Published in Journals: Agronomy, Applied Sciences, Climate, Forests, Remote Sensing, Sustainability and IJGI

Topic Reprint

Climate Change Impacts and Adaptation

Interdisciplinary Perspectives—Volume II

Edited by
Cheng Li, Fei Zhang, Mou Leong Tan and Kwok Pan Chun

mdpi.com/topics

MDPI

Climate Change Impacts and Adaptation: Interdisciplinary Perspectives—Volume II

Climate Change Impacts and Adaptation: Interdisciplinary Perspectives—Volume II

Topic Editors

Cheng Li
Fei Zhang
Mou Leong Tan
Kwok Pan Chun

MDPI

Basel • Beijing • Wuhan • Barcelona • Belgrade • Novi Sad • Cluj • Manchester

Topic Editors

Cheng Li
College of Plant Protection
Yangzhou University
Yangzhou
China

Fei Zhang
College of Geography and
Environmental Sciences
Zhejiang Normal University
Jinhua
China

Mou Leong Tan
School of Humanities
Universiti Sains Malaysia
Pulau Pinang
Malaysia

Kwok Pan Chun
CATE School of Architecture
and Environment
University of the West of
England
Bristol
UK

Editorial Office
MDPI AG
Grosspeteranlage 5
4052 Basel, Switzerland

This is a reprint of the Topic, published open access by the journals *Agronomy* (ISSN 2073-4395), *Applied Sciences* (ISSN 2076-3417), *Climate* (ISSN 2225-1154), *Forests* (ISSN 1999-4907), *Remote Sensing* (ISSN 2072-4292), *Sustainability* (ISSN 2071-1050) and *ISPRS International Journal of Geo-Information* (ISSN 2220-9964), freely accessible at: https://www.mdpi.com/topics/2578M074VX.

For citation purposes, cite each article independently as indicated on the article page online and as indicated below:

Lastname, A.A.; Lastname, B.B. Article Title. *Journal Name* **Year**, *Volume Number*, Page Range.

Volume II
ISBN 978-3-7258-5821-7 (Hbk)
ISBN 978-3-7258-5822-4 (PDF)
https://doi.org/10.3390/books978-3-7258-5822-4

Set
ISBN 978-3-7258-5817-0 (Hbk)
ISBN 978-3-7258-5818-7 (PDF)

© 2025 by the authors. Articles in this book are Open Access and distributed under the Creative Commons Attribution (CC BY) license. The book as a whole is distributed by MDPI under the terms and conditions of the Creative Commons Attribution-NonCommercial-NoDerivs (CC BY-NC-ND) license (https://creativecommons.org/licenses/by-nc-nd/4.0/).

Contents

About the Editors . . . . . **ix**

Preface . . . . . **xi**

Bernard Twaróg
Assessing Polarisation of Climate Phenomena Based on Long-Term Precipitation and Temperature Sequences
Reprinted from: *Sustainability* **2024**, *16*, 8311, https://doi.org/10.3390/su16198311 . . . . . **1**

Xinlong Li, Junli Tan, Xina Wang, Qian Shang, Hao Li and Xuefang Li
Analysis of Future Drought Risk and Wheat Meteorological Disaster in Ningxia (Northwest China) Based on CMIP6 and SPEI
Reprinted from: *Agronomy* **2024**, *14*, 3051, https://doi.org/10.3390/agronomy14123051 . . . . . **33**

Ju-Young Shin, Jiyeon Park, Kyungmin Sung and Yongseok Kim
Recent Spatiotemporal Changes of Subhourly Extreme Rainfall Events in Seoul
Reprinted from: *Appl. Sci.* **2025**, *15*, 1672, https://doi.org/10.3390/app15031672 . . . . . **59**

Jiayao Li, Shunwu Zhou, Dong Guo, Dingzhu Hu, Yao Yao and Minghui Wu
The Variation Characteristics of Stratospheric Circulation under the Interdecadal Variability of Antarctic Total Column Ozone in Early Austral Spring
Reprinted from: *Remote Sens.* **2024**, *16*, 619, https://doi.org/10.3390/rs16040619 . . . . . **75**

Simona Perčič, Katarina Bitenc, Majda Pohar, Anka Uršič, Tanja Cegnar and Ana Hojs
Assessing Heatwave-Related Deaths among Older Adults by Diagnosis and Urban/Rural Areas from 1999 to 2020 in Slovenia
Reprinted from: *Climate* **2024**, *12*, 148, https://doi.org/10.3390/cli12090148 . . . . . **93**

Cor A. Schipper, Titus W. Hielkema and Alexander Ziemba
Impact of Climate Change on Biodiversity and Implications for Nature-Based Solutions
Reprinted from: *Climate* **2024**, *12*, 179, https://doi.org/10.3390/cli12110179 . . . . . **110**

Xian Liu, Hengkai Li, Yanbing Zhou, Yang Yu and Xiuli Wang
The Impact of Seasonal Climate on Dryland Vegetation NPP: The Mediating Role of Phenology
Reprinted from: *Sustainability* **2024**, *16*, 9835, https://doi.org/10.3390/su16229835 . . . . . **135**

Carmela Sandoval-García, Jorge Méndez-González, Flores Andrés, Eulalia Edith Villavicencio-Gutiérrez, Fernando Paz-Pellat, Celestino Flores-López, et al.
Mapping the Future: Climate-Induced Changes in Aboveground Live-Biomass Carbon Density Across Mexico's Coniferous Forests
Reprinted from: *Forests* **2024**, *15*, 2032, https://doi.org/10.3390/f15112032 . . . . . **154**

Cheng Li, Hongda Yao, Zhaozhe Li, Fang Wu, Bo Liu, Yongping Wu, et al.
A Bibliometric Analysis of Global Research on Climate Change and Agriculture from 1985 to 2023
Reprinted from: *Agronomy* **2024**, *14*, 2729, https://doi.org/10.3390/agronomy14112729 . . . . . **175**

Xin Wang, Rui Xue, Ming Lu and Jiangyue Wu
Riders Under the Heat: Exploring the Impact of Extreme Heat on the Integration of Bike-Sharing and Public Transportation in Shenzhen, China
Reprinted from: *ISPRS Int. J. Geo-Inf.* **2024**, *13*, 438, https://doi.org/10.3390/ijgi13120438 . . . . **190**

Doo-Ho Choi, Cheol-Soon Ko, Youn-Lee Oh, Ji-Hoon Im, Minji Oh and Eun-Ji Lee
Investigation of Climatic Factors Affecting the Amount of Foraged Matsutake Mushrooms in Korea
Reprinted from: *Forests* **2024**, *15*, 2165, https://doi.org/10.3390/f15122165 . . . . . **213**

Kristine Vander Mijnsbrugge, Mattias Bollen, Stefaan Moreels, Eduardo Notivol Paino, Kris Vandekerkhove, Luc De Keersmaeker, et al.
Timing of Drought and Severity of Induced Leaf Desiccation Affect Recovery, Growth and Autumnal Leaf Senescence in *Fagus sylvatica* L. Saplings
Reprinted from: *Forests* **2025**, *16*, 5, https://doi.org/10.3390/f16010005 . . . . . **223**

Bashiri Iddy Muzzo, R. Douglas Ramsey and Juan J. Villalba
Changes in Climate and Their Implications for Cattle Nutrition and Management
Reprinted from: *Climate* **2025**, *13*, 1, https://doi.org/10.3390/cli13010001 . . . . . **241**

Zhenwei Yang, Xujing Yang, Yuheng Huang, Yalin Zhang, Yao Guo, Meichen Feng, et al.
Potential Impacts of Climate Change on the Spatial Distribution Pattern of Naked Oats in China
Reprinted from: *Agronomy* **2025**, *15*, 362, https://doi.org/10.3390/agronomy15020362 . . . . . **272**

Maryly Weyll Sant'Anna, Maurício Lamano Ferreira, Leonardo Ferreira da Silva and Pedro Luiz Côrtes
Climate Change and Arbovirus: A Review and Bibliometric Analysis
Reprinted from: *Climate* **2025**, *13*, 35, https://doi.org/10.3390/cli13020035 . . . . . **290**

Nabeeha Javed, Shahzada Sohail Ijaz, Qaiser Hussain, Muhammad Ansar, Abdulwahed Fahad Alrefaei, Bader O. Almutairi, et al.
Potential of Modified Reduced Tillage with Cover/Green Manure Crop for Climate Change Mitigation in a Smallholder Rainfed Farming System
Reprinted from: *Sustainability* **2024**, *16*, 4781, https://doi.org/10.3390/su16114781 . . . . . **311**

Everaldo B. de Souza, Brenda C. S. Silva, Emilene M. F. Serra, Melgris J. Becerra Ruiz, Alan C. Cunha, Paulo J. P. O. Souza, et al.
Small Municipalities in the Amazon under the Risk of Future Climate Change
Reprinted from: *Climate* **2024**, *12*, 95, https://doi.org/10.3390/cli12070095 . . . . . **327**

Muamer Abuzwidah, Ahmed Elawady, Ayat Gamal Ashour, Abdullah Gokhan Yilmaz, Abdallah Shanableh and Waleed Zeiada
Flood Risk Assessment for Sustainable Transportation Planning and Development under Climate Change: A GIS-Based Comparative Analysis of CMIP6 Scenarios
Reprinted from: *Sustainability* **2024**, *16*, 5939, https://doi.org/10.3390/su16145939 . . . . . **346**

Juanjuan Zhong, Ye Duan, Caizhi Sun and Hongye Wang
Analysis of the Impact of the Digital Economy on Carbon Emission Reduction and Its Spatial Spillover Effect—The Case of Eastern Coastal Cities in China
Reprinted from: *ISPRS Int. J. Geo-Inf.* **2024**, *13*, 293, https://doi.org/10.3390/ijgi13080293 . . . . **364**

Everjoy Magwegwe, Taruberekerwa Zivengwa and Mashford Zenda
Adaptation and Coping Strategies of Women to Reduce Food Insecurity in an Era of Climate Change: A Case of Chireya District, Zimbabwe
Reprinted from: *Climate* **2024**, *12*, 126, https://doi.org/10.3390/cli12080126 . . . . . **384**

Jorge Armando Hernández-López, Diana Ximena Puerta-Cortés and Hernán J. Andrade
Predictive Analysis of Adaptation to Drought of Farmers in the Central Zone of Colombia
Reprinted from: *Sustainability* **2024**, *16*, 7210, https://doi.org/10.3390/su16167210 . . . . . **402**

Shobha Poudel, Rabin Thapa and Bhogendra Mishra
A Farmer-Centric Cost–Benefit Analysis of Climate-Smart Agriculture in the Gandaki River Basin of Nepal
Reprinted from: *Climate* **2024**, *12*, 145, https://doi.org/10.3390/cli12090145 . . . . . **420**

Weiting Xiong, Yedong Zhang and Jingang Li
Examining the Causal and Heterogeneous Influence of Three-Dimensional Urban Forms on CO_2 Emissions in 285 Chinese Cities
Reprinted from: *ISPRS Int. J. Geo-Inf.* **2024**, *13*, 372, https://doi.org/10.3390/ijgi13110372 . . . . **442**

Ankita Pokhrel, Ping Fang and Gaurav Bastola
Integrating Remote Sensing and Community Perceptions for Sustainable Climate Adaptation Strategies in Mountain Ecosystems
Reprinted from: *Sustainability* **2025**, *17*, 18, https://doi.org/10.3390/su17010018 . . . . . **458**

Shufen Cao, Min Pang, Yongtan Ma, Qianyu Dong and Yongping Tao
Risk Spillover Effects in Energy Markets Under Climate Change: Evidence from the Chinese Market
Reprinted from: *Sustainability* **2025**, *17*, 2126, https://doi.org/10.3390/su17052126 . . . . . **491**

Juhyun Hong and Chang-Young Jeon
Linking Perceptions, Emotions, and Actions: How Psychological Distance, Media Framing, and Guilt About Climate Crisis Promote Communication and Pro-Environmental Behavior
Reprinted from: *Sustainability* **2025**, *17*, 2409, https://doi.org/10.3390/su17062409 . . . . . **511**

Carlos Bautista-Capetillo, Hugo Pineda-Martínez, Luis Alberto Flores-Chaires and Luis Felipe Pineda-Martínez
Agriculture Resilient at Three Irrigation Modules of Zacatecas, Mexico: Water Scarcity and Climate Variability
Reprinted from: *Agronomy* **2025**, *15*, 800, https://doi.org/10.3390/agronomy15040800 . . . . . **533**

Patricio Silva-Ávila, Jorge Rojas Hernández and Ricardo O. Barra
Knowledge Alliances for Global Change Adaptation: A Relational Approach Based on Traditional Ecological Knowledge, Territorial Management, and Community Practices in the Chilean Context
Reprinted from: *Sustainability* **2025**, *17*, 3653, https://doi.org/10.3390/su17083653 . . . . . **553**

Armando Prata and Marcela Matos
Compassion Towards Nature and Well-Being: The Role of Climate Change Anxiety and Pro-Environmental Behaviors
Reprinted from: *Sustainability* **2025**, *17*, 4349, https://doi.org/10.3390/su17104349 . . . . . **581**

Boqi Peng, Busheng Xie, Wei Wang and Lixin Wu
Enhancing Seasonal PM2.5 Estimations in China through Terrain–Wind–Rained Index (TWRI): A Geographically Weighted Regression Approach
Reprinted from: *Remote Sens.* **2024**, *16*, 2145, https://doi.org/10.3390/rs16122145 . . . . . **611**

Ahmad Abd Rabuh, Richard M. Teeuw, Doyle Ray Oakey, Athanasios V. Argyriou, Max Foxley-Marrable and Alan Wilkins
Sustainable Geoinformatic Approaches to Insurance for Small-Scale Farmers in Colombia
Reprinted from: *Sustainability* **2024**, *16*, 5104, https://doi.org/10.3390/su16125104 . . . . . **630**

James Arthur Dyer, Angela Pearson and Raymond Louis Desjardins
Interpolation of Nitrogen Fertilizer Use in Canada from Fertilizer Use Surveys
Reprinted from: *Agronomy* **2024**, *14*, 1700, https://doi.org/10.3390/agronomy14081700 . . . . . **652**

Yadong Liu, Hongmei Li, Lin Zhu, Bin Chen, Meirong Li, Huijuan He, et al.
Revealing Cropping Intensity Dynamics Using High-Resolution Imagery: A Case Study in Shaanxi Province, China
Reprinted from: *Remote Sens.* **2024**, *16*, 3832, https://doi.org/10.3390/rs16203832 . . . . . **670**

Subhasmita Das, Debabrata Nandi, Rakesh Ranjan Thakur, Dillip Kumar Bera, Duryadhan Behera, Bojan Đurin and Vlado Cetl
A Novel Approach for Ex Situ Water Quality Monitoring Using the Google Earth Engine and Spectral Indices in Chilika Lake, Odisha, India
Reprinted from: *ISPRS Int. J. Geo-Inf.* **2024**, *13*, 381, https://doi.org/10.3390/ijgi13110381 . . . . **688**

Rafael De Miguel González, Juan Mar-Beguería, María Sebastián López and Ondrej Kratochvíl
GIS-Based Dashboards as Advanced Geospatial Applications for Climate Change Education and Teaching the Future
Reprinted from: *ISPRS Int. J. Geo-Inf.* **2025**, *14*, 89, https://doi.org/10.3390/ijgi14020089 . . . . . **715**

Chakrit Chawalit, Wuttichai Boonpook, Asamaporn Sitthi, Kritanai Torsri, Daroonwan Kamthonkiat, Yumin Tan, et al.
Geoinformatics and Machine Learning for Shoreline Change Monitoring: A 35-Year Analysis of Coastal Erosion in the Upper Gulf of Thailand
Reprinted from: *ISPRS Int. J. Geo-Inf.* **2025**, *14*, 94, https://doi.org/10.3390/ijgi14020094 . . . . . **728**

About the Editors

Cheng Li

Cheng Li is an Associate Professor at the Department of Ecology, School of Plant Protection, Yangzhou University, China. He earned his Ph.D. in Applied Meteorology from the Nanjing University of Information Science and Technology. With a strong academic background, Dr. Li has authored approximately 60 peer-reviewed articles in high-impact journals and has presented his research at numerous prestigious conferences. He serves as a Topic Editor, Guest Editor, and Topical Advisory Panel Member for several international journals. Dr. Li has been honored with the Young Elite Scientists Sponsorship Program of Jiangsu Province and the National Scholarship for Doctoral Students in China.

Fei Zhang

Fei Zhang is a professor at the College of Geography and Environmental Sciences, Zhejiang Normal University. He is mainly engaged in remote sensing research on eco-environments in arid zones, with a focus on remote sensing research on the water environment, remote sensing image classification, urbanization dynamic detection, and image processing. To date, he has published more than 100 journal papers as the first author or corresponding author. He is a Guest Editor of journals such as *Water* and *Remote Sensing*, and he is also an Editorial Board Member of journals such as the *Journal of Lake Science*, *Spectroscopy and Spectral Analysis* and *the International Journal of Geomatics*.

Mou Leong Tan

Mou Leong Tan is an Associate Professor at the Geography Section, School of Humanities, Universiti Sains Malaysia. His research focuses on hydrology, climatology, remote sensing, and geographic information systems (GISs). Dr. Tan currently serves as the President of the Malaysian Geographical Association (GeogMalaysia), Vice President of Water Watch Penang (WWP), and is a professional member of the Institution of Geospatial and Remote Sensing Malaysia (IGRSM). He has led more than ten national and international research projects and has published over 150 research papers, with an H-index of 38 and over 5,000 citations. He has received several prestigious awards, including the "Malaysia Water Award for Young Water Leadership", the "Top Research Scientist Malaysia" award, and the "Malaysia Research Star Award". From 2021 to 2024, he was listed among the top 2% of the world's most highly cited scientists under environmental engineering by Stanford University.

Kwok Pan Chun

Kwok Pan Chun is a Senior Lecturer in Environmental Management and Geography at the School of Architecture and Environment, University of the West of England. His core research interests include nonstationary spatiotemporal processes, numerical modelling for hydroclimate, and land use management. Dr. Chun is currently leading a UK Research Council-funded project titled Land Use Change Investigation and Regional Climate (LIRIC), collaborating with researchers in South America and Asia to advance Sustainable Development Goal 13: Climate Action. He also leads an International Association of Hydrological Sciences (IAHS) working group that challenges existing power dynamics and colonial legacies, aligning with UN frameworks and contributing to the broader goals of IAHS cross-cutting initiatives.

Preface

The idea for *Climate Change Impacts and Adaptation: Interdisciplinary Perspectives* took shape in 2022, when record-breaking heatwaves, floods and droughts were simultaneously affecting every continent. As the young and responsible editors we had spent the preceding decade documenting regional climate signals and their cascading impacts, yet we were struck by how rarely disciplinary insights were assembled into a coherent, scale-relevant body of evidence that decision-makers could act upon. Against this backdrop, we issued an open call to the global research community in 2023, inviting submissions of original work that crossed traditional boundaries between climatology, ecosystem science, geospatial analysis and social practice. Ultimately, we presents a curated selection of 69 research articles and reviews that collectively address the pressing challenges posed by climate change across a variety of sectors and regions.

We organised the contributions into four overlapping streams. Part I includes observed regional climate changes, demonstrating how advanced detection techniques can now resolve sub-national signals. Part II quantifies biophysical and socio-economic impacts of climate change on water, food, health and infrastructure systems, emphasising compound and cascading risks. Part III evaluates adaptation measures ranging from drought-tolerant cultivars and urban green infrastructure to community-based early-warning systems, offering empirical evidence on costs, co-benefits and limits to implementation. Part IV explores the application of new technologies and methodologies, including remote sensing, machine learning, statistical modeling, and participatory approaches.

Our purpose is twofold: to provide researchers with a consolidated reference of cutting-edge, interdisciplinary methods that reduce uncertainty in impact assessment; and to offer practitioners a portfolio of rigorously tested adaptation options that can be transferred across similar socio-ecological contexts. We address the volume to graduate students beginning their careers at the climate–society interface, to scientists engaged in regional down-scaling or risk-modelling exercises, and to planners tasked with translating global targets into local investments. By integrating remote-sensing products, citizen-science data, machine-learning algorithms and participatory narratives, we hope that the findings and methodologies presented here exemplify the epistemic diversity that effective climate response now demands.

We thank the reviewers for their meticulous critiques, and the editorial office for sustaining an efficient publication process. Finally, we dedicate this volume to the communities whose lived experience of climate extremes motivates the search for robust, just and timely adaptation solutions.

Cheng Li, Fei Zhang, Mou Leong Tan, and Kwok Pan Chun
Topic Editors

sustainability

MDPI

Article

Assessing Polarisation of Climate Phenomena Based on Long-Term Precipitation and Temperature Sequences

Bernard Twaróg

Department of Geoengineering and Water Management, Faculty of Environmental and Energy Engineering, Cracow University of Technology, 31-155 Cracow, Poland; btwarog@pk.edu.pl; Tel.: +48-602129566

Abstract: This article presents an analysis of monthly precipitation totals based on data from the Global Precipitation Climatology Centre and monthly mean temperatures from the National Oceanic and Atmospheric Administration for 377 catchments located worldwide. The data sequences, spanning 110 years from 1901 to 2010, are analysed. These long-term precipitation and temperature sequences are used to assess the variability in climate characteristics, referred to here as polarisation. This article discusses the measures of polarisation used in the natural sciences. This study adopts two measures to evaluate the phenomenon of polarisation. The first measure is defined based on a stationary time series, calculated as the ratio of the amplitude of values to the standard deviation. The second measure is proposed as the difference in trends of these values. Based on the analysis of monthly precipitation data in the studied catchments, polarisation components are confirmed in 25% of the cases, while in the remaining 75%, they are not. For temperature data, polarisation is confirmed in 12.2% of the cases and not in the remaining 88.8%. The trend analysis employs Mann–Kendall tests at a 5% significance level. The Pettitt test is used to determine the point of trend change for precipitation and temperature data. This article underscores the complex relationship between climate polarisation and sustainable development, reaffirming that sustainable development cannot be pursued in isolation from the challenges posed by climate change. It emphasises the importance of integrating environmental, social, and economic strategies to adapt to extreme climatic events and mitigate their effects. This research is supported by detailed graphical analyses, with the results presented in tabular form.

Keywords: polarisation of climatic phenomena; GPCC data; NOAA data; monthly precipitation; average temperature; climate trends; Mann–Kendall test; Pettitt test; sustainability

1. Introduction

Analyses of historical observations of climate variables clearly indicate the anthropogenic causes of climate change [1–3]. Numerous studies at various spatial and temporal scales have thoroughly explored the impact of projected changes in the climate system on hydrology and water resources [3–6]. After air temperature, fresh water is proving to be the second most reactive environmental variable to climate change [7–10]. Despite the numerous existing studies and analyses of the temporal and spatial characteristics of precipitation and temperature, the timeliness of these studies is becoming increasingly appreciated [11–18], especially in the context of documenting the impact of human activities on regional climate factors [19–21]. Increasing computational capabilities and comprehensive analyses based on long measurement series [8,22,23] are attracting attention, especially in the context of the search for the justification of theses on the polarisation of extreme climatic events [24–30].

The increased interest in climatic factors such as precipitation and temperature [13,31,32] is also due to the consequences of floods and periods of hydrological drought [33]. Studies on the variability in precipitation and temperature over different periods [5,9,14,34–36] have made it possible to analyse statistical trends and assess the signal of these changes [32,37–39]. The

results of these analyses provide information about the moments of trend change and the form of them. In the context of the importance of the variability in climatic factors, it is important to apply statistical techniques [4,40] that allow for the detection of changes and trends [2,38], in, among other sources, data relating to monthly precipitation totals and monthly average temperatures.

Climate change predicted by the IPCC (Intergovernmental Panel on Climate Change) occurs as a result of increases in greenhouse gas emissions, which are mainly caused by the industrialisation of the world, the burning of fossil fuels and changes in land use [3,10,41,42]. According to the Intergovernmental Panel on Climate Change [43], both natural forces and human activities contribute to changes in climate patterns, including increases in land and ocean surface temperatures, changes in spatial and temporal precipitation patterns, increases in the frequency of extreme events, rising sea levels, and increased El Niño [3,4,31,34]. It is clearly emphasised that human influence significantly outweighs the action of natural forces. The warming of the Earth is evident in data that show a 0.85 °C increase in global temperature from 1901 to 2012 [44]. To see changes in precipitation and temperature trends, anomalous values and statistical models are used to measure the timing of the trend change and its magnitude. The change in trends of various climate variables can be quantified using global atmospheric circulation models (GCMs) or, for example, using statistical models that identify the moment of change in the trend and its magnitude [8].

The polarisation of climatic elements is a phenomenon in which certain climatic elements or features tend to separate into two extreme or opposite categories [45,46]. This means that over time, certain climatic features become more clearly concentrated in the two opposite extremes, which can lead to increased variability and diversity in atmospheric conditions. Polarisation can manifest itself as a clear separation between extremes of temperature, precipitation, or other climatic parameters, with implications for long-term patterns and trends in the climate of an area. The property of bimodality emphasises the concentration of features in two opposite extremes [8,47–49]. The polarisation of precipitation events can be defined as a process in which the frequency and intensity of extreme precipitation events, such as rainstorms, hail, storms, or floods, increases. Simultaneously, the normal precipitation condition is becoming less frequent. In the case of temperature phenomena, polarisation can be defined as a process in which the frequency and intensity of extreme temperatures, such as heat waves or extreme cold, increases. Again, the normal state of temperatures is becoming increasingly rare. Both of these phenomena are part of a broader process of climate change that affects atmospheric circulation and processes, leading to increased weather variability and a greater risk of extreme weather. Polarisation can be interpreted as a change in the nature of the occurrence of extreme events, where extreme events, specifically extreme temperatures and precipitation, are becoming more frequent, while normal conditions are becoming less frequent.

It is important to note the strong connection between the variability in climatic phenomena, described here as polarisation, and sustainable development [50,51]. Changes in the frequency and intensity of extreme weather events, such as droughts, floods, or heatwaves, have a direct impact on the ability of societies and economies [52–54] to achieve sustainable development goals [55,56]. These phenomena not only test the resilience of infrastructure and socioeconomic systems but can also exacerbate existing inequalities, destabilise local and global markets, and accelerate environmental degradation [57,58].

In this study, the phenomenon of polarisation is analysed using selected river basins, identified as areas particularly vulnerable to extreme climatic events, both in terms of temperature and precipitation. Numerous studies indicate a significant impact of climate variability on river flow values, which are sensitive to changes in both precipitation and temperature. Researchers [35] have demonstrated the polarisation of climatic phenomena, identifying increasing trends primarily in the magnitude of floods in German river basins, attributing these changes to climate change. Additionally, seasonal analyses revealed that these changes were more pronounced in winter than in summer. Abrupt changes

in both mean values and variance can be attributed to climatic factors (e.g., changes in climate regimes) as well as anthropogenic effects (e.g., construction of dams, changes in land use, vegetation cover, and shifts in measurement locations) [59,60]. The interpretation of statistical analyses must be conducted in the context of observed physical [3,7,61], social, and economic phenomena [3,14,19,62]. Therefore, predicting temporal trends in precipitation and temperature is crucial in social and urban planning [63].

The world's rivers play a key role in linking the atmosphere, hydrosphere, and biosphere by transporting 40% of precipitation runoff and 95% of sediment to the oceans [64,65]. The shaping of river flow depends on many factors, such as precipitation, temperature, evaporation, soil conditions, landforms, and land use changes [66]. With the available long-term precipitation and temperature data, it is important to conduct long-term analyses of this data in order to understand the polarisation of climate phenomena and its potential consequences [67]. In addition, such analyses provide valuable information that can be used to develop decision-making tools for the purposes of effectively managing extreme events, such as droughts and floods, and to mitigate ecological damage in regions particularly vulnerable to these hazards [67].

When assessing climate polarisation, a process in which certain climatic features become concentrated in two opposing categories, there are strong links between precipitation and temperature [34,67,68]. An increase in global temperatures can lead to an increase in the amount of water vapour in the atmosphere. More water vapour in the atmosphere increases the potential for cloud formation and precipitation, especially in areas with higher temperatures where there is access to more thermal energy As a result, more water vapour may in turn increase precipitation, meaning that areas with higher temperatures may experience more precipitation. Conversely, lower temperatures can result in reduced precipitation. In extreme cases, such as prolonged droughts or floods, fluctuations in temperature and precipitation can have catastrophic consequences, including the failure of crops and damage to property [60,69].

Long-term data series make it possible to identify temperature and precipitation trends and help to determine whether a region is experiencing changes in polarity. Furthermore, the analysis of precipitation–temperature interactions provides a better link between important atmospheric phenomena, such as El Niño and La Niña cycles [70,71], which affect global climate patterns. An example of this is the fact that rising temperatures can affect the occurrence of intense precipitation, while reduced precipitation can contribute to extreme heat waves [60]. It is important to consider the amount of precipitation and temperature along with other climate phenomena as their interaction can affect the overall effect of climate polarisation [72]. The magnitudes and relationships between precipitation and temperature are crucial for assessing the polarisation of climate phenomena and its consequences for the environment, economy, and society. This knowledge is essential for implementing preventive measures to mitigate the negative effects of climate change.

The main focus of this study is the analysis of long-term precipitation and temperature data sequences with the aim of introducing the concept of climate extremes polarisation, using river basins as a case study. Section 1 provides a literature review and presents the background on extreme climate variability, which serves as the foundation for analysing polarisation phenomena. Section 2 explores the interactions between polarisation and sustainable development. Section 3 outlines the temporal and spatial scope of the data utilised in the analysis. Section 4 examines the phenomenon of polarisation in extreme climatic events, specifically in terms of precipitation and temperature, and discusses its significant consequences for ecosystems, economies, and infrastructure. Section 5 details the methodologies employed in constructing the polarisation measure and proposes the introduction of a static measure based on stationary time series as well as a dynamic measure based on trends. Sections 6 and 7 present established statistical techniques for trend analysis and trend change point detection. Section 8 discusses and assesses the results of the analyses. Finally, Section 9 presents the conclusions.

2. Interactions between Polarisation and Sustainable Development

The polarisation of climatic phenomena, such as extreme precipitation and temperatures, presents additional challenges to the implementation of sustainable development [53,73], which strives for the harmonious coexistence of the economy, society, and the environment. Sustainable development is particularly vulnerable to disruptions resulting from global climate change, which can lead to the degradation of natural resources crucial for maintaining ecological balance. Such changes can also destabilise economies and cause social issues, such as migration driven by environmental changes [69].

In the context of natural resource conservation, the intensification of phenomena like droughts or floods can lead to the degradation of ecosystems and the depletion of water resources, threatening the ability of future generations to meet their needs. Variable climatic conditions also increase risks for agriculture, especially in urban areas where urban farming plays an increasingly important role in sustainable resource management [36,74]. Uneven distribution of rainfall and fluctuating temperatures can reduce agricultural productivity, impacting food security and economic stability in cities [75].

From the perspective of social justice, climate change can exacerbate existing inequalities, particularly among the poorest communities, which have limited capacity for adaptation [76]. Therefore, sustainable development must incorporate adaptive strategies that ensure equity and justice in resource access and protect the most vulnerable social groups. The long-term perspective of sustainable development requires integrating economic activities with ecological principles, taking into account dynamic climate changes [55]. Industry, transportation, and energy sectors must adapt their strategies, introducing innovations that minimise greenhouse gas emissions and support the development of a circular economy [52,54]. It is also necessary to strengthen policies and strategies at the global level that support sustainable development in the face of global climate challenges. Although the polarisation of climatic phenomena brings many challenges, it can also contribute to positive effects in the context of sustainable development [73].

Potential negative impacts:

- Degradation of natural resources: extreme phenomena such as droughts and floods can accelerate the degradation of natural resources, threatening ecological balance and future generations [77];
- Social inequality: the poorest communities, with limited capacity to adapt to climate change, are the most vulnerable to its negative effects, potentially deepening social inequalities [78];
- Impact on agriculture: variable and extreme climatic conditions can reduce agricultural productivity, affecting food security and economic stability, especially in urban areas [79,80];
- Challenges to infrastructure and industry: extreme weather events can disrupt the functioning of infrastructure and industry, leading to economic destabilisation [50];
- Risk to economic stability: economic losses caused by extreme events can lead to economic recessions, hindering the implementation of sustainable development strategies [50,79];
- Increased pressure on resources: growing pressure on limited natural resources can lead to conflicts over their availability, destabilising communities and economies [36,76].

Potential positive impacts:

- Acceleration of innovation and adaptation: extreme climatic conditions can stimulate the development of innovative technologies and adaptive strategies that minimise the negative impacts of climate change [51,60,81];
- Increased environmental awareness: climate polarisation can lead to greater social awareness of climate change, fostering more sustainable actions [82];
- Support for pro-environmental policies: support for sustainable development policies, such as reducing greenhouse gas emissions, protecting natural resources, and promoting the circular economy, is increasing [55,83];

- Increased efficiency and resilience of systems: communities and industries may strive for greater efficiency in resource use, reducing waste and supporting sustainable management [55];
- Growth of local and resilient Systems: local initiatives, such as urban agriculture, are gaining importance, increasing self-sufficiency and supporting sustainable development [53,84];
- Promotion of sustainable energy: climate change may accelerate the transition to renewable energy sources, which are more resilient to climate disruptions [51,54];
- Strengthening global cooperation: shared climate challenges may lead to closer international cooperation in support of sustainable development [85].

Sustainable development can play a key role in mitigating the effects of climate polarisation. However, it may also face challenges related to costs, delays in responses, and potential conflicts of interest. To effectively minimise negative impacts, an integrated approach is essential, combining sustainable development goals with adaptation to dynamically changing climatic conditions.

3. Preparation of Data for Analysis

This paper examines global trends in monthly precipitation totals and monthly mean temperatures from the area of 377 river basins distributed over all continents. Assuming 509.9×10^6 square kilometres of land area on the earth, the analysis covers 12.76% of the total land area of the globe [86]. Table 1 shows the areas covered by the analysis. The regions in the text are identified by code $WMO_REG = n$, where $n = 1, ..., 6$ (Table 1, Figure 1).

Table 1. Areas covered by the analysis [86].

Region WMO	Continent	Land Area	Area Catchment	Coverage of the Continents
WMO_REG		10^6 km^2	10^6 km^2	%
1	Africa	30.3	8.43	27.83%
2	Asia	44.3	20.3	45.86%
3	South America	17.8	12.6	70.57%
4	North America	24.2	13.0	53.87%
5	Australia and Oceania	8.5	1.1	13.07%
6	Europe	10.5	6.7	64.10%
	Antarctica	13.1	0.0	0.00%
	Total land area	148.7	65.1	43.77%
	Earth, total	509.9	65.1	12.76%

Rainfall data from the GPCC and temperature data from NOAA for each month from 1901 to 2010, calculated based on grid data with a spatial resolution of $0.5^\circ \times 0.5^\circ$ in latitude and longitude, were converted to catchment areas. This process generated a sequence of monthly data, which were then analysed in this study. Spatial data preparation involved the use of GIS interpolation techniques. The monthly precipitation/average temperature was calculated as a weighted average of the corresponding characteristic (precipitation/temperature) assigned to the grid cells covering the catchment area, with the weight proportional to the area of the grid cell [86]. The interpolation program was written in MATLAB (version R2021a) (The MathWorks, Inc.: Natick, MA, USA) by the author.

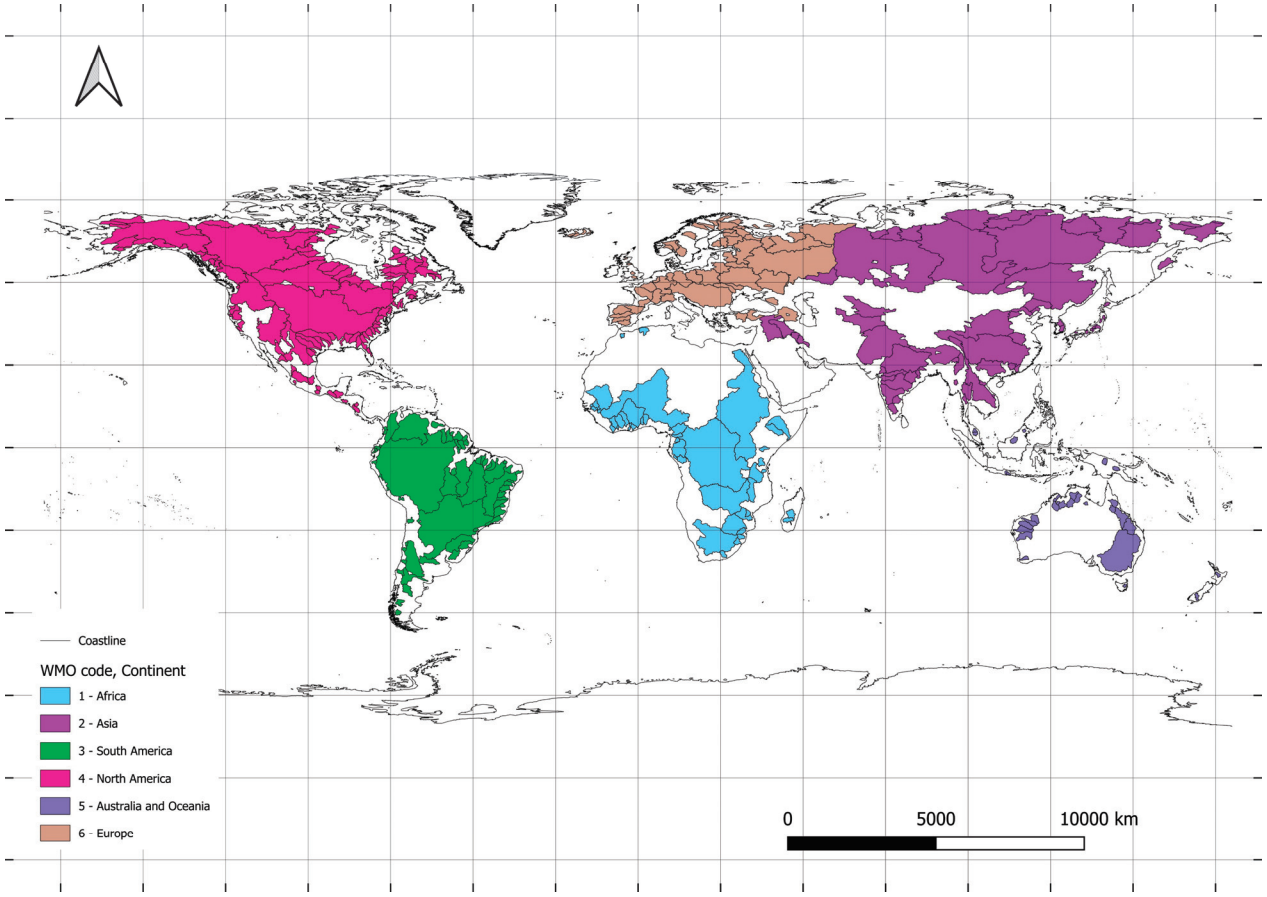

Figure 1. Analysed catchments—WMO code and continent are marked.

The area of one of the smallest catchments in this study, Skjern A (Europe, Denmark) is, according to calculations, 1090 km^2. An area of 0.5° × 0.5° at the latitude of Denmark covers an area of 3100 km^2. The location of this catchment area, for calculations of precipitation or temperature, requires the consideration of five neighbouring areas of 0.5° × 0.5°. With even such a small catchment area, precipitation and temperature characteristics are averaged. The calculated values of the sequences were subjected to a simple statistical analysis, determining the basic statistics: the minimum and maximum value, the mean, and the standard deviation of the sample. The data were analysed in monthly as well as calendar year cross-sections. Analyses of temperature data covered the years 1901 to 2010.

4. The Polarisation of Precipitation and Temperature Phenomena

The assessment of temporal variability and extreme events in air temperature and precipitation typically involves analysing a set of indicators that define these conditions. The concept of an extreme event assumes the existence of a normal state [39]. In this context, polarisation can be understood as a shift in the occurrence of extremes, with extreme temperatures and precipitation becoming more frequent, while the normal state becomes less common [87]. This polarisation can result from various factors, including human activity and climate change, which influence precipitation cycles, the intensity of extreme events, and temperature patterns. Consequently, polarisation represents the evolution of climatic features, leading to an increase in the frequency of extreme events and a destabilisation of the typical climate state. This shift can have significant consequences for ecosystems, the economy, and human quality of life.

The analysis of precipitation and temperature polarisation is crucial due to their central role in global energy and water cycles, as well as their impact on climate change. These variables are particularly important for managing freshwater resources and mitigating

the risks of floods and droughts. Increasing evidence suggests that human activities are accelerating climate change, leading to shorter periods of intense precipitation and longer dry spells marked by high temperatures and low precipitation [87]. The growing evidence of polarisation in extreme events, such as floods and droughts, underscores the uneven and intense impact of human activity on the climate.

This article examines long-term sequences of precipitation and temperature to evaluate the polarisation of climate phenomena. In climate science, "polarisation" describes the process by which certain areas of the planet experience more extreme temperature and/or precipitation conditions. This can lead to significant local environmental changes, including shifts in the distribution of plant and animal species, alterations in weather patterns, and changes in sea levels [88]. Long-term sequences of precipitation and temperature are critical for studying climate polarisation, providing detailed records that help identify trends and patterns. By analysing these sequences, researchers can pinpoint areas where the climate is becoming increasingly polarised and monitor changes over time. The use of these sequences offers a high degree of accuracy and precision, thanks to advanced measurement techniques and rigorous quality control measures [27,89,90].

The impact of polarisation extends across various aspects of life on Earth, affecting ecosystems, the economy, and infrastructure, as well as altering the size and location of water resources. In ecosystems, extreme temperature and precipitation changes influence biodiversity and ecosystem functioning, potentially leading to shifts in the distribution of plant and animal species, with negative consequences for entire ecosystems [88]. In agriculture, polarisation can reduce available water resources, impacting crop yields and food production [17,36,91,92]. For infrastructure, polarisation can lead to damage or destruction of roads, bridges, buildings, and water management systems. Given the complex and dynamic nature of the climate, polarisation is variable and difficult to predict, making it challenging to foresee its specific consequences in any given region [93,94].

The interaction between polarisation and other climate phenomena can trigger events such as hurricanes, tornadoes, or droughts, where one phenomenon may amplify or weaken another, complicating the understanding of climate change. Anthropogenic factors, particularly greenhouse gas emissions, play a significant role in driving the polarisation of climate factors [17,67,92].

The summary of causes and effects of polarisation presented below shows the complex nature of this phenomenon, where the clear separation of the two extreme categories leads to a variety of consequences, producing effects that dominate on many levels.

Causes of polarisation of precipitation phenomena:

- Changes in atmospheric circulation: fluctuations in atmospheric circulation, such as changes in belt and monsoon patterns, can concentrate precipitation in certain regions, while other areas experience precipitation deficits [95];
- El Niño and La Niña phenomena: these can lead to abrupt changes in ocean surface temperature, which affects rainfall patterns; areas that are normally wet can experience drought during El Niño, and dry areas can become flooded during La Niña [46];
- Topographical changes: high mountain ranges can affect the movement of air masses and cloud formation, leading to more rainfall on one side of the mountain and droughts on the other [46];
- Urbanisation and land use changes: urban growth and land use changes can alter the microclimate and affect the distribution of precipitation in an area [46].

Causes of polarised temperature phenomena:

- Melting of glaciers and reduction in ice cover: these can affect surface albedo, which can lead to faster warming in polar areas and cooling in oceanic areas [49,96];
- Changes in atmospheric circulation: may bring higher temperatures to tropical areas, while areas under the influence of lows may experience cooling [95];
- Changes in greenhouse gases: increases in greenhouse gas concentrations can lead to an overall warming of the climate, but some areas may experience faster temperature increases than others [72];

- Impact of urban areas: cities create so-called "heat islands" where concrete and asphalt absorb and retain heat, which can lead to significant heating of urban areas [97].

Effects of polarised precipitation events:

- Increased weather variability: polarisation of precipitation can lead to abrupt and unpredictable changes in weather patterns, which can make planning for agricultural and infrastructure activities difficult [36];
- Risk of natural disasters: extremes of rainfall can increase the risk of natural disasters, such as floods in areas of increased rainfall or droughts in areas of decreased rainfall [60];
- Impact on water availability: precipitation polarisation can lead to reduced water availability in drought-affected areas and increased risk of soil erosion during periods of intense rainfall [98];
- Impact on ecosystems: extreme precipitation conditions can affect ecosystem structures and services, with potential implications for biodiversity and ecosystem products [84].

Effects of polarised temperature phenomena:

- Human health risks: temperature extremes, both heat and cold, can pose a risk to human health, leading to heat- or cold-related diseases [60];
- Effects on agriculture and food production: extreme temperatures can affect plant growth processes, leading to reduced yields and loss of quality in agricultural products [80];
- Changes in species distribution: extreme temperatures can affect the distribution areas of different animal and plant species, which can disrupt the balance of ecosystems [99];
- Changes in water levels: glacial melting and ocean warming associated with temperature polarisation can lead to rising sea and ocean levels [100].

Interaction effects of precipitation and temperature polarisation:

- Increased risk of natural disasters: the combination of extreme rainfall and temperatures can amplify the risk of floods, landslides, and other natural disasters [76];
- Impact on agri-food production: extreme precipitation and temperatures can negatively affect food production, which can lead to food security problems [60];
- Changes in the landscape: the interaction of extreme rainfall and temperatures can lead to changes in the landscape, such as soil erosion and degradation of natural areas [60].

5. The Concept of Polarisation Measure

The concept of measuring climate polarisation is based on measuring the degree of diversity and variability in climate elements in a given area. This measure is used to determine the level of polarisation of climate elements in the region of interest. Polarisation refers to the extremes of parameters such as temperature, precipitation, humidity, etc., occurring in a specific area. A high level of polarisation indicates significant differences between maximum and minimum values, which can lead to an increased risk of extreme weather events. The measure of polarisation can be determined from various climatic parameters, such as temperature, precipitation, humidity, and atmospheric pressure. This can be calculated on different spatial and temporal scales, for example, for the entire country over the course of a year, for a specific region over the course of a month, or for individual weather stations over the course of a day. Depending on the purpose of the study and the availability of data, the measure of polarisation can be determined for different combinations of parameters. It is worth noting that a high level of polarisation does not necessarily mean unfavourable climatic conditions. For example, some regions have significant temperature differences between summer and winter, which can have a positive impact on seasonal tourism. However, in other cases, high polarisation can lead to serious problems, such as droughts, floods, or storms. Therefore, a measure of polarisation can be useful in identifying areas that require special attention when planning climate change adaptation activities.

Different approaches are possible for constructing measures of polarisation in climate phenomena, depending on the type and scale of the data under analysis. One of the basic methods is to use probabilistic techniques based on classical theories of one- or multi-dimensional random variables with distributions built using Copula functions [63,101,102]. Other, simpler methods are based on statistical characteristics [4,10,40,47]. A simple concept is to construct indicators measuring the degree of extremity that a phenomenon can take, for example, by measuring the dispersion relative to the long-term average. An example of such an indicator is the coefficient of variation. Another way to create a polarisation indicator is to define it as the degree of extremity compared to the mean value relative to the variability measured by the dispersion measure [12,103,104]. Such indicators can be based on classical measures, such as variance, standard deviation, mean deviation, and the coefficient of variation, or on positional measures, such as range, quartile deviation, and the coefficient of variation [47].

Further methods of building indicators are based on the idea of unevenness [85,105], which can also be a measure of polarisation. One such indicator is kurtosis [106], which is influenced by the intensity of extreme values, so it measures what is happening in the "tails" of the distribution. Other types of indicators are measures that have their genesis in economics and econometrics. One such example is the Gini index, also called the Gini coefficient [78,104,107–109], built using the Lorentz curve, which describes the degree of concentration of a one-dimensional distribution of a random variable with non-negative values [108]. The Gini index ranges from a minimum value of zero, when all values are equal, to a theoretical maximum of one in an infinite population in which every element except one has a magnitude of zero. In the context of climate change, the Gini index can be used to measure inequality in exposure to the effects of climate change, such as droughts, floods, or sea level rises [72]. Higher values of the Gini index indicate greater inequality in the occurrence of these phenomena. Several other examples of measures can be cited, including the following:

- The concentration ratio [110] determines the degree of concentration of values at one end of the distribution and is similar to the Gini coefficient. However, it should be noted that the Gini coefficient may be less useful in analysing asymmetric distributions, which means that other indicators such as the concentration ratio or Lorenz curve should be considered in such cases.
- The GMD (Gini mean difference) index [111] is an inequality measure used in statistical and econometric analysis to measure polarisation or inequality in a sample distribution. Unlike the Gini coefficient, which measures unevenness, the GMD index enables the analysis of unevenness in the distribution of any variable, such as income, age, weight, height, precipitation, or temperature. The GMD index ranges from zero to one, where zero indicates complete evenness in the distribution and one indicates the concentration of all values in one class. The higher the GMD index value, the greater the unevenness in the variable distribution.
- The Theil index [78,112] is a measure of inequality in the distribution of quantitative variables, based on the idea of information entropy, taking into account differences between groups of values in the distribution, similar to the Gini coefficient, but with a greater emphasis on extreme values.
- The Lorenz indicator [105,108] is an inequality indicator in a distribution, which is based on the Lorenz curve. It is often used to measure income inequality but can also be used to measure inequality in other quantitative variables, including climate change studies. Higher values of the Lorenz curve indicate greater inequality in the occurrence of climate change effects such as droughts, floods, or sea level rises, meaning that some regions or social groups are more vulnerable to the effects of climate change than others.
- The Atkinson index [104] is a measure of inequality in the distribution of quantitative variables, which is based on the idea of absolute deviations. It takes into account the differences between groups of values in the distribution; it is similar to the Gini index, but focuses more on average values than extreme values.

- Range relates to values calculated as max–min usually referring to the difference between the maximum and minimum values of a given variable in a specific period of time. In the case of assessing the polarisation of precipitation and temperature, max–min can be used as a measure of the amplitude of these variables in a given period.

In this study, two measures are adopted to evaluate the phenomenon of polarisation, the first P_1 is built based on a stationary time series, the second P_2 is based on calculated trends. The first measure is defined as follows:

$$P_1 = \frac{S_{max} - S_{min}}{\sigma}, \tag{1}$$

where for precipitation:

S_{max}, [mm]—the maximum value of monthly precipitation totals over the 110-year period;

S_{min}, [mm]—the minimum value of monthly precipitation totals over the 110-year period;

σ, [mm]—the standard deviation of monthly precipitation over the 110-year period;

for temperature:

S_{max}, [°C]—the maximum value of monthly average temperature over the 110-year period;

S_{min}, [°C]—the minimum value of monthly average temperature over the 110-year period;

σ, [°C]—the standard deviation of monthly average temperature over the 110-year period;

P_1, []—a measure for assessing the phenomenon of polarisation, based on a stationary time series.

The second measure is defined as follows:

$$P_2 = trend(S_{max} - S_{min}) - trend(\sigma), \tag{2}$$

where for precipitation:

$trend(S_{max} - S_{min})$, [mm/year]—this is the trend of the amplitude of changes over a 110-year period, calculated based on annual extreme values;

$trend(\sigma)$, [mm/year]—this is the trend of the standard deviation over a 110-year period, calculated based on annual extreme values;

for temperature:

$trend(S_{max} - S_{min})$, [°C/year]—this is the trend of the amplitude of changes over a 110-year period, calculated based on annual extreme values;

$trend(\sigma)$, [°C/year]—this is the trend of the annual standard deviation over a 110-year period.

The above measure can be interpreted as the ratio of the trend in variability in the amplitude to the trend in variability in the standard deviation. The trend in variability in the amplitude refers to the direction and speed of changes in the maximum and minimum values of a given variable over time, while the trend in variability in the standard deviation refers to the direction and speed of changes in the variability in the values of a given variable around their mean over time.

The amplitude of change values can be useful in identifying extreme climate conditions, such as periods of drought or heat waves, as well as periods of intense precipitation or extremely low temperatures. However, max–min as a single measure may be limited in its usefulness because it does not take into account other factors such as the length and intensity of the period, as well as other variables that affect weather conditions. Due to the fact that it ignores all data except for two extreme values, it does not provide information about the diversity of individual feature values in the population. Therefore, along with max–min values, other measures such as mean values, standard deviations, or cumulative indices are typically used to obtain a more comprehensive and diverse view of climate

variability. For example, max–min values can be calculated for individual months, seasons or years, and then compared with mean values, standard deviations, or other measures to better describe climate variability over time and space.

The adopted measure, which is the ratio of the max–min values to the standard deviation σ, can be used as a measure to evaluate the polarisation of precipitation and temperature. The $max - min$ values refer to the amplitude of changes in a given variable over a period of time, while the standard deviation σ refers to the degree of variability in these values around their mean. By applying this measure, we can see how large the amplitude of changes is in relation to the variability around the mean. Values of this measure greater than 1 suggest that the amplitude of changes is greater than the variability around the mean. If the variability is relatively low compared to the amplitude, it may indicate the occurrence of periods of extreme climatic conditions, such as periods of drought or heatwaves, as well as periods of intense rainfall or extremely low temperature. However, the use of a single measure may be limited because it does not take into account other factors affecting climate variability. Therefore, it is worth using it together with other measures that show the character of climate variability. Note that the values of this measure for precipitation and temperature will always take a non-negative value.

The second form of adopted measures could be dynamic indicators showing the variability in the indicator over a longer period of time. The simplest indicators are based on the idea of a trend coefficient. Trend is a long-term feature referring to the general direction of changes over time in the value of a variable. Trend can indicate an increase, decrease, or stabilisation of the variable over time. In time series analysis, the trend coefficient is one of the basic elements that help to forecast future values of the variable. The trend can be analysed for different time scales, from short-term cycles to long-term trends [2]. Trend analysis is applied in many fields, such as economics, finance, meteorology, earth sciences, medicine, sociology, and marketing. In scientific research, trend analysis is often used to study changes in long-term time series, such as climate change, demographic changes, or evolution of species.

The values of this measure according to the direction of change and the relationship of the components of the measure are interpreted in Table 2. The compatible signs of the components $trend(max - min)$ and $trend(\sigma)$ were assumed. This assumption is based on the experience obtained in this analysis. In the calculations carried out for all catchments in both precipitation and temperature data at a significance level of 5%, if $trend(max - min)$ exists, then $trend(\sigma)$ also exists and vice versa. Both components are highly correlated and have the same signs.

Table 2. Trends in the components of measure P_2 and their relationships and relevance to climate change.

Both Values	Impact on Climate Changes
$(+)$	Relation: $[trend(max - min) > trend(\sigma)]$ Result: $[trend(max - min) - trend(\sigma)] \rightarrow$ POSITIVE
Increasing range of temperature change: A Trend(Range) value greater than Trend(STD) for temperature suggests that the range of temperature change in an area is increasing over the period under study. This means that the maximum and minimum temperatures in the area vary more than they did previously, which may mean that the temperature varies more over the year or over the years. Increasing range of precipitation changes: Similarly, if the Trend(Range) for precipitation is greater than the Trend(STD) for rainfall, this suggests that the range of precipitation change in the area is also increasing. This may indicate more extreme rainfall conditions or drier periods in the study area. No change in the stability of temperature and precipitation: The Trend(STD) value measures the stability of temperature and precipitation, and the fact that it is positive for both indicators means that variability in these factors in the area is present, but the increase is not as significant as the extent of change. This could mean that there is no clear change in the seasonal or annual patterns of variability in temperature and precipitation, but the extremes are changing. Possible climate change: An increasing range of changes in temperature and precipitation may be a signal of possible climate change in an area. These may be the results of changes in the atmosphere, such as changes in atmospheric circulation or other climatic factors that affect the local climate.	

Table 2. *Cont.*

Both Values	Impact on Climate Changes
$(-)$	Relation: $[trend(max - min) > trend(\sigma)]$ Result: $[trend(max - min) - trend(\sigma)] \rightarrow$ POSITIVE
Declining range of change in temperature and precipitation: The Trend(Range) value for temperature and Trend(Range) value for precipitation suggest that the range of change in temperature and precipitation in an area is decreasing over the study period. This means that the difference between maximum and minimum temperature and the range of change in precipitation is decreasing. There are no clear trends in the stability of temperature and precipitation: The Trend(STD) value measures the stability of temperature and precipitation, and the fact that it is smaller than the Trend(Range) for these parameters suggests that variability is present but is not as significant as the decreasing range of change. This could mean that the variability in temperature and precipitation in an area remains relatively constant, but the range of variation is decreasing. No clear trend of increasing range: If the Trend(Range) for temperature and Trend(Range) for precipitation are both negative, there are no clear trends to suggest a significant increase in the range of change for these parameters in the area. Potential climate change: A decreasing range of change in temperature and precipitation may be a signal of potential climate change in an area. These may be the results of changes in the atmosphere, such as changes in atmospheric circulation or other climatic factors that affect the local climate.	
$(+)$	Relation: $[trend(max - min) < trend(\sigma)]$ Result: $[trend(max - min) - trend(\sigma)] \rightarrow$ NEGATIVE
Stability of the range of change in temperature and precipitation: If the Trend(Range) for temperature and Trend(Range) for precipitation are smaller than the Trend(STD) for these parameters, this suggests that the range of change in temperature and precipitation in the area is more stable or changes less over the time period studied. This means that there is no tendency for the range of temperature and precipitation changes to increase significantly. Stability of temperature and precipitation: The Trend(STD) value measures the stability of temperature and precipitation, and the fact that it is greater than the Trend(Range) for these parameters indicates the presence of variability, but this variability is not as significant as the range of change. This could mean that the variability in temperature and precipitation in the area remains relatively constant. No clear trend of increasing range: If the Trend(Range) for temperature and Trend(Range) for precipitation are less than Trend(STD), there are no clear trends to suggest a significant increase in the range of change of these parameters in the area. Fluctuations around mean values: It is worth noting that although the range of change may be relatively stable, there may still be fluctuations around the mean values of temperature and precipitation in the area.	
$(-)$	Relation: $[trend(max - min) < trend(\sigma)]$ Result: $[trend(max - min) - trend(\sigma)] \rightarrow$ NEGATIVE
Declining range of change in temperature and precipitation: The Trend(Range) value for temperature and Trend(Range) value for precipitation suggest that the range of change in temperature and precipitation in an area is decreasing over the study period. This means that the difference between maximum and minimum temperature and the range of change in precipitation is decreasing. Stability of temperature and precipitation: The Trend(STD) value measures the stability of temperature and precipitation, and the fact that it is greater than Trend(Range) for these parameters suggests that variability is present but is not as significant as the decreasing range of change. This could mean that the variability in temperature and precipitation in an area remains relatively constant, but the range of these changes is decreasing. No clear trend of increasing range: If the Trend(Range) for temperature and Trend(Range) for precipitation are both negative, there are no clear trends to suggest a significant increase in the range of change for these parameters in the area. Possible climate change: A decreasing range of change in temperature and precipitation may be a signal of potential climate change in the area. These could be the results of changes in the atmosphere, such as changes in atmospheric circulation or other climatic factors that affect the local climate.	
$(-)\ or (+)$	Relation: $[trend(max - min) = trend(\sigma)]$ Result : $[trend(max - min) - trend(\sigma)] \rightarrow$ ZERO
Stability of the range of change in temperature and precipitation: The equality between Trend(Range) and Trend(STD) for temperature and precipitation suggests that the range of changes in temperature and precipitation in an area is relatively stable and does not show a clear tendency to increase or decrease over the study period. Stability of temperature and precipitation: The Trend(STD) value measures the stability of temperature and precipitation, and the fact that it is equal to the Trend(Range) for these parameters indicates the presence of variability, but that this variability is not the dominant trend over the period analysed. This means that the variability in temperature and precipitation in the area remains relatively constant. No clear upward or downward trends: No difference between Trend(Range) and Trend(STD) for temperature and precipitation means that there is no clear trend suggesting a significant increase or decrease in the range of variation in these parameters in the area. Climate stability: Equality between Trend(Range) and Trend(STD) may suggest that the climate in an area is relatively stable over the study period and does not show significant changes in temperature and precipitation.	

6. Detecting a Change Point in the Trend

Various methods can be applied to determine change points in a time series [8,113–116]. In this analysis, the non-parametric Pettitt change point test (PCPT) [117] was used to detect the occurrence of changes. The Pettitt test (PCPT) is a non-parametric test for detecting sudden changes in a time sequence. It is used to detect the turning point where a sudden change, known as a "jump", occurs in the time series. The Pettitt test (PCPT) involves comparing the sum of ranks of two subsets of data, which are divided by a threshold value, to determine whether there is a statistically significant change in the time sequence.

This test can be applied to analyse data with any distribution, and the test result is not dependent on the data having a normal distribution. The result of the Pettitt test (PCPT) is a test statistic value, which is compared with the critical value for the level of significance

to determine whether the null hypothesis of no sudden changes in the time sequence can be rejected. The rank is given after sorting and is dependent on the variable that gives the order of the records in the set.

The PCPT has been widely used to detect changes in observed climatic and hydrological time series [8,16,98,118]. The Pettitt test is also applicable to investigate an unknown change point by considering a sequence of random variables $(X_1, X_2, ..., X_T)$, which have a change point at τ. As a result $(X_1, X_2, ..., X_\tau)$ has a common distribution $F_1(\cdot)$, but $(X_{\tau+1}, X_{\tau+2}, ..., X_T)$ have a different distribution $F_2(\cdot)$, where $F_1(\cdot) \neq F_2(\cdot)$. The null hypothesis, H_0: no change (but $\tau = T$), is tested against the alternative hypothesis, H_1: change (lub $1 \leq \tau < T$), using the non-parametric statistic $K_T = max|U_{t,T}| = max\,(K_{T+}, K_{T-})$, where the following applies:

$$U_{t,T} = \sum_{i=1}^{t} \sum_{j=t+1}^{T} sgn(X_t - X_j), \tag{3}$$

$$sgn(X_t - X_j) = \begin{bmatrix} 1 & (X_t - X_j) > 0 \\ 0 & (X_t - X_j) = 0 \\ -1 & (X_t - X_j) < 0 \end{bmatrix}, \tag{4}$$

$K_{T+} = maxU_{t,T}$ for the downward shift and $K_{T-} = -minU_{t,T}$ or the upward shift [116]. The confidence level associated with K_{T+} lub K_{T-} is approximately determined as follows:

$$\rho = \exp\left(\frac{-6{K_T}^2}{T^3 + T^2}\right), \tag{5}$$

when p is smaller than the specified confidence level (for example, in this study, 0.95 was adopted), the null hypothesis is rejected. The approximate probability of significance for the change point is defined as follows:

$$P = 1 - \rho, \tag{6}$$

It is obvious that in the case of a significant change point, the series is segmented at the change point into two sub-time series.

The main aim of this study is to investigate the existence of change points in the time series of monthly sum precipitation and monthly average temperature characteristics. For time series showing a significant change point, the trend test is applied to partial series, and if the change point is not significant, the trend test is applied to the entire time series [8].

The Pettitt change point test (PCPT) is highly valuable in the context of sustainable development, as it enables the identification of tipping points where significant shifts in precipitation or temperature have occurred. A sudden decrease or increase in precipitation may indicate the need to adjust water resource management systems to adapt to new climatic conditions. The results of this test can highlight the urgency for swift responses to evolving climate patterns. Detecting a change point can signal the immediate need for adaptive measures to minimise potential negative impacts of climate change, such as floods, droughts, or shifts in water availability.

7. Trend Test

To examine the trend in a given time series, the Mann–Kendall test (MKT) can be applied. Originally, this test was used by Mann [119], and later, Kendall derived the distribution of the test statistic in 1975 [116]. This test is independent of the type of distribution, and we do not need to adopt any specific form of the data distribution function [120]. This test was widely recommended by the World Meteorological Organization for public applications and has been used in many scientific studies to assess trends in water resource data [2,8,116]. Therefore, the MKT has been recognised as an excellent tool for trend detection by other scholars in similar applications. It should also be noted that the MKT

considers only the relative values of all elements in the series $X = \{x_1, x_2, \ldots, x_n\}$. for analysis. The test statistic for the MKT is given by the following:

$$S = \sum_{i=1}^{n-1} \sum_{j=i+1}^{n} sgn(x_j - x_i), \tag{7}$$

$$sgn(x_j - x_i) = \begin{bmatrix} 1 & (x_j - x_i) > 0 \\ 0 & (x_j - x_i) = 0 \\ -1 & (x_j - x_i) < 0 \end{bmatrix}, \tag{8}$$

where x_j, x_i are the consecutive values of the data and n is the number of elements in the data. Under the null hypothesis of no trend, and assuming that the data are independent and identically distributed with a zero mean and a variance $V(S)$ denoted by σ^2, which is calculated as (t_i—the repeated values in the analysed sequence):

$$V(S) = \sigma^2 = \frac{1}{18}\left(n \cdot (n-1) \cdot (2n+5) - \sum_{i=1}^{m} t_i \cdot (t_i - 1) \cdot (2t_i + 5)\right), \tag{9}$$

To test a hypothesis, the standard normal distribution is used, denoted as the test statistic Z, which is defined as follows for the trend test:

$$Z = \begin{bmatrix} \frac{S-1}{\sigma} & S > 0 \\ 0 & S = 0 \\ \frac{S+1}{\sigma} & S < 0 \end{bmatrix}, \tag{10}$$

In the two-sided test for trend, the null hypothesis is represented as follows: H_0: there is no trend in the dataset, which will be rejected if the calculated Z statistic is greater than the critical value of this statistic obtained from the standard normal distribution table corresponding to the previously established level of significance. A positive value of Z indicates an increasing trend, and a negative value indicates a decreasing trend.

The magnitude of the trend is estimated using a non-parametric slope estimator based on the median proposed by Sen [121] and extended by Hirsch [122]. The slope estimator is given as follows:

$$\beta = Median\left[\frac{x_j - x_k}{j - k}\right] \text{ for all } k < j, \tag{11}$$

where $1 < k < j < n$, and β is treated as the median of all possible pairs of combinations for the entire dataset.

The Mann–Kendall Test (MKT) allows for the identification of long-term trends in precipitation and temperature, which is crucial for understanding whether persistent climate changes are occurring that could impact sustainable development. The results of the MKT can inform decisions related to climate and environmental policies. If the test reveals significant changes in the climate, it may necessitate the implementation of appropriate measures, such as adjustments to water resource management regulations, to ensure ecological and socioeconomic stability.

8. Results and Discussion

In the present study, the following properties of long-term sequences of monthly precipitation totals and monthly mean temperatures were investigated for 377 catchments across six WMO regions. The scope of the research and calculations included the following:

- Determining the values of long-term monthly series over a 110-year period;
- Calculating statistics related to the average values for each calendar month, including the minimum, maximum, mean, and standard deviation;
- Determining trend values using the Mann–Kendall test (MKT) to evaluate trends;
- Examining whether the long-term series exhibited change points using the Pettitt test (PCPT);

- Investigating whether the sub-series (after the identified change point up to 2010) showed a significant trend and how this trend differed from the long-term series in cases where change points were identified.

Of all the catchments analysed in terms of monthly precipitation totals, only one—the Lagarfljót River catchment in Iceland (Europe)—satisfied all four tests (MKT for RANGE, MKT for STD, PCPT for trend change, and MKT for new trend) simultaneously. This means that, at the 5% significance level, the P_2 measure trend was identified for this catchment, the year of the trend change was determined, and a new trend was additionally recognised. The RANGE trend not only changed in value but also in direction, shifting from negative to positive, with a change from (−0.136) to (0.310) in 1953. Similarly, the STD trend changed from (−0.533) to (0.889) in the same year.

In the case of the Lagarfljót catchment, both the values and directions of the RANGE and STD trends shifted. The change in the RANGE trend from negative to positive in 1953 indicates an increase in the maximum monthly precipitation values in the study area. Additionally, the change in the STD trend reflects a shift in the variability of this phenomenon. The primary driver behind these changes appears to be the economic and demographic development in the region. In 1947, the town of Egilsstaðir was founded along the banks of the Lagarfljót River, becoming the largest town in eastern Iceland and its main service, transport, and administrative centre. By the 1950s, Iceland experienced a significant increase in the use of oil for heating, contributing to increased CO_2 emissions, rising temperatures, and potentially influencing changes in precipitation patterns [123].

However, this remains a hypothesis, as it is challenging to directly link local emissions to specific climate changes without more advanced analyses, such as climate modelling. Even though global emissions were lower at that time, asserting that local CO_2 emissions alone caused synoptic climate changes in the region would require further evidence. Only detailed simulations and analyses could confirm whether local emission changes had a measurable impact on precipitation patterns, particularly within a global context.

Based on the analysis of monthly precipitation data from the 377 catchments, it was found that for 93 catchments (25% of the total), the trends in polarisation coefficients (RANGE and STD) for monthly precipitation totals were statistically significant at the 5% level. In contrast, no significant trends were identified in the remaining 75% of the catchments.

Analysis of the P_1 polarisation coefficient values (Figure 2, Table 3) across the ten largest catchments, with areas ranging from 1,705,383 to 4,640,300 km^2, reveals notable variations in precipitation patterns. The coefficient of variation within these catchments ranges from 0.29 to 1.0, indicating a significant disparity in the consistency of monthly precipitation totals. Meanwhile, the P_1 measure, spans from 4.25 in the Yenisei catchment (Russian Fed., Asia) to 5.54 in the Mississippi River catchment (United States, North America). Across all analysed catchments, the P_1 measure exhibits an even broader range, from 3.81 in the Ganges catchment (India, Asia) to 12.78 in the Copper River catchment (United States, North America). These findings highlight substantial differences in precipitation variability and extremes between different regions. Higher P_1 values suggest that some catchments, particularly the Copper River, experience more pronounced fluctuations in monthly precipitation, which could indicate greater susceptibility to extreme weather events such as floods or droughts. Conversely, lower P_1 values, like those observed in the Ganges, may indicate more stable precipitation patterns, although this does not necessarily imply a lower risk of extreme events. The wide range of P_1 values across these large catchments underscores the importance of regional climate characteristics and their impact on hydrological extremes.

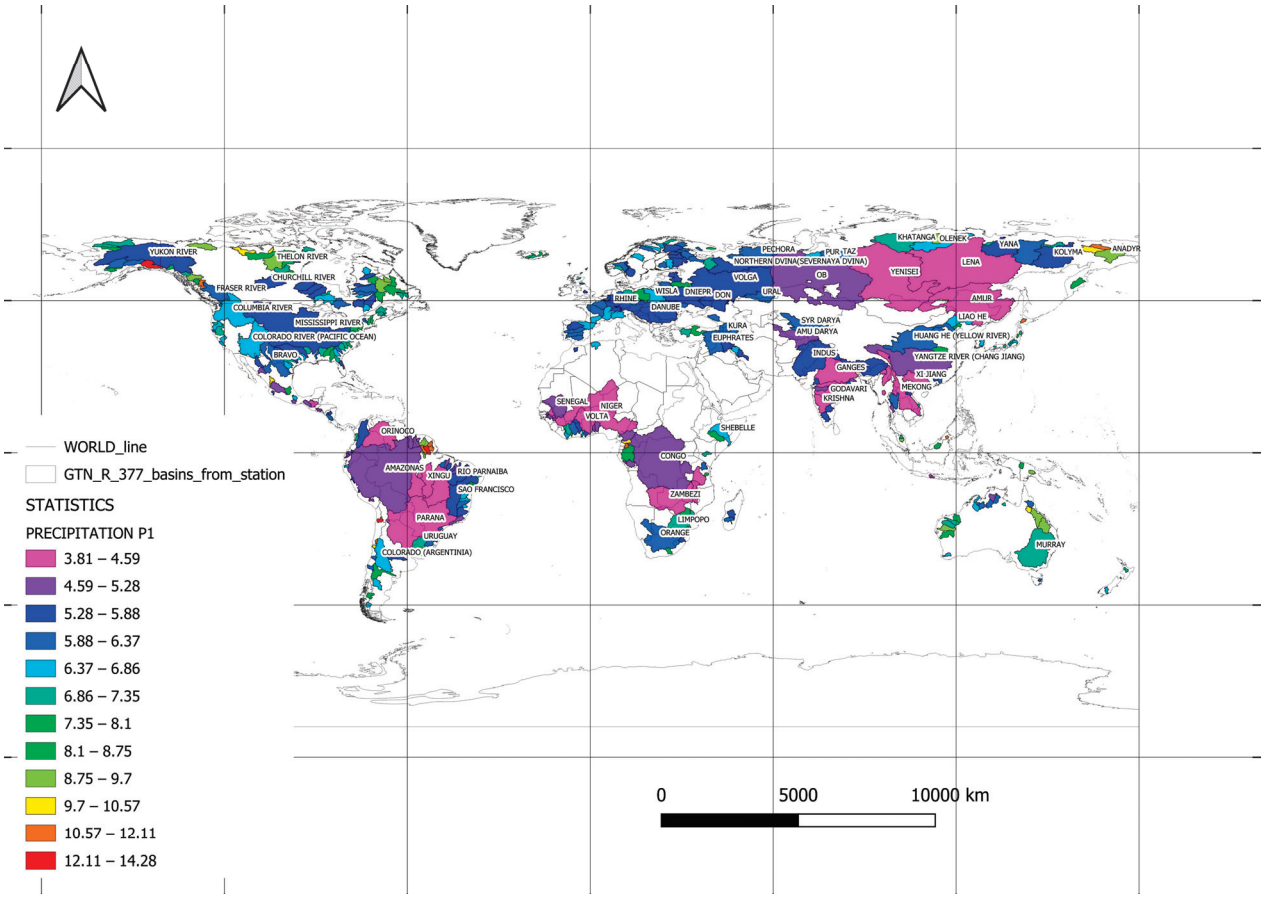

Figure 2. Polarisation measure P_1 for monthly precipitation totals of the period 1901 to 2010.

Table 3. P1 measure values for precipitation in the ten largest catchments.

No	WMO	River	Country	Continent	Area	C_v	P_1
					[km^2]		
138	3	Amazonas	Brazil	South America	4,640,300	0.292	4.909
2	1	Congo	Congo, The De	Africa	3,475,000	0.288	5.049
187	4	Mississippi River	United States	North America	2,964,255	0.412	5.536
94	2	Ob	Russian Fed.	Asia	2,949,998	0.501	4.996
14	1	Nile	Egypt	Africa	2,900,000	0.712	4.262
93	2	Yenisei	Russian Fed.	Asia	2,440,000	0.641	4.249
91	2	Lena	Russian Fed.	Asia	2,430,000	0.731	4.570
125	3	Parana	Argentina	South America	2,346,000	0.582	4.529
92	2	Amur	Russian Fed.	Asia	1,730,000	0.998	4.506
50	2	Yangtze River (Chang Jiang)	China	Asia	1,705,383	0.661	5.285
							MAX
180	4	Copper River	United States	North America	62,678	0.710	12.781
							MIN
78	2	Ganges	India	Asia	835,000	1.240	3.812

The values (Figure 3, Table 4) of the P_2 polarisation component trends are shown at the 5% significance level. The following values were obtained from the next ten largest catchments ranging from 244,000 to 2,900,000 km^2: the P_2 measure takes values from −0.895 (Brahmaputra, Bangladesh, Asia) to 0.444 (Uruguay, Uruguay, South America). The range of values of this measure for all analysed catchments meeting the 5% significance criterion takes values from −0.966 (Purari, Papua New Guinea, Australia and Oceania) to 0.945 (Han-Gang (Han River), Korea, Rep., Asia).

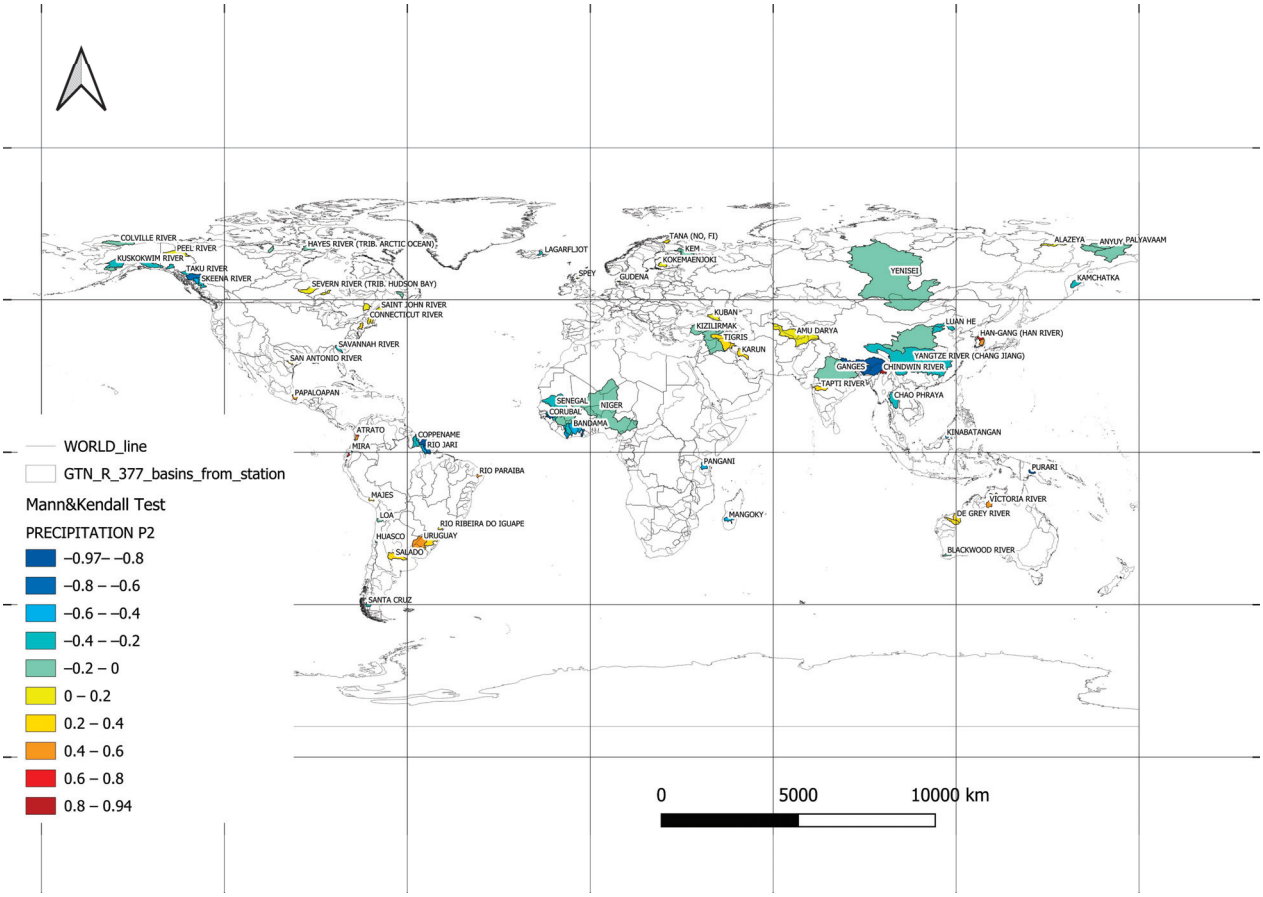

Figure 3. Watersheds in which significant polarisation trends were identified for monthly precipitation sums during the period from 1901 to 2010 at a significance level of 5%.

Figure 4 shows the spatial location of the analysed catchments, where significant trend change-points in the P_2 polarisation coefficients of monthly precipitation were recognised at the 5% significance level (Table 4). For the catchments of the rivers of Africa, the years of changes in rainfall trends mainly occur in the late nineteen-sixties to the nineteen-seventies. Changes in trends can be linked to processes of decolonisation, independence, and economic development in the area. The apogee of this process occurred between 1960 and 1968, and 1960 is referred to as the "Year of African Independence" [124]. For the catchments of the rivers of Asia, the years of changes in rainfall trends mainly occur in the range of the nineteen-fifties to the nineteen-sixties in the area of Russia, the nineteen-forties to the nineteen-sixties in the area of China, and from the nineteen-thirties to the nineteen-seventies in the area of India. The 1950s in Russia saw intensive economic development, industrialisation, and intensive agricultural development [125]. The year 1949 was the beginning of land reform and nationalisation of the main economic sectors in China. The 1970s was the Cultural Revolution, where economic development collapsed [126]. For the catchment areas of South American rivers, years of changes in precipitation trends mainly occur in the period from the nineteen-forties to the nineteen-seventies. The 1960s and 1970s

were a watershed period in the economic development of Latin American countries [127]. In the area of North America, this period is from the nineteen-forties to the nineteen-sixties on the west coast and through the nineteen-sixties for the east coast. This is a period of industrial and demographic boom [126]. For the catchments of the rivers of the Australia–Oceania area, trend changes have been shown in the years from the nineteen-fifties to the nineteen-seventies. This is a period of intense industrial development and demographic growth, as well as the decolonisation of Oceania and its economic development [126].

Table 4. Trend values of P_2 polarisation components for precipitation at 5% significance level in the ten largest catchments.

No	WMO	River	Country	Continent	Area	P_2	Year (STD)	Year (RANGE)
					[km^2]	[mm/year]	[year]	[year]
14	1	Nile	Egypt	Africa	2,900,000	−0.052	1964	1967
93	2	Yenisei	Russian Fed.	Asia	2,440,000	−0.053	1975	1954
50	2	Yangtze River	China	Asia	1,705,383	−0.305	1932	1939
78	2	Ganges	India	Asia	835,000	−0.170		
49	2	Huang He (Yellow River)	China	Asia	730,036	−0.151		
75	2	Brahmaputra	Bangladesh	Asia	636,130	−0.895	1955	1955
96	2	Amu Darya	Uzbekistan	Asia	450,000	0.062	1947	1951
73	2	Euphrates	Iraq	Asia	274,100	−0.103		
31	1	Senegal	Senegal	Africa	268,000	−0.302	1967	1967
135	3	Uruguay	Uruguay	South America	244,000	0.444	1945	1940
						MAX		
76	2	Han-Gang (Han River)	Korea, Rep.	Asia	25,046	0.945	1962	1953
						MIN		
295	5	Purari	Papua New Guinea	Australia and Oceania	11,100	−0.966	1950	1950

The reasons for the change in precipitation trends in the analysed catchments may be related to a variety of climatic, geographical, and anthropogenic factors. Potential causes of changes in rainfall trends by region are outlined below:

- Africa: changes in atmospheric circulation, including fluctuations in the rainfall belt and belt patterns, El Niño and La Niña phenomena, deforestation, overgrazing of animals and changes in land use, and land degradation [31,46];
- Asia: diversity of topography can affect air mass movements and precipitation formation; changes in atmospheric circulation such as monsoons; increasing urbanisation and infrastructure development can create the so-called "heat island effect", which affects the microclimate; air pollution including particulate matter, which affects condensation and cloud formation [31,128];
- South America: atmospheric circulation fluctuations, including those associated with El Niño and La Niña; topography of the region, including the Andes; deforestation; conversion of land for agriculture and urbanisation [46];
- North America: changes in atmospheric circulation such as the North Atlantic Oscillation, deforestation, urbanisation and land use change, and greenhouse gas emissions [31,44];

- Australia and Oceania: El Niño–La Niña cycle, changes in ocean circulation, variation in ocean surface temperature and atmospheric pressure between western and eastern areas of the Indian Ocean, deforestation, change in water use and air pollution, intensive agriculture, and overexploitation of water resources [31,46].

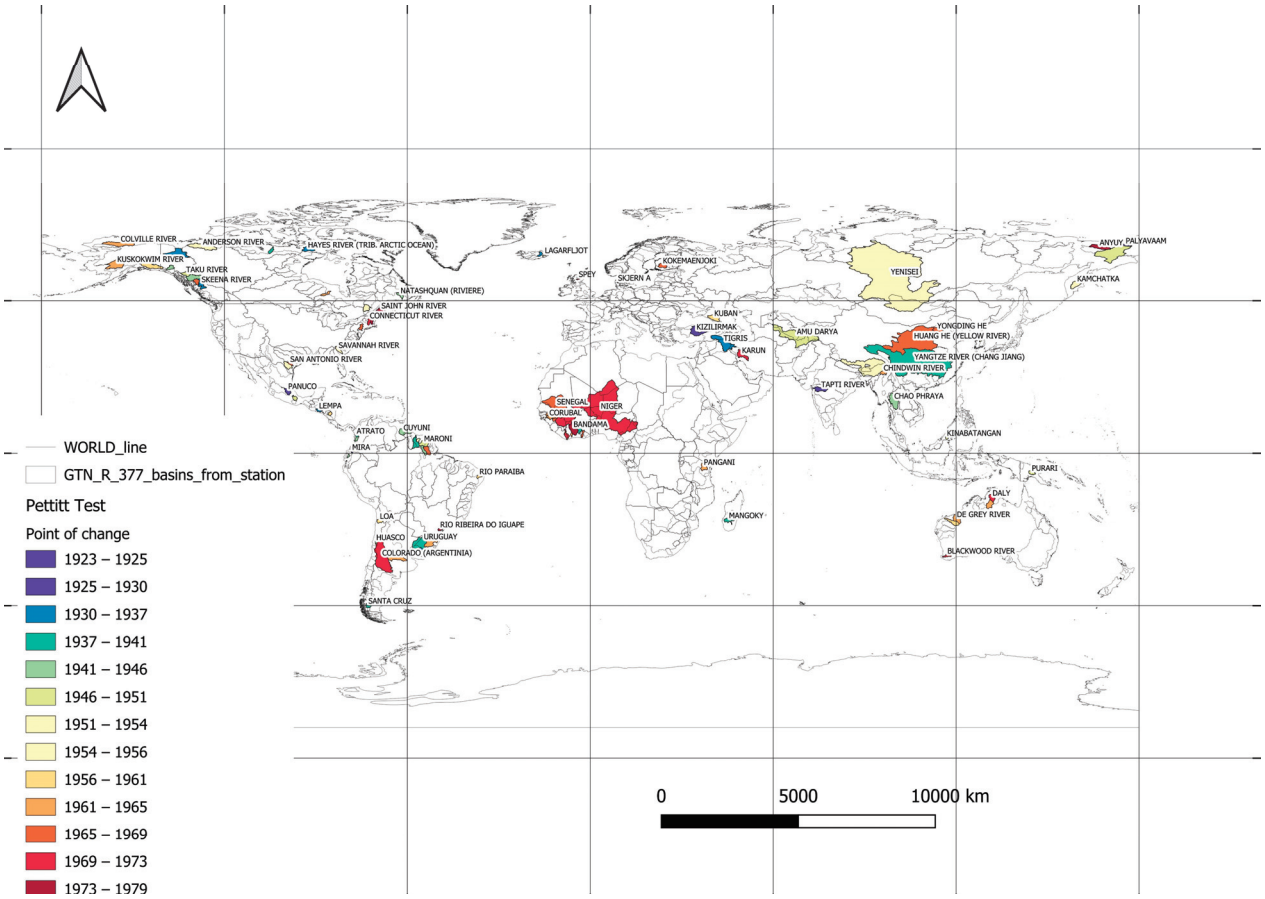

Figure 4. Watersheds in which change-points in the trend of factors related to precipitation polarisation for monthly precipitation sums during the period from 1901 to 2010 were identified at a significance level of 5%.

Based on the analysis of the data of monthly average temperatures in the analysed catchments, it should be noted that for 46/377 catchments, i.e., in 12.2% of the analysed catchments, the trends of polarisation coefficients in the range of temperatures were proven at the significance level of 5%, and in the remaining 88.8, they were not confirmed.

The analysis of the temperature polarisation index (Figure 5, Table 5) across ninety-three catchments reveals significant variability in the P_1 index, ranging from a high of 10.43 for the Sepik River catchment (Australia and Oceania, Papua New Guinea) to a low of 3.26 for the Indigirka River catchment (Asia, Russian Fed.). These results indicate that the Sepik River catchment experiences the most pronounced temperature fluctuations among the studied regions, which could suggest a greater vulnerability to extreme temperature events. On the other hand, the lower P_1 value for the Indigirka River catchment suggests more stable temperature conditions, although this does not necessarily correlate with a lower risk of temperature extremes. The observed variation in the P_1 index among the catchments underscores the diverse nature of temperature polarisation across different geographic regions. For instance, the Sepik River, with the highest P_1 value, may be more susceptible to dramatic temperature swings, which could have significant implications for local ecosystems and human activities. In contrast, catchments like the Indigirka River, with lower P_1 values, may experience more consistent temperature patterns, though they

are not immune to extreme events. The data also show some interesting patterns among the larger catchments, such as the Amazonas in Brazil and the Congo in Africa, which exhibit relatively high P_1 values, suggesting notable temperature variability. Meanwhile, catchments like the Mississippi River in the United States and the Yangtze River in China show lower P_1 values, indicating less temperature variability.

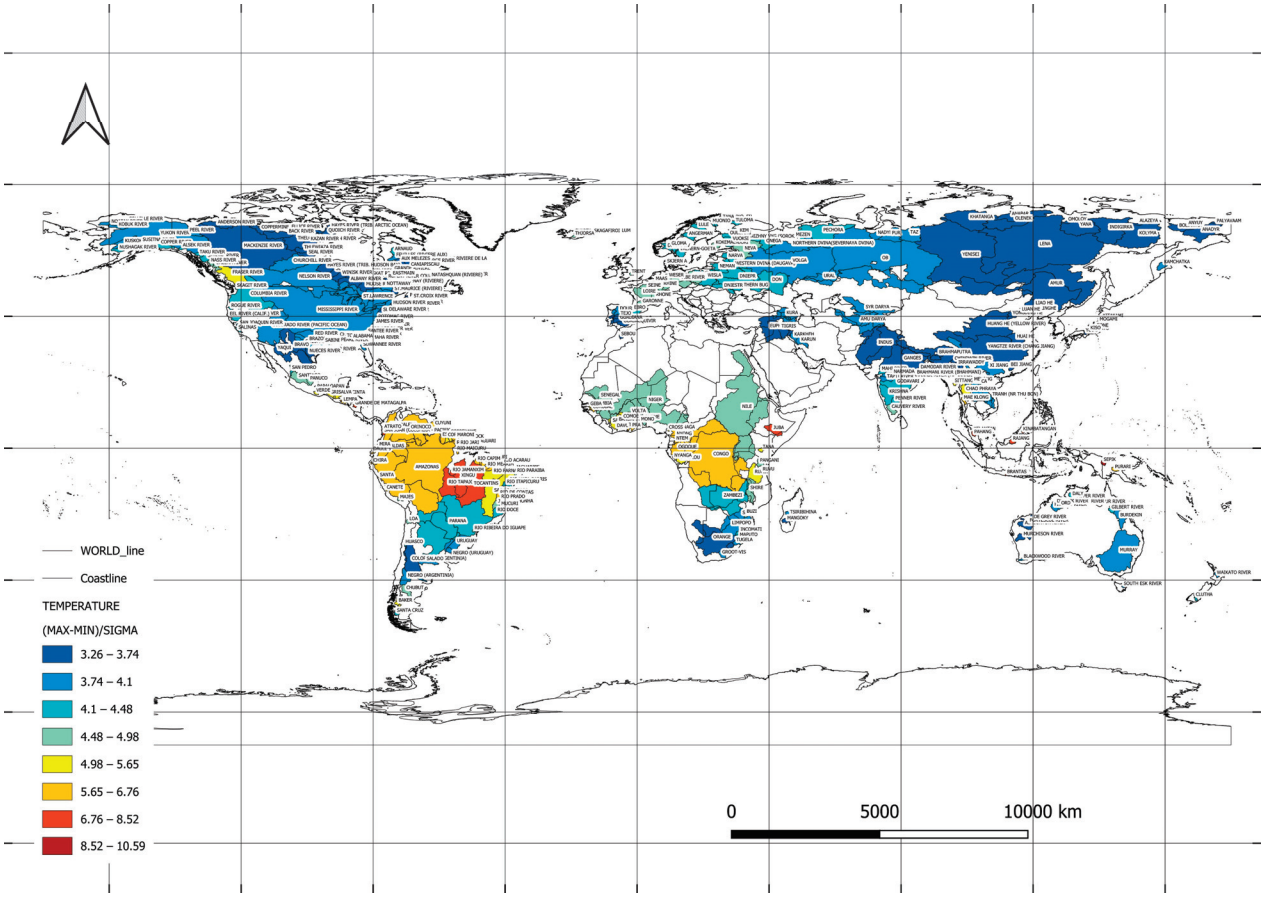

Figure 5. Polarisation measure P_1 for monthly temperature totals of the period 1901 to 2010.

The values (Figure 6, Table 6) of the P_2 polarisation component trends are shown at the 5% significance level. The following values were obtained from the next ten largest catchments ranging from 120,764 to 1,730,000 km^2: the P_2 measure takes values from −0.018 (Amur, Russian Fed., Asia) to 0.005 (Sao Francisco, Brazil, South America). The range of values of this measure for all analysed catchments meeting the 5% significance criterion takes values from −0.018 (Amur, Russian Fed., Asia) to 0.022 (Arnaud, Canada, North America).

Figure 7 shows the spatial location of the analysed catchments, where significant trend change-points in the P_2 polarisation coefficients of monthly mean temperatures were recognised at the 5% significance level (Table 6). For the catchments of African rivers, the years of changes in precipitation trends mainly occur in the nineteen-sixties to nineteen-eighties.

Table 5. P_1 measure values for temperature in the ten largest catchments.

No	WMO	River	Country	Continent	Area	C_v	P_1
					[km^2]	[]	[]
138	3	Amazonas	Brazil	South America	4,640,300	0.031	5.952
2	1	Congo	The Democratic Republic of Congo	Africa	3,475,000	0.028	6.736
187	4	Mississippi River	United States	North America	2,964,255	1.003	3.885
94	2	Ob	Russian Fed.	Asia	2,949,998	−22.694	3.820
14	1	Nile	Egypt	Africa	2,900,000	0.082	4.857
93	2	Yenisei	Russian Fed.	Asia	2,440,000	−2.663	3.590
91	2	Lena	Russian Fed.	Asia	2,430,000	−1.861	3.385
125	3	Parana	Argentina	South America	2,346,000	0.145	4.276
92	2	Amur	Russian Fed.	Asia	1,730,000	−10.070	3.420
50	2	Yangtze River (Chang Jiang)	China	Asia	1,705,383	0.652	3.428
							MAX
294	5	Sepik	Papua New Guinea	Australia and Oceania	40,922	0.042	10.435
							MIN
102	2	Indigirka	Russian Fed.	Asia	305,000	−1.294	3.257

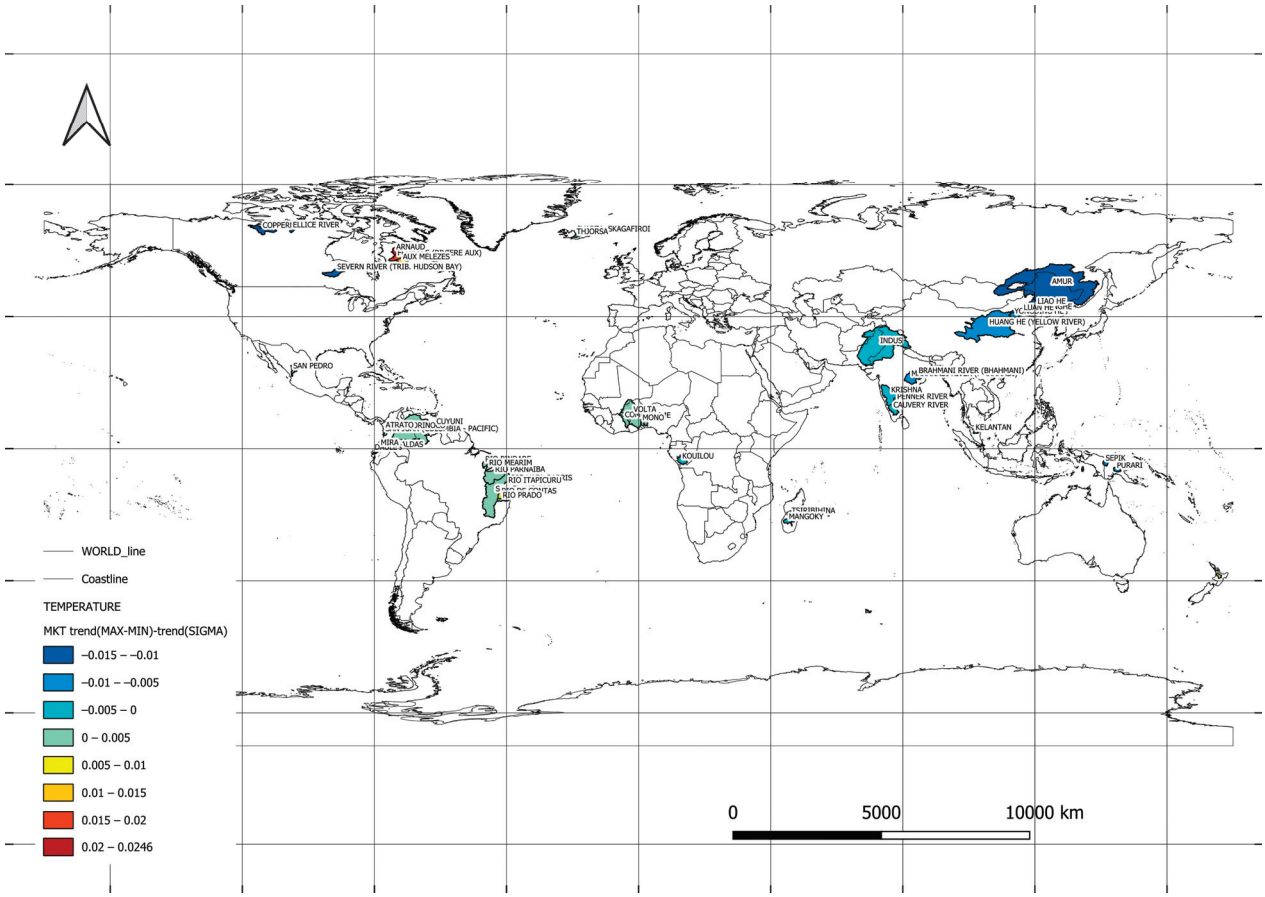

Figure 6. Watersheds in which significant polarisation trends were identified for monthly mean temperatures during the period from 1901 to 2010 at a significance level of 5%.

Table 6. Trend values of P_2 polarisation components for the next ten largest catchments at 5% significance level for temperature.

No	WMO	River	Country	Continent	Area	P_2	Year (STD)	Year (RANGE)
					[km^2]	[°C/year]	[year]	[year]
92	2	Amur	Russian Fed.	Asia	1,730,000	−0.018	1956	1954
123	3	Orinoco	Venezuela	South America	836,000	0.004	1957	1957
58	2	Indus	Pakistan	Asia	832,418	−0.006	1950	1973
49	2	Huang He (Yellow River)	China	Asia	730,036	−0.006	1975	1971
156	3	Sao Francisco	Brazil	South America	622,600	0.005	1932	1932
25	1	Volta	Ghana	Africa	394,100	0.002	1968	1978
152	3	Rio Parnaiba	Brazil	South America	322,823	0.004	1958	1958
88	2	Godavari	India	Asia	299,320	−0.004	1955	1955
87	2	Mahanadi River	India	Asia	132,090	−0.009	1961	1955
48	2	Liao He	China	Asia	120,764	−0.013	1957	1970
						MAX		
258	4	Arnaud	Canada	North America	26,900	0.022	1987	1987
						MIN		
92	2	Amur	Russian Fed.	Asia	1,730,000	−0.0182	1956	1954

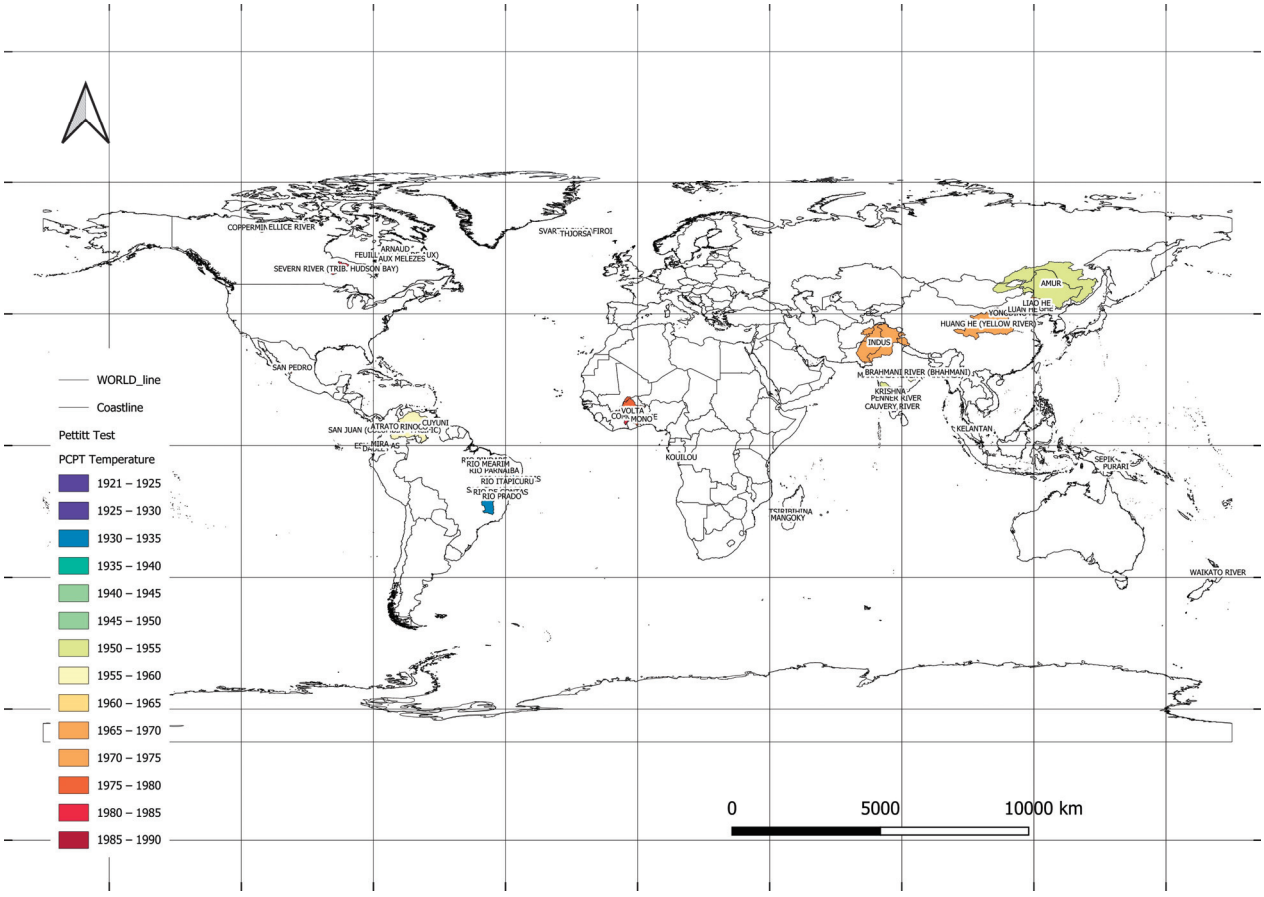

Figure 7. Watersheds in which change points in the trend of factors related to temperature polarisation for monthly mean temperatures during the period from 1901 to 2010 were identified at a significance level of 5%.

For the catchments of Asian rivers, the years of changes in precipitation trends mainly occur in the nineteen-forties to the nineteen-sixties. For the catchments of South American rivers, years of changes in rainfall trends mainly occur in the nineteen-thirties to the nineteen-sixties.

For the catchment area of North America, this period for the west coast is in the years following the start of the nineteen-eighties. For the catchments of the rivers of the Australia–Oceania area, trend changes have been identified in the nineteen-fifties.

Changes in temperature trends in continental catchments are the result of a complex interaction of both natural climatic and anthropogenic factors. The causes of changing trends are outlined below:

- Africa: changes in atmospheric circulation: fluctuations in the belts and monsoons; changes in the oceanic system: phenomena such as El Niño and La Niña. Greenhouse gas emissions; land use change: urbanisation, deforestation, and agriculture [8,31,46,76];
- Asia: monsoon changes: changes in intensity and timing of monsoons; topography: hills, mountains, and valleys; air pollution: dust and gas emissions can affect cloud formation and solar absorption; urbanisation: creation of heat island effect in urbanised areas [31,46,49];
- South America: changes in ocean circulation: fluctuations in ocean surface temperature; changes in land use: excessive deforestation and conversion of land to agriculture [8,31,46];
- North America: changes in atmospheric circulation: influence of circulations such as AO and NAO; greenhouse gas emissions: increase in greenhouse gas concentrations; land use change: urbanisation and deforestation [8,31,46]; and
- Australia and Oceania: changes in ocean cycles: El Niño and La Niña fluctuations; GHG emissions: increase in GHG concentrations; changes in water management: over-intensive use of water resources [8,31,46,76].

The polarisation index taking into account both precipitation and temperature phenomena is shown in Figure 8 and Table 7. On the horizontal axis is the polarisation index P_2 of monthly precipitation totals, while on the vertical axis is the polarisation index P_2 of monthly average temperatures. The points depicting the polarisation phenomenon farthest from the center of the system indicate a high intensity of polarisation.

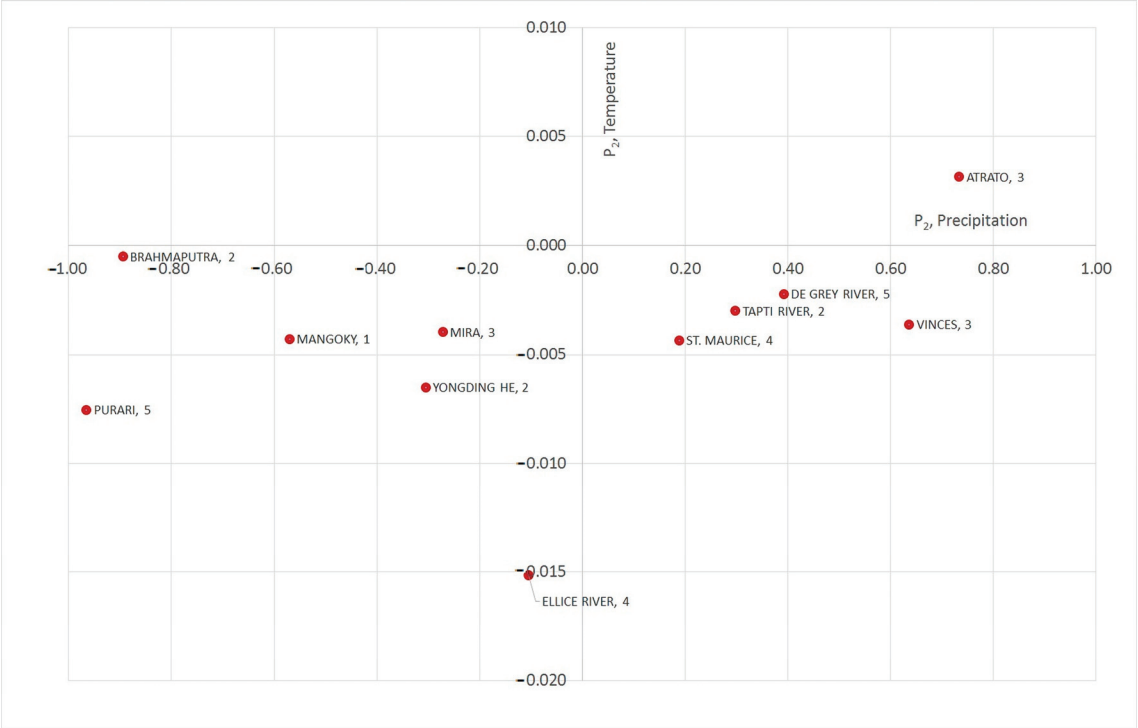

Figure 8. A picture of polarisation phenomena in the area of precipitation and temperature, taking into account WMO regions.

Table 7. Trend values of P_2 polarisation components at 5% significance level for precipitation and temperature.

					Precipitation			Temperature		
No	**WMO**	**River**	**Country**	**Area**	**tr (STD)**	**tr (RANGE)**	**P_2**	**tr (STD)**	**tr (RANGE)**	**P_2**
						mm/year			°C/year	
15	1	Mangoky	Madagascar	53,225	−0.2059	−0.7757	−0.5697	−0.0018	−0.0061	−0.0043
45	2	Yongding He	China	42,500	−0.0854	−0.3907	−0.3053	−0.0050	−0.0115	−0.0065
75	2	Brahmaputra	Bangladesh	636,130	−0.2147	−1.1095	−0.8948	−0.0017	−0.0022	−0.0005
81	2	Tapti River	India	61,575	0.1281	0.4256	0.2975	−0.0024	−0.0054	−0.0030
114	3	Atrato	Colombia	9432	0.3500	1.0835	0.7336	0.0014	0.0046	0.0032
168	3	Mira	Ecuador	4960	−0.1104	−0.3822	−0.2719	−0.0021	−0.0060	−0.0039
171	3	Vinces	Ecuador	4400	0.1595	0.7957	0.6361	−0.0011	−0.0047	−0.0036
233	4	Ellice River	Canada	16,900	−0.0433	−0.1476	−0.1043	−0.0077	−0.0228	−0.0152
263	4	St. Maurice	Canada	42,000	0.0762	0.2647	0.1885	−0.0052	−0.0096	−0.0043
295	5	Purari	Papua New Guinea	11,100	−0.3654	−1.3310	−0.9656	−0.0033	−0.0108	−0.0075
301	5	De Grey River	Australia	49,600	0.1442	0.5358	0.3916	−0.0026	−0.0048	−0.0022

The concordance of the sign of the trend (RANGE) and trend (STD) for monthly precipitation and temperature is due to the fact that, in most cases, the variability in precipitation is correlated with changes in their maximum and minimum values. Similarly, in the area of temperature, the concordance of the sign of the trend (RANGE) and the trend (STD) for monthly temperatures is due to the fact that, in most cases, the variability in temperatures is correlated with changes in their maximum and minimum values. The characteristics of the river basins where polarisation was found in both the precipitation and

temperature areas also included locations relating to Köppen–Geiger (K-G) classification areas [129,130].

The catchment area of the Mangoky River (Africa) is located on the island of Madagascar in the regions Bsh (arid, summer dry, hot arid) and Aw (equatorial, winter dry). It is characterised by negative values of both trends of precipitation polarisation factors and negative values of both trends of temperature polarisation factors. This indicates a decrease in the anomalies of precipitation and temperature factors. The decrease in the anomalies of precipitation factors while there is a decrease in temperature anomalies indicates a certain compatible relationship between the two factors in the catchment. This means that as precipitation anomalies decrease and stabilise, there may be a tendency toward lower temperatures or less extreme temperature changes.

The Yongding He River catchment is located in Asia in the Bsk (arid, dry summer) and Dwb (snow, dry winter and warm summer) regions. It is characterised by negative values of both trends of precipitation polarisation factors and negative values of both trends of temperature polarisation factors. This indicates a decrease in the anomalies of precipitation and temperature factors.

The catchment area of the Brahmaputra River is located in Asia in the regions: ET (polar, polar tundra) and Cwa (warm temperature, dry winter, hot summer). It is characterised by negative values of both trends of precipitation polarisation factors and negative values of both trends of temperature polarisation factors. This indicates a decrease in the anomalies of precipitation and temperature factors.

The Tapti River catchment is located in Asia in the Aw (equatorial, monsoonal) and As (equatorial, summer dry) regions. It is characterised by positive values of both trends of precipitation polarisation factors and negative values of both trends of temperature polarisation factors. This indicates an increase in precipitation factor anomalies with a decrease in temperature anomalies.

The Atrato River catchment is located in South America in the Af (equatorial, fully humid) region. It is characterised by positive values of both trends of precipitation polarisation factors and positive values of both trends of temperature polarisation factors. This indicates an increase in precipitation factor anomalies and temperature anomalies. If the region has positive values of both trends of precipitation polarisation factors and positive values of both trends of temperature polarisation factors, this indicates an increase in precipitation factor anomalies and temperature anomalies. Positive values of the precipitation polarisation factor trends suggest an increase in precipitation and greater variability in precipitation in the region. This could mean that precipitation becomes more abundant or more frequent and intense rainfall occurs. Positive trend values of temperature polarisation factors indicate an increase in temperature and greater temperature variability in the region.

The Mira River catchment is located in South America in the ET (polar, polar tundra) and Cfb (warm temperature, fully humid, warm summer) region. It is characterised by negative values of both trends of precipitation polarisation factors and negative values of both trends of temperature polarisation factors. This indicates a decrease in the anomalies of precipitation and temperature factors.

The Vinces River (South America) catchment is located at the boundary of the areas As (equatorial, dry summer), Am (equatorial, monsoonal), and Cfc (warm temperature, fully humid and cool summer). It is characterised by positive values of both trends of precipitation polarisation factors and negative values of both trends of temperature polarisation factors. This indicates an increase in precipitation factor anomalies with a decrease in temperature anomalies. This means that the amount of precipitation may be increasing or there may be more variability in precipitation in the area. In contrast, temperatures are less variable or stable, with decreasing temperature anomalies. An increase in precipitation factor anomalies while temperature anomalies are decreasing indicates a certain inverse relationship between the two factors in the catchment. This means that with higher precipitation, there may be a tendency towards lower temperatures or less extreme temperature changes.

The Ellice River catchment is located in North America, on the border of regions ET (polar, polar tundra) and Dfc (snow, fully humid, cool summer). It is characterised by negative values of both trends of precipitation polarisation factors and negative values of both trends of temperature polarisation factors. This indicates a decrease in the anomalies of precipitation and temperature factors.

The catchment area of the St. Maurice River is located in North America, on the border of the Dfb (snow, fully humid, cool summer) and Dfc (snow, fully humid, warm summer) regions. It is characterised by positive values of both precipitation polarisation factor trends and decreasing values of temperature polarisation factor trends. This indicates an increase in precipitation factor anomalies with a decrease in temperature anomalies.

The Purari River catchment is located in Australia and Oceania, in the Af (equatorial, fully humid) region. It is characterised by negative values of both trends of precipitation polarisation factors and negative values of both trends of temperature polarisation factors. This indicates a decrease in the anomalies of precipitation and temperature factors.

The De Grey River catchment is located in Australia and Oceania, in the Bwh (arid, winter dry, hot arid) region. It is characterised by positive values of both trends of precipitation polarisation factors and negative values of both trends of temperature polarisation factors. This indicates an increase in precipitation factor anomalies with a decrease in temperature anomalies.

Calming of precipitation and temperature anomalies (negative trends in both precipitation and temperature factors) are expected in the Brahmaputra and Yongding He catchments. For the Purari (Australia and Oceania) and Mangoky–Africa catchments, calculations indicate a calming of anomalies in both the temperature and precipitation variability area. Temperature and precipitation anomalies are to be expected in the Atrato River–South America catchments.

The analysis of K-G areas and catchments where trends in polarisation coefficients in both the area of monthly precipitation and monthly average temperatures have been recognised at the 5% significance level does not show associations of these catchment areas with the zones proposed by Köppen–Geiger [129,130].

In the calculations performed to determine the P_2 polarisation index, in addition to cases of trends with compatible signs (i.e., both positive and negative polarisation coefficients), there were also cases in which catchments showed opposite signs of P_2 polarisation coefficient trends in both precipitation and temperature sequence analysis. However, adopting a 5% significance level for the MKT resulted in the rejection of these cases. The concordance of the sign of the trend (max–min) and trend (STD) for precipitation is due to the fact that in most cases, the variability in precipitation is correlated with changes in its maximum and minimum values. In other words, when there are periods of increased precipitation, we usually also observe higher maximum and minimum values of precipitation, and thus an increase in variability relative to the average value. Similarly, when there are periods of increased drought, there are usually lower maximum and minimum precipitation values, and variability relative to the average is also lower. Note, however, that there are also periods in which maximum and minimum precipitation values may increase or decrease, but variability relative to the average remains constant or changes in the opposite direction.

9. Conclusions

This paper presents an analysis of monthly precipitation totals, based on the GPCC database, and monthly mean temperatures (NOAA data) for 377 catchments distributed worldwide, representing 12.76% of the Earth's total surface area. The study covers a 110-year period from 1901 to 2010, using grid data with a spatial resolution of 0.5° × 0.5° latitude and longitude. Data were analysed in monthly intervals across the calendar year. In total, this study examined 377 catchments × 110 years × 12 months = 497,640 precipitation data series, and the same number of temperature data series, resulting in approximately one million long-term series that characterise climatic phenomena in terms

of precipitation and temperature variability. Statistical characteristics for each calendar month were calculated, including minimum, maximum, and standard deviation values. Polarisation indices were computed based on the coefficients of amplitude and standard deviation, as well as the trends of these characteristics. Non-parametric Mann–Kendall Test (MKT) and Pettitt change-point test (PCPT) were used for trend analysis.

The analysis of monthly precipitation data across the catchments revealed that trends in the polarisation components (RANGE and STD) of monthly precipitation totals were confirmed at a 5% significance level in 25% of the catchments, while no significant trends were observed in the remaining 75%. Similarly, for the average monthly temperature data, trends in the polarisation coefficients were confirmed at a 5% significance level in 12.2% of the catchments, with no significant trends detected in the remaining 88.8%.

The analysis of temperature and precipitation polarisation is crucial due to its significant impact on various aspects of the natural and human environment. Based on long-term precipitation and temperature data, this paper demonstrates that polarisation processes are present and can lead to substantial changes in local environments. These changes may affect the distribution of plant and animal species, weather patterns, agriculture, the economy, and more. Moreover, precipitation and temperature variability play critical roles in global energy and water cycles, with potential consequences such as floods, droughts, and other natural disasters. Understanding the nature and timescales of these changes is essential for reducing the risk of extreme climate events such as droughts, heatwaves, heavy precipitation, flooding, or extreme cold.

A proper assessment of extreme event polarisation is vital for developing strategies to mitigate and minimise the impact of anthropogenic factors. Integrating adaptive and mitigative actions can help achieve long-term goals of balancing economic, social, and ecological needs. This paper presents methods for assessing the polarisation of precipitation and temperature variability, which can support the development of such strategies. Climate change trends suggest that polarisation is becoming more pronounced, with associated extremes intensifying and becoming more unevenly distributed. Analysing temperature and precipitation polarisation is critical for evaluating climate change and its environmental impacts, as well as for creating effective risk management strategies that minimise human impact on the environment, in line with the principles of sustainable development.

Funding: This research received no external funding.

Institutional Review Board Statement: This study did not require ethical approval.

Informed Consent Statement: Not applicable.

Data Availability Statement: The data presented in this study are available on request from the corresponding author. The data are not publicly available due to the size of the data structures.

Conflicts of Interest: The author declares no conflicts of interest.

References

1. Romanowicz, R.J.; Bogdanowicz, E.; Debele, S.E.; Doroszkiewicz, J.; Hisdal, H.; Lawrence, D.; Meresa, H.K.; Napiórkowski, J.J.; Osuch, M.; Strupczewski, W.G.; et al. Climate Change Impact on Hydrological Extremes: Preliminary Results from the Polish-Norwegian Project. *Acta Geophys.* **2016**, *64*, 477–509. [CrossRef]
2. Palaniswami, S.; Muthiah, K. Change Point Detection and Trend Analysis of Rainfall and Temperature Series over the Vellar River Basin. *Polish J. Environ. Stud.* **2018**, *27*, 1673–1682. [CrossRef] [PubMed]
3. Groves, D.G.; Yates, D.; Tebaldi, C. Developing and Applying Uncertain Global Climate Change Projections for Regional Water Management Planning. *Water Resour. Res.* **2008**, *44*, 1–16. [CrossRef]
4. Katz, R. Statistics of Extremes in Climatology and Hydrology. *Adv. Water Resour.* **2002**, *25*, 1287–1304. [CrossRef]
5. Herschy, R.W. The World's Maximum Observed Floods. *Flow Meas. Instrum.* **2002**, *13*, 231–235. [CrossRef]
6. Blöschl, G.; Bierkens, M.F.P.; Chambel, A.; Cudennec, C.; Destouni, G.; Fiori, A.; Kirchner, J.W.; McDonnell, J.J.; Savenije, H.H.G.; Sivapalan, M.; et al. Twenty-Three Unsolved Problems in Hydrology (UPH)—A Community Perspective. *Hydrol. Sci. J.* **2019**, *64*, 1141–1158. [CrossRef]
7. Lewis, S.C.; King, A.D. Evolution of Mean, Variance and Extremes in 21st Century Temperatures. *Weather Clim. Extrem.* **2017**, *15*, 1–10. [CrossRef]

8. Jaiswal, R.K.; Lohani, A.K.; Tiwari, H.L. Statistical Analysis for Change Detection and Trend Assessment in Climatological Parameters. *Environ. Process.* **2015**, *2*, 729–749. [CrossRef]
9. Heim, R.R. An Overview of Weather and Climate Extremes—Products and Trends. *Weather Clim. Extrem.* **2015**, *10*, 1–9. [CrossRef]
10. Sillmann, J.; Thorarinsdottir, T.; Keenlyside, N.; Schaller, N.; Alexander, L.V.; Hegerl, G.; Seneviratne, S.I.; Vautard, R.; Zhang, X.; Zwiers, F.W. Understanding, Modeling and Predicting Weather and Climate Extremes: Challenges and Opportunities. *Weather Clim. Extrem.* **2017**, *18*, 65–74. [CrossRef]
11. Młyński, D.; Cebulska, M.; Wałęga, A. Trends, Variability, and Seasonality of Maximum Annual Daily Precipitation in the Upper Vistula Basin, Poland. *Atmosphere* **2018**, *9*, 313. [CrossRef]
12. Młyński, D.; Wałęga, A.; Petroselli, A.; Tauro, F.; Cebulska, M. Estimating Maximum Daily Precipitation in the Upper Vistula Basin, Poland. *Atmosphere* **2019**, *10*, 43. [CrossRef]
13. Twardosz, R.C.M. Temporal Variability of Maximum Monthly Precipitation Totals in the Polish Western Carpathian Mts during the Period 1951–2005. *Pr. Geogr.* **2012**, *128*, 123–134. [CrossRef]
14. Ziernicka-Wojtaszek, A.; Kopcińska, J. Variation in Atmospheric Precipitation in Poland in the Years 2001–2018. *Atmosphere* **2020**, *11*, 794. [CrossRef]
15. Venegas-Cordero, N.; Kundzewicz, Z.W.; Jamro, S.; Piniewski, M. Detection of Trends in Observed River Floods in Poland. *J. Hydrol. Reg. Stud.* **2022**, *41*, 101098. [CrossRef]
16. Kundzewicz, Z.W.; Radziejewski, M. Methodologies for Trend Detection. *IAHS-AISH Publ.* **2006**, *308*, 538–549.
17. Kundzewicz, Z.W.; Robson, A. Detecting Trend and Other Changes in Hydrological Data. *World Clim. Program.-Water* **2000**, *1013*, 158.
18. Berezowski, T.; Szczeniak, M.; Kardel, I.; Michalowski, R.; Okruszko, T.; Mezghani, A.; Piniewski, M. CPLFD-GDPT5: High-Resolution Gridded Daily Precipitation and Temperature Data Set for Two Largest Polish River Basins. *Earth Syst. Sci. Data* **2016**, *8*, 127–139. [CrossRef]
19. Twaróg, B. Characteristics of Multi-Annual Variation of Precipitation in Areas Particularly Exposed to Extreme Phenomena. Part 1. the Upper Vistula River Basin. *E3S Web Conf.* **2018**, *49*, 00121. [CrossRef]
20. Yu, Y.; He, F.; Vavrus, S.J.; Johnson, A.; Wu, H.; Zhang, W.; Yin, Q.; Ge, J.; Deng, C.; Petraglia, M.D.; et al. Climatic Factors and Human Population Changes in Eurasia between the Last Glacial Maximum and the Early Holocene. *Glob. Planet. Change* **2023**, *221*, 104054. [CrossRef]
21. Chen, T.; Zou, L.; Xia, J.; Liu, H.; Wang, F. Decomposing the Impacts of Climate Change and Human Activities on Runoff Changes in the Yangtze River Basin: Insights from Regional Differences and Spatial Correlations of Multiple Factors. *J. Hydrol.* **2022**, *615*, 128649. [CrossRef]
22. Szolgayova, E.; Parajka, J.; Blöschl, G.; Bucher, C. Long Term Variability of the Danube River Flow and Its Relation to Precipitation and Air Temperature. *J. Hydrol.* **2014**, *519*, 871–880. [CrossRef]
23. Pechlivanidis, I.G.; Olsson, J.; Bosshard, T.; Sharma, D.; Sharma, K.C. Multi-Basin Modelling of Future Hydrological Fluxes in the Indian Subcontinent. *Water* **2016**, *8*, 177. [CrossRef]
24. Mudelsee, M.; Börngen, M.; Tetzlaff, G.; Grünewald, U. Extreme Floods in Central Europe over the Past 500 Years: Role of Cyclone Pathway 'Zugstrasse Vb'. *J. Geophys. Res. D Atmos.* **2004**, *109*, D23101. [CrossRef]
25. Vavrus, S.J.; Notaro, M.; Lorenz, D.J. Interpreting Climate Model Projections of Extreme Weather Events. *Weather Clim. Extrem.* **2015**, *10*, 10–28. [CrossRef]
26. Angélil, O.; Perkins-Kirkpatrick, S.; Alexander, L.V.; Stone, D.; Donat, M.G.; Wehner, M.; Shiogama, H.; Ciavarella, A.; Christidis, N. Comparing Regional Precipitation and Temperature Extremes in Climate Model and Reanalysis Products. *Weather Clim. Extrem.* **2016**, *13*, 35–43. [CrossRef]
27. Michaelides, S.; Levizzani, V.; Anagnostou, E.; Bauer, P.; Kasparis, T.; Lane, J.E. Precipitation: Measurement, Remote Sensing, Climatology and Modeling. *Atmos. Res.* **2009**, *94*, 512–533. [CrossRef]
28. Das, N.; Bhattacharjee, R.; Choubey, A.; Ohri, A.; Dwivedi, S.B.; Gaur, S. Time Series Analysis of Automated Surface Water Extraction and Thermal Pattern Variation over the Betwa River, India. *Adv. Sp. Res.* **2021**, *68*, 1761–1788. [CrossRef]
29. Reinking, R.F. An Approach to Remote Sensing and Numerical Modeling of Orographic Clouds and Precipitation for Climatic Water Resources Assessment. *Atmos. Res.* **1995**, *35*, 349–367. [CrossRef]
30. López-Bermeo, C.; Montoya, R.D.; Caro-Lopera, F.J.; Díaz-García, J.A. Validation of the Accuracy of the CHIRPS Precipitation Dataset at Representing Climate Variability in a Tropical Mountainous Region of South America. *Phys. Chem. Earth Parts A/B/C* **2022**, *127*, 103184. [CrossRef]
31. Becker, A.; Finger, P.; Meyer-Christoffer, A.; Rudolf, B.; Schamm, K.; Schneider, U.; Ziese, M. A Description of the Global Land-Surface Precipitation Data Products of the Global Precipitation Climatology Centre with Sample Applications Including Centennial (Trend) Analysis from 1901-Present. *Earth Syst. Sci. Data* **2013**, *5*, 71–99. [CrossRef]
32. Gómez, J.D.; Etchevers, J.D.; Monterroso, A.I.; Gay, C.; Campo, J.; Martínez, M. Spatial Estimation of Mean Temperature and Precipitation in Areas of Scarce Meteorological Information. *Atmosfera* **2008**, *21*, 35–56.
33. Easterling, D.R.; Kunkel, K.E.; Wehner, M.F.; Sun, L. Detection and Attribution of Climate Extremes in the Observed Record. *Weather Clim. Extrem.* **2016**, *11*, 17–27. [CrossRef]
34. Guimares Nobre, G.; Jongman, B.; Aerts, J.; Ward, P.J. The Role of Climate Variability in Extreme Floods in Europe. *Environ. Res. Lett.* **2017**, *12*, 084012. [CrossRef]

35. Petrow, T.; Merz, B. Trends in Flood Magnitude, Frequency and Seasonality in Germany in the Period 1951–2002. *J. Hydrol.* **2009**, *371*, 129–141. [CrossRef]
36. Singh, P.; Gupta, A.; Singh, M. Hydrological Inferences from Watershed Analysis for Water Resource Management Using Remote Sensing and GIS Techniques. *Egypt. J. Remote Sens. Sp. Sci.* **2014**, *17*, 111–121. [CrossRef]
37. Zhang, X.; Vincent, L.A.; Hogg, W.D.; Niitsoo, A. Temperature and Precipitation Trends in Canada during the 20th Century. *Atmos.-Ocean* **2000**, *38*, 395–429. [CrossRef]
38. Karmeshu, N. Trend Detection in Annual Temperature & Precipitation Using the Mann Kendall Test—A Case Study to Assess Climate Change on Select States in the Northeastern United States. *Mausam* **2015**, *66*, 1–6.
39. Dankers, R.; Hiederer, R. Extreme Temperatures and Precipitation in Europe: Analysis of a High-Resolution Climate Change Scenario. *JRC Sci. Tech. Rep.* **2008**, *EUR 23291*, 82. Available online: https://www.semanticscholar.org/paper/Extreme-Temperatures-and-Precipitation-in-Europe:-a-Rutger-Roland/05a831272412d5e53311e230bf171ff5f63f1751 (accessed on 14 April 2023).
40. Katz, R.W.; Parlange, M.B. Overdispersion Phenomenon in Stochastic Modeling of Precipitation. *J. Clim.* **1998**, *11*, 591–601. [CrossRef]
41. Roy, S.S.; Balling, R.C. Trends in Extreme Daily Precipitation Indices in India. *Int. J. Climatol.* **2004**, *24*, 457–466. [CrossRef]
42. Colmet-Daage, A.; Sanchez-Gomez, E.; Ricci, S.; Llovel, C.; Estupina, V.B.; Quintana-Seguí, P.; Carmen Llasat, M.; Servat, E. Evaluation of Uncertainties in Mean and Extreme Precipitation under Climate Change for Northwestern Mediterranean Watersheds from High-Resolution Med and Euro-CORDEX Ensembles. *Hydrol. Earth Syst. Sci.* **2018**, *22*, 673–687. [CrossRef]
43. Bernstein, L.; Bosch, P.; Canziani, O.; Chen, Z.; Christ, R.; Davidson, O.; Hare, W.; Huq, S.; Karoly, D.; Kattsov, V.; et al. Climate Change 2007: An Assessment of the Intergovernmental Panel on Climate Change. *Change* **2007**, *446*, 12–17.
44. Pitt, M.A. Increased Temperature and Entropy Production in the Earth's Atmosphere: Effect on Wind, Precipitation, Chemical Reactions, Freezing and Melting of Ice and Electrical Activity. *J. Mod. Phys.* **2019**, *10*, 966–973. [CrossRef]
45. Knoben, W.J.M.; Woods, R.A.; Freer, J.E. Global Bimodal Precipitation Seasonality: A Systematic Overview. *Int. J. Climatol.* **2019**, *39*, 558–567. [CrossRef]
46. *WMO Guide to Climatological Practices 2018 Edition*; WMO: Geneva, Switzerland, 2018; ISBN 9789263101006.
47. Ross, S.M. *Introduction to Probability and Statistics*; Elsevier: Amsterdam, The Netherlands, 2014; ISBN 978-0-12-394811-3.
48. Hao, Z. Application of Entropy Theory in Hydrologic Analysis and Simulation. Ph.D. Thesis, Texas A&M University, College Station, TX, USA, May 2016.
49. Rica, C. Tropical Meteorology Research Programme (Tmrp) Commission for Atmospheric Sciences (CAS). *Int. Organ.* **2006**, *16*, 241–243. [CrossRef]
50. Kuhlman, T.; Farrington, J. What Is Sustainability? *Sustainability* **2010**, *2*, 3436–3448. [CrossRef]
51. Eizenberg, E.; Jabareen, Y. Social Sustainability: A New Conceptual Framework. *Sustainability* **2017**, *9*, 68. [CrossRef]
52. McCormick, K.; Kautto, N. The Bioeconomy in Europe: An Overview. *Sustainability* **2013**, *5*, 2589–2608. [CrossRef]
53. Velten, S.; Leventon, J.; Jager, N.; Newig, J. What Is Sustainable Agriculture? A Systematic Review. *Sustainability* **2015**, *7*, 7833–7865. [CrossRef]
54. Lewandowski, M. Designing the Business Models for Circular Economy-towards the Conceptual Framework. *Sustainability* **2016**, *8*, 43. [CrossRef]
55. Staffas, L.; Gustavsson, M.; McCormick, K. Strategies and Policies for the Bioeconomy and Bio-Based Economy: An Analysis of Official National Approaches. *Sustainability* **2013**, *5*, 2751–2769. [CrossRef]
56. Müller, J.M.; Kiel, D.; Voigt, K.I. What Drives the Implementation of Industry 4.0? The Role of Opportunities and Challenges in the Context of Sustainability. *Sustainability* **2018**, *10*, 247. [CrossRef]
57. Lahti, T.; Wincent, J.; Parida, V. A Definition and Theoretical Review of the Circular Economy, Value Creation, and Sustainable Business Models: Where Are We Now and Where Should Research Move in the Future? *Sustainability* **2018**, *10*, 2799. [CrossRef]
58. Schaubroeck, T.; Schaubroeck, S.; Heijungs, R.; Zamagni, A.; Brandão, M.; Benetto, E. Attributional & Consequential Life Cycle Assessment: Definitions, Conceptual Characteristics and Modelling Restrictions. *Sustainability* **2021**, *13*, 7386. [CrossRef]
59. Chapman, J. A Nonparametric Approach to Detecting Changes in Variance in Locally Stationary Time Series. *Environmetrics* **2020**, *31*, e2576. [CrossRef]
60. Thornton, P.K.; Ericksen, P.J.; Herrero, M.; Challinor, A.J. Climate Variability and Vulnerability to Climate Change: A Review. *Glob. Change Biol.* **2014**, *20*, 3313–3328. [CrossRef]
61. Swanson, K.L.; Tsonis, A.A. Has the Climate Recently Shifted? *Geophys. Res. Lett.* **2009**, *36*, L06711. [CrossRef]
62. Balhane, S.; Driouech, F.; Chafki, O.; Manzanas, R.; Chehbouni, A.; Moufouma-Okia, W. Changes in Mean and Extreme Temperature and Precipitation Events from Different Weighted Multi-Model Ensembles over the Northern Half of Morocco. *Clim. Dyn.* **2022**, *58*, 389–404. [CrossRef]
63. Mesbahzadeh, T.; Miglietta, M.M.; Mirakbari, M.; Soleimani Sardoo, F.; Abdolhoseini, M. Joint Modeling of Precipitation and Temperature Using Copula Theory for Current and Future Prediction under Climate Change Scenarios in Arid Lands (Case Study, Kerman Province, Iran). *Adv. Meteorol.* **2019**, *2019*, 6848049. [CrossRef]
64. Gerten, D.; Rost, S.; von Bloh, W.; Lucht, W. Causes of Change in 20th Century Global River Discharge. *Geophys. Res. Lett.* **2008**, *35*, 1–5. [CrossRef]
65. Walling, D.E. Human Impact on Land–Ocean Sediment Transfer by the World's Rivers. *Geomorphology* **2006**, *79*, 192–216. [CrossRef]

66. Hunter, T.S.; Clites, A.H.; Campbell, K.B.; Gronewold, A.D. Development and Application of a North American Great Lakes Hydrometeorological Database—Part I: Precipitation, Evaporation, Runoff, and Air Temperature. *J. Great Lakes Res.* **2015**, *41*, 65–77. [CrossRef]
67. Chai, Y.; Yue, Y.; Zhang, L.; Miao, C.; Borthwick, A.G.L.; Zhu, B.; Li, Y.; Dolman, A.J. Homogenization and Polarization of the Seasonal Water Discharge of Global Rivers in Response to Climatic and Anthropogenic Effects. *Sci. Total Environ.* **2020**, *709*, 136062. [CrossRef] [PubMed]
68. Li, Z.; Shi, Y.; Argiriou, A.A.; Ioannidis, P.; Mamara, A.; Yan, Z. A Comparative Analysis of Changes in Temperature and Precipitation Extremes since 1960 between China and Greece. *Atmosphere* **2022**, *13*, 1824. [CrossRef]
69. Jahn, M. Economics of Extreme Weather Events: Terminology and Regional Impact Models. *Weather Clim. Extrem.* **2015**, *10*, 29–39. [CrossRef]
70. Zhang, X.; Alexander, L.; Hegerl, G.C.; Jones, P.; Tank, A.K.; Peterson, T.C.; Trewin, B.; Zwiers, F.W. Indices for Monitoring Changes in Extremes Based on Daily Temperature and Precipitation Data. *Wiley Interdiscip. Rev. Clim. Change* **2011**, *2*, 851–870. [CrossRef]
71. Allan, R.P.; Soden, B.J. Atmospheric Warming and the Amplification of Precipitation Extremes. *Science* **2008**, *321*, 1481–1484. [CrossRef]
72. Christensen, J.H.; Kanikicharla, K.K.; Aldrian, E.; An, S.I.; Albuquerque Cavalcanti, I.F.; de Castro, M.; Dong, W.; Goswami, P.; Hall, A.; Kanyanga, J.K.; et al. Climate Phenomena and Their Relevance for Future Regional Climate Change. In *Climate Change 2013—The Physical Science Basis*; Working Group I Contribution to the Fifth Assessment Report of the Intergovernmental Panel on Climate Change; Cambridge University Press: Cambridge, UK, 2013; Volume 9781107057, pp. 1217–1308. [CrossRef]
73. Cardona, O.D.; Van Aalst, M.K.; Birkmann, J.; Fordham, M.; Mc Gregor, G.; Rosa, P.; Pulwarty, R.S.; Schipper, E.L.F.; Sinh, B.T.; Décamps, H.; et al. Determinants of Risk: Exposure and Vulnerability. In *Managing the Risks of Extreme Events and Disasters to Advance Climate Change Adaptation*; Special Report of the Intergovernmental Panel on Climate Change; Cambridge University Press: Cambridge, UK, 2012; Volume 9781107025, pp. 65–108. [CrossRef]
74. Kolokytha, E.; Oishi, S.; Teegavarapu, R.S.V. *Sustainable Water Resources Planning and Management under Climate Change*; Kolokytha, E., Ed.; Springer Science+Business Media: Singapore, 2016; ISBN 9789811020513.
75. Powell, J.P.; Reinhard, S. Measuring the Effects of Extreme Weather Events on Yields. *Weather Clim. Extrem.* **2015**, *12*, 69–79. [CrossRef]
76. Lal, P.N.; Mitchell, T.; Aldunce, P.; Auld, H.; Mechler, R.; Miyan, A.; Romano, L.E.; Zakaria, S.; Dlugolecki, A.; Masumoto, T.; et al. *National Systems for Managing the Risks from Climate Extremes and Disasters*; Cambridge University Press: Cambridge, UK, 2012; Volume 9781107025, ISBN 9781139177245.
77. Knapp, A.K.; Beier, C.; Briske, D.D.; Classen, A.T.; Yiqi, L.; Reichstein, M.; Smith, M.D.; Smith, S.D.; Bell, J.E.; Fay, P.A.; et al. Consequences of More Extreme Precipitation Regimes for Terrestrial Ecosystems. *Bioscience* **2008**, *58*, 811–821. [CrossRef]
78. Sitthiyot, T.; Holasut, K. A Simple Method for Measuring Inequality. *Palgrave Commun.* **2020**, *6*, 112. [CrossRef]
79. Vermeulen, S.J.; Challinor, A.J.; Thornton, P.K.; Campbell, B.M.; Eriyagama, N.; Vervoort, J.M.; Kinyangi, J.; Jarvis, A.; Läderach, P.; Ramirez-Villegas, J.; et al. Addressing Uncertainty in Adaptation Planning for Agriculture. *Proc. Natl. Acad. Sci. USA* **2013**, *110*, 8357–8362. [CrossRef] [PubMed]
80. Ramirez-Villegas, J.; Lau, C.; Köhler, A.K.; Signer, J.; Jarvis, A.; Arnell, N.W.; Osborne, T.M.; Hooker, J. Climate Analogues: Finding Tomorrow's Agriculture Today. *Work. Pap. No. 12* **2011**, *12*, 40.
81. Matos, S.; Viardot, E.; Sovacool, B.K.; Geels, F.W.; Xiong, Y. Innovation and Climate Change: A Review and Introduction to the Special Issue. *Technovation* **2022**, *117*, 102612. [CrossRef]
82. Pfleiderer, P.; Schleussner, C.F.; Mengel, M.; Rogelj, J. Global Mean Temperature Indicators Linked to Warming Levels Avoiding Climate Risks. *Environ. Res. Lett.* **2018**, *13*, 059501. [CrossRef]
83. Stephan, G. Intergenerational Fairness and Climate Change Adaptation Policy: An Economic Analysis. *Green Low-Carbon Econ.* **2023**, *1*, 105–109. [CrossRef]
84. Langdon, J.G.R.; Lawler, J.J. Assessing the Impacts of Projected Climate Change on Biodiversity in the Protected Areas of Western North America. *Ecosphere* **2015**, *6*, 1–14. [CrossRef]
85. Nicolli, F.; Gilli, M.; Vona, F. Inequality and Climate Change: Two Problems, One Solution. *Fond. Eni Enrico Mattei Inequal.* **2023**. [CrossRef]
86. Twaróg, B. Application of Shannon Entropy in Precipitation Conditions and Application of Shannon Entropy in Assessing Changes in Precipitation Conditions and Temperature Based on Long-Term Sequences Using the Bootstrap Method. *Atmosphere* **2024**, *15*, 898. [CrossRef]
87. Hosseinzadehtalaei, P.; Tabari, H.; Willems, P. Climate Change Impact on Short-Duration Extreme Precipitation and Intensity–Duration–Frequency Curves over Europe. *J. Hydrol.* **2020**, *590*, 125249. [CrossRef]
88. Persson, J.; Blennow, K.; Gonçalves, L.; Borys, A.; Dutca, I.; Hynynen, J.; Janeczko, E.; Lyubenova, M.; Martel, S.; Merganic, J.; et al. No Polarization-Expected Values of Climate Change Impacts among European Forest Professionals and Scientists. *Sustainability* **2020**, *12*, 2659. [CrossRef]
89. Rudolf, B.; Beck, C.; Grieser, J.; Schneider, U. Global Precipitation Analysis Products of the GPCC. *Internet Publ.* **2005**, *112*, 3819–3837.

90. Arheimer, B.; Pimentel, R.; Isberg, K.; Crochemore, L.; Andersson, J.C.M.; Hasan, A.; Pineda, L. Global Catchment Modelling Using World-Wide HYPE (WWH), Open Data, and Stepwise Parameter Estimation. *Hydrol. Earth Syst. Sci.* **2020**, *24*, 535–559. [CrossRef]
91. Iverson, L.R.; McKenzie, D. Tree-Species Range Shifts in a Changing Climate: Detecting, Modeling, Assisting. *Landsc. Ecol.* **2013**, *28*, 879–889. [CrossRef]
92. Franklin, J. Mapping Species Distributions: Spatial Inference and Prediction. *Oryx* **2010**, *44*, 615. [CrossRef]
93. Viner, D.; Ekstrom, M.; Hulbert, M.; Warner, N.K.; Wreford, A.; Zommers, Z. Understanding the Dynamic Nature of Risk in Climate Change Assessments—A New Starting Point for Discussion. *Atmos. Sci. Lett.* **2020**, *21*, e958. [CrossRef]
94. Rosenzweig, C.; Parry, M. Potential Impact of Climate Change on World Food Supply. *Nature* **1992**, *367*, 133–138. [CrossRef]
95. Tabari, H.; Willems, P. Lagged Influence of Atlantic and Pacific Climate Patterns on European Extreme Precipitation. *Sci. Rep.* **2018**, *8*, 5748. [CrossRef]
96. Gibbins, G.; Haigh, J.D. Entropy Production Rates of the Climate. *J. Atmos. Sci.* **2020**, *77*, 3551–3566. [CrossRef]
97. Kharin, V.V.; Zwiers, F.W.; Zhang, X.; Wehner, M. Changes in Temperature and Precipitation Extremes in the CMIP5 Ensemble. *Clim. Change* **2013**, *119*, 345–357. [CrossRef]
98. Verstraeten, G.; Poesen, J.; Demarée, G.; Salles, C. Long-Term (105 Years) Variability in Rain Erosivity as Derived from 10-Min Rainfall Depth Data for Ukkel (Brussels, Belgium): Implications for Assessing Soil Erosion Rates. *J. Geophys. Res. Atmos.* **2006**, *111*, 1–11. [CrossRef]
99. Lovell, R.S.L.; Blackburn, T.M.; Dyer, E.E.; Pigot, A.L. Environmental Resistance Predicts the Spread of Alien Species. *Nat. Ecol. Evol.* **2021**, *5*, 322–329. [CrossRef] [PubMed]
100. Stocker, T.F.; Clarke, G.K.C.; Le Treut, H.; Lindzen, R.S.; Meleshko, V.P.; Mugara, R.K.; Palmer, T.N.; Pierrehumbert, R.T.; Sellers, P.J.; Trenberth, K.E.; et al. Physical Climate Processes and Feedbacks. In *Climate Change 2001: The Scientific Basis*; Contribution of Working Group I to the Third Assessment Report of the Intergovernmental Panel on Climate Change; Cambridge University Press: Cambridge, UK, 2001; Volume 881, pp. 419–457.
101. Chen, L.; Guo, S. *Copulas and Its Application in Hydrology and Water Resources*; Springer: Singapore, 2019; ISBN 978-981-13-0573-3.
102. Hou, W.; Yan, P.; Feng, G.; Zuo, D. A 3D Copula Method for the Impact and Risk Assessment of Drought Disaster and an Example Application. *Front. Phys.* **2021**, *9*, 656253. [CrossRef]
103. Santos-Gómez, J.D.; Fontalvo-García, J.S.; Giraldo Osorio, J.D. Validating the University of Delaware's Precipitation and Temperature Database for Northern South America. *Dyna* **2015**, *82*, 86–95. [CrossRef]
104. Amiel, Y.; Cowell, F. *Thinking about Inequality*; Cambridge University Press: Cambridge, UK; New York, NY, USA, 1999; ISBN 9780511492266.
105. Lorenz, M.O. Methods of Measuring the Concentration of Wealth. *Publ. Am. Stat. Assoc.* **1905**, *9*, 209–219. [CrossRef]
106. Mccright, A.M.; Dunlap, R.E. The Politicization of Climate Change and Polarization in the American Public's Views of Global Warming, 2001–2010. *Sociol. Q.* **2011**, *52*, 155–194. [CrossRef]
107. Ogwang, T. Calculating a Standard Error for the Gini Coefficient: Some Further Results: Reply. *Oxf. Bull. Econ. Stat.* **2004**, *66*, 435–437. [CrossRef]
108. Damgaard, C.; Weiner, J. Describing Inequality in Plant Size or Fecundity. *Ecology* **2000**, *81*, 1139. [CrossRef]
109. Panek, T. Polaryzacja Ekonomiczna w Polsce. *Wiadomości. Stat.* **2017**, *1*, 41–62.
110. Samson, P.-M. *Concentration of Measure Principle and Entropy-Inequalities*; Springer: New York, NY, USA, 2017; ISBN 9781493970049.
111. Yitzhaki, S. Gini's Mean Difference: A Superior Measure of Variability for Non-Normal Gini's Mean Difference: A Superior Measure of Variability for Non-Normal Distributions. *Metron. Lxi* **2016**, *2*, 285–316.
112. Conceição, P.; Ferreira, P. Young Person's Guide to the Theil Index: Suggesting Intuitive Interpretations and Exploring Analytical Applications. *World* **2000**, 1–54. [CrossRef]
113. Buishand, T.A. Some Methods for Testing the Homogeneity of Rainfall Records. *J. Hydrol.* **1982**, *58*, 11–27. [CrossRef]
114. Chen, J.; Gupta, A.K. Parametric Statistical Change Point Analysis. 2013–2015. *Angew. Chemie Int. Ed.* **2021**, *6*, 951–952. [CrossRef]
115. Radziejewski, M.; Bardossy, A.; Kundzewicz, Z.W. Detection of Change in River Flow Using Phase Randomization. *Hydrol. Sci. J.* **2000**, *45*, 547–558. [CrossRef]
116. Salarijazi, M. Trend and Change-Point Detection for the Annual Stream-Flow Series of the Karun River at the Ahvaz Hydrometric Station. *African J. Agric. Res.* **2012**, *7*, 4540–4552. [CrossRef]
117. Pettitt, A.N. A Non-Parametric Approach to the Change-Point Problem. *J. R. Stat. Soc. Ser. C Appl. Stat.* **1979**, *28*, 126–135. [CrossRef]
118. Conte, L.C.; Bayer, D.M.; Bayer, F.M. Bootstrap Pettitt Test for Detecting Change Points in Hydroclimatological Data: Case Study of Itaipu Hydroelectric Plant, Brazil. *Hydrol. Sci. J.* **2019**, *64*, 1312–1326. [CrossRef]
119. Mann, H.B. Nonparametric Tests Against Trend. *Econometrica* **1945**, *13*, 245–259. [CrossRef]
120. Yue, S.; Pilon, P.; Phinney, B.; Cavadias, G. The Influence of Autocorrelation on the Ability to Detect Trend in Hydrological Series. *Hydrol. Process.* **2002**, *16*, 1807–1829. [CrossRef]
121. Sen, P.K. Estimates of the Regression Coefficient Based on Kendall's Tau. *J. Am. Stat. Assoc.* **1968**, *63*, 1379–1389. [CrossRef]
122. Hirsch, R.M.; Slack, J.R.; Smith, R.A. Techniques of Trend Analysis for Monthly Water Quality Data. *Water Resour. Res.* **1982**, *18*, 107–121. [CrossRef]

123. Production and Consumption Gross Energy Consumption by Source. Available online: https://statice.is/statistics/environment/energy/production-and-consumption/ (accessed on 14 April 2023).
124. Everett, K.; Hardick, E.; Johnson, D. *The Year of Africa*; The African Presence; The Ohio State University: Columbus, OH, USA, 2018; pp. 1–24. [CrossRef]
125. Khanin, G.I. The 1950s: The Triumph of the Soviet Economy. *Eur. Asia. Stud.* **2003**, *55*, 1187–1211. [CrossRef]
126. Levy, M.; Stewart, D.E.; Kent, C.H.W. Encyclopedia Britannica. 2023, pp. 1–15. Available online: https://www.britannica.com/topic/Encyclopaedia-Britannica-English-language-reference-work (accessed on 14 April 2024).
127. Love, J.L. The Rise and Decline of Economic Structuralism in Latin America: New Dimensions. *Lat. Am. Res. Rev.* **2023**, *40*, 100–125. [CrossRef]
128. van Eck, C.W.; Mulder, B.C.; Dewulf, A. Online Climate Change Polarization: Interactional Framing Analysis of Climate Change Blog Comments. *Sci. Commun.* **2020**, *42*, 454–480. [CrossRef]
129. Beck, H.E.; Zimmermann, N.E.; McVicar, T.R.; Vergopolan, N.; Berg, A.; Wood, E.F. Present and Future Köppen-Geiger Climate Classification Maps at 1-Km Resolution. *Sci. Data* **2018**, *5*, 180214. [CrossRef]
130. Kottek, M.; Grieser, J.; Beck, C.; Rudolf, B.; Rubel, F. World Map of the Köppen-Geiger Climate Classification Updated. *Meteorol. Z.* **2006**, *15*, 259–263. [CrossRef] [PubMed]

Disclaimer/Publisher's Note: The statements, opinions and data contained in all publications are solely those of the individual author(s) and contributor(s) and not of MDPI and/or the editor(s). MDPI and/or the editor(s) disclaim responsibility for any injury to people or property resulting from any ideas, methods, instructions or products referred to in the content.

agronomy

MDPI

Article

Analysis of Future Drought Risk and Wheat Meteorological Disaster in Ningxia (Northwest China) Based on CMIP6 and SPEI

Xinlong Li [1], Junli Tan [1,2,3,*], Xina Wang [4], Qian Shang [1], Hao Li [1] and Xuefang Li [1]

[1] College of Civil and Hydraulic Engineering, Ningxia University, Yinchuan 750021, China; lixinlong9905@163.com (X.L.); 18236441048@163.com (Q.S.); lihao053871@163.com (H.L.); flxx1606@163.com (X.L.)
[2] Ministry of Education Engineering Research Center for Efficient Utilization of Modern Agricultural Water Resources in Arid Regions, Yinchuan 750021, China
[3] Ningxia Engineering Technology Research Center of Water-Saving Irrigation and Water Resources Regulation, Yinchuan 750021, China
[4] College of Agriculture, Ningxia University, Yinchuan 750021, China; eunicexina-w@163.com
* Correspondence: tanjl@nxu.edu.cn; Tel.: +86-15109613396

Abstract: In arid areas, droughts caused by climate change seriously impact wheat production. Therefore, research on spatial and temporal variability of dry and hot wind events and drought risk under different development patterns of future climate can provide a reference for wheat cultivation planning in the study area. Based on meteorological data under three scenarios of the CMIP6 (Sixth International Coupled Model Comparison Program) shared socio-economic path (SSP), we introduced wheat dry hot wind discrimination criteria and calculated the Standardized Precipitation–Evapotranspiration Index (SPEI). Future temperature changes within the Ningxia Province were consistent, increasing at a rate of 0.037, 0.15 and 0.45 °C·(10 a^{-1}) under SSP126, 245 and 585 scenarios, respectively. Simultaneously, average annual precipitation would increase by 17.77, 38.73 and 32.12 mm, respectively. Dry hot wind frequency differed spatially, being higher in northern Ningxia and western Ningxia, and lower in southern Ningxia and eastern Ningxia. During the wheat growing period, there is an obvious increasing drought risk trend under the SSP585 model in May, and the possibility of drought risk in the middle period was highest under the SSP126 model. In June, SPEI was generally higher than in May, and the risk of alternating drought and flood was greater under the SSP585 model, while near-medium drought risk was lower under the SSP126 and SSP245 models. The influence of DHW (dry and hot wind) on wheat yield will increase with the increase of warming level. However, when DHW occurs, effective irrigation can mitigate the harm. Irrigation water can be sourced from various channels, including rainfall, diversion, and groundwater. These results provide scientific reference for sustainable agricultural production, drought risk and wheat meteorological disaster forecast in inland arid areas affected by climate change.

Keywords: drought disaster risk; dry hot wind; spatiotemporal variation; wheat

1. Introduction

Drought is a major cause of economic, environmental and agricultural losses [1]. Many studies suggest that the effects of future global warming will intensify. The risk of various disasters caused by continuous drought has become a major threat to human beings [2–4]. While any high temperature, low humidity or high wind speed extremes can negatively impact agricultural production, a combination of these can more severely impact crop yields [5]. It has been recorded that the frequency of dry hot wind (DHW) in China has been increasing in recent years due to climate warming [6,7]. Therefore, appropriate methodologies are required to accurately assess likely future drought trends

under different development models [8]. Dry hot wind (DHW) events can directly lead to wheat water imbalance, flower abortion and inhibit grain carbohydrate synthesis [9]. Furthermore, increased DHW frequency [10] may lead to late wheat seeding and shorter growing season [11,12], thus reducing crop yield per unit area [13]. Wheat is an important grain crop in the Ningxia irrigation area, where its output reaches 346,000 tons, accounting for 9% of the total grain output. DHW events mainly occur during the wheat mature growth stage [14]. To ensure stable wheat harvests and food security, it is critical to systematically assess the future frequency and spatiotemporal changes in DHW events.

Chinese research on DHW events began in the late 1950s [15], and by the early 1980s, the cooperative research group on the impact of DHW on wheat in north China made remarkable achievements in the DHW meteorological index and its damage mechanism. Previous studies have shown that the frequency of wheat DHW events in Ningxia has been increasing in the last 40 years, and the Z value of the trend test was greater than 0 at all experimental stations [16]. Additionally, Liu et al. [12] introduced wheat dry hot wind indices in the Ningxia irrigation area of the Yellow River diversion, while others explored ways to quantify DHW effects on wheat growth and yield through modeling and empirical studies [17]. Zhao et al. [18] found that average maximum temperature had the greatest influence on the key wheat phenological periods, followed by relative humidity and solar radiation, and the least sensitive climatic factors were precipitation, wind speed and reference crop evapotranspiration. Li et al. [9] found that spraying phosphorus and a sugar preparation on leaves alleviated the dry hot wind effect on winter wheat. Current studies are still limited to exploring DHW formation and mechanisms [19] and analyzing DHW spatiotemporal characteristics and changes in historical periods [12]. However, it is inadequate to simply combine local DHW changes with those caused by future global warming. Therefore, we combined these changes with CMIP6 data to analyze future DHW temporal and spatial changes in Ningxia during wheat growing period under different development paths, to provide references for prediction and prevention of DHW meteorological disasters.

Additionally, it is insufficient to discuss only DHW changes for the analysis of drought caused by future complex climate change. Quantification and classification of drought disasters are also important for prospective planning (risk analysis) and retrospective analysis [20]. As the need to understand weather and climate grows, so does the need for consistent quantitative procedures for extreme drought disaster mitigation and monitoring. Therefore, it is necessary to re-classify single-value drought by incorporating indices such as precipitation, temperature and evapotranspiration [20]. The standardized precipitation–evapotranspiration coefficient (SPEI) is based on precipitation and evapotranspiration, and has been widely used in drought disaster grade assessment research [21]. The reference evapotranspiration is calculated according to the Penman–Monteith formula [22]. SPEI uses a more comprehensive measure of water availability and climate water balance than the Standardized Precipitation Index (SPI). Therefore, drought disaster assessment has great potential [23], and many studies have assessed drought risk based on SPEI changes. Tan et al. used CMIP5 data combined with SPEI to analyze drought disaster risk in Ningxia Hui Autonomous Region under an RCP scenario [24]. Chen et al. used the Thornthwaite method and Penman–Monteith equation to calculate reference evapotranspiration, and calculated and compared the influence of the two methods on SPEI [25]. Li et al. used SPEI to analyze drought spatiotemporal evolution characteristics at different time scales in Yunnan Province [26]. Existing studies have proved that SPEI is suitable for evaluating drought risk levels over long time scales. However, to cope with future drought disasters and reduce their impacts, it is crucial to quantitatively predict their future risk, so we used SPEI to quantitatively assess drought disaster risk in Ningxia Province. Based on DHW and SPEI, drought hazard risk temporal and spatial changes under different development paths were analyzed, and especially during future wheat growing periods. Time variation characteristics were tested by Mann–Kendall, and GIS visualization spatial change characteristics were determined by the Kriging interpolation method. Using Global Climate Model (GCM)

climate data and three representative shared socio-economic approach (SSP) scenarios, we predicted future drought hazards and their risk levels in Ningxia. This study's innovation lies in its novel approach of using historical meteorological data as a reference to process future CMIP6 meteorological data through machine learning. This method not only aligns more closely with the actual meteorological changes in the study area, but also preserves the essential characteristics of these changes, thereby enhancing the data's credibility. By analyzing the frequency of dry hot wind (DHW) events and the variations in the Standardized Precipitation–Evapotranspiration Index (SPEI) during the future period, this study aims to explore the impacts of drought risk on wheat production. This research not only provides valuable data support for drought risk management in other regions, but also offers a methodology that can be extended and applied to other areas, contributing to scientific references for sustainable agricultural production and drought risk evaluate in inland arid regions affected by climate change.

2. Materials and Methods

2.1. Study Area

Ningxia is located in northwest China, in the upper reaches of the Yellow River (between 35°14′–39°23′ N and 104°17′–107°39′ E). It is located on the western edge of China's monsoon region and has a typical continental climate. Because of the barrier of Helan Mountain in the west, it retains the precipitation brought by the monsoon, and the abundant water resources brought by the Yellow River, so Ningxia lives up to the reputation of being the Oasis Beyond the Great Wall, and is one of the main production areas of spring wheat in China. However, the drought disaster caused by the typical high temperature and strong wind in northwest China has a great impact on the actual wheat production, so Ningxia Province is selected as the research area in this study. The northern part of the study area belongs to the plain area, located in the middle and upper reaches of the Yellow River, with good irrigation conditions. The central part is more arid due to low precipitation and high evaporation, and is far away from the irrigation water source. The southern part is at a higher elevation, with sufficient rainfall but lower temperatures, and the soil is more infertile. According to landform, climate, vegetation and agricultural production types, Ningxia can be divided into three agricultural ecological types: the Yellow River diversion irrigation area, the central arid area and the southern mountainous area (Figure 1). We selected the longitude and latitude coordinates of 12 major agricultural experimental sites in the research area as research test locations (Table 1).

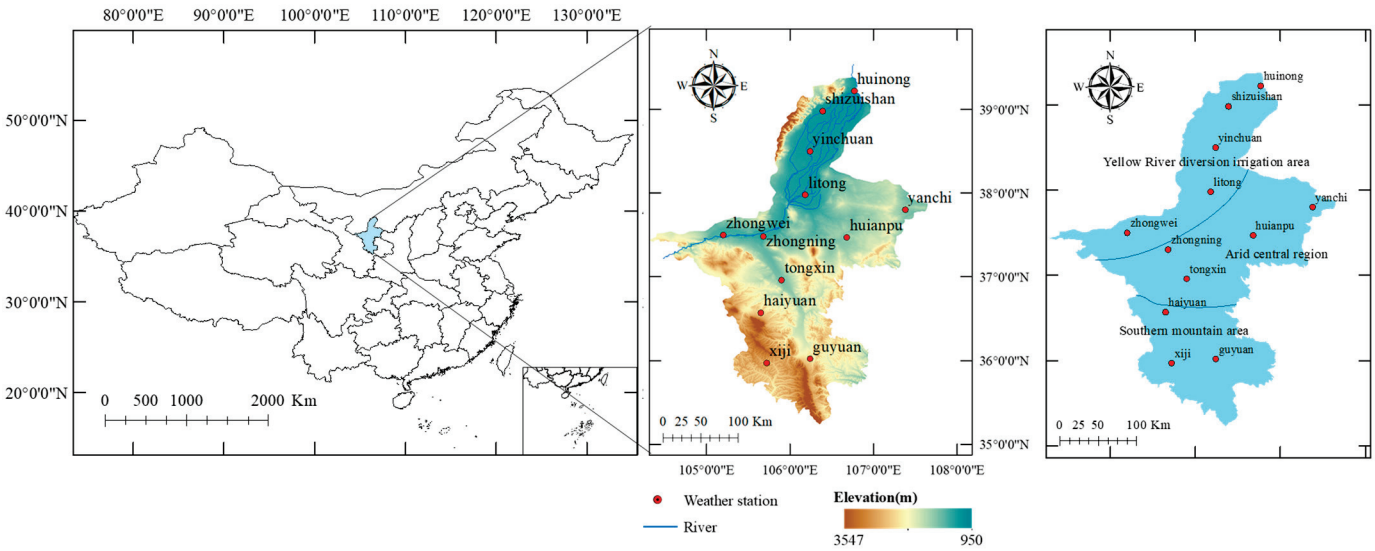

Figure 1. Geographical location, agro-ecological area distribution and DEM elevation of the study area.

Table 1. Information of latitude and longitude of test sites in the study area.

Agro-Ecological Region	Site Name	Latitude	Longitude	Elevation (m)
Ningxia Yellow River diversion irrigation area	huinong	39.22	106.77	1091
	shizuishan	38.98	106.39	1101.6
	yinchuan	38.5	106.24	1111.4
	zhongwei	37.5	105.2	1225.7
Arid area of central Ningxia	litong	37.98	106.18	1127.7
	zhongning	37.48	105.68	1183.3
	yanchi	37.8	107.38	1347.8
	tongxin	36.96	105.9	1343.9
Southern mountainous area of Ningxia	huianpu	37.47	106.68	1512.3
	xiji	35.97	105.72	1916.5
	guyuan	36.02	106.24	1753.2
	haiyuan	36.57	105.65	1853.7

2.2. Data Sources

We obtained historical daily meteorological data from 2001 to 2019 from the National Data Center for Meteorological Sciences (http://data.cma.cn, accessed on 18 December 2024). Wheat yield data by region were acquired from the National Statistics Center of China (https://www.stats.gov.cn/, accessed on 18 December 2024) and the China Statistical Yearbook. Future meteorological data were derived from global climate models (GCMs) provided by the World Climate Research Programme (WCRP), encompassing three future periods: short-term (ST, 2021–2045), middle-term (MT, 2046–2070) and long-term (LT, 2071–2098). GCMs were developed under the sixth phase of the Coupled Model Intercomparison Project (CMIP6; https://pcmdi.llnl.gov/CMIP6/, accessed on 18 December 2024) sixth assessment report (CMIP6-IPCC-AR6) [27]. The sixth Assessment report proposes five new climate change scenarios based on shared socio-economic pathways (SSPs), namely, SSP119, SSP126, SSP245, SSP370 and SSP585. We solely focused on investigating representative future climate scenario models, including the low (SSP126), medium (SSP245) and high warming level (SSP585) scenarios. SSP126 is an optimistic estimate predicated on effectively controlling global warming levels, SSP245 scenario represents future climate projections for countries predominantly pursuing sustainable development, and SSP585 scenario captures the ramifications of unconventional advancements. Meteorological variables selected for analysis included precipitation (pr, mm/s), surface down-welling shortwave radiation (rsds, MJ/m^2·day), surface wind speed (sfcWind, m/s), daily minimum near-surface recorded air temperature (T_{min}, Kelvin) and daily maximum near-surface air temperature (T_{max}, Kelvin). Temperature, rainfall and radiation data were obtained according to 0 °C = 273.15 Kelvin; 86,400 mm/s = 1 mm/day; 1 W/m^2·s = 11.574 MJ/m^2·day to convert to daily meteorological data. In the conducted study, we trained the machine learning model with Yinchuan 2015~2018 measured meteorological data and CMIP6 data, and used 2019~2022 CMIP6 data as the input of the trained machine learning model, and compared the results of eight machine learning methods on different kinds of meteorological data using the measured meteorological data as a reference. According to the results of the RMSE, lasso regression, support vector machine, neural network and random forest methods were selected to process RSDS, T_{min}, T_{max} and sfcWind data, respectively, in CMIP6 from 2020 to 2100. For detailed insights into the process and outcomes of applying machine learning methodologies to process CMIP6 data, please refer to the provided references [28]. The data for the selected GCM variables were all derived under an initial field of r1i1p1f1 (an experimental field with 1 for the number of runs, initial conditions, physical scheme and forcing data within the model).

2.3. DHW Discriminant Indices

According to Ningxia climatic characteristics and hazard nature [12], we determined the DHW indices. A maximum temperature tasmax $\geq$ 32 °C, minimum relative humidity hurs $\leq$ 30% and wind speed sfcWind $\geq$ 2 m/s on the day from the wheat filling stage to

the maturity stage was deemed a light DHW day. Under these conditions, transpiration of wheat is enhanced and plant water loss is accelerated, affecting photosynthesis and nutrient accumulation, which leads to insufficient irrigation of wheat kernels and lower thousand-grain weight, ultimately affecting yield and quality. If tasmax $\geq$ 34 °C, hurs $\leq$ 25% and sfcWind $\geq$ 3 m/s, it was deemed to be a heavy DHW day. Such conditions can cause rapid water loss in wheat plants, curling or even drying out of leaves, leading to premature cessation of growth and withering of seeds before they are fully ripe, which not only affects wheat plumping, but may also lead directly to early maturity and green blight, resulting in severe yield loss. Meteorological factors for the spring and winter wheat filling period in Ningxia were analyzed to determine the number of DHW meteorological days during the wheat growing period.

2.4. Standardized Precipitation–Evapotranspiration Index (SPEI)

SPEI is a new drought index proposed by Vicente-Serrano et al. [29], based on precipitation and temperature data with the advantage of combining multi-scalar features with the ability to include the effects of temperature changes on drought assessment. SPEI combines the trend and multi-temporal nature of the SPI with the sensitivity of the Palmer Drought Index (PDSI) to changes in evaporation due to temperature fluctuations. SPEI reflects the climate water balance on different time scales, with positive values indicating wetness and negative values indicating dryness. Under global warming, only PDSI and SPEI can show that increased drought severity is related to increased evapotranspiration. However, compared to PDSI, SPEI has the advantage of multiple scalars, which is crucial for drought analysis and monitoring. Since the FAO-56 Penman–Monteith (PM) equation accounts for not only temperature, but also the effects of wind speed and relative humidity in calculating Potential Evapotranspiration (PET), it is considered more physically accurate than the Thornthwaite equation, which solely considers temperature. Consequently, for the calculation of the Standardized Precipitation–Evapotranspiration Index (SPEI), the FAO-PM equation is used instead of the Thornthwaite equation. We used CMIP6 meteorological data to calculate monthly SPEI; soil water-holding capacity is not taken into account in crop drought impact assessments. Since wheat fertility in the study area is affected by dry weather concentrated in May, June and July, this study focused on the analysis of SPEI in May, June and July, when DHWs occur in wheat. The specific value can be calculated by the following formula:

$$D = P_i - PET_i \tag{1}$$

$$D_n^k = \sum_{i=0}^{k-1} P_{n-i} - PET_{n-i} \tag{2}$$

where D is the difference between potential evapotranspiration PET and precipitation P, k is the time scale (month) and n is the month of calculation. D^k represents the aggregate value of D on a time scale k. According to the Log-logistic distribution, the probability distribution function of D is given by the following formula:

$$F(x) = \left[1 + \left(\frac{\alpha}{x - \gamma}\right)^{\beta}\right]^{-1} \tag{3}$$

where α, β and γ are the scale, shape and origin parameters of the D value in the range, respectively. The $SPEI$ value is calculated by:

$$SPEI = W - \frac{C_0 + C_1 W + C_2 W^2}{1 + d_1 W + d_2 W + d_3 W^3} \tag{4}$$

where C_0 = 2.515517, C_1 = 0.802853, C_2 = 0.010328, d_1 = 1.432788, d_2 = 0.189269 and d_3 = 0.001308. The mean $SPEI$ is 0 and the standard deviation is 1. $SPEI$ is a standardized variable, so it can be compared with other $SPEI$ values over time and space.

The correlation test for the two sets of observations [30] is described below. The statistic S is calculated according to the formula.

$$S = \sum_{i=1}^{n-1} \sum_{j=i+1}^{n} \mathrm{sgn}(x_j - x_i) \quad (5)$$

where x_i and x_j are the sequential sequencing values, and n is the number of data sets.

2.5. WOFOST Model Optimization Method

The WOFOST model was jointly developed by Wageningen University and the World Food Research Center (CWFS) in the Netherlands. It is applicable to most crops by utilizing different crop parameters. The model's calculations are primarily performed through three modules: climate, crop and soil. Using daily meteorological data, the model incorporates dynamic explanatory variables for growth, including soil, management and crop parameters [31]. This allows the simulation of crop growth under three scenarios: optimal conditions, water-limited conditions and nutrient-limited conditions. The previous study calibrated the crop parameters of the WOFOST model based on changes in measured wheat yields and leaf area index (LAI), and validated the simulation of potential wheat yields (with adequate water and nutrient supply) in conjunction with the soil and meteorological conditions of the experimental sites. Crop parameters for the WOFOST model are selected as outlined in Table 2. Details on the optimization method and verification process of these model parameters can be found in Ref. [32].

Table 2. WOFOST model crop parameter values.

Crop Parameter	**AMAXTB0 ($kg \cdot hm^{-2} \cdot h^{-1}$)**	**AMAXTB1 ($kg \cdot hm^{-2} \cdot h^{-1}$)**	**AMAXTB1.3 ($kg \cdot hm^{-2} \cdot h^{-1}$)**	**CVO ($kg \cdot kg^{-1}$)**	**CVL ($kg \cdot kg^{-1}$)**
Significance	Maximum CO_2 assimilation rate at growth stage 0	Maximum CO_2 assimilation rate at growth stage 1	Maximum CO_2 assimilation rate at growth stage 1.3	Efficiency of dry matter conversion to seed	Efficiency of dry matter conversion to leaves
Value	35.25283831	39.0031	38.17566	0.765686	0.667321425
Parameter	CVS ($kg \cdot kg^{-1}$)	CVR ($kg \cdot kg^{-1}$)	EFFTB0 ($kg \cdot hm^{-2} \cdot h^{-1} \cdot J^{-1} \cdot m^2 \cdot s$)	EFFTB40 ($kg \cdot hm^{-2} \cdot h^{-1} \cdot J^{-1} \cdot m^2 \cdot s$)	KDIFTB0
Significance	Efficiency of conversion of dry matter to stems	Efficiency of dry matter conversion to roots	Single-leaf light energy utilization at 0 °C	Single-leaf light energy utilization at 40 °C	Scattered light extinction coefficient at growth stage 0
Value	0.72464208	0.667882	0.487338	0.476887	0.573684886
Parameter	KDIFTB2	SPAN (d)	SLATB0 ($hm^2 \cdot kg^{-1}$)	SLATB0.5 ($hm^2 \cdot kg^{-1}$)	SLATB2 ($hm^2 \cdot kg^{-1}$)
Significance	Scattered light extinction coefficient at growth stage 2	Leaf life cycle at 35 °C	Specific leaf area at growth stage 0	Specific leaf area at growth stage 0.5	Specific leaf area at growth stage 2
Value	0.654334798	33.02043	0.002004	0.001944	0.002072466
Parameter	TMPFTB0	TMPFTB10	TMPFTB15	TMPFTB25	TMPFTB35
Significance	Maximum CO_2 assimilation rate discount factor at mean temperature 0 °C	Maximum CO_2 assimilation rate discount factor at mean temperature 10 °C	Maximum CO_2 assimilation rate discount factor at mean temperature 15 °C	Maximum CO_2 assimilation rate discount factor at mean temperature 25 °C	Maximum CO_2 assimilation rate discount factor at mean temperature 35 °C
Value	0.099834809	0.56683	0.937174	0.956712	0.015038988
Parameter	TBASE	TSUM1 (°C·d)	TSUM2 (°C·d)	TMNFTB0	TMNFTB3
Significance	Minimum temperature for seedling emergence	Accumulated temperature from seedling emergence to flowering	Accumulated temperature from flowering to maturity	Total assimilation rate discount factor at 0 °C minimum temperature	Total assimilation rate discount factor at 3 °C minimum temperature
Value	−1.530764949	1269.892	1263.679	0.078391	0.913047808
Parameter	LAIEM ($hm^2 \cdot hm^{-2}$)	FOTB1 ($kg \cdot kg^{-1}$)	CFET	FLTB0 ($kg \cdot kg^{-1}$)	FLTB0.25 ($kg \cdot kg^{-1}$)
Significance	LAI at seedling emergence	Proportion of above-ground dry matter allocated to storage organs	Evapotranspiration rate correction factor	Proportion of above-ground dry matter allocated to leaves at growth stage 0	Proportion of above-ground dry matter allocated to leaves at growth stage 0.25

Table 2. *Cont.*

Crop Parameter	AMAXTB0 ($kg \cdot hm^{-2} \cdot h^{-1}$)	AMAXTB1 ($kg \cdot hm^{-2} \cdot h^{-1}$)	AMAXTB1.3 ($kg \cdot hm^{-2} \cdot h^{-1}$)	CVO ($kg \cdot kg^{-1}$)	CVL ($kg \cdot kg^{-1}$)
Value	0.129033698	0.956577	0.929755	0.601276	0.641848876
Parameter	FLTB0.5 ($kg \cdot kg^{-1}$)	FLTB0.646 ($kg \cdot kg^{-1}$)	DEPNR	TDWI ($kg \cdot hm^{-2}$)	Q10
Significance	Proportion of above-ground dry matter allocated to leaves at growth stage 0.5	Proportion of above-ground dry matter allocated to leaves at growth stage 0.646	Number of soil water depleting crop groups	gross initial dry weight	Rate of change in respiration at a temperature change of 10 °C
Value	0.450768093	0.296593	4.648691	182.6195	1.870266321
Parameter	RDI (cm)	RRI ($cm \cdot d^{-1}$)	RDMCR (cm)	AMAXTB2 ($kg \cdot hm^{-2} \cdot h^{-1}$)	
Significance	Initial root depth	Maximum daily increase in root depth	Maximum root depth	Maximum CO_2 assimilation rate at growth stage 2	
Value	11.94677171	1.290248	122.5433	4.84661	

Based on the revised WOFOST model and CMIP6 data, this study simulated the future growth and development of spring wheat under the climate change scenario year by year. For the detailed process and results of WOFOST correction and verification, and the simulation of spring wheat growth process year by year using WOFOST and CMIP6 data, see Ref. [28]. In this study, TRANSP and TWSO in the simulation results were used as the total transpiration of crops during the growing period, and TWSO was used as the yield. In addition, the change of growth period was based on the emergence date (DM), flowering date (FLWR) and harvest date (HALT) in the simulation results.

3. Results

3.1. Meteorological Changes Under Future Climate Scenarios

Meteorological variables (e.g., temperature, precipitation and wind speed) are important factors in climate change's impact on wheat production. Therefore, we used CMIP6 data to derive the average monthly precipitation, evaporation and temperature of each test site in the study area from 2015 to 2100 under three future climate change models (SSP126, SSP245 and SSP585) (Figure 2). The CMIP6 data spatial distribution was closely related to the latitude and longitude of the test site. Temperature change of all test sites was consistent, and the trend of the three models was high in the south and west, and low in the north and east. The average temperature in the SSP245 model was the highest, about 0.2 °C higher than in the other two models. In MT, SSP585 > SSP245 > SSP126, and the difference was about 0.5 and 0.6 °C. In LT, SSP585 > SSP245 > SSP126, and the difference was about 1.7 and 0.8 °C. Except for the three sites in the southern mountain area, the average monthly rainfall was SSP585 > SSP245 > SSP126, and the difference was about 1 and 0.5 mm. MT average monthly rainfall was SSP585 > SSP126 > SSP245, and the difference was about 0.7 mm. For LT, SSP585 > SSP245 > SSP126, and the difference was about 0.5 and 2 mm. The average monthly precipitation in the northern region was about 17 mm, for Zhongning, Zhongwei and Litong sites in the central region about 21 mm, Tongxin and Huianpu sites about 34 mm, and for Yanchi was about 40 mm. Average monthly precipitation in the southern region exceeded 40 mm. Due to the temperature and precipitation increase, average monthly evaporation significantly increased from ST to LT under each model. In addition to the three sites in the ST southern mountain area, the average monthly evaporation is SSP585 > SSP245 > SSP126, with a difference of about 1 mm. In MT, SSP585 > SSP126 > SSP245, and the difference was higher than ST. In LT, SSP585 > SSP245 > SSP126, differences were >1 mm and <1 mm, and the southern region was more different than the northern region. Specific results are set out in Table A1.

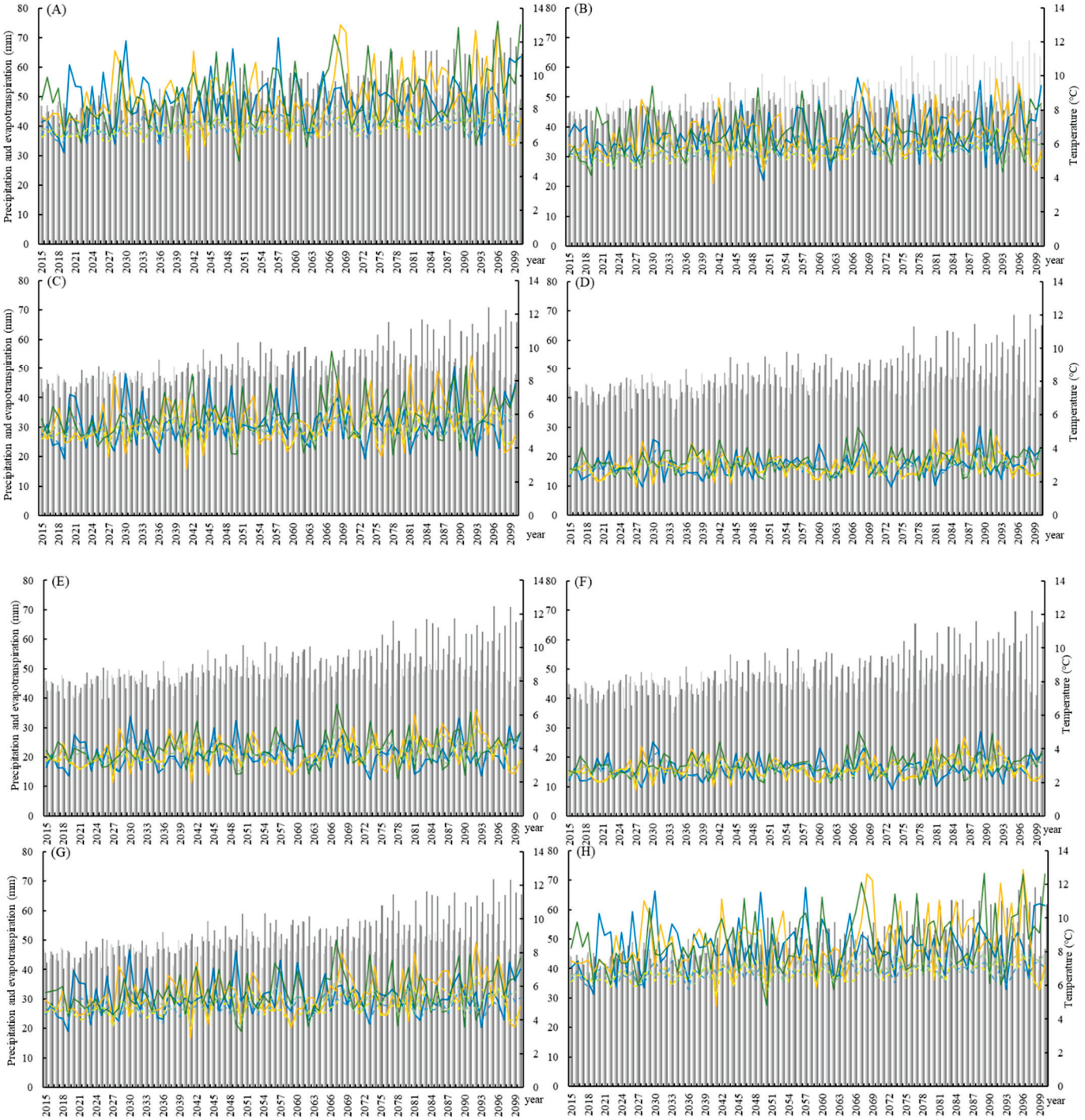

Figure 2. *Cont.*

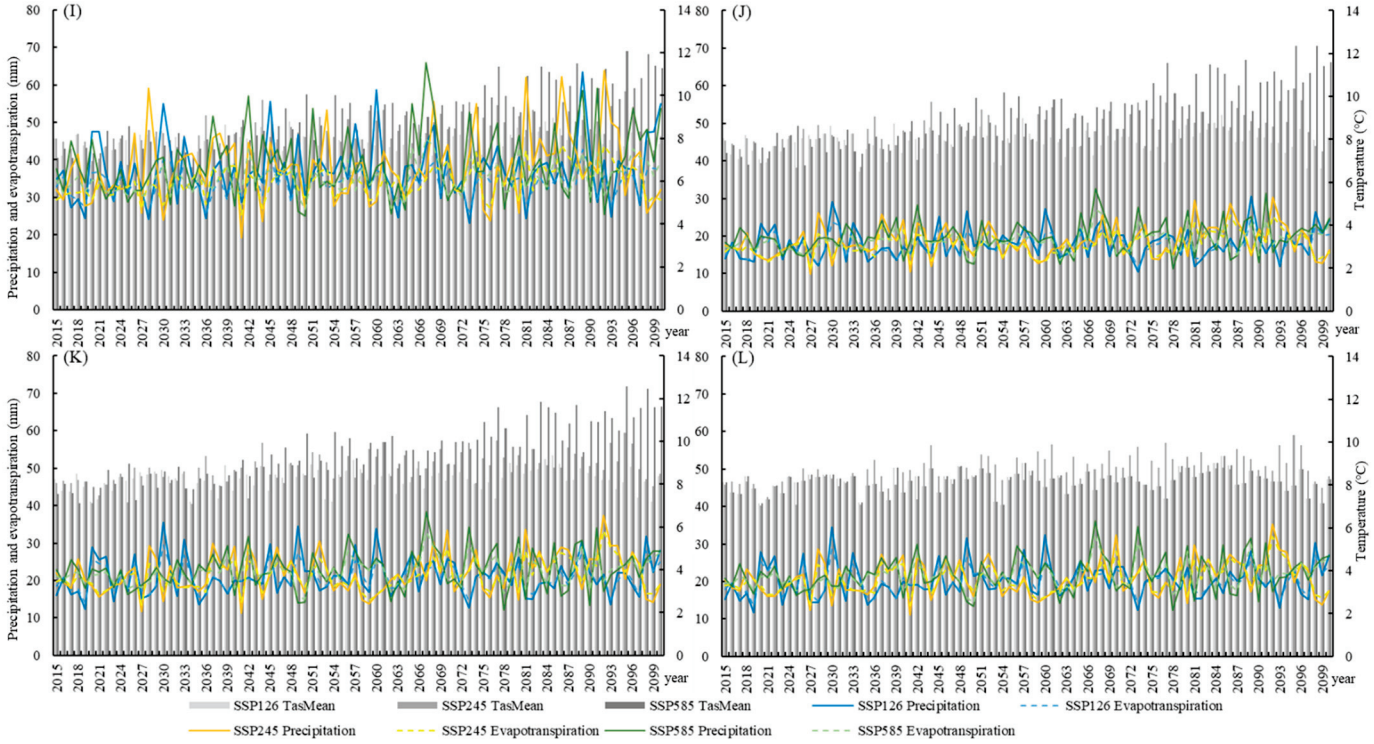

Figure 2. Monthly average temperature, precipitation and evaporation of each test site in the study area under SSP126, 245 and 585 models. Note: (**A**–**L**) represent 12 test sites in Guyuan, Haiyuan, Huianbao, Huinong, Litong, Shizuishan, Tongxin, Xiji, Yanchi, Yinchuan, Zhongning and Zhongwei, respectively.

The Ningxia DHW discriminating method was used to screen and derive statistics on future DHW days over the wheat growing period of the test sites in the SSP126, 245 and 585 model study areas. According to the regional distribution of wheat planting in Ningxia, Figure 3 shows the change trend of DHW in five representative test sites of Huinong, Yinchuan, Litong, Zhongning and Zhongwei. The frequency and intensity of DHW in the test stations located in the northern region are significantly higher compared to those in the central arid region. Under both the SSP126 and SSP245 models, the variation trend of DHW in the central arid region remains stable, while in the northern region, the DHW trend shows a slight increase over the long term. Test sites with the highest number of light and heavy DHW days in the three models during the 81 years from 2020 to 2100 were Yinchaun, with 359, 360 and 582 days, respectively. Under the SSP126 model, average annual DHW days were 3.67 in the southern mountainous area, 10.31 in the central arid area and 11.96 in the northern irrigation area. In the SSP245 model, the number of days were 2.98, 9.78 and 12.18 d, respectively, and in the SSP585 model, 6.54, 13.97 and 16.37 d, respectively.

In the study area overall, DHW occurrence days were closely related to geographical location, with more in the north and less in the south. Average annual DHW days were LT > ST > MT in the SSP126 model, and the differences between near- and long-term were small, all within 1 d. In the SSP245 model, average annual DHW days differed little in the near-, medium- and long-term, and LT was generally small. In the SSP585 model, average annual DHW days trended LT > MT > ST, and the difference was >1 d. Overall in the study area, the number of DHW days was highest in the SSP585 model, followed by SSP126 and finally SSP245. The difference of DHW days in the wheat growth period between SSP245 and SSP126 was only 0.26 d per year. The near- to long-term average annual DHW days of each site are listed in Table A2.

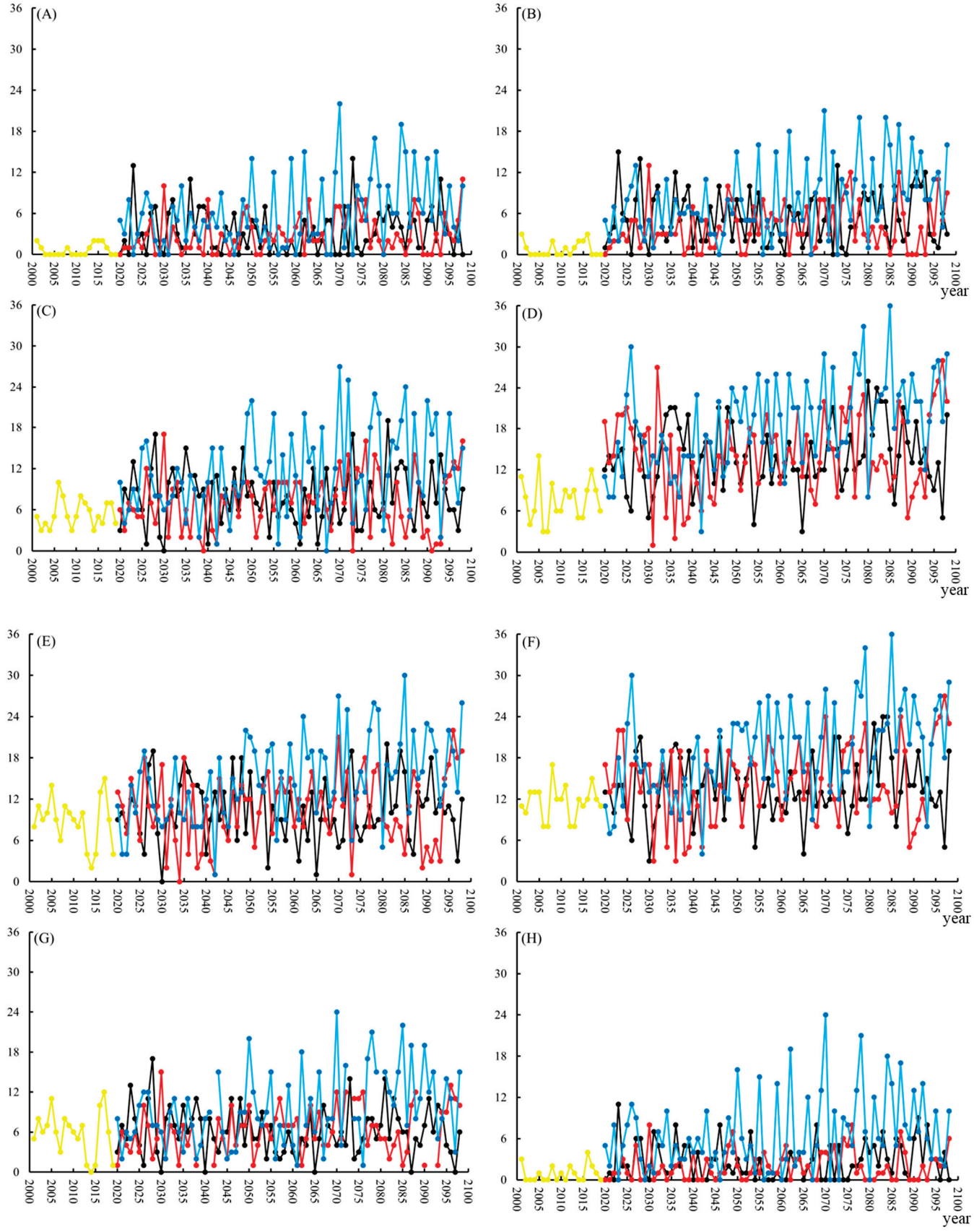

Figure 3. *Cont.*

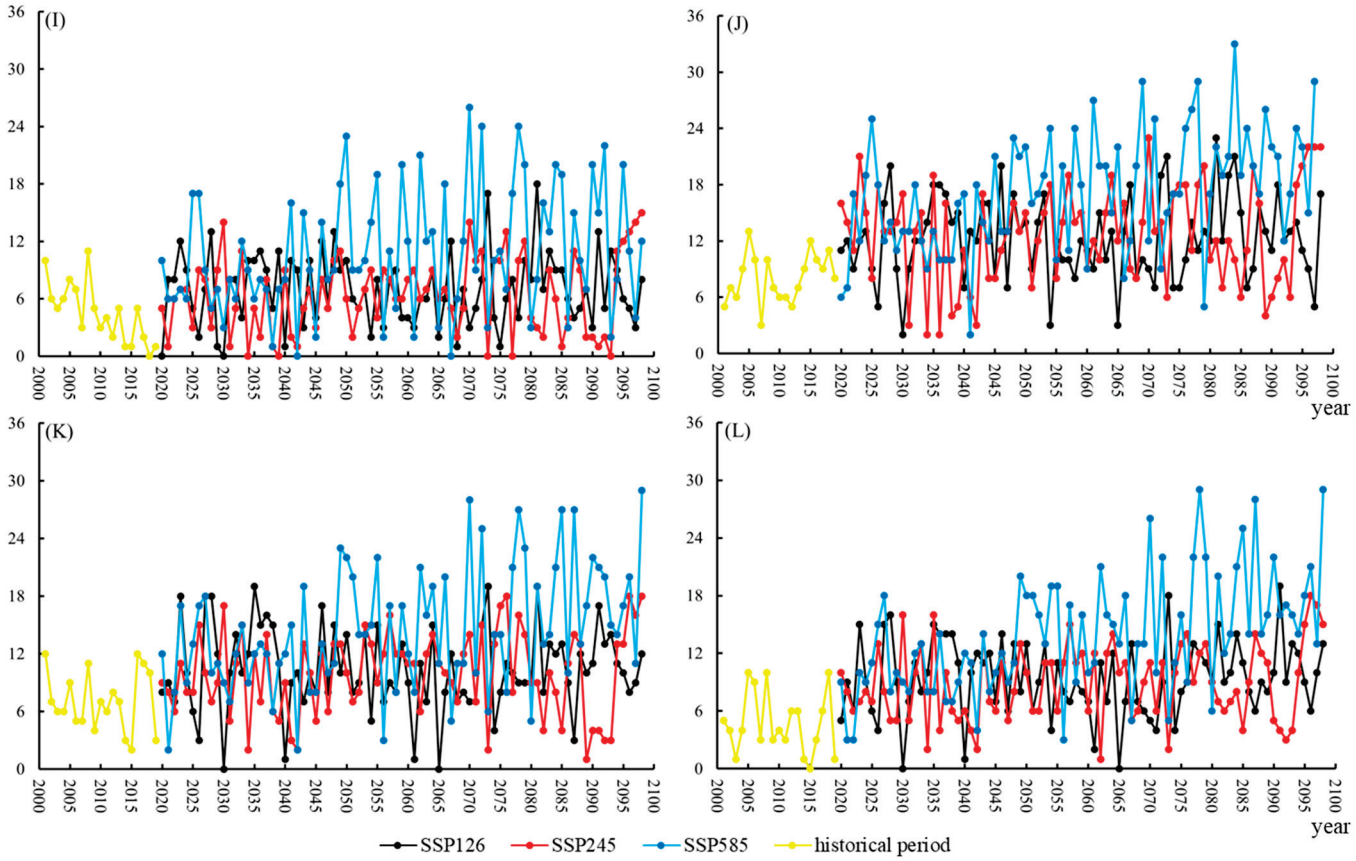

Figure 3. Future DHW days during wheat growth period under SSP126, 245 and 585 models were studied at 12 representative test sites. Note: (**A**–**L**) represent 12 test sites in Guyuan, Haiyuan, Huianbao, Huinong, Litong, Shizuishan, Tongxin, Xiji, Yanchi, Yinchuan, Zhongning and Zhongwei, respectively.

3.2. Future Wheat DHW Temporal and Spatial Changes in Ningxia

Mann–Kendall analysis and statistical tests were conducted on the total number of DHW days from 2015 to 2100 and during the wheat growth period at each test site (Table 3). The total number of DHW days in the SSP126 model decreased in all sites except Huinong. Under the SSP245 model, there was an obvious DHW day rising trend in Guyuan, Huianpu and Zhongning sites. Among them, the Guyuan upward trend was statistically significant, but for the other sites the trend was non-significant. In the SSP585 model, all sites showed an obvious and significant DHW day upward trend. A Z test score of >4 in the five sites in the northern region indicated that during the wheat growth period, there was a significant upward DHW day trend at each site.

Table 3. Mann–Kendall change trend test of total DHW days and wheat growing days at each test site under SSP126, 245 and 585 models.

Z Value	Southern Mountainous Area of Ningxia			Arid Area of Central Ningxia					Northern Region of Ningxia			
	guyaun	haiyuan	xiji	huianpu	tongxin	yanchi	zhongning	huinong	litong	shizuishan	yinchuan	zhongwei
SSP126	−0.37	−0.38	−0.03	−1.06	−1.28	−0.51	−0.64	0.15	−0.57	−0.14	−0.45	−0.36
confidence interval	-	-	-	-	-	-	-	-	-	-	-	-
SSP245	1.76	1.12	0.85	1.44	1.23	1.17	1.28	0.85	1.27	1.11	1.19	1.23
confidence interval	95%	-	-	90%	-	-	90%	-	-	-	-	-
SSP585	2.65	3.61	2.61	3.44	3.08	3.37	3.86	4.59	4.38	4.41	4.46	5.20
confidence interval	99%	99%	99%	99%	99%	99%	99%	99%	99%	99%	99%	99%

Note: "-" indicates no significance.

We conducted Mann–Kendall tests to determine significant changes in DHW days at each research site under the three future climate models during the wheat growth period (Figure 4). Under the SSP585 model, DHW days during the wheat growing period all began to trend insignificant upward before 2020 in Guyuan, Haiyuan and Xiji, while the DHW days in LT show a significant upward trend; this transformation appeared around 2068a. In the arid areas of central, Huianbao, Tongxin, Yanchi and Zhongning, DHW days significantly increased after 2050a, 2083a, 2049a and 2050a, respectively. There was a very significant increase in LT, and this change occurred in 2047a, 2059a, 2047a and 2048a, respectively. In Huinong, Litong, Shizuishan, Yinchuan and Zhongwei in the northern region, DHW days significantly increased after 2052a, 2050a, 2052a, 2051a and 2051a, respectively. There was a highly significant increase in LT, and mutations occurred in 2054a, 2050a, 2052a, 2051a and 2048a, respectively. There was no significant upward or downward trend in the SSP126 and SSP245 models, and no significant mutations were detected. Overall, under the SSP585 scenario, the risk of DHW increases across the entire study area. The rate of increase in DHW risk significantly accelerates in the northern and central arid regions after the 2050s, while in the southern mountainous region, this change occurs after the 2070s.

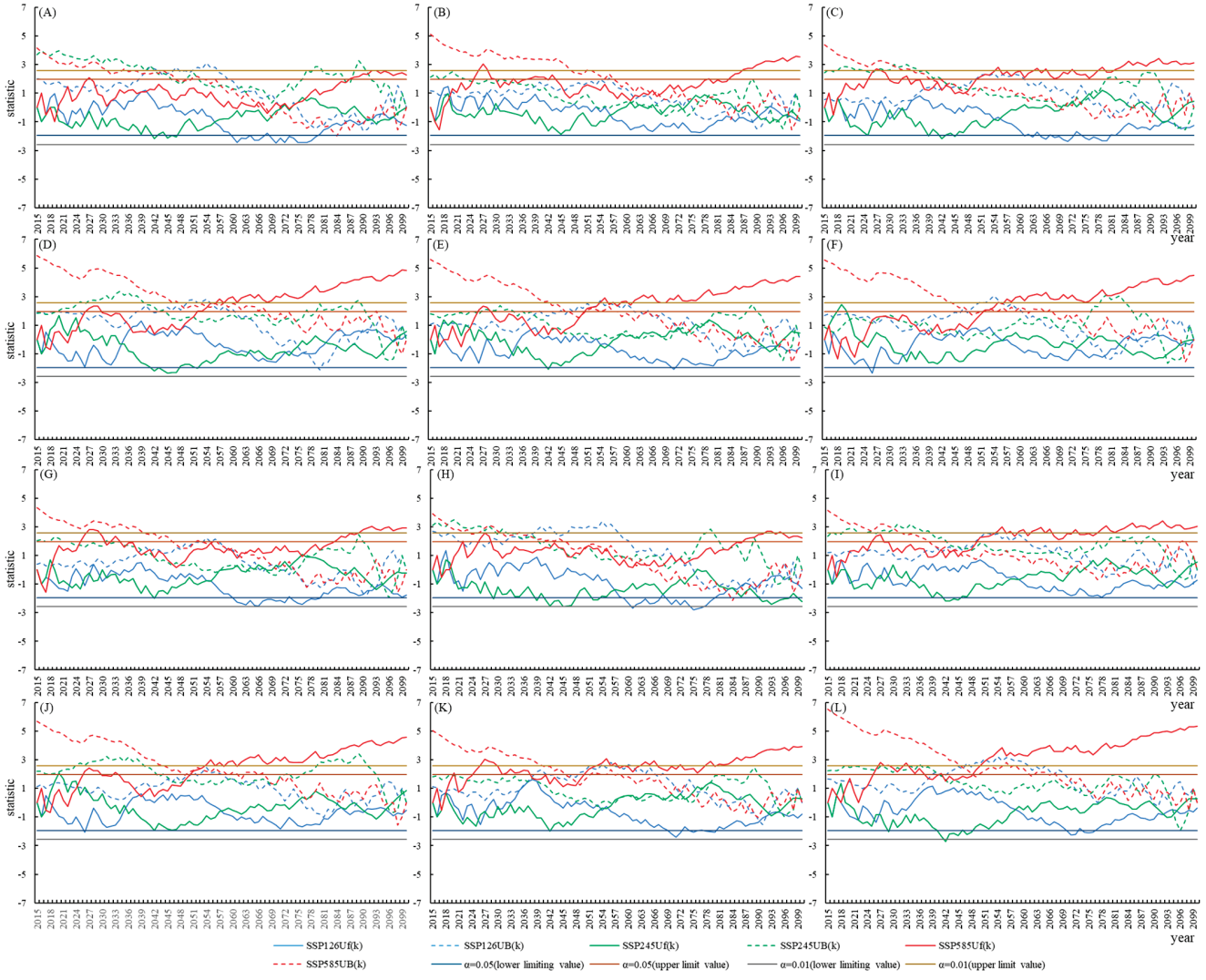

Figure 4. The variation trend of future DHW days in wheat growing period under SSP126, 245 and 585 models at each test site. Note: (**A**–**L**) represent 12 test sites in Guyuan, Haiyuan, Huianbao, Huinong, Litong, Shizuishan, Tongxin, Xiji, Yanchi, Yinchuan, Zhongning and Zhongwei, respectively.

We conducted a spatial analysis on DHW during the wheat growth period (Figure 5). There were significant spatial differences in DHW frequency, which was higher in the northern and western regions and lower in the southern and eastern regions. Overall, DHW frequency in the SSP585 model was significantly higher than in the other two models. For annual DHW days, MT was significantly lower in the SSP126 model. There is no significant difference between the three periods in the SSP245 model. In the SSP585 model, the spatial distribution was LT > MT > ST.

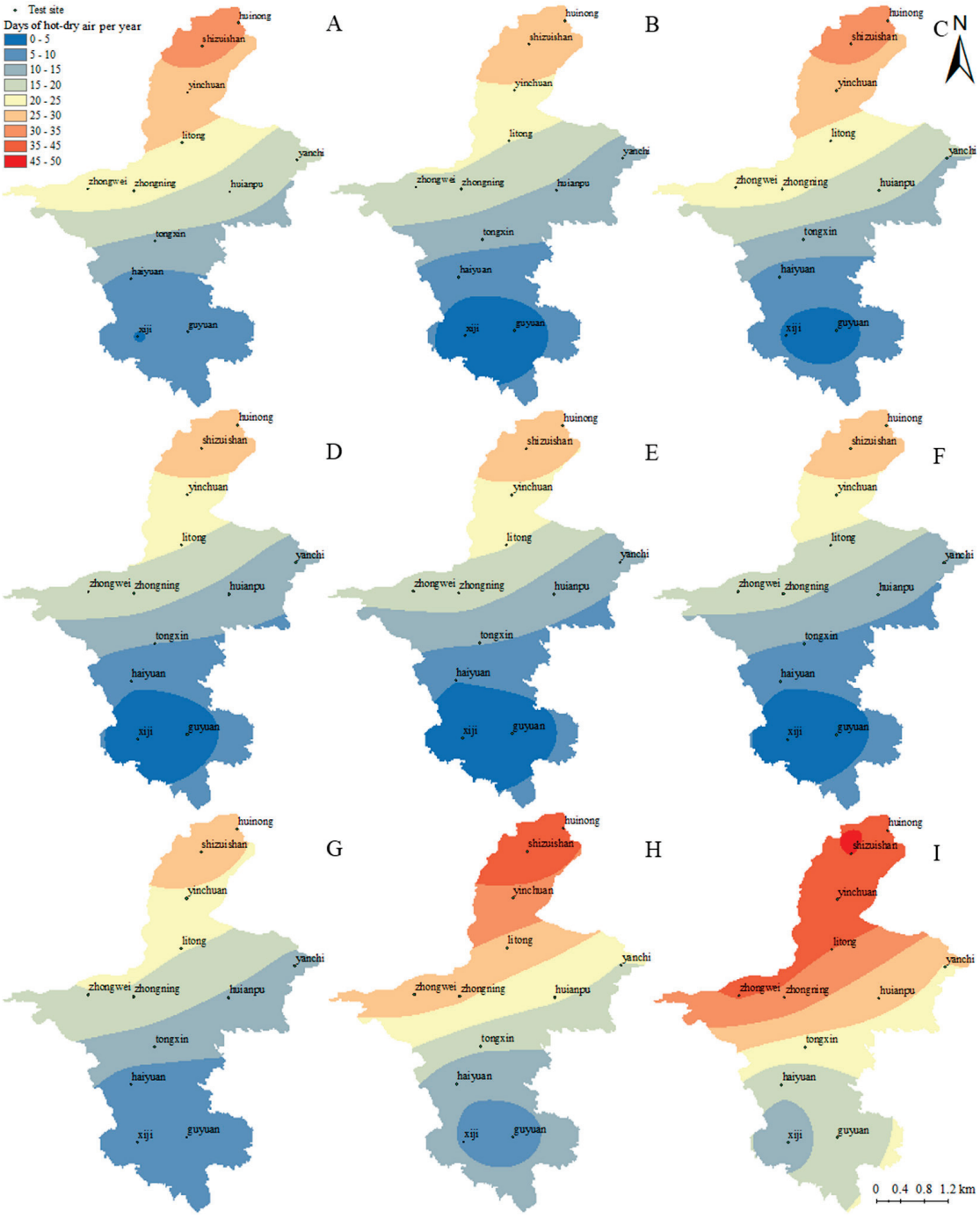

Figure 5. The variation trend of future DHW days in wheat growing period under SSP126, 245 and 585 models in the study area. Note: (**A**–**C**) represent the short-, medium- and long-term DHW average annual number of days under SSP126 model; (**D**–**F**) are under SSP245 model; (**G**–**I**) are under SSP585 model.

3.3. Drought Index Spatiotemporal Variation During the Wheat Growth Period

The identification of drought events and their severity characteristics are crucial for assessing and lowering drought disaster risk [33]. SPEI is derived from precipitation, evaporation and temperature changes in the form of water balance, and is currently a popular quantitative index for assessing drought degree and drought risk [34]. We used the Penman–Monteith equation to calculate future reference evapotranspiration in the study area, to calculate monthly SPEI [25]. According to the SPEI index drought classification criteria, 81a moderate drought months were identified (Table 4), and based on these, the study area drought risk was assessed as follows: southern mountain area > central arid area > northern region (SSP126 model); and southern mountainous area > northern region > central arid area (SSP245 and 585 models). For the wheat growth period in the study area, we selected the SPEI index from May to July of 2015 to 2100 for analysis. Drought risk was as follows: central arid area > southern mountainous area > northern region (SSP126 model); southern mountainous area > northern region > central arid area (SSP245 model); and southern mountainous area > central arid area > northern region (SSP585 model). Severe drought frequency was highest in the southern mountainous area, and extreme drought frequency was highest in the northern region. These results were consistent between the three future models.

Table 4. Number of drought risk months under three future climate models.

Future Climate Model	Drought Risk Level	Southern Mountainous Area of Ningxia			Arid Area of Central Ningxia				Northern Region of Ningxia				
		Guyaun	Haiyuan	Xiji	Huianpu	Tongxin	Yanchi	Zhongning	Huinong	Litong	Shizuishan	Yinchuan	Zhongwei
SSP126	Moderate drought	103	109	106	80	95	109	68	79	80	75	83	74
	Severe drought	31	28	30	16	17	12	14	16	12	18	14	14
	Extreme drought	1	1	1	2	1	2	0	5	2	4	4	1
SSP245	Moderate drought	110	94	114	85	82	87	70	87	84	85	86	73
	Severe drought	24	18	26	12	15	11	16	17	16	20	18	17
	Extreme drought	2	4	2	0	3	0	1	2	2	3	4	2
SSP585	Moderate drought	93	102	101	80	89	89	84	91	91	93	95	72
	Severe drought	20	20	18	16	17	15	15	18	18	18	17	9
	Extreme drought	4	4	4	1	4	1	2	3	2	6	6	1
SSP126 (Growth period)	Moderate drought	22	25	22	25	30	34	28	19	27	19	25	24
	Severe drought	12	9	11	7	7	4	7	7	5	10	8	6
	Extreme drought	0	0	0	2	0	2	0	2	1	1	1	0
SSP245 (Growth period)	Moderate drought	32	31	31	33	33	32	26	28	33	29	29	28
	Severe drought	10	8	10	5	6	4	5	5	6	6	7	7
	Extreme drought	0	0	0	0	0	0	0	0	1	1	2	0
SSP585 (Growth period)	Moderate drought	37	39	40	31	36	33	31	26	34	24	29	26
	Severe drought	4	4	2	4	3	3	2	3	4	5	3	1
	Extreme drought	0	0	0	0	0	0	0	1	0	1	2	0

For the wheat growth period in the study area, the SPEI index for May, June and July from 2015 to 2100a was used to examine temporal changes (Figures 6–8). The SPEI index change trend at all sites was similar, with low and high values alternating periodically. In May, under SSP585 mode, the frequency and extreme value of high SPEI values in LT of each site were greater than ST, and the frequency and amplitude of low LTSPEI values were also significantly higher than MT and ST. There was a clear trend of increasing drought risk. In the SSP245 model, the frequency and amplitude of high and low values from ST to LT increased significantly, indicating that drought risk was becoming unstable. The frequency and amplitude of MT low values were greatest in the SSP126 model, and the possibility of MT drought risk was the highest. In June, SPEI values generally increased compared to May, and the frequency and amplitude of high and low LT in the SSP585 model were

greater than ST and MT. In the SSP126 and SSP245 models, the frequency of high ST and MT was higher, and the amplitude of low values was smaller. In July, the frequency and amplitude of high values in the three models were greater than in May and June. The frequency and amplitude of low LT increased compared to June, but was still smaller than in May. The SPEI index in MT fluctuated less than ST and LT.

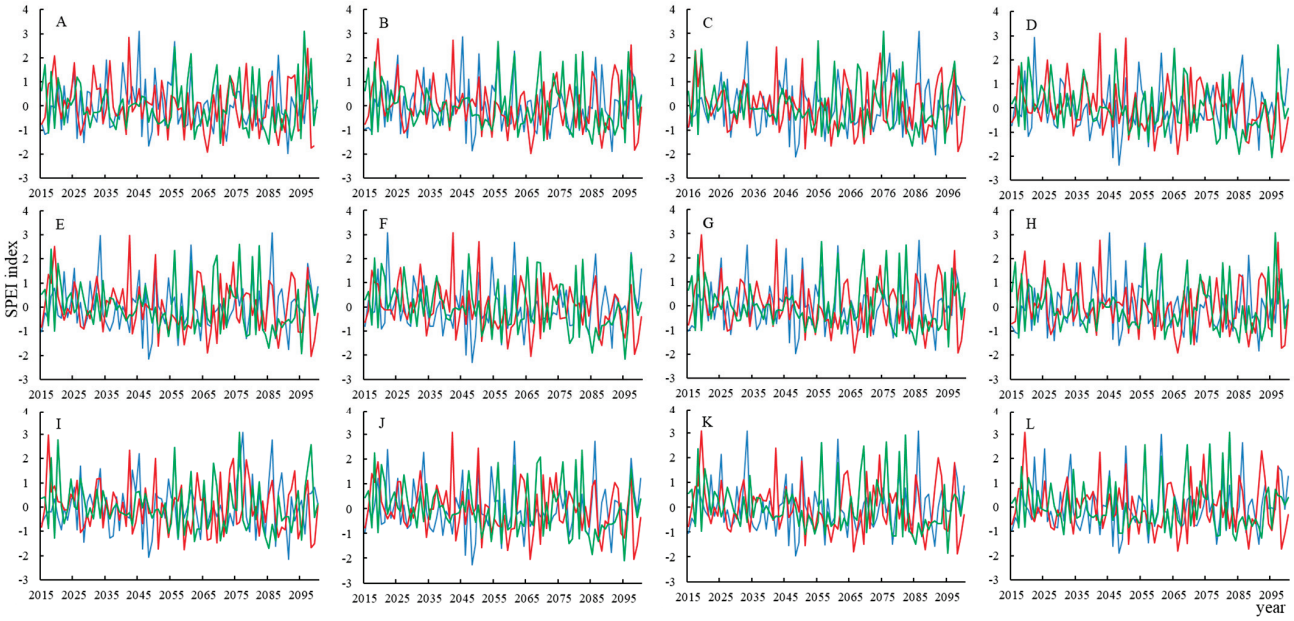

Figure 6. Changes of SPEI index in May under three future climate models. Note: (**A**–**L**) represent 12 test sites in Guyuan, Haiyuan, Huianbao, Huinong, Litong, Shizuishan, Tongxin, Xiji, Yanchi, Yinchuan, Zhongning and Zhongwei, respectively. The above, middle and below figures show the changes of SPEI values in May, June and July, respectively. The blue, green and red lines represent the changes of the SPEI index under SSP126, SSP245 and SSP585 scenarios respectively.

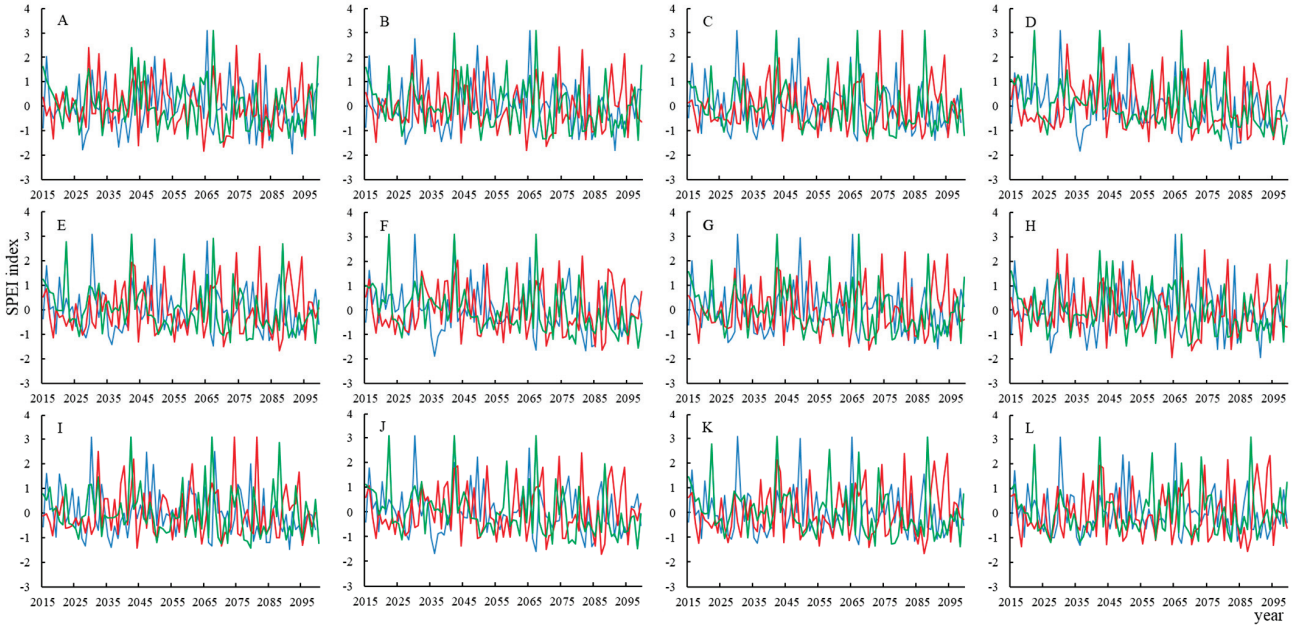

Figure 7. Changes of SPEI index in June under three future climate models. Note: (**A**–**L**) represent 12 test sites in Guyuan, Haiyuan, Huianbao, Huinong, Litong, Shizuishan, Tongxin, Xiji, Yanchi, Yinchuan, Zhongning and Zhongwei, respectively. The above, middle and below figures show the changes of SPEI values in May, June and July, respectively. The blue, green and red lines represent the changes of the SPEI index under SSP126, SSP245 and SSP585 scenarios respectively.

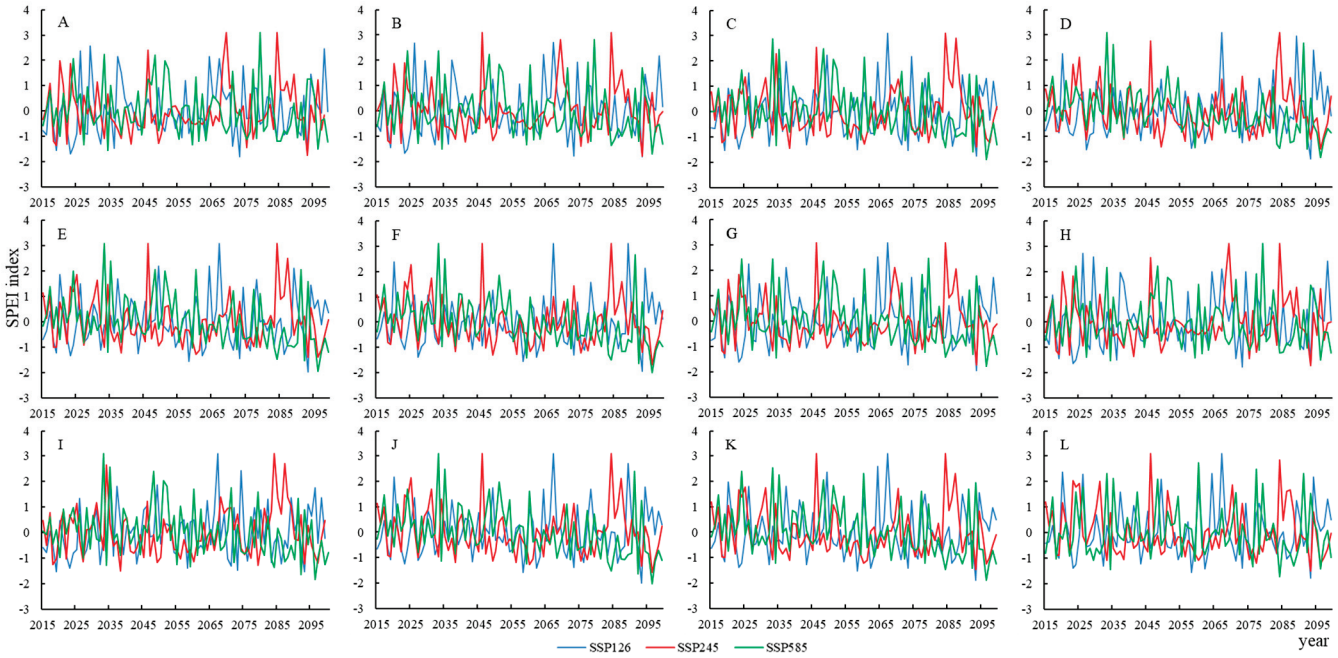

Figure 8. Changes of SPEI index in July under three future climate models. Note: (**A**–**L**) represent 12 test sites in Guyuan, Haiyuan, Huianbao, Huinong, Litong, Shizuishan, Tongxin, Xiji, Yanchi, Yinchuan, Zhongning and Zhongwei, respectively. The above, middle and below figures show the changes of SPEI values in May, June and July, respectively. The blue, green and red lines represent the changes of the SPEI index under SSP126, SSP245 and SSP585 scenarios respectively.

The optimized crop parameters were observed to effectively enhance the simulation results of the WOFOST model and minimize RMSE between the simulated and measured values. Furthermore, recent wheat yield simulations outperformed those from the early 21st century, with all stations except for the yields measured in Zhongning.

The SPEI index annual means under the three future climate models were selected and their spatial distribution analyzed by the Kriegin difference method (Figures 9–11). The SPEI index spatial distribution was less affected by latitude than by DHW days. The drought risk index in May, June and July was higher in MT, LT and ST, respectively, under the SSP126 model. In the SSP245 model, it was greater in MT, LT and MT, respectively, and in the SSP585 model, it was highest in LT. Its spatial distribution was less affected by latitude and longitude. Under the SSP585 model, spatial variation was significant, and the drought degree in the northern region was increasing monthly. There was no significant difference in the overall study area SPEI index under the SSP245 model. Overall, climate change was more consistent, while in the SSP126 model, the ML climate gradually became wetter.

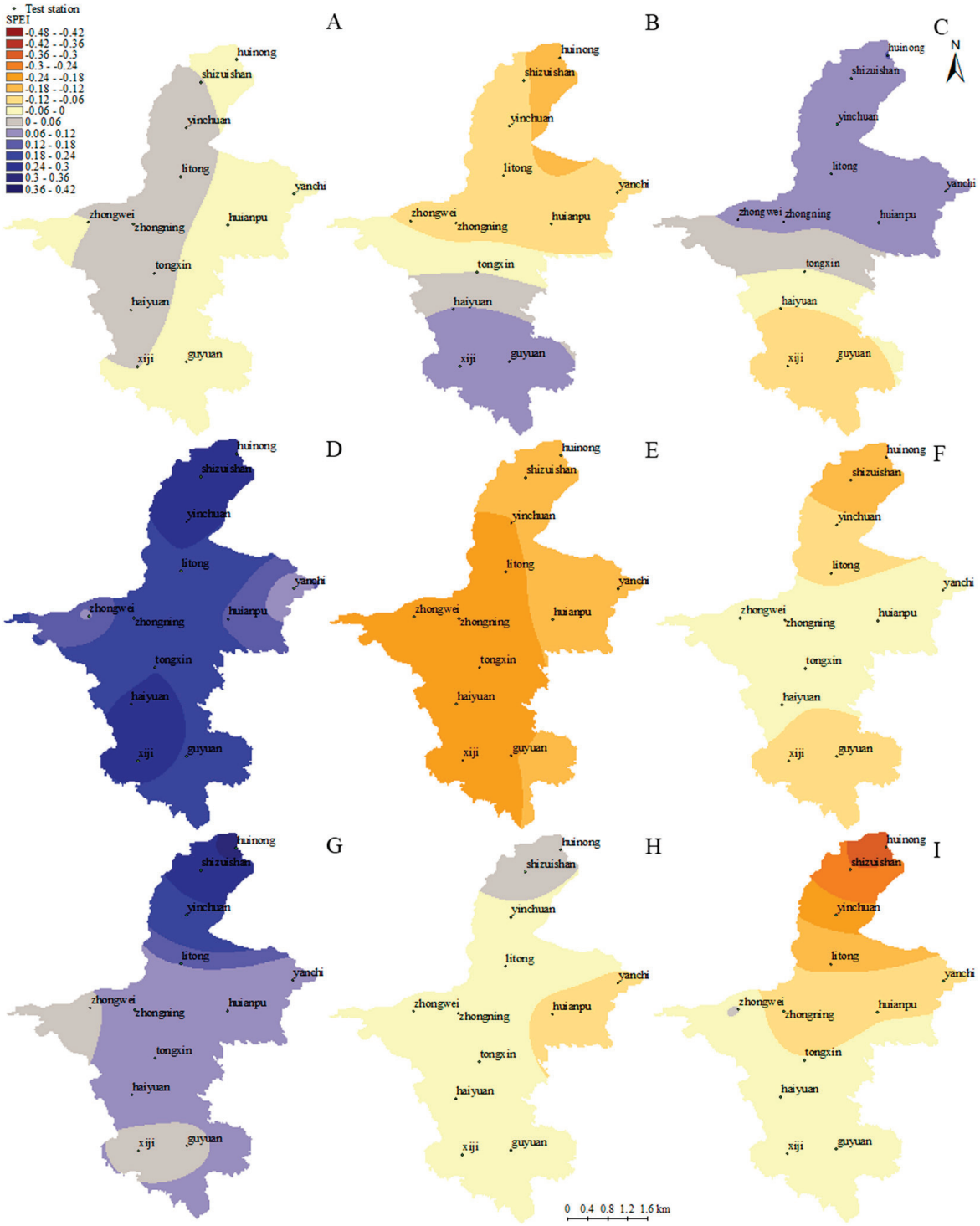

Figure 9. The SPEI index of May in the near to mid future under three climate change models in the study area. Note: (**A**–**C**) represent the average annual distribution of SPEI index in the near- to middle- and long-term under the SSP126 model; (**D**–**F**) represent the average annual distribution of SPEI index in the near- and long-term under the SSP245 model, respectively; and (**G**–**I**) represent the average annual distribution of SPEI index under the SSP585 model.

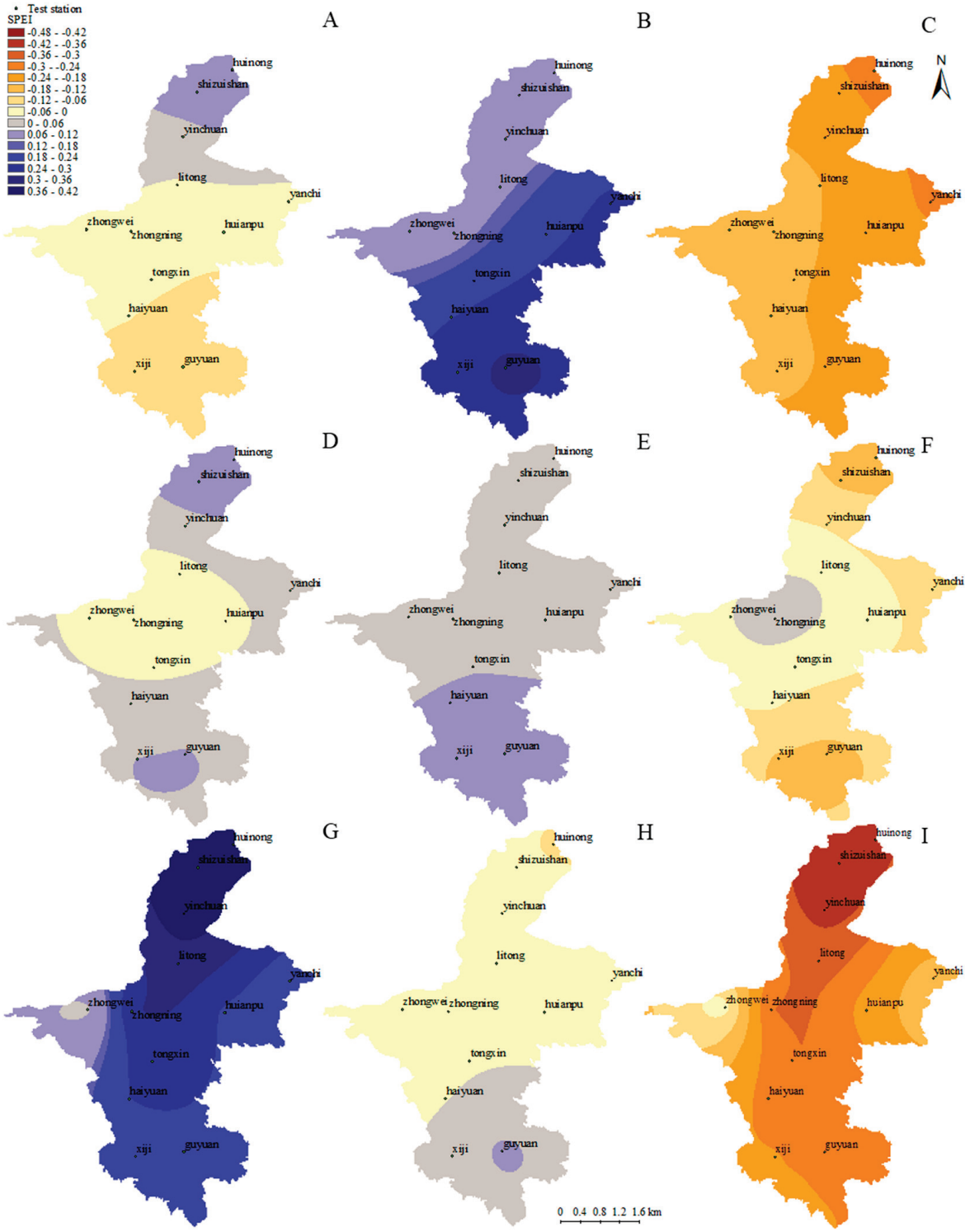

Figure 10. The SPEI index of June in the near- to mid-future under three climate change models in the study area. Note: (**A**–**C**) represent the average annual distribution of SPEI index in the near- to middle- and long-term under the SSP126 model; (**D**–**F**) represent the average annual distribution of SPEI index in the near- and long-term under the SSP245 model, respectively; and (**G**–**I**) represent the average annual distribution of SPEI index under the SSP585 model.

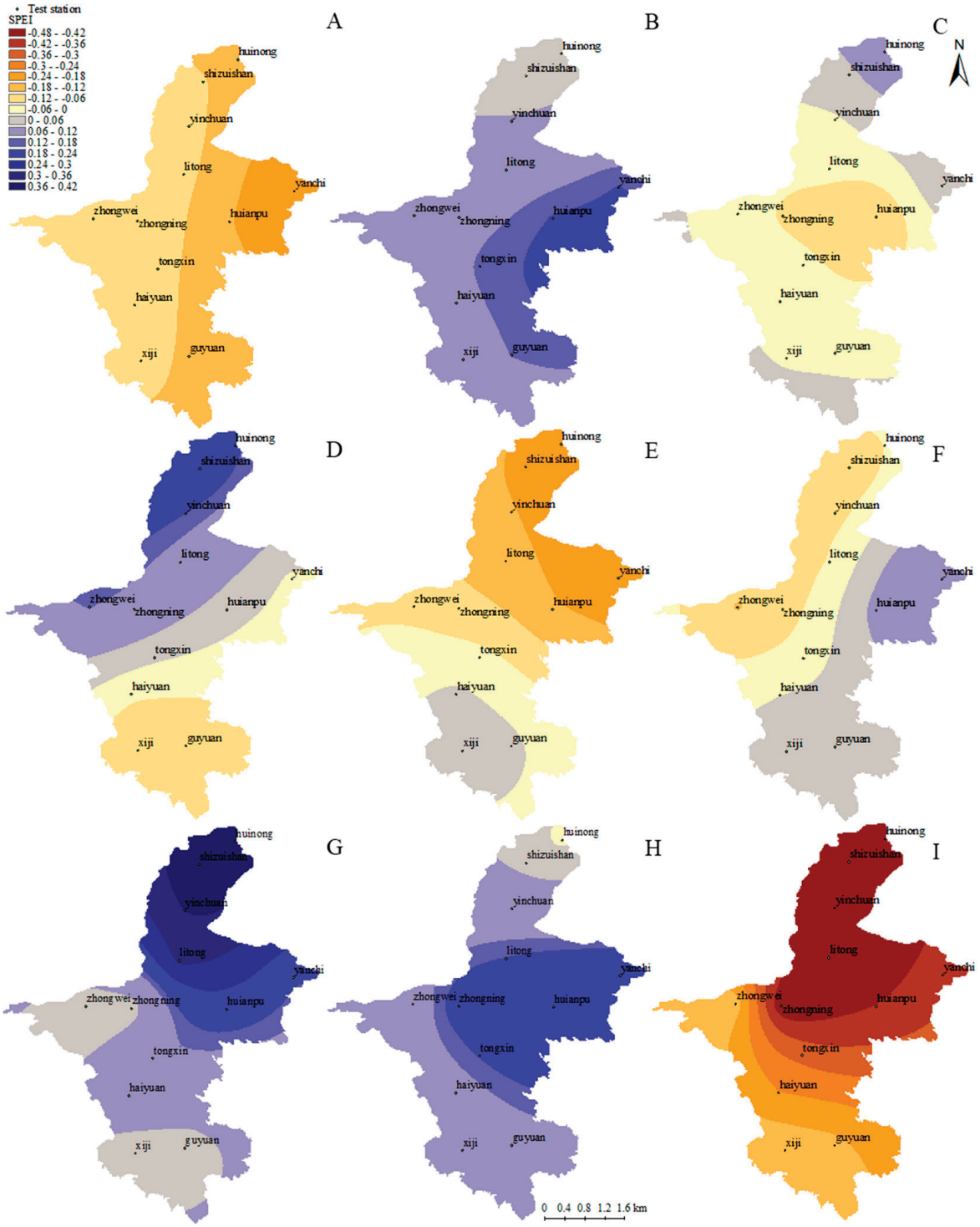

Figure 11. The SPEI index of July in the near- to mid-future under three climate change models in the study area. Note: (**A**–**C**) represent the average annual distribution of SPEI index in the near- to middle- and long-term under the SSP126 model; (**D**–**F**) represent the average annual distribution of SPEI index in the near- and long-term under the SSP245 model, respectively; and (**G**–**I**) represent the average annual distribution of SPEI index under the SSP585 model.

3.4. Effects of DHW and SPEI Index Changes on Wheat Yield

According to a previous study [28], we analyze the correlation between the total transpiration (TRANSP), yield (TWSO), flowering time (FLWR) and maximum leaf area index (LAIM) from the WOFOST model's simulation results for wheat from 2020 to 2098

and the annual number of DHW events, as well as the SPEI index for May, June and July (Figure 12). The most significant factor affecting TRANSP is LAIM, with correlation coefficients reaching 0.7 across all three scenarios. FLWR and TWSO also show significant effects: DHW has a notable impact under the SSP126 scenario, but not under the SSP245 and SSP585 scenarios. For TWSO, the impact of DHW increases with rising warming levels, with correlation coefficients of −0.142, −0.412 and −0.54 under the three scenarios, respectively. Additionally, the SPEI index for June shows a significant effect, being positively correlated in the SSP245 and SSP585 scenarios with coefficients of 0.195 and 0.328, respectively. In contrast, it is negatively correlated in the SSP126 scenario with a coefficient of −0.271, indicating that increased rainfall in SSP245 and SSP585 scenarios promotes wheat yield, while the SPEI index for May only has a significant effect in the SSP585 scenario. FLWR has a significant positive correlation with the SPEI indices for May and June under the SSP126 scenario, and with the SPEI indices for May and July under the SSP245 and SSP585 scenarios, respectively. DHW shows a negative correlation with the SPEI index across all three scenarios, with the strongest effect in the SSP585 scenario, with correlation coefficients of −0.512, −0.612 and −0.219 for May, June and July, respectively.

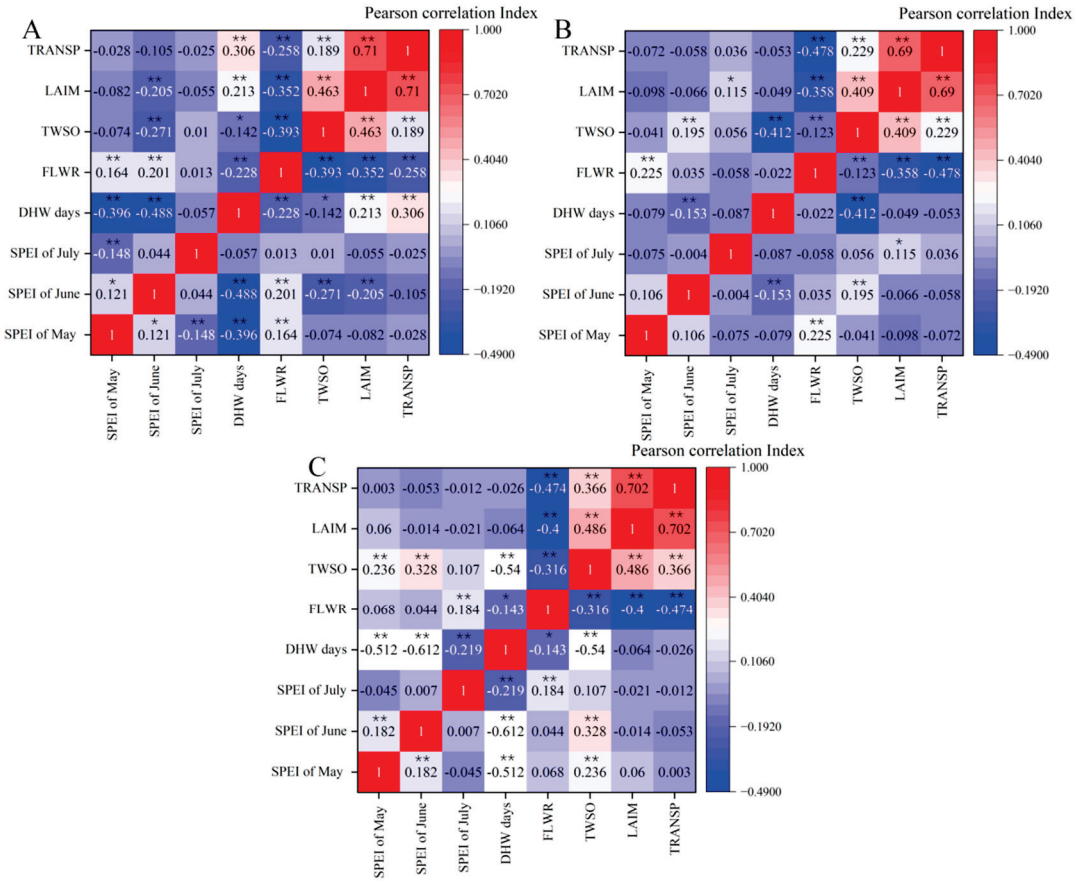

Figure 12. Pearson correlation analysis of SPEI index in May, June and July, DHW quantity in wheat growth period and four simulation results of wheat. Note: (**A**–**C**) represent the three development modes of SSP126, 245 and 585. * and ** indicating significant differences at the $p < 0.05$ and $p < 0.01$ levels, respectively.

4. Discussion

4.1. Wheat DHW Temporal and Spatial Variation Trends in Ningxia

The precipitation and temperature anomaly greatly influences drought variability. A decrease in regional precipitation and an increase in evaporation caused by warming may greatly exacerbate drought [35]. We statistically analyzed temperature, precipitation and wind speed changes in Ningxia province under different future climate scenarios by collating

CMIP6 data. According to meteorological changes, the spatiotemporal variation of dry hot wind in Huinong, Shizuishan and the other test sites was analyzed and temperature variation of each test site was consistent. Under SSP126, 245 and 585 conditions, temperature increased 0.037, 0.15 and 0.45 °C·(10 a^{-1}), respectively. Recent average annual temperatures in the northern region, central arid area and southern mountainous area were 7.75, 7.94 and 7.83 °C, respectively, which is consistent with Ma Yang et al. [36]. Under the SSP126, 245 and 585 scenarios, average annual precipitation increased by 17.77 mm, 38.73 mm and 32.12 mm from near- to long-term, respectively. Furthermore, annual evaporation increased by 11.96 mm, 30.85 mm and 28.18 mm, respectively, consistent with Zhang Shiyan et al. [37]. Thus, the future Ningxia Province climate will shift towards higher temperature and humidity, and high carbon emissions (SSP585) will accelerate the risk of warming and will not result in more precipitation than balanced carbon emissions (SSP245). This would increase extreme dry weather frequency. Dry hot wind weather statistics in each test site showed that Huinong and Shizuishan sites have the driest hot wind days. Under the SSP126 model, average annual DHW days were 5.71 in the southern mountainous area, 16.08 in the central arid area and 26.35 in the northern irrigation area. In the SSP245 model, there were 3.93, 12.58 and 23.29 d, respectively, and in the SSP585 model, 9.85, 20.85 and 32.35 d, respectively. Mann–Kendall trend test analysis showed that high warming levels will significantly affect the increasing hot wind days trend. Mutation was detected at all sites under the SSP585 model, indicating that the increased rate of dry hot wind days will be greatly improved, and drought risk is increasing rapidly in the long-term. DHW frequency was higher in the northern and western regions, and lower in the southern and eastern regions.

Li et al. [38] showed that the study area under the SSP585 model would be drier than in the other two scenarios, and expected future drought to be more severe in the long-term, than in the near- and medium-term. Feng et al. [39] investigated spatiotemporal variation of multi-variable complex hot, dry and strong wind extreme weather in northwest China, and found that both the upward trend in incidence and the increased likelihood of compound extreme weather posed a strong risk in the future. Tan et al. [24], based on CMIP5 data, used 20 global climate models and drought data to predict future climate change and related drought disasters in Ningxia, and found that the climate may become warmer and wetter in the 21st century, but drought disasters may also increase, which is a similar finding to our study. Compared with previous studies, we highlighted the impact of extreme weather on wheat by introducing the dry hot wind criterion, and analyzed specific test sites. We showed that future dry hot wind spatiotemporal variation in the study area may be caused by warming levels, which provides a key scientific basis for actual wheat drought risk prevention and mitigation in Ningxia.

4.2. Future Drought Temporal and Spatial Changes in Ningxia Based on the Drought Index

Drought status changes in the study area can be explained primarily by precipitation and evapotranspiration [40]. The increase of vegetation water demand under climate change is greater than the increase of rainfall. Therefore, even though precipitation may increase in some areas, more severe ecological droughts will still occur [41]. To determine the relative influences of precipitation, temperature and evapotranspiration, we introduced the SPEI index to quantitatively study drought/climate change effects in northwest China. In May, there was a clear trend of increased drought risk under the SSP585 model, but there was no obvious change in drought risk under the SSP245 model, and the probability of drought risk appearing in the middle period was the highest under the SSP126 model. In June, SPEI was generally higher than in May. The risk of alternating drought and flood was greater under the SSP585 model, while the risk of near-medium-term drought was lower under the SSP126 and SSP245 models. In July, the near-medium-term drought risk was greater than in May and June, and the long-term risk was higher than in June, but still lower than in May. Finally, we conducted Pearson correlation analysis on DHW, SPEI and the related indicators of the wheat simulation results. The study of DHW correlation indicates that DHW will have a significant impact on wheat yield under all scenarios, and

this impact increases with rising warming levels. However, increased rainfall tends to suppress the growth of DHW, with this effect being more pronounced under high-emission scenarios. In the SSP126 scenario, cooling caused by rainfall or post-rain dry hot winds will have a substantial effect on wheat yield, while in the SSP585 scenario, the advancement of high-temperature periods will also significantly affect wheat yield. High temperatures combined with high rainfall will lead to varying degrees of advancement in the flowering period. The results of the SPEI correlation analysis show that moderate high rainfall will promote wheat yield. However, the correlation results for DHW indicate that extreme high-temperature weather accompanied by high rainfall will negatively impact wheat yield. This highlights the limitations of studying the effects of a single indicator on wheat yield. Specific changes in the SPEI index categories are illustrated in Figure 13.

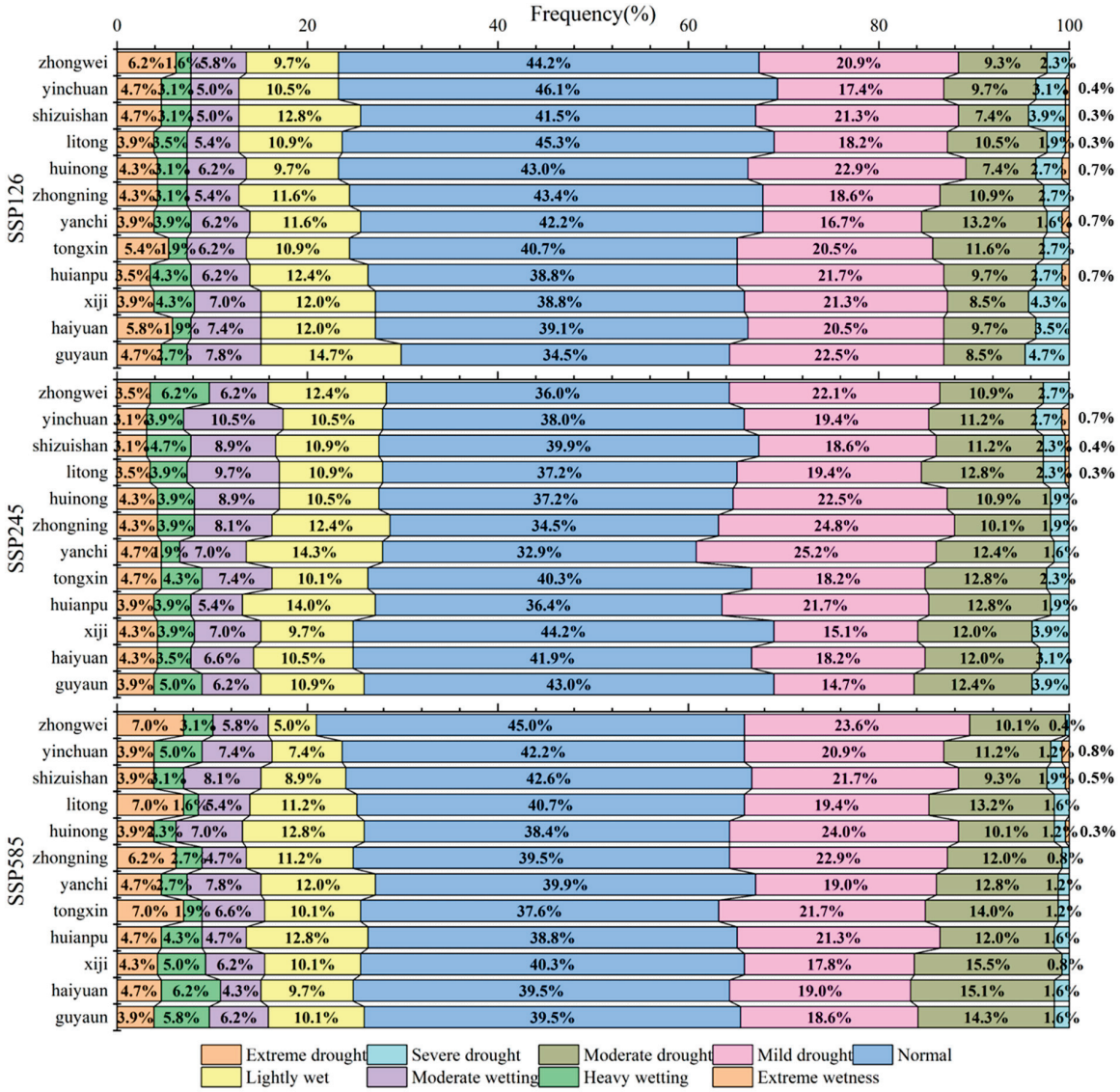

Figure 13. SPEI classification frequency. Note: SPEI ≤ -2.00 extreme drought, $-1.50 <$ SPEI ≤ -2.00 severe drought, $-1.00 <$ SPEI ≤ -1.50 moderate drought, $-0.50 <$ SPEI ≤ -1.00 mild drought, $-0.50 \leq$ SPEI ≤ 0.50 normal, $0.50 <$ SPEI ≤ 1.00 wet, $1.00 <$ SPEI ≤ 1.50 moderately wet, SPEI > 1.50 Extremely wet.

Based on the CMIP6 model, Liu et al. [42] found by analyzing the water balance between increasing evapotranspiration caused by rising temperature and increasing precipitation, that not all arid and semi-arid regions in northwest China will be wet in the future. In some areas, the drought trend would still be strong, and more severe in the high- than the low-

emission scenario. Based on CMIP5 data, according to Ma et al. [43], future changes will be characterized by significant contraction of the humid region and expansion of the arid/humid transition zone, results which are similar to our study. However, Zhang et al. [44] show that by the end of the 21st century, the area and severity of drought (based on scPDSI and SSIS) in the arid northwest will significantly trend downward. The reason for these differences may lie in the different index used to assess drought risk. The SPEI index predicts drought risk based on meteorological factors (precipitation, evapotranspiration), while Zhang et al. used an index based more on soil moisture analysis. Additionally, Tan et al. [24] showed that drought disaster risk in Ningxia may increase, reaching a maximum in the short-term, followed by the medium- and long-term. Conversely, we showed that the long-term risk increased significantly in the SSP585 model, while there was no significant change in the other two models. These differences reflect the different development models selected, and that the SPEI index was introduced to analyze the influence of evapotranspiration. However, Tan et al. [24] believe that compared with RCP2.6, drought disaster risk under the RCP4.5 scenario may further increase in the three periods, which concurs with our findings.

Referring to the future yield and fertility changes in the previous study and, in conjunction with the analysis of the future drought disaster risk for wheat in the study area, from the holistic perspective of the study area, the central arid zone faces the highest risk of drought disaster under SSP126 and SSP245 scenarios, with a greater distance to reach sufficient irrigation water. The southern mountainous area has limited access to light and heat resources, thus making the northern irrigation zone a suitable region for wheat cultivation. Specifically, for the experimental stations within the northern Yellow River Irrigation District, with the changing climatic conditions, advancing the sowing date appropriately can help achieve higher yields. Other than Yinchuan, Qingtongxia, where sowing can be advanced by an average of 1–3 days compared to the norm, under the SSP585 model, flowering can occur 4–8 days ahead of the average, which aids in making full use of rain and heat resources. Additionally, under the SSP585 scenario, the risk of drought will significantly increase across all stations in the study area in the future. However, the southern mountainous areas will not experience more severe drought due to yield reduction, and the rapid increase in temperature makes wheat cultivation more favorable. Therefore, if the rate of climate warming increases in the future, efforts should be made to develop and expand arable land in the southern mountainous areas to ensure the overall yield of wheat production.

Risk assessment is the core component of risk management, and its main purpose is to provide suggestions for risk-based decision-making and disaster risk management. Our results show that drought frequency and severity risk will increase, which will have a serious impact on agricultural production and economic development in Ningxia. Therefore, ways to reduce drought risk are the key issue. High-risk years and areas can also be avoided by adjusting planting areas and rationally planning grain reserves in advance [45], which requires the government to take corresponding measures. Additionally, for actual production practice, drought disaster damage can be alleviated by spring sowing in advance or artificial precipitation. Another approach is to improve crop adaptability and screen excellent drought-resistant varieties to reduce vulnerability [46]. Finally, governments could increase drought relief efforts such as efficient and water-saving agriculture development, reservoir and canal construction/renovation, planting structure adjustment, promotion of new drought resistant varieties, establishment of disaster preparedness and rescue systems and stockpiling a reserve of emergency materials [47].

5. Conclusions

Three CMIP6 development models were used to analyze future climate and dry hot wind meteorological changes in 12 test sites in Ningxia. The monthly SPEI index was calculated to analyze future spatiotemporal variation of drought conditions. In the study area overall, although temperature and precipitation would significantly increase, the risk of dry hot wind disaster and drought would also increase. Additionally, long-term drought risk would increase significantly under the high warming level model. During the wheat growing period,

there was a clear trend of increasing drought risk in May under the SSP585 model. Under the SSP245 model, there was no change in drought risk, and under the SSP126 model, the probability of drought risk appeared in the middle period and was the highest. In June, the SPEI index was generally higher than in May, and the risk of alternating drought and flood was greater under the SSP585 model, but the risk of near-medium drought was lower under the SSP126 and SSP245 models. The influence of DHW on wheat yield will increase with the increase of warming level, but the increase of rainfall will effectively inhibit the growth and harm of DHW, so the appropriate high rainfall will promote wheat yield.

Author Contributions: X.L. (Xinlong Li): conceptualization, data curation, investigation, methodology, software, writing—original draft and writing—review; J.T.: conceptualization, funding acquisition, investigation, supervision, writing—review and editing; X.W.: funding acquisition, investigation, supervision; Q.S.: conceptualization, data curation, software; H.L.: conceptualization, data curation, software; X.L. (Xuefang Li): conceptualization, data curation, software. All authors have read and agreed to the published version of the manuscript.

Funding: This work was supported by the National Key Research and Development Program of China [grant number 2018YFD0200405], the National Natural Science Foundation of China (52369010 and 31860590), the Natural Science Foundation of Ningxia [grant number 2022AAC02013], the National Key Research and Development Program of China [grant number 2021YFD1900605] and the Ningxia University First-class Discipline Construction (Hydraulic Engineering) Project [grant number NXYLXK2021A03].

Data Availability Statement: The data that have been used are confidential.

Conflicts of Interest: The authors declare that they have no known competing financial interests or personal relationships that could have influenced the work reported in this paper.

Appendix A

Table A1. Changes of near- and long-term average monthly temperature, precipitation and evaporation of each test point in the study area under SSP126, 245 and 585 models.

Research Site	Period	SSP126 Precipitation Monthly (mm)	SSP126 Evapotranspiration Monthly (mm)	SSP126 TasMean Monthly (°C)	SSP245 Precipitation Monthly (mm)	SSP245 Evapotranspiration Monthly (mm)	SSP245 TasMean Monthly (°C)	SSP585 Precipitation Monthly (mm)	SSP585 Evapotranspiration Monthly (mm)	SSP585 TasMean Monthly (°C)
A Guyuan	ST	46.69	38.61	8.07	46.68	37.86	8.32	46.63	38.58	8.17
	MT	49.79	40.61	8.26	49.23	39.82	8.93	49.32	40.54	9.41
	LT	48.99	40.08	8.30	51.81	40.82	9.12	52.18	42.30	10.79
B Haiyuan	ST	35.41	30.74	7.79	35.42	30.30	8.01	35.95	31.10	7.89
	MT	37.89	32.59	8.00	37.40	31.80	8.62	38.06	32.82	9.13
	LT	37.05	31.93	8.02	39.62	33.21	8.82	40.03	34.30	10.52
C Huianpu	ST	29.89	28.33	7.97	30.42	27.83	8.17	31.86	29.08	8.01
	MT	32.75	30.21	8.10	31.53	29.20	8.75	33.42	30.72	9.27
	LT	31.34	29.02	8.20	34.02	31.17	8.98	34.41	31.64	10.73
D Huinong	ST	15.80	15.12	7.40	16.86	15.94	7.62	18.00	17.01	7.40
	MT	17.52	16.61	7.46	16.95	16.16	8.12	17.97	16.96	8.71
	LT	17.32	16.41	7.54	18.13	17.18	8.43	18.95	17.95	10.26
E Litong	ST	20.05	19.49	7.94	20.50	19.44	8.13	21.79	20.59	8.01
	MT	22.06	21.06	8.10	21.31	20.24	8.71	22.95	21.72	9.28
	LT	20.87	20.11	8.15	22.98	22.01	8.97	23.36	22.49	10.75
F Shizuishan	ST	15.21	14.62	7.58	15.85	15.00	7.81	17.07	16.14	7.62
	MT	16.82	15.99	7.69	16.12	15.35	8.32	17.28	16.35	8.92
	LT	16.29	15.52	7.75	17.30	16.45	8.63	18.14	17.26	10.45
G Tongxin	ST	29.44	26.47	8.01	29.68	26.20	8.21	30.51	27.15	8.11
	MT	31.81	28.25	8.22	31.27	27.44	8.83	32.52	28.83	9.36
	LT	30.68	27.38	8.25	33.36	29.20	9.04	33.48	29.87	10.77
H Xiji	ST	45.79	37.92	7.64	45.46	37.13	7.90	45.55	37.79	7.76
	MT	48.56	39.86	7.86	48.13	39.08	8.50	48.17	39.73	8.99
	LT	48.02	39.43	7.87	50.76	40.09	8.69	51.21	41.65	10.35
I Yanchi	ST	35.45	32.94	7.70	36.27	32.44	7.93	37.79	33.75	7.67
	MT	38.81	34.96	7.74	37.23	33.97	8.45	38.96	35.11	8.95
	LT	37.76	33.98	7.88	40.09	35.61	8.69	40.83	36.30	10.44
J Yinchuan	ST	17.31	16.74	7.77	17.79	16.85	7.98	19.05	18.01	7.82
	MT	19.08	18.17	7.90	18.33	17.42	8.53	19.73	18.67	9.11
	LT	18.20	17.45	7.96	19.73	18.82	8.81	20.37	19.50	10.62
K Zhongning	ST	20.23	20.10	8.09	20.80	20.19	8.26	21.98	21.23	8.18
	MT	22.35	21.82	8.29	21.76	21.01	8.88	23.45	22.64	9.44
	LT	21.05	20.80	8.33	23.42	23.03	9.11	23.63	23.35	10.87
L Zhongwei	ST	19.22	19.30	8.04	19.99	19.64	8.21	21.04	20.58	8.04
	MT	21.37	21.07	8.23	20.80	20.32	8.82	22.23	21.74	8.23
	LT	20.38	20.25	8.26	22.28	22.08	9.05	22.73	22.57	8.26

Table A2. The average DHW days during wheat growing period were measured under SSP126, 245 and 585 models.

Dry Hot Wind Days (d)	Southern Mountainous Area of Ningxia			Arid Area of Central Ningxia				Northern Region of Ningxia				
	guyaun	haiyuan	xiji	huianpu	tongxin	yanchi	zhongning	huinong	litong	shizuishan	yinchuan	zhongwei
SSP126 ST	3.47	5.47	2.67	8.27	6.60	6.97	10.57	13.83	10.63	13.53	12.53	9.57
SSP126 MT	2.23	4.69	2.08	7.04	5.42	6.31	9.42	12.54	9.15	12.85	11.27	8.19
SSP126 LT	3.80	5.53	3.10	8.43	6.23	7.70	10.93	15.57	11.10	15.13	13.20	10.37
SSP245 ST	2.17	3.23	1.63	6.40	5.00	5.67	9.07	13.63	9.30	13.17	11.57	8.17
SSP245 MT	2.96	4.46	2.08	7.73	6.46	6.81	10.77	14.19	11.58	14.81	13.27	9.19
SSP245 LT	3.43	4.53	2.30	7.90	5.70	6.57	9.50	15.60	11.30	15.50	12.57	8.93
SSP585 ST	3.77	5.20	4.13	7.90	6.27	7.30	10.20	13.60	10.17	14.00	12.37	8.73
SSP585 MT	5.50	7.42	6.50	11.81	8.73	11.46	14.58	19.58	15.73	19.85	17.92	14.27
SSP585 LT	7.90	10.37	8.07	13.60	11.03	12.70	17.13	22.30	17.67	22.07	20.17	17.17

References

1. Musolino, D.A.; Massarutto, A.; de Carli, A. Does drought always cause economic losses in agriculture? An empirical investigation on the distributive effects of drought events in some areas of Southern Europe. *Sci. Total Environ.* **2018**, *633*, 1560–1570. [CrossRef] [PubMed]
2. Zhang, Q.; Yu, H.; Sun, P.; Singh, V.P.; Shi, P. Multisource data based agricultural drought monitoring and agricultural loss in China. *Glob. Planet. Change* **2019**, *172*, 298–306. [CrossRef]
3. Trenberth, K.E.; Dai, A.; van der Schrier, G.; Jones, P.D.; Barichivich, J.; Briffa, K.R.; Sheffield, J. Global warming and changes in drought. *Nat. Clim. Change* **2014**, *4*, 17–22. [CrossRef]
4. Spinoni, J.; Vogt, J.V.; Naumann, G.; Barbosa, P.; Dosio, A. Will drought events become more frequent and severe in Europe? *Int. J. Clim.* **2018**, *38*, 1718–1736. [CrossRef]
5. Tavakol, A.; Rahmani, V.; Harrington, J.J. Temporal and spatial variations in the frequency of compound hot, dry, and windy events in the central United States. *Sci. Rep.* **2020**, *10*, 15691. [CrossRef]
6. Cai, D.; Shoukat, M.R.; Zheng, Y.; Tan, H.; Meng, F.; Yan, H. Optimizing Center Pivot Irrigation to Regulate Field Microclimate and Wheat Physiology under Dry-Hot Wind Conditions in the North China Plain. *Water* **2022**, *14*, 708. [CrossRef]
7. Wang, S.; Zheng, H.; Liu, S.; Miao, Y.; Li, J. Numerical Study on the Stomatal Responses to Dry-Hot Wind Episodes and Its Effects on Land-Atmosphere Interactions. *PLoS ONE* **2016**, *11*, e0162852. [CrossRef]
8. Huang, S.; Leng, G.; Huang, Q.; Xie, Y.; Liu, S.; Meng, E.; Li, P. The asymmetric impact of global warming on US drought types and distributions in a large ensemble of 97 hydro-climatic simulations. *Sci. Rep.* **2017**, *7*, 5891. [CrossRef]
9. Li, S.; Zhang, L.; Huang, B.; He, L.; Zhao, J.; Guo, A. A comprehensive index for assessing regional dry-hot wind events in Huang-Huai-Hai Region, China. *Phys. Chem. Earth Parts A/B/C* **2020**, *116*, 102860. [CrossRef]
10. Zhao, H.; Zhang, L.; Kirkham, M.B.; Welch, S.M.; Nielsen-Gammon, J.W.; Bai, G.; Luo, J.; Andresen, D.A.; Rice, C.W.; Wan, N.; et al. Winter wheat yield loss attributed to compound hot-dry-windy events. *Nat. Commun.* **2022**, *13*, 7233. [CrossRef]
11. Zhao, C.; Zhang, Y.; Wang, Z.; Li, D. Effects of Freezing Damage and Dry Hot Wind on Wheat Production and Defense Countermeasures in Hebei Province. *Guizhou Nong Ye Ke Xue* **2011**, *39*, 80–82.
12. Liu, J.; Zhang, X.; Ma, G.; Cao, N.; Ma, L. Analysis of spectral characteristics of dry hot air hazard of spring wheat in Ningxia. *Trans. Chin. Soc. Agric. Eng.* **2012**, *28*, 189–199. [CrossRef]
13. Xu, Y.; Wu, Y.; Ji, B.; Song, J.; Lv, G.; Zhang, W.; Liu, B.; Bai, W. Effect of phosphorus and sugar preparation on resistance to dry hot air and yield of winter wheat. *J. Wheat Crops* **2022**, *42*, 236–245.
14. Xiao, G.; Zheng, F.; Qiu, Z.; Yao, Y. Impact of climate change on water use efficiency by wheat, potato and corn in semiarid areas of China. *Agric. Ecosyst. Environ.* **2013**, *181*, 108–114. [CrossRef]
15. Huo, Z.; Shang, Y.; Wu, D.; Wu, L.; Fan, Y.; Wang, P.; Yang, J.; Wang, C. Research progress on dry hot air disaster of wheat in China. *J. Appl. Meteorol.* **2019**, *30*, 129–141.
16. Li, X.; Tan, J.; Dong, L.; Wang, X. Analysis and prediction of dry hot air change characteristics and influencing factors of spring wheat in Ningxia. *Agric. Res. Arid Areas* **2023**, *41*, 283–292. [CrossRef]
17. Qi, Y.; Wang, H.; Zhang, K.; Wang, R.; Lei, J. Effects of climate change on spring wheat growth and yield in semi-arid region of the Loess Plateau: A case study of Dingxi City. *J. Ecol. Environ.* **2019**, *28*, 1313–1321. [CrossRef]
18. Zhao, J.; Pu, F.; Li, Y.; Xu, J.; Li, N.; Zhang, Y.; Guo, J.; Pan, Z. Assessing the combined effects of climatic factors on spring wheat phenophase and grain yield in Inner Mongolia, China. *PLoS ONE* **2017**, *12*, e0185690. [CrossRef]
19. Liu, L.; Liu, J.; Wu, D.; Xu, Y.; Jiang, C. Temporal and Spatial Variations of Dry-hot Windy Days in North China Under the Condition of Climatic Change in the Future. *Ke Ji Dao Bao* **2012**, *30*, 24–27. [CrossRef]
20. Zargar, A.; Sadiq, R.; Naser, B.; Khan, F.I. A review of drought indexes. *Environ. Rev.* **2011**, *19*, 333–349. [CrossRef]
21. Beguería, S.; Vicente-Serrano, S.M.; Reig, F.; Latorre, B. Standardized precipitation evapotranspiration index (SPEI) revisited: Parameter fitting, evapotranspiration models, tools, datasets and drought monitoring. *Int. J. Clim.* **2014**, *34*, 3001–3023. [CrossRef]
22. Tirivarombo, S.; Osupile, D.; Eliasson, P. Drought monitoring and analysis: Standardised Precipitation Evapotranspiration Index (SPEI) and Standardised Precipitation Index (SPI). *Phys. Chem. Earth Parts A/B/C* **2018**, *106*, 1–10. [CrossRef]
23. Vicente-Serrano, S.M.; Van der Schrier, G.; Beguería, S.; Azorin-Molina, C.; Lopez-Moreno, J. Contribution of precipitation and reference evapotranspiration to drought indexes under different climates. *J. Hydrol.* **2015**, *526*, 42–54. [CrossRef]

24. Tan, C.; Yang, J.; Wang, X.; Qin, D.; Huang, B.; Chen, H. Drought disaster risks under CMIP5 RCP scenarios in Ningxia Hui Autonomous Region, China. *Nat. Hazards.* **2020**, *100*, 909–931. [CrossRef]
25. Chen, H.; Sun, J. Changes in Drought Characteristics over China Using the Standardized Precipitation Evapotranspiration Index. *J. Clim.* **2015**, *28*, 5430–5447. [CrossRef]
26. Li, Y.; Wang, Z.; Zhang, Y.; Li, X.; Huang, W. Drought variability at various timescales over Yunnan Province, China: 1961–2015. *Theor. Appl. Climatol.* **2019**, *138*, 743–757. [CrossRef]
27. Zhou, T.; Zou, L.; Chen, X. Review of the sixth International Coupling Model Comparison Program (CMIP6). *Adv. Clim. Chang. Res.* **2019**, *15*, 445–456.
28. Li, X.; Tan, J.; Wang, X.; Han, G.; Qian, Z.; Li, H.; Wang, L.; Niu, G. Responses of spring wheat yield and growth period to different future climate change models in the yellow river irrigation area based on CMIP6 and WOFOST models. *Agr. Forest Meteorol.* **2024**, *353*, 110071. [CrossRef]
29. Vicente-Serrano, S.M.; Beguería, S.; López-Moreno, J.I. A Multiscalar Drought Index Sensitive to Global Warming: The Standardized Precipitation Evapotranspiration Index. *J. Clim.* **2010**, *23*, 1696–1718. [CrossRef]
30. Helsel, D.R.; Frans, L.M. Regional Kendall test for trend. *Environ. Sci. Technol.* **2006**, *40*, 4066–4073. [CrossRef]
31. Wu, D.; Ouyang, B.; Zhao, X.; Yu, Q.; Luo, Y. Applicability of crop growth model WOFOST in North China Plain. *Chin. J. Plant Ecol.* **2003**, *5*, 594–602.
32. Li, X.; Tan, J.; Li, H.; Wang, L.; Niu, G.; Wang, X. Sensitivity Analysis of the WOFOST Crop Model Parameters Using the EFAST Method and Verification of Its Adaptability in the Yellow River Irrigation Area, Northwest China. *Agronomy* **2023**, *13*, 2294. [CrossRef]
33. Li, B.; Liang, Z.; Zhang, J.; Wang, G. A revised drought index based on precipitation and pan evaporation. *Int. J. Clim.* **2017**, *37*, 793–801. [CrossRef]
34. Stagge, J.H.; Tallaksen, L.M.; Gudmundsson, L.; Van Loon, A.F.; Stahl, K. Candidate Distributions for Climatological Drought Indexes (SPI and SPEI). *Int. J. Clim.* **2015**, *35*, 4027–4040. [CrossRef]
35. Naumann, G.; Alfieri, L.; Wyser, K.; Mentaschi, L.; Betts, R.A.; Carrao, H.; Spinoni, J.; Vogt, J.; Feyen, L. Global Changes in Drought Conditions Under Different Levels of Warming. *Geophys. Res. Lett.* **2018**, *45*, 3285–3296. [CrossRef]
36. Ma, Y.; Cui, Y.; Zhang, W.; Li, X. Prediction of future temperature change in Ningxia section of Yellow River Basin based on CMIP6 model. *Arid. Meteorol.* **2023**, *41*, 43–53.
37. Zhang, S.; Hu, Y.; Li, Z. Variation trend and forecast of precipitation in northwest China. *Adv. Clim. Change Res.* **2022**, *18*, 683–694.
38. Li, S.; Miao, L.; Jiang, Z.; Wang, G.; Gnyawali, K.R.; Zhang, J.; Zhang, H.; Fang, K.; He, Y.; Li, C. Projected drought conditions in Northwest China with CMIP6 models under combined SSPs and RCPs for 2015–2099. *Adv. Clim. Chang. Res.* **2020**, *11*, 210–217. [CrossRef]
39. Feng, Y.; Sun, F.; Liu, F. Temporal and spatial variations of multivariate hot, dry and windy climate extremes in Northwest China. *Int. J. Clim.* **2023**, *43*, 8005–8018. [CrossRef]
40. Yao, N.; Li, L.; Feng, P.; Feng, H.; Li Liu, D.; Liu, Y.; Jiang, K.; Hu, X.; Li, Y. Projections of drought characteristics in China based on a standardized precipitation and evapotranspiration index and multiple GCMs. *Sci. Total Environ.* **2020**, *704*, 135245. [CrossRef]
41. Tietjen, B.; Schlaepfer, D.R.; Bradford, J.B.; Lauenroth, W.K.; Hall, S.A.; Duniway, M.C.; Hochstrasser, T.; Jia, G.; Munson, S.M.; Pyke, D.A.; et al. Climate change-induced vegetation shifts lead to more ecological droughts despite projected rainfall increases in many global temperate drylands. *Global Change Biol.* **2017**, *23*, 2743–2754. [CrossRef] [PubMed]
42. Liu, Y.; Tian, J.; Fu, Y.; Zhu, B.; He, X.; Gao, M.; Odamtten, M.T.; Kong, R.; Zhang, Z. Will the arid and semi-arid regions of Northwest China become warmer and wetter based on CMIP6 models? *Hydrol. Res.* **2022**, *53*, 29–50. [CrossRef]
43. Ma, D.; Deng, H.; Yin, Y.; Wu, S.; Zheng, D. Sensitivity of arid/humid patterns in China to future climate change under a high-emissions scenario. *J. Geogr. Sci.* **2019**, *29*, 29–48. [CrossRef]
44. Zhang, G.; Gan, T.Y.; Su, X. Twenty-first century drought analysis across China under climate change. *Clim. Dynam.* **2022**, *59*, 1665–1685. [CrossRef]
45. Masipa, T.S. The impact of climate change on food security in South Africa: Current realities and challenges ahead. *Jamba* **2017**, *9*, 411. [CrossRef]
46. Cooper, M.; Messina, C.D. Breeding crops for drought-affected environments and improved climate resilience. *Plant Cell* **2023**, *35*, 162–186. [CrossRef]
47. Yuan, X.; Su, C.; Umar, M.; Shao, X.; LOBONŢ, O. The race to zero emissions: Can renewable energy be the path to carbon neutrality? *J. Environ. Manag.* **2022**, *308*, 114648. [CrossRef]

Disclaimer/Publisher's Note: The statements, opinions and data contained in all publications are solely those of the individual author(s) and contributor(s) and not of MDPI and/or the editor(s). MDPI and/or the editor(s) disclaim responsibility for any injury to people or property resulting from any ideas, methods, instructions or products referred to in the content.

applied sciences

MDPI

Article

Recent Spatiotemporal Changes of Subhourly Extreme Rainfall Events in Seoul

Ju-Young Shin [1], Jiyeon Park [1], Kyungmin Sung [2,*] and Yongseok Kim [3]

[1] Department of Civil and Environmental Engineering, Kookmin University, Seoul 02707, Republic of Korea
[2] Korea Adaptation Center for Climate Change, Korea Environment Institute, Sejong 30116, Republic of Korea
[3] Climate Change Assessment Division, National Institute of Agricultural Sciences, Wanju 55365, Republic of Korea
* Correspondence: kmsung@kei.re.kr

Abstract: This study aims to examine the spatiotemporal variations of extreme rainfall events in Seoul, South Korea, utilizing subhourly rainfall data collected from an extensive observation network. Employing the Mann–Kendall trend detection test and Moran's *I* index, this study analyzed temporal trends and spatial distributions in the extreme rainfall time series at 37 weather stations. The findings revealed that the annual maximum precipitation (AMP) series for various durations in Seoul generally exhibited a decreasing trend, with a marked decline observed for durations of 300 and 360 min. Furthermore, the study identified notable changes in the spatial patterns of AMP events, particularly for subhourly AMP events. The results indicate an intensification in the spatial concentration of AMP distribution. Consequently, despite the overall reduction in AMP, the likelihood of urban flooding may increase. This suggests that existing hydraulic design criteria, based on past concepts that temporal and spatial variability are constant, may no longer adequately represent extreme rainfall events. Therefore, revising these criteria to account for the evolving nature of extreme rainfall patterns is imperative.

Keywords: rainfall pattern; annual maximum precipitation; Moran's *I*; trend detection test; climate change; urban inundation

1. Introduction

In recent decades, South Korea has made substantial efforts toward flood defense, achieving minimal flood damage from rainfall events with a frequency of less than 100 years. These efforts have primarily targeted fluvial flooding, as evidenced by the construction of levees and dams along major rivers. Although damage from fluvial flooding has significantly decreased, pluvial flooding has become more prevalent because of climate change.

For example, Seoul has experienced sporadic urban flooding, with notable incidents occurring in 2010, 2011, 2018, and 2022. Over the past 15 years, flooding has affected the city approximately 25% of the time. As Seoul is South Korea's capital, even minor flooding there can result in considerable economic damage. To mitigate the effects of urban flooding and devise effective future strategies, comprehensive investigations and analyses of the current patterns and characteristics of extreme rainfall events are essential. Such efforts will significantly enhance our understanding of extreme rainfall phenomena in Seoul.

Extensive research has been conducted on the temporal and spatial changes in rainfall characteristics owing to climate change [1–4]. Numerous studies have specifically examined the impact of climate change on rainfall patterns in South Korea. For example, Jung, et al. [5] identified a statistically significant trend of increasing annual maximum

precipitation (AMP) in certain regions of South Korea. Although the increase in AMP was not statistically significant, trends showing an increase in probable rainfall values have also been observed [6]. Additionally, some studies have investigated the spatial and temporal changes associated with climate change across various variables, including drought and soil erosion [7–11].

Many studies have focused on large geographic areas rather than smaller urban areas when analyzing rainfall patterns. Urban flooding is typically evaluated through simulations using rainfall data rather than direct surface water observations because of the intermittent nature of these events [12–14]. Generally, high-resolution spatiotemporal rainfall data are essential for effectively assessing and analyzing the impact of urban flooding [15]. However, a lack of long-term high-resolution rainfall data, particularly in South Korea, has resulted in a deficiency in studies on urban flooding and its effects in the context of climate change. To prevent urban flooding and mitigate the damage from urban inundation, it is crucial to investigate the spatiotemporal variations in urban flooding. Therefore, examining the spatiotemporal variations of rainfall patterns in urban areas based on high-resolution data is required to achieve these goals.

This study aims to examine the spatiotemporal changes in extreme rainfall in Seoul based on subhourly rainfall data derived from an extensive observation network. It attempts to address the following hypotheses to improve our understanding of extreme rainfall events in Seoul:

(1) Temporal characteristics of extreme rainfall in Seoul have changed.
(2) Spatial patterns of extreme rainfall in Seoul have been altered.

In the current study, the spatial patterns refer to the dispersion and autocorrelation of AMPs. The dispersion and autocorrelation represent the spatial clustering of AMPs. The temporal characteristics of extreme rainfall indicate trends in AMP series and spatial patterns. Temporal trends in the extreme rainfall time series were analyzed using the Mann–Kendall trend detection (MK) test, while the spatial patterns of extreme rainfall events in Seoul were examined based on the coefficients of variation (CV) and Moran's I. It was assumed that the spatial pattern of extreme rainfall had changed when temporal trends in CV and Moran's I were detected. This study's findings will help us better understand the variations in extreme rainfall in Seoul, particularly in urban areas of South Korea. This will enhance our capacity to mitigate and prevent urban flooding and inundation.

2. Study Area and Data Description

Seoul, the capital and largest metropolis of South Korea, is strategically located along the Han River in the northwestern part of the country. The city is surrounded by mountains, which enhance its scenic beauty. Seoul has a humid continental climate characterized by four distinct seasons. Summers are typically hot and humid, while winters are cold and dry, with the city experiencing a monsoon season during the summer months. As one of the most densely populated cities globally, Seoul has a population exceeding 9 million.

For disaster prevention and monitoring in urban areas, the Korea Meteorological Administration (KMA) has installed approximately 700 automatic weather stations (AWSs) across South Korea. To analyze extreme rainfall events in Seoul, AWSs located within and near the city were investigated. AWSs with an operational period of less than 20 years were excluded from the analysis. The AWSs were chosen to ensure that the Thiessen polygons formed by the AWSs could cover the entire administrative area of Seoul. The final selection included 37 AWSs located within and near Seoul. Figure 1 depicts the locations of the selected AWSs and their Thiessen polygons.

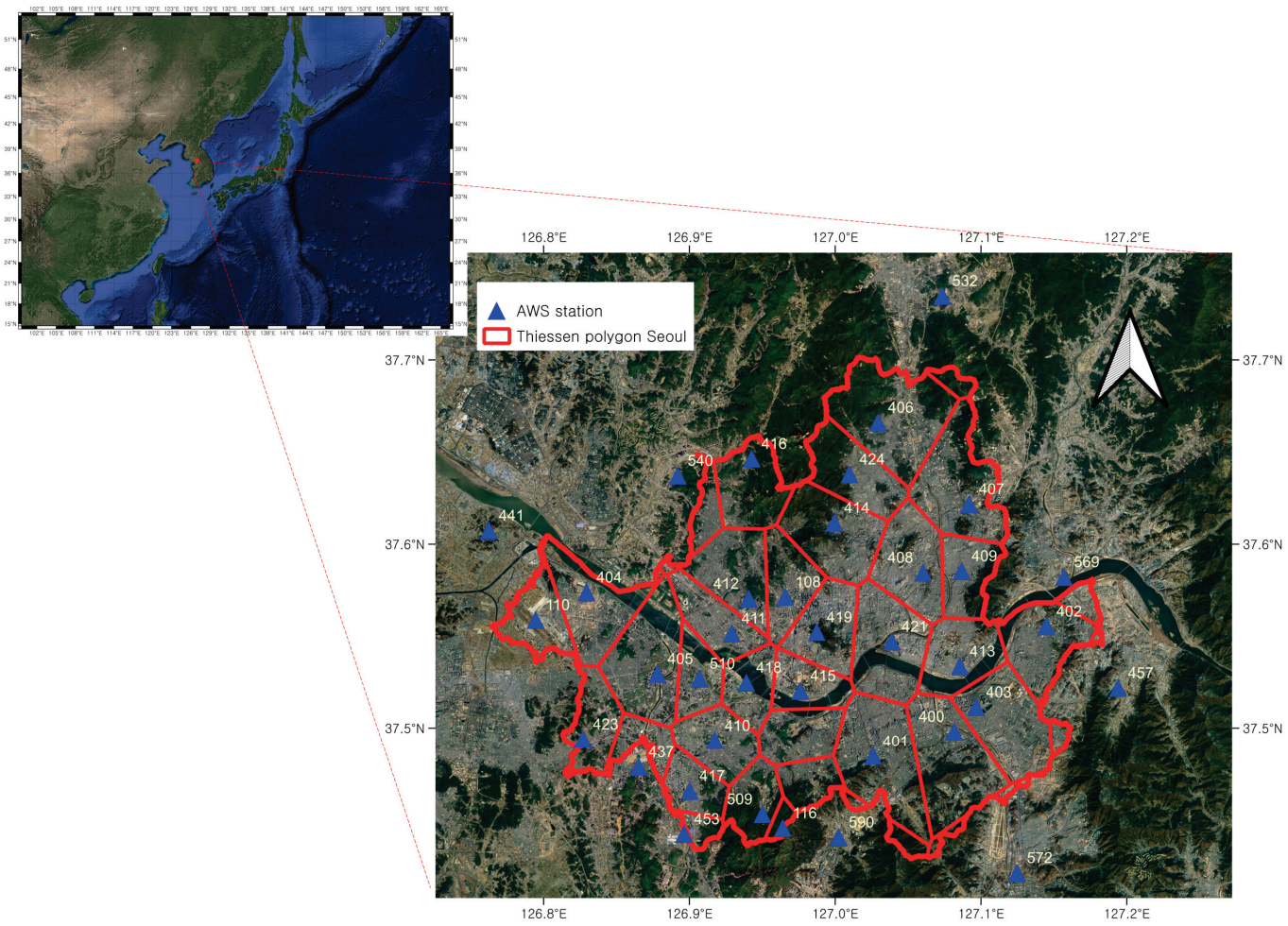

Figure 1. Locations of selected AWS stations and their Thiessen polygons in Seoul.

The average area of each Thiessen polygon was 15.71 km^2, indicating that each AWS represented an area of approximately 4 km by 4 km. This spatial resolution is considered adequate for analyzing the characteristics of rainfall events in urban areas. The names, altitudes (elevation: EL.(m)), and observation start years of the selected AWSs are summarized in Table S1. The KMA AWSs record cumulative rainfall data every minute, which are then aggregated every 15 min. In this study, 15 min cumulative rainfall data were collected for each station from their observation start year until 2024, with recordings taken at 0, 15, 30, and 45 min past each hour.

In this study, extreme precipitation events were defined as AMP events. In urban areas, the impact of rainfall events on drainage systems varies based on their duration and intensity, which are influenced by the size of the drainage basin. Urban inundation can result from short-duration rainfall events lasting less than an hour or from longer events lasting 4–5 h [16–18]. Thus, using 15 min cumulative rainfall data, the AMPs for durations of 15, 30, 45, 60, 120, 180, 240, 300, and 360 min were calculated. The current study used seven durations: three subhourly durations (15, 30, and 45 min) and four hourly durations (60, 120, 180, 240, 300, and 360 min).

Figure 2 presents basic statistics of the AMP events for the selected AWS stations in Seoul. As the duration increased, the mean and standard deviation of the AMPs also increased, accompanied by larger dispersion among stations. The coefficients of skewness and kurtosis showed the smallest values at 30 min, increased between 30 and 240 min, and then exhibited a decreasing trend after 240 min. The calculated statistics indicate that the

characteristics of extreme rainfall events in Seoul vary significantly depending on their duration and location.

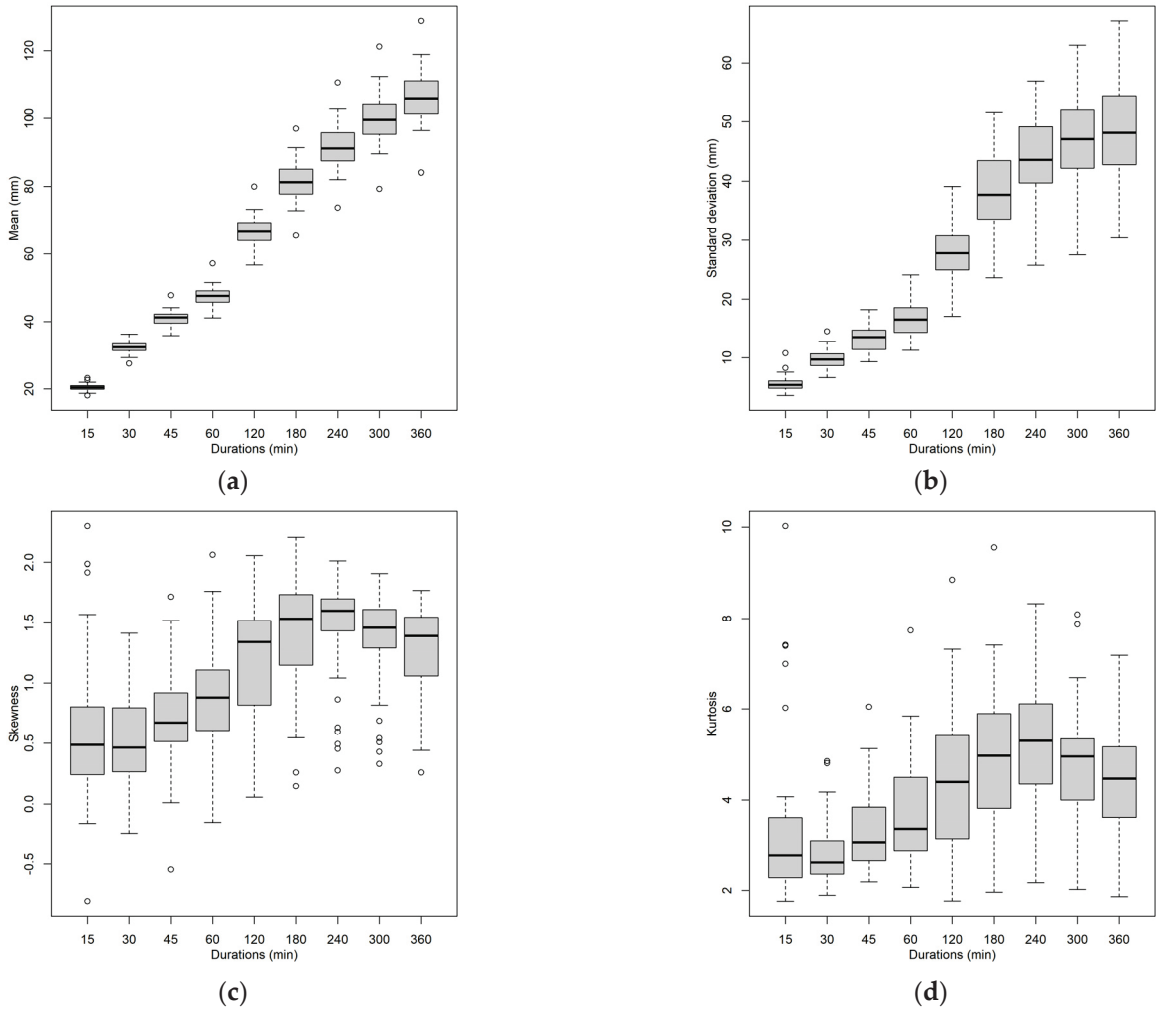

Figure 2. Basic statistics of the annual maximum precipitation (AMP) series for selected stations, including (**a**) mean, (**b**) standard deviation, (**c**) coefficient of skewness, and (**d**) coefficient of kurtosis.

3. Methodology

3.1. Mann–Kendall Trend Detection Test

The MK test is a statistical method used to detect and analyze trends in time series data [19,20]. This test is particularly valuable for examining long-term (e.g., longer than 20 years) changes in natural phenomena, including but not limited to climate data and hydrological records [21,22]. As a nonparametric method, the MK test is versatile and robust because it does not require any assumptions concerning data distribution. This procedure involves comparing the ranks between pairs of observed values to ascertain whether there is an overall increasing or decreasing trend. Specifically, the test evaluates whether the observed data exhibit a monotonic increase or decrease over time. The MK test can determine the statistical significance of the identified trend through *p*-values, which quantify the likelihood that the observed trend occurred by chance. This feature makes the MK test a powerful tool for hypothesis testing. Furthermore, the MK test is renowned for its effectiveness in handling datasets with substantial noise or non-normality from measuring noise, human error, and the nature of positive numbers, making it a preferred choice in environmental and climate research, where data irregularities are common [23,24].

The test statistic (S) used in the MK test is expressed as follows:

$$S = \sum_{i=1}^{n-1} \sum_{j=i+1}^{n} sign(y_j - y_i),\ sign(\alpha) = \begin{cases} 1\ if\ \alpha > 0 \\ 0\ if\ \alpha = 0 \\ -1\ if\ \alpha < 0 \end{cases} \quad (1)$$

where y_i and y_j represent the sequential data values and n denotes the total number of observations in the time series. A positive S-statistic signifies an increasing trend, whereas a negative S-statistic indicates a decreasing trend. According to Mann [25] and Kendall [26], when n exceeds 8, the S-statistic approximates a normal distribution with its variance, which is mathematically expressed as follows:

$$\mathrm{V(S)} = \frac{n(n-1)(2n+5) - \sum_{l=1}^{n} t_l l(l-1)(2l+5)}{18} \quad (2)$$

where t_l indicates the number of ties of extent l. The standard MK statistic Z is computed using Equation (3).

$$\mathrm{Z} = \begin{cases} \frac{S-1}{\sqrt{V(S)}} & for\ S > 0 \\ 0 \quad for\ S = 0 \\ \frac{S+1}{\sqrt{V(S)}} & for\ S < 0 \end{cases} \quad (3)$$

Under the null hypothesis of no trend, the Z-statistic follows the standard normal distribution.

3.2. Moran's I Index and Its Statistical Test for Spatial Dependence

Moran's I is a statistical measure developed to detect spatial autocorrelation, which indicates the degree to which a given variable is similar to itself in nearby locations [27]. It is widely used in spatial statistics to analyze and quantify the similarity or dissimilarity of a variable across space. Essentially, Moran's I assesses whether the observed pattern is clustered, dispersed, or random. This method is particularly valuable in fields such as geography, environmental science, and water resources, where understanding spatial relationships is crucial for interpreting patterns and trends in data [28–31]. Moran's I, therefore, indicates the spatial clustering pattern. It is calculated using the following formula:

$$I = \frac{N}{W} \frac{\sum_{i=1}^{N} \sum_{j=1}^{N} w_{ij}(x_i - \overline{x})(x_j - \overline{x})}{\sum_{i=1}^{N}(x_i - \overline{x})} \quad (4)$$

where N represents the number of observations; w_{ij} denotes the weight between locations i and j; x_i and x_j are the values at locations i and j, respectively; $\overline{x}$ signifies the mean of the variable; and W is the sum of all weights ($\sum_{i=1}^{N} \sum_{j=1}^{N} w_{ij}$). In this study, w_{ij} is given by the following equation:

$$w_{ij} = \frac{1}{d_{ij}} \quad (5)$$

where d_{ij} is distance (km) between location locations i and j.

Moran's I ranges from -1 to 1. Values approaching 1 indicate a strong positive spatial autocorrelation, suggesting that similar values cluster spatially. Conversely, values nearing -1 indicate strong negative spatial autocorrelation, implying that dissimilar values are located adjacently. Values close to 0 suggest the absence of spatial autocorrelation. To assess the significance of Moran's I, the z-value is computed using the expected value and variance of the statistic. The expected value is given by $E(I) = -\frac{1}{N-1}$, while the variance is derived using a more intricate formula. Typically, the significance is evaluated through Monte Carlo simulations or randomization tests, which offer robust assessments of the

spatial patterns in the data. In this study, Moran's I and its hypothesis test were computed using the "Spatial Dependence: Weighting Schemes, Statistics" package in R 4.3.1 [32].

3.3. Coefficients of Variation for Estimating Spatial Dispersion

In the current study, the CVs of AMP values at various stations within the same year were utilized to represent the spatial dispersion of AMP. A high CV value suggests a significant likelihood of localized heavy rainfall during AMP events. Conversely, a low CV value implies that all AMP values may originate from a single large system, such as a monsoon or typhoon. The annual CV of AMP can be determined using the following formula:

$$CV_t = \frac{\sigma_t}{\overline{x}_t} = \frac{1}{\overline{x}_t} \frac{\sum_{i=1}^{N} (x_{it} - \overline{x}_t)^2}{N} \quad (6)$$

where N represents the number of observations, x_{it} and x_j are the values at locations I in year t, $\overline{x}$ is the mean of the variable in year t, and σ_t is the standard deviation of x_{it} in year t.

4. Results

4.1. Temporal Changes in Extreme Rainfall Events

Figure 3 presents the observed AMP at the selected stations across different durations for each year, represented through boxplot visualizations. For the 15 min duration, the box sizes in Figure 3 remained relatively consistent across different years. However, from the 30 min duration onwards, there were substantial variations in the box sizes each year. For durations exceeding 1 h, the spatial pattern of AMP in the Seoul region demonstrated significant interannual differences, with these variations becoming more pronounced as the duration increased.

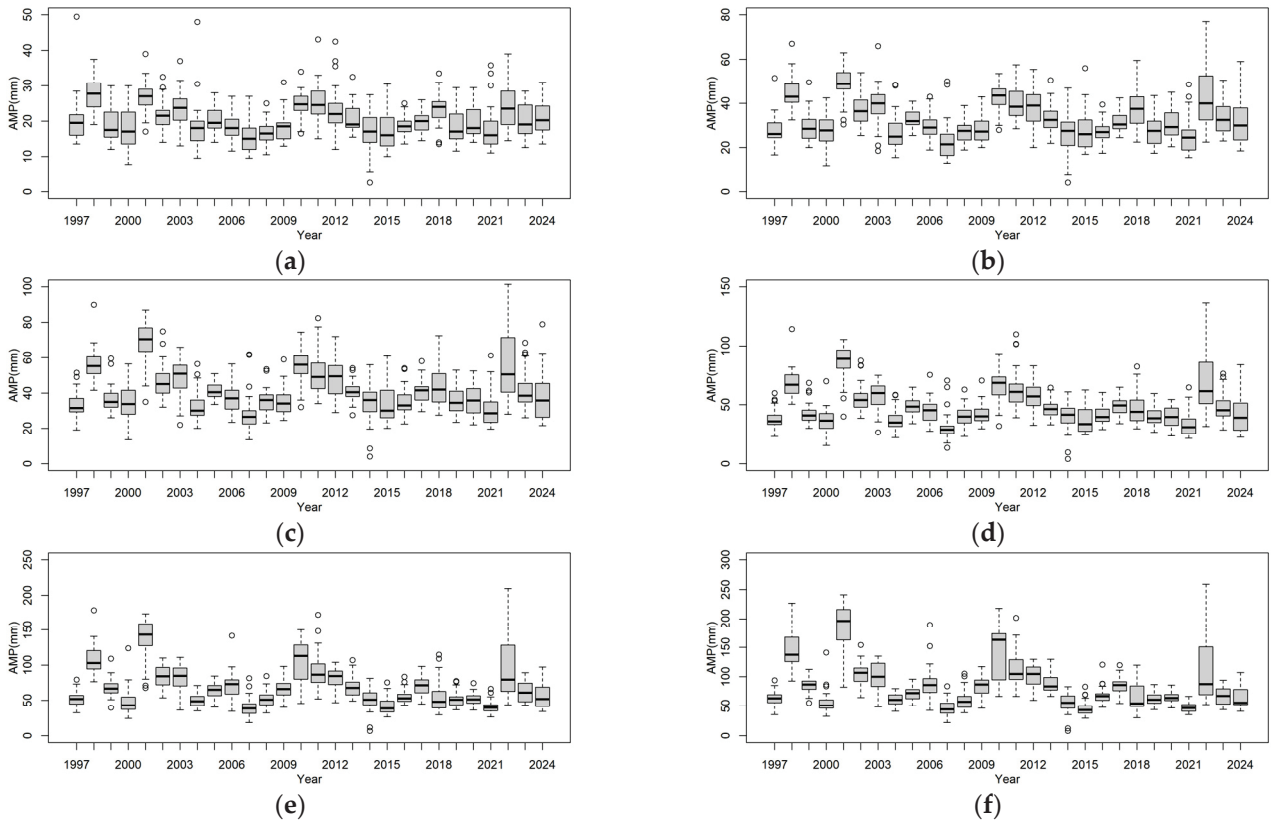

Figure 3. *Cont.*

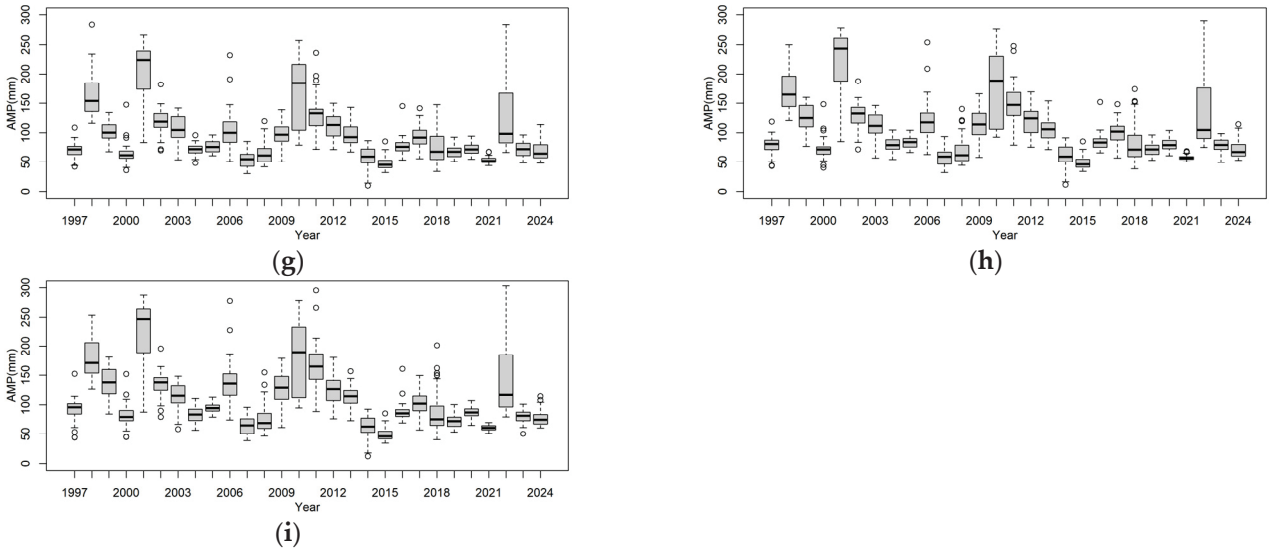

Figure 3. Boxplots of annual maximum precipitation (AMP) for selected stations for each year at various durations: (**a**) 15 min, (**b**) 30 min, (**c**) 45 min, (**d**) 60 min, (**e**) 120 min, (**f**) 180 min, (**g**) 240 min, (**h**) 300 min, and (**i**) 360 min.

The annual AMP mean series from the selected stations for each duration were plotted to examine the temporal variations in AMP across Seoul, as shown in Figure 4. Furthermore, the MK test was applied to the AMP mean series across all durations to assess the statistical significance of these temporal changes. The AMP mean series exhibited a decreasing trend over time across all durations, with the rate of decline less pronounced for shorter durations. For durations of 300 and 360 min, the MK test revealed statistically significant decreasing trends at significance levels of 10% and 5%, respectively. The AMP means in Seoul demonstrated a gradual decline, which became more pronounced with increasing duration. Notably, the AMP means for subhourly durations in 2018 were relatively larger than in other years, whereas the AMP means for hourly durations in 2018 were comparatively smaller. Since Seoul experienced significant flood damage in 2018, it can be inferred that extreme rainfall during subhourly durations contributed to urban flooding in the city.

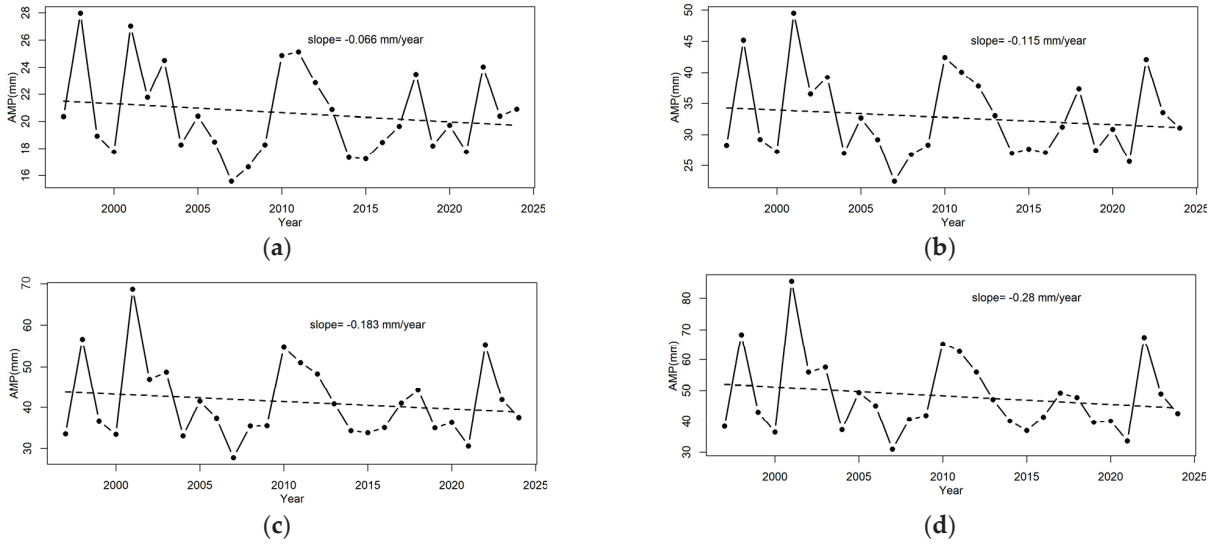

Figure 4. *Cont.*

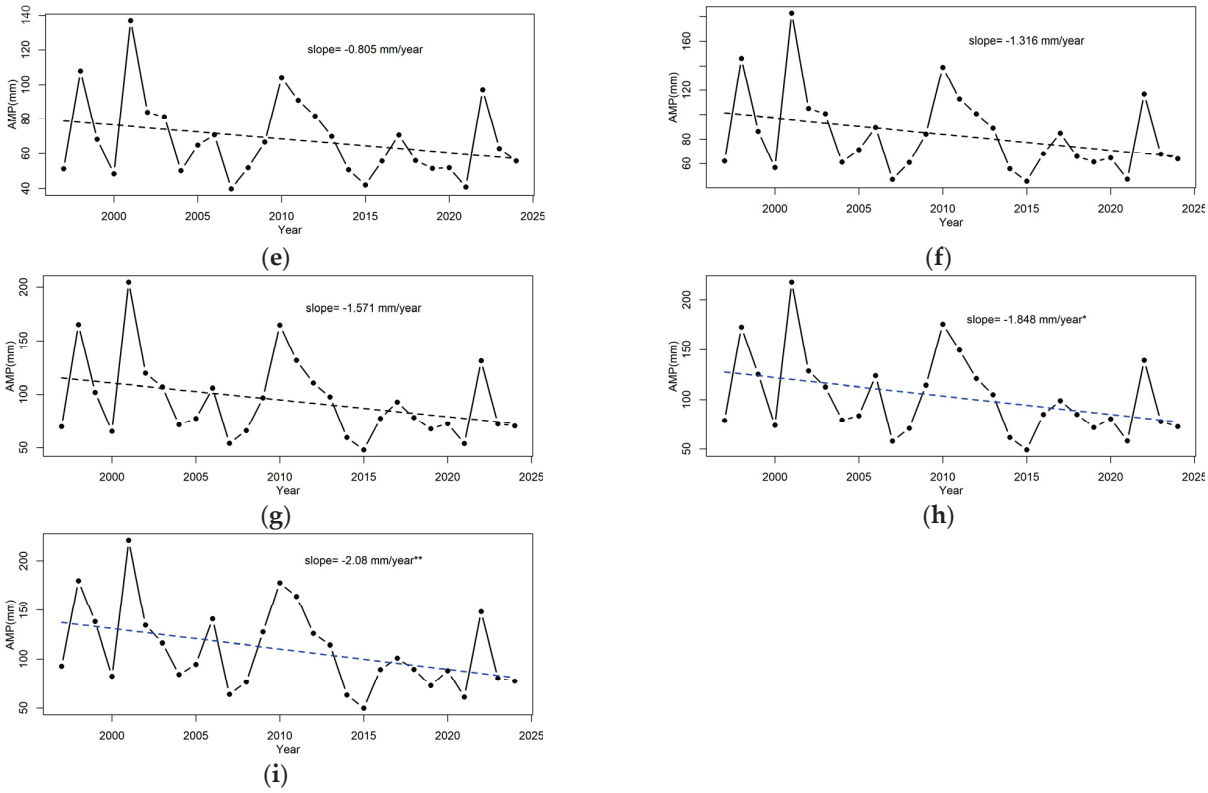

Figure 4. Time series of annual maximum precipitation (AMP) mean for each year at various durations: (**a**) 15 min, (**b**) 30 min, (**c**) 45 min, (**d**) 60 min, (**e**) 120 min, (**f**) 180 min, (**g**) 240 min, (**h**) 300 min, and (**i**) 360 min. The blue linear lines indicate statistically significant increasing and decreasing trends, respectively, detected at the 10% significance level. The black dashed line means linear regression line without statistically significant trend. Additionally, ** and * indicate statistically significant trends at the 5% and 10% significance levels, respectively.

4.2. Spatial Pattern Changes in Extreme Rainfall Events

To examine the alterations in the spatial distribution of AMP across Seoul, the CVs for the AMP series over selected durations were computed and are depicted in Figure 5. CVs were calculated from the AMP of different stations in the same year. Thus, CVs may be able to indirectly represent the spatial distribution or dispersion of AMPs. This figure reveals that the changes in the CV series for AMP varied depending on the duration considered. For the 15 min duration, the CV series showed a decreasing trend. In contrast, increasing trends were observed for durations of 30, 45, 60, 120, 180, and 240 min, with the 45 min and 60 min durations showing statistically significant trends. Meanwhile, for the 300 min and 360 min durations, the slope estimates were nearly zero, indicating no discernable trends in the CV series for these durations. These findings highlight significant changes in the spatial patterns of extreme rainfall events in Seoul, particularly for subhourly durations.

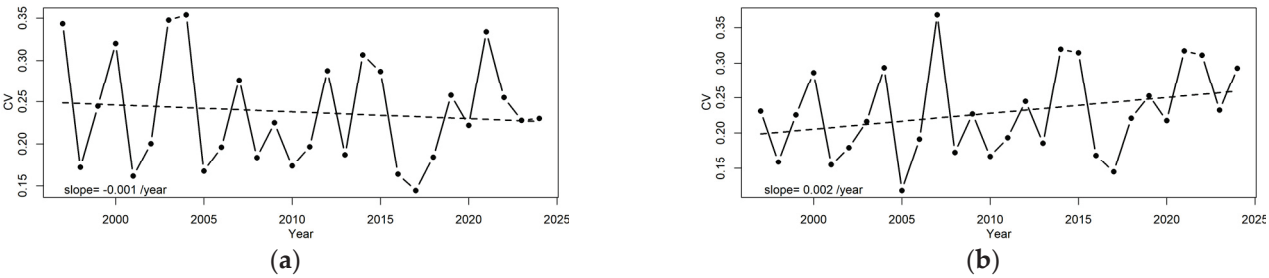

Figure 5. *Cont.*

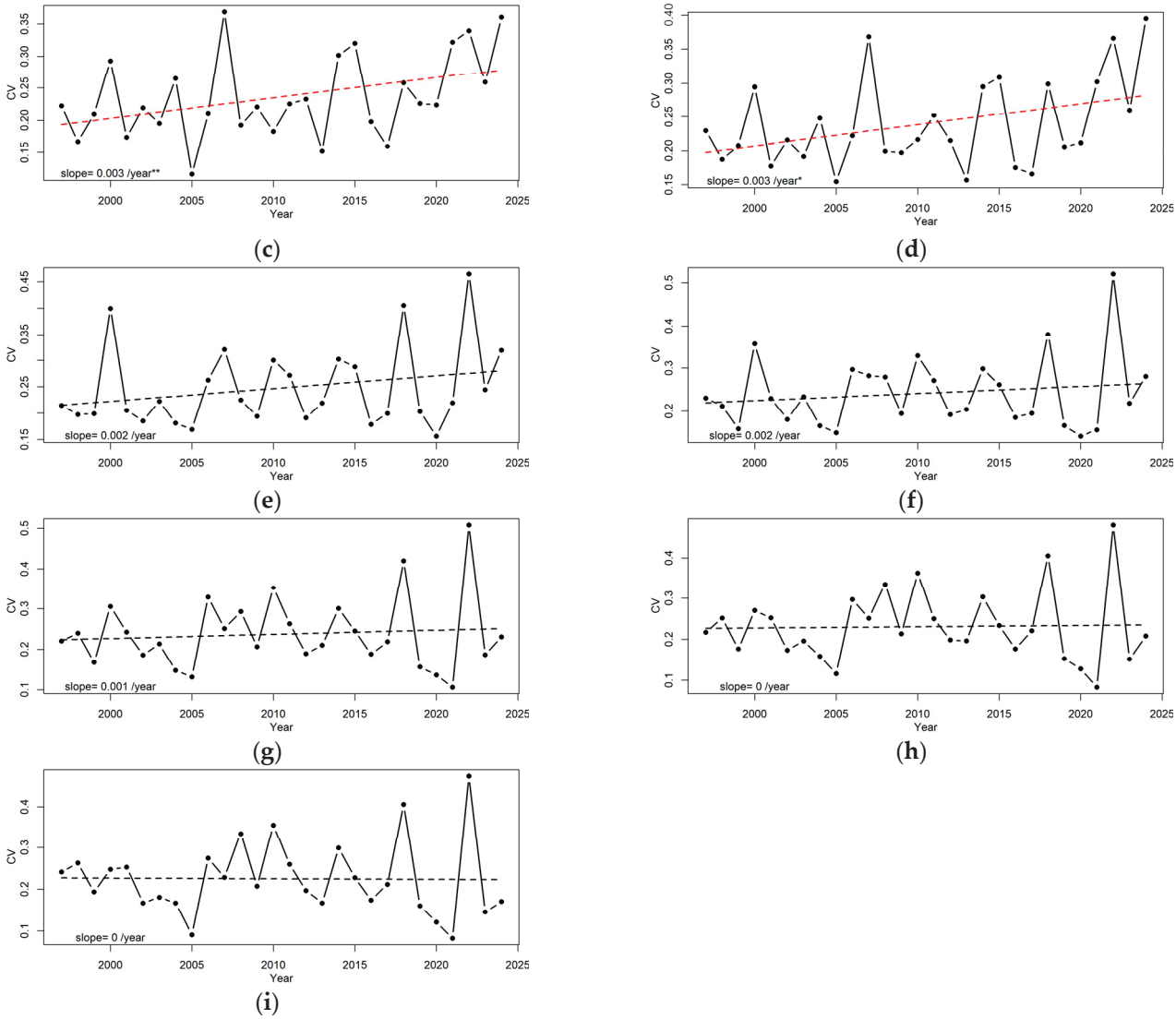

Figure 5. Time series of coefficients of variation (CVs) for annual maximum precipitation at various durations: (**a**) 15 min, (**b**) 30 min, (**c**) 45 min, (**d**) 60 min, (**e**) 120 min, (**f**) 180 min, (**g**) 240 min, (**h**) 300 min, and (**i**) 360 min. The red linear lines indicate statistically significant increasing and decreasing trends, respectively, detected at the 10% significance level. The black dashed line means linear regression line without statistically significant trend. Additionally, ** and * indicate statistically significant trends at the 5% and 10% significance levels, respectively.

To comprehensively analyze the changes in the spatial distribution of extreme rainfall, the Moran's *I* time series for AMP was calculated for each duration; these are presented in Figure 6. The findings of the Moran's *I* series aligned with the results of the CV series presented in Figure 5 but were not exactly the same. For all durations considered, the Moran's *I* series exhibited increasing trends. Specifically, these trends were statistically significant at the 5% significance level for the 30 min, 45 min, 60 min, and 120 min durations and at the 10% significance level for the 180 min duration. A high Moran's *I* value reflects strong spatial autocorrelation, indicating that the AMP recorded at different rainfall gauge stations within a given spatial domain occurs under the same rainfall event. As the duration increased, the likelihood of AMP occurring because of rainfall from larger systems, such as typhoons and monsoons, also rose. Consequently, the value of Moran's *I* increased with longer durations, and the probability of statistically significant autocorrelations rose. This trend was evident in the growing number of years with statistically significant Moran's *I* values as the duration lengthened. As shown in Figure 6b, Moran's *I* values were not

statistically significant before 2011, but significant autocorrelations were detected in six subsequent years. Similar patterns are evident in Figure 6c,d, particularly in AMP for subhourly durations.

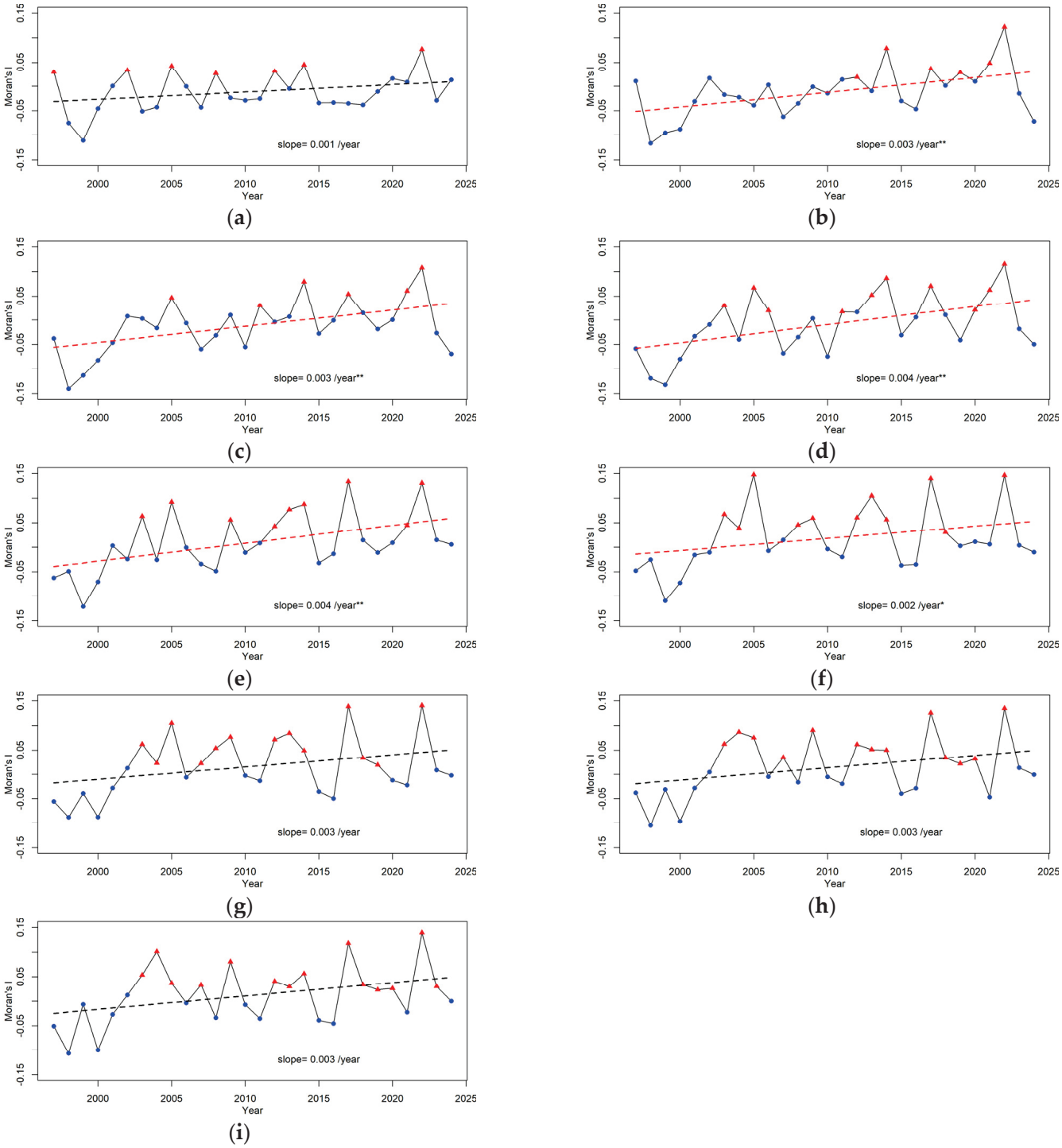

Figure 6. Time series of Moran's *I* index from annual maximum precipitation in Seoul for various durations: (**a**) 15 min, (**b**) 30 min, (**c**) 45 min, (**d**) 60 min, (**e**) 120 min, (**f**) 180 min, (**g**) 240 min, (**h**) 300 min, and (**i**) 360 min. Red triangles indicate a significant positive spatial autocorrelation with a 5% significance level based on Moran's *I* index values while blue circles indicate insignificance correlation. The red linear lines indicate statistically significant increasing and decreasing trends, respectively, detected at the 10% significance level. The black dashed line means linear regression line without statistically significant trend. Additionally, ** and * indicate statistically significant trends at the 5% and 10% significance levels, respectively.

A high CV indicates significant dispersion in AMP values across individual rain gauge stations within a given year. In contrast, a high Moran's *I* signifies strong spatial autocorrelation of these data. In other words, high CV and Moran's *I* values suggest that AMPs are concentrated in a narrow area within the domain. Analysis revealed that both CV and Moran's *I* for subhourly durations, such as 30 and 45 min, showed statistically significant increases over time at the 5% significance level. This finding indicates an increasing frequency of localized heavy rainfall events, or intense downpours, during subhourly durations in Seoul.

As shown in Figure 6i, for a 6 h duration, Moran's *I* often exhibited statistical significance annually. Although Moran's *I* values showed an increasing trend, the MK test revealed no statistical significance. Figure 7 provides a reillustration of Figure 5i. In Figure 7, the linear slope is nearly zero, indicating that the CV series exhibited almost no trend. By connecting the CV values of years with high CVs using a red dashed line and those of years with low CVs using a blue dashed line, we observe a gradual increase in the variability of CV values. A high CV value indicates the occurrence of strong, localized heavy rainfall that contributed to the formation of the AMP. In contrast, a low CV value implies that the AMP occurred evenly across Seoul because of large-scale systems, such as typhoons and monsoons, rather than localized heavy rainfall. Observing the red and blue dashed lines reveals that for the 6 h duration, rainfall events may be influenced by both localized heavy rainfall and large-scale systems. Since urban flooding typically occurs during subhourly durations, a 6 h duration implies a high probability that urban flooding has already taken place. However, when the drainage basin is large, the 6 h duration may warrant consideration. For areas or hydraulic structures affected by the 6 h duration in Seoul, a more detailed analysis is necessary to determine appropriate design criteria and implement damage mitigation measures.

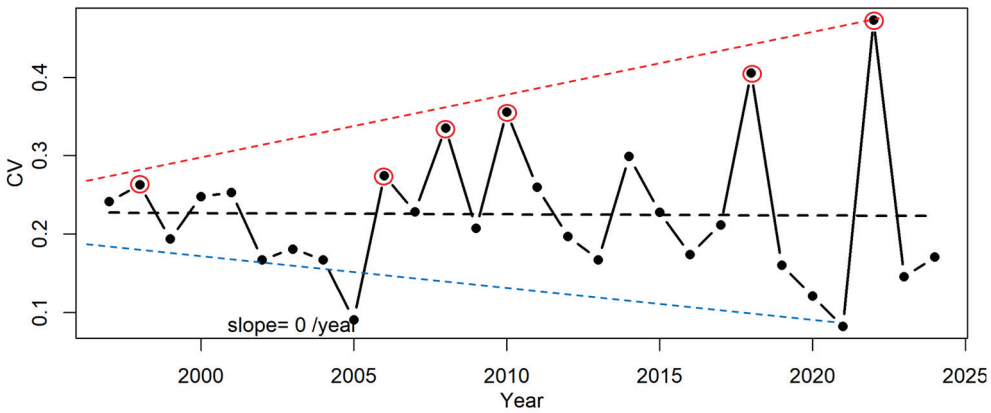

Figure 7. Time series of coefficients of variation (CVs) for annual maximum precipitation for 360 min in Seoul. The black dashed line indicates the linear slope of the CV.

5. Discussion

The present study analyzed whether the following two hypotheses are true: (1) temporal characteristics of extreme rainfall in Seoul have changed; (2) spatial patterns of extreme rainfall in Seoul have been altered. Regarding the first hypothesis, "temporal characteristics of extreme rainfall in Seoul have changed", the analysis results of the current study indicated that temporal changes indeed occurred. Firstly, the mean AMP series in Seoul showed a decreasing trend, and for the AMP with a duration of 5–6 h, a statistically significant decreasing trend was confirmed through the MK test with a 5% significance level. The reduction in the AMP values across Seoul will consequently lead to a decrease in the quantile values used for the design criteria of hydraulic infrastructure. The decrease

in rainfall quantiles implies a lower value of design criteria for hydraulics infrastructure within Seoul. Several factors, including impervious areas, drainage systems, and rainfall intensity, influence urban flooding. If other factors are constant, it can be inferred that climate change will lead to a reduction in urban flooding damage in the Seoul area based on the aforementioned results.

The hypothesis "spatial patterns of extreme rainfall in Seoul have been altered" was addressed by indicating that the spatial characteristics of extreme rainfall were indeed changing. The spatial patterns of AMP in Seoul were changing based on the duration of AMP, with this phenomenon being particularly noticeable for subhourly durations. The analysis results indicated an increasing frequency of localized heavy rainfall events in Seoul, highlighting an intensification of localized extreme rainfall in the city. While the overall AMP across Seoul exhibited a decreasing trend—suggesting that design criteria for hydraulic structures should be reduced and urban flood damage should decrease—the frequency of urban flood damage has increased. This paradoxical phenomenon can be partially explained by the findings of this study. Although the overall AMP decreased, the increased frequency of localized heavy rainfall events can lead to high-intensity rainfall in small areas that are part of the watershed in the city, causing urban flooding and damage. In large, sparsely populated river basins, decreases in AMP can lead to reduced flood damage because they may not result in increased water levels within river channels. However, in densely populated urban areas, localized heavy rainfall can occur more frequently and cause damage, as high-intensity rainfall events can lead to temporary inundation in small, concentrated regions. This suggests that recent urban flooding and inundation in Seoul may be largely driven by the intensification of localized extreme rainfall events. Consequently, there is a pressing need to reevaluate urban infrastructure and drainage systems, emphasizing the importance of implementing more meticulous countermeasures to address the impact of climate change. This point must be considered in research and policy decisions such as stormwater management, sewer management, urban planning, and emergency action plans for flash urban inundation [33–38].

In 2018, Seoul experienced significant urban flooding damage [39]. Upon examining Figure 4, it becomes evident that in 2018, AMP values were notably high during subhourly durations of 15, 30, 45, and 60 min. However, for durations exceeding 1 h, the AMP values in 2018 were not significant. Despite the lack of substantial AMP values for longer durations, urban flooding damage occurred that year. Figure 5 shows a high CV in 2018, indicating significant variability in rainfall intensities. Except for the 15 min duration, CV values were elevated for subhourly durations, and for hourly durations, the CV was higher than in other years. Additionally, Figure 3 reveals that while the median value of the box plot for 2018 was low, there were outlier points significantly above the median. These outliers likely represented extreme rainfall events much higher than typical values, contributing to urban flooding and associated damage. These findings confirm that the urban flooding in Seoul in 2018 resulted from localized heavy rainfall events. Furthermore, the high CV in 2022 suggests that the flooding events in that year were also caused by localized heavy rainfall.

The spatial heterogeneity of extreme rainfall events caused by localized heavy rainfall cannot be adequately addressed by traditional at-site frequency analysis. Each site is analyzed separately to estimate the rainfall quantiles. In cases where localized heavy rainfall results in extremely high AMP values at certain points, the rainfall quantile values will increase, while at other points, the AMP may show a decreasing trend, leading to a reduction in the rainfall quantile values. Since localized heavy rainfall has occurred within the city, there remains the possibility of such events happening at any other point. Therefore, if the rainfall quantile is not calculated considering this phenomenon across the entire region

of the city, this could lead to an underestimation of the rainfall quantile and consequently an increase in the vulnerability of hydraulic structures to climate change. As an alternative to address these issues, it is necessary to use regional frequency analysis (RFA) for estimating rainfall quantiles in urban areas. RFA involves performing frequency analysis by grouping sites that possess homogeneous hydrological characteristics [40]. By conducting frequency analysis on rainfall sites located in proximity and determined to be homogeneous regions, it is believed that the issues arising from spatial heterogeneity can be mitigated. RFA has the advantage of being able to be adopted swiftly, as considerable research has already been done on nonstationary frequency analysis for hydrometeorological variables [41–43].

It has been confirmed that the spatiotemporal characteristics of extreme rainfall differ significantly according to duration and exhibit different patterns of change in Seoul. For the design of hydraulic structures within cities, rainfall frequency analysis is conducted, and the results are used to derive the intensity–duration–frequency (IDF) curve to calculate the value of design criteria for hydraulic structures [44,45]. Existing IDF formulas have the drawback of not adequately considering these spatiotemporal variations. Although studies on IDF curves considering nonstationarity were conducted [46–48], there was a limitation in not addressing the nonstationarity in the spatial aspect. A newly proposed IDF curve that considers spatiotemporal characteristics is necessary for addressing spatiotemporal changes.

In this study, while the analysis based on annual maxima allowed us to examine overall phenomena, there are some limitations in making strict judgments about the intensification of localized heavy rainfall. These constraints arise because the analysis focused on AMP values rather than specific rainfall events representing extreme rainfall in Seoul. The data used in our analysis spanned 28 years, with one datapoint added each year, making the trend detection test results somewhat reliable but accompanied by significant uncertainty. Furthermore, variations in the starting years of the rainfall gauge stations introduced additional uncertainty to the findings. Urban inundation and flood damage result not solely from increased rainfall intensity but from a combination of factors, such as pipeline maintenance, operation and installation of pumping stations, increase in impervious surfaces, and neglect in managing trenches. Therefore, factors beyond those identified in this study may also contribute to the rise in urban inundation and flood damage.

6. Conclusions

This study investigated spatiotemporal changes in subhourly extreme rainfall events in Seoul, focusing on the implications for urban flooding in the context of changing climate patterns. The AMP mean series in Seoul showed a general decreasing trend across various durations, with statistically significant declines observed for longer durations, specifically 300 and 360 min. Despite this overall reduction, the study identified significant changes in the spatial distribution of extreme rainfall events, particularly for subhourly durations. This was evidenced by increasing trends in both the CV and Moran's *I* index, indicating a higher spatial concentration of extreme rainfall.

These findings highlight a paradox: although the overall AMP showed a decreasing trend, the intensification and localization of extreme rainfall increase the likelihood and impact of urban flooding. Localized extreme rainfall events of shorter durations (e.g., subhourly) have intensified, potentially increasing the risk of urban flooding. The increased frequency of localized heavy rainfall events further exacerbates the challenges associated with urban flood management.

Given the current methodology for determining design criteria for urban hydraulic structures, there is a high possibility of design criterion values gradually decreasing,

potentially making these structures more vulnerable to extreme rainfall events. As climate change continues to alter rainfall patterns, leading to more frequent and intense downpours, it is critical to develop design criteria for urban hydraulic facilities that can account for these changes.

Supplementary Materials: The following supporting information can be downloaded at: https://www.mdpi.com/article/10.3390/app15031672/s1, Table S1: Information of selected AWS stations in Seoul.

Author Contributions: Conceptualization, J.-Y.S.; methodology, J.-Y.S.; software, J.-Y.S. and J.P.; validation, J.-Y.S. and K.S.; formal analysis, J.-Y.S. and J.P.; investigation, J.-Y.S. and Y.K.; resources, Y.K.; data curation, J.-Y.S. and J.P.; writing—original draft preparation, J.-Y.S. and K.S.; writing—review and editing, J.-Y.S. and K.S.; visualization, J.-Y.S. and J.P.; supervision, J.-Y.S.; project administration, J.-Y.S. and Y.K.; funding acquisition, Y.K. All authors have read and agreed to the published version of the manuscript.

Funding: This work was carried out with the support of the "Cooperative Research Program for Agriculture Science and Technology Development (Project No. RS-2024-00332198)", Rural Development Administration, Republic of Korea.

Institutional Review Board Statement: Not applicable.

Informed Consent Statement: Not applicable.

Data Availability Statement: The data utilized in this study are publicly accessible and can be downloaded from https://data.kam.go.kr (accessed on 1 February 2025).

Acknowledgments: This work was carried out with the support of "Cooperative Research Program for Agriculture Science and Technology Development (Project No. RS-2024-00332198)" Rural Development Administration, Republic of Korea.

Conflicts of Interest: The authors declare no conflicts of interest.

References

1. Palmer, P.I.; Wainwright, C.M.; Dong, B.; Maidment, R.I.; Wheeler, K.G.; Gedney, N.; Hickman, J.E.; Madani, N.; Folwell, S.S.; Abdo, G.; et al. Drivers and impacts of Eastern African rainfall variability. *Nat. Rev. Earth Environ.* **2023**, *4*, 254–270. [CrossRef]
2. Tamm, O.; Saaremäe, E.; Rahkema, K.; Jaagus, J.; Tamm, T. The intensification of short-duration rainfall extremes due to climate change—Need for a frequent update of intensity–duration–frequency curves. *Clim. Serv.* **2023**, *30*, 100349. [CrossRef]
3. Zhou, S.; Yu, B.; Zhang, Y. Global concurrent climate extremes exacerbated by anthropogenic climate change. *Sci. Adv.* **2023**, *9*, eabo1638. [CrossRef]
4. Zhang, W.; Zhou, T.; Wu, P. Anthropogenic amplification of precipitation variability over the past century. *Science* **2024**, *385*, 427–432. [CrossRef]
5. Jung, Y.; Shin, J.-Y.; Ahn, H.; Heo, J.-H. The Spatial and Temporal Structure of Extreme Rainfall Trends in South Korea. *Water* **2017**, *9*, 809. [CrossRef]
6. Lee, M.; An, H.; Lee, J.; Um, M.-J.; Jung, Y.; Kim, K.; Jung, K.; Kim, S.; Park, D. Spatiotemporal Variability of Regional Rainfall Frequencies in South Korea for Different Periods. *Sustainability* **2023**, *15*, 16646. [CrossRef]
7. Azam, M.; Maeng, S.J.; Kim, H.S.; Lee, S.W.; Lee, J.E. Spatial and Temporal Trend Analysis of Precipitation and Drought in South Korea. *Water* **2018**, *10*, 765. [CrossRef]
8. Shin, J.-Y.; Kim, T.; Heo, J.-H.; Lee, J.-H. Spatial and temporal variations in rainfall erosivity and erosivity density in South Korea. *CATENA* **2019**, *176*, 125–144. [CrossRef]
9. Kwon, M.; Kwon, H.-H.; Han, D. Spatio-temporal drought patterns of multiple drought indices based on precipitation and soil moisture: A case study in South Korea. *Int. J. Climatol.* **2019**, *39*, 4669–4687. [CrossRef]
10. Shin, J.-Y.; Kim, K.R.; Kim, J.; Kim, S. Long-term trend and variability of surface humidity from 1973 to 2018 in South Korea. *Int. J. Climatol.* **2021**, *41*, 4215–4235. [CrossRef]
11. Moazzam, M.F.U.; Rahman, G.; Munawar, S.; Farid, N.; Lee, B.G. Spatiotemporal Rainfall Variability and Drought Assessment during Past Five Decades in South Korea Using SPI and SPEI. *Atmosphere* **2022**, *13*, 292. [CrossRef]
12. Chen, G.; Hou, J.; Wang, T.; Lv, J.; Jing, J.; Ma, X.; Yang, S.; Deng, C.; Ma, Y.; Ji, G. The effect of spatial–temporal characteristics of rainfall on urban inundation processes. *Hydrol. Process.* **2022**, *36*, e14655. [CrossRef]

13. Wang, M.; Fu, X.; Zhang, D.; Chen, F.; Liu, M.; Zhou, S.; Su, J.; Tan, S.K. Assessing urban flooding risk in response to climate change and urbanization based on shared socio-economic pathways. *Sci. Total Environ.* **2023**, *880*, 163470. [CrossRef]
14. Fan, C.; Hou, J.; Li, D.; Chen, G.; Guan, B.; Wang, T.; Pinpin, L.; Gao, X. Characteristics and drivers of flooding in recently built urban infrastructure during extreme rainfall. *Urban Clim.* **2024**, *56*, 102018. [CrossRef]
15. Lei, N.; Gao, L.; Liu, S.; Zhou, Z. The Spatiotemporal Clustering of Short-Duration Rainstorms in Shanghai City Using a Sub-Hourly Gauge Network. *Earth Space Sci.* **2024**, *11*, e2023EA003442. [CrossRef]
16. Berne, A.; Delrieu, G.; Creutin, J.-D.; Obled, C. Temporal and spatial resolution of rainfall measurements required for urban hydrology. *J. Hydrol.* **2004**, *299*, 166–179. [CrossRef]
17. Saghafian, B.; Farazjoo, H.; Bozorgy, B.; Yazdandoost, F. Flood Intensification due to Changes in Land Use. *Water Resour. Manag.* **2008**, *22*, 1051–1067. [CrossRef]
18. Smith, J.A.; Baeck, M.L.; Meierdiercks, K.L.; Nelson, P.A.; Miller, A.J.; Holland, E.J. Field studies of the storm event hydrologic response in an urbanizing watershed. *Water Resour. Res.* **2005**, *41*, W10413. [CrossRef]
19. Khaliq, M.N.; Ouarda, T.B.M.J.; Gachon, P.; Sushama, L.; St-Hilaire, A. Identification of hydrological trends in the presence of serial and cross correlations: A review of selected methods and their application to annual flow regimes of Canadian rivers. *J. Hydrol.* **2009**, *368*, 117–130. [CrossRef]
20. Ouarda, T.B.M.J.; Charron, C.; Niranjan Kumar, K.; Marpu, P.R.; Ghedira, H.; Molini, A.; Khayal, I. Evolution of the rainfall regime in the United Arab Emirates. *J. Hydrol.* **2014**, *514*, 258–270. [CrossRef]
21. Shin, J.-Y.; Kang, M.; Kim, K.R. Outdoor thermal stress changes in South Korea: Increasing inter-annual variability induced by different trends of heat and cold stresses. *Sci. Total Environ.* **2022**, *805*, 150132. [CrossRef]
22. Javari, M. Spatial variability of rainfall trends in Iran. *Arab. J. Geosci.* **2017**, *10*, 78. [CrossRef]
23. Khaliq, M.N.; Ouarda, T.B.M.J.; Gachon, P.; Sushama, L. Temporal evolution of low-flow regimes in Canadian rivers. *Water Resour. Res.* **2008**, *44*, W08436. [CrossRef]
24. Khaliq, M.N.; Ouarda, T.B.M.J.; Gachon, P. Identification of temporal trends in annual and seasonal low flows occurring in Canadian rivers: The effect of short- and long-term persistence. *J. Hydrol.* **2009**, *369*, 183–197. [CrossRef]
25. Mann, H.B. Nonparametric Tests Against Trend. *Econometrica* **1945**, *13*, 245–259. [CrossRef]
26. Kendall, M.G. *Rank Correlation Methods*; Griffin: Oxford, UK, 1948.
27. Moran, P.A.P. Notes on Continuous Stochastic Phenomena. *Biometrika* **1950**, *37*, 17–23. [CrossRef]
28. Zhang, J.; Han, D. Assessment of rainfall spatial variability and its influence on runoff modelling: A case study in the Brue catchment, UK. *Hydrol. Process.* **2017**, *31*, 2972–2981. [CrossRef]
29. Zhang, J.; Han, D.; Song, Y.; Dai, Q. Study on the effect of rainfall spatial variability on runoff modelling. *J. Hydroinform.* **2018**, *20*, 577–587. [CrossRef]
30. Zhang, L.; Hou, Q.; Duan, Y.; Liu, W. Spatial correlation between water resources and rural settlements in the Yanhe watershed based on bivariate spatial autocorrelation methods. *Land* **2023**, *12*, 1719. [CrossRef]
31. Zhuang, Q.; Liu, S.; Zhou, Z. Spatial heterogeneity analysis of short-duration extreme rainfall events in megacities in China. *Water* **2020**, *12*, 3364. [CrossRef]
32. Bivand, R. R Packages for Analyzing Spatial Data: A Comparative Case Study with Areal Data. *Geogr. Anal.* **2022**, *54*, 488–518. [CrossRef]
33. Li, P.; Zhuang, L.; Lin, K.; She, D.; Chen, Q.; Wang, Q.; Xia, J. New perspectives on urban stormwater management in China, with a focus on extreme rainfall events. *Nat. Hazards* **2024**. [CrossRef]
34. Miller, A.J.; Welty, C.; Duncan, J.M.; Baeck, M.L.; Smith, J.A. Assessing urban rainfall-runoff response to stormwater management extent. *Hydrol. Process.* **2021**, *35*, e14287. [CrossRef]
35. Muttil, N.; Nasrin, T.; Sharma, A.K. Impacts of Extreme Rainfalls on Sewer Overflows and WSUD-Based Mitigation Strategies: A Review. *Water* **2023**, *15*, 429. [CrossRef]
36. Nasrin, T.; Sharma, A.K.; Muttil, N. Impact of Short Duration Intense Rainfall Events on Sanitary Sewer Network Performance. *Water* **2017**, *9*, 225. [CrossRef]
37. Reu Junqueira, J.; Serrao-Neumann, S.; White, I. A systematic review of approaches for modelling current and future impacts of extreme rainfall events using green infrastructure. *J. Clean. Prod.* **2021**, *290*, 125173. [CrossRef]
38. Szeląg, B.; Kiczko, A.; Łagód, G.; De Paola, F. Relationship Between Rainfall Duration and Sewer System Performance Measures Within the Context of Uncertainty. *Water Resour. Manag.* **2021**, *35*, 5073–5087. [CrossRef]
39. Lee, S.; Choi, Y.; Ji, J.; Lee, E.; Yi, S.; Yi, J. Flood Vulnerability Assessment of an Urban Area: A Case Study in Seoul, South Korea. *Water* **2023**, *15*, 1979. [CrossRef]
40. Hosking, J.R.M.; Wallis, J.R. *Regional Frequency Analysis*; Cambridege University Press: Cambridege, UK, 1997.
41. El Adlouni, S.; Ouarda, T.B.M.J.; Zhang, X.; Roy, R.; Bobée, B. Generalized maximum likelihood estimators for the nonstationary generalized extreme value model. *Water Resour. Res.* **2007**, *43*, W03410. [CrossRef]

42. Khaliq, M.N.; Ouarda, T.B.M.J.; Ondo, J.C.; Gachon, P.; Bobée, B. Frequency analysis of a sequence of dependent and/or non-stationary hydro-meteorological observations: A review. *J. Hydrol.* **2006**, *329*, 534–552. [CrossRef]
43. Kim, H.; Shin, J.-Y.; Kim, T.; Kim, S.; Heo, J.-H. Regional frequency analysis of extreme precipitation based on a nonstationary population index flood method. *Adv. Water Resour.* **2020**, *146*, 103757. [CrossRef]
44. Gnecco, I.; Palla, A.; La Barbera, P.; Roth, G.; Giannoni, F. Defining intensity–duration–frequency curves at short durations: A methodological framework. *Hydrol. Sci. J.* **2023**, *68*, 1499–1512. [CrossRef]
45. Lanciotti, S.; Ridolfi, E.; Russo, F.; Napolitano, F. Intensity–Duration–Frequency Curves in a Data-Rich Era: A Review. *Water* **2022**, *14*, 3705. [CrossRef]
46. Ouarda, T.B.; Yousef, L.A.; Charron, C. Non-stationary Intensity-Duration-Frequency curves integrating information concerning teleconnections and climate change. *Int. J. Climatol.* **2019**, *39*, 2306–2323. [CrossRef]
47. Silva, D.F.; Simonovic, S.P.; Schardong, A.; Goldenfum, J.A. Assessment of non-stationary IDF curves under a changing climate: Case study of different climatic zones in Canada. *J. Hydrol. Reg. Stud.* **2021**, *36*, 100870. [CrossRef]
48. Yan, L.; Xiong, L.; Jiang, C.; Zhang, M.; Wang, D.; Xu, C.-Y. Updating intensity–duration–frequency curves for urban infrastructure design under a changing environment. *WIREs Water* **2021**, *8*, e1519. [CrossRef]

Disclaimer/Publisher's Note: The statements, opinions and data contained in all publications are solely those of the individual author(s) and contributor(s) and not of MDPI and/or the editor(s). MDPI and/or the editor(s) disclaim responsibility for any injury to people or property resulting from any ideas, methods, instructions or products referred to in the content.

remote sensing

MDPI

Article

The Variation Characteristics of Stratospheric Circulation under the Interdecadal Variability of Antarctic Total Column Ozone in Early Austral Spring

Jiayao Li [1,2,3], Shunwu Zhou [1], Dong Guo [1,*], Dingzhu Hu [1], Yao Yao [1] and Minghui Wu [1]

[1] Key Laboratory of Meteorological Disaster, Ministry of Education (KLME)/Joint International Research Laboratory of Climate and Environment Change (ILCEC)/Collaborative Innovation Center on Forecast and Evaluation of Meteorological Disasters (CIC-FEMD), Nanjing University of Information Science & Technology, Nanjing 210044, China; lijyao@outlook.com (J.L.); zhou@nuist.edu.cn (S.Z.); hudz@nuist.edu.cn (D.H.); yyao@nuist.edu.cn (Y.Y.); 202083300283@nuist.edu.cn (M.W.)

[2] Key Laboratory for Meteorological Disaster Monitoring and Early Warning and Risk Management of Characteristic Agriculture in Arid Regions, China Meteorological Administration, Yinchuan 750002, China

[3] Ningxia Hui Autonomous Region Climate Center, Yinchuan 750002, China

* Correspondence: 002344@nuist.edu.cn

Abstract: Antarctic Total Column Ozone (TCO) gradually began to recover around 2000, and a large number of studies have pointed out that the recovery of the Antarctic TCO is most significant in the austral early spring (September). Based on the Bodeker Scientific Filled Total Column Ozone and ERA5 reanalysis dataset covering 1979–2019, the variation characteristics of the Antarctic TCO and stratospheric circulation for the TCO 'depletion' period (1979–1999) and the 'recovery' period (2000–2019) are analyzed in September. Results show that: (1) Stratospheric elements significantly related to the TCO have corresponding changes during the two eras. (2) The interannual variability of the TCO and the above-mentioned stratospheric circulation elements in the recovery period are stronger than those in the depletion period. (3) Compared with the depletion period, due to the stronger amplitude of the planetary wave 1, stronger Eliassen–Palm (EP) flux corresponds to EP flux convergence, larger negative eddy heat flux, and positive eddy momentum flux in the stratosphere during the recovery period. The polar temperature rises in the lower and middle stratosphere and the polar vortex weakens in the middle and upper stratosphere, accompanied by the diminished area of PSC. This contributes to the understanding of Antarctic ozone recovery.

Keywords: antarctic total column ozone; depletion period; recovery period; stratospheric circulation; Eliassen–Palm flux

1. Introduction

From the late 1970s to the early 1990s, the Total Column Ozone (TCO) decreased rapidly over Antarctica during the austral spring (September–November), forming the Antarctic ozone hole [1], which was mainly caused by the significant increase in ozone-depleting substances (ODSs) as a result of additional anthropogenic emissions of chlorofluorocarbons (CFCs) and bromocarbons [2]. Although ozone depletion will be exacerbated by the large amounts of volcanic aerosols produced by volcanic eruptions [3], ozone has been showing signs of healing since around 2000 [4–7], which is the year of peak ODSs [8,9]. Studies have shown that ozone recovery is most evident in September [10], and the signal of increasing ozone is strongest between 1 and 20 September due to the changes in ODSs [11]. As one of the reasons for ozone recovery in September, Solomon et al. [10] suggest that, on the one hand, it is the chemical impact that is attributed to the gradual reduction in halogenated gases due to the implementation of the Montreal Protocol. On the other hand, it is the dynamic impact due to the influence of stratospheric temperature and circulation.

The interdecadal trends of Antarctic ozone can be well explained by the changes in ODSs [12,13], while the interannual variation in ozone is mainly influenced by stratospheric temperature [14,15] and planetary waves [16–18]. When the Antarctic stratospheric temperature decreases to a certain temperature, Polar Stratospheric Clouds (PSC) begin to form and the area gradually increases, resulting in the heterogeneous chemical process of chlorine gas on the surface of these PSCs to destroy ozone [6]. Additionally, the cooling stratospheric temperature enhances the meridional temperature gradient from mid-latitude to polar regions, strengthens the polar vortex through the thermal wind balance [19], and delays the rupture time of the polar vortex [20]. Low-ozone concentration airs are restricted by the dynamic properties of a stronger and later burst of polar vortexes in the polar regions, providing material isolation for ozone hole development [21,22]. In addition, more upward or downward Eliassen–Palm (EP) flux, corresponding to the divergence of EP flux, propagates to the stratosphere and weakens the residual circulation and the ozone transport from mid-latitude to polar regions. The accompanying anomalous upward adiabatic cooling reduces the stratospheric temperature and enhances the polar vortex to eventually affect the ozone hole [23,24].

Antarctic ozone has an important impact on changes in the climate system. For example, the loss of Antarctic ozone cools the stratospheric polar region through radiation cooling and strengthens the circumpolar westerlies and polar vortex. The influence of Antarctic ozone depletion extends to the troposphere through complex interplays [25], enhances the southern annular mode, strengthens the westerly jet, shifts toward the pole, and deepens the Amundsen Sea lows. Moreover, the Hadley call and the subtropical arid zone move towards the polar region [26–29]. In addition, the existence of the Antarctic ozone hole also affects the ocean [30,31] and sea ice [32,33]. The climate effect of ozone recovery seems to be opposite to the climate change caused by ozone depletion [26–28,34]. In conclusion, there is a close but complex causal relationship between Antarctic ozone and stratospheric circulation. However, under the interdecadal change in TCO around 2000, the characteristics of stratospheric circulation anomalies and planetary waves are not well understood in the two preceding and following eras of the TCO 'depletion' period (1979–1999) and the 'recovery' period (2000–2019). Therefore, this paper plans to investigate the variation characteristics of stratospheric circulation and planetary waves during the two eras. The article is organized as follows. The data and methods are briefly described in Section 2. In Section 3, the variation characteristics of TCO, stratospheric temperature, polar vortex, and PSC area over Antarctica are studied by diagnosing the recovery period and the depletion period. The variation characteristics of planetary waves during the two eras are then discussed. Finally, the conclusion and discussion are given in Section 4.

2. Data and Methods

2.1. Data

The timeframe of all datasets is from 1979 to 2019.

The TCO dataset is provided by the Bodeker Scientific Filled Total Column Ozone (BS–TCO) Database V3.5.1, with a horizontal resolution of $1^\circ \times 1.25^\circ$ [35].

Stratospheric temperature, geopotential height, and wind field are obtained from the European Center for Medium-Range Weather Forecasts (ECMWF) ERA5, with a horizontal resolution of $0.25^\circ \times 0.25^\circ$ [36].

The indices used in this study are as follows:

(1) Polar TCO index from the BS–TCO dataset is TCO averaged over 63°S~90°S [10].
(2) Polar TCO index from Satellite (S–TCO) is provided by the National Aeronautics and Space Administration (NASA) Goddard Space Flight Center online database, missing for 1994 and 1995.
(3) Equivalent effective stratospheric chlorine (EESC) is obtained from the Goddard Space Flight Center, which has been widely used to relate predictions of human-generated ODS abundances to future ozone changes [5,12]. It uses the parameters suggested by Newman et al. [8,13] and corresponds to the WMO A1-2014 scenarios, with an age

spectrum width of 2.75 year (symbol a is an abbreviation of year), a constant factor of 60, and a mean age-of-air of 5.5 a. This parameter is different from the classical EESC, which is thought to be more suitable for the polar region.

(4) The index of the PSC area is also from the NASA Goddard Space Flight Center.

(5) Due to the close correlation between TCO and polar (60°S~90°S) temperature, in particular with 50 hPa [12], the index of stratospheric temperature is represented by temperature averaged over 60°S~90°S (polar temperature, PT) at 50 hPa.

(6) In the same way as the temperature, the polar vortex is greatly related to TCO, in which a 10 hPa polar vortex variability explains approximately 85% of the variance of polar TCO anomalies [37]. The index of the stratospheric polar vortex is also represented by geopotential height averaged over 60°S~90°S (polar geopotential height, PGH) at 10 hPa.

(7) Additionally, the index of the stratospheric polar vortex is calculated by the zonal-mean zonal wind (U) at 60°S (U at 60°S, U60) and 30 hPa, which has the highest correlation with TCO and approaches the center of the mean position of the polar vortex in the mid-stratosphere. The polar vortex tends to enhance (weaken) the reduced (elevated) PGH and the accelerating (decelerating) U60.

2.2. Methods

With the methods of linear regression analysis, the tendency rate of the TCO, stratospheric temperature, polar vortex, and PSC area were analyzed in the two eras. Correlation analysis was used to explore the relationship between the TCO and stratospheric temperature, polar vortex, and PSC area. Additionally, all datasets were detrended to eliminate the correlation coefficient. Wavelet analysis was used to analyze the interannual variability of total Antarctic ozone and stratospheric elements [38]. The main dynamic processes are discussed by planetary wave, which is expressed by EP flux. EP flux has been widely used to diagnose the propagation of atmospheric fluctuations and wave–flow interaction [39,40]. The formulas for EP flux and its divergence are as follows in spherical p coordinates [41]:

$$F = \left(F_\varphi,\ F_p\right) = \left(-a\cos\varphi(\overline{v'u'}),\ fa\cos\varphi\ (\overline{v'\theta'})/\overline{\theta}_p\right) \quad (1)$$

$$\nabla\cdot F = \frac{1}{a\cos\varphi}\frac{\partial}{\partial\varphi}(F_\varphi\cos\varphi) + \frac{\partial}{\partial p}(F_p) \quad (2)$$

where F is EP flux, $\nabla\cdot F$ is its divergence (EP div), u and v represent zonal and meridional wind, θ is the potential temperature, a is the radius of the Earth, f is the Coriolis parameter, φ is the latitude, p is the pressure (hPa), the overbars denote zonal averages, and the primes denote departure from the zonal average. $\overline{v'\theta'}$ is the eddy heat flux (EHF). $\overline{v'u'}$ is the eddy momentum flux (EMF). EP flux convergence (divergence) will lead to the weakening (strengthening) of zonal flow. The EHF, being consistent with EP flux divergence [42], is related to the vertical component of EP flux [43] and reflects upward wave propagations [44]. The propagation of planetary waves can change EMF by adjusting the wave-driving rate of the polar vortex [39]. In the southern hemisphere, a negative EHF reflects upward wave propagation, while a positive EMF reflects the enhanced poleward motion [45]. Table 1 shows the abbreviations and full names of terms used in the text.

Table 1. Abbreviations and full names of terms used in the text.

Abbreviations	The Full Name
TCO	Total Column Ozone
ODSs	Ozone-Depleting Substances
EESC	Equivalent Effective Stratospheric Chlorine
PSC area	Polar Stratospheric Cloud Area
PT	Temperature Averaged Over 60°S~90°S
PGH	Geopotential Height Averaged Over 60°S~90°S
U60	Zonal-Mean Zonal Wind (U) at 60°S
EMF	Eddy Momentum Flux
EHF	Eddy Heat Flux

3. Results

3.1. The Variation Characteristics of Antarctic Total Column Ozone and Stratospheric Circulation during the Recovery Period and Depletion Period

Antarctic ozone is related to stratospheric temperature [14]. Stratospheric temperature affects the formation of PSCs on the one hand and cooperates with polar vortex on the other [6,22]. The Antarctic ozone experiences an interdecadal change characteristic of decreasing before 2000 and then rising after 2000 [7]. In consideration of that the variations in temperature, wind, and geopotential height are interrelated within the framework of a common physical process. So, do stratospheric temperature, polar vortex, and PSC area change correspondingly?

3.1.1. The Temporal Characteristics of Antarctic Total Column Ozone

Based on the BS–TCO, S–TCO, and EESC data, Figure 1a shows the time series of Antarctic polar TCO in September and EESC during the past 41 years (1979–2019). The polar TCO derived from different datasets shows consistent interannual variation and linear trend. The polar TCO coming from BS–TCO and S–TCO both increase at a rate of 22.2 Du·decade^{-1}, with an average of 193.6 Du and 212.2 Du, respectively, in the recovery period. The trend from the BS–TCO dataset has passed the 0.05 significance test. The polar TCO coming from BS–TCO and S–TCO decreases significantly at a rate of 48.4 Du·decade^{-1} with an average of 212.6 Du and 49.6 Du·decade^{-1} with an average of 235.2 Du, respectively, in the depletion period. The trend and average are very different between the two periods. Following the phasing out of ODSs under the Montreal Protocol, the level of EESC stops rising before 2000 and decreases after 2000 in the polar stratosphere, corresponding to the depletion and recovery of TCO. The trend in the recovery period is numerically about twice as slow as the trend in the depletion period, partly due to the slow decreasing rate and long atmospheric lifetime of EESC, partly possibly due to short data records. Since the trend values obtained from the two datasets exhibit little difference and the S–TCO is incomplete, the BS–TCO dataset is used in the following analysis.

Antarctic ozone is directly related to the heterogeneous chemical process on the surface of PSC [6,46]. Figure 1b shows the time series of polar TCO and PSC area in the last 41 years. It can be seen that the PSC area is similar to the evolution of polar TCO and significantly related to polar TCO with a determination coefficient of about 0.7. The PSC area decreases slowly at a rate of 2.6 million·Km^2·decade^{-1} with an average of 17.5 million·Km^2 in the recovery period, corresponding to the increased polar TCO. The PSC area increases significantly at a rate of 2.7 million·Km^2·decade^{-1} with an average of 14.9 million·Km^2 in the depletion period, being consistent with the decreased polar TCO. Therefore, the PSC area first increases and then decreases around 2000.

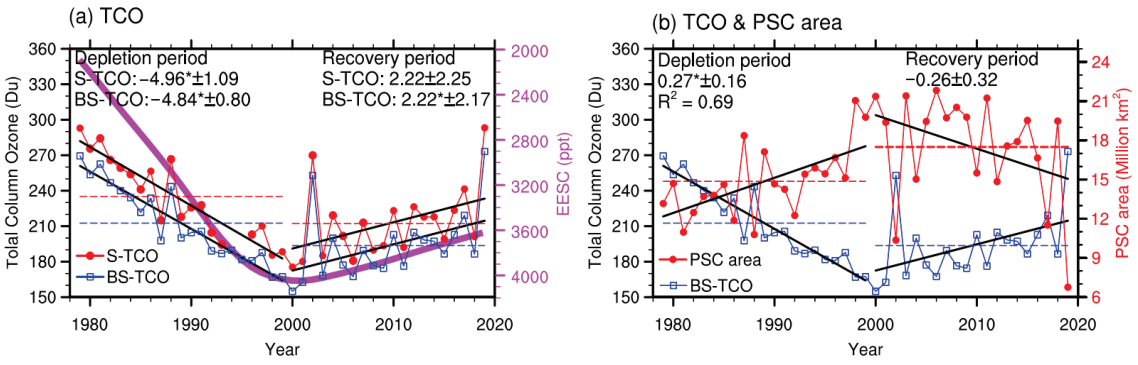

Figure 1. Time series of (**a**) Antarctic polar TCO averaged over 63°S~90°S (dotted lines unit: Du) and EESC (purple line unit: ppt), as well as (**b**) polar TCO (blue square line) and PSC area (red dotted line, units: million·Km^2) in September during 1979–2019. The left Y coordinate is for polar TCO. The right Y coordinate is for the inverse scale of EESC in (**a**) and for the PSC area in (**b**). The values on the top of the figure are linear trends in the recovery period (2000–2019) and depletion period (1979–1999). R^2 in (**b**) is the determination coefficient for the whole period. * Indicates that the linear trends and correlation coefficients are significant at the 0.05 confidence level. The black lines are linear fits of the time series during the two periods. The dashed lines are the averages of the time series during the two periods.

3.1.2. The Temporal Characteristics of Stratospheric Temperature and Polar Vortex

The evolution characteristics of stratospheric temperature, geopotential height, and zonal wind have been analyzed in the recent 41 years. Figure 2 shows the time series of the polar TCO, 50 hPa PT, 10 hPa PGH, and 30 hPa U60 in the recent 41 years; 50 hPa PT, 10 hPa PGH, and 30 hPa U60 have a remarkable correlation with polar TCO with a determination coefficient of about 0.5. During the recovery period, 50 hPa PT and 10 hPa PGH increase at a rate of 1.8 K·decade^{-1} with an average of 195.5 K and 11.4 dagpm·decade^{-1} with an average of 2836.1 dagpm, respectively, while 30 hPa U60 decreases at a rate of 1.4 m·s^{-1}·decade^{-1} with an average of 60.1 m·s^{-1}. It can be seen that the trends of each stratospheric circulation element are not obvious, but correspond to the slow increase in TCO. During the depletion period, 50 hPa PT and 10 hPa PGH show a decreasing trend at a rate of 0.7 K·decade^{-1} with an average of 194.1 K and 6.1 dagpm·decade^{-1} with an average of 2825.3 dagpm, respectively, while 30 hPa U60 increases at a rate of 1.3 m·s^{-1}·decade^{-1} with an average of 62.6 m·s^{-1}. It shows that the cooling temperature, the reduced geopotential height, and the accelerating zonal wind correspond to the decreased polar TCO.

The above analysis results show that TCO and the temperature at 50 hPa, as well as the geopotential height at 10 hPa (PSC area and the zonal wind at 30 hPa), maintain a significant and stable positive (negative) relationship during the whole analysis period. In the depletion period, the stratospheric temperature decreases significantly, while the polar vortex increases significantly, and the zonal wind is stronger. At this time, the PSC area increases significantly, corresponding to the sharp decrease in TCO. In the recovery period, the higher stratospheric temperature, the weaker polar vortex, the smaller zonal wind, and the decreased PSC area, in which the trends are not obvious, agree with the slow increase in TCO.

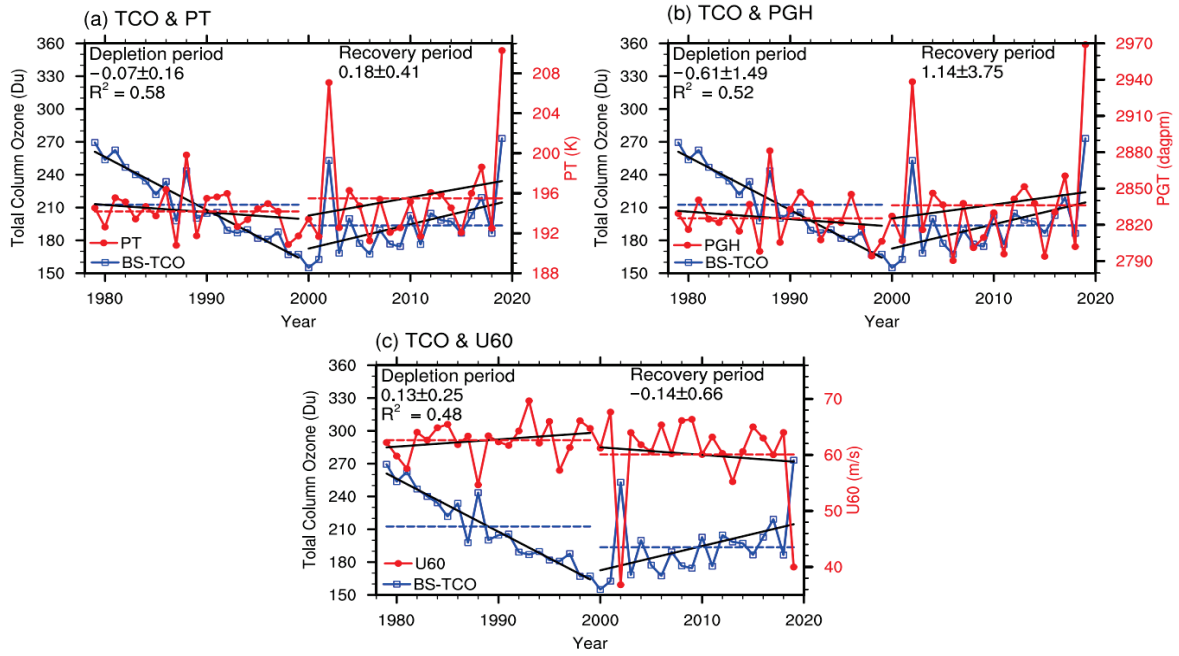

Figure 2. Same as Figure 1b, but for (**a**) 50 hPa PT averaged over 60°S~90°S (red dotted line, unit: K), (**b**) 10 hPa PGH averaged over 60°S~90°S (red dotted line, unit: dagpm), and (**c**) 30 hPa U60 (red dotted line, unit: m·s^{-1}).

3.1.3. The Spatial Characteristics of Antarctic Total Column Ozone and Stratospheric Circulation

To compare the spatial difference in TCO, stratospheric temperature, and polar vortex over Antarctica between the two eras, the composite of TCO and 50 hPa temperature anomalies, as well as 10 hPa geopotential height and 30 hPa zonal wind anomalies in comparison with the climatic mean state, are displayed in Figure 3 during the two periods. This indicates that significantly negative TCO anomalies are observed from Queen Maud Land to West Antarctica (cold shadings in Figure 3a) and the anomaly centers are located in the Haakon VII Sea (near 0°) during the recovery period. The positive TCO anomalies in Wilkes Land and its northern areas (warm shadings in Figure 3a) correspond to the positive anomaly center of the temperature (red contours in Figure 3a) and geopotential height (warm shadings in Figure 3c), as well as the anomalous eastward wind around 60°S (blue contours in Figure 3c). The distributions of TCO and stratospheric circulation anomalies during the depletion period are opposite to those during the recovery period Therefore, notable changes in TCO, stratospheric temperature, and polar vortex anomalies can be seen between the two periods. The positive (negative) TCO anomalies over Antarctica agree with the warming (cooling) of polar temperature and the weakening (strengthening) of the polar vortex.

Aiming at further understanding the linear trends of Antarctic TCO, stratospheric temperature, and polar vortex in the two eras, the spatial distributions of linear trends of TCO, 50 hPa temperature, 10 hPa geopotential height, and 30 hPa zonal wind are shown in Figure 4. During the recovery period, TCO (warm shadings in Figure 4a) and stratospheric temperature (red contours in Figure 4a) show a significant increasing trend over Antarctica, with the center located in the Ross Sea (near 180°). Geopotential height increases in the southern South Pacific (warm shadings in Figure 4c), accompanied by the decelerating zonal wind (blue contours in Figure 4c). During the depletion period, TCO (cold shadings in Figure 4b) and temperature (blue contours in Figure 4b) decrease significantly over Antarctica. Geopotential height decreases considerably over West Antarctica (cold shadings in Figure 4d) in combination with the accelerating zonal wind (red contours in Figure 4d).

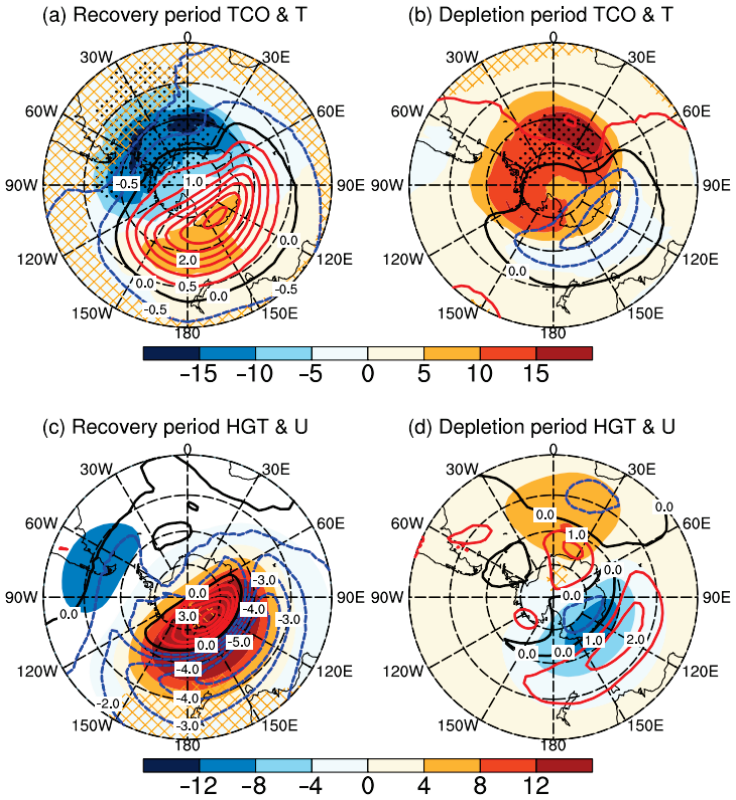

Figure 3. Composite of (**a**,**b**) Antarctic TCO (shadings, unit: Du) and 50 hPa temperature (contours, unit: K), and (**c**,**d**) 10 hPa geopotential height (shadings, unit: dagpm), and 30 hPa zonal wind (contours, unit: $m \cdot s^{-1}$) anomalies in September during the (**a**,**c**) recovery period and (**b**,**d**) depletion period, in comparison with the climatic mean state. The climatic mean state is the average value of each element from 1980 to 2010. The dotted areas and yellow grid areas represent the anomalies in the (**a**,**b**) TCO and temperature, and (**c**,**d**) geopotential height and zonal wind that are statistically significant at the 0.1 confidence level, respectively. The outermost latitude is 30°S and the latitude interval is 15°.

3.1.4. The Interannual Variability of Antarctic Total Column Ozone and Stratospheric Circulation

The spatial characteristics of Antarctic TCO, stratospheric temperature, and polar vortex are significantly different between the recovery and depletion periods. For the purpose of contrasting the degree of interannual variation of the TCO and stratospheric circulation over Antarctica during the two periods, Figure 5 shows the composite variance of the TCO and 50 hPa temperature, as well as 10 hPa geopotential height and 30 hPa zonal wind during the two periods. As can be seen, the largest interannual variances of each element are located in Wilkes Land and its north during the recovery period (Figure 5a,c), and in the northeast of Queen Maude Land during the depletion period (Figure 5b,d). In addition, the interannual variance in the recovery period is greater than that in the depletion period and the center is consistent with that of the abnormal center on the whole (Figure 3). Therefore, the interannual variance distributions of TCO, stratospheric temperature, and polar vortex in the two periods are significantly different.

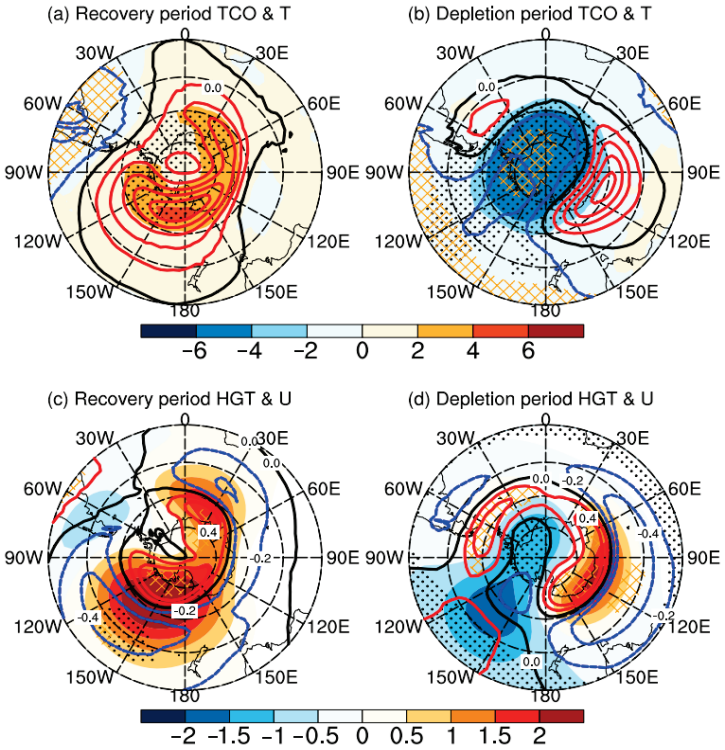

Figure 4. Same as Figure 3, but for the spatial distributions of the linear trends. The units of the trend of Total Column Ozone, 50 hPa temperature, 10 hPa geopotential height, and 30 hPa zonal wind are Du·a^{-1}, K·a^{-1}, dagpm·a^{-1}, and m·s^{-1}·a^{-1}, respectively.

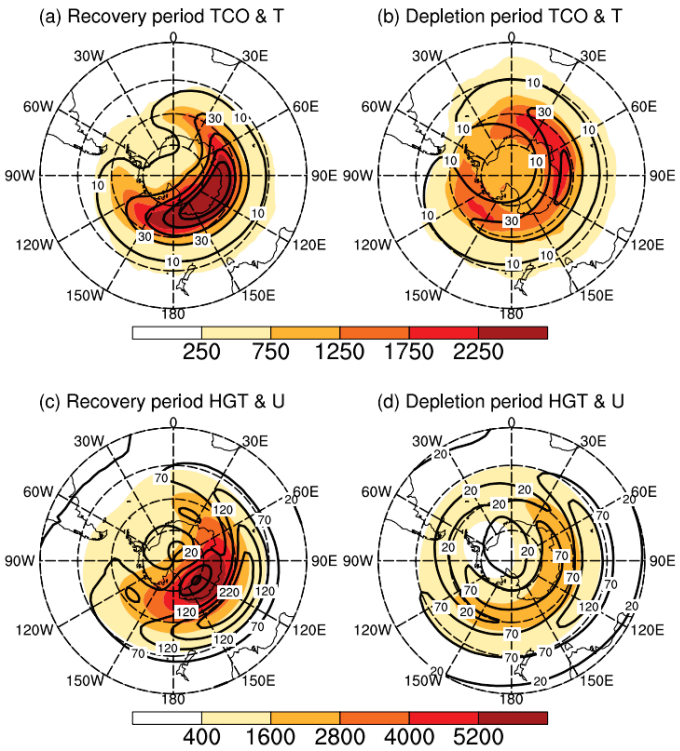

Figure 5. Composite variances of (**a**,**b**) Antarctic Total Column Ozone (shadings, unit: Du^2) and 50 hPa temperature (contours, unit: K^2), and (**c**,**d**) 10 hPa geopotential height (shadings, unit: dagpm^2) and 30 hPa zonal wind (contours, unit: m^2·s^{-2}) in September during the (**a**,**c**) recovery period and (**b**,**d**) depletion period.

To further understand the interannual variability of Antarctic TCO and stratospheric circulation during the two periods, Figure 6 shows the Morlet wavelet analysis of polar TCO and 50 hPa PT during the two periods. As can be seen, the interannual variation in polar TCO and 50 hPa PT in the two periods is similar to the main cycle being 2–4 years. Lu et al. [47] and Zou and Gao [48] found that the Antarctic ozone has a quasi-biennial oscillation period, which is consistent with the results of this paper. In the 2–4 year cycle, the maximum power spectrum of the polar TCO was 1878 in the recovery period and 322 in the depletion period, while the maximum power spectrum of 50 hPa PT was 50 in the recovery period and 6.75 in the depletion period. The wavelet analysis of the PSC area, 10 hPa PGH, and 30 hPa U60 were similar to 50 hPa PT. Therefore, the power spectrum of the TCO and stratospheric circulation in the 2–4 year cycle during the recovery period are much greater than that during the depletion period, showing stronger interannual variability characteristics.

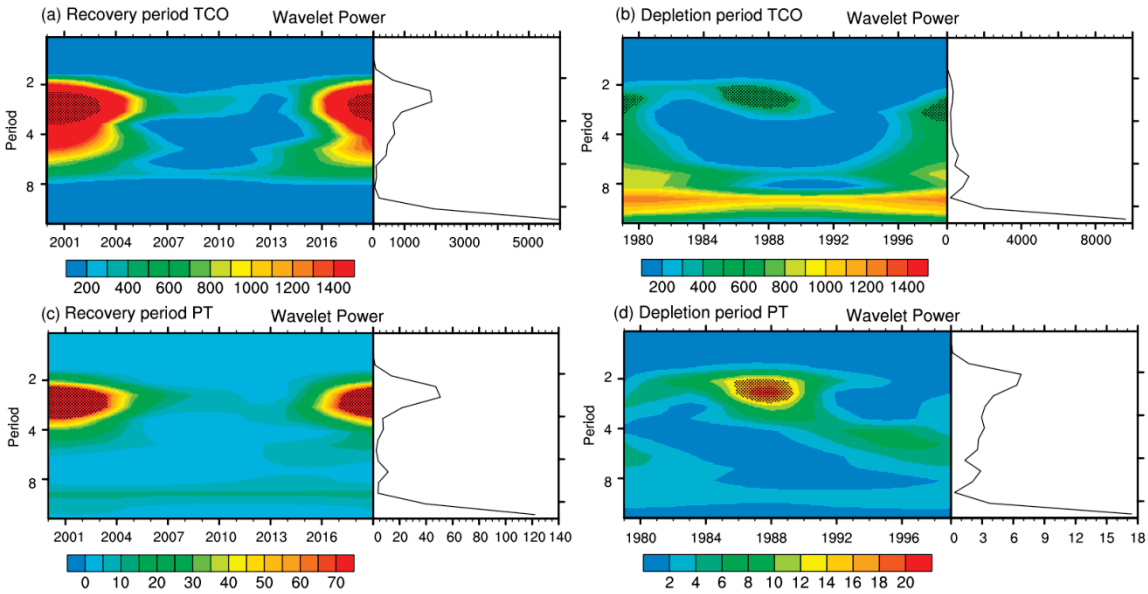

Figure 6. Morlet wavelet analysis of the (**a**,**b**) Antarctic polar TCO and (**c**,**d**) 50 hPa PT in September during the (**a**,**c**) recovery period and (**b**,**d**) depletion period. The black dots on the **left** represent passing the 0.05 confidence level and the power spectrum is on the **right**.

Combined with the above analysis results, it can be seen that the TCO is closely related to the PSC area, 50 hPa temperature, 10 hPa geopotential height, and 30 hPa zonal wind in the two eras. The relationship of each element is stable under the interdecadal change in the TCO: the rising (falling) of polar temperature, as well as the elevated (reduced) geopotential height, and the decelerating (accelerating) zonal wind result in the weakening (strengthening) of the polar vortex, combining with the increased (diminished) PSC area, thus, corresponding to the recovery (depletion) of the TCO. Additionally, the interannual variability of the TCO and stratospheric circulation in the recovery period is much greater than that in the depletion period.

3.2. The Variation Characteristics of Planetary Waves on Antarctic Total Column Ozone during the Recovery Period and Depletion Period

The above analyses prove that the 50 hPa temperature, 10 hPa geopotential height, and 30 hPa zonal wind are different during the recovery and depletion period. Are there also differences in the change in stratospheric circulation at each stratospheric layer between the two periods? First, the composite difference in stratospheric temperature, geopotential height, and zonal wind anomalies as a function of altitude and latitude were compared between the two periods. Compared with the depletion period, the temperature and geopo-

tential height are positive anomalies in the polar region during the recovery period. The large value of temperature (geopotential height) is located in the lower and middle stratosphere (the middle and upper stratosphere). The zonal wind shows a negative anomaly near 60°S in the middle and upper stratosphere. Not only are the 50 hPa temperature, 10 hPa geopotential height, and 30 hPa zonal wind significantly different, but the temperature in the middle and lower stratosphere and the polar vortex in the middle and upper stratosphere are also significantly different between the two periods.

The linear trends of stratospheric temperature and polar vortex during the recovery and depletion periods are further analyzed. Figure 7 exhibits the linear trend of stratospheric temperature and geopotential height as a function of altitude and latitude in the two periods. It illustrates that the temperature shows a positive trend throughout the stratosphere and the maximum trends appear in the lower and middle stratosphere during the recovery period (Figure 7a). Additionally, the geopotential height shows a positive trend (Figure 7c), and the zonal wind shows a negative trend in the middle and upper stratosphere, indicating a rising temperature in the lower and middle stratosphere and the gradual weakening of the polar vortex in the middle and upper stratosphere. During the depletion period, the temperature shows a negative trend in the middle and lower stratosphere, and the maximum trend is in the middle stratosphere (Figure 7b), corresponding to the negative trend of geopotential height (Figure 7d) and the positive trend of zonal wind in the middle and upper stratosphere. This demonstrates the falling temperature in the lower and middle stratosphere and the strengthening polar vortex in the middle and upper stratosphere. The trends of stratospheric circulation are not obvious, consistent with the result from Figure 2. This is possibly because of its inhomogeneity in zonal distribution. As a consequence, the changes in temperature and polar vortex in the recovery period are opposite to that in the depletion period. The changes in temperature are mainly located in the middle and lower stratosphere, while the changes in polar vortex are in the middle and upper stratosphere.

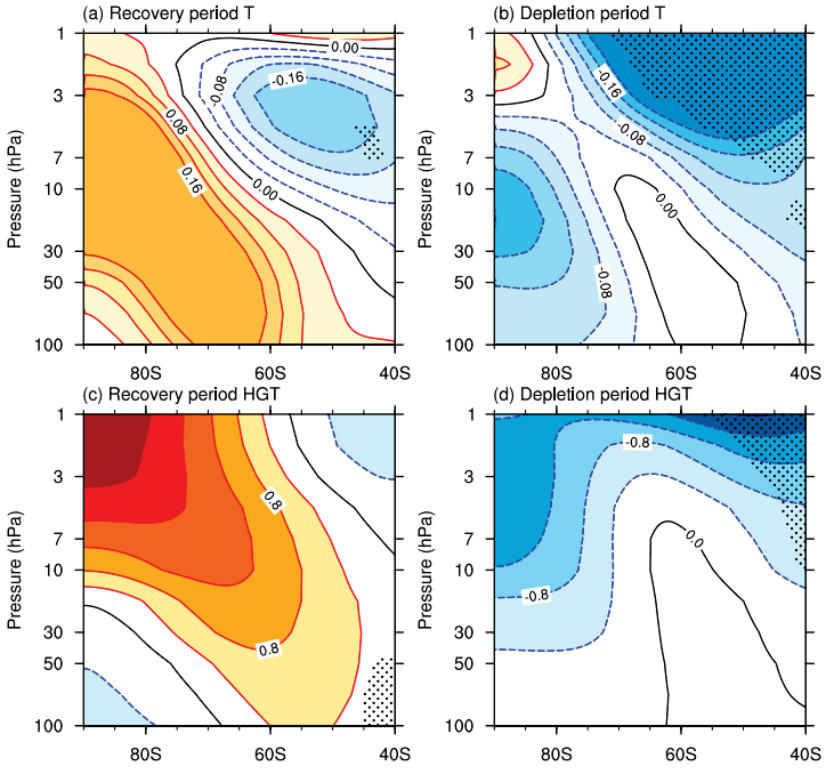

Figure 7. The linear trends of (**a**,**b**) temperature (unit: K·a^{-1}) and (**c**,**d**) geopotential height (unit: dagpm·a^{-1}) as a function of altitude and latitude in September during the (**a**,**c**) recovery period and (**b**,**d**) depletion period. The dotted areas are significant at the 0.01 confidence level.

The stratospheric temperature and polar vortex driven by planetary waves can affect the Antarctic ozone [23,24]. The difference in EP flux and EP flux divergence in the two periods are compared. The anomaly distribution in the recovery period is the opposite of that in the depletion period. In the recovery period, there is more upward EP flux and EP flux convergence in the stratosphere. The more downward EP flux corresponds to EP flux divergence during the depletion period, indicating the significant differences in EP flux and EP flux divergence between the two periods.

The linear trends of EP flux and EP flux divergence calculated from waves 1–3 as a function of altitude and latitude in the two periods are further displayed in Figure 8. During the recovery period, the stronger EP flux propagates from the troposphere to the stratosphere and EP flux convergence occurs in the middle and upper stratosphere above 10 hPa (cold shadings in Figure 8a). The stronger planetary wave forcings correspond to the positive trend of polar temperature in the lower and middle stratosphere and polar geopotential height in the middle and upper stratosphere (Figure 7a,c), as well as the negative trend of zonal flow in the middle and upper stratosphere being consistent with the recovery of the TCO. Additionally, in the vicinity of 3 hPa, EP flux is from the weak EP flux divergence in the low latitude (warm shadings in Figure 8a) to the EP flux convergence in the polar region. The stronger poleward movements are in favor of the transport of ozone-rich air from the equator to the polar, thus being consistent with the recovery of the TCO in the polar regions. In addition, the weak EP flux divergence exists near the polar region below 10 hPa (warm shadings in Figure 8a), which corresponds to the positive trend of zonal wind and the negative trend of geopotential height (cold shadings in Figure 7c). During the depletion period, the weaker EP flux exists from the troposphere to the stratosphere, corresponding to EP flux divergence at high latitudes in the middle stratosphere (warm shadings in Figure 8b). The weaker planetary wave forcings correspond to the negative trend of polar temperature in the lower and middle stratosphere and the polar geopotential height in the middle and upper stratosphere (Figure 7b,d). At this time, zonal flow accelerates in the middle and upper stratosphere, in favor of the depletion of the TCO. Additionally, EP flux is from EP flux divergence in the polar region to EP flux convergence in the low latitudes (cold shadings in Figure 8b). The weaker poleward movements are in favor of the transport of ozone from the polar to the equator, thus being consistent with the depletion of the TCO in the polar regions.

Eddy heat flux and eddy momentum flux can reflect the direction of planetary waves [40,45]. Figure 9 shows the difference in the linear trends of EHF and EMF calculated by waves 1–3 as a function of altitude and latitude between the two periods. During the recovery period, EHF decreases largely near the polar region of 10 hPa (Figure 9a), accompanied by more and stronger EP flux and EP flux convergence (Figure 8a). Compared with the recovery period, the smaller decreased EHF near the upper stratospheric polar region corresponds to weaker EP flux and EP flux divergence at high latitudes during the depletion period (Figure 8b). In addition, the increased EMF above 30 hPa at midlatitudes indicates that the poleward movements enhance (Figure 9b), and the planetary waves bring the ozone from the middle and low latitudes to the polar regions (Figure 8a), in keeping with the decelerating zonal flow and the increased ozone. During the depletion period, the decreased EMF in the stratosphere indicates that the poleward movements weaken and more planetary waves carry ozone away from the polar region (Figure 8b). This agrees with the accelerating zonal flow and the decreased ozone.

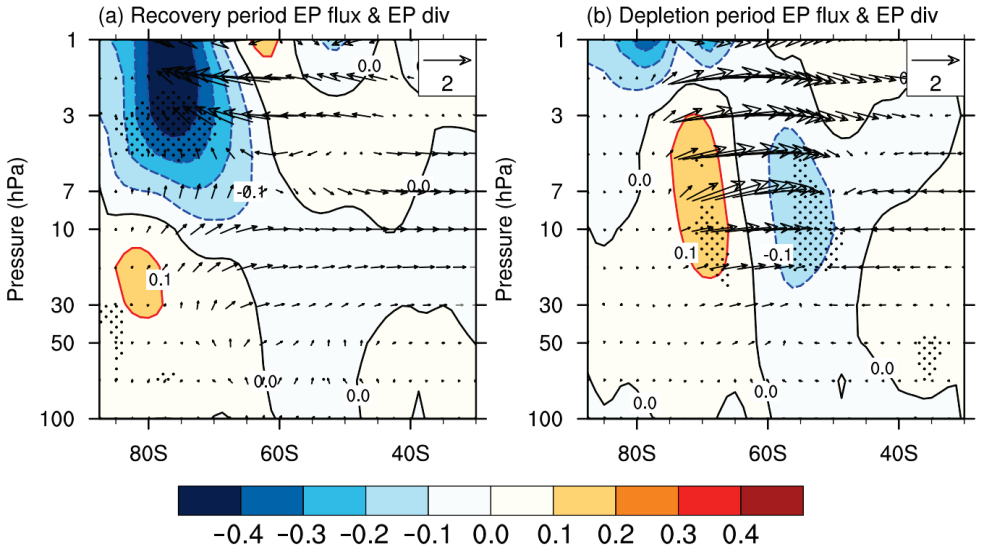

Figure 8. The linear trends of EP flux (vectors, unit: $m^3 \cdot s^{-2} \cdot a^{-1}$) and EP flux divergence (shadings, unit: $m \cdot s^{-2} \cdot a^{-1}$) calculated from waves 1–3 as a function of altitude and latitude in September during the (**a**) recovery period and (**b**) depletion period. EP flux vectors are multiplied by the square root of $1000.0/p$ in both the vertical and horizontal directions, where p is pressure (hPa). Red vectors and dotted areas indicate that the EP flux and EP flux divergence are significant at the 0.05 confidence level according to Student's t-test.

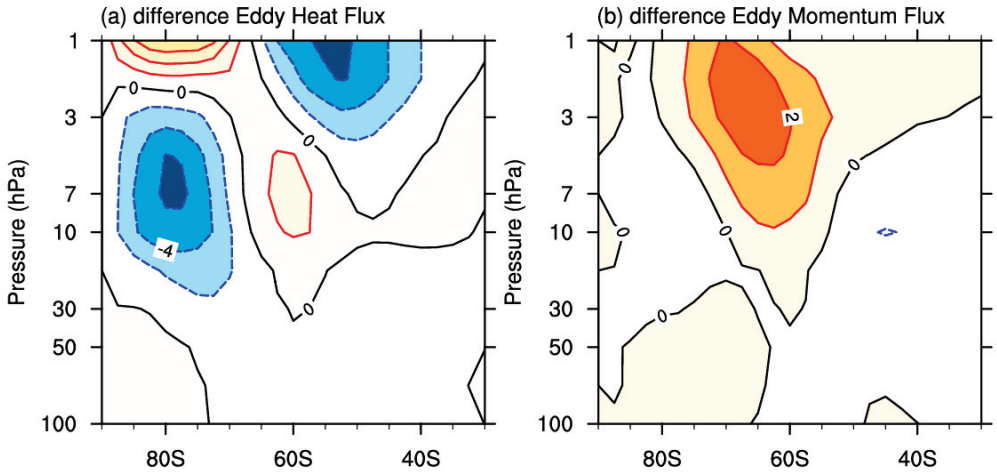

Figure 9. Difference in the linear trends of (**a**) eddy heat flux (unit: $K \cdot m \cdot s^{-1} \cdot a^{-1}$) and (**b**) eddy momentum flux (unit: $m^2 \cdot s^{-2} \cdot a^{-1}$) calculated from waves 1–3 as a function of altitude and latitude in September between the recovery period and depletion period.

Planetary waves, particularly for wave 1, dominate the total wave in the stratosphere [42,49], Figure 10 shows the climatological distributions and composite anomalies for geopotential height calculated from wave 1, as well as the linear trends for geopotential height and temperature calculated from wave 1, at 100 hPa in September during the recovery period and depletion period. This demonstrates that positive geopotential height is observed from the east of the southern Indian Ocean to the center of the South Pacific (red contours in Figure 10a,b), while negative geopotential height is over the east of the South Pacific to the South Atlantic (blue contours in Figure 10a,b) during the two periods. During the recovery period, positive anomalies in the southeast Pacific (warm shadings in Figure 10a) and negative anomalies in the South Atlantic (cold shadings in Figure 10a) are superimposed with the climatological geopotential height, indicating the larger amplitude of geopotential height. From the perspective of the linear trend, the

geopotential height wave 1 and temperature wave 1 are in different phases (Figure 10b), resulting in stronger baroclinic disturbance. During the depletion period, the anomalies for geopotential height are with out-of-phase superposition on the climatological geopotential height (Figure 10c). The geopotential height wave 1 and temperature wave 1 are in the same phases (Figure 10d), leading to weaker baroclinic disturbance.

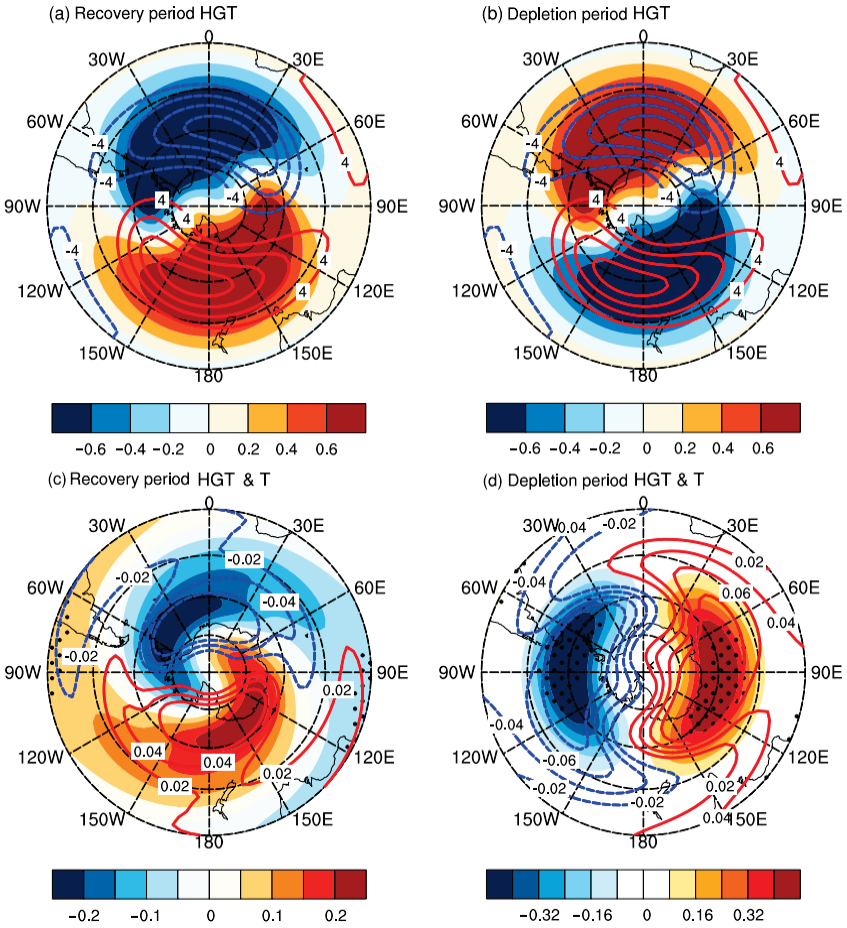

Figure 10. The (**a**,**b**) climatological distributions (contours) and composite anomalies (shadings) (unit: dagpm) for geopotential height calculated from wave 1 and (**c**,**d**) the linear trends for geopotential height (shadings, unit: dagpm·a^{-1}) and temperature (contours, unit: K·a^{-1}) calculated from wave 1 at 100 hPa in September during the (**a**,**c**) recovery period and (**b**,**d**) depletion period. Dotted areas are significant at the 0.05 confidence level according to Student's t-test.

In summary, the stronger (weaker) planetary wave amplitudes and baroclinic disturbances lead to stronger (weaker) upward planetary wave propagation from the troposphere to the stratosphere, as well as EP flux convergence (divergence), larger (smaller) negative EHF, and positive (negative) EMF. This is in accordance with the rising (falling) temperature in the lower and middle stratosphere and the weakened (enhanced) polar vortex in the middle and upper stratosphere, in combination with the diminished (increased) PSC area, being advantageous to the recovery (depletion) of the TCO.

4. Conclusions and Discussion

Based on the BS–TCO and ERA5 datasets during 1979–2019, this study explores the variation characteristics of TCO, stratospheric temperature, polar vortex, and PSC area over Antarctica under the interdecadal change in TCO around 2000 for the TCO 'depletion' period (1979–1999) and the 'recovery' period (2000–2019). The variation characteristics of

planetary waves are then discussed during the two periods. The results are concluded as follows.

The TCO over Antarctica in September increases significantly after 2000 and decreases significantly before 2000 as a result of the change in ODSs. During the whole period, the TCO and the temperature, as well as the geopotential height (PSC area and the zonal wind) maintain a significant and stable positive (negative) relationship. Correspondingly, around 2000, the polar temperature in the middle and lower stratosphere experiences a process of first cooling and then warming, the polar vortex in the middle and upper stratosphere first strengthens and then weakens, and the PSC area first increases and then diminishes. The trends of stratospheric polar temperature and the polar vortex are not significant but are consistent with the changes in the TCO. However, the interannual variability of the TCO and the above-mentioned stratospheric circulation elements in the recovery period are stronger than in the depletion period. The complete picture of the variation characteristics of the TCO and stratospheric circulation during the recovery and depletion periods is presented in Figure 11.

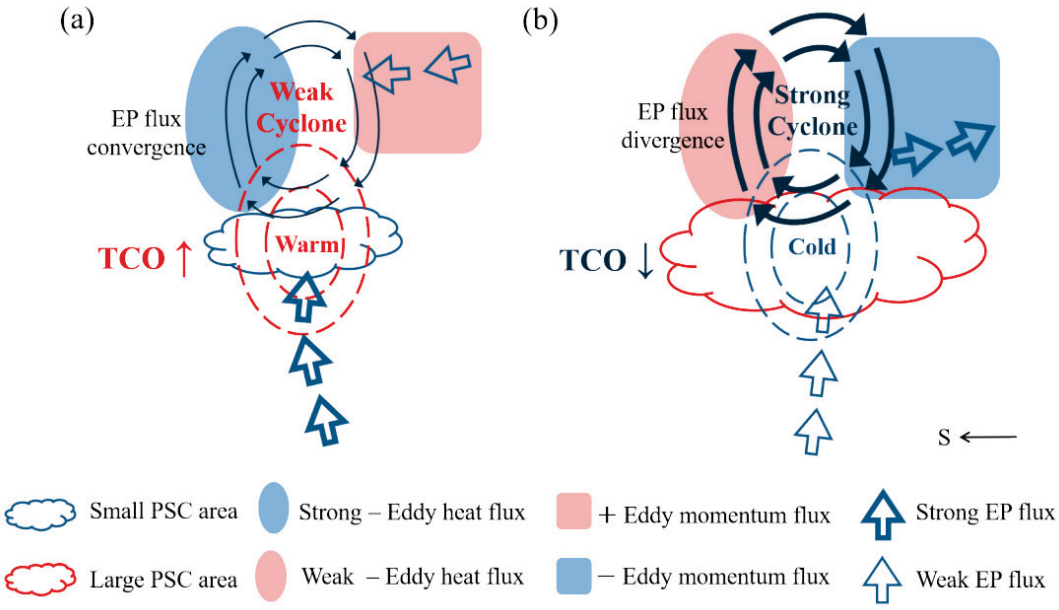

Figure 11. Schematic diagram of the possible pathways for different evolutions of the Antarctic Total Column Ozone during the (**a**) recovery period and (**b**) depletion period.

During the recovery period (Figure 11a), due to the stronger amplitude of planetary wave 1 and the baroclinic disturbance in the upper troposphere (Figure 10a), stronger upward EP flux existed in the stratosphere, accompanied by EP flux convergence (Figure 8a), larger negative eddy heat flux, and positive eddy momentum flux (Figure 9) in the middle and upper stratosphere. The polar temperature rose (Figures 2a, 4a and 7a) in the lower and middle stratosphere and the polar vortex weakened (Figures 2b, 4c and 7c) in the middle and upper stratosphere. The area of PSC diminished (Figure 1b), in keeping with the recovery of the Antarctic TCO (Figures 1a and 4a). During the depletion period (Figure 11b), the weaker planetary wave 1 amplitude and baroclinic disturbance in the upper troposphere (Figure 10c,d), resulted in weaker EP flux, together with EP flux divergence in the middle stratosphere (Figure 8b), smaller negative eddy heat flux and negative eddy momentum flux (Figure 9), when compared with the recovery period. The polar temperature fell (Figures 2a, 4b and 7b) in the middle and low stratosphere and the polar vortex was enhanced (Figures 2b, 4d and 7d) in the middle and upper stratosphere, accompanied by the increased area of PSC (Figure 1b), corresponding to the depletion of the Antarctic TCO (Figures 1a and 4b).

The varying characteristics of the Antarctic ozone and stratospheric circulation are compared in this paper using monthly data from the past 41 years during the Antarctic TCO recovery period and depletion period. Stratospheric elements significantly related to the TCO experienced corresponding changes. The stronger interannual variability of the TCO and the stratospheric circulation elements possibly means that the dynamic processes of stratospheric circulation had a closer relationship with the TCO in the recovery period. But the time series of the TCO in Figures 1 and 2 both have three local maximums in 1988, 2002, and 2019, because of sudden stratospheric warming [50,51]. Regarding the cause of the sudden stratospheric warming, some studies have suggested that it is due to the interaction between planetary waves and zonal winds [43], so this paper takes the three years of sudden stratospheric warming events into consideration as well. The results obtained after removing the data in these years are similar to those in this paper, so these three years do not affect the results presented in this paper. It is worth mentioning that the temporal and spatial characteristics of the Antarctic TCO from ECMWF are similar to those from BS–TCO. In addition, EP flux has a 2–4-year cycle and the power spectrum during the recovery period is much greater than that during the depletion period, showing stronger interannual variability characteristics. But the difference and interannual variability of EP flux are not significant between the two periods. Therefore, it is not analyzed deeply in this paper.

Due to the complex relationship between ozone and stratospheric temperature, and the continuous increase in greenhouse gases contributing to the cooling of the lower stratosphere in the depletion period and hindering the warming of the stratosphere in the recovery period [52], the order of precedence between TCO and stratospheric circulation is more difficult to distinguish. Solomon et al. [10] studied the contribution of dynamic and chemical processes to the ozone recovery trend through models and emphasized the important contribution of dynamic processes to ozone recovery in September. Additionally, an example of the relationship between stratospheric sudden warming and ozone studied for Syowa station in Antarctica based on the daily data, points out that stratospheric warming is affected by dynamic processes and ozone changes have a weak effect on stratospheric warming [53,54]. In conclusion, the formation of Antarctic ozone is influenced by atmospheric dynamics and atmospheric chemistry. It is necessary to select typical cases to analyze and further investigate the level of influence of dynamic processes on the TCO [55] using coupled dynamic chemical models in the recovery periods. In terms of the diagnosis of large-scale dynamic transport processes, a variety of diagnostic methods should be used for dynamic analysis, such as the residual circulation and reflective surfaces. Residual circulation driven by planetary wave activity [49] can also affect Antarctic ozone, but the long-term trends of this are still controversial [4,56]. All these problems need to be studied further.

Author Contributions: Conceptualization, methodology, J.L. and S.Z.; Writing—original draft, J.L.; Writing—review and editing, J.L. and M.W.; validation, D.G. and Y.Y.; funding acquisition, S.Z.; supervision, D.H. and Y.Y. All authors have read and agreed to the published version of the manuscript.

Funding: This work was funded by grants from the project of the National key research and development plan (Grant No. 2022YFF0801703), a key project of the National Natural Science Foundation (Grant No. 42030602), a major project of the National Natural Science Foundation of China (Grant No. 42192512), and an integration project of National Natural Science Foundation of China major research program (Grant No. 91837311).

Data Availability Statement: The dataset of the total ozone column is provided by Bodeker Scientific Filled Total Column Ozone (BS–TCO) Database V3.5.1 at https://doi.org/10.5281/zenodo.4535247 for this study (accessed on 1 October 2021). The polar ozone index from the satellite and the area of PSC formed of nitric acid trihydrate are from the National Aeronautics and Space Administration (NASA) Goddard Space Flight Center online database (https://ozonewatch.gsfc.nasa.gov/, accessed on 11 November 2021). The EESC dataset was obtained from https://acd-ext.gsfc.nasa.gov/Data_services/automailer/restricted/automailer (accessed on 27 November 2022). The stratospheric wind, geopotential height, and temperature datasets come from the European Center for Medium-

Range Weather Forecasts (ECMWF) ERA5 at https://cds.climate.copernicus.eu/cdsapp#!/dataset/reanalysis-era5-pressure-levels-monthlymeans?tab=form (accessed on 14 December 2021).

Conflicts of Interest: The authors declare no conflicts of interest.

References

1. Farman, J.C.; Gardiner, B.G.; Shanklin, J.D. Large losses of total ozone in Antarctica reveal seasonal ClOx/NOx interaction. *Nature* **1985**, *315*, 207–210. [CrossRef]
2. World Meteorological Organization/United Nations Environment Programme (WMO/UNEP). *Scientific Assessment of Ozone Depletion: 2014*; Global Ozone Research and Monitoring Project Report No. 55; World Meteorological Organization/United Nations Environment Programme (WMO/UNEP): Geneva, Switzerland, 2014.
3. Yu, P.; Davis, S.M.; Toon, O.B.; Portmann, R.W.; Bardeen, C.G.; Barnes, J.E.; Telg, H.; Maloney, C.; Rosenlof, K.H. Persistent stratospheric warming due to 2019–2020 Australian wildfire smoke. *Geophys. Res. Lett.* **2021**, *48*, e2021GL092609. [CrossRef]
4. Hu, D.Z.; Guo, Y.P.; Wang, F.Y.; Xu, Q.; Li, Y.P.; Sang, W.J.; Wang, X.; Liu, M. Brewer-Dobson Circulation: Recent-Past and Near-Future Trends Simulated by Chemistry-Climate Models. *Adv. Meteorol.* **2017**, *2017*, 2913895. [CrossRef]
5. World Meteorological Organization (WMO). *Scientific Assessment of Ozone Depletion: 2018*; Global Ozone Research and Monitoring Project-Report No. 58; World Meteorological Organization (WMO): Geneva, Switzerland, 2018; Volume 588.
6. Hu, Y.-Y. The discovery of the Antarctic ozone hole. *Chin. Sci. Bull.* **2020**, *65*, 1797–1803. (In Chinese) [CrossRef]
7. Stone, K.A.; Solomon, S.; Kinnison, D.E.; Mills, M.J. On recent large Antarctic ozone holes and ozone recovery metrics. *Geophys. Res. Lett.* **2021**, *48*, e2021GL095232. [CrossRef]
8. Newman, P.A.; Daniel, J.S.; Waugh, D.W.; Nash, E.R. A new formulation of equivalent effective stratospheric chlorine (EESC). *Atmos. Chem. Phys.* **2007**, *7*, 4537–4552. [CrossRef]
9. Chipperfield, M.P.; Bekki, S.; Dhomse, S.; Harris, N.R.P.; Hassler, B.; Hossaini, R.; Steinbrecht, W.; Thiéblemont, R.; Weber, M. Detecting recovery of the stratospheric ozone layer. *Nature* **2017**, *549*, 211–218. [CrossRef]
10. Solomon, S.; Ivy, D.J.; Kinnison, D.; Mills, M.J.; Neely, R.R., III; Schmidt, A. Emergence of healing in the Antarctic ozone layer. *Science* **2016**, *353*, 269–274. [CrossRef]
11. Strahan, S.E.; Douglass, A.R.; Damon, M.R. Why do Antarctic ozone recovery trends vary? *J. Geophys. Res. Atmos.* **2019**, *124*, 8837–8850. [CrossRef]
12. Bian, L.G.; Lin, Z.; Zheng, X.D.; Ma, Y.F.; Lu, L.H. The trend of Antarctic ozone hole and its influencing factors. *Adv. Clim. Chang. Res.* **2012**, *3*, 68–75.
13. Newman, P.A.; Nash, E.R.; Kawa, S.R.; Montzka, S.A.; Schauffler, S.M. When will the Antarctic ozone hole recover? *Geophys. Res. Lett.* **2006**, *33*, L12814. [CrossRef]
14. Kravchenko, V.O.; Evtushevsky, O.M.; Grytsai, A.V.; Klekociuk, A.R.; Milinevsky, G.P.; Grytsai, Z.I. Quasi-stationary planetary waves in late winter Antarctic stratosphere temperature as a possible indicator of spring total ozone. *Atmos. Chem. Phys.* **2012**, *12*, 2865–2879. [CrossRef]
15. Shantikumar, S.N.; Vemareddy, P.; Song, H.-J. Effect of lower stratospheric temperature on total ozone column (TOC) during the ozone depletion and recovery phases. *Atmos. Res.* **2020**, *232*, 104686.
16. Chen, W.; Huang, R.H. The numerical Study of Seasonal and lnterannual Variabilities of Ozone due to Planetary Wave Transport in the Middle Atmosphere: Part I. The Case of Steady Mean Flows. *Sci. Atmos. Sin.* **1996**, *20*, 513–523. (In Chinese)
17. Chen, W.; Huang, R.H. A Numerical Study of Seasonal and lnterannual Variabilities of Ozone due to Planetary Wave Transport in the Middle Atmosphere: Part II. The Case of Wave-Flow Interaction. *Sci. Atmos. Sin.* **1996**, *20*, 703–712. (In Chinese)
18. Zheng, B.; Chen, Y.J.; Shi, C.H. Relationship of Zonal Ozone Seasonal Variations and Planetary Wave in the Stratosphere. *Plateau Meteorol.* **2006**, *25*, 366–374. (In Chinese)
19. Thompson, D.W.J.; Solomon, S. Interpretation of recent Southern Hemisphere climate change. *Science* **2002**, *296*, 895–899. [CrossRef]
20. Keeble, J.; Braesicke, P.; Abraham, N.L.; Roscoe, H.K.; Pyle, J.A. The impact of polar stratospheric ozone loss on Southern Hemisphere stratospheric circulation and climate. *Atmos. Chem. Phys.* **2014**, *14*, 13705–13717. [CrossRef]
21. Waugh, D.W.; Plumb, R.A.; Elkins, J.W.; Fahey, D.W.; Boering, K.A.; Dutton, G.S.; Volk, C.M.; Keim, E.; Gao, R.-S.; Daube, B.C.; et al. Mixing of polar vortex air into middle latitudes as revealed by tracer-tracer scatter plots. *J. Geophys. Res.* **1997**, *102*, 13119–13134. [CrossRef]
22. Zhang, Y.; Li, J.; Zhou, L.B. The Relationship between Polar Vortex and Ozone Depletion in the Antarctic Stratosphere during the Period 1979–2016. *Adv. Meteorol.* **2017**, *2017*, 3078079. [CrossRef]
23. Li, C.C.; Guo, S.C.; Yi, Q.; Li, H.F. Relationship between atmospheric ozone and polar vortex intensity in the mid-high latitude over the Northern Hemisphere in winter. *Plateau Meteorol.* **2016**, *35*, 1290–1297. (In Chinese)
24. Seidel, D.J.; Li, J.; Mears, C.; Moradi, I.; Nash, J.; Randel, W.J.; Saunders, R.; Thompson, D.W.J.; Zou, C.-Z. Stratospheric temperature changes during the satellite era. *J. Geophys. Res. Atmos.* **2016**, *121*, 664–681. [CrossRef]
25. Kidston, J.; Scaife, A.; Hardiman, S.; Mitchell, D.; Butchart, N.; Baldwin, M.; Gray, L. Stratospheric influence on tropospheric jet streams, storm tracks and surface weather. *Nat. Geosci.* **2015**, *8*, 433–440. [CrossRef]

26. Son, S.W.; Gerber, E.P.; Perlwitz, J.; Polvani, L.M.; Gillett, N.P.; Seo, K.-H.; Eyring, V.; Shepherd, T.G.; Waugh, D.; Akiyoshi, H.; et al. The impact of stratospheric ozone on Southern Hemisphere circulation changes: A multimodel assessment. *J. Geophys. Res.* **2010**, *115*, D00M07. [CrossRef]
27. Polvani, L.M.; Waugh, D.W.; Correa, G.J.P.; Son, S.-W. Stratospheric ozone depletion: The main driver of twentieth-century atmospheric circulation changes in the Southern Hemisphere. *J. Clim.* **2011**, *24*, 795–812. [CrossRef]
28. Banerjee, A.; Fyfe, J.C.; Polvani, L.M.; Waugh, D.; Chang, K.-L. A pause in Southern Hemisphere circulation trends due to the Montreal protocol. *Nature* **2020**, *579*, 544–548. [CrossRef]
29. Zambri, B.; Solomon, S.; Thompson, D.W.J.; Fu, Q. Emergence of Southern Hemisphere stratospheric circulation changes in response to ozone recovery. *Nat. Geosci.* **2021**, *14*, 638–644. [CrossRef]
30. Ferreira, D.; Marshall, J.; Bitz, C.M.; Solomon, S.; Plumb, A. Antarctic ocean and sea ice response to ozone depletion: A two-time-scale problem. *J. Clim.* **2015**, *28*, 1206–1226. [CrossRef]
31. Seviour, W.J.M.; Gnanadesikan, A.; Waugh, D.W. The Transient Response of the Southern Ocean to Stratospheric Ozone Depletion. *J. Clim.* **2016**, *29*, 7383–7396. [CrossRef]
32. Turner, J.; Comiso, J.C.; Marshall, G.J.; Lachlan-Cope, T.A.; Bracegirdle, T.; Maksym, T.; Meredith, M.P.; Wang, Z.; Orr, A. Non-annular atmospheric circulation change induced by stratospheric ozone depletion and its role in the recent increase of Antarctic sea ice extent. *Geophys. Res. Lett.* **2009**, *36*, L08502. [CrossRef]
33. Zhang, J.K.; Tian, W.S.; Pyle, J.A.; Keeble, J.; Abraham, N.L.; Chipperfield, M.P.; Xie, F.; Yang, Q.H.; Mu, L.J.; Ren, H.-L.; et al. Responses of Arctic Sea Ice to Stratospheric Ozone Depletion. *Sci. Bull.* **2022**, *67*, 1182–1190. [CrossRef]
34. Xia, Y.; Hu, Y.Y.; Liu, J.P.; Huang, Y.; Xie, F.; Lin, J.T. Stratospheric Ozone-induced Cloud Radiative Effects on Antarctic Sea Ice. *Adv. Atmos. Sci.* **2020**, *37*, 505–514. [CrossRef]
35. Bodeker, G.E.; Kremser, S.; Tradowsky, J.S. BS Filled Total Column Ozone Database V3.5.1 (3.5.1). *Zenodo* **2021**. [CrossRef]
36. Hersbach, H.; Bell, B.; Berrisford, P.; Biavati, G.; Horányi, A.; Muñoz Sabater, J.; Nicolas, J.; Peubey, C.; Radu, R.; Rozum, I.; et al. ERA5 monthly averaged data on pressure levels from 1979 to present. *Copernic. Clim. Chang. Serv. (C3S) Clim. Data Store (CDS)* **2019**, *10*, 252–266.
37. Seviour, W.J.M.; Hardiman, S.C.; Gray, L.J.; Butchart, N.; Maclachlan, C.; Scaife, A.A. Skillful Seasonal Prediction of the Southern Annular Mode and Antarctic Ozone. *J. Clim.* **2014**, *27*, 7462–7474. [CrossRef]
38. Torrence, C.; Compo, G. A practical guide to wavelet analysis. *Bull. Am. Meteorol. Soc.* **1998**, *79*, 61–78. [CrossRef]
39. Orr, A.; Bracegirdle, T.J.; Hoskings, J.S.; Jung, T.; Haigh, J.D.; Phillips, T.; Feng, W. Possible dynamical mechanisms for Southern Hemisphere climate change due to the ozone hole. *J. Atmos. Sci.* **2012**, *69*, 2917–2932. [CrossRef]
40. Lubis, S.W.; Silverman, V.; Matthes, K.; Harnik, N.; Omrani, N.-E.; Wahl, S. How does downward planetary wave coupling affect polar stratospheric ozone in the Arctic winter stratosphere? *Atmos. Chem. Phys.* **2017**, *17*, 2437–2458. [CrossRef]
41. Dunkerton, T.; Hsu, C.F.; McIntyre, M.E. Some Eulerian and Lagrangian Diagnostics for a Model Stratospheric Warming. *J. Atmos. Sci.* **1981**, *38*, 819–844. [CrossRef]
42. Dunn-Sigouin, E.; Shaw, T.A. Comparing and contrasting extreme stratospheric events, including their coupling to the tropospheric circulation. *J. Geophys. Res.* **2015**, *120*, 1374–1390. [CrossRef]
43. Song, B.-G.; Chun, H.-Y. Residual circulation and temperature changes during the evolution of stratospheric sudden warming revealed in MERRA. *Atmos. Chem. Phys.* **2016**, preprint.
44. Chemke, R.; Polvani, L.M. Linking midlatitudes eddy heat flux trends and polar amplification. *NPJ Clim. Atmos. Sci.* **2020**, *3*, 8. [CrossRef]
45. Orr, A.; Lu, H.; Martineau, P.; Gerber, E.P.; Marshall, G.J.; Bracegirdle, T.J. Is our dynamical understanding of the circulation changes associated with the Antarctic ozone hole sensitive to the choice of reanalysis dataset? *Atmos. Chem. Phys.* **2021**, *21*, 7451–7472. [CrossRef]
46. Huck, P.E.; McDonald, A.J.; Bodeker, G.E.; Struthers, H. Interannual variability in Antarctic ozone depletion controlled by planetary waves and polar temperature. *Geophys. Res. Lett.* **2005**, *32*, L13819. [CrossRef]
47. Lu, L.H.; Bian, L.G.; Jia, P.Q. Short-term climatic change of Antarctic ozone. *Q. J. Appl. Meteorol.* **1997**, *8*, 402–412. (In Chinese)
48. Zou, H.; Gao, Y.Q. QBO and ENSO Signals in Total Ozone over 60~70°S. *Clim. Environ. Res.* **1997**, *1*, 62–71. (In Chinese)
49. Wang, Z.; Zhang, J.; Wang, T.; Feng, W.; Hu, Y.H.; Xu, X.R. Analysis of the Antarctic Ozone Hole in November. *J. Clim.* **2021**, *34*, 6513–6529. [CrossRef]
50. Shen, X.C.; Wang, L.; Osprey, S. The Southern Hemisphere sudden stratospheric warming of September 2019. *Sci. Bull.* **2020**, *65*, 1800–1802. [CrossRef]
51. Roy, R.; Kuttippurath, J.; Lefèvre, F.; Raj, S.; Kumar, P. The sudden stratospheric warming and chemical ozone loss in the Antarctic winter 2019: Comparison with the winters of 1988 and 2002. *Theor. Appl. Climatol.* **2022**, *149*, 119–130. [CrossRef]
52. Maycock, A.C.; Randel, W.J.; Steiner, A.K.; Karpechko, A.Y.; Christy, J.; Saunders, R.; Thompson, D.W.J.; Zou, C.-Z.; Chrysanthou, A.; Abraham, N.L.; et al. Revisiting the mystery of recent stratospheric temperature trends. *Geophys. Res. Lett.* **2018**, *45*, 9919–9933. [CrossRef]
53. Zou, H. Stratospheric sudden warming and its relationship with ozone on Antarctica in august. 1988. *Antarct. Res.* **1990**, *2*, 61–66. (In Chinese)
54. Xiong, K.; Hu, R.M.; Shi, G.Y. Antarctic total ozone change correlated to the stratosphere wind and temperature during the polar night. *Antarct. Res.* **1992**, *4*, 45–50. (In Chinese)

55. Shi, C.H.; Chen, Y.J.; Zheng, B.; Liu, Y. A comparison with the contribution of dynamics and chemistry in ozone's seasonal variation in the stratosphere. *Chin. J. Atmos. Sci.* **2010**, *34*, 399–406. (In Chinese)
56. Tian, W.S.; Huang, J.L.; Qie, K.; Wang, T.; Xu, M. Review of the general atmospheric circulation in the stratosphere and its variation features. *J. Meteorol. Sci.* **2020**, *40*, 628–638. (In Chinese)

Disclaimer/Publisher's Note: The statements, opinions and data contained in all publications are solely those of the individual author(s) and contributor(s) and not of MDPI and/or the editor(s). MDPI and/or the editor(s) disclaim responsibility for any injury to people or property resulting from any ideas, methods, instructions or products referred to in the content.

climate

MDPI

Article

Assessing Heatwave-Related Deaths among Older Adults by Diagnosis and Urban/Rural Areas from 1999 to 2020 in Slovenia

Simona Perčič [1,*], Katarina Bitenc [1], Majda Pohar [1], Anka Uršič [2], Tanja Cegnar [3] and Ana Hojs [1]

[1] Centre for Environmental Health, National Institute of Public Health Slovenia, Zaloška 29, 1000 Ljubljana, Slovenia; katarina.bitenc@nijz.si (K.B.); majda.pohar@nijz.si (M.P.); ana.hojs@nijz.si (A.H.)
[2] Medical Faculty, University of Ljubljana, Vrazov trg 2, 1000 Ljubljana, Slovenia; au6262@student.uni-lj.si
[3] Slovenian Environment Agency, Vojkova 1b, 1000 Ljubljana, Slovenia; tanja.cegnar@gov.si
* Correspondence: simona.percic@nijz.si

Abstract: Background: The association between mortality and heatwaves is well documented. Heatwaves frequency, intensity, and duration increase with global climate change. The most vulnerable group for dying during heatwaves is older people. Knowing which diseases contribute to a higher number of deaths during heatwaves is important for planning appropriate public health preventive measures. Methods: We assessed the short-term association between the number of deaths for older adults (75+ years) and heatwaves in the years 1999 to 2020 in Slovenia. We estimated the relative risks (RR) with a 95% confidence interval for the number of deaths for the observed diagnosis (all causes, circulatory, respiratory) and urban vs. rural areas associated with heatwaves in Slovenia for each year, comparing the number of deaths during heatwaves with reference days. Results: Most years showed no significant increase in deaths during heatwaves for those aged 75 and older. However, in 2006, 2007, 2014, and 2015, there was a significant increase in deaths during heatwaves. For the general population, heatwaves were associated with an increase in deaths due to all causes: 10% more in 2006 and 26% more in both 2007 and 2014. For those aged 75 and older, heatwaves were associated with an increase in deaths due to all causes: 22% more in 2007, 27% more in 2014, and 28% more in 2015. For those aged 75 and older, heatwaves were associated with an increase in deaths due to circulatory system diseases: 25% more in 2006, 33% more in 2007, 30% more in 2014, and 27% more in 2015. Regarding urban vs. rural areas, in 2006 and 2012, the elderly in urban areas were more affected, with 33% and 26% more deaths, respectively. In contrast, in 2007, 2014, and 2015, old age population in rural areas was more affected, with 29%, 26%, and 31% more deaths, respectively. Conclusions: According to the literature data, older adults are most susceptible to the effects of extreme heat due to physiological changes that occur with aging, chronic diseases, certain medications, a sedentary lifestyle, and social isolation. The results of our study will help in planning appropriate preventive public health measures to better protect older adults during the next heatwaves in Slovenia.

Keywords: climate change; heatwaves; excess deaths

1. Introduction

Human-caused greenhouse gas emissions have resulted in a noticeable increase in global temperatures, associated with more frequent, prolonged, and intense heatwaves and hot summers [1,2]. In Slovenia, every decade over the past 30 years has been warmer than the previous ones, with the exception of the period from 2001 to 2010, which was not statistically significantly warmer than 1991 to 2000 [3]. The temperature of the atmosphere in Slovenia in the first two decades of this millennium (2001–2020) was 1.8 [1.5 to 2.0] °C above that in the period 1850–1900, and in the last decade (2011–2020) by 2.1 [1.9 to 2.4] °C [3]. However, climate change projections for Europe, including Slovenia, suggest that temperatures will keep increasing rapidly, along with their health impacts, unless significant measures for mitigation and adaptation are put in place [4,5].

Heatwaves are among the extreme weather events globally that have the most significant impact in terms of death tolls, particularly highlighted over the past two decades (since the notorious 2003 disaster in France) [6]. This heightened awareness of the immediate health effects of heatwaves has prompted the development of prevention plans and adaptation strategies aimed at safeguarding vulnerable groups [7,8]. Older adults are especially at risk from extreme heat due to age-related physiological changes, limited access to healthcare, chronic conditions, specific medications, social isolation, a sedentary lifestyle, and the availability of air conditioning, all of which impair body temperature regulation and increase the risk of dehydration [9,10]. Heatwaves can also trigger or worsen adverse drug reactions in older adults who take diuretics, serotonergic antidepressants, ACE inhibitors, proton pump inhibitors, non-dopaminergic anti-parkinsonian drugs, antiepileptics, and beta-blockers [11]. As life expectancy increases, the demographic composition of society is shifting, with the 60+ age group projected to make up 21.1% of Europe's population by 2050 [12]. By 2060, the 65+ age group will constitute over 35% of Slovenia's population, raising concerns about a rise in chronic non-communicable diseases among this population [13]. This demographic change is particularly relevant to heatwaves, as older individuals are more susceptible to extreme temperatures, heightening health risks and placing additional pressure on healthcare systems.

The future impact of heatwaves on human health remains uncertain, with many unanswered questions about whether this effect will remain stable, increase, or decrease over time [14]. Numerous studies examining heatwaves across various periods and emission scenarios suggest that the link between heatwave intensity and increased mortality may stay consistent over time [15–18]. However, progressive adaptation to heat, along with the implementation of prevention plans targeting vulnerable subgroups, could potentially reduce the impact of heatwaves [19,20]. Currently, little is known about the factors driving these changes, but identifying them is crucial for better supporting vulnerable groups and managing future risks. Previous studies have proposed several possible explanations, such as improvements in healthcare, heightened awareness, and the adoption of adaptation strategies like air conditioning and early warning systems, but there is limited quantitative evidence to support these claims. Only a few studies have quantitatively linked changes in vulnerability to specific factors, such as the prevalence of air conditioning and other socio-economic factors [19,21].

The varied topography and the interplay of different geographical units (e.g., the Adriatic Sea, the Alps, and the Pannonian Plain) are reflected in the great spatial diversity of Slovenia's climate. Mountain, Mediterranean, and temperate continental climate types are thus intertwined in a relatively small area so that even in small areas, there is a wide range of climatic conditions.

In the central part of Slovenia, where valleys predominate among the hills, most people live in the Ljubljana basin.

There are large differences in the amount and distribution of precipitation. Due to the orographic effect, the amount of precipitation increases from the sea towards the interior of Slovenia, reaching a maximum at the Dinaric–Alpine barrier. A slightly smaller but noticeable maximum of precipitation also occurs in the Kamnik–Savinja Alps due to the effect of the uplift of air masses. Behind the Dinaric barrier to the northeast, precipitation decreases rapidly with distance from the sea and the orographic barrier.

Slovenia does not have a distinctly dry or wet part of the year, but significant differences exist between months or seasons. The sub-Mediterranean climate is characterized by two rainfall maxima: the first occurs in late spring, the second in autumn. The Alpine climate is characterized by a peak in autumn, with a slightly less pronounced maximum in late spring and early summer. In the east of the country, where the influence of the continental climate is pronounced, the highest rainfall occurs during summer showers and storms, with the driest months being in winter.

Temperatures tend to drop with altitude. The average annual temperature drops by 5.3 °C for every 1000 m. Not only altitude but also the slope and orientation of the terrain

have a major influence on temperature conditions. In closed valleys and basins, lakes of cold air with a temperature reversal often occur in the cold half, and the spatial distribution of temperature then differs considerably from the average. The spatial distribution of mean annual temperature follows the relief of Slovenia. The warmest temperatures are on the coast, in the Vipava Valley and in Brda.

It is also warmer in the rest of the Primorska region and in the lowlands of eastern Slovenia. The coldest temperatures are in the mountains, where the average annual temperature does not exceed 0 °C at the highest peaks. Temperature fluctuations are smallest in the Primorska region due to the influence of the sea and in the mountains, where we are already very close to a free atmosphere. The warmest area extends across the Vipava Valley and most of the Karst, and from the coast, it extends to the Karst rim. The second warmest thermal belt covers the whole eastern half of the country (except for the higher hills) and the Ljubljana basin.

The upward trend in average summer temperature is the highest of all seasons. All regions are experiencing an increase in both warm and hot days. The frequency of cold and icy days has decreased significantly throughout Slovenia, including in Primorska.

In summer, there is more sunshine in Primorska and the lowlands and basins because convection breaks out in the rugged mountainous terrain, resulting in more cloud cover. The opposite is true in the cold half of the year. Except for Primorska, the valleys receive less sunshine than the mountainous areas because fog or low clouds often linger in the valleys and valleys due to the occurrence of cold air lakes. There is also an increasing trend in the duration of solar irradiation.

In Slovenia, research has already been conducted on the short-term impact of heatwaves on mortality within certain vulnerable subgroups of the population [22]. International studies have primarily found an association between increased mortality and heatwaves due to cardiovascular, cerebrovascular, and respiratory diseases, particularly among the elderly [10].

The aim of this study was to assess the short-term association between heatwaves and the number of deaths for older adults (75 years and more), the most vulnerable population, in the period from 1999 to 2020 in Slovenia, to see whether any differences appeared after the increase in duration, frequency, and intensity of the heatwaves and more intense public health measures and inter-sectoral cooperation after the year 2015 in Slovenia.

2. Methods

2.1. Study Area

The Republic of Slovenia is a country located in Southern Central Europe, spanning 20,273 square kilometers (7827 sq. mi). Its population was 1,978,334 in 1999, 2,050,189 in 2011, and 2,108,977 in 2021 [23]. Slovenia experiences four major climate systems: the coastal climate in littoral Slovenia, the central climate in central Slovenia, a more continental climate in the northeastern region, and an alpine climate in the mountainous areas. The country's terrain, which is predominantly hilly except for the coastal region and the northwestern area dominated by the Alps, has a significant impact on its weather (Slovenian Environment Agency, Climate in Slovenia).

2.2. Time Period

In each observed year, independently from each other, we chose the period from May to September because this is the hottest part of the year in Slovenia. Analyses were conducted from 1999 to 2020 because in Slovenia, in 1999, the International Classification of Diseases (ICD)—9 changed to the ICD—10, which is still used today.

2.3. Number of Deaths Source

Data on all underlying causes of mortality, categorized by age group, diagnosis, and municipality, for the months of May through September from 1999 to 2020, were retrieved from the Mortality database of the National Institute of Public Health (NIPH), following the

International Classification of Diseases, Tenth Revision (ICD-10). Since the published data do not specify the time or location of death, making it impossible to identify individuals, we believe that Ethical Approval is not required.

2.4. Definition of Heatwave, Heatwave Deaths, and Reference Periods Deaths

To evaluate heat load, we employed pseudo-equivalent temperatures. We calculated the average from three weather monitoring stations representing Slovenia's different climate regions: littoral Slovenia, central Slovenia, and the more continental northeastern Slovenia [24]. Although the sample size is relatively small, several studies have shown that sample sizes need to be large enough to achieve statistical significance; some studies, including those initiated by an expert group under the World Meteorological Organization, recommend samples of at least one million [25]. Since Slovenia lacks cities of such scale, we used mortality data for the entire country. For consistency, we also aggregated the meteorological data [25].

Drawing from previous studies and the methodology used to compile the environmental indicators "Heatwaves and the daily number of deaths" within the indicator group "Human health and ecosystem resilience", we based our assessment on the average values from the three weather stations representing Slovenia's most populous climate regions: Bilje (Nova Gorica) in western Slovenia, Ljubljana in the central region, and Murska Sobota, located on the plains of northeastern Slovenia. The sparsely populated mountainous region, where heat stress is rare, was excluded from the analysis.

A heatwave was defined as a period of two or more consecutive days with a pseudo-equivalent daily temperature exceeding 56.0 °C. This temperature was calculated by summing the air temperature and the partial pressure of water vapor multiplied by 1.5 [26]. Temperature data were sourced from the Slovenian Environment Agency. The pseudo-equivalent temperature index, which accounts for the combined effects of air temperature and humidity on thermal discomfort in hot, humid conditions, has been used in Slovenia for several decades [26].

The heatwave periods in our study included all heatwaves that occurred between May 1 and September 30 during the years from 1999 to 2020 in Slovenia, as identified by previous meteorological analyses (Figure **??**).

The non-heatwave (reference) periods were defined in line with earlier studies [22,27]. We determined the length of the reference period, representing the number of days outside of heatwaves from May to September. For each year, the reference period matched the total number of heatwave days in that year. The reference days were selected using a consistent approach across all 22 years. Half of the reference period days were taken from the beginning of May (starting on May 1), while the other half were taken from the beginning of September (starting on September 1). If the total number of reference days was odd, an extra day was added to May. The number of deaths during the reference periods was calculated for each year separately and designated as A_0. Similarly, heatwave-related deaths were calculated for each year and labeled as A_1. Both heatwave deaths and reference period deaths were defined as any death recorded by ICD-10 during the respective periods.

The "lag" effect should be taken into account when determining the heatwave and reference periods. Previous studies suggest considering a lag period lasting from 0 to 3 days [28–30] or even longer. After descriptively analyzing several heatwaves, we chose not to include the days immediately following a heatwave in our heatwave periods. Therefore, for the heatwaves in our study, we defined the "lag" as 0 days.

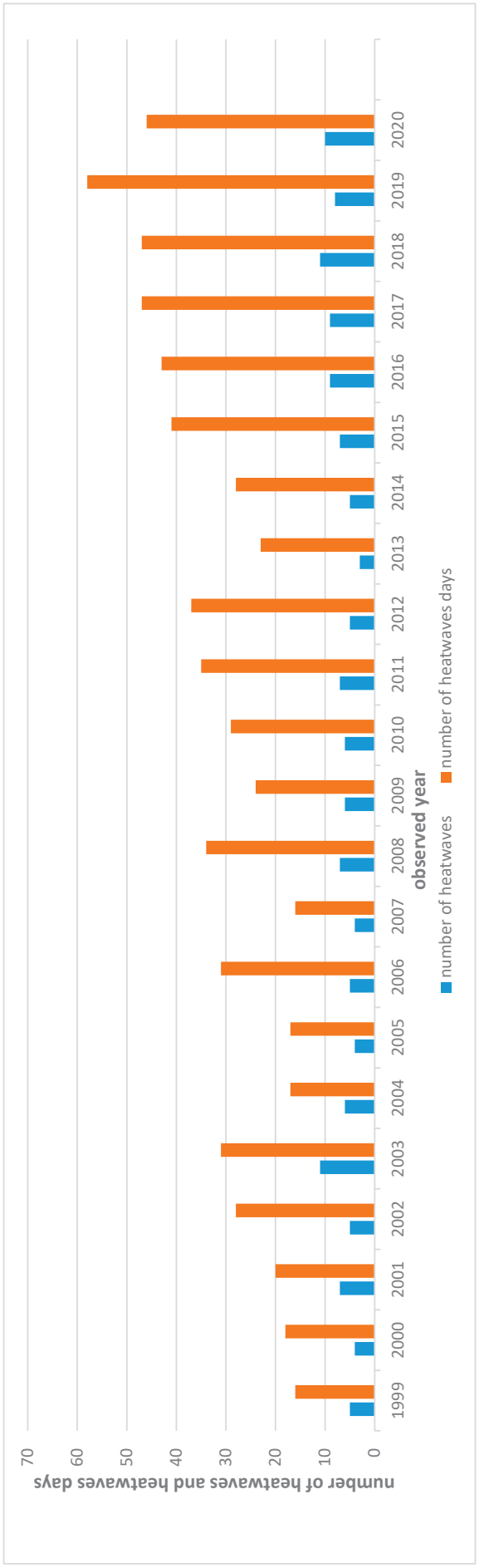

Figure 1. Number of heatwaves and number of days during heatwaves, from the year 1999 to 2020, in Slovenia.

2.5. Definitions of Subgroups

To examine the risks associated with different causes of death, we calculated the relative risks (RRs) and 95% confidence intervals (95% CI) for dying from all causes (ICD 10, A00-T98) for both the general population and old age population. We also calculated these risks for circulatory system diseases (ICD 10, I00-I99) and respiratory system diseases (ICD 10, J00-J99) specifically for those aged 75 and older.

Defining urban versus rural areas in Slovenia posed a challenge, as the country has only two cities with populations exceeding 100,000: Ljubljana, which is the capital, and Maribor. In our research, we categorized these two municipalities as urban areas, while the remaining fifty-six Slovenian municipalities were classified as rural. The analysis of rural versus urban areas was conducted specifically for the elderly population (aged 75 and older).

2.6. Statistical Analysis: Relative Risks, 95% Confidence Interval and Excess Deaths

All data were processed and analyzed using Microsoft Excel, version 2010 (Microsoft, Redmond, WA, USA). Following previous studies, we employed a simplified relative risk (RR) approach, comparing the number of deaths during heatwave periods with those during reference periods [22,27], separately for each observed year (1999–2020). We assumed, as in previous research [22,27], that the population size remained constant within each observed year. The RR was calculated to evaluate the impact of heatwaves by dividing the number of deaths during heatwave periods (A_1) by the number of deaths during reference periods (A_0), as shown in (Equation (1)).

$$RR = \frac{A_1}{A_0} \tag{1}$$

We calculated 95% confidence intervals (95% CI) for the RR using a simple approach for person–time incidence ratios (Equation (2)) [27]:

$$95\ \%\ CI = e^{lnRR \pm 1.96\ \sqrt{\frac{1}{A_1}+\frac{1}{A_0}}} \tag{2}$$

Statistically significant mortality increases during heatwaves belonged to the subgroups where the lower limit of the 95% CI was above or equal to 1.00.

Excess deaths were calculated from the RR in terms of percent (%). For example, if RR = 1.05, then 5% of excess deaths during heatwaves appeared in the observed year. On the contrary, if RR = 0.95, then 5% of decreased deaths during heatwaves appeared in the observed year.

3. Results

3.1. Analysis of Number of Deaths during Heatwaves for Each Year from 1999 to 2020

Analyses of the number of deaths during heatwaves were performed independently for each of the observed years. Most years showed no significant increase in deaths during heatwaves for both the general population and those aged 75 and older, regardless of diagnosis or urban/rural location. However, in 2006, 2007, 2014, and 2015, there was a significant increase in deaths during heatwaves (Table 1).

- For the general population, heatwaves were associated with an increase in deaths due to all causes: 10% (95% CI: 0–21%) more in 2006; 26% more in both 2007 (95% CI: 12–42%) and 2014 (95% CI: 14–40%).
- For those aged 75 and older, heatwaves were associated with an increase in deaths due to all causes: 22% more (95% CI: 4–44%) in 2007, 27% more (95% CI: 12–43%) in 2014, and 28% more (95% CI: 15–41%) in 2015.
- For those aged 75 and older, heatwaves were associated with an increase in deaths due to circulatory system diseases: 25% more (95% CI: 5–48%) in 2006, 33% more (95% CI: 6–67%) in 2007, 30% more (95% CI: 1–55%) in 2014, and 27% more (95% CI: 1–48%) in 2015.

Regarding urban vs. rural areas, in 2006 and 2012, the elderly population in urban areas was more affected, with 33% (95% CI: 2–72%) and 26% (95% CI: 1–57%) more deaths, respectively. In contrast, in 2007, 2014, and 2015, the elderly population in rural areas was more affected, with 29% (95% CI: 13–47%), 26% (95% CI: 9–45%), and 31% (95% CI: 16–47%) more deaths, respectively.

In Figure **??**, excess deaths due to all causes and circulatory system diseases for the elderly population (75+ years old) during heatwaves in Slovenia in the past 22 years (1999–2020) are shown. Additionally, in Figure **??**, heatwave duration in days and the number of heatwaves over the 22 years in Slovenia are also shown.

3.2. Reports for Air Pollution in Slovenia for the Observed Years (2006, 2007, 2014, 2015)

Slovenia is one of the countries with the highest PM10 levels in Europe. PM10 emissions per capita and per land area are also among the highest in the European Union. High emissions are due to the widespread use of wood for domestic heating in technically outdated stoves and boilers. Low-wind conditions and pronounced long-lasting temperature inversions are frequent in the colder part of the year in basins and valleys across continental Slovenia. These unfavorable meteorological conditions significantly contribute to elevated PM10 levels. In the last five years, PM10 levels at most urban monitoring stations exceeded the allowed number of exceedances in continental Slovenia. However, there were fewer exceedances in the Primorska region (Mediterranean part of Slovenia), where low wind and stable atmospheric conditions are much less frequent. Levels during winter are much higher than in the warmer part of the year also because of wood combustion in domestic heating appliances. After 2008, the yearly limit value for PM10 was exceeded only at the monitoring site Ljubljana Centre, which is under the direct influence of traffic. Due to lower PM levels in the warmer part of the year, the yearly limit value for PM2.5 has never been exceeded at any of the monitoring sites [31].

Ozone pollution is predominantly a regional issue. In Slovenia, ozone pollution is characterized by the pronounced influence of trans-boundary pollution, which classifies Slovenia as one of the most ozone-affected countries in Europe. The maximum daily eight-hour mean value for the protection of human health was exceeded at most monitoring sites. Lower concentrations were measured at the sites, which are under the direct influence of traffic. The highest concentrations were measured in the Primorska region, which is significantly influenced by trans-boundary pollution. The highest yearly average concentrations were measured at high-altitude monitoring sites (e.g., Krvavec) [31].

As the mortality rate for older people during heatwaves increased in 2006, 2007, 2014, and 2015, we checked the air pollution reports for the observed years in Slovenia. We wondered whether air pollution was higher in the observed years than in other years, which is a factor that can also contribute to increased mortality.

Ambient air in Slovenia in 2006 and in 2007 was—as in recent years—overly polluted with PM10 particles with the highest concentrations at urban sites, which are influenced by emissions from traffic (Maribor) and also local industry (cities of Zasavje region). The allowed annual number of exceedances of the daily limit value was exceeded at all urban monitoring stations in 2006 and 2007—most notably in Maribor and Zasavje—while in rural monitoring stations, it was exceeded in Rakičan near Murska Sobota. In 2006 and 2007, ozone concentrations exceeded the limit values in all places except the typical traffic sites (Maribor, Zagorje). As in previous years, the most polluted regions with ozone were the coastal and Primorska regions (Otlica, Nova Gorica, Koper). The alert threshold for ozone was exceeded once in Otlica [31].

Table 1. Relative risks (RR) for number of deaths during heatwaves and 95% confidence interval (CI) due to diagnosis, urban/rural area, for age group 75+ years, from 1999 to 2020 in Slovenia.

	1999	**2000**	**2001**	**2002**	**2003**
Underlying Cause of Death (ICD-10 code)	**RR (95% CI)**	**RR (95% CI)**	**RR (95% CI)**	**RR (95% CI)**	**RR (95% CI)**
ALL, all causes (A00-T98)	0.96 (0.85–1.08)	1.06 (0.94–1.19)	1.09 (0.97–1.21)	1.04 (0.95–1.14)	1.03 (0.94–1.12)
ALL, all causes, age group 75+ years (A00-T98)	0.91 (0.76–1.09)	1.14 (0.96–1.36)	1.09 (0.93–1.28)	1.04 (0.94–1.18)	1.02 (0.92–1.16)
ALL, circulatory diseases, age group 75+ years (I00-I99)	0.8 (0.63–1.02)	1.17 (0.92–1.49)	1.19 (0.94–1.51)	1.09 (0.9–1.32)	0.89 (0.47–1.06)
ALL, respiratory diseases, age group 75+ years (J00-J99)	1.2 (0.69–2.3)	1.03 (0.54–1.96)	0.90 (0.53–1.53)	1.05 (0.66–1.69)	0.98 (0.65–1.48)
ALL, urban area, age group 75+ years (A00-T98)	1.04 (0.63–1.74)	1.04 (0.72–1.49)	1.18 (0.85–1.65)	1.08 (0.82–1.42)	1.11 (0.86–1.43)
ALL, rural area, age group 75+ years (A00-T98)	0.85 (0.71–1.03)	1.16 (0.95–1.41)	1.07 (0.89–1.28)	1.03 (0.89–1.19)	1.00 (0.87–1.15)
	2004	**2005**	**2006**	**2007**	**2008**
Underlying Cause of Death (ICD-10 code)	**RR (95% CI)**	**RR (95% CI)**	**RR (95% CI)**	**RR (95% CI)**	**RR (95% CI)**
ALL, all causes (A00-T98)	1.03 (0.91–1.16)	1.01 (0.9–1.14)	1.10 (1.00–1.21)	1.26 (1.12–1.42)	1.02 (0.93–1.11)
ALL, all causes, age group 75+ years (A00-T98)	1.01 (0.86–1.19)	0.98 (0.84–1.15)	1.07 (0.95–1.21)	1.22 (1.04–1.44)	1.01 (0.90–1.13)
ALL, circulatory diseases, age group 75+ years (I00-I99)	1.05 (0.81–1.33)	1.08 (0.85–1.35)	1.25 (1.05–1.48)	1.33 (1.06–1.67)	0.99 (0.84–1.16)
ALL, respiratory diseases, age group 75+ years (J00-J99)	1.10 (0.64–1.88)	1.29 (0.71–2.31)	1.13 (0.79–1.69)	1 (0.52–2.07)	0.95 (0.65–1.38)
ALL, urban area, age group 75+ years (A00-T98)	1.18 (0.84–1.66)	1.06 (0.77–1.47)	1.33 (1.02–1.72)	1.07 (0.77–1.49)	0.98 (0.78–1.23)
ALL, rural area, age group 75+ years (A00-T98)	0.94 (0.78–1.13)	0.94 (0.79–1.13)	1.09 (0.95–1.26)	1.29 (1.13–1.47)	1.02 (0.90–1.16)
	2009	**2010**	**2011**	**2012**	**2013**
Underlying Cause of Death (ICD-10 code)	**RR (95% CI)**	**RR (95% CI)**	**RR (95% CI)**	**RR (95% CI)**	**RR (95% CI)**
ALL, all causes (A00-T98)	1.01 (0.91–1.11)	1.05 (0.96–1.14)	1.01 (0.93–1.09)	1.03 (0.95–1.11)	
ALL, all causes, age group 75+ years (A00-T98)	0.96 (0.84–1.1)	1.03 (0.91–1.15)	1.03 (0.93–1.15)	1.07 (0.96–1.19)	0.96 (0.86–1.09)
ALL, circulatory diseases, age group 75+ years (I00-I99)	1.04 (0.85–1.26)	0.97 (0.87–1.15)	1.01 (0.87–1.18)	1.07 (0.92–1.24)	0.99 (0.83–1.17)
ALL, respiratory diseases, age group 75+ years (J00-J99)	0.86 (0.52–1.40)	1.27 (0.84–1.93)	0.84 (0.57–1.23)	0.81 (0.56–1.17)	1.23 (0.79–1.91)
ALL, urban area, age group 75+ years (A00-T98)	1.17 (0.89–1.53)	1.25 (0.98–1.60)	1.02 (0.82–1.28)	1.26 (1.01–1.57)	1.04 (0.84–1.27)
ALL, rural area, age group 75+ years (A00-T98)	0.90 (0.77–1.05)	0.96 (0.84–1.1)	1.03 (0.92–1.16)	1.02 (0.9–1.14)	0.93 (0.8–1.07)

Table 1. *Cont.*

	2014	2015	2016	2017	2018
Underlying Cause of Death (ICD-10 code)	**RR (95% CI)**	**RR (95% CI)**	**RR (95% CI)**	**RR (95% CI)**	**RR (95% CI)**
ALL, all causes (A00-T98)	1.26 (1.14–1.40)	1.07 (0.99–1.16)	0.99 (0.91–1.06)	1.01 (0.94–1.09)	1.01 (0.92–1.08)
ALL, all causes, age group 75+ years (A00-T98)	1.27 (1.12–1.43)	1.28 (1.15–1.41)	1.07 (9.96–1.19)	0.98 (0.90–1.06)	0.99 (0.89–1.09)
ALL, circulatory diseases, age group 75+ years (I00-I99)	1.3 (1.1–1.55)	1.27 (1.1–1.48)	1.02 (0.87–1.18)	0.97 (0.86–1.11)	1.02 (0.85–1.21)
ALL, respiratory diseases, age group 75+ years (J00-J99)	1.03 (0.65–1.63)	1.08 (0.75–1.55)	0.83 (0.55–1.23)	0.98 (0.67–1.44)	0.97 (0.58–1.63)
ALL, urban area, age group 75+ years (A00-T98)	1.29 (0.99–1.68)	1.17 (0.95–1.45)	1.14 (0.92–1.43)	0.98 (0.87–1.11)	1.10 (0.90–1.36)
ALL, rural area, age group 75+ years (A00-T98)	1.26 (1.09–1.45)	1.31 (1.16–1.47)	1.05 (0.93–1.18)	0.97 (0.86–1.1)	1.05 (0.90–1.23)
	2019	**2020**			
Underlying Cause of Death (ICD-10 code)	**RR (95% CI)**	**RR (95% CI)**			
ALL, all causes (A00-T98)	1 (0.94–1.06)	1.06 (0.99–1.13)			
ALL, all causes, age group 75+ years (A00-T98)	0.96 (0.87–1.03)	1.03 (0.95–1.12)			
ALL, circulatory diseases, age group 75+ years (I00-I99)	0.89 (0.80–1.00)	1.05 (0.93–1.2)			
ALL, respiratory diseases, age group 75+ years (J00-J99)	0.88 (0.79–1.01)	1.02 (0.68–1.55)			
ALL, urban area, age group 75+ years (A00-T98)	1.08 (0.92–1.28)	0.98 (0.83–1.17)			
ALL, rural area, age group 75+ years (A00-T98)	1.03 (0.92–1.16)	1.04 (0.95–1.15)			

Legend: ALL—both sexes; —statistically significant association.

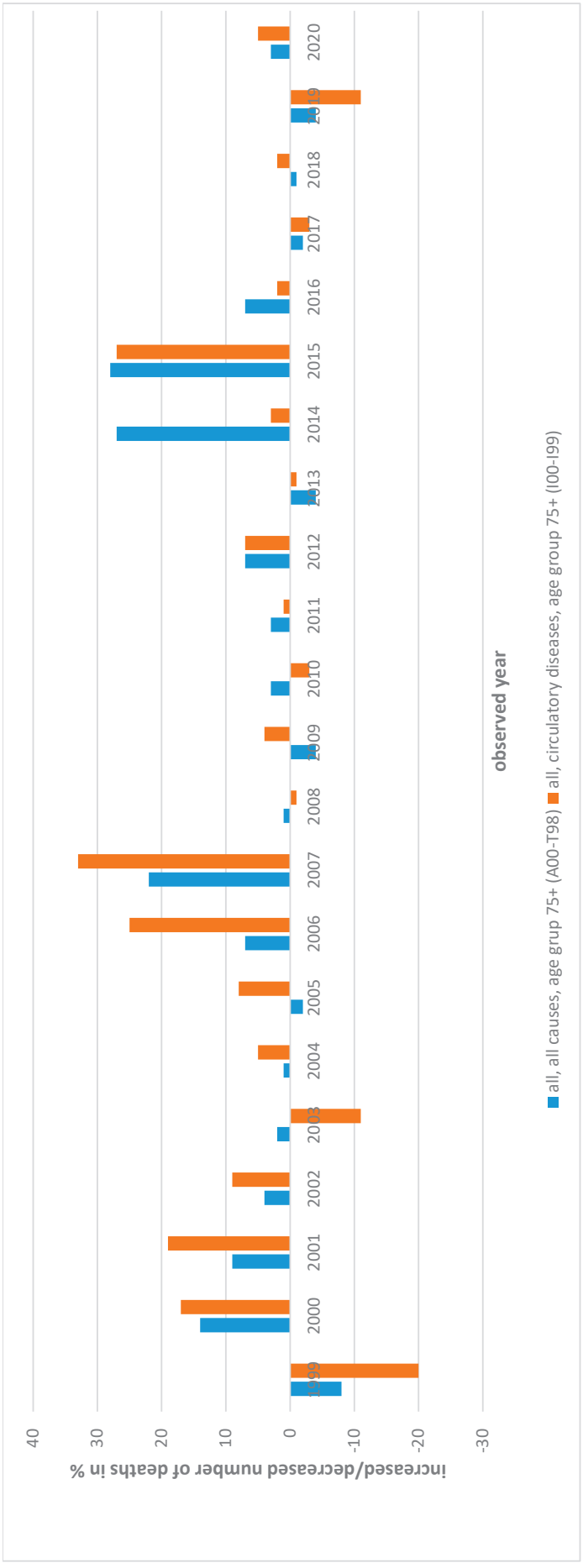

Figure 2. Increased/decreased number of deaths, in %, due to all causes and due to the circulatory system causes, for the age group 75+ years from 1999 to 2020 in Slovenia.

PM10 levels in 2014 were lower than in the previous years. This is attributed mainly to favorable meteorological conditions. The number of days that exceeded the daily limit value was higher than the allowed 35 only at Ljubljana Centre, Zagorje, and two monitoring sites in Celje. The first year when the yearly limit value was not exceeded at any monitoring site was 2014. The yearly limit value for PM2.5 was not exceeded either [31]. In 2014, ozone levels were lower than in the previous years. The first year without exceedances of the information threshold since the beginning of measurements in Slovenia was 2014. The allowed number of exceedances of the maximum daily eight-hour mean value was exceeded only in the Primorska region, which belongs to the Mediterranean part of Slovenia, and at elevated monitoring sites [31].

In 2015, the PM10 levels were slightly higher than in 2014. This could be mainly attributed to the less favorable meteorological conditions. More than 35 exceedances of the daily limit value were measured at the monitoring sites Ljubljana Center, Celje AMP Gaji, Celje, Zagorje, Trbovlje, Murska Sobota Rakičan, Ljubljana Bežigrad, and Novo mesto. In 2015, as well as in 2014, there were no exceptions to the yearly PM10 limit value recorded on any of the measuring sites. Similarly, the yearly limit value for PM2.5 was not exceeded anywhere. In general, a decreasing trend of PM levels was observed after 2002, although there are significant yearly variations due to different meteorological conditions in each year. The decrease in PM levels is attributed mainly to a decrease in industrial emissions [31]. In 2015, levels of ozone pollution were slightly higher than in 2014 [31].

4. Discussion

Slovenia experiences extreme weather events annually, with heatwaves during the summer classified as such events, potentially leading to increased mortality. When interpreting our conclusions about heatwaves in Slovenia, it is crucial to recognize that the findings are highly influenced by the definition of heatwaves, which lacks a universally accepted standard.

The elderly group is the most vulnerable during heatwaves due to reduced body temperature regulation that comes with aging [32,33]. Additionally, this group often suffers from chronic medical conditions like heart disease and chronic obstructive pulmonary disease (COPD) [34]. Therefore, the combined risks of age and co-morbidities heighten their susceptibility to heat-related illnesses.

Some previous foreign studies assessed increased mortality during heatwaves for the elderly population. A study in Brisbane (Australia) found increased mortality due to all causes for the elderly (60+ years old) in time series analysis from 2010 to 2019 [35]. In Iran, a study was conducted in the southwestern city of Dezful, which found that during the years 2013 to 2019, mortality for those over 75 years old significantly increased [36]. Regarding risk factors associated with heatwave mortality for those over 65 years old, a Chinese study conducted from 2008 to 2018 assessed that functional aging is an underlying factor in enhancing heatwave resilience in the elderly population [37]. The findings of the literature review by Liu and co-workers indicate that underlying regional climate conditions need to be accounted for when assessing the risk of heat-related cardiovascular disease-related mortality, as well as the characteristics of the population and disease subgroups. Increasing temperatures, in conjunction with an increase in the proportion of older people in the population, might result in a rise in poor cardiovascular health outcomes associated with climate change [38]. In England, a study by Thompson and co-workers assessed mortality during heatwaves in the year 2020. Significant excess mortality was observed for cardiovascular disease, respiratory disease, Alzheimer's, and Dementia across all three heatwaves, which appeared in 2020 in persons aged 65+ years. There was no evidence that the heatwaves affected the proportional increase in people dying at home and not seeking heat-related health care [39].

In our study, in most of the observed years, there were no statistically significant excess deaths during heatwaves for all populations or for those 75+ years old according to diagnosis and urban/rural areas. However, in 2006, 2007, 2014, and 2015, the association

between heatwaves and the number of deaths showed that older people die more, mainly because of cardiovascular diseases. These findings align with previous research on mortality during heatwaves [40–42]. However, during these years, including 2012, older adults in both urban and rural areas were equally affected. Earlier studies have generally indicated a higher risk of heatwave-related mortality in urban areas, attributing this to the urban heat island effect [43–45], which is often considered the primary factor [46,47]. Conversely, other studies have shown that heat-related mortality risk was actually higher in rural areas than in urban ones [48,49], suggesting that lower levels of non-climatic factors—such as air conditioner availability, education, healthcare infrastructure, and the aging population in rural areas—contribute to the increased risk in rural regions [47,49]. As far as air pollution is concerned, in the observed years 2006, 2007, 2014, and 2015, when mortality for older adults increased, we found no higher levels of PM and ozone than in other observed years [31].

Some findings from our study differ from other reported research on mortality during extreme heat. Unlike many previous studies [50,51], we did not find statistically significant evidence of an increase in deaths among older adults due to respiratory diseases during heatwaves. Additionally, some of our results showed no significant association between heatwaves and mortality, especially in the most recent years, beginning in 2015. Despite increased summer heat stress, the number of heatwave-related deaths among the elderly in Slovenia did not rise. The underlying factors behind this phenomenon remain unclear. While past studies have suggested possible reasons, such as improvements in healthcare, heightened awareness, and the adoption of adaptive measures like air conditioning and early warning systems, the evidence is still limited [20,23].

On the other hand, Slovenia has implemented more extensive public health interventions since 2015: (i) Heatwaves are now recognized as hazardous weather events, with the National Weather Service issuing warnings since 2011, which were enhanced in 2016 with special alerts for vulnerable populations. (ii) Several mass-media campaigns have been launched to inform the public, particularly older adults and those with circulatory diseases, about preventive measures during heatwaves through internet publications, TV, radio, and newspapers. (iii) Primary care centers are also actively addressing the issue, warning chronically ill patients—such as those on antihypertensive medications or with mental health conditions—of the potential complications related to their medication use during heatwaves. Public health efforts specifically focus on the vulnerable subgroups (older adults, children, pregnant women, chronically ill individuals). Our massages are short and easy to understand and consider physiological as well as socio-economic factors:

Take care of old-age individuals (identify lonely elderly individuals).

Use air conditioning in your home, if possible.

Drink water (take care of the old age individuals; make sure they drink water even if they are not thirsty).

Do not drink alcohol, sweet drinks, or coffee.

Avoid big cities; go to nature or public places with air conditioning, such as libraries and shopping centers.

Dress in light clothes and protect your head with hats.

In case of polypharmacy, contact your personal doctor.

We recommend being physically active early in the morning or late in the afternoon.

Use the freely available drinking water in the fountains to freshen yourself in the big cities.

The vulnerability of older adults is associated with both physiological and social factors [9,10], and this issue may worsen in the future. In 2022, people aged 65 and over made up 21.1% of Slovenia's population, a figure projected to rise to 30.9% by 2060 [13]. Despite a considerable decline in recent decades, circulatory system diseases continue to be the leading cause of death in Slovenia, responsible for 38% of all deaths in 2019 (45% in women and 31% in men) [52]. More women than men succumbed to circulatory system diseases in 2019, with the highest number of deaths occurring among those aged 75 and above in both sexes. In women, these deaths were mainly due to cerebrovascular diseases, whereas in men, ischemic heart disease was the more frequent cause. Among those under

75, more men than women died from circulatory system diseases [53]. The most frequent reasons for outpatient visits at both specialist and primary care levels include hypertensive diseases, peripheral vascular diseases, and cardiac arrhythmias [52]. Elevated cholesterol and triglyceride levels, commonly associated with aging, along with hypertension, are key contributors to atherosclerosis [53]. Atherosclerosis, particularly when combined with hypertension, is the primary factor leading to acute coronary syndrome, cerebral stroke, chronic kidney diseases, and heart failure [53]. Risk factors linked to hypertension include high cholesterol, obesity, high salt intake, alcohol consumption, and low physical activity. The accelerated rise in peripheral resistance caused by hypertension, resulting from vascular smooth muscle hypertrophy [54] and vascular rarefaction [55], impairs core temperature regulation due to reduced control of blood flow in the skin [56]. These effects can be further aggravated by medications, such as certain psychotropic and cardiovascular drugs, that affect thermoregulatory capacity [57].

Physiological cardiovascular issues in older adults make them particularly vulnerable during heatwaves. Older individuals struggle more to regulate their body temperature through vasodilation and sweating when temperatures rise [58]. Existing heart conditions in the elderly hinder their ability to effectively increase cardiac output, resulting in insufficient blood flow to the skin during elevated core temperatures [59]. Additionally, older adults are more susceptible to dehydration, which further strains the heart and other organs [60,61]. The combined impact of dehydration-induced hemoconcentration and pulmonary inflammation (as discussed later) can lead to acute coronary syndrome and cerebral stroke [62]. Severe health outcomes related to excessive heat, such as heat syncope, heat exhaustion, heat cramps, and heat stroke [63], are well-documented. When core temperatures exceed 40 °C, and the body cannot cool itself through vasodilation and sweating, it can result in multi-organ dysfunction syndrome [64].

As people age, their lungs undergo physiological changes that can impair ventilation even in the absence of disease, and these changes are coupled with a weakened immune system [65]. During heatwaves, poor outdoor air quality exacerbates these lung functions, with elevated ground-level ozone being a major contributor. This ozone causes local inflammation that can become systemic [66]. In Slovenia, the western regions are particularly exposed to high ozone levels. Additionally, older adults are more vulnerable to infections and pathogens [67]. Heatwaves often lead to an increase in vector-borne, water-borne, and food-borne diseases [65]. The combination of respiratory infections or inflammation due to poor air quality can also accelerate the development of atherosclerotic plaques [67]. Air pollution-induced inflammation in the respiratory tract can enhance coagulation through various mechanisms [67], which, coupled with impaired cardiovascular responses, increases the risk of thrombotic events [65,68]. Furthermore, inflammation and infection can worsen chronic obstructive pulmonary disease (COPD) and asthma, conditions that are common among the elderly [69]. In Slovenia, 16% of adults had asthma in 2010 [70], and COPD affects just over 10% of the population [71], both conditions associated with high morbidity and mortality.

In our study, we did not analyze the particularly vulnerable old population subgroups or diagnoses within the old population, such as mental illnesses (because of small daily observed outcome—deaths), diseases that are transmitted through food and water (because these causes increase primarily morbidity, less mortality), other diseases that are associated with higher mortality for older people during heatwaves (endocrine diseases, diseases of the kidney, diseases of the digestive system—again because of small daily outcome—deaths), and socio-economical vulnerability (because it would be necessary to analyze individual parameters such as, e.g., social isolation, loneliness, air conditioning, education, etc., and this goes beyond analysis in the present article).

Limitations and Strengths of the Study

We acknowledge that our study has several limitations. The analysis is based on a very small number of daily deaths due to Slovenia's small population, and as shown in

Table 1, the confidence intervals for some statistical subgroups are quite broad, making the results speculative and incomplete. Additionally, because of the limited number of daily deaths, we could only analyze a few variables without considering other major diagnoses associated with increased mortality during heatwaves among older adults. Furthermore, the study only recorded the underlying causes of death, leaving out potential contributions from other diseases, injuries, conditions, or events. We also did not account for confounding factors that could affect death rates during the summer, such as summer smog, other outdoor air pollutants, indoor living conditions, and socio-economic status.

The strengths of our study are that the results most likely indirectly show that with public health measures and inter-sectoral cooperation, we might improve people's awareness and help them behave more safely during days of high heat. For now, little is known about the factors that contribute to stabilization in mortality of older people age population during heatwaves despite increased heat load in the last observed summers. Further studies should focus on a better assessment of public health interventions and impact of each individual intervention.

In future analyses, we will use a new heatwave definition (the Australian one) [72], which is more common internationally. Due to the small observed sample, we intend to extend our analysis using the Poisson regression model and conduct an analysis for each climate region separately.

5. Conclusions

Our findings suggest that, overall, older people in Slovenia did not experience more deaths during heatwaves, especially in recent years. The number of deaths increased only in a few years (2006, 2007, 2012, 2014, and 2015) and was mainly due to circulatory system causes in both urban and rural areas. Mortality related to circulatory system issues in older adults, especially during extreme heat events, should be addressed with targeted prevention strategies due to its potentially severe consequences. The discussion highlights that physiological adaptation, demographic factors, and socio-economic conditions all play distinct roles in influencing the population's vulnerability to heatwaves. When evaluating future health risks in the context of projected climate change, it is essential to consider the potential effects of these factors.

Author Contributions: Conceptualization, S.P., K.B., M.P., A.U., T.C. and A.H., data curation, S.P., A.H. and T.C.; formal analysis, S.P. and T.C.; investigation, S.P., K.B., M.P., A.U. and A.H.; methodology, S.P. and T.C., administration, K.B. and A.U.; resources, S.P. and T.C.; supervision, S.P. and A.H.; validation, K.B., M.P., A.U. and T.C.; visualization, S.P.; writing—original draft preparation, S.P., K.B., M.P., A.U., T.C. and A.H.; writing—review and editing, S.P., K.B. and A.H. All authors have read and agreed to the published version of the manuscript.

Funding: This document was prepared as part of the Pharaon project, which received funding from the European Union's Horizon 2020 Research and Innovation Programme under Grant Agreement No. 857188.

Institutional Review Board Statement: It is impossible to identify the individual in the published data in the paper as the data are not specified for time or area of death. Therefore, we do not consider Ethical Approval to be necessary.

Informed Consent Statement: Not applicable.

Data Availability Statement: Data are available at a reasonoble request.

Conflicts of Interest: The authors declare no conflicts of interest.

References

1. Perkins-Kirkpatrick, S.E.; Lewis, S.C. Increasing trends in regional heatwaves. *Nat. Commun.* **2020**, *11*, 3357. [CrossRef] [PubMed]
2. IPCC. *Climate Change 2021: The Physical Science Basis*; Masson-Delmotte, V., Zhai, P., Pirani, A., Connors, S.L., Péan, C., Chen, Y., Goldfarb, L., Gomis, M.I., Matthews, J.B.R., Berger, S., et al., Eds.; Cambridge University Press: Cambridge, UK, 2021.
3. Berkeley Earth. Available online: https://berkeleyearth.org/ (accessed on 29 October 2023).

4. Martínez-Solanas, È.; Quijal-Zamorano, M.; Achebak, H.; Petrova, D.; Robine, J.M.; Herrmann, F.R.; Rodó, X.; Ballester, J. Projections of temperature-attributable mortality in Europe: A time series analysis of 147 contiguous regions in 16 countries. *Lancet Planet Health* **2021**, *5*, e446–e454. [CrossRef] [PubMed]
5. Ocena Podnebnih Sprememb v Sloveniji do Konca 21. Stoletja. Available online: https://meteo.arso.gov.si/uploads/probase/www/climate/text/sl/publications/OPS21_Porocilo.pdf (accessed on 23 October 2023).
6. European Environment Agency. *Climate Change, Impacts and Vulnerability in Europe 2012*; EEA Report No 12/2012; EEA: Kebnhaven, Denmark, 2012.
7. Fouillet, A.; Rey, G.; Wagner, V.; Laaidi, K.; Empereur-Bissonnet, P.; Le Tertre, A.; Frayssinet, P.; Bessemoulin, P.; Laurent, F.; De Crouy-Chanel, P.; et al. Has the impact of heat waves on mortality changed in France since the European heat wave of summer 2003? A study of the 2006 heat wave. *Int. J. Epidemiol.* **2008**, *37*, 309–317. [CrossRef]
8. Casanueva, A.; Burgstall, A.; Kotlarski, S.; Messeri, A.; Morabito, M.; Flouris, A.D.; Nybo, L.; Spirig, C.; Schwierz, C. Overview of Existing Heat-Health Warning Systems in Europe. *Int. J. Environ. Res. Public Health* **2019**, *16*, 2657. [CrossRef] [PubMed]
9. Åström, D.O.; Forsberg, B.; Rocklöv, J. Heat wave impact on morbidity and mortality in the elderly population: A review of recent studies. *Maturitas* **2011**, *69*, 99–105. [CrossRef]
10. Kenney, W.L.; Munce, T.A. Invited review: Aging and human temperature regulation. *J. Appl. Physiol. (1985)* **2003**, *95*, 2598–2603. [CrossRef]
11. Sommet, A.; Durrieu, G.; Lapeyre-Mestre, M.; Montastruc, J.L.; Association of French PharmacoVigilance Centres. A comparative study of adverse drug reactions during two heat waves that occurred in France in 2003 and 2006. *Pharmacoepidemiol. Drug Saf.* **2012**, *21*, 285–288. [CrossRef]
12. United Nation. *World Population Ageing 2013 ST/ESA/SER.A/348*; Department of Economic and Social Affairs, Population Division: New York, NY, USA, 2013.
13. Statistical Office of the Republic of Slovenia. EUROPOP2023 Population Projections-Demographic Balances and Selected Indicators, Slovenia, 2022–2100. Available online: https://pxweb.stat.si/SiStatData/pxweb/sl/Data/Data/05U3019S.px/ (accessed on 27 October 2023).
14. Linares, C.; Mirón, I.J.; Montero, J.C.; Criado-Álvarez, J.J.; Tobías, A.; Díaz, J. The time trend temperature-mortality as a factor of uncertainty analysis of impacts of future heat waves. *Environ. Health Perspect.* **2014**, *122*, A118. [CrossRef]
15. Martinez, G.S.; Baccini, M.; De Ridder, K.; Hooyberghs, H.; Lefebvre, W.; Kendrovski, V.; Scott, K.; Spasenovska, M. Projected heat-related mortality under climate change in the metropolitan area of Skopje. *BMC Public Health* **2016**, *16*, 407. [CrossRef]
16. Wu, J.; Zhou, Y.; Gao, Y.; Fu, J.S.; Johnson, B.A.; Huang, C.; Kim, Y.M.; Liu, Y. Estimation and uncertainty analysis of impacts of future heat waves on mortality in the eastern United States. *Environ. Health Perspect.* **2014**, *122*, 10–16. [CrossRef]
17. Peng, R.D.; Bobb, J.F.; Tebaldi, C.; McDaniel, L.; Bell, M.L.; Dominici, F. Toward a quantitative estimate of future heat wave mortality under global climate change. *Environ. Health Perspect.* **2011**, *119*, 701–706. [CrossRef]
18. Roldán, E.; Gómez, M.; Pino, M.R.; Pórtoles, J.; Linares, C.; Díaz, J. The effect of climate-change-related heat waves on mortality in Spain: Uncertainties in health on a local scale. *Stoch. Environ. Res. Risk A* **2016**, *30*, 831–839. [CrossRef]
19. Bobb, J.F.; Peng, R.D.; Bell, M.L.; Dominici, F. Heat-related mortality and adaptation to heat in the United States. *Environ. Health Perspect.* **2014**, *122*, 811–816. [CrossRef] [PubMed]
20. Díaz, J.; Carmona, R.; Mirón, I.J.; Ortiz, C.; Linares, C. Comparison of the effects of extreme temperatures on daily mortality in Madrid (Spain), by age group: The need for a cold wave prevention plan. *Environ. Res.* **2015**, *143 Pt A*, 186–191. [CrossRef]
21. Ng, C.F.S.; Boeckmann, M.; Ueda, K.; Zeeb, H.; Nitta, H.; Watanabe, C.; Honda, Y. Heat-related mortality: Effect modification and adaptation in Japan from 1972 to 2010. *Glob. Environ. Change* **2014**, *9*, 234–243. [CrossRef]
22. Perčič, S.; Kukec, A.; Cegnar, T.; Hojs, A. Number of Heat Wave Deaths by Diagnosis, Sex, Age Groups, and Area, in Slovenia, 2015 vs. 2003. *Int. J. Environ. Res. Public Health* **2018**, *15*, 173. [CrossRef]
23. Republic of Slovenia Statistical Office. Population of Slovenia. Available online: https://www.google.com/search?sxsrf=ACYBGNTJ6IA1Lb1L92EqTGYAVmhU2HdxgA:1571495426941&source=hp&ei=Ah6rXar6NuuXmwXdxYS4AQ&q=prebivalstvo+slovenije&oq=prebivastvo&gs_l=psy-ab.1.0.0i13l10.2340055.2346463.2348400...0.0..0.304.1473.8j2j1j1.....0....1..gws-wiz.....10..35i362i39j35i39j0j0i10j0i203.XYQvALUynys#spf=1571497774642 (accessed on 18 October 2023).
24. Slovenian Environment Agency (ARSO). National Meteorological Service of Slovenia. Available online: http://meteo.arso.gov.si/met/en/climate/ (accessed on 23 October 2023).
25. Michelozzi, P.; Kirchmayer, U.; Katsouyanni, K.; Biggeri, A.; McGregor, G.; Menne, B.; Kassomenos, P.; Anderson, H.R.; Baccini, M.; Accetta, G.; et al. Assessment and prevention of acute health effects of weather conditions in Europe, the PHEWE project: Background, objectives, design. *Environ. Health* **2007**, *6*, 12. [CrossRef]
26. Vida, M. *Medicinska Meteorologija*; Medicinska Fakulteta: Ljubljana, Slovenia, 1990.
27. Joe, L.; Hoshiko, S.; Dobraca, D.; Jackson, R.; Smorodinsky, S.; Smith, D.; Harnly, M. Mortality during a Large-Scale Heat Wave by Place, Demographic Group, Internal and External Causes of Death, and Building Climate Zone. *Int. J. Environ. Res. Public Health* **2016**, *13*, 299. [CrossRef] [PubMed]
28. Anderson, B.G.; Bell, M.L. Weather-related mortality: How heat, cold, and heat waves affect mortality in the United States. *Epidemiology* **2009**, *20*, 205–213. [CrossRef]
29. Bao, J.; Wang, Z.; Yu, C.; Li, X. The influence of temperature on mortality and its Lag effect: A study in four Chinese cities with different latitudes. *BMC Public Health* **2016**, *16*, 375. [CrossRef]

30. Baccini, M.; Kosatsky, T.; Analitis, A.; Anderson, H.R.; D'Ovidio, M.; Menne, B.; Michelozzi, P.; Biggeri, A.; PHEWE Collaborative Group. Impact of heat on mortality in 15 European cities: Attributable deaths under different weather scenarios. *J. Epidemiol. Community Health* **2011**, *65*, 64–70. [CrossRef] [PubMed]
31. Slovenian Environment Agency. Air Qality–Yearly Reports. Available online: http://rte.arso.gov.si/zrak/kakovost%20zraka/poro%C4%8Dila%20in%20publikacije/kakovost_letna.html (accessed on 9 September 2024).
32. Van Someren, E.J. More than a marker: Interaction between the circadian regulation of temperature and sleep, age-related changes, and treatment possibilities. *Chronobiol. Int.* **2000**, *17*, 313–354. [CrossRef]
33. Son, J.; Liu, J.C.; Bell, M.L. Temperature-related mortality: A systematic review and investigation of effect modifiers. *Environ. Res. Lett.* **2019**, *14*, 073004. [CrossRef]
34. Sherina, M.S.; Rampal, L.; Mustaqim, A. Factors associated with chronic illness among the elderly in a rural community in Malaysia. *Asia Pac. J. Public Health* **2004**, *16*, 109–114. [CrossRef] [PubMed]
35. Franklin, R.C.; Mason, H.M.; King, J.C.; Peden, A.E.; Nairn, J.; Miller, L.; Watt, K.; FitzGerald, G. Heatwaves and mortality in Queensland 2010–2019: Implications for a homogenous state-wide approach. *Int. J. Biometeorol.* **2023**, *67*, 503–515. [CrossRef]
36. Aghababaeian, H.; Ostadtaghizadeh, A.; Ardalan, A.; Asgary, A.; Akbary, M.; Yekaninejad, M.S.; Sharafkhani, R.; Stephens, C. Mortality Risk Related to Heatwaves in Dezful City, Southwest of Iran. *Environ. Health Insights* **2023**, *17*, 11786302231151538. [CrossRef]
37. Xi, D.; Liu, L.; Zhang, M.; Huang, C.; Burkart, K.G.; Ebi, K.; Zeng, Y.; Ji, J.S. Risk factors associated with heatwave mortality in Chinese adults over 65 years. *Nat. Med.* **2024**, *30*, 1489–1498. [CrossRef]
38. Liu, J.; Varghese, B.M.; Hansen, A.; Zhang, Y.; Driscoll, T.; Morgan, G.; Dear, K.; Gourley, M.; Capon, A.; Bi, P. Heat exposure and cardiovascular health outcomes: A systematic review and meta-analysis. *Lancet Planet Health* **2022**, *6*, e484–e495. [CrossRef]
39. Thompson, R.; Landeg, O.; Kar-Purkayastha, I.; Hajat, S.; Kovats, S.; O'Connell, E. Heatwave Mortality in Summer 2020 in England: An Observational Study. *Int. J. Environ. Res. Public Health* **2022**, *19*, 6123. [CrossRef]
40. Chen, K.; Bi, J.; Chen, J.; Chen, X.; Huang, L.; Zhou, L. Influence of heat wave definitions to the added effect of heat waves on daily mortality in Nanjing, China. *Sci. Total Environ.* **2015**, *506–507*, 18–25. [CrossRef]
41. Kim, E.J.; Kim, H. Effect modification of individual- and regional-scale characteristics on heat wave-related mortality rates between 2009 and 2012 in Seoul, South Korea. *Sci. Total Environ.* **2017**, *595*, 141–148. [CrossRef] [PubMed]
42. Ma, W.; Zeng, W.; Zhou, M.; Wang, L.; Rutherford, S.; Lin, H.; Liu, T.; Zhang, Y.; Xiao, J.; Zhang, Y.; et al. The short-term effect of heat waves on mortality and its modifiers in China: An analysis from 66 communities. *Environ. Int.* **2015**, *75*, 103–109. [CrossRef] [PubMed]
43. Gabriel, K.M.; Endlicher, W.R. Urban and rural mortality rates during heat waves in Berlin and Brandenburg, Germany. *Environ. Pollut.* **2011**, *159*, 2044–2050. [CrossRef] [PubMed]
44. Burkart, K.; Schneider, A.; Breitner, S.; Khan, M.H.; Krämer, A.; Endlicher, W. The effect of atmospheric thermal conditions and urban thermal pollution on all-cause and cardiovascular mortality in Bangladesh. *Environ. Pollut.* **2011**, *159*, 2035–2043. [CrossRef] [PubMed]
45. Hajat, S.; Kovats, R.S.; Lachowycz, K. Heat-related and cold-related deaths in England and Wales: Who is at risk? *Occup. Environ. Med.* **2007**, *64*, 93–100. [CrossRef]
46. Kovats, R.S.; Hajat, S. Heat stress and public health: A critical review. *Annu. Rev. Public Health* **2008**, *29*, 41–55. [CrossRef]
47. Hu, K.; Guo, Y.; Hochrainer-Stigler, S.; Liu, W.; See, L.; Yang, X.; Zhong, J.; Fei, F.; Chen, F.; Zhang, Y.; et al. Evidence for Urban-Rural Disparity in Temperature-Mortality Relationships in Zhejiang Province, China. *Environ. Health Perspect.* **2019**, *127*, 37001. [CrossRef]
48. Zeng, W.; Lao, X.; Rutherford, S.; Xu, Y.; Xu, X.; Lin, H.; Liu, T.; Luo, Y.; Xiao, J.; Hu, M.; et al. The effect of heat waves on mortality and effect modifiers in four communities of Guangdong Province, China. *Sci. Total Environ.* **2014**, *482–483*, 214–221. [CrossRef]
49. Chen, K.; Zhou, L.; Chen, X.; Ma, Z.; Liu, Y.; Huang, L.; Bi, J.; Kinney, P.L. Urbanization Level and Vulnerability to Heat-Related Mortality in Jiangsu Province, China. *Environ. Health Perspect.* **2016**, *124*, 1863–1869. [CrossRef]
50. D'Ippoliti, D.; Michelozzi, P.; Marino, C.; de'Donato, F.; Menne, B.; Katsouyanni, K.; Kirchmayer, U.; Analitis, A.; Medina-Ramón, M.; Paldy, A.; et al. The impact of heat waves on mortality in 9 European cities: Results from the EuroHEAT project. *Environ. Health* **2010**, *9*, 37. [CrossRef]
51. Conti, S.; Masocco, M.; Meli, P.; Minelli, G.; Palummeri, E.; Solimini, R.; Toccaceli, V.; Vichi, M. General and specific mortality among the elderly during the 2003 heat wave in Genoa (Italy). *Environ. Res.* **2007**, *103*, 267–274. [CrossRef] [PubMed]
52. Health in Slovenia. Available online: https://nijz.si/wp-content/uploads/2022/07/zdravje_v_sloveniji_eng_e-verzija.pdf (accessed on 18 October 2023).
53. American Heart Association. Available online: https://www.heart.org/en/health-topics/cholesterol/about-cholesterol/atherosclerosis (accessed on 18 October 2023).
54. Folkow, B. Physiological aspects of primary hypertension. *Physiol. Rev.* **1982**, *62*, 347–504. [CrossRef]
55. Greene, A.S.; Tonellato, P.J.; Lui, J.; Lombard, J.H.; Cowley, A.W., Jr. Microvascular rarefaction and tissue vascular resistance in hypertension. *Am. J. Physiol.* **1989**, *256 Pt 2*, H126–H231. [CrossRef]
56. Carberry, P.A.; Shepherd, A.M.; Johnson, J.M. Resting and maximal forearm skin blood flows are reduced in hypertension. *Hypertension* **1992**, *20*, 349–355. [CrossRef] [PubMed]
57. Allen, A.; Segal-Gidan, G. Heat-related illness in the elderly. *Clin. Geriatr.* **2007**, *15*, 37–45.

58. Kenney, W.L.; Craighead, D.H.; Alexander, L.M. Heat waves, aging, and human cardiovascular health. *Med. Sci. Sports Exerc.* **2014**, *46*, 1891–1899. [CrossRef]
59. Cui, J.; Arbab-Zadeh, A.; Prasad, A.; Durand, S.; Levine, B.D.; Crandall, C.G. Effects of heat stress on thermoregulatory responses in congestive heart failure patients. *Circulation* **2005**, *112*, 2286–2292. [CrossRef]
60. Schols, J.M.; De Groot, C.P.; van der Cammen, T.J.; Olde Rikkert, M.G. Preventing and treating dehydration in the elderly during periods of illness and warm weather. *J. Nutr. Health Aging* **2009**, *13*, 150–157. [CrossRef]
61. Watso, J.C.; Farquhar, W.B. Hydration Status and Cardiovascular Function. *Nutrients* **2019**, *11*, 1866. [CrossRef]
62. Keatinge, W.R.; Coleshaw, S.R.; Easton, J.C.; Cotter, F.; Mattock, M.B.; Chelliah, R. Increased platelet and red cell counts, blood viscosity, and plasma cholesterol levels during heat stress, and mortality from coronary and cerebral thrombosis. *Am. J. Med.* **1986**, *81*, 795–800. [CrossRef]
63. Knochel, J.P. Heat stroke and related heat stress disorders. *Dis. Mon.* **1989**, *35*, 301–377. [PubMed]
64. Glazer, J.L. Management of heatstroke and heat exhaustion. *Am. Fam. Physician* **2005**, *71*, 2133–2140. [PubMed]
65. Wang, L.; Green, F.H.; Smiley-Jewell, S.M.; Pinkerton, K.E. Susceptibility of the aging lung to environmental injury. *Semin. Respir. Crit. Care Med.* **2010**, *31*, 539–553. [CrossRef] [PubMed]
66. Bélanger, D.; Berry, P.; Bouchet, V.; Charron, D.; Clarke, K.L.; Doyon, B.; Fleury, M.; Furgal, C.; Gosselin, P.; Lamy, S.; et al. *Human Health in a Changing Climate: A Canadian Assessment of Vulnerabilities and Adaptive Capacity*; Séguin, J., Ed.; Health Canada: Ottawa, ON, Canada, 2008. Available online: www.sindark.com/NonBlog/Articles/hc-cc-report/CCandHealth.pdf (accessed on 19 October 2019).
67. Bevan, G.H.; Al-Kindi, S.G.; Brook, R.; Rajagopalan, S. Ambient Air Pollution and Atherosclerosis: Recent Updates. *Curr. Atheroscler. Rep.* **2021**, *23*, 63. [CrossRef]
68. Robertson, S.; Miller, M.R. Ambient air pollution and thrombosis. *Part. Fibre Toxicol.* **2018**, *15*, 1. [CrossRef]
69. Mazzoli-Rocha, F.; Fernandes, S.; Einicker-Lamas, M.; Zin, W.A. Roles of oxidative stress in signaling and inflammation induced by particulate matter. *Cell Biol. Toxicol.* **2010**, *26*, 481–498. [CrossRef]
70. Šuškovič, S.; Camlek, T.; Gril, M.; Hudoklin, I.; Klobučar, A.; Koren, I.; Koterle, M.; Terzin, K.; Mežnar, B.; Silič, A. Prevalenca astme pri odraslih v Sloveniji. *Zdrav. Vestn.* **2011**, *80*, 451–457.
71. Blanco, I.; Diego, I.; Bueno, P.; Fernández, E.; Casas-Maldonado, F.; Esquinas, C.; Soriano, J.B.; Miravitlles, M. Geographical distribution of COPD prevalence in Europe, estimated by an inverse distance weighting interpolation technique. *Int. J. Chron. Obstruct. Pulmon. Dis.* **2017**, *13*, 57–67. [CrossRef]
72. Nairn, J.R.; Fawcett, R. *Defining Heatwaves: Heatwave Defined as a Heat-Impact Event Servicing all Community and Business Sectors in Australia*; Technical Report 060; Centre for Australian Weather and Climate Research (CAWCR): Kent Town, SA, Australia, 2013; 84p.

Disclaimer/Publisher's Note: The statements, opinions and data contained in all publications are solely those of the individual author(s) and contributor(s) and not of MDPI and/or the editor(s). MDPI and/or the editor(s) disclaim responsibility for any injury to people or property resulting from any ideas, methods, instructions or products referred to in the content.

climate

MDPI

Article

Impact of Climate Change on Biodiversity and Implications for Nature-Based Solutions

Cor A. Schipper [1,*], Titus W. Hielkema [1] and Alexander Ziemba [2,3]

[1] Ministry of Infrastructure and Water Management, P.O. Box 2232, 3500 GE Utrecht, The Netherlands; titus.hielkema@minienw.nl
[2] Deltares, P.O. Box 177, 2600 MH Delft, The Netherlands; alex.ziemba@deltares.nl
[3] Applied Mathematics, Delft University of Technology, Mekelweg 2, 2628 CD Delft, The Netherlands
* Correspondence: ecotox@zeelandnet.nl; Tel.: +31-653-794-288

Abstract: The Intergovernmental Panel on Climate Change (IPCC) provides regular scientific assessments on climate change, its implications, and potential future risks based on estimated energy matrixes and policy pathways. The aim of this publication is to assess the risks climate change poses to biodiversity using projected IPCC climate scenarios for the period 2081–2100, combined with key species-sensitivity indicators and variables as a response to climate change projections. In doing so, we address how climate-change-driven pressures may affect biodiversity. Additionally, a novel causal relationship between extreme ambient temperature exposure levels and the corresponding effects on individual species, noted in this paper as the Upper Thermal-Tolerance Limit and Species Sensitivity Distribution (UTTL-SSD), provides a compelling explanation of how global warming affects biodiversity. Our study indicates that North American and Oceanian sites with humid continental and subtropical climates, respectively, are poised to realize temperature shifts that have been identified as potential key tipping-point triggers. Heat stress may significantly affect approximately 60–90% of mammals, 50% of birds, and 50% of amphibians in North American and Oceanian sites for durations ranging from 5 to 84 days per year from 2080. In the humid temperate oceanic climate of European sites, the climate conditions remain relatively stable; however, moderate cumulative effects on biodiversity have been identified, and additional biodiversity-assemblage threat profiles exist to represent these. Both the integration of IPCC-IUCN profiles and the UTTL-SSD response relationship for the species communities considered have resulted in the identification of the projected threats that climate pressures may impose under the considered IPCC scenarios, which would result in biodiversity degradation. The UTTL-SSD responses developed can be used to highlight potential breakdowns among trophic levels in food web structures, highlighting an additional critical element when addressing biodiversity and ecosystem concerns.

Keywords: climate change; flooding; adaptation; resilience; biodiversity; global; IUCN; IPCC

1. Introduction

Understanding the localized impacts of climate change projections on ecosystems is of the utmost importance for nature conservation strategies aiming to adapt to local climatic processes [1]. Increases in heat-related stress can result in a variety of effects, including increased metabolic rates, behavioral changes, and/or mortality [2–5]. The potential consequences of climate change on biodiversity in the long-term, and the transitional phases in the mid-term, are insufficiently known [6]. The literature confirms that mid- and long-term predictions on the effects of climate pressures on biodiversity, within local and regional scales, exhibit complex interactions, multiple drivers of change, and involve complex food webs with spatial variations in ecosystems [7–13] (Table A1). Changing climate conditions are caused by multiple factors and compounding bioclimatic pressures [14], such as temperature increases and changes in the water cycle. The combined stressors of drought

and extreme heatwaves, as predicted by climate scenario models, could have a high, and often negative, impact on organisms' physiology [15–17]. Ref. [18] showed that, if the monitored variation in thermal-tolerance levels for species continues, naturally adaptive responses in thermal limits from organisms will have a limited potential to serve as an adaptation strategy for most species' preservation. This has particular relevance, given the unprecedented rate of contemporary climate change. The resultant potential ecological regime shift, denoted by impacts observed as tipping points in external bioclimatic drivers and ecosystem responses, stands to cause a major change in ecosystems' structure and/or function [19]. Ref. [20] used catastrophe theory to detect a regime shift for marine species; in doing so, he concluded that ocean warming will cause potentially irreversible regime shifts in ecosystems on a global scale. A mechanism that could reduce the risk of overheating is physiological thermal tolerance, such as the reversible change known as acclimation [21]. Moreover, exposure of ectotherms to combined heat stress and drought can exacerbate physiological stress of organisms through additive effects [22,23]. Given the likelihood of increasing single and combined heat stressors with a limited pathway for species' adaptation, particularly given the rate of change predicted, particular attention is given to these elements within this application.

As there stands to be considerable potential for severe shifts in biodiversity composition and ecosystem functioning due to climate change, there is a need to assess the progress of climate adaptation in areas for nature conservation, resulting in an applied Nature-based Solution (NbS) [24,25]. Some of these studies consider ecological indicators to assess biodiversity conservation potential. Several authors have developed estimations on the potential effects of projected climate pressures on ecosystems [7,26–29]. Ref. [30] developed a model to assess the efficiency of NbS by coupling local IPCC bioclimatic projections with management plans for NbS sites. This application used UN Sustainable Development Goals (SDGs) for metrics and assessment purposes [31].

Readily applicable methodologies for evaluating biodiversity vulnerability levels to projected bioclimatic pressures are available, particularly those which can account for climate resilience solutions and adaptation strategies. However, to the best of our knowledge, studies in the existing literature have not attempted to conduct an analysis of NbS based on existing threats to biodiversity and long-term bioclimatic projections for the period 2081–2100—the core application considered in this work. As extremes become more common and intensify, investigating global assessments of climate change in relation to extreme heat stress, drought, and precipitation events requires key datasets compiled from scientific sources, and for this data to be carefully considered in future model risk assessments [32–34].

Our study shows the novel relationship between Upper Thermal-Tolerance Limit and Species Sensitivity Distribution (UTTL-SSD), where critical temperatures provide compelling insights into how climate change stands to affect biodiversity. This analysis aims to assess the effectiveness of NbS sites by enhancing an impact model, incorporating local IUCN biodiversity threats to vertebrates and invertebrates, and establishing connections with IPCC bioclimatic projections. This adds to the body of evidence concerning the role that an NbS plays in adaption strategies regarding the increasing bioclimatic pressures associated with climate biodiversity threats.

Within the scope of this paper, we consider biodiversity in the general sense, regarding it as encompassing species diversity, as well as structural and functional elements within ecological systems. It is acknowledged that biodiversity assessments are inherently complex and rely on an intricate understanding of ecosystem composition and relationships, and this study does not delve into the nuances of the ecosystems considered. Within our analysis, the term biodiversity is used to indicate a terminus point for pressures and climate-change system drivers and NbS influences, which are related to species diversity and structural or functional implications on ecological systems. As such, biodiversity is defined as the diversity or richness within species, between species, or of the habitat and ecosystems, in line with the ICBD definition (The International Convention on Biological Diversity).

In our paper, the IPCC bioclimatic variables and IUCN spatial data are used to (1) analyze global NbS sites and the projected increases in bioclimatic variables in climate classification systems, focusing on mean annual temperature, heat waves (i.e., days warmer than 35 °C and 40 °C annually), max 5-day precipitation, consecutive dry days, and sea level rise; (2) judge the impact of bioclimatic processes on biodiversity in different climate zones and at multiple trophic levels; and (3) gain evidence for the role played by NbSs in adapting to climate change while considering biodiversity. The outcomes and impact measures of this assessment can be used to inform planning processes, improve and enhance resilience, or promote measures for the conservation of biodiversity. NbS sites from Europe, Oceania, and North America are utilized, with various global regions represented in the database being developed, and they are shown to have a range of impacts.

2. Methodology

The selection criteria for the NbS sites considered are primarily driven by a desire to maintain similarity and comparability. The criteria were based on their functionalities, namely, providing flood protection, serving socioeconomic growth, possessing a high intrinsic value for biodiversity and healthy ecosystems, regulating emissions, erosion reduction, and serving the wellbeing of humans [30]. Four Köppen–Geiger climate zones for the present day (1980–2016) have been selected [35]. These are located in Europe, Oceania, and North America [36–38], Figure 1. This was performed with the acknowledgement that tropical ecosystems are most vulnerable to climate change and will likely suffer the greatest impacts. Integrating local threat profiles with projected bioclimatic changes allows for effective nature conservation planning and climate adaptation at the NbS site.

The flow of data processing and analysis in the proposed Bioclimatic–Biodiversity Impact model (BBI) model is outlined in Figure 1, and consists of three methodological steps. Step 1 consists of building the IPCC Sixth Coupled Model Intercomparison Project (IPCC CMIP6) [39], IUCN biodiversity threats [40], and GlobTherm datasets [18,41] for the sites.

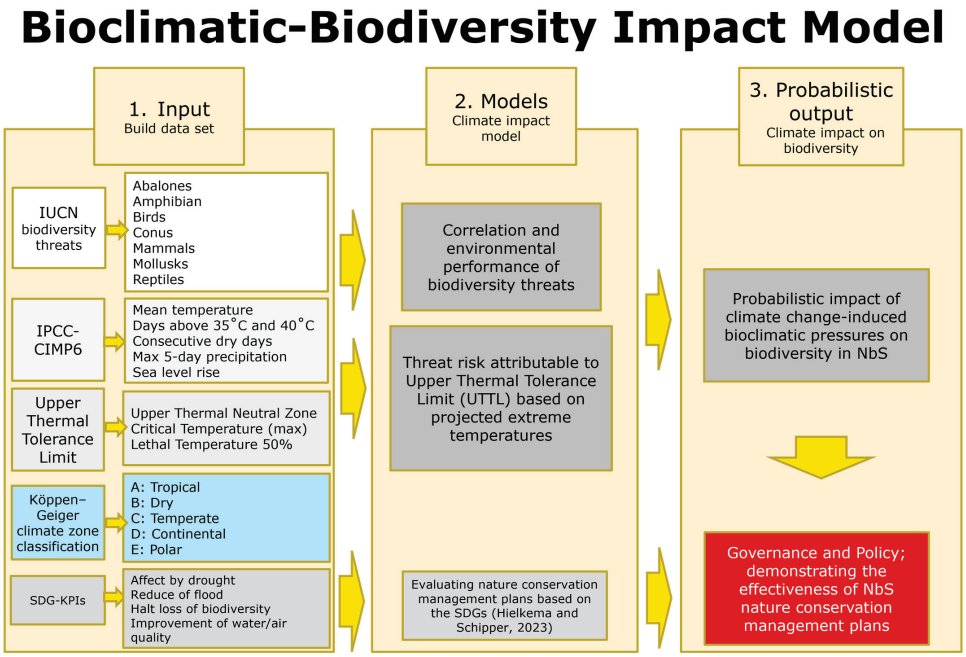

Figure 1. Schematization of the BBI model. The diagram outlines the flow of processed data from the IPCC climate change-induced variable on the IUCN biodiversity threat used to assess potential biodiversity degradation and places these in relation to local vulnerabilities to demonstrate effectiveness management plans in Köppen–Geiger climate zone projections for 2081–2100.

In Step 2, present-day IUCN biodiversity threats are analyzed for the relevant climate zones to create a biodiversity sensitivity map, which is then evaluated within the context of the IPCC projections under emissions scenarios SSP1-2.6 and SSP5-8.5. Furthermore, the GlobTherm data are analyzed to construct the Potentially Affected Fraction (PAF) of species groups to temperature extremes using the sigmoid shape Upper Thermal-Tolerance Limit and Species Sensitivity Distribution (UTTL-SSD) response relationship [42,43].

In Step 3, forecasts of probabilistic outputs are produced by correlations, tipping points, and food-web interactions for external bioclimatic drivers for selected species per region. It provides insights on potential biodiversity degradation in NbS sites and ranks these in relation to local biodiversity threats and vulnerabilities, demonstrating the effectiveness of management plans in climate zone projections for 2081–2100. Finally, the IPCC-SSD relationship demonstrates the effectiveness of management plans, considering the bioclimatic projections.

2.1. Building the Datasets

The IPCC model predictions are based on five scenarios, two of which are used in this body of work, namely, the SSP1-2.6 and SSP5-8.5 scenarios. Scenario SSP1-2.6 represents low greenhouse gas emissions and CO_2 emissions declining to net zero around or after 2050, followed by global net negative CO_2 emissions. Scenario SSP5-8.5 represents very high greenhouse gas emissions and CO_2 emissions of about double the current levels by 2050 [39]. Utilizing the lower and upper emission pathways allows for a thorough assessment of the full spectra of IPCC scenarios and to identify all threatened areas under best- and worst-case situations. The IPCC offers spatial data from CMIP6 for a range of bioclimatic variables, temporal domains (both historical data and projections), and Shared Socio-economic Pathways (SSP) [44]. Bioclimatic data were collected for mean annual temperature (in degrees °C), days warmer than 35 °C and 40 °C annually (biases adjusted using ISIMIP3 method [45]), max 5-day precipitation (in mm), consecutive dry days (CDDs) and sea level rise (SLR; in meters). In addition to SSP1-2.6 and SSP5-8.5 scenarios, bioclimatic data were collected for the baseline periods 1850–1900 (for mean temperature) and 1995–2014 (for precipitation, drought, and sea level rise). These data were collected as averages over the NbS site surface area. From the baseline and projection datasets, the changes in bioclimatic variables between periods were calculated manually.

Local biodiversity threat profiles were produced, based on the IUCN biodiversity-threat spatial data and species' thermal-tolerance limits. Firstly, the IUCN provides spatial data for threatened species and the direct threats to species. The IUCN connects threats for different species groups to the bioclimatic pressures via the IUCN Threats Classification Scheme (version 3.3. retrieved on 8 March 2022 https://www.iucnredlist.org/resources/threat-classification-scheme) [40]. Key factors of note used in this study are temperature increases and extremes, storms and pluvial flooding, droughts, and habitat shifting and alteration (sea level rise included; Table 2). The IUCN data were modified in the same process as described by [46,47], and used to generate a spatial biodiversity sensitivity map. Following the IUCN species distribution data [40], species were selected based on the overlap of their distribution with the coordinates of the NbS sites under consideration. Additionally, the species had to be scored as extant, native, and resident, so that invasive species were excluded. This ensured that species not adapted to local climate conditions were not evaluated and did not skew the evaluation of native ecosystems. Ten key species groups that play a central role in several ecosystem services were selected, namely, amphibians [48]; birds, fish, and mammals [49]; reptiles, insects, and arachnids [21]; and, lastly, abalones and conus for coastal areas or mollusks for river catchments [50]. The sensitivity of biodiversity assemblages to bioclimatic pressures was evaluated based on the count of local species threatened by the bioclimatic pressure.

Secondly GlobTherm database [18,40] was used, which represents a composite dataset of thermal-tolerance limits of species globally. The dataset consists of marine, fresh water, and terrestrial organisms and assesses the ecological impact of temperature in Oceania,

North America, and Europe. The data cover land, marine, fresh water, and brackish water biomes, representing 10 taxonomic groups. The Upper Thermal-Tolerance Limit (UTTL) was then defined by considering the measure of upper thermal tolerance that allows the greatest taxon coverage. The limits considered were the Upper Thermal Neutral Zone (UTNZ), Critical Thermal Maximum (CT_{max}), or the Lethal Temperature for 50% (LT50) depending on species group. The UTNZ and CT_{max} describe critical temperatures at which key ecological functions are lost, such as locomotion and the ability to gain nutrition or maintain basal metabolism for UTNZs (only applicable for endotherms). LT50 describes lethal temperatures at which mortality in 50% of individuals occurs, where mortality is considered as the death of the entire individual or a portion thereof, such as leaf die-off in a tree [40]. UTTL data points were selected for the climate zones (for the period 1980–2016) of the NbS sites per continent (Table 1).

Table 1. Overview of the climate zones in NbS sites in 1980–2016 and 2081–2100 following the Köppen–Geiger climate classification scheme. Abbreviations: Dfa = humid continental climate with hot summer; Dfb = humid continental climate with warm summer; Cfa = humid subtropical climate areas; Cfb = temperate oceanic climate areas. Different colors show the changes in the zones in the 21st century.

		Köppen–Geiger Classification	
Continent	**NbS Sites**	**1980–2016**	**2081–2100**
North America	Long Beach Island	Dfa	Cfa
	Springhouse Runs	Dfa/Cfa	Cfa
	Mill River Taunton	Dfa	Cfa
	Upper Mississippi River	Dfa/Dfb	Cfa/Dfa
Oceania	Tomago Wetland AS	Cfb/Dfa	Cfa/Cfb
	Taumanu NZ	Cfb	Cfa/Cfb
Europe	Zwin	Cfb	Cfb/Cfa
	Weijerswold	Cfb	Cfb
	Lower Saxony	Cfb	Cfb
	Medway	Cfb	Cfb
	Ringkobing fjord	Cfb	Cfb
	Klarälven Värmland	Dfb	Cfb/Dfb

2.2. Climate Impact Model

2.2.1. Upper Thermal-Tolerance Limit and Species Sensitivity–Response Relationship

In the second step of the BBI model, the relevant adverse effects of emerging threats can be assessed for a Potentially Affected Fraction (PAF) of species [51,52]. As the PAF includes the variation in sensitivity among all species tested, it gives a more ecologically relevant indication of the risk of an environmental pressure. This approach shifts away from a binary 'risk' or 'no-risk' evaluation for the most sensitive species, and rather addresses the likelihood that different effects are predicted based on a statistical analysis of all species tested [42]. In our study, the PAF of species was converted into SSD curves to use causal relationships between temperature exposure level and effects realized for individual species. The SSDTOOLS package was used to plot SSD curves in R statistical software version 4.2.2 [53], and the curve represents the best fit of the data to the sigmoid function [54–56]. The SSD curves consist of at least six species; if this was not possible, the SSD curve was omitted. From these SSD curve calculations, the Upper Thermal-Tolerance Limit sensitivity of species' tipping points was derived as the percentage of species threatened above 35 °C and 40 °C.

2.2.2. Correlating IPCC Projections with IUCN Data

The direct threats to species in NbS sites were correlated with the projected changes in bioclimatic pressures using the Spearman's correlation coefficient [57]. The Spearman correlation coefficient p is a measure of the strength and direction of monotonic association between two independent variables. The interpretation of the Spearman correlation relies on several factors: the closer p is to +1 or -1, the stronger the monotonic relationship. A Spearman's correlation was run to determine the relationship of selected IPCC SSP1-2.6 and SSP5-8.5 variables for temperature, drought, and precipitation with the number of species threatened by the respective IUCN biodiversity threat. Correlating IPCC projections with IUCN data gives insights into the effects of projected changes in bioclimatic pressures on local biodiversity in NbS sites. A positive correlation (bioclimatic pressure has threatened many species and is projected to increase until 2100) indicates the climatic pressure poses a threat of biodiversity loss in the NbS site.

2.3. Probabilistic Climate Impact on Biodiversity

The effect of heat stress on an ecosystem as a whole can be simulated by integrating projected heat stress among species with food web interactions. Simplified food webs were constructed for East Australian, North American, and European NbS sites to simulate the predicted effects of temperature rise on various trophic levels [58,59]. This is performed by utilizing only the species groups considered and detailed above. The interactions were based on the SSP5 climate scenario and the percentage estimates of species within a given species group which are threatened by heat stress, as shown in the UTTL-SSD curves.

The degree to which NbS for Nature Conservation Management (NCM) plans consider climate change scenarios and address their impact on biodiversity is key to determining how such plans contribute to the active or potential conservation of threatened species. NCM plans must not only be appointed for species currently under threat, but should also include species potentially threatened as a result of changing bioclimatic conditions. To this end, forecasts resulting in probabilistic outputs were produced using PAF and an analysis of biodiversity threat profiles to external bioclimatic drivers for selected species groups; this was repeated for each considered region. Plotting resultant thermal-tolerance limits of species regarding the UTTL-SSD response relationship provided insights into possible tipping points and biodiversity degradation as a result of external bioclimatic drivers due to the effects of global warming on ecosystems. In line with [30], the NCM plans of the 12 considered sites were compared using the UTTL-SSD response relationship to determine the degree to which climate change is considered and affecting these sites. This is performed to enhance the BBI model and assess the vulnerability of biodiversity in NbS sites for different climate zones in relation to climate change scenarios. Additionally, we also correlated predicted changes and how they may be affecting local biodiversity. The statistical Spearman's correlation is more limited as it does not describe potential tipping points, but it can highlight the local bioclimatic pressures of concern for nature conservation planning.

3. Results

3.1. Building Datasets

Twelve NbS sites are selected across Northwest Europe (six), Eastern North America (four), and East Oceania (two), including six coastal sites and six river sites. The NbS sites are located in four different climate zones following the Köppen–Geiger climate classification for the present day (1980–2016) and the future (2081–2100) (Table 1). Some North American and Oceanian NbS sites considered are located in multiple climate zones, due to the sites' location and low level of confidence in prescribing only one climate zone. When looking at current and 2081–2100 classifications, projected climate change results in the zones altering for most of the NbS sites.

The IPCC CMIP6 model projects great bioclimatic variabilities among NbS sites and continents (Tables 3 and 4). In the European NbS sites, most significant projected changes

are longer periods of drought (CDD, SSP1: 0.28–2.08 days; SSP5: 1.44–8.49 days) and more extreme precipitation (max. 5d, SSP1: 3.40–7.47%; SSP5: 14.16–19.78%). In North American NbS sites, the temperature rises (mean annual, SSP1: 2.29–2.78 °C; SSP5: 5.74–6.99 °C) and precipitation intensifies (max5d, SSP1: 5.23–7.63%; SSP5: 17.42–21.51%) most significantly. Sea level may rise most at the coast of Long Beach Island (North America), with changes from 0.69 m (SSP1) to 0.97 m (SSP5), while at the other coastal NbS sites, sea level rises were documented from 0.4 m (SSP1) to 0.7 m (SSP5). In absolute numbers, North American sites are projected to experience higher levels of precipitation and fewer consecutive dry days than Europe (under SSP5; $F(2, 9) < 5.2$, $p < 0.05$). Conversely, Europe is set to experience longer dry periods and a stronger increases in consecutive dry days compared to North American sites under SSP5 ($p = 0.07$) and Oceanian sites under both SSP1 ($p = 0.04$) and SSP5 ($p = 0.06$). Precipitation increases similarly in Europe compared to North American and Oceanian sites under SSP1 ($F(2, 9) = 4.619$, $p = 0.36$) and SSP5 (NA: $p = 0.05$, OC: $p = 0.54$). Extreme temperatures—that is, days warmer than 35 °C and 40 °C—will be more likely in North American and Australian sites, with rare events in Europe. Under SSP5 especially, extremely hot days will be more frequent.

The biodiversity sensitivity maps (Figure 2) show the number of species threatened for North American, Oceanian, and European areas and for temperature extremes, storms and flooding, droughts, and habitat shifting and alteration. The biodiversity sensitivity maps show that North American NbS sites are threatened by the combination of drought, temperature, precipitation, and habitat shifting and alteration, with mostly mammals and birds coming under pressure. European NbS sites are threatened by the combination of temperature, droughts, and habitat shifting and alteration, with mostly birds, mammals, and mollusks under pressure. Oceanian NbS sites are threatened by the combination of temperature, precipitation, drought, and habitat shifting and alteration, with mostly birds and mammals under pressure. It is important to note that in the majority of cases where species are coming under threat, it is a result of habitat shifting and alteration. This holds especially true for birds and mammals. For birds, this is most notable in Springhouse Runs stream and Tomago Wetland, where large numbers of bird species are threatened, due to habitat shifting and alteration.

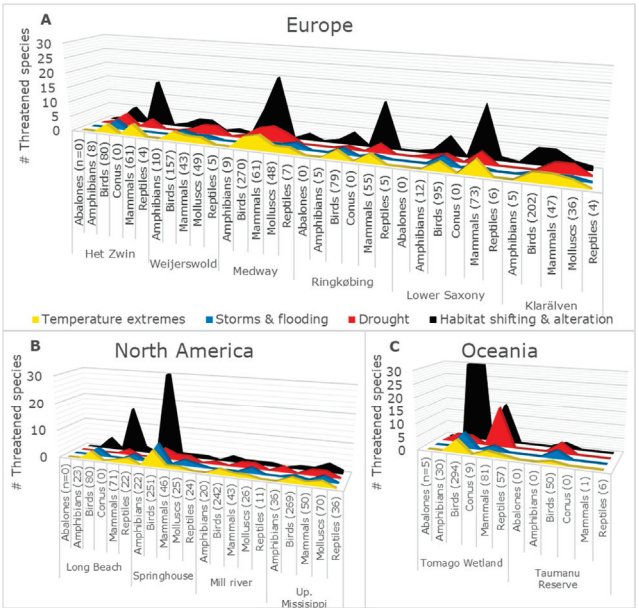

Figure 2. Number of threatened species of abalones, amphibians, birds, conus, mammals, mollusks, and reptiles in NbS sites in Europe (**A**), North America (**B**), and Oceania (**C**) due to temperature extremes, storms and flooding, droughts, and habitat shifting and alteration. The total number of endemic species present in the IUCN database is given in parentheses.

3.2. Bioclimatic Impact on Biodiversity

Forecasts generating probabilistic outputs are made through the application of the Potentially Affected Fraction. Subsequently, an analysis of biodiversity threat profiles and climate projections for selected species groups is generated per region. Figures 2–4 and 3–5 show the SSD curves generated for the UTTL–SSD response relationship for different species groups per continent. To provide insights in species degradation aspects linked to projected extreme temperature, the figures show the 35 °C and 40 °C lines, indicating that species on the left side experience heat stress at those temperatures (not indicated for aquatic species). The UTTL-SSD curves show many species groups are sensitive to heat stress, indicating a potentially dramatic decline in species in NbS sites due to frequent heatwaves in North America and Oceania.

In North America, many species have a thermal-tolerance level below 35 °C (Figures 2 and 3), while temperatures among NbS sites are projected to exceed 35 °C for 5-to-24 days in 2100 under SSP1 and 33-to-84 days under SSP5 (Table 4). Approximately 60% of mammals and 50% of birds have a UTNZ lower than 35 °C and approximately 45% of amphibians have a maximum CT_{max} lower than 35 °C. The majority of species have a thermal-tolerance level below 40 °C, but 40+ °C days are much less frequent.

In European sites, extreme warm days are not projected to be frequent. It is only under SSP5 where 0 to 9 days are expected to exceed temperatures of 35 °C (Table 3). Approximately 70% of birds and mammals (combined) have a UTNZ lower than 35 °C (Figures 3 and 4).

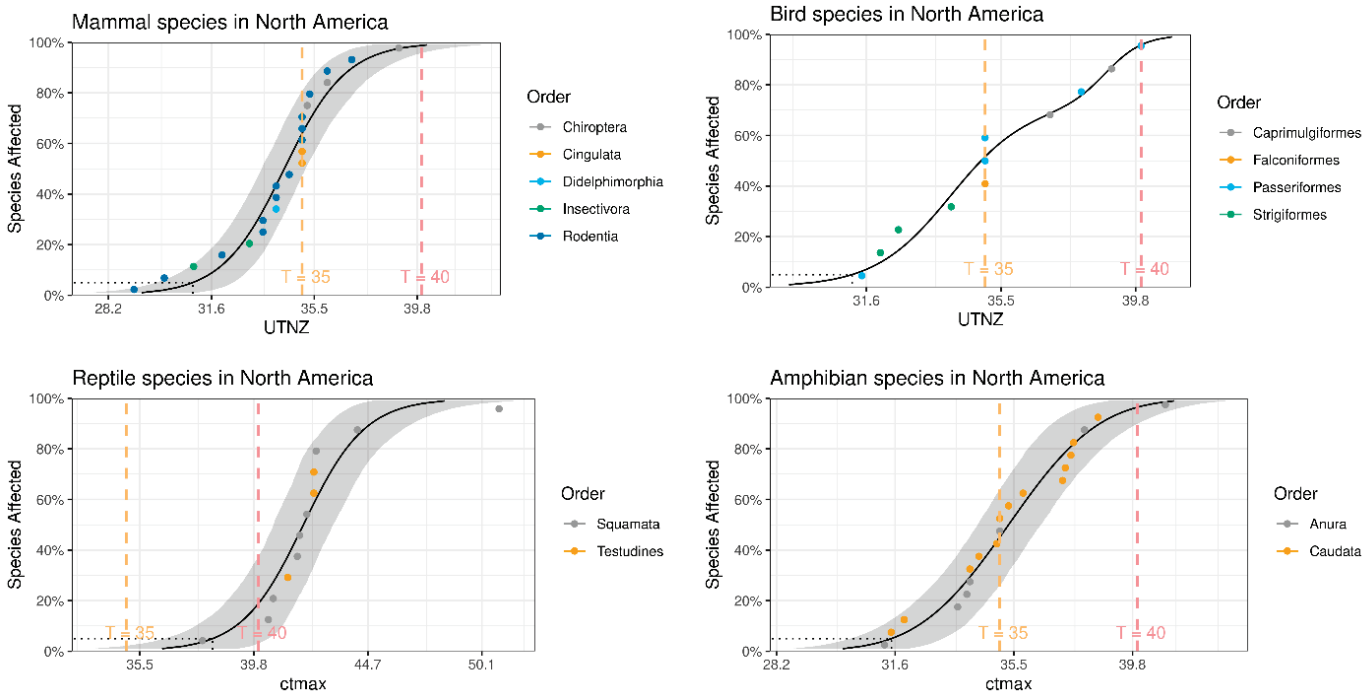

Figure 3. The Species Sensitivity Distributions for North America. The UTNZ and CTmax SSD–response relationship of invertebrate and vertebrate species is shown as sigmoid curves [40]. The percentage of affected species at temperature (°C) is represented by the solid black line, with the model-averaged 95% confidence interval indicated by the shaded band, and the 5% affected species threshold by the black dotted line. In 2100 in North America, the ambient temperatures are projected to exceed 35 °C for 5–25 days (SSP1) and 33–85 days (SSP5) and to exceed 40 °C during 0–2 days (SSP1) and 5–22 days (SSP5). Note that large group of species show high sensitivity to the extreme temperatures projected in 2100.

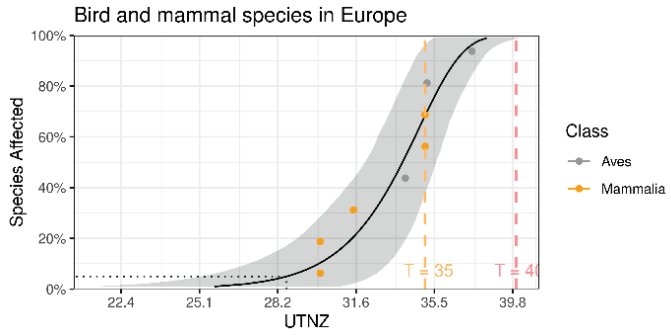

Figure 4. The Species Sensitivity Distributions for Europe. The UTNZ SSD–response relationship of vertebrate species is shown as sigmoid curves [40]. The percentage of affected species at temperature (°C) is represented by the solid black line, with the model-averaged 95% confidence interval indicated by the shaded band, and the 5% affected species threshold by the black dotted line. In 2100, in Europe, the ambient temperatures are projected to exceed 35 °C for 0–1 days (SSP1) and 0–9 days (SSP5) and exceed 40 °C during 0 days (SSP1) and 0–2 days (SSP5). Note that while many species show high sensitivity to extreme temperatures, the projections show extreme temperature will be very uncommon in 2100.

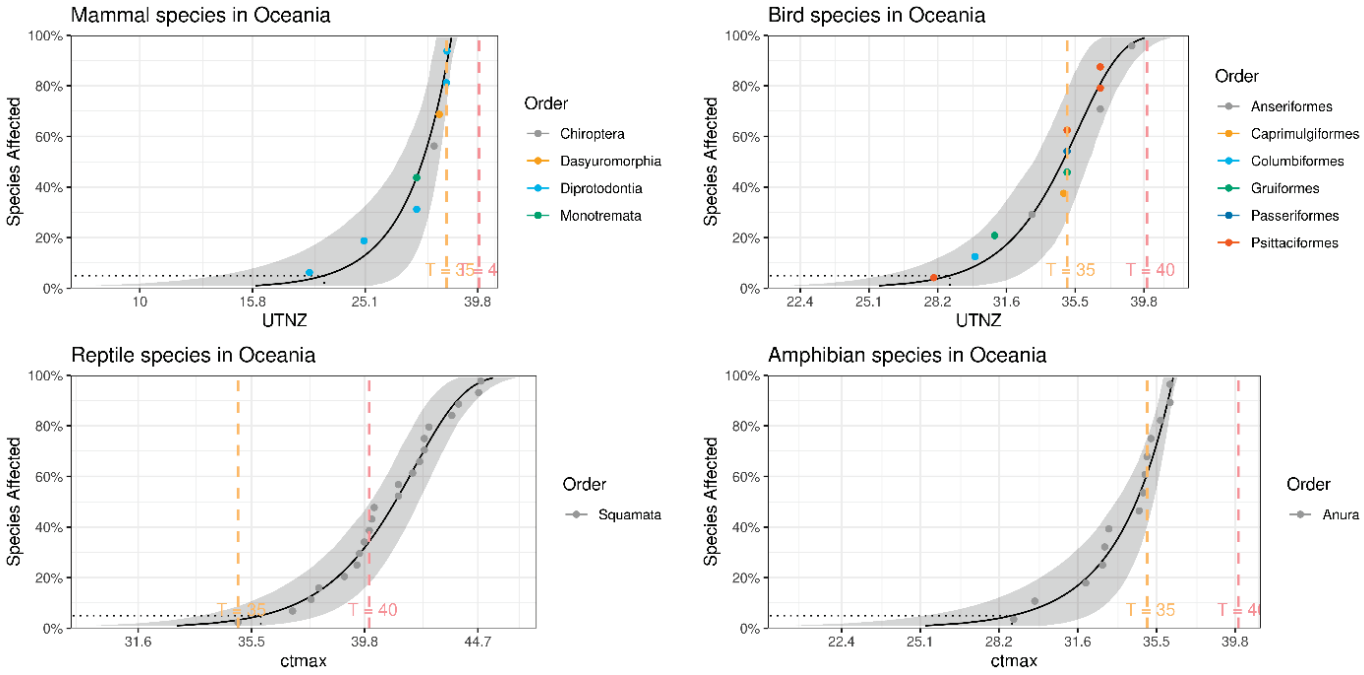

Figure 5. The Species Sensitivity Distributions for Oceania. The UTNZ and CT_{max} SSD–response relationship of invertebrate and vertebrate species is shown as sigmoid curves [40]. The percentage of affected species at temperature (°C) is represented by the solid black line, with the model-averaged 95% confidence interval indicated by the shaded band, and the 5% affected species threshold by the black dotted line. In 2100, in Oceanian sites, the ambient temperatures are projected to exceed 35 °C for 0 and 14 days (SSP1) and 0 and 41 days (SSP5), and to exceed 40 °C for 0 and 1 days (SSP1) and 0 and 7 days (SSP5). Note that large group of species show high sensitivity to extreme temperatures, which are projected to occur frequently only in East Australia in 2100.

In Oceanian sites, extreme warm days are only projected to occur in Tomago Wetland (Table 4), while many species have a thermal-tolerance level below 35 °C (Figure 5 and Table 4). Temperatures exceed 35 °C on 14 (SSP1) to 41 days (SSP5) and temperatures exceed 40 °C during 1 (SSP1) to 7 days (SSP5). Approximately 90% of mammals and 55% of birds have a UTNZ below 35 °C and approximately 60% of amphibians have a CT_{max} below 35 °C. In total, 100% of these species have a temperature tolerance below 40 °C.

The outcome of correlating the current biodiversity threats with the projections of changing bioclimatic pressures mean annual temperature, max 5-day precipitation, and droughts (CCD) gives no clear positive correlations among all sites considered on a global scale (Table 5). However, on regional scales, moderate (rho > 0.4), strong (rho > 0.6), and very strong (rho > 0.8) positive correlations were found for precipitation and drought among European NbS sites and future climate zones Cfa (North America and Oceania) and Cfb (Europe). Positive correlations highlight an imbalance in the climate pressures of concern, where biodiversity in some sites, per continent or climate zone, stand to be particularly vulnerable and exceptionally influenced under the considered projected intensifying climate conditions. For instance, in Europe, drought is projected to intensify, particularly in NbS sites where biodiversity shows sensitivity to droughts (rho (6) = 0.78, $p = 0.06$)—as is the case for the Medway Catchment and Het Zwin.

3.3. The Effect of Intensifying Climatic Conditions on Ecosystems as a Whole

The effect of heat stress among species was integrated with food-web interactions based on the percentage estimates of species affected by heat stress (Figure 6). This assessment aims to indicate what percentage of a certain species group stands to be at risk and potentially removed from the food-web dynamics, or at least significantly reduced. The majority of potentially affected food-web interactions exist amongst the higher trophic levels. These extreme temperature pressures are indicative of a dramatic decline in species by limiting food-web interactions and, potentially, overall biomass. Extinction events are seldom reversible without considerable conservation efforts; if caused by persistent and increasingly severe climactic pressures, reversibility or mitigation is highly unlikely. This highlights that through heat waves, a reduction in the number of species and trophic levels is realized, which has a direct impact and influence on the number of key species characteristics.

In Oceanian sites, considerable impacts on biodiversity are caused by extreme temperatures, based on the UTTL-SSD curves and IUCN data. However, drought and habitat shifting and alteration also have a profound impact on the populations of birds, mammals, and amphibians. Multiple species experience a cumulative risk of extreme temperatures and drought, namely, species of the genus bat *Vespadelus*, frog *Pseudophryne*, and pigeon *Hemiphaga*, based on the UTTL-SSD and IUCN data assessments, and the bird species *Larus bulleri*, koala *Phascolarctos cinereus*, and bat *Pteropus poliocephalus*, based on the IUCN data assessment. In North America and Europe, UTTL-SSD and IUCN datasets showed no matching species or genus. Based on the IUCN dataset, in North America, cumulative impact by extreme heat and drought did exist for mollusks *Cyclonaias tuberculate*, *Lampsilis cariosa*, *Ligumia recta*, and *Margaritifera margaritifera*, and the skunk *Mephitis mephitis*. In European sites, heat and drought impact the bats *Eptesicus serotinus*, *Myotis nattereri*, *and Plecotus auratus*, and mollusk *Margaritifera margaritifera*.

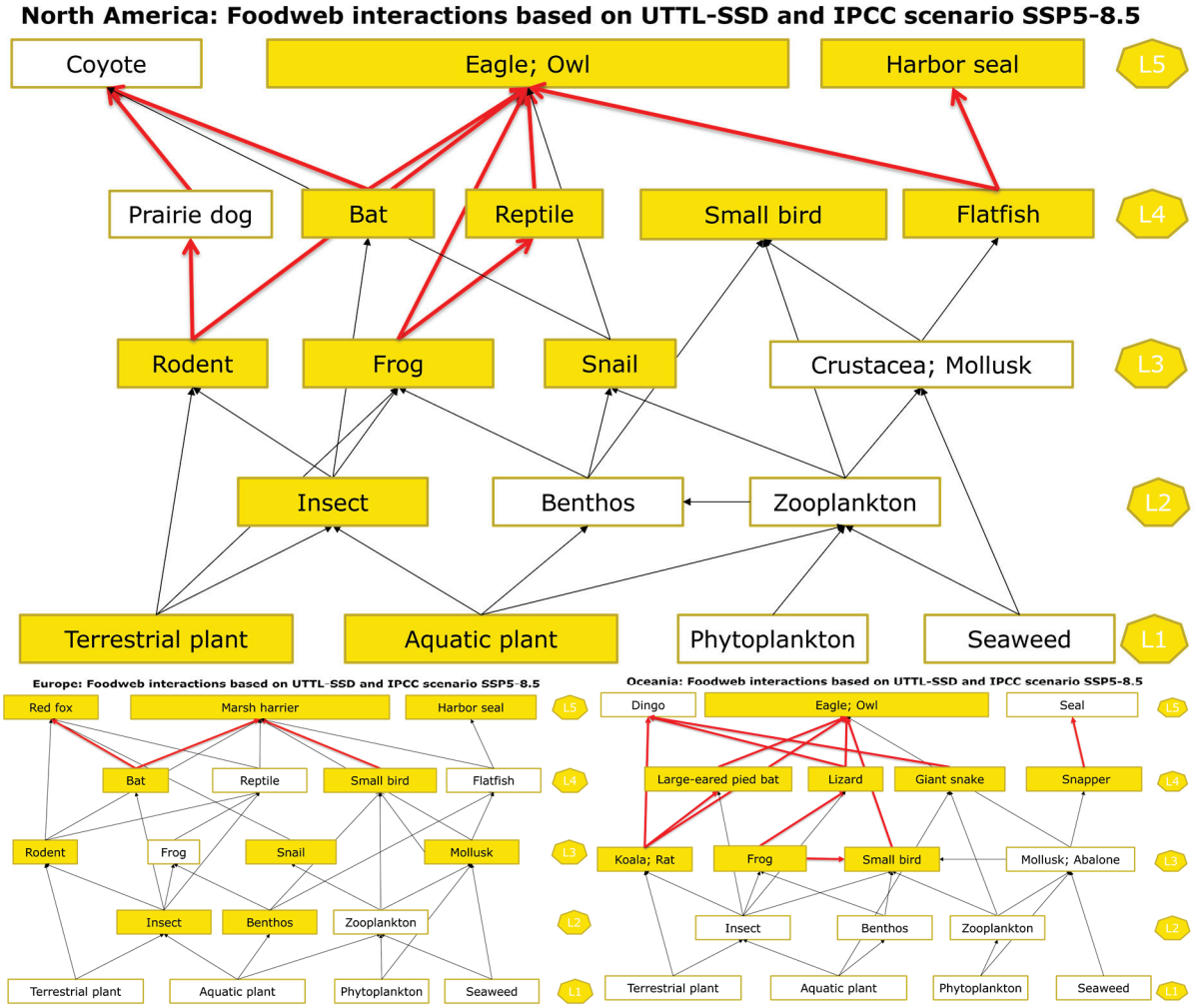

Figure 6. Visualization of food-web interactions at risk among key species groups in North America (**top**), Europe (**bottom left**), and Oceania (**bottom right**). Arrows show predator–prey interactions, with red arrows indicating prey is under pressure due to extreme temperatures. Thresholds result from extreme temperature IPCC projections for 2081–2100 under scenario SSP5-8.5 and UTTL-SSD response relationships. Species groups without UTTL-SSD data are shown in white.

4. Discussion

When considering the effects of changing climatic conditions in NbS sites, one should not only look at the multiple scales that the impacts of climate change have on biodiversity, but also the consequences that the cumulative impacts have in relation to increasing climate pressures on ecosystems. These bioclimatic changes are also dependent on the behavioral and evolutionary mechanisms of species, available connectivity to other habitats, species interactions, and range shifts in the environment that are impacting ecosystems [9]. These shifts in ecosystems, coupled with habitat degradation induced by phenomena such as sea level rise, wildfires, alterations in stream temperature, and shifts in species distributions, pose significant challenges and impose significant stressors [7,8,10,12].

The aim of this publication is to assess the risks posed to biodiversity from referenced IPCC scenarios in response to climate change, utilizing key species-sensitivity indicators and variables. In doing so, we address how climate-change-driven bioclimatic pressures may affect biodiversity based on the IPCC-IUCN-profiles and using the UTTL-SSD response relationship for species groups. Ref. [60] expresses a need to use climate change projections to take action on heat waves, extreme precipitation events, and extreme droughts, a claim reaffirmed through this body of work. However, a novel point of concern that has been raised is how are NbS nature-conservation management plans integrating climate change

and impact scenarios in the context of biodiversity? Using these relationships and their impacts in medium- and long-term projections would be needed to support or inform the conservation of (potentially) threatened species in the face of climate pressures. This study highlights the fact that the conservation of these species in the currently denoted NbS sites may not be possible.

Models have been developed to provide response profiles and quantify the impacts of bioclimatic pressures on species distribution [61]. These response profiles are considered "fingerprints", and are indicative of which species are affected by changing subsets of climate pressure variables and which are not [35]. Ref. [62] have suggested that conservation plans need to explore the relationships between biodiversity and ecosystem dynamics in response to climate extremes to understand the implications of systems being disrupted by periodic extreme events. To do so, further emphasis is needed on the development or larger applications of predictive models that consider the interactions between atmospheric processes, behavioral and migration patterns, and ecosystems. Such coupled models would allow for a prediction of the effectiveness of niche-model interventions over alternative frameworks for site-specific investigations, thereby building resilience and allowing for more comprehensive predictions of climate change's impacts on ecosystems [25,63,64].

Previous studies have shown that the relative proportion of species threatened, from the IUCN Red List in combination with IUCN predictors, is a relevant indicator to assess climate change effects on bioclimatic variables and biodiversity. However, most studies were not conducted for NbS sites over multiple transects based on climate zones. In our study, the global IPCC climate projections are coupled to today's IUCN biodiversity threats to enhance understanding regarding the effectiveness of applying NbSs for climate adaptation and biodiversity conservation. The method of migrating species to support or replace declining population structures is not analyzed within the scope of this study; however, it will likely play a significant role in shifting populations and replacing those no longer suited to certain regions. An analysis on foreign species migrating due to shifting habitats and suitability ranges is outside of the scope of this research, as to gather this information would require a critical analyses into food-web dynamics and the supplantation of endemic species, potentially leading to structural and functional shifts in ecological composition. This shifting of biomes has been cited to result in waves of what would now be considered as invasive species and drastic alterations to food webs, especially in 2080–2100 timelines.

4.1. NbS Nature-Conservation Management Planning

The BBI model incorporates projections on future bioclimatic pressures through species threat profiles that show species vulnerabilities based on empirical research, as well as UTTL-SSD response relationships, to highlight species tipping points for temperature extremes, highlighting bioclimatic pressures that need to be the focal point of nature conservation planning. In North American sites, climate conditions are projected to transition from a humid continental climate to a more humid subtropical climate. Temperatures are expected to increase by 2 °C to 7 °C, with a higher frequency of heat waves. Biodiversity in four NbS sites is especially threatened by heatwaves, particularly for species of higher trophic levels, with heat stress significantly affecting approximately 60% of mammals, 50% of birds, and 45% of amphibians for durations ranging from 5 to 84 days per year from 2080. Additionally, the intensification of droughts and precipitation events, habitat shifts and alterations, and the cumulative effects thereof, pose significant threats to mammals and birds, among other species. Examination of the nature-conservation management plans of the North American NbS sites reveals a significant deficiency in planning for increased resilience to rising temperatures, precipitation, and drought [30], indicating a need for substantial improvements.

In Oceanian sites, climate conditions are projected to shift from a temperate oceanic climate to a more subtropical climate. Frequent heatwaves are expected, as well as intensified precipitation events, particularly in the NbS site in New Zealand. Biodiversity in two NbS case studies, again mainly those of higher trophic levels, faces considerable

threats from heatwaves, with heat stress affecting approximately 90% of mammals, 55% of birds, and 60% of amphibians significantly for durations of 14 to 41 days annually, from 2080. Furthermore, the intensification of droughts, precipitation events, and habitat shifts and alterations, along with cumulative effects, threatens birds and mammals, among other species. While nature conservation management plans for the Oceanian NbS sites in this region do address these concerns and aim to enhance resilience to increasing bioclimatic pressures, the potentially high percentage of species that will experience heat stress remains alarming.

In European sites, climate conditions are projected to remain relatively stable, with only the Klarälven Varmland site experiencing a shift from a humid continental climate to a more temperate oceanic climate. However, droughts and precipitation events are expected to intensify. While birds and mammals in this region are sensitive to heat waves, such events will remain rare in the European sites. Biodiversity is nonetheless sensitive to temperature increases, and the intensification of droughts, precipitation events, and habitat shifts and alterations pose threats to birds, mammals, and mollusks. Examination of the nature conservation management plans for the European NbS sites indicates that there are strategies in place to address concerns related to increasing temperatures, precipitation, and habitat shifts. However, there is a notable lack of planning to enhance resilience to intensifying droughts, necessitating significant improvements in these areas.

4.2. Effects of Temperature Rise on Biodiversity

There is a realistic chance that, even under the most ambitious action scenario SSP1-1.9, global warming will exceed 1.5 °C in the next decade; even 2 °C is within reach, based on emissions scenarios SSP3-7.0 and SSP5-8.5 [65,66]. However, the IPCC projects additional extreme warming hereafter. NbS sites are widely applied as a climate adaptation strategy; however, they are not always applied in an effective manner, and often only in the consideration of floods. Some studies have used global datasets, with a temporal resolution including historical periods and extending to future time horizons by including a post-processing of climate simulations [67]. We have shown that biodiversity is threatened due to more frequent extreme temperatures, based on the UTTL-SSD response relationship, temperature projections under scenarios SSP1-2.6 and SSP5-8.5, and empirical data on species threats.

Many species groups that are threatened by projected extreme-temperature conditions reside in higher trophic levels (Figure 6), potentially destabilizing the balance of food webs and consequently reducing ecosystem self-regulation and increasing the risk of biodiversity loss. Further intensive investigations on the effects of climate change and resulting probabilistic redistributions of ecosystems and habitats on Earth would be useful to study the multi-scale implications of climate impact responses. Based on such studies, as we demonstrated in our examples, the internal UTTL-SSD response relationship can be related to habitat-based SSDs for ecological risk assessment of global-warming-induced tipping points.

Ref. [68] suggest that disruptions to ecological assemblages caused by climate change will be abrupt, and the result of resilience breakdowns. Within any given ecological assemblage, the exposure of most species to climate conditions beyond their realized niche limits occurs almost simultaneously. Based on our study of the biodiversity assemblages, biodiversity threats and projections for bioclimatic projections suggest serious biodiversity breakdowns within several ecosystems in North America and East Australia, which is further substantiated with the UTTL-SSD response relationships. The impact may be undervalued due to the cumulative effects of extreme temperature and droughts on biodiversity in combination with habitat alterations.

4.3. Cumulative Impacts on Biodiversity

The striking conclusions based on the UTTL-SSD response relationship can be seen as a metaphor for the sensitivity of the species, linked to other extreme weather events. Our

study highlights the need for research on species tipping points for the climate pressures of droughts, extreme precipitation, and sea level rise. Changing climate conditions are caused by a chain of effects and compounding bioclimatic pressures [14], such as changes in temperature and the water cycle. However, there is no empirical evidence for biodiversity showing a tipping response to all environmental drivers; trying to formulate or suggest a "manageability" that is, in fact, not feasible is still advised in many cases, and is adverse to conservation targets [69]. The applied BBI model shows the temporal changes in composition and the spatial changes in the UTTL-SSD response relationship of climate zones. By using the UTTL-SSD response relationship in the climate Köppen–Geiger zones, the number of affected species interactions in an ecological ecosystem may be clarified. Still, because of the cumulative bioclimatic and anthropogenic pressure on biodiversity, the species tipping response will be hard to pinpoint.

Sensitive species are often negatively impacted, due to cumulative bioclimatic pressures, as seen in North American and East Australian sites, where climate zones shift from humid continental climate conditions to a more humid subtropical climate. The impact is most notably felt by populations of amphibians, birds, mammals, and fish, placing these at high risk of impacts resulting from habitat changes. This is especially pronounced for the Tomago Wetland, as it shows high percentages of threatened species. As sensitive species are exposed to risks caused by extreme high temperature and further so by cumulative effects, these shifts are expected to have reasonable impacts on multiple populations.

It is reasserted that tropical ecosystems are most vulnerable to climate change. In these climate zones, temperature shifts have been identified as a key tipping point and trigger for amphibian, bird, and mammal decline, while thresholds may be exceeded for cumulative effects of hot days above 35 °C during prolonged periods of drought. Drought-adaptation condition mechanisms exist in the combination of ecological processes, physiological strategies, and morphological habitat changes [22,70]. However, when droughts, extreme temperature, and heatwaves occur together, biodiversity elements show considerable differences regarding drought tolerance and species mortality throughout the food web [71–74].

5. Conclusions

This paper illustrates the benefits of integrating IPCC climate change pathways with IUCN biodiversity threats and upper thermal-tolerance levels for a range of species groups. It demonstrates that doing so enhances the degree to which climate resilience is considered in nature conservation planning for NbS sites and can highlight issues with implementation strategies for medium- and long-term periods. By applying the Bioclimatic–Biodiversity Impact model, the causal relationship between extreme ambient temperature exposure level and the level of effect on individual species can be explored. In doing so, a compelling explanation of how climate change affects species can be developed. The bioclimatic projections suggest serious biodiversity breakdowns within several ecosystems in North American and East Australian NbS sites under scenarios SSP1-2.6 and SSP5-8.5 in 2081–2100. This is further substantiated with the analysis conducted using the UTTL-SSD response relationships and the future climate predictions for these regions. The UTTL-SSD response to extreme ambient temperature has been identified as a key tipping-point trigger for many species of amphibians, birds, and mammals in their respective food webs. The UTTL-SSD responses can be used to highlight potential risk among trophic levels in food web structures. Our results indicated the potential destabilization of food webs, particularly links within the higher trophic levels. To better align the ambitions and conservation targets of NbS sites, NCM plans must better consider the multiple pressures on the horizon resulting from climate change and the pending crises related to this. NCM plans that seek to protect threatened species cannot effectively do so without the incorporation of coupled stressors represented in various policy pathways, and focusing on those pathways remains realistic, despite current levels of action or inaction. Further investigations are needed regarding the effects and tipping points for climate pressures (e.g., drought) on biodiversity and the resulting probabilistic redistributions of ecosystems and habitats on Earth.

Author Contributions: Conceptualization, C.A.S. and T.W.H.; methodology, C.A.S. and T.W.H.; formal analysis, C.A.S. and T.W.H.; investigation, C.A.S. and T.W.H.; writing—original draft preparation, C.A.S., T.W.H. and A.Z.; writing—review and editing, C.A.S., T.W.H. and A.Z. All authors have read and agreed to the published version of the manuscript.

Funding: This research received no external funding.

Data Availability Statement: The data presented in this study are openly available in Tables 3 and 4.

Acknowledgments: This paper benefited greatly from discussions evaluating the sustainable measures with RWS colleagues in the EU Interreg Cluster for Cloud to Coast Climate Change adaptation (C5a). We are grateful to Vincent Escaravage (WMR) for advising with the statistical PDA and Alicia Hamer (WMR) for supporting with the sigmoidal curve fit. We would like to thank the collegial Gerben Dekker (RWS) and Berry Gersonius, as well as the external contributors, for their time devoted to this manuscript, because we feel their comments helped to improve the quality of the manuscript.

Conflicts of Interest: The authors declare no conflicts of interest.

Appendix A

Table A1. Overview of climate change impact on biodiversity used to assess climate change impacts in geographical areas. Different policy strategies and abiotic factors are realized in Asia, Africa, Europe, America, and Australia, respectively.

Reference	[7]	[8]	[75]	[76]	[9]	[10]	[11]	[12]
Geographical area	Europe	America	Europe, America, New Zealand, and Australia	Global	North America	Asia, Africa, Europe, America, and Australia	Global	Australia
Site	Mediterranean	Canada, North America, and Mexico	Global distribution of seaweed Undaria	Global oceans	Columbia river	Earth observation data and hydrodynamic modelling	Global	New South Wales, Australian Capital Territory, Victoria, Queensland, South, Western Australia, and Tasmania
Policy strategy	Intergovernmental Panel on Climate Change's (IPCC)	RAMSAR Wetlands	Managing marine NIS	Consistency of fisheries and marine ecosystem models (MEMs)	National Climate Assessment (NCA), 4th National Climate Assessment	I Insight into the total potential cost reduction of these Nature-based Solutions	Global Climate change, biodiversity loss, and food security	Forest Fire Danger Index (FFDI)
Framework	AOGCM simulation model	Johnson wetland simulation model	NIS management plan	Empirical data simulation model	Ecosystems, ecosystem services, and biodiversity	Model study of wave–vegetation interaction	Review	Continuous Haines index model
Period studied	1960–1989/ 2070–2099	1980–2004	1971–2016	1970–2005	Literature review 1991–2019	1997– 2017	None	1930–2019
Bioclimate indicators	Temperature and precipitation	Temperature and sea-level rise	Temperature	Increasing temperature	Warming stream temperature	Waves	Temperature	Temperature, rainfall, and soil moisture

Table A1. *Cont.*

Reference	[7]	[8]	[75]	[76]	[9]	[10]	[11]	[12]
Abiotic impact factors	Mediterranean climate extent (MCE) information	Coastal storm, changes in local precipitation and in humidity	Salinity, light, day length, nutrients, and wave exposure	No information	Temperature, acidification, drought, increasing CO_2, N_2 deposition, precipitation, water balance, sediment deposition, oxygen level, and stratification	Reduce wave impact	Reduce global cereal production	Including wind speed, humidity, fuel moisture deficit, and rainfall
Habitat loss and fragmentation	All terrestrial biomes	Coastal marshes	No information	No information	Climate change ecosystem impact	Data from salt marshes and mangrove map	Climate-change-driven migration, gene flow, and habitat fragmentation	Forest ecosystems
Biodiversity im-pact/changes in	Habitat loss	No information	May be driving ecosystem change in environments	Decreasing primary production; decrease of biomass fish stocks	Growth changes in invertebrates and vertebrates, genetic changes, changes in primary production, and changes in food web.	Salt marshes or mangrove vegetation	geographical distributions of species and ecosystems, and species range shifts	vegetation, biomass, and litter fractions of forested areas
Pollution, Nutrient loading and acidification	No information	water pollution from upstream	Growth of sporophyte and gametophyte stages is positively related to nutrients	No information	Affecting water quality	No information	Reduce the availability of water for crop	No information
Assessment	Quantitative of AOGCMs under multiple emissions scenarios	Quantitative	Qualitative	Quantitative	Qualitative literature review	Quantitative Sentinel-2 A and Landsat-8 images	None	Multivariate regression analysis

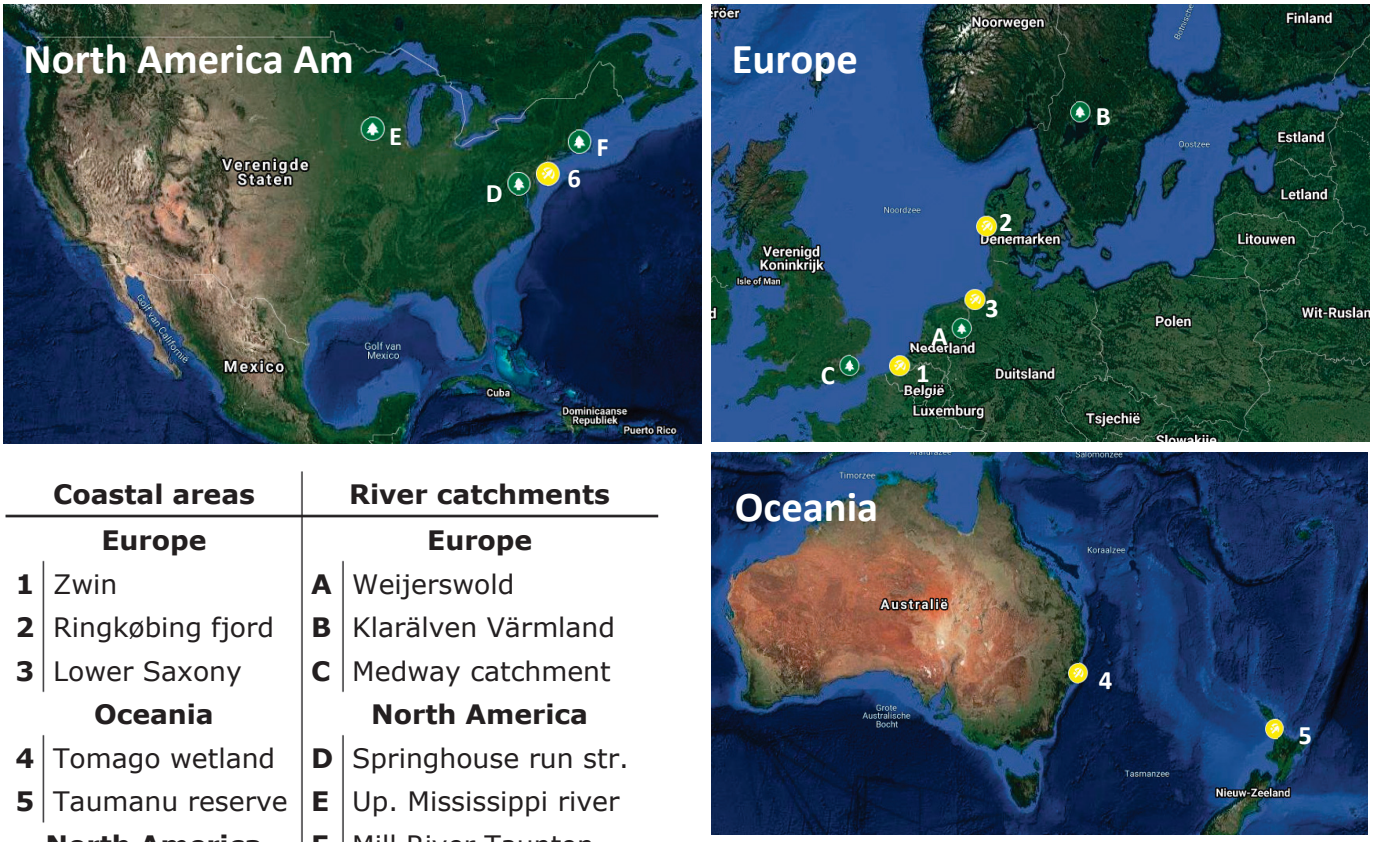

Coastal areas		River catchments	
Europe		**Europe**	
1	Zwin	**A**	Weijerswold
2	Ringkøbing fjord	**B**	Klarälven Värmland
3	Lower Saxony	**C**	Medway catchment
Oceania		**North America**	
4	Tomago wetland	**D**	Springhouse run str.
5	Taumanu reserve	**E**	Up. Mississippi river
North America		**F**	Mill River Taunton
6	Long Beach		

Figure 1. Overview of the NbS sites considered in this publication. The set consists of six coastal areas from Europe, Oceania, and North America, and six river catchments from Western Europe and North America.

Table 2. The IUCN direct threats to species with the threat description and examples. These data are used to assess vulnerability of biodiversity in sites for specific threats. IUCN direct threats will be linked to bioclimatic variables and their projected change according to the IPCC variables, to analyze potential threats of biodiversity loss.

IUCN Direct Threats	Threat Description	Linked IPCC Bioclimatic Variable
Temperature extremes	Periods in which temperatures exceed or go below the normal range of variation due to heat waves, cold spells, oceanic temperature changes, etc.	Mean annual temperature
Storms and flooding	Extreme precipitation and/or wind events, due to multiple types of storms.	Max 5-day precipitation
Droughts	Periods in which rainfall falls below the normal range of variation due to severe lack of rain, loss of surface water sources, etc.	Consecutive dry days
Habitat shifting and alteration	Major changes in habitat composition and site due to sea level rise, desertification, etc.	Sea level rise

Table 3. Below, the IPCC model data on the bioclimatic conditions across NbS sites in Europe are detailed. Data are given for the periods 1850–1900 for temperature mean and 1995–2014 for precipitation and drought. CMIP6 model data with projections under the SSP1-2.6 and SSP5-8.5 scenarios are given for the periods 2021–2024 for temperature extremes and 2081–2100 for all climatic variables.

			Europe					
	Europe		**Het Zwin**	**Ringkøbing Fjord**	**Lower Saxony**	**Weijerswold**	**Klarälven Varmland**	**Medway Catchment**
Temperature change			Temperature mean: (annual) change in °C (rel. to baseline)					
	1850–1900	Baseline	10.13	8.31	8.73	9.06	3.53	10.21
	2081–2100	SSP1-2.6	1.88	1.92	1.99	2.00	2.59	1.77
		SSP5-8.5	4.59	4.53	4.77	4.89	6.14	4.44
			Temperature extremes: Number of days > **35** °C					
	2021–2040	SSP1-2.6	0.04	0.00	0.29	0.75	0.10	0.13
		SSP5-8.5	0.04	0.00	0.40	0.79	0.16	0.16
	2081–2100	SSP1-2.6	0.05	0.00	0.53	0.99	0.19	0.20
		SSP5-8.5	1.17	0.00	3.98	9.00	3.99	3.91
			Temperature extremes: Number of days > **40** °C					
	2021–2040	SSP1-2.6	0.00	0.00	0.00	0.01	0.00	0.00
		SSP5-8.5	0.00	0.00	0.00	0.01	0.00	0.00
	2081–2100	SSP1-2.6	0.00	0.00	0.02	0.04	0.00	0.00
		SSP5-8.5	0.03	0.00	0.42	1.53	0.42	0.16
Change in water cycle			Precipitation (max 5 day): in % (rel. to baseline)					
	1995–2014	Baseline	56.18	57.28	54.83	54.85	53.68	52.74
	2081–2100	SSP1-2.6	3.40	5.43	7.47	4.68	6.48	6.70
		SSP5-8.5	14.16	15.20	17.08	15.31	14.88	19.78
			Drought (CDD): in days (rel. to baseline)					
	1995–2014	Baseline	20.61	21.27	19.65	19.24	18.81	22.22
	2081–2100	SSP1-2.6	0.69	0.69	0.56	0.28	0.95	2.08
		SSP5-8.5	6.49	3.99	4.25	4.49	1.44	8.49
			Sea level rise (in meters)					
	2081–2100	SSP1-2.6	0.43	0.42	0.43	*River areas*		
		SSP5-8.5	0.68	0.67	0.68			

Colors indicate the level of change relative to global values. Values under percentile (p) 25 are indicated in green, values between p25 and p75 in yellow and above p75 in red. Drought-specific values in between the positive and negative median are indicated in green, and values larger than p90 and smaller than p10 are indicated in red, and values in between in yellow.

Table 4. IPCC model data on the bioclimatic conditions across NbS sites in North America and Oceania are provided below. The data considered are mean temperature for 1850–1900 and precipitation and droughts for 1995–2014. CMIP6 model data with projections under the SSP1-2.6 and SSP5-8.5 scenarios are provided for the periods 2021–2024 in the context of temperature extremes and 2081–2100 for all climatic variables. Colors indicating the same percentile are coded as detailed in Table 3.

	North America & Oceania		Oceania			North America		
			Tomago Wetland	**Taumanu Reserve**	**Long Beach Island**	**Springhouse Runs Str.**	**Upper Mississippi River**	**Mill River Taunton**
Temperature change			Temperature mean: (annual) change in °C (rel. to baseline)					
	1850–1900	Baseline	17.33	15.62	13.03	13.16	8.50	10.70
	2081–2100	SSP1-2.6	1.89	1.61	2.29	2.37	2.78	2.44
		SSP5-8.5	4.72	4.14	5.74	5.84	6.99	5.97
			Temperature extremes: Number of days > **35** °C					
	2021–2040	SSP1-2.6	10.03	0.00	13.39	20.92	10.55	3.56
		SSP5-8.5	11.19	0.00	14.72	23.60	11.81	3.95
	2081–2100	SSP1-2.6	14.47	0.00	16.31	24.92	13.82	5.19
		SSP5-8.5	41.00	0.03	60.66	84.68	66.02	33.61
			Temperature extremes: Number of days > **40** °C					
	2021–2040	SSP1-2.6	0.68	0.00	0.83	0.94	0.56	0.11
		SSP5-8.5	0.65	0.00	0.91	1.30	0.70	0.18
	2081–2100	SSP1-2.6	1.02	0.00	1.14	1.57	0.99	0.25
		SSP5-8.5	7.22	0.00	12.24	21.54	18.99	5.49
Change in water cycle			Precipitation (max. 5 day): in % (rel. to baseline)					
	1995–2014	Baseline	115.04	104.30	109.98	106.10	85.54	101.58
	2081–2100	SSP1-2.6	−0.21	6.00	5.83	5.23	5.95	7.52
		SSP5-8.5	12.82	15.83	19.57	17.42	21.51	19.62
			Drought (CDD): in days (rel. to baseline)					
	1995–2014	Baseline	24.96	18.09	15.51	16.27	18.62	15.27
	2081–2100	SSP1-2.6	−1.51	0.15	0.12	−0.20	0.36	0.61
		SSP5-8.5	1.08	0.64	1.74	1.19	1.44	2.85
	Sea level rise (in meters)							
	2081–2100	SSP1-2.6	0.39	0.39	0.69	*River areas*		
		SSP5-8.5	0.70	0.70	0.97			

Colors indicate the level of change relative to global values. Values under percentile (p) 25 are indicated in green, values between p25 and p75 in yellow and above p75 in red. Drought-specific values in between the positive and negative median are indicated in green, and values larger than p90 and smaller than p10 are indicated in red, and values in between in yellow.

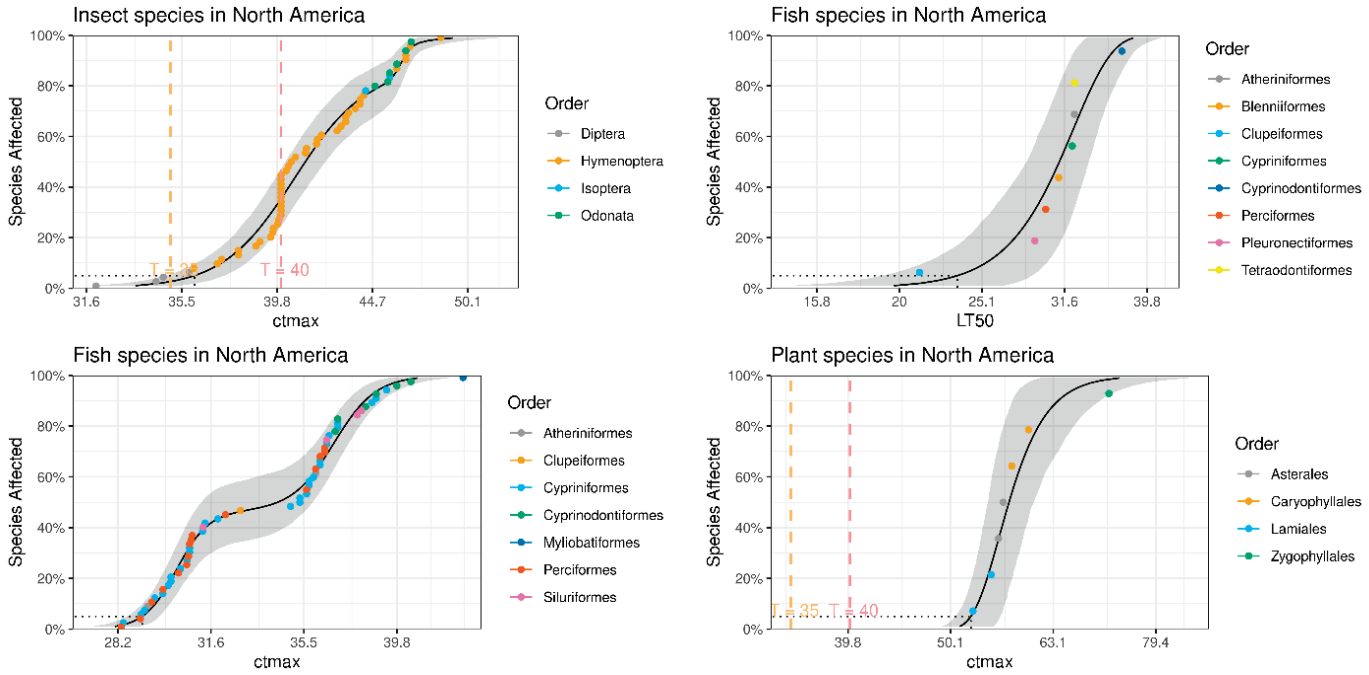

Figure 2. The Species Sensitivity Distributions for North America are presented below. The CTmax- and LT50-SSD response relationships for invertebrates, vertebrates, and plant species are shown as sigmoid curves [40]. The percentage of affected species at temperature (°C) is represented by the solid black line, with the model-averaged 95% confidence interval indicated by the shaded band, and the 5% affected species threshold by the black dotted line. In 2100, in North America, the ambient temperatures are projected to exceed 35 °C for 5–25 days (SSP1) and 33–85 days (SSP5) and to exceed 40 °C for 0–2 days (SSP1) and 5–22 days (SSP5). Note that groups of species, such as reptiles and insects, show high sensitivity to the extreme temperatures projected in 2100.

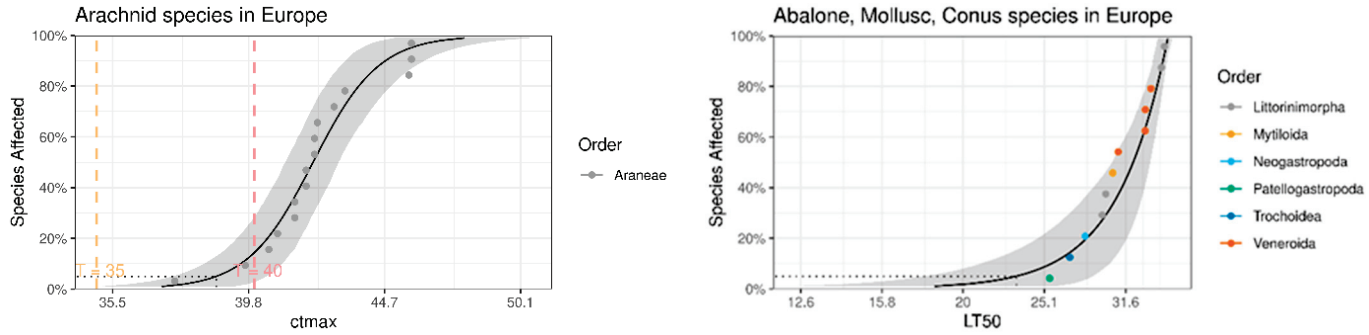

Figure 3. The Species Sensitivity Distributions for Europe are detailed below. The CTmax- and LT50-SSD response relationships for invertebrate species are shown as sigmoid curves [40]. The percentage of affected species at temperature (°C) is represented by the solid black line, with the model-averaged 95% confidence interval indicated by the shaded band, and the 5% affected species threshold by the black dotted line. In 2100, in Europe, the ambient temperatures are projected to exceed 35 °C for 0–1 days (SSP1) and 0–9 days (SSP5), and nearly never exceed 40 °C for 0 days (SSP1) and 0–2 days (SSP5). Note that while many species show high sensitivity to extreme temperatures, the projections for extreme temperature will be very uncommon in 2100.

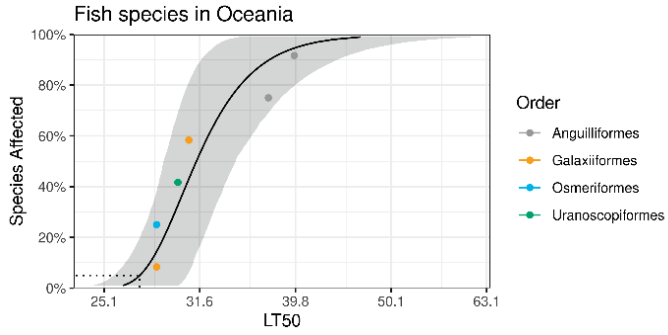

Figure 4. The Species Sensitivity Distributions for Oceania are detailed below. The LT50-SSD–response relationships for fish species are shown as sigmoid curves [40]. The percentage of affected species at temperature (°C) is represented by the solid black line, with the model-averaged 95% confidence interval indicated by the shaded band, and the 5% affected species threshold by the black dotted line. In 2100, in Oceanian sites, the ambient temperatures are projected to exceed 35 °C for 0 and 14 days (SSP1) and 0 and 41 days (SSP5), and to exceed 40 °C for 0 and 1 days (SSP1) and 0 and 7 days (SSP5).

Table 5. Spearman's correlation comparison between the number of IUCN species currently threatened and the corresponding IPCC projections of the climate pressure in 2100 for all Köppen–Geiger climate zones, continents, coastal areas, and river catchments, separately. Rho > 0.8 is considered a very strong correlation, rho > 0.6 is considered strong, and rho > 0.4 is considered moderate. Rho values > 0.4 are in bold.

IUCNxIPCC Correlation		**Temperature**		**Precipitation**		**Drought**	
		SSP1	SSP5	SSP1	SSP5	SSP1	SSP5
All	Rho	−0.396	−0.347	−0.289	0.218	0.086	0.385
n = 12	p	0.202	0.269	0.363	0.497	0.791	0.216
Climate Zones (Present)							
Cfb (n = 7)	Rho	0.000	0.164	0.164	**0.436**	0.327	**0.546**
	p	1.000	0.726	0.726	0.328	0.474	0.205
Dfa (n = 4)	Rho	−0.738	−0.738	−0.949	−0.105	−0.949	−0.105
	p	0.262	0.262	0.051	0.895	0.051	0.895
Dfb (n = 1)							
Climate Zones (Future)							
Cfa (n = 5)	Rho	0.100	**0.950**	−0.900	**0.900**	−0.900	**0.600**
	p	0.950	0.100	0.083	0.083	0.083	0.350
Cfb (n = 6)	Rho	**0.783**	−0.696	**0.406**	**0.638**	0.116	**0.783**
	p	0.066	0.125	0.425	0.173	0.827	0.066
Dfa (n = 1)							
Continents		**Temperature**		**Precipitation**		**Drought**	
EU (n = 6)	Rho	−0.783	−0.696	**0.406**	**0.638**	0.116	**0.783**
	p	0.066	0.125	0.425	0.173	0.827	0.066
NA (n = 4)	Rho	−0.738	−0.738	−0.949	−0.105	−0.949	−0.105
	p	0.262	0.262	0.051	0.895	0.051	0.089
OC (n = 2)							
Type							
Coastal (n = 6)	Rho	0.265	**0.530**	−0.265	0.088	−0.177	**0.618**
	p	0.312	0.280	0.612	0.868	0.738	0.191
Riverine (n = 6)	Rho	−0.841	−0.841	−0.232	0.058	0.058	**0.551**
	p	0.036	0.036	0.658	0.913	0.913	0.257

References

1. Pearce-Higgins, J.; Antão, L.; Bates, R.; Bowgen, K.; Bradshaw, C.; Duffield, S.; Ffoulkes, C.; Franco, A.; Geschke, J.; Gregory, R.; et al. A framework for climate change adaptation indicators for the natural environment. *Ecol. Indic.* **2022**, *136*, 108690. [CrossRef]
2. Pershing, A.J.; Alexander, M.A.; Hernandez, C.M.; Kerr, L.A.; Le Bris, A.; Mills, K.E.; Nye, J.A.; Record, N.R.; Scannell, H.A.; Scott, J.D.; et al. Response to Comments on "Slow adaptation in the face of rapid warming leads to collapse of the Gulf of Maine cod fishery". *Science* **2016**, *352*, 423. [CrossRef] [PubMed]
3. Jay, A.; Reidmiller, D.R.; Avery, C.W.; Barrie, D.; DeAngelo, B.J.; Dave, A.; Dzaugis, M.; Kolian, M.; Lewis, K.L.M.; Reeves, K.; et al. Overview. In *Impacts, Risks, and Adaptation in the United States: Fourth National Climate Assessment, Volume II*; Reidmiller, D.R., Avery, C.W., Easterling, D.R., Kunkel, K.E., Lewis, K.L.M., Maycock, T.K., Stewart, B.C., Eds.; U.S. Global Change Research Program: Washington, DC, USA, 2018; pp. 33–71. [CrossRef]
4. Vinagre, C.; Dias, M.; Cereja, R.; Abreu-Afonso, F.; Flores, A.A.; Mendonça, V. Upper thermal limits and warming safety margins of coastal marine species—Indicator baseline for future reference. *Ecol. Indic.* **2019**, *102*, 644–649. [CrossRef]
5. Fausnacht, D.W.; Kroscher, K.A.; McMillan, R.P.; Martello, L.S.; Baumgard, L.H.; Selsby, J.T.; Hulver, M.W.; Rhoads, R.P. Heat Stress Reduces Metabolic Rate While Increasing Respiratory Exchange Ratio in Growing Pigs. *Animals* **2021**, *11*, 215. [CrossRef] [PubMed]
6. Hallegatte, S.; Rogelj, J.; Allen, M.; Clarke, L.; Edenhofer, O.; Field, C.B.; Friedlingstein, P.; van Kesteren, L.; Knutti, R.; Mach, K.J.; et al. Mapping the climate change challenge. *Nat. Clim. Change* **2016**, *6*, 663–668. [CrossRef]
7. Klausmeyer, K.R.; Shaw, M.R. Climate Change, Habitat Loss, Protected Areas and the Climate Adaptation Potential of Species in Mediterranean Ecosystems Worldwide. *PLoS ONE* **2009**, *4*, e6392. [CrossRef]
8. Mitsch, W.J.; Hernandez, M.E. Landscape and climate change threats to wetlands of North and Central America. *Aquat. Sci.* **2013**, *75*, 133–149. [CrossRef]
9. Weiskopf, S.R.; Rubenstein, M.A.; Crozier, L.G.; Gaichas, S.; Griffis, R.; Halofsky, J.E.; Hyde, K.J.; Morelli, T.L.; Morisette, J.T.; Muñoz, R.C.; et al. Climate change effects on biodiversity, ecosystems, ecosystem services, and natural resource management in the United States. *Sci. Total. Environ.* **2020**, *733*, 137782. [CrossRef]
10. van Zelst, V.T.; Dijkstra, J.T.; van Wesenbeeck, B.K.; Eilander, D.; Morris, E.P.; Winsemius, H.C.; Ward, P.J.; de Vries, M.B. Cutting the costs of coastal protection by integrating vegetation in flood defences. *Nat Commun.* **2021**, *12*, 6533. [CrossRef]
11. Muluneh, M.G. Impact of climate change on biodiversity and food security: A global perspective—A review article. *Agric. Food Secur.* **2021**, *10*, 36. [CrossRef]
12. Canadell, J.G.; Meyer, C.P.; Cook, G.D.; Dowdy, A.; Briggs, P.R.; Knauer, J.; Pepler, A.; Haverd, V. Multi-decadal increase of forest burned area in Australia is linked to climate change. *Nat. Commun.* **2021**, *12*, 6921. [CrossRef] [PubMed]
13. Trégarot, E.; D'Olivo, J.P.; Botelho, A.Z.; Cabrito, A.; Cardoso, G.O.; Casal, G.; Cornet, C.C.; Cragg, S.M.; Degia, A.K.; Fredriksen, S.; et al. Effects of climate change on marine coastal ecosystems—A review to guide research and management. *Biol. Conserv.* **2024**, *289*, 110394. [CrossRef]
14. Rezaei, S.; Mohammadi, A.; Shadloo, S.; Ranaie, M.; Wan, H.Y. Climate change induces habitat shifts and overlaps among carnivores in an arid and semi-arid ecosystem. *Ecol. Inform.* **2023**, *77*, 102247. [CrossRef]
15. Todgham, A.E.; Stillman, J.H. Physiological Responses to Shifts in Multiple Environmental Stressors: Relevance in a Changing World. *Integr. Comp. Biol.* **2013**, *53*, 539–544. [CrossRef]
16. Rozen-Rechels, D.; Dupoué, A.; Lourdais, O.; Chamaillé-Jammes, S.; Meylan, S.; Clobert, J.; Le Galliard, J. When water interacts with temperature: Ecological and evolutionary implications of thermo-hydroregulation in terrestrial ectotherms. *Ecol. Evol.* **2019**, *9*, 10029–10043. [CrossRef]
17. Tripathy, K.P.; Mukherjee, S.; Mishra, A.K.; Mann, M.E.; Williams, A.P. Climate change will accelerate the high-end risk of compound drought and heatwave events. *Proc. Natl. Acad. Sci. USA* **2023**, *120*, e2219825. [CrossRef] [PubMed]
18. Bennett, J.M.; Sunday, J.; Calosi, P.; Villalobos, F.; Martínez, B.; Molina-Venegas, R.; Araújo, M.B.; Algar, A.C.; Clusella-Trullas, S.; Hawkins, B.A.; et al. The evolution of critical thermal limits of life on Earth. *Nat. Commun.* **2021**, *12*, 1198. [CrossRef]
19. Moore, J.C. Predicting tipping points in complex environmental systems. *Proc. Natl. Acad. Sci. USA* **2018**, *115*, 635–636. [CrossRef]
20. Sguotti, C.; Blöcker, A.M.; Färber, L.; Blanz, B.; Cormier, R.; Diekmann, R.; Letschert, J.; Rambo, H.; Stollberg, N.; Stelzenmüller, V.; et al. Irreversibility of regime shifts in the North Sea. *Front. Mar. Sci.* **2022**, *9*, 945204. [CrossRef]
21. Gunderson, A.R.; Stillman, J.H. Plasticity in thermal tolerance has limited potential to buffer ectotherms from global warming. *Proc. R. Soc. B Biol. Sci.* **2015**, *282*, 20150401. [CrossRef]
22. Vicente-Serrano, S.M.; Quiring, S.M.; Peña-Gallardo, M.; Yuan, S.; Domínguez-Castro, F. A review of environmental droughts: Increased risk under global warming? *Earth-Sci. Rev.* **2019**, *201*, 102953. [CrossRef]
23. Dezetter, M.; Le Galliard, J.-F.; Leroux-Coyau, M.; Brischoux, F.; Angelier, F.; Lourdais, O. Two stressors are worse than one: Combined heatwave and drought affect hydration state and glucocorticoid levels in a temperate ectotherm. *J. Exp. Biol.* **2022**, *225*, 243777. [CrossRef] [PubMed]
24. Clavero, M.; Villero, D.; Brotons, L. Climate Change or Land Use Dynamics: Do We Know What Climate Change Indicators Indicate? *PLoS ONE* **2011**, *6*, e18581. [CrossRef] [PubMed]
25. Chausson, B.; Turner, D.; Seddon, N.; Chabaneix, C.A.J.; Girardin, V.; Kapos, I.; Key, D.; Roe, A.; Smith, S.; Woroniecki, N.; et al. Mapping the effectiveness of Nature-based Solutions for climate change adaptation. *Glob Change Biol.* **2020**, *26*, 6134–6155. [CrossRef]

26. Aplet, G.H.; Mckinley, P.S. A portfolio approach to managing ecological risks of global change. *Ecosyst. Health Sustain.* **2017**, *3*, e01261. [CrossRef]
27. Aurelle, D.; Thomas, S.; Albert, C.; Bally, M.; Bondeau, A.; Boudouresque, C.; Cahill, A.E.; Carlotti, F.; Chenuil, A.; Cramer, W.; et al. Biodiversity, climate change, and adaptation in the Mediterranean. *Ecosphere* **2022**, *13*, e3915. [CrossRef]
28. Hoveka, L.N.; van der Bank, M.; Davies, T.J. Winners and losers in a changing climate: How will protected areas conserve red list species under climate change? *Divers. Distrib.* **2022**, *28*, 782–792. [CrossRef]
29. Jan, S.A.; Shinwari, Z.K.; Habib, N.; Ali, S.; Afridi, M.S.; Khan, M. Impact of Climate Change on Marine Biodiversity: Current Challenges and Future Perspectives. *Proc. Pak. Acad. Sci. B Pak. Acad. Sci. Life Environ. Sci.* **2023**, *60*, 29–47.
30. Hielkema, T.W.; Cor, A. Schipper, Berry Gersonius. Global nature conservation and the apparent ineffective adaptation to climate pressures. *Aquat. Ecosyst. Health Manag.* **2023**, *26*, 33–46. [CrossRef]
31. Schipper, C.A.; Dekker, G.; Visser, B.D.; Bolman, B.; Lodder, Q. Characterization of SDGs towards climate resilient coastal infrastructure: Sustainability performance and cross-linking cumulative consequences. *Sustainability* **2020**, *13*, 1560. [CrossRef]
32. Seneviratne, S.I.; Corti, T.; Davin, E.L.; Hirschi, M.; Jaeger, E.B.; Lehner, I.; Orlowsky, B.; Teuling, A.J. Investigating soil moisture—Climate interactions in a changing climate: A review. *Earth-Sci. Rev.* **2010**, *99*, 125–161. [CrossRef]
33. Zscheischler, J.; Westra, S.; Van Den Hurk, B.J.J.M.; Seneviratne, S.I.; Ward, P.J.; Pitman, A.; AghaKouchak, A.; Bresch, D.N.; Leonard, M.; Wahl, T.; et al. Future climate risk from compound events. *Nat. Clim. Change* **2018**, *8*, 469–477. [CrossRef]
34. Woolway, R.I.; Tong, Y.; Feng, L.; Zhao, G.; Dinh, D.A.; Shi, H.; Zhang, Y.; Shi, K. Multivariate extremes in lakes. *Nat. Commun.* **2024**, *15*, 4559. [CrossRef]
35. Beck, H.E.; Zimmermann, N.E.; McVicar, T.R.; Vergopolan, N.; Berg, A.; Wood, E.F. Present and future Köppen-Geiger climate classification maps at 1-km resolution. *Sci. Data* **2018**, *5*, 180214. [CrossRef]
36. Bridges, T.S.; Bourne, E.M.; King, J.K.; Kuzmitski, H.K.; Moynihan, E.B.; Suedel, B.C. *Engineering with Nature: An Atlas*; ERDC/EL SR-18-8; U.S. Army Engineer Research and Development Center: Vicksburg, MS, USA, 2018. [CrossRef]
37. Bridges, T.S.; Bourne, E.M.; Suedel, B.C.; Moynihan, E.B.; King, J.K. *Engineering with Nature: An Atlas, Volume 2*; ERDC SR-21-2; U.S. Army Engineer Research and Development Center: Vicksburg, MS, USA, 2021. [CrossRef]
38. Sayers, P.; Gersonius, B.; Özerol, G.; Nugraha, E.; Schipper, C.A. A Framework for Cloud to Coast Adaptation: Maturity and Experiences from across the North Sea. *Land* **2022**, *11*, 950. [CrossRef]
39. IPCC. Summary for Policymakers. In *Climate Change 2021: The Physical Science Basis Contribution of Working Group I to the Sixth Assessment Report of the Intergovernmental Panel on Climate Change*; Masson Delmotte, V., Zhai, A.P., Pirani, S.L., Connors, C., Péan, S., Berger, N., Caud, Y., Chen, L., Goldfarb, M.I., Gomis, M., et al., Eds.; Cambridge University Press: Cambridge, UK; New York, NY, USA, 2021; pp. 3–32. [CrossRef]
40. IUCN, 2019. The International Union for Conservation of Nature (IUCN) Red List of Threatened Species: Spatial Data. Available online: https://www.iucnredlist.org/resources/spatial-data-download (accessed on 18 February 2022).
41. Bennett, J.M.; Calosi, P.; Clusella-Trullas, S.; Martínez, B.; Sunday, J.; Algar, A.C.; Araújo, M.B.; Hawkins, B.A.; Keith, S.; Kühn, I.; et al. GlobTherm, a global database on thermal tolerances for aquatic and terrestrial organisms. *Sci. Data* **2018**, *5*, 180022. [CrossRef]
42. Posthuma, L.; Suter, G.W., II; Traas, T.P.; Species Sensitivity Distributions in Ecotoxicology. CRC Press, 2001. Available online: https://www.routledge.com/Species-Sensitivity-Distributions-in-Ecotoxicology/Posthuma-II-Traas/p/book/9781566705783 (accessed on 18 July 2023).
43. Schipper, C.A.; Rietjens, I.M.C.M.; Burgess, R.M.; Murk, A.J. Application of bioassays in toxicological hazard, risk and impact assessments of dredged sediments. *Mar. Pollut. Bull.* **2010**, *60*, 2026–2042. [CrossRef]
44. Gutiérrez, J.M.; RG Jones, G.T.; Narisma, L.M.; Alves, M.; Amjad, I.V.; Gorodetskaya, M.; Grose, N.A.B.; Klutse, S.; Krakovska, J.; Li, D.; et al. *Climate Change 2021: The Physical Science Basis. Contribution of Working Group I to the Sixth Assessment Report of the Intergovernmental Panel on Climate Change*; Masson-Delmotte, V.P., Zhai, A., Pirani, S.L., Connors, C., Péan, S., Berger, N., Caud, Y., Chen, L., Goldfarb, M.I., Gomis, M., et al., Eds.; Cambridge University Press: Cambridge, UK, 2021; In Press. Interactive Atlas. Available online: http://interactive-atlas.ipcc.ch/ (accessed on 8 March 2022).
45. Lange, S. Trend-preserving bias adjustment and statistical downscaling with ISIMIP3BASD (v1.0). *Geosci. Model Dev.* **2019**, *12*, 3055–3070. [CrossRef]
46. Bellard, C.; Leclerc, C.; Courchamp, F. Combined impacts of global changes on biodiversity across the USA. *Sci. Rep.* **2015**, *5*, 11828. [CrossRef]
47. Bellard, C.; Leclerc, C.; Leroy, B.; Bakkenes, M.; Veloz, S.; Thuiller, W.; Courchamp, F. Vulnerability of biodiversity hotspots to global change. *Glob. Ecol. Biogeogr.* **2014**, *23*, 1376–1386. [CrossRef]
48. Pottier, P.; Lin, H.Y.; Oh, R.R.; Pollo, P.; Rivera-Villanueva, A.N.; Valdebenito, J.O.; Yang, Y.; Amano, T.; Burke, S.; Drobniak, S.M.; et al. A comprehensive database of amphibian heat tolerance. *Sci. Data* **2022**, *9*, 600. [CrossRef]
49. Khaliq, I.; Hof, C.; Prinzinger, R.; Böhning-Gaese, K.; Pfenninger, M. Global variation in thermal tolerances and vulnerability of endotherms to climate change. *Proc. R. Soc. B Biol. Sci.* **2014**, *281*, 20141097. [CrossRef]
50. Compton, T.J.; Rijkenberg, M.J.; Drent, J.; Piersma, T. Thermal tolerance ranges and climate variability: A comparison between bivalves from differing climates. *J. Exp. Mar. Biol. Ecol.* **2007**, *352*, 200–211. [CrossRef]
51. Aldenberg, T.; Slob, W. Confidence Limits for Hazardous Concentrations Based on Logistically Distributed NOEC Toxicity Data. *Ecotoxicol. Environ. Saf.* **1993**, *25*, 48–63. [CrossRef]

52. Aldenberg, T.; Jaworska, J.S.; Traas, T.P. Normal species sensitivity distributions and probabilistic ecological risk assessment. In *Species Sensitivity, Distributions in Ecotoxicology*; Posthuma, L., Suter, G.W., II, Traas, T.P., Eds.; CRC Press: Boca Raton, FL, USA, 2002.
53. R Core Team. *R: A language and Environment for Statistical Computing*; R Foundation for Statistical Computing: Vienna, Austria, 2021. Available online: https://www.R-project.org/ (accessed on 10 September 2024).
54. Kemp, L.; Xu, C.; Depledge, J.; Ebi, K.L.; Gibbins, G.; Kohler, T.A.; Rockström, J.; Scheffer, M.; Schellnhuber, H.J.; Steffen, W.; et al. Climate Endgame: Exploring catastrophic climate change scenarios. *Proc. Natl. Acad. Sci. USA* **2022**, *119*, e2108146119. [CrossRef]
55. Cox, N.; Young, B.E.; Bowles, P.; Fernandez, M.; Marin, J.; Rapacciuolo, G.; Böhm, M.; Brooks, T.M.; Hedges, S.B.; Hilton-Taylor, C.; et al. A global reptile assessment highlights shared conservation needs of tetrapods. *Nature* **2022**, *605*, 285–290. [CrossRef]
56. Valdez, J.W.; Callaghan, C.T.; Junker, J.; Purvis, A.; Hill, S.L.L.; Pereira, H.M. The undetectability of global biodiversity trends using local species richness. *Ecography* **2023**, *2023*, e06604. [CrossRef]
57. Spearman, C. The Proof and Measurement of Association between Two Things. *Am. J. Psychol.* **1904**, *15*, 72–101. [CrossRef]
58. Rayner, T.S.; Pusey, B.J.; Pearson, R.G.; Godfrey, P.C. Food web dynamics in an Australian Wet Tropics river. *Mar. Freshw. Res.* **2010**, *61*, 909–917. [CrossRef]
59. Boonstra, R.; Andreassen, H.P.; Boutin, S.; Hušek, J.; Ims, R.A.; Krebs, C.J.; Skarpe, C.; Wabakken, P. Why Do the Boreal Forest Ecosystems of Northwestern Europe Differ from Those of Western North America? *BioScience* **2016**, *66*, 722–734. [CrossRef]
60. Griggs, D.; Stafford-Smith, M.; Warrilow, D.; Street, R.; Vera, C.; Scobie, M.; Sokona, Y. Use of weather and climate information essential for SDG implementation. *Nat. Rev. Earth Environ.* **2021**, *2*, 2–4. [CrossRef] [PubMed]
61. Araújo, M.B.; Luoto, M. The importance of biotic interactions for modelling species distributions under climate change. *Glob. Ecol. Biogeogr.* **2007**, *16*, 743–753. [CrossRef]
62. Mahecha, M.D.; Bastos, A.; Bohn, F.J.; Eisenhauer, N.; Feilhauer, H.; Hickler, T.; Kalesse-Los, H.; Migliavacca, M.; Otto, F.E.L.; Peng, J.; et al. Biodiversity and Climate Extremes: Known Interactions and Research Gaps. *Earth's Futur.* **2023**, *12*, e2023EF003963. [CrossRef]
63. Kearney, M. Habitat, environment and niche: What are we modelling? *Oikos* **2006**, *115*, 186–191. [CrossRef]
64. Buckley, L.B.; Carrington, E.; Dillon, M.E.; García-Robledo, C.; Roberts, S.B.; Wegrzyn, J.L.; Urban, M.C. Characterizing biological responses to climate variability and extremes to improve biodiversity projections. *PLOS Clim.* **2023**, *2*, e0000226. [CrossRef]
65. UN (2017a). *The Sustainable Development Goals Report*; United Nations: New York, NY, USA, 2017. Available online: https://unstats.un.org/sdgs/files/report/2017/TheSustainableDevelopmentGoalsReport2017.pdf (accessed on 20 January 2021).
66. IPCC. *Climate Change 2023: Synthesis Report Contribution of Working Groups I., II. and III to the Sixth Assessment Report of the Intergovernmental Panel on Climate Change*; Core Writing Team, Lee, H., Romero, J., Eds.; IPCC: Geneva, Switzerland, 2023; pp. 35–115. [CrossRef]
67. Noce, S.; Caporaso, L.; Santini, M. A new global dataset of bioclimatic indicators. *Sci. Data* **2020**, *7*, 398. [CrossRef]
68. Trisos, C.H.; Merow, C.; Pigot, A.L. The projected timing of abrupt ecological disruption from climate change. *Nature* **2020**, *580*, 496–501. [CrossRef]
69. Hillebrand, H.; Kuczynski, L.; Kunze, C.; Rillo, M.C.; Dajka, J.-C. Thresholds and tipping points are tempting but not necessarily suitable concepts to address anthropogenic biodiversity change—An intervention. *Mar. Biodivers.* **2023**, *53*, 43. [CrossRef]
70. Wang, C.; Li, Z.; Chen, Y.; Ouyang, L.; Li, Y.; Sun, F.; Liu, Y.; Zhu, J. Drought-heatwave compound events are stronger in drylands. *Weather. Clim. Extrem.* **2023**, *42*, 100632. [CrossRef]
71. Biber, M.F.; Voskamp, A.; Hof, C. Potential effects of future climate change on global reptile distributions and diversity. *Glob. Ecol. Biogeogr.* **2023**, *32*, 519–534. [CrossRef]
72. Lebreton, J.-D. The impact of global change on terrestrial Vertebrates. *Comptes Rendus Biol.* **2011**, *334*, 360–369. [CrossRef] [PubMed]
73. Okello, M.M.; Kenana, L.; Maliti, H.; Kiringe, J.W.; Kanga, E.; Warinwa, F.; Bakari, S.; Ndambuki, S.; Massawe, E.; Sitati, N.; et al. Population density of elephants and other key large herbivores in the Amboseli ecosystem of Kenya in relation to droughts. *J. Arid. Environ.* **2016**, *135*, 64–74. [CrossRef]
74. Vorste, R.V.; Obedzinski, M.; Pierce, S.N.; Carlson, S.M.; Grantham, T.E. Refuges and ecological traps: Extreme drought threatens persistence of an endangered fish in intermittent streams. *Glob. Change Biol.* **2020**, *26*, 3834–3845. [CrossRef] [PubMed]
75. Epstein, G.; Smale, D.A. *Undaria pinnatifida*: A case study to highlight challenges in marine invasion ecology and management. *Ecol. Evol.* **2017**, *7*, 8624–8642. [CrossRef]
76. Lotze, H.K.; Tittensor, D.P.; Bryndum-Buchholz, A.; Eddy, T.D.; Cheung, W.W.L.; Galbraith, E.D.; Barange, M.; Barrier, N.; Bianchi, D.; Blanchard, J.; et al. Global ensemble projections reveal trophic amplification of ocean biomass declines with climate change. *Proc. Natl. Acad. Sci. USA* **2019**, *116*, 12907–12912. [CrossRef]

Disclaimer/Publisher's Note: The statements, opinions and data contained in all publications are solely those of the individual author(s) and contributor(s) and not of MDPI and/or the editor(s). MDPI and/or the editor(s) disclaim responsibility for any injury to people or property resulting from any ideas, methods, instructions or products referred to in the content.

sustainability

MDPI

Article

The Impact of Seasonal Climate on Dryland Vegetation NPP: The Mediating Role of Phenology

Xian Liu [1], Hengkai Li [1,*], Yanbing Zhou [2,*], Yang Yu [1] and Xiuli Wang [3]

[1] School of Civil and Surveying & Mapping Engineering, Jiangxi University of Science and Technology, Ganzhou 341000, China; 6120220131@mail.jxust.edu.cn (X.L.); 1220211013@mail.jxust.edu.cn (Y.Y.)
[2] Information Technology Research Center, Beijing Academy of Agriculture and Forestry Sciences, Beijing 100097, China
[3] School of Economics and Management, Jiangxi University of Science and Technology, Ganzhou 341000, China; 9120040029@jxust.edu.cn
* Correspondence: giskai@jxust.edu.cn (H.L.); zhouyb@nercita.org.cn (Y.Z.)

Abstract: Dryland ecosystems are highly sensitive to climate change, making vegetation monitoring crucial for understanding ecological dynamics in these regions. In recent years, climate change, combined with large-scale ecological restoration efforts, has led significant greening in China's arid areas. However, the mechanisms through which seasonal climate variations regulate vegetation growth are not yet fully understood. This study hypothesizes that seasonal climate change affects net primary productivity (NPP) of vegetation by influencing phenology. We focused on China's Windbreak and Sand-Fixation Ecological Function Conservation Areas (WSEFCAs) as representative regions of dryland vegetation. The Carnegie–Ames–Stanford Approach (CASA) model was used to estimate vegetation NPP from 2000 to 2020. To extract phenological information, NDVI data were processed using Savitzky–Golay (S–G) filtering and threshold methods to determine the start of season (SOS) and end of season (EOS). The structural equation model (SEM) was constructed to quantitatively assess the contributions of climate change (temperature and precipitation) and phenology to variations in vegetation NPP, identifying the pathways of influence. The results indicate that the average annual NPP in WSEFCAs increased from 55.55 gC/(m^2·a) to 75.01 gC/(m^2·a), exhibiting uneven spatial distribution. The pathways through which seasonal climate affects vegetation NPP are more complex and uneven. Summer precipitation directly promoted NPP growth (direct effect = 0.243, $p < 0.001$) while also indirectly enhancing NPP by significantly advancing SOS (0.433, $p < 0.001$) and delaying EOS (−0.271, $p < 0.001$), with an indirect effect of 0.133. This finding highlights the critical role of phenology in vegetation growth, particularly in regions with substantial seasonal climate fluctuations. Although the overall ecological environment of WSEFCAs has improved, significant regional disparities remain, especially in northwestern China. This study introduces causal mediation analysis to systematically explore the mechanisms through which seasonal climate change impacts vegetation NPP in WSEFCAs, providing new insights into the broader implications of climate change and offering scientific support for ecological restoration and management strategies in arid regions.

Keywords: arid regions; causal mediation analysis; climate change; vegetation phenology; vegetation net primary productivity

1. Introduction

Net primary productivity (NPP) refers to the net accumulation of organic matter by vegetation through photosynthesis over a given period. It is a key metric for measuring the carbon sources and sinks of ecosystems and plays a significant role in the study of the global carbon cycle [1,2]. Arid–semi-arid ecosystems have been shown to exert a significant influence on the trend and interannual variability of the global terrestrial carbon sink over the past three decades [3]. These regions are particularly sensitive to climate change

and are often considered "outposts" of global change [4,5]. Changes in NPP in arid and semi-arid regions not only reflect the health of these ecosystems, but also exert a profound influence on the global carbon cycle [6]. Consequently, the monitoring and assessment of ecosystems in arid and semi-arid zones using indicators such as NPP represents a crucial step in understanding the ecological dynamics of these vulnerable regions. Furthermore, it provides invaluable data to support for the response to global climate change and the sustainable development of ecosystems.

Vegetation phenology, as the response time of vegetation to seasonal changes, is among the most sensitive ecological indicators of climate change [7,8]. In arid–semi-arid regions, the extreme and fluctuating climatic conditions result in a more pronounced response of phenology to environmental changes [9]. The dynamics of vegetation phenology in these regions exert a direct influence on the seasonal fluctuations of NPP. In recent years, researchers have identified that warmer temperatures and altered precipitation patterns in arid regions may result in the advancement or postponement of climatic events [10,11], which in turn amplifies or weakens the seasonal dynamics of NPP. Such dynamic changes influence the carbon balance and ecosystem stability [12,13]. Consequently, a comprehensive investigation of vegetation phenology dynamics and its response to climate change in the arid zone constitutes a crucial foundation for understanding ecosystem functions in the arid zone.

In addressing environmental challenges such as desertification and soil degradation, China has established Windbreak and Sand-Fixation Ecological Function Conservation Areas (WSEFCAs) and initiated a series of ecological restoration initiatives in arid and semi-arid regions. Among these, the Three North Shelter Forest Project (TNSFP, 1979–2050) stands out as a prominent example [14,15]. WSEFCAs have played a key role in preventing wind and sand encroachment and safeguarding the ecological environment [16]. However, these regions experience significant seasonal climate changes, with high temperatures and droughts in the summer being particularly impactful on vegetation growth. These changes not only affect the growth cycle of vegetation but also lead to significant fluctuations in phenological events [17,18]. Drought has been shown to impair vegetation productivity [19], whereas climate warming may prolong growing seasons, thereby increasing crop yields in certain instances [20].

However, the effects of seasonal climate change on vegetation NPP are particularly complex, exhibiting substantial spatial variability and inconsistency [21]. In particular, the role that vegetation phenology plays in this phenomenon has not been widely explored [22]. To gain a deeper understanding of the complex mechanisms by which seasonal climate change affects dryland vegetation NPP, this study employed structural equation modeling (SEM). As a quantitative research method [23], SEM is capable of being widely utilized to explore direct and indirect relationships between multiple factors by establishing links between empirical data and theoretical analysis [24,25]. For example, Chen et al. [26] employed SEM to examine the multifaceted impacts of climate change and human activities on vegetation cover alterations in northern China. Similarly, Liu et al. [27] utilized SEM to ascertain the moderating influence of hydrothermal conditions on Normalized Difference Vegetation Index (NDVI) responses. These studies have demonstrated the unique advantages of SEM in revealing multifactor interactions in ecosystems. Accordingly, the present study employs SEM models for mediating effect analysis, thereby facilitating a comprehensive investigation of the complex factors and interactions that influence vegetation growth.

The present study sought to examine the intricate interrelationship between NPP and climatic variables, as well as the associated phenological shifts, in arid and semi-arid regions of China that are particularly vulnerable to ecological disruption. It hypothesized that the quantitative contributions of climate and phenological changes to vegetation growth and their impact pathways vary significantly across seasons. To validate this hypothesis, the principal objectives of this study are as follows: (1) reveal the spatial and temporal dynamics of vegetation NPP in China's arid protected areas during the period 2000–2020 and the contrasting differences in different regions; (2) identify the regularity of vegetation phenology under

different climatic and topographic conditions; (3) quantitatively analyze the mechanisms of the contribution of climatic factors and changes in vegetation phenology to NPP and their pathways of influence, especially to explore the regulatory mechanism of phenological changes on NPP under seasonal climate changes. The findings of this study contribute to our understanding of the dynamic processes by which dryland ecosystems respond to climate change. They also provide a scientific basis for the development of strategies for the conservation of these ecosystems and for the sustainable management of arid zones.

2. Materials and Methods

2.1. Study Area

The WSEFCA is situated in the arid and semi-arid zones of northern China (Figure 1), covering a total area of 374,000 square kilometers. The study area covers geographic regions, from the Tarim River Basin in the Xinjiang Uygur Autonomous Region to the Horqin and Maowusu Sandy lands in the Inner Mongolia Autonomous Region, featuring varied topographies. This area is a desertification-sensitive and fragile zone under continental climate conditions in China. The annual average temperature ranges from approximately 4 °C to 8 °C, and the annual precipitation increases gradually from 150 mm in the western part of the region to 250 mm in the eastern part [28]. These climatic conditions pose significant challenges for vegetation growth. At the beginning of this century, China launched a series of sand-prevention and -control programs aimed at effectively combating land desertification and wind erosion. These programs were designed to effectively address the threats of land desertification and wind erosion. The implementation of these programs has contributed to improved vegetation cover and mitigated the process of land desertification to some extent.

2.2. Data Sources

In this study, the years 2000, 2005, 2010, 2015 and 2020 were selected as the study time points with the aim of comprehensively analyzing the characteristics and influence mechanisms of vegetation NPP changes in the vegetation of the WSEFCA under climate change within this period.

The NDVI is derived from the MODIS MOD13A3 product of the National Aeronautics and Space Administration (NASA), with a spatial resolution of 1 km × 1 km and a temporal resolution of 30 days. The MODIS data are widely applicable in the study of global and regional vegetation changes, ecological monitoring and the response to natural disasters and extreme climatic events, among other areas of research. The MODIS data were employed to estimate vegetation NPP in the WSEFCA, thereby furnishing pivotal information for an in-depth understanding of the research topic (Table 1).

Table 1. Sources of data.

Data	Description	Resolution	Period	Source
Vegetation type	National 1:1,000,000 vegetation type map	Raster/1 km		China National Data Center for Glaciology and Geocryology, accessed on 10 November 2022. (http://www.ncdc.ac.cn)
NDVI	MOD13A3	Raster/1 km		NASA, accessed on 14 May 2023. (https://ladsweb.modaps.eosdis.nasa.gov/)
DEM	SETMDEMUTM	Raster/90 m	2000	Geospatial data cloud, accessed on 3 July 2023. (https://www.gscloud.cn)
	ASTER_GDEM_30M	Raster/30 m	2009	
	GDEMV2	Raster/30 m	2015	
	GDEMV3	Raster/30 m	2019	
Meteorological data	Precipitation and temperature	Gridded/0.5°	2000–2020	CRU TS v. 4.07, accessed on 15 November 2022. (https://crudata.uea.ac.uk/cru/data/hrg/)
	Solar radiation	Gridded/0.1°	2000–2020	ERA5-Land monthly averaged data from 1981 to present, accessed on 15 November 2022. (https://cds.climate.copernicus.eu)
Phenological data	Start of Season	Point	2001–2016	Vegetation phenology data set from major ecological observation stations in China, accessed on 27 July 2023. (https://doi.org/10.11922/sciencedb.449)

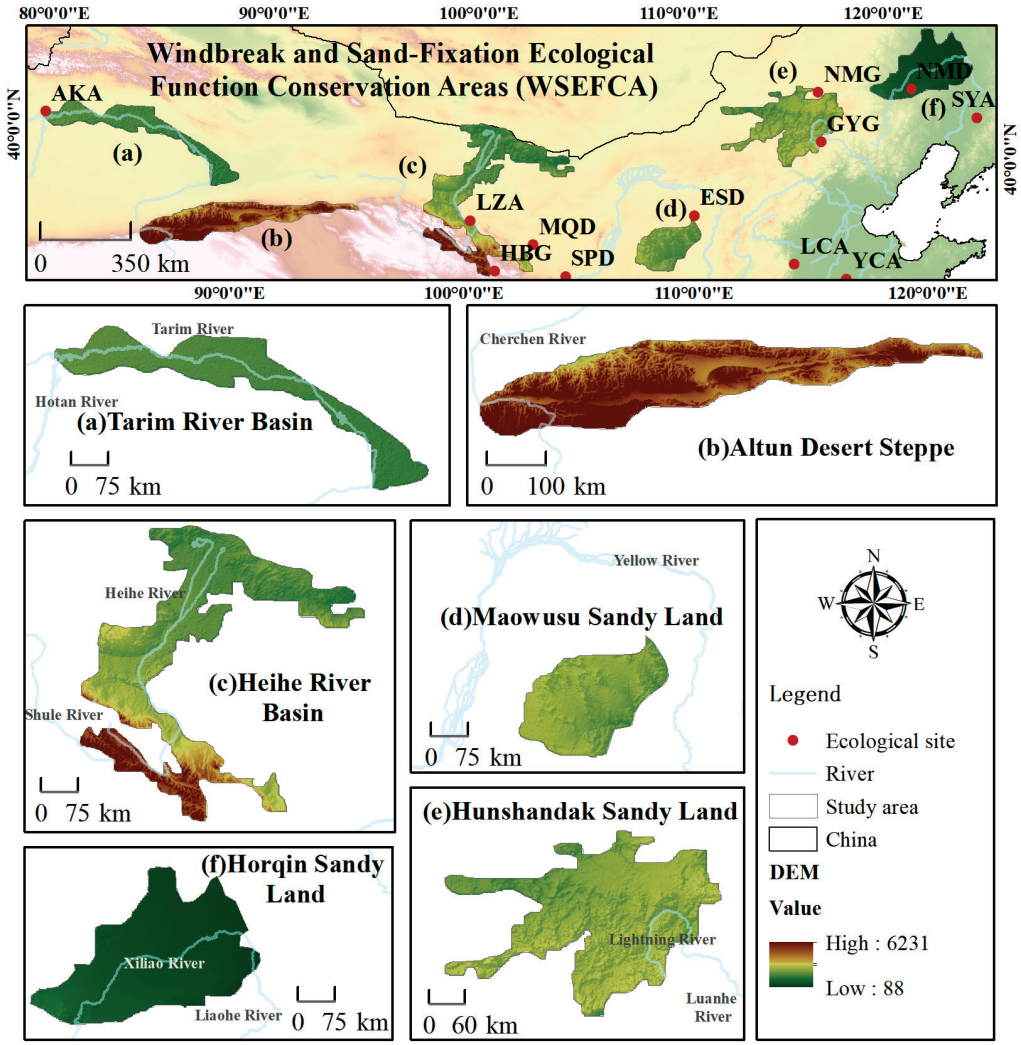

Figure 1. Study area. (**a**) Tarim River Basin (Tarim); (**b**) Altun Desert Steppe (Altun); (**c**) Heihe River Basin (Heihe); (**d**) Maowusu Sandland (Maowusu); (**e**) Hunshandak Sandland (Hunshandak); (**f**) Horqin Sandland (Horqin). Field observation stations: Aksu (AKA); Linze (LZA); Haibei (HBG); Minle (MQD); Shapotou (SPD); Ordos (ESD); Luancheng (LCA); Yucheng (YCA); Guyuan (GYG); Inner Mongolia (NMG); Naiman (NMD); Shenyang (SYA).

The temperature and precipitation data came from the CRU TS dataset of the UK National Center for Atmospheric Science (NCAS), with a spatial and temporal resolution of 0.5° per month. This dataset is one of the most widely utilized climate datasets currently available [29]. The radiometric data were derived from the ERA5-Land reanalysis product, which was provided by the European Center for Medium-Range Weather Forecasts (ECMWF), with a spatial and temporal resolution of 0.1°/month. The data have been demonstrated to have significant utility in arid and semi-arid regions [30].

The phenology validation data were selected from the vegetation climate dataset of major ecological observatories in China [31]. The dynamic thresholds for SOS and EOS of vegetation were validated using the 2015 phenology observation data from 12 stations, including Aksu, Ansai, Cele, Ordos, Haibei and Inner Mongolia.

The digital elevation model (DEM) data were obtained from the Geospatial Data Cloud, which facilitated a deeper understanding of the interrelationships between topography and vegetation and provided crucial support for the analysis of structural equation modeling. Considering that the resolution of the radiation data in this study is 10 km, we set the spatial resolution at 1 km to ensure data consistency and avoid errors caused by

downscaling. All data were resampled to this uniform resolution, ensuring data uniformity for subsequent analyses.

2.3. Methods

The objective of this study is to elucidate the role of vegetation phenology in complex dryland ecosystems under the influence of climate change. The specific research focuses, and technical route are as follows: First, based on remote sensing and meteorological data, the Carnegie–Ames–Stanford Approach (CASA) model was constructed to estimate vegetation NPP at different time periods, revealing the evolution of vegetation productivity in the WSEFCA. NDVI was used to extract phenological information and analyze the characteristics of changes in the growing season of vegetation within the study area. Second, using Structural Equation Modeling (SEM), the contributions of climate and phenology to vegetation NPP changes were quantified, establishing a causal mechanism chain between climate, phenology and vegetation NPP. This clarified the pathways through which climate change impacts vegetation growth in arid regions and identified the dominant factors driving vegetation change. The technical route is shown in Figure 2.

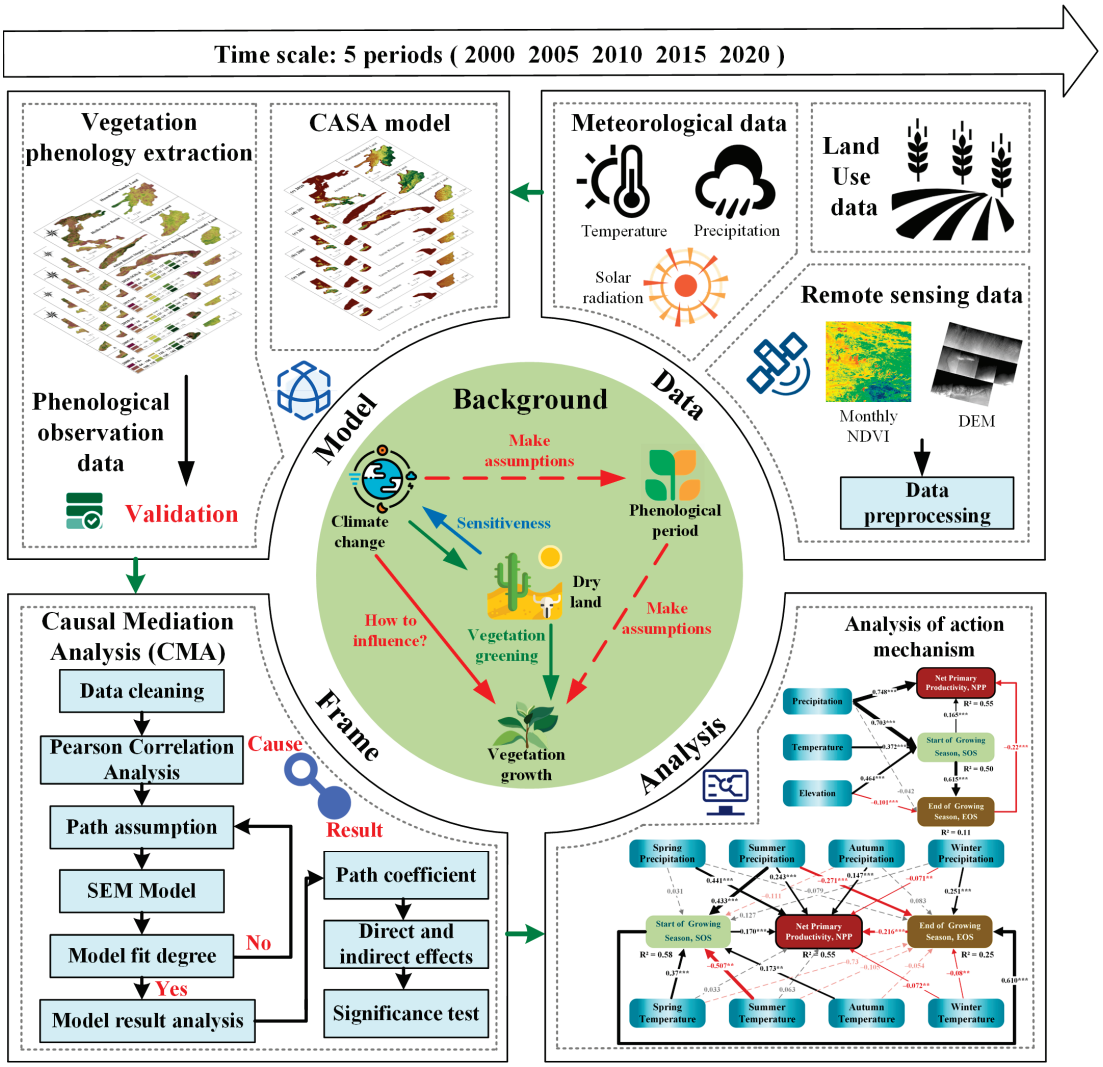

Figure 2. Technical route. (Analysis of action mechanism: The solid line indicates a significant relationship ($p < 0.05$), while the dashed line indicates a non-significant relationship. The black line indicates the positive paths, and the red line indicates the negative paths. The asterisks *** and ** indicate significance levels of 0.001 and 0.05).

2.3.1. Estimation of Vegetation NPP

In this study, we employed an improved light use efficiency model to estimate vegetation NPP, which is better suited to the conditions in China than the classical CASA model and has been extensively utilized in arid and semi-arid regions [32,33]. The NPP estimation model, based on remote sensing, was constructed based on the following variables: vegetation types, NDVI, temperature, precipitation and solar radiation data. The specific model construction process is as follows:

$$NPP(x,\ t) = APAR(x,\ t) \times \varepsilon(x,\ t) \tag{1}$$

In this equation, x represents the computational unit (pixel). t denotes the time scale (months). $APAR$ and ε are defined as photosynthetically active radiation absorbed by vegetation and the actual light use efficiency, respectively. The formulas for calculating $APAR$ (x, t) and ε (x, t) are as follows:

$$APAR(x,\ t) = SOL(x\ ,t) \times FPAR(x,\ t) \times 0.5 \tag{2}$$

$$\varepsilon(x,\ t) = T_{\varepsilon 1}(x,\ t) \times T_{\varepsilon 2}(x,\ t) \times \varepsilon_{max} \tag{3}$$

In this context, SOL and $FPAR$ represent the absorption rates of total solar radiation and incident photosynthetically active radiation by vegetation, respectively. $T_{\varepsilon 1}(x, t)$ and $T_{\varepsilon 2}(x, t)$ reflect the stress effects of low and high temperatures on light use efficiency. W_{ε} is the water stress coefficient, while ε_{max} denotes the maximum light energy utilization under ideal conditions, which varies in value depending on the vegetation type.

The global vegetation maximum light energy utilization [34] is not well-suited for the present study area. To ensure the accuracy of the model, we selected the simulated maximum light energy utilization data of Chinese vegetation types [35] for the calculation. In the subsequent study, the reliability of the model was further enhanced through the assurance that the number of rows and columns of the vegetation type data matched the meteorological raster data.

2.3.2. Information Extraction of Vegetation Phenology

In the process of extracting vegetation surface phenology, satellite remote sensing data were used as the primary source of information. However, as satellite data are affected by atmospheric conditions, cloud cover and other factors, they exhibit irregularities and abrupt changes, which present challenges to the accurate extraction of vegetation phenology [18]. The development of remote sensing technology has greatly improved the accuracy of vegetation phenology extraction [36,37]. To address these challenges, we employed the Savitzky–Golay (S–G) filtering method [38] to process the satellite remote sensing data into a smooth time series. The S-G filtering can retain both the position and peaks of the time series data while effectively eliminating noise in the data during the processing of the time series data [39]. The characteristics of this method render it optimal for processing satellite remote sensing data, thereby providing a more reliable and uniform foundation for subsequent vegetation phenology extraction.

$$Y_j = \frac{\sum_{i=-m}^{i=m} C_i Y_{j+1}}{N} \tag{4}$$

In this equation, Y_j represents the NDVI series data after smoothing, Y_{j+1} denotes the original NDVI time series data, C_i signifies the S-G filter coefficient and N represents the size of the sliding window.

The most utilized methodologies for the extraction of vegetation phenology data are primarily the threshold method and the maximum ratio method. In consideration of the operational feasibility and spatio-temporal applicability [40], the dynamic threshold method was employed for the extraction of climate parameters from the smoothed NDVI

time series. Following the introduction of the dynamic thresholding method for climate feature extraction, the recommendation of setting the threshold for SOS and EOS to 0.2 [41] was widely adopted by numerous climate researchers. However, the determination of thresholds is dependent on the specific plant species and geographical location in question, and therefore requires careful consideration during the selection process. Accordingly, a range of dynamic thresholds, spanning from 10% to 80%, were established in this study. The results were validated using ground monitoring data (Table 2), and the dynamic thresholds of 40% and 60% were ultimately selected for vegetation SOS and vegetation EOS, ensuring that the extracted climatic parameters were consistent with the actual ground conditions.

$$NDVI_{radio} = \frac{NDVI_t - NDVI_{min}}{NDVI_{max} - NDVI_{min}} \quad (5)$$

Table 2. Phenology (SOS and EOS) extracted from different thresholds (A1/A2) and ground-based monitoring data in 2015.

A1/A2	SOS	EOS
10%	87.71	321.95
20%	92.51	316.79
30%	105.85	306.74
40%	119.05	297.19
50%	129.54	287.73
60%	141.69	278.00
70%	154.55	267.48
80%	168.98	255.84
Ground monitoring data	122.81	278.14

In this equation, $NDVI_{radio}$ is the first year in which the threshold is exceeded, $NDVI_t$ is the NDVI value at a given time t, $NDVI_{max}$ and $NDVI_{min}$ are the maximum and minimum values in the annual cycle of the NDVI time series, respectively.

2.3.3. Analysis of Causal Mediation

SEM is a multivariate statistical technique used to analyze complex relationships between variables [42]. There are three key advantages of SEM over traditional regression analysis in mediation effects analysis. First, SEM permits the incorporation of measurement error into variables, thereby yielding more precise estimates than are possible with ordinary regression analysis. Second, SEM is capable of handling multiple dependent and multiple mediating variables simultaneously, facilitating the clear identification of the strength of each relationship. Finally, SEM quantitatively distinguishes between direct and indirect effects, thereby revealing the mediating mechanism. In recent years, SEM has been widely applied in ecological research [43]. Based on these advantages, we utilized SEM to quantify the mediating role of phenology between climate and vegetation NPP.

During the process of selecting model variables, we focused primarily on temperature and precipitation as the key climatic factors. This choice was not only supported by existing literature but also validated by the results of correlation analysis (Table 3). Although other climatic factors, such as wind speed, may also have some influence on vegetation growth, their relative impact was comparatively smaller and therefore not included in our model. This simplified design helps to concentrate on the main driving factors, thereby highlighting the direct regulatory effects of temperature and precipitation on NPP.

Table 3. Correlation analysis results (* significant at the 0.05 level, ** significant at the 0.01 level).

	Wind Speed	Temperature	SOS	Precipitation	NPP	EOS
Wind Speed	1.000	−0.108 *	0.061	−0.040	−0.013	−0.005
Temperature	−0.108 *	1.000	0.012	−0.291 **	−0.227 **	0.077
SOS	0.061	0.012	1.000	0.035	−0.084	0.639 **
Precipitation	−0.040	−0.291 **	0.035	1.000	0.613 **	0.045
NPP	−0.013	−0.277 **	−0.084	0.613 **	1.000	−0.056
EOS	−0.005	0.077	0.639 **	0.045	−0.056	1.000

If the model's fit was insufficient, the path assumptions were revised in accordance with the findings until the model achieved an acceptable level of fit. Once the SEM model was successfully developed, the total effects were decomposed into direct and indirect effects, and the significance of the indirect effects was tested using the Bootstrap method [44]. This allowed us to uncover both the causal relationships and the mediating mechanisms. Figure 3 illustrates the workflow for developing the vegetation NPP change mechanism.

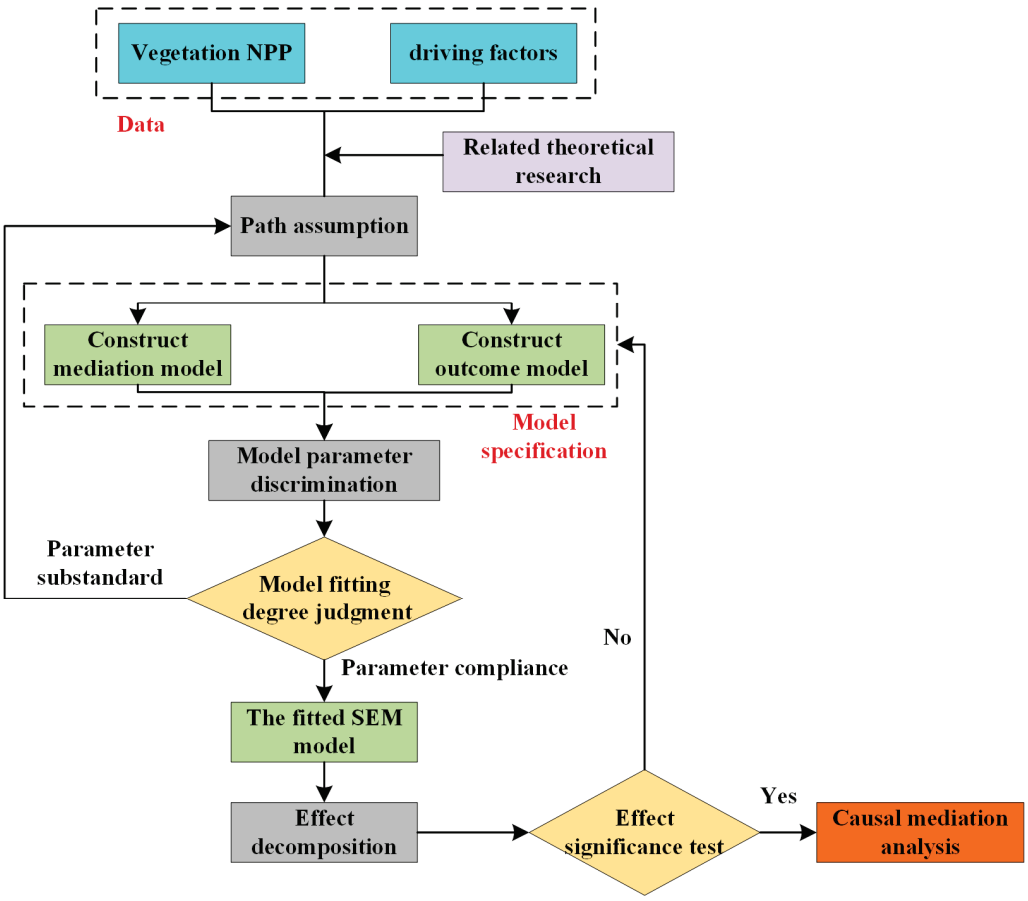

Figure 3. Model diagram of the driving mechanism of vegetation NPP change in the WSEFCA.

2.3.4. Data Statistics and Analysis

In this study, we conducted a statistical analysis of variables such as temperature, precipitation and NDVI to provide climate context and data support. According to Table 4, the annual average precipitation is 16.37 mm, with a standard deviation of 13.224, indicating significant temporal and spatial variability in precipitation. The maximum precipitation recorded was 53.54 mm in 2010, while the minimum was 0.61 mm in 2020. The annual average temperature is 6.616 °C, with a standard deviation of 3.828, showing relatively stable fluctuations over time. The lowest temperature recorded was −5.424 °C in 2000,

and the highest was 13.45 °C in 2020. The annual average NDVI is 0.1092, with a standard deviation of 0.1676; the maximum value is 0.6218 and the minimum is −0.1956, indicating relatively stable changes in vegetation cover in the region. Additionally, the average DEM of the study area is 1574.127 m, with a standard deviation of 1176.76 m, reflecting significant topographic variability in the region.

Table 4. Statistical results of selected raw data.

	Year	Maximum	Minimum	Mean	Standard Deviation
Precipitation (mm)	2000	1.34	47.57	15.011	11.021
	2005	2.073	49.575	15.293	11.952
	2010	1.104	53.538	17.402	13.942
	2015	1.518	40.80	16.515	12.976
	2020	0.61	48.461	17.624	16.23
annual average		1.329	47.9888	16.369	13.2242
Temperature (degree centigrade)	2000	−5.424	13.26	6.42	3.88
	2005	−5.41	13.61	6.77	3.79
	2010	−5.4	13.2	6.28	3.74
	2015	−5.4	13.72	6.69	3.89
	2020	−5.17	13.45	6.92	3.84
annual average		−5.3608	13.448	6.616	3.828
NDVI	2000	−0.196	0.53	0.1	0.06
	2005	−0.196	0.6	0.11	0.06
	2010	−0.194	0.646	0.106	0.057
	2015	−0.2	0.658	0.11	0.595
	2020	−0.192	0.675	0.12	0.066
annual average		−0.1956	0.6218	0.1092	0.1676
DEM (m)		66	6063	1574.127	1176.76

These statistical analyses provide essential data support for subsequent in-depth studies on the impacts of climate change, vegetation NPP and phenological changes.

3. Results

3.1. Characteristics of Spatial and Temporal Changes of NPP in Typical Ecological Function Reserve Areas

The NPP of WSEFCA showed a significant upward trend over the past two decades, with the average value rising from 55.55 gC/(m^2·a) in 2000 to 75.01 gC/(m^2·a) in 2020 (Figure 4). The long-term pattern of vegetation NPP indicates a gradual improvement in the ecological condition in the WSEFCA, particularly in the Hunsandak and Horqin.

As the ecological restoration efforts progressed, a noticeable diversification in the spatial distribution of NPP became evident (Figure 4A). However, the NPP levels in the Altun, the Tarim and the northern part of the Heihe remain relatively low, with values ranging between 0 and 90 gC/(m^2·a). However, an increase in NPP was observed in some regions in 2010 and 2015. For instance, at the southeastern border of the Hunsandak and Maowusu, the vegetation NPP gradually shifted from low to medium-high levels, exceeding 200 gC/(m^2·a) in most areas. Meanwhile, the Horqin demonstrated a sustained high level of vegetation NPP.

With regard to seasonal fluctuations, the annual mean NPP in each region exhibited a discernible upward trajectory from 2000 to 2020. This trend was particularly pronounced during the summer months, when the mean vegetation NPP reached its highest point and demonstrated a consistent annual increase, consistently remaining above 10 gC/(m^2·a). By 2020, the mean summer vegetation NPP had reached 15.11 gC/(m^2·a) (Figure 4B). This highlights the significant influence of seasonal variations on vegetation growth. However, the changes in vegetation NPP among different regions showed significant variation (Figure 4C).

The highest annual mean vegetation NPP was recorded in the Horqin, followed by the Hunsandak and the Maowusu, which demonstrated a substantial enhancement of NPP across all three regions. In comparison, the vegetation NPP in the Tarim, Altun and Heihe exhibited minimal alteration and lower mean values, suggesting that the ecological environment of these regions situated in northwestern China still requires further enhancement.

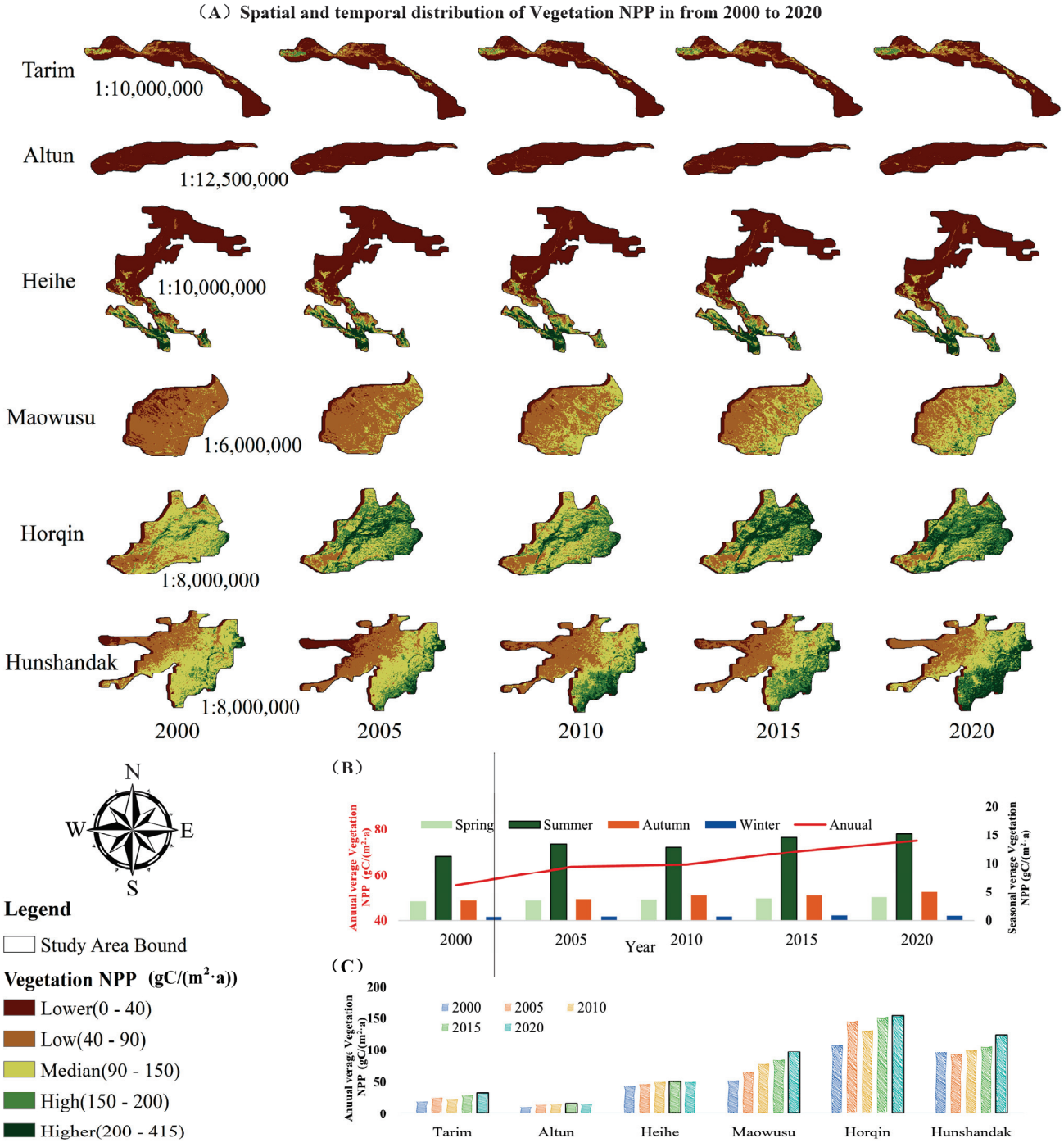

Figure 4. Spatial and temporal evolution of vegetation NPP ((**A**) spatial pattern of vegetation NPP in the study area in 2000, 2005, 2010, 2015 and 2020; (**B**) changes in vegetation NPP in different years and seasons; and (**C**) changes in vegetation NPP in different regions (black lines indicate the years with the highest values).

3.2. Spatial and Temporal Characteristics of Vegetation Climatic Changes

From 2000 to 2020, the vegetation SOS in the WSEFCA exhibited a spatial pattern of gradual delay from east to west (Figure 5A). Significant differences in SOS were observed among regions. The Tarim and the Altun showed an overall trend of advancement, while the Horqin and the Maowusu exhibited the opposite pattern, with SOS gradually advancing as longitude increases. In contrast, the SOS in the Hunshandake and the northern part of the Heihe has shown a delaying trend, reflecting the different climate responses in these regions.

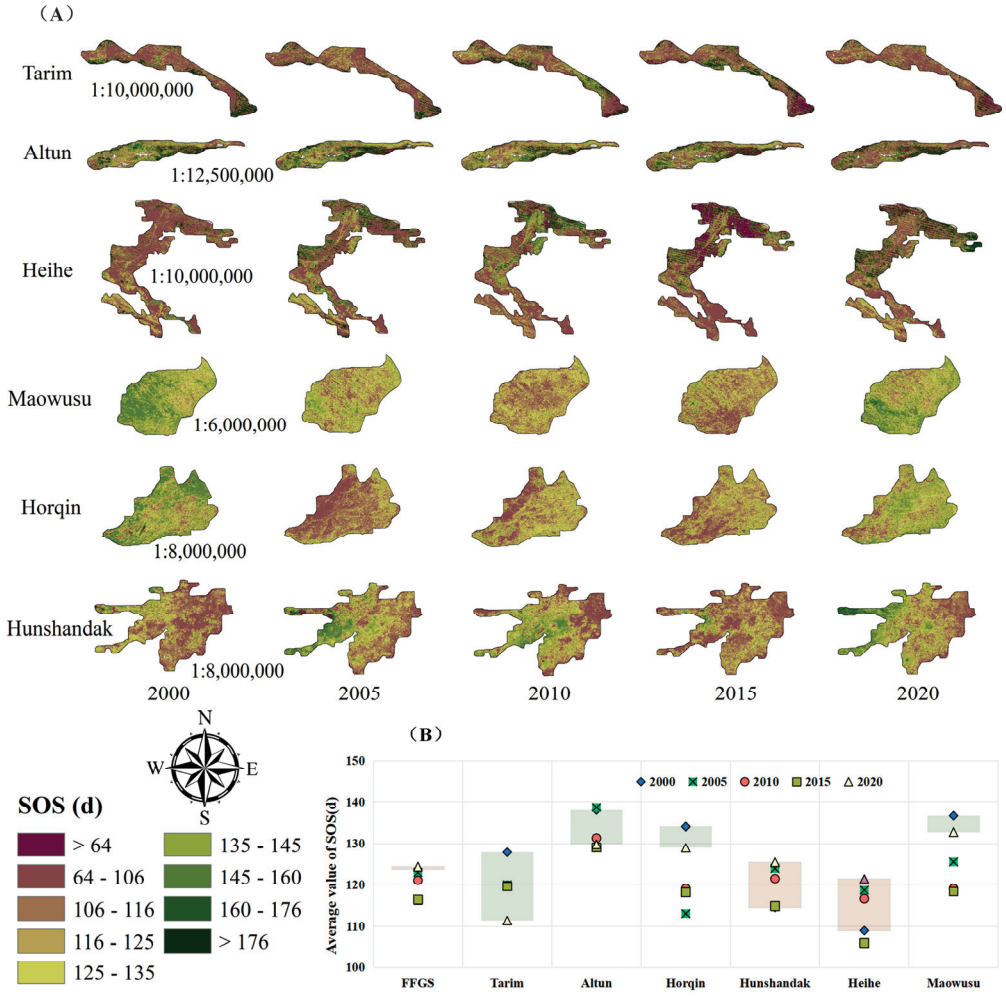

Figure 5. Spatial and temporal evolution of SOS. (**A**) Spatial patterns of vegetation SOS in the study area for the years 2000, 2005, 2010, 2015 and 2020. (**B**) Changes in vegetation SOS in different regions (green boxes represent advancing times, orange represents delaying times).

The spatial pattern of EOS showed similarities to that of SOS, yet also demonstrated regional specificity (Figure 6A). In the Tarim, the advancement of EOS is particularly pronounced, especially in the northwestern and southeastern regions. Meanwhile, the overall change in the Hunshandake is relatively stable; however, a significant delay in EOS was observed in the northeastern part in 2015. By comparison, the changes in EOS in the Horqin and the Maowusu are relatively minor. These discrepancies illustrate the varying effects of climate change on vegetation phenology across diverse topographic regions.

The interannual variation of SOS and EOS exhibits complexity within the subregions (Figures 5B and 6B). In the Tarim and Altun, both SOS and EOS demonstrated notable advancement, with SOS advancing by approximately 2 to 3 days and EOS advancing by 10 to 15 days per decade on average. The trend of SOS and EOS in the Horqin and Mauwusu

was consistent, with advancement followed by postponement. In contrast, the mean values of SOS in the Heihe and the Hunsandak exhibited a relatively stable 10-day difference over the 20-year period.

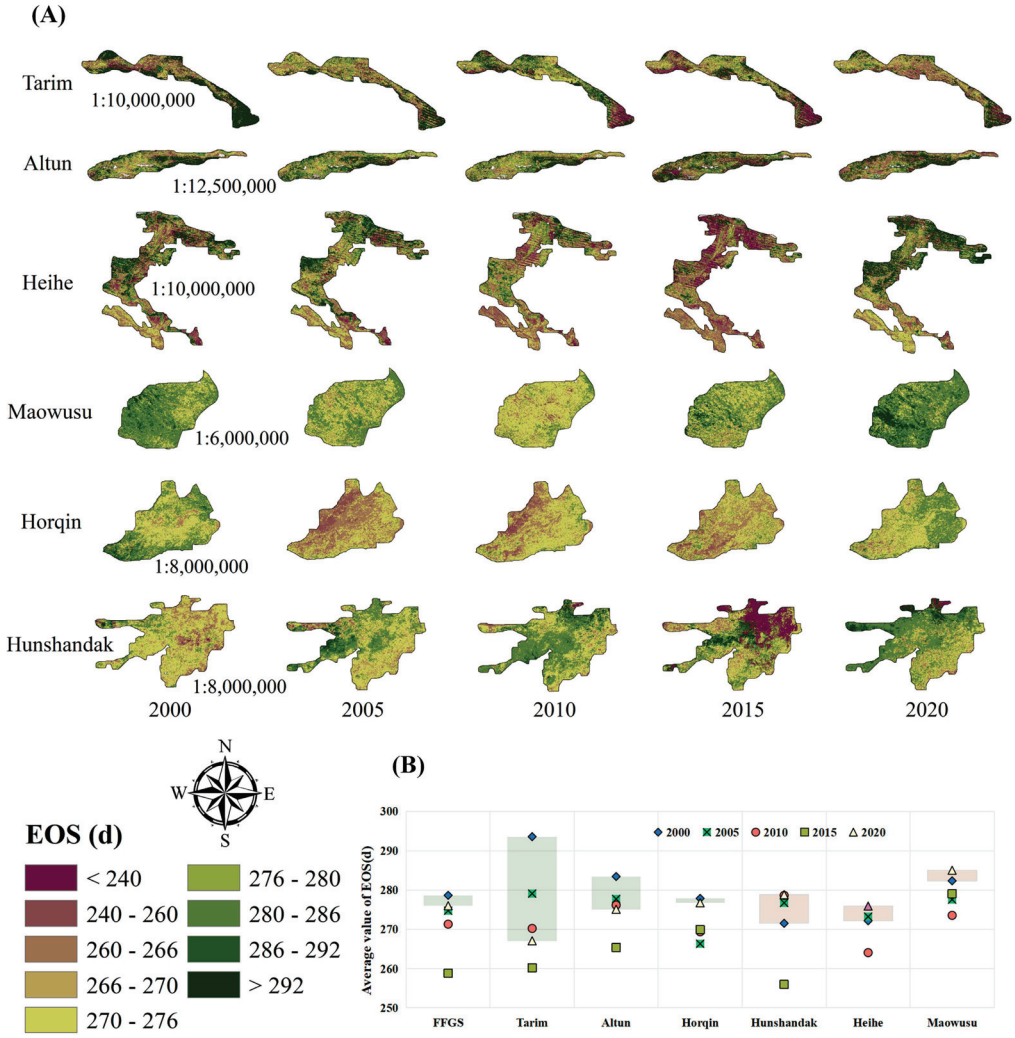

Figure 6. Spatial and temporal evolution of EOS. (**A**) Spatial patterns of vegetation EOS in the study area for the years 2000, 2005, 2010, 2015 and 2020. (**B**) Changes in vegetation EOS in different regions (green boxes represent advancing times, orange represents delaying times).

3.3. Influence Pathways of Climate and Phenology Changes on Vegetation NPP Changes

The final model fitted by SEM is shown in Figure 7. This model provides effectively captures the interactions among the variables and reveals the pathways through which climatic factors influence vegetation NPP across multiple temporal scales (annual and seasonal). The model showed strong goodness of fit at both the annual and seasonal scales (Table 5), indicating robust explanatory power.

Table 5. Fitting of the model.

	CHISQ	GFI	CFI	RMR	SRMR	RMSEA
Annual scale	0.036	0.998	0.999	0.014	0.007	0.034
Seasonal scale	0.103	0.997	0.998	0.019	0.01	0.021

First, the pathways of climate change effects on vegetation NPP exhibited a significant relationship from an annual scale perspective (Appendix A, Figure A1). The mean annual

precipitation had a strongly significant effect on SOS and NPP ($p < 0.001$), but not on EOS ($p > 0.05$). Furthermore, precipitation indirectly increased NPP via its influence (with an indirect effect of 0.116 and a total effect amounting to 0.819). Although the direct effect of precipitation on EOS was not significant, the total effect of precipitation on EOS was 0.432, as indicated by the indirect effect of SOS on EOS (Appendix A, Table A1). Meanwhile, EOS exhibited a significant negative direct effect on NPP (with an impact coefficient of −0.220). Although DEM lacked a direct effect on NPP alterations, it exerted a modest total effect on NPP via the indirect influences of SOS and EOS (with indirect effects of 0.077 and 0.022, respectively).

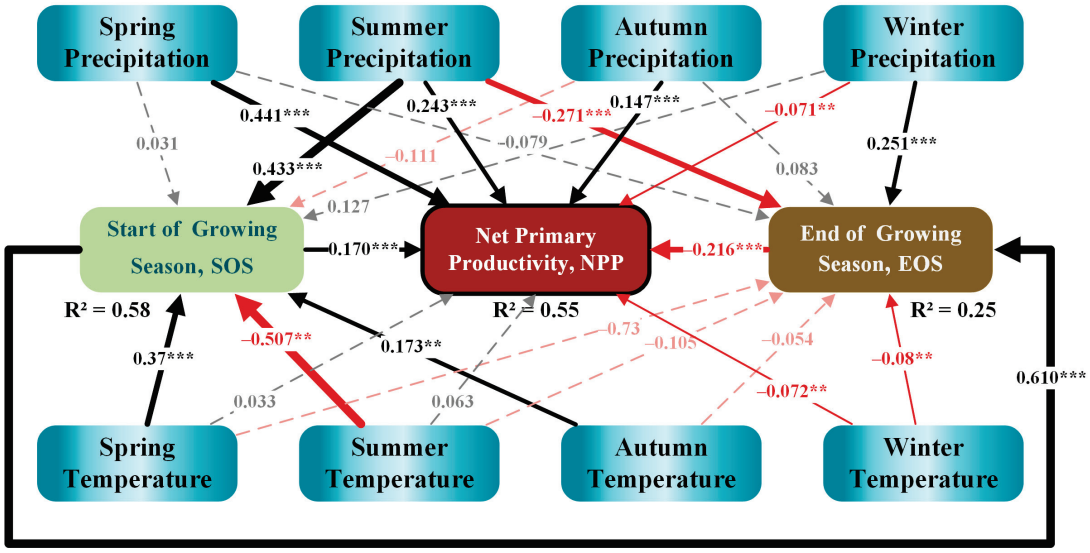

Figure 7. The relationships between climatic factors and NPP, SOS and EOS on seasonal scales. The values on the lines represent standardized throughput coefficients, and the thickness of the arrows indicates the magnitude of the standardized coefficients. A solid line indicates a significant relationship ($p < 0.05$), while a dashed line indicates a non-significant relationship. Black lines indicate positive paths, and red lines indicate negative paths. The asterisks *** and ** indicate significance levels of 0.001 and 0.05, respectively. R^2 denotes the degree of coexplanation of the variable in question.

The patterns observed at the annual scale demonstrated a greater complexity of influence at the seasonal scale (Figure 7). Spring precipitation exerts a considerable direct influence on NPP, with an effect coefficient of 0.441. This represents one of the most pronounced direct effects of seasonal precipitation on NPP variability. This indicates that spring precipitation plays a crucial role in regulating NPP. The impact of summer precipitation on NPP was more intricate. It exerted a direct effect of 0.243 and also exerted an indirect influence on NPP alterations through a substantial positive effect on SOS (with an impact coefficient of 0.433) and a negative effect on EOS (with an impact coefficient of −0.271). This indirect effect was 0.133, indicating that the contribution of summer precipitation is influenced by the combined effects of multiple pathways, exhibiting a complex pattern of indirect effects. The direct effect of fall and winter precipitation on NPP was smaller, with values of 0.147 and −0.071, respectively. Additionally, the indirect effect of winter precipitation on NPP through the EOS was −0.054, resulting in a total effect of −0.125 (Table 6). This further demonstrates that the negative impact of winter precipitation on NPP is indirectly mediated through the EOS pathway.

Another crucial climatic factor, temperature, also exerted diverse influences on NPP at varying temporal scales. The mean annual air temperature exhibited a highly significant direct effect on SOS ($p < 0.001$, with an effect coefficient of 0.372), whereas seasonal air temperature effects demonstrated more nuanced differences. For example, summer tem-

peratures had a significant negative effect on SOS ($p < 0.05$, with an impact coefficient of −0.507). In contrast, the positive effects of spring and fall temperatures on SOS indirectly supported NPP growth, reflecting that temperature changes in different seasons have varying regulatory effects on vegetation growth.

Table 6. Results of direct, indirect and total effects of seasonal changes in temperature, precipitation, SOS, EOS and NPP (slash indicates no indirect effect, NS indicates that the pathway is not significant, spring precipitation (PRE-Spring), spring temperatures (TEMP-Spring)).

Paths	Direct Effects	Paths	Indirect Effects	Paths	Total Effects
PRE-Spring → NPP	0.441	/	/	PRE-Spring → NPP	0.441
PRE-Summer → SOS	0.433	PRE-Summer → SOS → NPP	0.074	PRE-Summer → SOS	0.433
PRE-Summer → EOS	−0.271	PRE-Summer → EOS → NPP	0.059	PRE-Summer → EOS	−0.007
PRE-Summer → NPP	0.243	PRE-Summer → SOS → EOS	0.264	PRE-Summer → NPP	0.376
PRE-Autumn → NPP	0.147	/	/	PRE-Autumn → NPP	0.147
PRE-Winter → EOS	0.251	PRE-Winter → EOS → NPP	−0.054	PRE-Winter → EOS	0.251
PRE-Winter → NPP	−0.071			PRE-Winter → NPP	−0.125
TEMP-Spring → SOS	0.37	TEMP-Spring → SOS → NPP	0.063	TEMP-Spring → SOS	0.37
TEMP-Spring → NPP	NS			TEMP-Spring → NPP	0.063
TEMP-Summer → SOS	−0.507	TEMP-Summer → SOS → NPP	−0.086	TEMP-Summer → SOS	0.37
TEMP-Summer → NPP	NS			TEMP-Summer → NPP	−0.086
TEMP-Autumn → SOS	0.173	TEMP-Autumn → SOS → NPP	0.029	TEMP-Autumn → SOS	0.173
TEMP-Autumn → NPP	NS			TEMP-Autumn → NPP	0.029
TEMP-Winter → EOS	−0.08	TEMP-Winter → EOS → NPP	0.016	TEMP-Winter → EOS	−0.072
TEMP-Winter → NPP	−0.072			TEMP-Winter → NPP	−0.064
SOS → EOS	0.610	SOS → EOS → NPP	−0.132	SOS → EOS	0.610
SOS → NPP	0.170	/	/	SOS → NPP	0.038
EOS → NPP	−0.216	/	/	EOS → NPP	−0.216

4. Discussion

This study reveals the spatial and temporal characteristics of the NPP of vegetation in the WSEFCA over the past two decades. Overall, vegetation NPP has exhibited a significant upward trend, which was closely related to changes in climatic conditions within the region. In particular, the increase in vegetation NPP was especially in years when precipitation increased precipitation, indicating that precipitation is the primary driving factor influencing vegetation productivity [28]. However, when both precipitation and temperature are considered together, the increase in NPP is not uniform. In fact, significant differences are observed between seasons and regions. For example, the NPP elevation in the Hunsandak, Maowusu and Horqin was particularly significant in years of relatively abundant precipitation. The climate conditions in these regions are relatively mild, with abundant rainfall, reaching over 300 mm annually. As a result, the vegetation in these areas is highly responsive to water availability, which promotes vegetation recovery [45–47]. In contrast, in regions with high temperatures and low precipitation, such as the Tarim River Basin and the Arjin Desert Steppe, the increase in NPP was relatively modest, and the overall level remained low. The ecosystem recovery in these regions is relatively delayed, with extreme high temperatures and high evaporation rates severely limiting plant growth. In the Tarim River Basin, summer temperatures often exceed 40 °C, while annual rainfall is less than 50 mm. These extreme climatic conditions directly contribute to the low level of vegetation productivity in the area [48,49]. Similarly, the Heihe River Basin exhibited comparable outcomes, further indicating that in the arid regions of northwestern China, NPP levels are typically low and highly susceptible to precipitation fluctuations due to a significant scarcity of water resources [50]. Recent studies have also shown that vegetation growth in these arid regions is more severely affected by climate change, with extreme precipitation events posing additional challenges to ecosystem recovery [51,52].

Further exploring the impact of climate change and phenological changes on NPP, this study reinforces the necessity of comprehending the interdependent relationships between climate, phenology and vegetation. It has been demonstrated that there are notable differences in the impact of climatic variables on vegetation phenology across different seasons. To illustrate,

spring temperature has been demonstrated to exert a pronounced influence on SOS, whereas fall precipitation has been shown to exert a significant impact on EOS [7,8]. This seasonal difference has been validated to varying degrees in arid and semi-arid regions around the world, thereby confirming the critical role of climatic factors on vegetation growth [5,53]. The results demonstrated that the impact of climatic factors on SOS is generally more pronounced than that on EOS. The positive effect of warmer spring temperatures on SOS is observed to be driven by the promotion of early vegetation emergence and growth, which in turn led to an increase in NPP. However, the rise in summer temperatures has a significant negative effect on SOS. It is found that higher temperatures potentially led to an earlier growing season, which in turn inhibited NPP accumulation by shortening the growing season. While warmer temperatures often facilitate early growth, in extreme climatic conditions, this advancement may negatively impact NPP on an annual basis [9]. Recent literature also supports this view, suggesting that extreme climate events may have a significant impact on vegetation phenology and weaken the potential for NPP growth [54]. Additionally, the rise in precipitation has a considerable positive impact on SOS, yet a detrimental effect on EOS. This suggests that, while increased precipitation typically fosters vegetation growth, excessive precipitation may alternatively precipitate water stress in arid ecosystems, thereby constraining vegetation expansion [55,56]. This underscores that the impact of phenological shifts on NPP is not solely contingent on the overall precipitation levels but is also profoundly shaped by the cumulative effect of local precipitation patterns and climate variability.

Furthermore, the prolongation of vegetation phenology resulting from climate change may augment NPP in the immediate term. However, in the long term, recurrent extreme climatic occurrences may offset this impact, particularly in regions characterised by elevated climate variability [57]. This intricate dynamic indicates that future research must prioritize investigating the direct and indirect impacts of climate change on phenological events. A multi-scale and multi-factor analysis approach will facilitate a more comprehensive understanding of the mechanisms through which climate change affects NPP, thereby providing a scientific foundation for the management and restoration of ecosystems.

The results demonstrated that the duration of the vegetation growing season was progressively extended with the intensification of seasonal precipitation and temperature fluctuations, which led to an increase in vegetation NPP. However, ecosystems may experience heightened levels of water stress and heat stress as summer temperatures continue to rise and precipitation patterns become increasingly erratic [58,59]. In dryland ecosystems, there is considerable spatial heterogeneity in temperature and precipitation, with a high degree of uncertainty [22]. It is therefore imperative that future ecological restoration strategies give special consideration to the potential challenges posed by water carrying capacity and seasonal climate change in these regions. The spatial distribution of water and heat is significantly influenced by local topography and soil conditions, thereby increasing the complexity of ecological restoration. In order to effectively address the uncertainties posed by future climate change, ecological restoration strategies must prioritize nature-based solutions and incorporate a comprehensive assessment of the dual impacts of local climate variability on vegetation growth. In particular, when considering the restoration of windbreaks in future climate scenarios, it is essential to address both the enhancement of plant water use efficiency and the sustainable management of soil moisture. It is imperative to increase ground cover in order to enhance soil moisture retention and to adapt to climate change by optimizing vegetation structure. Furthermore, in regions experiencing prolonged periods of drought, it is essential to implement more adaptive vegetation-restoration strategies that prioritize the introduction of drought-tolerant species and the effective management of water resources. This approach is crucial to ensure the long-term resilience and stability of the ecosystem. Furthermore, future restoration strategies should prioritize the monitoring of vegetation phenology dynamics under climate change scenarios, with a particular emphasis on the study of response mechanisms to seasonal climate change.

Although this study focuses on the effects of climatic and phenological changes on vegetation growth, while the effects of human activities are relatively less addressed. Anthropogenic activities exert a more pronounced influence on vegetation cover (e.g., ecological restoration projects) within the study area. However, a more comprehensive investigation is required to elucidate the precise nature of these impacts. Subsequent studies will investigate the role of human activities in ecological restoration in greater detail, particularly in the context of interactions with climate change. This will provide a crucial foundation for the development of more precise and sustainable restoration strategies.

5. Conclusions

This study focuses on WSEFCA, utilizing an SEM model to construct a relational network that quantitatively evaluates the impact of climatic factors and phenological events on vegetation NPP. It reveals the crucial role phenology plays in climate-driven NPP changes under arid and semi-arid conditions. The results indicate that while the overall ecological environment of these conservation areas has improved, significant regional disparities persist, particularly in northwestern China, where further ecological improvements are needed. In the arid and semi-arid regions, summer precipitation notably advances spring SOS and delays autumn EOS, thereby indirectly enhancing the growth potential of vegetation NPP. The study further demonstrates that climate change indirectly influences vegetation growth cycles and productivity by regulating phenological events.

This research provides a basis for formulating more precise strategies for ecological protection and restoration. In other similar arid regions, ecological restoration efforts should also focus on the relationship between regional climate and phenological changes, in order to develop location-specific strategies to address the impact of climate change on vegetation productivity. Future ecological management strategies should fully consider the regulatory effects of climate change on phenology and NPP to effectively address the challenges of ecological restoration in global arid zones.

Author Contributions: X.L.: Data curation, Formal analysis, Methodology, Software, Writing—original draft. H.L.: Conceptualization, Funding acquisition, Methodology, Resources, Writing—review and editing. Y.Z.: Conceptualization, Project administration, Validation, Writing—review and editing. Y.Y.: Data curation, Formal analysis, Software. X.W.: Investigation, Project administration, Supervision. All authors have read and agreed to the published version of the manuscript.

Funding: This research was funded by The Key Projects of Jiangxi Natural Science Foundation, grant number 20232ACB203025, and the Science and Technology Project of the Jiangxi Provincial Department of Natural Resources, grant number ZRKJ20232523.

Institutional Review Board Statement: Not applicable.

Informed Consent Statement: Not applicable.

Data Availability Statement: Data derived from public domain resources.

Conflicts of Interest: The authors declare no conflicts of interest.

Appendix A

Table A1. Results of direct, indirect, and total effects of annual changes in temperature, precipitation, SOS, EOS, and NPP (slashes indicate no indirect effects, NS indicates the path is not significant).

Paths	Direct Effects	Paths	Indirect Effects	Paths	Total Effects
PRE → SOS	0.703	PRE → SOS → NPP	0.116	PRE → SOS	0.703
PRE → EOS	NS	PRE → EOS → NPP	NS	PRE → EOS	0.432
PRE → NPP	0.748	PRE → SOS → EOS	0.432	PRE → NPP	0.819
TEMP → SOS	0.372	TEMP → SOS → NPP	0.061	TEMP → SOS	0.372
		TEMP → SOS → EOS	0.229	TEMP → EOS	0.229
				TEMP → SOS	0.061

Table A1. *Cont.*

Paths	Direct Effects	Paths	Indirect Effects	Paths	Total Effects
DEM → SOS	0.464	DEM → SOS → EOS	0.285	DEM → SOS	0.464
DEM → EOS	−0.101	DEM → SOS → NPP	0.077	DEM → EOS	0.149
		DEM → EOS → NPP	0.022	DEM → NPP	0.099
SOS → EOS	0.615	SOS → EOS → NPP	−0.135	SOS → EOS	0.615
SOS → NPP	0.165			SOS → NPP	0.030
EOS → NPP	−0.220	/		EOS → NPP	−0.220

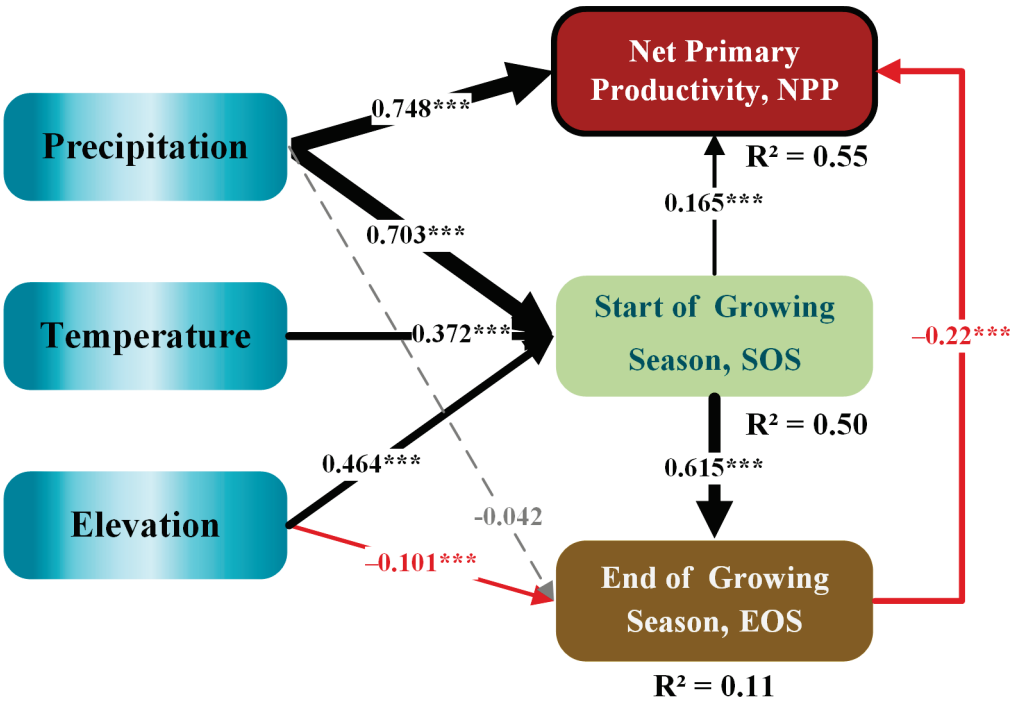

Figure A1. The relationships between climatic factors and NPP, SOS, and EOS on annual scales. The values on the lines represent standardized throughput coefficients, and the thickness of the arrows indicates the magnitude of the standardized coefficients. A solid line indicates a significant relationship ($p < 0.05$), while a dashed line indicates a non-significant relationship. Black lines indicate positive paths, and red lines indicate negative paths. The asterisks *** indicate a significance level of 0.001. R^2 denotes the degree of coexplanation of the variable in question.

References

1. Field, C.B.; Behrenfeld, M.J.; Randerson, J.T.; Falkowski, P. Primary production of the biosphere: Integrating terrestrial and oceanic components. *Science* **1998**, *281*, 237–240. [CrossRef] [PubMed]
2. Li, H.; Wu, Y.; Liu, S.; Xiao, J. Regional contributions to interannual variability of net primary production and climatic attributions. *Agric. For. Meteorol.* **2021**, *303*, 108384. [CrossRef]
3. Poulter, B.; Frank, D.; Ciais, P.; Myneni, R.B.; Andela, N.; Bi, J.; Broquet, G.; Canadell, J.G.; Chevallier, F.; Liu, Y.Y.; et al. Contribution of semi-arid ecosystems to interannual variability of the global carbon cycle. *Nature* **2014**, *509*, 600–603. [CrossRef] [PubMed]
4. Wang, S.; Fu, B.; Wei, F.; Piao, S.; Maestre, F.T.; Wang, L.; Jiao, W.; Liu, Y.; Li, Y.; Li, C.; et al. Drylands contribute disproportionately to observed global productivity increases. *Sci. Bull.* **2023**, *68*, 224–232. [CrossRef] [PubMed]
5. Li, J.; Liu, L.; Zheng, J.; Yu, X.; Tian, R.; Han, W.; Guan, J. Increasing influence of minimum temperature on grassland spring phenology in arid Central Asia. *Agric. For. Meteorol.* **2024**, *355*, 110122. [CrossRef]
6. Lyu, J.; Fu, X.; Lu, C.; Zhang, Y.; Luo, P.; Guo, P.; Huo, A.; Zhou, M. Quantitative assessment of spatiotemporal dynamics in vegetation NPP, NEP and carbon sink capacity in the Weihe River Basin from 2001 to 2020. *J. Clean. Prod.* **2023**, *428*, 139384. [CrossRef]
7. Li, C.; Wang, R.; Cui, X.; Wu, F.; Yan, Y.; Peng, Q.; Qian, Z.; Xu, Y. Responses of vegetation spring phenology to climatic factors in Xinjiang, China. *Ecol. Indic.* **2021**, *124*, 107286. [CrossRef]

8. Jiang, Q.; Yuan, Z.; Yin, J.; Yao, M.; Qin, T.; Lü, X.; Wu, G. Response of vegetation phenology to climate factors in the source region of the Yangtze and Yellow Rivers. *J. Plant Ecol.* **2024**, *17*, rtae046. [CrossRef]
9. Ji, Z.; Wang, L. Differential responses of vegetation phenology to climatic elements during extreme events on the Chinese loess plateau. *Sci. Total Environ.* **2024**, *933*, 173146. [CrossRef]
10. Mou, C.; Sun, G.; Luo, P.; Wang, Z.; Luo, G. 4Flowering Responses of Alpine Meadow Plant in the Qinghai-Tibetan Plateau to Extreme Drought Imposed in Different Periods. *Chin. J. Appl. Environ. Biol.* **2013**, *19*, 272–279. [CrossRef]
11. Chen, L.; Hänninen, H.; Rossi, S.; Smith, N.G.; Pau, S.; Liu, Z.; Feng, G.; Gao, J.; Liu, J. Leaf senescence exhibits stronger climatic responses during warm than during cold autumns. *Nat. Clim. Change* **2020**, *10*, 777–780. [CrossRef]
12. Kang, X.; Hao, Y.; Cui, X.; Chen, H.; Huang, S.; Du, Y.; Li, W.; Kardol, P.; Xiao, X.; Cui, L. Variability and changes in climate, phenology, and gross primary production of an alpine Wetland ecosystem. *Remote Sens.* **2016**, *8*, 391. [CrossRef]
13. Richardson, A.D.; Black, T.A.; Ciais, P.; Delbart, N.; Friedl, M.A.; Gobron, N.; Hollinger, D.Y.; Kutsch, W.L.; Longdoz, B.; Luyssaert, S.; et al. Influence of spring and autumn phenological transitions on forest ecosystem productivity. *Philos. Trans. R. Soc. B Biol. Sci.* **2010**, *365*, 3227–3246. [CrossRef] [PubMed]
14. Chen, C.; Park, T.; Wang, X.; Piao, S.; Xu, B.; Chaturvedi, R.K.; Fuchs, R.; Brovkin, V.; Ciais, P.; Fensholt, R.; et al. China and India lead in greening of the world through land-use management. *Nat. Sustain.* **2019**, *2*, 122–129. [CrossRef]
15. Xu, L.; Gao, G.; Wang, X.; Fu, B. Distinguishing the effects of climate change and vegetation greening on soil moisture variability along aridity gradient in the drylands of northern China. *Agric. For. Meteorol.* **2023**, *343*, 109786. [CrossRef]
16. Jie, X.; Yu, X.; Gaodi, X.; Yangyang, W.; Yuan, J.; Wenhui, C. Assessment of wind erosion prevention service and its beneficiary areas identification of national key ecological function zone of windbreak and sand fixation type in China. *Acta Ecol. Sin.* **2019**, *39*, 5857–5873. [CrossRef]
17. Li, H.; Feng, J.; Bai, L.; Zhang, J. Populus euphratica Phenology and Its Response to Climate Change in the Upper Tarim River Basin, NW China. *Forests* **2021**, *12*, 1315. [CrossRef]
18. Han, H.; Bai, J.; Ma, G.; Yan, J.; Wang, X.; Ta, Z.; Wang, P. Seasonal responses of net primary productivity of vegetation to phenological dynamics in the Loess Plateau, China. *Chin. Geogr. Sci.* **2022**, *32*, 340–357. [CrossRef]
19. Kang, W.; Wang, T.; Liu, S. The response of vegetation phenology and productivity to drought in Semi-Arid regions of northern China. *Remote Sens.* **2018**, *10*, 727. [CrossRef]
20. Liu, Z.; Liu, Y.; Li, Y. Extended warm temperate zone and opportunities for cropping system change in the Loess Plateau of China. *Int. J. Climatol.* **2018**, *39*, 658–669. [CrossRef]
21. Wu, L.; Ma, X.; Dou, X.; Zhu, J.; Zhao, C. Impacts of climate change on vegetation phenology and net primary productivity in arid Central Asia. *Sci. Total Environ.* **2021**, *796*, 149055. [CrossRef] [PubMed]
22. Smith, W.K.; Dannenberg, M.P.; Yan, D.; Herrmann, S.; Barnes, M.L.; Barron-Gafford, G.A.; Biederman, J.A.; Ferrenberg, S.; Fox, A.M.; Hudson, A.; et al. Remote sensing of dryland ecosystem structure and function: Progress, challenges, and opportunities. *Remote Sens. Environ.* **2019**, *233*, 111401. [CrossRef]
23. Hayes, A.F.; Montoya, A.K.; Rockwood, N.J. The Analysis of Mechanisms and Their Contingencies: PROCESS versus Structural Equation Modeling. *Australas. Mark. J.* **2017**, *25*, 76–81. [CrossRef]
24. Schweiger, E.W.; Grace, J.B.; Cooper, D.; Bobowski, B.; Britten, M. Using structural equation modeling to link human activities to wetland ecological integrity. *Ecosphere* **2016**, *7*, e01548. [CrossRef]
25. Ren, L.; Li, J.; Li, C.; Dang, P. Can ecotourism contribute to ecosystem? Evidence from local residents' ecological behaviors. *Sci. Total Environ.* **2021**, *757*, 143814. [CrossRef] [PubMed]
26. Chen, M.; Xue, Y.; Xue, Y.; Peng, J.; Guo, J.; Liang, H. Assessing the effects of climate and human activity on vegetation change in Northern China. *Environ. Res.* **2024**, *247*, 118233. [CrossRef] [PubMed]
27. Liu, B.; Tang, Q.; Zhou, Y.; Zeng, T.; Zhou, T. The Sensitivity of Vegetation Dynamics to Climate Change across the Tibetan Plateau. *Atmosphere* **2022**, *13*, 1112. [CrossRef]
28. Ling, H. Spatio-temporal dynamics of vegetation in key ecological function zone of wind-break and sand-fixation over the last 20 years. *Acta Ecol. Sin.* **2021**, *41*, 8341–8351. [CrossRef]
29. Harris, I.; Osborn, T.J.; Jones, P.; Lister, D. Version 4 of the CRU TS monthly high-resolution gridded multivariate climate dataset. *Sci. Data* **2020**, *7*, 109. [CrossRef]
30. Xue, C.; Wu, H.; Jiang, X. Temporal and Spatial Change Monitoring of Drought Grade Based on ERA5 Analysis Data and BFAST Method in the Belt and Road Area during 1989–2017. *Adv. Meteorol.* **2019**, *2019*, 4053718. [CrossRef]
31. Zhou, Y.; Liu, J. A MODIS EVI based dataset of vegetation phenology for the key ecological observation stations in China (2001–2016) [Dataset]. *Sci. Data Bank* **2017**. [CrossRef]
32. Yin, C.; Luo, M.; Meng, F.; Sa, C.; Yuan, Z.; Bao, Y. Contributions of climatic and anthropogenic drivers to net primary productivity of vegetation in the Mongolian Plateau. *Remote Sens.* **2022**, *14*, 3383. [CrossRef]
33. He, T.; Dai, X.; Li, W.; Zhou, J.; Zhang, J.; Li, C.; Dai, T.; Li, W.; Lu, H.; Ye, Y.; et al. Response of net primary productivity of vegetation to drought: A case study of Qinba Mountainous area, China (2001–2018). *Ecol. Indic.* **2023**, *149*, 110148. [CrossRef]
34. Potter, C.S.; Randerson, J.T.; Field, C.B.; Matson, P.A.; Vitousek, P.M.; Mooney, H.A.; Klooster, S.A. Terrestrial ecosystem production: A process model based on global satellite and surface data. *Glob. Biogeochem. Cycles* **1993**, *7*, 811–841. [CrossRef]
35. Zhu, W.; Pan, Y.; He, H.; Yu, D.; Hu, H. Simulation of maximum light use efficiency for some typical vegetation types in China. *Chin. Sci. Bull.* **2006**, *51*, 457–463. [CrossRef]

36. Kong, D.; McVicar, T.R.; Xiao, M.; Zhang, Y.; Peña-Arancibia, J.L.; Filippa, G.; Xie, Y.; Gu, X. phenofit: An R package for extracting vegetation phenology from time series remote sensing. *Methods Ecol. Evol.* **2022**, *13*, 1508–1527. [CrossRef]
37. Li, Y.; Zhang, W.; Schwalm, C.R.; Gentine, P.; Smith, W.K.; Ciais, P.; Kimball, J.S.; Gazol, A.; Kannenberg, S.A.; Chen, A.; et al. Widespread spring phenology effects on drought recovery of Northern Hemisphere ecosystems. *Nat. Clim. Change* **2023**, *13*, 182–188. [CrossRef]
38. Savitzky, A.; Golay, M.J.E. Smoothing and differentiation of data by simplified least squares procedures. *Anal. Chem.* **1964**, *36*, 1627–1639. [CrossRef]
39. Sisheber, B.; Marshall, M.; Mengistu, D.; Nelson, A. Tracking crop phenology in a highly dynamic landscape with knowledge-based Landsat–MODIS data fusion. *Int. J. Appl. Earth Obs. Geoinf.* **2022**, *106*, 102670. [CrossRef]
40. Guo, J.; Yang, X.; Niu, J.; Jin, Y.; Xu, B.; Shen, G.; Zhang, W.; Zhao, F.; Zhang, Y. Remote sensing monitoring of green-up dates in the Xilingol grasslands of northern China and their correlations with meteorological factors. *Int. J. Remote Sens.* **2018**, *40*, 2190–2211. [CrossRef]
41. Jonsson, P.; Eklundh, L. Seasonality extraction by function fitting to time-series of satellite sensor data. *IEEE Trans. Geosci. Remote Sens.* **2022**, *40*, 1824–1832. [CrossRef]
42. Hou, D.; Al-Tabbaa, A.; Chen, H.; Mamic, I. Factor analysis and structural equation modelling of sustainable behaviour in contaminated land remediation. *J. Clean. Prod.* **2014**, *84*, 439–449. [CrossRef]
43. Lu, J.; Qin, T.; Yan, D.; Lv, X.; Yuan, Z.; Wen, J.; Xu, S.; Yang, Y.; Feng, J.; Li, W. Response of vegetation to drought in the source region of the Yangtze and Yellow Rivers based on causal analysis. *Remote Sens.* **2024**, *16*, 630. [CrossRef]
44. Cheung, M.W. Comparison of approaches to constructing confidence intervals for mediating effects using structural equation models. *Struct. Equ. Model. A Multidiscip. J.* **2007**, *14*, 227–246. [CrossRef]
45. Chen, A.; Yang, X.; Xu, B.; Jin, Y.; Guo, J.; Xing, X.; Yang, D.; Wang, P.; Zhu, L. Monitoring the spatiotemporal dynamics of aeolian desertification using Google Earth Engine. *Remote Sens.* **2021**, *13*, 1730. [CrossRef]
46. Lin, M.; Hou, L.; Qi, Z.; Wan, L. Impacts of climate change and human activities on vegetation NDVI in China's Mu Us Sandy Land during 2000–2019. *Ecol. Indic.* **2022**, *142*, 109164. [CrossRef]
47. Zhang, J.; Wang, J.; Liu, L.; Liu, H.; Liu, Y.; Li, M. On potential salient climatic factors tied to late-summer compound drought and heatwaves around Horqin sandy land, Northeast China. *Theor. Appl. Climatol.* **2024**, *155*, 6829–6842. [CrossRef]
48. Liu, S.; Zhao, H.; Dong, S.; Su, X.; Liu, Q.; Zhang, X. Landscape dynamics along a river corridor in alpine desert region and its driving factor analysis: A case study in Altun National Nature Reserve. *Chin. J. Ecol.* **2014**, *33*, 1647–1654. Available online: https://www.researchgate.net/publication/288442867_Landscape_dynamics_along_a_river_corridor_in_alpine_desert_region_and_its_driving_factor_analysis_A_case_study_in_Altun_National_Nature_Reserve (accessed on 27 July 2024).
49. Zhang, Y.; Lu, Y.; Sun, G.; Li, L.; Zhang, Z.; Zhou, X. Dynamic Changes in Vegetation Ecological Quality in the Tarim Basin and Its Response to Extreme Climate during 2000–2022. *Forests* **2024**, *15*, 505. [CrossRef]
50. Feng, J.; Yan, D.; Li, C.; Gao, Y.; Liu, J. Regional Frequency Analysis of Extreme Precipitation after Drought Events in the Heihe River Basin, Northwest China. *J. Hydrol. Eng.* **2014**, *19*, 1101–1112. [CrossRef]
51. Ma, S.; Ren, J.; Wu, C.; He, Q. Extreme precipitation events trigger abrupt vegetation succession in emerging coastal wetlands. *Catena* **2024**, *241*, 108066. [CrossRef]
52. Tuo, M.; Xu, G.; Zhang, T.; Guo, J.; Zhang, M.; Gu, F.; Wang, B.; Yi, J. Contribution of climatic factors and human activities to vegetation changes in arid grassland. *Sustainability* **2024**, *16*, 794. [CrossRef]
53. Dong, T.; Liu, J.; Shi, M.; He, P.; Li, P.; Liu, D. Seasonal scale climatic factors on Grassland phenology in Arid and Semi-Arid Zones. *Land* **2024**, *13*, 653. [CrossRef]
54. Ying, H.; Zhang, H.; Zhao, J.; Shan, Y.; Zhang, Z.; Guo, X.; Rihan, W.; Deng, G. Effects of spring and summer extreme climate events on the autumn phenology of different vegetation types of Inner Mongolia, China, from 1982 to 2015. *Ecol. Indic.* **2019**, *111*, 105974. [CrossRef]
55. He, Z.; Du, J.; Chen, L.; Zhu, X.; Lin, P.; Zhao, M.; Fang, S. Impacts of recent climate extremes on spring phenology in arid-mountain ecosystems in China. *Agric. For. Meteorol.* **2018**, *260–261*, 31–40. [CrossRef]
56. Zhang, S.; Zhang, J.; Liang, S.; Liu, S.; Zhou, Y. A perception of the nexus "resistance, recovery, resilience" of vegetations responded to extreme precipitation pulses in arid and semi-arid regions: A case study of the Qilian Mountains Nature Reserve, China. *Sci. Total Environ.* **2022**, *843*, 157105. [CrossRef]
57. Shen, Y.; Shen, Y.; Guo, Y.; Zhang, Y.; Pei, H.; Brenning, A. Review of historical and projected future climatic and hydrological changes in mountainous semiarid Xinjiang (northwestern China), central Asia. *Catena* **2020**, *187*, 104343. [CrossRef]
58. Xu, B.; Arain, M.A.; Black, T.A.; Law, B.E.; Pastorello, G.Z.; Chu, H. Seasonal variability of forest sensitivity to heat and drought stresses: A synthesis based on carbon fluxes from North American forest ecosystems. *Glob. Change Biol.* **2019**, *26*, 901–918. [CrossRef]
59. Shao, H.; Zhang, Y.; Gu, F.; Shi, C.; Miao, N.; Liu, S. Impacts of climate extremes on ecosystem metrics in southwest China. *Sci. Total Environ.* **2021**, *776*, 145979. [CrossRef]

Disclaimer/Publisher's Note: The statements, opinions and data contained in all publications are solely those of the individual author(s) and contributor(s) and not of MDPI and/or the editor(s). MDPI and/or the editor(s) disclaim responsibility for any injury to people or property resulting from any ideas, methods, instructions or products referred to in the content.

forests

MDPI

Article

Mapping the Future: Climate-Induced Changes in Aboveground Live-Biomass Carbon Density Across Mexico's Coniferous Forests

Carmela Sandoval-García [1], Jorge Méndez-González [1,*], Flores Andrés [2], Eulalia Edith Villavicencio-Gutiérrez [3], Fernando Paz-Pellat [4], Celestino Flores-López [1], Eladio Heriberto Cornejo-Oviedo [1], Alejandro Zermeño-González [5], Librado Sosa-Díaz [4], Marino García-Guzmán [1] and José Ángel Villarreal-Quintanilla [6]

[1] Department of Forestry, Autonomous Agrarian University Antonio Narro, Calz. Antonio Narro 1923, Saltillo 25315, Coahuila, Mexico; ka_rmen7@hotmail.com (C.S.-G.)
[2] National Center for Disciplinary Research in Conservation and Improvement of Forest Ecosystems, National Institute for Forestry, Agriculture and Livestock Research, Progreso 5, Mexico City 04010, Coyoacán, Mexico; flores.andres@inifap.gob.mx
[3] National Institute for Forestry, Agriculture and Livestock Research, Progreso 5, Saltillo Experimental Station, Saltillo 25315, Coahuila, Mexico
[4] Postgraduate College, Campus Montecillo, Montecillo, Texcoco 56264, Edo. de México, Mexico
[5] Irrigation and Drainage Department, Autonomous Agrarian University, Antonio Narro. Calz. Antonio Narro 1923, Saltillo 25315, Coahuila, Mexico
[6] Department of Botany, Autonomous Agrarian University Antonio Narro, Calz. Antonio Narro 1923, Saltillo 25315, Coahuila, Mexico
* Correspondence: jmendezg@hotmail.com; Tel.: +52-84431-21141

Abstract: Climate variations in temperature and precipitation significantly impact forest productivity. Precipitation influences the physiology and growth of species, while temperature regulates photosynthesis, respiration, and transpiration. This study developed bioclimatic models to assess how climate change will affect the carbon density of aboveground biomass ($_{cd}$AGB) in Mexico's coniferous forests for 2050 and 2070. We used $_{cd}$AGB data from the National Forest and Soils Inventory (INFyS) of Mexico and 19 bioclimatic variables from WorldClim ver. 2.0. The best predictors of $_{cd}$AGB were obtained using machine learning techniques with the "caret" library in R. The model was trained with 80% of the data and validated with the remaining 20% using Generalized Linear Models (GLMs). Current $_{cd}$AGB prediction maps were generated using the best predictors. Future $_{cd}$AGB was calculated with the average of three general circulation models (GCMs) of future climate projections from the Coupled Model Intercomparison Project Phase 5 (CMIP5), under four Representative Concentration Pathways (RCPs): 2.6, 4.5, 6.0, and 8.5 W/m^2. The results indicate $_{cd}$AGB losses in all climate scenarios, reaching up to 15 Mg C ha^{-1}, and could occur under the RCP 8.5 scenario by 2070 in the central region of the country. Temperature-related variables are more important than precipitation variables. Bioclimatic variables can explain up to 20% of the total variance in $_{cd}$AGB. The temperature in the study area is expected to increase by 2.66 °C by 2050 and 3.36 °C by 2070, while precipitation is expected to fluctuate by ±10% relative to the current values, which could geographically redistribute the $_{cd}$AGB of the country's coniferous forests. These findings underscore the need for forest management to focus not only on biodiversity conservation but also on the carbon storage capacity of these ecosystems.

Keywords: aboveground biomass; bioclimatic models; climate change; coniferous forests; machine learning

1. Introduction

Forests occupy approximately 31% of the Earth's terrestrial surface, equivalent to around 4.06 billion hectares, and play a pivotal role in climate regulation by acting as major

carbon sinks. Global forests are estimated to sequester approximately 662 gigatonnes (Gt) of carbon, distributed as follows: 44% in living biomass, 45% in soil organic matter, and 11% in dead wood and litter [1].

In Mexico, forests cover approximately 64.8 million hectares, accounting for about 33% of the national land area [1]. These forests include a wide range of types, including temperate, broad-leaved, mixed, and tropical forests [2], and are estimated to store around 1.69 Gt of carbon [3]. Changes in temperature and precipitation patterns due to climate change have been shown to adversely affect forest growth, biomass accumulation, and carbon sequestration at a global scale [4,5].

The scientific basis for studying climate change is unequivocal, and the findings are irrefutable; climate change is present and highly likely to intensify in the coming years. Between 2011 and 2020, the global average surface temperature rose by 1.09 °C compared to the 1850–1900 baseline, with more pronounced warming observed in the Northern Hemisphere, particularly over land (1.59 °C) compared to oceans (0.88 °C). Precipitation patterns are shifting, with increases observed at higher latitudes and decreases in the subtropics. Climate projections indicate that extreme events will escalate in frequency and intensity, while the carbon sequestration capacity of global forest ecosystems is projected to diminish [6].

In Mexico, the average temperature increased by 0.31 °C per decade between 1971 and 2020, with the most pronounced effects occurring in the northern plateau during the summer months. According to projections under the SSP3-7.0 climate scenario, the average temperature is expected to increase by 0.82 °C between 2020 and 2039 and by 1.63 °C between 2040 and 2059. In addition, some northern states are likely to experience significant reductions in precipitation [7].

Precipitation and temperature are well established as primary drivers of forest biomass productivity [4]. Precipitation plays a pivotal role in plant physiology by regulating transpiration, nutrient uptake, stomatal conductance, and nutrient availability [8,9]. In addition to shaping species-specific growth strategies. Variations in precipitation availability also affect water use efficiency [10,11], with a direct relationship between precipitation levels and biomass productivity [2].

Similarly, temperature exerts significant control over plant growth by modulating fundamental physiological processes, including photosynthesis, respiration, and transpiration [4,12]. It also governs the rate of chemical reactions and CO_2 assimilation [13]. While rising temperatures may stimulate biomass accumulation in boreal forests, they tend to suppress growth in tropical forests [14]. Excessively high temperatures reduce growth rates, alter leaf pigmentation, impair root system development, and induce water stress, thereby disrupting normal growth patterns [15].

Plants from temperate climates exhibit a degree of cold tolerance, but extremely low temperatures negatively affect processes such as cell division, photosynthesis, and metabolic activity, leading to reduced productivity [16].

Climatic variations are driving forests to become increasingly dynamic systems [17], resulting in changes in tree species composition within ecosystems [11]. Simultaneous shifts in temperature and precipitation lead to either reductions or increases in ecosystem biomass, thereby altering global forest distribution patterns [18].

It is well established that temperature exerts both positive and negative effects on aboveground forest biomass [4,19,20]. Furthermore, annual precipitation is generally positively correlated with aboveground biomass [12,21], though this relationship is not fully consistent, as it depends on forest type and, more importantly, the specific bioclimatic variable being correlated [22]. These effects have been documented across various forest biomes, including temperate, tropical, and boreal ecosystems [14], as well as at the species level [8].

To estimate aboveground biomass in forest ecosystems, both dynamic variables (related to climate) and static variables (such as diameter at breast height, basal area, stand density, slope, aspect, and elevation, among others) have been jointly applied [8,23–25].

These mixed models, incorporating dynamic and static variables that influence aboveground biomass, demonstrate predictive capacities ranging from moderate (R^2 = 0.19) to very high (R^2 = 0.86), as indicated by their determination coefficients [8,23,24]. In some cases, these models include nine or more explanatory variables [8].

While these models are useful for identifying correlations between biomass and environmental variables, they are limited in their ability to quantify the direct impacts of climate change on aboveground biomass [8,23,26].

To effectively assess the impact of climate change on carbon density across different scales (species, genus, ecosystems), it is essential to use dynamic variables. Moreover, focusing on dynamic variables provides insights into how potential future climate fluctuations, in both temperature and precipitation, will affect carbon density. This supports effective forest management and informed conservation policies while facilitating the development of adaptive strategies to address the challenges posed by climate change.

Furthermore, forests are highly dynamic systems that undergo temporal changes due to natural disturbances, anthropogenic activities, and climatic fluctuations, which introduces additional complexity to the modeling process [25,27].

The research conducted by [22] indicated that, among ten conifer species, precipitation demonstrated a positive correlation with aboveground biomass density ($0 \leq \rho \leq 0.20$), whereas temperature exhibited a negative correlation ($-0.20 \leq \rho \leq 0$). Importantly, the magnitude and direction of the correlation between climatic variables and aboveground biomass in forest ecosystems are highly contingent upon several factors, such as spatial scale [28], forest type [4], and species-specific traits [12,23].

To deepen our understanding of how climate change specifically influences aboveground biomass, it is imperative to develop new modeling frameworks. These models should integrate dynamic climatic data to directly assess the effects of climate variability and enable future projections—an objective that cannot be fully achieved by models that rely solely on static stand or site-level variables.

Based on the above considerations, the primary objective of this study was to develop bioclimatic models specifically designed to assess the impact of climate change on the geospatial distribution of aboveground live biomass carbon density in Mexican pine forests. Bioclimatic models are defined as predictive tools that assess the relationships between climatic variables and biological responses. These models can be based on climatic variables alone or in conjunction with additional non-climatic covariates [29]. The analysis incorporated four distinct climate scenarios based on Representative Concentration Pathways (RCPs) 2.6, 4.5, 6.0, and 8.5 W/m^2, projected for 2050 and 2070. These models are intended to provide highly accurate information that can enhance forest management practices and contribute to climate change mitigation efforts. It is hypothesized that future climate projections will exert a significant influence on the aboveground biomass carbon density in the pine forests of Mexico.

2. Materials and Methods

2.1. Study Area Description

Conifers in Mexico are found from sea level up to over 4000 m in altitude, with the highest diversity concentrated in the Sierra Madre Occidental (SMOc) and the Sierra Madre Oriental (SMO), and Mexico hosts 49 species of pine, representing 40% of the approximately 120 pine species worldwide [30]. The distribution of these species spans approximately from 32 °N north latitude to 19 °N and from 105 °W west longitude to 98 °W on soils derived from igneous and metamorphic rocks [31]. These ecosystems are characterized by a climate with cold temperatures, with annual precipitation ranging from 350 to 1200 mm and average temperatures ranging from 6 to 28 °C [32] and with rainy summers and dry, cold winters, and they are dominated by coniferous trees such as pines (*Pinus* spp.), firs (*Abies* spp.), cedars (*Cupressus* spp.), and junipers (*Juniperus* spp.) [33] (Figure 1).

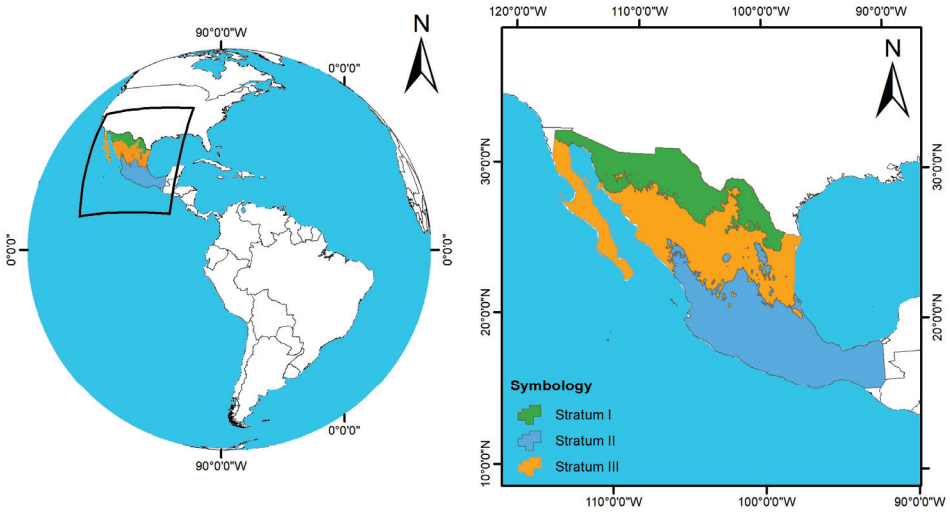

Figure 1. Study area in the global context (**left**) and regional context (**right**).

2.2. Data Acquisition and Cleaning Process

A total of 22 parameters, including type, topographic, species richness, biomass, carbon (aboveground and belowground), health indices, climate, geographic, and dasometric factors (Appendix A), were obtained from [2]. From there, we used data on carbon density in aboveground live biomass (henceforth referred to as $_{cd}$AGB), geographic coordinates (lat, long), and ID of each cluster, exclusively from the parameter type = "coniferous forests". The $_{cd}$AGB is the carbon stock per unit area of live biomass contained in living trees, including stems, branches, leaves, and seeds [34]. These data were calculated from the National Forest and Soil Inventory (INFyS) of Mexico (2009–2012) [2]. Additionally, we utilized 19 bioclimatic variables from WorldClim version 2.0, covering the period from 1970 to 2000 (Appendix B), in raster format with a resolution of 30 arcseconds, published in January 2020 [35]. These variables have been previously used in similar studies [8,9,12,14,28,36].

Using the "raster" library in R [37], we employed the geographic coordinates of each cluster to extract values for the 19 bioclimatic variables (Bios). To identify erroneous or atypical data in $_{cd}$AGB, we applied a Principal Component Analysis (PCA) to the centered and scaled matrix of $_{cd}$AGB and 19 Bios, using the "FactoMineR" v.2.9 library [38]. We considered outliers as those falling outside the 95% confidence ellipse of the PCA, which were subsequently excluded from the dataset to ensure the coherence and reliability of the results.

2.3. Predictive Modeling of $_{cd}$AGB

Due to the significant climatic variability recorded in the pine forests of the country [31], and in order to enhance predictions of $_{cd}$AGB, a bioclimatic stratification of Mexico's pine forest areas was conducted. We utilized 19 bioclimatic variables in raster format, employing the "GeoStratR" library [39], to create strata (geographical space) in the same format. The clusters from INFyS located within each generated stratum were separated for independent analysis.

For the selection of predictors (Bios) of $_{cd}$AGB, within each stratum, the machine learning (ML) technique employing 10-fold cross-validation was utilized, employing backward selection. A tuning grid ranging from 1 to 7 predictors (nvmax = 1:7) was considered [40]. The statistical significance of regression coefficients ($p < 0.05$) and the variance inflation factor (VIF) were evaluated to mitigate multicollinearity effects.

With the subset of predictors that met these criteria, the model was trained using the Generalized Linear Models (GLMs) method with the "identity" link function. For this purpose, 80% of the data (randomly obtained and by quantiles) were used. This approach (GLM) is suitable for continuous and positive response variables [2,9] in this type of study.

The model fitting was performed using the "caret" package in R [40]. Hypothesis tests ($\propto = 0.05$) were conducted on the regression coefficients ($H_0 : \beta_i = 0 \; vs \; H_1 : \beta_i \neq 0, \ldots, \beta_{ij}$) of the final model. We utilized the "lmg" metric to calculate the importance of each bioclimatic variable (as a percentage of the variance explained by the model), which provides a decomposition of the model's explained variance into non-negative contributions [41]. For the remaining 20% of the data, the model was validated using various techniques: Leave-One-Out Cross-Validation (LOOCV), Cross-Validation (CV; k = 10), Repeated Cross-Validation (RCV, k = 10, rep = 10), and Bootstrap (reps = 100). The evaluation included calculations of Root Mean Square Error (RMSE), Pseudo Coefficient of Determination (Rsquared), and Mean Absolute Error (MAE) to assess the model's performance. These validations were conducted using the "caret" R package [40].

2.4. Current and Future Prediction and Rate of Change of $_{cd}$AGB

Using the generated bioclimatic models, current predictions of $_{cd}$AGB were made for each stratum, employing the corresponding bioclimatic predictors. The raster library in R software [37] was used to predict $_{cd}$AGB values. Specifically, we applied the argument type = "response"—a function within the raster library—to generate $_{cd}$AGB prediction maps in raster format. This approach enabled the creation of spatially explicit maps that visualize the distribution and magnitude of predicted variables across the study area.

To predict future $_{cd}$AGB, raster layers from three different General Circulation Models (GCMs) were obtained: MIROC-6, GISS-E2, and CMCC-ESM2. From these models, only the bioclimatic predictors of $_{cd}$AGB for each stratum were selected. The GCMs are derived from future climate projections of the Coupled Model Intercomparison Project Phase 5 (CMIP5) at a resolution of 2.5 degrees. Four Representative Concentration Pathways (RCPs) developed by the Intergovernmental Panel on Climate Change [42] were used, characterized by their projected Total Radiative Forcing (TRF) for the year 2100, ranging from 2.6, 4.5, and 6.0 to 8.5 W/m^2, considering the years 2050 and 2070. These RCP scenarios are used to project potential future trajectories of climate change based on different emission levels and mitigation efforts.

The three layers of each GCM, RCP, and year were averaged using raster algebra. Using this average and the corresponding bioclimatic model, future prediction of $_{cd}$AGB was conducted for each stratum. Similarly, the R raster library [37] was employed with the argument type = "response" to generate raster maps of future $_{cd}$AGB predictions. To identify changes in future $_{cd}$AGB relative to the current scenario, the following expression was employed: $_{cd}$AGB (future) $-$ $_{cd}$AGB (current). The results are as follows: 0 if pixel values are equal in both scenarios; positive if $_{cd}$AGB is higher in the future; and negative if $_{cd}$AGB is higher in the current scenario.

To visualize the vulnerable areas of Mexico's coniferous forests to changes in $_{cd}$AGB due to climate change, a 40 km radius buffer was created around each site from the National Forest and Soil Inventory. This delineated the forested areas that were potentially affected. Subsequently, the number of pixels for each $_{cd}$AGB change category or rate within these buffer polygons was quantified. The resulting change rate was then presented in map form for each RCP and year.

In addition, uncertainty in future predictions of $_{cd}$AGB was quantified using the standard error: EE(θ) = $\sqrt{}$[Var(θ). This involved repeated predictions of $_{cd}$AGB from MIROC-6 + GISS-E2 + CMCC-ESM2, for each RCP and year, which were averaged using the raster library [37], and generating a raster map of EE(θ).

2.5. Bioclimatic Predictors: Current Analysis and Future Projections

In order to determine the influence of future bioclimatic predictors on the changes in $_{cd}$AGB of Mexican forests, the non-parametric Wilcoxon signed-rank test was employed. This test was used to evaluate whether there are significant differences between the medians of two samples: the current bioclimatic predictor and the future bioclimatic predictor (e.g., current Bio1 vs. Bio1 2050, RCP 4.0). A significance level of 95% was used.

For this purpose, the current and future values (average of 3 GCMs, RCP, and year) of the predictors for each stratum (Bios) were extracted the geographic coordinates of each cluster and employing the raster library [37]. These analyses were represented in violin plots, with temperature-derived Bios shown in orange and precipitation-derived Bios in blue, with statistical significance indicated by the * symbol at the top.

All statistical analyses, figures, and geographic processing were performed using R software version 4.3.1 [43].

3. Results

3.1. Distribution Carbon Density of Aboveground Live Biomass

The stratification process of the coniferous forests in Mexico resulted in three strata: stratum I, located in the northwest of the country (Figure 2a; n = 60), stratum II, in the central-southern part of the country (Figure 2b; n = 450), and stratum III, located in the Sierra Madre Occidental, SMO (Figure 2c; n = 463). The sample size for each stratum varies, as indicated in Table 1. This variation is determined by the geographic extent of each stratum generated during the stratification process and by the number of National Forest and Soil Inventory sites located within each stratum.

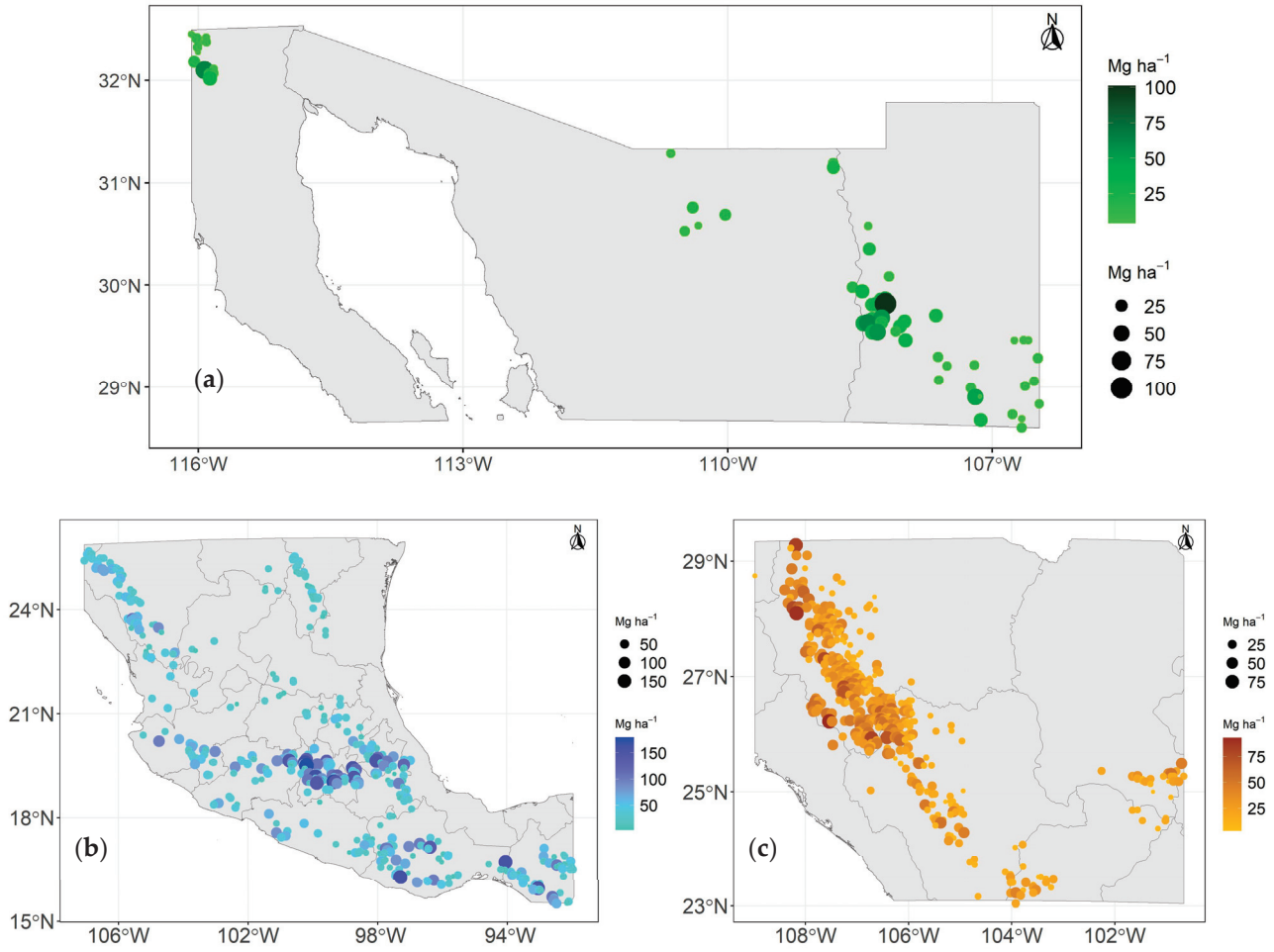

Figure 2. Distribution of sites from the National Forest and Soil Inventory (2009–2012): stratum I (**a**), stratum II (**b**), and stratum III (**c**). The size of the circles and the color gradient indicate the values of carbon density in the aboveground live biomass (Mg C ha^{-1}).

Table 1. Regression coefficients for the prediction of the carbon density of aboveground live biomass by stratum in the coniferous forests of Mexico.

Stratum	Coefficient	Estimate	2.5	97.5	Std. Err	*T* Value	Pr (>|t|)	Residual Deviance	VIF	Imp. (%)
I	β_0 (intercept)	64.8332	22.7606	97.3943	23.2221	2.79	0.00772 **			
(n = 48)	β_1 (Bio 5)	−0.1897	−0.2932	−0.0544	0.0737	−2.57	0.01355 *	13.246	1.02	10.33
	β_2 (Bio 18)	0.0586	0.0337	0.0829	0.0123	4.77	2.02×10^{-5} ***		1.02	8.74
II	β_0 (intercept)	87.6362	66.3661	108.9076	10.4558	8.38	1.22×10^{-15} ***			
(n = 360)	β_1 (Bio 5)	−0.2572	−0.3296	−0.1841	0.0376	−6.84	3.37×10^{-11} ***	172.17	1.03	8.04
	β_2 (Bio 12)	0.0190	0.0106	0.0272	0.0037	5.12	4.91×10^{-7} ***		1.03	3.35
III	β_0 (intercept)	26.6379	12.3682	40.4383	8.4994	3.13	0.00186 **			
(n = 370)	β_1 (Bio 10)	−0.0959	−0.1571	−0.0293	0.0391	−2.45	0.01461 *	132.39	1.16	3.28
	β_2 (Bio 13)	0.0933	0.0708	0.1160	0.0135	6.93	1.8×10^{-11} ***		1.16	14.95

β_0, β_1, and β_2: are the regression coefficients; 2.5 and 97.5: 95% confidence intervals of the regression coefficients; Std. Err: standard error of the regression coefficients; *Pr* (>|t|): The probability of obtaining a T-value more extreme than the observed one, assuming that the null hypothesis is true. VIF: variance inflation factor; Imp = importance value of the variables. Bio 05: Max Temperature of Warmest Month (°C); Bio 10: Mean Temperature of Warmest Quarter (°C); Bio 12: Annual Precipitation (mm); Bio 13: Precipitation of Wettest Month (mm); Bio 18: Precipitation of Warmest Quarter (mm). Statistical significance: "* $p < 0.05$": Significant; "** $p < 0.01$": Highly significant; "*** $p < 0.001$": Very highly significant.

3.2. Models for Predicting Carbon Density in the Aboveground Live Biomass

The bioclimatic variables selected by the algorithms were statistically significant ($p < 0.05$) for predicting $_{cd}$AGB. The predictors (Bios) of $_{cd}$AGB were represented by both precipitation variables (3 out of 6) and temperature variables (3 out of 6). However, at the stratum level, temperature variables were more important (Imp., Table 1) than precipitation variables. Bio 5 (Max Temperature of Warmest Month) was the best predictor of $_{cd}$AGB in strata I and II. No model exhibited multicollinearity (VIF < 1.16), which ensures that $_{cd}$AGB predictions are not overestimated.

The equations for estimating $_{cd}$AGB in each stratum are as follows:

$$\text{Stratum I: } {}_{cd}\text{AGB (Mg C ha}^{-1}) = 64.8332 + -0.1897 \times \text{Bio 5 (°C} \times 10) + 0.0586 \times \text{Bio 18 (mm)} \quad (1)$$

$$\text{Stratum II: } {}_{cd}\text{AGB (Mg C ha}^{-1}) = 87.6362 + -0.2572 \times \text{Bio 5 (°C} \times 10) + 0.0190 \times \text{Bio 12 (mm)} \quad (2)$$

$$\text{Stratum III: } {}_{cd}\text{AGB (Mg C ha}^{-1}) = 26.6379 + -0.0959 \times \text{Bio 10 (°C} \times 10) + 0.0933 \times \text{Bio 13 (mm)} \quad (3)$$

The mean of $_{cd}$AGB does not follow a pattern among strata; that is, it is not lower in stratum I and higher in stratum III. The mean $_{cd}$AGB in stratum II represents, on average, up to 1.6 times more than in strata I and III; and it ranges from 23.14 Mg C ha^{-1} (stratum I) to 42.57 Mg C ha^{-1} (stratum II), with maximum values reaching almost 180 Mg C ha^{-1} (Table 2), but it also has the highest variability (*CV* > 60%). None of the variables showed normality ($p < 0.0001$) according to the Shapiro–Wilk and Anderson–Darling tests (Table 2).

Table 2. Descriptive statistics of the observed carbon density of aboveground live biomass and its predictors (1950–2000 period) in the coniferous forests of Mexico.

Stratum	Parameter	*n*	Min	P25	Mean	Median	P75	Max	*SD*	*CV*	Shapiro *p*-Value	Anderson *p*-Value
I	$_{cd}$AGB	48	4.23	11.54	23.14	16.23	33.35	62.05	15.04	65	0.0001	0.0001
	Bio 5		27.7	28.7	29.97	29.6	30.75	36	1.76	5.89	0.0001	0.0001
	Bio 18		62	223	256.89	290	330.5	397	101.66	39.57	0.0001	0.0001
II	$_{cd}$AGB	360	4.46	19.87	42.57	34.35	54.75	179.69	33.01	77.54	0.0001	0.0001
	Bio 5		17.5	22.78	25.72	25.3	28.7	34.6	3.93	15.28	0.0001	0.0001
	Bio 12		426	895.25	1109.42	1092	1314.25	2216	367.25	33.1	0.0001	0.0001

Table 2. *Cont.*

Stratum	Parameter	*n*	Min	P25	Mean	Median	P75	Max	*SD*	*CV*	Shapiro	Anderson
											p-Value	*p*-Value
III	$_{cd}$AGB	370	3.15	12.76	26.26	23.24	35.98	92.92	16.56	63.05	0.0001	0.0001
	Bio 10		14.7	17.4	18.55	18.3	19.4	26.3	1.74	9.39	0.0001	0.0001
	Bio13		53	154	184.03	181	219	357	52.54	28.55	0.0001	0.0001

$_{cd}$AGB: carbon density of aboveground live biomass (Mg C ha^{-1}); Bio 5: Max Temperature of Warmest Month (°C); Bio18: Precipitation of Warmest Quarter (mm); Bio12: Annual Precipitation (mm); Bio10: Mean Temperature of Warmest Quarter (°C); Bio13: Precipitation of Wettest Month (mm); *n* = number of sites in the stratum; Min: minimum value; P25 and P75: 25th and 75th percentiles; Max: maximum value; *SD*: standard deviation; *CV*: coefficient of variation (%).

3.3. Validation of Predictive Models for $_{cd}$AGB

According to the pseudo R^2 derived from the validation procedure, bioclimatic variables explain an average of 19% of the $_{cd}$AGB (Table 3). The LOOCV method calculates the lowest R^2 (0.10), while the other methods yield an average R^2 of 0.22. According to the validation, when using the models to predict aboveground biomass carbon density with independent data from the training set, the estimation errors (RMSE) could range from 13.18 Mg C ha^{-1} (stratum III) to 42.42 Mg C ha^{-1} (stratum I), with the best estimates observed in stratum III.

Table 3. Validation of bioclimatic regression models for predicting the carbon density of aboveground live biomass in coniferous forests in Mexico.

Stratum	Method	Set	*n*	Pseudo R^2	RMSE	MAE
I		Training	48			
	LOOCV	Validation	12	0.031	38.319	30.806
	CV	Validation	12	0.177	29.908	29.379
	RCV	Validation	12	0.177	31.949	31.272
	Bootstrap	Validation	12	0.316	42.426	34.457
II		Training	360			
	LOOCV	Validation	90	0.128	29.938	21.789
	CV	Validation	90	0.249	28.493	21.720
	RCV	Validation	90	0.246	28.620	21.685
	Bootstrap	Validation	90	0.150	30.107	22.302
III		Training	370			
	LOOCV	Validation	92	0.153	13.887	10.699
	CV	Validation	92	0.231	13.181	10.543
	RCV	Validation	92	0.238	13.330	10.600
	Bootstrap	Validation	92	0.192	14.175	10.986

Where: LOOCV: Leave-One-Out Cross-Validation; CV: Cross-Validation; RCV: Repeated Cross-Validation; *n*: sample size; R^2: Coefficient of Determination; RMSE: Root Mean Square Error; MAE: Mean Absolute Error.

3.4. Current and Future Prediction of Carbon Density of Aboveground Live Biomass

Using the bioclimatic models generated here, at the INFyS sites, predictions range from 7.48 to 34.79 Mg C ha^{-1}, from 16.68 to 71.29 Mg C ha^{-1}, and from 10.98 to 41.91 Mg C ha^{-1} for strata I, II, and III, respectively (Figure 3a–c). The highest $_{cd}$AGB is observed/predicted in stratum II (Figure 3b) in the central region of the country. The highest differences between the observed $_{cd}$AGB and estimated $_{cd}$AGB are −19 and +30, −52 and +124, −29 and +56 Mg C ha^{-1}, respectively, for strata I, II, and III.

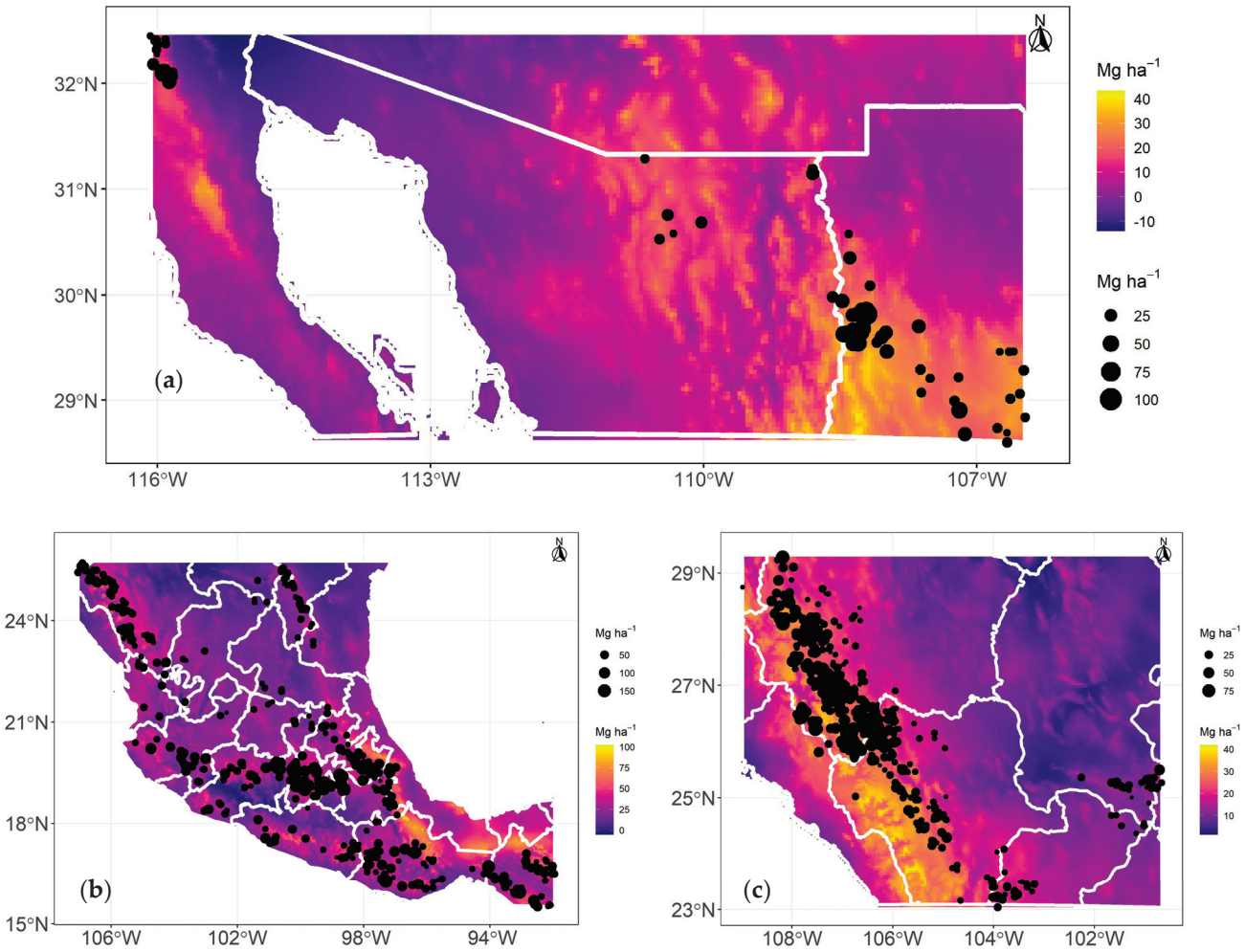

Figure 3. Prediction of current carbon density of aboveground live biomass in Mexican conifer forests through bioclimatic models: stratum I (**a**), stratum II (**b**), and stratum III (**c**). Circle size and color gradient indicate values of carbon density of aboveground live biomass (Mg C ha^{-1}).

According to future predictions of $_{cd}$AGB up to 2050 and 2070 (Figures 4–6) using the bioclimatic model for each stratum (Equations (1)–(3)), under any climate scenario (RCP), only reductions in $_{cd}$AGB are expected. Forests in stratum II (Figure 5a–h, situated in the central and southern regions of the country) would be the most affected, with decreases ranging from −5 to −10 Mg ha^{-1}, potentially up to −20 Mg C ha^{-1} by 2070, whereas those in stratum III (Figure 5a–h, SMO) would experience lesser impacts ranging from 0 to −5 Mg C ha^{-1} (Table 4). The most significant losses of $_{cd}$AGB are expected under RCP 8.5 and are anticipated to be greater by 2070.

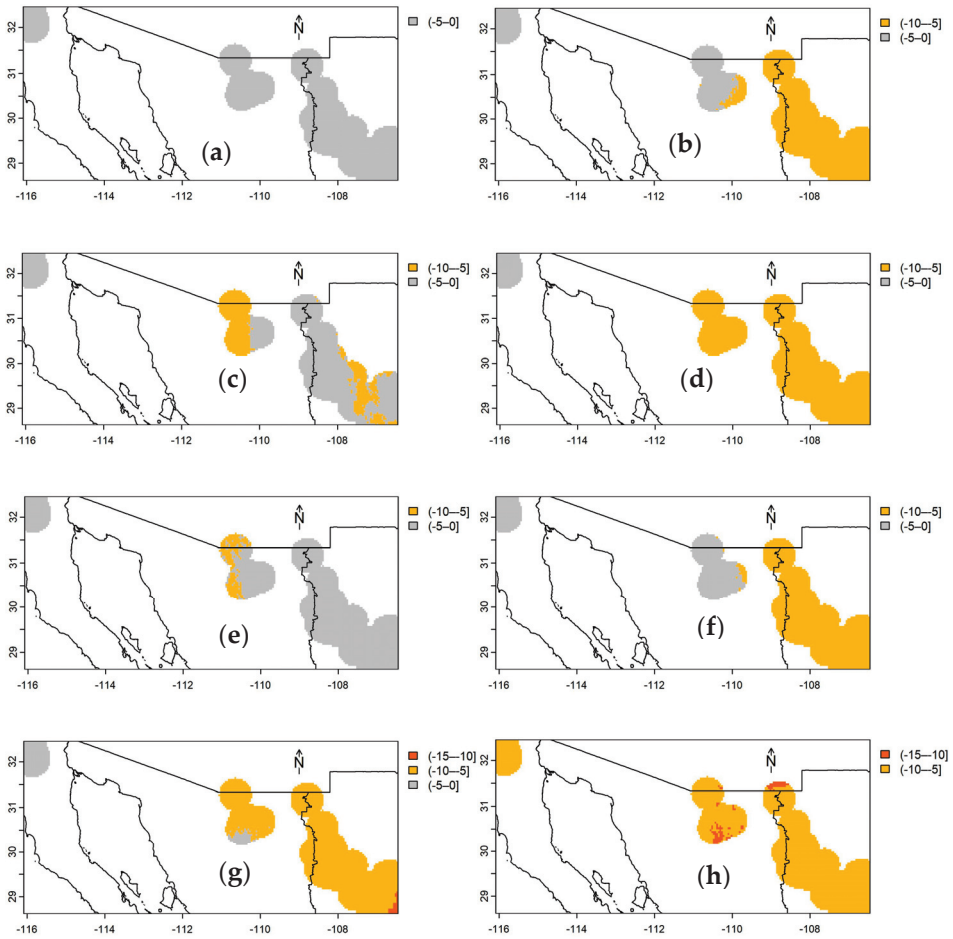

Figure 4. Changes in carbon density of aboveground live biomass in Mexican conifer forests under the RCP 2.6 to 8.5 scenarios (**a**–**d**) for the years 2050 and 2070 (**e**–**h**) in stratum I. Colored areas represent 40 km radius buffers around each INFyS site; uncolored areas correspond to other vegetation types different from conifer forests.

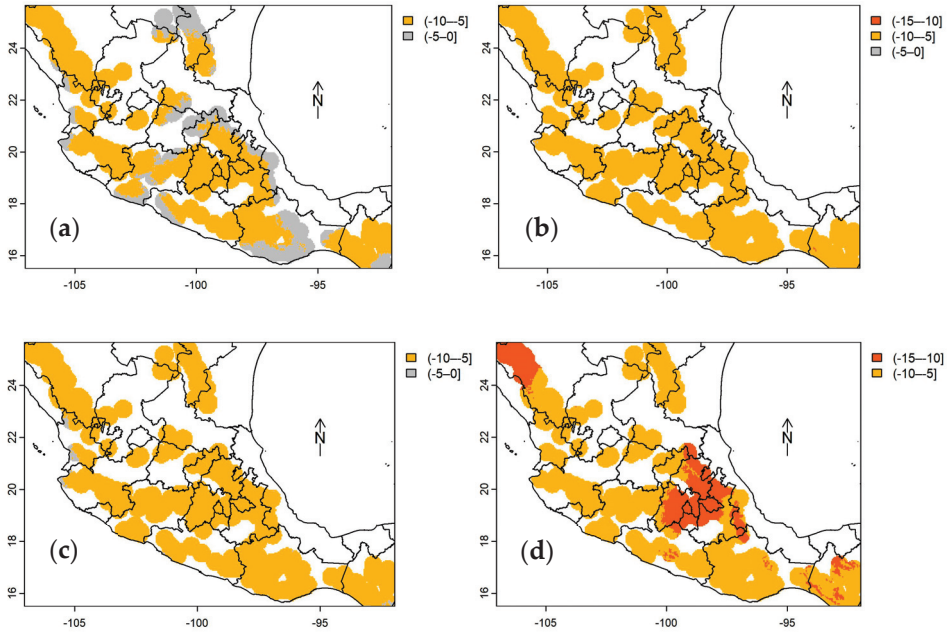

Figure 5. *Cont*.

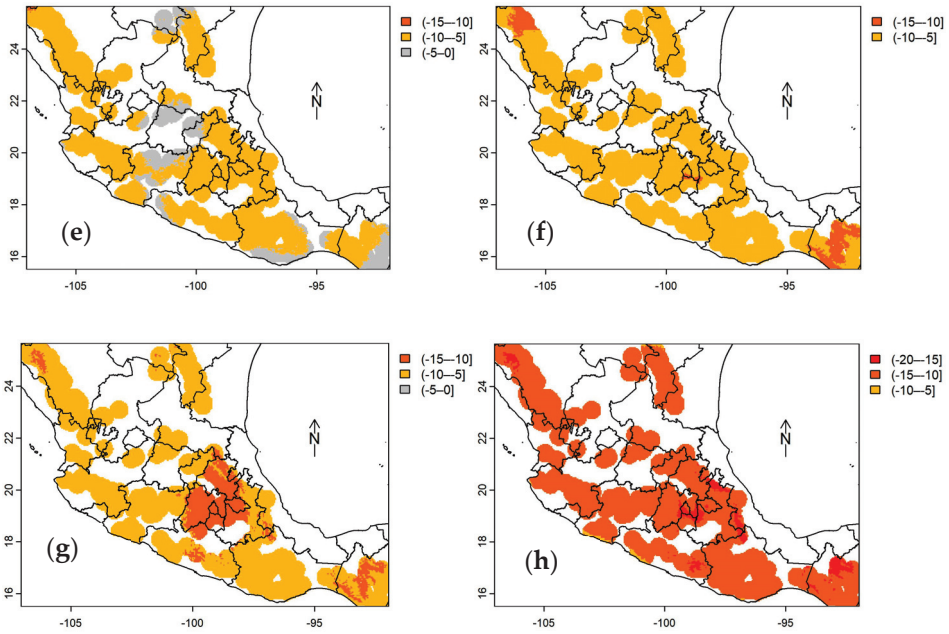

Figure 5. Changes in carbon density of aboveground live biomass in Mexican conifer forests under the RCP 2.6 to 8.5 scenarios (**a**–**d**), for the years 2050 and 2070 (**e**–**h**) in stratum II. Colored areas represent 40 km radius buffers around each INFyS site; uncolored areas correspond to other vegetation types different from conifer forests.

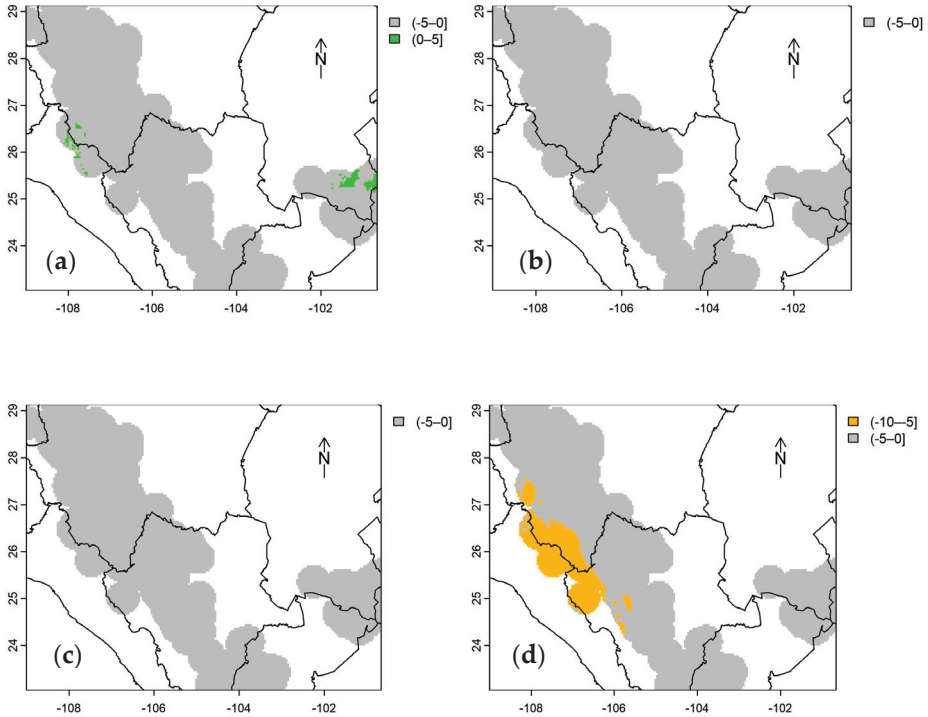

Figure 6. *Cont.*

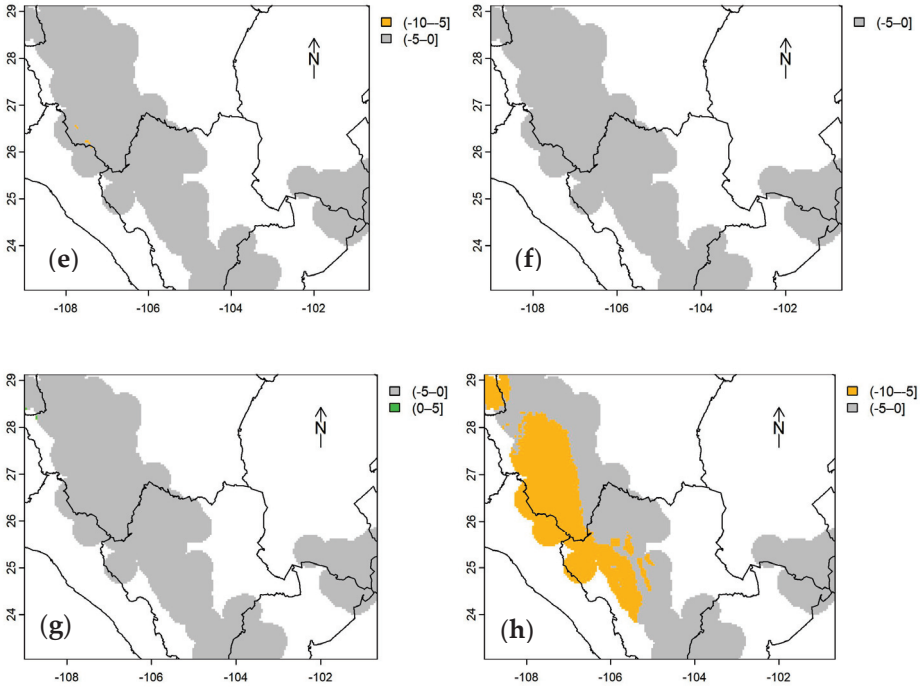

Figure 6. Changes in the carbon density of aboveground live biomass in Mexican conifer forests under the RCP 2.6 to 8.5 scenarios (**a**–**d**) for the years 2050 and 2070 (**e**–**h**) in stratum III. Colored areas represent 40 km radius buffers around each INFyS site; uncolored areas correspond to other vegetation types different from conifer forests.

Table 4. Number of pixels contained within the 40 km radius buffer around each sampling site of INFyS to differentiate changes in carbon density of aboveground live biomass in the conifer forests of Mexico under future climatic scenarios. Each pixel represents 0.98 × 0.98 km on each side.

Stratum	Changes in $_{cd}$AGB	RCP 26		RCP 45		RCP 60		RCP 85	
		2050	2070	2050	2070	2050	2070	2050	2070
I	(−20–−15])	0	0	0	0	0	0	0	0
	(−15—10])	0	0	0	0	0	35	0	107
	(−10–−5])	0	240	2361	2280	906	2885	3011	3180
	(−5–0])	3287	3047	926	1007	2381	367	276	0
	(0–5])	0	0	0	0	0	0	0	0
II	(−20–−15])	0	0	0	0	0	0	0	1148
	(−15–−10])	0	30	6	1526	0	3928	4796	22,466
	(−10–−5])	17,750	19,473	23,821	22,317	23,571	19,912	19,047	229
	(-5–0])	6093	4340	16	0	272	3	0	0
	(0–5])	0	0	0	0	0	0	0	0
III	(−20–−15])	0	0	0	0	0	0	0	0
	(−15–−10])	0	0	0	0	0	0	0	0
	(−10–−5])	0	6	0	0	0	0	1290	3281
	(−5–0])	9680	9819	9825	9825	9825	9822	8535	6544
	(0–5])	145	0	0	0	0	3	0	0

Observed carbon density of aboveground live biomass (Mg C ha^{-1}); RCP = Representative Concentration Pathway. The color of the box in column two corresponds to the color of the pixel in Figures 3–5.

3.5. Evaluation of Climate Projections on Variables Predicting $_{cd}$AGB

The Wilcoxon test provided sufficient evidence ($p < 0.0001$) to reject the null hypothesis (H0) of equal medians between the current Bio and the same Bio under a future climate scenario. In all cases, the median of the estimated temperature Bios for 2050 and 2070, projected by three General Circulation Models (GCMs), in any climate scenario (RCP; left, Figure 7), will be higher than the current median (Table 2). Generally, the temperature

is expected to increase by 2.66 °C (2050) and 3.36 °C (2070) compared to the present (Figure 7a,c,e). The coniferous areas in stratum II are predicted to be vulnerable due to a likely increase of +2.7 °C by 2050, whereas the less vulnerable areas will be in stratum III (+2.5 °C).

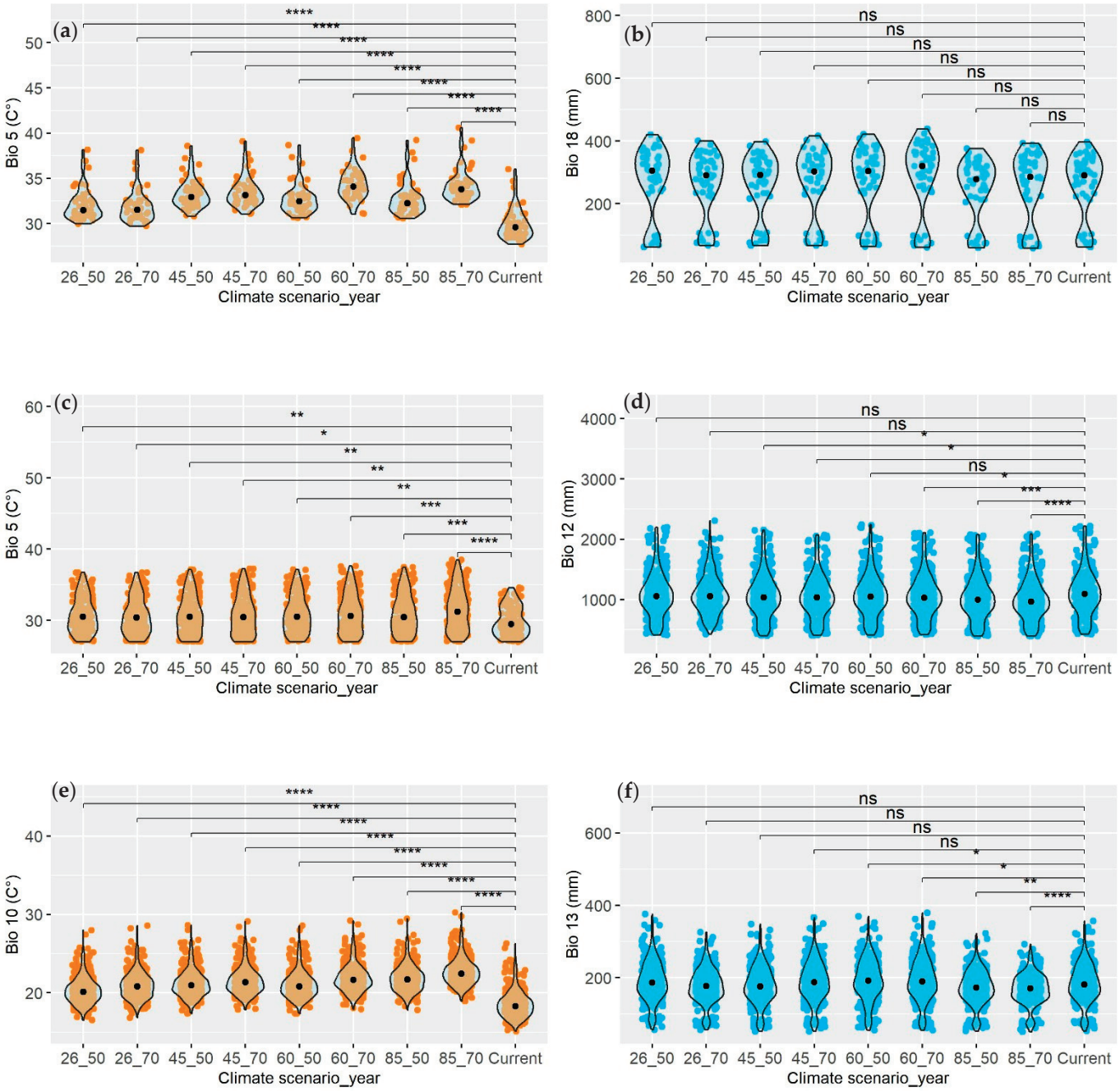

Figure 7. Wilcoxon test for comparing medians of the current variable with each climate scenario, in strata I (**a**,**b**), II (**c**,**d**), and III (**e**,**f**). Bio 05: Max Temperature of Warmest Month (°C); Bio 10: Mean Temperature of Warmest Quarter (°C); Bio 12: Annual Precipitation (mm); Bio 13: Precipitation of Wettest Month (mm); Bio 18: Precipitation of Warmest Quarter (mm). Significance levels: ns (Not significant), * (Significant at 0.05%), ** (Significant at 1%), *** (Significant at 0.1%), **** (Significant at 0.01%).

Generally, the test demonstrated that in the coniferous forests of Mexico, precipitation levels in 2050 and 2070 could statistically be the same ($p < 0.05$) as those currently recorded in stratum I (Figure 7b). In stratum II, precipitation is projected to decrease ($p < 0.0001$) by 5.3% (2050) and 6.4% (2070) (Figure 7d), while in stratum III, it could either increase or

decrease (Figure 7f). When analyzed individually (Current vs. Bio-RCP-Year), significant differences exist only for precipitation variables (right, Figure 7) and not for temperature variables (left, Figure 7).

The uncertainty (represented by the standard error) estimated for $_{cd}$AGB shown here (Figure 8), for the most critical scenario (RCP 85 | 2070), indicates that the standard error ranges from 2.5 Mg C ha^{-1} (stratum III) to 6 Mg C ha^{-1} (stratum II), well below the RMSE (Table 3) estimated with independent data. This uncertainty is similar in less critical climatic scenarios (RCP 26 | 2050).

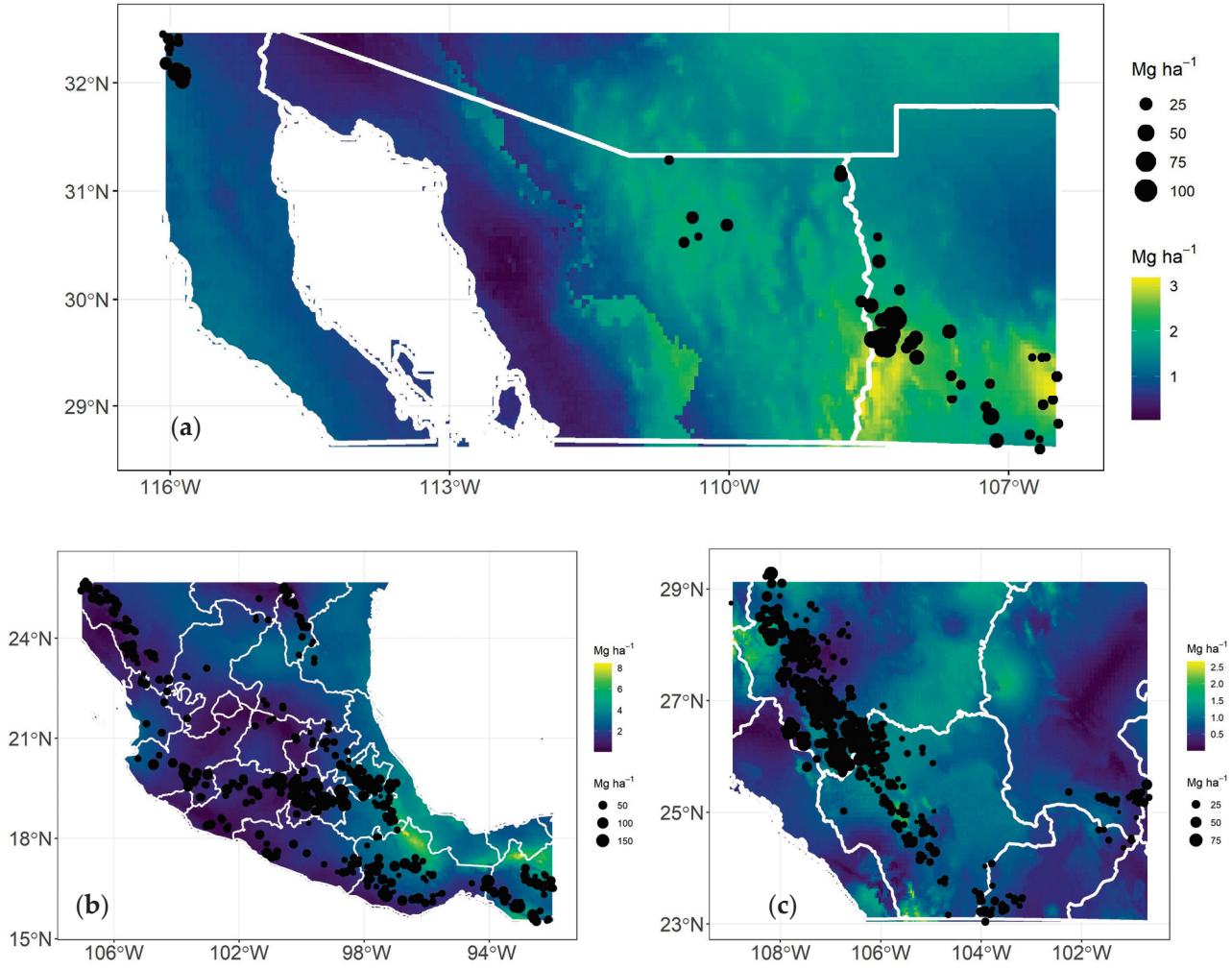

Figure 8. Estimated uncertainty (standard error) of carbon density of aboveground live biomass in Mexican conifer forests, for strata I (**a**), II (**b**), and III (**c**) under RCP 85 and for the year 2070.

4. Discussion

The selection of $_{cd}$AGB predictors through automated algorithms (stepwise, machine learning, neural networks, etc.) is generally efficient. These algorithms have been tested in natural forests [44,45], tropical rainforests [46], and even in plantations [19]. Although the variables selected by these algorithms are statistically significant, $p < 0.05$ [36], the models generated here exhibited multicollinearity effects (VIF > 10); consequently, these models had to be evaluated to mitigate this effect and enhance the accuracy of the predictions.

Some authors [47] have used linear procedures (lm) for predicting NPP (Net Primary Production) in grasslands, with favorable results. We tested this technique; however, it was demonstrated that in this type of study, it is difficult to meet all the assumptions of a regression model ($\varepsilon_i \sim N(0, \sigma^2)$), which is why the "glm" procedure was ultimately employed, as has been done in such studies [2,9]. In addition to these procedures, the

Random Forest [8,48,49] and Bayesian models [20] have also been used for predicting AGB (above-ground biomass) from temperature and precipitation variables.

4.1. Predictor Variables of Aboveground Biomass

In this study, the algorithms selected both temperature variables (Bio5 and Bio10) and precipitation variables (Bio12, Bio13, and Bio18) as the best predictors of $_{cd}$AGB. Temperature variables were the most important in the model (contributing 8 to 10% to the pseudo R^2) for strata I and II (Table 1, Figure 2a,b), but not for stratum III. According to some authors [21,47], on a global scale, precipitation and temperature variables are the best predictors of AGB. Specifically, annual mean temperature (Bio1) and temperature of the warmest quarter (Bio10) are climatic variables associated with biomass distribution on broad scales. Metrics demonstrate that temperatures appear to be more important than precipitation variables [28].

It has been demonstrated that hthe bioclimatic variables of temperature (Bio1 and Bio5) and precipitation (Bio12) are associated with the accumulation of AGB in forests [20], boreal ecosystems [19], temperate seasonal ecosystems [18], tropical rainforests [50], and tropical seasonal ecosystems [4,5]. As can be observed, Bio5 and Bio12 (Appendix A) are good predictors of AGB across different types of ecosystems. For instance, a study conducted in the SMO (stratum II of this same study) indicates that average temperature (Bio1) is the most important predictor for AGB in temperate forests [25].

In Australian forests, encompassing 15 types of forests predominantly dominated by eucalypts [8], it has been demonstrated that climatic variables are better predictors of AGB than soil variables, with Bio 9 (Mean Temperature of Driest Quarter) being the most important variable. Regardless of the metrics, as in our study, temperature variables appear to be the most important for predicting AGB (Table 1).

However, the relationship between bioclimatic variables and AGB is entirely dependent on the type of ecosystem, the species, and the region of the world. For this reason, other authors emphasize that the mean annual precipitation (MAP) has a relatively greater importance (0.19%) than the mean annual temperature (MAT) (0.05%) for predicting AGB in Larix plantations in northern and northeastern China. Furthermore, its importance is also dependent on the model structure [19].

Continuing with the previous narrative, the relationship between precipitation and AGB can be complex, as different responses may be observed depending on the type of forest and climatic conditions. This variable significantly influences the accumulation of different components of AGB (branches, stems, roots, and needles) in conifer plantations. Therefore, it is essential to consider it in predictive models and the evaluation of the climate–forest relationship [12]. However, climatic variables such as temperature and precipitation together can improve AGB estimates [21]. In tropical forests [51], 13 predictor variables of AGB were used, including geographical, topographical, hydrological, soil, and even species-related variables (e.g., coverage). They found that the relative influence of MAP on AGB is 37.6%, making it the most important, while MAT has a relative influence of less than 1%.

4.2. Correlation Between Bioclimatic Variables and Carbon Density

The correlation of $_{cd}$AGB with temperature variables (Bio 5 and Bio 10) in temperate forests of Mexico is negative but positive with precipitation variables (Table 1). Similar findings were reported by [23], who observed a negative correlation ($-0.46 > r < -0.63$; $-0.43 > r < -0.60$) between the stem biomass of *Larix gmelinii* and *Betula platyphylla* with MAT. Likewise, other studies have demonstrated that MAT is negatively correlated with AGB, either at the species level [12] or at the stand level [36].

Similar to this study, in temperate and dry forests, a positive correlation between $_{cd}$AGB and MAP has been observed [27]. This same relationship is found in other studies; for instance, [23] discovered that MAP positively correlates with the stem biomass of *Larix gmelinii* ($0.84 > r < 0.92$) and *Betula platyphylla* ($0.76 > r < 0.88$). Additionally, [12] observed

that MAP positively and significantly ($p < 0.05$) correlates with the AGB of *Pinus koraiensis* Siebold & Zucc., *Larix olgensis* A. Henry, and *Pinus sylvestris* var. mongolica Litv.

Furthermore, the study conducted by [28] reveals that, on a global scale (>6200 forests and 61 countries), MAT is positively correlated with foliage biomass, although the geographical patterns of correlation are inconsistent. The authors of [14] found that while temperature correlates positively in boreal forests, the opposite occurs in tropical forests. Studies conducted by [4] in boreal forests demonstrate that MAT can explain (R^2) between 26% and 45% of carbon density and is positively correlated; whereas MAP can explain between 28% and 67% of carbon density (both aboveground and belowground); however, the correlation between these two variables is positive when precipitation is between 0 and 1000 mm and negative when it exceeds 1000 mm.

In contrast to this study, in boreal and temperate forests, a positive relationship has been found between $_{cd}$AGB and MAT [18], but a negative one in humid regions [27].

4.3. Predictive Capacity of Bioclimatic Models

Model validation is crucial for assessing the predictive capacity of a model based on new data. In reality, within this context (AGB–climatic predictor relationship), few studies undertake this process [19,48,52,53]. As is known, when generating a model using the "glm" procedure, statistics such as R^2, RMSE, and MAE, are not computed. Upon validating our models, we were able to calculate these metrics and evaluate the predictive capacity of each model. We observed that bioclimatic variables can explain up to 22% of $_{cd}$AGB in these types of forests (Table 3), a reasonably significant value at the eco-region level [4], but not at the species level [12,23], where variables can explain up to 84% of AGB at this scale.

In general, the "cross-validation" technique has been the most commonly used to validate models for estimating AGB [19,36,53,54]; in this study, we used it along with three other techniques (Table 3). It is noteworthy that when dealing with climatic predictors, these can explain around 20% (Table 3), whereas predicting AGB from predictors derived from vegetation indices, e.g., normalized difference vegetation index (NDVI), spectral information [53], or satellite optical images and unmanned aerial vehicles [54], can explain (R^2) up to 80% of AGB. The inclusion of different predictor variables such as MAP, MAT, clay content, pH, dryness index, and stand age can explain up to 44.4% of $_{cd}$AGB in temperate forests [4].

However, exclusive stand predictors (diameter at breast height, age, and stand density) can explain up to 98% of the ABG variance [19]. The RMSE metric is entirely dependent on the units and scale of the dependent variables, which is why such distant differences are observed across studies.

4.4. Current and Future Projection of $_{cd}$AGB

Under any climate scenario (RCP—year), our models predict losses in $_{cd}$AGB ranging from 5 Mg C ha^{-1} (2050) to 20 Mg C ha^{-1} by 2070 (Figures 4–6) in Mexico's coniferous forests. Globally, positive changes in Total Carbon Density (TCD) are projected for temperate forests, averaging 2.23 Mg C ha^{-1} (RCP 26, 45, and 85; 2050) and 1.99 Mg C ha^{-1} by 2070. Specifically for Mexico, these authors [4] predict changes of $\pm$20 Mg C ha^{-1}. It is important to note that, for the country, only two plots were considered in [4], whereas our study was conducted at a finer scale, generating models from $n = 48$ to $n = 370$ (Table 2).

A study conducted by [55] under various simulation scenarios, altering temperature and precipitation, in Yunnan Province, China, suggests that the combined effects of these variables are more complex than anticipated. These effects can result in both gains and losses (as observed in this study) in carbon sequestration across different forest types, attributed to decreased precipitation and increased temperature. Our study shows a decrease in $_{cd}$AGB, primarily due to a temperature increase of 1 to 3 °C and a precipitation decrease of approximately 10%. Nearly three decades ago [56], the vulnerability of Mexico's forests to climate change was assessed, revealing that under these conditions (+2 °C and

−10% precipitation), the area of humid and dry temperate forests would significantly decrease (to less than half of their current size).

In a study conducted in the Brazilian Atlantic Forest (AF) [57], it was found that in 34.7% of the existing forest fragments, AGB could increase, while in 2.6%, it could decrease by the year 2100. Models predict an 8.5% increase in total carbon stock; additionally, 76.9% of AF would be suitable for a potential increase in AGB by 2100 under RCP 4.5, solely due to climate change. This contrasts with findings here, possibly due to differences in forest types and geographical location, but is similar to what was found by [36] in subtropical evergreen forests in China, showing a decrease in AGB by 2050–2070, varying according to different climate scenarios (RCP 2.6 > RCP 4.5 > RCP 6.0 > RCP 8.5).

5. Conclusions

The relationships between $_{cd}$AGB and climate are more complex than they may initially appear. Bioclimatic variables, especially those related to temperature, have proven to be significant predictors of $_{cd}$AGB in the developed models and can explain up to 19% of $_{cd}$AGB. Bio 5 (Max Temperature of Warmest Month) emerged as the most robust predictor. Predictions using bioclimatic models suggest that all strata of the country's coniferous forests, under any climate scenario (RCP—Year), will experience declines in $_{cd}$AGB (in the absence of anthropogenic activities) by 2050 and 2070, particularly under the RCP 8.5 scenario. It is expected that forests in stratum II will be the most affected, with significant reductions that could reach up to -20 Mg C ha^{-1} by the year 2070. The temperature projected by the GCMs for 2050 and 2070 will be significantly higher than current levels, with increases of up to 3.55 °C in stratum I by 2070. Precipitation could remain unchanged in stratum I, decrease (−10%) in stratum II, and vary (±10%) in stratum III. These future climate projections are expected to lead to a redistribution of $_{cd}$AGB in Mexican forests. The conclusions suggest an urgent need for adaptation and mitigation strategies to conserve biodiversity and ecosystem services provided by conifer forests in Mexico. Forest management should consider not only biodiversity conservation but also the carbon storage capacity of these ecosystems.

Author Contributions: Conceptualization, J.M.-G. and C.S.-G.; methodology, J.M.-G. and J.Á.V.-Q.; software, C.S.-G.; validation, E.H.C.-O., C.F.-L. and F.A.; formal analysis, J.M.-G.; investigation, F.P.-P. and E.E.V.-G.; resources, A.Z.-G. and L.S.-D.; data curation, C.S.-G., M.G.-G. and F.A.; writing—original draft preparation, C.S.-G.; writing—review and editing, E.H.C.-O., A.Z.-G. and E.E.V.-G.; visualization, L.S.-D. and M.G.-G.; supervision, J.M.-G.; project administration, J.M.-G. All authors have read and agreed to the published version of the manuscript.

Funding: This research was funded by AUTONOMOUS AGRARIAN UNIVERSITY ANTONIO NARRO, grant number 38111425103001-2185.

Data Availability Statement: Data are contained within the article.

Acknowledgments: The authors are grateful to the AUTONOMOUS AGRARIAN UNIVERSITY ANTONIO NARRO, for funding all stages of this study through Project No 38111425103001-2185.

Conflicts of Interest: The authors declare no conflicts of interest. The funders had no role in the design of the study; in the collection, analyses, or interpretation of data; in the writing of the manuscript; or in the decision to publish the results.

Appendix A. Comprehensive Dataset of Physical and Biological Biomass and Carbon Content Parameters in Mexico's National Forest Inventory

#	Name	Short Name	Unit
1	Identification (Cluster no.) *	ID	
2	Type* (Conifers forests) *	Type	
3	Tenure	Tenure	
4	Slope	Slope	deg
5	DEPTH, soil	Depth soil	m
6	Structural richness	Structural rich	
7	Tree richness	Tree rich	
8	Number of stumps	Stumps	#
9	Biomass, aboveground	Biom abovegr	t/ha
10	Biomass, belowground	Biom belowgr	t/ha
11	Biomass, total	Biom total	t/ha
12	Carbon, aboveground *	C abovegr	t/ha
13	Carbon, belowground	C belowgr	t/ha
14	Soil carbon stock	C stock	t/ha
15	Fires index	Fires	
16	Pests index	Pests	
17	Temperature, air, annual mean	MAAT	°C
18	Precipitation, annual mean	MAP	mm
19	Longitude *	Longitude	
20	Latitude *	Latitude	
21	Trees, diameter at breast height	DBH	cm
22	Height	Height	m

* Selected parameters for data analysis in the present study.

Appendix B. Bioclimatic Variables

Variable	Description	Units	Scale
Bio 1	Annual Mean Temperature	°C	Annual
Bio 2	Mean Diurnal Range (max temp–min temp)	°C	Monthly
Bio 3	Isothermality (Bio02/Bio07) (×100)	%	Annual
Bio 4	Temperature Seasonality (standard deviation × 100)	%	Annual
Bio 05	Max Temperature of Warmest Month	°C	Monthly
Bio 06	Min Temperature of Coldest Month	°C	Monthly
Bio 07	Temperature Annual Range (Bio5–Bio6)	°C	Annual
Bio 08	Mean Temperature of Wettest Quarter	°C	Quarterly
Bio 09	Mean Temperature of Driest Quarter	°C	Quarterly
Bio 10	Mean Temperature of Warmest Quarter	°C	Quarterly
Bio 11	Mean Temperature of Coldest Quarter	°C	Quarterly
Bio 12	Annual Precipitation	mm	Annual
Bio 13	Precipitation of Wettest Month	mm	Monthly
Bio 14	Precipitation of Driest Month	mm	Monthly
Bio 15	Precipitation Seasonality (Coefficient of variation)	%	Quarterly
Bio 16	Precipitation of Wettest Quarter	mm	Quarterly
Bio 17	Precipitation of Driest Quarter	mm	Quarterly
Bio 18	Precipitation of Warmest Quarter	mm	Quarterly
Bio 19	Precipitation of Coldest Quarter	mm	Quarterly

References

1. FAO. *El Estado de Los Bosques Del Mundo 2022*; FAO: Rome, Italy, 2022.
2. Arasa-Gisbert, R.; Vayreda, J.; Román-Cuesta, R.M.; Villela, S.A.; Mayorga, R.; Retana, J. Forest Diversity Plays a Key Role in Determining the Stand Carbon Stocks of Mexican Forests. *For. Ecol. Manag.* **2018**, 415–416, 160–171. [CrossRef]
3. Rodríguez-Veiga, P.; Saatchi, S.; Tansey, K.; Balzter, H. Magnitude, Spatial Distribution and Uncertainty of Forest Biomass Stocks in Mexico. *Remote Sens. Environ.* **2016**, *183*, 265–281. [CrossRef]

4. Guo, Y.; Peng, C.; Trancoso, R.; Zhu, Q.; Zhou, X. Stand Carbon Density Drivers and Changes under Future Climate Scenarios across Global Forests. *For. Ecol. Manag.* **2019**, *449*, 117463. [CrossRef]
5. Ma, Y.; Eziz, A.; Halik, Ü.; Abliz, A.; Kurban, A. Precipitation and Temperature Influence the Relationship between Stand Structural Characteristics and Aboveground Biomass of Forests—A Meta-Analysis. *Forests* **2023**, *14*, 896. [CrossRef]
6. IPCC. *Climate Change 2021—The Physical Science Basis*; Cambridge University Press: Cambridge, UK, 2021; pp. 3–32.
7. Climate Risk Profile: Mexico (2023): The World Bank Group.Washington, DC, USA. 41 p. Available online: https://climateknowledgeportal.worldbank.org/sites/default/files/country-profiles/15634-WB_Mexico%20Country%20Profile-WEB%20(2).pdf (accessed on 22 June 2024).
8. Bennett, A.C.; Penman, T.D.; Arndt, S.K.; Roxburgh, S.H.; Bennett, L.T. Climate More Important than Soils for Predicting Forest Biomass at the Continental Scale. *Ecography* **2020**, *43*, 1692–1705. [CrossRef]
9. Cysneiros, V.C.; Coelho de Souza, F.; Gaui, T.D.; Pelissari, A.L.; Orso, G.A.; Machado, S.d.A.; de Carvalho, D.C.; Silveira-Filho, T.B. Integrating Climate, Soil and Stand Structure into Allometric Models: An Approach of Site-Effects on Tree Allometry in Atlantic Forest. *Ecol. Indic.* **2021**, *127*, 107794. [CrossRef]
10. Gao, J.; Zhao, P.; Shen, W.; Rao, X.; Hu, Y. Physiological Homeostasis and Morphological Plasticity of Two Tree Species Subjected to Precipitation Seasonal Distribution Changes. *Perspect. Plant Ecol. Evol. Syst.* **2017**, *25*, 1–19. [CrossRef]
11. Yuan, J.; Yan, Q.; Wang, J.; Xie, J.; Li, R. Different Responses of Growth and Physiology to Warming and Reduced Precipitation of Two Co-Existing Seedlings in a Temperate Secondary Forest. *Front. Plant Sci.* **2022**, *13*, 946141. [CrossRef]
12. Xin, S.; Wang, J.; Mahardika, S.B.; Jiang, L. Sensitivity of Stand-Level Biomass to Climate for Three Conifer Plantations in Northeast China. *Forests* **2022**, *13*, 2022. [CrossRef]
13. Eamus, D. How Does Ecosystem Water Balance Affect Net Primary Productivity of Woody Ecosystems? *Funct. Plant Biol.* **2003**, *30*, 187–205. [CrossRef]
14. Liu, Y.; Yu, G.; Wang, Q.; Zhang, Y. How Temperature, Precipitation and Stand Age Control the Biomass Carbon Density of Global Mature Forests. *Glob. Ecol. Biogeogr.* **2014**, *23*, 323–333. [CrossRef]
15. Han, S.H.; Kim, D.H.; Kim, G.N.; Lee, J.C.; Yun, C.W. Changes on Initial Growth and Physiological Characteristics of Larix Kaempferi and Betula Costata Seedlings under Elevated Temperature. *Korean J. Agric. For. Meteorol.* **2012**, *14*, 63–70. [CrossRef]
16. Devi, V.; Kaur, A.; Sethi, M.; Avinash, G. Perspective Chapter: Effect of Low-Temperature Stress on Plant Performance and Adaptation to Temperature Change. In *Plant Abiotic Stress Responses and Tolerance Mechanisms*; IntechOpen: London, UK, 2023.
17. Pan, Y.; Birdsey, R.A.; Phillips, O.L.; Jackson, R.B. The Structure, Distribution, and Biomass of the World's Forests. *Annu. Rev. Ecol. Evol. Syst.* **2013**, *44*, 593–622. [CrossRef]
18. Keith, H.; Mackey, B.G.; Lindenmayer, D.B. Re-Evaluation of Forest Biomass Carbon Stocks and Lessons from the World's Most Carbon-Dense Forests. *Proc. Natl. Acad. Sci. USA* **2009**, *106*, 11635–11640. [CrossRef] [PubMed]
19. He, X.; Lei, X.; Zeng, W.; Feng, L.; Zhou, C.; Wu, B. Quantifying the Effects of Stand and Climate Variables on Biomass of Larch Plantations Using Random Forests and National Forest Inventory Data in North and Northeast China. *Sustainability* **2022**, *14*, 5580. [CrossRef]
20. Chen, X.; Luo, M.; Larjavaara, M. Effects of Climate and Plant Functional Types on Forest Above-Ground Biomass Accumulation. *Carbon Balance Manag.* **2023**, *18*, 5. [CrossRef]
21. Dai, L.; Ke, X.; Guo, X.; Du, Y.; Zhang, F.; Li, Y.; Li, Q.; Lin, L.; Peng, C.; Shu, K.; et al. Responses of Biomass Allocation across Two Vegetation Types to Climate Fluctuations in the Northern Qinghai–Tibet Plateau. *Ecol. Evol.* **2019**, *9*, 6105–6115. [CrossRef] [PubMed]
22. Girón-Gutiérrez, D.; Méndez-González, J.; Osorno-Sánchez, T.G.; Cerano-Paredes, J.; Soto-Correa, J.C.; Cambrón-Sandoval, V.H. Climate as a Driver of Aboveground Biomass Density Variation: A Study of Ten Pine Species in Mexico. *Forests* **2024**, *15*, 1160. [CrossRef]
23. Khan, D.; Muneer, M.A.; Nisa, Z.U.; Shah, S.; Amir, M.; Saeed, S.; Uddin, S.; Munir, M.Z.; Lushuang, G.; Huang, H. Effect of Climatic Factors on Stem Biomass and Carbon Stock of Larix Gmelinii and Betula Platyphylla in Daxing'anling Mountain of Inner Mongolia, China. *Adv. Meteorol.* **2019**, 1–10. [CrossRef]
24. David, H.C.; de Araújo, E.J.G.; Morais, V.A.; Scolforo, J.R.S.; Marques, J.M.; Péllico Netto, S.; MacFarlane, D.W. Carbon Stock Classification for Tropical Forests in Brazil: Understanding the Effect of Stand and Climate Variables. *For. Ecol. Manag.* **2017**, *404*, 241–250. [CrossRef]
25. López-Serrano, P.M.; Domínguez, J.L.C.; Corral-Rivas, J.J.; Jiménez, E.; López-Sánchez, C.A.; Vega-Nieva, D.J. Modeling of Aboveground Biomass with Landsat 8 Oli and Machine Learning in Temperate Forests. *Forests* **2020**, *11*, 11. [CrossRef]
26. Rezashobairi, S.; Lin, H.; Usoltsev, V.; Osmirko, A.; Tsepordey, I.; Ye, Z.; Anees, S. A Comparative Pattern for *Populus* Spp. and *Betula* Spp. Stand Biomass in Eurasian Climate Gradients. *Croat. J. For. Eng.* **2022**, *43*, 457–467. [CrossRef]
27. Stegen, J.C.; Swenson, N.G.; Enquist, B.J.; White, E.P.; Phillips, O.L.; Jørgensen, P.M.; Weiser, M.D.; Monteagudo Mendoza, A.; Núñez Vargas, P. Variation in Above-Ground Forest Biomass across Broad Climatic Gradients. *Glob. Ecol. Biogeogr.* **2011**, *20*, 744–754. [CrossRef]
28. Reich, P.B.; Luo, Y.; Bradford, J.B.; Poorter, H.; Perry, C.H.; Oleksyn, J. Temperature Drives Global Patterns in Forest Biomass Distribution in Leaves, Stems, and Roots. *Proc. Natl. Acad. Sci. USA* **2014**, *111*, 13721–13726. [CrossRef]
29. Ellis, C.J. Climate Change, Bioclimatic Models and the Risk to Lichen Diversity. *Diversity* **2019**, *11*, 54. [CrossRef]

30. Gernandt, D.S.; Pérez-De La Rosa, J.A. Biodiversity of Pinophyta (Conifers) in Mexico. *Rev. Mex. Biodivers.* **2014**, *85*, 215–223. [CrossRef]
31. Rzedowski, J.; Huerta, L. *Vegetación de México*; Editorial Limusa: Ciudad de México, Mexico, 2006.
32. Granados-Sánchez, D.; López-Ríos, G.F.; Hernández-García, M.A. Ecología Y Silvicultura Bosques Templados. *Rev. Chapingo Ser. Cienc. For. Y Ambiente* **2007**, *13*, 67–80.
33. Challenger, A. *Utilización y Conservación de Los Ecosistemas Terrestres de México*; Instituto de Biología: Distrito Federal, Mexico, 1998; 847p, ISBN 970-9000-02-0. Available online: https://biblioteca.ecosur.mx/cgi-bin/koha/opac-detail.pl?biblionumber=23389 (accessed on 12 August 2024).
34. Grupo Intergubernamental de Expertos sobre el Cambio Climático (IPCC). Orientación Sobre las Buenas Prácticas para uso de la Tierra, Cambio de uso de la Tierra y Silvicultura. Available online: https://www.ipcc-nggip.iges.or.jp/public/gpglulucf/gpglulucf_languages.html (accessed on 12 August 2024).
35. Fick, S.E.; Hijmans, R.J. WorldClim 2: New 1-km Spatial Resolution Climate Surfaces for Global Land Areas. *Int. J. Climatol.* **2017**, *37*, 4302–4315. [CrossRef]
36. Li, Y.; Li, M.; Wang, Y. Forest Aboveground Biomass Estimation and Response to Climate Change Based on Remote Sensing Data. *Sustainability* **2022**, *14*, 14222. [CrossRef]
37. Hijmans, R.J. raster: Geographic Data Analysis and Modeling. R package version 3.6-26. 2023. Available online: https://CRAN.R-project.org/package=raster (accessed on 6 October 2024).
38. Lê, S.; Josse, J.; Rennes, A.; Husson, F. FactoMineR: An R Package for Multivariate Analysis. *J. Stat. Softw.* **2008**, *25*, 1–18. [CrossRef]
39. Corcoran, D.C. GeoStratR: Simple Spatial Stratification of Rasters. 2024. Available online: https://sustainscapes.github.io/GeoStratR/ (accessed on 12 August 2024).
40. Kuhn, M. Building predictive models in R using the caret package. *J. Stat. Softw.* **2008**, *28*, 1–26. [CrossRef]
41. Grömping, U. Relative Importance for Linear Regression in R: The Package Relaimpo. *J. Stat. Softw.* **2006**, *17*, 1–27. [CrossRef]
42. IPCC. *Climate Change 2013: The Physical Science Basis. Contribution of Working Group I to the Fifth Assessment Report of the Intergovernmental Panel on Climate Change*; Stocker, T.F., Qin, D., Plattner, G.-K., Tignor, M., Allen, S.K., Boschung, J., Nauels, A., Xia, Y., Bex, V., Midgley, P.M., Eds.; Cambridge University Press: Cambridge, UK, 2013; p. 1535.
43. R Core Team. *R: A Language and Environment for Statistical Computing*; R Foundation for Statistical Computing: Vienna, Austria, 2024.
44. Luo, M.; Wang, Y.; Xie, Y.; Zhou, L.; Qiao, J.; Qiu, S.; Sun, Y. Combination of Feature Selection and Catboost for Prediction: The First Application to the Estimation of Aboveground Biomass. *Forests* **2021**, *12*, 216. [CrossRef]
45. Bjork, S.; Anfinsen, S.N.; Naesset, E.; Gobakken, T.; Zahabu, E. On the Potential of Sequential and Nonsequential Regression Models for Sentinel-1-Based Biomass Prediction in Tanzanian Miombo Forests. *IEEE J. Sel. Top. Appl. Earth Obs. Remote Sens.* **2022**, *15*, 4612–4639. [CrossRef]
46. Ortiz-Reyes, A.D.; Valdez-Lazalde, J.R.; Ángeles-Pérez, G.; de los Santos-Posadas, H.M.; Schneider, L.; Aguirre-Salado, C.A.; Peduzzi, A. Synergy of Landsat, Climate and LiDAR Data for Aboveground Biomass Mapping in Medium-Stature Tropical Forests of the Yucatan Peninsula, Mexico. *Rev. Chapingo Ser. Cienc. For. Ambiente* **2021**, *27*, 383–400. [CrossRef]
47. Zhang, H.; Feng, Z.; Shen, C.; Li, Y.; Feng, Z.; Zeng, W.; Huang, G. Relationship between the Geographical Environment and the Forest Carbon Sink Capacity in China Based on an Individual-Tree Growth-Rate Model. *Ecol. Indic.* **2022**, *138*, 108814. [CrossRef]
48. Cartus, O.; Kellndorfer, J.; Walker, W.; Franco, C.; Bishop, J.; Santos, L.; Fuentes, J.M.M. A National, Detailed Map of Forest Aboveground Carbon Stocks in Mexico. *Remote Sens.* **2014**, *6*, 5559–5588. [CrossRef]
49. Yan, M.; Xia, Y.; Yang, X.; Wu, X.; Yang, M.; Wang, C.; Hou, Y.; Wang, D. Biomass Estimation of Subtropical Arboreal Forest at Single Tree Scale Based on Feature Fusion of Airborne LiDAR Data and Aerial Images. *Sustainability* **2023**, *15*, 1676. [CrossRef]
50. Chen, L.; Ren, C.; Zhang, B.; Wang, Z.; Xi, Y. Estimation of Forest Above-Ground Biomass by Geographically Weighted Regression and Machine Learning with Sentinel Imagery. *Forests* **2018**, *9*, 582. [CrossRef]
51. Adhikari, H.; Heiskanen, J.; Siljander, M.; Maeda, E.; Heikinheimo, V.; Pellikka, P.K.E. Determinants of Aboveground Biomass across an Afromontane Landscape Mosaic in Kenya. *Remote Sens.* **2017**, *9*, 827. [CrossRef]
52. Zhang, L.; Jiang, Y.; Zhao, S.; Dong, M.; Chen, H.Y.H.; Kang, X. Different Responses of the Radial Growth of Conifer Species to Increasing Temperature along Altitude Gradient: Pinus Tabulaeformis in the Helan Mountains (Northwestern China). *Pol. J. Ecol.* **2016**, *64*, 509–525. [CrossRef]
53. Opelele, O.M.; Yu, Y.; Fan, W.; Chen, C.; Kachaka, S.K. Biomass Estimation Based on Multilinear Regression and Machine Learning Algorithms in the Mayombe Tropical Forest, in the Democratic Republic of Congo. *Appl. Ecol. Environ. Res.* **2021**, *19*, 359–377. [CrossRef]
54. Wang, Z.; Yi, L.; Xu, W.; Zheng, X.; Xiong, S.; Bao, A. Integration of UAV and GF-2 Optical Data for Estimating Aboveground Biomass in Spruce Plantations in Qinghai, China. *Sustainability* **2023**, *15*, 9700. [CrossRef]
55. Zhou, R.; Zhang, Y.; Peng, M.; Jin, Y.; Song, Q. Effects of Climate Change on the Carbon Sequestration Potential of Forest Vegetation in Yunnan Province, Southwest China. *Forests* **2022**, *13*, 306. [CrossRef]

56. Villers-Ruiz, L.; Trejo-Vazquez, I. Climate Research Clim Res Assessment of the Vulnerability of Forest Ecosystems to Climate Change in Mexico. *Clim. Res.* **1997**, *9*, 87–93. [CrossRef]
57. Ferreira, I.J.M.; Campanharo, W.A.; Fonseca, M.G.; Escada, M.I.S.; Nascimento, M.T.; Villela, D.M.; Brancalion, P.; Magnago, L.F.S.; Anderson, L.O.; Nagy, L.; et al. Potential Aboveground Biomass Increase in Brazilian Atlantic Forest Fragments with Climate Change. *Glob. Chang. Biol.* **2023**, *29*, 3098–3113. [CrossRef]

Disclaimer/Publisher's Note: The statements, opinions and data contained in all publications are solely those of the individual author(s) and contributor(s) and not of MDPI and/or the editor(s). MDPI and/or the editor(s) disclaim responsibility for any injury to people or property resulting from any ideas, methods, instructions or products referred to in the content.

agronomy

MDPI

Article

A Bibliometric Analysis of Global Research on Climate Change and Agriculture from 1985 to 2023

Cheng Li [1,2,3,†], Hongda Yao [3,†], Zhaozhe Li [3], Fang Wu [4], Bo Liu [5], Yongping Wu [6], Kwok Pan Chun [7], Thanti Octavianti [7], Xuefeng Cui [4,*] and Yang Xu [1,2,*]

[1] Jiangsu Key Laboratory of Crop Genetics and Physiology, Key Laboratory of Plant Functional Genomics of the Ministry of Education, Jiangsu Key Laboratory of Crop Genomics and Molecular Breeding, Yangzhou University, Yangzhou 225009, China; licheng@yzu.edu.cn
[2] Jiangsu Co-Innovation Center for Modern Production Technology of Grain Crops, Yangzhou University, Yangzhou 225009, China
[3] Department of Ecology, School of Plant Protection, Yangzhou University, Yangzhou 225009, China; 211801127@stu.yzu.edu.cn (H.Y.); 202331250023@mail.bnu.edu.cn (Z.L.)
[4] School of Systems Science, Beijing Normal University, Beijing 100875, China; fangw@mail.bnu.edu.cn
[5] College of Hydraulic Science and Engineering, Yangzhou University, Yangzhou 225009, China; boliu@yzu.edu.cn
[6] College of Physical Science and Technology, Yangzhou University, Yangzhou 225002, China; ypwu@yzu.edu.cn
[7] CATE School of Architecture and Environment, University of the West of England, Bristol BS16 1QY, UK; kwok.chun@uwe.ac.uk (K.P.C.); thanti.octavianti@uwe.ac.uk (T.O.)
* Correspondence: xuefeng.cui@bnu.edu.cn (X.C.); yangx@yzu.edu.cn (Y.X.)
† These authors contributed equally to this work.

Abstract: With increasing concentrations of atmospheric greenhouse gases, the interaction between climate change and agriculture is receiving widespread attention as part of food security and sustainable human development. However, a comprehensive summary of knowledge in the field of climate change and agriculture from a scientometric perspective is still lacking. Here, we selected 25,872 papers related to climate change and agriculture from the Web of Science Core Collection database for the period 1985 to 2023 and used VOSviewer software to reveal the research status and trends. The main results were as follows: (1) the number of papers in this field showed a rapidly increasing trend after 2007, with a clear interdisciplinary characteristic; (2) The United States was the most influential country in this field with 6819 papers and 363,109 citations. China had the second highest number of papers (3722 papers), but the Chinese Academy of Sciences was the most influential institution with the most papers. On an author level, Pete Smith was the most influential; (3) All keywords were divided into four different research topics, such as the impact of climate change on agriculture, climate change mitigation and adaptation in agriculture, and crop growth in response to climate change. Among them, some keywords related to climate change adaptation were the most recent topics of interest in this field. These findings provide effective scientific references for relevant scientists and practitioners to better conduct future theoretical and practical research on climate change and agriculture.

Keywords: climate change; agriculture; bibliometric analysis; visualization

1. Introduction

According to the latest data from the Intergovernmental Panel on Climate Change (IPCC), the global surface temperature during the period of 2011 to 2020 is 1.09 °C above the levels recorded between 1850 and 1900 [1]. Broadly speaking, climate change characterized by increasing temperature has altered the occurrence and severity of extreme weather and climate events [2], with widespread impacts on terrestrial ecosystems and human societies [3–5]. Agriculture, an essential foundation for sustainable economic and social

development, is not only considered one of the climate-impacted sectors but also an important source of greenhouse gas emissions [6–8]. In this context, research on climate change and agriculture has attracted great attention across regions, between countries, and among individuals [9,10].

Many scientists have conducted numerous theoretical and practical studies in the field of climate change and agriculture [11–14]. Some of these review papers, such as the traditional literature reviews and meta-analyses [15,16], reported from different perspectives in this field. They mainly focused on the relationship between weather, climate, and agricultural production [17]; climate change impact, mitigation, and adaptation in agriculture [18,19]; and quantitative methods to assess climate change impacts on agriculture [20]. However, most of these review papers had limited research scope and were easily influenced by scientists' personal preferences, resulting in a lack of quantitative analysis of the relevant scientific literature in this field from an objective perspective [21]. Bibliometric analysis is a widely used quantitative method for examining a large amount of the literature in terms of various aspects, including authors, documents, journals, keywords, and other indicators [22,23]. As the content and scope of research related to climate change and agriculture continue to deepen and expand, the knowledge structure and emerging trends of this field remain poorly understood using bibliometric analysis.

With the support of modern information technology, knowledge mapping has become an emerging technique that enables the visualization and analysis of complex bibliometric networks [24]. In addition, it can be viewed as an entry point for acquiring knowledge and new information in a specific field [25]. Currently, there are various commonly used knowledge mapping tools, such as VOSviewer 1.6.19, CiteSpace 6.3, Ucinet 6, and Bibexcel 2017 [26–30]. For example, VOSviewer is a typical knowledge mapping software developed by Leiden University based on the Java programming language [27]. Unlike other tools, its advantages lie in text mining capabilities that can identify co-occurrence networks of important terms and excellent visualization capabilities. In recent years, the VOSviewer software has been used to represent the knowledge structure and development of various research fields [31–33], especially several agriculture-related fields, such as agricultural drought [34], agricultural pollution [35], sustainable agriculture [36], and land use change and food security [37]. Despite the power and popularity of the VOSviewer software, there is still no research using this tool to investigate the growing publications on climate change and agriculture. Aiming to give a comprehensive summary of climate change and agriculture research, this study presents a bibliometric analysis to illustrate the knowledge structure and emerging trends in this field based on a trusted citation database and VOSviewer software. Therefore, the main research objectives are (1) to analyze the changes in the number of publications on climate change and agriculture, (2) to reveal research power (countries, institutions, and authors) through the visualization of collaboration networks, and (3) to identify the research trend using keyword co-occurrence analysis. The detailed result is of great importance for relevant researchers to understand the dynamics of this field and find new research directions.

2. Materials and Methods

2.1. Data

A scientific citation database is usually recognized as the data source for bibliometric analysis [38]. As the world's leading citation database, the Web of Science Core Collection (WoSCC) contains records of articles, conference proceedings, and books [39]. In this study, we used the WoSCC database to select the relevant publications for input data in bibliometric analysis. During the search process, we restricted the search period from 1985 to 2023 and set TS = (Climate Change AND Agriculture). In addition, the selected language was English, and the document types were articles and review articles. Finally, a total of 25,872 papers were selected for this study.

2.2. Methods

In this study, the software VOSviewer 1.6.19 (https://www.vosviewer.com/, accessed on 24 February 2024) was used to construct and visualize bibliometric networks. Users can select an item type in the VOSviewer software, such as authors, organizations, countries, and keywords, and set relevant parameters to generate analysis results and network graphs [40]. In a generated network graph, the dimension of the circle represents the importance of an item, while the width of the line between items indicates the intensity of the connections [41]. Guidelines for using VOSviewer software and data analysis steps can be found at https://www.vosviewer.com/. In addition, Origin 2021b software (https://www.originlab.com/, accessed on 24 February 2024) was also used to display data from the WoSCC database through graphs and charts.

3. Results and Discussion

3.1. Characteristics of Publications and Research Areas

According to the WoSCC database, a total of 25,872 papers on climate change and agriculture were identified from 1985 to 2023. Figure 1 shows the changes in publications on climate change and agriculture and the main subject categories from the WoSCC database. As shown in Figure 1a, the annual number of papers increased exponentially from 1985 to 2023 (R^2 = 0.96) and showed a rapid growth trend after 2007. A key reason was the publication of the IPCC Fourth Assessment Report in 2007, which provided an integrated perspective on the multifaceted nature and impacts of climate change and addressed a range of options and responses for adaptation and mitigation [42,43]. In addition, the IPCC was also awarded the Nobel Peace Prize that year [44], sparking greater interest in research on climate change and agriculture over the past decade [45,46]. As a result, 24,809 papers were published after 2007, accounting for 95.89% of all papers.

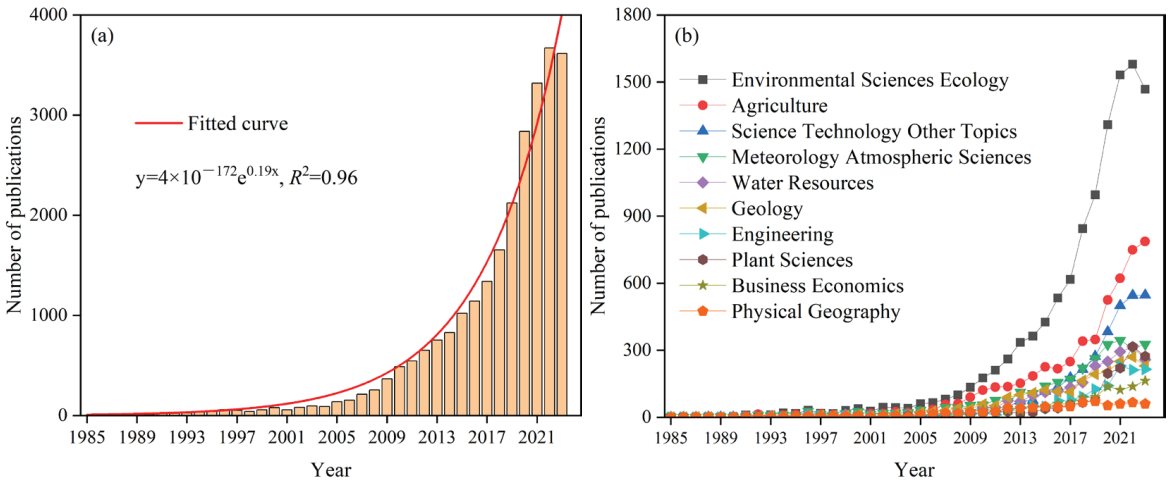

Figure 1. (**a**) Annual number of publications on climate change and agriculture from 1985 to 2023. (**b**) Annual publication output in the top ten research areas.

By analyzing the research areas from the WoSCC database (Figure 1b), the top ten research areas were Environmental Sciences Ecology (11,457 papers, 44.28% of 25,872 papers), Agriculture (5260 papers, 20.33%), Science Technology Other Topics (3254 papers, 12.58%), Meteorology Atmospheric Sciences (3050 papers, 11.79%), Water Resources (2349 papers, 9.08%), Geology (2306 papers, 8.91%), Engineering (1478 papers, 5.71%), Plant Sciences (1464 papers, 5.66%), Business Economics (1192 papers, 4.61%), Physical Geography (830 papers, 3.21%). Regarding changes in focus areas, Environmental Sciences Ecology, as the dominant research area, contributed more to this field after 2007, with Agriculture and Science Technology Other Topics increasing rapidly in recent years. The distribution of the above research areas also showed that climate change and agriculture research was

clearly interdisciplinary, which not only expanded our understanding of this field but also promoted its rapid and diverse development [47–49].

In order to identify principal journals on climate change and agriculture research, we set the minimum number of papers and the minimum number of citations to 50 and 100, respectively, in the VOSviewer software. A total of 97 of the 2991 source journals met the thresholds and were shown in the visualization network (Figure 2). As shown in Figure 2, the dimensions of different circles indicated the number of papers in different journals, and the source journals in the same color group were closely related to each other. Table 1 further shows the top ten journals published on climate change and agriculture research, each with more than 246 papers. As shown in Table 1, these ten journals published nearly 16% of all papers, suggesting that the papers in this field were not concentrated in a few journals [50]. Additionally, these ten journals were considered influential, with eight journals in Quartile 1 and two journals in Quartile 2. The top five journals were *Sustainability* (912 papers, 3.53%), *Science of the Total Environment* (589 papers, 2.28%), *Climatic Change* (445 papers, 1.72%), *Environmental Research Letters* (378 papers, 1.46%), *Water* (337 papers, 1.30%). Although the journal *Sustainability* published the largest number of papers in research on climate change and agriculture, its total number of citations was not very high. On the contrary, the top four journals with more than 17,500 citations were *Climatic Change*, *Agriculture Ecosystems and Environment*, *Science of the Total Environment*, and *Environmental Research Letters*, indicating that these four journals had a greater influence in this field.

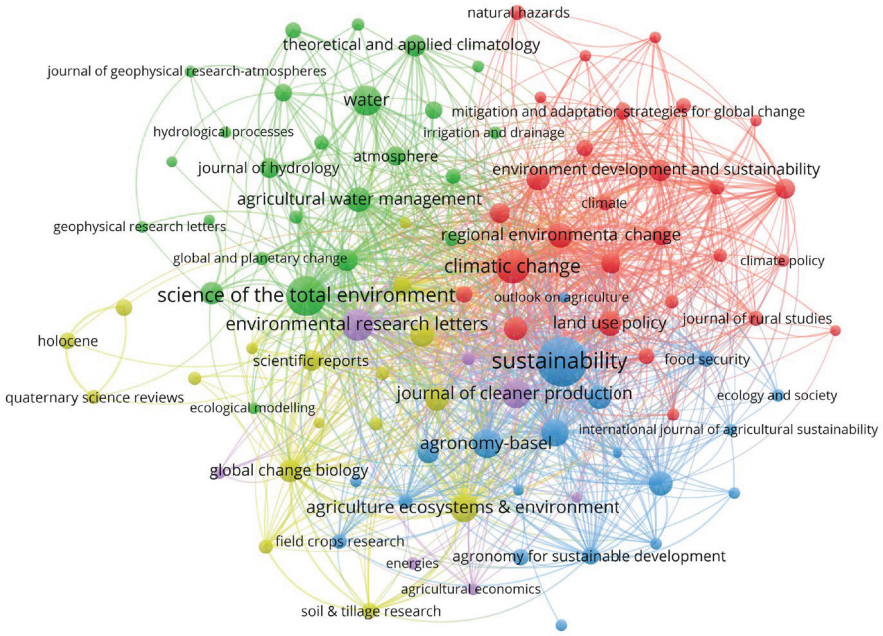

Figure 2. Visualization of principal journals on climate change and agriculture research.

Table 1. Top ten principal journals on climate change and agriculture research.

No.	Journal	No. of Papers	Ratio (%)	No. of Citations	Quartile in Category
1	*Sustainability*	912	3.53	14,061	Q2
2	*Science of the Total Environment*	589	2.28	21,451	Q1
3	*Climatic Change*	445	1.72	25,507	Q1
4	*Environmental Research Letters*	378	1.46	17,724	Q1
5	*Water*	337	1.30	5349	Q2
6	*Journal of Cleaner Production*	328	1.27	11,941	Q1
7	*Agronomy-Basel*	316	1.22	3878	Q1
8	*Agriculture Ecosystems and Environment*	301	1.16	22,037	Q1
9	*Agricultural Systems*	286	1.11	9974	Q1
10	*Regional Environmental Change*	246	0.95	7408	Q1

In order to identify influential papers on climate change and agriculture research, we set the minimum number of citations to 500 in the VOSviewer software. A total of 129 of the 25,872 papers met the thresholds and were shown in the visualization network (Figure 3). As shown in Figure 3, a larger circle indicates that the paper is more influential, while a thicker line indicates a stronger relationship between the two papers. Table 2 further shows the top ten influential papers published on climate change and agriculture research. As shown in Table 2, these ten papers were cited 25,107 times, with each of them cited more than 1260 times. However, the number of papers on climate change and agriculture research published in journals containing these most influential articles was not in the top ten, with the exception of *Environmental Research Letters*. An article published in the journal *Science* entitled "Food security: the challenge of feeding 9 billion people" took first place with 6990 citations [51]. In addition, "Global food demand and the sustainable intensification of agriculture" in the journal *Proceedings of the National Academy of Sciences of the United States of America* and "The impacts of climate change on water resources and agriculture in China" in the journal *Nature* took second to third place with 4518 and 2455 citations, respectively [52,53]. Interestingly, the three most cited papers were all published in multidisciplinary science journals with publishing histories spanning centuries. An important reason for this was that research papers published in high-quality journals were more likely to attract widespread attention and also promote more in-depth investigation of related hot topics in this field [54]. Regarding the timing of publication, nine of the ten most influential papers were published in the five-year period around 2012, suggesting that this period was important for the development of knowledge systems on climate change and agriculture research.

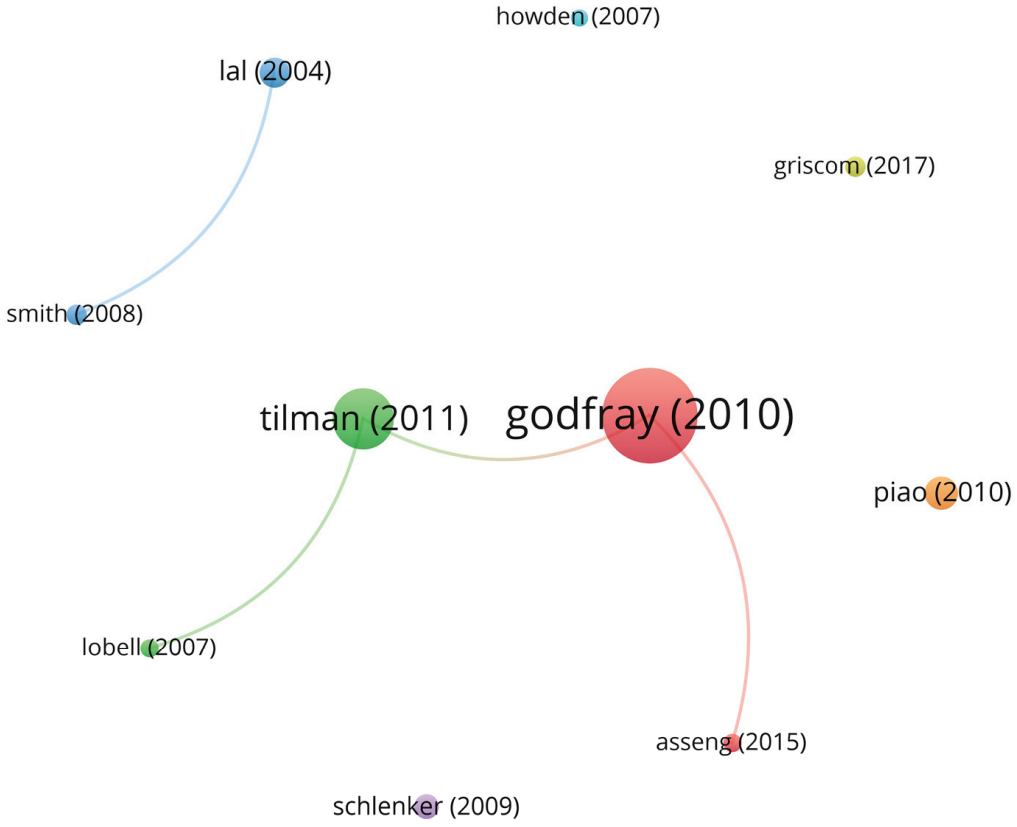

Figure 3. Visualization of influential papers on climate change and agriculture research [51–53,55–61].

Table 2. Top ten influential papers on climate change and agriculture research.

No.	Document	Title	Source	No. of Citations
1	[51]	Food security: The challenge of feeding 9 billion people	*Science*	6990
2	[52]	Global food demand and the sustainable intensification of agriculture	*Proceedings of the National Academy of Sciences of the United States of America (PNAS)*	4518
3	[53]	The impacts of climate change on water resources and agriculture in China	*Nature*	2455
4	[55]	Soil carbon sequestration to mitigate climate change	*Geoderma*	2201
5	[56]	Nonlinear temperature effects indicate severe damages to US crop yields under climate change	*PNAS*	1880
6	[57]	Greenhouse gas mitigation in agriculture	*Philosophical Transactions of the Royal Society B*	1550
7	[58]	Natural climate solutions	*PNAS*	1516
8	[59]	Rising temperatures reduce global wheat production	*Nature Climate Change*	1371
9	[60]	Global scale climate–crop yield relationships and the impacts of recent warming	*Environmental Research Letters*	1358
10	[61]	Adapting agriculture to climate change	*PNAS*	1268

3.2. Cooperation Networks of Climate Change and Agriculture Research

3.2.1. Country Co-Authorship

According to the WoSCC database, 190 countries participated in climate change and agriculture research. We set the minimum number of papers and the minimum number of citations in the VOSviewer software to 100 and 200, respectively [33,40]. A total of 62 of the 190 countries met the thresholds and were divided into six different color groups in the cooperation network (Figure 4). As shown in Figure 4, the larger the circle, the greater the collaboration between countries and researchers from different countries in this field.

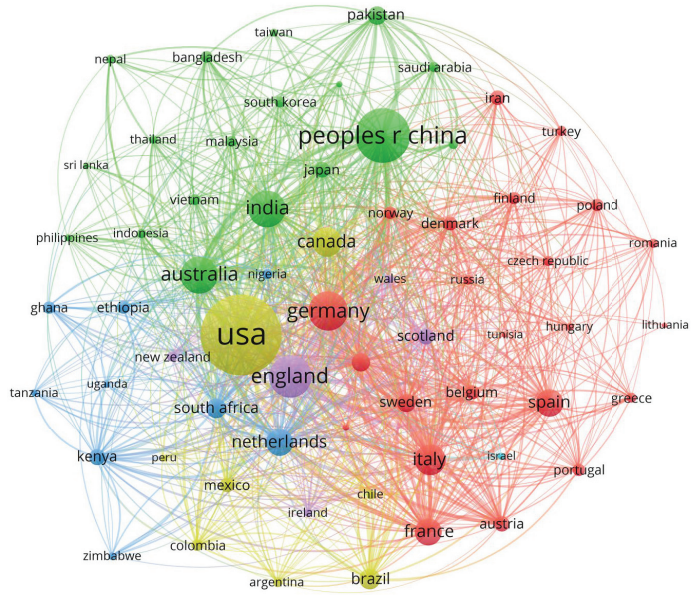

Figure 4. Visualization of the cooperation network of countries published on climate change and agriculture research.

Table 3 further shows the top ten influential countries published on climate change and agriculture research. At least 1212 papers were published in each of these ten influential countries, eight of which were developed Western countries, and only China and India were developing countries [62]. In particular, the USA ranked first in the total number of papers and citations. Moreover, the USA (63 links and 7172 total link strength) had the largest circle and densest lines in the cooperation network, indicating that it held a crucial position in this field and carried out extensive cooperation with other countries

(Figure 4). China had the second highest number of papers (3722 papers), but its total number of citations and total link strength was much lower than that of the USA (Table 3). Although India also published a large number of papers, its average number of citations per paper was much lower than that of other countries, and its collaboration with other countries was limited (Table 3 and Figure 4). In addition to these ten influential countries, it was undeniable that other countries had also made positive contributions to this field (Figure 4). In the future, more attention should be paid to cross-country cooperation in order to sustain the rapid development in this field [49]. In particular, cooperation could be established with countries where the literature was less available (e.g., Africa, which is highly vulnerable to climate change) in order to enhance their local knowledge [63].

Table 3. Top ten influential countries published on climate change and agriculture research.

No.	Country	No. of Papers	No. of Citations	Total Link Strength
1	USA	6819	363,109	7172
2	P. R. China	3722	124,376	3860
3	England	2450	152,233	4929
4	Germany	2207	116,180	4485
5	India	2017	60,024	1934
6	Australia	2000	101,704	3284
7	Italy	1469	69,516	2575
8	Canada	1363	65,962	1943
9	Spain	1244	46,324	2128
10	France	1212	70,259	2684

3.2.2. Institution Co-Authorship

According to the WoSCC database, 15,460 institutions participated in climate change and agriculture research. We set the minimum number of papers and the minimum number of citations in the VOSviewer software to 100 and 200, respectively [33,40]. A total of 80 of the 15,460 institutions met the thresholds and were divided into five different color groups in the cooperation network (Figure 5). As shown in Figure 5, a larger circle indicates that the institution is more influential, while a thicker line indicates a higher degree of cooperation between institutions.

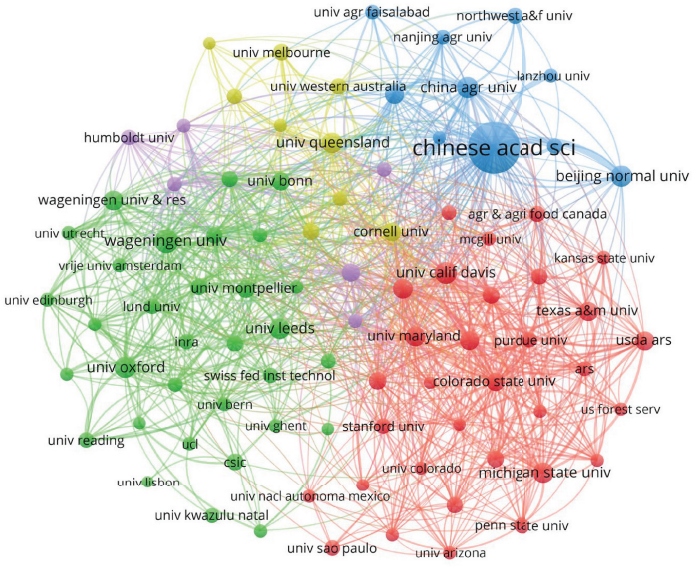

Figure 5. Visualization of the cooperation network of institutions published on climate change and agriculture research.

Table 4 further presents the top ten influential institutions published on climate change and agriculture research. Of these ten influential institutions, there were three each in the

USA and China, two in England, and one each in the Netherlands and Australia. Moreover, each of these institutions published at least 222 papers. The Chinese Academy of Sciences ranked first in the total number of papers and citations and also showed extensive cooperation with other institutions in different countries (Figure 5). In addition, some institutions in the USA (e.g., the University of Florida and the University of California, Davis) also cooperated more with other institutions (Figure 5). The average number of citations per paper in Chinese institutions was less than 40 times, although they published a large number of papers. In comparison, institutions in Western countries had a higher average number of citations per paper, ranging from 47.49 to 86.90 times (Table 4). Interestingly, institutions from the same country were more closely linked to each other than to institutions from different countries in the cooperation network (Figure 5), which suggested that future research should strengthen cooperation with institutions from different countries in order to realize high-level scientific outputs in this field [64].

Table 4. Top ten influential institutions published on climate change and agriculture research.

No.	Institution	No. of Papers	No. of Citations	Total Link Strength	Country
1	Chinese Academy of Sciences	1121	42,066	624	China
2	Wageningen University	505	30,558	481	Netherlands
3	University of California, Davis	261	15,371	276	USA
4	Beijing Normal University	254	8971	190	China
5	China Agricultural University	254	9266	250	China
6	University of Oxford	254	22,073	269	England
7	Michigan State University	231	12,617	235	USA
8	University of Queensland	231	10,971	211	Australia
9	University of Leeds	229	14,247	176	England
10	University of Florida	222	14,381	298	USA

3.2.3. Author Co-Authorship

According to the WoSCC database, there were 87,743 authors who published on climate change and agricultural research. In order to identify principal authors in this field, we set the minimum number of papers and the minimum number of citations in the VOSviewer software to 20 and 100, respectively [33,40]. A total of 65 of the 87,743 authors met the thresholds and were divided into 22 different color groups in the cooperation network (Figure 6). As shown in Figure 6, the larger the circle, the more papers the author published, and authors with the same circle color cooperated closely with each other.

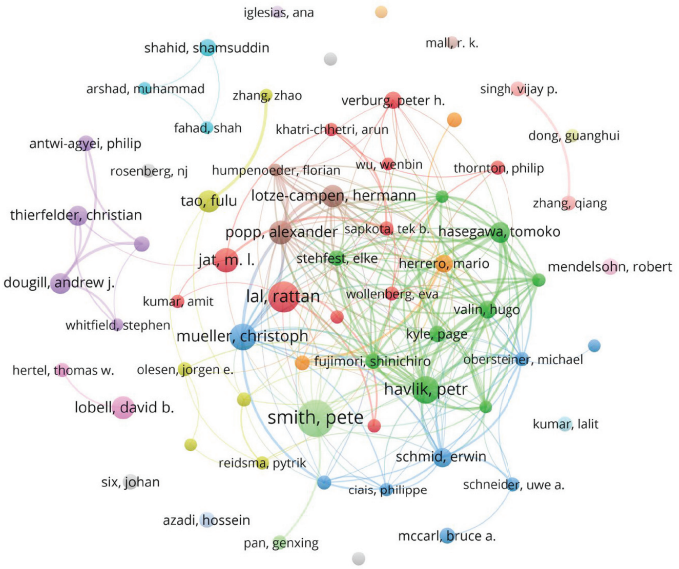

Figure 6. Visualization of the cooperation network of authors published on climate change and agriculture research.

Table 5 further presents the top ten influential authors published on climate change and agriculture research. As shown in Table 5, each of these ten influential authors published at least 37 papers. Notably, authors who published at least 50 papers with more than 5000 citations included Pete Smith, Rattan Lal, Petr Havlik, and Christoph Müller. Taking author Pete Smith as an example shows that he not only belonged to the same group as Genxing Pan but also carried out extensive cooperation with Rattan Lal, Petr Havlik, M. L. Jat, and Philip K. Thornton from other color groups (Figure 6). In contrast to Pete Smith, the authors David B. Lobell, with the highest average citations per paper (189.52 times), and Thomas W. Hertel were part of a group, but their cooperation with other authors was limited (Figure 6). Overall, most influential authors had strong tiers within their respective groups, and cooperation between different groups should be strengthened, which could serve as an important reference for newcomers, as well as those seeking potential cooperators in this field [65].

Table 5. Top ten influential authors published on climate change and agriculture research.

No.	Author	No. of Papers	No. of Citations	Total Link Strength	Affiliations
1	Smith, Pete	77	10,920	46	University of Aberdeen
2	Lal, Rattan	63	5537	20	The Ohio State University
3	Havlik, Petr	52	5932	206	International Institute for Applied Systems Analysis
4	Müller, Christoph	51	5805	92	Potsdam Institute for Climate Impact Research (PIK)
5	Jat, M. L.	45	2860	17	International Maize and Wheat Improvement Center
6	Popp, Alexander	43	4245	140	PIK
7	Lobell, David B.	42	7960	4	Stanford University
8	Tao, Fulu	41	2680	21	Chinese Academy of Sciences
9	Lotze-Campen, Hermann	40	4571	125	PIK
10	Dougill, Andrew J.	37	1849	45	University of Leeds

3.3. Keywords Co-Occurrence Analysis

All keywords, including author keywords and keywords plus, are usually considered an important aspect of presenting the core content of papers, which can reflect the dynamics and trends of research in a certain field [66,67]. In this study, we selected all keywords to analyze the co-occurrence of keywords related to climate change and agriculture research.

After analyzing the co-occurrence of all keywords using the full counting method, there were a total of 55,861 keywords, of which 169 met the threshold of 200 and were divided into four different color groups in the visualization network (Figure 7). As shown in Figure 7, a keyword with a larger circle indicated that it occurred more frequently, whereas a thicker connecting line indicated a higher intensity of co-occurrence between keywords. Meanwhile, Table 6 shows the top 10 keywords with the highest frequency of co-occurrence in each color group resulting from the co-occurrence analysis of keywords (Figure 7). The top 17 co-occurrences of all keywords were “climate change”, “agriculture”, “impact”, “adaption”, “management”, “food security”, “variability”, “land use”, “temperature”, “drought”, “model”, “yield”, “vulnerability”, “sustainability”, “precipitation”, “water”, and “growth”, each appearing more than 1000 times (Table 6). Of the two search terms in this field, “climate change” and “agriculture” were the most common, and both were strongly related to other keywords.

As shown in Figure 7, four color groups presented different research topics. The red group represented the climate change impacts on agriculture, with two key terms being “climate change” and “impact”. Some keywords related to climate change mainly included “temperature”, “drought”, “precipitation”, “water resources”, “variability”, and “trends”. A number of keywords related to impact assessment were “model”, “simulation”, “scenarios”, “remote sensing”, “gis”, and “prediction”. The representative research regions were mainly in China, the USA, India, and European countries.

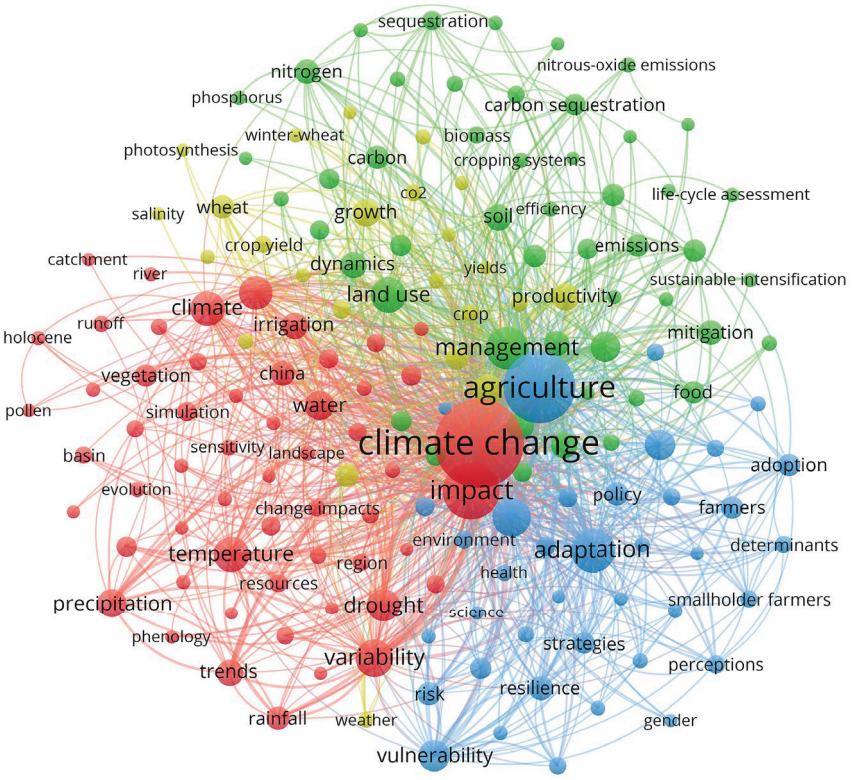

Figure 7. Visualization of the co-occurrence network of most frequent keywords published on climate change and agriculture research.

Table 6. The top 10 keywords with the highest frequency of co-occurrence in each color group in Figure 7.

No.	Red Group		Green Group		Blue Group		Yellow Group	
	K	O	K	O	K	O	K	O
1	Climate change	11,648	Management	2469	Agriculture	7464	Yield	1339
2	Impact	4581	Land use	1722	Adaptation	2755	Growth	1000
3	Variability	1871	Biodiversity	984	Food security	1964	Productivity	974
4	Temperature	1647	Soil	909	Vulnerability	1295	Responses	709
5	Drought	1490	Conservation	899	Sustainability	1174	Wheat	688
6	Model	1484	Dynamics	865	Resilience	745	Maize	634
7	Precipitation	1136	Nitrogen	766	Policy	692	Rice	412
8	Water	1111	Mitigation	733	Risk	667	Crop yield	388
9	Irrigation	931	Carbon	677	Farmers	649	Crop production	374
10	Trends	918	Greenhouse-gas emissions	659	Adoption	612	CO_2	363

The green group represented climate change mitigation in agriculture, focusing primarily on the following two aspects: agricultural management as well as greenhouse gas emissions and mitigation potential (Figure 7). The keywords related to agricultural management were "land use", "conservation agriculture", "sustainable agriculture", "deforestation", "tillage", "cropping systems", and "sustainable intensification". Some keywords related to greenhouse gas emissions and mitigation mainly included "carbon", "nitrogen", "methane", "soil", "biomass", "organic matter", "carbon sequestration", "biodiversity", and "life-cycle assessment".

The blue group represented climate change adaptation in agriculture, which mainly focused on conceptual studies and climate adaptation strategies (Figure 7). The former mainly included the keywords "adaptation", "food security", and "adaptive capacity", while the latter mainly included keywords "adaptation strategies", "climate-smart agriculture", and "smallholder farmers". In addition, Africa, particularly Sub-Saharan Africa and Southeast Asia, were important hotspots for research on agricultural adaptation to climate change.

The yellow group represented crop growth in response to climate change, which had a high degree of overlap with the red group and the green group (Figure 7). Agronomic keywords related to crop growth included "yield", "productivity", "photosynthesis", "stress", and "water use efficiency". Several keywords related to crop types were "wheat", "maize", and "rice". Additionally, other commonly used keywords such as "responses", "CO_2", "weather", and "global warming" also appeared in this group.

Note: K represents keywords, while O represents co-occurrences (frequency of keywords). Four color groups presented different research topics.

Figure 8 shows an overlay map by year in which papers were published to reflect the evolution of climate change and agriculture research. In Figure 8, blue keywords represent earlier research topics, while yellow keywords represent more recent research topics [68]. In particular, most yellow keywords were found in the right part of Figure 8, suggesting that attention has recently shifted to climate change adaptation in agriculture. Keywords such as "adaptation strategies", "adoption", "perceptions", "gender", "smallholder farmers", and "climate-smart agriculture" have been the latest research hotspots that appeared to have gained more attention in recent years.

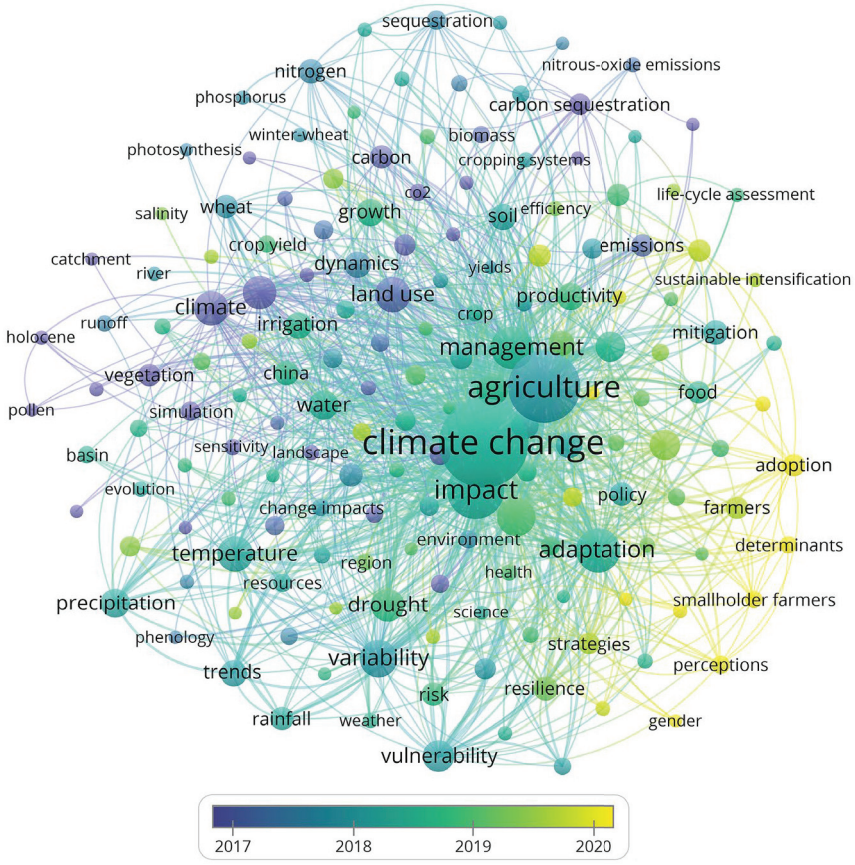

Figure 8. Visualization of the co-occurrence overlay of most frequent keywords published on climate change and agriculture research. The years in which specific keywords frequently occur are shown by different colors.

Taking agricultural greenhouse gas emissions in relation to political efforts as an example, major economies around the world proposed a variety of plans to reduce emissions, including international commitments, policy measures, technological innovations, market mechanisms, and environmental protection strategies [69]. However, the effectiveness of these political efforts was easily influenced by various factors, such as the complex international environment, side effects of emission reduction measures, the involvement of a large number of stakeholders, and the unfamiliarity of farmers with climate change [70].

As an important starting point for the discussion, identifying political efforts conducive to incentivizing emissions reductions and promoting sustainable agriculture requires a concerted effort from policymakers, economic actors, farmers, and researchers [71].

3.4. Limitations

The limitations of our study arise mainly from two aspects. First, the literature data used for the analysis were only from the WoSCC database, ignoring the literature from other databases [72]. This was primarily attributed to the fact that the existing VOSviewer software is prone to formatting errors when merging the literature data from different databases [73]. Therefore, a small number of relevant papers from other databases may not be included in this study. Second, different parameter settings in the VOSviewer software may generate different results, which may contain some synonyms that need to be replaced due to differences in the presentation of relevant information [64]. Both two aspects may affect the reliability of the bibliometric results. As the WoSCC database is constantly updated, we will collect more literature data on climate change and agriculture and invite more scientists with expertise to further summarize research progress in relevant sub-fields by incorporating a systematic review or a scoping review.

4. Conclusions

Using the WOSCC database and the VOSviewer software, this study analyzed 25,872 papers on climate change and agriculture research from 1985 to 2023 in terms of the number of publications, research power, and keywords. The main results were as follows:

(1) The annual number of papers increased exponentially from 1985 to 2023 and showed a rapid growth trend after 2007, with 95.89% of the total number of papers being published during this period. Furthermore, climate change and agriculture research was characterized by interdisciplinarity and diversity in terms of research areas and journals;
(2) The USA had the leading position in this field, with the highest number of papers and total citations, and cooperated closely with other countries. In addition to the USA, China and some European countries also have great influence in this field. Furthermore, the most influential institutions and authors were mainly distributed in these countries;
(3) The most prominent keywords were “climate change”, “agriculture”, “impact”, “adaptation”, and “management”. Although four distinct research topics have been identified over the decades, in recent years, the research focus has shifted toward climate change adaptation in agriculture.

Overall, this bibliometric analysis presents a distinct and intriguing snapshot of climate change and agriculture research, allowing relevant researchers to understand the knowledge structure, emerging trends, and how progress is being made in this field. As a starting point for future research, some valuable suggestions could be given to scientists/countries that claim to have less literature to improve their local knowledge.

Author Contributions: Conceptualization, C.L., X.C. and Y.X.; methodology, C.L. and H.Y.; software, H.Y.; formal analysis, H.Y., Z.L. and F.W.; data curation, F.W. and B.L.; writing—original draft preparation, C.L. and H.Y.; writing—review and editing, Z.L., F.W., B.L., Y.W., K.P.C., T.O., X.C. and Y.X.; funding acquisition, C.L., Y.W., K.P.C., X.C. and Y.X. All authors have read and agreed to the published version of the manuscript.

Funding: This research was funded by the National Key Research and Development Program of China (2023YFF1303702), the Key Research and Development Program of Jiangsu Province (BE2022343), the Young Scientific and Technological Talents Support Project of Jiangsu Association for Science and Technology (TJ-2023-032), the National Natural Science Foundation of China (42275029, 41801013), the Royal Society International Exchanges 2022 (IEC\NSFC\223132), the Qinglan Project of Jiangsu Province, and the Qinglan Project of Yangzhou University.

Data Availability Statement: The data presented in this study are available upon request from the corresponding author.

Conflicts of Interest: The authors declare no conflicts of interest.

References

1. IPCC. Climate Change 2021: The Physical Science Basis. In *Contribution of Working Group I to the Sixth Assessment Report of the Intergovernmental Panel on Climate Change*; Masson-Delmotte, V., Zhai, P., Pirani, A., Connors, S.L., Péan, C., Berger, S., Caud, N., Chen, Y., Goldfarb, L., Gomis, M.I., et al., Eds.; Cambridge University Press: Cambridge, UK, 2021.
2. Rawat, A.; Kumar, D.; Khati, B.S. A review on climate change impacts, models, and its consequences on different sectors: A systematic approach. *J. Water Clim. Change* **2024**, *15*, 104–126. [CrossRef]
3. Malhi, Y.; Franklin, J.; Seddon, N.; Solan, M.; Turner, M.G.; Field, C.B.; Knowlton, N. Climate Change and Ecosystems: Threats, Opportunities and Solutions. *Philos. Trans. R. Soc. B* **2020**, *375*, 20190104. [CrossRef] [PubMed]
4. Piao, S.; Wang, X.; Park, T.; Chen, C.; Lian, X.; He, Y.; Bjerke, J.W.; Chen, A.; Ciais, P.; Tømmervik, H.; et al. Characteristics, drivers and feedbacks of global greening. *Nat. Rev. Earth Environ.* **2020**, *1*, 14–27. [CrossRef]
5. Dietz, T.; Shwom, R.L.; Whitley, C.T. Climate Change and Society. *Annu. Rev. Sociol.* **2020**, *46*, 135–158. [CrossRef]
6. Ray, D.; Gerber, J.; MacDonald, G.; West, P.C. Climate variation explains a third of global crop yield variability. *Nat. Commun.* **2015**, *6*, 5989. [CrossRef]
7. Crippa, M.; Solazzo, E.; Guizzardi, D.; Monforti-Ferrario, F.; Tubiello, F.N.; Leip, A. Food systems are responsible for a third of global anthropogenic GHG emissions. *Nat. Food* **2021**, *2*, 198–209. [CrossRef]
8. Li, C.; Jia, J.; Wu, F.; Zuo, L.; Cui, X. County-level intensity of carbon emissions from crop farming in China during 2000–2019. *Sci. Data* **2024**, *11*, 457. [CrossRef]
9. Abbass, K.; Qasim, M.Z.; Song, H.; Murshed, M.; Mahmood, H.; Younis, I. A review of the global climate change impacts, adaptation, and sustainable mitigation measures. *Environ. Sci. Pollut. Res.* **2022**, *29*, 42539–42559. [CrossRef]
10. Rivera-Ferre, M.G. From agriculture to food systems in the IPCC. *Glob. Change Biol.* **2020**, *26*, 2731–2733. [CrossRef]
11. Yuan, X.; Li, S.; Chen, J.; Yu, H.; Yang, T.; Wang, C.; Huang, S.; Chen, H.; Ao, X. Impacts of Global Climate Change on Agricultural Production: A Comprehensive Review. *Agronomy* **2024**, *14*, 1360. [CrossRef]
12. Azadi, H.; Moghaddam, S.M.; Burkart, S.; Mahmoudi, H.; Passel, S.V.; Kurban, A.; Lopez-Carr, D. Rethinking resilient agriculture: From Climate-Smart Agriculture to Vulnerable-Smart Agriculture. *J. Clean. Prod.* **2021**, *319*, 128602. [CrossRef]
13. McLeman, R.; Mayo, D.; Strebeck, E.; Smit, B. Drought adaptation in rural eastern Oklahoma in the 1930s: Lessons for climate change adaptation research. *Mitig. Adapt. Strateg. Glob. Change* **2008**, *13*, 379–400. [CrossRef]
14. Lee, C.C.; Zeng, M.; Luo, K. How does climate change affect food security? Evidence from China. *Environ. Impact Assess. Rev.* **2024**, *104*, 107324. [CrossRef]
15. Gaugler, T.; Stoeckl, S.; Rathgeber, A.W. Global climate impacts of agriculture: A meta-regression analysis of food production. *J. Clean. Prod.* **2020**, *276*, 122575. [CrossRef]
16. Mizik, T. Climate-Smart Agriculture on Small-Scale Farms: A Systematic Literature Review. *Agronomy* **2021**, *11*, 1096. [CrossRef]
17. Parolini, G. Weather, climate, and agriculture: Historical contributions and perspectives from agricultural meteorology. *Wiley Interdiscip. Rev. Clim. Change* **2022**, *13*, e766. [CrossRef]
18. Malhi, G.S.; Kaur, M.; Kaushik, P. Impact of Climate Change on Agriculture and Its Mitigation Strategies: A Review. *Sustainability* **2021**, *13*, 1318. [CrossRef]
19. Grigorieva, E.; Livenets, A.; Stelmakh, E. Adaptation of Agriculture to Climate Change: A Scoping Review. *Climate* **2023**, *11*, 202. [CrossRef]
20. Crane-Droesch, A. Machine learning methods for crop yield prediction and climate change impact assessment in agriculture. *Environ. Res. Lett.* **2018**, *13*, 114003. [CrossRef]
21. Totin, E.; Segnon, A.C.; Schut, M.; Affognon, H.; Zougmoré, R.B.; Rosenstock, T.; Thornton, P.K. Institutional Perspectives of Climate-Smart Agriculture: A Systematic Literature Review. *Sustainability* **2018**, *10*, 1990. [CrossRef]
22. Wang, Z.; Zhao, Y.; Wang, B. A bibliometric analysis of climate change adaptation based on massive research literature Data. *J. Clean. Prod.* **2018**, *199*, 1072–1082. [CrossRef]
23. Chen, G.; Bai, J.; Bi, C.; Wang, Y.; Cui, B. Global greenhouse gas emissions from aquaculture: A bibliometric analysis. *Agric. Ecosyst. Environ.* **2023**, *348*, 108405. [CrossRef]
24. Shiffrin, R.M.; Börner, K. Mapping knowledge domains. *Proc. Natl. Acad. Sci. USA* **2004**, *101*, 5183–5185. [CrossRef] [PubMed]
25. Huang, Y.; Glänzel, W.; Zhang, L. Tracing the development of mapping knowledge domains. *Scientometrics* **2021**, *126*, 6201–6224. [CrossRef]
26. Xu, Y.; Yang, Y.; Chen, X.; Liu, Y. Bibliometric Analysis of Global NDVI Research Trends from 1985 to 2021. *Remote Sens.* **2022**, *14*, 3967. [CrossRef]
27. Van Eck, N.J.; Waltman, L. Software survey: VOSviewer, a computer program for bibliometric mapping. *Scientometrics* **2010**, *84*, 523–538. [CrossRef]
28. Chen, C. Citespace ii: Detecting and visualizing emerging trends and transient patterns in scientific literature. *J. Am. Soc. Inf. Sci. Technol.* **2006**, *57*, 359–377. [CrossRef]

29. Borgatti, S.; Everett, M.; Freeman, L. *UCINET 6 for Windows: Software for Social Network Analysis*; Analytic Technology: Harvard, MA, USA, 2002.
30. Persson, O.; Danell, R.; Schneider, J.W. How to use Bibexcel for various types of bibliometric analysis. In *Celebrating Scholarly Communication Studies: A Festschrift for Olle Persson at his 60th Birthday*; Umeå University Library: Umeå, Sweden, 2009; pp. 9–24.
31. McAllister, J.T.; Lennertz, L.; Atencio Mojica, Z. Mapping a Discipline: A Guide to Using VOSviewer for Bibliometric and Visual Analysis. *Sci. Technol. Libr.* **2022**, *41*, 319–348. [CrossRef]
32. Bukar, U.A.; Sayeed, M.S.; Razak, S.F.A.; Yogarayan, S.; Amodu, O.A.; Mahmood, R.A.R. A Method for Analyzing Text Using VOSviewer. *MethodsX* **2023**, *11*, 102339. [CrossRef]
33. Sweileh, W.M. Bibliometric analysis of peer-reviewed literature on food security in the context of climate change from 1980 to 2019. *Agric. Food Secur.* **2020**, *9*, 11. [CrossRef]
34. Xiao, F.; Liu, Q.; Qin, Y.; Huang, D.; Liao, Y. Agricultural drought research knowledge graph reasoning by using VOSviewer. *Heliyon* **2024**, *10*, e27696. [CrossRef] [PubMed]
35. Li, B.; Hu, K.; Lysenko, V.; Khan, K.Y.; Wang, Y.K.; Jiang, Y.N.; Guo, Y. A scientometric analysis of agricultural pollution by using bibliometric software VoSViewer and Histcite (TM). *Environ. Sci. Pollut. Res.* **2022**, *29*, 37882–37893. [CrossRef] [PubMed]
36. Sarkar, A.; Wang, H.; Rahman, A.; Memon, W.H.; Qian, L. A bibliometric analysis of sustainable agriculture: Based on the Web of Science (WOS) platform. *Environ. Sci. Pollut. Res.* **2022**, *29*, 38928–38949. [CrossRef] [PubMed]
37. Cheng, P.; Tang, H.; Dong, Y.; Liu, K.; Jiang, P.; Liu, Y. Knowledge Mapping of Research on Land Use Change and Food Security: A Visual Analysis Using CiteSpace and VOSviewer. *Int. J. Environ. Res. Public Health* **2021**, *18*, 13065. [CrossRef]
38. Baraj, B.; Mishra, M.; Sudarsan, D.; da Silva, R.M.; Santos, C.A.G. Climate change and resilience, adaptation, and sustainability of agriculture in India: A bibliometric review. *Heliyon* **2024**, *10*, e29586. [CrossRef]
39. van Leeuwen, T. The application of bibliometric analyses in the evaluation of social science research. Who benefits from it, and why it is still feasible. *Scientometrics* **2006**, *66*, 133–154. [CrossRef]
40. Li, M.; Wang, Y.; Li, N.; Chou, S. Knowledge mapping on the sun-induced chlorophyll fluorescence technology research: A scientometric and visualization analysis. *Environ. Sci. Pollut. Res.* **2024**, *31*, 9150–9166. [CrossRef]
41. Yuan, B.Z.; Sun, J. Research trend of rice and greenhouse gases based on Web of Science: A bibliometric analysis. *All. Earth* **2023**, *35*, 16–30. [CrossRef]
42. Solomon, S.; Qin, D.; Manning, M.; Averyt, K.; Marquis, M. (Eds.) *Climate Change 2007—The Physical Science Basis: Working Group I Contribution to the Fourth Assessment Report of the IPCC*; Cambridge University Press: Cambridge, UK, 2007.
43. Fussel, H.M. An updated assessment of the risks from climate change based on research published since the IPCC Fourth Assessment Report. *Clim. Change* **2009**, *97*, 469–482. [CrossRef]
44. Ravishankara, A.R.; Randall, D.A.; Hurrell, J.W. Complex and yet predictable: The message of the 2021 Nobel Prize in Physics. *Proc. Natl. Acad. Sci. USA* **2022**, *119*, e2120669119. [CrossRef]
45. Hertel, T.W.; de Lima, C.Z. Climate impacts on agriculture: Searching for keys under the streetlight. *Food Policy* **2020**, *95*, 101954. [CrossRef]
46. Shahzad, A.; Ullah, S.; Dar, A.A.; Sardar, M.F.; Mehmood, T.; Tufail, M.A.; Shakoor, A.; Haris, M. Nexus on climate change: Agriculture and possible solution to cope future climate change stresses. *Environ. Sci. Pollut. Res.* **2021**, *7*, 1–22. [CrossRef] [PubMed]
47. Yu, Q.; Wu, W.; Yang, P.; Li, Z.; Xiong, W.; Tang, H. Proposing an interdisciplinary and cross-scale framework for global change and food security researches. *Agric. Ecosyst. Environ.* **2012**, *156*, 57–71. [CrossRef]
48. El Bilali, H.; Strassner, C.; Ben Hassen, T. Sustainable Agri-Food Systems: Environment, Economy, Society, and Policy. *Sustainability* **2021**, *13*, 6260. [CrossRef]
49. Yang, Q.; Du, T.; Li, N.; Liang, J.; Javed, T.; Wang, H.; Guo, J.; Liu, Y. Bibliometric Analysis on the Impact of Climate Change on Crop Pest and Disease. *Agronomy* **2023**, *13*, 920. [CrossRef]
50. Sawirdin, S.; Tian, A.; Shi, L.; Fu, W.; Cheng, S.; Halik, Ü.; Liang, J. A Bibliometric Analysis of the Research Progress and Trends during 2002–2022 on the Carbon Stocks in Terrestrial Ecosystems. *Forests* **2023**, *14*, 2051. [CrossRef]
51. Godfray, H.C.J.; Beddington, J.R.; Crute, I.R.; Haddad, L.; Lawrence, D.; Muir, J.F.; Pretty, J.; Robinson, S.; Thomas, S.M.; Toulmin, C. Food security: The challenge of feeding 9 billion people. *Science* **2010**, *327*, 812–818. [CrossRef]
52. Tilman, D.; Balzer, C.; Hill, J.; Befort, B.L. Global food demand and the sustainable intensification of agriculture. *Proc. Natl. Acad. Sci. USA* **2011**, *108*, 20260–20264. [CrossRef]
53. Piao, S.; Ciais, P.; Huang, Y.; Shen, Z.; Peng, S.; Li, J.; Zhou, L.; Liu, H.; Ma, Y.; Ding, Y. The impacts of climate change on water resources and agriculture in China. *Nature* **2010**, *467*, 43. [CrossRef]
54. Van Dalen, H.P.; Henkens, K. Signals in science—On the importance of signaling in gaining attention in science. *Scientometrics* **2005**, *64*, 209–233. [CrossRef]
55. Lal, R. Soil carbon sequestration to mitigate climate change. *Geoderma* **2004**, *123*, 1–22. [CrossRef]
56. Schlenker, W.; Roberts, M.J. Nonlinear temperature effects indicate severe damages to U.S. crop yields under climate change. *Proc. Natl. Acad. Sci. USA* **2009**, *106*, 15594–15598. [CrossRef] [PubMed]
57. Smith, P.; Martino, D.; Cai, Z.; Gwary, D.; Janzen, H.; Kumar, P.; McCarl, B.; Ogle, S.; O'Mara, F.; Rice, C.; et al. Greenhouse gas mitigation in agriculture. *Phil. Trans. R. Soc. B* **2008**, *363*, 789–813. [CrossRef] [PubMed]

58. Griscom, B.W.; Adams, J.; Ellis, P.W.; Houghton, R.A.; Lomax, G.; Miteva, D.A.; Schlesinger, W.H.; Shoch, D.; Siikamäki, J.V.; Smith, P.; et al. Natural climate solutions. *Proc. Natl. Acad. Sci. USA* **2017**, *114*, 11645–11650. [CrossRef]
59. Asseng, S.; Ewert, F.; Martre, P.; Rötter, R.P.; Lobell, D.; Cammarano, D.; Kimball, B.; Ottman, M.; Wall, G.; White, J.W. Rising temperatures reduce global wheat production. *Nat. Clim. Change* **2015**, *5*, 143. [CrossRef]
60. Lobell, D.B.; Field, C.B. Global scale climate–crop yield relationships and the impacts of recent warming. *Environ. Res. Lett.* **2007**, *2*, 014002. [CrossRef]
61. Howden, S.M.; Soussana, J.F.; Tubiello, F.N.; Chhetri, N.; Dunlop, M.; Meinke, H. Adapting agriculture to climate change. *Proc. Natl. Acad. Sci. USA* **2007**, *104*, 19691–19696. [CrossRef]
62. Leng, S.; Gao, X.; Pei, T.; Zhang, G.; Chen, L.; Chen, X.; He, C.; He, D.; Li, X.; Lin, C.; et al. *The Geographical Sciences During 1986–2015*; Springer: Berlin/Heidelberg, Germany, 2017.
63. Ogisi, O.D.; Begho, T. Adoption of climate-smart agricultural practices in sub-Saharan Africa: A review of the progress, barriers, gender differences and recommendations. *Farming Syst.* **2023**, *1*, 100019. [CrossRef]
64. Jiang, B.; Deng, X.; Chen, H.; Cui, L.; Tang, W. Research trends and hotspots in climate adaptation of the agricultural system: A bibliometric analysis. *Front. Sustain. Food Syst.* **2023**, *7*, 1158904. [CrossRef]
65. Aleixandre-Benavent, R.; Aleixandre-Tudó, J.; Castelló-Cogollos, L.; Aleixandre, J. Trends in scientific research on climate change in agriculture and forestry subject areas (2005–2014). *J. Clean. Prod.* **2017**, *147*, 406–418. [CrossRef]
66. Velasco-Muñoz, J.F.; Aznar-Sánchez, J.A.; Belmonte-Ureña, L.J.; López-Serrano, M.J. Advances in Water Use Efficiency in Agriculture: A Bibliometric Analysis. *Water* **2018**, *10*, 377. [CrossRef]
67. Yuan, B.; Sun, J. Trend and status of Food Science and Technology category based on the Essential Science Indicators during 2011–2021. *Food Sci. Technol.* **2022**, *42*, e91321. [CrossRef]
68. Lin, W.; De, K.; Wei, X.; Wang, W.; Zhang, L.; Xiang, X.; Li, F. Visual analysis of alpine meadow research trends and hotspots based on VOS viewer. *Front. Environ. Sci.* **2023**, *11*, 1095299. [CrossRef]
69. Nsabiyeze, A.; Ma, R.; Li, J.; Luo, H.; Zhao, Q.; Tomka, J.; Zhang, M. Tackling climate change in agriculture: A global evaluation of the effectiveness of carbon emission reduction policies. *J. Clean. Prod.* **2024**, *468*, 142973. [CrossRef]
70. Oenema, O.; Velthof, G.; Kuikman, P. Technical and policy aspects of strategies to decrease greenhouse gas emissions from agriculture. *Nutr. Cycl. Agroecosyst.* **2001**, *60*, 301–315. [CrossRef]
71. Liu, M.; Chen, X.; Jiao, Y. Sustainable Agriculture: Theories, Methods, Practices and Policies. *Agriculture* **2024**, *14*, 473. [CrossRef]
72. Ochoa-Noriega, C.A.; Aznar-Sánchez, J.A.; Velasco-Muñoz, J.F.; Álvarez-Bejar, A. The Use of Water in Agriculture in Mexico and Its Sustainable Management: A Bibliometric Review. *Agronomy* **2020**, *10*, 1957. [CrossRef]
73. Shi, S.; Yin, J. Global research on carbon footprint: A scientometric review. *Environ. Impact Assess. Rev.* **2021**, *89*, 106571. [CrossRef]

Disclaimer/Publisher's Note: The statements, opinions and data contained in all publications are solely those of the individual author(s) and contributor(s) and not of MDPI and/or the editor(s). MDPI and/or the editor(s) disclaim responsibility for any injury to people or property resulting from any ideas, methods, instructions or products referred to in the content.

International Journal of Geo-Information

MDPI

Article

Riders Under the Heat: Exploring the Impact of Extreme Heat on the Integration of Bike-Sharing and Public Transportation in Shenzhen, China

Xin Wang [1], Rui Xue [2], Ming Lu [3] and Jiangyue Wu [1,*]

[1] Shenzhen International School of Design/Future Design School, Harbin Institute of Technology, Shenzhen 518055, China; 23s035061@stu.hit.edu.cn
[2] Department of Urban and Rural Planning, School of Architecture and Urban Planning, Huazhong University of Science and Technology, Wuhan 430000, China; m202374212@hust.edu.cn
[3] Department of Urban and Rural Planning, School of Architecture and Design, Harbin Institute of Technology, Harbin 150001, China; hitlm1969@hit.edu.cn
* Correspondence: wujiangyue@hit.edu.cn

Abstract: Bike-sharing (BS) systems provide a widely used and convenient feeder mode for connecting to public transportation (PT) and is seen as an effective solution to the first- and last-mile problem. Amidst the critical challenges posed by global climate change and rising temperatures, enhancing the resilience of the BS and PT integration is essential to ensure sustainable urban mobility and adapt to increasing climate variability, yet empirical studies in this area remain limited. This study analyzes BS-PT integration usage under extreme heats events, focusing on a Chinese mega city's bike-sharing system. By defining extreme heat using the heat index, a more accurate measure of heat perception is established. We carefully categorize heatwaves based on the duration and temperature context of extreme heat to account for their potential impact on the integration's response. Then, integrating multi-source big data and applying geographically weighted regression (GWR), we explore the spatial–temporal variations in the response of BS-PT integration ridership during different temperatures, and further identify key factors that contribute to the response of BS-PT integrated travel. Results show that extreme heat significantly influences BS-PT integration, with users showing a greater willingness to shift towards more integrated uses under extreme heat during non-summer seasons, compared to solely using bike-sharing, to avoid outdoor heat exposure. The temporal heterogeneity of the integrated trips is highest during extreme heat in non-summer and lowest under continuous extreme-heat periods. GWR spatial regression reveals that land-use characteristics significantly affect BS-PT integration resilience, with notable spatial differences in the influence of various factors, such as office density and entropy. These findings enhance our understanding of how climate change affects public transportation, providing urban planners and policymakers with valuable insights for improving the adaptability of urban mobility systems to climate change.

Keywords: bike-sharing; public transport; extreme heat; multimodality; GWR

1. Introduction

Due to rapid urban expansion and increasing car ownership, the issues of traffic congestion and environmental pollution have become more severe. Bike-sharing, as an environmentally friendly transport mode, significantly contributes to sustainable mobility by eliminating emissions [1,2]. It also provides personal health benefits by promoting physical activities [3,4] and expands the service coverage of public transit [5,6]. This mode of transport has been widely adopted in various regions, including China, Australia, and Europe [7,8]. Beyond its function as an independent travel mode, bike-sharing plays a crucial role as a feeder mode for metro systems [9,10]. The integration of bike-sharing

(BS) and public transportation (PT) services effectively addresses the first- and last-mile problem [10]. In recent years, the rapid expansion of bike-sharing systems has been particularly notable in countries like China and Singapore. This integration is especially compelling in high-density urban areas [11].

The increasing frequency and intensity of extreme weather events, such as heatwaves, have escalated as a direct consequence of climate change. Extreme heat poses significant challenges to urban mobility, particularly for non-motorized modes of transport such as bike-sharing, which are highly sensitive to weather conditions [12]. During extreme weather events, the travel frequency of active travelers decreases because they are directly exposed to severe conditions, resulting in discomfort and safety risks [13,14]. This effect is more pronounced for bike-sharing systems than for individual cyclists, as shared bike users are more likely to alter their travel plans in response to adverse weather.

Existing studies have demonstrated the correlation between temperature variations and bike-sharing usage, highlighting the deterrent effect of extreme temperatures on bike-sharing [14–16]. However, the existing research has several limitations. First, there are few comprehensive studies on the specific impacts of extreme heats on the integration of BS and PT. Related studies typically examine bike-sharing and metro ridership independently, neglecting the integrated use of these modes. The spatiotemporal characteristics and explanatory factors of the integration likely differ from those of standalone BS due to the distinct attributes of the integration, such as not requiring full exposure to outdoor environments, offering a broader service range, and typically involving longer trip durations. Consequently, the usage patterns under extreme heat conditions may significantly differ between PT-BS integration and standalone BS. In addition, there is a lack of standardized definitions for extreme heat globally, leading to varied and sometimes simplistic criteria that fail to account for regional climatic differences in relevant studies [17].

Therefore, this study aims to fill these gaps by exploring how extreme heat influences BS-PT integration using reasonable and context-specific definitions for extreme heat and identifying the key factors contributing to the resilience of such integrated travel under different temperature conditions. The objectives of this study are to (1) identify the spatiotemporal distribution patterns of BS-PT integrated uses under extreme heat events to understand the substitution and complementary relationship with BS trips and where the integration offers greater resistance to extreme heats; and (2) identify the key factors affecting the BS-PT integration response.

This paper is structured in the following manner: Section 2 reviews the literature on the bike-sharing system, the integration usage, and the impact of weather. Section 3 describes the data, control groups, and models. Section 4 discusses the results of the data analysis and modeling. Finally, the paper concludes with the key findings, implications for practice and policy, and suggestions for future research.

2. Literature Review

2.1. Bike-Sharing System

Bike-sharing systems, which offer a flexible and sustainable mode of travel, are being promoted globally [18]. It serves as an effective solution to address issues arising from rapid urbanization and increased car dependency, such as vehicle emissions, traffic congestion, and air pollution, which negatively impact the urban environment and public health [19–21]. This system supports spontaneous and short-distance trips, seamlessly integrating with public transport to tackle the first- and last-mile problem [1,22,23]. Lack of connectivity is one of the biggest challenges in the development of public transport systems, especially rail transportation [24]. This addresses the challenge of providing first- and last-mile connections from residential areas and public transportation stations to final destinations. Efficient connections and transitions among different travel modes can significantly improve passenger satisfaction and travel efficiency [25].

Different regions exhibit varying travel patterns influenced by numerous factors, making in-depth research essential. As summarized by [26], cycling trips are influenced

by natural environment factors (weather and topography), built environment factors (land use and infrastructure), and temporal factors (calendar events and peak periods). Understanding these factors helps in tailoring strategies to promote cycling and optimize bike-sharing systems, ensuring their efficiency and accessibility in diverse urban settings.

2.2. The Integration of Bike-Sharing and Public Transportation

Due to their flexibility and affordability, bike-sharing (BS) systems are widely applied as feeder systems to public transportation (PT) to improve efficiency and address first- and last-mile issues [1,27]. Studies from the United States [7,28], Europe [2,29], and Australia [1] demonstrate BS-PT integration's ability to enhance multimodal connectivity, reduce car dependency, and improve commuter behavior.

The integration of BS-PT has garnered increasing attention in recent studies for multiple reasons. First, BS-PT integration has significantly enhanced demand for both public transportation and shared bikes because it offers passengers a travel option with higher flexibility and accessibility [1]. Second, BS enables a multimodal combination that is smarter, more eco-friendly, and more cost-effective, eliminating concerns about theft, vandalism, and maintenance [7]. Third, the integration is particularly advantageous in densely populated areas because of its ability to alleviate traffic congestion [11]. Therefore, the advantages provided by BS-PT integration have attracted research interest from multiple disciplines, including urban planning, transportation planning, and traffic engineering. Numerous studies have explored how BS and metro PT trips are integrated [2,30], the spatiotemporal heterogeneity under different factors such as built environment and socioeconomic groups [9,31], and models to quantify the interdependencies of bike-sharing and public transportation systems [30,32,33].

However, several weather-related studies mainly focused on the impact of long-term weather [26,33,34], but the impact of short-term weather (within a day), which can cause temporary but significant fluctuations that are likely to recur, has been overlooked. Researchers have identified distinct peak periods for both shared bikes [5] and their integration with public transportation [10] during morning and evening commuting hours. While both show increased usage during these peak periods, the patterns are not identical, indicating unique usage behaviors for integrated trips. Therefore, the response of the integration of BS-PT to extreme heats may vary across different times of a day. Given these insights, it is crucial to investigate how BS-PT integration reacts to extreme heats at various times throughout the day to enhance our understanding and improve the system's resilience, which is also vital for the system response and scheduling of BS services.

2.3. The Impact of Weather on the Integration of BS-PT

Active travel modes are significantly more affected by extreme weather events compared to motorized options [14]. Active travelers, who are directly exposed to harsh weather conditions, face increased discomfort and elevated risks. This exposure leads to a marked decrease in the frequency of trips during extreme weather [13,14]. This effect is particularly notable in bike-sharing systems, where users tend to have greater flexibility to adjust their travel plans in response to weather changes compared to cyclists who always use their own bikes. An, Zahnow, Pojani, and Corcoran [26] discovered that weather has a more significant influence on bike-sharing rates compared to factors such as calendar events, topography, infrastructure, and land-use mix. Among different factors of weather, temperature significantly influences the availability of bikes at bike-sharing system stations [35]. Temperature variations strongly affect bike-sharing decisions. Extreme temperatures, both high and low, deter bike-sharing, especially among recreational cyclists [14,36].

Existing weather-related studies have mainly focused on long-term weather impacts, such as seasonal variations and annual averages [33,34]. These studies have demonstrated how prolonged weather patterns influence cycling habits and infrastructure usage. However, they often neglect short-term influences, which can cause temporary but significant fluctuations that are likely to recur. This remains a research gap that requires further explo-

ration to understand the effects of long-term weather on bike-sharing-related usage [37]. In addition, the lack of standardized definitions for extreme heat globally leads to varied and sometimes simplistic criteria that fail to account for regional climatic differences [17]. Some previous studies on the impact of extreme heats on bike-sharing often considered only temperature [15], neglecting the fact that human perception of extreme heat depends on multiple environmental factors such as humidity and wind speed, not just the daily maximum temperature.

As global mean temperatures continue to rise, bike-sharing travel, which requires physical exertion, is likely to be significantly impacted by increased heat exposure [13]. The integration of the BS-PT model, as an emerging yet crucial component of bike-sharing trips, is also highly sensitive to temperature. Given the different characteristics of bike-sharing and its integration with public transportation, their responses to extreme heats may vary. However, the changes in mobility patterns during extreme heats remain unclear, and the extent of extreme heats' impact on users' spatiotemporal active travel patterns is not well understood. Substantial evidence indicates that bicycle ridership decreases under extreme heats conditions due to the discomfort and severe health risks like heat exhaustion and dehydration, which deter users [15]. In densely populated urban areas, extreme heats significantly exacerbate challenges to human mobility [38], particularly affecting non-motorized and public transportation. Therefore, establishing a comprehensive understanding of the relationship between extreme heats and the integration of BS and PT becomes essential. This insight is critical for the development and implementation of heat-resilient urban policies and strategies within existing transportation infrastructures.

2.4. Summary

First, the existing research on bike-sharing usage often focuses on stable factors like socioeconomic conditions and policies, which are crucial for long-term planning, but tends to overlook short-term weather variability. This oversight reveals a significant research gap. Understanding short-term weather impacts is essential for enhancing urban resilience, as cities must quickly adapt to extreme weather to maintain effective transportation networks. Unprecedented heatwaves have occurred widely across South America, North America, Europe, and Asia [39]. During these events, cities had to rapidly adapt with measures like adjusting public transportation and managing power usage, to ensure the resilience and continuity of urban services. Second, while research has separately examined bike-sharing [15] and metro ridership [40], the combined effects of integrated uses, especially under extreme weather conditions, remain underexplored. Understanding the impact of weather variability on this integration is vital for optimizing service response and scheduling, as the spatiotemporal characteristics of the integration likely differ from those of standalone BS due to the distinct attributes of the integration, such as not requiring full exposure to outdoor environments, offering a broader service range, and typically involving longer trip durations. Consequently, the usage patterns under extreme heat conditions may significantly differ between PT-BS integration and standalone BS. Lastly, most studies select relatively few instances of heatwaves, limiting the generalizability of their findings. There is also a lack of standardized definitions for extreme heats globally, leading to varied and sometimes overly simplistic definitions that do not account for regional climatic differences [17]. Therefore, investigating the integration of bike-sharing and public transportation, particularly rail transit, under different extreme heat conditions, can provide comprehensive insights into travel behaviors and needs.

This study addresses this gap by investigating the spatiotemporally varying effects of extreme heats on the integration of BS and PT, considering spatiotemporal heterogeneity, which is crucial as BS often serves as a first- and last-mile solution integrated with PT, reflecting actual travel patterns often neglected in previous studies. The main research questions are as follows:

- Do BS users shift towards more BS-PT integrated uses during extreme heat to avoid outdoor exposure, and how is this substitution and complementary relationship manifested?

- How does extreme heat affect BS-PT integrated uses, and what key factors contribute to the resilience of BS-PT integrated travel during different temperature conditions?

By integrating multi-source big data and geographically weighted regression methods, the study aims to enhance understanding of urban transport resilience and inform adaptable transport policies and infrastructure development.

3. Methodology

3.1. Study Area: Shenzhen, China

The city of Shenzhen, one of China's top-tier cities and a central hub in the Guangdong–Hong Kong–Macau Greater Bay Area, had a population of 17.68 million as of 2021, spanning an area of 1997.47 square kilometers (Figure 1). The metro is the backbone of public transportation in Shenzhen, constituting 40% of all public transport trips. The Shenzhen metro system includes 11 operational lines spanning 419 km. In 2021, the metro system accommodated an average daily passenger flow of 5.97 million [41]. The dockless bike-sharing (DBS) system was first introduced to Shenzhen in September 2016. Due to its compatibility with the city's infrastructural environment, the system experienced extremely rapid growth. As of 2021, Shenzhen boasted around 390,000 DBS bikes and 27.7 million registered users, with an average daily cycling volume of 1.38 million (Shenzhen Municipal Transportation Management Bureau).

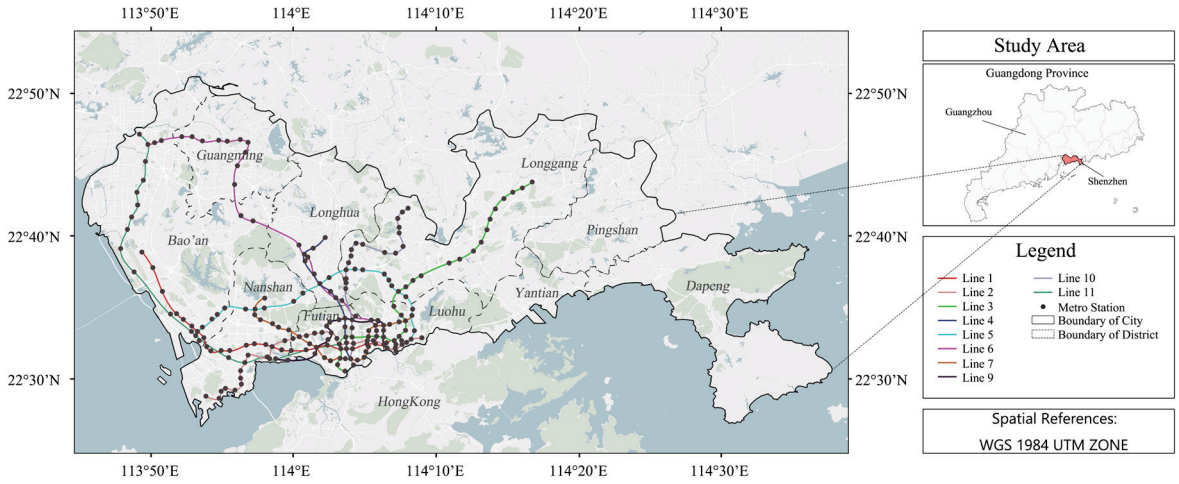

Figure 1. Study area.

According to the 2019 Shenzhen Bike-Sharing Development Evaluation Report, areas within a 2 km radius around metro stations are the most concentrated regions for bike-sharing usage, accounting for over 90% of hotspot cycling areas. Rides connecting to metro or bus services constitute approximately 52.3% of the average daily cycling volume. This spatiotemporal distribution highlights the citizens' need for "first- and last-kilometer" connections. Furthermore, the report indicates significant variations in bike-sharing usage between morning and evening peak hours at metro stations, with differences typically exceeding 2 percentage points, highlighting a noticeable imbalance. During weekday mornings, bike unlocking locations are dispersed, while locking locations are concentrated around metro stations, indicating a strong aggregation effect. Conversely, in the evenings, bike unlocking locations are concentrated around metro stations, with locking locations more dispersed, illustrating a significant dispersal effect. These spatiotemporal imbalances in the BS-PT integration provide a basis for categorizing multimodal travel types and underscore the necessity for more detailed studies on the spatiotemporal characteristics of integrated travel behaviors.

3.2. Data Resources

This study consolidates the diversified big data of Shenzhen City in 2021 from official sources, and the following Table 1 shows the sources and descriptions of the data.

Table 1. Data resources.

Data Category	Resources	Description
Bike-sharing data	The open data platform of the Shenzhen municipal government https://opendata.sz.gov.cn/ (accessed on 21 May 2024)	A total of 240 million trips were recorded between January and August 2021, with each line of data recording the user ID of the shared bike, the latitude and longitude of the start and end points of the trip, and the start and end times.
Point of interest (POI)	The application programming interface (API) of Amap https://lbs.amap.com/ (accessed on 12 June 2024)	This study selects six categories of POIs, including bus stations, residential sites, commercial sites, public facilities, recreational sites, transportation services, and workplace services.
Metro stations	The application programming interface (API) of Amap https://lbs.amap.com/ (accessed on 20 May 2024)	As of 2021, there were a total of 239 metro stations in Shenzhen.
Weather record	2345 historical data from the 2345 Weather website and NCDC National Weather Data Centre https://tianqi.2345.com/ (accessed on 5 June 2024) https://www.ncei.noaa.gov/cdo-web/ (accessed on 5 June 2024)	Each date with the maximum temperature, minimum temperature, wind speed, wind force, wind direction, air quality index, relative humidity, and rainfall data in 2021.
Road network	OpenStreetMap https://www.openstreetmap.org (accessed on 23 May 2024)	Urban road network data include spatial and vector information for various types of roads, such as highways, and main and branch roads.

3.3. Identification of Integrated Usage

The integration of BS and PT generally follows two patterns: (1) using bike-sharing to travel to the public transport station, known as access integration, and (2) using bike-sharing from the public transport station, referred to as egress integration [9,10], as illustrated in Figure 2. Since Shenzhen's BS-PT integration is often linked with the metro (Shenzhen Urban Transportation Planning and Design Institute, 2019), in this paper, "PT station" specifically refers to metro stations.

Figure 2. The different patterns of BS-PT integration.

The specific process for identifying the integration is as follows. Initially, the spatial relationship between shared bikes and public transport stations is established by aligning the real-time location data of bike-sharing systems with the fixed coordinates of public transport stations. Following the methodologies of [22,42], the integration is measured by counting the use of BS within a buffer zone around a public transport station (see Figure 3). It is fundamentally assumed that bike trips occurring near public transport stations qualify as integrated usage [22]. A survey by Guo et al. [22] with 1167 participants from 22 Shenzhen metro stations found that over 95% of commuters ended or began their shared bikes within 100 m of a station. This buffer size has been widely adopted in recent studies, which consistently report strong spatial correlations between bike-sharing and public transport stations [10,43,44]. Consequently, a 100 m buffer (see Figure 3) is used to determine if a bike-sharing trip is integrated.

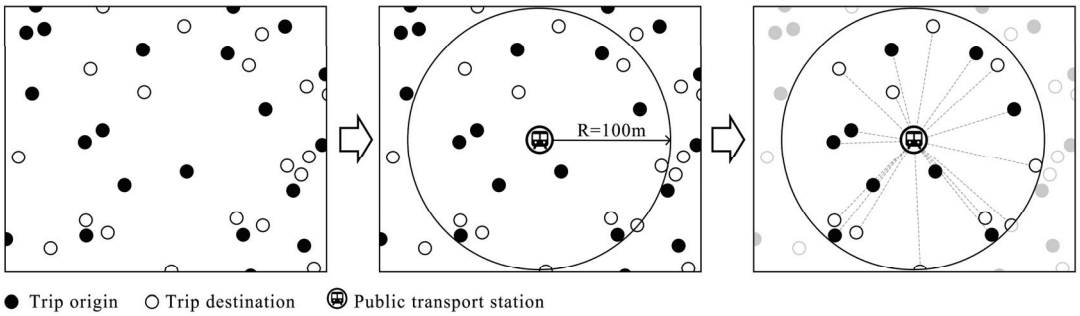

Figure 3. The process of identifying the integration.

3.4. Screening Weather Control Groups

Control groups under different weather conditions are screened to accurately assess and understand the specific impacts of temperature changes on travel behavior. According to the China Meteorological Administration, extreme high-temperature weather is broadly defined as when the daily maximum temperature exceeds 35 degrees Celsius. However, previous studies on the impact of high temperatures on bike-sharing often considered only temperature [15], neglecting the fact that human perception of extreme heat depends on multiple environmental factors such as humidity and wind speed, not just the daily maximum temperature. This is especially important in Shenzhen, where the annual average relative humidity exceeds 70%. Therefore, a more nuanced definition of extreme high-temperature weather is crucial.

In this study, a day is classified as having extreme high-temperature weather if the heat index reaches 32 °C or above. The heat index, developed by the U.S. National Weather Service [45], is a composite measure used to assess the actual temperature perceived by the human body under specific temperature and humidity conditions. It considers both air temperature and relative humidity, thus providing a more accurate reflection of human thermal perception than temperature alone. According to this index, a heat index exceeding 32 °C warrants "Extreme Caution" due to the potential for heat stroke, heat cramps, or heat exhaustion with prolonged exposure and/or physical activity.

The control groups were divided based on four different temperature conditions, considering the impacts of both temperature and duration. After excluding the impact of precipitation and the months with significant data fluctuations due to the pandemic (indicated by the gray shaded areas in the figure), the filtered results are presented in Figure 4.

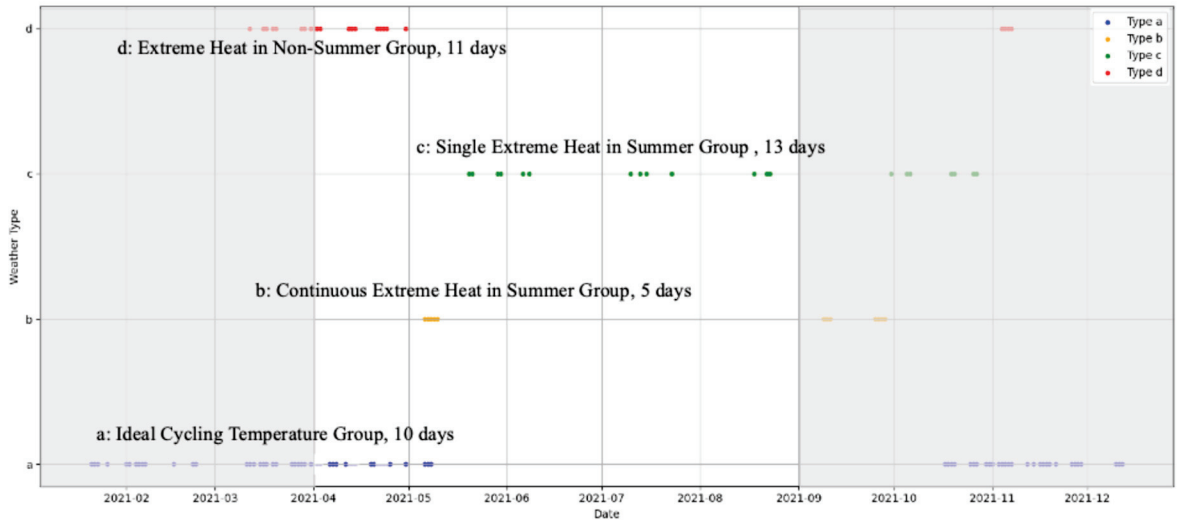

Figure 4. Weather control group (excluding all days with precipitation).

(1) Ideal Cycling Temperature Group (Group A)

Many studies have investigated the ideal temperature for cycling, yielding varying specific values. The ideal temperature range for cycling is typically between 17 °C and 33 °C; although in cities with continental climates, cyclists often ride in temperatures spanning from −4 °C to 40 °C [36,46,47]. In addition, the ideal temperature for bicycle riding was found to be 25–28 °C, where bike usage has been observed to increase by 60% compared to when the temperatures are at 0 °C [48]. Combining Shenzhen's high-humidity weather conditions, the ideal cycling temperature in this study is defined as days with a maximum temperature between 25 °C and 28 °C; this group provides a benchmark for understanding travel characteristics under the most comfortable conditions, with a total of 10 days selected.

(2) Continuous Extreme Heat Group (Group B)

According to the China Meteorological Administration's definition of consecutive extreme high-temperature weather, it is defined as such if the maximum temperature reaches 35 degrees Celsius for three or more consecutive days. Considering the comprehensive definition of temperatures with humidity mentioned earlier, this group is defined as experiencing three consecutive days with a heat index (HI) of 32 °C or above, which captures the cumulative effects of sustained high temperatures on travel behavior, with a total of 5 days selected.

(3) Single Extreme Heat Group in Summer (Group C)

Defined as experiencing sudden spikes in temperature during generally high summer averages (HI $\geq$ 32 °C), this group is designed to analyze the impact of abrupt high temperatures on travel behavior in summer, with a total of 13 days selected.

(4) Extreme Heat Group in Non-Summer (Group D)

Defined as experiencing abrupt temperature rises outside of summer, this group is designed to assess the immediate impact of single extreme high temperatures on travel behavior, with a total of 11 days selected.

(5) Statistical Justification for Temperature Grouping

To justify the division of data into four temperature groups, we conducted a one-way ANOVA, which confirmed significant differences in heat index values between groups ($F = 38.22$, $p < 0.01$). Descriptive statistics further support the validity of this grouping: mean heat index values range from 27.87 (Group A, ideal cycling conditions) to 48.40 (Group C, summer single-point extreme heat), with Group C showing the highest maximum heat index (59.30) and greater variability (SD = 4.31) compared to Group A (SD = 3.38).

Visualizations (Figure 5a,b) reinforce these findings, with minimal overlap between groups. Group A exhibits a narrow range (25–30), while Groups B and C extend into higher heat index ranges, exceeding 55 in Group C. Group D displays intermediate values (35–40). These results validate the robustness of the grouping, ensuring that each category reflects distinct and meaningful temperature scenarios.

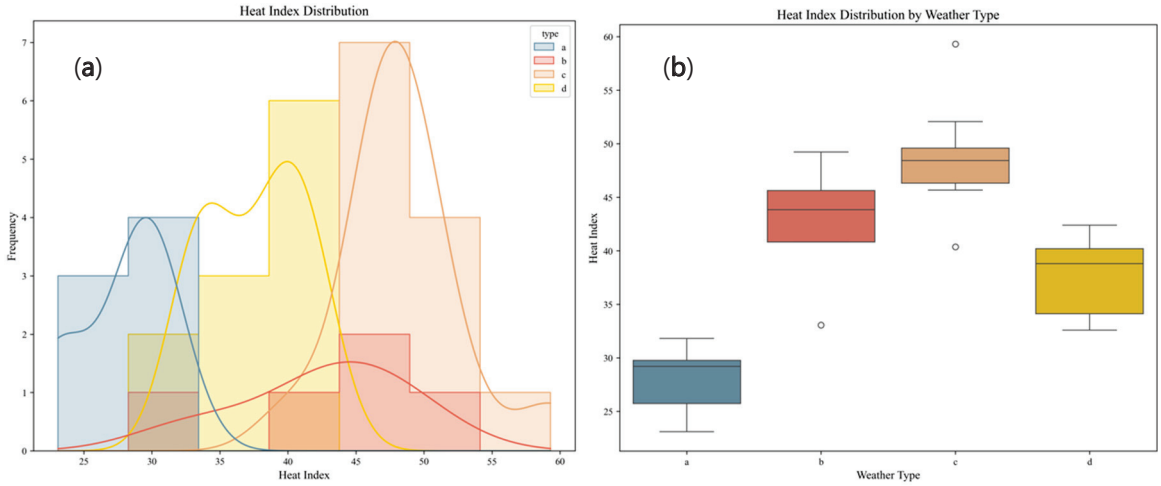

Figure 5. Heat index distribution and heat index distribution by weather groups. (**a**) Frequency distribution plot highlighting minimal overlap between groups. (**b**) Boxplot showing distinct heat index ranges for each group.

3.5. Geographically Weighted Regression

Spatial data often exhibit spatial autocorrelation and spatial heterogeneity, which can lead to biased estimates in traditional regression models. To address these challenges, geographically weighted regression (GWR) was developed, emphasizing the non-stationary relationships between independent and dependent variables across the geographical space. The advantages of GWR include its ability to model spatially varying relationships and account for spatial heterogeneity, which traditional methods like OLS cannot address. However, GWR has limitations, including computational demands and sensitivity to bandwidth selection [49]. Compared to methods like OLS, which assumes constant relationships, and Spatial Lag Models, which address spatial dependency but not localized variations, GWR offers geographically specific insights, making it particularly suitable for this study. This localized approach captures spatial variations more effectively, as described in Equation (1) [49].

$$y_i = \beta_0(u_i, v_i) + \sum_{j=1}^{m} \beta_j(u_i, v_i) x_{ij} + \epsilon_i \quad (1)$$

In this equation, $\beta_0(u_i, v_i)$ represents the local intercept for the i th observation, $\beta_j(u_i, v_i)$ refers to the local coefficient of the j th independent variable x_{ij}, ϵ_i is the random error term, and (u_i, v_i) represents the spatial coordinates of the i th observation. In this study, the independent variables include various built environment factors, while the dependent variable is the integrated usage under different weather conditions, such as ideal temperature and continuous extreme heat, as shown in Table 2. By employing GWR, we aim to uncover the spatially varying relationships between these factors and weather.

Spatial data often exhibit autocorrelation, where nearby locations show similar variable values, potentially biasing model estimates if unaccounted for [50]. Moran's I is a key tool for detecting spatial autocorrelation, which is widely applied in urban studies to analyze spatial patterns and support spatial modeling [51]. In public transportation research, it identifies spatial clustering in transit accessibility and travel behavior, revealing service inequities [52,53]. Additionally, Moran's I assesses urban green space distribution, informing environmental justice. For example, Li et al. [54] applied Moran's I to study the spatial variation in forest litter carbon density in subtropical forests, providing insights into environmental management. These applications underscore its relevance and robustness in detecting spatial clustering in urban research.

The Moran's I test results in Table 3 indicate significant spatial autocorrelations for all explanatory variables, with high Moran's I values and Z-scores, and p-values of 0. This suggests that the variables exhibit strong spatial clustering. These findings underscore the

necessity of using spatially explicit models such as geographically weighted regression (GWR) to account for spatial heterogeneity in the analysis.

Table 2. Summary statistics of variables.

Variable	Description	Mean	SD	Min	Max
Dependent Variables					
Access trips in Group A	Access integration during the ideal temperature days	21,325.1	9177	5623	33,805
Egress trips in Group A	Egress integration during the ideal temperature days	21,285.9	9160.6	5613	34,295
Access trips in Group B	Access integration during the continuous extreme heat days in summer	12,761.4	1656.3	10,701	14,937
Egress trips in Group B	Egress integration during the continuous extreme heat days in summer	12,401.6	2407.5	9287	15,589
Access trips in Group C	Access integration during the single extreme heat days in summer	21,210	1992	18,504	24,382
Egress trips in Group C	Egress integration during the single extreme heat days in summer	36,043.1	55,039	17,954	219,088
Access trips in Group D	Access integration during the extreme heat days in non-summer	26,386.8	9391.5	8462	39,440
Egress trips Group D	Egress integration during the extreme heat days in non-summer	26,581	9335.8	8441	39,638
Explanatory Variables					
Bus station density	Number of bus stations per unit area	6.07	2.12	0.16	11.32
Road density	Length of roads per unit area (Km/Km^2)	0.01	0.01	0	0.03
Residential POI	Number of residential areas	285.8	150.45	2	759
Commercial POI	Number of restaurants, shopping points, sports stadiums and life services, etc.	1330.66	754.64	33	3476
Public facility POI	Number of government agencies, and social groups, technology and cultural venues, healthcare services, public restrooms, etc.	739.82	462.39	22.	2075
Recreation POI	Number of parks, memorials, tourist attractions, squares, etc.	41.2	30.78	0	180
Transportation POI	Number of transportation-related points of interest	875.39	639.44	22	2594
Office POI	Number of bus stops, subway stations, parking lots, and high-speed rail stations	2082.45	1164.24	19	5971
Entropy	Measure of diversity of points of interest	2.01	0.14	1.36	2.31

Table 3. Moran's *I* test for each explanatory variable.

Variable	Moran's *I*	Z-Score	*p*-Value
Bus station density	0.628	14.76	0
Road density	0.784	18.384	0
Residential POI	0.744	17.451	0
Commercial POI	0.697	17.451	0
Public facility POI	0.789	18.508	0
Recreation POI	0.680	15.963	0
Transportation POI	0.856	20.07	0
Office POI	0.703	16.503	0
Entropy	0.466	10.981	0

4. Findings and Discussions

4.1. Temporal Variations in BS-PT Integration Response

Although bike-sharing trips in Shenzhen are consistently concentrated around metro stations [55], the temporal characteristics of BS-PT integrated trips differ significantly from those of standalone bike-sharing trips.

From Figure 6 (1), which shows the average number of bike-sharing trips per half hour in control groups, it is evident that bike-sharing usage remains highest in the ideal temperature group, consistent with previous studies [48]. The lowest usage is observed during extreme heats in non-summer seasons, likely due to the lower overall background temperatures, making sudden high temperatures more noticeable and thus more discouraging for bike-sharing trips, since they directly expose riders to the heat. This suggests that the impact of temperature on bike-sharing trip volumes is not simply linear, as previously suggested [56–58], where trip numbers always drop once a certain temperature is reached. The impact of continuous extreme heat in summer on overall bike-sharing trips is similar to that of single extreme heat in summer. Regarding the daily fluctuations in bike-sharing usage, the morning and evening peaks are similar across all four weather conditions, with no significant compensation at night, contrary to previous research [15].

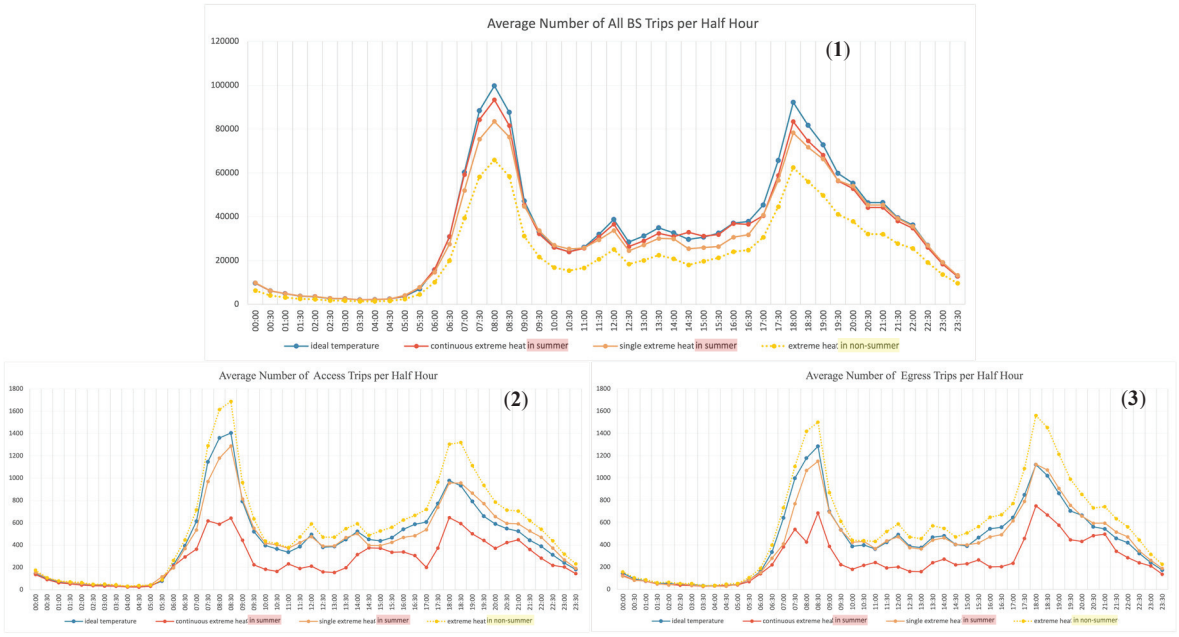

Figure 6. Average trip counts per half hour in control group.

From Figure 6 (2) and (3), it can be seen that under extreme heat in non-summer seasons, BS-PT integrated trips are actually the highest, even exceeding those under ideal riding conditions. This contrasts with standalone bike-sharing trips, which are lowest under extreme heats outside of summer. This may be because integrated trips offer more opportunities to avoid direct exposure to high temperatures, making more people choose connecting trips in such weather. In this sense, integrated trips supplement and substitute standalone bike-sharing trips. Continuous extreme heat significantly hinders integrated trips, especially when compared to overall bike-sharing usage, highlighting the negative impact of extreme heats on integrated and multimodal trips. Additionally, the temporal characteristics of integrated trips under ideal temperatures and single extreme heat in summer are similar, which indicates that single extreme heat in summer does not significantly negatively affect integrated trips and are almost equivalent to ideal cycling temperature.

Furthermore, in terms of access usage, the number of trips during the morning peak is almost 50% higher than during the evening peak, except for continuous extreme heats, consistent with previous research findings [10]. However, in terms of egress usage, the

numbers of trips during the morning and evening peaks are nearly identical regardless of temperature conditions. The lower evening temperatures compared to the daytime suggest that other transportation modes may substitute for bike-sharing access trips, while the number of bike-sharing egress trips remains unaffected. Under continuous extreme heats, the access and egress usage numbers during morning and evening peaks are nearly identical, possibly because the retained commuting integration during these peaks is essential and difficult to replace.

4.2. Spatial Variations in BS-PT Integration Response

Different control groups exhibit distinct spatial clustering patterns under varying temperatures and durations. Figures 7 and 8 illustrate the average travel volumes of access-integrated and egress-integrated uses on a day of extreme high temperatures.

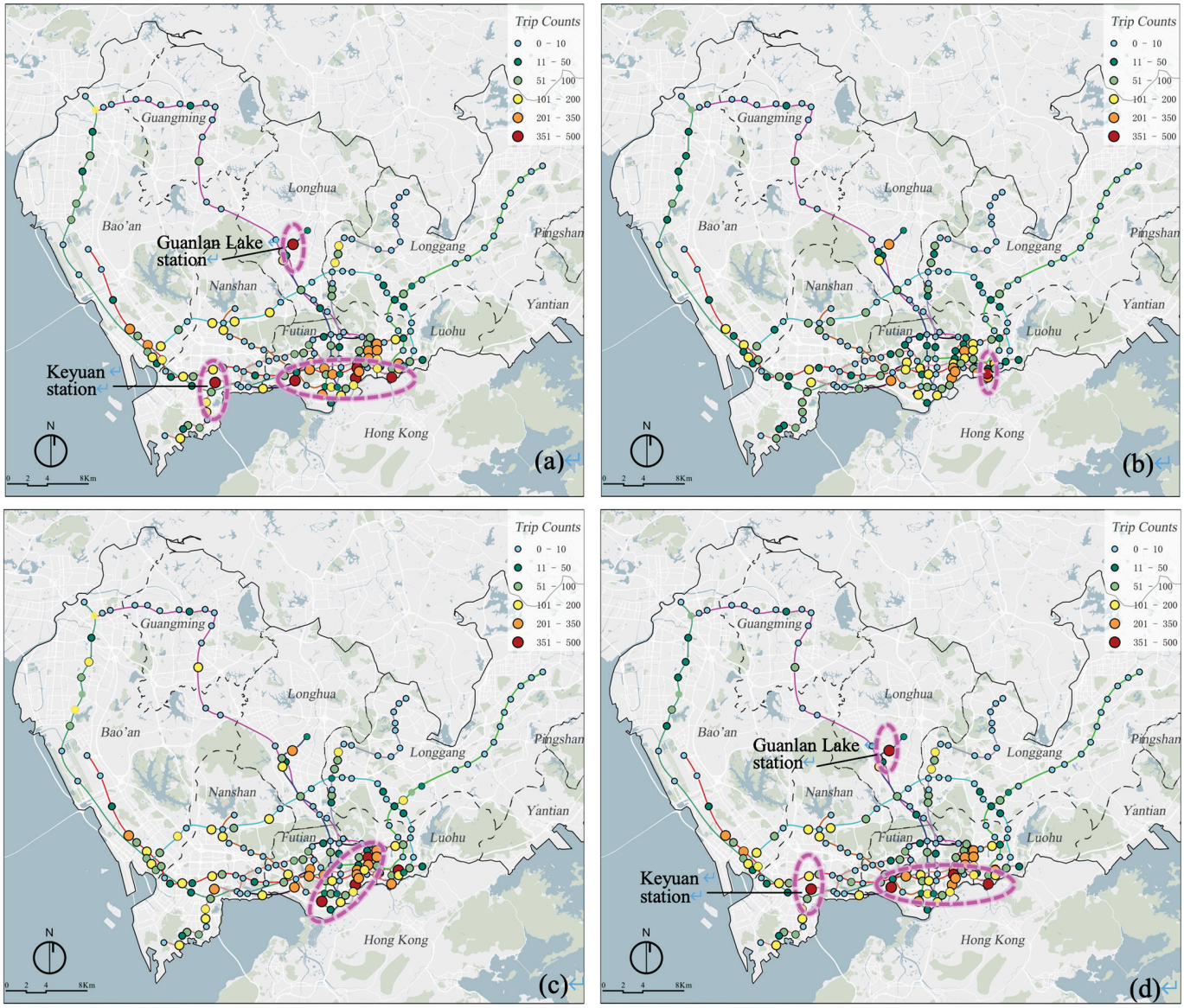

Figure 7. Different spatial clustering patterns of access-integrated uses in the control group. (**a**) Group A: Access-integrated uses under ideal cycling temperature. (**b**) Group B: Access-integrated uses under continuous extreme heat in summer. (**c**) Group C: Access-integrated uses under single extreme heat in summer. (**d**) Group D: Access-integrated uses under extreme heat in non-summer.

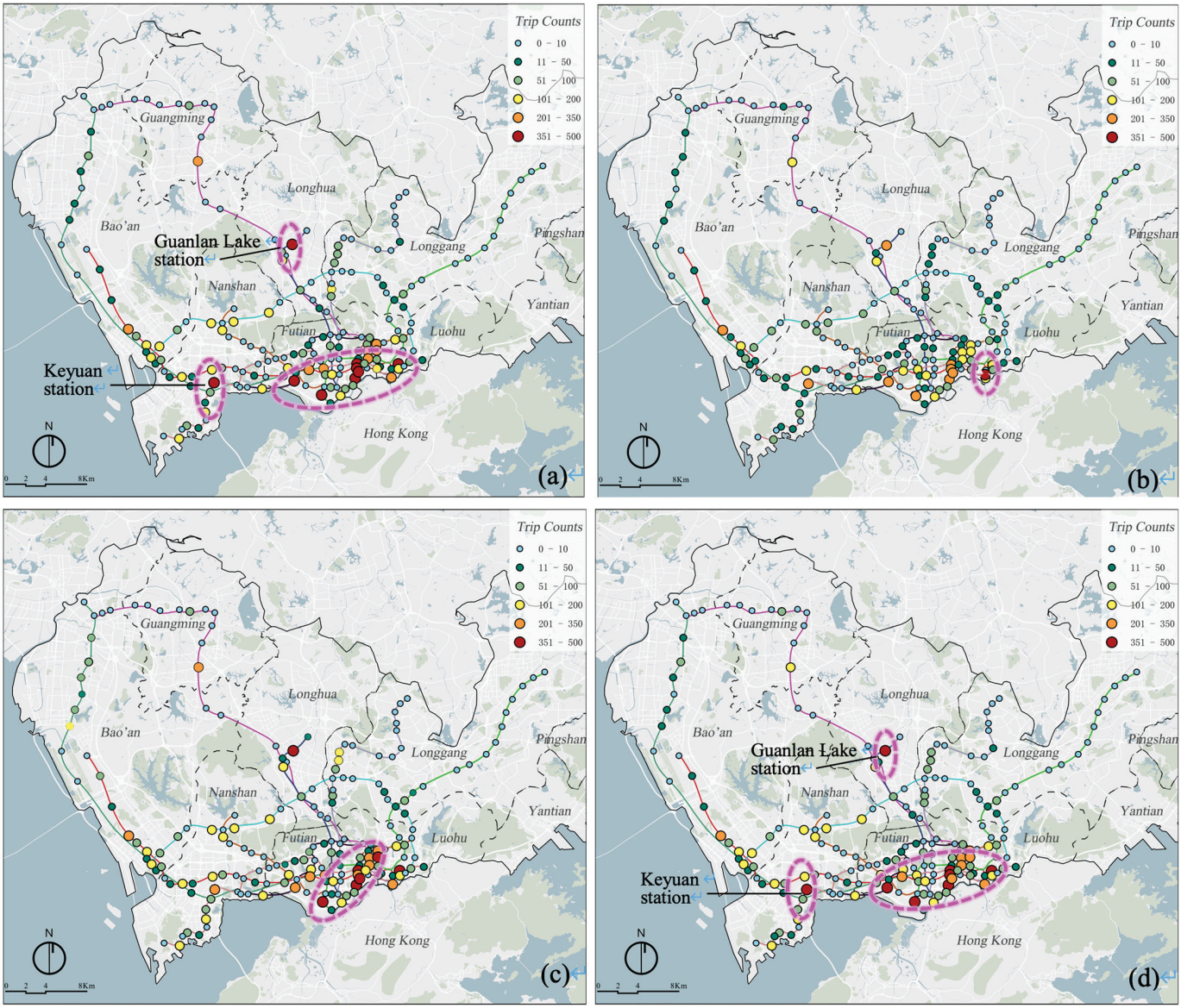

Figure 8. Different spatial clustering patterns of egress-integrated uses in control group. (**a**) Group A: Egress-integrated uses under ideal cycling temperature. (**b**) Group B: Egress-integrated uses under continuous extreme heat in summer. (**c**) Group C: Egress-integrated uses under single extreme heat in summer. (**d**) Group D: Egress-integrated uses under extreme heat in non-summer.

The distribution indicates a certain similarity in BS-PT integrated uses under different weather conditions, primarily concentrated in the high-density development CBD areas of Futian, Luohu, and Nanshan districts in southern Shenzhen. Additionally, there are varying degrees of concentration in Longhua district and at the Keyuan station in Nanshan district (Figure 7a). It is noteworthy that both of these stations are located in high-tech park office areas, reflecting Shenzhen's reputation for innovation and technology and closely relating to the start and end points of residents' commutes. The High-Tech Park in Nanshan district, which is agglomerated with a large number of high-tech companies, has created nearly 300,000 jobs within an 11.5 km^2 area, attracting thousands of companies. Furthermore, it is noteworthy that the travel data for Group A (ideal cycling temperature) in Figures 7a and 8a and Group D (single extreme heat in non-summer) in Figures 7d and 8d show similar spatial distributions. This indirectly proves that non-summer extreme heats not only do not inhibit the integrated uses but also promote them. The relationship between bike-sharing trip volume and temperature is not simply linear, where exceeding a threshold

results in a negative impact. Instead, it depends to a certain extent on the temperature context and the duration of high temperature.

On the other hand, there are significant geographical differences in the spatial aggregation of trips under different weather conditions. Comparing Group A in Figures 7a and 8a with Groups B in Figures 7b and 8b and C in Figures 7c and 8c show that extreme heat significantly reduces the integration volume at almost all stations, with the reduction from continuous extreme heats being greater than that from single extreme heats in summer. For stations with a medium integration volume (100–200), the impact of single extreme heats in summer is negligible. However, for continuous extreme heats, the integration volume significantly decreases. Stations with a daily average integration volume of more than 200 are more sensitive to temperature changes, with both single and continuous extreme heats significantly reducing the integration volume at these stations.

4.3. Factors Associated with BS-PT Integration Response

4.3.1. Modeling Results

Table 4 summarizes the mean coefficients and standard deviations for geographically weighted regression (GWR) models under four different weather conditions (A, B, C, and D) and two usage types (access and egress). These statistics offer insights into the spatial variability and significance of the model parameters, reflecting how various factors influence the dependent variable across different spatial contexts. The results indicate that the impact of variables varies significantly across different weather conditions and usage types, highlighting the importance of considering spatial heterogeneity in regression analysis.

Table 4. Modeling results of geographically weighted regression.

Variable	A Group				B Group				C Group				D Group			
	Access Use		Egress Use		Access Use		Egress Use		Access Use		Egress Use		Access Use		Egress Use	
	Coef.	STD	Coef.	STD	Coef.	STD	Coef.	STD	Coef.	STD	Coef.	STD	Coef.	STD	Coef.	STD
Bus station density	1185.449	2055.211	3685.24	3372.854	66.723	323.765	656.743	747.152	1627.278	1202.139	3082.21	2256.294	1245.158	2238.761	2517.585	2608.344
Road density	−97.193	410.61	−164.072	356.125	−18.75	59.992	−20.652	60.104	−37.116	245.8	−92.785	174.28	−88.559	290.501	−132.777	270.019
Residential POI	−77,841.265	98,140.21	−89,973.2	87,148.24	−12,075.8	12,330.54	−12,838.6	13,940.08	−45,680.2	48,104.53	−60,888.1	33,147.16	−56,154.7	66,417.36	−66,982.2	65,327.95
Commercial POI	−8.816	2.714	−8.981	3.196	−1.374	0.378	−1.463	0.537	−5.197	1.814	−5.013	1.988	−6.109	1.916	−6.312	2.491
Public facility POI	1.894	0.348	1.923	0.308	0.24	0.038	0.293	0.041	1.157	0.124	1.188	0.185	1.292	0.233	1.363	0.236
Recreation POI	0.601	2.243	0.838	2.404	0.162	0.304	0.111	0.338	0.426	0.972	0.303	1.486	0.452	1.626	0.492	1.894
Transportation POI	−6.014	6.113	−6.555	6.415	−1.326	0.811	−0.772	1.043	−4.209	3.711	−3.324	4.071	−4.146	3.961	−3.991	5.213
Office POI	2.192	1.661	2.534	1.665	0.295	0.228	0.369	0.247	1.594	0.756	1.927	0.892	1.487	1.122	1.718	1.281
Entropy	0.166	0.424	0.037	0.434	0.042	0.053	−0.007	0.079	−0.084	0.218	−0.107	0.201	0.122	0.328	0.068	0.317

Overall, bus station density consistently exhibits a positive impact on BS-PT integrated uses across all weather groups (A, B, C, and D), supporting the existing literature that highlights the importance of transit infrastructure density in promoting public transport usage [9,10]. Conversely, road density and commercial POIs show a generally negative impact on BS-PT integration, which contrasts with Zhou et al. (2023) [9], who found that commercial POIs were not significant, and road density had a positive correlation. On the other hand, the impact of other variables such as residential POIs and public facility POIs varies across different weather groups. For instance, residential POIs have a significant negative impact in Group A but show a less pronounced effect in other groups. Similarly, public facility POIs demonstrate a positive impact in Groups A and C but are less significant in Groups B and D. These variations suggest that the influence of built environment factors on public transport usage is context-dependent, varying with weather conditions and possibly reflecting differences in user behavior and mobility patterns under different environmental settings. This nuanced understanding underscores the need for tailored transportation planning and policy interventions that consider specific local and temporal conditions.

4.3.2. Spatial Heterogeneity of Influencing Factors

The impact of variables on the spatial distribution of BS-PT integrated access uses and egress uses is generally similar, both with a distinct east–west difference. The eastern

part of Shenzhen, including Longgang and Luohu districts, is primarily residential and industrial, while the western part, comprising Bao'an, Nanshan, and Guangming districts, is more commercial and technology-focused. Further analysis of the spatial variation in each influencing factor shows that the spatial heterogeneity of commercial, recreation, entropy, transportation, office, and residential POIs is similar. These variables exhibit a positive correlation at metro stations in the eastern parts of the city, specifically in Longgang and Luohu districts, and a negative correlation in the western parts of the city, including Bao'an, Nanshan, and Guangming districts. On the other hand, bus station, public facility, and road density POIs show a positive correlation in the eastern parts of the city and a negative correlation in the western parts.

This spatial heterogeneity distribution can be explained by Shenzhen's land-use planning and urban development policies: the western region emphasizes efficient economic activities and dense land use, while the eastern region prioritizes ecological preservation and low-density residential environments [59]. The western part of Shenzhen (e.g., Nanshan District) is characterized by the concentration of high-tech industries and highly commercialized development. These areas have a high density of commercial POIs, office POIs, and transportation POIs, along with higher densities of bus stations and roads. Consequently, these variables have a more significant impact on the number of trips at metro stations in these areas. Additionally, the high population density and diversified land use (including high-rise residential and commercial buildings) make the travel patterns in these regions more responsive to economic and social activities [59,60]. In contrast, the eastern part of Shenzhen (e.g., Longgang District and Dapeng District) focuses on ecological preservation and low-density development. Although these areas have more residential POIs and public facility POIs, they have relatively fewer transportation facilities, lower road density, and fewer bus stations. Consequently, the public transport infrastructure is less developed, which reduces the overall impact of variables like bus station density and road density on metro station usage. The reliance on private transportation in these regions further diminishes the influence of these variables on travel patterns. In addition, apart from entropy and office POIs showing a strong positive correlation in Futian District, the influence of other variables is insignificant in this area. This may be due to the high density of metro stations, high intensity of land development, and high level of land-use mix represented by Futian District as the city center [61]. The overall travel system is much more developed than that in the outskirts of the city [62], reducing the opportunities for people to choose BS-PT integration uses.

With changes in weather, the spatial heterogeneity of these influencing factors also varies (Figures 9–12). These changes are mainly manifested as follows: (1) The degree of correlation for certain influencing factors differs. For example, the positive correlation of commercial POIs under weather conditions A, C, and D is significantly stronger than under condition B. This may be because continuous extreme high-temperature weather discourages unnecessary commercial and recreational trips. (2) The nature of the correlation for certain influencing factors changes. For instance, under condition B, transportation POIs are negatively correlated with the number of integrated trips in the access mode in the northwest of Bao'an District and the north of Guangming District. However, under the same weather condition for the egress mode and under the other three weather conditions, the correlation is positive. This can be attributed to the fact that the northwest of Bao'an District is primarily composed of industrial parks and logistics bases where work locations are concentrated and far from transportation nodes. The north of Guangming District is dominated by high-tech parks and emerging industries, with many enterprises and research institutions, and offices are dispersed yet relatively concentrated in specific areas. During extreme high-temperature weather, workers in factories and logistics bases prefer to commute directly from home to work, reducing the time spent using shared bikes under high temperatures. For these users, choosing the egress mode often occurs during the evening peak after work, when the temperature and UV intensity are lower than during

the day, making it more comfortable. Therefore, employees may be more inclined to use shared bikes to travel from their workplace to the metro station.

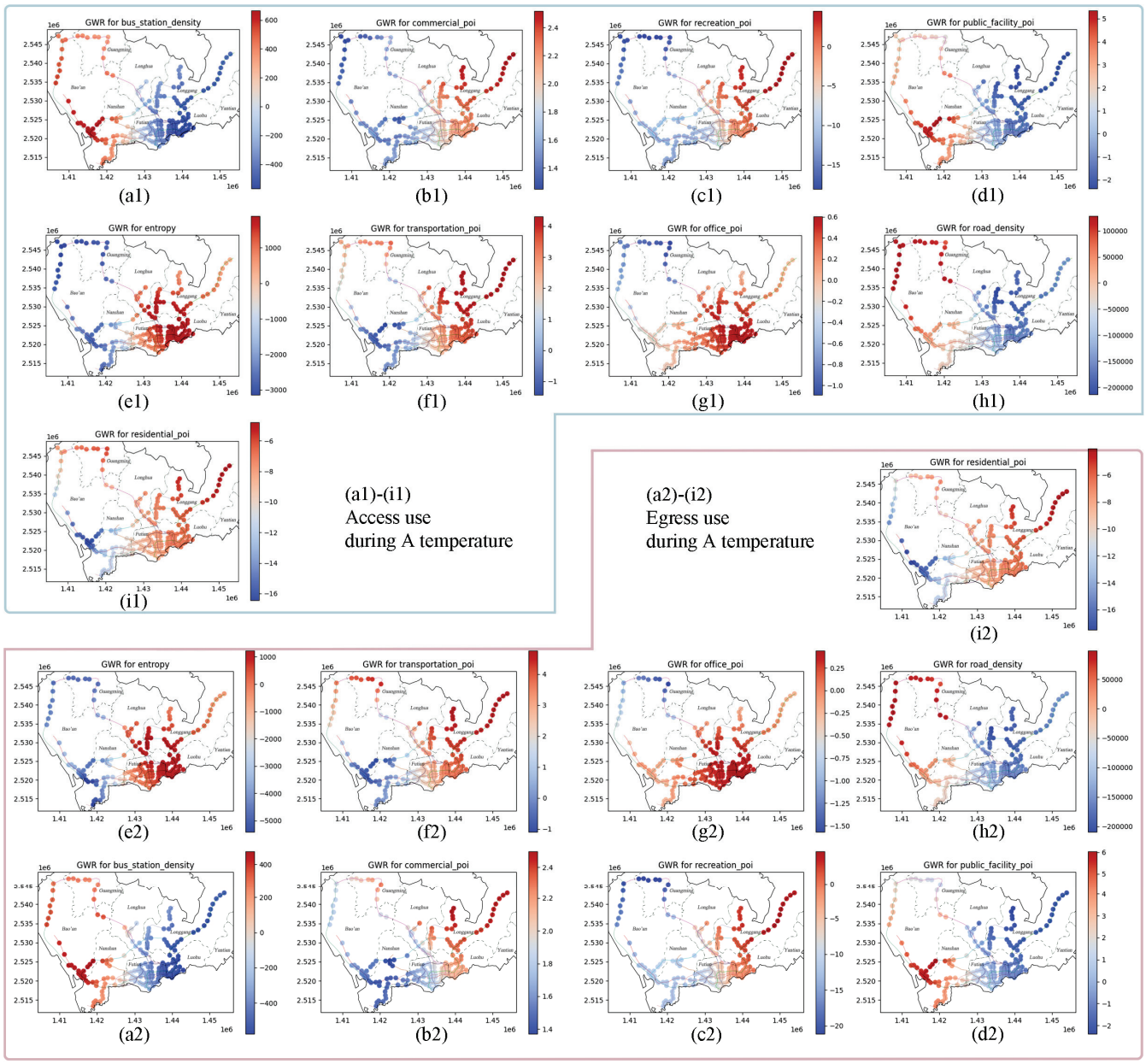

Figure 9. Impact of variables on the spatial distribution of integrated uses under ideal temperature. (**a1**–**i1**): Impact of bus station density, commercial POIs, recreation POIs, public facility POIs, entropy, transportation POIs, office POIs, road density, and residential POIs on access-integrated uses under ideal temperature conditions. (**a2**–**i2**): Impact of bus station density, commercial POIs, recreation POIs, public facility POIs, entropy, transportation POIs, office POIs, road density, and residential POIs on egress-integrated uses under ideal temperature conditions.

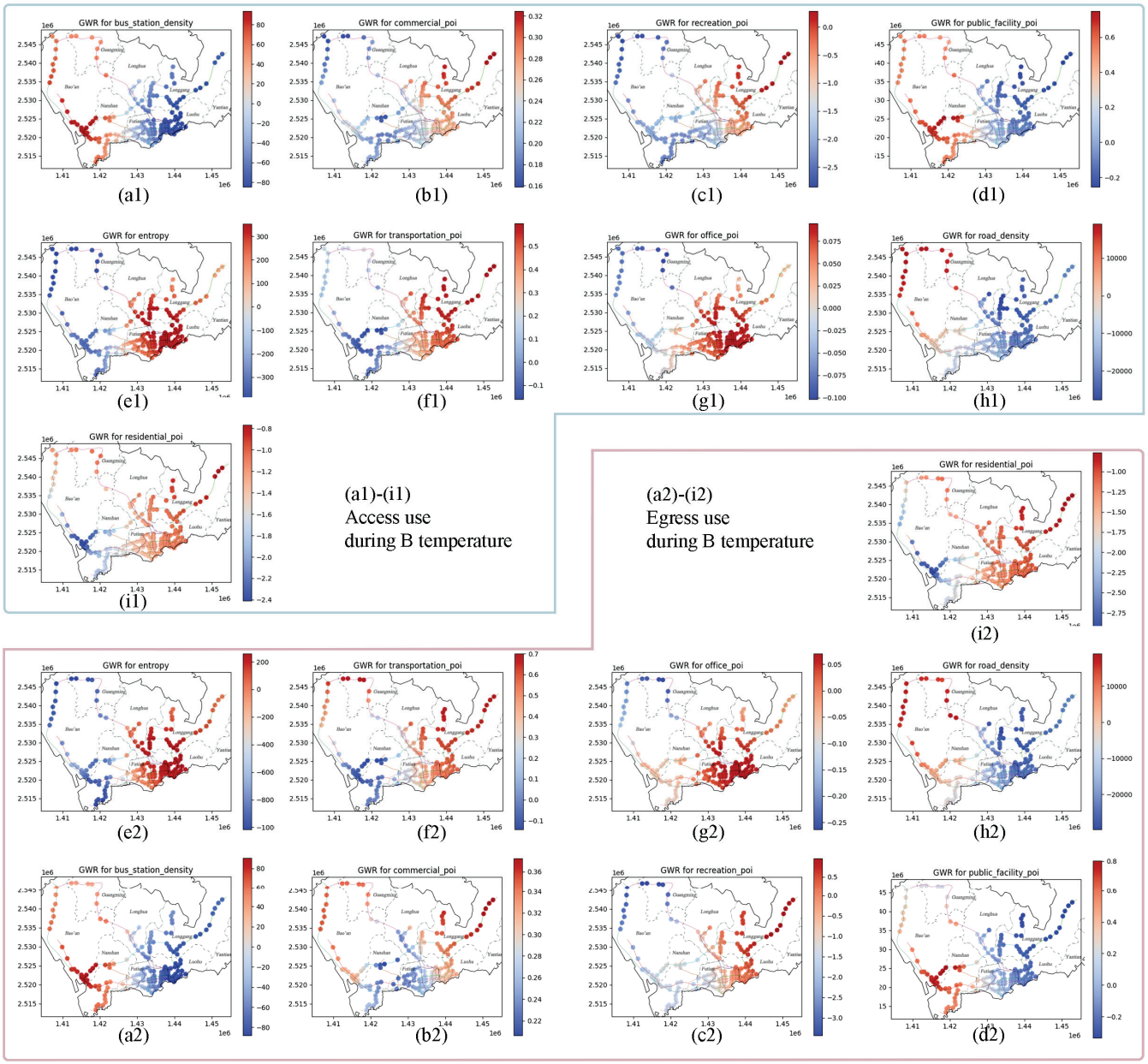

Figure 10. Impact of variables on the spatial distribution of integrated uses under continuous extreme heats in summer. (**a1**–**i1**): Impact of bus station density, commercial POIs, recreation POIs, public facility POIs, entropy, transportation POIs, office POIs, road density, and residential POIs on access-integrated uses under continuous extreme heats in summer. (**a2**–**i2**): Impact of bus station density, commercial POIs, recreation POIs, public facility POIs, entropy, transportation POIs, office POIs, road density, and residential POIs on egress-integrated uses under continuous extreme heats in summer.

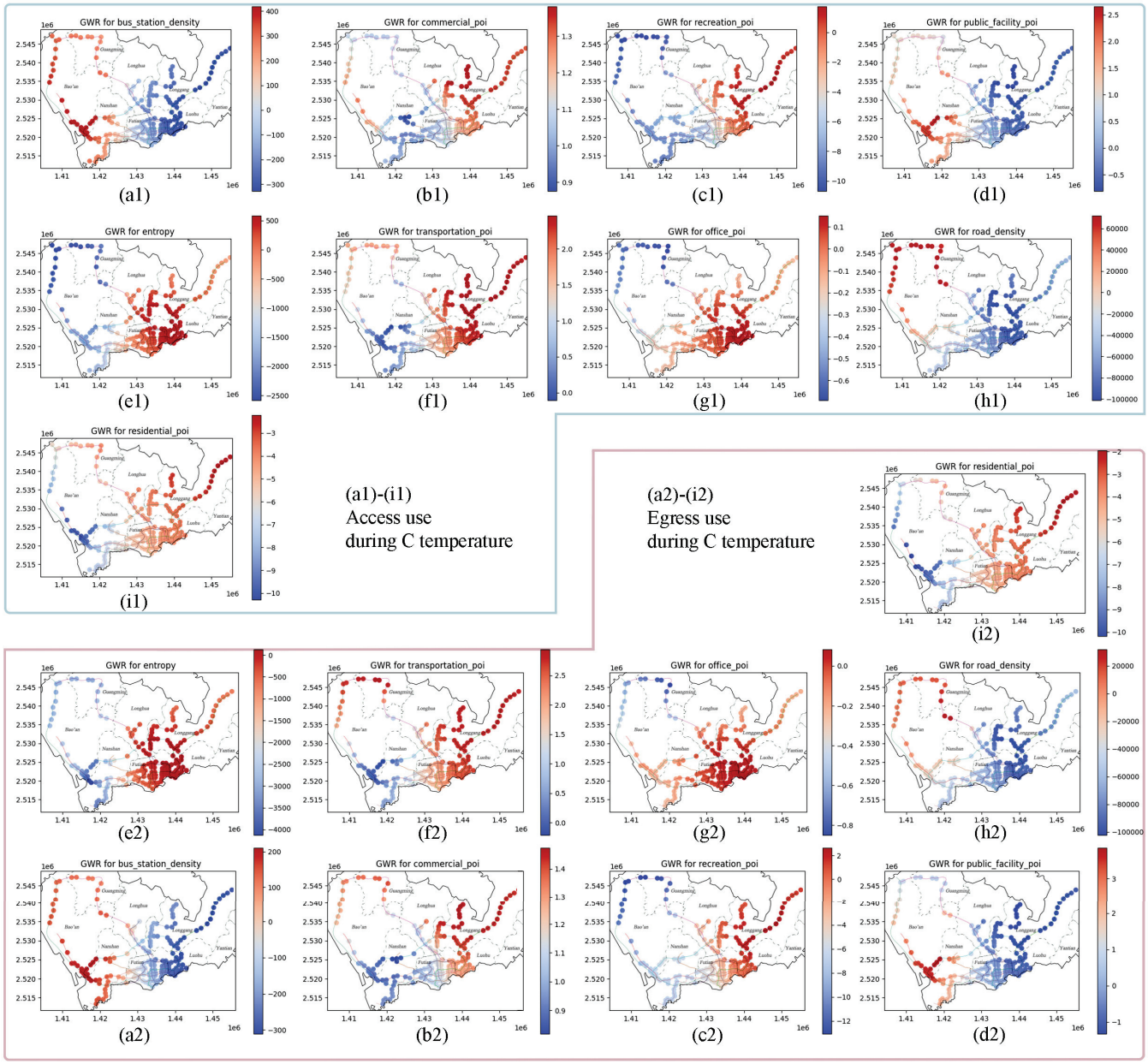

Figure 11. Impact of variables on the spatial distribution of integrated uses under single extreme heats in summer. (**a1–i1**): Impact of bus station density, commercial POIs, recreation POIs, public facility POIs, entropy, transportation POIs, office POIs, road density, and residential POIs on access-integrated uses under single extreme heats in summer. (**a2–i2**): Impact of bus station density, commercial POIs, recreation POIs, public facility POIs, entropy, transportation POIs, office POIs, road density, and residential POIs on egress-integrated uses under single extreme heats in summer.

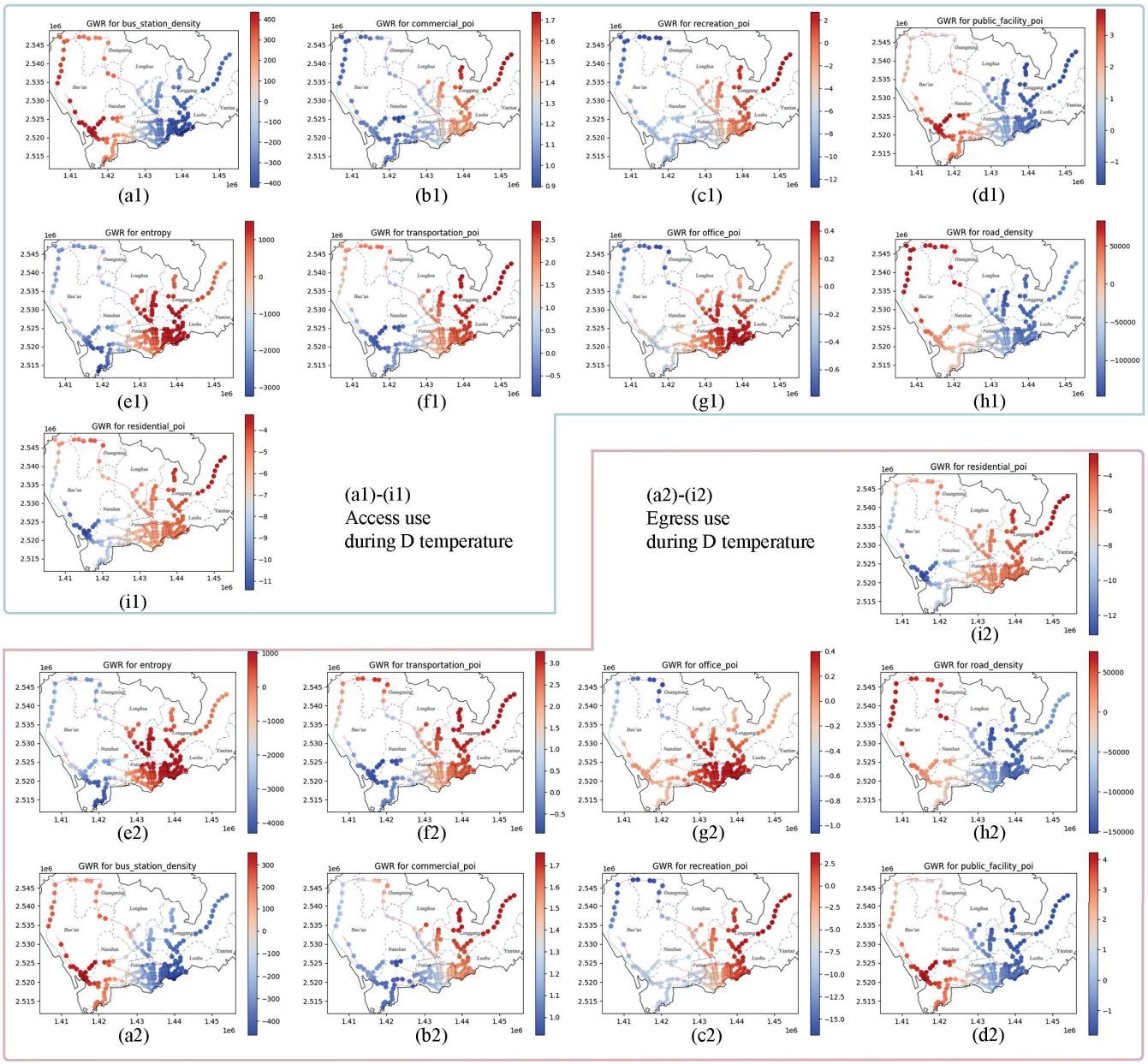

Figure 12. Impact of variables on the spatial distribution of integrated uses under extreme heat in non-summer. (**a1–i1**): Impact of bus station density, commercial POIs, recreation POIs, public facility POIs, entropy, transportation POIs, office POIs, road density, and residential POIs on access-integrated uses under extreme heat in non-summer. (**a2–i2**): Impact of bus station density, commercial POIs, recreation POIs, public facility POIs, entropy, transportation POIs, office POIs, road density, and residential POIs on egress-integrated uses under extreme heat in non-summer.

5. Conclusions

Recent extreme heat worldwide has increasingly challenged the resilience and sustainability of urban transportation systems, highlighting the urgent need for adaptive strategies to maintain sustainable mobility. This study aims to address these challenges by investigating how extreme heats influence the integration of bike-sharing (BS) and public transportation (PT), with a specific focus on Shenzhen. By defining several heat scenarios and applying geographically weighted regression (GWR) methods, we quantified the response of urban BS-PT integration usage under extreme heats, examining spatiotemporal dynamics and identifying factors contributing to this integration.

The study revealed several significant findings. Firstly, extreme heats significantly influence BS-PT integration, with users showing a greater willingness to shift towards more integrated uses under extreme heats outside of summer, compared to solely using bike-sharing to avoid outdoor exposure. This shift underscores the substitution and complementary relationship between BS and PT under extreme heats. The temporal analysis showed that BS-PT integrated trips peak under extreme heats outside of summer, likely due to the protective nature of PT against direct heat exposure. Conversely, continuous extreme heats negatively impact integrated trips, highlighting the sensitivity of multimodal travel to sustained high temperatures.

Methodologically, this study advances the application of GWR in transportation research, offering a nuanced analysis of how built environment factors influence BS-PT integration across different weather conditions. By employing GWR, we captured the spatial variability and context-dependent impacts of variables such as bus station density, road density, and commercial points of interest (POIs). This approach allows for more precise and localized policy recommendations, demonstrating the value of spatially disaggregated analysis in understanding and planning for urban transportation resilience.

Practically, the findings of this study have significant implications for urban transportation planning and policy. Identifying high-density areas like the CBDs of Futian, Luohu, and Nanshan as key hubs for BS-PT integration underscores the need for targeted infrastructure investments in these regions. Additionally, this research can guide bike-sharing operators and government agencies in optimizing resource allocation and management during heatwaves. By understanding BS-PT integration dynamics, operators can better distribute bikes and schedule maintenance, ensuring availability in high-demand areas. Targeted infrastructure improvements in regions with high demand but low resilience to heat can enhance user experience and encourage continued bike-sharing use, supporting broader public health and environmental sustainability goals by promoting active transportation.

Future research can build on this study by improving the precision of identifying integration behaviors. First, due to data limitations, our definition of integration was relatively coarse. Future research could utilize more detailed data and advanced methods to improve the accuracy of identifying integration behaviors. Second, extreme weather conditions include more than just high temperatures. This study excluded all rainy weather, yet precipitation significantly impacts cycling behavior. Considering the increasing frequency of heavy rainfall and flooding in recent years, future studies should also examine the effects of precipitation on cycling.

Author Contributions: Conceptualization, Xin Wang; methodology, Xin Wang and Jiangyue Wu; software, Xin Wang; validation, Xin Wang, Rui Xue, and Ming Lu; formal analysis, Xin Wang; investigation, Xin Wang; resources, Xin Wang; data curation, Xin Wang and Rui Xue; writing—original draft preparation, Xin Wang; writing—review and editing, Xin Wang, Ming Lu, and Jiangyue Wu; visualization, Xin Wang and Rui Xue; supervision, Ming Lu and Jiangyue Wu; project administration, Xin Wang. All authors have read and agreed to the published version of the manuscript.

Funding: This research received no external funding.

Data Availability Statement: The data supporting the reported results in this study are openly available. Detailed information can be found in Section 3.2 "Data Resources". The data categories and their sources are as follows: bike-sharing data—Shenzhen Municipal Government's open data platform, available at https://opendata.sz.gov.cn/; points of interest (POIs)—application programming interface (API) of Amap, available at https://lbs.amap.com/; metro stations—application programming interface (API) of Amap, available at https://lbs.amap.com/; weather records—2345 Historical Data from the 2345 Weather website and the NCDC National Weather Data Centre, available at https://tianqi.2345.com/ and https://www.ncei.noaa.gov/cdo-web/; road networks—OpenStreetMap, available at https://www.openstreetmap.org.

Acknowledgments: We would like to express our heartfelt gratitude to our supervisors for their invaluable guidance and continuous support throughout this research. We also appreciate the helpful feedback and assistance from our colleagues and peers, whose contributions have significantly enhanced the quality of this work.

Conflicts of Interest: The authors declare no conflicts of interest.

References

1. Fishman, E. Bikeshare: A review of recent literature. *Transp. Rev.* **2015**, *35*, 92–113. [CrossRef]
2. Martens, K. Promoting bike-and-ride: The Dutch experience. *Transp. Res. Part A Policy Pract.* **2007**, *41*, 326–338. [CrossRef]
3. Hou, Z.; Wu, K.; Zhang, H.M. Does bike sharing improve public health? A case study in New York City. *Int. J. Sustain. Transp.* **2022**, *17*, 1207–1216. [CrossRef]
4. Leister, E.H.; Vairo, N.; Sims, D.; Bopp, M. Understanding bike share reach, use, access and function: An exploratory study. *Sustain. Cities Soc.* **2018**, *43*, 191–196. [CrossRef]
5. Zhang, X.; Shen, Y.; Zhao, J. The mobility pattern of dockless bike sharing: A four-month study in Singapore. *Transp. Res. Part D Transp. Environ.* **2021**, *98*, 102961. [CrossRef]
6. Lin, D.; Zhang, Y.; Zhu, R.; Meng, L. The analysis of catchment areas of metro stations using trajectory data generated by dockless shared bikes. *Sustain. Cities Soc.* **2019**, *49*, 101598. [CrossRef]
7. Shaheen, S.A.; Guzman, S.; Zhang, H. Bikesharing in Europe, the Americas, and Asia. *Transp. Res. Rec. J. Transp. Res. Board* **2010**, *2143*, 159–167. [CrossRef]
8. Soriguera, F.; Jiménez-Meroño, E. A continuous approximation model for the optimal design of public bike-sharing systems. *Sustain. Cities Soc.* **2020**, *52*, 101826. [CrossRef]
9. Zhou, X.; Dong, Q.; Huang, Z.; Yin, G.; Zhou, G.; Liu, Y. The spatially varying effects of built environment characteristics on the integrated usage of dockless bike-sharing and public transport. *Sustain. Cities Soc.* **2023**, *89*, 104348. [CrossRef]
10. Guo, Y.; He, S.Y. Built environment effects on the integration of dockless bike-sharing and the metro. *Transp. Res. Part D Transp. Environ.* **2020**, *83*, 102335. [CrossRef]
11. Lin, J.-J.; Wang, N.-L.; Feng, C.-M. Public bike system pricing and usage in Taipei. *Int. J. Sustain. Transp.* **2017**, *11*, 633–641. [CrossRef]
12. Wang, H.; Noland, R.B. Bikeshare and Subway Ridership Changes During the COVID-19 Pandemic in New York City. *Transp. Policy* **2021**, *106*, 262–270. [CrossRef] [PubMed]
13. Nahal, T.; Mitra, R. Facilitators and barriers to winter cycling: Case study of a downtown university in Toronto, Canada. *J. Transp. Health* **2018**, *10*, 262–271. [CrossRef]
14. Helbich, M.; Böcker, L.; Dijst, M. Geographic heterogeneity in cycling under various weather conditions: Evidence from Greater Rotterdam. *J. Transp. Geogr.* **2014**, *38*, 38–47. [CrossRef]
15. Li, C.; Chen, G.; Wang, S. Urban mobility resilience under extreme heats: Evidence from bike-sharing travel in New York. *Travel Behav. Soc.* **2024**, *37*, 100821. [CrossRef]
16. Pucher, J.; Buehler, R.; Bassett, D.R.; Dannenberg, A.L. Walking and Cycling to Health: A Comparative Analysis of City, State, and International Data. *Am. J. Public Health* **2010**, *100*, 1986–1992. [CrossRef]
17. Shi, Y.; Ren, C.; Luo, M.; Ching, J.; Li, X.; Bilal, M.; Fang, X.; Ren, Z. Utilizing world urban database and access portal tools (WUDAPT) and machine learning to facilitate spatial estimation of heatwave patterns. *Urban Clim.* **2021**, *36*, 100797. [CrossRef]
18. Zhou, Y.; Zhao, M.; Lam, W.H.; Chen, A.; Sze, N.; Tang, S.; Chen, Y.; Zhang, T. Modeling the impact of dock-less bike-sharing system on outpatient trips. *Sustain. Cities Soc.* **2021**, *69*, 102853. [CrossRef]
19. Zhang, L.; Zhang, J.; Duan, Z.; Bryde, D. Sustainable bike-sharing systems: Characteristics and commonalities across cases in urban China. *J. Clean. Prod.* **2015**, *97*, 124–133. [CrossRef]
20. Ritchie, H.; Roser, M. Urbanization. 2018. Available online: https://ourworldindata.org/urbanization (accessed on 15 May 2024).
21. World Bank. Urban Development Overview. 2020. Available online: https://www.worldbank.org/en/topic/urbandevelopment/overview (accessed on 1 May 2024).
22. SGuo, Y.; Yang, L.; Lu, Y.; Zhao, R. Dockless bike-sharing as a feeder mode of metro commute? The role of the feeder-related built environment: Analytical framework and empirical evidence. *Sustain. Cities Soc.* **2021**, *65*, 102594. [CrossRef]
23. Cao, Y.; Shen, D. Contribution of shared bikes to carbon dioxide emission reduction and the economy in Beijing. *Sustain. Cities Soc.* **2019**, *51*, 101749. [CrossRef]
24. Chandra, S.; Quadrifoglio, L. A model for estimating the optimal cycle length of demand responsive feeder transit services. *Transp. Res. Part B Methodol.* **2013**, *51*, 1–16. [CrossRef]
25. Meng, M.; Rau, A.; Mahardhika, H. Public transport travel time perception: Effects of socioeconomic characteristics, trip characteristics and facility usage. *Transp. Res. Part A Policy Pract.* **2018**, *114*, 24–37. [CrossRef]
26. An, R.; Zahnow, R.; Pojani, D.; Corcoran, J. Weather and cycling in New York: The case of Citibike. *J. Transp. Geogr.* **2019**, *77*, 97–112. [CrossRef]
27. Lee, J.; Choi, K.; Leem, Y. Bicycle-based transit-oriented development as an alternative to overcome the criticisms of the conventional transit-oriented development. *Int. J. Sustain. Transp.* **2015**, *9*, 92–101. [CrossRef]

28. Saberi, M.; Ghamami, M.; Gu, Y.; Shojaei, M.H.; Fishman, E. Understanding the impacts of a public transit disruption on bicycle sharing mobility patterns: A case of Tube strike in London. *J. Transp. Geogr.* **2018**, *66*, 154–166. [CrossRef]
29. Mahajan, S.; Argota Sánchez-Vaquerizo, J. Global comparison of urban bike-sharing accessibility across 40 cities. *Sci. Rep.* **2024**, *14*, 20493. [CrossRef]
30. Fu, C.; Huang, Z.; Scheuer, B.; Lin, J.; Zhang, Y. Integration of dockless bike-sharing and metro: Prediction and explanation at origin-destination level. *Sustain. Cities Soc.* **2023**, *99*, 104906. [CrossRef]
31. Zhao, P.; Li, S. Bicycle-metro integration in a growing city: The determinants of cycling as a transfer mode in metro station areas in Beijing. *Transp. Res. Part A Policy Pract.* **2017**, *99*, 46–60. [CrossRef]
32. Kosmidis, I.; Müller-Eie, D. The synergy of bicycles and public transport: A systematic literature review. *Transp. Rev.* **2023**, *44*, 34–68. [CrossRef]
33. El-Assi, W.; Mahmoud, M.S.; Habib, K.N. Effects of built environment and weather on bike sharing demand: A station level analysis of commercial bike sharing in Toronto. *Transportation* **2017**, *44*, 589–613. [CrossRef]
34. Zi, W.; Xiong, W.; Chen, H.; Chen, L. TAGCN: Station-level demand prediction for bike-sharing system via a temporal attention graph convolution network. *Inf. Sci.* **2021**, *561*, 274–285. [CrossRef]
35. Ashqar, H.I.; Elhenawy, M.; Rakha, H.A. Modeling bike counts in a bike-sharing system considering the effect of weather conditions. *Case Stud. Transp. Policy* **2019**, *7*, 261–268. [CrossRef]
36. Brandenburg, C.; Matzarakis, A.; Arnberger, A. Weather and cycling—A first approach to the effects of weather conditions on cycling. *Meteorol. Appl.* **2007**, *14*, 61–67. [CrossRef]
37. Nankervis, M. The effect of weather and climate on bicycle commuting. *Transp. Res. Part A Policy Pract.* **1999**, *33*, 417–431. [CrossRef]
38. Jay, O.; Capon, A.; Berry, P.; Broderick, C.; de Dear, R.; Havenith, G.; Honda, Y.; Kovats, R.S.; Ma, W.; Malik, A.; et al. Reducing the health effects of hot weather and extreme heats: From personal cooling strategies to green cities. *Lancet* **2021**, *398*, 709–724. [CrossRef]
39. Georgescu, M.; Broadbent, A.M.; Krayenhoff, E.S. Quantifying the decrease in heat exposure through adaptation and mitigation in twenty-first-century US cities. *Nat. Cities* **2024**, *1*, 42–50. [CrossRef]
40. Wang, B.; Zhang, F.; Liu, J.; Tan, Z. The impacts of extreme hot weather on metro ridership: A case study of Shenzhen, China. *J. Transp. Geogr.* **2024**, *117*, 103899. [CrossRef]
41. Cheng, L. Exploring non-linear built environment effects on the integration of free-floating bike-share and urban rail transport: A quantile regression approach. *Transp. Res. Part A* **2022**, *162*, 175–187. [CrossRef]
42. Wu, X.; Lu, Y.; Lin, Y.; Yang, Y. Measuring the Destination Accessibility of Cycling Transfer Trips in Metro Station Areas: A Big Data Approach. *Int. J. Environ. Res. Public Health* **2019**, *16*, 2641. [CrossRef]
43. Saltykova, K.; Ma, X.; Yao, L.; Kong, H. Environmental impact assessment of bike-sharing considering the modal shift from public transit. *Transp. Res. Part D Transp. Environ.* **2022**, *105*, 103238. [CrossRef]
44. Yan, Y.; Chen, Q. Spatial heterogeneity and nonlinearity study of bike-sharing to subway connections from the perspective of built environment. *Sustain. Cities Soc.* **2024**, *105*, 105766. [CrossRef]
45. US Department of Commerce; National Oceanic and Atmospheric Administration; National Weather Service. What is the Heat Index? 1978. Available online: https://www.weather.gov/ama/heatindex (accessed on 5 June 2024).
46. Heinen, E.; van Wee, B.; Maat, K. Commuting by Bicycle: An Overview of the Literature. *Transp. Rev.* **2010**, *30*, 59–96. [CrossRef]
47. de Chardon, C.M.; Caruso, G.; Thomas, I. Bicycle sharing system "success" determinants. *Transp. Res. Part A Policy Pract.* **2017**, *100*, 202–214. [CrossRef]
48. Ahmed, F.; Rose, G.; Jacob, C. Impact of weather on commuter cyclist behaviour and implications for climate change adaptation. *Transp. Res. Forum* **2010**, *33*, 1–19.
49. Fotheringham, A.S.; Brunsdon, C.; Charlton, M. *Geographically Weighted Regression: The Analysis of Spatially Varying Relationships*; John Wiley & Sons: Hoboken, NJ, USA, 2002.
50. Anselin, L. *Spatial Econometrics: Methods and Models*; Springer: Berlin/Heidelberg, Germany, 1988.
51. Moran, P.A.P. Notes on Continuous Stochastic Phenomena. *Biometrika* **1950**, *37*, 17–23. [CrossRef]
52. Chen, S.K.; Wei, W.; Mao, B.H.; Guan, W. Analysis on urban traffic status based on improved spatio-temporal Moran's I. *Acta Phys. Sin.* **2013**, *62*, 148901. [CrossRef]
53. Zhang, C.; Lv, W.; Zhang, P.; Song, J. Multidimensional spatial autocorrelation analysis and its application based on improved Moran's I. *Earth Sci. Inform.* **2023**, *16*, 3355–3368. [CrossRef]
54. Li, H.; Calder, C.A.; Cressie, N. Beyond Moran's I: Testing for spatial dependence based on the spatial autoregressive model. *Geogr. Anal.* **2013**, *45*, 274–291. [CrossRef]
55. Shenzhen Urban Transportation Planning and Design Institute. Shenzhen Bicycle Sharing Development Evaluation Report. 2019. Available online: https://dcutp.com/index.php?s=/News/show/id/432.html (accessed on 5 May 2024).
56. Corcoran, J.; Li, T.; Rohde, D.; Charles-Edwards, E.; Mateo-Babiano, D. Spatio-temporal patterns of a Public Bicycle Sharing Program: The effect of weather and calendar events. *J. Transp. Geogr.* **2014**, *41*, 292–305. [CrossRef]
57. Gebhart, K.; Noland, R.B. The impact of weather conditions on bikeshare trips in Washington, DC. *Transportation* **2014**, *41*, 1205–1225. [CrossRef]

58. Lewin, A. Temporal and Weather Impacts on Bicycle Volumes. In Proceedings of the Transportation Research Board 90th Annual Meeting Transportation Research Board, Washington, DC, USA, 23–27 January 2011.
59. Cheng, J.; Chen, M.; Tang, S. Shenzhen—A typical benchmark of Chinese rapid urbanization miracle. *Cities* **2023**, *140*, 104421. [CrossRef]
60. Song, X.; Feng, Q.; Xia, F.; Li, X.; Scheffran, J. Impacts of changing urban land-use structure on sustainable city growth in China: A population-density dynamics perspective. *Habitat Int.* **2021**, *107*, 102296. [CrossRef]
61. Quattrone, G.; Chen, L. Shenzhen—How to further implement the sustainability and resilience towards 2030? *Cities* **2023**, *136*, 104263. [CrossRef]
62. Dou, P.; Chen, Y. Dynamic monitoring of land-use/land-cover change and urban expansion in Shenzhen using Landsat imagery from 1988 to 2015. *Int. J. Remote Sens.* **2017**, *38*, 5388–5407. [CrossRef]

Disclaimer/Publisher's Note: The statements, opinions and data contained in all publications are solely those of the individual author(s) and contributor(s) and not of MDPI and/or the editor(s). MDPI and/or the editor(s) disclaim responsibility for any injury to people or property resulting from any ideas, methods, instructions or products referred to in the content.

forests

MDPI

Article

Investigation of Climatic Factors Affecting the Amount of Foraged Matsutake Mushrooms in Korea

Doo-Ho Choi [1], Cheol-Soon Ko [2], Youn-Lee Oh [1], Ji-Hoon Im [1], Minji Oh [1] and Eun-Ji Lee [1,*]

[1] Mushroom Research Division, National Institute of Horticultural and Herbal Science, RDA, Eumseong 27709, Chungbuk, Republic of Korea; gamchoduho@korea.kr (D.-H.C.)
[2] Yangyang-gun Agriculture Technology Center, Geumsan-gun 32708, Chungcheongnam-do, Republic of Korea
* Correspondence: ejg1105@korea.kr

Abstract: *Tricholoma matsutake* is a valuable edible mushroom in Eastern Asia. Due to the challenges of artificial cultivation, *T. matsutake* cultivation has relied on foraging from pine forests. Changes in global climate variables, such as temperature and precipitation, could affect the amount of foraged *T. matsutake*. In this study, we investigated the correlation between the amount of foraged *T. matsutake* and climatic factors (average monthly temperature and precipitation) in Yangyang-gun using the augmented Dickey–Fuller test and the ordinary least squares method. Among the assessed correlations between the foraged *T. matsutake* and different climatic factors, the average temperature in August was significantly correlated with the amount of foraged *T. matsutake*, increasing by 1.5 tons when the temperature in August increased by 1 unit. Overall, this study identified a potentially strong positive correlation between the average temperature in August and amount of foraged *T. matsutak*e.

Keywords: *Tricholoma matsutake*; Yangyang-gun; temperature; precipitation; correlation coefficient

1. Introduction

Tricholoma matsutake, also known as matsutake mushroom, derives its name from two Japanese words: "matsu", meaning pine, and "take", meaning mushroom. *T. matsutake* has historically been a valuable and economically important food in Korea, Japan, and China. Due to its unique aroma, derived from the compound matsutakeol, *T. matsutake* is a commonly used food additive in soups and main dishes to enhance the overall aroma. It is also utilized as a medicinal fungus to prevent and treat several disorders, including diabetes and cardiovascular diseases [1–4].

Like other ectomycorrhizal fungi, matsutake mushrooms form symbiotic relationships with the root system of their hosts, contributing to the nutrient cycle of the forest ecosystem. *T. matsutake* establishes a symbiotic structure with its host, the pine tree, facilitating a nutrient exchange through interactions between the mushroom's hyphal system and the fine root hairs of the pine tree [5,6]. This relationship often leads to the development of specific formations known as fairy rings. They are discovered near pine trees and develop in gravel and weakly acidic soils with low nutrients and high amounts of sand that offer good drainage [7,8]. During summer, stormwater results in the formation of this gravel and sand mixture, while the pines in these forests exhibit tolerance to a broad spectrum of stress conditions [7–9]. In Korea, *T. matsutake* grows in Korean forests where red pine is the dominant species, characterized by slightly acidic and well-drained soils shaped by the climate of the Korean Peninsula [9,10].

Both soil and climatic conditions play important roles in the growth of *T. matsutake* in pine forests. The matsutake mushroom undergoes different developmental phases throughout its life cycle: the initiation and growth of the mycelium from March to June and the development of the fruiting body from late August to early October [11]. However, global climate change in the 21st century has significantly affected climatic factors

such as temperature and precipitation, potentially affecting the growth of *T. matsutake* in Korea [12–14]. A previous study identified a quantitative relationship between climatic factors and *T. matsutake* habitat suitability [15]. The study revealed that temperature and precipitation could potentially influence the development of matsutake mushrooms. Despite this evidence, few studies have demonstrated a significant relationship between the amount of foraged matsutake mushroom and climatic factors. Since foraged mushroom growth and productivity depend on climatic factors, analyzing the correlation between the amount of foraged *T. matsutake* and climatic factors is essential. In this study, we investigated the correlation between the amount of foraged *T. matsutake*, temperature, and precipitation in Yangyang-gun, Korea, from 2003 to 2023.

2. Materials and Methods

2.1. Conceptual Frameworks

Edible mushrooms, including *Tricholoma matsutake*, predominantly inhabit forested areas [16,17]. Previous studies have confirmed that changes in temperature and precipitation affect not only the vigor of woody and herbaceous plants in forests but also species composition and the herbaceous layer. These climatic changes may decrease mushroom mycelial activity and psychrophilic fungi while increasing the growth and abundance of thermophilic and xerophilic fungi. Such climatic factors may also result in a decrease in the development of mushroom fruiting bodies. Consequently, they may lead to a decrease in mushroom foraging [18–21].

Yangyang-gun is one of the most important provinces for *T. matsutake* foraging in Gangwon-do, Korea [11]. To assess the temporal variation in the amount of foraged matsutake mushrooms, data on the amount of *T. matsutake* foraged in Yangyang-gun between 1990 and 2023 were obtained from the National Forestry Cooperative Federation and Yangyang Institute of Technology. Figure 1 illustrates the data regarding the variation in the amount of foraged matsutake mushrooms from 1990 to 2023 [22].

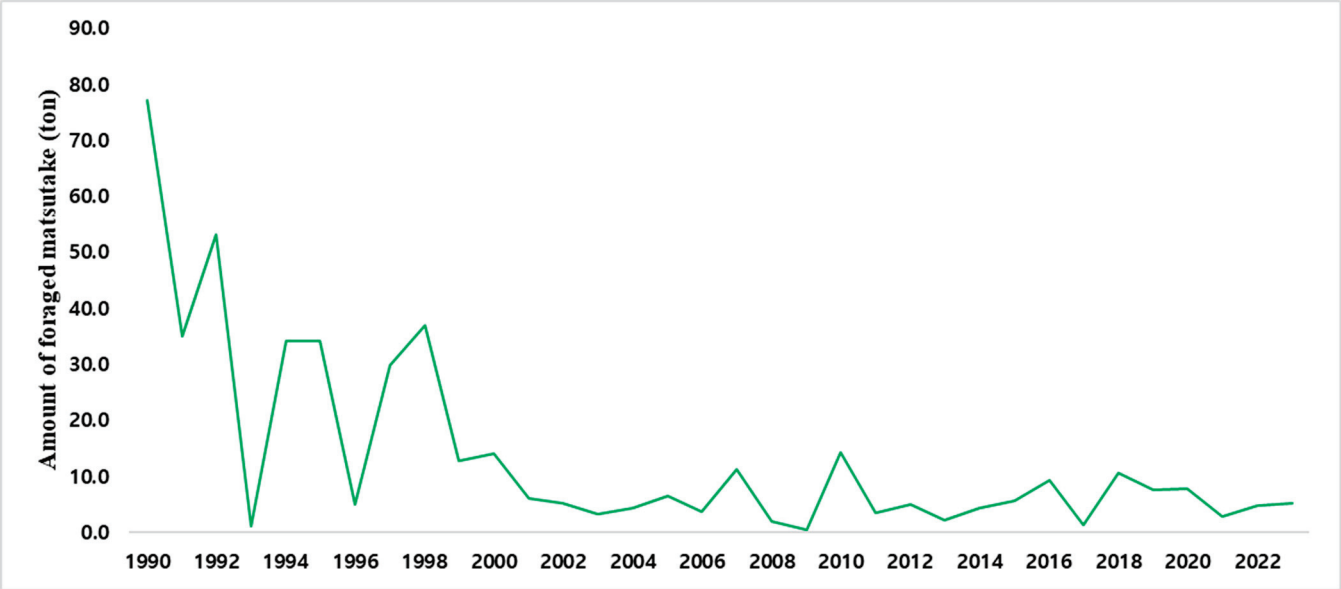

Figure 1. Amount of foraged *Tricholoma matsutake* in pine forests of Yangyang-gun, Korea, between 1990 and 2023.

Figure 1 illustrates a continuous decrease in the amount of foraged *T. matsutake* each year. Similarly to other mushroom species, temperature and precipitation are crucial factors for the growth of *T. matsutake* [15,18], thereby resulting in the continued decline and variability in the amount of foraged *T. matsutake*. In order to confirm the correlation

between matsutake mushrooms and climatic factors more accurately, climatic surveys in Yangyang-gun are necessary.

In the context of global climatic change, several studies also investigated climate change in Gangwon-do [23,24]. From the studies, an increase in temperature and a decreasing trend in precipitation in Gangwon-do have been identified. Similarly to other provinces in Gangwon-do, Yangyang-gun is also expected to undergo an increase in temperature and a decrease in precipitation. These climatic trends are expected to affect pine forest formation and the amount of *T. matsutake* foraged in Yangyang-gun. However, few studies have examined such climatic changes in this region over time. In this study, we investigated changes in the climatic factors of Yangyang-gun over 20 years. The amount of foraged *T. matsutake* (expressed in tons), temperature (expressed in degrees Celsius), and precipitation (expressed in millimeters) in Yangyang-gun are illustrated in Figure 2. Data from 2003 to 2023 are illustrated since the monitoring of the temperature and precipitation in Yangyang-gun began in 2003 [25].

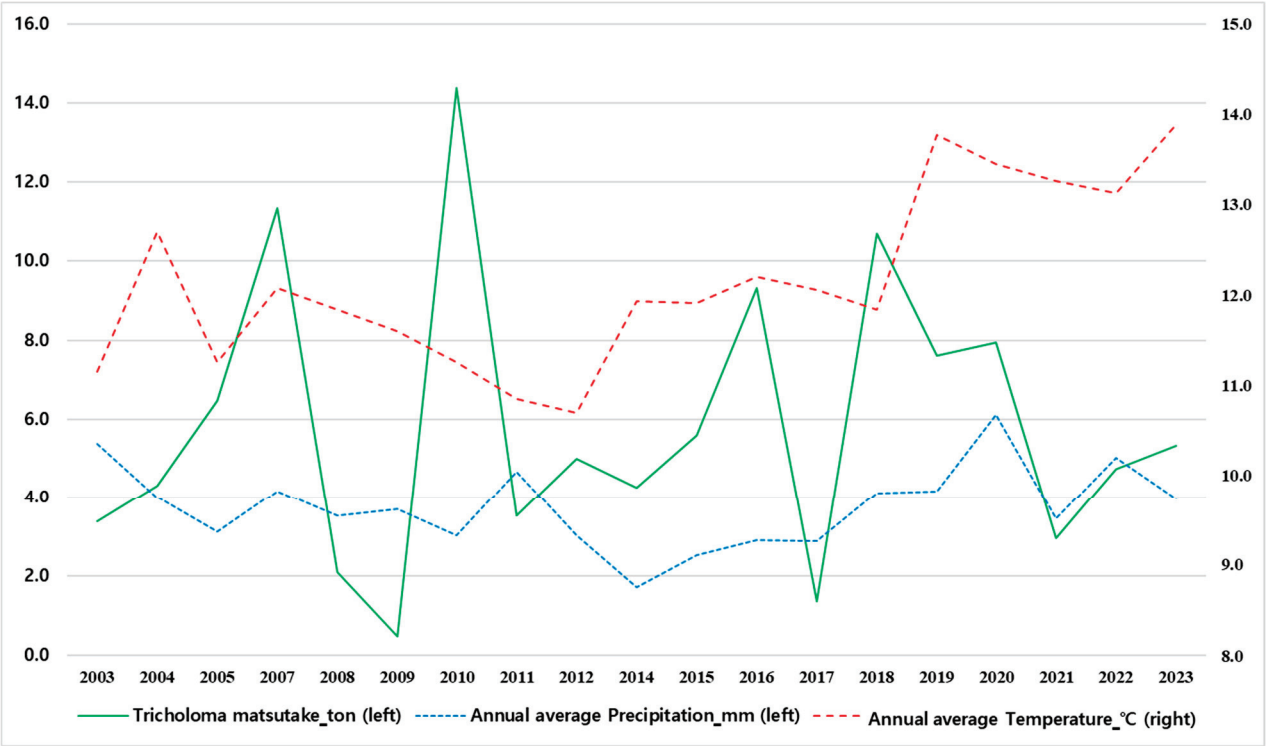

Figure 2. Amount of foraged *Tricholoma matsutake*, annual average temperature, and annual average precipitation in pine forests of Yangyang-gun, Korea, between 2003 and 2023.

Similarly to previous studies on temperature variations in Gangwon-do, Yangyang-gun has exhibited two types of climatic changes: an increase in temperature and a decreasing trend in precipitation. However, as shown in Figure 2, the correlation between the amount of *T. matsutake* foraged and climatic factors remains unclear. To investigate this relationship, a meta-analysis was carried out based on previous studies conducted by Kauserud's team in 2008, Alfranca's team in 2015, and Procházka's team in 2023 [18,19,21]. From these studies, data regarding the amount of foraged *T. matsutake*, temperature, and precipitation were analyzed.

2.2. Data of Foraged T. matsutake, Temperature, and Precipitation

Data on the amount of foraged *T. matsutake*, temperature, and precipitation were collected from publicly available datasets provided by the Institute of Korea. The amount of foraged *T. matsutake* in Yangyang-gun was investigated based on auction quantities

reported by the Korea Forest Service and Forestry Cooperative in Korea, which oversees the reported foraging of matsutake mushrooms [22]. From these data, foraged mushrooms from registered mushroom pickers were identified, and the amount of foraged *T. matsutake* in Yangyang-gun was inferred. The temperature and precipitation data in Yangyang-gun were obtained from reports by the Agricultural Weather Information Service in the Rural Development Administration in Korea [25]. Additional surveys in the mushroom habitats were conducted to ensure the reliability of the information regarding climatic factors. The average annual temperature is reported in degrees Celsius, and the average annual precipitation is reported in millimeters.

2.3. Stationarity Test

A comparison of the time series data was conducted to identify the correlation between the amount of mushrooms and climatic factors. This entails assessing the stationarity of the variables using a unit root test. In this study, we employed the Dickey–Fuller test, which is most commonly used for identifying variable correlations. This test comprises two versions: the simple version and the augmented version [18,19,26].

The simple version includes several types of equations depending on whether there is no trend and intercept (Equation (1)), only a trend (Equation (2)), or an intercept (Equation (3)). Each equation is presented below:

$$\Delta y_t = \beta y_{t-1} + \epsilon_t \quad (1)$$

$$\Delta y_t = \alpha + \beta y_{t-1} + \epsilon_t \quad (2)$$

$$\Delta y_t = \alpha + \delta t + \beta y_{t-1} + \epsilon_t \quad (3)$$

In the equations, Δy_t, α, δ, β, and ϵ_t represent the difference in the y_t, intercept, slope of trend, the coefficient for the unit root test, and the error term, respectively. However, in the simple version of the Dickey–Fuller test, analyzing the correlation between factors for each time period is unfeasible due to the unavailability of a lagged term. Thus, there is a limit to identifying the correlation between the amount of foraged *T. matsutake* and climatic factors.

To analyze the correlation between the amount of foraged *T. matsutake*, temperature, and precipitation in relation to annual variations, the augmented Dickey–Fuller (ADF) test was used, incorporating the trend, conception, and lagged term (Equation (4)). The relevant equation for the ADF test is presented below:

$$\Delta y_t = \alpha + \delta t + \beta y_{t-1} + \sum_{i=1}^{p} \beta_i \Delta y_{t-i} + \epsilon_t \quad (4)$$

In the equation, Δy_{t-i} corresponds to the lagged term, and $\sum_{i=1}^{p} \beta_i \Delta y_{t-i}$ corresponds to the number of lagged terms to control the correlation. In addition, the results of the ADF test were ascertained using the following formula (Equation (5)):

$$tDF = \frac{\hat{I}}{SE\left(\hat{I}\right)} \quad (5)$$

The null hypothesis was set as $I = 0$, indicating a unit root in the time series. For the alternative hypothesis, $I < 0$ suggests stationarity exists.

In summary, the level of stationarity in the correlation between the variables (annual amount of foraged *T. matsutake*, average monthly temperature, and precipitation) was assessed using the ADF test incorporating trend, conception, and lagged terms.

Among the regression methods, linear regression offers an advantage for quantitatively assessing the correlation between the foraged *T. matsutake* and climatic factors. In this study, the ordinary least squares (OLS) method was employed, the most commonly and widely used method. If stationarity is identified in the ADF test, the OLS method can be

used to analyze the correlation between the amount of foraged *T. matsutake* and climatic factors [18,27].

In the theoretical regression function, the amount of foraged mushrooms (in this study, PM) is the dependent variable, and the climatic factors (in this study, average monthly temperature and precipitation) are the independent variables. The following formula (Equation (6)) was used for the regression:

$$y = \beta_0 + \beta_n X_n + \epsilon \quad (6)$$

In the equation, y, X, β_0, β_n, and ϵ correspond to the mean of the dependent variable (foraged *T. matsutake*), independent variable (climatic factors), intercept, slope of trend, and error term, respectively. In OLS, this equation is most commonly employed for determining variable correlation.

To ensure the reliability of the regression model, the sum of squared residuals (SSR, also denoted as Q) was calculated based on the correlation between the variables in Equation (6). The following formula (Equation (7)) was used in the regression:

$$Q = \min_{\beta_0 \beta_1 \beta_2} \sum_{i=1}^{n} (y_i - \beta_0 - \beta_1 X_{1i} - \beta_2 X_{2i}, \ldots, \beta_n X_{ni})^2 \quad (7)$$

Based on the SSR results, the suitability of the OLS model for assessing the correlation between the variables was evaluated, and the amount of foraged *T. matsutake* was calculated based on changes in the climatic factors.

3. Results and Discussion

Prior to investigating the relationship between the amount of foraged *T. matsutake* and climatic factors in a time series, it was necessary to analyze the descriptive statistics for the dependent variable (foraged *T. matsutake*). This analysis aimed to ascertain the reliability of the correlation between the foraged *T. matsutake* and climatic factors. The results are provided in Table 1.

Table 1. Descriptive statistics for the variable foraged *Tricholoma matsutake* (2003–2023).

Variable	Mean	Median	Minimum	Maximum
Foraged *T. matsutake*	5829.6	4999.1	481.0	14,380.2
Foraged *T. matsutake* (log)	8.4	8.5	6.2	9.6

The descriptive statistics for the foraged *T. matsutake* revealed significant differences between the minimum and maximum, as well as between the mean and median. These results indicated an asymmetric data distribution, potentially impeding the correlation analysis. Thus, the foraged *T. matsutake* foraging data were logarithmically transformed to achieve a symmetrical distribution and stabilize the correlation analysis. Following this transformation, a normal distribution was obtained using the logged data, as evidenced by the relatively close relationship between the mean and median and the considerable difference between the minimum and maximum.

From the ADF test in this study, the stationarity level for the amount of foraged *T. matsutake* in the correlation analysis was not presented. To obtain stationarity, diffusion was processed against the data in 2006 and 2013, which exhibited the lowest correlation between the mushroom and climatic factors. With the diffused data, the stationarity level of each variable (foraged *T. matsutake*, average monthly temperature, and precipitation) was evaluated, and the results are provided in Table 2.

Table 2. Augmented Dickey–Fuller test between foraged *Tricholoma matsutake* and climatic factors across different months.

		Annual	January	February	March	April	May	June	July	August	September	October	November	December
Temp.	ADF statistic	−3.09	−2.74	−5.08	−2.57	−3.64	−2.50	−2.83	−3.58	−4.00	−0.53	1.10	−3.12	−4.14
	p-value	0.11	0.22	<0.01	0.29	0.03	0.33	0.18	0.03	<0.01	0.98	1.00	0.10	<0.01
Prec.	ADF statistic	−3.55	−3.92	−4.22	−4.47	−2.49	−3.81	−4.74	−2.20	−1.15	−3.66	−3.10	−3.50	−0.89
	p-value	0.03	<0.01	<0.01	<0.01	0.33	0.02	<0.01	0.49	0.92	0.03	0.11	0.04	0.96

In foraged *Tricholoma matsutake*, ADF statistic: −5.08, *p*-value: <0.01. Significance level $\alpha = 0.05$.

The results of the ADF test indicated stationarity in the amount of foraged *T. matsutake* in relation to the average temperature in February, August, and December and the average precipitation in January, February, March, and June. The correlation with the amount of foraged *T. matsutake* could be assessed using these variables. In addition, the correlation coefficient, which measures the strength and direction of relationships between two variables, was calculated to identify the degree of similarity between the mushroom and climatic factors with stationarity. Among the correlation coefficients, the average temperature in August exhibited the highest values of the stationarity coefficient in relation to the amount of foraged *T. matsutake* at 0.68 (Table 3). This result suggested a moderately close relationship between the average temperature in August and the foraged *T. matsutake*. In the graph, the relationship between the log-transformed amount of foraged *T. matsutake* and the average temperature in August is clearly evident (Figure 3).

Table 3. Correlation coefficients between *Tricholoma matsutake* foraging and climatic factors exhibiting stationarity.

	Temp. (February)	Temp. (August)	Temp. (December)	Prec. (January)	Prec. (February)	Prec. (March)	Prec. (June)
Corr. with *Tricholoma matsutake*	−0.15	0.68	0.20	0.14	0.14	−0.01	−0.10

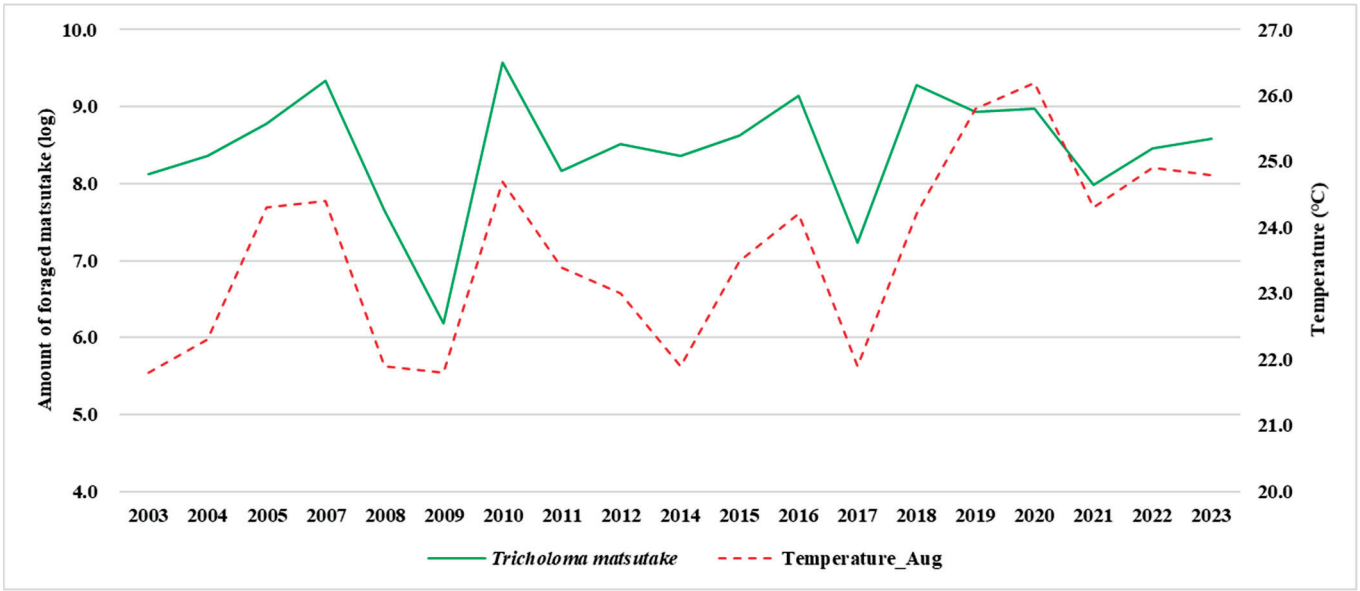

Figure 3. Amount of foraged *Tricholoma matsutake* and the average temperature in August in the pine forest of Yangyang-gun, Korea, between 2003 and 2023.

To calculate the amount of foraged *T. matsutake* based on climatic factors exhibiting stationarity, an OLS model was employed to evaluate the correlation between the foraged

matsutake mushroom, temperature, and precipitation. The reliability of the model was evaluated using the R^2, t-statistic, and *p*-value, ensuring data robustness. The OLS model's results are summarized in Table 4.

Table 4. Linear regression of the correlation between foraged *T. matsutake* and climatic factors.

Corr. with *Tricholoma matsutake*	Model	R^2	t-Statistic	*p*-Value
Temp. (February)	$\log(\hat{y}_i) = 8.5101 + (-0.0618) \cdot x_i$	0.02	−0.61	0.55
Temp. (August)	$\log(\hat{y}_i) = (-0.7465) + 0.3883 \cdot x_i$	0.46	3.81	<0.01
Temp. (December)	$\log(\hat{y}_i) = 8.3492 + 0.0793 \cdot x_i$	0.04	0.86	0.40
Prec. (January)	$\log(\hat{y}_i) = 8.3463 + 0.1127 \cdot x_i$	0.02	0.60	0.56
Prec. (February)	$\log(\hat{y}_i) = 8.3088 + 0.1152 \cdot x_i$	0.02	0.60	0.56
Prec. (March)	$\log(\hat{y}_i) = 8.4431 + (-0.0047) \cdot x_i$	0.00	−0.03	0.98
Prec. (June)	$\log(\hat{y}_i) = 8.5413 + (-0.0238) \cdot x_i$	0.01	−0.41	0.69

Significance level $\alpha = 0.05$.

Based on the results, only a correlation between the foraged *T. matsutake* and average temperature in August was identified, thereby demonstrating the reliability of the data.

Using the climatic factors that exhibited high reliability, results for the amount of foraged *T. matsutake* prediction were constructed using the OLS model. Based on the model results, a 1.5-ton increase in foraged *T. matsutake* was predicted for every 1-unit increase in August's average temperature. For the recommended conditions for maximum prediction stability, the August temperature should be between 21.8 °C and 26.2 °C. If the temperature falls outside this range, the model's predictive power diminishes due to a shift in the temperature pattern, making it impossible to utilize the previously established relationship between the mushroom foraging and temperature. A new correlation coefficient and model must be developed to address such alterations in temperature patterns.

Previous studies on matsutake mushrooms have examined the relationships between the growth of *T. matsutake* and climatic factors [11,15]. Unfortunately, few studies have investigated the direct relationship between the amount of foraged matsutake mushroom and climatic factors. We compared the results of this study to other studies that examined the correlation between the amount of wild mushrooms harvested and climatic factors. In wild mushrooms, an increase in precipitation causes a higher degree of mushroom foraging [18,28,29]. In the case of the investigation in the Czech Republic into wild mushroom using the ADF test and OLS method, a 21-ton increase in foraged wild mushroom was predicted for every 1-unit increase in the average precipitation. The effects on foraged wild mushroom growth of temperature have also been identified [19,30,31]. For example, using ADF and the Phillips–Perron (PP) test, the correlation coefficient for wild mushroom according to the temperature was 0.61. In addition, high humidity and favorable soil conditions play an important role in the growth and amount of wild mushrooms [28,32]. This relationship can also be identified in the results showing that mushroom production is expected to increase by 23% to 93% when the soil moisture and temperature rise.

As seen in other studies, the increase in the amount of foraged wild mushroom, temperature, and precipitation have a positive relationship. However, this comparison is bound to be limited due to the different growth conditions between wild mushrooms and *T. matsutake*. Specifically, regarding the soil conditions, while wild mushrooms can grow in a wide range of soil temperatures, *T. matsutake* requires a narrow range of soil temperatures, between 19 °C and 20 °C. Unlike other wild mushrooms, *T. matsutake* requires the pine tree as its host. Additionally, regarding the *T. matsutake* habitat condition, there are specific requirements for soil conditions, such as weak acidity, low nutrient content, and appropriate drainage [6,8,16]. Therefore, a comparison with other studies regarding the correlation between foraged *T. matsutake* and climatic factors is still necessary to derive more meaningful results from this study.

As mentioned, there are no reports of a significant correlation between the amount of foraged *T. matsutake* and climatic factors. Instead, several studies have investigated the

correlation between climatic factors and the growth of matsutake mycelia in fairy rings in pine forests [6,8,16,32]. These studies suggest that climatic factors, including temperature and precipitation, contribute to the development of *T. matsutake* mycelia within 5 cm below ground at fairy rings. These findings highlight the positive effect of temperature and precipitation on the dominance of *T. matsutake* mycelium and the formation of matsutake mushrooms in sterile and dry soils. As climatic factors can influence the soil conditions for matsutake mushrooms, it can be inferred that both temperature and precipitation are closely related to *T. matsutake* foraging [6,33].

From the correlation analysis, the correlation coefficient of the average temperature in August was 0.68. In comparison with the previous study [19], this correlation coefficient degree indicates a sufficiently high correlation between the amount of foraged matsutake mushroom and the average temperature in August. This positive correlation, however, does not always guarantee a close relationship between matsutake mushroom foraging and climatic factors. In this study, the linear relationships derived using the ADF test and OLS model alone do not fully investigate the correlation between the foraged matsutake mushroom and climatic factors. Furthermore, the t-statistics (3.81) and *p*-value (<0.01) confirmed that the ADF-OLS model has statistical significance and reliability, but the R^2 result (0.46) confirmed that the model does not account for half of the data variability in this investigation. The linear relationship and R^2 result indicate that although the model in this study presents, to some extent, a correlation between matsutake mushroom foraging and the average temperature in August, this temperature cannot be considered the only affecting factor. In other words, in addition to the factors with stationarity in this study, various factors including factors with non-stationarity are likely to affect matsutake mushroom foraging. Despite these limitations, by investigating the relationship between mushroom foraging and temperature in this study, the amount of foraged *T. matsutake* could be predicted with some reliability, and above all, we were able to secure the factor that significantly influenced the amount of foraged matsutake mushrooms. And this factor, the average temperature in August, could potentially be one of several factors influencing mushroom foraging.

Due to the significant impact of non-stationary factors on growth, it is essential to ensure their stationarity. As mentioned in the above paragraph, the soil conditions, including the soil temperature, soil moisture, and microorganisms in fairy rings, are also expected to significantly affect variables associated with *T. matsutake* foraging. The capacity to increase the correlation coefficient from moderate to high regarding the average temperature in August is a subject of interest. Due to the accelerating global climate change in the 21st century [19,20], temperature, a crucial factor in matsutake mushroom foraging, may become more optimal during other months compared to August. To respond to this changing climate, various Machine Learning (ML) techniques, such as classification trees, random forest, linear and radial support vector machine, and neural networks, are expected for the investigation of the non-linear relationship between the amount of foraged *T. matsutake* and various environmental factors [34]. In conclusion, continuously ongoing and continuously revised investigations regarding the linear and non-linear relationships between mushroom foraging and relevant factors are essential to improve the quality of the obtained data and address climatic changes.

4. Conclusions

Since the emergence of human societies, *Tricholoma matsutake* has been recognized as a popular and valuable mushroom that grows in the sterile, dry soil of pine forests. Temperature and precipitation influence the growth of matsutake mushrooms and the amount of foraged *T. matsutake*. In this study, employing a 20-year-period meta-analysis on climate variables in Yangyang-gun, we identified a significant positive correlation between matsutake mushroom foraging and the average temperature in August. The correlation coefficient at 0.68 and the relation between a 1-unit increase in temperature and a 1.5-ton increase in mushroom foraging indicated the significant effect of the average temperature

in August on *T. matsutake* foraging. These results are in line with the results of previous studies. However, this relationship is only expected to be one of several relationships between mushroom foraging and external environmental factors. Moreover, the findings of this study are predicated on linear relationships and necessitate the examination of non-linear relationships. Nevertheless, the average temperature in August still significantly affects the amount of foraged *T. matsutake*. Additionally, with the continuous investigation regarding the correlation between mushroom foraging and the aforementioned factors, the development of a more reliable model to predict the amount of foraged *T. matsutake* will provide an improved predictive value.

Supplementary Materials: The following supporting information can be downloaded at: https://www.mdpi.com/article/10.3390/f15122165/s1, Table S1. Yearly amount of foraged pine mushroom and monthly average temperature. Table S2. Yearly amount of foraged pine mushroom and monthly average precipitation.

Author Contributions: Conceptualization, D.-H.C., Y.-L.O. and E.-J.L.; Methodology, D.-H.C.; Software, D.-H.C. and E.-J.L.; Validation, Y.-L.O., J.-H.I., M.O. and E.-J.L.; Investigation, C.-S.K.; Resources, C.-S.K.; Data curation, C.-S.K.; Writing—original draft, D.-H.C.; Visualization, D.-H.C.; Supervision, E.-J.L. All authors have read and agreed to the published version of the manuscript.

Funding: This study was conducted within the postdoctoral research program support project as part of the results conducted by the Rural Development Administration (grant number PJ017355022024).

Data Availability Statement: Data is contained within the article or Supplementary Material.

Conflicts of Interest: The authors declare no conflicts of interest.

References

1. Pueschel, V.A.; Schieberle, P. Changes in the key aroma compounds of matsutake mushroom (*Tricholoma matsutake* Sing.) from Canada during pan-frying elucidated by application of the sensomics approach. *Eur. Food Res. Technol.* **2021**, *47*, 51–65.
2. Hosford, D.; Pilz, D.; Molina, R.; Amaranthus, M. *Ecology and Management of the Commercially Harvested American Matsutake Mushrooms*; USDA Forest Service PNW-GTR-412; USDA Forest Service: Washington, DC, USA, 1997.
3. Lee, N.Y.; Choi, D.H.; Kim, M.G.; Jeong, M.J.; Kwon, H.J.; Kim, D.H.; Kim, Y.G.; Luccio, E.; Arioka, M.; Yoon, H.J.; et al. Biosynthesis of (R)-(-)-1-Octen-3-ol in Recombinant *Saccharomyces cerevisiae* with Lipoxygenase-1 and Hydroperoxide Lyase Genes from *Tricholoma matsutake*. *J. Microbiol. Biotechnol.* **2020**, *30*, 296–305. [PubMed]
4. Cheng, H.; Jia, Y.; Wang, L.; Liu, X.; Liu, G.; Li, L.; He, C. Isolation and structural elucidation of a novel homogenous polysaccharide from *Tricholoma matsutake*. *Nat. Prod. Res.* **2015**, *30*, 58–64. [PubMed]
5. Tedersoo, L.; Bahram, M.; Zobel, M. How mycorrhizal associations drive plant population and community biology. *Science* **2020**, *367*, eaba1223.
6. Yamanaka, T.; Yamada, A.; Furukawa, H. Advances in the cultivation of the highly-prized ectomycorrhizal mushroom *Tricholoma matsutake*. *Mycoscience* **2020**, *61*, 49–57.
7. Li, J.; Li, J. Regeneration and restoration of broad-leaved Korean pine forests in Lesser Xing'an Mountains of Northeast China. *Acta Ecol. Sin.* **2003**, *23*, 1268–1277.
8. Yamada, A. Cultivation studies of edible ectomycorrhizal mushrooms: Successful establishment of ectomycorrhizal associations in vitro and efficient production of fruiting bodies. *Mycoscience* **2022**, *63*, 242–253. [CrossRef]
9. Lee, C.S.; Chun, Y.M.; Lee, H.; Pi, J.H.; Lim, C.H. *Establishment, Regeneration, and Succession of Korean Red Pine (Pinus densiflora S. et Z.) Forest in Korea*; IntechOpen: London, UK, 2018.
10. Korea Forest Service. *Statistical Yearbook of Forestry*; Korea Forest Service: Daejeon, Republic of Korea, 2018.
11. Shim, K.M.; Ko, C.S.; Lee, Y.S.; Kim, G.Y.; Lee, J.T.; Kim, S.J. Correlation coefficients between pine mushroom emergence and meteorological elements in Yangyang country, Korea. *Korean J. Agric. For. Meteorol.* **2007**, *9*, 188–194. [CrossRef]
12. Fan, X.; Miao, C.; Duan, Q.; Shen, C.; Wu, Y. Future Climate Change Hotspots Under Different 21st Century Warming Scenarios. *Earths Future* **2021**, *9*, e2021EF002027.
13. Moberg, A.; Jones, P.D. Trends in indices for extremes in daily temperature and precipitation in central and western Europe, 1901–1999. *Int. J. Climatol.* **2005**, *25*, 1149–1171.
14. Hong, S.H.; Lee, Y.H.; Lee, G.; Lee, D.H.; Adhikari, P. Predicting Impacts of Climate Change on Northward Range Expansion of Invasive Weeds in South Korea. *Plants* **2021**, *10*, 1604. [CrossRef] [PubMed]
15. Guo, Y.; Li, X.; Zhao, Z.; Wei, H.; Gao, B.; Gu, W. Prediction of the potential geographic distribution of the ectomycorrhizal mushroom *Tricholoma matsutake* under multiple climate change scenarios. *Sci. Rep.* **2017**, *10*, 46221. [CrossRef] [PubMed]
16. Hur, T.C.; Park, H.; Ka, K.H.; Joo, S.H. Dynamic Changes of Soil Physicochemical Properties in the Fairy-rings of *Tricholoma matsutake*. *J. Korean For. Soc.* **2004**, *93*, 26–34.

17. Barbati, A.; Corona, P.; Marchetti, M. A forest typology for monitoring sustainable forest management: The case of European Forest Types. *Plant Biosyst.* **2007**, *141*, 93–103. [CrossRef]
18. Procházka, P.; Soukupová, J.; Jr Tomšík, K.; Mullen, K.J.; Čábelková, I. Climatic Factors Affecting Wild Mushroom Foraging in Central Europe. *Forests* **2023**, *14*, 382. [CrossRef]
19. Alfranca, O.; Voces, R.; Diaz-Balteiro, L. Influence of Climate and Economic Variables on the Aggregated Supply of a Wild Edible Fungi (*Lactarius deliciosus*). *Forests* **2015**, *6*, 2324–2344. [CrossRef]
20. Morera, A.; LeBlanc, H.; Aragón, J.M.; Bonet, J.A.; de-Miguel, S. Analysis of climate change impacts on the biogeographical patterns of species-specific productivity of socioeconomically important edible fungi in Mediterranean forest ecosystems. *Ecol. Inform.* **2024**, *81*, 102557. [CrossRef]
21. Kauserud, H.; Stige, L.C.; Vik, J.O.; Økland, R.H.; Høiland, K.; Stenseth, N.C. Mushroom Fruiting and Climate Change. *Proc. Natl. Acad. Sci. USA* **2008**, *105*, 3811–3814. [CrossRef]
22. National Forestry Cooperative Federation. Available online: https://m.nfcf.or.kr/forest/user.tdf?a=user.songi.SongiApp&c=1003&mc=MOB_CST01 (accessed on 26 June 2024).
23. Kim, H.G.; Park, C.Y. Landslide susceptibility analysis of photovoltaic power stations in Gangwon-do, Republic of Korea. *Geomat. Nat. Hazards Risk* **2021**, *12*, 2328–2351. [CrossRef]
24. Hong, M.; Song, C.; Kim, M.; Kim, J.; Roh, M.; Ko, Y.; Cho, K.; Son, Y.; Jeon, S.; Kraxner, F.; et al. Modeling-Based Risks Assessment and Management of Climate Change in South Korean Forests. *Forests* **2023**, *14*, 745. [CrossRef]
25. Rural Development Administration. Available online: http://weather.rda.go.kr/weather/observation.do (accessed on 26 June 2024).
26. Kočenda, E.; Černý, A. *Elements of Time Series Econometrics: An Applied Approach*; Karolinum: Prague, Czech Republic, 2015; ISBN 978-80-246-3199-8.
27. Hindls, R.; Hronová, S.; Seger, J.; Fischer, J. *Statistika pro Ekonomy*, 8th ed.; Professional Publishing: Prague, Czech Republic, 2007; ISBN 978-80-86946-43-6.
28. Karavani, A.; Cáceres, M.D.; de Aragón, J.M.; Bonet, J.A.; de-Miguel, S. Effect of climatic and soil moisture conditions on mushroom productivity and related ecosystem services in Mediterranean pine stands facing climate change. *Agric. For. Meteorol.* **2018**, *248*, 432–440. [CrossRef]
29. Procházka, P.; Soukupová, J.; Mullen, K.J.; Jr Tomšík, K.; Čábelková, I. Wild Mushrooms as a Source of Protein: A Case Study from Central Europe, Especially the Czech Republic. *Foods* **2023**, *12*, 934. [CrossRef] [PubMed]
30. Chiu, C.I.; Yeh, H.T.; Li, P.L.; Kuo, C.Y.; Tsai, M.J.; Li, H.F. Foraging Phenology of the Fungus-Growing Termite Odontotermes formosanus (Blattodea: Termitidae). *Environ. Entomol.* **2018**, *47*, 1509–1516. [CrossRef]
31. Oviya, R.; Sobanbabu, G.; Anbazhagan, P.; Revathy, N.; Mahalakshmi, P.; Manonmani, K.; Mareeswari, P.; Vijayasamundeeswari, A.; Shanmugaiah, V.; Mehetre, S.; et al. Studying Soil Ecology and Growth Conditions of *Phellorinia herculeana*, a Wild Edible Mushroom. *Processes* **2022**, *10*, 1797. [CrossRef]
32. Lee, K.H.; Jo, S.Y.; Kim, S.C. The Relationship between Tree-Ring Growth in *Pinus densiflora* S. et Z. and the Corresponding Climatic Factors in Korea. *J. Korean Wood Sci. Technol.* **2022**, *50*, 81–92. [CrossRef]
33. Narimatsu, M.; Koiwa, T.; Masaki, T.; Sakamoto, Y.; Ohmori, H.; Tawaraya, K. Relationship between climate, expansion rate, and fruiting in fairy rings('shiro') of an ectomycorrhizal fungus *Tricholoma matsutake* in a *Pinus densiflora* forest. *Fungal Ecol.* **2015**, *61*, 18–28. [CrossRef]
34. Martínez-Rodrigo, R.; Águeda, B.; Ágreda, T.; Altelarrea, J.M.; Fernández-Toirán, L.M.; Rodríguez-Puerta, F. Assessment of Mycological Possibility Using Machine Learning Models for Effective Inclusion in Sustainable Forest Management. *Sustainability* **2024**, *16*, 5656. [CrossRef]

Disclaimer/Publisher's Note: The statements, opinions and data contained in all publications are solely those of the individual author(s) and contributor(s) and not of MDPI and/or the editor(s). MDPI and/or the editor(s) disclaim responsibility for any injury to people or property resulting from any ideas, methods, instructions or products referred to in the content.

forests

MDPI

Article

Timing of Drought and Severity of Induced Leaf Desiccation Affect Recovery, Growth and Autumnal Leaf Senescence in *Fagus sylvatica* L. Saplings

Kristine Vander Mijnsbrugge [1,*], Mattias Bollen [1], Stefaan Moreels [1], Eduardo Notivol Paino [2], Kris Vandekerkhove [1], Luc De Keersmaeker [1], Arno Thomaes [1], Sanne Verdonck [1] and Margot Vanhellemont [1]

[1] Department for Forest Ecology and Management, Research Institute for Nature and Forest (INBO), 9500 Geraardsbergen, Belgium; mattias.bollen34@gmail.com (M.B.); stefaan.moreels@inbo.be (S.M.); kris.vandekerkhove@inbo.be (K.V.); luc.dekeersmaeker@inbo.be (L.D.K.); arno.thomaes@inbo.be (A.T.); sanne.verdonck@inbo.be (S.V.); margot.vanhellemont@inbo.be (M.V.)

[2] Department for Environment, Agricultural and Forest Systems, Agri-Food Research and Technology Centre of Aragon (CITA), 50059 Zaragosa, Spain; enotivol@cita-aragon.es

* Correspondence: kristine.vandermijnsbrugge@inbo.be

Abstract: Increased water limitations due to climate change will pose severe challenges to forest ecosystems in Europe. We investigated the response of potted saplings of *Fagus sylvatica* L., one of the major European tree species, to a spring and a summer water-withholding period with control–control (C-C), control–drought (C-D), drought–control (D-C) and drought–drought (D-D) treatments. We focused on recovery capacity and phenological and growth traits and questioned the extent to which an earlier drought influenced the response to a second drought in the same growing season. To examine the impact of the level of drought stress, a distinction was made between saplings with less or more than half of their leaves desiccated due to the spring drought (D<50 and D>50). The timing of the drought influenced the immediate post-drought response: saplings severely affected by the spring drought (D>50) resprouted, whereas saplings severely affected by the summer drought (C-D and D<50-D) did not. The spring treatment influenced the onset of visual symptoms in the summer drought, with saplings less affected in the spring drought (D<50-D) developing symptoms three days later than the saplings not subjected to drought in the spring (C-D), whereas severely affected saplings (D>50-D) had not yet display symptoms seventeen days after the first visual symptoms in the spring control saplings (C-D). The timing of autumnal leaf senescence displayed the legacies of the spring treatment. The saplings heavily affected by the spring drought showed a slower decrease in relative chlorophyll content and delayed leaf senescence (D>50-C and D>50-D), which may enable the repair of damaged tissues. The saplings that were less affected by the spring drought (D<50-C) showed earlier autumnal leaf senescence, which is likely an acclimation response. Interestingly, a larger diameter increment in autumn for all of the saplings that experienced the summer drought (C-D, D<50-D and D>50-D) may indicate the recovery of hydraulic capacity by new xylem growth. Our results underline the plasticity of young *F. sylvatica* saplings in response to (repeated) drought.

Keywords: autumnal leaf phenology; recurrent drought stress; relative chlorophyll content; resprouting

1. Introduction

Forests play a key role in water and nutrient cycles, provide a diverse range of ecosystem services and are essential for the preservation and sustenance of biodiversity [1,2]. Increasing severe weather phenomena such as heat waves, droughts and storms, occurring due to climate change, can lead to increased tree mortality and result in the release of net atmospheric CO_2. Forests face vulnerability to various extreme climate events, with drought and its related disturbances globally exerting the most significant impact [3,4]. It is assumed that trees will probably not be able to adapt to abrupt increases in aridity through evolutionary mechanisms due to their extended generation cycles and the incapacity to migrate away from stressful conditions. The prospect of global warming causing extended and intensified droughts underscores the importance of investigating the impacts of drought on woody plants [4,5].

Trees shedding leaves is a common phenomenon during drought as a life-saving strategy [6]. Leaf shedding typically occurs after stomatal closure [7], and xylem embolisms in the leaves may be the main driver of leaf mortality during drought [8–10]. The shedding of leaves in response to drought diminishes the evaporative leaf surface area, thereby assisting woody perennials in postponing the initiation of cavitation in the conductive tissues of the stem [11,12]. Leaf shedding alleviates water stress on the remaining foliage of woody plants, effectively slowing down the rate of desiccation [13,14]. Yet, shedding leaves without complete nutrient resorption results in net nutrient losses, which may limit post-drought resprouting and photosynthesis and have long-term implications for tree performance [15]. Defoliation due to severe drought can lead to partial crown dieback and eventually result in tree mortality in the following years [16]. Rebuilding an affected crown after a severe drought demands additional carbon investment, sourced from non-structural carbohydrate reserves or from the assimilation of remaining or newly grown leaves once drought stress subsides [17].

While considerable focus has been dedicated to identifying the physiological factors leading to tree mortality during drought, it is equally crucial to comprehend the mechanisms involved in the recovery of trees that withstand dry periods [18]. Drought resilience can be quantified by evaluating both the disturbance impact and the rate of recovery following the disturbance [19]. The pace of post-drought hydraulic recovery is primarily determined by the magnitude of the negative water potential reached and the time spent at this extreme [4]. When little or no cavitation (i.e., formation of vapor-filled cavities or air bubbles in the xylem network) has occurred, recovery from drought after rainfall occurs rapidly and stomata open to assimilate new carbon from the atmosphere as plants rehydrate. When cavitation thresholds have been surpassed, the recovery of photosynthesis is considerably slower and proceeds in coordination with the gradual restoration of hydraulic conductance from the roots to the tree crown [20]. When extensive aboveground biomass loss occurs due to drought, the recovery process may be accelerated through resprouting from epicormic buds [20]. A reduction in growth or physiological processes can be compensated for by investment in other processes or tissues and, a process called compensatory recovery [17]. For instance, after drought stress, *Fagus sylvatica* saplings can delay autumnal leaf senescence, maintaining photosynthesis at a higher level for a longer time [21,22].

In this study, we conducted a controlled recurrent drought experiment on *F. sylvatica* saplings. We withheld water from potted saplings in the spring and summer of the same growing season, followed by rewatering. In the experiment, we aimed to subject saplings to varying levels of drought stress, ranging from mild to severe, which was assessed based on the visual symptoms that developed during the drought periods. The factorial design allowed the study of the potential influence of former drought exposure. We hypothesized

that the responses to the imposed droughts would depend on (i) the timing of the drought in the growing season, (ii) the severity of the drought effects and (iii) whether saplings had already experienced a drought. We were particularly interested in the recovery process and focused on the timing of autumnal leaf senescence and the influence on growth traits.

2. Materials and Methods

2.1. Source Material

We used 288 *Fagus sylvatica* saplings belonging to ten provenances (Table S1). The ten genetic backgrounds were evenly distributed between the different treatments (see Section 2.2), but no provenance-dependent analyses were performed because of the low number of saplings for each provenance in each treatment group. Vander Mijnsbrugge et al. [23] described the seed collection in 2016, the germination in 2017, the establishment of a common garden of potted seedlings in 2017, and a temperature manipulation experiment with the potted seedlings in 2018. After the temperature treatment in 2018, we moved the potted seedlings to an outdoor container field at the Research Institute for Agriculture and Fisheries in Melle (Belgium), where the saplings were watered using automatic sprinklers. In the winter of 2019–2020, we transferred the saplings to 4 L pots (height 17 cm, diameter 21 cm). All pots were filled with standard nursery potting soil (1.5 kg/m^3 NPK 12 + 14 + 24, organic matter 20%, pH 5.0–6.5, E.C. 450 µS/cm and dry matter 25%) without additional fertilizer. The organic matter content and the pH range promote the water-holding capacity of the potting soil, while a dry matter content of 25% indicates a relatively aerated mixture. All saplings remained in the pots during the experiment and had access to the same type and amount of potting soil.

2.2. Drought Treatments

In the middle of May 2022, we moved all potted saplings to a greenhouse, in which an automatic grey shade net protected the saplings from heavy solar radiation. We performed spring and summer drought treatments following a full-factorial design in the growing season of 2022 (Figure 1). At the start and end of both treatments, we brought all saplings to full water saturation: we placed the pots overnight in a water basin with the water level reaching 5 cm above the base of the pots. At the start of the two treatments, we took the pots out of the basin and let any excess water drain naturally over the course of a few hours. During the first treatment (spring), half of the pots—the drought group—did not receive any watering (n = 144), while the other half—the control group—were watered on a regular basis by experienced technical staff, keeping the saplings well-moisturized (n = 144). The ten provenances were evenly (and randomly within each provenance) distributed among the control and drought groups (Table S2). For the second treatment (summer), we split both the control and drought groups of the spring treatment in half, with each half then being the control or drought group in the summer treatment (Figure 1). In addition, the ten provenances were equally (and randomly within each provenance) distributed over the control and drought groups (Table S3). The four treatment groups of the experiment are hereafter called control–control (C-C), control–drought (C-D), drought–control (D-C) and drought–drought (D-D), indicating the combination of the groups in the spring and summer treatments.

The spring treatment lasted from May 23 until June 15, and the summer treatment took place from August 8 until September 12. The spring treatment was ended when there was a distribution of saplings across the different visual drought stress groups (see results), from saplings displaying up to 100% desiccated leaves, as well as saplings without any desiccated leaves. A small number of saplings, for which all leaves were desiccating during the spring drought treatment (15 from a total of 144 saplings), were placed overnight in

a water basin on June 13 (n = 7) and June 14 (n = 8) to keep mortality to a minimum and to have a reasonable amount of saplings in all visual drought stress groups (Table S2). To reduce sapling mortality to a minimum during the summer drought treatment, we again placed the saplings that were severely desiccated early on during the treatment in a water basin before the end of the summer drought treatment (Table S4, Figure S1). After the two subsequent treatments, we kept the saplings in the greenhouse until December 2022, ensuring they were consistently maintained under well-watered conditions, as assessed by knowledgeable technical staff. Seven saplings were not alive anymore in the spring of 2023.

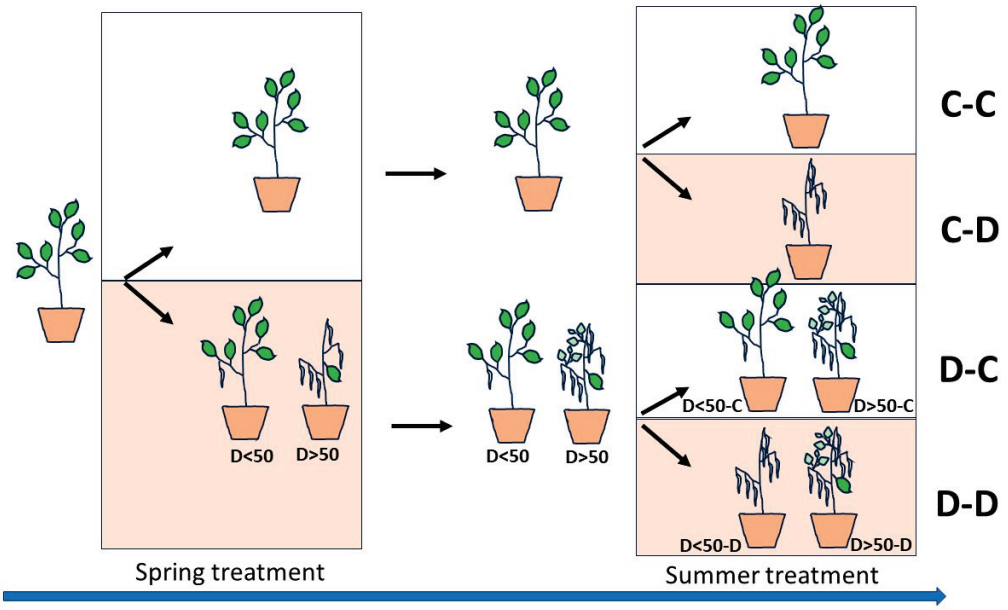

Figure 1. Schematic representation of the two succeeding droughts in the growing season of 2022. For a potted sapling, the two consecutive treatments were either C-C (control–control), i.e., the control group during the spring treatment and the control group during the summer treatment, C-D (control–drought), D-C (drought–control) or D-D (drought–drought). The severity of the spring drought was categorized according to the proportion of desiccated leaves, with D<50 representing less than half of the leaves desiccated, and D>50 representing more than half.

2.3. Measurements and Observations

We weighed all the pots at the start of each of the two drought treatments (i.e., after the overnight water basin) and on a weekly basis throughout the treatments. The weight reduction of the pots served as an indicator of water scarcity. For the summer treatment, we calculated the relative weight loss as the difference in weight of a pot between the initial water-saturated condition (on August 8) and its weight on August 22, divided by the initial weight at the saturated condition.

For all the saplings, we measured stem diameter with a measuring rod at 1 cm above the soil level and sapling height up to the place on the stem that was still alive. We performed the measurements at the beginning of the spring drought treatment (May 23), in-between the two drought treatments (August 1) and at the end of 2022 (December 26 for diameters) or the start of the growing season in 2023 (April 25 for heights). Height measurements in December 2022 were not reliable as it only became clear at the time of the spring budburst in 2023 which part of the stem had died off.

To identify the onset of visual drought stress symptoms on the saplings in the spring and summer drought treatments and to track the progress of desiccation, we scored the saplings of the drought groups phenotypically (protocol: see Table 1). During the spring treatment, visual drought symptoms became evident on June 10, and we scored all saplings

on June 13–15. For the summer drought treatment, we scored the saplings 3 times a week from August 20 until September 12.

Table 1. Four scoring protocols used to visually assess the effects of: drought stress on the saplings during the water withholding period [9,24], final leaf desiccation after drought, post-drought recovery and autumnal leaf senescence.

Score	Drought Stress * (% Leaves)	Leaf Desiccation (% Leaves)	Post-Drought Resprouting	Autumnal Leaf Senescence (% Green Leaves)
1	none	none	normal buds	100% (all leaves still green)
2	≤33%	1%–50%	swollen buds starting to open	75%–99% (first leaves turning yellow)
3	34%–66%	51%–75%	first leaves protruding from the buds	50%–75% (combination of green, yellow and first browning leaves)
4	67%–100%	76%–95%	first leaves unfolding	25%–50% (more than half of the leaves turning yellow to brown)
5		>95%	first leaves elongating	<25% (a majority or only yellow and brown leaves)
6				a majority to all leaves brown

* visual signs of drought stress: leaves curling up or becoming more rigid; leaves turning pale green to grey; later on, most of the affected leaves turned brown.

Following the first (spring) drought treatment, when it became visually evident which leaves had dried up and which ones had regained turgor, we assessed the proportion of desiccated leaves on the saplings of the drought group on June 21 using a scoring protocol (Table 1). The distribution of the saplings among the different categories of desiccated leaves and their further division among the control and drought groups in the summer treatment are shown in Table 2. The first results indicated that distinguishing saplings with less than 50% desiccated leaves (D<50, consisting of the groups with 0% and 1%–50% leaf desiccation) and saplings with more than 50% desiccated leaves (D>50, consisting of the groups with 51%–75%, 76%–95% and 96%–100% leaf desiccation) was justified (see Figure 2b). On July 14, we evaluated the post-drought recovery of the saplings in the drought group, focusing on buds that initiated new growth (i.e., resprouting). Budburst in woody saplings is normally observed in spring. We adapted a spring protocol for the post-drought new leaf phenology (Table 1). After the second (summer) drought treatment, only a few of the desiccated saplings displayed bud swelling, with a minor number of small leaves that hardly protruded from the buds and did not properly unfold. Therefore, no recovery was scored after the summer drought treatment.

Table 2. Number of saplings in the different categories of desiccated leaves after the spring drought period (n_D) and their further division among the D-C and D-D treatment groups ($n_{D\text{-}C}/n_{D\text{-}D}$).

Proportion of Desiccated Leaves	n_D	$n_{D\text{-}C}/n_{D\text{-}D}$
0%	78	39/39
1%–50%	11	7/4
51%–75%	11	8/3
76%–95%	14	9/5
96%–100%	30	10/20

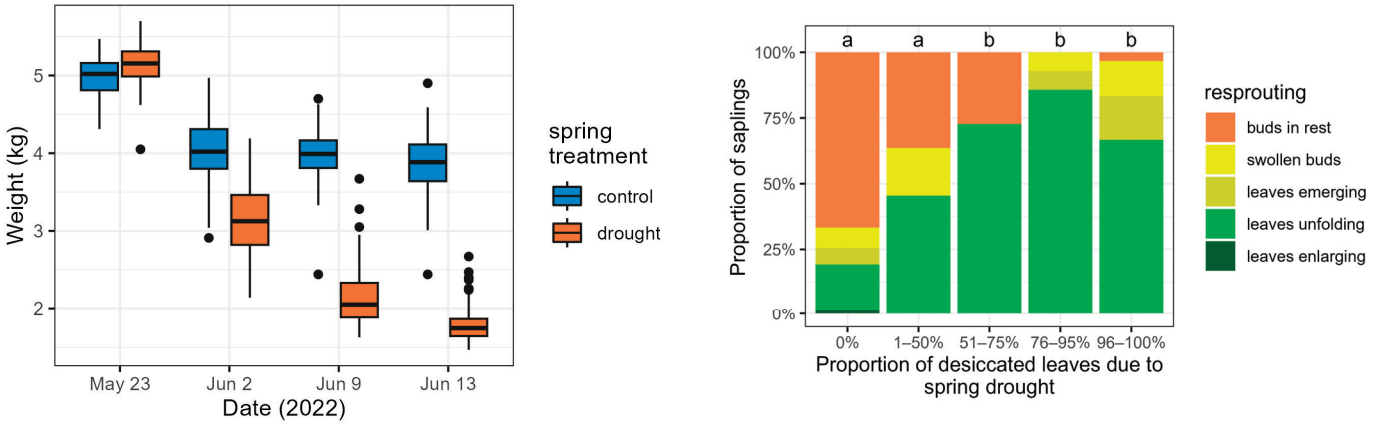

(**a**) (**b**)

Figure 2. Weight of the pots during the spring treatment for the control saplings and the saplings subjected to drought (**a**) and proportion of the saplings that had experienced drought in the different resprouting categories after the spring drought, according to the proportion of desiccated leaves (**b**). The lowercase b denotes a significant difference with the saplings that had zero desiccated leaves.

We used a chlorophyll content meter (CCM-200, Edaphic Scientific, Melbourne, Australia) that determines the relative chlorophyll content as the ratio of optical transmission at 931 nm (near-infra-red) to optical transmission at 653 nm (green). We measured the relative chlorophyll content on one representative damage-free and mature leaf on a short shoot at the middle of each sapling during the growing season: May 31, July 4 and 18 (beginning of the spring drought, and two times after the end of the spring drought), as well as on August 1, September 26 and October 24 (before the summer drought, and two times after the end of the summer drought). Saplings that were totally desiccated due to the drought treatments were, quite evidently, not measured.

In the autumn of 2022, we scored leaf senescence in all groups of saplings twice a week from October 26 to November 28, observing the entire sapling and giving a mean score (Table 1). Leaves desiccated due to the previous drought treatments were omitted from the scoring.

2.4. Statistical Analysis

We analyzed all data using the open-source statistical software R, version 4.4.2. [25]. We applied linear and general linear mixed models using the lme4 package [26] and addressed ordinal data with cumulative logistic regression using the ordinal package [27]. Figures were made with ggplot2 [28]. Mixed-effects modeling proved advantageous for the analysis of ecological data due to its ability to accommodate nested data, handle unbalanced datasets, and incorporate random effects [29]. In the context of experimental studies on tree seedlings and saplings, growth traits are often analyzed using (general) linear mixed models, whereas phenological data can be effectively processed with cumulative logistic regression (e.g., [30,31]). The independent variables applied in the fixed parts of the mixed models are explained in Table 3. In the presented model formulas, each β is an indication of the effect of each independent variable on the response variable. A unique plant identifier was added as a random effect to account for repeated measures on the same saplings when applicable.

Table 3. Variables used as fixed effects in the mixed models. Abbreviations of the variables are explained in the description using bold text.

Variable	Description	Type
DAY	day of measurement	continuous
DAY_{cat}	**cat**egorical time variable for spring or summer treatments	categorical, 3 levels spring: first week (May 31) and after treatment (July 4 and 18) summer: before (August 1) and after treatment (September 26 and October 24)
DES	proportion of **des**iccated leaves after the spring drought	categorical, 5 levels: none (score 1) ≤50% (score 2) 51%–75% (score 3) 76%–95% (score 4) >95% (score 5)
D_{spring}	sapling **d**iameter at the start of the **spring** treatment (May 23)	continuous (in mm)
D_{summer}	sapling **d**iameter in-between the two treatments, before the **summer** treatment (August 1)	continuous (in mm)
H_{spring}	sapling **h**eight at the start of the **spring** treatment (May 23)	continuous (in cm)
H_{summer}	sapling **h**eight in-between the two treatments, before the **summer** treatment (August 1)	continuous (in cm)
TR_{spring}	**spring tr**eatment	categorical, 3 levels: C = control D<50 = drought resulting in less than half of the leaves being desiccated D>50 = drought resulting in more than half of the leaves being desiccated
TR_{full}	**full**, i.e., combined spring and summer treatments (leaf desiccation categorized as in TR_{spring})	categorical, 6 levels: C-C = control–control C-D = control–drought D<50-C and D>50-C = drought–control D<50-D and D>50-D = drought–drought

2.4.1. Recovery After the Spring Drought Period

We examined the relationship between the occurrence of post-drought resprouting after the spring treatment and the severity of the experienced drought stress. For this, we looked at the saplings in the drought group and studied the effect of the level of leaf desiccation and initial sapling height on the recovery by resprouting (RES). We used cumulative logistic regression to model the probability of having resprouted up to a given resprouting level (p_R), i.e., having reached a certain resprouting level or a lower level:

$$\log(p_{RES}/(1 - p_{RES})) = \beta_0 - \beta_1 DES - \beta_2 H_{spring}$$

2.4.2. Onset of Visual Drought Symptoms in the Summer Treatment

We examined whether the onset of visual drought symptoms in the summer treatment (ODR_{summer}) was dependent on the effects of the spring treatment. During the summer treatment, none of the saplings in the drought group that had more than half of their leaves desiccated due to the spring drought (D>50-D) showed visual drought symptoms before the end of the treatment. Hence, we used only part of the drought group, i.e., the saplings with less than half of their leaves desiccated after the spring treatment (D<50-D), and all controls from the spring treatment (C-D) for the modeling. We first transformed

the scores of visual symptoms into binary data. All saplings without visual drought symptoms were given a score of 0, and all others scored 1. We fit a logistic regression with $p_{ODRsummer}$, showing the probability of displaying drought symptoms on a given day during the summer drought treatment:

$$\log(p_{ODRsummer}/1 - p_{ODRsummer}) = \beta_0 + \beta_1 H_{summer} + \beta_2 TR_{full} + \beta_3 DAY$$

The difference in time between the onset of the visual drought symptoms in the C-D and D<50-D groups was calculated based on the coefficients of the model above and using the mean summer sapling height.

2.4.3. Relative Chlorophyll Content

We used the measurements of the relative chlorophyll content (RCC) in the leaves for two purposes. Firstly, we quantified the experienced drought stress caused by the spring drought, by comparing the relative chlorophyll content of the spring drought group with the controls. Secondly, the relative chlorophyll content measurements in summer and autumn completed the picture of the autumnal leaf senescence process together with the visual observations.

The RCC_{spring} model accounted for the measurements in the first week of the spring drought treatment (May 31) and the two measurements after the treatment (July 4 and 18):

$$RCC_{spring} = \beta_0 + \beta_1 H_{spring} + \beta_2 TR_{spring} + \beta_3 DAY_{cat} + \beta_4 TR_{spring} DAY_{cat}$$

By including the interaction term between DAY_{cat} and TR_{spring}, the model allowed for the possibility that the change in RCC_{spring} over time (DAY_{cat}) differed among the treatment groups (TR_{spring}).

The relative chlorophyll content at the beginning of (August 1) and after (September 26 and October 24) the summer treatment (RCC_{summer}) was modeled with the same model structure as above but with H_{summer} and TR_{full}.

2.4.4. Autumnal Leaf Senescence

To examine the effect of the treatments on autumnal leaf senescence (SEN), the probability of having attained—on a given day—a given leaf senescence score or a lower score (p_{SEN}) was modeled by employing a generalized linear mixed model (cumulative logistic regression):

$$\log(p_{SEN}/(1 - p_{SEN})) = \beta_0 - \beta_1 TR_{full} - \beta_2 DAY$$

The timelapse between autumnal leaf senescence for the control–control group and the different spring and summer treatments was calculated based on the coefficients of the fitted model.

2.4.5. Change in Sapling Heights and Diameters

To evaluate the effects of the drought in each treatment on sapling growth, we modeled the change in sapling height and diameter for all the saplings, taking into account the initial height and diameter. We calculated the height and diameter increment by subtracting the height and diameter on May 23 from those on August 1 for the spring treatment (HI_{spring} and DI_{spring}), and by subtracting the height and diameter on August 1 from those on April 25, 2023 (height) or December 26, 2022 (diameter) for the summer treatment (HI_{summer} and DI_{summer}). We applied a linear model for the change in height caused by the spring treatment:

$$IH_{spring} = \beta_0 + \beta_1 H_{spring} + \beta_2 TR_{spring}$$

For the modeling of the change in height caused by the summer treatment (IH_{summer}), the same model structure was applied with H_{summer} and TR_{full}. For the changes in diameter (DI_{spring} and DI_{summer}), the initial heights were replaced by initial diameters (D_{spring} and D_{summer}).

3. Results

3.1. Spring Treatment: Drought Symptoms, Recovery and Relative Chlorophyll Content

In the spring treatment, the reduction in weight of the pots demonstrated the water scarcity experienced by the saplings (Figure 2a). In the group of saplings that had experienced drought, saplings for which more than half of the leaves had desiccated (categories 51%–75%, 76%–95% and 96%–100%) resprouted significantly more after the drought in comparison to the saplings without leaf desiccation due to the drought (Figure 2b, Table S5). The categories of 51%–75%, 76%–95% and 96%–100% post-drought desiccated leaves are grouped and designated as D>50, whereas the categories of 0% and 1%–50% desiccated leaves are grouped and designated as D<50.

The relative chlorophyll content increased less or diminished in the saplings of the drought group of the spring treatment when compared to the controls (significant interaction terms between the date, i.e., July 4, and treatment groups are shown in Table S6, Figure 3). Later on in July, the relative chlorophyll content in the saplings with more than half of their leaves desiccated due to the drought (D>50) diminished relatively quickly (significant interaction terms between the date, i.e., July 18, and treatment groups are shown in Table S6, Figure 3). The noticeably different reaction of the relative chlorophyll content in the leaves of the D<50 and D>50 groups further justified the division of the group that experienced spring drought in the two subgroups, i.e., with more or less than half of their leaves desiccated due to the drought.

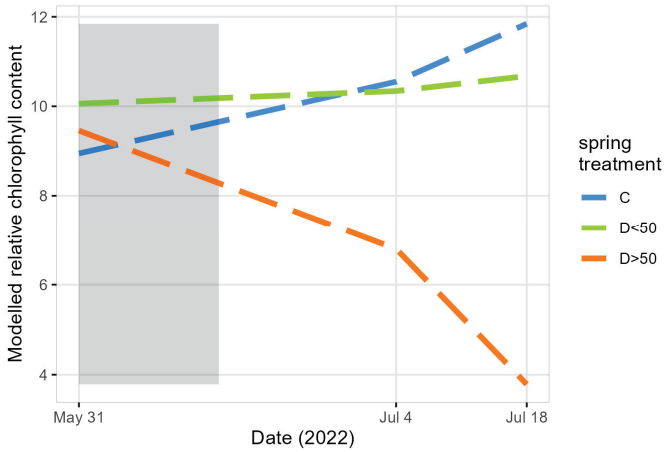

Figure 3. The modeled relative chlorophyll content in the leaves of the saplings at the beginning (May 31) and after (July 4 and 18) the spring treatment. C: controls and D: drought group with less (D<50) or more (D>50) than half of their leaves desiccated due to the spring drought. The spring drought treatment period is indicated in grey.

3.2. Summer Treatment: Drought Symptoms, Recovery and Relative Chlorophyll Content

The weight loss of the pots during the summer treatment demonstrated the water scarcity experienced by the saplings (Figure 4). The pot's weight showed variability that could be related to the spring treatment. The pots of saplings with more than half of their leaves desiccated due to the spring drought (D>50-D) lost weight less quickly than the pots of saplings with less than half of their leaves desiccated (D<50-D) and the control plots of the spring treatment (C-D). On August 22 (the first saplings were taken out of the drought

to avoid mortality on August 24), the mean relative weight loss of the pots in the D>50-D treatment was 30.8% ± 5.3%, which was significantly higher than the relative weight loss of the pots in the D<50-D (53.9% ± 5.4%) or C-D (60.5% ± 5.6%) treatment groups.

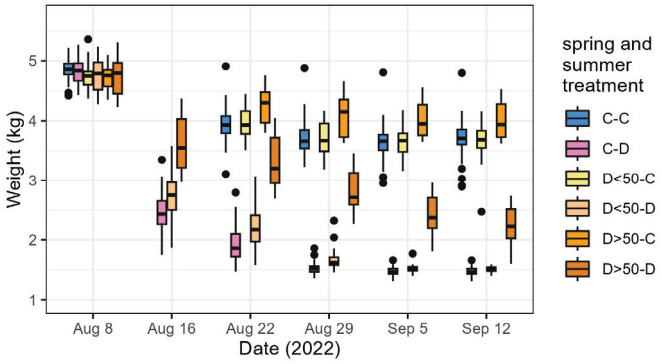

Figure 4. Box plot presenting weight of the pots during the summer drought treatment for the six different combinations of the two consecutive treatments, i.e., C-C: control–control, C-D: control–drought, D<50-C and D<50-D: less than half of leaves desiccated due to the spring drought followed by control or drought, D>50-C and D>50-D: more than half of leaves desiccated due to the spring drought followed by control or drought.

The control–drought saplings (C-D) and the drought–drought saplings with less than half of their leaves desiccated due to the spring drought (D<50-D) developed symptoms before the end of the summer treatment (Figures S1 and 5). The difference in the onset of visual drought symptoms between C-D and D<50-D was significant (Table S7), with the D<50-D group displaying visual drought symptoms 3.3 days later. The saplings on which more than half of the leaves had desiccated due to the spring drought, as well as those in the drought group of the summer treatment, did not display any drought symptoms by the end of the summer treatment (D>50-D in Figure 5). Therefore, it could be deduced that the onset of visual drought symptoms in this group would have taken place more than 17 days later than in the C-D group.

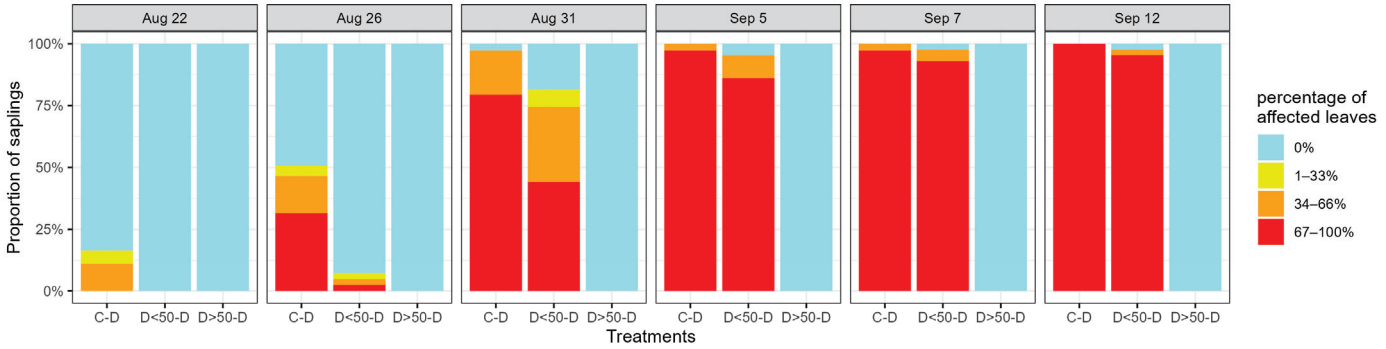

Figure 5. Development of visual drought symptoms during the summer drought treatment for the saplings that were in the control group (C-D) during the spring treatment and in the drought group with less (D<50-D) or more (D>50-D) than half of their leaves desiccated due to the spring drought.

3.3. Timing of Autumnal Leaf Senescence

The timing of leaf senescence was studied based on two methods: measurements of relative chlorophyll content in the leaves and visual observations of leaf decoloration. When comparing the relative chlorophyll content before and after the summer drought period, the two groups of saplings with more than half of their leaves desiccated due to the spring drought (D>50-C and D>50-D) showed a rise in relative chlorophyll content whereas the control–control group showed a decline (significant interaction terms between the date,

i.e., September 26, and treatment groups are shown in Table S6, Figure 6). When looking at the change in relative chlorophyll content after the summer treatment, the saplings that had more than half of their leaves desiccated due to the spring drought (D>50-C and D>50-D) displayed a diminishment that was less steep in comparison to the C-C group (significant interaction terms between the date, i.e., October 24, and treatment groups are shown in Table S6, Figure 6).

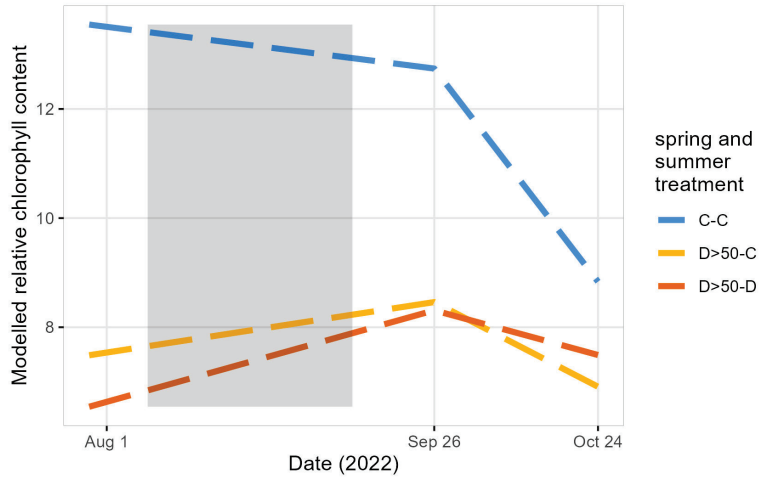

Figure 6. The modeled relative chlorophyll content in the leaves of the saplings before (August 1) and after (September 26 and October 24) the summer treatment. C: control and D: drought group with D>50: more than half of their leaves desiccated due to the spring drought. The summer drought period is indicated in grey. Only treatment groups significantly differing from C-C are shown.

Among the drought–control saplings, the group with less than half of their leaves desiccated due to the spring drought (D<50-C) decolored 3.3 days earlier than the control–control (C-C) group, while the saplings on which more than half of the leaves had desiccated due to the spring drought decolored 7.6 (D>50-C) and 9.3 (D>50-D) days later (Table S8, Figure 7). It should be noted that the D<50-D group lost the majority or all of their leaves due to the summer drought and did not resprout afterwards, and no relative chlorophyll content measurements nor leaf decoloration observations could be performed on this group of saplings.

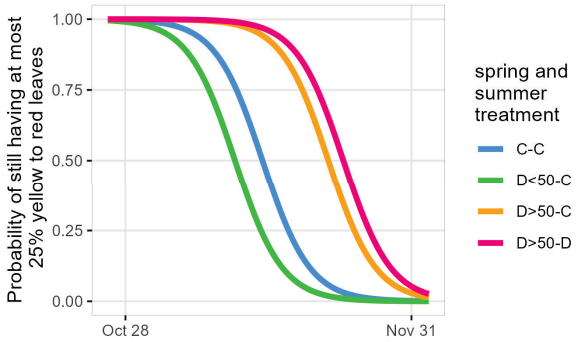

Figure 7. Modeled timing of autumnal leaf decoloration. C: control and D: drought groups with D<50 and D>50: less and more than half of their leaves desiccated due to the spring drought. Only treatment groups significantly differing from C-C are shown.

3.4. Changes in Height and Diameter

The spring drought caused a smaller height increment between May 23 and August 1 in the group of saplings with less than half of their leaves desiccated due to the spring drought (D<50) compared to the controls (C), while the height of saplings with more than

half of their leaves desiccated (D>50) was reduced due of the top parts dying off (Figure 8a, significant treatment groups are shown in Table S9). During the summer drought, we observed no change in height between August 1 and April 25, 2023 in the control–control group (C-C) and several treatment groups (D<50-C, D>50-C and D>50-D) (no significant treatment groups in Table S9), while sapling height decreased in the control–drought group (C-D) and in the drought–drought group with less than half of their leaves desiccated due to the spring drought (D<50-D) due to the top parts dying off (Figure 8b, significant treatment groups are shown in Table S9).

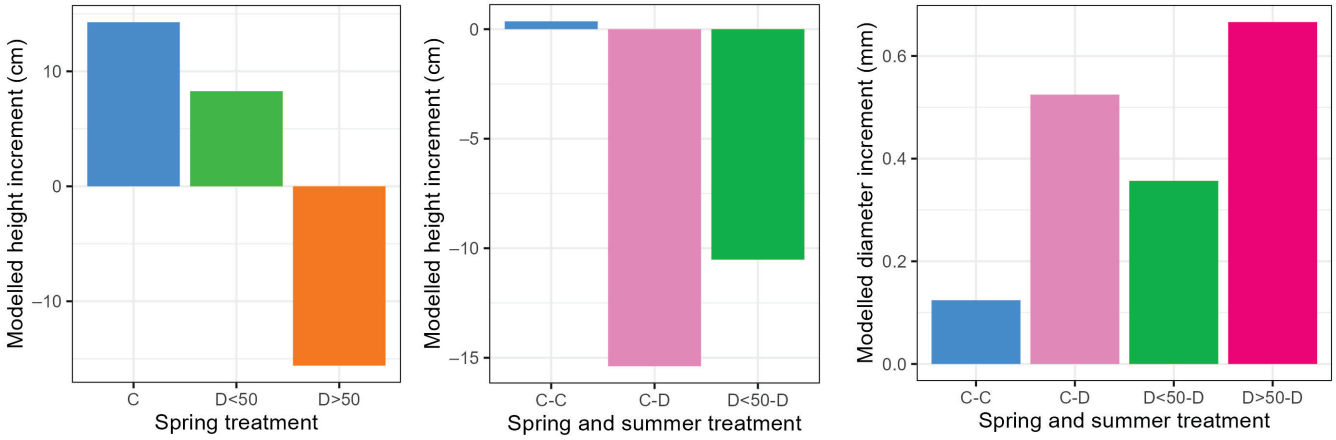

Figure 8. Modeled sapling height increment for the spring treatment (between May 23 and August 1) (**a**), for the summer treatment (between August 1 and April 25, 2023) (**b**) and modeled diameter increment for the summer treatment (between August 1 and December 26) (**c**). The saplings are in a control (C) or drought (D) group in the spring or spring and summer treatments (separated by a hyphen) and have less or more than half of their leaves desiccated due to the spring drought (D<50 or D>50). Only groups that differed significantly from the control (**a**) or control–control group (**b**,**c**) are shown.

The spring drought did not cause significantly larger or smaller diameter increments (between May 23 and August 1) for the different treatment groups in comparison to the control (no significant treatment groups in Table S9). Interestingly, all the sapling groups that experienced drought in the summer treatment (C-D, D<50-D and D>50-D) displayed a larger diameter increment (between August 1 and December 26) in comparison to the C-C group (Figure 8c, significant treatment groups are shown in Table S9). The modeled diameter increment during the second part of the growing season, i.e., after August 1, was 17% of the diameter increment of the entire growing season for the control saplings (group C-C), 47% for the saplings that only experienced the summer drought (group C-D), 31% for the saplings with less than half of their leaves desiccated after the spring drought and subjected to the summer drought (group D<50-D) and 65% for the saplings that were deeply affected by the spring drought and subjected to the summer drought (D>50-D).

Six out of the seven saplings that were not alive anymore in the spring of 2023 belonged to the control–drought group (C-D). The deceased saplings displayed a larger diameter increment than the C-C group between August 1 and December 26 (Figure S2, significant treatment group in Table S10), similar to the surviving saplings in the C-D group.

3.5. Summary Modeling Results

The extent of leaf desiccation following the spring drought treatment (D<50 vs. D>50) significantly affected subsequent processes, including the likelihood of new shoot formation during the recovery phase, the onset of visual drought symptoms in the summer treatment,

changes in relative chlorophyll content throughout the growing season, the timing of autumnal leaf senescence and the occurrence of partial stem dieback and growth reduction (Figure 9). Notably, diameter growth was stimulated by the summer drought treatment, regardless of whether saplings had experienced drought in the spring treatment (Figure 9).

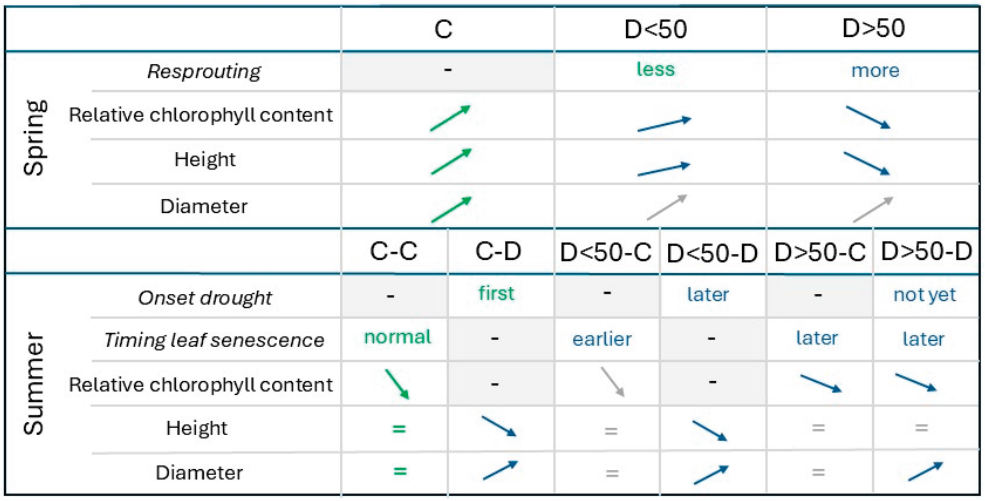

Figure 9. Schematic representation of the results from the modeling of the response variables for the spring and summer treatments. The saplings were in a control (C) or drought group (D) in the spring treatment or in the combined spring and summer treatment (separated by a hyphen). The spring drought caused less than half or more than half of the leaves to desiccate (D<50 or D>50). Italic: response variable specific to either the spring or summer treatment; grey background: not measured; arrows: increase or decrease; equality sign: no change; green: standard group to which the others are compared; blue: significantly different from the standard group; grey: no significant difference with regard to the standard group.

4. Discussion

Leaf wilting and shedding are commonly observed responses of *F. sylvatica* to water shortage during the growing season [16,32]. In our experiment, the wilting and curling of the first leaves indicated the onset of a rapid progression towards wilting in the majority of sapling leaves, as evident in the spring and summer drought treatments.

4.1. Post-Drought Resprouting

The phenomenon of post-drought resprouting has been well-documented across various woody species [20,24]. Resprouting, whether after drought or fire, appears to be influenced more by the severity of the stress rather than by the type of stress [17,18,20]. In our experiment, we observed a correlation between the formation of new shoots in saplings following the spring drought and the degree of leaf loss due to desiccation. Saplings with more than half of their leaves desiccated exhibited significantly higher rates of resprouting. Interestingly, in the recovery phase after the summer drought treatment, we observed no resprouting. This underscores that a sapling's resprouting capability not only hinges on the severity of drought stress but also on the timing of the drought within the growing season.

Priming, i.e., the process by which a phenotype adapts to environmental pressures, instigates stress memory, which enhances a plant's response to future stress [33,34]. Mild drought stress typically prompts reversible stomatal closure and osmotic regulation without significantly impacting growth or other essential processes [18], whereas intense drought stress, triggering active repair mechanisms and profound metabolic changes, can serve as a priming event, leading to stress memory [17,18]. In our experiment, losing less than half of their foliage to desiccation due to the spring drought may be categorized as mild stress, although it still resulted in a few days' delay in the onset of visual drought symptoms

during the summer drought compared to the control–drought group (i.e., D<50-D vs. C-D). Losing more than half of their foliage due to the spring drought caused a delay in symptom onset that was at least five times longer during the summer drought (D>50-D vs. C-D). The ability to withstand the summer drought hence depended on the level of stress experienced in the spring drought. It can be hypothesized that saplings with extensive post-drought leaf desiccation in spring (D>50) achieved stomatal closure during the summer drought earlier than the saplings that were in the control group during the spring treatment (C-D). Previous studies on beech saplings have indicated that stomatal conductance remains reduced following severe drought, thereby enhancing intrinsic water use efficiency [35].

4.2. Timing of Autumnal Leaf Senescence

Following the summer treatment, the relative chlorophyll content in saplings with more than half of their leaves desiccated due to the spring drought (D>50-C and D>50-D) remained lower than in the double control group (C-C). As these saplings resprouted, newly formed leaves most probably did not have sufficient time to develop higher levels of chlorophyll content. However, the rate of decrease in chlorophyll content was significantly slower in these saplings compared to the double control group. This trend continued in autumnal leaf decoloration. Saplings heavily impacted by the spring drought (D>50-C and D>50-D) exhibited delayed autumnal leaf senescence. This post-drought delay in leaf senescence has already been documented in *F. sylvatica* [21,22], as well as in other species such as *Quercus petraea* (Matt.) Liebl. and *Frangula alnus* Mill. [30,36]. Delayed leaf senescence may prolong photosynthesis, potentially compensating for carbon losses caused by drought and aiding in a plant's recovery [22]. In contrast, saplings in which less than half of the leaves desiccated due to the spring drought and which were in the control group during the summer treatment (D<50-C) exhibited significantly earlier leaf decoloration compared to saplings that experienced no drought (C-C). Both earlier and later timing of autumnal leaf senescence in the same experiment has already been documented in a controlled drought experiment on *Cornus sanguinea* L. [24]. In the study, *C. sanguinea* saplings with minimal to no visual drought symptoms exhibited earlier senescence compared to control saplings. Conversely, saplings displaying pronounced visual symptoms experienced a delayed senescence, while those with intermediate symptoms did not show any significant deviation from the control group. These contrasting trajectories of post-drought leaf senescence, observed in our experiment with *F. sylvatica*, corroborate the findings in the *C. sanguinea* study. It was already hypothesized that these observations may concern a trade-off between risk-minimizing acclimation (resulting in earlier senescence) and life-saving repair of drought-induced injuries (leading to later senescence) [18].

4.3. Drought Affects Sapling Size

The extent of leaf desiccation resulting from the spring drought had a significant impact on sapling height. Those with more than half of their leaves desiccated (D>50) were shorter after the spring drought due to the loss of the upper parts of their stems. The summer treatment impacted the height of the saplings in the D<50-D and C-D groups, similarly resulting in reduced height. Partial crown dieback following drought is common in adult *F. sylvatica* trees [16]. More interestingly, all saplings subjected to drought during the summer treatment (C-D, D<50-D and D>50-D) displayed a higher diameter increment in the later part of the growing season, from before the summer treatment until the season's end, compared to the control group (C-C). In climatologically normal years, adult *F. sylvatica* tress typically exhibit peak radial growth around the end of May or the beginning of June [37]. By the end of June, these trees have completed approximately three-quarters of their annual radial growth [38]. Cambial cell divisions typically cease by the end of July or

mid-August [38,39]. It can be hypothesized that in our experiment, the late-season radial growth represented a specific response to hydraulic impairment. Research has suggested that the primary response to hydraulic impairment in trees is the regeneration of the xylem through active vascular cambium [40] and not the refilling of embolized conduits [4]. Interestingly, the six saplings from the C-D group that did not survive the experiment also exhibited late-season radial growth, suggesting that they did not die from hydraulic impairment caused by the summer drought but rather from carbon starvation resulting from the demands of the post-drought radial growth repair [41].

5. Conclusions

The timing of the drought events within the growing season significantly influenced the recovery through resprouting, growth and the timing of autumnal leaf senescence in *F. sylvatica* saplings. Our results suggest stress memory, particularly when saplings experienced significant foliage loss due to spring drought. Earlier leaf senescence (e.g., 3 days earlier for a group of saplings that experienced spring drought) can be viewed as an acclimation strategy aimed at preventing impairments from putative new drought events. Delayed leaf senescence (e.g., 7 days later and longer for different groups of drought-treated saplings) likely provided essential time for recovery from drought-induced damage. This result likely reflects a trade-off between minimizing risks and prioritizing necessary life-saving repair processes. Saplings subjected to summer drought did not resprout but formed additional secondary xylem: they performed up to 65% of their diameter increment in the second part of the growing season compared to 17% for the control plants. Our findings contribute to a deeper understanding of forest responses to the anticipated increase in drought frequency.

Supplementary Materials: The following supporting information can be downloaded at: https://www.mdpi.com/article/10.3390/f16010005/s1, Figure S1: Timing and number of saplings that were taken out of the summer drought treatment and were rewatered, according to the spring and summer treatments. C-D: control–drought; D<50-D and D>50-D: drought–drought with plants with less and more than half of their leaves desiccated due to the spring drought; Figure S2: Boxplot for the diameter increment between August 1 and December 26, according to both treatments and whether plants survived the subsequent winter or not. C-C: control–control; C-D: control–drought; D-C: drought–control; D-D: drought–drought; Table S1: The ten provenances of *Fagus sylvatica* (l = local, nl = non-local) with the number of saplings (n); Table S2: Spring treatment. Number of saplings in the treatment groups (control and drought) and only for the droughted saplings: rewatered two days early (June 13), one day early (June 14) and on the last day of the treatment. Provenance codes in Table S1; Table S3: Summer treatment. Number of saplings in the treatment groups, with C control and D drought during the spring and summer drought treatments. Provenance codes in Table S1; Table S4: Summer treatment. Number of saplings rewatered two to nineteen days before the end of the treatment (September 12) in the control–drought group (C-D) and in the drought–drought group, in which the saplings showed less than 50% leaf desiccation due to the spring drought (D<50-D). All saplings of the drought–drought group with more than 50% leaf desiccation were rewatered on September 12. Provenance codes in Table S1; Table S5: Test statistics for the modeling of resprouting after the spring treatment (only droughted plants). A leaf desiccation (DES) score of 1 (no leaves desiccated) is the standard to which the other scores are compared. H_{spring} is the initial height on May 23; Table S6: Test statistics for the modeling of the relative chlorophyll content at the spring and summer treatments. The controls in the spring (C) and summer (C-C) treatments are the standard to which the other groups are compared, with D<50 being the droughted plants with less than half of their leaves desiccated due to the spring drought and D>50 being those with more than half. H_{spring} and H_{summer} are the initial heights for the spring and summer treatments. For the time variable in the spring treatment, May 23 is the standard to which July 4 and July 18 are compared. For the time

variable in the summer treatment, August 1 is the standard to which September 26 and October 24 are compared; Table S7: Test statistics for the modeling of the onset of visual drought symptoms in the summer treatment. Control–drought (C-D) is the standard to which the group of saplings with less than half of their leaves desiccated due to the spring drought (D<50-D) is compared. DAY is the day of observation, H_{summer} is the initial height on August 1; Table S8: Test statistics for the modeling of the timing of autumnal leaf decoloration. The control–control group is the standard to which the other treatment groups are compared. The two succeeding treatments are coded with C as control, D as drought, D<50 as drought with less than half of the leaves desiccated due to the spring drought and D>50 as more than half. DAY is the day of observation; Table S9: Test statistics for the modeling of height and diameter increments for the spring and summer treatments. The controls in the spring (C) and summer (C-C) treatments are the standard to which the other treatment groups are compared, with D<50 being the droughted saplings with less than half of their leaves desiccated due to the spring drought and D>50 being those with more than half. H_{spring} and H_{summer} are the initial heights on May 23 and August 1, respectively, in the height increment models, and D_{spring} and D_{summer} are the initial diameters on May 23 and August 1, respectively, in the diameter increment models; Table S10: Test statistics for the modeling of the diameter increment for the summer treatment. Included are the control–control (C-C), surviving saplings in the control–drought (C-Ds) and deceased saplings in the control–drought (C-Dd) groups. The C-C group is the standard to which the other groups are compared. D_{summer} is the initial diameter on August 1.

Author Contributions: Conceptualization, K.V.M., S.M., L.D.K., A.T. and M.V.; methodology, K.V.M., M.B., S.M., E.N.P., K.V., L.D.K., A.T., S.V. and M.V.; formal analysis, K.V.M., M.B. and M.V.; investigation, K.V.M., M.B., S.M., E.N.P., K.V. and S.V.; data curation, K.V.M. and M.B.; writing—original draft preparation, K.V.M. and M.B.; writing—review and editing, K.V.M., M.B., E.N.P., K.V., L.D.K., A.T., S.V. and M.V.; supervision, K.V.M. and M.V. All authors have read and agreed to the published version of the manuscript.

Funding: This research received no external funding.

Data Availability Statement: The dataset for this study is available at https://doi.org/10.5281/zenodo.10912281 (accessed on 3 April 2024).

Acknowledgments: We extend our gratitude to Marc Schouppe and Nico De Regge for their diligent care of the saplings, as well as to the Research Institute for Agriculture and Fisheries in Melle (Belgium) for providing essential infrastructure support. Special thanks also for Samuel Van de Walle for his invaluable assistance with data collection during the spring drought treatment, Tom Huysmans for his support during the summer drought treatment and Milan Van Reybrouck and Joren Dierckxsens for helping with the measurements.

Conflicts of Interest: The authors declare no conflicts of interest.

References

1. Pan, Y.; Birdsey, R.A.; Fang, J.; Houghton, R.; Kauppi, P.E.; Kurz, W.A.; Phillips, O.L.; Shvidenko, A.; Lewis, S.L.; Canadell, J.G.; et al. A Large and Persistent Carbon Sink in the World's Forests. *Science* **2011**, *333*, 988–993. [CrossRef] [PubMed]
2. Bonan, G.B. Forests and climate change: Forcings, feedbacks, and the climate benefits of forests. *Science* **2008**, *320*, 1444–1449. [CrossRef]
3. Reichstein, M.; Bahn, M.; Ciais, P.; Frank, D.; Mahecha, M.D.; Seneviratne, S.I.; Zscheischler, J.; Beer, C.; Buchmann, N.; Frank, D.C.; et al. Climate extremes and the carbon cycle. *Nature* **2013**, *500*, 287–295. [CrossRef] [PubMed]
4. Choat, B.; Brodribb, T.J.; Brodersen, C.R.; Duursma, R.A.; López, R.; Medlyn, B.E. Triggers of tree mortality under drought. *Nature* **2018**, *558*, 531–539. [CrossRef]
5. Trenberth, K.E.; Dai, A.; van der Schrier, G.; Jones, P.D.; Barichivich, J.; Briffa, K.R.; Sheffield, J. Global warming and changes in drought. *Nat. Clim. Change* **2014**, *4*, 17–22. [CrossRef]
6. Munne-Bosch, S.; Alegre, L. Die and let live: Leaf senescence contributes to plant survival under drought stress. *Funct. Plant Biol.* **2004**, *31*, 203–216. [CrossRef] [PubMed]
7. Martin-StPaul, N.; Delzon, S.; Cochard, H. Plant resistance to drought depends on timely stomatal closure. *Ecol. Lett.* **2017**, *20*, 1437–1447. [CrossRef] [PubMed]

8. Blackman, C.J.; Creek, D.; Maier, C.; Aspinwall, M.J.; Drake, J.E.; Pfautsch, S.; O'Grady, A.; Delzon, S.; Medlyn, B.E.; Tissue, D.T.; et al. Drought response strategies and hydraulic traits contribute to mechanistic understanding of plant dry-down to hydraulic failure. *Tree Physiol.* **2019**, *39*, 910–924. [CrossRef] [PubMed]
9. Blackman, C.J.; Brodribb, T.J.; Jordan, G.J. Leaf hydraulics and drought stress: Response, recovery and survivorship in four woody temperate plant species. *Plant Cell Environ.* **2009**, *32*, 1584–1595. [CrossRef]
10. Cardoso, A.A.; Batz, T.A.; McAdam, S.A.M. Xylem Embolism Resistance Determines Leaf Mortality during Drought in Persea americana. *Plant Physiol.* **2020**, *182*, 547–554. [CrossRef]
11. Hochberg, U.; Windt, C.W.; Ponomarenko, A.; Zhang, Y.-J.; Gersony, J.; Rockwell, F.E.; Holbrook, N.M. Stomatal Closure, Basal Leaf Embolism, and Shedding Protect the Hydraulic Integrity of Grape Stems. *Plant Physiol.* **2017**, *174*, 764–775. [CrossRef] [PubMed]
12. Wolfe, B.T.; Sperry, J.S.; Kursar, T.A. Does leaf shedding protect stems from cavitation during seasonal droughts? A test of the hydraulic fuse hypothesis. *New Phytol.* **2016**, *212*, 1007–1018. [CrossRef] [PubMed]
13. Vilagrosa, A.; Bellot, J.; Vallejo, V.R.; Gil-Pelegrin, E. Cavitation, stomatal conductance, and leaf dieback in seedlings of two co-occurring Mediterranean shrubs during an intense drought. *J. Exp. Bot.* **2003**, *54*, 2015–2024. [CrossRef] [PubMed]
14. Schuldt, B.; Buras, A.; Arend, M.; Vitasse, Y.; Beierkuhnlein, C.; Damm, A.; Gharun, M.; Grams, T.E.E.; Hauck, M.; Hajek, P.; et al. A first assessment of the impact of the extreme 2018 summer drought on Central European forests. *Basic Appl. Ecol.* **2020**, *45*, 86–103. [CrossRef]
15. Marchin, R.; Zeng, H.; Hoffmann, W. Drought-deciduous behavior reduces nutrient losses from temperate deciduous trees under severe drought. *Oecologia* **2010**, *163*, 845–854. [CrossRef] [PubMed]
16. Walthert, L.; Ganthaler, A.; Mayr, S.; Saurer, M.; Waldner, P.; Walser, M.; Zweifel, R.; von Arx, G. From the comfort zone to crown dieback: Sequence of physiological stress thresholds in mature European beech trees across progressive drought. *Sci. Total Environ.* **2021**, *753*, 141792. [CrossRef] [PubMed]
17. Ruehr, N.K.; Grote, R.; Mayr, S.; Arneth, A. Beyond the extreme: Recovery of carbon and water relations in woody plants following heat and drought stress. *Tree Physiol* **2019**, *39*, 1285–1299. [CrossRef] [PubMed]
18. Gessler, A.; Bottero, A.; Marshall, J.; Arend, M. The way back: Recovery of trees from drought and its implication for acclimation. *New Phytol.* **2020**, *228*, 1704–1709. [CrossRef] [PubMed]
19. Ingrisch, J.; Bahn, M. Towards a Comparable Quantification of Resilience. *Trends Ecol. Evol.* **2018**, *33*, 251–259. [CrossRef]
20. Zeppel, M.J.B.; Harrison, S.P.; Adams, H.D.; Kelley, D.I.; Li, G.; Tissue, D.T.; Dawson, T.E.; Fensham, R.; Medlyn, B.E.; Palmer, A.; et al. Drought and resprouting plants. *New Phytol.* **2015**, *206*, 583–589. [CrossRef] [PubMed]
21. Arend, M.; Sever, K.; Pflug, E.; Gessler, A.; Schaub, M. Seasonal photosynthetic response of European beech to severe summer drought: Limitation, recovery and post-drought stimulation. *Agric. For. Meteorol.* **2016**, *220*, 83–89. [CrossRef]
22. Pflug, E.E.; Buchmann, N.; Siegwolf, R.T.W.; Schaub, M.; Rigling, A.; Arend, M. Resilient Leaf Physiological Response of European Beech (*Fagus sylvatica* L.) to Summer Drought and Drought Release. *Front. Plant Sci.* **2018**, *9*, 187. [CrossRef] [PubMed]
23. Vander Mijnsbrugge, K.; Malanguis, J.M.; Moreels, S.; Lauwers, A.; Thomaes, A.; De Keersmaeker, L.; Vandekerkhove, K. Growth Recovery and Phenological Responses of Juvenile Beech (*Fagus sylvatica* L.) Exposed to Spring Warming and Late Spring Frost. *Forests* **2021**, *12*, 1604. [CrossRef]
24. Vander Mijnsbrugge, K.; Vandepitte, J.; Moreels, S.; Mihaila, V.-V.; De Ligne, L.; Notivol, E.; Van Acker, J.; Van den Bulcke, J. Timing of autumnal leaf senescence in a common shrub species depends on the level of preceding summer drought symptoms. *Environ. Exp. Bot.* **2023**, *216*, 105539. [CrossRef]
25. R_Core_Team. *R: A Language and Environment for Statistical Computing*; R Foundation for Statistical Computing: Vienna, Austria, 2022.
26. Bates, D.; Machler, M.; Bolker, B.M.; Walker, S.C. Fitting Linear Mixed-Effects Models Using lme4. *J. Stat. Softw.* **2015**, *67*, 1–48. [CrossRef]
27. Christensen, R.H.B. Ordinal: Regression Models for Ordinal Data. R Package Version 2015.6-28. 2015. Available online: http://www.cran.r-project.org/package=ordinal/ (accessed on 12 April 2018).
28. Wickham, H. *ggplot2: Elegant Graphics for Data Analysis*; Springer: New York, NY, USA, 2016.
29. Zuur, A.; Ieno, E.; Walker, N.; Saveliev, A.; Smith, G. *Mixed Effects Models and Extensions in Ecology with R*; Springer: New York, NY, USA, 2009.
30. Vander Mijnsbrugge, K.; Turcsan, A.; Maes, J.; Duchene, N.; Meeus, S.; Steppe, K.; Steenackers, M. Repeated Summer Drought and Re-watering during the First Growing Year of Oak (*Quercus petraea*) Delay Autumn Senescence and Bud Burst in the Following Spring. *Front. Plant Sci.* **2016**, *7*, 419. [CrossRef] [PubMed]
31. Mariën, B.; Dox, I.; De Boeck, H.J.; Willems, P.; Leys, S.; Papadimitriou, D.; Campioli, M. Does drought advance the onset of autumn leaf senescence in temperate deciduous forest trees? *Biogeosciences* **2021**, *18*, 3309–3330. [CrossRef]
32. Leuschner, C. Drought response of European beech (*Fagus sylvatica* L.)—A review. *Perspect. Plant Ecol. Evol. Syst.* **2020**, *47*, 125576. [CrossRef]

33. Hilker, M.; Schmülling, T. Stress priming, memory, and signalling in plants. *Plant Cell Environ.* **2019**, *42*, 753–761. [CrossRef]
34. Walter, J.; Jentsch, A.; Beierkuhnlein, C.; Kreyling, J. Ecological stress memory and cross stress tolerance in plants in the face of climate extremes. *Environ. Exp. Bot.* **2013**, *94*, 3–8. [CrossRef]
35. Gallé, A.; Feller, U. Changes of photosynthetic traits in beech saplings (*Fagus sylvatica*) under severe drought stress and during recovery. *Physiol. Plant.* **2007**, *131*, 412–421. [CrossRef] [PubMed]
36. Vander Mijnsbrugge, K.; De Clerck, L.; Van der Schueren, N.; Moreels, S.; Lauwers, A.; Steppe, K.; De Ligne, L.; Campioli, M.; Van den Bulcke, J. Counter-Intuitive Response to Water Limitation in a Southern European Provenance of *Frangula alnus* Mill. in a Common Garden Experiment. *Forests* **2020**, *11*, 1186. [CrossRef]
37. Puchalka, R.; Prislan, P.; Klisz, M.; Koprowski, M.; Gricar, J. Tree-ring formation dynamics in *Fagus sylvatica* and *Quercus petraea* in a dry and a wet year. *Dendrobiology* **2024**, *91*, 1–15. [CrossRef]
38. Čufar, K.; Prislan, P.; de Luis, M.; Gričar, J. Tree-ring variation, wood formation and phenology of beech (*Fagus sylvatica*) from a representative site in Slovenia, SE Central Europe. *Trees* **2008**, *22*, 749–758. [CrossRef]
39. Martinez del Castillo, E.; Longares, L.A.; Gričar, J.; Prislan, P.; Gil-Pelegrín, E.; Čufar, K.; de Luis, M. Living on the Edge: Contrasted Wood-Formation Dynamics in *Fagus sylvatica* and *Pinus sylvestris* under Mediterranean Conditions. *Front. Plant Sci.* **2016**, *7*, 370. [CrossRef] [PubMed]
40. Brodribb, T.J.; Bowman, D.J.; Nichols, S.; Delzon, S.; Burlett, R. Xylem function and growth rate interact to determine recovery rates after exposure to extreme water deficit. *New Phytol.* **2010**, *188*, 533–542. [CrossRef]
41. Trugman, A.T.; Detto, M.; Bartlett, M.K.; Medvigy, D.; Anderegg, W.R.L.; Schwalm, C.; Schaffer, B.; Pacala, S.W. Tree carbon allocation explains forest drought-kill and recovery patterns. *Ecol. Lett.* **2018**, *21*, 1552–1560. [CrossRef]

Disclaimer/Publisher's Note: The statements, opinions and data contained in all publications are solely those of the individual author(s) and contributor(s) and not of MDPI and/or the editor(s). MDPI and/or the editor(s) disclaim responsibility for any injury to people or property resulting from any ideas, methods, instructions or products referred to in the content.

climate

MDPI

Review

Changes in Climate and Their Implications for Cattle Nutrition and Management

Bashiri Iddy Muzzo *, R. Douglas Ramsey and Juan J. Villalba

Department of Wildland Resources, Quinney College of Natural Resources, Utah State University, Logan, UT 84322-5230, USA; doug.ramsey@usu.edu (R.D.R.); juan.villalba@usu.edu (J.J.V.)
* Correspondence: iddy.muzzo@usu.edu

Abstract: Climate change is a global challenge that impacts rangeland and pastureland landscapes by inducing shifts in temperature variability, precipitation patterns, and extreme weather events. These changes alter soil and plant conditions, reducing forage availability and chemical composition and leading to nutritional stress in cattle. This stress occurs when animals lack adequate water and feed sources or when these resources are insufficient in quantity, composition, or nutrient balance. Several strategies are essential to address these impacts. Genetic selection, epigenetic biomarkers, and exploration of epigenetic memories present promising avenues for enhancing the resilience of cattle populations and improving adaptation to environmental stresses. Remote sensing and GIS technologies assist in locating wet spots to establish islands of plant diversity and high forage quality for grazing amid ongoing climate change challenges. Establishing islands of functional plant diversity improves forage quality, reduces carbon and nitrogen footprints, and provides essential nutrients and bioactives, thus enhancing cattle health, welfare, and productivity. Real-time GPS collars coupled with accelerometers provide detailed data on cattle movement and activity, aiding livestock nutrition management while mitigating heat stress. Integrating these strategies may offer significant advantages to animals facing a changing world while securing the future of livestock production and the global food system.

Keywords: epigenetics; plant diversity; plant secondary compounds; GIS and remote sensing; water quality

1. Introduction

Climate change is widely considered the most significant global challenge of the 21st century, with its impact being experienced worldwide (recent long-term shifts in temperature, precipitation patterns, and the frequency and intensity of extreme weather events). The primary cause of climate change is the greenhouse effect, which occurs when gases such as carbon dioxide, methane, and nitrous oxide in the Earth's atmosphere act like the glass in a greenhouse, trapping the sun's heat and preventing it from escaping into space, leading to global warming [1]. Human activities, including industries, burning of fossil fuels, and deforestation, are the primary drivers of climate change, with carbon dioxide emissions being the largest contributor. Among these, the energy sector is the largest contributor, followed by transportation, manufacturing, agriculture, and forestry [2]. As of 2020, the concentration of CO_2 in the atmosphere has increased by 48% above pre-industrial levels (before 1750) [2]. Although other greenhouse gases such as methane and nitrous oxide are emitted in smaller quantities by human activities such as livestock farming, they still contribute to global warming over different timescales. Moreover, non-greenhouse gas pollutants such as soot have varying warming and cooling effects and can

affect air quality. Soon et al. [3] reveal that natural causes such as changes in solar radiation or volcanic activity are estimated to have contributed much less to global warming between 1890 and 2010 than human activities. Moreover, combined human and natural drivers have been shown to have a greater influence on long-term increases in global temperature [4].

The increase of atmospheric greenhouse gases not only leads to rising sea levels and more frequent extreme weather events but also leads to changes in ecological communities [5]. Climate change indirectly affects agricultural systems, particularly livestock production. Cattle, as an essential source of food and income for millions of people worldwide, are expected to face significant challenges as the global demand for beef and dairy products is projected to rise in the coming decades [6]. As a result of climate changes, cattle are expected to face significant challenges, with nutritional stress being one of the most critical factors affecting their health and productivity. Forage is an important component of the beef and dairy industry, playing a vital role in human livelihoods and food security. Climate change has the potential to adversely impact forage nutritive value and quantity through alterations in precipitation patterns, temperature, extreme weather events [7], and plant distribution and abundance [8], as well as through reductions in forage accessibility. Changes in rainfall patterns resulting from climate change, including shifts in timing and intensity, have significant implications for plant growth. These changes ultimately affect the quantity and quality of forage. In semi-arid climates, increased rainfall can provide the necessary moisture for plants to thrive, resulting in enhanced productivity and greater forage quantity. Moreover, increased rainfall in these regions has been found to promote plant diversity, which contributes to a more balanced diet for grazing animals through improvements in overall forage quality [9]. However, increased rainfall in humid climates may have the opposite effect, leading to a reduction in forage quantity and quality. Excess water can result in waterlogging, which can damage plant roots and impede nutrient uptake, decreasing productivity and forage quality [10].

Changes in temperature due to climate change can also affect the quality and quantity of cattle forage. Higher temperatures during the growing period can lead to increased plant growth and productivity, resulting in greater forage quantity [11]. However, prolonged temperatures can lead to drought, which may reduce both the quantity and quality of forage by accelerating plant maturity, stunting growth, and increasing plant die-off [12]. Additionally, high temperatures can cause heat stress in livestock, resulting in reduced feed intake and weight gain [13]. On the other hand, a decrease in temperatures due to climate change can lead to shorter growing seasons and a delay in the onset of plant growth, potentially leading to decreased forage quantity [14]. Cold temperatures can also reduce the digestibility of forage and its quality as a feed source for livestock [15]. The impact of temperature on forage quality and quantity can vary depending on the specific plant species and the region in which they are grown. For instance, the same plant species can benefit from increasing temperatures in one area, but not in a different location, whereas in other areas, the quality and quantity of forage may decline as temperatures increase [11]. In Australia, increasing temperatures may benefit certain pasture species such as kikuyu grass (*Pennisetum clandestinum*) in the southeastern region of the country, but it can lead to a decrease in forage quantity and quality in the northern region due to increased water stress [16]. Similarly, in the United States, certain forage species, such as *Sporobolus cryptandrus* and *A. purpurea*, may benefit from both increased temperatures and elevated carbon dioxide levels, leading to increments in forage production [17]. However, other studies have reported that increased temperatures can reduce the nutritional quality of forage species such as alfalfa (*Medicago sativa*) and reduce the growth of cool-season grasses [18]. More frequent extreme weather events due to climate change can lead to an increase in droughts, floods, and wildfires, as reported by [19]. These events can have

significant impacts on forage availability and quality [20,21], as well as on the ability of animals to access forage. Nutritional stress occurs when an animal does not get enough nutrients to maintain its health and productivity, which can happen when an animal does not have access to enough water or high-quality feed, or when the available feed is not well-balanced in terms of nutrient content [7]. This narrative review article describes how climate change impacts cattle nutrition, synthesizing current knowledge on its effects on soil and plant water availability and quality, as well as on cattle health. Furthermore, it explores potential mitigation strategies and proposes practical management approaches to help alleviate the adverse effects of climate change on cattle production systems.

2. Discussion

2.1. Impact of Climate Change on Soil

Soil Microbes and Nutrient Cycling

Climate change has a profound indirect impact on cattle through its effects on soil microbial communities, which are vital for nutrient cycling and availability. Changes in temperature and moisture levels can significantly impact the composition and function of soil microorganisms [22]. Temperature plays a crucial role in shaping microbial communities and their metabolic activities. Research indicated that temperature influences enzyme activity, microbial growth rates, and community composition [23]. Warmer temperatures generally accelerate microbial metabolic rates by increasing enzymatic activity and enhancing organic matter decomposition and nutrient cycling. In contrast, excessively high temperatures can denature enzymes and proteins, reducing microbial activity and potentially leading to cell death [24]. Conversely, lower temperatures slow down microbial metabolic processes, decreasing enzyme activity and nutrient cycling efficiency [25]. Different microbial species have distinct optimal temperature ranges for their growth and shifts in temperature can favor temperature-tolerant species, altering the composition of the community and affecting the decomposition of organic matter and rates of nutrient cycling [26].

Climate change can increase water availability in some regions, providing optimal soil moisture conditions that support microbial activity. Optimal soil moisture levels facilitate microbial activity by ensuring sufficient water for nutrient solubilization and enzyme function [27]. In contrast, dry conditions limit microbial activity due to water scarcity, leading to decreased nutrient cycling [28]. Conversely, waterlogged soils restrict oxygen diffusion, favoring anaerobic processes and potentially shifting microbial communities towards anaerobic species such as denitrifiers and methanogens, impacting nutrient pathways and greenhouse gas production [29,30]. This balance between aerobic and anaerobic microbial processes, influenced by soil moisture levels, significantly affects overall soil function and nutrient cycling dynamics [22]. The highlighted changes in temperature and moisture levels, impacting the composition and function of soil microbes, also substantially influence the breakdown and release of essential forage nutrients such as nitrogen, phosphorus, and potassium. Research conducted by [31] demonstrated that warming and increased nitrogen deposition affected the stability and complexity of soil microbial networks, with warming promoting bacterial network stability and nitrogen addition decreasing it. Additionally, Qiu et al. [32] found that warming reduced fungal abundance but not bacterial abundance, leading to a shift in the microbial community's composition in semi-arid grasslands. Moreover, Wang et al. [33] highlighted the importance of microbial network complexity in driving soil multifunctionality, showing that altered precipitation regimes affected soil functions mediated by microbial communities. These studies collectively emphasize the fundamental role of soil microbes in nutrient cycling processes and the potential consequences of climate change on ecosystem functioning.

Changes in soil nutrient availability, driven by altered microbial activity and plant composition, can affect the concentration of essential micronutrients and minerals in the forage. For instance, shifts in plant species can affect the availability of critical nutrients such as phosphorus and calcium, which are essential for cattle health and productivity, as different plant species have varying abilities to uptake these nutrients from the soil [34]. In conclusion, modifications of plant species composition due to climate change may impact soil nutrient availability, further influencing the nutritional quality and balance of forage accessible to cattle. Alterations in temperature and moisture levels can shift the composition and function of soil microbes, affecting the breakdown and release of essential nutrients such as nitrogen, phosphorus, and potassium [35]. These changes in nutrient cycling can influence plant growth and nutrient content, affecting the forage available to cattle. As the microbial community structure shifts, nutrient utilization and recycling efficiency in the soil ecosystem can be disrupted, potentially leading to nutrient imbalances that compromise plant health and productivity. Bainard et al. [36] reported that increased plant species diversity enhances the soil's nutrient content, potentially mitigating some negative effects of climate change on soil fertility.

2.2. Impact of Climate Change on Forage Plants

2.2.1. Plant Growth, Establishment, and Phenology

Higher temperatures during the growing period can lead to increased plant growth and productivity, resulting in greater forage quantity. A rise in temperature causes an increase in CO_2 concentration levels [37,38]. The relationship between atmospheric CO_2 and temperature can be considered a "hen-or-egg" problem, where it is not always clear which is the cause and which is the effect [39]. However, recent studies suggest that the dominant direction is temperature (T) $\rightarrow$ CO_2, meaning that changes in CO_2 follow changes in temperature [40]. This can be attributed to biochemical reactions, such as increased soil respiration and CO_2 emission at higher temperatures [39]. Photosynthesis, the fundamental process by which green plants convert carbon dioxide and water into organic compounds and oxygen, varies across different plant species and their respective photosynthetic pathways C3, C4, and CAM. C3 plants such as fescue and ryegrass grass species rely exclusively on the Calvin cycle for CO_2 assimilation. In contrast, C4 plants such as Bermuda grass and crabgrass follow a typical pathway involving enzymes and a four-carbon compound, exhibiting high photosynthetic rates and a distinct advantage under conditions conducive to high transpiration rates. In the future, increased temperatures with CO_2 levels are expected to favor C4 plants over C3 plants [41]. C4 plants have a more efficient photosynthetic process and are better able to concentrate CO_2, which allows them to thrive in high-CO_2 environments [42]. The increased temperatures are expected to have a negative impact on photosynthesis, particularly in C3 plants [41] as these plants have limited rubisco activity at high temperatures, which can decrease their photosynthetic efficiency [43]. Therefore, under increased temperatures, C4 plants may have a competitive advantage over C3 plants. Overall, the interaction between CO_2 levels and temperature can have different effects on C4 and C3 plants, with elevated CO_2 favoring C4 plants and increased temperatures potentially favoring C3 plants. The prolonged increased temperature during sprouting of the forage hastens plant maturity and reduces plant growth and die-off [44]. In this period, temperatures promote stem-over-leaf growth, resulting in lower digestibility of both leaves and stems due to high cell wall concentrations and low soluble sugar concentrations [45]. Moreover, the growth of various organs decreases gradually, leading to weaker plants and a slowdown in growth during summer [46]. Temperature and variety are important factors that modify tuber initiation and growth, with temperature having a considerable influence [47]. Elevated

temperatures can affect seed germination and subsequent seedling vigor, but in the case of fodder tree *Trichilia emetica*, exposure to elevated temperatures did not disrupt metabolic and ultrastructural integrity and may have even improved germinative development and seedling growth rates [48]. While climate change is typically associated with temperature increases, localized cooling can occur in specific regions, such as higher latitudes, elevated altitudes, or as a result of particular atmospheric phenomena such as volcanic eruptions or La Niña events [39].

A decline in temperature due to climate change can result in a shorter growing season, delaying the onset of plant growth and potentially reducing the quantity of overall forage available for grazing. Cold temperatures constrain the time available for active plant growth, slowing down metabolic rates and diminishing nutrient assimilation, ultimately impacting biomass production [49]. The structural changes induced by cold stress can compromise the digestibility of forage, diminishing its quality as a feed source for cattle. These declines in temperature have multifaceted effects on various stages of plant growth and development. Cold temperatures impede metabolic processes during germination and seedling establishment, delaying germination and compromising seedling vigor [50]. In the vegetative stage, plants experience reduced photosynthesis and nutrient uptake, leading to stunted growth as cell expansion and elongation are hindered [51]. Reproductive development is hampered by cold stress during flowering, disrupting pollination and fertilization processes and diminishing seed or fruit production [49]. Cold temperature stress also affects the structural integrity of plant cells, leading to cell membrane fluidity issues and ice crystal formation, causing cellular damage [52]. Plants exhibit metabolic adaptations, such as the accumulation of compatible solutes, to serve as cryoprotectants against freezing temperatures [53]. Some plants also undergo cold acclimation, a process involving physiological changes induced by non-freezing low temperatures, enhancing their tolerance to subsequent cold temperature stress. Phenological shifts in grassland species, influenced by climate change and land use practices, have been extensively studied, revealing species-specific responses to changing environmental conditions [54,55]. These changes in flowering phenology can impact the availability and quality of forage for cattle, with late-flowering species and those with specific functional traits advancing their flowering under future climate conditions, potentially affecting nutrient uptake and storage in plants [55]. Additionally, alterations in precipitation patterns can drive phenological shifts, influencing flower and fruit production in temperate grasslands and ultimately impacting the nutritional quality of forage available to cattle [56]. Furthermore, vegetation phenology, including the start and end of the growing season, responds to climate fluctuations, affecting gross primary productivity and potentially influencing nutrient availability in the soil and the nutritional balance of forage [57].

2.2.2. Plant Species Composition, Forage Biomass, and Nutritional Quality

Climate change causes shifts in plant species composition (PSC), forage biomass production, and nutritional quality. As temperatures rise and precipitation patterns change, the abundance and distribution of plant species adjust, leading to altered competitive dynamics within plant communities [58]. For instance, Liu et al. [59] found that an increase in temperature of 1.2 °C (0.38 per decade) led to increased above-ground net primary productivity (ANPP) in grass, decreased ANPP in sedge, and relatively stable ANPP in forbs. These shifts in species composition can result in changes to the nutrient profile of forages, with forbs generally being high in protein and low in fiber relative to grasses [60]. Studies by Zhang [61] in northern Tibet and Yoshihara [62] in Mongolian drylands demonstrate that warming can lead to an increase in acid detergent fiber (ADF) content and a decrease in digestibility, affecting the overall forage quality of the diet. Petit Bon [63] further highlights

how environmental perturbations can alter plant community nutrient concentrations, with varying effects on different functional plant types. Sebastià [64] reported the significant impact of management practices on forage nutritive value, demonstrating that sainfoin swards managed under different regimes by displaying varying nutrient profiles, with cattle-grazed swards exhibiting a higher nutritional quality that declines faster compared to sheep-grazed or mown swards. Habermann [65] showed that elevated CO_2 levels and warming can synergistically decrease forage digestibility and modify nutrient content, illustrating the intricate interplay between climate change and forage quality in grassland ecosystems. Climate change-induced shifts in PSC directly impact the nutritional quality and abundance of forage available to cattle. Sebastià [64] explained that changes in PSC, including alterations in the relative abundance of grasses, sedges, and forbs, can significantly influence the protein and fiber content of forage, thereby affecting its suitability as a feed source. Furthermore, climate-induced alterations in plant growth cycles and species dominance can lead to variations in forage biomass production, affecting the quantity of feed available for cattle and potentially leading to nutritional stress.

On the other hand, climate change impacts water availability, causing it to become more limited in semi-arid and temperate climates as the probability of summer droughts increases [66]. Forage production is dependent on adequate water supply [67], and soil water deficits typically limit biomass production, particularly in soil types that tend to show low water holding capacities, such as coarse-textured soils [68,69]. Irrigation amends this problem but with the predicted interannual variabilities in rainfall and thus water availability [70], it becomes crucial to better understand the relationship between water inputs and the quantity and quality of the forage produced. For instance, the total alfalfa yield was 100% greater on average for irrigated compared to unirrigated treatments. However, treatments with high levels of irrigation (to bring root zone extractable soil water (ESW) levels to 15% of field capacity at 35% ESW depletion), or with 34% less irrigation than those higher levels, produced similar amounts of forage after four harvests [68]. Despite multiple studies on the negative impacts of soil water availability on forage biomass production, knowledge regarding the influence of drought on important characteristics of the nutritive value of forages is inconsistent and limited [59,71]. In general, perennial forage plants growing under moderate water deficits tend to present greater nutritive quality than those forages grown under irrigation [72], provided that the deficit was not severe and initiated early in the growth of the herbage [73,74]. In contrast, long and extreme drought events due to climate change inhibit tillering and branching, accelerate the death of tillers and the senescence of leaves, and relocate protein, nitrogen, and soluble carbohydrates from leaves to roots, reducing the nutritive value of the forage [73,75,76]. Under moderate water restrictions, in vitro dry matter digestibility (IVDMD) in alfalfa is greater and the contents of cell walls are lower under prolonged water deficits that reduce plant water potential (ψw) than in control plants grown without a water deficit [77]. Improvements in forage quality have been attributed to a greater leaf-to-stem ratio (LSR) in water-stressed plants, given that water stress has the greatest effect on reducing stem growth [77]. Alternatively, the high forage nutritive value in plants grown under a water deficit could be better explained by a retardation of the rate of plant maturation rather than by a differential effect on leaf-to-stem growth [72,73]. In fact, forage quality in alfalfa declines with maturation [78], and the mean maturity stage decreases with increasing water stress [79]. Consistent with this idea, increments of IVDMD in alfalfa have been primarily associated with plant maturity [77]. Nevertheless, the same authors showed that increments in stem crude protein (CP) contents and declines in cellulose concentration in alfalfa stems and leaves under water stress were not fully accounted for by differences in plant maturity. Research on other legumes such as birdsfoot trefoil, sainfoin, clover, and cicer milkvetch shows similar patterns in response

to water stress to those described for alfalfa [69,71], although alfalfa yields tend to be less affected by drought than for the other species. Droughted alternative legumes produced biomass with lower contents of ADF, NDF, and lignin than alfalfa, with birdsfoot trefoil and cicer milkvetch producing the highest-quality forage [69]. Nevertheless, because of its superior yield (and persistence) under drought, it was concluded that alfalfa would produce more nutrients per unit of area than the alternative legumes [69].

2.2.3. Plant Secondary Compounds

Plant secondary metabolites (PSMs) are a diverse group of chemical compounds, including alkaloids, terpenoids, and phenolics, that are not directly involved in essential plant growth but are crucial for the plant's defense against abiotic and biotic stressors [80,81]. These compounds also aid in protecting plants from pathogens, attracting pollinators, and thriving in diverse environmental conditions. PSMs play significant roles in plant communication, ecosystem functioning, and defense responses to stress [82,83]. When plants encounter stressors such as drought or herbivory, specific receptors on the plant cells are activated, signaling the stress and triggering various biochemical pathways. These pathways involve molecules such as calcium ions, reactive oxygen species (ROS), and plant hormones such as jasmonic acid and salicylic acid. These molecules activate transcription factors that upregulate genes responsible for the biosynthesis of PSMs, which are formed by converting primary metabolites into alkaloids, terpenoids, and phenolic compounds [82,84]. For instance, during drought, phenolic compounds such as flavonoids and tannins accumulate in plants as protective mechanisms against oxidative damage and to minimize water loss. Abscisic acid, another plant hormone, helps with water conservation by regulating stomatal closure. In response to herbivore feeding, some plants produce alkaloids, such as nicotine in tobacco, which act as neurotoxins to deter herbivores. Similarly, terpenoids such as menthol in mint release strong odors and flavors to discourage herbivores from feeding [85,86]. In addition to protecting plants from herbivory and stress, certain PSMs, such as condensed tannins, provide benefits beyond plant defense. These compounds can improve livestock productivity by enhancing plant protein utilization and reducing enteric methane emissions [87]. Furthermore, PSMs can benefit soils by increasing carbon sequestration and reducing nitrogen losses [88], while also improving meat and milk quality through reduced fat biohydrogenation and extended shelf life [89]. With the ongoing effects of climate change, the production and accumulation of PSMs in plants are expected to change. A meta-analysis of the effects of global climate change on medicinal and aromatic PSMs revealed that phenolic and terpenoid levels generally increase with elevated carbon dioxide but decrease with higher nitrogen concentrations. Additionally, total alkaloid concentrations increase significantly with higher nitrogen levels.

Elevated temperatures also lead to alterations in plant secondary metabolites (PSMs) in plants, affecting their interactions with herbivores and overall plant performance. Temperature increases can influence both the types and concentrations of PSMs, thereby affecting plant–herbivore interactions and plant defense strategies [90,91]. Moreover, elevated temperatures may increase the concentrations of certain toxic compounds, such as aristolochic acids, which can alter herbivore growth and nutritional intake [91,92]. Such changes in PSM concentrations can have dual effects on herbivores. On the one hand, they may enhance plant resistance to herbivores, but on the other, they may reduce the palatability and nutritional value of forage, which can limit feed intake and affect herbivore health [93,94]. Research by Balluffi-Fry [95] suggests that increased temperatures could elevate PSM levels, potentially improving plant resistance to pests and diseases, but also reduce the overall quality of forage for grazing animals. Certain PSMs can be toxic to cattle, especially when consumed in large quantities, leading to reduced feed intake and potential health prob-

lems [96–98]. As ambient temperatures continue to rise, Beck and Gregorini [99] emphasize the growing challenge of managing livestock diets that reduce PSM content while maintaining adequate protein levels. Furthermore, Villalba and Manteca [100] highlight the importance of identifying areas within grazing landscapes that facilitate heat dissipation, helping livestock manage temperature-related stress. They also stress that animals accustomed to complex landscapes and diverse plant types may have an advantage in adapting to environmental changes.

Changes in rainfall patterns, a critical aspect of climate change, can lead to water deficits, which in turn can affect the concentration of PSMs in plants. Water stress limits photosynthetic activity by disrupting the balance between light capture and utilization, which leads to the generation of ROS. To cope with this, plants activate mechanisms for ROS detoxification, which often involve phenolic compounds, such as tannins, known for their antioxidant properties [101,102]. Consequently, under mild water stress, plants are likely to produce more carbon-based PSMs, such as tannins, due to a higher concentration of carbohydrates. However, as water deficits become more severe, plants reduce their carbon gain, prioritizing primary metabolites over PSMs. This can lead to a decrease in the production of PSMs in more extreme drought conditions [103–105]. The impact of water deficits on PSMs is non-linear and varies depending on the severity of the stress. For instance, condensed tannin concentrations in tanniferous legumes such as *Lotus corniculatus* and *Lotus uliginosus* can either increase, remain stable, or decrease in response to water stress, depending on the degree of water limitation [68,106–108].

PSMs also have an important role in herbivore thermoregulation. The energy required for thermoregulation in mammals such as cattle is derived from their diet, which makes PSMs an important factor in determining their ability to maintain stable body temperatures under varying environmental conditions. Studies have shown that PSMs can interfere with thermoregulation by uncoupling mitochondrial oxidative phosphorylation, thus reducing the available energy for maintaining body temperature. Additionally, the detoxification processes that break down PSMs are thermogenic, meaning they generate additional heat, further challenging animals in warmer conditions. Beale [93] found that PSMs in grazing forage could negatively impact thermoregulation, especially in hotter climates. Supporting studies have shown that temperature affects the tolerance of herbivores to PSMs. For example, Windley and Shimada [109] showed that mice acclimated to cooler temperatures exhibited improved liver function and tannin tolerance when consuming tannin-rich acorns. However, at higher temperatures, liver function decreased, which impaired the detoxification of PSMs. Similarly, Beale [110] observed that temperature influenced the detoxification of PSMs in herbivorous marsupials. The findings indicate that ambient temperatures increase the detoxification burden of herbivores, reducing food intake and making it more difficult for them to manage diets high in PSMs. Longer acclimation periods may be required to fully understand these impacts.

2.3. Impact of Climate Change on Cattle

2.3.1. Heat Stress

Climate change causes an increase or decrease in the frequency and intensity of extreme temperature events, leading to both heat stress (HS) and cold stress in cattle, indirectly affecting their nutritional status. Higher temperatures cause heat stress in cattle, reducing feed intake and digestion efficiency, leading to weight loss and decreased productivity [13]. This decline in productivity during HS is not solely due to reduced feed intake. However, it is also linked to compromised gastrointestinal tract function and increased permeability, allowing antigens to enter the circulation [111]. Consequently, nutrient partitioning shifts to support immune responses, characterized by increased insulin secretion and altered

metabolism in response to the activated immune system, ultimately reducing animal productivity during higher-temperature months [112]. HS has been extensively studied in dairy cows, with findings indicating a significant negative impact on productivity. For instance, Chen [113] conducted a meta-analysis using data from 31 studies (34 trials) and found that HS led to decreased dry matter intake (DMI), energy-corrected milk (ECM), and milk protein concentration, with reductions of 4.13% and 3.25% in DMI and ECM, respectively, for each unit increase in the temperature-humidity index (THI). Additionally, Souza [114] reported that pregnant nonlactating heat-stressed dairy cows experienced reduced DMI as the THI increased, emphasizing the importance of environmental conditions in influencing feed intake. Sammad [115] and Safa [116] reported contrasting results, showing that HS affects metabolic, endocrinological, and inflammatory parameters and alters milk yield, milk composition, and feed efficiency in dairy cows. Furthermore, Antanaitis [117] showed that HS negatively affected behaviors such as rumination and drinking time, showing the detrimental effects of HS on dairy cow health and productivity. Nevertheless, Chen [113] revealed that HS did not affect milk fat concentration or feed efficiency. During moderate-to-severe heat stress, when compared to a thermoneutral period, dairy cows experience a significant decrease in milk production, which can be attributed to a complex interplay of altered metabolic, endocrinological, and inflammatory parameters [13,113]. HS causes physiological changes, including hyperthermia, impacting feed intake and milk yield and ultimately compromising dairy production [118].

Regarding biological responses to HS, Baumgard and Rhoads [111] stated that energy allocation is shifted towards protective mechanisms, diminishing milk production and increasing susceptibility to diseases and mortality in dairy cattle. In beef cattle, HS also poses a significant challenge, particularly during summer in temperate regions and dry seasons in tropical regions, leading to various detrimental effects on animal productivity and well-being. Studies have shown that exposure to heat stress results in elevated rectal temperatures in beef cattle, reduced feed intake, body weight loss, and changes in behavior, such as increased stepping and altered body posture [119,120]. Additionally, heat stress negatively impacts reproductive rates in beef cattle, with pregnancy rates being lower under moderate stress conditions compared to mild stress conditions [121,122]. Heat stress exacerbates the susceptibility of animals to PSCs by disrupting detoxification processes [123], impairing liver and kidney function, and reducing the activity of enzymes involved in metabolizing toxic compounds. This disruption, coupled with heat-induced oxidative stress and increased reactive oxygen species [124], intensifies the harmful effects of PSMs such as tannins and flavonoids, leading to greater cellular damage. Furthermore, heat stress impairs gut function, alters the gut microbiome, and reduces digestion efficiency [125], which might result in higher concentrations of PSMs in the gut in cattle forage containing PSMs. In identifying HS indicators for dairy cows, Chen [126] exhibited that HS can induce changes in blood parameters such as cortisol, glucose, and interleukin-6, with heat-tolerant cows exhibiting lower levels of these indicators compared to heat-sensitive cows. Genetic studies have identified potential genetic markers associated with heat stress tolerance in Chinese Holstein cattle, highlighting genes such as PDZRN4 and PRKG1 as important for this trait [127]. Lemal [128] also explored using sensor data, such as activity and rumination sensors, to evaluate heat stress in dairy cattle, indicating the complexity of the relationship between sensor traits and production traits under heat stress conditions. Cold stress increases the energy requirements of cattle to maintain their body temperature, which can result in higher forage intake. Research on Simmental crossbred bulls exposed to long-term cold stress showed decreased body weight and average daily gain, increased dry matter intake, and altered physiological behaviors, indicating heightened energy demands [129].

2.3.2. Cold Stress

After highlighting the impact of heat stress caused by elevated temperatures, it is equally important to consider cold stress (CS) in cattle. Cold stress occurs when ambient temperatures drop below the animal's thermal comfort zone, leading to physiological challenges in maintaining their core body temperature. Key factors contributing to cold stress include low ambient temperatures, wind chill that exacerbates heat loss, and wet conditions that diminish the insulating properties of an animal's coat. Additionally, cattle with low body condition scores or compromised health, as well as younger animals, are more vulnerable due to insufficient fat insulation and lower metabolic heat production.

CS reduces forage intake as animals prioritize energy conservation over feeding. The mechanism behind this reduced intake involves prioritizing energy expenditure for thermoregulation rather than digestion. Research by Chase [130] indicated that cattle exposed to CS reduced their dry matter intake by approximately 30%, leading to decreased nutrient availability that impacts overall health and productivity. Similarly, a study by Kim [131] found that beef cattle subjected to CS conditions consumed 25% less feed than their counterparts in thermally neutral environments. Conversely, a study by Delfino and Mathison [132] reported that while feed intake decreased, the efficiency of nutrient utilization improved, suggesting that cattle may adapt their feeding behavior under specific CS conditions to optimize energy use. Under cold conditions, the rate of passage of feed through the digestive system may also slow down, affecting nutrient absorption and energy utilization and further diminishing digestive efficiency. For instance, Wang [133] demonstrated that cold-stressed cattle exhibited a significantly slower rate of rumen evacuation, resulting in less efficient digestion and nutrient absorption. A study by Nardone [134] suggested that some cattle could maintain rumen function under mild CS, indicating variability in response based on individual animal factors and environmental conditions. Additionally, Coloma-García [135] indicated that cattle exposed to prolonged cold stress exhibited a 15% decrease in the digestibility of dry matter, emphasizing the impact of cold stress on nutrient absorption. Moreover, cold stress compels cattle to expend more energy to maintain body temperature, leading to decreased activity levels and potential weight loss, which can adversely affect their welfare. The increased energy expenditure can result in an additional caloric requirement of 10–20% during cold weather, which cattle may not compensate for if forage intake is reduced. The consequences of CS extend to milk production, which may decline as the energy required to sustain body temperature detracts from the energy available for lactation, significantly impacting dairy operations during winter months. Berian [136] found that lactating cows exposed to CS experienced a reduction in milk yield compared to cows in thermally neutral conditions. Similarly, a study by Sahib [137] demonstrated that dairy cows subjected to CS had an average drop of 12% in milk production due to increased energy demands for thermoregulation. In beef cattle, research by Wagner [138] indicated that CS led to reduced weight gain in heifers, as those experiencing cold stress consumed approximately 20% less feed compared to control groups, impacting their overall growth rates. In another study, Cantalapiedra-Hijar et al. [139] found that steers exposed to CS conditions exhibited a significant decline in average daily gain, emphasizing the long-term implications of CS on beef production systems. Additionally, a study by Ames [140] reported that beef cattle experiencing cold stress had lower feed efficiency, with a 15% reduction in the conversion of feed to body weight gain. Physiologically, CS can alter critical parameters such as increased heart and respiratory rates, as ruminants work harder to maintain their body temperature, indicating heightened stress levels that may necessitate management interventions. Young [141] found that dairy cows exposed to prolonged CS exhibited increased heart rates, which could be linked to decreased milk yields and altered feeding behavior. Similarly, Lees et al. [142] observed that beef cattle

at different growth stages experienced changes in heart rate, rectal temperature, and dry matter intake under extreme cold stress, emphasizing the increased energy requirements in such conditions. Hence, CS can elevate the energy demands of cattle to maintain body temperatures, potentially driving an increase in forage intake to meet these heightened requirements. In contrast, a study by Colditz and Hine [143] suggested that certain beef cattle breeds demonstrated resilience to CS, maintaining normal heart rates and growth performance despite environmental challenges. By comprehensively addressing these aspects, the discussion of cold stress can be effectively balanced with that of heat stress.

2.3.3. Health

Livestock, especially beef and dairy cattle, are significantly impacted by climate change-induced weather fluctuations, with factors such as rising temperatures, erratic rainfall, and intermittent drought promoting different causative agents of disease, compromising their health. Changes in precipitation patterns, particularly increased intensity and frequency, have an important role in altering the distribution and abundance of vector-borne diseases such as ticks, consequently affecting the spread of diseases such as Lyme, Anaplasmosis, Babesiosis, and Theileriosis to new areas [144,145]. Bryer [146] showed that increased humidity, often associated with higher precipitation levels, prevents ticks from desiccating. Deshpande [147] reported that this environmental factor helps ticks stay hydrated and promotes vegetation growth, which provides suitable habitats for ticks to thrive. Moreover, the rise in humidity levels contributes to an increase in the availability of hosts such as rodents, which are essential for ticks' feeding and reproduction cycles. *Ixodes ricinus*, a common tick species in Europe, transmits various pathogens, including Lyme borreliosis and tick-borne encephalitis [148]. Climate change models predict potential range expansions of tick areas with milder winter conditions, leading to increased survival rates and higher probabilities of tick bites [149–151]. Milder winter temperatures reduce tick mortality by preventing exposure to lethal cold conditions [152]. Warmer winters allow ticks to avoid freezing, which could disrupt their bodily fluids and metabolic functions [153], ultimately improving their chances of survival during the winter months. Additionally, the decreased severity of cold conditions reduces the energy expenditure required for survival processes, further enhancing tick survival rates [154]. Waterlogging in tropical cattle boma areas due to high-intensity rainfall can lead to foot disorders in cattle, such as foot rot diseases [155]. Urban-Chmiel [154] showed that foot disorders are prevalent in cattle, with laminitis and its consequences being a significant issue, especially during the rainy season. Additionally, waterlogging can increase soil concentrations of certain elements such as iron and manganese, potentially causing leaf abnormalities, which may affect the overall health of the cattle in these areas [155]. Furthermore, rainfall has been linked to increased leptospiral infections in cattle, with higher seropositivity and urine PCR positivity during rainy seasons compared to dry seasons, indicating a correlation between rainfall and cattle health issues [156].

2.4. Impact of Climate Change on Water for Cattle

Water Availability and Quality

Climate change impacts water availability and quality for cattle through alterations in precipitation patterns, increased temperatures, and more frequent extreme weather events. Rainfall patterns, including distribution, intensity, and timing, are evidence of changing climate affecting cattle via various interconnected mechanisms. Alizadeh [157] showed that these patterns are altered due to rising global temperatures, increasing evaporation rates, loading the atmosphere with more moisture, and intensifying precipitation events in some regions, potentially causing flooding. This scenario has led to significant cattle losses, with

farmers experiencing the deaths of a substantial number of cattle due to the adverse effects of climate change. Conversely, higher temperatures can exacerbate drought conditions by accelerating evapotranspiration rates [158]. For example, prolonged droughts in regions such as the western United States have reduced surface water availability, forcing ranchers to rely more on groundwater resources, which can become depleted or contaminated over time [159]. Prolonged droughts as a result of climate change lead to water scarcity in beef cattle, which affects their intake, weight gain, and reproductive success and can even lead to death in severe cases [160]. Free-grazing cattle tend to walk longer distances to find water during a drought, which has detrimental effects on their health and productivity. Maurya [161] reported that cattle walking long distances in search of water can lead to increased energy expenditure, impacting the maintenance energy requirements of cattle by up to 24% compared to stall-fed animals. Additionally, walking stress induces physiological and metabolic changes, altering hormonal concentrations and potentially reducing dairy cows' growth, milk production, and reproductive performance [162]. However, the physiological responses to long-distance walking, including changes in adrenal and thyroid hormone concentrations, showcase the stress and adaptation mechanisms involved in local cattle breeds such as Tanzania shorthorn zebu (TSZ). The TSZ cattle withstand drought due to their small body size, skin color, and hair coats, which are adapted to reflect sunlight and reduce heat absorption [163]. Climate change-induced temperatures also increase the temperature of water sources, negatively impacting cattle. Cattle drink less hot water primarily due to body thermoregulatory and physiological reasons. He [164] demonstrated that beef cattle consuming heated water in colder seasons experienced disruptions in serum metabolism, rumen microbial fermentation, and the metabolome, leading to altered glucose and fatty acid metabolism. Conversely, Golher [165] highlighted that providing cooler water sources can aid in regulating body temperature and maintaining metabolic balance in cattle. In the hot season, due to climate change with warmer water, cattle will tend to increase their energy demands for thermoregulation, affecting glucose and fatty acid metabolism, altering rumen microbial fermentation, and causing stress-induced metabolic changes. Bewley [166] found that prolonged water consumption with higher temperatures decreased the reticular temperatures of dairy cows. Singh [167] found that cows consumed more water at 37 °C than at 25 °C and 15 °C. In contrast, Grossi et al. [168] reported no significant difference in animal performance when provided with water at different temperatures of 17 °C and 24 °C. Pereyra et al. [169] conducted three experiments. They found that water temperatures of 18 °C and 31 °C had no effect on water consumption by dairy cows but recommended providing fresh water to improve thermoregulation and animal performance under heat stress conditions. Another set of trials within the same study showed that providing a simple cloth shade over the water trough can prevent a significant effect on water temperature, which may modify water intake behavior in dairy cattle. Moreover, changes in water quality due to increased weather events and water temperature can also affect animal health and productivity [170]. The increased occurrence of weather events due to climate change, such as flooding in mining areas, reduces water quality by introducing mineral content such as selenium, sulfur, and copper into animal water sources. Water with high concentrations of these minerals has been shown to be toxic to cattle [171] and may lead to death. Generally, these changes in water quality and availability due to climate change, as Bownik and Wlodkowic [172] showed, significantly impact animal behavior and movement, reducing their nutritional intake.

2.5. Mitigation Strategies

2.5.1. Cattle Selection, Breeding, and Epigenetics

Selection, breeding, and epigenetics strategies significantly enhance cattle's adaptability to climate change effects (Figure 1). Selection involves choosing individuals with desirable traits to serve as parents for the next generation. Breeders can improve livestock resilience by selecting individuals with traits such as heat tolerance, disease resistance, and efficient nutrient utilization [173]. Rexroad [174] pointed out that genomic analysis aids in identifying genetic markers associated with these traits, facilitating tailored breeding programs to enhance adaptability in cattle populations. A current study on genetic variations in diverse cattle populations has revealed genes such as HSPB2, HSPB3, HSP20, HSP90AB1, HSF4, HSPA1B, and CLPB linked to climate adaptation [175]. For example, in their study, they show that variations in the HSP70 gene are associated with heat tolerance in cattle such as the Brahman breed. Genetic variants in HSP70 in cattle breeds improve their ability to withstand high temperatures and thermal stress [175]. Tian [176] conducted a whole-genome sequencing study on crossbred and Mongolian cattle populations that revealed significant genetic diversity and distinct clustering based on geographic distribution, with identified candidate genes such as TRPM8, NMUR1, PRKAA2, SMTNL2, and OXR1 that are associated with immune response and cold adaptation and crucial for developing cattle populations better suited to cope with climate change challenges. By systematically selecting for these advantageous traits, breeders can ensure the sustainability of livestock production systems via breeding programs in the face of evolving environmental pressures.

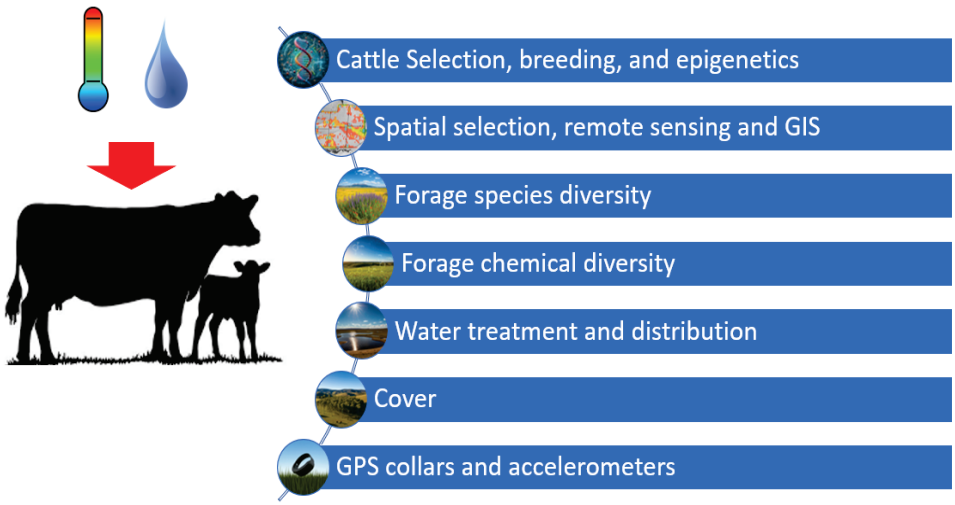

Figure 1. A framework of mitigation strategies to improve cattle resilience under climate change stress. Seven key management areas are highlighted: (1) Breeding and Epigenetics: Developing heat-tolerant and disease-resistant cattle with climate-adaptive traits passed down across generations. (2) Remote Sensing and GIS Mapping: Tracking optimal grazing zones and cattle movements as vegetation changes, enabling adaptive land use. (3) Forage Diversity: Enhancing forage species variety to ensure a stable food supply under changing environmental conditions. (4) Chemical Diversity in Forage: Incorporating tannin-rich plants and other chemically diverse forages to improve nutrient utilization and reduce methane emissions, thus contributing to environmental sustainability. (5) Water Treatment and Distribution: Establishing reliable water access systems, particularly important in drought-prone regions, to maintain cattle hydration and health. (6) Vegetation Cover Management: Promoting shade and ground cover to create cooler grazing areas, reduce soil erosion, and retain moisture. (7) GPS Collars and Accelerometers: Employing wearable technologies to monitor cattle movement, behavior, and physiological responses, allowing for precise, data-driven adaptive management.

Breeding involves strategically applying selected climate adaptation and resilience traits that cattle possess, enhancing the climate change stress resilience of future cattle populations. In livestock production, breeding can involve both inbreeding and crossbreeding techniques. Inbreeding, while altering genetic footprints within cattle genomes and impacting phenotypic variance, can potentially influence adaptive traits negatively due to reduced genetic diversity [177]. Conversely, crossbreeding techniques offer a promising avenue to improve resilience to climate stress by introducing genetic diversity from cattle breeds with adaptive traits into non-resilient populations [178], thereby enhancing overall climate resilience across cattle populations. In Rwanda, which has a tropical climate, Niyonzima [179] found that crossbred cows (Ankole-Friesian) with higher heat tolerances had better milk production and fertility than purebred cows. In the southwest U.S., Castaño-Sánchez [180] revealed that crossbreed cattle (Criollo × Angus) exhibited lower water use, fuel consumption, nitrogen footprints, and production costs regardless of the finishing diet. Muzzo et al. [163] emphasized that crossbreeding can produce offspring with more desirable traits of climate and disease resilience and adaptability to local conditions.

On the other hand, epigenetics studies have an important role in understanding how cattle might adapt to climate change. Holliday [181] defined epigenetics as biochemical and structural changes in chromatin without alterations in the DNA sequence. In the context of the effect of climate change on cattle, epigenetics serves as molecular mechanisms influencing cattle in terms of gene expression, physiology, and phenotypic variation to adapt to stress due to the changing climate, with the potential to cause transgenerational effects. Epigenetic mechanisms, such as DNA methylation, histone modifications, and non-coding RNAs, can provide a bridge between environmental stressors and phenotypic responses, allowing organisms to acclimate and cope with rapidly changing climates. Identifying epigenetic biomarkers and exploring epigenetic memories and diversity present promising avenues for enhancing the resilience of cattle populations, improving adaptation to environmental stresses, and facilitating the development of climate-resilient cattle breeds. For example, Creole cattle breeds in tropical environments, when compared to their Spanish ancestors, reveal differential methylation, impacting genes related to immune responses, heat resistance, and energy management, highlighting adaptation mechanisms [182]. Similarly, the methylation patterns of heat stress-related genes in Sahiwal and Frieswal cattle under heat stress conditions offer insights into the molecular mechanisms of adaptation to tropical climates, indicating similarities in their responses due to acclimatization [183]. By unraveling these epigenetic mechanisms, we can pave the way for developing climate-resilient cattle breeds that can thrive in challenging environmental conditions, ultimately ensuring sustainable cattle production in the face of climate change challenges. Concurrently, integrating selection, breeding, and epigenetics can produce a comprehensive approach that ensures that cattle are resilient, healthy, and productive in various environmental conditions, supporting sustainable cattle production systems in the face of ongoing climate changes.

2.5.2. Spatial Selection, Remote Sensing, and GIS

In the current era of climate change challenges, the use of remote sensing and geographic information systems (GISs) has an important role in assisting farmers in locating pasture areas that are greener than the surrounding area and thus inferring localized higher soil moisture ("wet spots") that can assist in establishing forage for sustaining livestock during dry periods (Figure 1).

Remote sensing instruments mounted to satellites, unpiloted aerial systems (UASs), or piloted aircraft offer a variety of data in the form of multi-spectral imagery for real-time or near-real-time monitoring of vegetation health, soil moisture levels, and land cover

transformations [184]. The normalized difference vegetation index (NDVI) and enhanced vegetation index (EVI) are remote sensing-derived vegetation indices used to measure plant density and health [185], facilitating the identification of productive regions even amidst varying climatic conditions. NDVI, obtained by normalizing near-infrared and red-light reflectance differentials, can evaluate vegetation vigor areas where the leaf area index is less than 3. The EVI provides similar capabilities in more dense vegetation areas [186]. Additionally, Bhaga [187] explained that indices such as the soil moisture index (SMI), which uses remote sensing data to estimate soil moisture content, and the normalized difference water index (NDWI), which monitors water levels in vegetation, enable the evaluation of drought resilience and identifying areas with adequate water availability.

Geographic information systems (GISs) leverage the wealth of data offered by remote sensing technologies, particularly in the realm of climate change. Combining spatial and temporal data from diverse data sources such as high- and low-resolution satellite images, UAS-captured imagery, and other spatial data such as fences, topography, and even livestock movement recorded with GPS, etc., provides a holistic view of landscape dynamics and a platform to monitor environmental conditions, including changes in vegetation health, soil moisture, and land cover patterns. GISs empower the creation of intricate maps and models crucial for informed decision-making. Historical imagery from satellites such as Landsat and the Moderate Resolution Imaging Spectroradiometer (MODIS) offer several decades of information [188] and is invaluable for analyzing long-term trends and understanding the impacts of climate change on vegetation, water, and soil conditions [189]. These and other platforms provide decades of information at a temporal repeat rate spanning 1 to 16 days, providing both long-term and high-temporal-grain data to evaluate surface conditions.

Previous research by Poitras [190] demonstrated the effectiveness of satellite imagery in identifying vegetation hotspots in rangeland ecosystems. Combining data from multiple remote sensing platforms allows a comprehensive assessment of vegetation health, phenology, and responses to climatic events over time, thus aiding in identifying areas that consistently exhibit higher levels of photosynthetically active vegetation ("green spots"), indicating forage availability and quality for a particular temporal period. Identifying periodic green areas can help ranchers or pastoralists allocate their cattle grazing regimes and stocking density based on the estimated carrying capacity of their grazing area. In addition, a suitable mix of soil and water indices can help identify "wet spots" for better establishment of seeded forage species. This approach aligns with the principles employed in developing the Islands of Diversity Location Tool (IDLT) by researchers at Utah State University. This tool assisted in identifying suitable areas for establishing islands of plant diversity "feed patches" with plants containing different phytochemicals across a 55-acre pasture of grass monoculture (Figure 2), a demonstration research field of the ongoing Smart Foodscape project [81]. Additionally, remote sensing provides a reliable and cost-effective means of measuring and evaluating mitigation and adaptation strategies against the effects of climate change, enhancing resilience and promoting sustainable agricultural intensification. Therefore, remote sensing and GIS tools significantly enhance the selection of optimal "green spots" for establishing forage in rangeland areas with limited precipitation. However, identifying the most resilient and adaptable forage species in rangeland areas using these tools requires further research. The identification of forage species adapted to specific ecosites requires the development of testing plots to gather information on species establishment, persistence, and tolerance to grazing. Regos [191] suggested that integrating ecological niche models and eco-evolutionary mechanisms through GIS and remote sensing can dynamically model geographic range shifts and assess evolutionary rescue probabilities. These approaches allow researchers to predict species responses to

climate change more accurately. For instance, integrating models such as AdaptR and incorporating adaptive capacity, phenotypic plasticity, and evolutionary adaptation into species distribution modeling help to reduce projected range losses and enhance species resilience [192]. This integration supports the development of effective strategies for forage establishment and ecosystem management in the face of ongoing climate change.

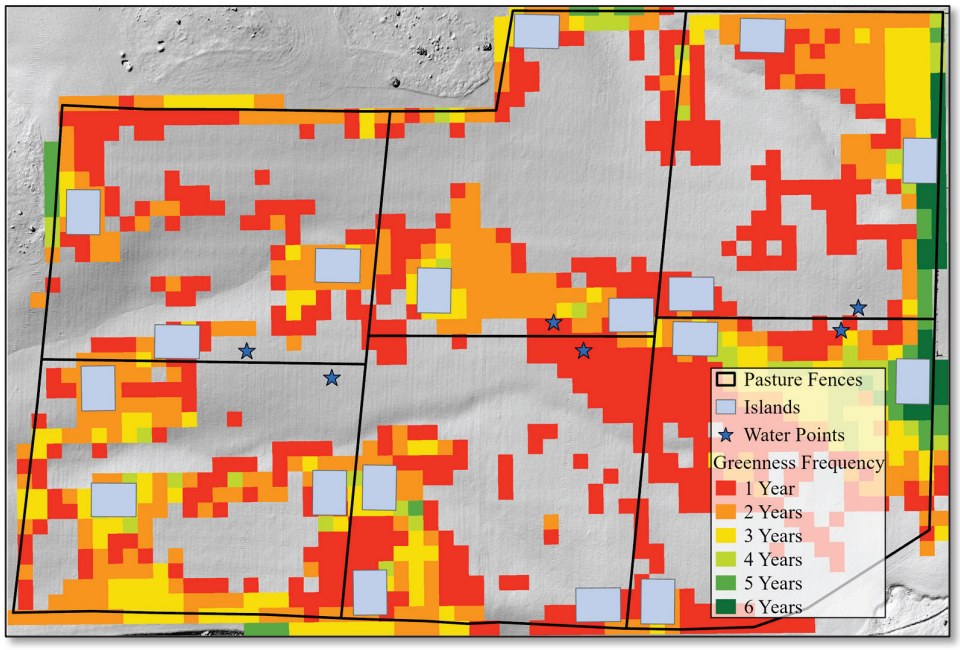

Figure 2. Map identifying areas within a 55-acre grass monoculture pasture—partitioned into 6 paddocks of approximately 9 acres in size, showing the frequency of pixels with above-average greenness across a 7-year period. Colors refer to the number of years a given pixel is 1 standard deviation above the NDVI mean for that year and is considered a surrogate for moisture availability. This frequency layer was derived from NDVI values from Sentinel-2 imagery processed using the IDLT tool. Light blue boxes identify locations with above-average moisture availability that would provide the best chance to successfully establish "feed patches". Gray areas represent below-average moisture zones that would be unsuitable for forage patch establishment.

2.5.3. Forage Species and Chemical Diversity to Attenuate the Negative Impacts of Climate Fluctuations on Livestock Performance

The establishment of islands of plant diversity "feed patches" within grazing landscapes facing long drought conditions enhances forage availability and quality, mitigating cattle nutrition stress (Figure 1). Wet spots identified within the landscape using the above-highlighted principles provide established forages with self-sustaining resources to grow and mature, providing essential nutrients to cattle grazing most grass monoculture landscapes even during extended dry periods. During the dry season, the nutritive value of these grasses declines while perennial legumes are revealed to fix atmospheric N2 [193], persist for years without additional planting [194], and provide a significant input of nutrients for the ruminant animal [195]. In addition, legumes and some forbs are of greater nutritional value than grasses [196]. Diverse legumes with different biochemical profiles, such as protein, non-fibrous carbohydrates, and plant secondary compounds (PSMs), such as condensed tannins (CTs) complement grasses, increase the diversity of feed resources that improve animal fitness [197] while decreasing carbon and N footprints [125]. In support of this, Lagrange and Villalba [198] and Lagrange [199] showed that cattle and sheep consuming combinations of alfalfa (ALF; *Medicago sativa*), birdsfoot trefoil (BFT; *Lotus corniculatus*), and sainfoin (SF; *Onobrychis viciifolia*) showed reduced urinary N excretions and improved body weight gains and N retention. This forage diversity motivates animal

intake by offering numerous orosensorial and post-ingestive stimuli [200]. Moreover, allowing animals to choose pastures of different chemical and organoleptic profiles contributes to improved intake, animal welfare, and performance [201,202]. Diverse pastures grazed in specific sequences improved dry matter intake compared to repeated allocations of monotonous pastures [203]. Mote [204] reported that providing sheep with a tannin-rich ration followed by terpenes doubled their intake of food with terpenes relative to the reverse sequence, suggesting that temporal allocation of diverse forages impacts foraging behavior and potentially performance.

The availability of taxonomically diverse forage alternatives allows ruminants to select diets that meet their nutrient requirements while incorporating bioactives that are medicinal or prophylactic (e.g., antioxidants). Doses of these biochemicals in diverse diets are typically below the thresholds of toxicity [205] and thus more beneficial than consuming individual plant species [206,207]. Incorporating a diversity of forage species into grazing systems is essential for reducing the metabolic burden of herbivores associated with detoxifying PSMs. A monotonous diet dominated by a single species can elevate the metabolic rate of herbivores, leading to an increased internal heat load, particularly under changing climate conditions with rising temperatures and frequent heat waves [5]. A diverse forage landscape allows herbivores to consume various plants, each with different PSMs, effectively diluting the intake of any single toxin and reducing the detoxification load on their organs [176,207]. Moreover, the interaction between diverse PSMs can enhance detoxification efficiency, as some compounds may mitigate the toxicity of others [125]. For instance, studies have shown that sheep grazing on mixed diets experienced less heat stress and improved health compared to those on monocultures [208]. Similarly, cattle fed diverse forages exhibited lower internal temperatures and enhanced growth rates [202]. Studies by Jordán [209] further support this, showing that goats grazing on diverse Mediterranean shrublands had improved protein utilization and lower liver enzyme activity compared to those on single-species diets. Moreover, diverse forages stimulate the expression of various detoxification enzymes, enhancing the herbivore's ability to metabolize a broader range of toxins [210]. This enzymatic adaptability is vital as different plants produce distinct PSMs, each requiring specific pathways for detoxification. Key enzymes involved in this process include cytochrome P450 enzymes, which facilitate the oxidation of organic compounds, and glutathione S-transferases, which conjugate toxins with glutathione for excretion. Additionally, the presence of antioxidant compounds in diverse forages can alleviate oxidative stress associated with PSM metabolism, as antioxidants help neutralize reactive oxygen species generated during detoxification [211]. These findings underscore that promoting plant diversity is a crucial adaptive strategy for grazing systems, enabling herbivores such as cattle to maintain better health and productivity in warmer environments, thereby addressing the challenges posed by climate change. Integrating shrubs into pasturelands represents a vital strategy for enhancing forage diversity and adapting to climate variability and climate change. The establishment of shrub islands can significantly extend the grazing season by providing evergreen forage that remains available during periods when traditional pastures are dormant, particularly in the face of increased drought frequency and changing precipitation patterns. This incorporation of shrubs enhances the nutritional profile of the forage, offering increased levels of protein, minerals, and vitamins that are often lacking in pasturelands devoid of such vegetation, thus supporting livestock health and resilience during climate-induced stressors. Research has demonstrated the potential contributions of forage shrubs to both economic returns and environmental management. For instance, Monjardino [212] pointed out that incorporating perennial forage shrubs in Australian agriculture can enhance farm profitability by an average of 24% while providing reliable "out-of-season" feed, thus reducing supplementary feed

costs and improving animal production, as demonstrated using the model of an integrated dryland agricultural system (MIDAS). Additionally, these shrubs improve water use efficiency and carbon storage, addressing challenges associated with climate change. Revell [213] highlighted the importance of breeding and incorporating shrubs, such as tagasaste (*Chamaecytisus palmensis*) and saltbush (*Atriplex* spp.), into farming systems and within fences in the southwest of Western Australia to improve diet quality, maintain soil health, and support livestock nutrition amidst increasing climate variability. Further investigations by Revell [214] confirmed that Australian perennial shrub species can enhance the feed base for grazing livestock, particularly in low- and medium-rainfall zones, by providing high-quality forage options during periods of scarcity. Additionally, Robertson and [215] provided an overview of the role of perennial pastures, including shrubs, in cropping systems in southern Australia, underscoring the need for ongoing research to explore the future benefits of these systems. In summary, incorporating shrubs into pasture systems not only extends the grazing season but also improves the nutritional quality of forage available to livestock, making this diversification essential for optimizing grazing systems amid the challenges posed by climate variability. Further research is needed regarding optimal synergistic or associative benefits derived from diverse supplementary forages established in these wet spots on livestock nutrition, health, and welfare, as well as their impact on the environment. Utilizing techniques such as ground cover fabric to enhance seedbed conditions can aid in the successful establishment of native forbs, contributing to improved forage quality for livestock [216]. Additionally, the inclusion of native tree islands in silvopastoral systems can further enhance biodiversity and ecosystem functioning in tropical regions, providing alternative forage sources while restoring degraded areas for conservation purposes [217]. Understanding the functional traits of plant species on islands is crucial for predicting establishment success, biotic interactions, and evolutionary pathways, highlighting the importance of considering ecological strategies when selecting species for restoration efforts [218].

2.5.4. Water Treatment, Water Points, and Strategic Shade Allocation

Ensuring high-quality water is fundamental to cattle health, as poor water quality can lead to various health issues that adversely affect productivity and welfare (Figure 1). Implementing effective water treatment methods is essential, particularly in regions where natural water sources may be contaminated due to climate change effects. Filtration systems, including sand filters, membrane filters, and UV light treatment, are commonly employed to remove particulates and pathogens in water points. Chemical treatments such as chlorination effectively disinfect water by killing harmful bacteria and viruses. A supportive study by Kim [219] indicated that disinfectants such as chlorine and ozone can effectively reduce *Escherichia coli* O157:H7 levels in contaminated water, achieving significant reductions when applied in specific concentrations. Maintaining a chlorine concentration of 1–3 parts per million (ppm) is recommended for effective livestock water treatment [11]. Lactic acid combined with acidic calcium sulfate reduced *Escherichia coli*, while no effect was observed on the amount of water consumed by cattle drinking water that contained compounds [220]. Cattle consuming water treated with 0.1% lactic acid and 0.9% acidic calcium sulfate (pH 2.1) drank an average of 18.6 L per day, comparable to untreated water consumption [221]. In local or rural settings, biofiltration systems that utilize layers of gravel, sand, and activated carbon can effectively remove contaminants while being cost-efficient. Rainwater harvesting also presents an effective method for ensuring water availability during dry periods, provided proper treatment measures are implemented to maintain water quality. A study by Richards [222] demonstrated that implementing rainwater harvesting systems in remote areas resulted in a 30% increase in

water availability for livestock, thereby reducing dependence on unreliable surface water sources. Furthermore, research by Sobsey [223] found that biofiltration systems improved water quality by reducing total coliform bacteria levels by up to 95%, ensuring that cattle had access to safe drinking water. Establishing reliable water sources and effective water treatment methods can significantly enhance cattle health, productivity, and resilience against climate-related challenges.

The impact of climate change on water availability is a pressing issue that requires immediate attention. Developing accessible water sources is essential for maintaining cattle hydration, especially during heat stress or drought. Water is vital for various physiological functions, including digestion, nutrient absorption, and thermoregulation. As climate change exacerbates water scarcity, cattle are forced to walk longer distances to access water, particularly in free rangeland grazing systems. Water points are not just sources of water but also strategic tools that can be placed within 1 to 2 km (0.6 to 1.2 miles) of grazing areas to minimize the time and energy cattle expend walking to water. A study by Hunt [224] demonstrated that cattle within 1 km of water sources exhibited improved distribution across pastures, while distances exceeding 2 km reduced grazing efficiency and increased localized overgrazing. Cattle walking distances can increase energy costs by 10% to 24% compared to stall-fed animals, highlighting the importance of minimizing travel distance to water. A study found that energy costs for locomotion varied, with horizontal movement costing approximately 2.8 to 2.9 kJ/kg of body weight per kilometer. Cattle with access to water points less than 1 km away had a 15% improvement in their intake, ultimately enhancing their performance.

Conversely, the scarcity of water resources in drought-prone areas leads to cattle congestion at water points, resulting in overgrazing and pasture nutrient depletion. This ultimately causes the degradation of grazing areas. Muzzo and Provenza [225] recommended investing in increasing the number of water points to encourage cattle to utilize a broader area, promoting better pasture health and nutrient cycling in response to climate change. In areas with water scarcity, increasing the number of water points within strategic distances of 1 to 2 km enhances cattle performance, reduces animal congestion at water points, and maintains pasture health. Furthermore, integrating water point placement with vegetation assessments could optimize grazing management, as cattle are more likely to utilize areas with better forage availability near water sources.

In addition to water availability, providing cover and shade is essential for effective thermoregulation in cattle. Shade structures, tree plantings, and other forms of cover can significantly reduce heat stress, improving animal welfare and performance. Shade reduces plasma cortisol levels, indicating lower stress, which is vital for maintaining appetite and growth rates [226]. Tree shade significantly lowers black globe temperatures (BGTs), with studies showing shaded areas averaging 30.2 °C compared to 35.5 °C outside [227]. Cattle under shade exhibited lower rectal temperatures (RTs) and respiration rates (RRs), indicating better thermoregulation. Non-shaded cows had an average RT of 40.1 °C, while shaded cows had an RT of 39.3 °C [227]. Titto [228] reported that cattle with access to shade altered their behavior, spending more time grazing and ruminating, which is crucial for their overall health and productivity. Cattle under shade minimize their heat load, reducing the energy expenditure required for thermoregulation and allocating more energy to production. For example, shade use in hot climates increased significantly; over 50% of Holstein dairy and Belgian Blue beef cattle utilized shade, maintaining normal RR and panting scores compared to those without shade [229]. Cows with access to shade exhibited higher milk yields and better milk composition, with significant differences in solids-not-fat yield and lactose percentage [230]. Yearling Hereford steers gained an additional 19 lbs over the summer when shade was available [231]. Therefore, farmers can improve resilience to

climate variability by incorporating water treatment, water points, and shade allocation strategies, ultimately fostering sustainable cattle systems.

2.5.5. Real-Time GPS Coupled with Accelerometer Collars

Cattle exhibit divergent foraging and site preferences, resulting in discrete behavioral events [232]. Such events include grazing, walking, resting, or ruminating activities. Grazing activities are determined by bite size formation, the bite size rate, and time spent foraging. Cattle allocate their grazing activities across different spatial scales and this consists of a hierarchy, from a feeding patch where they graze specific forage species, to a feeding station that includes multiple patches, and ultimately to the broader landscape, which encompasses the entire grazing area and influences their long-term movement patterns, influenced by their physiological state, the pasture's structure and composition, and past experiences [233]. Using their senses, animals perform different activities, enabling them to select more profitable patches within feeding stations. In these stations, cattle initially recognize greener patches as indicative of greater nutritional quality, while forage abundance is another variable determining where to graze. Additionally, flat terrains are preferred over steep slopes, and grazing distribution is partly influenced by proximity to water and shelter and previous experience [234]. Hence, understanding both grazing events and distribution helps determine effective cattle grazing behaviors and, indirectly, animal performance and welfare.

In the 1990s, global positioning system (GPS) technology emerged and now allows researchers to accurately monitor livestock grazing patterns. Data from collar-mounted GPS units can be collected over weeks or even months at fine temporal intervals to help evaluate livestock movement and thus assist the rancher in improving techniques used to manage grazing distribution. While livestock instinctively seek the best available forage, climate change alters forage distribution, abundance, and quality over time, creating immediate and long-term challenges for cattle nutrition. Understanding grazing patterns and forage selection through tools such as GPS technology enables adaptive management to mitigate these effects by optimizing resource use, preventing overgrazing, improving forage quality, and ensuring the sustainability of grazing systems under climate change challenges. GPS units attached to collars can accurately track cattle movements and grazing patterns [235], providing valuable insights into the time cattle spend foraging, resting, and walking. Using real-time GPS collars, ranchers can accurately monitor cattle behavior and grazing patterns, allowing them to analyze the data within short time ranges and subsequently re-allocate cattle based on their preferences for forage and grazing conditions, helping to mitigate nutritional stress. A longer time spent grazing at a given location indicates a preference for the forage available at that location. For instance, Bello [236] found that real-time GPS collars can be used to identify locations where cattle prefer to forage and thus provide information for targeted interventions, such as enhancing forage availability or creating additional favorable locations, helping to ensure consistent access to nutritious feed during periods of reduced availability.

Current real-time GPS collars also measure air temperatures, offering valuable insights into cattle behavior and habitat preferences. Ranchers can analyze integrated temperature and GPS data to identify specific areas where cattle spend more time due to favorable temperature conditions, allowing for targeted improvements. The data can also help them to understand cattle movement patterns and behavior, enabling farmers to adapt grazing practices to enhance animal welfare and optimize livestock management strategies based on temperature preferences and comfort levels. GPS collars with integrated accelerometers monitor various animal behaviors, including periods when a cow is lying down or grazing. Ramezani [237] successfully used accelerometers to detect periods of lying down, rumi-

nation, and activity times in weaned calves during regrouping events, and Versluijs [238] identified common behaviors in free-ranging cattle, such as feeding, resting, walking, scratching, and self-grooming. Hence, an accelerometer provides valuable insights into cattle activity levels and behavior, which are crucial for managing climate change-induced stress. Accelerometers enable timely interventions. Džermeikaitė [239] demonstrated that real-time data from accelerometers helped manage heat stress by allowing farmers to respond promptly to temperature-induced stress, thereby improving animal welfare and productivity. Similarly, Sprinkle [240] highlighted the benefits of integrating accelerometer data with GPS for predictive analysis, assisting in managing grazing areas more effectively and mitigating the impacts of climate variability. However, some studies, such as those by Riaboff [241], have pointed out that accelerometers may sometimes provide inaccurate data under certain environmental conditions or with specific animal behaviors. Despite these challenges, real-time temperature–GPS collars coupled with accelerometers offer a comprehensive approach to managing cattle nutritional stress amidst climate challenges. These advanced technologies enable monitoring of behavioral responses and activity alterations in cattle exposed to heat stress, aiding in assessing the variability of stress experienced. Therefore, using these innovative tools and nutritional interventions, livestock producers can effectively address nutritional stress challenges in the face of climate change.

3. Conclusions

Climate change is linked to increasing levels of greenhouse gases in the atmosphere, leading to rising temperatures, altered precipitation patterns, and more frequent extreme weather events, which impact ecological systems and agricultural practices. Cattle nutrition and productivity are particularly impacted by changes in climate due to reductions in forage quality and productivity. Extreme weather events, such as flooding and droughts, may also reduce water availability and/or accessibility, with negative connotations for cattle nutrition and health. Soil microbial communities, crucial for nutrient cycling, are significantly impacted by temperature and moisture regimes. Extreme weather events such as flooding and droughts intensify these issues by reducing both water access and forage quality, further complicating cattle management. The shifts in climate also affect soil microbial communities, which are crucial for nutrient cycling. While warmer temperatures may increase microbial activity in some ecosystems, excessive heat or dryness can hinder nutrient cycling, disrupting the availability of essential nutrients for cattle. Additionally, changing plant communities, including shifts from C3 to C4 plants and alterations in plant secondary compound concentrations, may further impact forage quality and the nutritional balance of grazing cattle. In response to these challenges, several integrated strategies are needed to strengthen cattle resilience. Genetic selection, breeding for heat tolerance, disease resistance, and epigenetic research can enhance cattle adaptability. Remote sensing and GIS technologies offer valuable tools for monitoring water availability, plant health, and optimal grazing areas. Diversifying plant species, including perennial legumes and shrubs, helps to improve forage quality, enhance cover, and extend grazing seasons while reducing environmental impacts. Moreover, strategic management practices, such as developing water points, using GPS technology, and creating thermoregulatory structures, support cattle resilience in real-time by improving the management of forage, habitat, and environmental stressors. Real-time GPS collars combined with accelerometers provide detailed data on cattle movement and activity, aiding in the management of nutritional and heat stress. These strategies collectively enhance cattle resilience, health, and productivity amidst climate change challenges.

Author Contributions: B.I.M.: Conceptualization, Writing—review and editing original draft. J.J.V.: Review and editing original draft. R.D.R.: Review and editing original draft. All authors have read and agreed to the published version of the manuscript.

Funding: This work is supported by AFRI Sustainable Agricultural Systems Coordinated Agricultural Project (SAS-CAP) Award Number: 2021-69012-35952 from the USDA National Institute of Food and Agriculture.

Conflicts of Interest: The authors declare no conflicts of interest.

References

1. Gupta, A.; Anand, A.; Arora, D.; Bhattacharya, A.M.; Chahal, P.; Chauhan, R.; Dhall, A.; Dikshit, V.; Gulati, R.; Haque, A.J.; et al. *Conservation, Sustainability, and Environmental Justice in India*; Lexington Books: Lanham, MD, USA, 2020.
2. Friedlingstein, P.; Jones, M.W.; O'Sullivan, M.; Andrew, R.M.; Bakker, D.C.E.; Hauck, J.; Le Quéré, C.; Peters, G.P.; Peters, W.; Pongratz, J.; et al. Global Carbon Budget 2021. *Earth Syst. Sci. Data* **2022**, *14*, 1917–2005. [CrossRef]
3. Soon, W.; Connolly, R.; Connolly, M.; Akasofu, S.I.; Baliunas, S.; Berglund, J.; Bianchini, A.; Briggs, W.M.; Butler, C.J.; Cionco, R.G.; et al. The Detection and Attribution of Northern Hemisphere Land Surface Warming (1850–2018) in Terms of Human and Natural Factors: Challenges of Inadequate Data. *Climate* **2023**, *11*, 179. [CrossRef]
4. Forster, P.M.; Smith, C.J.; Walsh, T.; Lamb, W.F.; Lamboll, R.; Hauser, M.; Ribes, A.; Rosen, D.; Gillett, N.; Palmer, M.D.; et al. Indicators of Global Climate Change 2022: Annual Update of Large-Scale Indicators of the State of the Climate System and Human Influence. *Earth Syst. Sci. Data* **2023**, *15*, 2295–2327. [CrossRef]
5. Zhao, S.; Liu, M.; Tao, M.; Zhou, W.; Lu, X.; Xiong, Y.; Li, F.; Wang, Q. The Role of Satellite Remote Sensing in Mitigating and Adapting to Global Climate Change. *Sci. Total Environ.* **2023**, *904*, 166820. [CrossRef] [PubMed]
6. Henchion, M.; Moloney, A.P.; Hyland, J.; Zimmermann, J.; McCarthy, S. Review: Trends for Meat, Milk and Egg Consumption for the next Decades and the Role Played by Livestock Systems in the Global Production of Proteins. *Animal* **2021**, *15*, 100287. [CrossRef]
7. Cheng, M.; McCarl, B.; Fei, C. Climate Change and Livestock Production: A Literature Review. *Atmosphere* **2022**, *13*, 140. [CrossRef]
8. Kelly, A.E.; Goulden, M.L. Rapid Shifts in Plant Distribution with Recent Climate Change. *Proc. Natl. Acad. Sci. USA* **2008**, *105*, 11823–11826. [CrossRef] [PubMed]
9. Harrison, S.; Spasojevic, M.J.; Li, D. Climate and Plant Community Diversity in Space and Time. *Proc. Natl. Acad. Sci. USA* **2020**, *117*, 4464–4470. [CrossRef] [PubMed]
10. Sprunger, C.D.; Lindsey, A.; Lightcap, A. Above- and Belowground Linkages during Extreme Moisture Excess: Leveraging Knowledge from Natural Ecosystems to Better Understand Implications for Row-Crop Agroecosystems. *J. Exp. Bot.* **2023**, *74*, 2845–2859. [CrossRef] [PubMed]
11. Izaurralde, R.C.; Thomson, A.M.; Morgan, J.A.; Fay, P.A.; Polley, H.W.; Hatfield, J.L. Climate Impacts on Agriculture: Implications for Forage and Rangeland Production. *Agron. J.* **2011**, *103*, 371–381. [CrossRef]
12. Apgaua, D.M.G.; Tng, D.Y.P.; Forbes, S.J.; Ishida, Y.F.; Vogado, N.O.; Cernusak, L.A.; Laurance, S.G.W. Elevated Temperature and CO_2 Cause Differential Growth Stimulation and Drought Survival Responses in Eucalypt Species from Contrasting Habitats. *Tree Physiol.* **2019**, *39*, 1806–1820. [CrossRef] [PubMed]
13. Blond, B.; Majkić, M.; Spasojević, J.; Hristov, S.; Radinović, M.; Nikolić, S.; Anđušić, L.; Čukić, A.; Došenović Marinković, M.; Vujanović, B.D.; et al. Influence of Heat Stress on Body Surface Temperature and Blood Metabolic, Endocrine, and Inflammatory Parameters and Their Correlation in Cows. *Metabolites* **2024**, *14*, 104. [CrossRef]
14. Crous, K.Y. Plant Responses to Climate Warming: Physiological Adjustments and Implications for Plant Functioning in a Future, Warmer World. *Am. J. Bot.* **2019**, *106*, 1049. [CrossRef]
15. Kennedy, P.M.; Milligan, L.P. Effects of Cold Exposure on Digestion, Microbial Synthesis and Nitrogen Transformations in Sheep. *Br. J. Nutr.* **1978**, *39*, 105–117. [CrossRef]
16. Bell, M.J.; Eckard, R.J.; Harrison, M.T.; Neal, J.S.; Cullen, B.R. Effect of Warming on the Productivity of Perennial Ryegrass and Kikuyu Pastures in South-Eastern Australia. *Crop Pasture Sci.* **2013**, *64*, 61–70. [CrossRef]
17. Havrilla, C.A.; Bradford, J.B.; Yackulic, C.B.; Munson, S.M.; Caroline Havrilla, C.A.; Jarvis, S. Divergent Climate Impacts on C 3 versus C 4 Grasses Imply Widespread 21st Century Shifts in Grassland Functional Composition. *Divers. Distrib.* **2023**, *29*, 379–394. [CrossRef]
18. Sanz-Sáez, Á.; Erice, G.; Aguirreolea, J.; Irigoyen, J.J.; Sánchez-Díaz, M. Alfalfa Yield under Elevated CO_2 and Temperature Depends on the Sinorhizobium Strain and Growth Season. *Environ. Exp. Bot.* **2012**, *77*, 267–273. [CrossRef]
19. Sisco, M.R.; Bosetti, V.; Weber, E.U. When Do Extreme Weather Events Generate Attention to Climate Change? *Clim. Change* **2017**, *143*, 227–241. [CrossRef]

20. Giridhar, K.; Samireddypalle, A.; Giridhar, K.; Samireddypalle, A. Impact of Climate Change on Forage Availability for Livestock. In *Climate Change Impact on Livestock: Adaptation and Mitigation*; Springer: New Delhi, India, 2015; pp. 97–112. [CrossRef]
21. Chaplin-Kramer, R.; George, M.R. Effects of Climate Change on Range Forage Production in the San Francisco Bay Area. *PLoS ONE* **2013**, *8*, e57723. [CrossRef]
22. Visconti-Moreno, E.F.; Valenzuela-Balcázar, I.G. Pores Distribution Influences the Soil Microorganism's Response to Changes in Temperature and Moisture. *Eurasian J. Soil Sci.* **2023**, *12*, 28–36. [CrossRef]
23. Agom, O.; Gbadebo, A. Effects of Climate Change and Global Warming on Enzymes. *Rev. Gestão Soc. Ambient.* **2024**, *18*, e06079. [CrossRef]
24. Choudhary, P.; Bhatt, S.; Chatterjee, S. From Freezing to Functioning: Cellular Strategies of Cold-Adapted Bacteria for Surviving in Extreme Environments. *Arch. Microbiol.* **2024**, *206*, 1–13. [CrossRef] [PubMed]
25. Kumar, S.; Najar, I.N.; Sharma, P.; Tamang, S.; Mondal, K.; Das, S.; Sherpa, M.T.; Thakur, N. Temperature—A Critical Abiotic Paradigm That Governs Bacterial Heterogeneity in Natural Ecological System. *Environ. Res.* **2023**, *234*, 116547. [CrossRef] [PubMed]
26. Xiao, X.; Ma, Z.; Zhang, J.; Sun, B.; Zhou, J.; Liang, Y. Coupling Temperature-Dependent Spatial Turnover of Microbes and Plants Using the Metabolic Theory of Ecology. *New Phytol.* **2023**, *238*, 383–392. [CrossRef]
27. Zhang, J.; Yang, L.; Yu, M.; Chen, X. Response of Extreme Rainfall to Atmospheric Warming and Wetting: Implications for Hydrologic Designs Under a Changing Climate. *J. Geophys. Res. Atmos.* **2023**, *128*, e2022JD038430. [CrossRef]
28. Li, W.; Su, T.; Shen, Y.; Ma, H.; Zhou, Y.; Lu, Q.; Wang, G.; Liu, Z.; Li, J. Effects of Warming Seasonal Rotational Grazing on Plant Communities' Structure and Diversity in Desert Steppe. *Ecol. Evol.* **2023**, *13*, e9748. [CrossRef] [PubMed]
29. Rojas, Y.P.; Ghezzehei, T. Determining Soil Microbial Activity Based on Soil Moisture and Average Functions. In Proceedings of the EGU General Assembly 2023, Vienna, Austria, 24–28 April 2023; p. EGU23-899. [CrossRef]
30. Chatterjee, D.; Saha, S. Response of Soil Properties and Soil Microbial Communities to the Projected Climate Change. In *Advances in Crop Environment Interaction*; Springer: Singapore, 2018; pp. 87–136.
31. Li, D.; Wu, C.; Wu, J. Soil Fungal Community Has Higher Network Stability than Bacterial Community in Response to Warming and Nitrogen Addition in a Subtropical Primary Forest. *Appl. Environ. Microbiol.* **2024**, *90*, e00001-24. [CrossRef]
32. Qiu, Y.; Zhang, K.; Zhao, Y.; Zhao, Y.; Wang, B.; Wang, Y.; He, T.; Xu, X.; Bai, T.; Zhang, Y.; et al. Climate Warming Suppresses Abundant Soil Fungal Taxa and Reduces Soil Carbon Efflux in a Semi-Arid Grassland. *mLife* **2023**, *2*, 389–400. [CrossRef] [PubMed]
33. Wang, X.; Zhang, Q.; Zhang, Z.; Li, W.; Liu, W.; Xiao, N.; Liu, H.; Wang, L.; Li, Z.; Ma, J.; et al. Decreased Soil Multifunctionality Is Associated with Altered Microbial Network Properties under Precipitation Reduction in a Semiarid Grassland. *iMeta* **2023**, *2*, e106. [CrossRef]
34. Huntley, B.J. Soil, Water and Nutrients. In *Ecology Angola*; Springer International Publishing: Cham, Switzerland, 2023; pp. 127–147. [CrossRef]
35. Naylor, D.; McClure, R.; Jansson, J. Trends in Microbial Community Composition and Function by Soil Depth. *Microorganisms* **2022**, *10*, 540. [CrossRef] [PubMed]
36. Bainard, L.D.; Evans, B.; Malis, E.; Yang, T.; Bainard, J.D. Influence of Annual Plant Diversity on Forage Productivity and Nutrition, Soil Chemistry, and Soil Microbial Communities. *Front. Sustain. Food Syst.* **2020**, *4*, 560479. [CrossRef]
37. Danar Dewa, D.; Buchori, I. Impacts of Rapid Urbanization on Spatial Dynamics of Land Use-Based Carbon Emission and Surface Temperature Changes in the Semarang Metropolitan Region, Indonesia Dimas Danar Dewa · Imam Buchori. *Environ. Monit. Assess.* **2023**, *195*, 259. [CrossRef] [PubMed]
38. Fischer, M.; Günther, M.; Pischinger, S.; Kramer, U.; Nederlof, C.; van Almsick, T. Influence of Desulfurization Strategies for Methane Gaseous Direct Injection Engine on Carbon Dioxide Emissions. *J. Nat. Gas. Sci. Eng.* **2022**, *108*, 104822. [CrossRef]
39. Koutsoyiannis, D.; Kundzewicz, Z.W. Atmospheric Temperature and CO_2: Hen-Or-Egg Causality? *Sci* **2020**, *2*, 83. [CrossRef]
40. Lacis, A.A.; Schmidt, G.A.; Rind, D.; Ruedy, R.A. Atmospheric CO_2: Principal Control Knob Governing Earth's Temperature. *Science* **2010**, *330*, 356–359. [CrossRef]
41. Sage, R.F.; Kubien, D.S. The Temperature Response of C3 and C4 Photosynthesis. *Plant Cell Environ.* **2007**, *30*, 1086–1106. [CrossRef]
42. Jobe, T.O.; Rahimzadeh Karvansara, P.; Zenzen, I.; Kopriva, S. Ensuring Nutritious Food Under Elevated CO_2 Conditions: A Case for Improved C4 Crops. *Front. Plant Sci.* **2020**, *11*, 563726. [CrossRef] [PubMed]
43. Wijewardene, I.; Shen, G.; Zhang, H. Enhancing Crop Yield by Using Rubisco Activase to Improve Photosynthesis under Elevated Temperatures. *Stress Biol.* **2021**, *1*, 2. [CrossRef] [PubMed]
44. McDowell, N.G. Mechanisms Linking Drought, Hydraulics, Carbon Metabolism, and Vegetation Mortality. *Plant Physiol.* **2011**, *155*, 1051–1059. [CrossRef]
45. Buanafina, M.M.d.O.; Morris, P. The Impact of Cell Wall Feruloylation on Plant Growth, Responses to Environmental Stress, Plant Pathogens and Cell Wall Degradability. *Agronomy* **2022**, *12*, 1847. [CrossRef]

46. Ashworth, A.J.; Kharel, T.; Sauer, T.; Adams, T.C.; Philipp, D.; Thomas, A.L.; Owens, P.R. Spatial Monitoring Technologies for Coupling the Soil Plant Water Animal Nexus. *Sci. Rep.* **2022**, *12*, 3508. [CrossRef] [PubMed]
47. More, S.J.; Ravi, V.; Raju, S. Tropical Tuber Crops. In *Vegetables for Nutrition and Entrepreneurship*; Springer: Singapore, 2019; Volume 1, pp. 719–758. [CrossRef]
48. Sershen; Perumal, A.; Varghese, B.; Govender, P.; Ramdhani, S.; Berjak, P. Effects of Elevated Temperatures on Germination and Subsequent Seedling Vigour in Recalcitrant Trichilia Emetica Seeds. *S. Afr. J. Bot.* **2014**, *90*, 153–162. [CrossRef]
49. Bhattacharya, A. *Physiological Processes in Plants Under Low Temperature Stress*; Springer: Singapore, 2022.
50. Abobatta, W.F. The Influence of Climate Change on Interactions between Environmental Stresses and Plants. In *Plant Stress Mitigators: Types, Techniques and Functions*; Academic Press: Cambridge, MA, USA, 2023; pp. 425–434. [CrossRef]
51. Anjum, S.A.; Ashraf, U.; Zohaib, A.; Tanveer, M.; Naeem, M.; Ali, I.; Tabassum, T.; Nazir, U. Žemės Ūkio Augalų Reakcija į Sausros Sukurtą Stresą: Apžvalga. *Zemdirbyste* **2017**, *104*, 267–276. [CrossRef]
52. Yadav, S.K. Cold Stress Tolerance Mechanisms in Plants. A Review. *Agron. Sustain. Dev.* **2010**, *30*, 515–527. [CrossRef]
53. Bhandari, K.; Nayyar, H. Low Temperature Stress in Plants: An Overview of Roles of Cryoprotectants in Defense. In *Physiological Mechanisms and Adaptation Strategies in Plants Under Changing Environment*; Springer: New York, NY, USA, 2014; Volume 1, pp. 193–265. ISBN 9781461485919.
54. Ojo, T.A.; Kirkman, K.; Tedder, M. Effects of Warming and Rainfall Variation on Grass Phenology and Regenerative Responses in Mesic Grassland. *S. Afr. J. Bot.* **2024**, *174*, 107–115. [CrossRef]
55. Plos, C.; Hensen, I.; Korell, L.; Auge, H.; Römermann, C. Plant Species Phenology Differs between Climate and Land-Use Scenarios and Relates to Plant Functional Traits. *Ecol. Evol.* **2024**, *14*, e11441. [CrossRef] [PubMed]
56. Kangombe, F.N.; Throop, H.; Sala, O.; Vivoni, E.; Pigg, K.; Hultine, K.; Kwembeya, E. Environmental Drivers of Vegetative and Flowering Phenology in Drylands. Doctoral Dissertation, Arizona State University, Tempe, AZ, USA, 2023.
57. Fang, H.; Sha, M.; Xie, Y.; Lin, W.; Qiu, D.; Tu, J.; Tan, X.; Li, X.; Sha, Z. Shifted Global Vegetation Phenology in Response to Climate Changes and Its Feedback on Vegetation Carbon Uptake. *Remote Sens.* **2023**, *15*, 2288. [CrossRef]
58. Schüle, M.; Heinken, T.; Fartmann, T. Long-Term Effects of Environmental Alterations in Protected Grasslands—Land-Use History Determines Changes in Plant Species Composition. *Ecol. Eng.* **2023**, *188*, 106878. [CrossRef]
59. Liu, H.; Mi, Z.; Lin, L.; Wang, Y.; Zhang, Z.; Zhang, F.; Wang, H.; Liu, L.; Zhu, B.; Cao, G.; et al. Shifting Plant Species Composition in Response to Climate Change Stabilizes Grassland Primary Production. *Proc. Natl. Acad. Sci. USA* **2018**, *115*, 4051–4056. [CrossRef]
60. French, K.E. Species Composition Determines Forage Quality and Medicinal Value of High Diversity Grasslands in Lowland England. *Agric. Ecosyst. Environ.* **2017**, *241*, 193–204. [CrossRef]
61. Zhang, G.; Dai, E.; Dawaqiongda; Luobu; Fu, G. Effects of Climate Change and Fencing on Forage Nutrition Quality of Alpine Grasslands in the Northern Tibet. *Plants* **2023**, *12*, 3182. [CrossRef] [PubMed]
62. Yoshihara, Y.; Aoki, R.; Kinugasa, T.; Sasaki, T. Predicted Effects of Simulated Ambient Warming and Moisture on Forage Nutrient Quality and Community Composition in Mongolian an Arid Grassland. *Rangel. J.* **2022**, *44*, 159–164. [CrossRef]
63. Petit Bon, M.; Bråthen, K.A.; Ravolainen, V.T.; Ottaviani, G.; Böhner, H.; Jónsdóttir, I.S. Herbivory and Warming Have Opposing Short-Term Effects on Plant-Community Nutrient Levels across High-Arctic Tundra Habitats. *J. Ecol.* **2023**, *111*, 1514–1530. [CrossRef]
64. Sebastià, M.T.; Banagar, F.; Palero, N.; Ibáñez, M.; Plaixats, J. Quality Production of Sainfoin Swards Challenged by Global Change in Mountain Areas in the Western Mediterranean. *Agronomy* **2023**, *14*, 6. [CrossRef]
65. Habermann, E.; Dias de Oliveira, E.A.; Contin, D.R.; San Martin, J.A.B.; Curtarelli, L.; Gonzalez-Meler, M.A.; Martinez, C.A. Stomatal Development and Conductance of a Tropical Forage Legume Are Regulated by Elevated [CO_2] under Moderate Warming. *Front. Plant Sci.* **2019**, *10*, 609. [CrossRef] [PubMed]
66. Bykova, O.; Chuine, I.; Morin, X. Highlighting the Importance of Water Availability in Reproductive Processes to Understand Climate Change Impacts on Plant Biodiversity. *Perspect. Plant Ecol. Evol. Syst.* **2019**, *37*, 20–25. [CrossRef]
67. Neal, J.S.; Fulkerson, W.J.; Hacker, R.B. Differences in Water Use Efficiency among Annual Forages Used by the Dairy Industry under Optimum and Deficit Irrigation. *Agric. Water Manag.* **2011**, *98*, 759–774. [CrossRef]
68. Carter, P.R.; Sheaffer, C.C. Alfalfa Response to Soil Water Deficits. I. Growth, Forage Quality, Yield, Water Use, and Water-Use Efficiency1. *Crop Sci.* **1983**, *23*, 669–675. [CrossRef]
69. Peterson, P.R.; Sheaffer, C.C.; Hall, M.H. Drought Effects on Perennial Forage Legume Yield and Quality. *Agron. J.* **1992**, *84*, 774–779. [CrossRef]
70. Dumont, B.; Andueza, D.; Niderkorn, V.; Lüscher, A.; Porqueddu, C.; Picon-Cochard, C. A Meta-Analysis of Climate Change Effects on Forage Quality in Grasslands: Specificities of Mountain and Mediterranean Areas. *Grass Forage Sci.* **2015**, *70*, 239–254. [CrossRef]
71. Küchenmeister, K.; Küchenmeister, F.; Kayser, M.; Wrage-Mönnig, N.; Isselstein, J. Influence of Drought Stress on Nutritive Value of Perennial Forage Legumes. *Int. J. Plant Prod.* **2013**, *7*, 693–710.

72. Wilson, J.R. Effects of Water Stress on in Vitro Dry Matter Digestibility and Chemical Composition of Herbage of Tropical Pasture Species. *Aust. J. Agric. Res.* **1983**, *34*, 377–390. [CrossRef]
73. Buxton, D.R. Quality-Related Characteristics of Forages as Influenced by Plant Environment and Agronomic Factors. *Anim. Feed. Sci. Technol.* **1996**, *59*, 37–49. [CrossRef]
74. Reddy, G.S.N.; Matsumoto, G.I.; Shivaji, S. Sporosarcina Macmurdoensis Sp. Nov., from a Cyanobacterial Mat Sample from a Pond in the McMurdo Dry Valleys, Antarctica. *Int. J. Syst. Evol. Microbiol.* **2003**, *53*, 1363–1367. [CrossRef] [PubMed]
75. Durand, J.-L.; Gonzalez-Dugo, V.; Gastal, F. How Much Do Water Deficits Alter the Nitrogen Nutrition Status of Forage Crops? *Nutr. Cycl. Agroecosystems* **2021**, *88*, 231–243. [CrossRef]
76. Liu, Y.; Wu, Q.; Ge, G.; Han, G.; Jia, Y. Influence of Drought Stress on Afalfa Yields and Nutritional Composition. *BMC Plant Biol.* **2018**, *18*, 13. [CrossRef] [PubMed]
77. Halim, R.A.; Buxton, D.R.; Hattendorf, M.J.; Carlson, R.E. Water-Stress Effects on Alfalfa Forage Quality After Adjustment for Maturity Differences. *Agron. J.* **1989**, *81*, 189–194. [CrossRef]
78. Kalu, B.A.; Fick, G.W. Quantifying Morphological Development of Alfalfa for Studies of Herbage Quality1. *Crop Sci.* **1981**, *21*, 267–271. [CrossRef]
79. Van Soest, P.J. Acknowledgments. In *Nutritional Ecology of the Ruminant*; Cornell University Press: Ithaca, NY, USA, 1994; pp. ix–xii.
80. Tariq, A.; Ahmed, A. Plant Phenolics Production: A Strategy for Biotic Stress Management. In *Plant Phenolics in Biotic Stress Management*; Springer Nature: Singapore, 2024; pp. 441–454. [CrossRef]
81. Villalba, J.J.; Ramsey, R.D.; Athanasiadou, S. Review: Herbivory and the Power of Phytochemical Diversity on Animal Health. *Animal* **2024**, 101287. [CrossRef]
82. Rahman, A.; Albadrani, G.M.; Waraich, E.A.; Awan, T.H.; Yavaş, İ.; Hussain, S.; Rahman, A.; Albadrani, G.M.; Waraich, E.A.; Awan, T.H.; et al. Plant Secondary Metabolites and Abiotic Stress Tolerance: Overview and Implications. In *Plant Abiotic Stress Responses and Tolerance Mechanisms*; IntechOpen: London, UK, 2023.
83. La, V.H.; Kim, T.H.; Calderon-Urrea, A.; Janda, T. Editorial: Plant Signaling in Response to Environmental Stresses. *Front. Plant Sci.* **2023**, *14*, 1282465. [CrossRef] [PubMed]
84. Ahmad, N.; Xu, Y.; Zang, F.; Li, D.; Liu, Z. The Evolutionary Trajectories of Specialized Metabolites towards Antiviral Defense System in Plants. *Mol. Hortic.* **2024**, *4*, 1–11. [CrossRef]
85. Ray, R. Using Natural Variation in Nicotiana Attenuata to Elucidate Its Defense Response Against Herbivory. Doctoral Dissertation, Friedrich Schiller University Jena, Jena, Germany, 1990.
86. Montesinos-Navarro, A.; López-Climent, M.F.; Pérez-Clemente, R.M.; Arenas-Sánchez, C.; Sánchez-Martín, R.; Gómez-Cadenas, A.; Verdú, M. Plant Metabolic Response to Stress in an Arid Ecosystem Is Mediated by the Presence of Neighbors. *Ecology* **2024**, *105*, e4247. [CrossRef] [PubMed]
87. Waghorn, G. Beneficial and Detrimental Effects of Dietary Condensed Tannins for Sustainable Sheep and Goat Production—Progress and Challenges. *Anim. Feed. Sci. Technol.* **2008**, *147*, 116–139. [CrossRef]
88. Lorenz, K.; Lal, R. The Depth Distribution of Soil Organic Carbon in Relation to Land Use and Management and the Potential of Carbon Sequestration in Subsoil Horizons. *Adv. Agron.* **2005**, *88*, 35–66. [CrossRef]
89. Ortiz-López, B.; Mariezcurrena-Berasain, M.D.; Barajas-Cruz, R.; Velázquez-Garduño, G.; Pliego, A.B.; Adegbeye, M.J.; Salem, A.Z.M.; Mariezcurrena-Berasain, M.A. Sustainable Evaluation of Tannin Extract Biomass as a Feed Product Additive: Effects on Growth Performance, Meat Fatty Acid Profile, and Lipid Oxidation in Bullocks. *Biomass Convers. Biorefinery* **2024**, *14*, 5101–5107. [CrossRef]
90. Sun, Y.; Alseekh, S.; Fernie, A.R. Plant Secondary Metabolic Responses to Global Climate Change: A Meta-Analysis in Medicinal and Aromatic Plants. *Glob. Change Biol.* **2023**, *29*, 477–504. [CrossRef]
91. Laftouhi, A.; Cordero, M.A.W.; Mahraz, M.A.; Zerkani, H.; Hmamou, A.; Idrissi, A.M.; Imane, T.; Eloutassi, N.; Rais, Z.; Taleb, A.; et al. Study of the Physiological Behavior of Some Plants in Response to Climate Change Conditions. *Pol. J. Environ. Stud.* **2024**, *33*, 3733–3745. [CrossRef]
92. González-Teuber, M.; Palma-Onetto, V.; Aguirre, C.; Ibáñez, A.J.; Mithöfer, A. Climate Change-Related Warming-Induced Shifts in Leaf Chemical Traits Favor Nutrition of the Specialist Herbivore Battus Polydamas Archidamas. *Front. Ecol. Evol.* **2023**, *11*, 1152489. [CrossRef]
93. Beale, P.K.; Foley, W.J.; Moore, B.D.; Marsh, K.J. Warmer Ambient Temperatures Reduce Protein Intake by a Mammalian Folivore. *Philos. Trans. R. Soc. B* **2023**, *378*, 20220543. [CrossRef] [PubMed]
94. Zhou, C.; Lv, C.; Miao, T.; Ma, X.; Xia, C. Interactive Effects of Rising Temperature, Elevated CO_2 and Herbivory on the Growth and Stoichiometry of a Submerged Macrophyte Vallisneria Natans. *Sustainability* **2023**, *15*, 1200. [CrossRef]
95. Balluffi-Fry, J.; Leroux, S.J.; Wiersma, Y.F.; Richmond, I.C.; Heckford, T.R.; Rizzuto, M.; Kennah, J.L.; Vander Wal, E. Integrating Plant Stoichiometry and Feeding Experiments: State-Dependent Forage Choice and Its Implications on Body Mass. *Oecologia* **2022**, *198*, 579–591. [CrossRef]

96. Acamovic, T.; Brooker, J.D. Biochemistry of plant secondary metabolites and their effects in animals. *Proc. Nutr. Soc.* **2005**, *64*, 403–412. [CrossRef] [PubMed]
97. Torres-Fajardo, R.A.; González-Pech, P.G.; Sandoval-Castro, C.A.; Torres-Acosta, J.F.d.J. Small Ruminant Production Based on Rangelands to Optimize Animal Nutrition and Health: Building an Interdisciplinary Approach to Evaluate Nutraceutical Plants. *Animals* **2020**, *10*, 1799. [CrossRef]
98. Reddy, P.R.K.; Elghandour, M.M.M.Y.; Salem, A.Z.M.; Yasaswini, D.; Reddy, P.P.R.; Reddy, A.N.; Hyder, I. Plant Secondary Metabolites as Feed Additives in Calves for Antimicrobial Stewardship. *Anim. Feed. Sci. Technol.* **2020**, *264*, 114469. [CrossRef]
99. Beck, M.R.; Gregorini, P. How Dietary Diversity Enhances Hedonic and Eudaimonic Well-Being in Grazing Ruminants. *Front. Vet. Sci.* **2020**, *7*, 486377. [CrossRef] [PubMed]
100. Villalba, J.J.; Manteca, X. A Case for Eustress in Grazing Animals. *Front. Vet. Sci.* **2019**, *6*, 303. [CrossRef] [PubMed]
101. Reddy, A.R.; Chaitanya, K.V.; Vivekanandan, M. Drought-Induced Responses of Photosynthesis and Antioxidant Metabolism in Higher Plants. *J. Plant Physiol.* **2004**, *161*, 1189–1202. [CrossRef] [PubMed]
102. Gourlay, G.; Constabel, C.P. Condensed Tannins Are Inducible Antioxidants and Protect Hybrid Poplar against Oxidative Stress. *Tree Physiol.* **2019**, *39*, 345–355. [CrossRef] [PubMed]
103. Popović, B.M.; Štajner, D.; Ždero-Pavlović, R.; Tumbas-Šaponjac, V.; Čanadanović-Brunet, J.; Orlović, S. Water Stress Induces Changes in Polyphenol Profile and Antioxidant Capacity in Poplar Plants (*Populus* Spp.). *Plant Physiol. Biochem.* **2016**, *105*, 242–250. [CrossRef]
104. Bryant, J.P.; Stuart Chapin, F.; Klein Bryant, D.R.; Bryant, J.P.; Chapin, F.S. Herbivore-Plant Interactions at Northern Latitudes. *Oikos* **1983**, *40*, 357–368. [CrossRef]
105. Horner, J.D. Nonlinear Effects of Water Deficits on Foliar Tannin Concentration. *Biochermcal Syst. Ecol.* **1990**, *18*, 211–213. [CrossRef]
106. Matyssek, R.; Schnyder, H.; Oßwald, W.; Ernst, D.; Munch, J.C.; Pretzsch, H. *Ecological Studies 220 Growth and Defence in Plants Resource Allocation at Multiple Scales*; Springer: Berlin/Heidelberg, Germany, 2012.
107. AbdElgawad, H.; Peshev, D.; Zinta, G.; Van Den Ende, W.; Janssens, I.A.; Asard, H. Climate Extreme Effects on the Chemical Composition of Temperate Grassland Species under Ambient and Elevated CO_2: A Comparison of Fructan and Non-Fructan Accumulators. *PLoS ONE* **2014**, *9*, e92044. [CrossRef]
108. Anuraga, M.; Duarsa, P.; Hill, M.; Lovett, J. Soil Moisture and Temperature Affect Condensed Tannin Concentrations and Growth in Lotus Corniculatus and Lotus Pedunculatus. *Aust. J. Agric. Res.* **1993**, *44*, 1667–1681. [CrossRef]
109. Windley, H.R.; Shimada, T. Cold Temperature Improves Tannin Tolerance in a Granivorous Rodent. *J. Anim. Ecol.* **2020**, *89*, 471–481. [CrossRef] [PubMed]
110. Beale, P.K.; Connors, P.K.; Dearing, M.D.; Moore, B.D.; Krockenberger, A.K.; Foley, W.J.; Marsh, K.J. Warmer Ambient Temperatures Depress Detoxification and Food Intake by Marsupial Folivores. *Front. Ecol. Evol.* **2022**, *10*, 888550. [CrossRef]
111. Baumgard, L.H.; Rhoads, R.P. Effects of Heat Stress on Postabsorptive Metabolism and Energetics. *Annu. Rev. Anim. Biosci.* **2013**, *1*, 311–337. [CrossRef] [PubMed]
112. Bernabucci, U.; Lacetera, N.; Baumgard, L.H.; Rhoads, R.P.; Ronchi, B.; Nardone, A. Metabolic and Hormonal Acclimation to Heat Stress in Domesticated Ruminants. *Animal* **2010**, *4*, 1167–1183. [CrossRef] [PubMed]
113. Chen, L.; Thorup, V.M.; Kudahl, A.B.; Østergaard, S. Effects of Heat Stress on Feed Intake, Milk Yield, Milk Composition, and Feed Efficiency in Dairy Cows: A Meta-Analysis. *J. Dairy. Sci.* **2024**, *107*, 3207–3218. [CrossRef] [PubMed]
114. Souza, V.C.; Moraes, L.E.; Santos, J.E.P.; Baumgard, L.H.; Mueller, N.D.; Kebreab, E. Modeling the Relationship between Heat Stress, Feed Intake, and Day Relative to Calving in Nonlactating Dairy Cows. *J. Dairy. Sci.* **2023**, *106*, 8942–8952. [CrossRef]
115. Sammad, A.; Wang, Y.J.; Umer, S.; Lirong, H.; Khan, I.; Khan, A.; Ahmad, B.; Wang, Y. Nutritional Physiology and Biochemistry of Dairy Cattle under the Influence of Heat Stress: Consequences and Opportunities. *Animals* **2020**, *10*, 793. [CrossRef] [PubMed]
116. Safa, S.; Kargar, S.; Moghaddam, G.A.; Ciliberti, M.G.; Caroprese, M. Heat Stress Abatement during the Postpartum Period: Effects on Whole Lactation Milk Yield, Indicators of Metabolic Status, Inflammatory Cytokines, and Biomarkers of the Oxidative Stress. *J. Anim. Sci.* **2019**, *97*, 122–132. [CrossRef]
117. Antanaitis, R.; Džermeikaitė, K.; Krištolaitytė, J.; Ribelytė, I.; Bespalovaitė, A.; Bulvičiūtė, D.; Palubinskas, G.; Anskienė, L. The Impacts of Heat Stress on Rumination, Drinking, and Locomotory Behavior, as Registered by Innovative Technologies, and Acid–Base Balance in Fresh Multiparous Dairy Cows. *Animals* **2024**, *14*, 1169. [CrossRef]
118. Giannone, C.; Bovo, M.; Ceccarelli, M.; Torreggiani, D.; Tassinari, P. Review of the Heat Stress-Induced Responses in Dairy Cattle. *Animals* **2023**, *13*, 3451. [CrossRef]
119. Ross, A.D.; Bryden, W.L.; Bakau, W.; Burgess, L.W. Induction of Heat Stress in Beef Cattle by Feeding the Ergots of Claviceps Purpurea. *Aust. Vet. J.* **1989**, *66*, 247–249. [CrossRef] [PubMed]
120. Idris, M.; Uddin, J.; Sullivan, M.; McNeill, D.M.; Phillips, C.J.C. Non-Invasive Physiological Indicators of Heat Stress in Cattle. *Animals* **2021**, *11*, 71. [CrossRef] [PubMed]

121. Dash, S.; Chakravarty, A.K.; Singh, A.; Upadhyay, A.; Singh, M.; Yousuf, S. Effect of Heat Stress on Reproductive Performances of Dairy Cattle and Buffaloes: A Review. *Vet. World* **2016**, *9*, 235. [CrossRef] [PubMed]
122. Fernandez-Novo, A.; Pérez-Garnelo, S.S.; Villagrá, A.; Pérez-Villalobos, N.; Astiz, S. The Effect of Stress on Reproduction and Reproductive Technologies in Beef Cattle—A Review. *Animals* **2020**, *10*, 2096. [CrossRef]
123. Hemantaranjan, A. Heat Stress Responses and Thermotolerance. *Adv. Plants Agric. Res.* **2014**, *1*, 1–10. [CrossRef]
124. Alemu, T.W.; Pandey, H.O.; Salilew Wondim, D.; Gebremedhn, S.; Neuhof, C.; Tholen, E.; Holker, M.; Schellander, K.; Tesfaye, D. Oxidative and Endoplasmic Reticulum Stress Defense Mechanisms of Bovine Granulosa Cells Exposed to Heat Stress. *Theriogenology* **2018**, *110*, 130–141. [CrossRef]
125. Patra, A.K.; Saxena, J. A New Perspective on the Use of Plant Secondary Metabolites to Inhibit Methanogenesis in the Rumen. *Phytochemistry* **2010**, *71*, 1198–1222. [CrossRef]
126. Chen, H.; Fan, W.; Zhang, H.; Yue, P.; Wang, R.; Zhang, W.; Mai, K. Effects of Dietary Methionine on Growth and Body Composition, Indicators of Digestion, Protein Metabolism and Immunity, and Resistance to Heat Stress of Abalone Haliotis Discus Hannai. *Aquaculture* **2023**, *563*, 738978. [CrossRef]
127. Czech, B.; Wang, Y.; Szyda, J. Genome-Wide Association Study of Heat Stress Response in *Bos taurus*. *bioRxiv* **2023**. [CrossRef]
128. Lemal, P.; Tran, M.-N.; Schroyen, M.; Gengler, N. 143 Validation Strategies of Sensor Data in the Context of Heat Stress Detection. *J. Anim. Sci.* **2023**, *101*, 36–37. [CrossRef]
129. Nickles, K.R.; Relling, A.E.; Garcia-Guerra, A.; Fluharty, F.L.; Parker, A.J. Environmental Stress during the Last Trimester of Gestation in Pregnant Cows and Its Effect on Offspring Growth Performance and Response to Glucose and Adrenocorticotropic Hormone. *J. Anim. Sci.* **2023**, *101*, skac332. [CrossRef] [PubMed]
130. Chase, L.E. Cold Stress: Effects on Nutritional Requirements, Health and Performance. In *Reference Module in Food Science*; Elsevier: Amsterdam, The Netherlands, 2016. [CrossRef]
131. Kim, W.-S.; Nejad, J.G.; Lee, H.-G. Impact of Cold Stress on Physiological, Endocrinological, Immunological, Metabolic, and Behavioral Changes of Beef Cattle at Different Stages of Growth. *Animals* **2023**, *13*, 1073. [CrossRef]
132. Delfino, J.G.; Mathison, G.W. Effects of Cold Environment and Intake Level on the Energetic Efficiency of Feedlot Steers. *J. Anim. Sci.* **1991**, *69*, 4577–4587. [CrossRef] [PubMed]
133. Wang, S.; Li, Q.; Peng, J.; Niu, H. Effects of Long-Term Cold Stress on Growth Performance, Behavior, Physiological Parameters, and Energy Metabolism in Growing Beef Cattle. *Animals* **2023**, *13*, 1619. [CrossRef] [PubMed]
134. Nardone, A.; Ronchi, B.; Lacetera, N.; Ranieri, M.S.; Bernabucci, U. Effects of Climate Changes on Animal Production and Sustainability of Livestock Systems. *Livest. Sci.* **2010**, *130*, 57–69. [CrossRef]
135. Coloma-García, W.; Mehaba, N.; Such, X.; Caja, G.; Salama, A.A.K. Effects of Cold Exposure on Some Physiological, Productive, and Metabolic Variables in Lactating Dairy Goats. *Animals* **2020**, *10*, 2383. [CrossRef] [PubMed]
136. Berian, S. Effect of Cold Stress on Milk Yield, Physiological and Hemato-Biochemical Profile of Cross Bred Dairy Cattle. *J. Anim. Res.* **2019**, *9*, 335–338. [CrossRef]
137. Sahib, Q.S.; Aafaq, I.; Ahmed, H.A.; Sheikh, G.G.; Ganai, I.A. Mitigating Cold Stress in Livestock by Nutritional Interventions: A Comprehensive Review. *Indian. J. Anim. Res.* **2024**, *58*, 353–363. [CrossRef]
138. Wagner, D.G. Effects of Cold Stress on Cattle Performance and Management Factors to Reduce Cold Stress and Improve Performance. *Bov. Pract.* **1988**, *23*, 88–93. [CrossRef]
139. Cantalapiedra-Hijar, G.; Abo-Ismail, M.; Carstens, G.E.; Guan, L.L.; Hegarty, R.; Kenny, D.A.; Mcgee, M.; Plastow, G.; Relling, A.; Ortigues-Marty, I. Review: Biological Determinants of between-Animal Variation in Feed Efficiency of Growing Beef Cattle. *Animal* **2018**, *12*, S321–S335. [CrossRef] [PubMed]
140. Ames, D.R. Adjusting Rations for Climate. *Vet. Clin. N. Am. Food Anim. Pract.* **1988**, *4*, 543–550. [CrossRef] [PubMed]
141. Young, B.A. Cold Stress as It Affects Animal Production. *J. Anim. Sci.* **1981**, *52*, 154–163. [CrossRef]
142. Lees, A.M.; Sejian, V.; Wallage, A.L.; Steel, C.C.; Mader, T.L.; Lees, J.C.; Gaughan, J.B. The Impact of Heat Load on Cattle. *Animals* **2019**, 9. [CrossRef]
143. Colditz, I.G.; Hine, B.C. Resilience in Farm Animals: Biology, Management, Breeding and Implications for Animal Welfare. *Anim. Prod. Sci.* **2016**, *56*, 1961–1983. [CrossRef]
144. Paz, S. Climate Change Impacts on Vector-Borne Diseases in Europe: Risks, Predictions and Actions. *Lancet Reg. Health—Eur.* **2021**, *1*, 100017. [CrossRef] [PubMed]
145. Chikezie, F.M.; Opara, K.N.; Ubulom, P.M.E. Impacts of Changing Climate on Arthropod Vectors and Diseases Transmission. *Niger. J. Entomol.* **2024**, *40*, 179–192. [CrossRef]
146. Bryer, K.E. Effects of Temperature and Humidity on the Mortality of the Tick Dermacentor Reticulatus in the UK. Doctoral Dissertation, University of Bristol, Bristol, UK, 2020.
147. Deshpande, G.; Beetch, J.E.; Heller, J.G.; Naqvi, O.H.; Kuhn, K.G. Assessing the Influence of Climate Change and Environmental Factors on the Top Tick-Borne Diseases in the United States: A Systematic Review. *Microorganisms* **2023**, *12*, 50. [CrossRef]

148. Domatskiy, V.N.; Sivkova, E.I. The Influence of Climatogeographic Conditions on the Expansion of the Range of Ixodes Ticks. *Entomol. Appl. Sci. Lett.* **2023**, *10*, 1–9. [CrossRef]
149. Hoch, T.; Madouasse, A.; Jacquot, M.; Wongnak, P.; Beugnet, F.; Bournez, L.; Cosson, J.F.; Huard, F.; Moutailler, S.; Plantard, O.; et al. Seasonality of Host-Seeking Ixodes Ricinus Nymph Abundance in Relation to Climate. *Peer Community J.* **2024**, *4*, e2. [CrossRef]
150. Brunner, J.L.; Killilea, M.; Ostfeld, R.S. Overwintering Survival of Nymphal Ixodes Scapularis (Acari: Ixodidae) Under Natural Conditions. *J. Med. Entomol.* **2012**, *49*, 981–987. [CrossRef] [PubMed]
151. Lemery, J.; Knowlton, K.; Sorensen, C. (Eds.) *Global Climate Change and Human Health: From Science to Practice*; John Wiley & Sons: Hoboken, NJ, USA, 2021; p. 636.
152. Ogden, N.H.; Ben Beard, C.; Ginsberg, H.S.; Tsao, J.I. Possible Effects of Climate Change on Ixodid Ticks and the Pathogens They Transmit: Predictions and Observations. *J. Med. Entomol.* **2021**, *58*, 1536–1545. [CrossRef] [PubMed]
153. Alexandre, J.; Dionizio, R.; Augusto, J.; Afonso, B.; Silmara, G.; Soares, L.; Pajeú E Silva, B.; Filipe, J.; Cajueiro, P.; Teles Coutinho, L.; et al. Occurrence of Foot Diseases in Cattle Attended at the Clínica de Bovinos de Garanhuns: Epidemiological, Clinical, Therapeutic and Economic Aspects. *Ciência Anim. Bras.* **2022**, *23*, e-72731. [CrossRef]
154. Urban-Chmiel, R.; Mudroň, P.; Abramowicz, B.; Kurek, Ł.; Stachura, R. Lameness in Cattle—Etiopathogenesis, Prevention and Treatment. *Animals* **2024**, *14*, 1836. [CrossRef] [PubMed]
155. Chepkwony, R.; Castagna, C.; Heitkönig, I.; Van Bommel, S.; Van Langevelde, F. Associations between Monthly Rainfall and Mortality in Cattle Due to East Coast Fever, Anaplasmosis and Babesiosis. *Parasitology* **2020**, *147*, 1743–1751. [CrossRef] [PubMed]
156. Correia, L.; Loureiro, A.P.; Lilenbaum, W. Effects of Rainfall on Incidental and Host-Maintained Leptospiral Infections in Cattle in a Tropical Region. *Vet. J.* **2017**, *220*, 63–64. [CrossRef] [PubMed]
157. Alizadeh, O. Changes in the Mean and Variability of Temperature and Precipitation over Global Land Areas. *Environ. Res. Clim.* **2023**, *2*, 035006. [CrossRef]
158. Luppichini, M.; Bini, M.; Giannecchini, R.; Zanchetta, G.; Luppichini, M.; Bini, M.; Giannecchini, R.; Zanchetta, G. The Effects of the Temperature Increase on the Rainfall Regimes in North-Central Italy. In Proceedings of the EGUGA, Vienna, Austria, 23–28 April 2023; p. EGU-5430. [CrossRef]
159. Lall, U.; Josset, L.; Russo, T. A Snapshot of the World's Groundwater Challenges. *Annu. Rev. Environ. Resour.* **2020**, *45*, 171–194. [CrossRef]
160. Godde, C.M.; Mason-D'Croz, D.; Mayberry, D.E.; Thornton, P.K.; Herrero, M. Impacts of Climate Change on the Livestock Food Supply Chain; a Review of the Evidence. *Glob. Food Sec.* **2021**, *28*, 100488. [CrossRef] [PubMed]
161. Maurya, V.P.; Sejian, V.; Kumar, K.; Singh, G.; Naqvi, S.M.K. Walking Stress Influence on Livestock Production. In *Environmental Stress and Amelioration in Livestock Production*; Springer: Berlin/Heidelberg, Germany, 2012; pp. 75–95. ISBN 9783642292057. [CrossRef]
162. Sejian, V.; Maurya, V.P.; Naqvi, S.M.K. Effect of Walking Stress on Growth, Physiological Adaptability and Endocrine Responses in Malpura Ewes in a Semi-Arid Tropical Environment. *Int. J. Biometeorol.* **2012**, *56*, 243–252. [CrossRef] [PubMed]
163. Muzzo, B.I.; Maleko, D.D.; Thacker, E.; Provenza, F.D. Review: Rangeland Management in Tanzania: Opportunities, Challenges, and Prospects for Sustainability. *Int. J. Trop. Drylands* **2023**, *7*, 2. [CrossRef]
164. He, T.; Yi, G.; Wang, X.; Sun, Y.; Li, J.; Wu, Z.; Guo, Y.; Sun, F.; Chen, Z. Effects of Heated Drinking Water during the Cold Season on Serum Biochemistry, Ruminal Fermentation, Bacterial Community, and Metabolome of Beef Cattle. *Metabolites* **2023**, *13*, 995. [CrossRef]
165. Golher, D.M.; Patel, B.H.M.; Bhoite, S.H.; Syed, M.I.; Panchbhai, G.J.; Thirumurugan, P. Factors Influencing Water Intake in Dairy Cows: A Review. *Int. J. Biometeorol.* **2021**, *65*, 617–625. [CrossRef]
166. Bewley, J.M.; Grott, M.W.; Einstein, M.E.; Schutz, M.M. Impact of Intake Water Temperatures on Reticular Temperatures of Lactating Dairy Cows. *J. Dairy Sci.* **2008**, *91*, 3880–3887. [CrossRef]
167. Singh, A.K.; Bhakat, C.; Singh, P. A Review on Water Intake in Dairy Cattle: Associated Factors, Management Practices, and Corresponding Effects. *Trop. Anim. Health Prod.* **2022**, *54*, 1–13. [CrossRef]
168. Grossi, S.; Rossi, L.; Dell'anno, M.; Biffani, S.; Sgoifo Rossi, C.A. Effects of Heated Drinking Water on the Growth Performance and Rumen Functionality of Fattening Charolaise Beef Cattle in Winter. *Animals* **2021**, *11*, 2218. [CrossRef] [PubMed]
169. Valeria González Pereyra, A.; Maldonado May, V.; Catracchia, C.G.; Alejandra Herrero, M.; Flores, M.C.; Mazzini, M. Influence of water temperature and heat stress on drinking water intake in dairy cows. *J. Agric. Res* **2010**, *70*, 328–336. [CrossRef]
170. Coffey, R.; Paul, M.J.; Stamp, J.; Hamilton, A.; Johnson, T. A Review of Water Quality Responses to Air Temperature and Precipitation Changes 2: Nutrients, Algal Blooms, Sediment, Pathogens. *JAWRA J. Am. Water Resour. Assoc.* **2019**, *55*, 844–868. [CrossRef] [PubMed]
171. Giri, A.; Bharti, V.K.; Kalia, S.; Arora, A.; Balaje, S.S.; Chaurasia, O.P. A Review on Water Quality and Dairy Cattle Health: A Special Emphasis on High-Altitude Region. *Appl. Water Sci.* **2020**, *10*, 1–16. [CrossRef]

172. Wagner, J.J.; Engle, T.E. Invited Review: Water Consumption, and Drinking Behavior of Beef Cattle, and Effects of Water Quality. *Appl. Anim. Sci.* **2021**, *37*, 418–435. [CrossRef]
173. Arya, A.; Sharma, P.; Trivedi, M.M.; Modi, R.J.; Patel, Y.G. Article No.JSRR.116804 Review Article Arya et Al. *J. Sci. Res. Rep.* **2024**, *30*, 427–436. [CrossRef]
174. Rexroad, C.; Vallet, J.; Matukumalli, L.K.; Reecy, J.; Bickhart, D.; Blackburn, H.; Boggess, M.; Cheng, H.; Clutter, A.; Cockett, N.; et al. Genome to Phenome: Improving Animal Health, Production, and Well-Being—A New USDA Blueprint for Animal Genome Research 2018–2027. *Front. Genet.* **2019**, *10*, 431609. [CrossRef]
175. Nayak, S.S.; Panigrahi, M.; Rajawat, D.; Ghildiyal, K.; Sharma, A.; Jain, K.; Bhushan, B.; Dutt, T. Deciphering Climate Resilience in Indian Cattle Breeds by Selection Signature Analyses. *Trop. Anim. Health Prod.* **2024**, *56*, 1–14. [CrossRef] [PubMed]
176. Tian, R.; Asadollahpour Nanaie, H.; Wang, X.; Dalai, B.; Zhao, M.; Wang, F.; Li, H.; Yang, D.; Zhang, H.; Li, Y.; et al. Genomic Adaptation to Extreme Climate Conditions in Beef Cattle as a Consequence of Cross-Breeding Program. *BMC Genom.* **2023**, *24*, 186. [CrossRef] [PubMed]
177. Gutierrez-Reinoso, M.A.; Aponte, P.M.; Garcia-Herreros, M. Genomic Analysis, Progress and Future Perspectives in Dairy Cattle Selection: A Review. *Animals* **2021**, *11*, 599. [CrossRef]
178. de Brito, A. *Effects of Dietary Forage and Protein Supplements on Production, Nitrogen Utilization and Microbial Protein Synthesis in Lactating Dairy Cows*; The University of Wisconsin-Madison: Madison, WI, USA, 2004.
179. Niyonzima, Y.B.; Strandberg, E.; Hirwa, C.D.; Manzi, M.; Ntawubizi, M.; Rydhmer, L. The Effect of High Temperature and Humidity on Milk Yield in Ankole and Crossbred Cows. *Trop. Anim. Health Prod.* **2022**, *54*, 1–11. [CrossRef] [PubMed]
180. Castaño-Sánchez, J.P.; Rotz, C.A.; McIntosh, M.M.; Tolle, C.; Gifford, C.A.; Duff, G.C.; Spiegal, S.A. Grass Finishing of Criollo Cattle Can Provide an Environmentally Preferred and Cost Effective Meat Supply Chain from United States Drylands. *Agric. Syst.* **2023**, *210*, 103694. [CrossRef]
181. Holliday, R. Epigenetics: A Historical Overview. *Epigenetics* **2006**, *1*, 76–80. [CrossRef] [PubMed]
182. Sevane, N.; Martínez, R.; Bruford, M.W. Genome-Wide Differential DNA Methylation in Tropically Adapted Creole Cattle and Their Iberian Ancestors. *Anim. Genet.* **2019**, *50*, 15–26. [CrossRef]
183. Verma, S.; Taube, F.; Malisch, C.S. Examining the Variables Leading to Apparent Incongruity between Antimethanogenic Potential of Tannins and Their Observed Effects in Ruminants—A Review. *Sustainability* **2021**, *13*, 2743. [CrossRef]
184. Kowalski, K.; Senf, C.; Okujeni, A.; Hostert, P. Large-Scale Remote Sensing Analysis Reveals an Increasing Coupling of Grassland Vitality to Atmospheric Water Demand. *Glob. Chang. Biol.* **2024**, *30*, e17315. [CrossRef] [PubMed]
185. Priya, M.V.; Kalpana, R.; Pazhanivelan, S.; Kumaraperumal, R.; Ragunath, K.P.; Vanitha, G.; Nihar, A.; Prajesh, P.J.; Vasumathi, V. Monitoring Vegetation Dynamics Using Multi-Temporal Normalized Difference Vegetation Index (NDVI) and Enhanced Vegetation Index (EVI) Images of Tamil Nadu. *J. Appl. Nat. Sci.* **2023**, *15*, 1170–1177. [CrossRef]
186. Mallick, K.; Verfaillie, J.; Wang, T.; Ortiz, A.A.; Szutu, D.; Yi, K.; Kang, Y.; Shortt, R.; Hu, T.; Sulis, M.; et al. Net Fluxes of Broadband Shortwave and Photosynthetically Active Radiation Complement NDVI and near Infrared Reflectance of Vegetation to Explain Gross Photosynthesis Variability across Ecosystems and Climate. *Remote Sens. Environ.* **2024**, *307*, 114123. [CrossRef]
187. Bhaga, T.D.; Dube, T.; Shekede, M.D.; Shoko, C. Impacts of Climate Variability and Drought on Surface Water Resources in Sub-Saharan Africa Using Remote Sensing: A Review. *Remote Sens.* **2020**, *12*, 4184. [CrossRef]
188. Bellini, E. *Assessing Grassland Development by Means of Modelling and Remote Sensing Approaches: Current Situation and Future Projections*; University of Florence: Florence, Italy, 2023.
189. König, S.; Thonfeld, F.; Förster, M.; Dubovyk, O.; Heurich, M. Assessing Combinations of Landsat, Sentinel-2 and Sentinel-1 Time Series for Detecting Bark Beetle Infestations. *GISci. Remote Sens.* **2023**, *60*, 2226515. [CrossRef]
190. Poitras, T.B.; Villarreal, M.L.; Waller, E.K.; Nauman, T.W.; Miller, M.E.; Duniway, M.C. Identifying Optimal Remotely-Sensed Variables for Ecosystem Monitoring in Colorado Plateau Drylands. *J. Arid. Environ.* **2018**, *153*, 76–87. [CrossRef]
191. Regos, A.; Gonçalves, J.; Arenas-Castro, S.; Alcaraz-Segura, D.; Guisan, A.; Honrado, J.P. Mainstreaming Remotely Sensed Ecosystem Functioning in Ecological Niche Models. *Remote Sens. Ecol. Conserv.* **2022**, *8*, 431–447. [CrossRef]
192. Bibi, Z.; Maqsood, M.J.; Idrees, A.; Rafique, H.; Butt, A.A.; Ali, R.; Arif, Z.; Nabi, M.U. Retracted: Exploring the Role of Phenotypic Plasticity in Plant Adaptation to Changing Climate: A Review. *Asian J. Res. Crop Sci.* **2024**, *9*, 1–9. [CrossRef]
193. Temperton, V.M.; Mwangi, P.N.; Scherer-Lorenzen, M.; Schmid, B.; Buchmann, N. Positive Interactions between Nitrogen-Fixing Legumes and Four Different Neighbouring Species in a Biodiversity Experiment. *Oecologia* **2007**, *151*, 190–205. [CrossRef]
194. Pirhofer-Walzl, K.; Eriksen, J.; Rasmussen, J.; Høgh-Jensen, H.; Søegaard, K.; Rasmussen, J. Effect of Four Plant Species on Soil 15N-Access and Herbage Yield in Temporary Agricultural Grasslands. *Plant Soil* **2013**, *371*, 313–325. [CrossRef]
195. Moorby, J.M.; Fraser, M.D. Review: New Feeds and New Feeding Systems in Intensive and Semi-Intensive Forage-Fed Ruminant Livestock Systems. *Animal* **2021**, *15*, 100297. [CrossRef]
196. Lee, M.A. A Global Comparison of the Nutritive Values of Forage Plants Grown in Contrasting Environments. *J. Plant Res.* **2018**, *131*, 641–654. [CrossRef]

197. Provenza, F.D.; Villalba, J.J.; Dziba, L.E.; Atwood, S.B.; Banner, R.E. Linking Herbivore Experience, Varied Diets, and Plant Biochemical Diversity. *Small Rumin. Res.* **2003**, *49*, 257–274. [CrossRef]
198. Lagrange, S.; Villalba, J.J. Tannin-Containing Legumes and Forage Diversity Influence Foraging Behavior, Diet Digestibility, and Nitrogen Excretion by Lambs 1,2 3995 Tannin-Containing Legumes and Forage Intake. *J. Anim. Sci.* **2019**, *97*, 3994–4009. [CrossRef] [PubMed]
199. Lagrange, S.; Beauchemin, K.A.; MacAdam, J.; Villalba, J.J. Grazing Diverse Combinations of Tanniferous and Non-Tanniferous Legumes: Implications for Beef Cattle Performance and Environmental Impact. *Sci. Total Environ.* **2020**, *746*, 140788. [CrossRef] [PubMed]
200. Villalba, J.J.; Provenza, F.D.; K Clemensen, A.; Larsen, R.; Juhnke, J. Preference for Diverse Pastures by Sheep in Response to Intraruminal Administrations of Tannins, Saponins and Alkaloids. *Grass Forage Sci.* **2011**, *66*, 224–236. [CrossRef]
201. Villalba, J.J.; Provenza, F.D.; Gibson, N.; López-Ortíz, S. Veterinary Medicine: The Value of Plant Secondary Compounds and Diversity in Balancing Consumer and Ecological Health. In *Sustainable Food Production Includes Human and Environmental Health*; Springer: Berlin/Heidelberg, Germany, 2014; pp. 165–190. [CrossRef]
202. Garrett, K.; Beck, M.R.; Marshall, C.J.; Maxwell, T.M.R.; Logan, C.M.; Greer, A.W.; Gregorini, P. Varied Diets: Implications for Lamb Performance, Rumen Characteristics, Total Antioxidant Status, and Welfare. *J. Anim. Sci.* **2021**, *99*, skab334. [CrossRef]
203. Jensen, T.L.; Provenza, F.D.; Villalba, J.J. Influence of Diet Sequence on Intake of Foods Containing Ergotamine d Tartrate, Tannins and Saponins by Sheep. *Appl. Anim. Behav. Sci.* **2013**, *144*, 57–62. [CrossRef]
204. Kamler, J.F.; Ballard, W.B.; Gilliland, R.L.; Mote, K. Coyote (Canis Latrans) Movements Relative to Cattle (Bos Taurus) Carcass Areas. *West. N. Am. Nat.* **2004**, *64*, 53–58.
205. Villalba, J.J.; Provenza, F.D.; Manteca, X. Links between Ruminants' Food Preference and Their Welfare. *Animal* **2010**, *4*, 1240–1247. [CrossRef]
206. Tilman, D. *Plant Strategies and the Dynamics and Structure of Plant Communities*; Princeton University Press: Princeton, NJ, USA, 1988; Volume 26.
207. Gregorini, P.; Villalba, J.J.; Chilibroste, P.; Provenza, F.D. Grazing Management: Setting the Table, Designing the Menu and Influencing the Diner. *Anim. Prod. Sci.* **2017**, *57*, 1248–1268. [CrossRef]
208. Distel, R.A.; Arroquy, J.I.; Lagrange, S.; Villalba, J.J. Designing Diverse Agricultural Pastures for Improving Ruminant Production Systems. *Front. Sustain. Food Syst.* **2020**, *4*, 596869. [CrossRef]
209. Jordán, M.J.; Martínez-Conesa, C.; Bañón, S.; Otal, J.; Quílez, M.; García-Aledo, I.; Romero-Espinar, P.; Sánchez-Gómez, P. The Combined Effect of Mediterranean Shrubland Pasture and the Dietary Administration of Sage By-Products on the Antioxidant Status of Segureña Ewes and Lambs. *Antioxidants* **2020**, *9*, 938. [CrossRef]
210. Athanasiadou, S.; Tzamaloukas, O.; Kyriazakis, I.; Jackson, F.; Coop, R.L. Testing for Direct Anthelmintic Effects of Bioactive Forages against Trichostrongylus Colubriformis in Grazing Sheep. *Vet. Parasitol.* **2005**, *127*, 233–243. [CrossRef] [PubMed]
211. Saed-Moucheshi, A.; Shekoofa, A.; Pessarakli, M. Reactive Oxygen Species (ROS) Generation and Detoxifying in Plants. *J. Plant Nutr.* **2014**, *37*, 1573–1585. [CrossRef]
212. Monjardino, M.; Revell, D.; Pannell, D.J. The Potential Contribution of Forage Shrubs to Economic Returns and Environmental Management in Australian Dryland Agricultural Systems. *Agric. Syst.* **2010**, *103*, 187–197. [CrossRef]
213. Revell, C.K.; Ewing, M.A.; Nutt, B.J. Breeding and Farming System Opportunities for Pasture Legumes Facing Increasing Climate Variability in the South-West of Western Australia. *Crop Pasture Sci.* **2012**, *63*, 840–847. [CrossRef]
214. Revell, D.K.; Norman, H.C.; Vercoe, P.E.; Phillips, N.; Toovey, A.; Bickell, S.; Hulm, E.; Hughes, S.; Emms, J. Australian Perennial Shrub Species Add Value to the Feed Base of Grazing Livestock in Low- to Medium-Rainfall Zones. *Anim. Prod. Sci.* **2013**, *53*, 1221–1230. [CrossRef]
215. Robertson, M.; Revell, C. Perennial Pastures in Cropping Systems of Southern Australia: An Overview of Present and Future Research. *Crop Pasture Sci.* **2014**, *65*, 1084–1090. [CrossRef]
216. Landeen, M.; Jones, C.; Jensen, S.; Whittaker, A.; Summers, D.D.; Eggett, D.; Petersen, S.L. Establishing Seed Islands for Native Forb Species on Rangelands Using N-Sulate Ground Cover Fabric. *Nativ. Plants J.* **2021**, *22*, 51–63. [CrossRef]
217. Santos-Gally, R.; Boege, K. Biodiversity Islands: The Role of Native Tree Islands Within Silvopastoral Systems in a Neotropical Region. In *Biodiversity Islands: Strategies for Conservation in Human-Dominated Environments*; Springer International Publishing: Cham, Switzerland, 2022; pp. 117–138. [CrossRef]
218. Schrader, J.; Wright, I.J.; Kreft, H.; Westoby, M. A Roadmap to Plant Functional Island Biogeography. *Biol. Rev.* **2021**, *96*, 2851–2870. [CrossRef]
219. Kim, N.H.; Cho, T.J.; Rhee, M.S. Current Interventions for Controlling Pathogenic *Escherichia coli*. *Adv. Appl. Microbiol.* **2017**, *100*, 1–47. [CrossRef]
220. Charles, A.S.; Baskaran, A.; Murcott, C.; Schreiber, D.; Hoagland, T.; Venkitanarayanan, K. Reduction of *Escherichia coli* O157:H7 in Cattle Drinking-Water by Trans-Cinnamaldehyde. *Foodborne Pathog. Dis.* **2008**, *5*, 763–771. [CrossRef]

221. Zhao, T.; Zhao, P.; West, J.W.; Bernard, J.K.; Cross, H.G.; Doyle, M.P. Inactivation of Enterohemorrhagic Escherichia Coli in Rumen Content- or Feces-Contaminated Drinking Water for Cattle. *Appl. Environ. Microbiol.* **2006**, *72*, 3268–3273. [CrossRef] [PubMed]
222. Richards, S.; Rao, L.; Connelly, S.; Raj, A.; Raveendran, L.; Shirin, S.; Jamwal, P.; Helliwell, R. Sustainable Water Resources through Harvesting Rainwater and the Effectiveness of a Low-Cost Water Treatment. *J. Environ. Manag.* **2021**, *286*, 112223. [CrossRef]
223. Sobsey, M.D.; Khatib, L.A.; Hill, V.R.; Alocilja, E.; Pillai, S. *Pathogens in Animal Wastes and the Impacts of Waste Management Practices on Their Survival, Transport and Fate*; ASABE: St. Joseph, MI, USA, 2006; pp. 609–666. [CrossRef]
224. Hunt, L.P.; Mcivor, J.G.; Grice, A.C.; Bray, S.G. Principles and Guidelines for Managing Cattle Grazing in the Grazing Lands of Northern Australia: Stocking Rates, Pasture Resting, Prescribed Fire, Paddock Size and Water Points—A Review. *Rangel. J.* **2014**, *36*, 105–119. [CrossRef]
225. Muzzo, B.I.; Provenza, F.D. Review of strategies for overcoming challenges of beef production in Tanzania. *Livestock Res. Rural Development* **2018**, *30*, 199.
226. Masters, D.G.; Blache, D.; Lockwood, A.L.; Maloney, S.K.; Norman, H.C.; Refshauge, G.; Hancock, S.N. Shelter and Shade for Grazing Sheep: Implications for Animal Welfare and Production and for Landscape Health. *Anim. Prod. Sci.* **2023**, *63*, 623–644. [CrossRef]
227. Valtorta, S.E.; Leva, P.E.; Gallardo, M.R. Evaluation of Different Shades to Improve Dairy Cattle Well-Being in Argentina. *Int. J. Biometeorol.* **1997**, *41*, 65–67. [CrossRef] [PubMed]
228. Titto, C.G.; Titto, E.A.L.; Titto, R.M.; Mourão, G.B. Heat Tolerance and the Effects of Shade on the Behavior of Simmental Bulls on Pasture. *Anim. Sci. J.* **2011**, *82*, 591–600. [CrossRef] [PubMed]
229. Van Laer, E.; Moons, C.P.H.; Ampe, B.; Sonck, B.; Vandaele, L.; De Campeneere, S.; Tuyttens, F.A.M. Effect of Summer Conditions and Shade on Behavioural Indicators of Thermal Discomfort in Holstein Dairy and Belgian Blue Beef Cattle on Pasture. *Animal* **2015**, *9*, 1536–1546. [CrossRef]
230. Davison, T.M.; Silver, B.A.; Lisle, A.T.; Orr, W.N. The Influence of Shade on Milk Production of Holstein-Friesian Cows in a Tropical Upland Environment. *Aust. J. Exp. Agric.* **1988**, *28*, 149–154. [CrossRef]
231. McIlvain, E.H.; Shoop, M.C. Shade for Improving Cattle Gains and Rangeland Use (El Uso de Sombreadores Para Mejorar Las Ganancias de Novillas y Pastoreo de Animales). *J. Range Manag.* **1971**, *24*, 181. [CrossRef]
232. Moreno García, C.A.; Maxwell, T.M.R.; Hickford, J.; Gregorini, P. On the Search for Grazing Personalities: From Individual to Collective Behaviors. *Front. Vet. Sci.* **2020**, *7*, 502292. [CrossRef]
233. Gregorini, P.; Tamminga, S.; Gunter, S.A. Behavior and Daily Grazing Patterns of Cattle. *Prof. Anim. Sci.* **2006**, *22*, 201–209. [CrossRef]
234. Lyons, R.K.; Machen, R.V. *Livestock Grazing Distribution: Considerations and Management*; Texas AgriLife Extension: College Station, TX, USA, 2023.
235. Heins, B.J.; Pereira, G.M.; Sharpe, K.T. Precision Technologies to Improve Dairy Grazing Systems. *JDS Commun.* **2023**, *4*, 318–323. [CrossRef]
236. Bello, R.-W.; Talib, A.Z.H.; Mohamed, A.S.A. A Framework for Real-Time Cattle Monitoring Using Multimedia Networks. *Int. J. Recent Technol. Eng. (IJRTE)* **2020**, *8*, 974–979. [CrossRef]
237. Ramezani Gardaloud, N.; Guse, C.; Lidauer, L.; Steininger, A.; Kickinger, F.; Öhlschuster, M.; Auer, W.; Iwersen, M.; Drillich, M.; Klein-Jöbstl, D. Short Communications: An Ear-Attached Accelerometer Detects Effects of Regrouping on Lying, Rumination, and Activity Times in Calves. *Vet. Res. Commun.* **2023**, *47*, 2333–2337. [CrossRef] [PubMed]
238. Versluijs, E.; Niccolai, L.J.; Spedener, M.; Zimmermann, B.; Hessle, A.; Tofastrud, M.; Devineau, O.; Evans, A.L. Classification of Behaviors of Free-Ranging Cattle Using Accelerometry Signatures Collected by Virtual Fence Collars. *Front. Anim. Sci.* **2023**, *4*, 1083272. [CrossRef]
239. Džermeikaitė, K.; Bačėninaitė, D.; Antanaitis, R. Innovations in Cattle Farming: Application of Innovative Technologies and Sensors in the Diagnosis of Diseases. *Animals* **2023**, *13*, 780. [CrossRef]
240. Sprinkle, J.E.; Sagers, J.K.; Hall, J.B.; Ellison, M.J.; Yelich, J.V.; Brennan, J.R.; Taylor, J.B.; Lamb, J.B. Predicting Cattle Grazing Behavior on Rangeland Using Accelerometers. *Rangel. Ecol. Manag.* **2021**, *76*, 157–170. [CrossRef]
241. Riaboff, L.; Shalloo, L.; Smeaton, A.F.; Couvreur, S.; Madouasse, A.; Keane, M.T. Predicting Livestock Behaviour Using Accelerometers: A Systematic Review of Processing Techniques for Ruminant Behaviour Prediction from Raw Accelerometer Data. *Comput. Electron. Agric.* **2022**, *192*, 106610. [CrossRef]

Disclaimer/Publisher's Note: The statements, opinions and data contained in all publications are solely those of the individual author(s) and contributor(s) and not of MDPI and/or the editor(s). MDPI and/or the editor(s) disclaim responsibility for any injury to people or property resulting from any ideas, methods, instructions or products referred to in the content.

agronomy

MDPI

Article

Potential Impacts of Climate Change on the Spatial Distribution Pattern of Naked Oats in China

Zhenwei Yang [1,2], Xujing Yang [1,2], Yuheng Huang [1,2], Yalin Zhang [1,2], Yao Guo [1,2], Meichen Feng [1,2,*], Mingxing Qin [2,3], Ning Jin [4], Muhammad Amjad [1,2], Chao Wang [1,2], Meijun Zhang [1,2] and Wude Yang [1,2]

[1] College of Agriculture, Shanxi Agricultural University, Taigu 030801, China; yzw5221@163.com (Z.Y.); yangxujing0521@163.com (X.Y.); dingzi_wangyi@163.com (Y.H.); zhangyalin1111@163.com (Y.Z.); 16603475962@163.com (Y.G.); amjadmalik3125@gmail.com (M.A.); wcqxx2005@126.com (C.W.); meijunz@126.com (M.Z.); sxauywd@126.com (W.Y.)
[2] Smart Agriculture College, Shanxi Agricultural University, Taigu 030801, China; qmx758@163.com
[3] College of Resources and Environment, Shanxi Agricultural University, Taigu 030801, China
[4] Department of Resources and Environmental Engineering, Shanxi Institute of Energy, Jinzhong 030600, China; j.n.--0613@163.com
* Correspondence: fmc101@163.com; Tel.: +86-354-6285019

Abstract: Naked oats, a significant minor cereal crop in China popular for its nutrient richness, have experienced a surge in production in recent years, fueled by the escalating demand for wholesome healthy food. However, the dispersed and disorganized cultivation plan of naked oats poses a significant constraint on its industrial progression. Considering the dual influence of cultivation, management techniques, and global climate change on the production of naked oats, this study explores the potential impacts of climate change on the spatial distribution and yield of this cereal crop. Leveraging CMIP6 climate models (BCC-CSM2-MR, CanESM5, CNRM-ESM2-1) and an optimized MaxEnt model (RM = 0.5, FC = LQ), we simulated potential climate-suitable zones for naked oats from 1990 to 2020 and forecasted alterations under various emission scenarios from 2021 to 2100. The model achieved an average accuracy test with high value (AUC = 0.945) in predicting suitable areas; with precipitation seasonality (Coefficient of Variation) (bio15, 21.70%) and topsoil pH (H_2O) (T_PH_H_2O, 21.00%) as key factors, both climate and soil properties have a greater influence. Simulation results showed that the climatically suitable area for naked oats increased under all scenarios, with the largest increase in the optimal growing area under ssp126 in the 2030s. The increase was 3.93% with an area of 0.77×10^6 km^2. The study also compared the data from the main producing counties of naked oats in Shanxi Province from 2020 to 2022 for statistical purposes, and found that 39 counties were in high climatic suitability zones and 39 counties were in remarkably high climatic suitability zones. The agreement rate between planting areas and climatically suitable areas was as high as 97.44%. Further, the growing area expanded westward, increasing the production intensity. This study reveals the current spatial distribution pattern of naked oats, providing a scientific rationale for addressing climate change through multi-scenario predictions. Our findings have implications for optimizing cultivation layout and identifying optimal zones, supporting sustainable agricultural development strategies in China.

Keywords: naked oats; climate change; CMIP6; MaxEnt; spatial distribution

1. Introduction

According to the Fifth Assessment Report (AR5) of the Intergovernmental Panel on Climate Change (IPCC), global temperatures have increased by 0.65 °C to 1.06 °C since 1880,

with projections indicating a sustained upward trend in the coming decades [1,2]. Staple foods high in carbohydrates, particularly cereals, frequently exhibit a greater environmental footprint compared to nutrient-dense foods, such as fruits and vegetables [3]. There is a paucity of research examining the impacts of climate change on oat production. However, numerous climatic factors including temperature, CO_2 concentration, ozone levels, water availability and salinity can influence plant yields, with these effects showing geographical variability. An elevation in CO_2 level is anticipated to stimulate plant growth, exerting a beneficial influence, whereas a decline in water resources poses detrimental effects [4].

Historical climate, geology, and other environmental factors interact intricately to determine the geographic distribution patterns of species [5]. Species Distribution Models (SDMs) determine the relationship between species distribution and environmental factors by relating samples of species distribution to related variables. This resultant relationship is subsequently applied to the study area to predict the distribution of the target species [6]. SDMs have emerged as an indispensable tool for elucidating the intricate interactions between the spatial pattern of species' geographical distribution and environment in the context of evolving global climatic conditions [7,8]. Primary SDMs encompass the Genetic Algorithm for Rule-set Prediction (GARP) [9], Generalized Additive Models (GAM), Random Forest (RF), and Maximum Entropy MaxEnt [10]. Presently, an ever-growing number of SDMs are set to investigate species' historical geographical distribution process and future distribution trends amidst climate change. Comparative assessments among various models have demonstrated that MaxEnt surpasses others in terms of sample tolerance and prediction accuracy, particularly when dealing with limited sample sizes, generating highly satisfactory simulation outcomes [11]. The MaxEnt model is now largely employed for predicting species' potential climate-suitable habitats [12] and invasion trends of alien species [13], and suggesting biodiversity conservation initiatives [14] and endangered species protection efforts [15].

Around 70 diverse types of oats are grown worldwide, with hulled and naked oats (*Avena nuda* L.) being the two most prevalent varieties [16], the latter commonly referred to as "youmai", "yumai", and "lingdangmai" in China. Predominantly distributed across Inner Mongolia, Gansu, Shanxi, Hebei, and other regions, naked oats constitute a vital minor cereal crop in China, accounting for an impressive 90% share of cultivated oats. These large-seeded Chinese oat types are the most widely grown because of their exceptional drought resistance, cold tolerance, and flexibility. In recent years, improvement in quality of life and dietary habits have stimulated a growing demand for food safety, nutrition, and healthcare, resulting in an emerging trend in the consumption of oats and oat-based products. Consequently, China's oat market harbors substantial potential [17].

However, the cultivated area of oats in China experiences significant annual variations, with the planting area increasing from 3.62×10^5 hm^2 in 2022. Most of these producing areas are located in arid and semi-arid regions that rely upon rain-fed agriculture and have fragile ecological conditions. The existing scattered and unplanned layout of cultivation poses significant obstacles to the development of the oat industry [14]. Therefore, in order provide a scientific foundation for oat production planning, investigating the suitability of naked oat cultivation distribution is indispensable.

Our previous study investigated the potential geographic distribution of ruderal oats under climate change, with a special focus on production in North China [18]. The current study extends this work by providing a comprehensive analysis of the suitability of naked oat cultivation distribution across broader regions in China. Using the MaxEnt model, this study aims to clarify the relationship between environmental climatic parameters and naked oats, estimate trends in climate-suitable regions under various emission scenarios, and analyze the current climate suitability for multiple varieties of naked oats. By

identifying areas where climate conditions are expected to become more favorable for oat cultivation, this research aims to provide actionable recommendations for optimizing the spatial distribution of oat production in China, thereby contributing to regional agricultural planning.

2. Materials and Methods

2.1. Data Acquisition

2.1.1. Species Distribution Data

The natural distribution records of hulled oats across China were initially obtained by consulting various resources, including the Global Biodiversity Information Facility (http://www.gbif.org (accessed on 20 February 2023)), the National Specimen Information Infrastructure of China (http://www.Nsii.org (accessed on 21 February 2023)), the Chinese Virtual Herbarium (http://www.cvh.org (accessed on 22 February 2023)), and authoritative books such as the Flora of China (Higher Plants). Distribution points lacking geographical information and those with duplicate data were excluded from the analysis. To compl ete missing latitude and longitude data, Google Earth was utilized to locate and mark corresponding geographical coordinates, with precision extending to the county level. This process yielded comprehensive latitude and longitude information for all distribution points. It is noteworthy that employing distinct databases and sampling methodologies for acquiring sample data points may introduce certain geographical sampling biases [19], potentially impeding the predictive performance of the model. To address this issue, the present study employed the ENM Tools utility to perform overfitting reduction on the species distribution point data [20], thereby generating spatial grids corresponding to the environmental layer resolution (30″, approximately 0.81 km^2) (Figure 1).

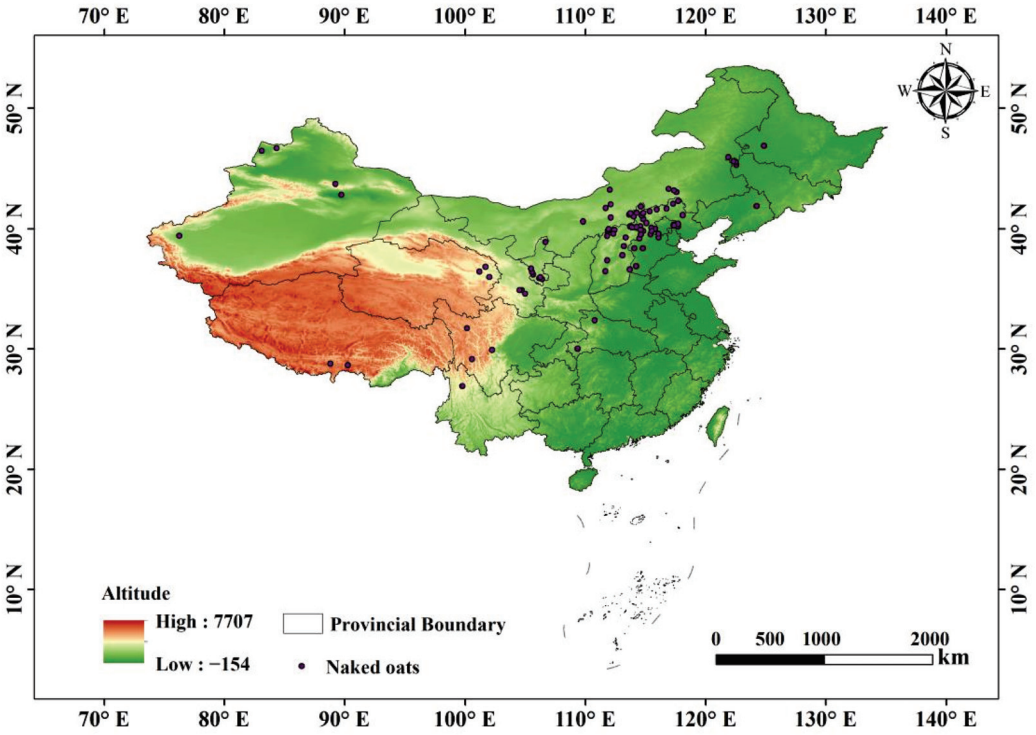

Figure 1. Sample distribution points map.

2.1.2. Geographic and Environmental Data

The geographic base map utilized in the model analysis is a 1:4 million vector map of China's administrative districts, sourced from the National Centre for Basic Geo-graphic

Information (https://www.ngcc.cn (accessed on 17 April 2023)). The current climate data (1990–2020) for monthly maximum temperature, monthly minimum temperature, and monthly precipitation were obtained from Loess Plateau Sub Center, National Earth System Science Data Centre, National Science and Technology Infrastructure of China (http:/loess.geodata.cn (accessed on 18 April 2023)), with a spatial resolution of 0.0083333º (approximately 1 km). This dataset was derived from global 0.5º climate data provided by CRU and high-resolution data from WorldClim. The Delta spatial downscaling method was applied to scale these data to the Chinese context with high validation accuracy achieved against 496 independent meteorological observation points [21]. Subsequently, the data set was processed using the "dismo" [22] and "terra" [23] packages in R to generate 19 bioclimatic variables (Bio1–Bio19). The future period (2021–2100) selected for this study was obtained from the World Climate Data website database (http://www.worldclim.org, version 1.4 (accessed on 15 June 2023)). Four Shared Socio-economic Pathways (SSPs), namely 126, 245, 370, and 585, for the three climate models, namely BCC-CSM2-MR [24], CanESM5, and CNRM-ESM2-1, were selected on the basis of the Coupled Model Intercomparison Project Phase 6 (CMIP6) [25–27]. The bioclimatic variables predicted under [28] (IPCC) were used to simulate potential changes in the distribution range of naked oats under different emission scenarios in the future (2021–2100). These pre-dicted bioclimatic variables (bio1–bio19) were treated as mean values at 20-year intervals from 2021–2100.

Multiple factors, including light, soil type, temperature, and moisture influence plant growth, having a key role in bioclimatic variables. To improve the predictive power of the model, a topographic factor (elevation, slope, and slope direction), a soil factor (effective soil water content, carbonate or lime content, sulphate content, pH, organic carbon content, exchangeable sodium, and conductivity), a total of 29 environmental factor layers, using soil data from the Harmonised World Soil Database version 1.2 (HWSD, http://www.Fao.org (accessed on 25 July 2023)) [29], and the elevation data used in the modelling were also obtained from HWSD.

2.2. Model Construction

2.2.1. MaxEnt

The model used in this study is Maxent 3.4.3 [30], which requires only environmental layers and a small amount of distribution point data to obtain good model simulation results compared to other species distribution models [31,32]. MaxEnt, called the 'Maximum Entropy Principle', applies five different characteristic constraints (linear, product, hinge, quadratic, and threshold) regarding environmental variables to calculate the potential geographic distribution probability of the species. The estimated MaxEnt probability distribution of location (x) is the weighted sum of the environmental features (f) divided by the exponent of normalization constant ($Z\lambda$) to ensure that the probability values range from 0 to 1 and sum to one, where λ denotes the vector of feature weights, n denotes the number of environmental features, and $Z\lambda$ is the normalization constant ensuring that the probability distributions in the study region sum to one.

2.2.2. Parameter Optimization and Model Evaluation Methods

The default parameters of the MaxEnt model were set by its developers based on the comparison of their model results with realistic distributions in their studies of bird, mammal, reptile, and plant distributions [32]. However, since the MaxEnt model is a complex model in machine learning, it is sensitive to sampling bias and the complexity of the model is related to the feature functions (FC): LQPTH (L is linear liner, Q is quadratic, P is multiplicative product, T is threshold and H is fragmented hinge) and Regularization multiplier (RM) are significantly correlated [33]. In order to avoid the influence of over-

fitting on the migration ability of the model, this paper applies the 'kuenm' package in R4.2.3 to cross-combination validation of the RM (0–4) of the model starting from 0 and increasing upward every 0.5 up to 4 with the FC (LQPTH), and finally selects the model that has a significance, omission rates <5%, and with a frequency of the data (LQPTH) that has a significant correlation with the LQPTH. Omission rates <5% and smaller delta AICc values (the difference between the calibrated optimal model and the current model's Akaike informativeness criterion) were chosen as the optimal parameter combinations to run the final model [34].

When the MaxEnt 3.4.4 model was run, the georeferenced distribution points of naked oats needed to be converted into csv format. Resolutions of the environmental factor layer and the extent of the study area used in the modelling needed to be standardized. All the environmental factor layers and oat distribution point data were imported into MaxEnt software, and the number of random background points was set to ten thousand. A total of 75% of the oat distribution points would be used for model calculations whereas the remaining 25% would be used for model testing [33]. To improve the accuracy of results, the experiment was repeated ten times. Response curves of the individual environmental factors were selected to be plotted, the knife-cut method (Jackknife) was used to assess the contribution and replacement importance of each environmental factor to the oat distribution, and the environmental factors that produced a higher training gain were the key bioclimatic variables. To calibrate the accuracy of MaxEnt model assessment, the predictive effect was evaluated using a Receiver operating characteristic (ROC) curve that was independent of the threshold [32], and the value of Area under the curve (AUC) of the ROC curve was used as a measure of model accuracy. The AUC value is between 0 and 1.0, and the closer the value is to 1.0, the better the prediction of the model. Based on the AUC value, the model prediction effect is classified into several grades: 0.5–0.6 indicates that the model prediction effect is unqualified, 0.6–0.7 is poor, 0.7–0.8 is fair, 0.8–0.9 is good, and 0.9–1 is excellent [33].

2.2.3. Correlation Analysis of Environmental Factors

During the construction of the species distribution model, a high correlation between variables may lead to errors in the simulation of the model [35,36]. Therefore, in this study, the SDM Toolbox tool in ArcGIS 10.5 [37] was used to assess the correlation between all 29 variables using a Pearson correlation coefficient approach(Figure 2), removing environmental factor layers with correlations higher than 0.8, and retaining variables with high biological significance to the species and low correlations (Pearson correlation coefficient $|r| < 0.8$) for the MaxEnt analysis [38,39]. Finally, five climatic factors such as mean diurnal range (bio2) and precipitation of wettest month (bio13); three topographic factors such as altitude, slope, and aspect; and five soil factors such as pH (T_PH_H_2O) and carbonate or lime content (T_$CaCO_3$) of the topsoil layer were selected to figure in the modelling. The set of outcome variables contains the 13 bold factors used to construct the model (Table 1).

Table 1. Environmental factors used for modeling after screening.

Variable	Description	Unit
bio1	Annual mean temperature	°C
bio2	**Mean diurnal range**	**°C**
bio3	Isothermality	×100
bio4	**Temperature seasonality**	**×100**
bio5	Max temperature for warmest month	°C
bio6	Min temperature for coldest month	°C
bio7	Temperature annual range	°C
bio8	Mean temperature of wettest quarter	°C

Table 1. *Cont.*

Variable	Description	Unit
bio9	Mean temperature of driest quarter	°C
bio10	Mean temperature of warmest quarter	°C
bio11	Mean temperature of coldest quarter	°C
bio12	Annual precipitation	mm
bio13	**Precipitation of wettest month**	**mm**
bio14	**Precipitation of driest month**	**mm**
bio15	**Precipitation seasonality**	**×100**
bio16	Precipitation of wettest quarter	Mm
bio17	Precipitation of driest quarter	Mm
bio18	Precipitation of warmest quarter	Mm
bio19	Precipitation of coldest quarter	Mm
Slope	**Slope**	°
Altitude	**Altitude**	**m**
Aspect	**Aspect**	°
T_CACO_3	**Topsoil Calcium Carbonate**	**% weight**
T_CASO_4	**Topsoil Gypsum**	**% weight**
T_ECE	Topsoil Salinity (Elco)	dS/m
T_ESP	**Topsoil Sodicity (ESP)**	**%**
T_OC	Topsoil Organic Carbon	% weight
$T_PH_H_2O$	**Topsoil pH (H_2O)**	**−log(H+)**
AWC_CLASS	**AWC Range**	**code**

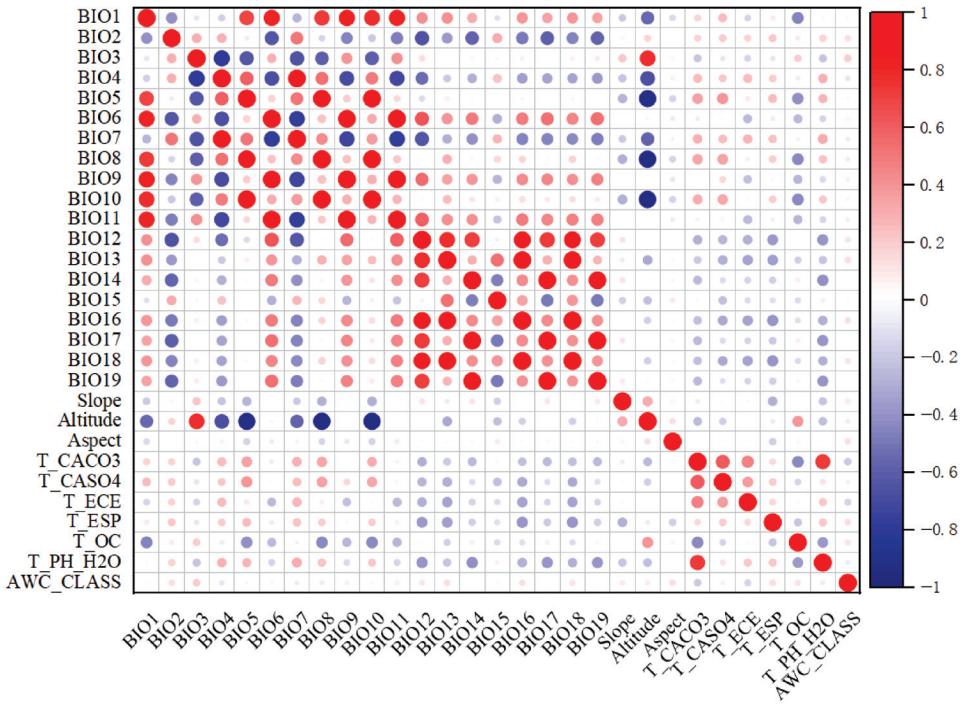

Figure 2. Correlation analysis of environmental factors.

3. Results and Analyses

3.1. Potential Geographical Distribution of Naked Oats in the Current Period

3.1.1. Model Parameter Optimization and Accuracy Evaluation

To reduce MaxEnt model over-fitting, this paper optimizes the modulation multiplicity and feature combination selection. The ENMeval package used to optimize the MaxEnt parameter settings includes auc.diff.avg (AUC difference average), auc.val.avg (AUC validation set average), AICc (corrected Akaike Information Criterion difference), and bias

rate (or.10p.avg). When FC = LQ and RM = 0.5 (Figure 3), delta.AICc is 0, auc.div.avg has the highest value, and or.10p.avg is also lower at parameter 0.5, which shows better stability and highest value, which indicates that the combined model has strong predictive ability and therefore the model is optimal.

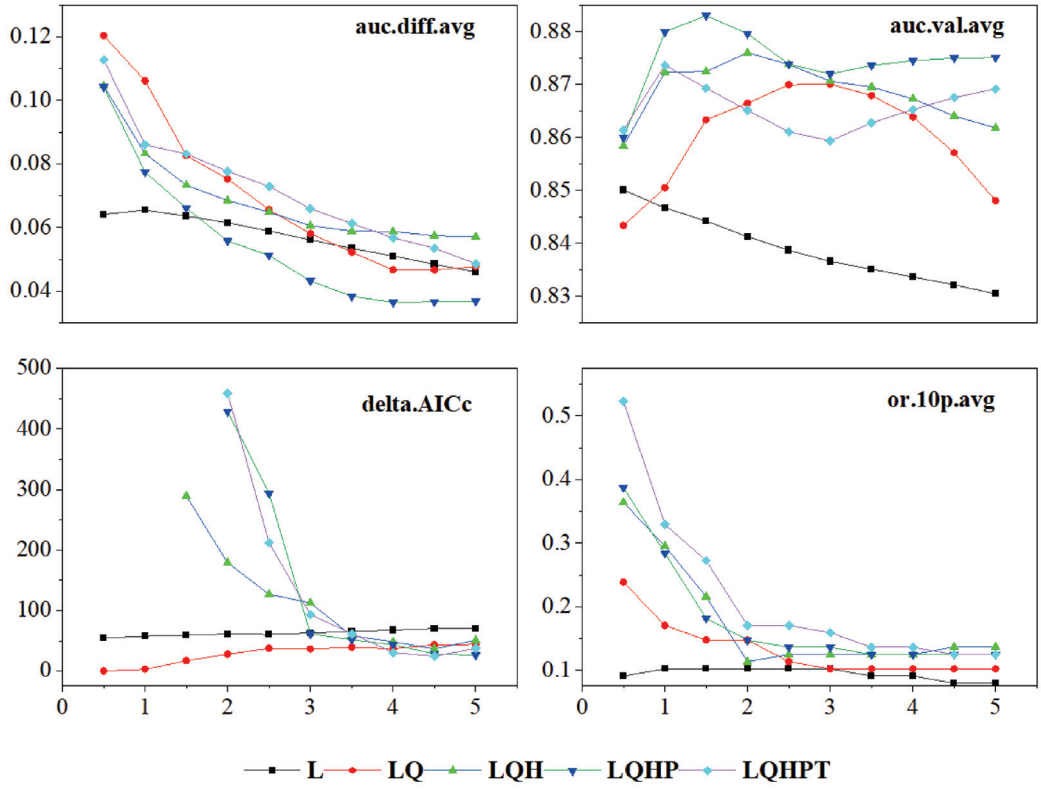

Figure 3. Trend analysis of model parameter optimization and accuracy assessment.

Twenty-five percent of geographical distribution points of naked oats were randomly selected as the test set and 75% as the training data, then the MaxEnt model was repeatedly run ten times. The results of the model accuracy test are shown in (Figure 4). The omission rate curves of the ten simulation runs have low omission rates under different thresholds and have minute fluctuations. Combined with the current and future climate scenarios, the average value of AUC of the subject's working curve in the MaxEnt prediction results are all greater than 0.94. This shows that the model prediction results are highly credible and convincing. These results can be used for the study of the potential geographic distribution of naked oats across the country.

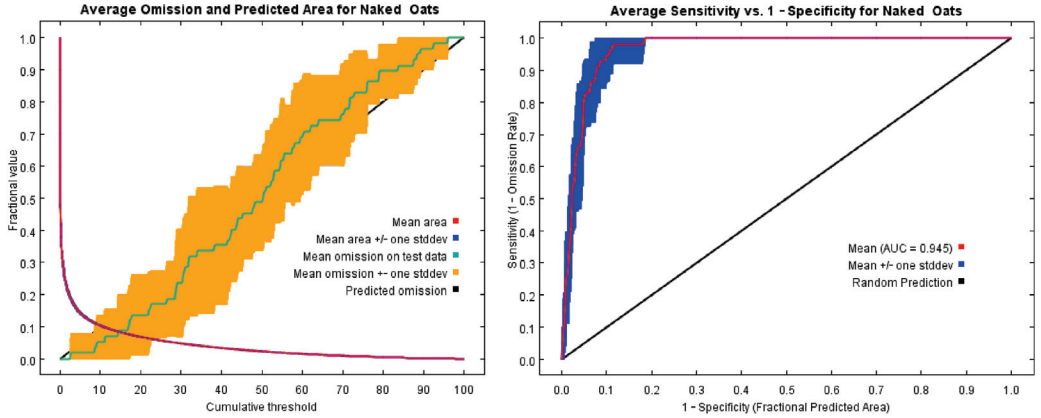

Figure 4. ROC curve and omission rate curve under the optimized MaxEnt model.

3.1.2. Analysis of Dominant Climatic Factors Affecting the Geographical Distribution of Oats

The dominant climate factors affecting the simulation of oat habitat distribution after 10 runs of the model along with their corresponding contribution rates as well as replacement importance values were analyzed using the Jackknife test (Table 2). Response curves of the environmental factors showed how logistic predictions of the MaxEnt model changed with each environmental curve, and Figure 5 shows the response curves of the six environmental factors with the highest contribution to the influence of oat distribution.

Table 2. Contribution of each environmental factor in MaxEnt model.

Variable	Percent Contribution/%	Permutation Importance/%
bio15	21.70	12.10
T_PH_H_20	21.00	9.30
AWC_CLASS	15.80	14.60
bio4	8.10	13.20
bio14	7.80	2.20
altitude	6.00	24.20
T_$CASO_4$	5.70	0.40
bio13	4.70	18.30
T_$CACO_3$	3.40	3.50
slope	2.30	0.10
bio2	1.40	1.30
T_ESP	1.20	0.30
aspect	0.60	0.50

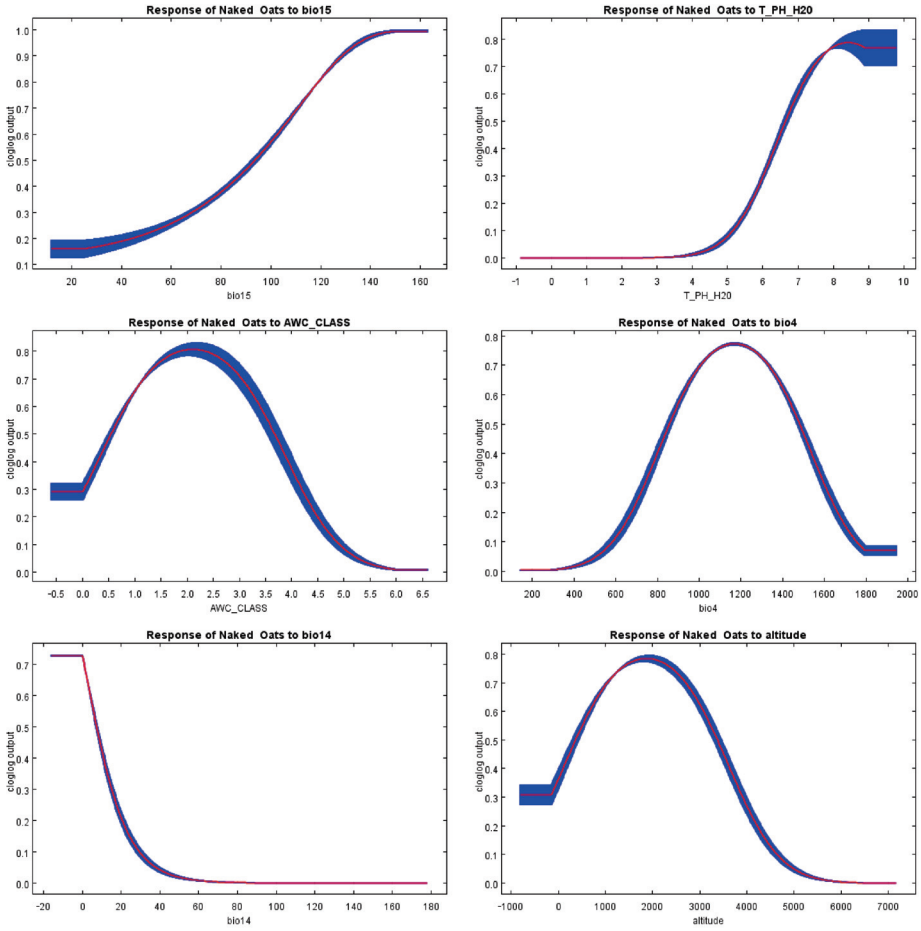

Figure 5. Response curve of environmental factors.

The top six environmental factors contributing to the distribution of naked oats are precipitation seasonality (Coefficient of Variation) (bio15, 21.70%), topsoil pH (H_2O) (T_PH_H_2O, 21.00%), AWC Range (AWC_CLASS, 15.80%), temperature seasonality (standard deviation × 100) (bio4, 8.10%), precipitation of driest month (bio14, 7.80%) and altitude (6.00%). These six environmental covariates accounted for 80.40% of the total contribution.

3.1.3. The Spatial Distribution of Climatically Suitable Areas for Naked Oats Under Current Climatic Conditions

Based on the suitability of oat habitat under the current climate scenario, the response curve of environmental variables (Figure 5) was drawn by combining the results of the Pearson correlation analysis (Figure 2). The area with a geographic distribution probability greater than 0.05 was set as a suitable area, while the area with a geographic distribution probability greater than 0.50 was a highly suitable area.

The main environmental factor affecting naked oats is precipitation seasonality (Coefficient of Variation) (bio15), with naked oats showing high suitability for growth when this value lies in the range of 95–150. The subsequent environmental factors with a high contribution are topsoil pH (H_2O)(T_PH_H_2O) with a high-suitability zone threshold interval of 6.6–8.5; AWC range (AWC_CLASS) with a high-aptitude zone threshold interval of 0.6–3.7; temperature seasonality (standard deviation × 100) (bio4) with a high-aptitude zone threshold interval of 850–1480; precipitation of driest month (bio14) with a high-aptitude zone threshold interval of 0–14 mm; and altitude with a high-aptitude zone threshold interval of 400–3400 m.

3.2. Spatial Distribution of Climatically Suitable Areas for Naked Oats Under Current Climate Conditions

Figure 6 shows the potential spatial distribution of naked oats simulated by the MaxEnt model under current climatic conditions (1990–2020). The logistic results output from the MaxEnt model are expressed as different probabilities ranging from 0–1. Furthermore, this result is classified into five suitability classes using the reclassification tool in ArcGIS 10.5. In this classification, 0–0.05 is considered a non-suitable zone, 0.05–0.30 a low-suitability zone, 0.30–0.50 a medium-suitability zone, 0.50–0.70 a high-suitability zone, and 0.70–1 an optimum zone.

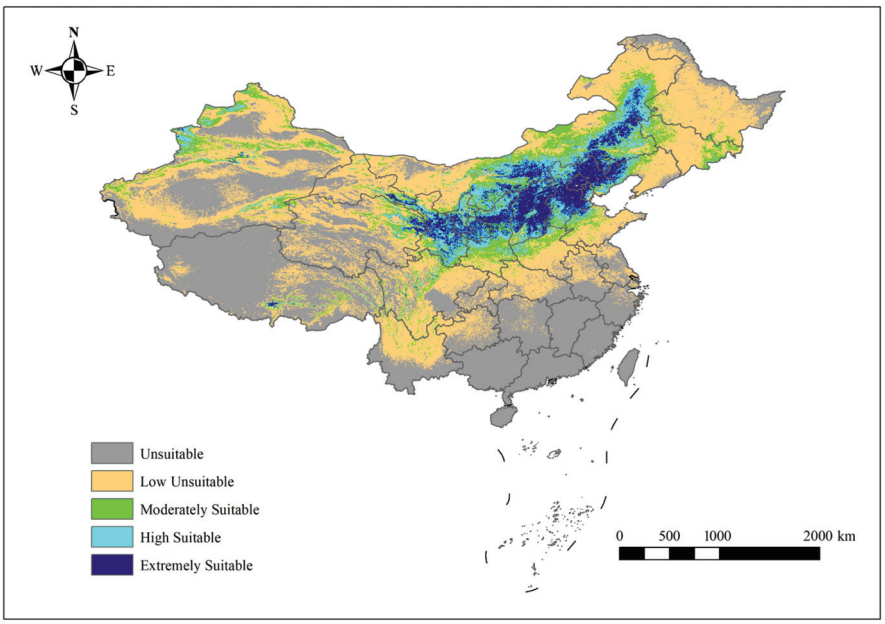

Figure 6. The distribution of suitable habitats for naked oats in China during the current period.

Most suitable and highly suitable areas for naked oats are distributed in Shanxi, Hebei, Beijing, Tianjin, western Liaoning, southeastern Gansu, Ningxia, southern Inner Mongolia, northern Shaanxi, and other areas. While the medium-suitability area expands to North China and Northwest China, the low-suitability area is distributed in the edge area of the medium-suitability area, presenting the transitional characteristics of the outward expansion. Most of the areas of the South and Southwest belong to the unfamiliar areas, and the climatic conditions are unfavorable for oat cultivation.

3.3. Potential Distribution of Naked Oats Under Future Climate Models

3.3.1. Simulation of the Potential Distribution of Naked Oats Under Future Climate Models

We averaged the predictions of three GCM models to create the distribution map of climate suitability zones for the future period, which helped to reduce the impact of using a single GCM model on the simulation results. Figure 7 shows the distribution of oat suitability zones under different future climate-change scenarios (ssp126, ssp245, ssp370, ssp585). The highest zone of naked oats is still mainly distributed in Shanxi, Hebei, Beijing, and Tianjin. In the future, highly suitable areas for naked oats sativa will be distributed in Shanxi, Hebei, Beijing, Tianjin, and other areas, the moderately suitable areas will be distributed in the transition zone, the middle-fitness zone will mainly be distributed around the highly suitable zone, while the low-suitability and unsuitable zones are widely distributed in the western provinces.

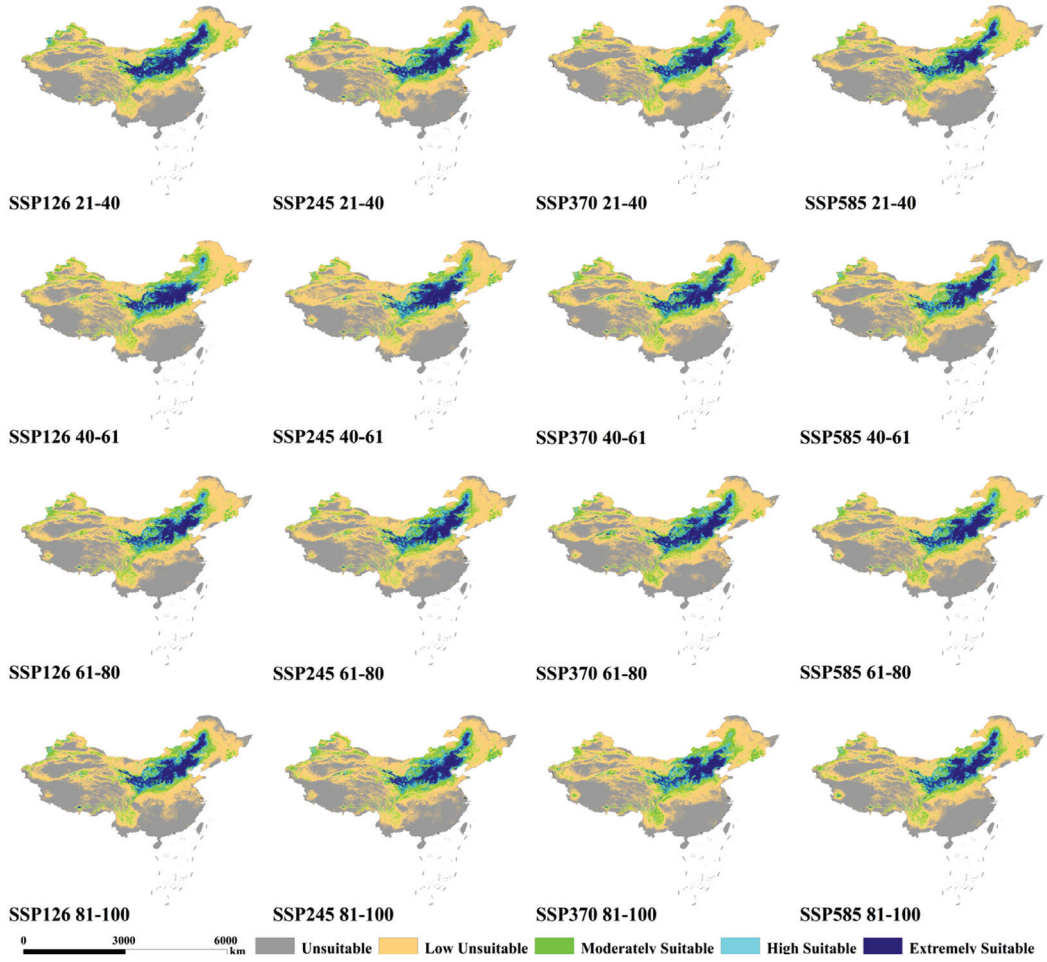

Figure 7. Distribution of naked oats suitable areas in the coming period.

Figure 8 shows that the most suitable areas for naked oats under four future climate-change scenarios increase slowly, while the suitable areas for naked oats planting may

become more concentrated in the future. Meanwhile, the area of the high-suitability zone decreases under all four climate-change scenarios. A decrease in the area of the medium-suitability zone is in the ssp370 climate-change scenario for the 2030 period, the ssp245 and ssp885 scenarios for 2050 period, and the ssp126 scenario for the 2090 period. The area of the remaining medium-suitability zone increased. In addition to this, the area of the low-suitability zone varies from scenario to scenario over time, e.g., it increases the most in the ssp245 scenario in the 2050 period and decreases the most in the ssp370 scenario in the 2070 period.

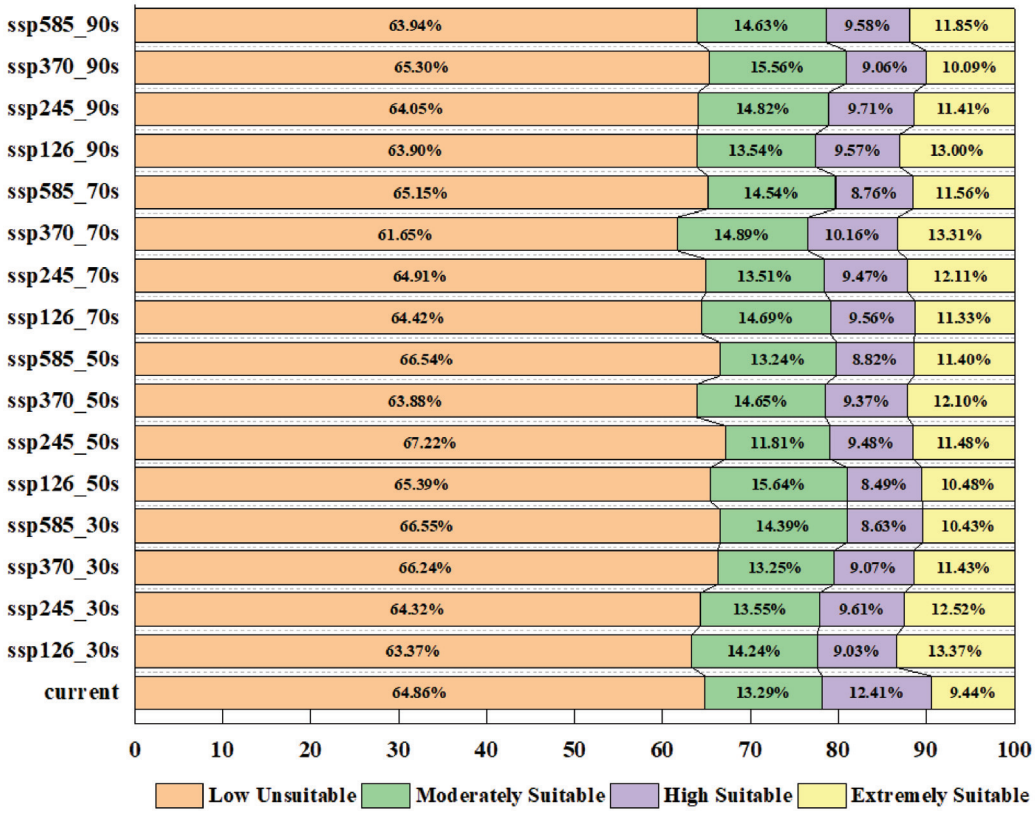

Figure 8. Distribution of naked oats in the future period in relation to the area of each suitable area.

Under the ssp126 climate-change scenario, the largest increase in the moderately suitable area for naked oats was observed in the 2070s, with a growth of 1.53%. In contrast, under the ssp585 scenario, the most significant decrease in the moderately suitable area for naked oats occurred in the 2050s, with a reduction of 0.47%. These findings suggest that the impact on the moderately suitable area for naked oats may vary under different climate-change scenarios, indicating potential uncertainty in future projections.

3.3.2. Changes in the Distribution of Oat Habitat Area Under Future Climate Models

From Table 3, the most suitable area for oats increases in all four periods, with the largest increase in the 2030s period, with an area of 0.77×10^{6} km^2. In contrast, the highly suitable area for oats decreases to varying degrees across all four decades. The largest highly suitable area is found in the 2050s under the ssp245 scenario with 0.87×10^6 km^2, while the smallest highly suitable area is in the 2070s under the ssp585 scenario, measuring 0.48×10^6 km^2. The low-suitability areas exhibit varying degrees of expansion. The maximum area of naked oats was 4.04×10^6 km^2 under the ssp245 scenario in the period of the 2050s, and the minimum area was 3.52×10^6 km^2 under the ssp370 scenario in the period of the 2070s. The non-fitness area decreased in the next four periods, indicating that

the conditions for oat cultivation may improve in the future and become more suitable for oat growth.

Table 3. Naked Oats Area under Different Climate-Change Scenarios.

Period	Type	Unsuitable Areas ($\times 10^6$ km^2)	Low-Suitability Areas ($\times 10^6$ km^2)	Moderately Suitable Areas ($\times 10^6$ km^2)	Highly Suitable Areas ($\times 10^6$ km^2)	Most Suitable Areas ($\times 10^6$ km^2)
	Current	3.87	3.71	0.76	0.71	0.54
2030s	ssp126	3.84	3.65	0.82	0.52	0.77
	ssp245	3.76	3.75	0.79	0.56	0.73
	ssp370	4.08	3.65	0.73	0.50	0.63
	ssp585	4.03	3.70	0.80	0.48	0.58
2050s	ssp126	3.58	3.93	0.94	0.51	0.63
	ssp245	3.58	4.04	0.71	0.57	0.69
	ssp370	3.72	3.75	0.86	0.55	0.71
	ssp585	4.16	3.62	0.72	0.48	0.62
2070s	ssp126	3.95	3.64	0.83	0.54	0.64
	ssp245	3.89	3.70	0.77	0.54	0.69
	ssp370	3.89	3.52	0.85	0.58	0.76
	ssp585	3.87	3.72	0.83	0.50	0.66
2090s	ssp126	4.06	3.54	0.75	0.53	0.72
	ssp245	3.73	3.76	0.87	0.57	0.67
	ssp370	3.74	3.82	0.91	0.53	0.59
	ssp585	3.86	3.67	0.84	0.55	0.68

3.4. Consistency Between Climatic Suitability Zones and Actual Yield of Naked Oats Under Climate Change Conditions

Figure 9 overlays the climatic suitability distribution map of naked oats to retain the maximum value of each raster, generating the total climatic suitability distribution map, dividing the suitability grade into five grades according to Figure 6, overlaying the potential climate suitability class map and vector map of major planting areas of naked oats sativa under the current climate model generated by the model simulation for analysis. And if a county is categorized as a highly suitable area (habitat suitability > 0.5), then the planting area is considered to have consistency with the climate suitability zone; a county that is categorized as a low-suitability zone is considered to have no consistency. The bar chart represents the number of major planting counties with different climatic suitability for naked oats, and the pie chart represents the proportion of consistency and inconsistency.

Considering the feasibility of obtaining statistical data, the study selected the main production counties of naked oats in Shanxi Province (average annual production greater than ten tons) to yield data from 2020 to 2022. A total of thirty-nine counties with annual production greater than ten tons was superimposed upon the climatically suitable area rating map and the map of the main planting areas of naked oats, to statistically measure the consistency between the main planting counties of naked oats and the climatically suitable areas of naked oats simulated by the model. The study shows that oat production is in a high climatic suitability zone and remarkably high climatic suitability zone in 39 and 38 counties, respectively. And the consistency ratio between planting areas and climatic suitability zones accounts for 97.44%, which indicates that the distribution of major oat producing counties and climatic suitability zones under the current climatic conditions have a high degree of consistency.

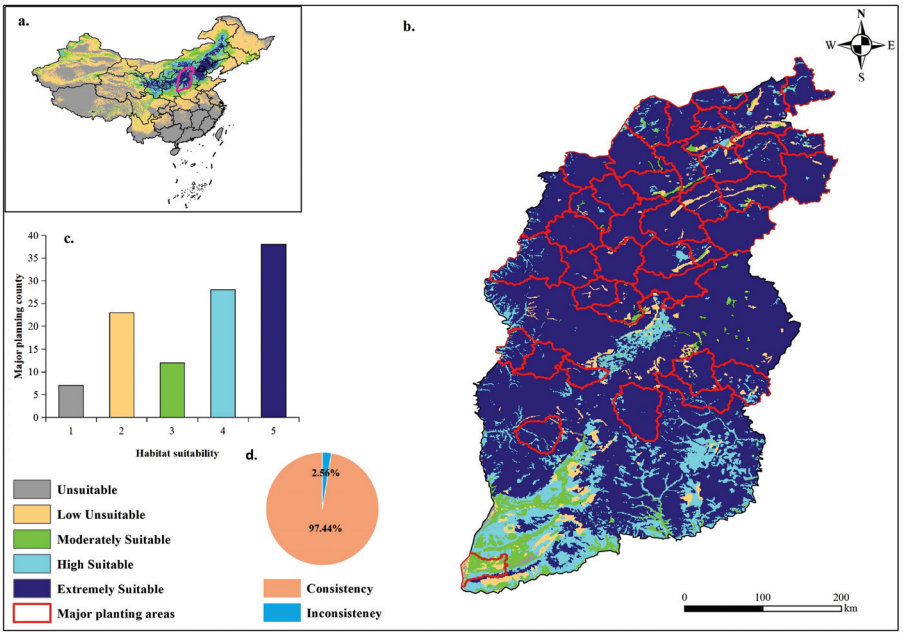

Figure 9. (**a**) A schematic representation of the geographical positioning of Shanxi Province within the territorial extent of China. (**b**) Consistency between climatically suitable areas and actual yield of oat. (**c**) Number of counties in each suitable area. (**d**) Map of consistency between plantingareas and climatically suitable areas.

3.5. Location and Migration Trends of the Center of Mass in the Total Suitable Area of Naked Oats Under Climate Change

In this study, we used a geographic distribution metric tool to fit the range of species distribution under different future emission pathways to a single center-of-mass (center) point and created a vector file to predict the trend and extent of species change over time by tracking the changes in center-of-mass. We also mapped the distribution of naked oats under four emission pathways, namely ssp126, ssp245, ssp370, and ssp585, under the four-climate suitability (habitat suitability > 0.5) distribution. Center-of-mass transfer maps (Figure 10) were used to assess the potential migration trends and migration distances of naked oats under the influence of climate change. And thus, we analyzed the potential impacts of center-of-mass trends and distances on the consistency of such climatic suitability and planting areas under the current climatic conditions.

Under present climatic conditions the centroid coordinates of the climate suitability zone for ruderal oats are suited at (107.64° E, 36.49° N). The distribution of the centroid of mass of ruderal oats exhibited varying migration angles and distances across four distinct decades: 2030s, 2050s, 2070s, and 2090s. In the SSP126 scenario, the migration direction sequentially followed a northwest-southwest-southeast-southwest trajectory. In the SSP245 scenario, the migration direction sequentially shifted from northwest to northeast, then southeast, and finally northwest. Under the SSP370 climate-change scenario the migration direction predominantly remained northwest with a final shift to the southeast. Under the SSP585 climate-change scenario, the migration direction sequentially followed a northwest-southwest-northwest trajectory with a northwest persistence at the end. Notably, the 2030s exhibited the greatest migration distance among four decades with SSP245 yielding the farthest migration distance. The study reveals that the migration distance under the high-emission scenario (SSP585) was less than that under the medium-emission scenario (SSP245). Under various emission pathways, accompanied by the potential climate suitability zones, a potential decrease in consistency may result in heightened instability in agricultural production, thereby posing a potential threat to food security. Consequently, it

is recommended that relevant departments and research institutions intensify their efforts in investigating the impact of climate change on crop distribution, to furnish a scientific rationale for formulating agricultural policies and measures that adapt to climate change.

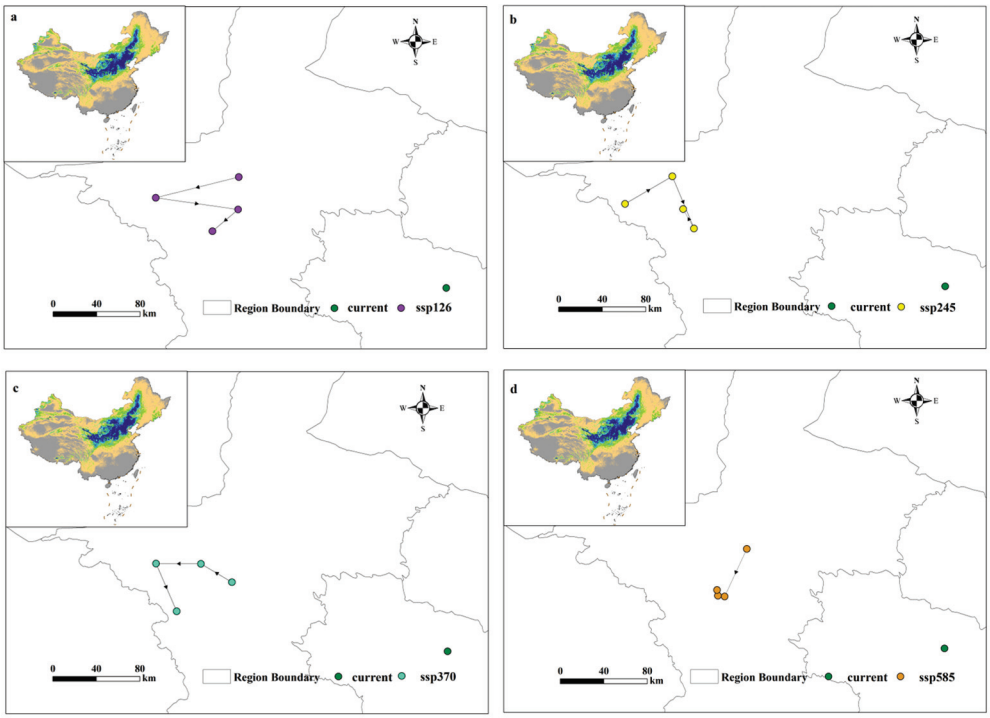

Figure 10. Trends in the centroid shift of climatically suitable areas for naked oats under different emission scenarios ((**a**) SSP1-2.6 scenario; (**b**) SSP2-4.5 scenario; (**c**) SSP3-7.0 scenario; (**d**) SSP5-8.5 scenario).

4. Discussion

4.1. Differences in the Effects of Different Environmental Factors on Naked Oats

In-depth analysis of the environmental factors contributing to the growth of naked oats revealed that the growth of naked oats was particularly responsive to temperature and precipitation, especially precipitation seasonality (coefficient of variation) (bio15) and temperature seasonality (bio4), the latter of which showed significant regional and interspecific differences across regions and species [40].

Compared with other environmental factors, elevation, slope, and slope direction had lower contribution rates in the modelling, indicating that their direct role in defining climatic suitability zones for naked oats was limited. Studies indicate that the significance of soil diminishes as the spatial extent of the environmental factor grid cells used in the analyses increases [41]. However, the contribution analysis primarily reflects the direct influence of the factors on model fit within MaxEnt [42–44]. Notably, the present study expands the analysis of environmental factors to include soil variables within the 0–30 cm layer, such as topsoil pH (H_2O) (T_PH_H_2O), total carbonate content (T_$CACO_3$), exchangeable sodium percentage (T_ESP), and total sulfate content (T_$CASO_4$), as well as available water capacity range (AWC_CLASS). These soil factors, along with other climatic variables, collectively play a significant role in determining the habitat suitability of naked oats. The top six environmental factors influencing the distribution of naked oats include two soil variables: topsoil pH (H_2O) (T_PH_H_2O, 21.00%) and available water capacity range (AWC_CLASS, 15.80%). This highlights the significance of soil conditions in shaping the geographical distribution of the crop.

4.2. Naked Oats Distribution Range Change and Yield Risk

Compared with the simulation results under current climate conditions (1990–2020), the center-of-mass offset distance of naked oats is smaller and shows higher stability under the next four scenarios. However, the climatically suitable areas for naked oats exhibit a slowing trend with the intensification of greenhouse gas emission pathways. This climate change-driven reduction in suitable areas, combined with decreased consistency, poses a potential threat to naked oats yields. In comparison to the previous study by Qin et al. [18], which focused solely on North China, the present study provides a more comprehensive understanding of the potential geographical distribution of naked oats across a wider range of regions in China. The use of higher-resolution data (30 arc-seconds) allows for finer spatial details, enabling more accurate capture and resolution of spatial variability and patterns. Additionally, the introduction of a consistency study between climate suitability zones and actual yields of naked oats under climate change adds another layer of validation to the predictive model. The results indicate a high consistency between the predicted suitability zones and observed yields, further supporting the accuracy and reliability of the findings. This study emphasizes the importance of developing prompt and region-specific planting and management strategies to effectively address the yield risks posed by climate change, ensuring the sustainability and resilience of oat production.

4.3. The Guiding Role of Ecological Niche Modelling in Oat Planting Management

China has a vast territory spanning from cold to tropical temperature zones, in which naked oats are distributed in mesothermal, warm temperate and subtropical regions. In this study, we focused on naked oats and refined their growing area into specific climate zones through MaxEnt model simulation. It is worth noting that, although naked oats are adapted to arid and high-altitude environments, its seed germination requires a remarkably elevated level of water, up to about 65% of the seed weight [45]. This characteristic suggests that yield expansion may be achieved through rational extension of planting areas.

However, the pursuit of yield is often accompanied by a tendency towards homogenization of planting strategies and studies have warned that this trend poses a serious threat to biodiversity. Neglecting ecological adaptability in the selection and promotion of planting varieties, coupled with the impact of climate change, may lead to the homogenization of local varieties, migration of climatically suitable areas and the reduction of area, which may trigger the risk of extinction of local varieties and ultimately damage the species' richness and diversity of germplasm resources.

Therefore, while promoting the expansion of oat planting area and yield enhancement, we must attach significant importance to biodiversity protection and take scientific planning and management measures to ensure the harmonious coexistence of agricultural production and ecological balance.

4.4. Uncertainty Analysis

Although the model used in this study provides a powerful tool for prediction, the uncertainty inherent in it cannot be ignored. This stems from the limitations in the selection of sample distribution points and the incomplete consideration of environmental factors during the modelling process, which may limit the model's ability to capture the complex ecological processes in a comprehensive manner. In addition, the model did not adequately incorporate the hierarchical differences in land-use status within each suitable area when simulating the land-use status and trends in different areas, which further increased the uncertainty of the prediction results.

As climate warming continues, the frequent occurrence of extreme weather conditions has become a challenge that cannot be ignored. These extreme weather events may not

only pose a direct risk to plant growth periods but may also indirectly affect fruit yields by inducing an increase in pests and diseases, posing a complex and far-reaching impact on agroecosystems. Therefore, when developing agricultural strategies to adapt to climate change, modelling uncertainty and the multifaceted impacts of future climate change need to be considered to ensure scientific and effective decision-making.

5. Conclusions

This study presents a comprehensive examination of the potential geographical distribution of naked oats under contemporary and projected climatic conditions. By integrating climatic and soil variables, we have elucidated key environmental determinants of habitat suitability and underscored the necessity of considering these factors in agricultural planning. The robustness of our findings is further corroborated by the strong correspondence between the predicted suitability zones and actual crop yields. These results underscore the imperative to devise region-specific cropping strategies to mitigate the risks associated with climate change and secure sustainable production of naked oats.

Author Contributions: Conceptualization, Z.Y. and M.F.; Methodology, Z.Y.; Software, Z.Y. and X.Y.; Validation, Z.Y., X.Y. and Y.H.; Formal analysis, Z.Y. and M.F.; Investigation, Z.Y., X.Y., Y.H., Y.Z. and Y.G.; Resources, M.F., M.Q., W.Y. and C.W.; Data curation, Z.Y. and X.Y.; Writing—original draft, Z.Y.; Writing—review & editing, M.F., W.Y., C.W., M.Z., M.Q., N.J., Y.Z., Y.G. and M.A.; Visualization, Z.Y. and Y.H.; Supervision, M.F.; Project administration, M.F.; Funding acquisition, M.F. All authors have read and agreed to the published version of the manuscript.

Funding: The Shanxi Modern Agricultural Industry Technology System (coarse cereals) (2024CYJSTX03-03, 2024CYJSTX03-18) supported this work.

Data Availability Statement: The raw data supporting the conclusions of this article will be made available by the authors on request.

Acknowledgments: Acknowledgement for the data support from "Loess Plateau SubCenter, National Earth System Science Data Center, National Science & Technology Infrastructure of China (http://loess.geodata.cn (accessed on 18 April 2023))".

Conflicts of Interest: The authors declare no conflict of interest.

References

1. IPCC. *Climate Change 2013-the Physical Science Basis: Working Group I Contribution to the Fifth Assessment Report of the Intergovernmental Panel on Climate Change*; Cambridge University Press: Cambridge, UK, 2014.
2. Li, W.Q.; Xu, Z.F.; Shi, M.M.; Chen, J. Predicting changes in potential geographic distribution patterns of tetrapod willow in Asia under different climate scenarios. *J. Ecol.* **2019**, *39*, 3224–3234. (In Chinese)
3. Clark, M.A.; Springmann, M.; Hill, J.; Tilman, D. Multiple health, and environmental impacts of foods. *Proc. Natl. Acad. Sci. USA* **2019**, *116*, 23357–23362. [CrossRef]
4. Ainsworth, E.A.; Long, S.P. 30 years of free-air carbon dioxide enrichment (FACE): What have we learned about future crop productivity and its potential for adaptation? *Glob. Change Biol.* **2021**, *27*, 27–49. [CrossRef] [PubMed]
5. Huang, E.; Chen, Y.; Fang, M.; Zheng, Y.; Yu, S. Environmental drivers of plant distributions at global and regional scales. *Glob. Ecol. Biogeogr.* **2021**, *30*, 697–709. [CrossRef]
6. Qazi, A.W.; Saqib, Z.; Zaman-ul-Haq, M. Trends in species distribution modelling in context of rare and endemic plants: A systematic review. *Ecol. Process.* **2022**, *11*, 1–11. [CrossRef]
7. Shen, J.; Lantso, D.; Wang, W.; Wang, H.; Wang, W.; Zhao, J. Dynamics of three good forage grasses in the Tibetan Plateau under climate change. *Grassl. Sci.* **2024**, 1–22. (In Chinese)
8. Zurell, D.; Franklin, J.; König, C.; Bouchet, P.J.; Dormann, C.F.; Elith, J.; Fandos, G.; Feng, X.; Guillera-Arroita, G.; Guisan, A.; et al. A standard protocol for reporting species distribution models. *Ecography* **2020**, *43*, 1261–1277. [CrossRef]
9. Yang, A.; Gomez, J.P.; Blackburn, J.K. Exploring environmental coverages of species: A new variable contribution estimation methodology for rulesets from the genetic algorithm for rule-set prediction. *PeerJ* **2020**, *8*, e8968. [CrossRef] [PubMed]

10. Kaky, E.; Nolan, V.; Alatawi, A.; Gilbert, F. A comparison between Ensemble and MaxEnt species distribution modelling approaches for conservation: A case study with Egyptian medicinal plants. *Ecol. Inform.* **2020**, *60*, 101150. [CrossRef]
11. Barber, R.A.; Ball, S.G.; Morris, R.K.A.; Gilbert, F. Target-group backgrounds prove effective at correcting sampling bias in Maxent models. *Divers. Distrib.* **2022**, *28*, 128–141. [CrossRef]
12. Kariyawasam, C.S.; Kumar, L.; Ratnayake, S.S. Potential risks of plant invasions in protected areas of Sri Lanka under climate change with special reference to threatened vertebrates. *Climate* **2020**, *8*, 51. [CrossRef]
13. Petrosyan, V.; Osipov, F.; Feniova, I.; Dergunova, N.; Warshavsky, A.; Khlyap, L.; Dzialowski, A. The TOP 100 most dangerous invasive alien species in Northern Eurasia: Invasion trends and species distribution modelling. *NeoBiota* **2023**, *82*, 23–56. [CrossRef]
14. Wang, F.; Yuan, X.; Sun, Y.; Liu, Y. Species distribution modeling based on MaxEnt to inform biodiversity conservation in the Central Urban Area of Chongqing Municipality. *Ecol. Indic.* **2024**, *158*, 111491. [CrossRef]
15. Lian, Y.; Bai, Y.; Huang, Z.; Ali, M.; Wang, J.; Chen, H. Spatio-Temporal Changes and Habitats of Rare and Endangered Species in Yunnan Province Based on MaxEnt Model. *Land* **2024**, *13*, 240. [CrossRef]
16. Xia, Z.; Cholewa, J.M.; Dardevet, D.; Huang, T.; Zhao, Y.; Shang, H.; Yang, Y.; Ding, X.; Zhang, C.; Wang, H.; et al. Effects of oat protein supplementation on skeletal muscle damage, inflammation and performance recovery following downhill running in untrained collegiate men. *Food Funct.* **2018**, *9*, 4720–4729. [CrossRef]
17. Liu, L.; Assaha, D.V.M.; Islam, M.S.; Rajendran, K.; Theivasigamani, P.; Soufan, W.; Ayman, E.S.; Ueda, A. Effect of NaCl on physiological, biochemical, and ionic parameters of naked oat (*Avena nuda* L.) line Bayou1. *Front. Sustain. Food Syst.* **2024**, *7*, 1336350. [CrossRef]
18. Qin, M.; Gao, X.; Feng, M.; Jin, N.; Wang, C.; Cheng, W. Modeling of the potential geographical distribution of naked oat under climate change. *Front. Plant Sci.* **2023**, *13*, 1009577. [CrossRef]
19. Hortal, J.; Jiménez-Valverde, A.; Gómez, J.F.; Lobo, J.M.; Baselga, A. Historical bias in biodiversity inventories affects the observed environmental niche of the species. *Oikos* **2008**, *117*, 847–858. [CrossRef]
20. Warren, D.L.; Glor, R.E.; Turelli, M. ENMTools: A toolbox for comparative studies of environmental niche models. *Ecography* **2010**, *33*, 607–611. [CrossRef]
21. Peng, S.; Ding, Y.; Liu, W.; Li, Z. 1 km monthly temperature and precipitation dataset for China from 1901 to 2017. *Earth Syst. Sci. Data* **2019**, *11*, 1931–1946. [CrossRef]
22. Robert, J.; Hijmans, S.P.; Leathwick, J.; Elith, J. *dismo: Species Distribution Modeling, R Package*, Version 1.3-3; R Foundation for Statistical Computing: Vienna, Austria, 2020.
23. Hijmans, R.J. *terra: Spatial Data Analysis, R Package*, Version 1.3-4; R Foundation for Statistical Computing: Vienna, Austria, 2021.
24. Wu, T.; Lu, Y.; Fang, Y.; Xin, X.; Li, L.; Li, W.; Jie, W.; Zhang, J.; Liu, Y.; Zhang, L.; et al. The Beijing climate center climate system model (BCC-CSM): The main progress from CMIP5 to CMIP6. *Geosci. Model Dev.* **2019**, *12*, 1573–1600. [CrossRef]
25. Zhou, Y.; Zhang, Z.; Zhu, B.; Cheng, X.; Yang, L.; Gao, M.; Kong, R. MaxEnt modeling based on CMIP6 models to project potential suitable zones for Cunninghamia lanceolata in China. *Forests* **2021**, *12*, 752. [CrossRef]
26. Pérez, M.S.; Arroyo, T.P.F.; Barrera, C.S.V.; Sosa-Gutiérrez, C.; Torres, J.; Brown, K.A.; Pérez, G.G. Predicting the impact of climate change on the distribution of Rhipicephalus sanguineus in the Americas. *Sustainability* **2023**, *15*, 4557. [CrossRef]
27. Fu, C.; Li, M.; Tian, C.F.; Song, Y.; Yi, X.; Wang, X. Prediction of potential suitable regions of Prunus pseudocerasus based on MaxEnt model under climate change. *J. Nanjing For. Univ. (Nat. Sci. Ed.)* **2024**, *48*, 235–242.
28. Kriegler, E.; O'Neill, B.C.; Hallegatte, S.; Kram, T.; Lempert, R.J.; Moss, R.H.; Wilbanks, T. The need for and use of socio-economic scenarios for climate change analysis: An innovative approach based on shared socio-economic pathways. *Glob. Environ. Change* **2012**, *22*, 807–822. [CrossRef]
29. Fao, I.; Isric, I. *JRC: Harmonized World Soil Database (Version, 1.2.)*; F.A.O.: Rome, Italy; IIASA: Laxenburg, Austria, 2012.
30. Phillipss, J.; Andersonr, P.; Schapirer, E. Maximum entropy modeling of species geographic distributions. *Ecol. Model.* **2006**, *190*, 231–259. [CrossRef]
31. Merow, C.; Smith, M.J.; Silander, J.A. A practical guide to MaxEnt for modeling species' distributions: What it does, and why inputs and settings matter. *Ecography* **2013**, *36*, 1058–1069. [CrossRef]
32. Elith, J.; Graham, C.H.; Anderson, R.P.; Dudi'k, M. Novel Methods Improve Prediction of Species' Distributions from Occurrence Data. *Ecography* **2006**, *29*, 129–151. [CrossRef]
33. Phillips, S.J. Transferability, sample selection bias and background data in presence-only modelling: A response to Peterson et al. (2007). *Ecography* **2008**, *31*, 272–278. [CrossRef]
34. Araujo, M.B.; Pearson, R.G.; Thuiller, W.; Erhard, M. Validation of species–climate impact models under climate change. *Glob. Change Biol.* **2005**, *11*, 1504–1513. [CrossRef]
35. Thuiller, W.; Albert, C.; Araújo, M.B.; Berry, P.M.; Cabeza, M.; Guisan, A.; Hickler, T.; Midgley, G.F.; Paterson, J.; Schurr, F.M.; et al. Predicting global change impacts on plant species' distributions: Future challenges. *Perspect. Plant Ecol. Evol. Syst.* **2008**, *9*, 137–152. [CrossRef]

36. Boria, R.A.; Olson, L.E.; Goodman, S.M.; Anderson, R.P. Spatial filtering to reduce sampling bias can improve the performance of ecological niche models. *Ecol. Model.* **2014**, *275*, 73–77. [CrossRef]
37. Brown, J.L.; Bennett, J.R.; French, C.M. SDMtoolbox 2.0: The next generation Python-based GIS toolkit for landscape genetic, biogeographic and species distribution model analyses. *PeerJ* **2017**, *5*, e4095. [CrossRef] [PubMed]
38. Brown, J.L. SDM toolbox: A python-based GIS toolkit for landscape genetic, biogeographic and species distribution model analyses. *Methods Ecol. Evol.* **2014**, *5*, 694–700. [CrossRef]
39. Jayasinghe, S.L.; Kumar, L. Modeling the climate suitability of tea [*Camellia sinensis* (L.) O. Kuntze] in Sri Lanka in response to current and future climate change scenarios. *Agric. For. Meteorol.* **2019**, *272*, 102–117. [CrossRef]
40. Li, L.; He, L.; Xi, L.; Zhiang, F.; Guanglong, O. Study on the distribution and climate dominant factors of geographical substitution of Pinus elliottii forests in South China. *J. Southwest For. Univ. (Nat. Sci.)* **2024**, *44*, 97–105. (In Chinese)
41. Pearson, R.G.; Dawson, T.P. Predicting the impacts of climate change on the distribution of species are bioclimate envelope models useful. *Glob. Ecol. Biogeogr.* **2003**, *12*, 361–371. [CrossRef]
42. Zhao, J.; Lan, C.; Zhuo, M.; Wang, W.; Shen, J.P. Response of Highland Barley to climate change in Tibetan Plateau based on Maxent model. *Chin. J. Eco-Agric.* **2024**, *32*, 1626–1638. (In Chinese)
43. Zhang, L.; Qi, S.; Zhao, T.; Li, P.; Wang, X. Applying Specific Habitat Indicators to Study Asteraceae Species Diversity Patterns in Mountainous Area of Beijing, China. *Forests* **2024**, *15*, 1348. [CrossRef]
44. Duan, X.; Li, J.; Wu, S. MaxEnt modeling to estimate the impact of climate factors on distribution of *Pinus densiflora*. *Forests* **2022**, *13*, 402. [CrossRef]
45. Delshadi, S.; Ebrahimi, M.; Shirmohammadi, E. Reducing Water Stress, Germination and Shoot Nutrients Accumulation of *Avena sativa* L. Following Application of Plant Growth-Promoting Bacteria. *Commun. Soil Sci. Plant Anal.* **2024**, *55*, 1175–1189. [CrossRef]

Disclaimer/Publisher's Note: The statements, opinions and data contained in all publications are solely those of the individual author(s) and contributor(s) and not of MDPI and/or the editor(s). MDPI and/or the editor(s) disclaim responsibility for any injury to people or property resulting from any ideas, methods, instructions or products referred to in the content.

climate

MDPI

Review

Climate Change and Arbovirus: A Review and Bibliometric Analysis

Maryly Weyll Sant'Anna [1,*], Maurício Lamano Ferreira [2], Leonardo Ferreira da Silva [3] and Pedro Luiz Côrtes [1,4]

[1] Postgraduate Programme in Environmental Science, Institute of Energy and Environment, University of São Paulo, São Paulo 05508-010, SP, Brazil; plcortes@usp.br
[2] Department of Basic and Environmental Sciences, Lorena School of Engineering, University of São Paulo, Lorena 12602-810, SP, Brazil; lamano@usp.br
[3] Postgraduate Program in Architecture and Urbanism of Mackenzie Presbyterian University, São Paulo 01302-907, SP, Brazil; leonardoferreira.silva@mackenzista.com.br
[4] School of Communication and Arts, University of São Paulo, São Paulo 05508-020, SP, Brazil
* Correspondence: marylysantanna@usp.br

Abstract: The rise in Earth's temperature is capable of influencing the occurrence of catastrophic natural events, contributing to outbreaks of arboviruses in endemic areas and new geographical regions. This study aimed to conduct a bibliometric review and analysis of research activities on climate change with a focus on human arboviruses, using the Scopus database. A total of 1644 documents were found related to the topic between 1934 and 2023. The United States continues to lead in the number of academic publications. Dengue was the arbovirosis with the highest number of publications, followed by West Nile fever, Zika and chikungunya fever. Due to the rise in global temperature, a trend of arbovirus dissemination to non-endemic areas is observed, with a possible global increase in morbidity and mortality. Consequently, more effective measures are expected from epidemiological surveillance, vector control services, governmental authorities and, crucially, social engagement in combating and preventing new outbreaks.

Keywords: arboviruses; climate change; vector-bone diseases

1. Introduction

The rapid increase in global warming observed in recent years has contributed to a higher frequency and intensity of extreme events, such as heavy rainfall and prolonged periods of drought [1]. Since the 1970s, an increase of 0.2 °C per decade has been observed [2,3], and the predicted global increase in terrestrial temperatures by the year 2100 is between 1.0 and 4.5 °C [4]. This situation puts human life at risk of extinction, as the planet is about to reach irreversible levels of warming and, consequently, great vulnerability to catastrophic natural events [5]. Anthropogenic activities mainly influence these climatic oscillations and contribute to significant modifications in terrestrial and marine ecosystems, resulting in social and economic losses, as well as negative impacts on human health and well-being [4].

Among the health implications related to climate variations, there is an increase in outbreaks of different diseases [6]. Vector-borne diseases, especially those transmitted by mosquitoes, are among those that show a strong association with climatic factors [7]. Variations in temperature, humidity and performance influence the epidemiology of these diseases, as they not only alter the metabolism and reproduction of vectors and pathogens but are also capable of modifying the habitats of these insects, contributing to an increase in their density and spread to new areas [7,8].

Among vector-borne diseases, arboviruses are of great interest for public health due to their high morbidity and mortality [9,10]. Recently, dengue was considered the fastest-growing arbovirus in the world, putting about 40% of the population at risk of illness due to the absence of effective antiviral treatments and widely available vaccines [11]. In addition to dengue, Zika and chikungunya are also considered serious public health problems worldwide, especially in tropical and subtropical regions, where in addition to climatic factors that favor vector reproduction there are serious socioeconomic problems that make it difficult to implement measures to prevent and control these diseases [12–14]. Furthermore, as the Earth's temperature reaches higher levels, there is a greater territorial expansion of arboviruses into currently non-endemic temperate zones, where there are a high number of susceptibles [14].

Frequent outbreaks of these arboviral diseases increase global awareness of the importance of controlling these diseases in the face of climatic variations observed in recent years [15,16]. Insect vectors expand their distribution to new geographical areas as environments change and become more suitable for their survival [17]. These arboviral diseases can cause subclinical manifestations to severe conditions, as observed in dengue hemorrhagic fever and the neurological sequelae of Zika and chikungunya [15,16].

The literature provides strong evidence of the influence of climatic factors on the increase in cases of arboviral diseases [18]. However, the occurrence of these diseases involves multiple socio-environmental factors, such as human and animal mobility, land use (deforestation, reforestation, agricultural activity), access to sufficient basic sanitation and adequate assistance to health services, among others [18]. In addition, these diseases have the potential to cause large outbreaks, result in debilitating illnesses and impose significant public health costs [19]. Therefore, verifying the profile of international research activities on the influence of climate change on arboviral outbreaks can help in the academic understanding of this subject, in the identification of possible control measures for new outbreaks and in the knowledge gaps that need to be filled [20].

In this way, the methodology chosen was the bibliometric review as it is a rigorous method that has the ability to explore and analyze large volumes of scientific data already published [20]. Furthermore, this type of analysis helps to indicate research trends, main authors and journals following scientific rigor. In addition, the use of a review methodology, such as the PRISMA methodology, could limit the academic production analyzed. To date, there have been few bibliometric studies analyzing the relationship between climate change and arboviruses.

Therefore, the aim of this study was to carry out a review of existing academic production on the relationship between climate change and human arboviruses, through the bibliometric aspects of research, and thereby contribute to the identification of possible gaps in the subject and the direction of new studies.

2. Materials and Methods

2.1. Database

To obtain the database, SciVerse Scopus was used; it is considered a legitimate database for conducting bibliometric studies due to its ease of data extraction for tabulation and the quality and quantity of articles in its repository [19,21]. Scopus stores more than 6.5 million articles before 1970, with the oldest records dating back to 1788, making it one of the most comprehensive databases to date [22]. All types of published documents related to climate change and arboviruses were included, regardless of year and language.

2.2. Search Strategy

All documents related to arboviruses and climate change were collected from the past up to 8 October 2023. To retrieve documents related to arboviruses and avoid false-positive results, titles containing the following terms were used: arbovirus OR "arthropod-borne viruses" OR arboviruses OR "Cache Valley virus" OR chikungunya OR dengue OR "Eastern equine encephalitis virus" OR "Jamestown Canyon virus" OR "Japanese encephalitis" OR "La Crosse virus" OR "Mayaro virus" OR "Murray valley encephalitis virus" OR "O'nyong nyong virus" OR Oropouche OR "Ross River virus" OR "St. Louis encephalitis virus" OR "sindbis" OR "Venezuelan virus equine encephalitis virus" OR "West Nile virus" OR "Western equine encephalitis virus" OR "Yellow fever" OR zika. The disease terms were taken from the list of human arboviruses on the United States Centers for Disease Control and Prevention (CDC) website [23], with the addition of Oropouche.

Subsequently, all titles, abstracts and keywords related to climate change were included, such as "global warming" OR "climate change" OR "greenhouse effect" OR "greenhouse gas" OR "changing climate" OR "extreme weather" OR "climate variability" OR "rising temperature" OR "heat wave" OR drought OR flood OR rainfall. Finally, to validate the search results and avoid false positives, all titles, abstracts and keywords related to "dengue-negative" OR "Cell stress" were excluded.

The search was summarized as follows: (TITLE (arbovirus OR "arthropod-borne viruses" OR arboviruses OR "Cache Valley virus" OR chikungunya OR dengue OR "Eastern equine encephalitis virus" OR "Jamestown Canyon virus" OR "Japanese encephalitis" OR "La Crosse virus" OR "Mayaro virus" OR "murray valley encephalitis virus" OR "O'nyong nyong virus" OR Oropouche OR "Ross River virus" OR "St. Louis encephalitis virus" OR "sindbis" OR "Venezuelan virus equine encephalitis virus" OR "West Nile virus" OR "Western equine encephalitis virus" OR "Yellow fever" OR zika) AND TITLE-ABS-KEY ("global warming" OR "climate change" OR "greenhouse effect" OR "greenhouse gas" OR "changing climate" OR "global warming" OR "extreme weather" OR "climate variability" OR "rising temperature" OR "heat wave" OR drought OR flood OR rainfall) AND NOT TITLE-ABS-KEY ("dengue-negative" OR "Cell stress").

2.3. Validation

The research queries were validated following the first stage of the validation method adopted by Sweileh [19], where the 50 most cited documents in the literature were analyzed to ensure the studies' alignment with the relationship between climate change and arboviruses, and no false-positive results were found.

2.4. Data Analysis

The data were exported from Scopus and tabulated using Microsoft Office Excel 2010. During the analysis, the top ten ranked items for most bibliometric indicators were obtained and displayed in descending order from 1 to 10 using the standard ranking (SCR), used in bibliometrics studies [24]. Descriptive statistics were used to determine frequency, percentage and sum. The h-index was used to evaluate researcher performance and is defined as follows: if a researcher's h-index is 9, it means that their 9 most cited publications received at least 9 citations each; if it is 13, the 13 most cited publications received at least 13 citations each [22]. Therefore, this index is capable of evaluating both the number of publications (quantity) and the number of citations (impact) of a given scientific production or researcher [24]. The impact factor for journals was obtained from Journal Citation Reports [25]. The data were exported from Scopus were imported into QGIS v3.22.9 software [26] to create thematic maps.

In addition, the data obtained from Scopus were processed using VOSviewer 1.6.20, a software specialized in bibliometrics visualization and analysis, widely used in science studies to explore and represent bibliographic data in an interactive and comprehensible manner. Its main function lies in the ability to create maps and networks from large datasets, allowing the identification of patterns, trends and relationships between publications, authors, keywords and other bibliometric elements [27].

The software stands out for its ability to generate clear and informative visualizations, facilitating the understanding of the structure and dynamics of scientific production in a specific area of knowledge. Through its clustering and mapping algorithms, VOSviewer helps researchers identify emerging research areas, collaborations between authors and the evolution of scientific themes over time, contributing to an in-depth analysis of the research landscape [28]. Thus, the co-occurrence analysis of keywords was performed, considering only terms with a minimum frequency of three occurrences, in order to identify the main themes and research trends in the area.

In the figures generated by VOSviewer, each color represents a different cluster formed based on the volume of collaborations between countries or keywords. The clusters are established by the proximity and density of the connections, highlighting groups (such as countries or keywords) that frequently interact in scientific publications. The size of each circle is proportional to the number of publications or the centrality of a country or keyword in the network of collaborations. The lines connecting the circles indicate direct collaborations, with thicker lines reflecting a greater number of joint publications.

3. Results

3.1. Volume, Growth of Publications and Types

The research found 1644 documents related to climate change and arboviruses in the period between 1934 and 2023. Figure 1 shows that until 2007, the production of literature on this topic was low, with an ascending global trend beginning in 2010, reaching its highest intensity in 2021. However, from 2022 and 2023 onwards, a trend of reduction in the global number of publications is observed when compared to the previous two years (Table S1).

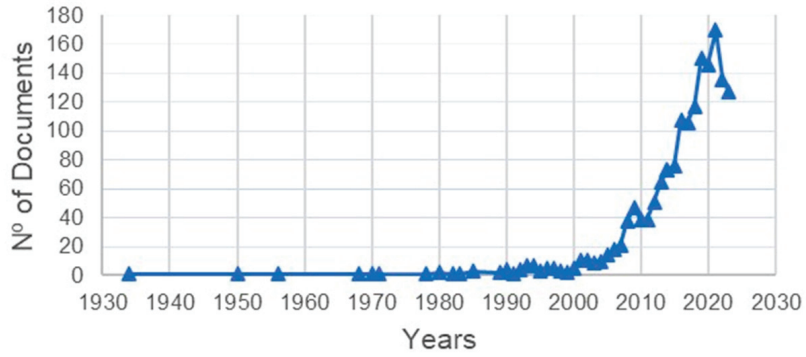

Figure 1. Documents related to arboviruses and climate change by year. Source: Scopus, 2023.

Regarding the retrieved documents, nine different types were found. Among them, articles represented 71.8% (n = 1181), followed by reviews with 12.0% (n = 201). Other percentages included conference papers, 7.4% (n = 122); letters, 3.1% (n = 51); notes, 1.8% (n = 29); book chapters, 1.7% (n = 28); editorials, 1.3% (n = 22); brief surveys, 0.4%; errata, 0.2% (n = 3); and undefined, 0.1% (n = 1). The documents were published in 13 languages. The most prevalent language was English with 1575 (95.8%), followed by Portuguese (n = 28; 1.7%) and Spanish (n = 21; 1.2%). Other languages appeared in smaller proportions, representing less than 1%.

3.2. Number of Citations

During the analysis of the selected articles, it was identified that the article titled "The global distribution and burden of dengue" [29], published in *Nature* in 2013 was the most cited document among the 1644 studies with a total of 6192 citations. Other studies that had over 500 citations were as follows: "Epidemiology of dengue: past, present and future prospects" [30], with 708 citations; "Potential effect of population and climate changes on global distribution of dengue fever: an empirical model" [31], with 690 citations; "Global spread and persistence of dengue" [32] with 664 citations. These articles had the magnitude of dengue and its potential for global dissemination in the face of climatic oscillations already evidenced in previous years as their main theme.

3.3. Country, Author and Publication Journal

The analysis of keyword recurrences by country, shown in Figure 2, indicates the proximity and density of the links, highlighting groups of countries that frequently work together on scientific publications. Nine clusters were identified, distinguished by different colors. The first cluster (red) was represented by the United States of America and included the United Kingdom, Canada, Mexico, Argentina, Portugal and Spain, among other countries. The second cluster (green) included India, Japan, Iraq and Nepal, among other countries. The third group (dark blue) was represented by Malaysia and included South Africa, Saudi Arabia and Nigeria, among other countries. The fourth group (lime green) was represented by Germany, Pakistan, Israel and Romania, among other countries. The fifth group (purple) was represented by Brazil, France, Bangladesh, Thailand, Norway and Switzerland, among others. China led the sixth cluster (light blue), which included Italy, Morocco and Denmark, among others. The seventh cluster (orange) was represented by Australia, New Zealand, Ethiopia, Indonesia and Ghana. The eighth cluster (brown) was for Puerto Rico, and finally, the ninth (rose) was for Senegal. Further details of the clusters can be found in Supplementary Table S2.

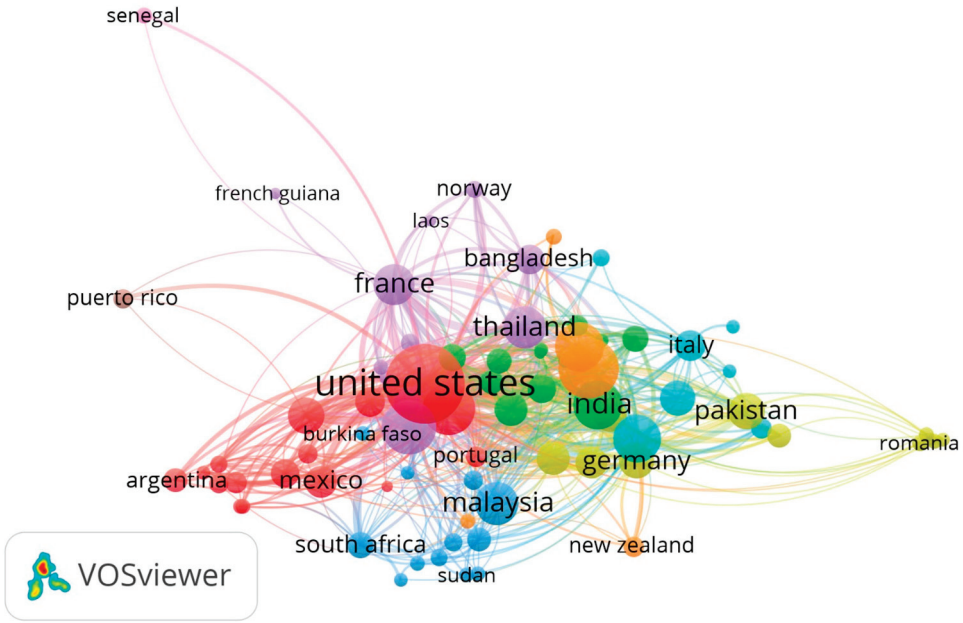

Figure 2. Recurrences of keywords by country. Source: Scopus, processed with VOSviewer.

This study showed a balance between the number of publications related to arboviral diseases and environmental factors between the Northern and Southern Hemispheres. The countries with the highest number of publications in the global north were the United States (n = 406) and the United Kingdom (n = 136). In the global south, the countries with

the highest number of publications were Australia (*n* = 198) and Brazil (*n* = 156), as shown in Figure 3.

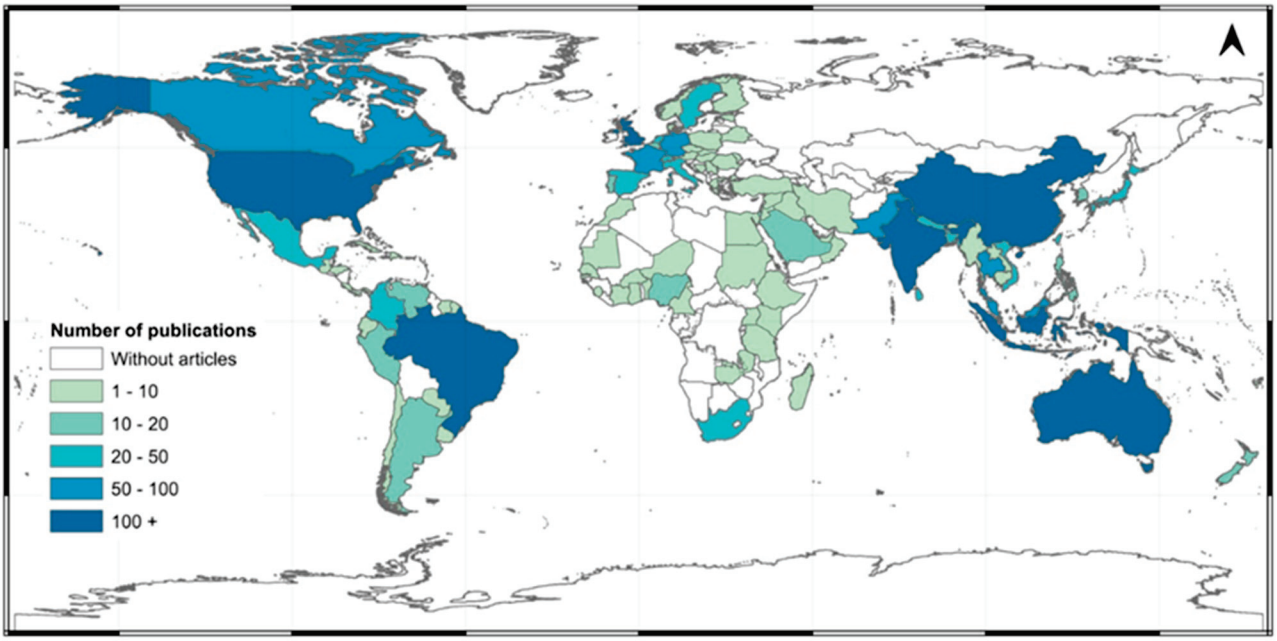

Figure 3. Publications related to climate change and arboviruses by country. Source: SciVal Scopus. Processed with QGIS v3.22.9 software.

Other countries such as Indonesia (*n* = 115), India (*n* = 113), China (*n* = 110), Malaysia (*n* = 85), Thailand (*n* = 79) and France (*n* = 74) also show a significant global percentage in scientific production on the subject of climate change and arboviruses.

In analyzing the 10 authors found in this selection, the following were identified: Hu, W. (*n* = 34); Tong, S. (*n* = 24); Liu, Q. (*n* = 23); Rocklöv, J. (*n* = 22), followed by others described in Table 1. The author with the highest h-index was Tong, S. (*n* = 79). The identification of the 10 most productive research centers found in this analysis is described in Table 2. Australia hosted four large study centers in this area of analysis; Brazil was responsible for two centers; China, the United Kingdom, the United States and France presented one each.

Table 1. The ten most active authors in publishing articles on arboviruses and climate change.

Rank	Author Name	Frequency (*n* = 1644)	h-Index *
1st	Hu, W.	34	44
2nd	Tong, S.	24	79
3rd	Liu, Q.	23	54
4th	Rocklöv, J.	22	54
5th	Bi, P.	16	49
6th	Lowe, R.	16	35
7th	Harley, D.	14	24
8th	Wilder-Smith, A.	13	62
9th	Bambrick, H.	12	24
10th	Viennet, E.	12	14

Source: SciVal Scopus. * h-index: indicates a balance between the productivity (academic output) and citation impact (citation count) of an organization's publications.

Table 2. The 10 most productive research centers in the field of arboviruses and climate change.

Rank	Research Center	Frequency (*n* = 1644)	Country
1st	The University of Queensland	50	Australia
2nd	Queensland University of Technology	47	Australia
3rd	Fundação Oswaldo Cruz	43	Brazil
4th	London School of Hygiene & Tropical Medicine	41	U.K.
5th	Chinese Center for Disease Control and Prevention	34	China
6th	The Australian National University	32	Australia
7th	University of Florida	30	United States
8th	Universidade de São Paulo	28	Brazil
9th	QIMR Berghofer Medical Research Institute	27	Australia
10th	Institut Pasteur Paris	26	France

Source: SciVal Scopus.

The 10 most productive journals found in this analysis represent 22.1 per cent (363) of this study's sample. The journal *Plos Neglected Tropical Diseases* had the highest number of publications (100; 6.08%), followed by *Plos One* (48; 2.9%) and *Medical Entomology* (33; 2%). Other relevant journals are described in Table 3.

Table 3. The 10 most productive journals in the field of arboviruses and climate change.

Rank	Journal	Frequency (*n* = 1644)	JIF *
1st	*PLOS Neglected Tropical Diseases*	100 (6.1%)	3.8
2nd	*PLOS ONE*	48 (2.9%)	3.7
3rd	*American Journal of Tropical Medicine and Hygiene*	42 (2.5%)	3.3
4th	*Journal of Medical Entomology*	33 (2.0%)	2.1
5th	*Inter. Journal of Environmental Research and Public Health*	31 (1.9%)	4614
6th	*Acta Tropica*	24 (1.45%)	2.7
7th	*Viruses*	23 (1.4%)	4.7
8th	*Parasites & Vectors*	21 (1.3%)	3.2
9th	*Science of The Total Environment*	21 (1.3%)	9.8
10th	*BMC Infectious Diseases*	20 (1.2%)	3.7

Source: SciVal Scopus. * JIF: the impact factor of journals is measured by the sum of citations received in the year of calculation divided by the total number of articles published in the previous two years.

3.4. Keywords

The citations of the most frequently found infectious disease/pathogen terms in the Scopus filter keywords revealed that terms related to dengue led the studies with 1468 occurrences; West Nile fever appears in second place, with 371 occurrences, followed by Zika with 354 occurrences and chikungunya fever with 281 occurrences. Other arboviruses such as Japanese encephalitis, yellow fever and Ross River fever appear in fewer occurrences (Table 4).

In addition, the keywords most frequently appearing in the selected articles were identified using VOSviewer. Each colored cluster in Figure 4 represents the co-occurrence network of all keywords, extracted from the titles, abstracts and keyword lists of the 1644 Scopus articles. In the network, the nodes and larger words reflect their greater occurrence, the colors indicate the clusters and the lines show the interrelationship of the

keywords. The analysis revealed the existence of 1000 items distributed in seven major areas of published studies, each centered on specific aspects.

Table 4. Frequency of diseases or pathogens found in the keyword filter.

Disease/Pathogen	Frequency (Keyword by Filter)
Dengue/virus/fever/hemorrhagic fever	1468
West Nile virus/fever/flavivirus	371
Zika virus/fever/virus infection	354
Chikungunya/virus/fever	281
Japanese encephalitis/virus/encephalitis, Japanese	164
Yellow fever	53
Ross River vírus	48

Source: SciVal Scopus.

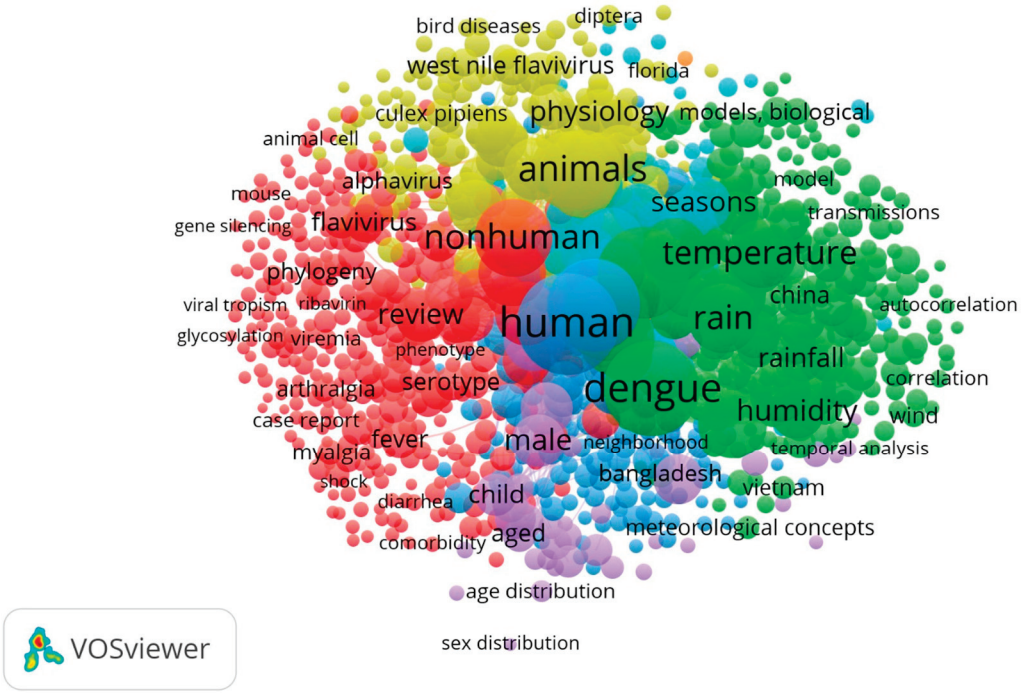

Figure 4. Highlighting the recurrence of words. Source: Scopus processed with VOSviewer.

As shown in Figure 4, the first cluster (dark blue) was represented by the word "human". In the second cluster (green), the most frequent word was "dengue", followed by terms such as "temperature", "rain", "humidity" and others. The third cluster (red) was represented by the words "nonhuman", "review" and others. The fourth cluster (lime green) was represented by the words "animal" and "physiology". In the fifth cluster (purple), "female", "child" and "aged" are the most prominent words. In the sixth cluster (light blue), the most important words were "seasons", "forest" and "distribution". And finally, the seventh cluster (orange) was represented by the words "disease outbreaks", "immunity" and "import disease". This may demonstrate the great diversity of areas of knowledge involved in research related to arboviral diseases.

4. Discussion

4.1. Environmental Movements and Arbovirus Publications

This study pointed out that in the first two decades of the 21st century, there has been a significant increase in the number of publications related to arboviruses and climate

variations, probably due to the relevance that climate studies have reached in this period. This increase occurred in parallel with the growth of international conferences supporting sustainable development and environmental conservation, which began in the middle of the 20th century [19]. Furthermore, recent years have been marked by a global alert about unprecedented planetary warming and the risks of this climatic scenario for human health and survival [1].

One of the main events in defense of the environment was the first United Nations Conference on Environment and Sustainable Development held in Stockholm in 1979 [33]. Although the Conference focused on local pollution sources, such as oil spills in oceans, it was able to drive the beginning of a series of global events and conferences on the topic, contributing to the promotion of terrestrial biodiversity conservation movements [34].

Among these events are the Villach Conference in 1985, pointing out possible climate changes and the importance of governmental commitments; the Brundtland Report in 1987, Our Common Future, addressing the importance of environmental conservation for future generations; and the Toronto Conference in 1988, warning political leaders about the seriousness of socio-environmental issues [34]. Also, in 1988, the Intergovernmental Panel on Climate Change (IPCC) was established, with the purpose of analyzing and reporting scientific data on changes in the global climate [19,35], which contributed to the increase in scientific publications on the theme of climate influence on human health [19].

From then on, other movements occurred, such as the United Nations Conference on Environment and Development in 1992, in Rio de Janeiro, and the signing of the Kyoto Protocol in 1997, the first international treaty that sought to control emissions of so-called greenhouse gases [34]. In addition, at the beginning of the 21st century, the 61st World Health Assembly held in Geneva in 2008, recognized that climate variations were capable of interfering with human health, contributing to the increase in chronic and infectious diseases [36], driving the increase in publications relating climate change and human health. This evidence was confirmed in 2014 with the publication of the IPCC Fifth Assessment Report (AR5) which issued an alert about the global danger of delaying mitigation actions and neglecting scientific studies that point to the environmental and socioeconomic disasters of global warming [37].

In the first decades of the 21st century, the IPCC published AR6 (sixth report) ratifying the anthropogenic influence on the increase in global temperature and the risk to terrestrial life in the face of these changes [38]. During the publication of AR6, in March 2023, an alert was issued to the industrial sector about the urgent need to replace fossil fuels and immediately implement sustainable development, given the imminent risk of disappearance of polar regions, damage to terrestrial biodiversity, increase in infectious diseases and mortality related to climatic factors, facts already experienced in the present generation [38]. These alerts issued by the IPCC continue to drive scientific publications that associate climatic aspects with the increase in arbovirus outbreaks, mainly due to environmental imbalance, represented by the increase in frequency and intensity of extreme climate events, such as floods and droughts.

The slowdown in research in 2022 and 2023 was probably due to the COVID-19 pandemic that began in 2020. It is likely that the social isolation measures encouraged by the World Health Organisation, as well as the impacts of the pandemic, such as resource restrictions, limited mobility, laboratory closures, changes in research priorities, funding challenges and workforce reductions, have contributed to the delays in publication processes.

4.2. Chronology of Research into Arboviruses and Climate

The oldest document found was published in 1934 in the United States and was a Public Health letter relating the period of high temperatures to the increase in infectious diseases, including the dengue outbreak in Miami, Florida [39]. In the mid-20th century, the influence of climatic factors, such as precipitation, on the prevalence of the *Haemagogus* vector and the incidence of sylvatic yellow fever in forest areas of Brazil and Colombia was identified [40]. Other publications occurred in 1968 and came from the northern region of Queensland, Australia [41,42]. Both studies pointed to an increase in the population of arbovirus vectors during the rainy season.

In the 1960s, the study by Standfast and Barrow [42] indicated a higher probability of arbovirus outbreaks in humans through the bite of *Culex annulirostris* during the dry season, suggesting that control of artificial breeding sites may be useful in combat vectors. In addition, the study by Doherty et al. [41] does not exclude the possibility that Murray Valley encephalitis viruses, active in northwest Queensland during the rainy season, may survive year-round in the rainforest, demonstrating the importance of maintaining control measures during both dry and rainy seasons [41,42].

At the end of the 1970s, a study in Massachusetts observed an increase in cases of Eastern Equine Encephalitis in humans after long periods of heavy rainfall and contributed to evaluating the predictive value of precipitation volume in the appearance of arboviruses [43], helping to strengthen the association of climatic variations with the occurrence of arbovirus outbreaks. In addition, in the 1980s, an epidemiological study in Selangor, Malaysia, presented strong statistical evidence of the association between dengue outbreaks and high precipitation volume [44].

Confirming these findings, other studies in the last decade of the 20th century pointed to a strong association between environmental factors and arbovirus cases, warning of the possible risk that climate changes would bring to the emergence of outbreaks of these diseases [45–48]. Also in this decade, a study in Eastern Europe pointed to the influence of environmental factors (heavy rains, floods, temperature rise above the annual average) and human activities (irrigation) in the formation of ecological niches that promote the reproduction of insect vectors, allowing for an increase in the incidence of West Nile fever in Eastern Europe during the rainy months [49].

At the beginning of the 21st century, scientific evidence already confirmed the influence of the effect of climate variability of multi-year cycles, such as El Niño and La Niña and the so-called Decadal Oscillations, such as the PDO (Pacific Decadal Oscillation), on the epidemiology of vector-borne diseases [8], confirming the implication of climatic variations in the biological cycle of insects. Furthermore, it was corroborated that climatic oscillations associated with natural phenomena, such as the El Niño–Southern Oscillation, tend to increase the frequency and intensity of outbreaks of vector diseases, especially in tropical regions [50–52].

Based on this knowledge, mapping and climate modeling studies have gained significant ground in 21st-century publications. These studies use the recording of disease incidence and data on environmental variables, such as temperature and rainfall, in a variation of time and space to understand the current and future distribution of arboviruses, as well as to predict the risk of the population falling ill due to these arboviruses [53,54]. In addition, projections of vector distribution and disease risk are often based on climate scenarios, according to the representative concentration pathways (RCPs) defined by the IPCC for each period, and provide useful information for planning actions to control these arboviruses in endemic and non-endemic regions [53,55,56]. Climate projections for the coming years indicate a growing increase in the Earth's temperature, which could influence the increase in the frequency and intensity of arboviral disease outbreaks in endemic and

non-endemic regions. Health and epidemiological surveillance services in areas at risk must therefore remain alert in order to control and prevent possible outbreaks.

4.3. Expansion of Arboviruses to New Ecological Niches

Environmental factors such as urbanization, global trade and transport systems, and land use/cover, including deforestation of forest areas, have contributed to the increase in and global spread of these diseases [8,57,58]. In addition, anthropogenic changes in land use are capable of influencing biodiversity loss, causing modifications in vector behavior, contributing to their expansion and consequently to the spread of pathogens [59]. Among these modifications, land use for the agricultural sector has been considered the dominant cause of tropical deforestation, occupying about 40% of the Earth's surface and contributing to significant changes in the forest ecosystem [60]. Agriculture, including livestock production, is considered the largest user of land and water in the world, being the main source of contamination by nitrates and ammonia in groundwater and surface water, as well as the release of greenhouse gases (GHGs), such as methane and nitrous oxide, influencing the increase in the Earth's temperature [61]. In addition, the destruction of ecosystems influenced by deforestation can contribute to the spread of vectors in urban centers.

The scientific literature confirms that the urbanization process, accelerated by rapid human population growth, influenced the intercontinental spread of arboviruses through various mechanisms, such as favoring the change in the vector's feeding behavior from zoophilia to anthropophilia, accentuated by human occupation in forest areas and the reproductive adaptation of insects in domestic or peridomiciliary containers, such as tires, shoes, support pots for potted plants, water reservoirs [9,62]. In addition to the urbanization process, the global expansion of *Aedes aegypti* and *Ae. albopictus* has been associated with the increase in global connectivity existing in international trade routes and human movement, whether by sea, land or air [57,63]. This connectivity can influence the spread of eggs resistant to long periods of desiccation that may be present in internationally traded plants or objects [57,63].

Furthermore, modifications in the ecophysiological capacity of mosquitoes, including genetic and environmental components, are capable of influencing the dispersal and survival of species in extreme temperatures (severe winter or heat waves), expanding new survival niches [64]. Thus, the greater the ecophysiological plasticity of the species, the broader its territorial distribution and risk of population illness will be [64].

It is observed that *Ae. albopictus* presents greater acclimatization compared to *Ae. aegypti*, having a greater adaptive capacity to different climates through the production of eggs more resistant to cold [58,64,65]. This is possible due to a genetic variation in its ability to undergo diapause and, therefore, to hibernate in colder locations [63]. The presence of *Ae. albopictus* has been reported in about 28 European countries with greater abundance in southern Europe, including Italy, Spain, southern France, the Balkans, Greece and Portugal [65], which justifies the recording of dengue and chikungunya cases in European countries.

Thus, a significant expansion of these species is predicted, with the distribution of *Ae. aegypti* being more intense in tropical and subtropical regions of South America, the Caribbean Islands, the southeastern United States, and the Pacific coast of Canada and the United States [54]. As for *Ae. albopictus*, an expansion is predicted with greater intensity in temperate regions of Europe, from the southwest to the north of the United States and southern Canada [54]. This has occurred due to climate change, especially rising temperatures, as this interaction creates habitats that drive the continuous expansion of these species into new climatically suitable urban areas [9]. Therefore, it is possible that this expansion will occur intensively in the coming years, regardless of the environmental

changes that may occur, due to the growth of global interaction and the process of urban agglomeration, which could put around half of the world's population at risk of falling ill with arboviruses by the year 2050 [9].

4.4. Global Academic Production

In general, bibliometric studies point to the Global North with a high percentage of publications in various areas, especially in studies related to human health and the environment [19,66,67]. However, this study showed a balance in the number of publications between the Global North and the Global South, due to strong production in Australia and Brazil. The United States, on the other hand, leads the way in the number of academic publications related to the subject of analysis. This sovereignty is probably due to the economic power of the United States and the large number of high-level research institutions in its territory, which leads many international researchers to express a desire for technical cooperation with American institutions [67].

This association can be best exemplified in Figure 2, where the thicker lines represent a greater number of co-authored publications between the linked countries. The groupings show how scientific collaborations are regionalized, with a great deal of technical cooperation between the United States and Brazil. In addition, the top ten authors found in this analysis have Australian, European or Chinese affiliations. It was noted that in this analysis, Australia and Brazil together house more than 50% of the top ten research centers related to arboviruses and climate change. This finding justifies the high academic production on this subject found in the Global South.

In addition, this balance may have been influenced by the high endemicity of arboviruses in tropical regions, present to a greater extent in the countries of the Global South. It was observed that in the Southern Hemisphere, the countries with the greatest scientific contribution in the area of arboviruses and climate change are precisely those with a high incidence of cases, including Australia, Brazil and Southeast Asia, a fact also identified in other studies [68–70]. This finding may confirm the importance of the countries of the Global South in scientific production on the subject of arboviruses, potentially contributing to the control and prevention of arbovirus outbreaks in regions of low endemicity.

4.5. Dengue, Zika and Chikungunya

Dengue is considered an arboviral disease with the greatest impact on global public health due to its large magnitude and capacity for high morbidity, especially in tropical and subtropical regions, and is already considered endemic in more than 125 countries [6,71–73]. Estimates suggest that the global incidence of dengue fever reaches 390 million cases per year, with about 96 million symptomatic cases, resulting in 500,000 hospitalizations and 25,000 deaths [74,75]. In addition to dengue, Zika and chikungunya are also considered emerging diseases of great importance for global public health due to the great expansion to different regions of the Americas, Africa, Asia, the Indian Ocean and temperate areas in Europe [76–78]. Besides sharing similar geographical areas, both diseases share the same vectors, *Ae. aegypti* and *Ae. Albopictus*, and common symptoms.

The Zika virus (ZIKV) was discovered in 1947 in Uganda and for a long time remained neglected by public health, until the emergence of the microcephaly outbreak in Brazil recorded after a Zika virus epidemic in the country in 2015 [79]. Given the intensity of the cases, the expansion of the disease and possible severe congenital outcomes in 2016, the Zika virus was declared a Public Health Emergency of International Concern by the World Health Organization [80], becoming part of international control programs.

In most cases, the effects of the Zika virus tend to be mild and transient, being considered less aggressive than chikungunya; with symptoms lasting between 1 and

2 weeks [81]. However, some cases can generate cardiac and respiratory compromise, with a risk of death in immunocompromised individuals [82]. Furthermore, there is a possible association between viral infections and the emergence of neurological syndromes, such as Guillain–Barré syndrome (GBS) and its risk of teratogenic effects, such as possible motor and cognitive impairments and auditory and visual disorders [82].

The chikungunya virus (CHIKV) was discovered in 1952 on the Makonde Plateau, in the province of Tanzania, East Africa, receiving this name derived from the Kimakonde verb kungunyala which means "that which bends over", referring to the physical position adopted by those with the disease [76]. Its clinical manifestations involve the presence of fever, skin rash, myalgia, intense arthralgia and in some cases, severe hemorrhages, neurological impairment and long-lasting arthritis similar to rheumatoid arthritis [83]. From 2000 onwards, large outbreaks began with high frequency and expansion to new areas, suggesting possible genetic adaptations of the virus and its vector, with *Aedes* mosquitoes being its main transmitters [84].

Currently, CHIKV has been reported in about 60 countries in Africa, Asia, Europe and the Americas, maintaining its sylvatic cycles in Africa and regions of Asia [76]. However, its urban transmission between humans and mosquitoes is significant, presenting a pandemic potential recognized by the Coalition for Epidemic Preparedness Innovations (CEPI) as a priority pathogenic agent for vaccine development, which sanctions its relevance in global public health [76].

4.6. Other Arboviruses: West Nile Fever, Japanese Encephalitis, Yellow Fever and Ross River Fever

The West Nile fever virus (WNV) was discovered in 1937 in Uganda, but its probable origin was in the Middle East, from where it spread to Africa, Asia, Europe, Australia and North America [85]. WNV is one of the flaviviruses with a wide global distribution, and until the early 1990s, it was characterized by subclinical infection and mild feverish conditions [85]. However, in 1999 in New York City (USA), it was associated with cases of human and equine encephalitis, as well as mortality of migratory birds, which may be related to the intercontinental spread of the virus [86]. The virus transmission occurs through the bite of mosquitoes belonging to the *Culex* genus, such as *Culex pipiens* and *Cx. modestus*, which allows transmission to non-avian species [85,86]. Climatic factors such as temperature and performance can influence the population density of mosquitoes, influencing the amplification of transmission and distribution of the disease in endemic regions [85,86].

The Japanese encephalitis virus (JEV) is a single-stranded RNA virus of the flavivirus genus and is considered the main agent of human encephalitis in the Asian Pacific region, having already been identified in northern Australia and in Angola, Africa [87–89]. JEV is responsible for approximately 68,000 cases and about 13,600–20,400 deaths annually, with neurological complications and sequelae in about 50% of cases, mainly in children [90].

The main source of disease transmission occurs through the bite of *Culex* mosquitoes contaminated with the virus [91]. Several bird species are considered natural reservoirs, but pigs are the main hosts and are responsible for maintaining and amplifying disease outbreaks in society [87,89]. Humans and other mammalian species, such as horses, are considered dead-end hosts due to the absence of viremia in these species [91]. Despite the existence of vaccines, there is still a high number of cases annually, and with the increase in global warming, an expansion of the vector mosquito's territory and consequent increase in the number of susceptible to the virus is expected [90].

Yellow fever (YF) is also caused by the infection of an RNA virus of the flavivirus genus, capable of affecting humans and nonhuman primates (NHPs), occurring in countries of South America and Africa [92]. In the South American region, viral transmission occurs

in two cycles, the sylvatic cycle, where NHPs are infected through the bite of *Haemagogus* spp. and *Sabethes* spp. Mosquitoes, and the urban cycle, where the infection reaches humans through the bite of insects of the genus *Aedes* sp., the same vector of dengue, Zika and chikungunya [93]. On the African Continent, human transmission involves sylvatic and domestic vector species, contributing to the frequent occurrence of large outbreaks [94].

Viral infection in humans can cause symptoms ranging from mild cold-like conditions to more severe symptoms, such as hemorrhagic fever, jaundice, renal failure and cardiovascular disturbance [95]. The fatality rate can vary between 5 and 50% [95]. Despite the existence of effective vaccines, YF outbreaks still occur sporadically in endemic regions, such as in 2015 and 2016 in Angola and the Democratic Republic of Congo (DRC) and in Brazil and Nigeria in 2017 and 2018 [92,93], which demonstrates the need for vector control programs and monitoring of new cases, in order to prevent the expansion of the disease to non-endemic areas where *Aedes* is present.

Ross River fever (RRF) is an arbovirus caused by an alphavirus, Ross River virus (RRV), of the *Togaviridae* family, endemic to Australia and South Pacific islands, which was first isolated in 1972 in the Queensland region [96,97]. In addition, RRV is responsible for about 1451 to 9551 reported cases annually, as well as the occurrence of seasonal outbreaks in the Australian region which are associated with environmental conditions conducive to vector reproduction [98]. The disease transmission involves multiple hosts such as mammals, birds, marsupials and about 40 vector mosquitoes, including *Cx annulirostris*, *Ocherotatus vigilax*, *Ae. Camptorhynchus* and *Aedes. vigilax* [96,99].

The clinical manifestations of RRF include fever, myalgia, lethargy and skin rash and chronic arthralgia, similar to chikungunya [99]. In 2020, the number of reported cases was higher than in previous years, and the epidemic peak period lasted longer than in previous years [100]. This fact may have been due to global warming and heat islands in large urban centers, which may be favoring the annual prolongation in the months of greater permanence of vector mosquitoes [100].

This study presented the most relevant arboviral diseases in the research database. Only mosquito-borne diseases were described in this analysis. Other arboviral diseases, including those transmitted by ticks, such as tick-borne encephalitis and Crimean-Congo hemorrhagic fever, although highly relevant to global public health, had a low number of publications in this research database and were therefore not discussed in this research.

4.7. Prevention, Control and Surveillance

Given this scenario, it is necessary to intensify efforts to control arboviruses worldwide through multivariate intervention measures [9,101]. The best ways of preventing and reducing morbidity from arboviruses continue to be vector control measures and human behavioral interventions, such as educating the population to prevent possible breeding sites near their homes, i.e., avoiding the accumulation of standing water without adequate treatment [71]. Other adjuvant measures in the control of arboviruses would be the improvement of basic sanitation and urban infrastructure, as these social factors are associated with an increase in cases [102]; the use of insecticides and larvicides by vector control services; and the maintenance of community educational campaigns, which present significant results when carried out in a timely manner and integrated with other forms of control [102,103].

In order to contain the permanence of mosquitoes inappropriately introduced in non-endemic areas, high-risk border areas need to maintain entomological surveillance continuously and more effectively, due to the existence of great human and animal mobilization, as well as the high flow of interaction actions on commercial routes [9,101]. As a vector surveillance measure, the collection and laboratory analysis of adult mosquito

samples, the implementation of integrated sentinel surveillance of vectors and diseases (with genomic identifications of the virus found) and early warning systems based on climate, using available technologies, can be included [104].

A measure that could be adopted in these areas would be the use of chemical larvicides such as pyriproxyfen (PPF), associated with biological larvicides such as the entomopathogenic fungus *Beauveria bassiana* contributing to the reduction in vector population density and consequent reduction in the risk of arbovirus transmission [71]. The use of biological larvicides functions as a good ecological alternative in combat vectors, given the resistance acquired by insects to chemical larvicides [105,106]. The use of the fungus *Beauveria bassiana*, for example, can shorten the survival of *Ae. aegypti* mosquitoes, can hinder viral replication of dengue in their midgut and can still be transmitted through mating to new populations [107].

An emerging strategy for controlling Aedes-borne diseases would be the use of *Wolbachia*, an intracellular bacterium, existing in most insect species, which has the ability to block virus transmission in hematophagous arthropods [75,108]. The strategy consists of the regular release of Wolbachia-infected females into a wild insect population, with the aim of manipulating reproductive outcomes and ensuring that the surviving reproductive population is infected [109]. Studies show that the introduction of *Ae. aegypti* mosquitoes infected with *Wolbachia* (wMel strain) can contribute to reducing the incidence of dengue cases and other arboviruses in urban areas with low or moderate endemicity [75].

In addition, maintaining biodiversity can be considered a control measure, since forest conservation and the presence of wild or domestic animals are considered protective factors against arbovirus transmission to humans [110]. This is because an increase in the number of host species and the presence of less competent and more resistant vectors reduces the possibility of arbovirus transmission to more susceptible hosts [111].

Thus, the global reduction in arboviruses requires the use of diversified and comprehensive strategies, involving political, social and technological efforts. The growing trend in the number of cases, as well as the spread of arboviruses to new areas, demonstrates the need and urgency to improve early warning systems for possible outbreaks. It is therefore imperative to develop epidemiological surveillance strategies that consider not only biomedical aspects, but also the socio-environmental, economic and geopolitical dimensions that influence the spread of these arboviruses, given the role of socio-environmental factors in the epidemiology of arboviral diseases. As observed in other studies [5,57,60], the interconnection between global warming, urbanization, human mobility and changes in ecosystems suggests that effective control of these diseases requires international collaboration, investment in research, strengthening of public health systems and implementation of proactive prevention policies that take into account the dynamism and unpredictability of vectors in a scenario of global climate change.

5. Limitations

The main limitation of this study was the use of a single research platform, which, despite being considered one of the most comprehensive, does not cover all the existing publications on the subject. Because of this limitation, there is a potential citation bias. In addition, due to the large area of knowledge analyzed, social and climatic aspects were not covered in greater depth.

6. Considerations

This study presented a brief review of the academic literature and bibliometric aspects of climate change research, with a focus on human arboviruses. The literature found points to a strong association between terrestrial warming and the risk of new outbreaks of

arboviral diseases in endemic and non-endemic areas. It is therefore necessary to invest in research, strengthen public health systems and implement proactive prevention policies that take into account the dynamism and unpredictability of the vectors in a scenario of global climate change. It is hoped that this review will contribute to the development of new scientific studies on this subject.

Supplementary Materials: The following supporting information can be downloaded at https://www.mdpi.com/article/10.3390/cli13020035/s1: Table S1: Database used in the research; Table S2: Country clusters found in the VOSviewer analysis.

Author Contributions: Conceptualization, M.W.S. and P.L.C.; methodology, M.W.S., L.F.d.S. and P.L.C.; validation, M.W.S. and P.L.C.; formal analysis, M.W.S., M.L.F. and P.L.C.; research, M.W.S., M.L.F. and P.L.C.; writing, M.W.S., M.L.F., L.F.d.S. and P.L.C. proofreading and editing, M.W.S., M.L.F. and L.F.d.S.; visualisation, M.W.S. and L.F.d.S.; supervision, M.L.F. and P.L.C. All authors have read and agreed to the published version of the manuscript.

Funding: This research received no external funding.

Data Availability Statement: Details of this research can be found in the supplementary tables. Other data can be made available on request.

Acknowledgments: We thank Alec Briam Lacerda (Universidade de São Paulo, São Paulo) for providing the Figure produced by QGIS. The author M.L.F. thanks the "Conselho Nacional de Desenvolvimento Científico e Tecnológico" (CNPq) for the scholarship under Project Number 307185/2023-0. The author L.F.d.S. thanks the Coordination for the Improvement of Higher Education Personnel—Brazil (CAPES)—Financing Code 001 and the Universidade Presbiteriana Mackenzie.

Conflicts of Interest: The authors declare no conflict of interest.

References

1. Whitehorn, J.; Yacoub, S. Global warming and arboviral infections. *Clin. Med.* **2019**, *19*, 149–152. [CrossRef]
2. Celik, S. The Effects of Climate Change on Human Behaviors. In *Environment, Climate, Plant and Vegetation Growth*; Fahad, S., Hasanuzzaman, M., Alam, M., Ullah, H., Saeed, M., Ali Khan, I., Adnan, M., Eds.; Springer International Publishing: Berlin/Heidelberg, Germany, 2020; pp. 577–589.
3. Samset, B.H.; Fuglestvedt, J.S.; Lund, M.T. Delayed emergence of a global temperature response after emission mitigation. *Nat. Commun.* **2020**, *11*, 3261. [CrossRef]
4. Climate Change 2022: Impacts, Adaptation and Vulnerability. 2022. Available online: www.ipcc.ch/report/ar6/wg2/ (accessed on 10 October 2023).
5. van Daalen, K.R.; Romanello, M.; Rocklöv, J.; Semenza, J.C.; Tonne, C.; Markandya, A.; Dasandi, N.; Jankin, S.; Achebak, H.; Ballester, J.; et al. The 2022 Europe report of the Lancet Countdown on health and climate change: Towards a climate resilient future. *Lancet Public Health* **2022**, *7*, e942–e965. [CrossRef]
6. El-Sayed, A.; Kamel, M. Climatic changes and their role in emergence and re-emergence of diseases. *Environ. Sci. Pollut. Res.* **2020**, *27*, 22336–22352. [CrossRef]
7. Tidman, R.; Abela-Ridder, B.; de Castañeda, R.R. The impact of climate change on neglected tropical diseases: A systematic review. *Trans. R. Soc. Trop. Med. Hyg.* **2021**, *115*, 147–168. [CrossRef] [PubMed]
8. Githeko, A.K.; Lindsay, S.W.; Confalonieri, U.E.; Patz, J.A. Climate change and vector-borne diseases: A regional analysis. *Bull. World Health Organ.* **2000**, *78*, 1136–1147. Available online: https://www.scielosp.org/pdf/bwho/v78n9/v78n9a09.pdf (accessed on 10 October 2023).
9. Kraemer, M.U.G.; Reiner, R.C.; Brady, O.J.; Messina, J.P.; Gilbert, M.; Pigott, D.M.; Yi, D.; Johnson, K.; Earl, L.; Marczak, L.B.; et al. Past and future spread of the arbovirus vectors Aedes aegypti and Aedes albopictus. *Nat. Microbiol.* **2019**, *4*, 854–863. [CrossRef]
10. Young, P.R. Arboviruses: A Family on the Move. In *Dengue and Zika: Control and Antiviral Treatment Strategies. Advances in Experimental Medicine and Biology*; Hilgenfeld, R., Vasudevan, S., Eds.; Springer: Singapore, 2018; Volume 1062. [CrossRef]
11. Carreto, C.; Gutiérrez-Romero, R.; Rodríguez, T. Climate-driven mosquito-borne viral suitability index: Measuring risk transmission of dengue, chikungunya and Zika in Mexico. *Int. J. Health Geogr.* **2022**, *21*, 15. [CrossRef]
12. Mordecai, E.A.; Caldwell, J.M.; Grossman, M.K.; Lippi, C.A.; Johnson, L.R.; Neira, M.; Rohr, J.R.; Ryan, S.J.; Savage, V.; Shocket, M.S.; et al. Thermal biology of mosquito-borne disease. *Ecol. Lett.* **2019**, *22*, 1690–1708. [CrossRef] [PubMed]

13. World Health Organization. *Laboratory Testing for Zika Virus and Dengue Virus Infections: Interim Guidance, 14 July 2022*; WHO/ZIKV_DENV/LAB/2022.1; World Health Organization: Geneva, Switzerland, 2022. Available online: https://apps.who.int/iris/handle/10665/359857 (accessed on 10 October 2023).
14. Webb, C.E.; Doggett, S.L. Exotic mosquito threats require strategic surveillance and response planning. *Public Health Res. Pract.* **2016**, *26*, 2651656. [CrossRef] [PubMed]
15. Ferreira, M.L.B.; de Albuquerque, M.; de Brito, C.A.A.; Franca, R.F.D.; Moreira, A.J.P.; Machado, M.I.D.; Melo, R.P.; Medialdea-Carrera, R.; Mesquita, S.D.; Santos, M.L.; et al. Neurological disease in adults with Zika and chikungunya virus infection in Northeast Brazil: A prospective observational study. *Lancet Neurol.* **2020**, *19*, 826–839. [CrossRef] [PubMed]
16. Weetman, D.; Kamgang, B.; Badolo, A.; Moyes, C.L.; Shearer, F.M.; Coulibaly, M.; Pinto, J.; Lambrechts, L.; McCall, P.J. Aedes Mosquitoes and Aedes-Borne Arboviruses in Africa: Current and Future Threats. *Int. J. Environ. Res. Public Health* **2018**, *15*, 220. [CrossRef] [PubMed]
17. Bartlow, A.W.; Manore, C.; Xu, C.; Kaufeld, K.A.; Valle, S.D.; Ziemann, A.; Fairchild, G.; Fair, J.M. Forecasting zoonotic infectious disease response to climate change: Mosquito vectors and a changing environment. *Vet. Sci.* **2019**, *6*, 40. [CrossRef]
18. Caminade, C.; McIntyre, K.M.; Jones, A.E. Impact of recent and future climate change on vector-borne diseases. *Ann. N. Y. Acad. Sci.* **2019**, *1436*, 157–173. [CrossRef] [PubMed]
19. Sweileh, W.M. Bibliometric analysis of peer-reviewed literature on climate change and human health with an emphasis on infectious diseases. *Glob. Health* **2020**, *16*, 44. [CrossRef]
20. Donthu, N.; Kumar, S.; Mukherjee, D.; Pandey, N.; Lim, W.M. How to conduct a bibliometric analysis: An overview and guidelines. *J. Bus. Res.* **2021**, *133*, 285–296. [CrossRef]
21. Leal Filho, W.; Ternova, L.; Parasnis, S.A.; Kovaleva, M.; Nagy, G.J. Climate change and zoonoses: A review of concepts, definitionsand bibliometrics. *Int. J. Environ. Res. Public Health* **2022**, *19*, 893. [CrossRef]
22. Scopus. ScopusContentCoverageGuideWEB.pdf. 2023. Available online: https://assets.ctfassets.net/o78em1y1w4i4/EX1iy8VxBeQKf8aN2XzOp/c36f79db25484cb38a5972ad9a5472ec/Scopus_ContentCoverage_Guide_WEB.pdf (accessed on 10 October 2023).
23. CDC. Centers for Disease Control and Prevention, National Center for Emerging and Zoonotic Infectious Diseases (NCEZID); Division of Vector-Borne Diseases (DVBD). 2022. Available online: https://search.cdc.gov/search/?query=vector%20borne%20diseases&dpage=1 (accessed on 10 October 2023).
24. Zyoud, S.H. Dengue research: A bibliometric analysis of worldwide and Arab publications during 1872–2015. *Virol. J.* **2016**, *13*, 78. [CrossRef]
25. JCR. Journal Citation Reports Help Center. 2022. Available online: https://journalcitationreports.zendesk.com/hc/en-gb/articles/28350221001745-2022 (accessed on 10 October 2023).
26. Quantum GIS. Internet. 2023. Available online: http://qgis.osgeo.org/ (accessed on 10 October 2023).
27. Zupic, I.; Cater, T. Bibliometric Methods in Management and Organization. *Organ. Res. Methods* **2015**, *18*, 429–472. [CrossRef]
28. Raboaca, M.S.; Bizon, N.; Grosu, O.V. Energy management strategies for hybrid electric vehicles-vosviwer bibliometric analysis. In Proceedings of the 2020 12th International Conference on Electronics, Computers and Artificial Intelligence (ECAI), Bucharest, Romania, 25–27 June 2020; IEEE: Piscataway, NJ, USA, 2020; pp. 1–8.
29. Bhatt, S.; Gething, P.W.; Brady, O.J.; Messina, J.P.; Farlow, A.W.; Moyes, C.L.; Drake, J.M.; Brownstein, J.S.; Hoen, A.G.; Sankoh, O.; et al. The global distribution and burden of dengue. *Nature* **2013**, *496*, 504–507. [CrossRef]
30. Murray, N.E.A.; Quam, M.B.; Wilder-Smith, A. Epidemiology of dengue: Past, present and future prospects. *Clin. Epidemiol.* **2013**, *5*, 299–309. [CrossRef]
31. Hales, S.; De Wet, N.; Maindonald, J.; Woodward, A. Potential effect of population and climate changes on global distribution of dengue fever: An empirical model. *Lancet* **2002**, *360*, 830–834. [CrossRef]
32. Kyle, J.L.; Harris, E. Global spread and persistence of dengue. *Annu. Rev. Microbiol.* **2008**. [CrossRef] [PubMed]
33. Ivanova, M. Designing the United Nations Environment Programme: A story of compromise and confrontation. *Int. Environ. Agreem. Politics Law. Econ.* **2007**, *7*, 337–361. [CrossRef]
34. Bodansky, D. The history of the global climate change regime. In *International Relations and Global Climate Change*, 1st ed.; Press Cambridge: London, UK, 2001; pp. 34–40.
35. Gupta, J. A history of international climate change policy. *Wiley Interdiscip. Rev. Clim. Change* **2010**, *1*, 636–653. [CrossRef]
36. McMichael, A.J.; Neira, M.; Heymann, D.L. World Health Assembly 2008: Climate change and health. *Lancet* **2008**, *371*, 1895–1896. [CrossRef]
37. Pachauri, R.K.; Allen, M.R.; Barros, V.R.; Broome, J.; Cramer, W.; Christ, R.; Church, J.A.; Clarke, L.; Dahe, Q.; Dasgupta, P. *Climate Change 2014: Synthesis Report. Contribution of Working Groups I, II and III to the Fifth Assessment Report of the Intergovernmental Panel on Climate Change*; IPCC: Geneva, Switzerland, 2014.

38. Lee, H.; Calvin, K.; Dasgupta, D.; Krinner, G.; Mukherji, A.; Thorne, P.; Trisos, C.; Romero, J.; Aldunce, P.; Barret, K. IPCC, 2023: Climate Change 2023: Synthesis Report, Summary for Policymakers. In *Contribution of Working Groups I, II and III to the Sixth Assessment Report of the Intergovernmental Panel on Climate Change*; Core Writing Team, Lee, H., Romero, J., Eds.; IPCC: Geneva, Switzerland, 2023; pp. 8–40.
39. Ravenel, M.P. Our correspondent speaks of the American Public Health Association Meeting at Pasadena—The Poliomyelitis Situation—The Drought and Typhoid—Dengue Fever in Florida—And Medical Insurance. *Public Health* **1934**, *48*, 77–78. [CrossRef]
40. Kumm, H.W. Seasonal variations in rainfall: Prevalence of Haemagogus and incidence of jungle yellow fever in Brazil and Colombia. *Trans. R. Soc. Trop. Med. Hyg.* **1950**, *43*, 673–682. [CrossRef]
41. Doherty, R.L.; Standfast, H.A.; Wetters, E.J.; Whitehead, R.H.; Barrow, G.J.; Gorman, B.M. Virus isolation and serological studies of arthropodborne virus infections in a high rainfall area of North Queensland. *Trans. R. Soc. Trop. Med. Hyg.* **1968**, *62*, 862–867. [CrossRef]
42. Standfast, H.A.; Barrow, G.J. Studies of the epidemiology of arthropod-borne virus infections at Mitchell River Mission, Cape York Peninsula, North Queensland. *Trans. R. Soc. Trop. Med. Hyg.* **1968**, *62*, 418–429. [CrossRef] [PubMed]
43. Grady, G.F.; Maxfield, H.K.; Hildreth, S.W.; Timperi, R.J.; Gilfillan, R.F.; Rosenau, B.J.; Francy, D.B.; Calisher, C.H.; Marcus, L.C.; Madoff, M.A. Eastern equine encephalitis in massachusetts, 1957-1976: A prospective study centered upon analyses of mosquitoes. *Am. J. Epidemiol.* **1978**, *107*, 170–178. [CrossRef] [PubMed]
44. Li, C.F.; Lim, T.W.; Han, L.L.; Fang, R. Rainfall, abundance of Aedes aegypti and dengue infection in Selangor, Malaysia. *S. Asian J. Trop. Med. Public Health* **1985**, *16*, 560–568. [PubMed]
45. Doggett, S.L.; Russell, R.C.; Clancy, J.; Haniotis, J.; Cloonan, M.J. Barmah Forest virus epidemic on the south coast of New South Wales, Australia, 1994-1995: Viruses, vectors, human casesand environmental factors. *J. Med. Entomol.* **1999**, *36*, 861–868. [CrossRef] [PubMed]
46. Patz, J.A.; Balbus, J.M. Methods for assessing public health vulnerability to global climate change. *Clim. Res.* **1996**, *6*, 113–125. [CrossRef]
47. Patz, J.A.; Martens, W.J.M.; Focks, D.A.; Jetten, T.H. Dengue fever epidemic potential as projected by general circulation models of global climate change. *Environ. Health Perspect.* **1998**, *106*, 147–153. [CrossRef] [PubMed]
48. Russell, R.C. Mosquito-borne arboviruses in Australia: The current scene and implications of climate change for human health. *Int. J. Parasitol.* **1998**, *28*, 9673874. [CrossRef] [PubMed]
49. Hubálek, Z.; Halouzka, J. West Nile fever-A reemerging mosquito-borne viral disease in Europe. *Emerg. Infect. Dis.* **1999**, *5*, 643–650. [CrossRef] [PubMed]
50. Cazelles, B.; Chavez, M.; McMichael, A.J.; Hales, S. Nonstationary influence of El Nino on the synchronous dengue epidemics in Thailand. *PLoS Med.* **2005**, *2*, e106. [CrossRef]
51. Kelly-Hope, L.A.; Purdie, D.M.; Kay, B.H. El Nino southern oscillation and Ross River virus outbreaks in Australia. *Vector-Borne Zoonotic Dis.* **2004**, *4*, 210–213. [CrossRef]
52. Weaver, S.C.; Reisen, W.K. Present and future arboviral threats. *Antivir. Res.* **2010**, *85*, 328–345. [CrossRef]
53. Bonnin, L.; Tran, A.; Herbreteau, V.; Marcombe, S.; Boyer, S.; Mangeas, M.; Menkes, C. Predicting the Effects of Climate Change on Dengue Vector Densities in Southeast Asia through Process-Based Modeling. *Environ. Health Perspect.* **2022**, *130*, 127002. [CrossRef]
54. Kamal, M.; Kenawy, M.A.; Rady, M.H.; Khaled, A.S.; Samy, A.M. Mapping the global potential distributions of two arboviral vectors Aedes aegypti and Ae. albopictus under changing climate. *PLoS ONE* **2018**, *13*, e0210122. [CrossRef] [PubMed]
55. Lowe, R.; Gasparrini, A.; Van Meerbeeck, C.J.; Lippi, C.A.; Mahon, R.; Trotman, A.R.; Rollock, L.; Hinds, A.Q.J.; Ryan, S.J.; Stewart-Ibarra, A.M. Nonlinear and delayed impacts of climate on dengue risk in Barbados: A modelling study. *PLoS Med.* **2018**, *15*, e1002613. [CrossRef]
56. Outammassine, A.; Zouhair, S.; Loqman, S. Global potential distribution of three underappreciated arboviruses vectors (Aedes japonicus, Aedes vexans and Aedes vittatus) under current and future climate conditions. *Transbound. Emerg. Dis.* **2022**, *69*, E1160–E1171. [CrossRef] [PubMed]
57. Findlater, A.; Bogoch, I.I. Human mobility and the global spread of infectious diseases: A focus on air travel. *Trends Parasitol.* **2018**, *34*, 772–783. [CrossRef]
58. Medlock, J.M.; Hansford, K.M.; Schaffner, F.; Versteirt, V.; Hendrickx, G.; Zeller, H.; Bortel, W.V. A review of the invasive mosquitoes in Europe: Ecology, public health risksand control options. *Vector-Borne Zoonotic Dis.* **2012**, *12*, 435–447. [CrossRef] [PubMed]
59. Plowright, R.K.; Reaser, J.K.; Locke, H.; Woodley, S.J.; Patz, J.A.; Becker, D.J.; Oppler, G.; Hudson, P.J.; Tabor, G.M. Land use-induced spillover: A call to action to safeguard environmental, animaland human health. *Lancet Planet. Health* **2021**, *5*, e237–e245. [CrossRef]

60. Patz, J.A.; Olson, S.H.; Uejio, C.K.; Gibbs, H.K. Disease Emergence from Global Climate and Land Use Change. *Med. Clin. N. Am.* **2008**, *92*, 1473–1491. [CrossRef]
61. Bruinsma, J. *World Agriculture: Towards 2015/2030: An FAO Study*; Routledge: London, UK, 2017. [CrossRef]
62. Powell, J.R.; Tabachnick, W.J. History of domestication and spread of Aedes aegypti-a review. *Mem. Inst. Oswaldo Cruz* **2013**, *108*, 11–17. [CrossRef]
63. Kraemer, M.U.; Sinka, M.E.; Duda, K.A.; Mylne, A.Q.; Shearer, F.M.; Barker, C.M.; Moore, C.G.; Carvalho, R.G.; Coelho, G.E.; Van Bortel, W. The global distribution of the arbovirus vectors Aedes aegypti and Ae. albopictus. *eLife* **2015**, *4*, e08347. [CrossRef] [PubMed]
64. Kramer, I.M.; Pfeiffer, M.; Steffens, O.; Schneider, F.; Gerger, V.; Phuyal, P.; Braun, M.; Magdeburg, A.; Ahrens, B.; Groneberg, D.A.; et al. The ecophysiological plasticity of Aedes aegypti and Aedes albopictus concerning overwintering in cooler ecoregions is driven by local climate and acclimation capacity. *Sci. Total Environ.* **2021**, *778*, 146128. [CrossRef] [PubMed]
65. Medlock, J.M.; Hansford, K.M.; Vaux, A.G.C.; Cull, B.; Gillingham, E.; Leach, S. Assessment of the public health threats posed by vector-borne disease in the United Kingdom (UK). *Int. J. Environ. Res. Public Health* **2018**, *15*, 2145. [CrossRef] [PubMed]
66. Leal, W.; Scheday, S.; Boenecke, J.; Gogoi, A.; Maharaj, A.; Korovou, S. Climate Change, Health and Mosquito-Borne Diseases: Trends and Implications to the Pacific Region. *Int. J. Environ. Res. Public Health* **2019**, *16*, 12. [CrossRef] [PubMed]
67. Yang, L.; Liu, C.; Bi, P.; Vardoulakis, S.; Huang, C. Local actions to health risks of heatwaves and dengue fever under climate change: Strategies and barriers among primary healthcare professionals in southern China. *Environ. Res.* **2020**, *187*, 109688. [CrossRef]
68. Ho, Y.-S.; Siu, E.; Chuang, K.-Y. A bibliometric analysis of dengue-related publications in the Science Citation Index Expanded. *Future Virol.* **2016**, *11*, 631–648. [CrossRef]
69. Li, C.; Ojeda-Thies, C.; Renz, N.; Margaryan, D.; Perka, C.; Trampuz, A. The global state of clinical research and trends in periprosthetic joint infection: A bibliometric analysis. *Int. J. Infect. Dis.* **2020**, *96*, 696–709. [CrossRef]
70. Mota, F.B.; Galina, A.C.; da Silva, R.M. Mapping the dengue scientific landscape worldwide: A bibliometric and network analysis. *Mem. Inst. Oswaldo Cruz* **2017**, *112*, 354–363. [CrossRef] [PubMed]
71. Lin, Y.; Fang, K.; Zheng, Y.; Wang, H.-l.; Wu, J. Global burden and trends of neglected tropical diseases from 1990 to 2019. J. *Travel Med.* **2022**, *29*, taac031. [CrossRef]
72. Soni, S.; Gill, V.J.S.; Singh, J.; Chhabra, J.; Gill, G.J.S.; Bakshi, R. Dengue, Chikungunyaand Zika: The Causes and Threats of Emerging and Re-emerging Arboviral Diseases. *Cureus* **2023**, *15*, e41717. [CrossRef]
73. Zhang, Y.; Wang, L.; Wang, G.; Xu, J.; Zhang, T. An ecological assessment of the potential pandemic threat of Dengue Virus in Zhejiang province of China. *BMC Infect. Dis.* **2023**, *23*, 473. [CrossRef] [PubMed]
74. Sahu, M.C.; Samantaray, R.K.; Pal, A.; Pati, S. Recent advances on pathogenesis, diagnosis, prevention, immunological aspectsand vectors of dengue: A review. Asian Pac. *J. Trop. Biomed.* **2023**, *13*, 325–338. [CrossRef]
75. Ogunlade, S.T.; Adekunle, A.I.; Meehan, M.T.; McBryde, E.S. Quantifying the impact of Wolbachia releases on dengue infection in Townsville, Australia. *Sci. Rep.* **2023**, *13*, 14932. [CrossRef] [PubMed]
76. Bartholomeeusen, K.; Daniel, M.; LaBeaud, D.A.; Gasque, P.; Peeling, R.W.; Stephenson, K.E.; Ng, L.F.P.; Ariën, K.K. Chikungunya fever. *Nat. Rev. Dis. Primers* **2023**, *9*, 17. [CrossRef]
77. Mayer, S.V.; Tesh, R.B.; Vasilakis, N. The emergence of arthropod-borne viral diseases: A global prospective on dengue, chikungunya and zika fevers. *Acta Trop.* **2017**, *166*, 155–163. [CrossRef] [PubMed]
78. Obadia, T.; Gutierrez-Bugallo, G.; Duong, V.; Nunez, A.I.; Fernandes, R.S.; Kamgang, B.; Hery, L.; Gomard, Y.; Abbo, S.R.; Jiolle, D.; et al. Zika vector competence data reveals risks of outbreaks: The contribution of the European ZIKAlliance project. *Nat. Commun.* **2022**, *13*, 8. [CrossRef] [PubMed]
79. Fauci, A.S.; Morens, D.M. Zika virus in the Americas—Yet another arbovirus threat. *N. Engl. J. Med.* **2016**, *374*, 601–604. [CrossRef] [PubMed]
80. Lessler, J.; Chaisson, L.H.; Kucirka, L.M.; Bi, Q.; Grantz, K.; Salje, H.; Carcelen, A.C.; Ott, C.T.; Sheffield, J.S.; Ferguson, N.M. Assessing the global threat from Zika virus. *Science* **2016**, *353*, aaf8160. [CrossRef]
81. Cao-Lormeau, V.-M.; Blake, A.; Mons, S.; Lastère, S.; Roche, C.; Vanhomwegen, J.; Dub, T.; Baudouin, L.; Teissier, A.; Larre, P. Guillain-Barré Syndrome outbreak associated with Zika virus infection in French Polynesia: A case-control study. *Lancet* **2016**, *387*, 1531–1539. [CrossRef] [PubMed]
82. Puntasecca, C.J.; King, C.H.; LaBeaud, A.D. Measuring the global burden of chikungunya and Zika viruses: A systematic review. *PLoS Neglected Trop. Dis.* **2021**, *15*, e0009055. [CrossRef] [PubMed]
83. Kucharz, E.J.; Cebula-Byrska, I. Chikungunya fever. *Eur. J. Intern. Med.* **2012**, *23*, 325–329. [CrossRef]
84. Burt, F.J.; Rolph, M.S.; Rulli, N.E.; Mahalingam, S.; Heise, M.T. Chikungunya: A re-emerging virus. *Lancet* **2012**, *379*, 662–671. [CrossRef]

85. Ronca, S.E.; Ruff, J.C.; Murray, K.O. A 20-year historical review of West Nile virus since its initial emergence in North America: Has West Nile virus become a neglected tropical disease? *PLoS Neglected Trop. Dis.* **2021**, *15*, e0009190. [CrossRef]
86. Luethy, D. Eastern, Western, and Venezuelan Equine Encephalitis and West Nile Viruses: Clinical and Public Health Considerations. *Vet. Clin. Equine Pract.* **2023**, *39*, 99–113. [CrossRef] [PubMed]
87. Filgueira, L.; Lannes, N. Review of emerging Japanese encephalitis virus: New aspects and concepts about entry into the brain and inter-cellular spreading. *Pathogens* **2019**, *8*, 111. [CrossRef]
88. Hsieh, J.T.; St. John, A.L. Japanese encephalitis virus and its mechanisms of neuroinvasion. *PLoS Pathog.* **2020**, *16*, e1008260. [CrossRef] [PubMed]
89. Mulvey, P.; Duong, V.; Boyer, S.; Burgess, G.; Williams, D.T.; Dussart, P.; Horwood, P.F. The ecology and evolution of Japanese encephalitis virus. *Pathogens* **2021**, *10*, 1534. [CrossRef] [PubMed]
90. Sharma, K.B.; Vrati, S.; Kalia, M. Pathobiology of Japanese encephalitis virus infection. *Mol. Asp. Med.* **2021**, *81*, 100994. [CrossRef]
91. Auerswald, H.; Maquart, P.-O.; Chevalier, V.; Boyer, S. Mosquito vector competence for Japanese encephalitis virus. *Viruses* **2021**, *13*, 1154. [CrossRef] [PubMed]
92. Chen, L.H.; Wilson, M.E. Yellow fever control: Current epidemiology and vaccination strategies. *Trop. Dis. Travel. Med. Vaccines* **2020**, *6*, 1. [CrossRef] [PubMed]
93. Giovanetti, M.; de Mendonça, M.C.L.; Fonseca, V.; Mares-Guia, M.A.; Fabri, A.; Xavier, J.; de Jesus, J.G.; Gräf, T.; dos Santos Rodrigues, C.D.; Dos Santos, C.C. Yellow fever virus reemergence and spread in Southeast Brazil, 2016–2019. *J. Virol.* **2019**, *94*. [CrossRef]
94. Monath, T.P.; Vasconcelos, P.F. Yellow fever. *J. Clin. Virol.* **2015**, *64*, 160–173. [CrossRef] [PubMed]
95. Silva, N.I.O.; Sacchetto, L.; De Rezende, I.M.; Trindade, G.d.S.; LaBeaud, A.D.; De Thoisy, B.; Drumond, B.P. Recent sylvatic yellow fever virus transmission in Brazil: The news from an old disease. *Virol. J.* **2020**, *17*, 9. [CrossRef] [PubMed]
96. Damtew, Y.T.; Tong, M.; Varghese, B.M.; Hansen, A.; Liu, J.; Dear, K.; Zhang, Y.; Morgan, G.; Driscoll, T.; Capon, T.; et al. Associations between temperature and Ross river virus infection: A systematic review and meta-analysis of epidemiological evidence. *Acta Trop.* **2022**, *231*, 106454. [CrossRef]
97. Harley, D.; Sleigh, A.; Ritchie, S. Ross River virus transmission, infectionand disease: A cross-disciplinary review. *Clin. Microbiol. Rev.* **2001**, *14*, 909–932. [CrossRef]
98. Koolhof, I.S.; Gibney, K.B.; Bettiol, S.; Charleston, M.; Wiethoelter, A.; Arnold, A.-L.; Campbell, P.T.; Neville, P.J.; Aung, P.; Shiga, T. The forecasting of dynamical Ross River virus outbreaks: Victoria, Australia. *Epidemics* **2020**, *30*, 100377. [CrossRef]
99. Mostafavi, H.; Tharmarajah, K.; Vider, J.; West, N.P.; Freitas, J.R.; Cameron, B.; Foster, P.S.; Hueston, L.P.; Lloyd, A.R.; Mahalingam, S. Interleukin-17 contributes to Ross River virus-induced arthritis and myositis. *PLoS Pathog.* **2022**, *18*, e1010185. [CrossRef] [PubMed]
100. Qian, W.; Hurst, C.; Glass, K.; Harley, D.; Viennet, E. Spatial and temporal patterns of Ross River virus in Queensland, 2001–2020. Trop. *Med. Infect. Dis.* **2021**, *6*, 145. [CrossRef]
101. Schaffner, F.; Bellini, R.; Petrić, D.; Scholte, E.-J.; Zeller, H.; Marrama Rakotoarivony, L. Development of guidelines for the surveillance of invasive mosquitoes in Europe. *Parasites Vectors* **2013**, *6*, 209. [CrossRef]
102. Wilder-Smith, A.; Gubler, D.J.; Weaver, S.C.; Monath, T.P.; Heymann, D.L.; Scott, T.W. Epidemic arboviral diseases: Priorities for research and public health. *Lancet Infect. Dis.* **2017**, *17*, e101–e106. [CrossRef] [PubMed]
103. Bouzid, M.; Brainard, J.; Hooper, L.; Hunter, P.R. Public health interventions for Aedes control in the time of Zikavirus–A meta-review on effectiveness of vector control strategies. *PLoS Neglected Trop. Dis.* **2016**, *10*, e0005176. [CrossRef] [PubMed]
104. Tsheten, T.; Gray, D.J.; Clements, A.C.; Wangdi, K. Epidemiology and challenges of dengue surveillance in the WHO South-East Asia Region. *Trans. R. Soc. Trop. Med. Hyg.* **2021**, *115*, 583–599. [CrossRef]
105. Banu, A.N.; Balasubramanian, C. Myco-synthesis of silver nanoparticles using Beauveria bassiana against dengue vector, Aedes aegypti (Diptera: Culicidae). *Parasitol. Res.* **2014**, *113*, 2869–2877. [CrossRef] [PubMed]
106. Smith, L.B.; Kasai, S.; Scott, J.G. Pyrethroid resistance in Aedes aegypti and Aedes albopictus: Important mosquito vectors of human diseases. *Pestic. Biochem. Physiol.* **2016**, *133*, 1–12. [CrossRef] [PubMed]
107. Dong, Y.; Morton Jr, J.C.; Ramirez, J.L.; Souza-Neto, J.A.; Dimopoulos, G. The entomopathogenic fungus Beauveria bassiana activate toll and JAK-STAT pathway-controlled effector genes and anti-dengue activity in Aedes aegypti. *Insect Biochem. Mol. Biol.* **2012**, *42*, 126–132. [CrossRef]
108. Ogunlade, S.T.; Adekunle, A.I.; McBryde, E.S.; Meehan, M.T. Modelling the ecological dynamics of mosquito populations with multiple co-circulating Wolbachia strains. *Sci. Rep.* **2022**, *12*, 14. [CrossRef]
109. Utarini, A.; Indriani, C.; Ahmad, R.A.; Tantowijoyo, W.; Arguni, E.; Ansari, M.R.; Supriyati, E.; Wardana, D.S.; Meitika, Y.; Ernesia, I. Efficacy of Wolbachia-infected mosquito deployments for the control of dengue. *N. Engl. J. Med.* **2021**, *384*, 2177–2186. [CrossRef] [PubMed]

110. Keesing, F.; Belden, L.K.; Daszak, P.; Dobson, A.; Harvell, C.D.; Holt, R.D.; Hudson, P.; Jolles, A.; Jones, K.E.; Mitchell, C.E. Impacts of biodiversity on the emergence and transmission of infectious diseases. *Nature* **2010**, *468*, 647–652. [CrossRef] [PubMed]
111. Catenacci, L.S.; Ferreira, M.S.; Fernandes, D.; Padda, H.; Travassos-da-Rosa, E.S.; Deem, S.L.; Vasconcelos, P.F.; Martins, L.C. Individual, household and environmental factors associated with arboviruses in rural human populations, Brazil. *Zoonoses Public Health* **2021**, *68*, 203–212. [CrossRef] [PubMed]

Disclaimer/Publisher's Note: The statements, opinions and data contained in all publications are solely those of the individual author(s) and contributor(s) and not of MDPI and/or the editor(s). MDPI and/or the editor(s) disclaim responsibility for any injury to people or property resulting from any ideas, methods, instructions or products referred to in the content.

sustainability

MDPI

Article

Potential of Modified Reduced Tillage with Cover/Green Manure Crop for Climate Change Mitigation in a Smallholder Rainfed Farming System

Nabeeha Javed [1], Shahzada Sohail Ijaz [1,*], Qaiser Hussain [1], Muhammad Ansar [2], Abdulwahed Fahad Alrefaei [3], Bader O. Almutairi [3], Wajid Zaman [4,*] and Munazza Yousra [5]

[1] Institute of Soil & Environmental Sciences, PMAS Arid Agricultural University, Rawalpindi 46000, Pakistan
[2] Department of Agronomy, PMAS Arid Agricultural University, Rawalpindi 46000, Pakistan
[3] Department of Zoology, College of Science, King Saud University, P.O. Box 2455, Riyadh 11451, Saudi Arabia
[4] Department of Life Sciences, Yeungnam University, Gyeongsan 38541, Republic of Korea
[5] Land Resources Research Institute, NARC, Islamabad 45500, Pakistan
* Correspondence: shahzadasohail@uaar.edu.pk (S.S.I.); wajidzaman@yu.ac.kr (W.Z.)

Abstract: Soil can function as a reservoir and a source of greenhouse gases (GHGs), contingent on its management. This study assesses the potential of a modified reduced tillage (MRT) approach involving the use of cover or green manure crops as a substitute for crop residues to mitigate GHG emissions from soil within smallholder rainfed farming systems. A two-year field experiment with different tillage techniques (moldboard plow, tine cultivator, and modified reduced tillage) and crop rotations (summer fallow–wheat and cover/green manure–wheat) was conducted at Rawalpindi, Pakistan. The results showed that MRT reduced carbon dioxide (CO_2) and nitrous oxide (N_2O) emissions by 8% and 15.3%, respectively, from soil while maintaining consistently higher soil moisture than conventional tillage techniques. The modified reduced tillage reduced the global warming potential (GWP) and greenhouse gas intensity (GHGI) by 15.8% and 20.7%, respectively. The net ecosystem exchange (NEE) was unaffected by the tillage systems. Therefore, adopting the MRT technique and incorporating green manure is a viable strategy for curtailing GHG emissions from soil, particularly in the context of smallholder rainfed farming systems. Extended, multi-year studies under various climate scenarios and agronomic practices are needed to understand the long-term impacts of MRT and crop rotations on GHG emissions.

Keywords: greenhouse gases; smallholder rainfed farming; dryland; reduced tillage; global warming potential; greenhouse gas intensity

1. Introduction

Greenhouse gases, including carbon dioxide (CO_2), nitrous oxide (N_2O), and methane (CH_4), are being released into the atmosphere at an accelerated rate [1], resulting in various adverse effects, such as global warming [2]. Agriculture is accountable for approximately 12% of human-caused greenhouse gas emissions [3]. The primary contributors to agriculture are arable soils (5.27%) and animal intestinal fermentation (3.21%) [4,5]. Consequently, there has been a growing emphasis on the potential of soil to function as a sink and source of atmospheric gases, contingent on its management [6]. Soil respiration significantly impacts the global carbon cycle by releasing CO_2 from the carbon pool of soil into the atmosphere [7]. Soil organic carbon (SOC) plays a critical role in the global carbon cycle, serving as the most substantial terrestrial carbon reservoir following fossil fuel deposits [8]. This means it contains substantial carbon that is vital for maintaining the atmospheric carbon balance [9]. Even slight changes in SOC resulting from shifts in agricultural practices can influence the global carbon balance because it is a substantial reservoir of soil organic carbon in terrestrial ecosystems [8]. Increasing soil organic matter (SOM) and soil carbon stocks are crucial

for climate change mitigation and adaptation, owing to their profound effects on carbon sequestration, greenhouse gas emissions reduction, soil health, and ecosystem resilience [9]. Furthermore, nitrification and denitrification processes within the soil contribute to N_2O production, a significant greenhouse gas [10]. The application of nitrogenous fertilizers to enhance crop productivity amplifies N_2O emissions [11]. Agricultural soils generally range from minor CH_4 emitters to small CH_4 sinks in the atmosphere [12]. The interplay between the soil carbon changes and N_2O emissions predominantly governs the global warming potential (GWP) [13], which provides an overall assessment of greenhouse gas sources and sinks within a crop production system. Conventional cropping patterns often result in a net release of CO_2 and N_2O, diminishing the atmospheric CH_4 sink [14].

Conservation tillage is being increasingly adopted worldwide, presenting a practical approach for soil conservation, enhanced crop productivity, and reduced input expenses [15–17]. In addition, conservation tillage is recommended as a strategy to mitigate the GWP caused by N_2O and CH_4 emissions during crop cultivation because of its capacity for soil carbon storage [18]. Conservation tillage has positive effects on the soil properties, including improved soil organic carbon, increased moisture retention, reduced soil bulk density, satisfactory crop yields, and economic returns [19].

The Pothwar Plateau in Pakistan is a semi-arid region characterized by its hilly terrain, limited water resources, and highly variable rainfall patterns [20]. These conditions make sustainable agricultural practices essential for enhancing productivity and preserving soil health [21]. Among the various soil management strategies, biofilm mulching has become a promising technique [22]. Biofilm mulch conserves soil moisture by reducing evaporation, moderating soil temperature, suppressing weed growth, and improving soil structure [23]. Biofilm mulching does not mitigate GHG emissions directly, but can complement other sustainable approaches by maintaining favorable microclimate conditions that reduce the need for frequent tillage [24]. The cost and availability of biofilm materials and varying degradation rates can limit their widespread use and require careful disposal to avoid soil contamination [25–27]. The Pothwar Plateau covers an area of approximately 1.8 million hectares, and approximately 80% of farmers in the region adopt the practice of summer fallowing that involves intensive plowing with a moldboard plow and tine cultivator [28]. Previous research in the region has confirmed the benefits of reduced tillage, specifically chisel plowing with crop residue retention, which enhances moisture conservation, soil carbon sequestration, aggregate formation, and wheat yield compared to conventional tillage methods [28,29]. No-till and minimum tillage have limitations because of reduced rainwater infiltration and lower crop yields [30]. Consequently, local farmers are more likely to adopt reduced tillage. The primary challenge in promoting reduced tillage is the availability of crop residue, which farmers often use as feed for their livestock. Incorporating cover/green manure crops during the summer fallow period offers an alternative to crop residue, providing soil cover during the heavy monsoon rains to conserve moisture, prevent soil erosion, suppress weeds, and enhance soil organic matter. Despite these insights, the comprehensive impacts of reduced tillage on GHG emissions, GWP, and GHGI in smallholder rainfed farming systems are unclear. This study hypothesizes that implementing a modified reduced tillage system and a cover/green manure crop can mitigate GHG emissions. Consequently, this research was conducted in Pakistan's Pothwar plateau with the following objectives: (1) quantify GHG emissions, (2) assess the global warming potential, and (3) evaluate the greenhouse gas intensity associated with modified, reduced tillage practices compared to conventional tillage methods.

2. Materials and Methods

2.1. Site, Treatments, and Experimental Design

A two-year field study was conducted at the Research Farm of Pir Mehr Ali Shah, Arid Agriculture University in Rawalpindi, Pakistan (32°10′ N, 73°55′ E), from 2018–2020. The research site is located within the Pothwar plateau in northern Punjab province, which has a subtropical dryland climate. Annual rainfall ranges from 400 mm in southern areas

to 1137 mm in northern areas, with approximately 65% occurring during the July–August monsoon months. During this period, local farmers practice summer fallowing and intensive plowing with a moldboard plow and a frequent tine cultivator to conserve moisture and manage weeds before wheat planting in November. The study was conducted in an existing long-term experiment initiated in 2011 comparing conservation tillage systems to conventional tillage. The experimental site has sandy clay loam soils classified as Udic Haplustalfs. The soil has 51% sand, 27% silt, and 21% clay, with intermediate drainage. It has an alkaline pH of 7.87 and no salinity issues (electrical conductivity: 0.57 dS/m). The nitrate and available phosphorus levels are deficient at 4.3 mg/kg and 3.8 mg/kg, respectively. Organic matter content is relatively low at 5.04 g/kg compared to the critical limit, while extractable potassium is adequate at 138 mg/kg [30].

This study used a split-plot randomized complete block design with three replications. The primary plots accommodate the tillage systems, while the sub-plots pertain to crop rotations: (a) fallow–wheat (F–W), and (b) cover/green manure crop-wheat (GM–W). The main plots measured 13 m $\times$ 10 m, and the sub-plots measured 4 m $\times$ 10 m. The tillage treatments were started in July in each main plot. Subsequently, each main plot was subdivided into two subplots. The first subplot (fallow–wheat rotation) remained uncultivated from July to October, with weed control achieved through repeated tine cultivator tillage. The second subplot (green manure–wheat) involved sowing sesbania at a seed rate of 40 kg /ha in July, followed by green manuring at flower initiation towards the end of September. Wheat was sown at a seed rate of 100 kg/ha across all main and subplots on November 15, with the application of urea 100 kg/ha and diammonium phosphate 50 kg/ha fertilizer.

2.2. GHG Measurements and Calculations

A collar equipped with a groove was positioned randomly in the field, and a chamber rim was inserted into this groove to quantify gas evolution. The rate of soil CO_2 was assessed using the CO_2 Analyzer (Lutron GC-2028, Lutron, Coopersburg, PA, USA). Gas samples were collected weekly during the initial month of primary tillage, bi-weekly during the subsequent month, and monthly throughout the year. This sampling regimen was consistent across both experimental years (2018 to 2020). From July 2019 to July 2020, the CH_4 and N_2O fluxes were monitored using a static chamber technique. Although the static chamber technique is widely accepted for its simplicity and cost-effectiveness, it has inherent limitations in capturing the spatial and temporal variability of greenhouse gas emissions. Several strategies were used to mitigate these limitations. Repeated measurements were taken throughout different seasons to capture the temporal variability. The spatial variability was addressed by taking replicated measurements within each treatment plot. Standardized protocols were used for chamber placement, sampling time, and gas analysis to ensure the consistency and reliability of the data. The chamber, constructed from PVC and measuring 0.342 m, was placed randomly in the field to capture the gas emissions. Portable infrared methane gas detectors ((ATO-GAS-CH_4) and (ATO-GAS-N_2O), Australian Taxation Office, Canberra, Australia) were used to detect the gases within the chamber. The soil water content at a depth of 0–15 cm was assessed using time domain reflectometry (TDR, Mogadore, OH, USA), and the temperature was measured with the help of a soil thermometer to a 5 cm depth [31]. The environmental data were synchronized with GHG flux measurements by aligning the timestamps of the recorded data. The GHG flux data were logged concurrently with the environmental measurements to ensure temporal alignment.

2.3. GHG Data Analysis

The rate of GHG emissions from the soil surface was calculated by measuring the change in gas concentration over 15 min using four samples. The average flux and standard deviation were then calculated from three plots. The formula used to calculate the gas emission rate was the following:

$$f = \Delta C/\Delta t \cdot V/A \cdot m/Vm$$

where $\Delta C/\Delta t$, A, V, m, and Vm are the changes in gas concentration during chamber closure time, area of soil covered by the chamber, chamber volume, molecular weight of the gas, and gas molar volume, respectively. The results were then extrapolated to one hour and one square meter [32]. The gas emissions for each type of gas were converted to kg CO_2-C per hectare per hour using the methodology reported elsewhere [33]. Negative fluxes indicate that the soil is absorbing gas, while positive fluxes indicate net emissions from the soil.

The net global warming potential (NGWP) equation given by [34] was used, in which the IPCC factors (34 and 298) for the conversion of CH_4 and N_2O to CO_2 equivalent were used [35]. The GHGI was determined by dividing the NGWP by the grain yield of the wheat [presented elsewhere].

$$\text{NGWP} = 34 \times \text{CH}_4 \left(\text{kg ha}^{-1}\right) + 298 \times \text{N}_2\text{O} \left(\text{kg ha}^{-1}\right) + \text{CO}_2 \left(\text{kg ha}^{-1}\right)$$

$$\text{GHGI} = \text{NGWP/yield}(\text{kg CO}_2 - \text{eq kg} - 1 \text{ grain yield})$$

The net ecosystem exchange (NEE) of CO_2 was calculated using the equation reported elsewhere [36], where NEE is the difference between total seasonal soil respiration (Rh) and net primary productivity (NPP):

$$\text{NEE} = \text{Rh–NPP}$$

The NPP was calculated using the equation reported in a previous study [37], where NPP = 0.446 × Wmax × −0.00067. Here, Wmax stands for the maximum biomass.

Throughout the two-year study, weather data were collected continuously using an automatic weather station, which included information on rainfall and maximum and minimum daily temperatures. The annual precipitation during this period was 629.59 mm and 1014.26 mm in the first and second experimental years, respectively. In particular, the highest precipitation was recorded in June, with 137.51 mm and 178 mm in the first and second years, respectively. On the other hand, the lowest precipitation levels occurred in November of the first year (0.6 mm) and December of the second year (16 mm) (Figure 1).

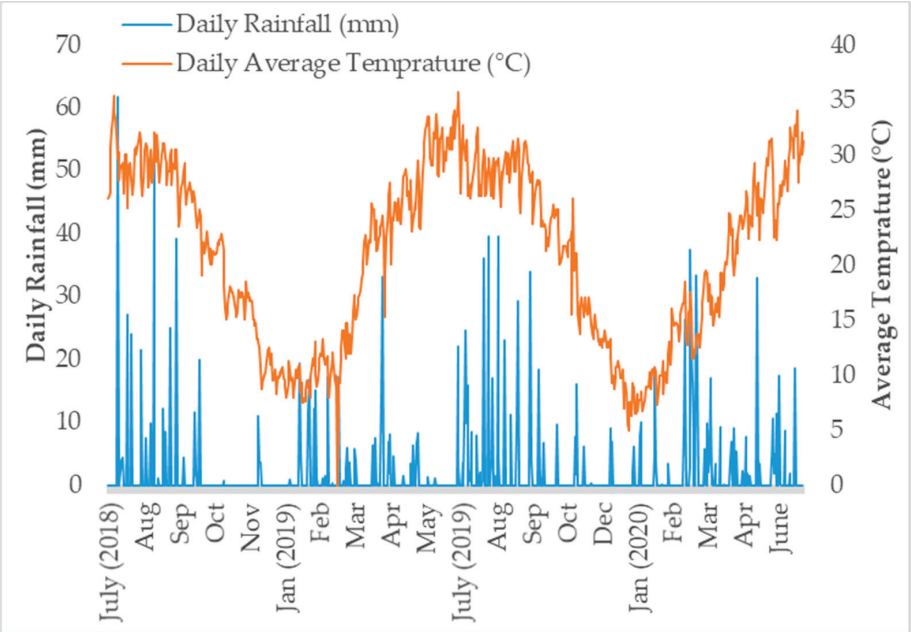

Figure 1. Daily rainfall and average temperature during the experimental period 2018–2020.

2.4. Statistical Analysis

The collected data for various characteristics were analyzed using Analysis of Variance (ANOVA) within a split-plot design framework. The mean comparisons were conducted at the 5% significance level using a least significant difference (LSD) test. All statistical analyses were conducted using the software package Statistix 8.1 [38].

3. Results

3.1. Soil Moisture Content and Temperature

The MRT system consistently maintained a higher soil moisture content most of the year than the MB and TC systems, regardless of crop rotations (Figure 2). The mean soil moisture followed the MRT > MB > TC pattern across the growing seasons in both years. A comparison of the tillage and rotation combinations showed that the volumetric water content of the MB (F–W) combination exhibited a higher initial level in July, which gradually diminished over time. In November (at the time of wheat sowing), the MRT (GM–W) combination displayed elevated moisture levels in both years.

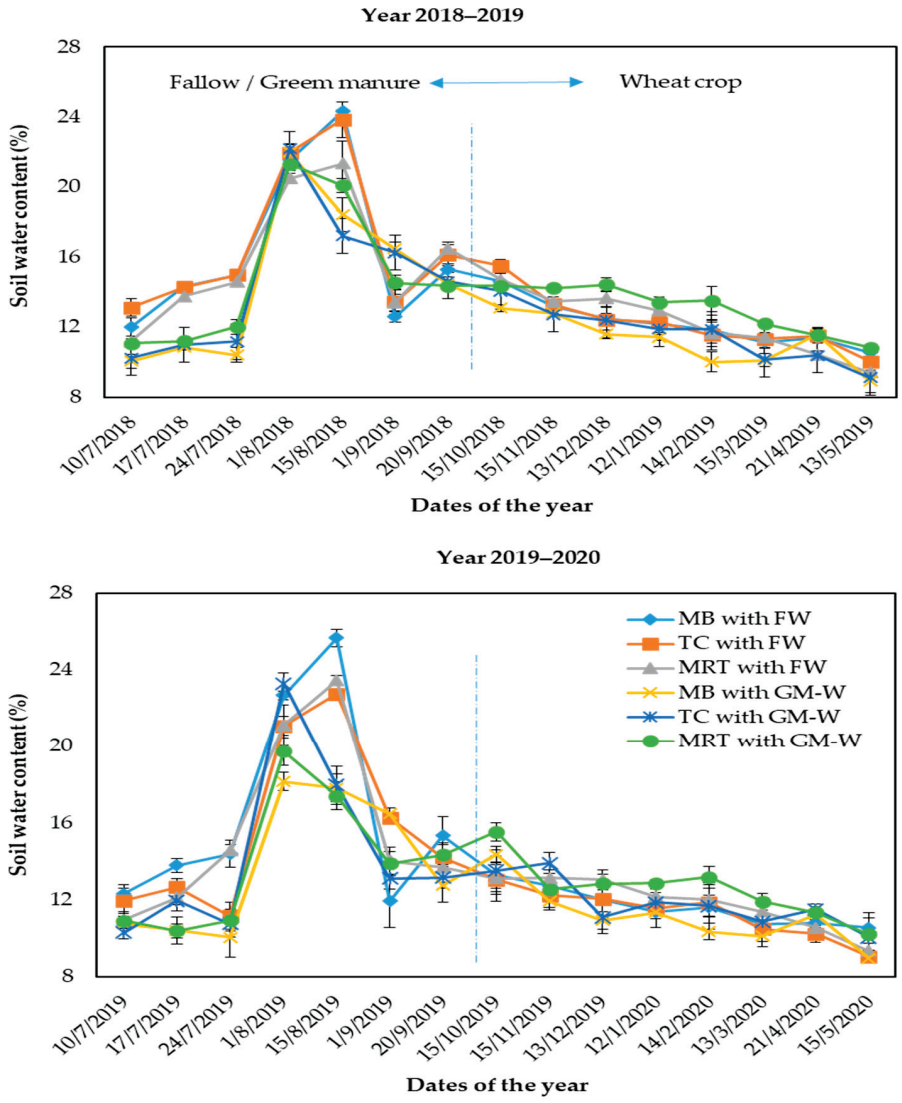

Figure 2. Soil moisture affected by the different tillage systems and crop rotations during 2018–2019 and 2019–2020. MB F–W (Moldboard with Fallow–Wheat); TC F–W (Tine cultivator with Fallow–Wheat); MRT F–W (Modified with Reduced tillage Fallow–Wheat); MB GM–W (Moldboard with Green manure–Wheat); TC GM–W (Tine cultivator with Green manure–Wheat); MRT GM–W (Modified Reduced tillage with Green manure–Wheat).

The soil moisture levels varied with weather conditions, peaking in August and declining by May. In the first year, the moisture content ranged from 21.58% in August to 9.8% in May. In the second year, it ranged from 21% in August to 9.68% in May. Tillage systems and green manuring had minimal impact on the average 24 month soil temperature across the experimental years. On the other hand, minor temperature fluctuations were observed during the fallow period without green manuring, with MB consistently having the highest temperatures and MRT and TC showing lower temperatures. The peak temperatures occurred from June to August.

3.2. CO_2 Flux

The tillage systems significantly affected CO_2 emissions, with MRT showing significantly lower emissions than the MB system. In both years, a combination of MRT with green manuring resulted in the lowest average emissions (187.65 mg/m^2/h and 181.53 mg/m^2/h in the first and second years, respectively), while MB plowing with F-W rotation recorded the highest (215.7 mg/m^2/h and 209.24 mg/m^2/h in the first and second years, respectively). Regardless of the tillage method and experimental year, GM–W rotation consistently had lower CO_2 emissions than F–W rotation. An analysis of the sampling intervals showed that the peak CO_2 emissions occurred immediately after primary tillage in July, averaging 279 mg/m^2/h and 275 mg/m^2/h in the first and second years, respectively. Two weeks post-tillage, the emissions subsided to an average of 188 mg/m^2/h and 189 mg/m^2/h in the first and second years, respectively. Subsequently, the emissions gradually rose, peaking in August before declining to their lowest levels in January, averaging 154 mg/m^2/h and 152 mg/m^2/h in the first and second years, respectively. Soil respiration fluxes followed a consistent pattern, peaking during the warm months and declining during the colder periods, often correlating with the changes in soil temperature (Figure 3).

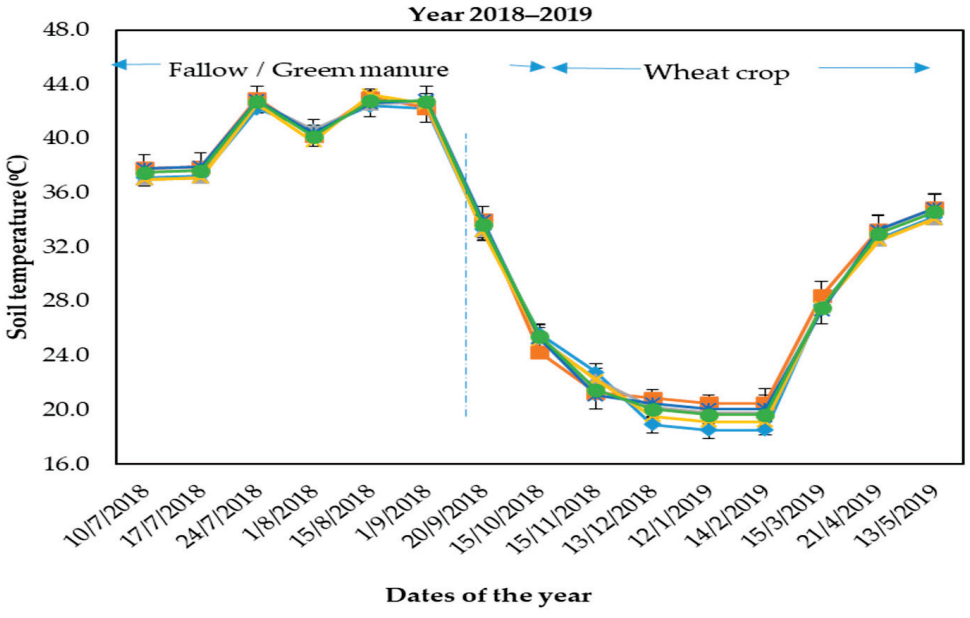

Figure 3. *Cont.*

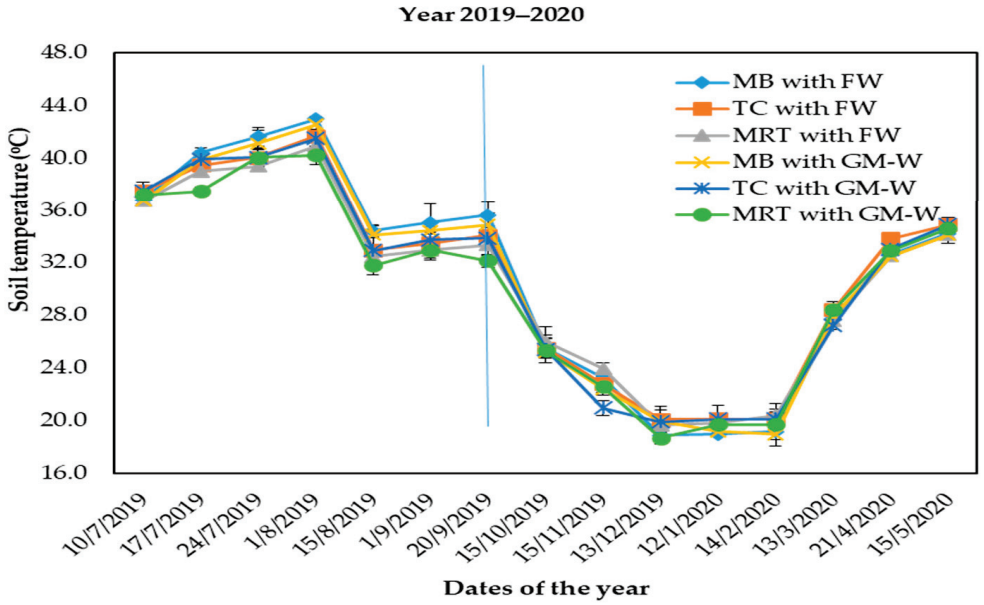

Figure 3. Soil temperature affected by different tillage systems and crop rotations during 2018–2020. MB F–W (Moldboard with Fallow–Wheat); TC F–W (Tine cultivator with Fallow–Wheat); MRT F–W (Modified with Reduced tillage Fallow–Wheat); MB GM–W (Moldboard with Green manure–Wheat); TC GM–W (Tine cultivator with Green manure–Wheat); MRT GM–W (Modified Reduced tillage with Green manure–Wheat).

The results indicated significant differences in cumulative CO_2 emission among the tillage treatments and crop rotations (Figure 4). During both years, the cumulative CO_2 was highest for the MB tillage and lowest for the MRT tillage, whereas the CO_2 content of TC remained in between these two tillage systems. Among the crop rotations, the differences among GM–W and F–W were non-significant for all tillage treatments in the first year. On the other hand, when comparing the crop rotation effect in the second year, MRT and TC emitted significantly lower CO_2 than the MB tillage.

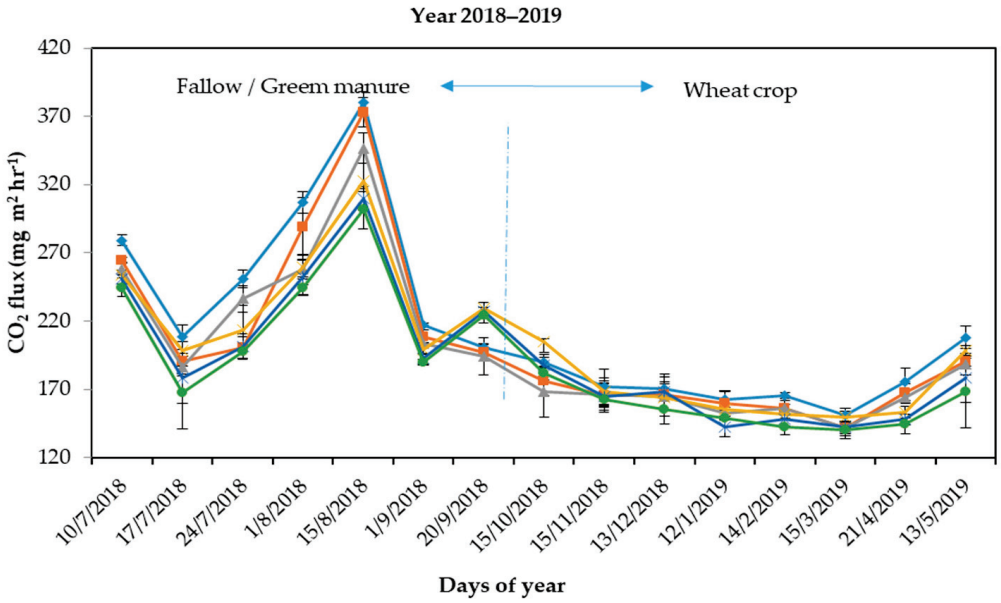

Figure 4. *Cont.*

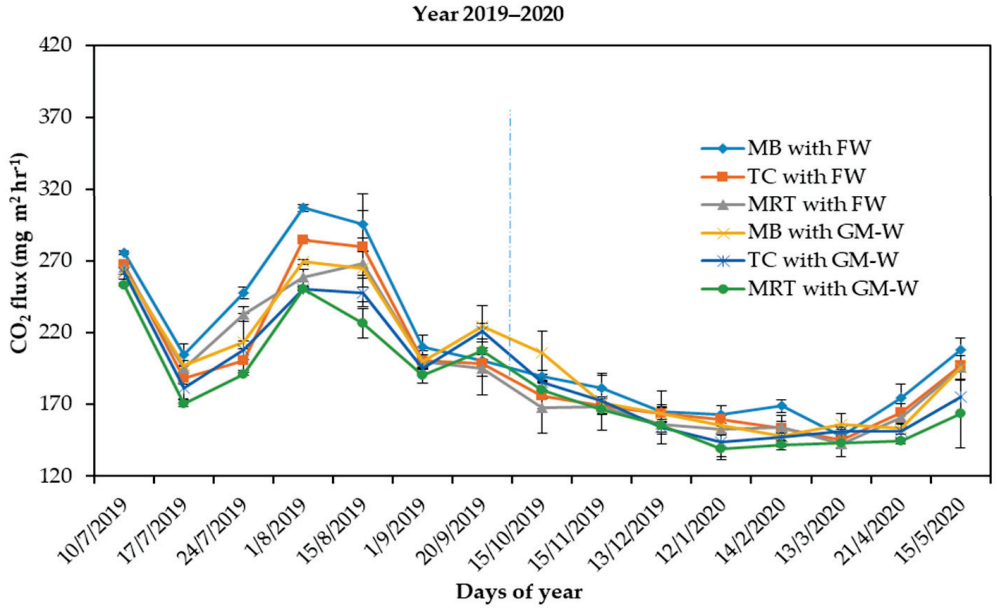

Figure 4. CO_2 flux affected by different tillage systems and crop rotations during the experimental period 2018–2020. MB F–W (Moldboard with Fallow–Wheat); TC F–W (Tine cultivator with Fallow–Wheat); MRT F–W (Modified Reduced tillage with Fallow–Wheat); MB GM–W (Moldboard with Green manure–Wheat); TC GM–W (Tine cultivator with Green manure–Wheat); MRT GM–W (Modified Reduced tillage with Green manure–Wheat).

3.3. N_2O Fluxes

Throughout the sampling intervals, MRT with green manuring had the lowest average soil N_2O emissions (0.20 mg/m^2/h), while MB with the F–W rotation had the highest (0.24 mg/m^2/h). The GM–W rotation generally had lower emissions than F–W, even though the emissions increased after green manure incorporation. The peak emissions occurred in July (0.30 mg/m^2/h), with the lowest observed in February (0.16 mg/m^2/h). Similar to CO_2 emissions, the N_2O fluxes were highest during the warm months and lowest during the cold periods, tracking soil temperature fluctuations. An examination of the cumulative N_2O emissions revealed distinct effects of the tillage treatments and crop rotations. The cumulative N_2O emissions were significantly lower under the MRT system than the MB and TC systems. Among the crop rotations, the cumulative N_2O emissions were significantly lower under GM–W rotation than F–W rotation (Figures 5–7).

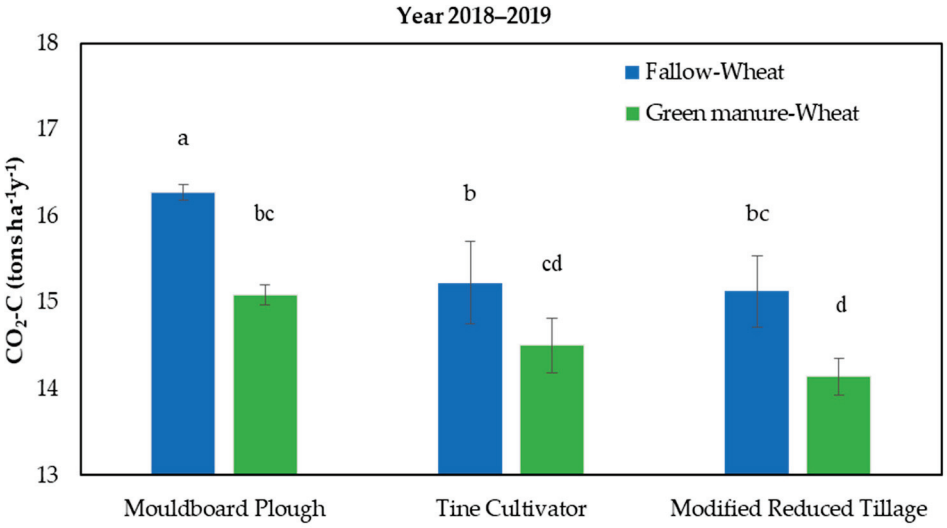

Figure 5. *Cont.*

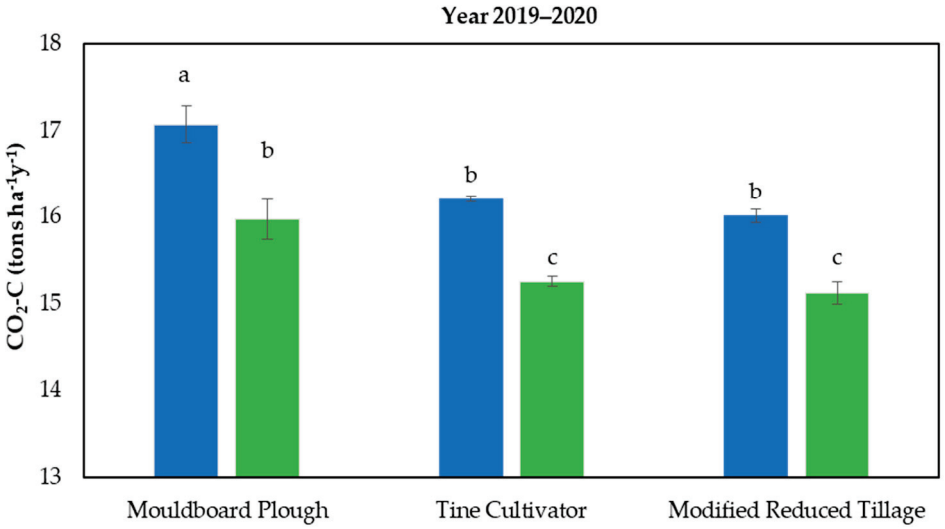

Figure 5. Cumulative CO_2 affected by different tillage systems and crop rotations during the experimental period 2018–2020. Treatments labeled with the same letter (e.g., "a", "b", "c", etc.) within each crop are not significantly different from each other. Treatments labeled with different letters are significantly different from each other within each crop.

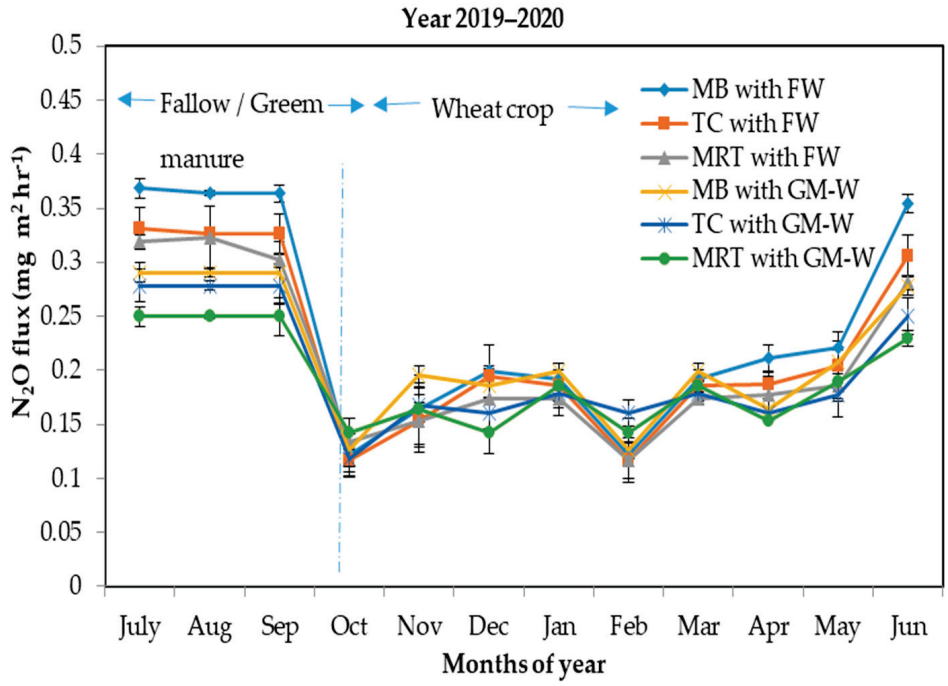

Figure 6. N_2O flux affected by the different tillage systems and crop rotations during the experimental period 2019–2020. MB F–W (Moldboard with Fallow–Wheat); TC F–W (Tine cultivator with Fallow–Wheat); MRT FW (Modified Reduced tillage with Fallow–Wheat); MB GM–W (Moldboard with Green manure–Wheat); TC GM–W (Tine cultivator with Green manure–Wheat); MRT GM–W (Modified Reduced tillage with Green manure–Wheat).

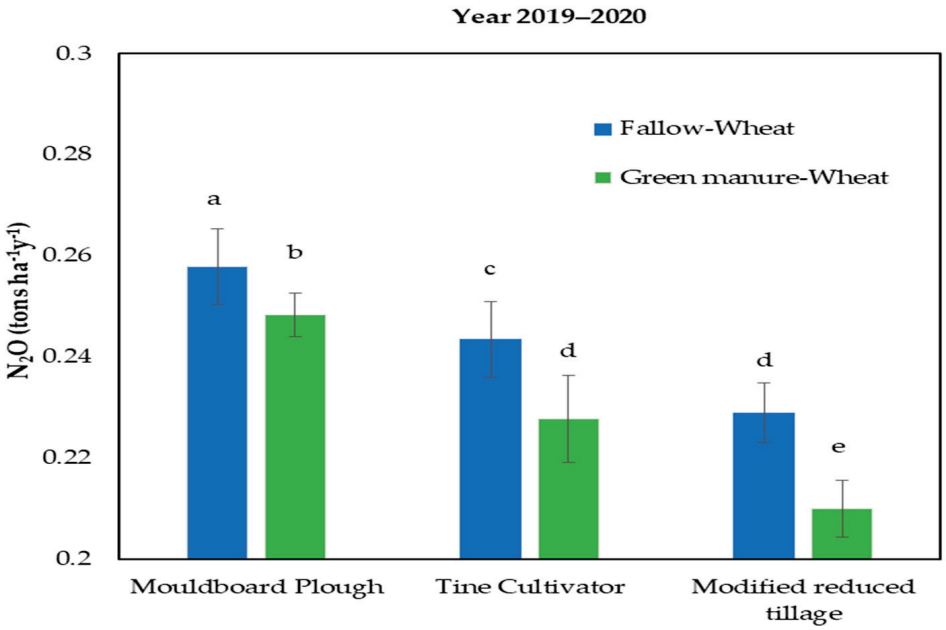

Figure 7. Cumulative N_2O affected by the different tillage systems and crop rotations during the experimental period 2019–2020. Letters denote homogeneous groups at $\alpha = 0.05$ significance level, where treatments with the same letter are not significantly different from each other.

3.4. Net Ecosystem Exchange (NEE), Global Warming Potential (GWP), and Greenhouse Gas Intensity (GHGI)

In the summer of the first year, the NEE for CO_2 showed the highest value in MB, followed by TC, and the lowest in MRT. Higher NEE values were observed for the F–W crop rotations than GM–W. This pattern persisted in the second-year summer data. A comparison of the results for winter revealed a significant overall decrease in NEE for both years. The highest NEE was recorded in the MB (F–W) combination plots at 3.35 t C ha^{-1}. The lowest was observed with the MRT (GM–W) combination plots at 2.55 t C ha^{-1} (Table 1).

Table 1. Net ecosystem exchange (NEE) affected by different tillage and crop rotations during 2018–2020.

	Tillage Systems	Crop Rotations	Summer Season NEE	Winter Season NEE Mg ha^{-1}	Annual NEE
Year 2019–2020 Year 2018–2019	MB	FW	9.28 A	3.35 A	12.63 A
		GW	2.93 C	2.08 A	5.01 C
	TC	FW	8.62 B	1.91 A	10.53 B
		GW	2.36 D	2.95 A	5.31 C
	MRT	FW	8.54 B	2.25 A	10.79 B
		GW	1.93 D	2.53 A	4.46 C
	MB	FW	8.44 A	3.49 A	11.93 A
		GW	2.14 B	2.42 A	4.56 B
	TC	FW	7.90 A	2.24 A	10.24 A
		GW	1.58 B	2.66 A	4.24 B
	MRT	FW	7.66 A	2.65 A	10.31 A
		GW	1.23 B	4.00 A	3.88 B

Different capital letters indicate statistically significant differences between means within each column at the 0.05 level. Means sharing the same letter are not significantly different from each other according to a post hoc test.

The MB tillage system yielded the highest GWP, followed closely by TC, and the least under MRT in 2019–2020, because GWP is primarily influenced by N_2O emissions because

of its higher warming potential in both crop rotations (Table 2). Compared to the MB plots, both TC and MRT treatments resulted in a 6.57% and 14.11% reduction in GHGI, respectively, under the fallow–wheat crop rotation and by 11.58% and 20.7% under the green manure–wheat rotation (Table 2).

Table 2. Global warming potential (GWP) and greenhouse gas intensity (GHGI) affected by different tillage and crop rotations during 2018–2020.

Tillage Systems	Crop Rotations	GWP t C ha^{-1} $year^{-1}$	GHGI t C ha^{-1} $year^{-1}$
Moldboard Plough	Fallow–Wheat	93.90 A	31.44 A
	Green manure–Wheat	89.94 AB	28.95 BC
Tine Cultivator	Fallow–Wheat	88.58 BC	29.32 AB
	Green manure–Wheat	83.10 BCD	25.14 CD
Modified Reduced Tillage	Fallow–Wheat	84.38 CD	25.64 C
	Green manure–Wheat	77.65 D	22.79 D

Different capital letters indicate statistically significant differences between means within each column at the 0.05 level. Means sharing the same letter are not significantly different from each other according to a post hoc test.

4. Discussion

4.1. Soil Moisture and Soil Temperature Affected by Different Tillage Practices and Crop Rotations

Minimizing tillage practices positively impacted soil properties, while excessive tillage practices negatively affected properties, such as the soil water content. A comparison among tillage systems showed that MRT resulted in a higher soil moisture content. This aligns with previous findings [39], in that chisel plow cultivation preserved the maximum moisture. Deep tillage practices, particularly with a chisel plow and disk, were reported to enhance soil water content, with shallow tillage having a less pronounced effect [40]. Green manure crops in the GM–W rotation absorbed moisture during their growth period, leading to less moisture conservation during summer than in the F–W rotation. On the other hand, after incorporating the green manure crop, particularly under MRT tillage, GM–W rotation consistently exhibited the highest moisture levels. This is crucial during wheat sowing in rainfed farming systems, where the combination of MRT tillage and GM–W rotation yielded the highest moisture content. Sesbania green manure incorporation adds organic matter to the soil, enhancing soil structure and water retention, as noted by [41].

These results revealed higher temperatures under moldboard plowing and chisel plowing for fallow–wheat rotation. This temperature increase was attributed to soil disturbance and closely linked to changes in the soil heat flux. Soil heat flux depends on the changes in soil heat capacity and thermal conductivity resulting from tillage practices, which impact soil structure, bulk density, and water content [42]. This finding relates to the impact of both MB and TC because they contribute to increased soil evaporation by inverting the soil during tillage, leading to higher soil temperatures [43]. The presence of a cover/green manure crop served as a surface cover with reduced heat conductivity and increased heat reflection compared to bare MB and TC because they contribute to increased soil evaporation by inverting the soil during tillage, leading to higher soil temperatures [43].

4.2. Effect of Tillage Practices and Crop Rotations on CO_2 Emission

These results suggest that MRT yields lower CO_2 emissions than MB. This reduction can be attributed to less soil disturbance in MRT, which reduces the exposure of soil organic matter to microbial decomposition [44]. The GM–W rotation consistently resulted in lower CO_2 emissions than the F–W rotation, regardless of the tillage system or experimental year. This pattern was especially evident during the summer season. Integrating cover or green manure crops likely enhanced soil organic matter and microbial biomass, promoting carbon sequestration and reducing emissions [45]. CO_2 emissions were highest immediately after primary tillage in July. This initial peak was attributed to the disruption of the soil structure and increased microbial activity that accelerates organic matter decomposition [46]. The

emissions declined two weeks post-tillage, but peaked again in August before gradually decreasing to their lowest levels in January. The seasonal variation highlights the influence of temperature and microbial activity on CO_2 emissions [47]. The findings are specific to the dryland conditions of the Pothwar plateau. The soil type, texture, and climatic conditions significantly influence CO_2 emissions and may vary in other regions [48]. Although the two-year study provided valuable initial insights, longer-term experiments will be needed to assess the sustainability and cumulative impacts of MRT and crop rotations on CO_2 emissions and soil health [49]. The peaks in CO_2 emissions immediately after tillage suggest that the timing of the measurements critically affects the results. More frequent sampling could provide a detailed understanding of emission dynamics over time [50]. Furthermore, the variations in soil moisture, temperature, and organic matter content across different treatments may influence the microbial activity and CO_2 emissions, necessitating controlled experimental conditions [51].

4.3. Impact of Tillage Practices and Crop Rotations on N_2O Emissions

The N_2O fluxes increased after plowing in the MB and TC systems and increased slightly after chiseling in the MRT system. Conventional tillage practices led to reduced bulk densities and smaller volumetric soil water content, improving the soil aeration and enabling N_2O to escape before denitrification to N_2 [52]. In contrast, the MRT and TC systems maintained a better soil structure and higher soil moisture content, which can suppress N_2O emissions by promoting denitrification to N_2, reducing the overall emissions [44,48]. Various factors, including water-filled pore space, mineral nitrogen concentration, air-filled porosity, soil moisture content, and soil structure density, contribute to increased N_2O emissions following modified reduced tillage [53,54]. For example, a high soil moisture content can produce anaerobic conditions that favor denitrification. In contrast, well-aerated soils promote nitrification. Both can lead to increased N_2O emissions depending on the specific soil and environmental conditions [55]. Significant N_2O emissions were observed during the initial weeks of the fallow season, consistent with previous studies, suggesting that a lack of crop cover and increased soil aeration promote microbial processes that release N_2O [56]. Overall, tillage systems did not significantly affect the total N_2O emissions during the experimental period, but the MB treatment exhibited higher N_2O fluxes during the fallow season than TC and MRT. Climate change impacts N_2O emissions, with increased temperatures and precipitation contributing to elevated emissions. Sustainable tillage practices are crucial for mitigating greenhouse gas emissions, considering the interactions between climate and soil properties. The soil type and management strategies also influence N_2O emissions, highlighting the importance of conservation practices in reducing emissions [57,58]. Additionally, organic matter contributions to nitrous oxide emissions following nitrate addition are not proportional to substrate-induced soil carbon priming, indicating that the relationship between soil management practices and N_2O emissions can be complex, and are influenced by factors such as the type and quantity of organic matter present [59].

4.4. Net Ecosystem Exchange (NEE), Global Warming Potential (GWP), and Greenhouse Gas Intensity (GHGI) Influenced by Tillage Practices and Cropping Sequence

The net ecosystem exchange (NEE) of CO_2 represents the balance between carbon (C) outputs from soil heterotrophic respiration (organic matter decomposition) and C inputs from autotrophic C assimilation (plant photosynthesis). The MRT system led to lower NEE, likely due to the treatment effects on the soil temperature, a strong driver of NEE CO_2 [60]. The effect of temperature on soil, root, and leaf respiration contributed to this outcome. Both tillage practice and crop incorporation influence the soil temperature by altering the soil organic matter content, surface insulation, and radiation [61–63]. In green manure crop rotation, crop residues incorporated into the soil reduce heat input, resulting in lower NEE CO_2 fluxes. On the other hand, plant residue incorporation removes this barrier between the soil and the atmosphere, allowing for heat exchange. The NEE CO_2 was higher during

the warm periods and varied with the crop growth stages, indicating the influence of seasonal temperature variations [64,65]. The net GWP was influenced significantly by N_2O emissions and SOC sequestration [66]. Addressing this will require effective agricultural management approaches that maximize soil carbon storage and reduce N_2O emissions in rainfed agriculture. This is crucial for mitigating greenhouse gas emissions and promoting sustainable productivity. The GHGI index is a useful tool for comparing the environmental and economic benefits of different agricultural management strategies, considering their impact on GHG emissions and crop yields [67]. The present study found that the variability in GHGI within modified reduced tillage treatments closely mirrored the variations in net GWP. While crop yield was pivotal in determining the GHGI, the N_2O fluxes were the primary driver of GHGI variations, as reported elsewhere [65].

While the static chamber technique provided valuable data on GHG fluxes in this study, it is vital to consider the limitations of the method. The static chamber method can sometimes fail to capture the full extent of the spatial and temporal variability in greenhouse gas emissions. Variations in the soil type, moisture content, and temperature can lead to fluctuations in gas fluxes that static chambers might not fully capture.

These limitations were addressed by conducting repeated measurements across different intervals and following strict protocols for gas sampling and analysis. Nevertheless, these constraints should be considered when interpreting the results because they might have led to underestimations or overestimations of the actual gas fluxes.

5. Conclusions

This study's findings suggest that transitioning from conventional tillage practices to modified reduced tillage, coupled with a cover/green manure crop, significantly reduce CO_2 and N_2O emissions, lowering the overall global warming potential and the greenhouse gas intensity. Peak emissions occurred in July, with the lowest levels occurring in February, indicating that fluxes were highest during warm months and lowest during cold periods, tracking soil temperature and moisture fluctuations. Conservation tillage approaches, such as MRT, are a promising avenue for climate-smart agriculture in smallholder rainfed areas of Pothwar and other similar regions. Future research will conduct extended, multi-year studies encompassing various climate scenarios and diverse agronomic practices that can provide a more comprehensive understanding of how modified reduced tillage affects greenhouse gas emissions over time.

Author Contributions: Conceptualization, Investigation, Validation, N.J., S.S.I., Q.H. and M.A.; Supervision, S.S.I.; Writing—original draft, N.J.; Methodology, Formal analysis, Data collection, N.J., S.S.I. and Q.H.; Writing—review and editing, N.J., S.S.I., Q.H., M.A., A.F.A., B.O.A., W.Z. and M.Y. All authors have read and agreed to the published version of the manuscript.

Funding: This study received financial assistance from the Higher Education Commission of Pakistan under a project entitled "Inter-Comparison of CENTURY and DSSAT Model Simulations to Improve Soil Based Climate Change Resilience and Adaptability of Rainfed Crop Production Systems in Pakistan" (HEC Project No. 3179) and Researchers supporting project number (RSP2024R414), King Saud University, Riyadh, Saudi Arabia.

Institutional Review Board Statement: Not applicable.

Informed Consent Statement: Not applicable.

Data Availability Statement: Data will be given on request.

Acknowledgments: We extend our appreciation to the Researchers Supporting Project (no. RSP2024R414), King Saud University, Riyadh, Saudi Arabia.

Conflicts of Interest: The authors state that they have no known conflicting financial interests or personal connections that seem to have an impact on the work published in this article.

References

1. Montzka, S.A.; Dlugokencky, E.J.; Butler, J.H. Non-CO_2 greenhouse gases and climate change. *Nature* **2011**, *476*, 43–50. [CrossRef]
2. Shakoor, A.; Shahbaz, M.; Farooq, T.H.; Sahar, N.E.; Shahzad, S.M.; Altaf, M.M.; Ashraf, M. A Global Meta-Analysis of Greenhouse Gases Emission and Crop Yield under No-Tillage as Compared to Conventional Tillage. *Sci. Total Environ.* **2021**, *750*, 142299. [CrossRef] [PubMed]
3. IPCC. *Climate Change Mitigation of Climate Change: Working Group I Contribution to the Fourth Assessment Report of the IPCC*; Cambridge University Press: Cambridge, UK, 2014.
4. EAT. Greenhouse Gas Emissions from Agriculture in the EU. Factsheet 1. 2015. Available online: http://www.europarl.europa.eu/RegData/etudes/BRIE/2015/571327/EPRS_BRI(2015)571327_EN.pdf (accessed on 2 July 2017).
5. Philippe, F.-X.; Nicks, B. Review on greenhouse gas emissions from pig houses: Production of carbon dioxide, methane and nitrous oxide by animals and manure. *Agric. Ecosyst. Environ.* **2014**, *199*, 10–25. [CrossRef]
6. Liu, T.Q.; Li, S.H.; Guo, L.G.; Cao, C.G.; Li, C.F.; Zhai, Z.B.; Ke, H.J. Advantages of nitrogen fertilizer deep placement in greenhouse gas emissions and net ecosystem economic benefits from no-tillage paddy fields. *J. Clean. Prod.* **2020**, *263*, 121322. [CrossRef]
7. Tong, L.S.; Xiao, H.B.; Xu, K.; Zhan, Y.M.; Shi, Z.H. Stoichiometric Regulations of Soil Respiration and Its Temperature Sensitivity under Erosion and Deposition Conditions. *Agric. Ecosyst. Environ.* **2021**, *319*, 107507. [CrossRef]
8. Zhou, L.M.; Jin, S.L.; Liu, C.A.; Xiong, Y.C.; Si, J.T.; Li, X.G.; Gan, Y.T.; Li, F.M. Ridge-Furrow and Plastic-Mulching Tillage Enhances Maize–Soil Interactions: Opportunities and Challenges in a Semiarid Agroecosystem. *Field Crops Res.* **2012**, *126*, 181–188. [CrossRef]
9. Houghton, R.A. Balancing the Global Carbon Budget. *Annu. Rev. Earth Planet. Sci.* **2007**, *35*, 313–347. [CrossRef]
10. Ren, W.; Banger, K.; Tao, B.; Yang, J.; Huang, Y.; Tian, H. Global pattern and change of cropland soil organic carbon during 1901–2010: Roles of climate, atmospheric chemistry, land use and management. *Geogr. Sustain.* **2020**, *1*, 59–69. [CrossRef]
11. Murphy, B.W.; Sparrow, L.A.; Salmon, S.U.; Abbott, T.S.; Raison, R.J.; Downie, A.L. Organic carbon stocks in soils of New South Wales, Australia. *Soil Res.* **2007**, *45*, 255–272. [CrossRef]
12. Gong, Y.; Li, P.; Sakagami, N.; Komatsuzaki, M. No-tillage with rye cover crop can reduce net global warming potential and yield-scaled global warming potential in the long-term organic soybean field. *Soil Tillage Res.* **2021**, *205*, 104747. [CrossRef]
13. Shcherbak, I.; Millar, N.; Robertson, G.P. Global meta-analysis of the nonlinear response of soil nitrous oxide (N_2O) emissions to fertilizer nitrogen. *Proc. Natl. Acad. Sci. USA* **2014**, *111*, 9199–9204. [CrossRef] [PubMed]
14. Smith, P.; Reay, D.; Smith, J. Agricultural methane emissions and the potential for mitigation. *Philos. Trans. R. Soc. A* **2021**, *379*, 20200451. [CrossRef] [PubMed]
15. Guenet, B.; Gabrielle, B.; Chenu, C.; Arrouays, D.; Balesdent, J.; Bernoux, M.; Zhou, F. Can N_2O Emissions Offset the Benefits from Soil Organic Carbon Storage? *Glob. Change Biol.* **2021**, *27*, 237–256. [CrossRef] [PubMed]
16. Dossou-Yovo, E.R.; Brüggemann, N.; Jesse, N.; Huat, J.; Ago, E.E.; Agbossou, E.K. Reducing soil CO_2 emission and improving upland rice yield with no-tillage, straw mulch and nitrogen fertilization in northern Benin. *Soil Tillage Res.* **2016**, *156*, 44–53. [CrossRef]
17. Madarász, B.; Jakab, G.; Szalai, Z.; Juhos, K.; Kotroczó, Z.; Tóth, A.; Ladányi, M. Long-Term Effects of Conservation Tillage on Soil Erosion in Central Europe: A Random Forest-Based Approach. *Soil Tillage Res.* **2021**, *209*, 104959. [CrossRef]
18. Wang, Z.; Li, Y.; Li, T.; Zhao, D.; Liao, Y. Conservation Tillage Decreases Selection Pressure on Community Assembly in the Rhizosphere of Arbuscular Mycorrhizal Fungi. *Sci. Total Environ.* **2020**, *710*, 136326. [CrossRef] [PubMed]
19. Kumar, V.; Saharawat, Y.S.; Gathala, M.K.; Jat, A.S.; Singh, S.K.; Chaudhary, N.; Jat, M.L. Effect of different tillage and seeding methods on energy use efficiency and productivity of wheat in the Indo-Gangetic Plains. *Field Crops Res.* **2013**, *142*, 1–8. [CrossRef]
20. Fan, J.; Luo, R.; Liu, D.; Chen, Z.; Luo, J.; Boland, N.; Ding, W. Stover retention rather than no-till decreases the global warming potential of rainfed continuous maize cropland. *Field Crops Res.* **2018**, *219*, 14–23. [CrossRef]
21. Xu, J.; Han, H.; Ning, T.; Li, Z.; Lal, R. Long-term effects of tillage and straw management on soil organic carbon, crop yield, and yield stability in a wheat-maize system. *Field Crops Res.* **2019**, *233*, 33–40. [CrossRef]
22. Khan, M.A.; Mahmood, K.; Ahmad, M. Agricultural Land Use in the Pothwar Plateau. *Pak. J. Agric. Res.* **2004**, *17*, 131–138.
23. Li, F.M.; Wang, J.; Xu, J.Z.; Xu, H.L.; Ma, L. Mulching Improves Yield and Water-Use Efficiency of Potato Cropping in China. *Field Crops Res.* **2013**, *83*, 297–311. [CrossRef]
24. Zhang, S.; Li, Q.; Zhang, X.; Wei, K.; Chen, L. Effect of Plastic Mulch on Soil Water, Temperature and Degradation of Phenolic Acids in Salvia miltiorrhiza Bunge. *Sci. Hortic.* **2016**, *204*, 15–22. [CrossRef]
25. Chen, X.; Stewart, P.S. Biofilm Removal Caused by Chemical Treatments. *Water Res.* **2007**, *41*, 965–974. [CrossRef] [PubMed]
26. Kasirajan, S.; Ngouajio, M. Polyethylene and Biodegradable Mulches for Agricultural Applications: A Review. *Agron. Sustain. Dev.* **2012**, *32*, 501–529. [CrossRef]
27. Stewart, P.S.; Franklin, M.J. Physiological Heterogeneity in Biofilms. *Nat. Rev. Microbiol.* **2008**, *6*, 199–210. [CrossRef]
28. Lal, R. Sequestering carbon in soils of arid ecosystems. *Land Degrad. Dev.* **2009**, *20*, 441–454. [CrossRef]
29. Sharif, M.; Ijaz, S.S.; Ali, S.; Ansar, M.; Hassan, A. Prediction of Tillage Operation Strategies for Dryland Wheat Production in a Degraded Loess Soil. *Arch. Agron. Soil Sci.* **2017**, *63*, 1137–1149. [CrossRef]
30. ur Rehman, S.; Ijaz, S.S.; Raza, M.A.; Din, A.M.U.; Khan, K.S.; Fatima, S.; Ansar, M. Soil Organic Carbon Sequestration and Modeling under Conservation Tillage and Cropping Systems in a Rainfed Agriculture. *Eur. J. Agron.* **2023**, *147*, 126840. [CrossRef]

31. Sharif, M.; Ijaz, S.S.; Ali, S.; Ansar, M.; Hassan, A. Buildup of Soil Organic Carbon and Stable Aggregates under Conservation Tillage in Loess Dryland Soil. *J. Biodivers. Environ. Sci.* **2015**, *6*, 446–453.
32. Wraith, J.M.; Robinson, D.A.; Jones, S.B.; Long, D.S. Spatially Characterizing Apparent Electrical Conductivity and Water Content of Surface Soils with Time Domain Reflectometry. *Comput. Electron. Agric.* **2005**, *46*, 239–261. [CrossRef]
33. Gomes, J.; Bayer, C.; de Souza Costa, F.; de Cássia Oiccolo, M.; Znatta, J.A.; Vieira, C.B.; Six, J. Soil nitrous oxide emissions in long-term cover crops-based rotations under subtropical climate. *Soil Tillage Res.* **2009**, *106*, 36–44. [CrossRef]
34. Zhang, A.; Cui, L.; Pan, G.; Li, L.; Hussain, Q.; Zhang, X.; Zheng, J.; Crowley, D. Effect of biochar amendment on yield and methane and nitrous oxide emissions from a rice paddy from Tai Lake Plain, China. *Agric. Ecosyst. Environ.* **2010**, *139*, 469–475. [CrossRef]
35. Huang, Y.; Ren, W.; Wang, L.; Hui, D.; Grove, J.H.; Yang, X.; Goff, B. Greenhouse gas emissions and crop yield in no-tillage systems: A meta-analysis. *Agric. Ecosyst. Environ.* **2018**, *268*, 144–153. [CrossRef]
36. Zheng, X.; Xie, B.; Liu, C.; Zhou, Z.; Yao, Z.; Wang, Y.; Wang, Y.; Yang, L.; Zhu, J.; Huang, Y.; et al. Quantifying net ecosystem carbon dioxide exchange of a short-plant cropland with intermittent chamber measurements. *Glob. Biogeochem.* **2008**, *22*, 3. [CrossRef]
37. Osaki, M.; Shinano, T.; Tadano, T. Carbon-nitrogen interaction in field crop production. *Soil Sci. Plant Nutr.* **1992**, *38*, 553–564. [CrossRef]
38. Steel, R.G.D.; Torrie, J.H.; Dicky, D.A. *Principles and Procedures of Statistics, A Biometrical Approach*, 3rd ed.; McGraw Hill, Inc. Book Co.: New York, NY, USA, 1997; pp. 352–358.
39. Makki, E.K.; El-amin Mohamed, A. Tillage implements performance and effect on some soil physical properties. *AMA Agric. Mech. Asia Afr. Lat. Am.* **2008**, *39*, 9.
40. Laddha, K.C.; Totawat, K.L. Effects of deep tillage under rainfed agriculture on production of sorghum (*Sorghum biocolor* L. Moench) intercropped with green gram (*Vigna radiata* L. Wilczek) in western India. *Soil Tillage Res.* 1997; 43, 241–250. [CrossRef]
41. Das, T.K.; Nath, C.P.; Das, S.; Biswas, S.; Bhattacharyya, R.; Sudhishri, S.; Chaudhari, S.K. Conservation Agriculture in rice-mustard cropping system for five years: Impacts on crop productivity, profitability, water-use efficiency, and soil properties. *Field Crops Res.* 2020; 250, 107781. [CrossRef]
42. Hillel, D. *Introduction to Environmental Soil Physics*; Elsevier: Amsterdam, The Netherlands, 2003.
43. Lichet, M.A.; Al-Kaisi, M. Strip-tillage effect on seedbed soil temperature and other soil physical properties. *Soil Tillage Res.* **2005**, *80*, 233–249. [CrossRef]
44. Six, J.; Ogle, S.; Breidt, F.J.; Conant, R.T.; Mosier, A.R.; Paustian, K. The potential to mitigate global warming with no-tillage management is only realized when practice is in the long term. *Glob. Change Biol.* **2004**, *10*, 155–160. [CrossRef]
45. Lal, R. Soil carbon sequestration impacts on global climate change and food security. *Science* **2004**, *304*, 1623–1627. [CrossRef]
46. Reicosky, D.C.; Archer, D.W. Moldboard plow tillage depth and short-term carbon dioxide release. *Soil Tillage Res.* **2007**, *94*, 109–121. [CrossRef]
47. Davidson, E.A.; Janssens, I.A. Temperature sensitivity of soil carbon decomposition and feedbacks to climate change. *Nature* **2006**, *440*, 165–173. [CrossRef]
48. Smith, P.; Martino, D.; Cai, Z.; Gwary, D.; Janzen, H.; Kumar, P.; Smith, J. Greenhouse gas mitigation in agriculture. *Philos. Trans. R. Soc. B Biol. Sci.* **2008**, *363*, 789–813. [CrossRef]
49. Post, W.M.; Kwon, K.C. Soil carbon sequestration and land-use change: Processes and potential. *Glob. Change Biol.* **2000**, *6*, 317–327. [CrossRef]
50. Parkin, T.B.; Kaspar, T.C. Nitrous oxide emissions from corn-soybean systems in the Midwest. *J. Environ. Qual.* **2006**, *35*, 1496–1506. [CrossRef]
51. Conant, R.T.; Paustian, K.; Elliott, E.T. Grassland management and conversion into grassland: Effects on soil carbon. *Ecol. Appl.* **2011**, *11*, 343–355. [CrossRef]
52. Chatskikh, D.; Olesen, J.E. Soil tillage enhanced CO_2 and N_2O emissions from loamy sand soil under spring barley. *Soil Tillage Res.* **2007**, *97*, 5–18. [CrossRef]
53. Oorts, K.; Merckx, R.; Gréhan, E.; Labreuche, J.; Nicolardot, B. Determinants of annual fluxes of CO_2 and N_2O in long-term no-tillage and conventional tillage systems in northern France. *Soil Tillage Res.* **2007**, *95*, 133–148. [CrossRef]
54. Beare, M.H.; Gregorich, E.G.; St-Georges, P. Compaction effects on CO_2 and N_2O production during drying and rewetting of soil. *Soil Biol. Biochem.* **2009**, *41*, 611–621. [CrossRef]
55. Butterbach-Bahl, K.; Baggs, E.M.; Dannenmann, M.; Kiese, R.; Zechmeister-Boltenstern, S. Nitrous oxide emissions from soils: How well do we understand the processes and their controls? *Philos. Trans. R. Soc. B Biol. Sci.* **2013**, *368*, 20130122. [CrossRef] [PubMed]
56. Venterea, R.T.; Burger, M.; Spokas, K.A. Nitrogen oxide and methane emissions under varying tillage and fertilizer management. *J. Environ. Qual.* **2005**, *34*, 1467–1477. [CrossRef] [PubMed]
57. Bouwman, A.F.; Boumans, L.J.M.; Batjes, N.H. Emissions of N_2O and NO from fertilized fields: Summary of available measurement data. *Glob. Biogeochem. Cycles* **2002**, *16*, 6-1–6-13. [CrossRef]
58. Mutegi, J.K.; Munkholm, L.J.; Petersen, B.M.; Hansen, E.M.; Petersen, S.O. Nitrous oxide emissions and controls as influenced by tillage and crop residue management strategy. *Soil Biol. Biochem.* **2010**, *42*, 1701–1711. [CrossRef]

59. Li, Y.; Moinet, G.Y.; Clough, T.J.; Whitehead, D. Organic matter contributions to nitrous oxide emissions following nitrate addition are not proportional to substrate-induced soil carbon priming. *Sci. Total Environ.* **2022**, *851*, 158274. [CrossRef]
60. Rastogi, M.; Singh, S.; Pathak, H. Emission of carbon dioxide from soil. *Curr. Sci.* **2002**, *82*, 510–517.
61. Schmidt, M.W.; Torn, M.S.; Abiven, S.; Dittmar, T.; Guggenberger, G.; Janssens, I.A.; Kleber, M.; Kögel-Knabner, I.; Lehmann, J.; Manning, D.A. Persistence of soil organic matter as an ecosystem property. *Nature* **2011**, *478*, 49–56. [CrossRef]
62. Azooz, R.; Lowery, B.; Daniel, T.; Arshad, M. Impact of tillage and residue management on soil heat flux. *Agric. For. Meteorol.* **1997**, *84*, 207–222. [CrossRef]
63. Beyaert, R.P.; Schott, J.W.; White, P.H. Tillage effects on corn production in a coarse-textured soil in southern Ontario. *Agron. J.* **2002**, *94*, 767–774. [CrossRef]
64. Wan, S.; Hui, D.; Wallace, L.; Luo, Y. Direct and indirect effects of experimental warming on ecosystem carbon processes in a tallgrass prairie. *Glob. Biogeochem. Cycles* **2005**, *19*, 9–13. [CrossRef]
65. Ussiri, D.A.; Lal, R. Long-term tillage effects on soil carbon storage and carbon dioxide emissions in continuous corn cropping system from an alfisol in Ohio. *Soil Tillage Res.* **2009**, *104*, 39–47. [CrossRef]
66. Lv, J.; Yin, X.; Dorich, C.; Olave, R.; Wang, X.; Kou, C.; Song, X. Net field global warming potential and greenhouse gas intensity in typical arid cropping systems of China: A 3-year field measurement from long-term fertilizer experiments. *Soil Tillage Res.* **2021**, *212*, 105053. [CrossRef]
67. Mosier, A.R.; Halvorson, A.D.; Reule, C.A.; Liu, X.J. Net global warming potential and greenhouse gas intensity in irrigated cropping systems in northeastern Colorado. *J. Environ. Qual.* **2006**, *35*, 1584–1598. [CrossRef] [PubMed]

Disclaimer/Publisher's Note: The statements, opinions and data contained in all publications are solely those of the individual author(s) and contributor(s) and not of MDPI and/or the editor(s). MDPI and/or the editor(s) disclaim responsibility for any injury to people or property resulting from any ideas, methods, instructions or products referred to in the content.

climate

MDPI

Article

Small Municipalities in the Amazon under the Risk of Future Climate Change

Everaldo B. de Souza [1,*], Brenda C. S. Silva [1], Emilene M. F. Serra [1], Melgris J. Becerra Ruiz [1], Alan C. Cunha [2], Paulo J. P. O. Souza [3], Luciano P. Pezzi [4], Edson J. P. da Rocha [5], Adriano M. L. Sousa [3], João de Athaydes Silva, Jr. [1], Alexandre M. C. do Carmo [1], Douglas B. S. Ferreira [6], Aline M. M. Lima [1], Flavio A. A dos Santos [5], Bergson C. Moraes [1], Maria de L. P. Ruivo [7], Peter M. Toledo [4] and Tercio Ambrizzi [8]

[1] Programa de Pos-Graduação em Ciências Ambientais (PPGCA), Instituto de Geociências (IG), Universidade Federal do Pará (UFPA), Belém 66075-110, PA, Brazil; brenda.silva@itec.ufpa.br (B.C.S.S.); emilene.serra@ig.ufpa.br (E.M.F.S.)
[2] Departamento de Engenharia Civil, Universidade Federal do Amapá (UNIFAP), Macapá 68900-070, AP, Brazil
[3] Instituto Sócio Ambiental e dos Recursos Hídricos, Universidade Federal Rural da Amazônia (UFRA), Belém 66077-830, PA, Brazil
[4] Instituto Nacional de Pesquisas Espaciais (INPE), São José dos Campos 12227-010, SP, Brazil
[5] Centro Gestor e Operacional do Sistema de Proteção da Amazônia (CENSIPAM), Belém 66617-420, PA, Brazil
[6] Instituto Tecnológico Vale (ITV), Belém 66055-090, PA, Brazil
[7] Museu Paraense Emilio Goeldi (MPEG), Belém 66077-830, PA, Brazil
[8] Instituto de Astronomia, Geofísica e Ciências Atmosféricas, Universidade de São Paulo (USP), São Paulo 05508-010, SP, Brazil
* Correspondence: everaldo@ufpa.br

Abstract: The focus of this work is on small municipalities (population below 50 thousand inhabitants) that cover around 87% of the territory of the Brazilian Legal Amazon (BLA). Based on a comprehensive integrated analysis approach using the three components hazard (climate extremes from CMIP6 future scenarios), exposure (directly affected population), and vulnerability (subdimensions of susceptibility and coping/adaptive capacity by using multidimensional indicators), the latter two using current datasets provided by the official Census IBGE 2022, we document a quantitative assessment of the risk R of natural disasters in the BLA region. We evidenced a worrying and imminent intensification of the curve of R in most Amazonian municipalities over the next two 25-year periods. The overall results of the highest proportions of R (total municipalities affected) pointed out the Amazonas, Roraima, Pará, and Maranhão as the main states, presenting projected categories of R high in the near future (2015 to 2039) and very high in the far future (2040 to 2064). The detailed assessment of the susceptibility and coping/adaptive capacity allowed us to elucidate the principal indicators that aggravate the degree of vulnerability: economy, the precariousness of urban infrastructure, medical services, communication, and urban mobility, whose combined factors, unfortunately, reveal a widespread poverty profile along the small Amazonian municipalities. Our scientific findings can assist decision makers in targeted strategies planning and public policies to minimize and mitigate ongoing and future climate change.

Keywords: disaster risk; vulnerability; climate extremes; CMIP6 projections; Brazilian Amazon

1. Introduction

The climate is changing, and we have a new normal [1]. Climate science is crucial in systemic understanding of ongoing and future global climate change that can exacerbate extreme atmospheric/oceanic phenomena [2–4], directly compromising human well-being. The occurrence of extreme weather and climate events in an area with exposed and vulnerable human and natural systems can very likely lead to natural disasters [5]. In recent decades, a novel category of extremes has become increasingly apparent, with several cities

around the globe experiencing successions of extremes of floods, droughts, and heat waves, with consequent significant damage in social and environmental dimensions [4].

In particular, Brazil is a continental country presenting profound social inequalities, with the north (Amazon) and northeast regions being characterized as the most vulnerable to natural hazards [6,7]. Studies of meteorological extremes (especially long-term droughts) from a climatological perspective, including aspects of socio-environmental vulnerability, are numerous for the Brazilian Northeast [8–11] and references therein. For the Amazon, most previous studies reported composites or case studies of droughts [12–14] and floods [15–17], which provoked serious impacts during the last few decades.

Climate extremes in the Amazon have amplified their frequency and intensity [2], but the populations and environments at risk have also increased. Given this complex picture of temporally dynamic physical and environmental changes interacting with the spatially diverse social dimension, we have a great scientific challenge of investigating future scenarios of the possible worsening of disaster risk. At the same time that the science of integrated Earth system modeling advances assertively in generating future climate change projections, further efforts are needed to downscale global prognoses to a level of regional and local analysis that may be applied to disaster risk assessment [18].

Considering that the demographic, social, and environmental differences throughout the Brazilian territory are significant [6], a complicating factor in interpreting the degree of vulnerability on a national scale [19], here we propose an approach on a regional scale with a focus on municipalities of the Brazilian Legal Amazon (BLA) that are considered to be small-sized (population below 50 thousand inhabitants, according to Instituto Brasileiro de Geografia e Estatística—IBGE). The justification for choosing the municipal analysis scale in the study area is that the results of the risk evaluation in locations with the same geographic characteristics can contribute to assisting decision makers in targeted strategies planning and public policies to minimize and mitigate the threat of ongoing and future climate change. Hence, we conducted a comprehensive integrated analysis to quantitatively assess the future risk of natural disasters within and between small municipalities of the BLA region, resulting from three components: hazard (climate extremes associated with droughts and floods), exposure (directly affected population and environment), and vulnerability (sub-dimensions of susceptibility and coping/adaptive capacity by using multidimensional indicators), the latter two using current datasets provided by the official Census IBGE 2022 [20]. It is important to mention that the hazard component includes an analysis of extreme climate indices extracted from historical and future General Circulation Models (GCMs) projections included in Phase 6 of the Coupled Model Intercomparison Project (CMIP6), which represent the most up-to-date simulations to investigate the impacts of climate change in different global emissions scenarios [21].

2. Materials and Methods

The official data from the 2022 Census coordinated by the IBGE [20] were used to select municipalities with a total population below 50,000 inhabitants (defined as small municipalities). Figure 1a shows the study area, highlighting a total of 671 small municipalities selected across the territory of the nine BLA states. MA, TO, MT and PA are the states with more than one hundred municipalities, while for AP, RR and AC, the total is below twenty (Figure 1b). Around 522 municipalities have a density <16 inhabitants/km^2 and 123 municipalities between 17 and 47 inhabitants/km^2, the total of which accounts for around 96% of the entire region (Figure 1c). An urbanized area <3 km^2 is observed in a total of 319 municipalities and values between 4 and 7 km^2 are verified in around 217 municipalities, both sets accounting for almost 80% of the entire sample (Figure 1b). So, the population living in small urbanized areas with low demographic density is a prominent geographic characteristic of this study area.

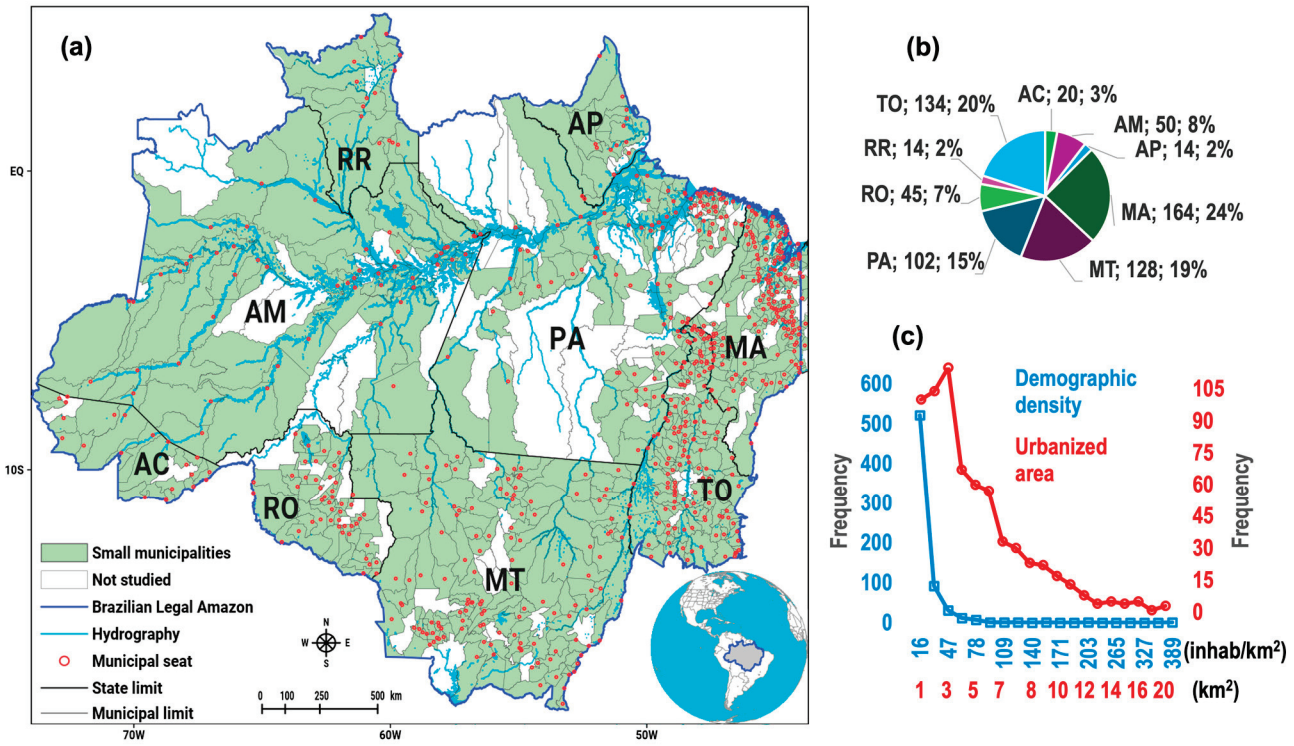

Figure 1. (**a**) Map of the study area highlighting the small municipalities (in green) and its municipal seats (red circles) in the BLA region, (**b**) total number of municipalities and respective percentage by state, (**c**) frequency distribution of demographic density (in blue) and urbanized area (in red) of the 671 municipalities. Acronyms indicate the nine states (AC—Acre, AM—Amazonas, AP—Amapá, MA—Maranhão, west of 44° W, MT—Mato Grosso, PA—Pará, RO—Rondônia, RR—Roraima and TO—Tocantins).

Based on a conceptual framework recommended in the Special Report on Managing the Risks of Extreme Events and Disasters to Advance Climate Change Adaptation (SREX) [5], we consider that the risk (R) of natural disaster is the result of the interaction (intercession) of three main components (Equation (1): first, the threat or hazard (H) of occurrence of extreme meteorological/climate events, second, the exposure (E) of the affected/impacted population and environment, and third, the respective degree of vulnerability (V) in multiple social, economic, environmental and local infrastructure dimensions:

$$R = H \times E \times V \quad (1)$$

Equation (1) is applied for the 671 small municipalities in the BLA using a total of 3 indicators for the component E, 17 indicators for the component V and 4 indicators for component H (see Table 1 with details of all multidimensional variables/indicators) and following the methodological procedures described in the flowchart in Figure 2, as sequentially explained below. Due to the indicators presenting different units, a minimum/maximum rescaling method [22] was adopted, in which each indicator is transformed (normalized) into an identical range between zero and one, through the expression:

$$I_n = (I_i - I_{min})/(I_{max} - I_{min}) \quad (2)$$

I_n is the normalized indicator, I_{min} and I_{max} are the minimum and maximum values, respectively, considering the entire sample of 671 municipalities of the respective indicator. The result is a score, with 0 being the best and 1 the worst in rank. After normalization employed in all indicators listed in Table 1, the components H, E and V were calculated according to the methodology described below. We used the quantile method to divide

the results into five intensity categories for the spatial analysis and maps containing a classification scheme defined as very low, low, moderate, high, and very high.

Table 1. List of all indicators and variables used to calculate the components E, V and H.

Components, Sub-Dimensions, Themes, Variables/Indicators and Units	Acronym	Reference Year, Source
Component E		
Total population (inhabitants)	TP	2022, IBGE Census
Demographic density (inhabitants/km^2)	DD	2022, IBGE Census
Urbanized area (km^2)	UA	2019, IBGE
Component V		
Sub-dimension S Susceptibility		
Public infrastructure		
Households by type of sewage system: rudimentary septic tank/hole, ditch, river, lake, stream or sea, without bathroom (total)	SW	2022, IBGE Census
Households by type of waste destination: burned or buried on the property; played on vacant land or public area (total)	WD	2022, IBGE Census
Households by form of water supply: no connection to general network (total)	WS	2022, IBGE Census
Housing conditions and dependent people		
Housing in a rooming house or tenement; residence unfinished (total)	HO	2022, IBGE Census
Children 0 to 4 years (total)	CH	2022, IBGE Census
Elderly people over 65 years old (total)	EL	2022, IBGE Census
Health (illnesses and family losses)		
Incidence of malaria	MA	2018/2022, DATASUS
Mortality from COVID-19 (accumulated people)	MC	2020/2021, DATASUS
Economy		
GDP per capita (Thousand BRL/inhabitants)	GP	2021, IBGE
C Coping/Adaptive Capacity		
Medical services		
Number of hospital beds (total)	HB	2022, DATASUS
Number of physicians (total)	NP	2022, DATASUS
Digital communication and urban mobility		
Broadband Internet (access/100 homes)	BI	2019, IBGE
Public transport (total buses/1000 inhabitants)	PT	2019, IBGE
Education		
IDEB Elementary Education—final years (concept)	ED	2021, MEC/INEP
Environment		
Accumulated deforestation (km^2)	DE	2000/2022, INPE
Existence of a civil defense department and specific legislation		
Municipal civil defense coordination or secretariat or fire department (yes/no)	CD	2019, IBGE
Public policy plan with municipal law instrument for planning and managing environmental disaster risks (yes/no)	IN	2019, IBGE
Component H		
Climate extremes associated with droughts and heat waves		
Relative changes of CDD for near and far future	C_CDD	Future, CMIP6 GCMs
Relative changes of WSDI for near and far future	C_WSDI	Future, CMIP6 GCMs
Climate extremes associated with floods and inundations		
Relative changes of R95p for near and far future	C_R95p	Future, CMIP6 GCMs
Relative changes of RX5day for near and far future	C_RX5day	Future, CMIP6 GCMs

Component E is of great relevance in integrated risk assessment, since the population is the central element that will directly suffer the possible damages, impacts and consequences of natural disasters. E is expressed by the simple mean of the three demographic indicators:

$$E = (TP + DD + UA)/3 \quad (3)$$

where TP, DD and UA are the total population, demographic density and urbanized area, respectively.

The assessment of component V is multidimensional including social, economic, environmental and public infrastructure variables and indicators, which are expressed by the sub-dimensions of susceptibility (S) and coping/adaptive capacity (C):

$$V = (S + C)/2 \quad (4)$$

S reveals the propensity of the municipality and people to suffer damage/loss and be negatively affected by the occurrence of climate extremes. We consider indicators that represent the lack of S, as below:

$$S = 0.15\,(0.33\,(SW + WD + WS)) + 0.15\,(0.33\,(HO + CH + EL)) + 0.1\,(0.5\,(MA + MC)) + 0.1\,GP \quad (5)$$

The acronyms of the indicators are described in detail in Table 1. The first term contains indicators that denote the precariousness of the public infrastructure of Amazonian households (critical or minimum conditions of sanitary sewage, waste destination and potable water supply), the second term reflects the fragility or insecurity of housing conditions (tenements or unfinished/degraded houses) and the presence of more dependent people (children and elderly), the third term characterizes health conditions (incidence of malaria, a disease endemic in the Amazon) and human losses given by the recent mortality rate from COVID-19, and the last term expresses the economic indicator (municipal GDP). The highest weights were assigned to the indicators of the first and second terms, which in the Amazon contribute more directly to the lack of S.

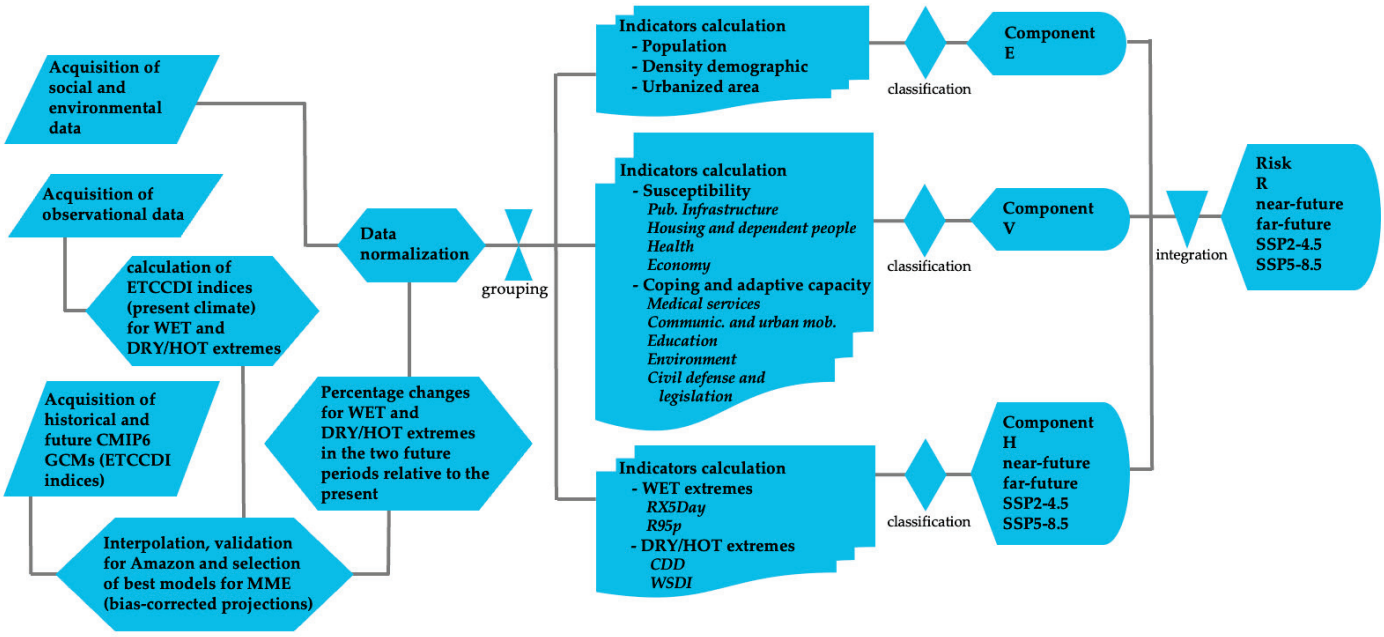

Figure 2. Flowchart of methodological procedures adopted for integrated risk assessment.

C was estimated by indicators that determine the immediate or short-term ability of the municipality to manage or react to the impact of an extreme event (coping capacity), as well as some characteristics of the adaptive capacity that enable the municipality to carry out actions and adaptation strategies in the medium and long term for the purposes of minimization of vulnerability:

$$C = 0.2(0.5(HB + NP)) + 0.1(0.5(BI + PT)) + 0.1(0.5(CD + IN)) + 0.05ED + 0.05D \quad (6)$$

Details of the acronyms are in Table 1. The first term emphasizes the medical services most used by the population in an emergency (receiving the highest weight), the second term represents the digital communication and urban mobility to obtain alert information and moving from the place of danger, the third term is the most important on the part of the municipal government responsible for the civil defense secretariats that deal with disaster response actions, as well as for the implementation of public policies registered in legal instruments focusing on the planning and management of climate and environmental risk, and the last terms indicate the aspects of education and environment.

The weight values used in the sub-dimensions S and C were established in accordance with the methodological framework used in the AdaptaBrasil platform, a project implemented by the Ministry of Science, Technology and Innovation (MCTI) from Brazil in partnership with the National Institute for Space Research (INPE), which developed a theoretical–methodological document to assess the risk of climate change impacts in some Brazilian strategic strategies sectors [23].

The indicators of the component H were obtained through a comprehensive analysis approach of extreme climate indices from historical and future projections of a total of 24 General Circulation Models (GCMs) included in the Coupled Model Intercomparison Project Phase 6 (CMIP6). Table A1 in Appendix A shows the complete list of GCMs used. These GCMs were used in the 6th Assessment Report of the Intergovernmental Panel on Climate Change [20] and the gridded data were acquired on the Copernicus platform [24]. We use two future scenarios considered intermediate (SSP2-4.5) and more extreme (SSP5-8.5) in terms of radiative forcing of global warming [20]. Due to the availability of historical simulation data, the present climate was defined from 1990 to 2014 (25 years). Continuing the subsequent chronological scale, the future time scale was subdivided into two 25-year periods, the near future (2015 to 2039) and the far future (2040 to 2064). Two observational databases are used to compare and validate CMIP6 model simulations for the present climate, the CHIRPS [25] that combines satellite images and station data to create a 0.25° gridded precipitation time series, and the CPC Unified [26] containing 0.5° gridded maximum and minimum air temperature generated through the optimal interpolation objective analysis technique using solely gauge data network. As in previous studies [27], all gridded databases (observations and GCMs) were interpolated into a 0.25° regular grid using the bilinear interpolation method, with the purpose of investigating climate extremes on a regional (municipal) scale over the Amazon.

We consider a set of absolute, threshold, duration, and percentile-based indices, defined by the Expert Team of Climate Change Detection and Indices, ETCCDI [28], to characterize two opposing types of climate extremes in the Amazon: very intense rainfall episodes generally associated with floods conditions (WET extremes), and the combination of drought and heat wave events (DRY/HOT extremes). Daily data from CHIRPS and CPC for the base period 1990 to 2014 (present climate) were used in the calculations of extreme climate indices of precipitation and air temperature, respectively. For the WET extremes, we use RX5day (annual maximum 5-day precipitation) and R95p (precipitation on days with daily precipitation > 95th percentile for the base period). For the DRY/HOT extremes, we use CDD (maximum number of consecutive dry days with precipitation <1 mm) describing the longest length of dry spells in a year, and the WSDI (annual count of days with at least 6 consecutive days when daily maximum temperature is above the 90th percentile centered on a 5-day window for the base period). The extreme indices gridded data for future projections were acquired directly from the Copernicus platform [24], containing pre-calculated and consistent ETCCDI indices from CMIP6 models that have the necessary daily resolved data for both historical and at least two of the future projections. Thus, the representative indices of WET and DRY/HOT extremes were extracted at the geographic points of the 671 small municipalities in the BLA for the GCM and observations in the present climate and only for the GCMS in the two periods of future climate. With the present climate time series of observed and simulated data, we calculated the statistical metrics of means, standard deviation (σ), Pearson correlation (r) and root mean squared error (RMSE) for all municipalities and in the end, we obtained the Taylor skill score, TSS [29], for each GCM and climate extreme:

$$TSS = 4(1 + r)/[\sigma + (1/\sigma)]^2 (1 + r_0) \quad (7)$$

where r is the correlation between the simulated and reference datasets, r_0 is the maximum correlation (between the 24 GCM), and σ is the standard deviation of the simulated dataset. TSS provided the overall rank of the models, and we also plotted the Taylor diagram to evaluate the performance of the GCMs. A selection of models that best represent

each extreme climate index over the Amazon (TSS $\geq$ 7.0) was made with the purpose of evaluating future projections with a more robust signal (less uncertainty). The set of these best GCMs was denominated as a multi-model ensemble (MME), in which the bias correction method (present climate simulation minus reference observation) was applied and then the percentage changes (C) of the extreme indices (EIs) in the future period relative to the present were obtained:

$$C = ((EI_{future} - EI_{present})/EI_{present})) \times 100 \quad (8)$$

As previously mentioned, the EIs for WET were RX5day and R95p and for DRY/HOT extremes, they were CDD and WSDI, all extracted from the MME considering the 25-year averages in the present (1990 to 2014) and the two subsequent periods of the near future (2015 to 2039) and far future (2040 to 2064) and taking into account the two CMIP6 scenarios SSP2-4.5 and SSP5-8.5.

Finally, the component H provides the threat of climate extremes associated with drought and flood episodes in the Amazon:

$$H = (H_{WET} + H_{DRY/HOT})/2 \quad (9)$$

$$H_{WET} = (C_CDD + C_WSDI)/2 \quad (10)$$

$$H_{DRY/HOT} = (C_RX5day + C_R95p)/2 \quad (11)$$

where C_CDD, C_WSDI, C_ RX5day and C_R95p are changes of CDD, WSDI, RX5day and R95p, respectively, for the two future periods using SSP2-4.5 and SSP5-8.5.

3. Results and Discussion

The spatial distribution of the components E and V in the domain of municipalities over the BLA is shown in Figure 3. To complement the interpretation of the results, Table 2 illustrates the respective percentages in the nine states for each intensity category. Although the maps indicate high spatial variability throughout the Amazon territory, the visual analysis of both components reveals that the two highest categories of E and V are predominantly distributed in the states of PA, MA, AM and MT, while TO exhibits more municipalities in the lowest categories (Figure 3). Analyzing sequentially the values in Table 2, the three states with the component E in the very high category are PA, MA and MT (totaling 15.2%), and those with high are MA, PA and AM (totaling 13.7%). Conversely, only the state of TO, with 11.6%, has the greatest concentration of municipalities with very low, while the states of MA, TO and MT contribute a total of 14% of municipalities in the low category. In terms of component V, the states with the largest number of municipalities in the very high category are PA, MA and AM (totaling 16.2%), and in the high category are MA, PA and MT (totaling 12.5%). In contrast, the states with the greatest abundance of municipalities in the very low category are TO (9.5%) and MT (6.7%) and the low category are TO (6.0%), MT (5.4%) and MA (3.9%), according to quantitative values in Table 2.

With the purpose of identifying which indicators of sub-dimensions S and C contribute to the worsening of vulnerability, boxplots and a radar chart (Figure 4) were constructed particularly for the sets of municipalities with component V categorized as very high and high in each Amazonian state. One should bear in mind that a value tending to 0 indicates the best score and a value close to 1 indicates the worst in the rank. In terms of susceptibility, the economy indicator is critically the most serious, compared to the others, with most states showing a boxplot position close to 1. Except for MT (favored by the soybean agricultural sector), all states show average economy values at the outer edge of the radar (close to 1). The second indicator with some prominence is the lack of public infrastructure (precarious conditions of sanitary sewage, waste destination and potable water supply), mainly in the states of PA, RO and MA with boxplots displaying values

from 0.1 to 0.7. In the indicator radar, these states also stand out with average values of 0.46, 0.39 and 0.38 in PA, RO and MA, respectively. The housing conditions/dependent people indicator shows relatively similar variations in the boxplots, and the states of PA and MT show average values reaching 0.32 in the radar. The health indicator is the lowest in all states, except RR with a highlighted value of 0.28 in the susceptibility quadrant of the indicator radar. On the other hand, the indicators of the sub-dimension coping/adaptive capacity reveal that digital communication/urban mobility and medical services are clearly the first and second highest contributors to the degree of vulnerability in Amazonian municipalities. The indicator radar shows that communication/urban mobility in all states is very close to 1. Medical services present values between 0.7 and 0.9 across states, and in the radar, the lowest value is seen in MT with 0.8 and the highest is verified in AC with 0.93. The education indicator is also problematic in most municipalities, with values oscillating between 0.5 and 0.7, with average values in the radar around 0.58 in RR and MA and reaching 0.7 in RO and TO. The environment indicator showed values below 0.3 and the radar illustrating that the states of PA, AM and MT are the worst in the region, with averages of 0.17, 0.14 and 0.13, respectively.

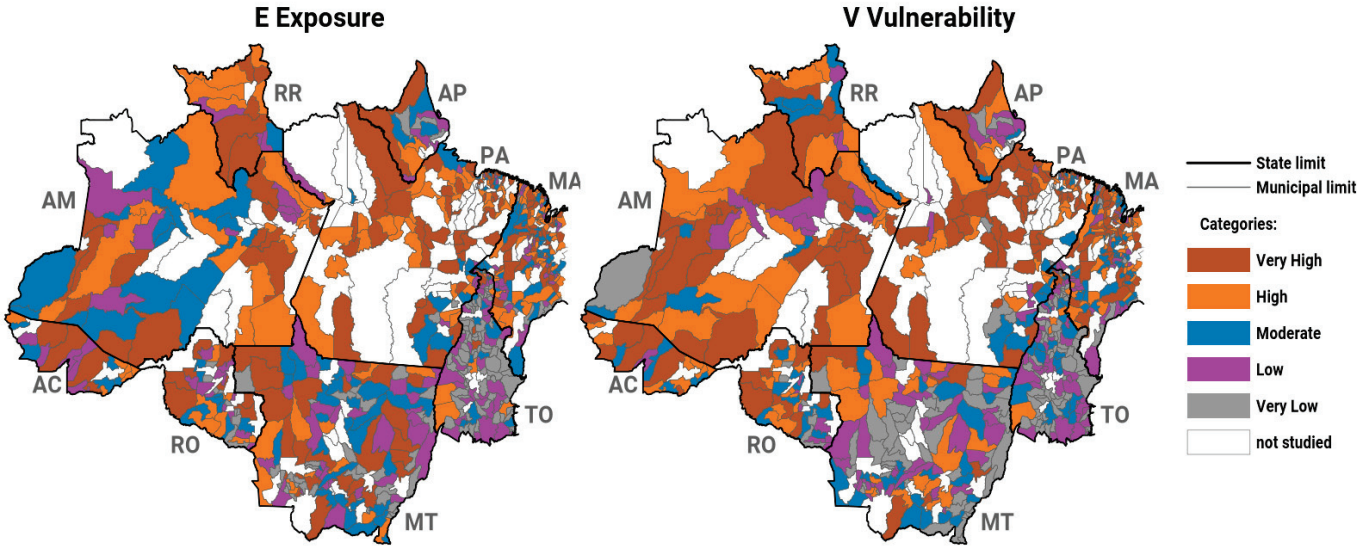

Figure 3. Components E and V in the small municipalities over BLA, considering the distribution in five intensity categories (color scale). The acronyms of the nine states are placed alongside.

Table 2. Percentages (relative to the total 671) of the number of municipalities in each state and intensity category of components E and V. Colors from white to gray to magenta indicate the increasing variation in %.

States	E Exposure Categories					V Vulnerability Categories				
	Very High	High	Moderate	Low	Very Low	Very High	High	Moderate	Low	Very Low
AC	0.6%	0.9%	0.7%	0.7%	0.0%	0.9%	1.2%	0.7%	0.1%	0.0%
AM	1.9%	2.1%	2.4%	1.0%	0.0%	3.0%	2.5%	1.0%	0.7%	0.1%
AP	0.3%	0.3%	0.4%	0.6%	0.4%	0.3%	0.4%	0.3%	0.6%	0.4%
MA	5.4%	7.0%	6.3%	4.8%	1.0%	6.0%	5.8%	7.3%	3.9%	1.5%
MT	3.4%	1.8%	4.3%	4.5%	5.1%	0.7%	3.1%	3.1%	5.4%	6.7%
PA	6.4%	4.6%	2.5%	1.3%	0.3%	7.3%	3.6%	2.5%	1.2%	0.6%
RO	1.2%	1.2%	1.2%	1.8%	1.3%	1.3%	1.8%	1.8%	0.9%	0.9%
RR	0.7%	0.7%	0.1%	0.4%	0.0%	0.6%	0.4%	0.6%	0.4%	0.0%
TO	0.6%	0.9%	2.1%	4.8%	11.6%	0.1%	0.9%	3.4%	6.0%	9.5%

Most of the characteristics of the indicators discussed above are supported by the extensive research conducted by [6] on the social vulnerability index at the level of Brazilian cities. In the quantitative maps, it was demonstrated that the north region (Amazon) contains the most socially vulnerable cities, with conditions of poverty, poor infrastructure, lack of public employment, among others, presenting the worst scores. This pattern is consistent with historical development patterns, aggravated by the fact that this region receives the smallest shares of federal public investment. Almeida et al. [19] also found very high vulnerability in northern Brazil, implying that these locations would have more difficulties in coping and recovering from the impacts of a given disaster.

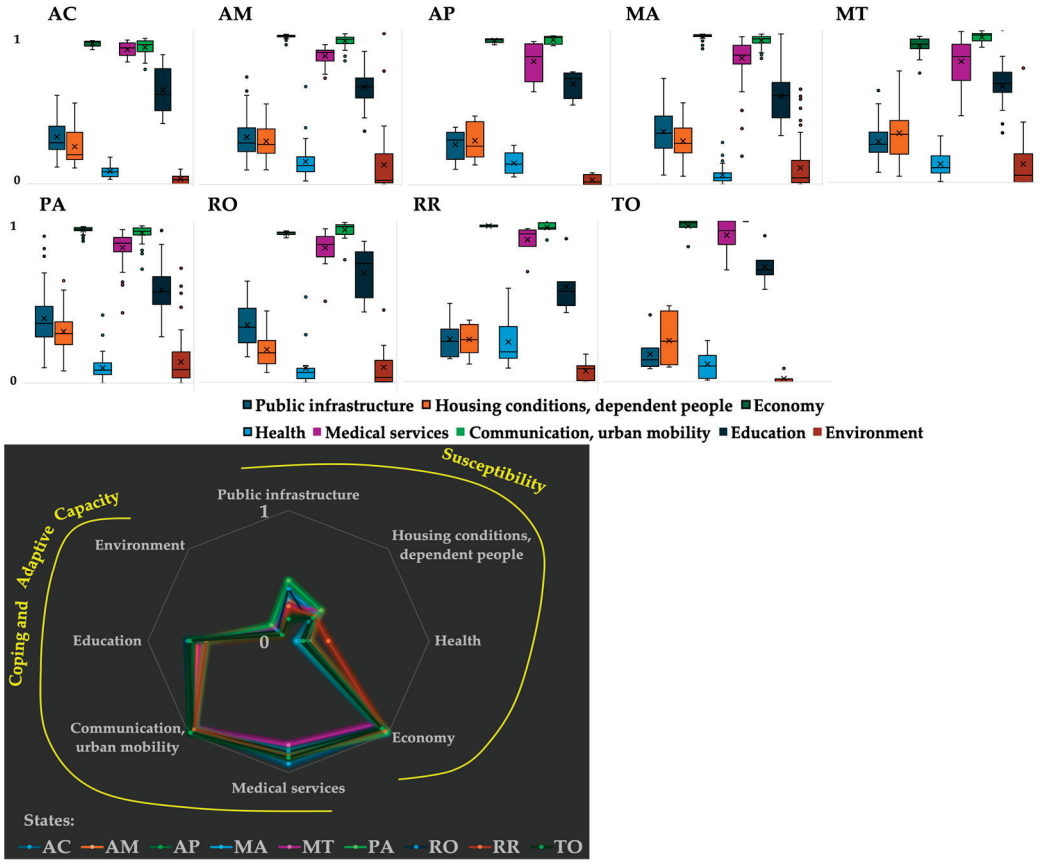

Figure 4. Boxplots (**top**) and radar (**bottom**) of the indicators of S and C for the sets of municipalities categorized with V very high and high in each state.

Instead of using simulated data from all 24 GCMS CMIP6, we evaluated the ability of these models to reproduce the observed patterns of extreme indices for the historical period (1990 to 2014). Through statistical analysis of the TSS, it was possible to rank quantitatively a list of the best GCMs in each extreme index, whose results are illustrated in Figure 5 (top graph), with blue bars highlighting the best models. We selected a total of eight GCMs for CDD and R95p and seven GCMs for WSDI and RX5Day. Similar performance analyses of the CMIP6 models conducted by [27] also found results similar to the rank obtained in this work. The selected models were then used to generate the multi-model ensemble (MME), which is considered to be the most assertive or with the lowest uncertainties in the projections of climate extremes for the Amazon. Thus, it is convenient to present the original observed patterns of the extreme indices in the present climate (1990 to 2014) and the corresponding MME patterns representative of the CMIP6 simulations (Figure 5, bottom). Analyzing the observations, we observe a northwest/southeast gradient of the CDD, indicating more frequent droughts in areas located on the south/southeast/eastern edge of the region, which is also coincident with the most intense manifestation of the WSDI, both indices being significant in MA, TO, MT and the

respective border areas with PA. The RX4Day and R95p reveal that precipitation extremes spread across all Amazonian states. Examining the CMIP6 simulations represented by the MME, a good consistency is noted both spatially and in magnitude of the extreme indices compared to the reference observations. Therefore, we mention that the CMIP6 simulations are able to reproduce the observed patterns of climate extremes in the Amazon, whose findings are consistent with previous analyses reported by [27,30]. Some previous observational studies using satellite and station databases [31] also investigated extreme indices in the Amazon, with spatial patterns similar to those presented here.

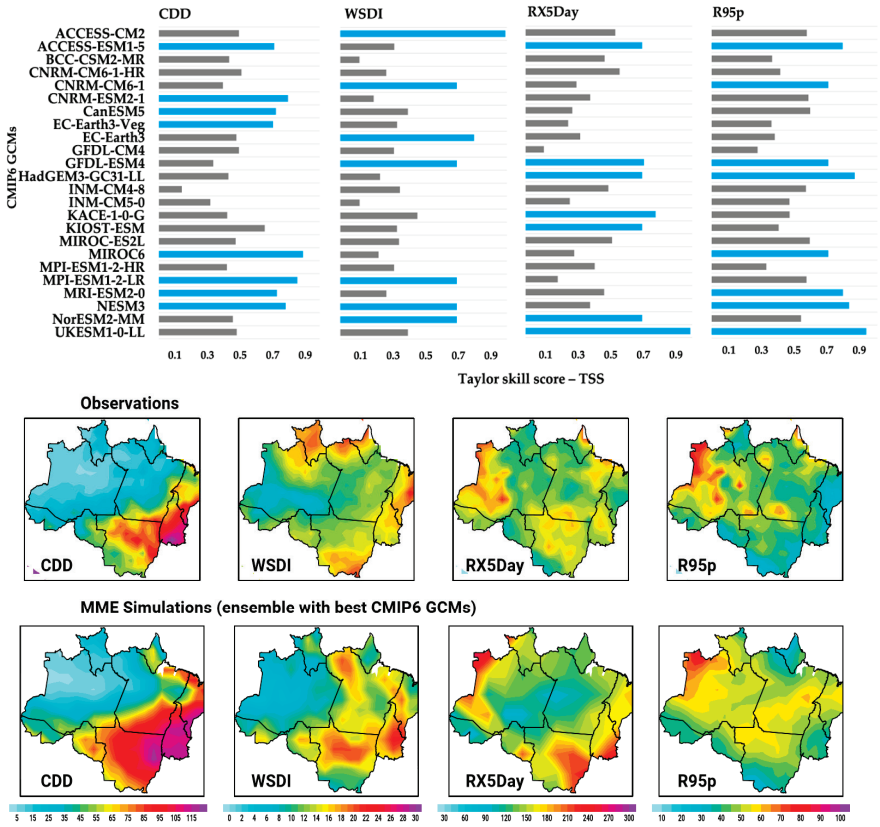

Figure 5. (**Top**) TSS for 24 GCMs with blue bars highlighting the best models; (**bottom**) original spatial patterns of CDD, WSDI, RX5Day and R95p for observations and simulations (MME using best CMIP6 GCMs) for the present climate (1990 to 2014).

After applying the bias correction method to the MME, the percentage changes in the two 25-year periods relative to the current climate were calculated and normalized. The maps of component H given by the MME considering both the effects of the WET and DRY/HOT extremes are shown in Figure 6. Analyzing the maps, for the near future (Figure 6, left panel) in both scenarios we verify an indication of the categories very low and low in a large number of the Amazonian states, except in the southeastern BLA encompassing the states of MA and TO and portions to the northeast MT and southeast PA. Some municipalities located in central AM and PA also display categories H moderate and high in this period. Examining the results for the far future (Figure 6, right panel), a widespread intensification of climate extremes over the Amazon territory, especially throughout the states of AM, PA, MA, TO and MT, is evident. In the SSP2-4.5 scenario, the categories H vary from moderate to very high, and in the SSP5-8.5 scenario, the high and very high categories predominate in these regions.

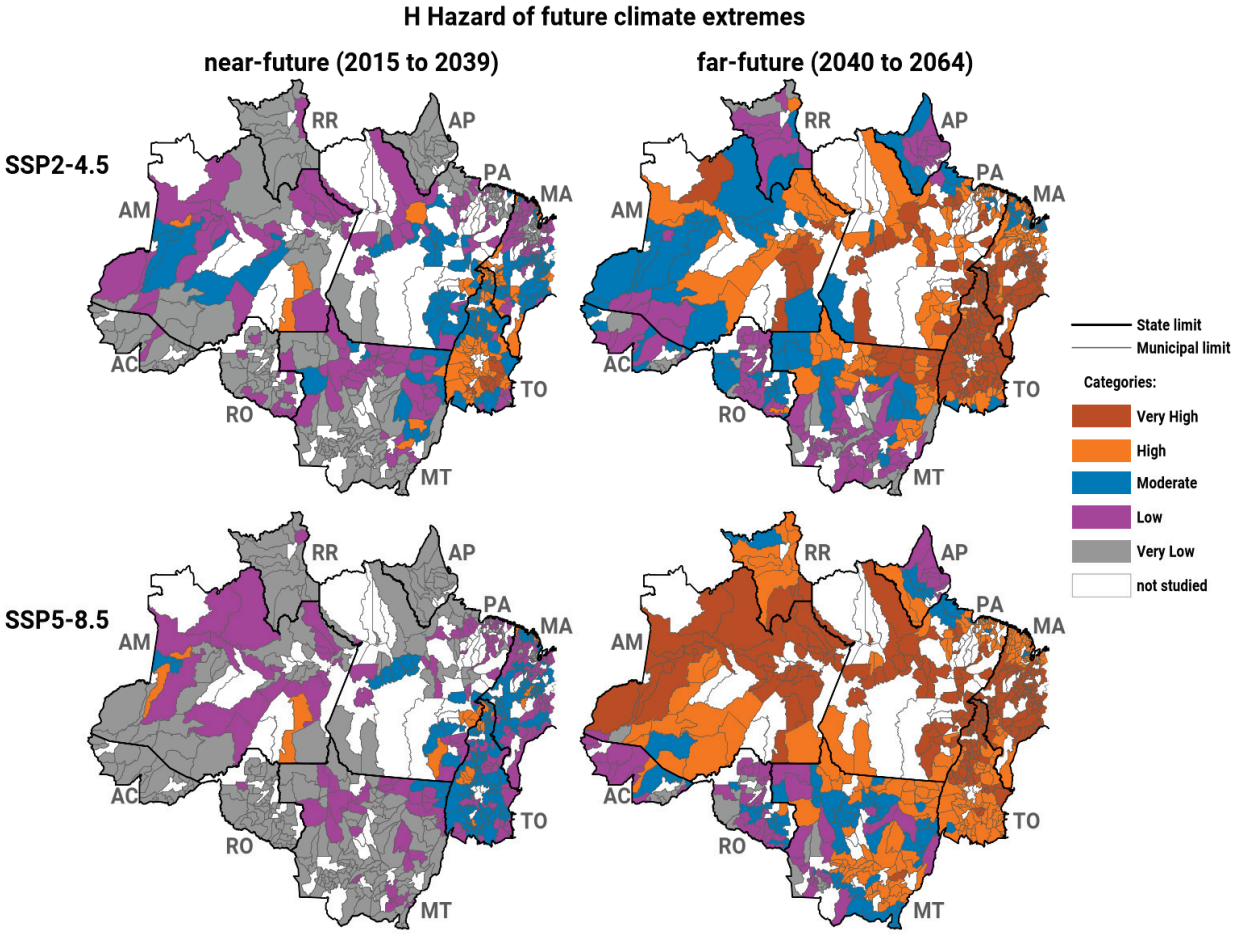

Figure 6. Component H considering WET and DRY/HOT extremes in the near and far future for SSP2-4.5 and SSP5-8.5 scenarios. Color scale indicates the distribution in five intensity categories. The acronyms of the nine states are placed alongside.

Our H mapping results are consistent with former evaluations of simulations with global and regional models. Previous studies based on CMIP5 future projections scenarios had already reported a significant increase in the number of consecutive dry days, amplifying droughts in the Amazon, with a more intense signal under RCP8.5 [7]. As the complete database of CMIP6 simulations was made available from 2020 onwards, there are still few studies reporting the results of climate extremes directed at sectors in South America. For the Amazon, in particular, Ferreira et al. [32] indicated results of reduced rainfall projections for the coming decades that are more prominent during the austral spring under the SSP5-8.5 scenario. Investigating the CMIP6 worst-case scenario in the middle (2046–2065) and far future (2081–2100), Medeiros et al. [30] showed that the extreme precipitation events are projected to be more severe, frequent, and long-lasting in all Brazilian regions, with the most pronounced changes expected in heavy rainfall and severe droughts in the central and northern portion, including the Amazon.

We now investigate the risk R of natural disasters (resulting from components E, V and H above mentioned) in the BLA region, whose maps are shown in Figure 7 for the near and far future in the two scenarios SSP2-4.5 and SSP5-8.5. The analysis of spatial distribution reveals the presence of high spatial variability mainly in the states located to the south/southeast (AC, RO, MT and TO) and to the north (AP and RR) portions of the BLA, where the categories R vary from very low to very high. The spatial configuration of R is somewhat more regular in the states of AM, PA and MA, where there is a greater presence of the categories R from moderate to high to very high in most municipalities.

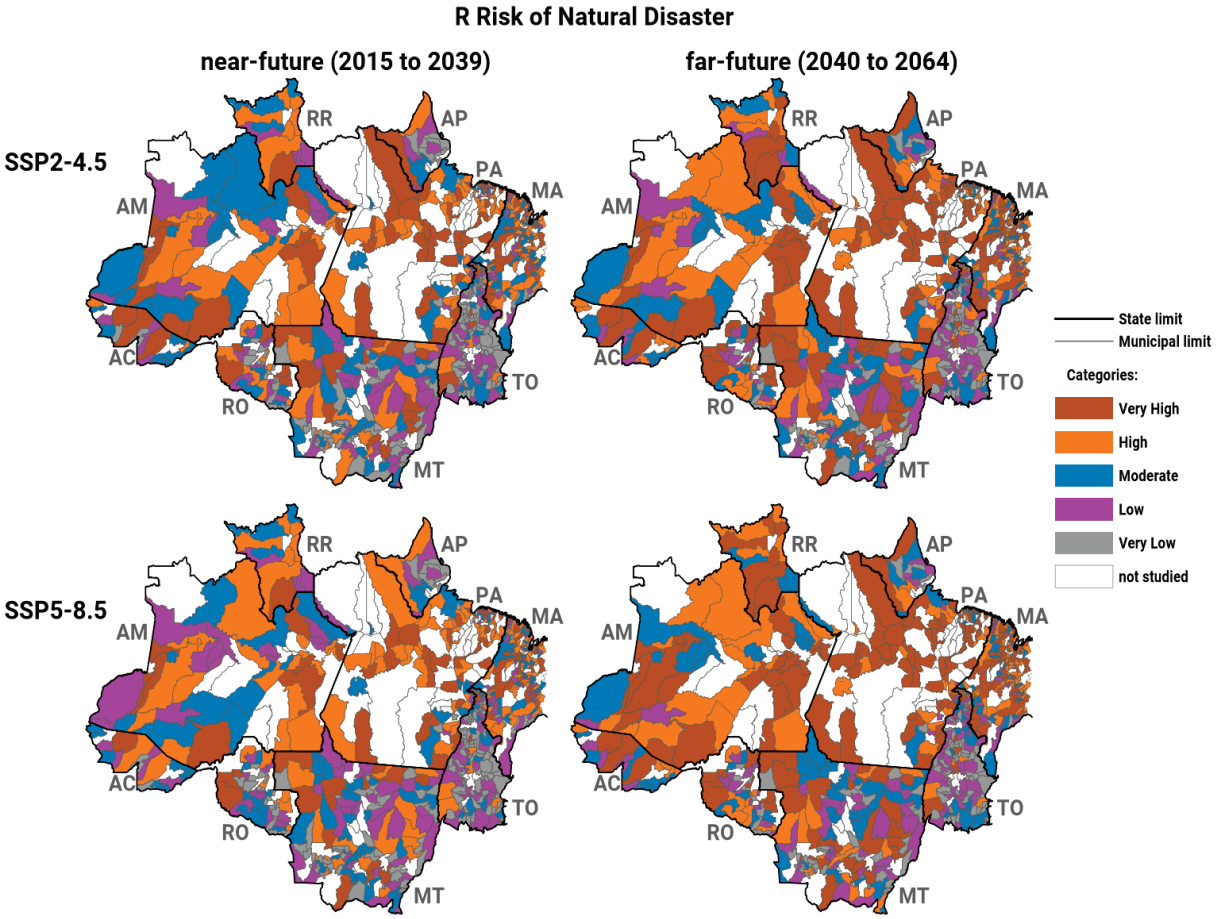

Figure 7. Risk map of natural disasters in the near and far future for SSP2-4.5 and SSP5-8.5 scenarios. The acronyms of the nine states are placed alongside.

In line with the results obtained in Figure 7, but for current climate indicators (2010 to 2013), the distribution map of the Disaster Risk Indicators in Brazil (DRIB) generated by Almeida et al. [19] also pointed out the majority of municipalities in AC, AM, PA and MA exhibiting the highest R rating. With a similar scope, Debortoli et al. [33] developed a disaster vulnerability map for 2011–2040 and 2041–2070 periods in Brazil, based on projections of the Eta regional model nested within two IPCC/AR5 global models. They showed a large number of municipalities depicting high vulnerability to natural disasters of hydrometeorological origin (in particular, flash floods) in all regions of the country, including the AP/PA border, AC and Manaus region in the AM state.

A general analysis of the results of the five disaster risk categories in terms of the proportions of the number of municipalities relative to the total for each state may be found in Table A2 in Appendix A. An objective question given the results in Figure 7 and Table A2 would be: Which risk category presents the highest proportion of municipalities considering the average between the two scenarios? And what is the evolution in the two future periods? For this point, we produced Figure 8, exhibiting for each state the average between SSP2-4.5 and SSP5-8.5 for the category containing the highest proportion of municipalities in the near and far future. The states with the most problematic configuration of increasing disaster risks are AM, RR, PA and MA, while the states TO, AP, MT and RO have lower categories (although still significant, as they occupy a significant proportion of the states). AM has a proportion of 31% of municipalities in the high category in the near future and 32% in the very high category in the far future. PA remains in the very high category with 45% of municipalities in the near future and 46% in the far future. MA ranges from 30% of municipalities in the high category in the near future to 33% in the very high category in the far future. RR presents 39% of municipalities in the very high

category in the near future, decreasing to 39% in the high category in the far future, whose result may be associated with redistribution to other categories. AC maintained 44% in the high category in the near future and 40% in the far future. RO remains in the low category with 29% in the near future and 28% of municipalities in the far future. MT shows 32% of municipalities in the very low category in the near future and 31% in the low category in the far future. The very low category prevails in AP with 36% in the near future and 35% in the far future. TO is also in the very low category with 49% in the near and 48% in the far future. Such information is most important in terms of application for disaster risk management, as it focuses on the most relevant results in each Amazonian state.

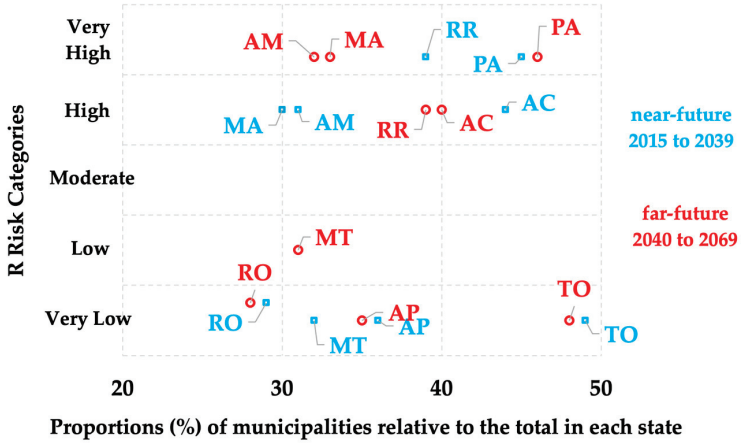

Figure 8. Average values between SSP2-4.5 and SSP5-8.5 for the category containing the highest proportion of municipalities for each Amazonian state in the near and far future.

The integrated perspective of all components is very interesting to analyze in the scatter plot in Figure 9. The disaster risk R curve can be interpreted by the polynomial trend line between the component V (vulnerability) and the combination of component H (hazard climate extremes) multiplied by component E (population exposure), as shown in Figure 9. This integrated analysis demonstrates in quantitative terms an intensification of R from the near future (2015 to 2039) to the far future (2040 to 2064). In the near future, the risk curve slopes positively with a smaller trend and an R^2 of 0.393 in SSP2-4.5 and a much higher R^2 of 0.507 in SSP5-8.5. Subsequently, in the far future, the diagonally positive R curve with R^2 of 0.506 in SSP2-4.5 increases significantly to the most extreme position with an R^2 of 0.523.

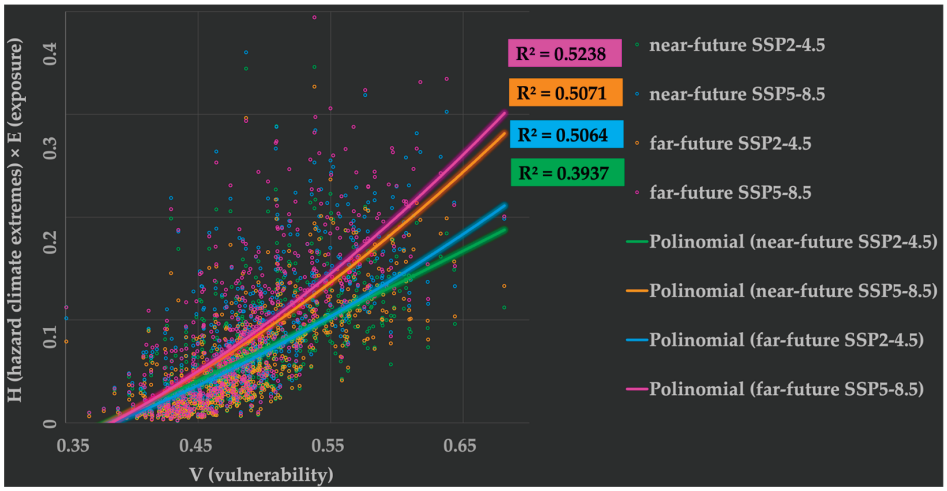

Figure 9. Scatterplot of V versus H × E in the near- and far-future for the SSP2-4.5 and SSP5-8.5 scenarios. The disaster risk curve is indicated by the colored lines.

4. Conclusions and Recommendation

Based on an integrated assessment approach of the risk R of natural disasters resulting from component H (hazard climate extremes associated with drought and flood episodes) from the latest future scenarios of climate change projections made by GCMs available in CMIP6 (we used a set of the best models validated for the Amazon), component E (exposure of the affected/impacted population), and component V (subdimensions of susceptibility and coping/adaptive capacity obtained from multiple social, economic, environmental and local infrastructure indicators), with these two later components from the current data provided by the official IBGE 2022 Census, this work concludes the following two fundamental points:

- The curve of R of natural disasters throughout the territory of small municipalities in the Amazon will intensify significantly over the next two 25-year periods. Although there is a high intra-municipal spatial variation, the overall results of the highest proportions of R (total municipalities affected) by state indicate that for AM, RR, PA, and MA, the prevailing categories are high and very high in the near and far future. The state of AC prevails in the moderate category in both the future periods, and the states RO, MT and AP move from category very low to low in the near to the far future.
- The detailed assessment of component V allowed us to elucidate that the economy indicator is the most serious in the scope of susceptibility, followed by indicators portraying the precariousness of urban infrastructure (households with problems in the supply of potable water, waste disposal, and sanitary sewage). Likewise, health (low availability of medical beds and hospitals), digital communication (access to broadband internet), and urban mobility (public transport) indicators, whose services are the most used by the population in the face of a climate emergency, also contributed negatively to the unfavorable situation of municipal vulnerability. These combined factors, unfortunately, reveal a widespread poverty profile among the small Amazonian municipalities, highlighting the need for greater public investments.

Therefore, our objective assessment highlighted the worrying and imminent threat of extreme phenomena exacerbated by climate change, as well as indicating a strong dependence on social and economic aspects that significantly aggravate the degree of vulnerability, thus implying an intensified disaster risk curve. Given this finding, it is crucial for all countries to meet Sustainable Development Goals, as a way of implementing aspects of mitigation and adaptation in the face of the intensification of climate extremes on a warmer planet [34]. An obvious option, that can bring positive results in the short to medium term, to reduce or flatten the risk curve is the implementation of effective strategic planning and decision-making actions by the government sector (municipal, state, and national), which is responsible for public policies to minimize and mitigate climate change. Thus, as a way of contributing scientific information for applications in the aforementioned government actions, it is convenient to point out a ranking of the top 10 municipalities in each state (highest R) that have the greatest chance of suffering negatively in the future. So, as a final recommendation in this work, we suggest that the results of the SSP5-8.5 scenario should only be considered for the near future period (2015 to 2039), whose time scale may be plausible for targeted strategy planning, as policies in Brazil are eminently pluriannual (maximum 5 years ahead). Figure 10 shows the mapped geographic locations of the top 10 municipalities, with Table 3 indicating the respective names and quantitative values of the components E, V, and R, which we consider to be priorities (from the point of view of scientific findings) in each Amazonian state.

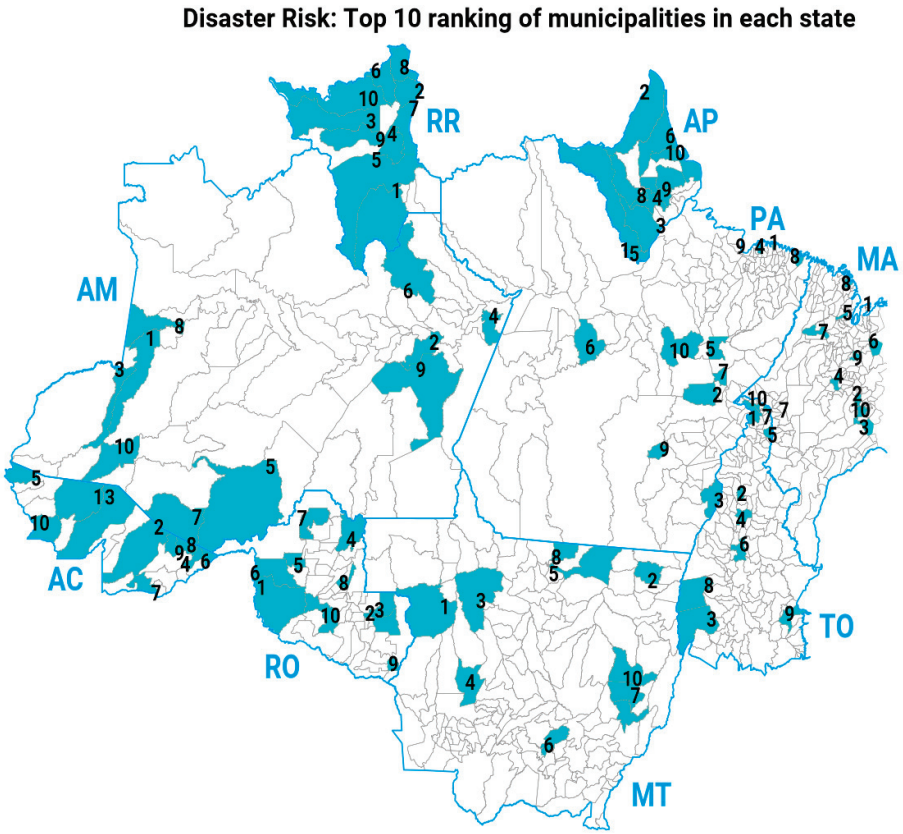

Figure 10. Locations of municipalities in each state in the top 10 ranking with the highest R in the SSP5-8.5 near future scenario. Numbers indicate the position in the rank and the names of the municipalities are given in Table 3. Acronyms of the nine states are placed alongside.

Table 3. List of the top 10 ranking municipalities in each state that presented the highest R in the SSP5-8.5 near future scenario.

State	Rank	Municipality	E × H	V	R	State	Rank	Municipality	E × H	V	R
AC	1	Tarauacá	0.17	0.60	0.09	AM	1	São Paulo de Olivença	0.22	0.58	0.12
	2	Sena Madureira	0.15	0.57	0.08		2	Autazes	0.26	0.61	0.11
	3	Feijó	0.16	0.60	0.08		3	Benjamin Constant	0.18	0.57	0.11
	4	Senador Guiomard	0.10	0.53	0.05		4	Barreirinha	0.16	0.59	0.11
	5	Mâncio Lima	0.10	0.54	0.05		5	Lábrea	0.18	0.61	0.10
	6	Acrelândia	0.08	0.50	0.04		6	Presidente Figueiredo	0.19	0.57	0.10
	7	Brasiléia	0.08	0.49	0.04		7	Boca do Acre	0.19	0.57	0.09
	8	Porto Acre	0.09	0.51	0.04		8	Santo Antônio do Içá	0.16	0.56	0.09
	9	Bujari	0.09	0.50	0.04		9	Borba	0.17	0.61	0.09
	10	Marechal Thaumaturgo	0.08	0.53	0.04		10	Eirunepé	0.16	0.57	0.08
AP	1	Laranjal do Jari	0.15	0.54	0.08	MA	1	Raposa	0.36	0.49	0.18
	2	Oiapoque	0.14	0.55	0.07		2	Presidente Dutra	0.27	0.51	0.15
	3	Mazagão	0.09	0.52	0.04		3	Colinas	0.25	0.54	0.14
	4	Porto Grande	0.08	0.52	0.03		4	Lago da Pedra	0.25	0.55	0.13
	5	Vitória do Jari	0.05	0.48	0.02		5	São Bento	0.21	0.60	0.13
	6	Calçoene	0.05	0.50	0.02		6	Vargem Grande	0.22	0.60	0.13
	7	Tartarugalzinho	0.05	0.47	0.02		7	Zé Doca	0.23	0.57	0.13
	8	Pedra Branca do Amapari	0.04	0.47	0.02		8	Cururupu	0.22	0.47	0.13
	9	Ferreira Gomes	0.03	0.45	0.01		9	São Mateus do Maranhão	0.23	0.54	0.13
	10	Amapá	0.03	0.46	0.01		10	São Domingos do Maranhão	0.20	0.57	0.12

Table 3. *Cont.*

State	Rank	Municipality	E × H	V	R	State	Rank	Municipality	E × H	V	R
MT	1	Juína	0.29	0.51	0.17	PA	1	Salinópolis	0.41	0.54	0.22
	2	Confresa	0.20	0.52	0.12		2	Itupiranga	0.26	0.62	0.16
	3	Juara	0.22	0.51	0.12		3	Conceição do Araguaia	0.26	0.55	0.16
	4	Campo Novo do Parecis	0.22	0.43	0.11		4	Curuçá	0.32	0.58	0.16
	5	Peixoto de Azevedo	0.21	0.56	0.11		5	Breu Branco	0.28	0.62	0.16
	6	Campo Verde	0.17	0.50	0.10		6	Uruará	0.30	0.64	0.15
	7	Água Boa	0.18	0.46	0.10		7	Jacundá	0.28	0.54	0.15
	8	Guarantã do Norte	0.20	0.51	0.10		8	Augusto Corrêa	0.24	0.53	0.14
	9	Nova Xavantina	0.17	0.55	0.09		9	Tucumã	0.24	0.55	0.14
	10	Canarana	0.16	0.49	0.09		10	Pacajá	0.26	0.63	0.13
RO	1	Guajará-Mirim	0.20	0.54	0.12	RR	1	Rorainópolis	0.17	0.51	0.09
	2	Pimenta Bueno	0.17	0.49	0.10		2	Normandia	0.15	0.45	0.07
	3	Espigão D'Oeste	0.15	0.56	0.09		3	Alto Alegre	0.11	0.61	0.07
	4	Machadinho D'Oeste	0.14	0.54	0.08		4	Cantá	0.14	0.55	0.06
	5	Buritis	0.17	0.54	0.08		5	Caracaraí	0.11	0.53	0.06
	6	Nova Mamoré	0.14	0.56	0.08		6	Pacaraima	0.10	0.53	0.06
	7	Candeias do Jamari	0.12	0.56	0.07		7	Bonfim	0.10	0.49	0.06
	8	Ouro Preto do Oeste	0.13	0.48	0.07		8	Uiramutã	0.08	0.48	0.04
	9	Colorado do Oeste	0.13	0.45	0.06		9	Mucajaí	0.08	0.49	0.04
	10	São Miguel do Guaporé	0.11	0.56	0.05		10	Amajari	0.08	0.52	0.04
TO	1	Araguatins	0.22	0.56	0.13						
	2	Colinas do Tocantins	0.22	0.50	0.13						
	3	Formoso do Araguaia	0.15	0.52	0.09						
	4	Guaraí	0.15	0.48	0.08						
	5	Tocantinópolis	0.13	0.51	0.08						
	6	Miracema do Tocantins	0.12	0.47	0.07						
	7	São Miguel do Tocantins	0.13	0.48	0.07						
	8	Lagoa da Confusão	0.12	0.48	0.06						
	9	Dianópolis	0.11	0.45	0.06						
	10	Augustinópolis	0.10	0.35	0.05						

Author Contributions: Conceptualization, methodology, formal analysis, E.B.d.S.; writing—original draft preparation, E.B.d.S., J.d.A.S.J., D.B.S.F. and T.A.; writing—review and editing, E.B.d.S., B.C.S.S., E.M.F.S., M.J.B.R., A.C.C., P.J.P.O.S., L.P.P., E.J.P.d.R., A.M.L.S., J.d.A.S.J., A.M.C.d.C., D.B.S.F., A.M.M.L., F.A.A.d.S., B.C.M., M.d.L.P.R., P.M.T. and T.A. All authors have read and agreed to the published version of the manuscript.

Funding: This research was supported by CNPQ processes 420142/2023-1 and 442261/2020-9, and the Universidade Federal do Pará (UFPA).

Data Availability Statement: Databases with respective sources and references were described in the Materials and Methods section.

Acknowledgments: B.C.S.S., E.M.F.S. and M.J.B.R. thank CAPES and CNPq for the scholarships. The authors thank CNPQ for support in research projects and scientific productivity fellow: A.M.M.L. (308770/2022-6), M.L.P.R. (307534/2021-9), A.M.L.S. (409167/2023-1), P.J.P.d.S (311681/2022-0), T.A. (304298/2014-0 and 301397/2019-8), and L.P.P. (CNPq/PROANTAR 443013/2018-7, ATMOS 2 CNPq/PROANTAR 440848/2023-7, and 303981/2023-7).

Conflicts of Interest: The authors declare no conflicts of interest.

Appendix A

Table A1. List of CMIP6 GCMs used in this work.

GCMs	Acronym	Country
1	ACCESS-CM2	Australia
2	ACCESS-ESM1-5	Australia
3	BCC-CSM2-MR	China
4	CNRM-CM6-1-HR	France
5	CNRM-CM6-1	France
6	CNRM-ESM2-1	France
7	CanESM5	Canada
8	EC-Earth3-Veg	Europe
9	EC-Earth3	Europe
10	GFDL-CM4	USA
11	GFDL-ESM4	USA
12	HadGEM3-GC31-LL	UK
13	INM-CM4-8	Russia
14	INM-CM5-0	Russia
15	KACE-1-0-G	Korea
16	KIOST-ESM	Korea
17	MIROC-ES2L	Japan
18	MIROC6	Japan
19	MPI-ESM1-2-HR	Germany
20	MPI-ESM1-2-LR	Germany
21	MRI-ESM2-0	Japan
22	NESM3	China
23	NorESM2-MM	Norway
24	UKESM1-0-LL	UK

In Table A2, taking into account the highest proportions, it is possible to highlight some important points in each state. AC displays R moderate in proportions of 50% and 36% in the near future and moderate 40% and high 40% in the far future in the SSP2-4.5 and SSP5-8.5 scenarios, respectively. AM presents R high in the proportion of 32% and high and very high both with 32% in the near future and moderate 30% and very high 34% in the far future in SSP2-4.5 and SSP5-8.5, respectively. In the state of AP, the R is very low with proportions of 43% and 29%, verified in both future periods in SSP2-4.5 and SSP5-8.5, respectively. The MA reveals R moderate with 30% and very high with 31% in the near future and high 29% very high 36% in the far future in SSP2-4.5 and SSP5-8.5, respectively. MT shows R very low with 35% and 28% in the near future and R very low with 36% and moderate with 29% in the far future in SSP2-4.5 and SSP5-8.5, respectively. The state of PA presents R high in the proportion of 37% and very high with 53% in the near future and R high with 37% and very high with 55% in the far future in SSP2-4.5 and SSP5-8.5, respectively. RO reveals R very low with 31% low with 27% in the near future and R very low with 33% and low with 23% in the far future in SSP2-4.5 and SSP5-8.5, respectively. RR shows a higher proportion of R high with 43% and very high with 36% in the near future and R high with 43% and R high and very high both with 36% in the far future in SSP2-4.5 and SSP5-8.5, respectively. In the state of TO, a proportion of 54% and 43% is noted in R very low in the near future and R very low with 57% and 41% in the far future in SSP2-4.5 and SSP5-8.5, respectively.

Table A2. Proportions of the number of municipalities in each respective state according to the R categories in the near and far future for SSP2-4.5 and SSP5-8.5 scenarios. Colors from white to gray to magenta indicate the increasing variation in %.

	Near-Future (2015 to 2039)										Far-Future (2040 to 2064)									
	SSP2-4.5					SSP5-8.5					SSP2-4.5					SSP5-8.5				
	Very High	High	Mod erate	Low	Very Low	Very High	High	Mod erate	Low	Very Low	Very High	High	Mod erate	Low	Very Low	Very High	High	Mod erate	Low	Very Low
AC	15%	10%	50%	20%	5%	15%	35%	35%	15%	0%	10%	15%	40%	30%	5%	15%	40%	30%	15%	0%
AM	20%	32%	30%	18%	0%	32%	32%	28%	8%	0%	20%	28%	30%	22%	0%	34%	32%	32%	2%	0%
AP	7%	7%	14%	29%	43%	14%	7%	21%	29%	29%	0%	14%	14%	29%	43%	14%	7%	21%	29%	29%
MA	20%	27%	30%	16%	6%	31%	29%	23%	15%	2%	17%	28%	29%	20%	6%	36%	26%	21%	15%	2%
MT	10%	10%	20%	24%	35%	15%	9%	24%	24%	28%	8%	13%	19%	25%	36%	17%	9%	29%	21%	25%
PA	33%	37%	15%	11%	4%	53%	26%	11%	9%	1%	29%	37%	19%	11%	4%	55%	25%	10%	9%	1%
RO	11%	16%	16%	27%	31%	18%	20%	11%	27%	24%	7%	20%	13%	27%	33%	20%	17%	18%	24%	21%
RR	7%	43%	21%	29%	0%	36%	29%	7%	29%	0%	7%	43%	21%	29%	0%	35%	37%	7%	21%	0%
TO	3%	5%	11%	26%	54%	6%	7%	12%	31%	43%	2%	5%	12%	24%	57%	7%	8%	12%	32%	41%

References

1. Trenberth, K.; Fasullo, J.; Shepherd, T. Attribution of climate extreme events. *Nat. Clim. Chang.* **2015**, *5*, 725–730. [CrossRef]
2. Vogel, M.; Hauser, M.; Seneviratne, S. Projected changes in hot, dry and wet extreme events' clusters in CMIP6 multi-model ensemble. *Environ. Res. Lett.* **2020**, *15*, 094021. [CrossRef]
3. Gu, L.; Chen, J.; Yin, J.; Slater, L.J.; Wang, H.M.; Guo, Q.; Feng, M.; Qin, H.; Zhao, T. Global increases in compound flood-hot extreme hazards under climate warming. *Geophys. Res. Lett.* **2022**, *49*, e2022GL097726. [CrossRef]
4. Zhou, S.; Yu, B.; Zhang, Y. Global concurrent climate extremes exacerbated by anthropogenic climate change. *Sci. Adv.* **2023**, *9*, eabo1638. [CrossRef]
5. IPCC. *Managing the Risks of Extreme Events and Disasters to Advance Climate Change Adaptation. A Special Report of Working Groups I and II of the Intergovernmental Panel on Climate Change*; Field, C.B., Barros, V., Stocker, T.F., Qin, D., Dokken, D.J., Ebi, K.L., Mastrandrea, M.D., Mach, K.J., Plattner, G.-K., Allen, S.K., et al., Eds.; Cambridge University Press: Cambridge, UK; New York, NY, USA, 2012; p. 582.
6. Hummell, B.M.L.; Cutter, S.L.; Emrich, C.T. Social Vulnerability to Natural Hazards in Brazil. *Int. J. Disaster Risk Sci.* **2016**, *7*, 111–122. [CrossRef]
7. Reboita, M.S.; Kuki, C.A.C.; Marrafon, V.H. South America climate change revealed through climate indices projected by GCMs and Eta-RCM ensembles. *Clim. Dyn.* **2022**, *58*, 459–485. [CrossRef]
8. Vieira, R.M.d.S.P.; Sestini, M.F.; Tomasella, J.; Marchezini, V.; Pereira, G.R.; Barbosa, A.A.; Santos, F.C.; Rodriguez, D.A.; Nascimento, F.R.D.; Santana, M.O.; et al. Characterizing spatio-temporal patterns of social vulnerability to droughts, degradation and desertification in the Brazilian northeast. *Environ. Sustain. Indic.* **2020**, *5*, 100016. [CrossRef]
9. Confalonieri, U.E.C.; Lima, A.C.L.; Brito, I.; Quintão, A.F. Social, environmental and health vulnerability to climate change in the Brazilian Northeastern Region. *Clim. Chang.* **2014**, *127*, 123–137. [CrossRef]
10. Dobkowitz, S.; Walz, A.; Baroni, G.; Pérez-Marin, A.M. Cross-Scale Vulnerability Assessment for Smallholder Farming: A Case Study from the Northeast of Brazil. *Sustainability* **2020**, *12*, 3787. [CrossRef]
11. Marengo, J.A.; Torres, R.R.; Alves, L.M. Drought in Northeast Brazil—Past, present, and future. *Theor. Appl. Climatol.* **2017**, *129*, 1189–1200. [CrossRef]
12. Zeng, N.; Yoon, J.-H.; Marengo, J.A.; Subramaniam, A.; Nobre, C.A.; Mariotti, A.; Neelin, J.D. Causes and impacts of the 2005 amazon drought. *Environ. Res. Lett.* **2008**, *3*, 014002. [CrossRef]
13. Marengo, J.A.; Tomasella, J.; Alves, L.M.; Soares, W.R.; Rodriguez, D.A. The drought of 2010 in the context of historical droughts in the amazon region. *Geophys. Res. Lett.* **2011**, *38*, L12703. [CrossRef]
14. Correa, S.H.; Paiva, R.C.D.; Espinoza, J.C.; Collischonn, W. Multi-decadal Hydrological Retrospective: Case study of Amazon floods and droughts. *J. Hydrol.* **2017**, *549*, 667–684. [CrossRef]
15. Satyamurty, P.; Costa, C.P.W.; Manzi, A.O.; Candido, L.A. A quick look at the 2012 record flood in the Amazon basin. *Geophys. Res. Lett.* **2013**, *40*, 1396–1401. [CrossRef]
16. Towner, J.; Cloke, H.L.; Lavado, W.; Santini, W.; Bazo, J.; de Perez, E.C.; Stephens, E.M. Attribution of Amazon floods to modes of climate variability: A review. *Meteorol. Appl.* **2020**, *27*, e1949. [CrossRef]
17. Espinoza, J.C.; Marengo, J.; Schongart, J.; Jimenez, J.C. The new historical flood of 2021 in the Amazon River compared to major floods of the 21st century: Atmospheric features in the context of the intensification of floods. *Weather. Clim. Extrem.* **2022**, *35*, 100406. [CrossRef]
18. Mansur, A.V.; Brondízio, E.S.; Roy, S.; Hetrick, S.; Vogt, N.D.; Newton, A. An assessment of urban vulnerability in the Amazon Delta and Estuary: A multi-criterion index of flood exposure, socio-economic conditions and infrastructure. *Sustain. Sci.* **2016**, *11*, 625–643. [CrossRef]
19. Almeida, L.Q.; Welle, T.; Birkmann, J. Disaster risk indicators in Brazil: A proposal based on the world risk index. *Int. J. Disaster Risk Reduct.* **2016**, *17*, 251–272. [CrossRef]

20. IBGE—Instituto Brasileiro de Geografia e Estatística. *Censo Demográfico 2022*; IBGE: Brasília, Brazil, 2023. Available online: https://sidra.ibge.gov.br/pesquisa/censo-demografico/demografico-2022 (accessed on 1 December 2023).
21. Eyring, V.; Bony, S.; Meehl, G.A.; Senior, C.A.; Stevens, B.; Stouffer, R.J.; Taylor, K.E. Overview of the Coupled Model Intercomparison Project Phase 6 (CMIP6) experimental design and organization. *Geosci. Model. Dev.* **2016**, *9*, 1937–1958. [CrossRef]
22. Cutter, S.L.; Boruff, B.J.; Shirley, W.L. Social vulnerability to environmental hazards. *Soc. Sci. Q.* **2003**, *84*, 242–261. Available online: http://www.jstor.org/stable/42955868 (accessed on 11 December 2023). [CrossRef]
23. AdaptaBrasil, 2022. Documento Teórico-Metodológico Para Avaliação De Risco De Impacto De Mudança Climática Nos Setores Estratégicos De Recursos Hídricos E Segurança Alimentar da Plataforma AdaptaBrasil MCTI—Versão 1.1. Available online: https://adaptabrasil.mcti.gov.br/sobre/metodologia (accessed on 10 June 2022).
24. Sandstad, M.; Schwingshackl, C.; Iles, C. Climate Extreme Indices and Heat Stress Indicators Derived from CMIP6 Global Climate Projections. Copernicus Climate Change Service (C3S) Climate Data Store (CDS). 2022. Available online: https://cds.climate.copernicus.eu/cdsapp#!/dataset/10.24381/cds.776e08bd?tab=overview (accessed on 10 November 2023).
25. Funk, C.; Peterson, P.; Landsfeld, M.; Pedreros, D.; Verdin, J.; Shukla, S.; Husak, G.; Rowland, J.; Harrison, L.; Hoell, A.; et al. The climate hazards infrared precipitation with stations—A new environmental record for monitoring extremes. *Sci. Data* **2015**, *2*, 150066. [CrossRef]
26. Chen, M.W.; Shi, P.; Xie, V.B.; Silva, V.E.; Kousky, R.; Higgins, W.; Janowiak, J.E. Assessing objective techniques for gauge-based analyses of global daily precipitation. *J. Geophys. Res.* **2008**, *113*, D04110. [CrossRef]
27. Monteverde, C.; De Sales, F.; Jones, C. Evaluation of the CMIP6 Performance in Simulating Precipitation in the Amazon River Basin. *Climate* **2022**, *10*, 122. [CrossRef]
28. Alexander, L.V.; Zhang, X.; Peterson, T.C.; Caesar, J.; Gleason, B.; Tank, A.M.G.K.; Haylock, M.; Collins, D.; Trewin, B.; Rahimzadeh, F.; et al. Global observed changes in daily climate extremes of temperature and precipitation. *J. Geophys. Res.* **2006**, *111*, D05109. [CrossRef]
29. Taylor, K.E. Summarizing multiple aspects of model performance in a single diagram. *J. Geophys. Res.* **2001**, *106*, 7183–7192. [CrossRef]
30. Medeiros, F.J.; Oliveira, C.P.; Diaz, A.A. Evaluation of extreme precipitation climate indices and their projected changes for Brazil: From CMIP3 to CMIP6. *Weather. Clim. Extrem.* **2022**, *38*, 100511. [CrossRef]
31. Funatsu, B.M.; Le Roux, R.; Arvor, D.; Espinoza, J.C.; Claud, C.; Ronchail, J.; Michot, V.; Dubreuil, V. Assessing precipitation extremes (1981–2018) and deep convective activity (2002–2018) in the Amazon region with CHIRPS and AMSU data. *Clim. Dyn.* **2021**, *57*, 827–849. [CrossRef]
32. Ferreira, G.W.d.S.; Reboita, M.S.; Ribeiro, J.G.M.; de Souza, C.A. Assessment of Precipitation and Hydrological Droughts in South America through Statistically Downscaled CMIP6 Projections. *Climate* **2023**, *11*, 166. [CrossRef]
33. Debortoli, N.S.; Camarinha, P.I.M.; Marengo, J.A.; Rodrigues, R.R. An index of Brazil's vulnerability to expected increases in natural flash flooding and landslide disasters in the context of climate change. *Nat. Hazards* **2017**, *86*, 557–582. [CrossRef]
34. IPCC. Summary for Policymakers. In *Climate Change 2023: Synthesis Report. Contribution of Working Groups I, II and III to the Sixth Assessment Report of the Intergovernmental Panel on Climate Change*; Core Writing Team, Lee, H., Romero, J., Eds.; IPCC: Geneva, Switzerland, 2023; pp. 1–34. [CrossRef]

Disclaimer/Publisher's Note: The statements, opinions and data contained in all publications are solely those of the individual author(s) and contributor(s) and not of MDPI and/or the editor(s). MDPI and/or the editor(s) disclaim responsibility for any injury to people or property resulting from any ideas, methods, instructions or products referred to in the content.

sustainability

MDPI

Article

Flood Risk Assessment for Sustainable Transportation Planning and Development under Climate Change: A GIS-Based Comparative Analysis of CMIP6 Scenarios

Muamer Abuzwidah [1,*], Ahmed Elawady [1], Ayat Gamal Ashour [1], Abdullah Gokhan Yilmaz [2], Abdallah Shanableh [1,3] and Waleed Zeiada [1,4]

[1] Civil and Environmental Engineering Department, College of Engineering, University of Sharjah, Sharjah P.O. Box 27272, United Arab Emirates; aelawady@sharjah.ac.ae (A.E.); u21200308@sharjah.ac.ae (A.G.A.); shanableh@sharjah.ac.ae (A.S.); wzeiada@sharjah.ac.ae (W.Z.)
[2] Department of Engineering, La Trobe University, Melbourne, VIC 3086, Australia; g.yilmaz@latrobe.edu.au
[3] Scientific Research Center, Australian University, Kuwait City P.O Box 1411, Kuwait
[4] Department of Public Works Engineering, Mansoura University, Mansoura 35516, Egypt
* Correspondence: mabuzwidah@sharjah.ac.ae; Tel.: +971-65050618

Abstract: Climate change is causing a range of environmental impacts, including increased flood frequency and intensity, posing significant risks to human populations and transportation infrastructure. Assessing flood risk under climate change is critical, but it is challenging due to uncertainties associated with climate projections and the need to consider the interactions between different factors that influence flood risk. Geographic Information Systems (GISs) are powerful tools that can be used to assess flood risk under climate change by gathering and integrating a range of data types and sources to create detailed maps of flood-prone areas. The primary goal of this research is to create a comprehensive GIS-based flood risk map that includes various climate change scenarios derived from the Coupled Model Intercomparison Project Phase 6 (CMIP6) models. This goal will leverage the Analytic Hierarchy Process (AHP) methodology to better understand the impacts of these climate change scenarios on the transportation network. Furthermore, this study aims to evaluate the existing flood risk map and assess the potential impacts of prospective climate scenarios on the levels of flood risk. The results showed that the northern and coastal regions of the United Arab Emirates (UAE) are at higher risk of flooding, with the majority of the population living in these areas. The projections for future flood risk levels indicate that under the SSP245 scenario, flood risk levels will generally be low, but some areas in the northern and eastern regions of the UAE may still face high to very high flood risk levels due to extensive urbanization and low-lying coastal regions. Under the SSP585 scenario, flood risk levels are projected to be significantly higher, with a widespread distribution of very high and high flood risk levels across the study area, leading to severe damage to infrastructure, property, and human lives. The recent publication of the CMIP6 models marks a significant advancement, and according to the authors' knowledge, there have been no studies that have yet explored the application of CMIP6 scenarios. Consequently, the insights provided by this study are poised to be exceptionally beneficial to researchers globally, underscoring the urgent necessity for holistic sustainable flood risk management approaches for geography, planning, and development areas. These approaches should integrate both sustainable transportation infrastructure development and risk mitigation strategies to effectively address the anticipated impacts of flooding events within the study region.

Keywords: transportation infrastructure; flood risk assessment; climate change; GIS; climate projections; geography; planning and development; flooding; risk mapping

1. Introduction

Climate change, which includes long-term shifts in the Earth's climate patterns, notably rising temperatures, elevated atmospheric carbon dioxide concentrations, and altered precipitation patterns, has profound and intricate implications for transportation systems worldwide [1]. One of its most significant impacts is the transformation of the natural environment. Climate-induced variations in temperature, precipitation, and sea levels can trigger ecosystem shifts, affecting plant growth patterns and animal migration routes. These changes not only threaten species with extinction but also result in a decline in critical ecosystem services, such as pollination, water purification, and carbon sequestration—aspects that directly intersect with the integrity and functionality of transportation infrastructure. The influence of climate change on human societies further underscores its relevance to transportation infrastructure. Rising temperatures and changing precipitation patterns lead to extreme weather, affecting agriculture, water resources, and infrastructure. This impacts transportation planning and asphalt performance, highlighting significant regional weather variations affecting pavement design [2]. Additionally, assessments of UAE's precipitation through GCMs highlight the need for adaptation due to significant projected rainfall variability [3].

Economic consequences, yet another facet of climate change's repercussions, hold critical importance for transportation infrastructure. Altered weather patterns can disrupt industries like agriculture, fishing, and forestry, leading to diminished productivity and increased operational costs—factors that ripple through supply chains and impact transportation systems that facilitate the movement of goods and people. Furthermore, the rising sea levels associated with climate change pose a substantial threat to coastal communities and the transportation infrastructure that supports them, translating into property loss and augmented costs for protective measures, making adaptation and resilience a paramount consideration for coastal transportation infrastructure. In essence, climate change's multifaceted impacts on the natural environment, human societies, and the global economy have intricate and far-reaching consequences for transportation systems. Adaptation and mitigation measures are essential to ensure the resilience and functionality of transportation networks in the face of a changing climate.

The adverse consequences of floods can be exacerbated under climate change, and it is, therefore, essential to understand and assess flood risk in a changing climate. Assessing flood risk under climate change is critical because floods pose a significant threat to human populations, transportation infrastructure, and the environment. As climate change alters weather patterns, the frequency and intensity of floods are expected to increase, making it essential to understand and manage flood risk. Floods can have severe consequences, including loss of life, damage to property and transportation infrastructure, and disruptions to communities and economies. The adverse impacts of floods can be exacerbated under climate change, as rising sea levels, changing precipitation patterns, and more frequent extreme weather events can increase the likelihood and severity of flooding [3,4]. A study analyzed urban expansion in over 6000 cities, tracking impervious surface area, population, and GDP changes, correlating these with economic growth and flood risks, to inform sustainable development strategies [3]. Another study that utilized CoastalDEM, a neural network-enhanced DEM, reveals that 190 million people currently live below projected 2100 high-tide lines under low emissions, tripling past estimates [4].

In the face of accelerating climate change, understanding its impacts on flood vulnerability emerges as a critical scientific and practical issue, particularly within the arid landscapes of the UAE. This research directly confronts the challenges posed by changing climate patterns on flood risk assessments, focusing on the vulnerabilities of transportation infrastructure in the UAE. By identifying and analyzing the specific factors that increase flood risks in this unique geographical context, our study seeks to inform and enhance the resilience of infrastructure planning and management against the backdrop of climate change. The emphasis on the UAE not only addresses a gap in the current literature but also serves as a case study for similar arid regions grappling with the complexities of climate-induced flood risks.

Assessing flood risk under climate change involves understanding the exposure, vulnerability, and hazards associated with flooding [5]. This allows for the identification and mapping of flood-prone areas and the estimation of the number of people, buildings, and critical transportation infrastructures located in these areas. It also involves understanding the characteristics of the assets at risk of flooding and the likelihood and severity of flooding in a given area. A key challenge in assessing flood risk under climate change is the uncertainty associated with climate projections [5]. Future climate conditions are subject to uncertainty due to various factors, including the complex nature of the climate system and the limitations of climate models [6]. As such, it is essential to use a range of climate projections and consider a range of possible outcomes in flood risk assessments. Another challenge is the need to consider the interactions between different factors that influence flood risk. For example, land-use changes and changes in precipitation patterns can influence the exposure and vulnerability of assets to flooding [7]. It is, therefore, important to consider these interactions when assessing flood risk. To mitigate the impacts of flooding under climate change, various strategies can be employed. These include structural measures such as flood walls, levees, and drainage systems, as well as non-structural measures such as land-use planning, early warning systems, and insurance [7]. The most effective strategy will depend on the local context, the level of flood risk, and the available resources.

Geographic Information Systems (GISs) are powerful tools that can be used to assess flood risk under climate change. GIS can be used to identify and map flood-prone areas; estimate the number of people, buildings, and critical infrastructures located in these areas; and model the potential impacts of flooding [7]. GISs can be used to gather and integrate a range of data types and sources to assess flood risk. These can include data on topography, land use, hydrology, climate, and infrastructure [8]. By integrating these data types, GISs can provide a comprehensive understanding of flood risk in a given area. One of the key strengths of a GIS in assessing flood risk is its ability to visualize and analyze spatial data. GISs can be used to create detailed maps of flood-prone areas and identify the assets located in these areas. This can assist decision-makers in prioritizing mitigation efforts and efficiently allocating resources.

Floods stand as among the most destructive natural calamities, inflicting substantial harm on transportation infrastructure, claiming lives, and disrupting routine activities. GISs have proven to be effective tools for identifying and mapping areas at high risk of flooding. Many studies have utilized GISs to assess flood risk in different parts of the world. For instance, Kourgialas and Karatzas utilized a GIS to assess flood risk on the Mediterranean island of Crete, Greece [9]. Six factors are integrated within a GIS framework to pinpoint the areas most susceptible to flooding, delineating five distinct flood risk levels that gauge the likelihood of a flooding occurrence within a single hydrological year. Rubio et al. evaluated flood risk in Metro Manila, the Philippines, employing a series of indicators tailored to urban environments, encompassing physical, social, economic, and ecological aspects [10]. The AHP method was used to determine optimal weights for each indicator. They then created spatial maps showing five levels of flood risk ranging from very low risk to very high risk using a GIS. Vanolya and Jelokhani-Niaraki investigated flood hazard maps in Mazandaran, Iran, using subjective and objective weights [11]. This study evaluates the accuracy of these maps based on historic flood occurrences within them and their assessment ratio. The results show that both types of weights produce similar results for very high-class floods but differ for other strategies with better values shown by subjective–objective weights. Osei et al. used a GIS-based approach with Digital Elevation Models (DEMs) to delineate flood-prone zones within the Tarkwa mining area [12]; morphological characteristics such as local slope and streamflow network were constructed using ArcGIS Pro 3.0. These features were subsequently employed to create a flooding susceptibility map by combining the slope map with the stream network maps.

While most of the studies focused on developing risk maps based on the current situation, only a few considered how climate change will impact the areas affected by flood. Oubennaceur et al. examined the influence of climate change on flood risk in two municipalities situated in southern Quebec, Canada [13]. The study employed a

modeling methodology to forecast forthcoming river flows and simulate flood hazard maps based on anticipated climate scenarios for the years 2050 and 2080. The results show that while peak-flow frequencies are expected to decrease slightly over time, depth, inundation areas, and monetary losses will also experience minor decreases. While the studies discussed in the conclusion demonstrate the effectiveness of GISs in assessing flood risk and developing flood hazard maps, there is still a research gap in understanding the social and economic impacts of floods on communities. Most of the studies mentioned in the conclusion focused on developing flood risk maps based on physical factors such as topography and hydrology. However, it is important to understand how floods affect communities, including the impact on infrastructure. Further exploration is essential to understand how climate change may affect flood hazards moving forward, especially in regions where infrastructure faces the greatest risk. To the best of our awareness, the application of CMIP6 scenarios in this context has not been previously explored. Thus, the primary aim of our study is to create Geographic Information System (GIS)-powered maps that depict flood risks under various climate change projections. The detailed goals of this study include the following:

1. Collection of historical climate databases from local weather stations;
2. Obtaining historical and future climate change scenario data from GCMs models;
3. Adopting and applying bias correction and downscaling methods to produce future climate projections;
4. Suggesting a structured framework for evaluating the effects of climate change on flood vulnerability;
5. Creation of a flood risk map utilizing GIS under various climate change scenarios using CMIP6 projections.

2. Study Area and Observed Data

The United Arab Emirates (UAE), located at the eastern end of the Arabian Peninsula, is a member of the Gulf Cooperation Council (GCC), situated from 22°50′ to 26° north latitude and 51° to 56°25′ east longitude, encompassing 83,600 km^2. It boasts a coastline of about 1318 km along the Arabian Gulf and the Gulf of Oman. The southern shoreline of the Arabian Gulf is distinguished by large salt flats that reach into the interior. The country's landscape is primarily dry, featuring extensive sand deserts, dunes, oases, rugged mountains, valleys, wetlands, mangrove forests, and salt flats.

Abu Dhabi, one of the emirates in the UAE, hosts most of the nation's oases, well known for their dense date palm populations. Situated in a region with a hot, arid climate, it experiences average temperatures ranging from 26 °C to 33.5 °C. The period from December to March marks the rainy season in the UAE, with annual precipitation typically falling between 140 and 200 mm, though areas with elevation may receive as much as 350 mm. Severe dust storms, or shamal winds, significantly impact visibility across UAE airports, influencing transportation safety. Other studies exploring the negative influences of adverse weather on driver behavior collectively point to the expansive consequences of climate change on transportation networks. This body of work stresses the necessity for improved predictive tools and safety protocols to lessen these impacts and bolster the resilience of transportation infrastructure [14,15]. Figure 1 illustrates the geographical and infrastructural features of the UAE. The climate data utilized in this analysis were collected from a variety of weather stations throughout the UAE, supplied by the National Center of Meteorology. In addition to climate data, this study utilized high-resolution land cover data from the Sentinel-2 10-m Land Use/Land Cover dataset provided by ESRI [16]. This comprehensive dataset allowed for detailed analysis of land cover variations across the UAE, crucial for assessing the impact of land use on flood risk. The Sentinel-2 data, with its 10-meter resolution, encompasses a wide range of land cover types, including urban fabric, agricultural lands, natural vegetation, water bodies, and barren areas. Following the acquisition of climate and land cover datasets, topographic data were sourced from the Shuttle Radar Topography Mission (SRTM) [17]. The SRTM data form a Digital Terrain Model (DTM) with a resolution

of 1 arc/second (~30 m), designed to provide a detailed representation of the Earth's bare surface. This resolution is particularly suited for flood risk assessment as it allows for the precise delineation of elevation contours. The SRTM data, which were collected during the 11-day Space Shuttle Endeavour mission in February 2000, have since become a benchmark for global topographic data used in various geospatial analyses.

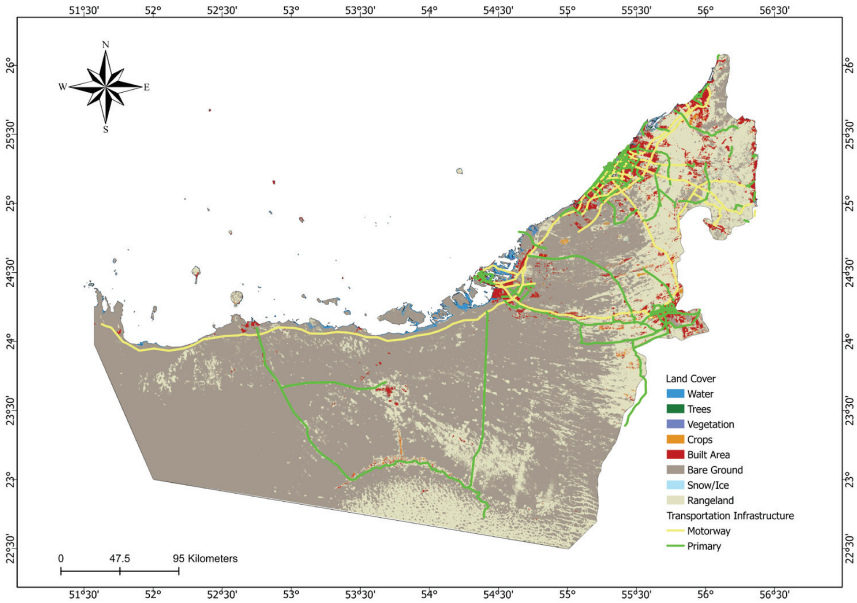

Figure 1. Land cover map of the United Arab Emirates with integrated transportation infrastructure.

3. Global Climate Model Data

The Coupled Model Intercomparison Project Phase 6 (CMIP6) is a multi-model initiative that provides updated climate projections for a wide range of scenarios. Shared Socioeconomic Pathways (SSPs) are a set of scenarios that describe different socioeconomic conditions and emissions pathways for the future. In this paragraph, we will discuss the CMIP6 data under different SSPs. The CMIP6 data provides valuable information on how the Earth's climate will respond to different socioeconomic conditions and emissions scenarios [18]. The UAE study maps temperature changes using GCMs, predicting significant increases, thus aiding decision-making for climate change mitigation strategies [19].

Under the SSP1-2.6 scenario, which represents a future with rapid decarbonization and sustainable development, the global mean surface temperature is projected to remain below 2 °C above pre-industrial levels, which is the target of the Paris Agreement. However, under the SSP5-8.5 scenario, which represents a future with high greenhouse gas emissions and limited climate policies, global mean surface temperature is projected to increase by over 4 °C by the end of the century, resulting in significant impacts on ecosystems and human societies. In addition to temperature projections, the CMIP6 data also provide information on other climate variables, such as precipitation, sea level, and ocean acidity. Under the SSP1-2.6 scenario, precipitation is projected to increase in many regions, particularly in the tropics and high-latitude areas, while sea level rise is expected to be limited to around 0.5 m by 2100. However, under the SSP5-8.5 scenario, precipitation is projected to decrease in many regions, particularly in the subtropics and mid-latitudes, while sea level rise is expected to exceed 1 m by 2100. Furthermore, the CMIP6 data also show that the impacts of climate change will vary depending on the region and sector. For example, under the SSP1-2.6 scenario, the Arctic is expected to experience significant warming, leading to the widespread melting of sea ice and permafrost. This could have significant impacts on the region's ecosystems and indigenous communities. In contrast, under the SSP5-8.5 scenario, the tropics are expected to experience more frequent and intense heatwaves, which could have significant impacts on agriculture, human health, and transportation infrastructure.

In this study, two Shared Socioeconomic Pathway (SSP) scenarios, specifically SSP2-4.5 and SSP5-8.5, were chosen for two CMIP6 models, CanESM5 and MIROC6, spanning both near-future (2021–2050) and far-future (2051–2100) timeframes [20,21]. The advantage of utilizing SSP scenarios lies in the ability to integrate estimated changes into flood risk with socioeconomic projections under varying SSP scenarios to explore flood risk dynamics. Presently, these two SSP scenarios incorporate a total of 19 CMIP6 General Circulation Models (GCMs). Each climate model encompasses daily precipitation data for both historical (2000–2020) and future (2021–2100) periods.

4. Methodology

Figure 2 presents the approach used to estimate flood risk vulnerability in the context of climate change scenarios, which consists of two primary phases: first, assessing the accuracy of CMIP6 global climate models by comparing them to historical data; second, using CMIP6 model outputs to forecast future flood risks, incorporating the evaluation and prioritization of factors through the Analytic Hierarchy Process (AHP). The preliminary analysis of CMIP6 GCMs involves a comparison of model-generated rainfall data against actual precipitation figures from a reference period in the past. The consistency between the modeled and real-world data acts as a measure of the CMIP model's proficiency in mirroring climate patterns pertinent to this research.

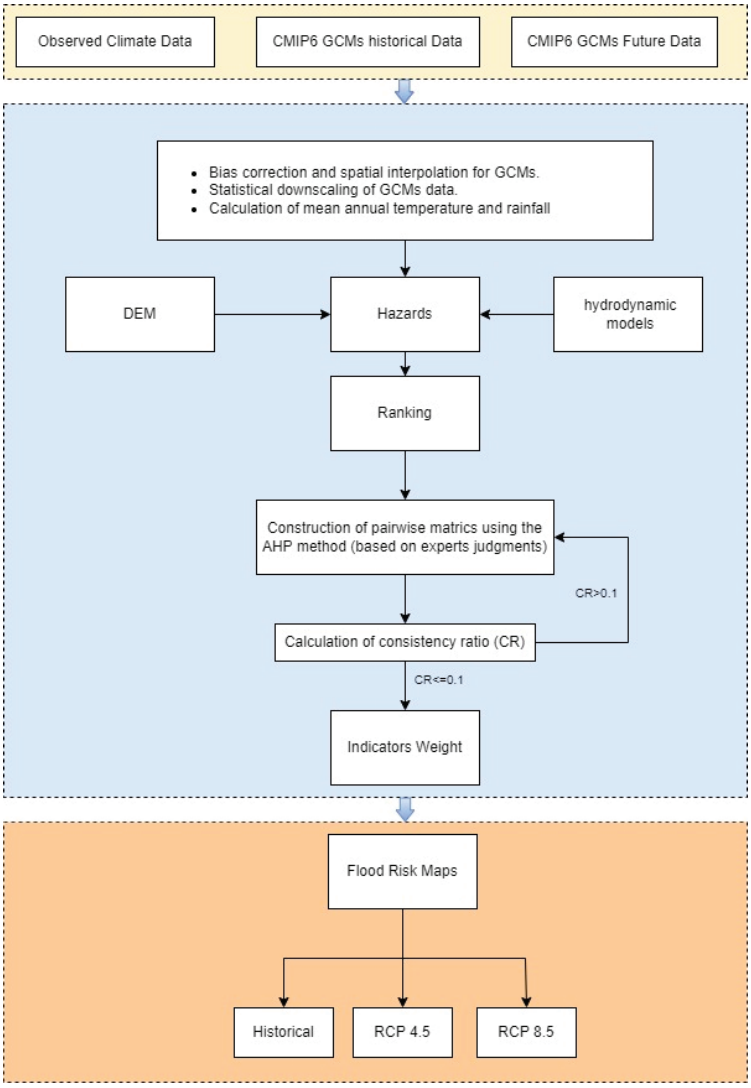

Figure 2. Methodology framework.

A high degree of concordance suggests that CMIP models are instrumental in exploring the effects of climate change scenarios on flood events. The reference period for historical climate model simulation data spanned from 2000 to 2020, with the periods 2021–2050 and 2051–2100 designated as the near and far future, respectively, based on SSP scenarios in line with the IPCC Sixth Assessment Report's guidelines. The calculation of mean annual precipitation was carried out for both the historical and future periods using each of the CMIP6 global climate models. The calculated baseline period values were subsequently incorporated into the authors' model for assessing national susceptibility to rainfall-induced flooding, which considers the impact of mean annual precipitation.

4.1. Statistical Downscaling and Global Climate Model Evaluation

Climate models at both global and regional scales are pivotal for projecting future climate variations. Numerous studies have applied these models, often incorporating bias correction techniques and real-world measurements to rectify consistent discrepancies in the prediction of weather elements such as temperature and precipitation. In the context of this study, bias correction was performed using the delta method, a strategy celebrated for its straightforwardness, efficacy in correcting biases, widespread use in the scientific literature, and ability to withstand comparison with other top methods. The delta change technique allows for the application of General Circulation Model (GCM) projections in hydrological modeling and studies at the watershed level, though in a somewhat indirect manner. It operates on the principle of applying change factors or ratios derived from comparing future projections to historical averages. These factors, when applied to historical observational series, adjust the data to reflect future climate scenarios. For the purpose of determining delta correction factors in this research, data on average monthly precipitation collected over a two-decade period (2000 to 2020) from 21 meteorological stations throughout the UAE were analyzed. Corrections were made for data under various Shared Socioeconomic Pathways (SSP2-4.5 and SSP5-8.5) employing the delta method. The computation of the delta factor was based on the following equation [22]:

$$\Delta \text{ month i } = \frac{\text{Future average monthly for month i (from model used)}}{\text{Historical average monthly for month i (from a model used)}}$$

Given the varied resolution of CMIP6 GCM data and the notable spatial diversity in the UAE's landscape, which influences precipitation and temperature projections, the technique of climate data interpolation was utilized to align accurately with other critical variables within the flood risk vulnerability model. Climate models provide data as a function of latitude and longitude along predefined grid lines covering the entire Earth's surface. Adjusting the data for UAE weather stations necessitated interpolation or extrapolation for each model. Interpolation entails predicting data from available datasets, while extrapolation involves making predictions beyond the dataset. Three types of interpolation were utilized to determine precise rainfall for each area based on the station's location within each model's grid. Interpolation was required when a station fell between two points, and interpolation between four points was necessary when it was situated in the middle of a square formed by those points.

4.2. Flood Risk Analysis

Flooding poses a critical danger to the safety of both public and private transportation networks [23], impacting worldwide transportation safety and infrastructure development efforts. In evaluating the spatial variation in flood risk across the study zone, five unique flood risk levels (RLs) were analyzed, identified as very high, high, moderate, low, and very low. These RLs were defined based on the likelihood of a flood occurring within a given hydrological year. Zones identified with a very high flood risk corresponded to a 2% probability of a flood event within a hydrological year (akin to a 50-year recurrence interval), while high-flood-risk areas had a 1% chance (matching a 100-year recurrence interval). A moderate flood risk was associated with a 0.5% chance (corresponding to

a 200-year recurrence interval). Areas under the very low flood risk category showed a likelihood of less than 0.2% (surpassing a 500-year recurrence interval), and those deemed to have a low flood risk presented a probability of 0.2% or less.

In the evaluation of flood risk factors, special attention was given to the role of elevation in determining flood susceptibility. Our analysis associated higher elevation levels with an increased risk of flash flooding. This decision was grounded in the specific geographical context of our study area, where steep terrains are prevalent, and the hydrological dynamics can lead to rapid water flow and accumulation during heavy rainfall events, thus precipitating flash floods. This phenomenon is not only theoretically supported but also evidenced by historical flood events within the region [24,25].

This classification considered the elements that determine the occurrence of floods. The final flood risk map was generated by combining seven separate theme map components that are closely related to flooding incidents. Based on a linear algebraic function that assigned relative weights to each element, this combination was determined. Within the ArcGIS environment, four separate thematic map-factors, including land cover (L), rainfall (R), elevation (E) and slope (S), were generated to estimate the final flood risk map.

The influence of each factor was categorized into five specific flood risk levels (RLs): very high, high, moderate, low, and very low. These distinct flood risk categories for each factor were established using Jenk's Natural Breaks method. Subsequently, a numerical score was allocated to each factor, quantifying the flood risk levels (RLs) in this manner: very high (RL) scores 10, high (RL) scores 8, moderate (RL) scores 5, very low (RL) scores 2, and low (RL) scores 1.

The Analytic Hierarchy Process (AHP) was used to assign weights to the significant elements since not all investigated factors have the same effect on flood generation. The AHP is a useful technique for many decision-making procedures in numerous disciplines, including finance, transportation, engineering, business, education, and politics. The AHP is the most often used method for multi-criteria decision-making (MCDM). Numerous researchers have recreated the AHP due to its numerous advantages in making vital decisions [26–29]. The Analytic Hierarchy Process (AHP) is a comprehensive mathematical framework that facilitates the assessment of both tangible and intangible elements in decision-making scenarios, taking into account the preferences of individuals or collective bodies. This method unfolds across various decision-making phases, during which values are attributed and alternative assessments are made according to the selected criteria. The procedure is initiated by establishing a hierarchical framework and creating a comparison matrix. This matrix is subsequently converted into a priority vector, followed by the computation of the consistency ratio using a specific random index value. Figure 3 displays the diagrammatic depiction of a three-tier hierarchical structure applied to a multi-criteria decision-making (MCDM) issue, as detailed by [30].

At the topmost tier is the goal of the decision, succeeded by the criteria at the intermediary level, and, when relevant, the bottom tier features the options under consideration. These alternatives are delineated at the most fundamental level. To maintain accuracy in the pairwise comparisons, it is crucial to clearly specify both the total number of criteria and the individual details of each criterion. Criteria ought to be categorized according to their common attributes, facilitating the application of AHP across a broad spectrum of criteria. Within the AHP, the significance of each criterion is established through pairwise comparisons once the hierarchical framework is in place. The comparative significance of each criterion is denoted by a scale from 1 to 9, based on pairwise evaluations, as shown in Table 1, and following discussions with decision-makers. Consequently, the pairwise comparison matrix for evaluating specific criteria is constructed according to the formula presented:

$$A = \begin{bmatrix} a_{11} & \cdots & a_{1n} \\ \vdots & \ddots & \vdots \\ a_{n1} & \cdots & a_{nn} \end{bmatrix} = \begin{bmatrix} a_{11} & \cdots & a_{1n} \\ \vdots & \ddots & \vdots \\ 1/a_{n1} & \cdots & a_{nn} \end{bmatrix}$$

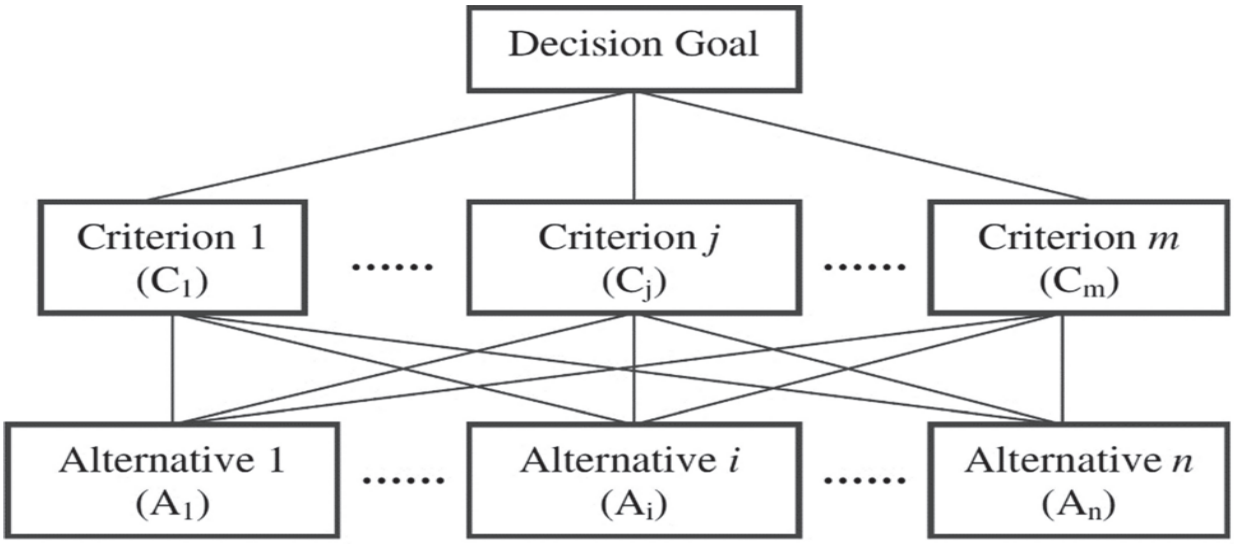

Figure 3. A three-level hierarchy for a MCDM problem.

Table 1. Scales for pairwise comparison in the AHP.

Importance Intensity (Scores)	Definition
1	Equal importance
3	Moderate importance of one over another
5	Strong importance of one over another
7	Very strong importance of one over another
9	Extreme importance of one over another
2, 4, 6, 8	Intermediate values
Reciprocals	Reciprocals for inverse comparison

To obtain the normalized matrix, the process involves calculating the totals of the elements within every column of the comparison matrix. Subsequently, every element within the comparison matrix is divided by the sum of its corresponding column. The creation of the weight vector follows, determined by averaging the values in each row of the normalized matrix. Furthermore, the priorities matrix is formed through the multiplication of the comparison matrix with the weight vector, executed as follows:

$$[AWi] = [A][Wi]$$

The maximum eigenvalue (λmax) is computed with the following:

$$\lambda max = \frac{1}{n}\sum_{i=1}^{n}\frac{AW_i}{W_i}$$

Within these formulas, "n" stands for the count of criteria, "A" stands for the matrix for pairwise comparisons, and "W" stands for the vector of weights. The method employed to extract the weight vector out of the pairwise comparison matrix is referred to as the principal right eigenvector method (EM) [23]. Given that decision-makers may not always provide completely consistent pairwise evaluations, it is recommended that matrix A for pairwise comparisons demonstrate a satisfactory consistency level. The consistency of the matrix can be evaluated through the consistency ratio (CR), ensuring the reliability of the comparisons [29]:

$$CI = \frac{(\lambda max - n)}{(n-1)}$$

$$CR = \frac{CI}{RI}$$

Here, CI stands for the consistency index, and RI stands for the random inconsistency index, which is determined from Table 2 based on the value of "n" obtained from Wang et al. [29].

Table 2. RI values depending on criteria numbers (n = 1–15).

n	1	2	3	4	5	6	7	8	9	10	11	12	13	14	15
RI	0.00	0.00	0.58	0.90	1.12	1.24	1.32	1.41	1.45	1.49	1.51	1.48	1.56	1.57	1.59

Should the consistency ratio (CR) be less than 0.10, the comparison matrix is considered to possess adequate consistency. Otherwise, the decision-making process is repeated to achieve the necessary level of consistency. A CR of 0.00 indicates optimal consistency [31]. Table 3 outlines the assigned weights and ratings for the factors and their respective categories. In the evaluation of these factors, the unique hydrological characteristics of the UAE, which lacks significant rivers or lakes, were taken into account. As a consequence, the selection and verification of parameters in our model were tailored to the region's conditions. Historical flood event data were analyzed, and expert consultations further substantiated the relevance of the selected factors to validate the weightings. This comprehensive approach was essential in a region where typical hydrological models may not apply, and it provided a foundation for an accurate and context-specific flood risk assessment [32].

Table 3. The weightings and ratings of the considered factors.

Factors	Flood Risk Levels	Weight of Effect (RL)	Value	Total Weight (%)
Land Cover	Very High	5	Bare Ground, Built Area	14.5
	High	4	Crops	
	Moderate	3	Rangeland	
	Low	2	Vegetation, Trees	
	Very Low	1	Water	
Rainfall (mm)	Very High	5	>22	38
	High	4	11–22	
	Moderate	3	7.6–11	
	Low	2	6–7.6	
	Very Low	1	0–6	
Elevation	Very High	5	>143	10.4
	High	4	117–143	
	Moderate	3	94–117	
	Low	2	46–94	
	Very Low	1	−6–46	
Slope	Very High	5	0–1.27	37.1
	High	4	1.27–5.6	
	Moderate	3	5.6–14.5	
	Low	2	14.5–30	
	Very Low	1	>30	
Sum	100			

The final proportion of each element's influence on flood risk was determined by dividing the individual weight of each factor by the total combined weight of all factors (that is, the aggregate of the weights for all six factors). Through the use of the weighted linear combination technique, each factor was then multiplied by its respective percentage weight. This process led to the creation of the ultimate flood risk map for the UAE by aggregating all the factors according to the equation provided below:

$$R = \sum x_i w_i = Fw_L + Rw_R + Ew_E + Sw_S$$

where

X_i = the map of each parameter i;
W_i = the weight of each parameter i;
L = land cover, R = rainfall, E = elevation, and S = slope.

Using geoinformatics and field measurement techniques, the aforementioned thematic maps/factors were determined and digitized. A Digital Elevation Model (DEM) of the study area was created using topographic maps. Using a DEM in a GIS environment, a 3D Analyst tool was used to generate a slope map. The occurrence of floods is inversely proportional to topographic characteristics such as slope and elevation. The slope of land is a critical factor in determining how water flows over the surface. If land is steeply sloped, water will flow downhill quickly and with greater force, leading to more rapid runoff and potential flooding. On the other hand, if land is relatively flat, water will flow more slowly and be absorbed into the soil more easily, reducing the risk of flooding. Elevation refers to the height of the land above sea level. Low-lying areas are more prone to flooding than areas at higher elevations, as water naturally flows downhill to lower elevations. In addition, areas close to bodies of water, such as rivers or lakes, are at a higher risk of flooding due to their proximity to the water source. In addition, the type of land cover in an area can also impact flooding. Natural vegetation, such as forests and wetlands, can absorb and slow down rainwater, reducing the amount of runoff and preventing flooding. However, when natural vegetation is replaced by impervious surfaces like concrete and asphalt, rainwater cannot be absorbed into the ground and instead runs off rapidly into rivers and streams, increasing the likelihood of flooding. Rainfall is one of the primary factors contributing to the risk of flooding. When rainfall occurs, the amount of water on the ground increases, and depending on the intensity and duration of the rainfall, the water may accumulate and cause flooding.

5. Results and Discussion

Figure 4 displays the present flood risk map of the UAE, categorized into five levels—very high, high, moderate, low, and very low. The map accurately represents the flood risk across the country. The map indicates that the northern region of the UAE is at a higher risk of flooding than the southern region, with the majority of the areas in the northern part of the country being classified as either very high or high risk. This is likely due to the fact that the northern part of the UAE receives more rainfall than the southern part, particularly during the winter months. The map also shows that the coastal areas of the UAE, particularly along the Arabian Gulf and the Gulf of Oman, are at a higher risk of flooding than the inland areas. This is due to a combination of factors such as high tides, storm surges, and heavy rainfall, which can lead to flash floods and the inundation of low-lying areas. These areas are characterized by high population density, extensive infrastructure, and large-scale development, which make them particularly vulnerable to flooding events. It is important to note that the majority of the population of the UAE lives in coastal cities, which means that they are particularly vulnerable to the impacts of flooding. In contrast, the inland regions of the UAE are generally at a lower risk of flooding, with most areas classified as being at moderate to very low risk. These regions are largely dominated by desert and semi-arid landscapes, with fewer population centers and less transportation infrastructure development. However, even these regions are not immune to the risks of

flooding, particularly in the case of extreme weather events such as cyclones and severe thunderstorms.

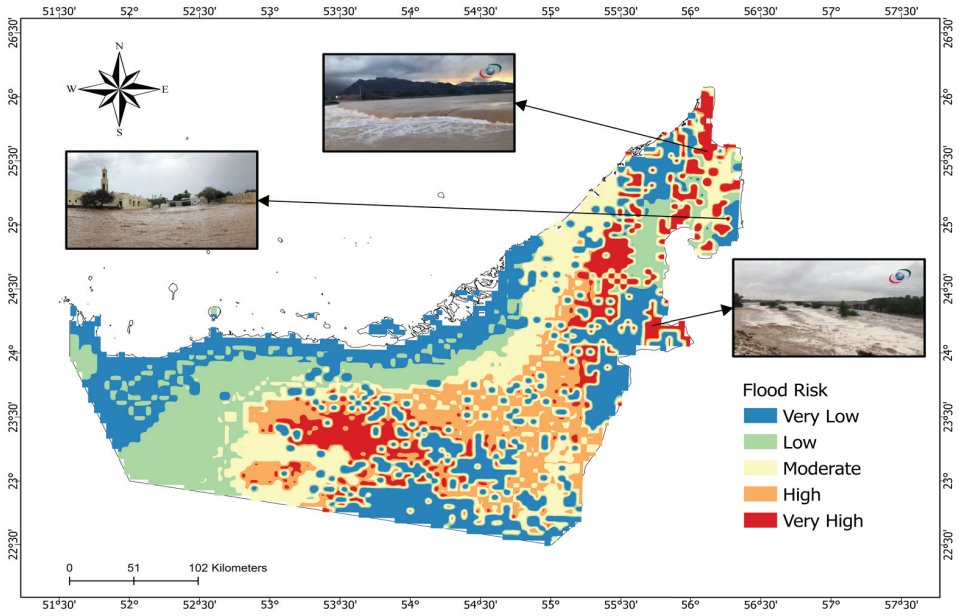

Figure 4. Current flood risk map for the UAE highlighting various levels of flood risk [images courtesy of the National Center of Meteorology, the UAE. Used with permission].

Figures 5 and 6 illustrate the flood risk projections for the UAE across two different Shared Socioeconomic Pathways (SSPs) for both near- and far-future scenarios, using the CanESM5 and MIROC6 climate models, respectively. Under SSP245, indicative of a sustainable path with reduced greenhouse gas emissions, the overall flood risk across the UAE is anticipated to be low for both timeframes. Nonetheless, specific locales in the UAE's northern and eastern parts are expected to exhibit high to very high levels of flood risk in the long-term future.

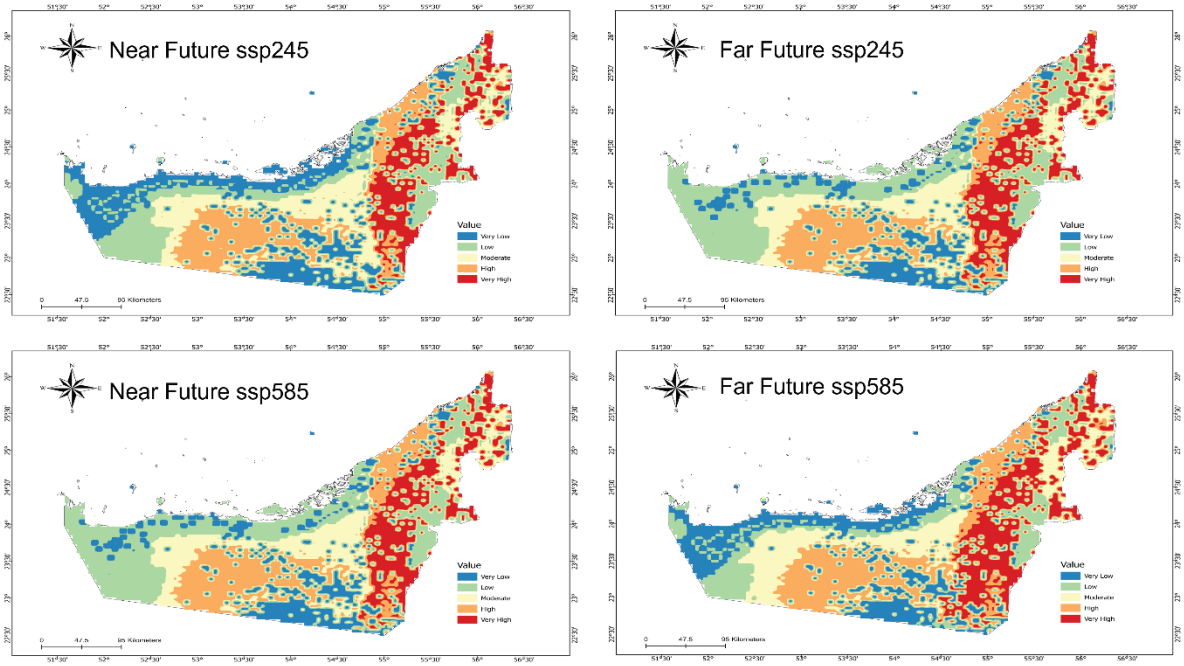

Figure 5. Projected flood risk map for the UAE using the CanESM5 model for near- and far-future scenarios (SSP245 and SSP585).

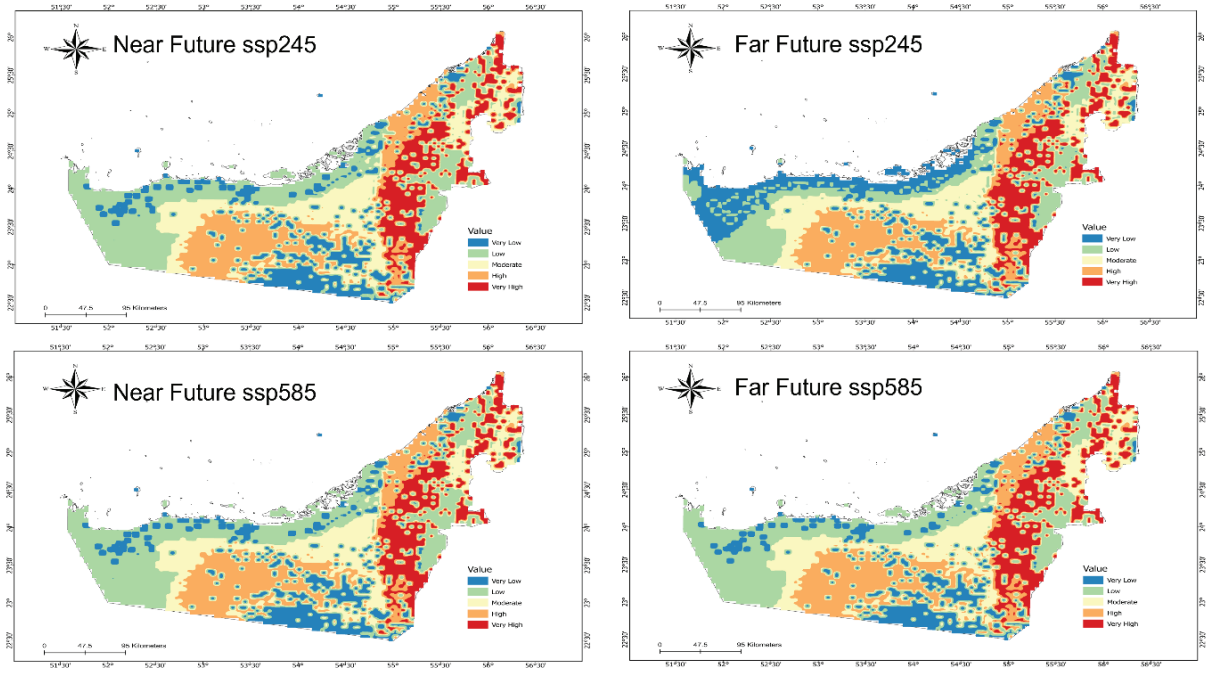

Figure 6. Projected flood risk map for the UAE using the MIROC6 model for near- and far-future scenarios (SSP245 and SSP585).

These areas are predominantly characterized by low-lying coastal regions and extensive urbanization, which increases the surface runoff and reduces the groundwater recharge. The potential impact of these high to very high flood risk levels can lead to severe damage to transportation infrastructure, property, and human life. Conversely, within the SSP585 scenario, indicating elevated greenhouse gas emissions, the flood risk levels exhibit notable disparities compared to SSP245, particularly in the far-future timeframe. The map presented shows a broad distribution of very high and high levels of flood risk across the UAE, with the most significant risks highlighted in the northern and eastern areas of the country. These areas are projected to experience an increase in precipitation intensity, duration, and frequency, resulting in severe flash floods and the inundation of coastal areas. The projected impact of these high flood risk levels can lead to devastating consequences for the UAE's economy, transportation infrastructure, and human life. Overall, flood risk levels in the near-future period were observed to be comparatively lower than those projected for the far-future period under both the SSP245 and SSP585 scenarios. Nevertheless, the severity and coverage of flood risk levels in the far-future period, particularly under SSP585, were notably greater than in other scenarios.

Tables 4–7 display the proportion of the UAE's land, transportation network, and major and minor roads exposed to flood risks under various climate change projections. Currently, 34% of the UAE's territory is categorized as having a very low level of flood risk. Under the CanESM5 SSP245 scenario for the near future, this figure declines to 25%, and drops further to 13% in the far-future scenario. The MIROC6 SSP245 scenarios for both the near and far future indicate a reduction in areas with very low flood risk to 13% and 25%, respectively. With the CanESM5 SSP585 scenarios for the near and far future, the percentages of areas classified under very low flood risk fall to 13% and 23%, respectively. Under the MIROC6 SSP585 projections for the near and far future, the area of the UAE facing very low flood risk is expected to decrease to 13% and 18%, respectively. The portion of the UAE at "low" flood risk is currently 19%. The CanESM5 SSP245 scenario for the near future predicts a reduction to 17%, but this increases to 29% in the far future. The MIROC6 SSP245 scenarios for both the near and far future forecast a rise to 29%. The CanESM5 SSP585 scenarios predict a fall to 15% in the near future and a rise to 29% in the far future. The MIROC6 SSP585 scenarios anticipate drops to 29% and 22% for the near and far future,

respectively. The levels of moderate and high flood risk remain fairly constant across all scenarios, fluctuating from 21% to 23% and from 14% to 22%, respectively. The very high flood risk level sees an escalation to 14% in both the near and far future under the CanESM5 SSP245 and MIROC6 SSP245 scenarios. For the CanESM5 and MIROC6 SSP585 scenarios, very high flood risk escalates to 18% and 14% for the near and far future, respectively.

Table 4. The percentage of UAE areas under different flood risk levels.

Flood Risk Level	Current	CanESM5				MIROC6			
		SSP245	SSP245	SSP585	SSP585	SSP245	SSP245	SSP585	SSP585
		Near Future	Far Future	Near Future	Far Future	Near Future	Far Future	Near Future	Far Future
Very Low	34%	25%	13%	13%	23%	13%	25%	13%	13%
Low	19%	17%	29%	29%	15%	29%	17%	29%	29%
Moderate	14%	22%	21%	22%	22%	22%	22%	22%	22%
High	23%	21%	22%	22%	23%	21%	22%	22%	22%
Very High	10%	14%	15%	15%	18%	14%	14%	14%	14%

Table 5. The percentage of UAE infrastructure under different flood risk levels.

Flood Risk Level	Current	CanESM5				MIROC6			
		SSP245	SSP245	SSP585	SSP585	SSP245	SSP245	SSP585	SSP585
		Near Future	Far Future	Near Future	Far Future	Near Future	Far Future	Near Future	Far Future
Very Low	36%	26%	13%	14%	23%	14%	26%	14%	14%
Low	17%	17%	28%	28%	16%	29%	17%	29%	28%
Moderate	15%	23%	21%	22%	22%	23%	22%	22%	22%
High	20%	18%	19%	19%	20%	18%	19%	19%	19%
Very High	12%	16%	18%	17%	20%	16%	16%	16%	17%

Table 6. The percentage of UAE major roads under different flood risk levels.

Flood Risk Level	Current	CanESM5				MIROC6			
		SSP245	SSP245	SSP585	SSP585	SSP245	SSP245	SSP585	SSP585
		Near Future	Far Future	Near Future	Far Future	Near Future	Far Future	Near Future	Far Future
Very Low	44%	27%	12%	12%	22%	13%	27%	13%	12%
Low	13%	20%	34%	34%	22%	34%	20%	34%	34%
Moderate	17%	17%	18%	17%	18%	17%	17%	17%	17%
High	9%	20%	20%	20%	20%	20%	21%	20%	21%
Very High	17%	16%	17%	17%	18%	17%	16%	17%	17%

For the CanESM5 SSP245 near-future scenario, the percentage of infrastructure under very low flood risk decreases to 26%, which is a significant decrease compared to the current scenario. In contrast, the MIROC6 SSP245 near-future scenario shows a slight decrease to 14%. In the far-future scenarios for both models, the percentage of infrastructure under very low flood risk decreases further. The CanESM5 SSP245 far-future scenario predicts that only 13% of infrastructure will be under very low flood risk, while MIROC6 SSP245 far-future scenario shows a decrease to 13%. In terms of the low flood risk level, the CanESM5

SSP245 near-future scenario predicts that the percentage of infrastructure under this level will remain the same as the current scenario, while MIROC6 SSP245 near-future scenario shows an increase to 29%. In the far-future scenarios for both models, the percentage of infrastructure under low flood risk level increases, but the CanESM5 SSP245 far-future scenario shows a more significant increase to 28% compared to the MIROC6 SSP245 far-future scenario, which shows an increase to 29%. Both models predict that the percentage of infrastructure under moderate and high flood risk levels will remain relatively stable in all scenarios, ranging from 21% to 23% and from 14% to 22%, respectively.

Table 7. The percentages of UAE minor roads under different flood risk levels.

Flood Risk Level	Current	CanESM5				MIROC6			
		SSP245	SSP245	SSP585	SSP585	SSP245	SSP245	SSP585	SSP585
		Near Future	Far Future	Near Future	Far Future	Near Future	Far Future	Near Future	Far Future
Very Low	37%	26%	13%	14%	23%	14%	26%	14%	14%
Low	17%	17%	29%	29%	16%	29%	17%	29%	29%
Moderate	15%	23%	21%	22%	22%	23%	22%	23%	22%
High	20%	18%	19%	19%	20%	18%	19%	18%	19%
Very High	12%	16%	18%	18%	20%	17%	17%	17%	17%

However, in terms of the very high flood risk category, both models project an increase in both near- and far-future scenarios. Across the CanESM5 SSP245 scenarios for the near and far future and the MIROC6 SSP245 scenarios for both timeframes, there is a consistent climb to 16% and 18%, respectively. Under the CanESM5 SSP585 scenarios for the near and far future, there is a rise to 17% and 14%, respectively, while in the MIROC6 SSP585 scenarios for both periods, there is an increase to 16% and 17%, respectively.

For major roads, CanESM5 SSP245 and SSP585 predict a decrease in the percentage of roads in the very low flood risk level, while MIROC6 SSP585 predicts an increase. In contrast, MIROC6 SSP245 predicts an increase in the percentage of major roads in the very low flood risk level. For low flood risk levels, all models predict an increase in the percentage of major roads in this category, except for the CanESM5 SSP245 far-future scenario, which predicts a decrease. For moderate flood risk levels, all models predict relatively consistent percentages across current and future scenarios. For high flood risk levels, the CanESM5 SSP245 near- and far-future scenarios predict an increase in percentage, while the other models predict a relatively consistent percentage across current and future scenarios. For very high flood risk levels, all models predict an increase in the percentage of major roads in this category.

For minor roads, the same trend can be observed in terms of an overall increase in flood risk levels predicted by all models. Similar to major roads, CanESM5 SSP245 and SSP585 predict a decrease in the percentage of minor roads in the very low flood risk level, while MIROC6 SSP585 predicts an increase. MIROC6 SSP245 predicts an increase in the percentage of minor roads in the very low flood risk level. For low flood risk levels, all models predict an increase in the percentage of minor roads in this category, except for CanESM5 SSP245 for future scenarios, which predicts a decrease.

For moderate flood risk levels, all models predict relatively consistent percentages across current and future scenarios. For high flood risk levels, CanESM5 SSP245 near- and far-future scenarios predict an increase in percentage, while the other models predict a relatively consistent percentage across current and future scenarios. For very high flood risk levels, all models predict an increase in the percentage of minor roads in this category.

The tables indicate that climate change is poised to elevate flood risk in the UAE. Across all climate scenarios, a notable pattern emerges: a rise in the percentage of areas, infrastructure, and roads facing moderate and high flood risk, coupled with a decline

in the percentage of areas, infrastructure, and roads facing very low and low flood risk. Of particular concern is the CanESM5 SSP245 far-future scenario, revealing a substantial uptick in the percentage of areas facing very high flood risk. This emphasizes the critical need to adopt efficient strategies for managing flood risks and implementing adaptation measures in the UAE to mitigate the potential consequences of climate change on the country's infrastructure and population.

6. Conclusions

In conclusion, the flood risk map of the UAE accurately depicts the country's flood-prone regions, with the northern and coastal regions being at higher risk. The majority of the population lives in coastal cities, making them particularly vulnerable to flooding events. The future flood risk map projections for both the CanESM5 and MIROC6 models indicate that under the SSP245 scenario, flood risk levels will generally be low across both time periods. Nevertheless, specific areas within the northern and eastern regions of the UAE may continue to face heightened levels of flood risk, ranging from high to very high, particularly in the far-future period, due to extensive urbanization and the presence of low-lying coastal zones. The SSP585 scenario predicts significantly higher levels of flood risk compared to SSP245, with widespread occurrences of very high and high flood risk levels throughout the UAE. The potential consequences of these increased flood risk levels could include substantial damage to transportation infrastructure, property, and human lives. It is expected that the proportion of areas classified as having very low flood risk will decrease in future scenarios, while the percentages of areas with moderate and high flood risk levels will remain relatively stable. Additionally, a significant reduction in the proportion of infrastructure exposed to very low flood risk is anticipated in future scenarios. The recent publication of the CMIP6 models marks a significant advancement, and according to the authors' knowledge, there have been no studies that have yet explored the application of CMIP6 scenarios. This study highlights the global need for sustainable flood risk management in transportation and planning, advocating for integrated approaches to mitigate flood impacts. It calls for combining sustainable geography with infrastructure development and risk strategies, aiming to address future flooding challenges effectively. Based on the findings of this study, opportunities for further research have been identified, as outlined in the following recommendations:

1. Diversify the use of GCMs: Future studies should consider incorporating a wider array of GCMs to capture a broader range of climate scenarios. This approach will help in obtaining more robust and comprehensive results.
2. Implement an Ensemble Approach: Adopting an ensemble approach with multiple GCMs can provide a more accurate representation of climate uncertainties. This method allows for the aggregation of different model outputs, leading to more reliable predictions.
3. Develop More Advanced Downscaling Techniques: To ensure that global climate model outputs are more applicable at regional or local scales, future research should invest in the development of sophisticated downscaling methods. These techniques should be capable of translating large-scale climate information into finer, more detailed local climate data.

Author Contributions: Conceptualization, M.A., A.E., W.Z., A.G.Y. and A.S.; methodology, M.A., A.E. and A.G.Y.; software, A.E. and A.G.A.; validation, M.A., A.E., W.Z. and A.G.Y.; formal analysis, A.E. and M.A.; investigation, M.A., A.E. and A.G.Y.; resources, A.E., A.G.A., M.A. and W.Z.; data curation, M.A., A.E., A.G.A. and W.Z.; writing original draft preparation, M.A., A.E., A.G.A. and W.Z.; writing review and editing, M.A., A.E., A.G.A. and W.Z.; visualization, M.A., A.E. and A.G.A.; supervision, M.A., W.Z. and A.S.; project administration, M.A. and A.S.; funding acquisition, M.A. and W.Z. All authors have read and agreed to the published version of the manuscript.

Funding: The authors extend their deepest gratitude to the Ministry of Energy and Infrastructure for funding this project (No29/04/2019) in title Potential Impact of Climate Change on Traffic Safety and Transportation System Performance in the UAE.

Institutional Review Board Statement: Not applicable.

Informed Consent Statement: Not applicable.

Data Availability Statement: The authors do not have permission to publish the data.

Conflicts of Interest: The authors declare no conflict of interest.

References

1. National Climate Assessment. *Impacts, Risks, and Adaptation in the United States: Fourth National Climate Assessment, Volume II*; U.S. Global Change Research Program: Washington, DC, USA, 2018.
2. Zeiada, W.; Mirou, S.; Ashour, A.; Hassan, R.; Abuzwidah, M. Development of Climate Data Inputs towards the Implementation of Mechanistic-Empirical Pavement Design in the UAE. In Proceedings of the 2nd International Conference on Civil Infrastructure and Construction (CIC 2023), Doha, Qatar, 5–8 February 2023; pp. 1341–1348. [CrossRef]
3. Zhong, C.; Guo, H.; Swan, I.; Gao, P.; Yao, Q.; Li, H. Evaluating Trends, Profits, and Risks of Global Cities in Recent Urban Expansion for Advancing Sustainable Development. *Habitat. Int.* **2023**, *138*, 102869. [CrossRef]
4. Kulp, S.A.; Strauss, B.H. New Elevation Data Triple Estimates of Global Vulnerability to Sea-Level Rise and Coastal Flooding. *Nat. Commun.* **2019**, *10*, 4844. [CrossRef] [PubMed]
5. Kundzewicz, Z.W.; Kanae, S.; Seneviratne, S.I.; Handmer, J.; Nicholls, N.; Peduzzi, P.; Mechler, R.; Bouwer, L.M.; Arnell, N.; Mach, K.; et al. Flood Risk and Climate Change: Global and Regional Perspectives. *Hydrol. Sci. J.* **2014**, *59*, 1–28. [CrossRef]
6. Pachauri, R.K.; Meyer, L.A. *Climate Change 2014: Synthesis Report. Contribution of Working Groups I, II and III to the Fifth Assessment Report of the Intergovernmental Panel on Climate Change*; Intergovernmental Panel on Climate Change: Geneva, Switzerland, 2014.
7. Arnell, N.W.; Brown, S.; Gosling, S.N.; Gottschalk, P.; Hinkel, J.; Huntingford, C.; Lloyd-Hughes, B.; Lowe, J.A.; Nicholls, R.J.; Osborn, T.J.; et al. The Impacts of Climate Change across the Globe: A Multi-Sectoral Assessment. *Clim. Chang.* **2016**, *134*, 457–474. [CrossRef]
8. Di Baldassarre, G.; Montanari, A.; Lins, H.; Koutsoyiannis, D.; Brandimarte, L.; Blschl, G. Flood Fatalities in Africa: From Diagnosis to Mitigation. *Geophys. Res. Lett.* **2010**, *37*. [CrossRef]
9. Kourgialas, N.N.; Karatzas, G.P. A Flood Risk Decision Making Approach for Mediterranean Tree Crops Using GIS; Climate Change Effects and Flood-Tolerant Species. *Environ. Sci. Policy* **2016**, *63*, 132–142. [CrossRef]
10. Rubio, C.J.; Yu, I.S.; Kim, H.Y.; Jeong, S.M. Index-Based Flood Risk Assessment for Metro Manila. *Water Sci. Technol. Water Supply* **2020**, *20*, 851–859. [CrossRef]
11. Mahmoody Vanolya, N.; Jelokhani-Niaraki, M. The Use of Subjective–Objective Weights in GIS-Based Multi-Criteria Decision Analysis for Flood Hazard Assessment: A Case Study in Mazandaran, Iran. *GeoJournal* **2021**, *86*, 379–398. [CrossRef]
12. Osei, B.K.; Ahenkorah, I.; Ewusi, A.; Fiadonu, E.B. Assessment of Flood Prone Zones in the Tarkwa Mining Area of Ghana Using a GIS-Based Approach. *Environ. Challenges* **2021**, *3*, 100028. [CrossRef]
13. Oubennaceur, K.; Chokmani, K.; Gauthier, Y.; Ratte-Fortin, C.; Homayouni, S.; Toussaint, J.P. Flood Risk Assessment under Climate Change: The Petite Nation River Watershed. *Climate* **2021**, *9*, 125. [CrossRef]
14. Mirou, S.M.; Elawady, A.T.; Ashour, A.G.; Zeiada, W.; Abuzwidah, M. Visibility Prediction through Machine Learning: Exploring the Role of Meteorological Factors. In Proceedings of the 2023 Advances in Science and Engineering Technology International Conferences ASET, Dubai, United Arab Emirates, 20–23 February 2023; pp. 1–6. [CrossRef]
15. Kaisari, N.K.; Abuzwidah, M.; Elawady, A.; Zeiada, W. Adverse Weather Impact on Driver Performance in the UAE. *E3S Web Conf.* **2022**, *347*, 01020. [CrossRef]
16. Esri. Global Land Cover. ArcGIS Living Atlas of the World. Available online: https://livingatlas.arcgis.com/landcover/ (accessed on 13 June 2024).
17. Mudd, S.M. *Topographic Data from Satellites*, 1st ed.; Elsevier B.V.: Amsterdam, The Netherlands, 2020; Volume 23, ISBN 9780444641779.
18. Masson-Delmotte, V.; Zhai, P.; Pirani, A.; Connors, S.L.; Péan, C.; Berger, S.; Caud, N.; Chen, Y.; Goldfarb, L.; Gomis, M.I.; et al. *Climate Change 2021: The Physical Science Basis*; Cambridge University Press: Cambridge, UK; New York, NY, USA, 2021; Volume 2. [CrossRef]
19. Ashour, A.G.; Mirou, S.M.; Hassan, R.N.; Zeiada, W.; Abuzwidah, M.; Shanableh, A. Assessment of Potential Temperature Increases in The UAE Due to Future Global Warming. In Proceedings of the 2022 Advances in Science and Engineering Technology International Conferences ASET, Dubai, United Arab Emirates, 21–24 February 2022; pp. 1–6. [CrossRef]
20. Ding, X.; Liao, W.; Lei, X.; Wang, H.; Yang, J.; Wang, H. Assessment of the Impact of Climate Change on Urban Flooding: A Case Study of Beijing, China. *J. Water Clim. Chang.* **2022**, *13*, 2692–3715. [CrossRef]
21. Tatebe, H.; Ogura, T.; Nitta, T.; Komuro, Y.; Ogochi, K.; Takemura, T.; Sudo, K.; Sekiguchi, M.; Abe, M.; Saito, F.; et al. Description and Basic Evaluation of Simulated Mean State, Internal Variability, and Climate Sensitivity in MIROC6. *Geosci. Model Dev.* **2019**, *12*, 2727–2765. [CrossRef]

22. Hassan, R.N.; Zeiada, W.A.; Abuzwidah, M.; Mirou, S.M.; Ashour, A.G. *Investigation of Historical and Future Air Temperature Changes in the UAE*; Springer International Publishing: Berlin/Heidelberg, Germany, 2022; ISBN 9783030798000.
23. Pregnolato, M.; Ford, A.; Wilkinson, S.M.; Dawson, R.J. The Impact of Flooding on Road Transport: A Depth-Disruption Function. *Transp. Res. Part D Transp. Environ.* **2017**, *55*, 67–81. [CrossRef]
24. Singh, G.; Pandey, A. Flash Flood Vulnerability Assessment and Zonation through an Integrated Approach in the Upper Ganga Basin of the Northwest Himalayan Region in Uttarakhand. *Int. J. Disaster Risk Reduct.* **2021**, *66*, 102573. [CrossRef]
25. Costache, R.; Barbulescu, A.; Pham, Q.B. Integrated Framework for Detecting the Areas Prone to Flooding Generated by Flash-Floods in Small River Catchments. *Water* **2021**, *13*, 758. [CrossRef]
26. Budayan, C. Evaluation of Delay Causes for BOT Projects Based on Perceptions of Different Stakeholders in Turkey. *J. Manag. Eng.* **2019**, *35*, 4018057. [CrossRef]
27. Negese, A.; Worku, D.; Shitaye, A.; Getnet, H. Potential Flood-Prone Area Identification and Mapping Using GIS-Based Multi-Criteria Decision-Making and Analytical Hierarchy Process in Dega Damot District, Northwestern Ethiopia. *Appl. Water Sci.* **2022**, *12*, 28. [CrossRef]
28. Aydin, M.C.; Sevgi Birincioğlu, E. Flood Risk Analysis Using Gis-Based Analytical Hierarchy Process: A Case Study of Bitlis Province. *Appl. Water Sci.* **2022**, *12*, 122. [CrossRef]
29. Yang, X.L.; Ding, J.H.; Hou, H. Application of a Triangular Fuzzy AHP Approach for Flood Risk Evaluation and Response Measures Analysis. *Nat. Hazards* **2013**, *68*, 657–674. [CrossRef]
30. Wang, Y.M.; Liu, J.; Elhag, T.M.S. An Integrated AHP-DEA Methodology for Bridge Risk Assessment. *Comput. Ind. Eng.* **2008**, *54*, 513–525. [CrossRef]
31. Saaty, T.L. How to Make a Decision: The Analytic Hierarchy Process. *Eur. J. Oper. Res.* **1990**, *48*, 9–26. [CrossRef]
32. Subramanian, N.; Ramanathan, R. A Review of Applications of Analytic Hierarchy Process in Operations Management. *Int. J. Prod. Econ.* **2012**, *138*, 215–241. [CrossRef]

Disclaimer/Publisher's Note: The statements, opinions and data contained in all publications are solely those of the individual author(s) and contributor(s) and not of MDPI and/or the editor(s). MDPI and/or the editor(s) disclaim responsibility for any injury to people or property resulting from any ideas, methods, instructions or products referred to in the content.

International Journal of
Geo-Information

MDPI

Article

Analysis of the Impact of the Digital Economy on Carbon Emission Reduction and Its Spatial Spillover Effect—The Case of Eastern Coastal Cities in China

Juanjuan Zhong [1], Ye Duan [1,*], Caizhi Sun [2] and Hongye Wang [3]

[1] School of Geography, Liaoning Normal University, Dalian 116029, China; zhongjuanjuan0705@163.com
[2] KRI—Center for Studies of Marine Economy and Sustainable Development, Liaoning Normal University, Dalian 116029, China; suncaizhi@lnnu.edu.cn
[3] School of Energy and Power Engineering, Dalian University of Technology, Dalian 116024, China; wanghongye@dlut.edu.cn
* Correspondence: dydl@lnnu.edu.cn

Abstract: The expansion of the digital economy is crucial for halting climate change, as carbon emissions from urban energy use contribute significantly to global warming. This study uses the Difference-in-Differences Model and the Spatial Durbin Model determine whether the digital economy may support the development of reducing carbon emissions and its geographic spillover effects in Chinese cities on the east coast. In addition, it looks more closely at the effects of lowering carbon emissions in space by separating them into direct, indirect, and spatial impact parts. The findings show that (1) from 2012 to 2021, the digital economy favored carbon emission reductions in China's eastern coastline cities, as supported by the robustness test. (2) The link between digital economy growth and carbon emissions is highly variable, with smart city development and urban agglomeration expansion both cutting city carbon emissions considerably. Successful digital economy strategies can lower CO_2 emissions from nearby cities. (3) Eastern coastal cities have a considerable spatial spillover impact, and the digital economy mitigates local energy consumption and carbon emissions while simultaneously enhancing environmental quality in nearby urban areas. This analysis proposes that the peak carbon and carbon neutrality targets can be met by increasing the digital economy and enhancing regional environmental governance cooperation.

Keywords: digital economy; carbon emission reduction; difference-in-differences model; spatial Durbin mode; eastern seaboard cities

1. Introduction

The extensive use of fossil fuels, primarily coal, brought on by the wave of industrialization and modernity has worsened environmental pollution and global warming [1]. China's eastern coastal region is a major agglomeration of its industrial development, and most of its cities, some of which are also coal resource cities, are experiencing rapid economic development. These cities have nearly half of the nation's digital economy and relatively high carbon emissions. Compared to other cities, East Coast cities show significant differences in digital economy development and carbon emissions, making them an ideal case study for examining the relationship between digital economy carbon emissions. Along with the increasing demand for energy, the environmental pressure is increasing. In this context, the digital economy is rapidly growing as a novel and productive force, presenting potential solutions to environmental obstacles. The digital economy effectively reduces energy and carbon emissions by optimizing energy use and industrial structure, reducing unnecessary economic activities, promoting the development of the carbon trading market, supporting carbon capture and storage technologies, and guiding the public to participate in carbon emission reduction in a variety of ways, demonstrating its great

potential and important role in the field of carbon emission reduction. The 14th Five-Year Plan and 2024 Government Work Report, which are key policy papers for China's economic development, highlight the importance of digitization as a crucial step towards improving and modernizing the country's economic system. China's coastal areas play a crucial role in promoting new, high-quality productive forces as they serve as the main zone for marine-based economic activity. Thus, it is crucial to analyze the link between the digital economy and energy-related carbon emissions in these places must be examined. Additionally, it is important to investigate the potential intermediate effects and variations in strategies for reducing emissions. This research is essential for promoting the strong growth of new productive forces and achieving the "double carbon" target at an earlier stage.

The purpose of this paper is to explore the relationship between the digital economy and carbon emission reduction in China's eastern coastal region through theoretical and empirical analyses so as to promote the green and low-carbon development of the region and other regions and to contribute to the realization of the "dual-carbon goal".

2. Literature Review

Owing to its unique functioning and potential, the digital economy has increased economic progress and rejuvenated the global economy. The current research primarily examines the economic impacts of the digital economy, with a particular emphasis on five key areas: economic growth [2–4], high-quality development [5–7], improvement of technological innovation [8,9], total factor productivity enhancement [10–13], and industrial structure upgrading [14,15]. Certain researchers also prioritize examining the motivating impact of the digital economy on the environment, such as network information through the dissemination of digital media, which may encourage public adoption of a green environmental preservation mindset that boosts environmental pollution control research [16,17]. Furthermore, the digital economy sector directly improves environmental circumstances. For instance, the digital economy has proven effective in reducing industrial pollutant emissions [18,19]. This has greatly strengthened the efficacy of governmental environmental management and elevated the caliber of urban settings [20–22]. Li, M. G. et al. [23] empirically analyzed the significant effect of DE on carbon pollution reduction using the quasi-natural experiment in the National Comprehensive Experimental Zone for Big Data (NCTZ), using the DID model and the mediated effects model.

The increase in carbon emissions resulting from energy consumption has worsened the problem of urban climate change in recent years. Previous literature has primarily focused on studying the digital economy and energy carbon reduction separately. Nevertheless, there is a scarcity of studies on the convergence of these two disciplines specifically examining the effects of informatization [24], information technology [25,26], and Internet development [27,28] on energy carbon emissions. Some experts suggest that the digital economy reduces carbon emissions and pollution, whereas others worry that it may increase carbon emissions. For instance, a study by Wu et al. found that the construction of smart cities (SCC) effectively reduces urban environmental pollution [29]. Additionally, there is evidence of a significant U-shaped relationship between the digital economy and the intensity of carbon emissions [30,31].

In summary, past studies on the digital economy and energy carbon emissions offer useful insights for this study. However, further exploration is required to further explore these topics. First, there is little existing literature on carbon emissions associated with energy consumption in the digital economy, and there is a lack of empirical literature examining the link between the digital economy and carbon emission reduction. In addition, most of the existing studies have been conducted at the level of all provinces and cities or individual provinces and cities, and there is a lack of in-depth studies on eastern coastal cities, for which studies are necessary in the eastern coastal region of China as a national pioneer zone for digital economy development. Secondly, the current research explored the correlation between the digital economy and carbon emission reduction from both theoretical and empirical perspectives. However, little attention has been paid to how the

development of the digital economy has had different impacts in different places. Finally, most studies have primarily investigated the influence of the two and their endogenous mechanisms, overlooking the spatial spillover effect caused by the development of the digital economy.

In view of this, by examining the relationship between policies and carbon emission reduction in the National Digital Economy Development Pilot Zone in East China's coastal cities, this study draws findings consistent with existing studies that digital economy development promotes urban carbon emission reduction and complements current research on the environmental impacts of the digital economy in coastal city regions based on existing studies. Secondly, this study investigates how the digital economy affects carbon emission reduction in different regions, focusing on analyzing and combining the different characteristics of different zones and the city's own characteristics along the eastern coast. Finally, it analyzes the spillover effects of digital economy policies on these cities, providing theoretical support and practical guidance for understanding the relationship between the digital economy, carbon emissions reduction, and global warming.

The paper is organized as follows. Section 2 presents relevant research, outlining applications of the digital economy in various fields and research on the relationship between the digital economy and carbon emissions. Section 3 briefly describes the policy and analyzes the mechanisms of the digital economy and energy carbon emissions. Section 4 briefly describes the estimation methodology and data used in the study. Section 5 presents the empirical results and a discussion. Section 6 further analyzes heterogeneity and spatial spillover effects. Section 7 concludes the paper. Finally, Section 8 contains a discussion of the article and policy recommendations.

3. Policy Proposals and Research Hypotheses

3.1. Policy Proposal

In the current era of the digital economy, data are crucial production components that contribute significantly to the advancement of consumption, investment, and employment. Nevertheless, the progress of China's digital economy is limited by fundamental technological limitations. To further advance the growth of the digital economy, China released the 'Implementation Program of the National Pilot Zone for the Innovative Development of the Digital Economy' in 2019 (hereafter referred to as the Pilot Zone Policy). This program specifically suggests the creation of pilot zones in Hebei (Xiong'an New Area), Zhejiang, Fujian, Guangdong, Chongqing, and Sichuan, among other regions, to foster innovative development in the digital economy. The government will implement a set of policies on the digital economy in conjunction with pilot zones to facilitate seamless integration of digital industrialization and industrial digitization. Simultaneously, enterprises will be guided by these policies to actively engage in digital transformation, establish clear objectives for transformation, and collectively drive the prosperous growth of the digital economy. Consequently, the pilot-zone policy node used in this study was 2019.

3.2. Research Hypothesis

According to the content of the national digital economy innovation and development policy and carbon emission factor-related literature research, the development of the digital economy improves digital governance capacity by upgrading technological innovation, adjusting industrial structure, and optimizing factor allocation, which is also an important focus point for reducing energy and carbon emissions. As a result, the logical analytical framework for digital economy development impacting carbon emission reduction in China's eastern coastal cities is built around three components: the industrial upgrading effect, the technology innovation effect, and the resource allocation effect.

3.2.1. Technological Innovation Effect

Digital technology is a significant catalyst for innovation in green technology [13]. Firstly, combining the digital economy with energy-saving and low-carbon technologies

allows established businesses to become knowledge- and technology-intensive, reducing carbon emissions and enhancing efficiency. Secondly, technological innovation can enhance the utilization of renewable energy sources, gradually replacing conventional energy sources such as coal and petroleum and driving the transition towards a diversified, cleaner, and lower-carbon energy structure. Thirdly, digital technology in industry optimizes pollution management measures and connects equipment and real-time collection of sewage data, thereby promoting environmentally friendly development of the industry and facilitating adjustments to the energy structure and utilization efficiency. Accordingly, the derivation of hypothesis 1 is as follows:

Hypothesis 1. *The digital economy delivers fresh kinetic energy to lower carbon emissions by enhancing technological innovation.*

3.2.2. Industrial Upgrading Effect

The digital economy is spearheading the shift in industrial structure from being reliant on capital and labor to being focused on digital and technological advancements [32]. From the perspective of industrial digitization, the rise of industries that rely on data as a fundamental component is accelerating the digital economy, enhancing the efficient allocation of resources, decreasing overall carbon emissions in the production chain, and facilitating the enhancement of carbon emission performance. At the level of digital industrialization, digital technology has significantly improved production efficiency in various industries and strengthened the market competition mechanism, which promotes industry integration and development. The streamlining of industrial structures has resulted in efficient allocation of resources in the production sector, leading to a decrease in carbon emissions [33]. Accordingly, derivation of hypothesis 2:

Hypothesis 2. *The digital economy presents new prospects for decreasing energy carbon emissions by altering the industrial structure.*

3.2.3. Factor Allocation Effect

Currently, China's coal consumption accounts for a significant proportion of the energy structure, and energy-consuming enterprises often rely on traditional production technologies and models to obtain economic benefits through large inputs of production factors. The digital economy uses data as a production component and has the benefits of replicability, scalability, and low cost. These advantages enable the optimization of resource flow, thereby improving the resource utilization efficiency and compensating for the limitations of traditional production factors [20]. The digital economy successfully integrates data elements into conventional production factors, generating a high-quality combination of production factors, boosting energy conservation, and minimizing carbon emissions. From a production standpoint, digital elements are seamlessly integrated into the production process to achieve efficient resource utilization, reduce excessive energy consumption in traditional industries, and enhance resource utilization efficiency. These digital elements are characterized as being green, sustainable, and of high quality, contributing to a more environmentally friendly and economically efficient production process. Accordingly, the derivation of hypothesis 3 is as follows:

Hypothesis 3. *The digital economy presents a new way of minimizing energy carbon emissions by optimizing component allocation.*

4. Research Design

4.1. Model Construction

Regarding the impact of the establishment of the National Pilot Zone for Innovative Development of the Digital Economy on China's eastern coastal cities, double-difference modeling is one of the methods used to effectively identify its causal effects. This study employs a double difference model to analyze the influence of pilot area policies on energy carbon emissions in eastern coastal cities to evaluate their carbon reduction effect:

$$C_{it} = \beta_0 + \beta_1 \text{treat}_i \times \text{post}_t + \beta_2 X_{it} + \mu_i + \mu_t + \varepsilon_{it} \quad (1)$$

where Equation (1) is a double fixed-effects model that considers the city and year. The explanatory variable C_{it} is the cumulative amount of carbon emissions from energy use in city i during time t. $treat_i \times post_t$ is the major independent variable in this study, which is the cross term between the time of policy enactment and whether it is a treatment group or not; β_1 is the coefficient that this study focuses on, as the true effect of the policy in eastern coastal cities; μ_i denotes the individual fixed effect; μ_t denotes the time fixed effect; and ε_{it} denotes the random error term.

4.2. Variable Description and Data Sources

4.2.1. Explained Variable: Energy Carbon Emissions (C)

Using the approach of the Wang X. M. et al. [34], CO_2 emissions from 31 types of energy sources in oversized industries were measured in 81 cities above the prefecture level on the east coast using the carbon emission factor approach.

4.2.2. Explanatory Variables

Pilot zone policy (*DID* = *treat* × *post*), *treat* × *post* is the dummy variable interaction term between each city and the time of policy implementation.

4.2.3. Mediating Variables

Technological innovation (*Pat*) is reflected by the number of patents granted per capita; industrial upgrading (*Ris*) is measured by the ratio of value-added of the third industry to the second industry, in which the secondary sector is industry (including extractive industries, manufacturing, water, electricity, steam, hot water, and gas) and construction; the tertiary sector is all industries other than those mentioned above, and mainly includes the distribution sector, the sector that serves production and living, and the sector that serves to improve the level of science and culture as well as the quality of the population; and resource allocation efficiency (*Tfp*) is reflected by the city's total factor productivity, in which the inputs are the fixed capital stock and the number of people in the workforce, and the output is the real GDP.

4.2.4. Control Variables

The impact of the digital economy on carbon emissions reduction does not necessarily work only through the national digital economy innovation and development pilot zone policy, but non-pilot zones can also utilize the digital economy to reduce carbon emission levels in their regions in other ways. Based on relevant literature, the following control variables were selected in this study: The level of economic development (*Pgdp*) is defined by the logarithm of urban per capita GDP; population density (*Pop*) is characterized by the total population divided by the land area at the end of the year; the degree of openness to the outside world (*Fdi*) is defined by the ratio of real foreign direct investment to GDP; the degree of urban construction (*H*) is defined by the area of land utilized for urban building; the intensity of environmental regulation (*Er*) is characterized by the ratio of the amount of environmental pollution investment completed to GDP; the relative share of energy consumption in overall energy consumption of each city is the defining characteristic

of energy consumption structure (*Ec*); and the intensity of energy consumption (*Ei*) is characterized by the GDP per unit of energy consumption.

4.2.5. Data Sources

Because of the constraints on the statistical information of certain cities, this study ultimately chose the panel data of 81 cities above the prefecture level on the east coast of China (excluding Hong Kong, Macao, and Taiwan) for 2012–2021. The primary sources of data on energy carbon emissions in this study are the 2013–2022 China Energy Statistical Yearbook, the China Environmental Yearbook, and the 2013–2022 statistical yearbooks of cities above the prefecture level. Additionally, some unpublished data from the Internet were obtained from the statistical bureaus of cities above the prefecture level. The 2013–2022 China Urban Statistical Yearbook, together with the Yearbooks of cities at different levels and above and the National Economic and Social Development Statistical Bulletins from prior years, provided more pertinent economic and social statistics. Interpolation was used to address the lack of data for specific years. Using known data points, the approach creates a continuous function or model that predicts missing values. Descriptive statistics of variables are detailed in Table 1.

Table 1. Variables defined in descriptive statistics.

Variable Category	Variable Symbol	Sample Size	Mean	Standard Deviation	Min	Max
Explained variable	*C*	810	4622.000	4648.000	23,766.000	99.040
Explanatory variable	*DID*	810	0.137	0.344	1.000	0.000
Mediating variable	*Ris*	810	1.157	0.551	5.348	0.338
	Pat	810	8.666	1.579	12.940	1.946
	Tfp	810	0.419	0.093	0.736	0.155
Control variable	*InPgdp*	810	11.110	0.518	12.120	9.972
	Pop	810	6.340	0.534	7.699	5.042
	Fdi	810	0.017	0.015	0.080	0.001
	H	810	224.300	208.600	1046.000	24.000
	Er	810	0.003	0.001	0.008	0.001
	Ec	810	7.533	19.000	135.000	0.071
	Ei	810	0.000	0.000	0.001	0.000

5. Analysis of Empirical Results

5.1. Benchmark Regression

Table 2 shows the benchmark regression findings for energy carbon emissions of the digital economy. Column 1 controls only for city fixed effects and year fixed effects, that is, the effect of policy variables on carbon emission reductions. However, since carbon emission reductions are also affected by other factors, column 2 is an addition of seven control variables to column 1, making the net effect of the results stronger. Column (1) displays the results with only city and time fixed effects controlled for, while column (2) includes additional control variables based on column (1). The results indicate that the double-difference coefficient is significantly negative at the 5% significance level. This suggests that the pilot zone policy efficiently decreases energy carbon emissions in coastal areas and provides a strong incentive to minimize carbon emissions.

Table 2. Benchmark regression results.

Variants	(1)	(2)
DID	−0.0767 (0.0855)	−0.1433 ** (0.0571)
InPgdp		0.0424 (0.1440)
Pop		−0.1454 (0.5518)
Fdi		6.8005 (4.2108)
H		−0.0003 (0.0003)
Er		0.2253 (8.5644)
Ec		−0.0025(0.0048)
Ei		4074.0598 *** (338.7760)
Cons	7.8738 *** (0.0416)	1.3493 (3.6953)
N	810	730
R^2	0.1320	0.567
Year	YES	YES
City	YES	YES

Values in parentheses are standard errors; *** and ** are each 1 significant at the 1% and 5% levels. Year and city control for time and individual fixed effects, respectively. Cons denotes the constant term below.

5.2. Parallel Trend Testing

The parallel trend test is the most important step in constructing the *DID* model and is a prerequisite for the *DID* model. Before using the *DID* model for empirical analysis, the parallel trend test must be carried out first. If the variables pass the parallel trend test, then the *DID* model can be constructed initially for empirical analysis, and vice versa. To verify whether this research sample meets the requirements of parallel trends, we created a model based on the methodology of Wang B.B. [35] and others:

$$C_{it} = \beta_0 + \sum_{j\geq -5}^{2} \theta_j treat_i \times post_t^j + \beta_1 X_{it} + \mu_i + \mu_t + \varepsilon_{it} \quad (2)$$

In Equation (2), $post_t^j$ is a dummy variable and $post_t^j$ takes 1 when $j > 0$, such as where t represents the jth year after the introduction of the pilot zone policy, and 0 otherwise; and $post_t^j$ takes 1 when $j < 0$, such as when t is the jth year before the policy, and 0 otherwise. This study examines the time leading up to the 5th phase of policy implementation in the pilot zone and compares it to the 5th phase of policy implementation itself. The pre-policy treatment period served as the reference period. The remaining variables are consistent with the basic regression.

Figure 1 provides a comprehensive display of the parallel trend test outcomes. The horizontal axis represents the number of years before and after the establishment of the test area, and the vertical axis represents carbon emissions. Dashed lines represent confidence intervals. Upon examining the effects of the pilot zone policy on carbon emission reduction in eastern coastal cities, it is evident that there is no substantial disparity in energy carbon emissions between the pilot and non-pilot zones prior to the implementation of the policy. Prior to the implementation of legislation, these locations had comparable patterns of carbon emissions, meeting the prerequisite conditions of parallel trends. During the initial year following the implementation of the *DID* coefficients, the pilot zones' DID coefficients exhibited a notable negative trend. This suggests that the energy and carbon emissions of coastal cities experienced a significant reduction after the policy was put into effect. This substantial change underscores the favorable impact of the digital economy on energy conservation and carbon reduction in eastern coastal cities. Furthermore, it demonstrates the considerable potential of the digital economy in environmental preservation.

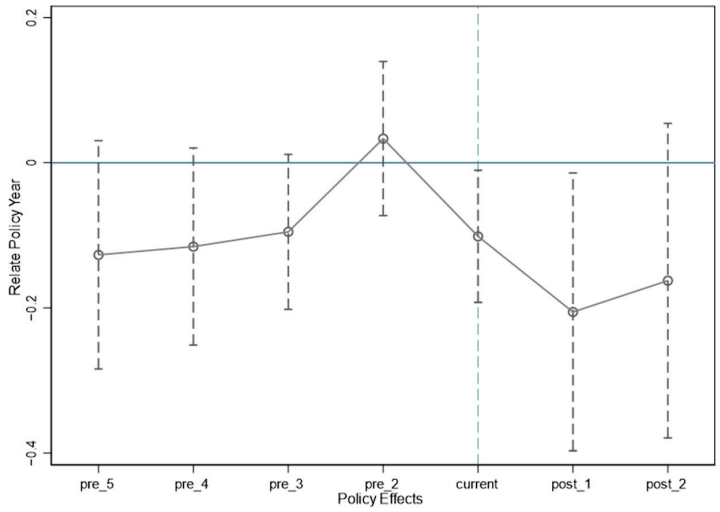

Figure 1. Parallel trend test.

5.3. Analysis of Results Based on PSM-DID Methodology

To ensure the accuracy of the first regression findings, ensure that the choice of experimental and control groups follows randomization, and remove any possible systematic errors, it is essential to conduct a thorough examination of the empirical data for their robustness. In this study, inspired by the literature of Shi D. C. [36] and others, the *PSM-DID* method was used for the measurement. The experimental and control groups were precisely selected through one-to-one nearest-neighbor matching to mitigate systematic estimation bias effectively. Logit regression was performed using policy dummy variables to obtain propensity matching scores, and cities with similar scores were selected as the control group. The post-matching test jointly supports this hypothesis, and the results show no significant difference between the groups, verifying the effectiveness of the *PSM-DID* method. Simultaneously, the probability distribution graph of the propensity score value (refer to Figure 2) visualizes the matching effect, and the distribution after matching is more convergent, proving that the matching effect is ideal and that the *PSM-DID* method is reliable.

Regression analysis was validated using *PSM-DID*. The regression results are shown in Table 3. The coefficients of the test area policy are significantly negative, indicating that the benchmark regression results are reliable. This suggests that the digital economy in eastern coastal cities has a reduction effect on energy carbon emissions, further confirming the reliability of the benchmark regression.

Table 3. *PSM-DID* methodology and regression results excluding other policy effects.

Variants	(1)	(2)	(3)
	PSM-DID		**Excluding Other Policy Effects**
DID	−0.1506 *** (0.0567)	−0.1512 ** (0.0573)	−0.1554 *** (0.0575)
D			−0.0539 (0.0561)
Cons	2.6877 (4.0043)	2.5941 (4.0063)	2.5381 (4.0150)
N	705	703	703
R^2	0.518	0.518	0.520
Control	YES	YES	YES
Year	YES	YES	YES
City	YES	YES	YES

The symbols *** and ** denote significance levels of estimated parameters at 1% and 5%, respectively. The standard errors are given in parentheses.

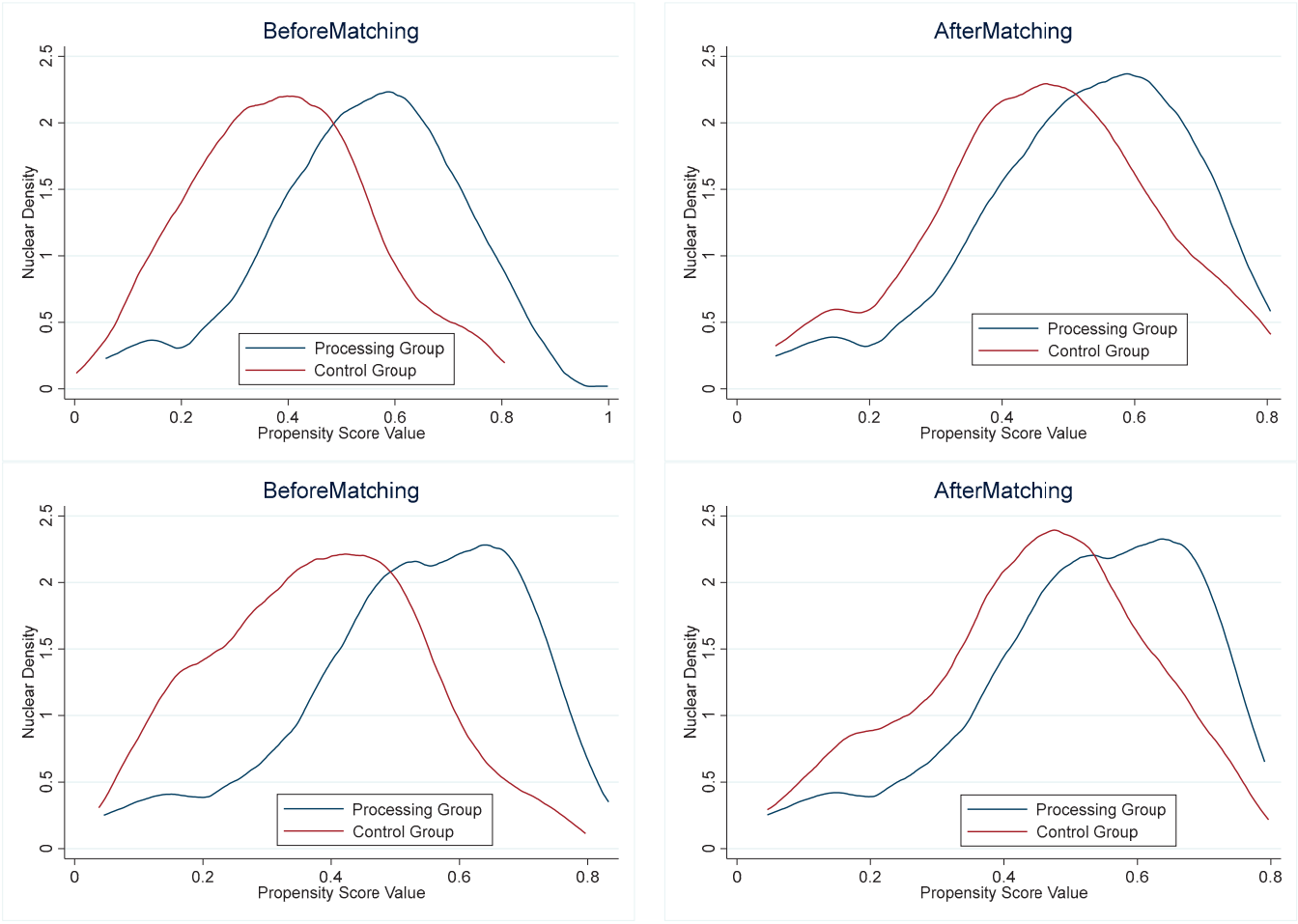

Figure 2. Density plot of probability distribution of propensity score.

5.4. Robustness Tests

5.4.1. Placebo Test

The placebo test, a key method to ensure the robustness of research findings, centers on the construction of virtual treatment groups or policy times. Inspired by the study of Ren S. G. et al. [37], this study innovatively utilizes the strategy of randomly assigning pilot cities. Of the 81 coastal cities above the prefecture level, a random selection of 30 cities was designated as the pseudo "pseudo experimental group" for the placebo test. These cities were considered to have adopted a pilot zone policy. Other cities naturally formed the control group. By iterating this procedure 500 times, we produced 500 sets of extraneous coefficients that include the regression coefficients, standard errors, and *p*-values of the "pseudo-policy dummy variables". If these coefficients approach 0, the dummy variables do not substantially impact the outcomes. Figure 3 demonstrates that the spurious coefficients are closely grouped around the value of 0 and follow a normal distribution. This suggests that the establishment of the test area had a minimal impact on the formation of the randomized "pseudo-experimental group". This strengthens the validity and dependability of the results.

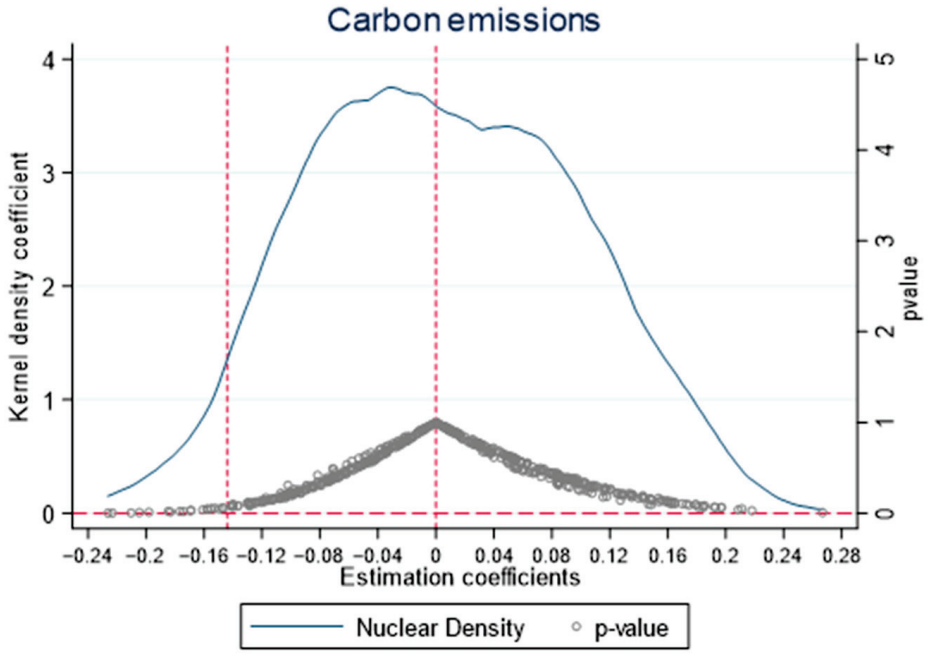

Figure 3. Placebo test.

5.4.2. Excluding Other Policy Effects

Considering the interference of other policies with the results, we performed a net effects test. The low-carbon city pilot strategy has gained widespread recognition for its significant contribution to lowering carbon emissions in metropolitan areas. Thus, this study integrates the policy into an analytical framework to thoroughly evaluate the policy impacts of establishing pilot zones. The policy has been implemented in stages since 2010, with the second stage of the policy being approved on 6 December 2012. Because of a delay in policy implementation, the second batch was processed in 2013. Thus, this analysis incorporates a multi-period difference model and creates the matching policy dummy variable *DID* (*treat* × *post*). The years 2010, 2013, and 2017 were considered key points in the implementation of this policy. This study uses a multi-period difference model and creates a policy dummy variable called *DID*. Additionally, a time dummy variable is established using the year of policy implementation as the reference point. Model (1) includes policy and temporal dummies for re-regression. Column (3) of Table 3 shows the regression findings. The findings indicate that the creation of the pilot zone alone has a substantial impact on decreasing energy and carbon emissions, even when considering the influence of other relevant policies. This shows the reliability of the baseline regression results.

5.4.3. Deletion of Central Cities

The data collected for this research include typical prefecture-level cities, province capital cities, sub-provincial cities, and municipalities. In view of the special characteristics of municipalities in terms of administrative mode and resource control, their common regression with other cities may introduce bias, and the sample data of municipalities are deleted in this study when conducting regression analysis. The regression coefficients in Column (1) of Table 4 indicate negative values, with a significance level of 5%. The emergence of the internet economy has had a substantial impact on decreasing energy-related carbon emissions. This further confirms the strength and dependability of previous conclusions.

Table 4. Deletion of central cities and addition of fixed effects.

Variants	(1)	(2)	(3)
	Delete Developed City	Increased Control for Fixed Effects	
DID	−0.1512 ** (0.0573)	−0.1433 ** (0.0575)	−0.1775 ** (0.0827)
Cons	2.5941 (4.0063)	1.4713 (3.7615)	1.6354 (3.6433)
N	703	729	711
R^2	0.518	0.970	0.979
Control	YES	YES	YES
Year	YES	YES	YES
City	YES	YES	YES

The symbols ** denote significance levels of estimated parameters at 5%, respectively. The standard errors are given in parentheses.

Furthermore, this study employs a high-dimensional fixed-effects model to thoroughly examine the relationships between variables. The purpose of this model is to minimize the potential influence of time-varying unobservable factors at the provincial level on the study's findings. China's eastern coastal cities include provincial-level municipalities; therefore, this study considers factors that exist at the provincial level but are not directly observable or measurable at the city level and that change over time. By doing so, this study aims to enhance the reliability and precision of the results. Columns (2) and (3) of Table 4 show the findings. Column (2) eliminates the influence of additional disruptive factors at the provincial level on the outcomes, while column (3) additionally eliminates the impact of unobservable factors at the provincial level caused by changes over time. Both columns yielded significantly negative results, reinforcing the reliability of the previous findings.

6. Further Analyses

6.1. Heterogeneity Test

6.1.1. Heterogeneity of City Location

In the analysis of heterogeneity, clear criteria for regional delineation are essential for a deeper understanding of the specific conditions and economic development patterns in different regions. Urban agglomeration engines driving China's economic growth possess notable advantages in scientific and technical innovation as well as in opening up to the global market. However, they have also emerged as primary contributors to carbon emissions over time [38]. Based on the geographic scope of the three major urban agglomerations of Beijing–Tianjin–Hebei, Yangtze River Delta, and Pearl River Delta, as well as their respective geographic locations on China's northern, central, and southern coasts, we categorize China's eastern coastal cities into three major regions: the north coast, the central coast, and the south coast [39]. Thus, this research experimentally investigates whether there are variations in the influence of digital economy growth on carbon emission reduction on the metropolitan agglomerations of the north coast, central coast, and south coast. Table 5 demonstrates that the digital economy significantly reduces energy carbon reduction in the North Coast, indicating a strong carbon control effect. However, on the Central Coast and the South Coast, although the regression coefficient remains negative, it is not significant. This phenomenon may be attributed to the suboptimal industrial structure of northern coastal cities, particularly exemplified by the Beijing–Tianjin–Hebei urban agglomeration. This region is still predominantly reliant on the highly polluting and energy-intensive secondary industries, resulting in significant energy consumption. Consequently, the cities around the northern shore have a greater drive and desire to enhance energy efficiency and mitigate environmental pollution.

Table 5. Urban regional heterogeneity.

Variants	(1)	(2)	(3)
	Northern Coastal Cities	**Central Coastal Cities**	**Southern Coastal Cities**
DID	−0.1900 ** (0.0719)	−0.0235 (0.0561)	−0.2950 (0.2529)
Cons	6.4134 (12.4846)	5.6214 (4.4617)	−0.0430 (5.4582)
N	253	216	261
R^2	0.760	0.800	0.503
Control	YES	YES	YES
Year	YES	YES	YES
City	YES	YES	YES

The symbols ** denote significance levels of estimated parameters at 5 %, respectively. The standard errors are given in parentheses.

6.1.2. Heterogeneity of Urban Resources

There are significant variations in economic development, social consumption, and Internet development levels among these cities. Some cities have better smart city infrastructure, which may result in different outcomes in terms of carbon emission reduction owing to the pilot zone policy. Thus, this study examines how the policy affects each coastal city.

The digital economy is growing rapidly due to data components [40]. This study measures urban Internet development by counting fixed Internet broadband users. The sample cities were divided into two groups by taking the average value of Internet development water in the corresponding year. Cities above the average value are defined as cities with high Internet development levels, and those below were defined as cities with low Internet development levels. City values above the average indicate strong Internet growth, while values below the average indicate poor Internet development. Since social consumption is closely tied to economic development, income, and employment, it is a useful indicator of a city's economic health. Social consumption may also reflect the progress of the digital economy. This study measures coastal city social consumption using aggregate retail sales of social consumer products. Above the average value of social water consumption for the corresponding year, a city is defined as having a high social consumption level and vice versa. Cities with a social consumption water value above the average have high social consumption, whereas those below the average have low social consumption. The regression analysis Table 6 shows that, in the sub-sample test results of heterogeneity analysis, the pilot zone legislation affects weaker cities more in terms of Internet growth, indicating that higher-level cities already had a foundation for using digital technology to transform the low-carbon economic development model. However, towns with limited Internet penetration have reduced carbon emissions more due to the strategy. The sub-sample test on social consumption levels shows that the pilot zone reduces energy and carbon emissions more significantly and statistically in places with lower social consumption. However, cities with higher social consumption have a smaller influence. High social consumption is linked to strong economic development and financial support for cities. These cities are more likely to support digital economy enterprises.

Table 6. Heterogeneity of urban characteristics.

Variants	(1)	(2)	(3)	(4)
	High Level of Social Consumption	**Low Level of Social Consumption**	**High Level of Internet Development**	**Low Level of Internet Development**
DID	−0.0619 (0.0775)	−0.1518 ** (0.0692)	−0.0636 (0.0674)	−0.1814 ** (0.0749)
Cons	4.4404 (5.5851)	−0.8134 (4.1823)	3.6693 (5.8080)	2.0533 (4.3155)
N	244	486	291	439
R^2	0.704	0.613	0.712	0.619
Control	YES	YES	YES	YES
Year	YES	YES	YES	YES
City	YES	YES	YES	YES

The symbols ** denote significance levels of estimated parameters at 5%, respectively. The standard errors are given in parentheses.

6.2. Mediating Effect Test

The regression findings show that the digital economy reduces energy and carbon emissions in the study area. This influence interacts with technical innovation, industrial upgrading, and resource allocation. In order to explore the intrinsic mechanism of this process more deeply, we draw on the relevant practices of Jiang T. [39] to validate the influence of digital economy growth on mediating variables. Subsequently, we create the mediating effect model as outlined below:

$$Mev_{it} = \beta_0 + \beta_1 treat_i \times post_t + \beta_2 X_{it} + \mu_i + \mu_t + \varepsilon_{it} \quad (3)$$

Mev_{it} in Equation (3) serves as a mediator, but the definitions of the other variables remain consistent with Equation (1). The results of the mediating impact examination are shown in Table 7: At a significance level of 1%, the estimated coefficient of the cross-multiplier term (*treat* × *post*) in Column (2) is considerably negative. This means that the development of the pilot region has a considerable impact on the promotion and application of technical innovation. This method facilitates the transition of the energy consumption structure towards diversity, cleanliness, and low carbonization. As a result, it enhances energy efficiency, promotes energy conservation, and reduces emissions. Thus, hypothesis 1 has been confirmed. Upon further examination of Column (3), it is evident that the calculated coefficient of the cross-multiplier component (*treat* × *post*) is significantly negative at the 5% significance level. This clearly demonstrates that the digital economy policy has a beneficial impact on promoting the progressive and efficient development of China's industrial structure, enhancing cooperative collaboration through the clustering of manufacturing and service industries, and facilitating the transformation of coastal regional cities towards environmentally friendly and low-carbon practices. Thus, hypothesis 2 has been confirmed. Furthermore, the data in Column (4) indicate that the coefficient and factor allocation are positively correlated and significant at the 5% level. This finding suggests that the integration of data elements with traditional production factors is an important trend in the era of the digital economy, which, through technological innovation, industrial synergy, and policy guidance, has led to the formation of a high-quality combination of highly efficient, innovative, and sustainable production factors that promote the high-quality development of the economy. Consequently, this integration enhances the efficiency of resource allocation; reduces energy consumption and carbon emissions in coastal cities; and contributes to the creation of a clean, aesthetically pleasing, harmonious, and well-organized urban environment. Thus, hypothesis 3 has been confirmed.

Table 7. Intermediation effects.

Variants	(1)	(2)	(3)	(4)
	Benchmark Regression	**Technological Innovation**	**Industrial Upgrading**	**Resource Allocation**
DID	−0.1433 ** (0.0571)	−0.1608 *** (0.0538)	0.1755 ** (0.0770)	0.0247 ** (0.0095)
Cons	1.3493 (3.6953)	−3.9506 ** (1.7749)	−9.5120 *** (2.9819)	0.5711 (0.5532)
N	730	730	730	730
R^2	0.567	0.079	0.725	0.092
Control	YES	YES	YES	YES
Year	YES	YES	YES	YES
City	YES	YES	YES	YES

The symbols *** and ** denote significance levels of estimated parameters at 1% and 5%, respectively. The standard errors are given in parentheses.

6.3. Tests for Spatial Spillover Effects

6.3.1. Spatial Autocorrelation and Durbin Model Applicability Test

The digital economy, with its notable geographical network properties, has the ability to lessen spatial correlation in the geographic dimension compared to the conventional form of economy. As a result, the spatial spillover effect is significantly enhanced [41]. All prior findings validate that cities in coastal areas see robust growth in the digital economy after the introduction of pilot zone legislation, resulting in a substantial decrease in energy-related carbon emissions. A city's development policies are often learned and emulated by other affiliated cities, making energy consumption variables of spatially affiliated cities have obvious spatial spillover effects [42]. This study utilized the Spatial Durbin Model with Double Difference (*SDM-DID*) to thoroughly investigate the process by which policy affects carbon emission reduction in the region and neighboring regions. Specifically, it aims to investigate the spillover effect of emission reduction from cities during the policy implementation. In this process, this study integrates geographic and economic distances and constructs geo-economic nested spatial weights *W*. Specifically, spatial weight matrices W_1 and W_2 are established based on the geographic and economic distances of the cities, respectively, where W_1 is measured by the latitudinal and longitudinal distances between the cities and W_2 is characterized by the reciprocal of the square of the disparity in per-capita GDP between the cities.

The results of *the Global Moran's I index* test for energy carbon emissions for various years are shown in Table 8. All *the Global Moran's I index* are larger than 0 and indicate a consistent rising trend. This study also includes a scatter plot of *the Local Moran's I index* in the year of the pilot zone policy (2019) (refer to Figure 4). The scatter plot and other evidence suggest that there is a strong spatial correlation in the impact of the policy implementation on carbon emission reduction in eastern coastal cities. This correlation satisfies the requirements for applying the double-difference spatial Durbin model.

Additionally, this research offers a valuable understanding into the potential degeneration of into double-difference space Durbin model. The potential for it to be converted into a dual-difference spatial lag or error model was analyzed. By arranging and analyzing the collected data and presenting the findings in Table 9, it is evident that the LR test disproves the initial hypothesis, hence validating the appropriateness of selecting this model. Based on this rationale and the Hausman test results, a double-fixed model including both time and space is used to effectively predict digital economic growth by reducing pollution.

Table 8. *Global Moran's I* index of energy carbon emissions.

Time	Matrix	*I*	E(*I*)	Sd(*I*)	*z*	*p*-Value
2017	W_1	0.083	−0.013	0.019	5.029	0.000
	W_2	0.105	−0.013	0.129	0.906	0.365
2018	W_1	0.101	−0.013	6.010	9.243	0.000
	W_2	0.141	0.013	0.129	1.185	0.236
2019	W_1	0.142	−0.013	0.020	8.020	0.000
	W_2	0.221	−0.013	0.132	1.772	0.076
2020	W_1	0.183	−0.013	0.020	9.973	0.000
	W_2	0.365	−0.013	0.134	2.825	0.005
2021	W_1	0.168	−0.013	0.020	9.243	0.000
	W_2	0.330	−0.013	0.134	2.560	0.010

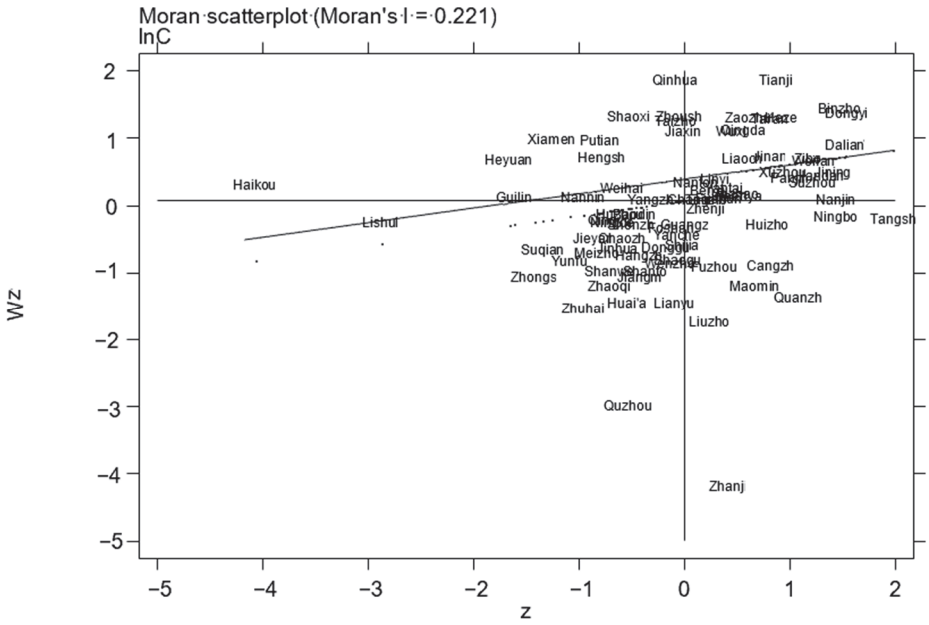

Figure 4. *Localized Global Moran's I Index* Chart for 2019.

Table 9. Model applicability test result.

Type of Test	Statistical Value	*p*-Value
LR_spatial_lag	2259.090	0.000
LR_spatial_error	38.850	0.000
Hausman Test	25.030	0.000

6.3.2. Spatial Spillover Effects of Policies

After an in-depth analysis, this study provides a comprehensive examination of the regression findings of the double-difference spatial Durbin model. It thoroughly breaks down the data to determine the direct, indirect, and overall effects of explanatory factors. The precise outcomes are shown in Table 10. After considering both geographical distance and economic distance, it was discovered that the coefficient of the spatial lag term has a significant negative impact on urban pollution emissions caused by the policy. This directly confirms the existence of a spatial spillover effect, where the policy implemented affects the energy and carbon emissions of eastern coastal cities. The presence of digital economic growth, regardless of other factors influencing energy, has a substantial impact on reducing both energy consumption and carbon emissions in the city. Furthermore, there is evidence to suggest that the digital economy has a favorable effect on energy consumption and carbon emissions in nearby cities. This phenomenon may be ascribed to the successful

promotion of the data element flow in each city via the pilot zone policy, resulting in the growth of both the city and its adjacent cities.

Table 10. Double-difference spatial Durbin model regression results.

Variants	(1) $SDM\text{-}W_1$	(2) $SDM\text{-}W_2$
Main	−0.1064 ** (0.0427)	−0.0888 ** (0.0425)
Wx	−1.1169 *** (0.3517)	−0.0823 ** (0.0429)
Indirect	−0.0961 ** (0.0435)	−0.0874 ** (0.0438)
Direct	−0.8284 *** (0.2562)	−0.0843 ** (0.0415)
Total	−0.9245 *** (0.2637)	−0.1717 *** (0.0644)
Control	YES	YES
Year	YES	YES
City	YES	YES
Rho	−0.3640 * (0.1917)	−0.0012 (0.0327)
$Sigma^2$	0.0736 *** (0.0037)	0.0746 *** (0.0037)
N	810	810

The symbols ***, **, and * denote significance levels of estimated parameters at 1%, 5%, and 10% levels, respectively. The standard errors are given in parentheses.

7. Conclusions

This study is based on balanced panel data of 81 cities along the east coast of China from 2012 to 2021. (1) The digital economy plays a crucial role in facilitating the decrease in carbon emissions in eastern coastal cities. The National Digital Economy Innovation and Development Pilot Zone policy significantly promotes the reduction in carbon emissions in China's eastern coastal cities. This conclusion holds true even after conducting rigorous tests to ensure the accuracy and reliability of the findings, such as PSM-DID, parallel trend, and placebo tests. (2) An examination of heterogeneity reveals that the digital economy provides a greater impact on lowering greenhouse gases in northern coastal cities compared to central and southern coastal areas. Additionally, this impact is particularly pronounced in coastal towns characterized by limited Internet infrastructure and reduced levels of social engagement. (3) The mediating effect test demonstrated that the digital economy, via technical innovation, industrial upgrading, and resource allocation, may significantly improve the digital governance capability and achieve the goal of reducing carbon emissions. (4) An additional examination using the double-difference spatial Durbin model demonstrates that the advancement of the digital economy diminishes local energy consumption and carbon emissions, while concurrently enhancing environmental conditions in adjacent areas. In terms of the spatial impact, the pilot area policy has a notable spillover effect on energy and carbon emissions in coastal cities. This suggests that the digital economy can effectively decrease energy and carbon emissions in both the pilot city and its neighboring cities. Furthermore, the development of the digital economy can facilitate inter-city collaboration and the joint governance of the urban environment in coastal regions.

Exploring the impact of the digital economy on carbon emission reduction in China's eastern coastal cities, as a new economic form, can help clarify the relationship between the digital economy and energy carbon emissions, as well as provide recommendations for furthering China's digital economy development strategy and the transformation and upgrading of traditional industries. For other developing countries similar to China, which are mainly industrialized and have large energy consumption, as well as developed cities with a high level of digital economy development and are committed to realizing the dual-carbon goal, the study results of the impact of the digital economy on the carbon emissions of China's eastern coastal cities can be used as a reference to implement carbon emission reduction measures in response to carbon emission reduction.

8. Discussions

Based on the quasi-natural experiment methodology of the National Pilot Zone for the Innovative Development of Digital Economy, this study measures for the first time the impact of digital economy on carbon emission reduction in coastal cities in eastern China. This study finds that the development of the digital economy significantly reduces urban carbon emissions, which is consistent with the findings of existing related literature [23,30,31]. According to a different study, the digital economy not only encourages local carbon emission reduction, but also inspires adjacent cities to follow suit.

The main contribution of this study is to provide more theoretical and empirical support for the impact of the digital economy on carbon emission reduction in China's eastern coastal cities, enriching the research results in this field. Based on the findings of this study, the following policy recommendations are proposed:

(1) Deepening the integration of the digital economy and green low-carbon development policies. Relying on the National Pilot Zone's achievements to improve the statistical monitoring and decision-making system using big data, AI, and blockchain. Ensuring a clear understanding of digital economy trends and risks. Creating a link between the digital economy and green low-carbon projects; encouraging the matching of supply and demand for green products and services via the digital economy platform; and hastening the marketization and commercialization of green, low-carbon technologies.

(2) Strengthening the synergy between technological innovation and industrial upgrading. Leveraging digital technology to enhance operational efficiency in production, management, sales, etc., encourages enterprises to adopt cloud computing, big data, and AI to innovate production methods and strengthens R&D, product upgrades, and service innovations to boost the competitiveness and sustainability of traditional industries. Fostering talent with an international vision and innovation. Assisting in digital economy growth; promoting the broad use of cloud computing, industrial Internet, and big data; and improving the application levels of fundamental technology. Encouraging the growth of businesses with creative potential in the fields of carbon capture and storage, clean energy utilization, and energy efficiency enhancement.

(3) Cities with diverse endowments should distribute the economic and social benefits of the digital economy considering local conditions. The results of the heterogeneity analysis in this study demonstrate that the growth of the digital economy has varying degrees of environmental welfare effects in various geographic locations and city characteristics, making it a useful resource for fostering the sector's development. Regional governments should develop targeted policies and plans to promote the development of the digital economy based on the size of the local city, the level of information technology, and the level of financial expenditure, rather than blindly copying the development experience of other regions to maximize the performance of the data-driven digital economy.

(4) Enhancing collaborative energy and carbon governance among cities. The combination of regional variability and phases of development has aided the rapid development of the digital economy. Eastern coastal towns continue to capitalize on their geographic advantages; expedite the upgrade of their information networks; establish digital industrial ecosystems that integrate collecting, transmission, and storage; and play a spreading role in the digital economy. Strengthening city exchanges on energy management, emission monitoring, and technology. Boosting city synergies in digital governance. Maximizing the "green" influence of the digital economy to promote sustainable urban development.

This study has made some headway in understanding how the Internet economy affects carbon emission reductions in coastal cities. However, there are still some restrictions and possibilities for future development:

(1) Based on the concept of data availability, this study's city panel data do not include all cities in China's eastern coastline provinces, and the representativeness of the sample needs to be enhanced. Future investigations are required in order to expand this database.

(2) This study has not thoroughly investigated the nonlinear relationship between national digital economy strategies and urban carbon emission reduction. In future research, we will further explore the nonlinear relationship to obtain a more exact and precise picture of the two.
(3) In this study, numerous control variables were chosen to correctly estimate the influence of the digital economy on energy and carbon emission reduction in coastal cities. Several elements are complex and can interact with each other. In the future, machine learning and other technologies can be used to improve performance. Furthermore, additional issues, such as environmental rules, may be addressed in the future.

Author Contributions: Conceptualization, Juanjuan Zhong and Ye Duan; methodology, Juanjuan Zhong; software, Juanjuan Zhong; validation, Ye Duan, Caizhi Sun; formal analysis, Juanjuan Zhong; investigation, Juanjuan Zhong; resources, Ye Duan; data curation, Juanjuan Zhong; writing—original draft preparation, Juanjuan Zhong; writing—review and editing, Ye Duan, Hongye Wang; visualization, Juanjuan Zhong; supervision, Ye Duan, Caizhi Sun; project administration, Ye Duan, Caizhi Sun; funding acquisition, Ye Duan, Caizhi Sun, Hongye Wang. All authors have read and agreed to the published version of the manuscript.

Funding: This study was supported by the National Natural Science Foundation of China (No. 72304056, No. 42101257), the Fundamental Research Funds for the Central Universities, China (DUT23RW405), the China Postdoctoral Science Foundation (No. 2020M670789), the National Key Fund for Social Sciences (No. 19AJY010) and Scientific Research Project of the Department of Education of Liaoning Province (No. JYTMS20231064).

Data Availability Statement: Data can be provided upon request.

Conflicts of Interest: The authors declare no conflicts of interest.

References

1. Zhao, Y.; Feng, Y.; Du, M.; Fraedrich, K. Annual and Seasonal Dynamics of CO_2 Emissions in Major Cities of China (2019–2022). *ISPRS Int. J. Geo-Inf.* **2024**, *13*, 181. [CrossRef]
2. Salahuddin, M.; Gow, J. The Effects of Internet Usage, Financial Development and Trade Openness on Economic Growth in South Africa: A Time Series Analysis. *Telemat. Inform.* **2016**, *33*, 1141–1154. [CrossRef]
3. Perez-Trujillo, M.; Lacalle-Calderon, M. The Impact of Knowledge Diffusion on Economic Growth across Countries. *World Dev.* **2020**, *132*, 104995. [CrossRef]
4. Xing, Z.; Huang, J.; Wang, J. Unleashing the Potential: Exploring the Nexus between Low-Carbon Digital Economy and Regional Economic-Social Development in China. *J. Clean. Prod.* **2023**, *413*, 137552. [CrossRef]
5. Jing, W.; Sun, B. Digital Economy Promotes High-Quality Economic Development: A Theoretical Analysis Framework. *Economist* **2019**, *2*, 66–73.
6. Zhang, Y.; Wang, M.; Liu, T. Spatial Effect of Digital Economy on High-Quality Economic Development in China and Its Influence Path. *Geogr. Res.* **2022**, *41*, 1826–1844.
7. Zhao, T.; Zhang, Z.; Liang, S. Digital Economy, Entrepreneurship, and High-Quality Economic Development: Empirical Evidence from Urban China. *Manag. World* **2020**, *36*, 65–76.
8. Cao, S.; Nie, L.; Sun, H.; Sun, W.; Taghizadeh-Hesary, F. Digital Finance, Green Technological Innovation and Energy-Environmental Performance: Evidence from China's Regional Economies. *J. Clean. Prod.* **2021**, *327*, 129458. [CrossRef]
9. Heo, P.S.; Lee, D.H. Evolution of the Linkage Structure of ICT Industry and Its Role in the Economic System: The Case of Korea. *Inf. Technol. Dev.* **2019**, *25*, 424–454. [CrossRef]
10. Lyu, Y.; Wang, W.; Wu, Y.; Zhang, J. How Does Digital Economy Affect Green Total Factor Productivity? Evidence from China. *Sci. Total Environ.* **2023**, *857*, 159428. [CrossRef]
11. Acemoglu, D.; Restrepo, P. The Race between Man and Machine: Implications of Technology for Growth, Factor Shares, and Employment. *Am. Econ. Rev.* **2018**, *108*, 1488–1542. [CrossRef]
12. Qiu, Z.; Zhou, Y. Development of Digital Economy and Regional Total Factor Productivity: An Analysis Based on National Big Data Comprehensive Pilot Zone. *Financ. Res.* **2021**, *47*, 4–17.
13. Wang, K.; Wu, G.; Zhang, G. Has the Development of the Digital Economy Improved Production Efficiency? *Economist* **2020**, *1*, 24–34.

14. Wu, J.; Lin, K.; Sun, J. Improving Urban Energy Efficiency: What Role Does the Digital Economy Play? *J. Clean. Prod.* **2023**, *418*, 138104. [CrossRef]
15. Zuo, P.; Jiang, Q.; Chen, J. Internet Development, Urbanization and the Upgrading of China's Industrial Structure. *Res. Quant. Tech. Econ.* **2020**, *37*, 71–91.
16. Xu, Y. Whether Informal Environmental Regulation from Social Pressure Constraints on China's Industrial Pollution? *Res. Financ. Trade* **2014**, *25*, 7–15.
17. Zhang, S.; Wang, Y.; Li, Y. Does Regional Haze Opinion Affect Air Quality? *Arid Zone Resour. Environ.* **2018**, *32*, 100–106.
18. Jiang, H.; Elahi, E.; Gao, M.; Huang, Y.; Liu, X. Digital Economy to Encourage Sustainable Consumption and Reduce Carbon Emissions. *J. Clean. Prod.* **2024**, *443*, 140867. [CrossRef]
19. Pan, W.; Xie, T.; Wang, Z.; Ma, L. Digital Economy: An Innovation Driver for Total Factor Productivity. *J. Bus. Res.* **2022**, *139*, 303–311. [CrossRef]
20. Guo, B.; Wang, Y.; Zhang, H. Will the Development of Digital Economy Improved Urban Air Quality—A Quasi-Natural Experiment Based on the National-Level Big Data Comprehensive Pilot Zone. *J. Guangdong Univ. Financ. Econ.* **2022**, *37*, 58–74.
21. Liu, H.; Cui, W.; Zhang, M. Exploring the Causal Relationship between Urbanization and Air Pollution: Evidence from China. *Sustain. Cities Soc.* **2022**, *80*, 103783. [CrossRef]
22. Zhang, H.; Duan, Y.; Yang, J.; Han, Z.; Wang, H. Can Green Finance Improve China's Haze Pollution Reduction? The Role of Energy Efficiency. *Environ. Dev.* **2023**, *45*, 100833. [CrossRef]
23. Liu, M.; Li, G. Research on the Impact of the Digital Economy on Carbon Pollution Based on the National Big Data Comprehensive Pilot Zone in China. *Sustainability* **2023**, *15*, 15390. [CrossRef]
24. Lange, S.; Pohl, J.; Santarius, T. Digitalization and Energy Consumption. Does ICT Reduce Energy Demand? *Ecol. Econ.* **2020**, *176*, 106760. [CrossRef]
25. Takase, K.; Murota, Y. The Impact of IT Investment on Energy: Japan and US Comparison in 2010. *Energy Policy* **2004**, *32*, 1291–1301. [CrossRef]
26. Zou, R.; Yang, J.; Feng, C. Does Informatization Alleviate Energy Poverty? A Global Perspective. *Energy Econ.* **2023**, *126*, 106971. [CrossRef]
27. Hao, Y.; Li, Y.; Guo, Y.; Chai, J.; Yang, C.; Wu, H. Digitalization and Electricity Consumption: Does Internet Development Contribute to the Reduction in Electricity Intensity in China? *Energy Policy* **2022**, *164*, 112912. [CrossRef]
28. Ren, S.; Hao, Y.; Xu, L.; Wu, H.; Ba, N. Digitalization and Energy: How Does Internet Development Affect China's Energy Consumption? *Energy Econ.* **2021**, *98*, 105220. [CrossRef]
29. Wu, D.; Xie, Y.; Lyu, S. Disentangling the Complex Impacts of Urban Digital Transformation and Environmental Pollution: Evidence from Smart City Pilots in China. *Sustain. Cities Soc.* **2023**, *88*, 104266. [CrossRef]
30. Cheng, Y.; Zhang, Y.; Wang, J.; Jiang, J. The Impact of the Urban Digital Economy on China's Carbon Intensity: Spatial Spillover and Mediating Effect. *Resour. Conserv. Recycl.* **2023**, *189*, 106762. [CrossRef]
31. Zhu, C.; Wang, Z.; Sun, B.; Yue, Y. Urban Digital Economy, Environmental Pollution, and Resident's Health–Empirical Evidence from China. *Front. Public Health* **2023**, *11*, 1238670. [CrossRef] [PubMed]
32. Wang, Y.; Liu, J.; Zhao, Z.; Ren, J.; Chen, X. Research on Carbon Emission Reduction Effect of China's Regional Digital Trade under the "Double Carbon" Target—Combination of the Regulatory Role of Industrial Agglomeration and Carbon Emissions Trading Mechanism. *J. Clean. Prod.* **2023**, *405*, 137049. [CrossRef]
33. Zhang, F.; Deng, X.; Phillips, F.; Fang, C.; Wang, C. Impacts of Industrial Structure and Technical Progress on Carbon Emission Intensity: Evidence from 281 Cities in China. *Technol. Forecast. Soc. Chang.* **2020**, *154*, 119949. [CrossRef]
34. Wang, X.; Wu, J.; Bai, B.; Wang, Z. Spatial Differentiation and Driving Factors of CO_2 Emissions: Analysis Based on 198 Cities at Prefecture Level and Above in China. *Econ. Geogr.* **2020**, *40*, 29–38.
35. Wang, B.; Mo, Q.; Qian, H. The Diffusion Models and Effects of the Local Environmental Policy Innovation—A Micro-Econometric Evidence from the Diffusion of River Chief Policy. *China Ind. Econ.* **2020**, *8*, 99–117.
36. Shi, D.; Ding, H.; Wei, P.; Liu, J. Can Smart City Construction Reduce Environmental Pollution? *China Ind. Econ.* **2018**, *6*, 117–135.
37. Ren, S.; Zheng, J.; Liu, D.; Chen, X. Does Emissions Trading System Improve Firm's Total Factor Productivity—Evidence from Chinese Listed Companies. *China Ind. Econ.* **2019**, *5*, 5–23.
38. Liu, M.; Li, S.; Li, Y.; Shi, J.; Bai, J. Evaluating the Synergistic Effects of Digital Economy and Government Governance on Urban Low-Carbon Transition. *Sustain. Cities Soc.* **2024**, *105*, 105337. [CrossRef]
39. Duan, Y.; Zhong, J.; Wang, H.; Sun, C. Analysis of the Spatial and Temporal Evolution of Energy-Related CO_2 Emissions in China's Coastal Areas and the Drivers of Industrial Enterprises above Designated Size—The Case of 82 Cities. *Sustainability* **2023**, *15*, 13374. [CrossRef]
40. Xie, F.; Zhang, S.; Zhang, Q.; Zhao, S.; Lai, M. Research on the Geographical Pattern, Evolution Model, and Driving Mechanism of Carbon Emission Density from Urban Industrial Land in the Yangtze River Economic Belt of China. *ISPRS Int. J. Geo-Inf.* **2024**, *13*, 192. [CrossRef]

41. Zhao, B. Impact of Digital Economy on Regional Innovation Performance and Its Spatial Spill over Effect. *Sci. Technol. Prog. Countermeas.* **2021**, *38*, 37–44.
42. Shao, S.; Fan, M.; Yang, L. Economic Restructuring, Green Technical Progress, and Low-Carbon Transition Development in China: An Empirical Investigation Based on the Overall Technology Frontier and Spatial Spillover Effect. *Manag. World* **2022**, *38*, 46–69+4–10.

Disclaimer/Publisher's Note: The statements, opinions and data contained in all publications are solely those of the individual author(s) and contributor(s) and not of MDPI and/or the editor(s). MDPI and/or the editor(s) disclaim responsibility for any injury to people or property resulting from any ideas, methods, instructions or products referred to in the content.

climate

MDPI

Article

Adaptation and Coping Strategies of Women to Reduce Food Insecurity in an Era of Climate Change: A Case of Chireya District, Zimbabwe

Everjoy Magwegwe [1], Taruberekerwa Zivengwa [2] and Mashford Zenda [3,*]

[1] SARChi Chair in South African Art and Visual Culture, Faculty of Art, Design and Architecture, University of Johannesburg, Bunting Campus, Auckland Park, 33 Twickenham Avenue, Johannesburg 2006, South Africa; emagwegwe@uj.ac.za
[2] Development Studies Department, Faculty of Arts and Humanities, Midland's State University, Private Bag 9055, Senga Road, Gweru, Zimbabwe; r2211253r@student.msu.ac.zw
[3] Centre for Ecological Intelligence, Faculty of Engineering and the Build Environment (FEBE), University of Johannesburg, Electrical and Electronic Engineering Science, Auckland Park Campus, Auckland Park, P.O. Box 524, Johannesburg 2006, South Africa
* Correspondence: mzenda@uj.ac.za

Abstract: The research investigated how women employ various adaptation and coping mechanisms to alleviate food insecurity resulting from the impacts of climate change. The documentation of the debate on the role of women in adaptation and coping with climate change is relatively limited. Climate change's effect on food security in semi-arid areas could potentially increase the population of individuals residing in severe poverty. Over the past three decades, Africa's sub-tropics have experienced irregular rainfall and prolonged droughts, which have negatively affected agriculture and food production. This research utilized a combination of qualitative and quantitative approaches within a mixed-method design, guided by the pragmatic paradigm. Based on the results of the study, water harvesting/dam construction and income generating projects (IGPs) were identified as the most effective coping strategies for women. This study recommends implementing awareness campaigns to educate women farmers about the negative effects of climate change and the need for integrated and comprehensive capacity-building frameworks. By understanding the challenges women face in adapting to and coping with climate change, it is hoped that more effective and sustainable solutions can be developed.

Keywords: adaptation; coping strategies; food insecurity; food production

1. Introduction

The report (2014) [1] from the Intergovernmental Panel on Climate Change (IPCC) asserts that greenhouse gas emissions are starting to impact the Earth's climate on a global scale. The IPCC and other researchers (Mikhaylov et al., 2020) [2] expect extreme weather events such as floods, droughts, and tropical storms to become more common and severe in Africa. This trend is consistent with recent climatic changes observed in southern Africa, including Zimbabwe (Phiri et al., 2021; Chanza and Musakwa, 2022; Rangarirai, Marnani and Rahhmat, 2023) [3–5].

Climate change poses a significant risk to food security in developing nations, notably in Africa, where the economy relies heavily on agriculture and is highly susceptible to climate-related impacts. As Zimbabwe's climate has shifted from semi-arid to arid, there is concern about the country's ability to feed its population (Govere, Nyamangara and Nyakutawa, 2019; Matsa, 2021) [6,7]. Climate-related risks, such as extended dry seasons, have become more common and severe, negatively impacting agricultural livelihoods, food security, and women's ability to cope with climate change (Govere et al., 2019; Mushore et al., 2021) [6,8].

The impact of climate change hits the poor harder, primarily because they depend more on natural resources and lack the resources to adjust to the shifting climate, as noted by Waha et al. (2013); Sujakhu et al. (2019); and Perkins (2021) [9–11]. Women are disproportionately impacted by climate change due to their higher representation among the world's impoverished populations and their increased dependence on threatened natural resources (Waha et al., 2013; Dewi et al., 2022) [9,12]. The varied effects of climate change on women and men stem from entrenched traditional roles, societal expectations, and unequal power dynamics, all of which constrain their abilities (Hlahla, 2022) [13].

Rural women encounter various obstacles that have adverse effects on their welfare and means of earning a living. These include an unequal distribution of responsibilities for procuring food, water, and fuel for cooking and heating (D'Exelle and Riedl, 2018; Tigabie et al., 2022) [14,15]. Despite playing a significant role in food production, processing, and preparation, women often lack access to and control over agricultural resources (Tigabie et al., 2022) [15]. In addition, they have limited access to maternal health services, resulting in lower rates of institutional delivery compared to urban women, primarily due to financial constraints (Amporfu and Grépin, 2019) [16]. The challenges faced by rural women also include constraints in providing adequate nutrition for their families, leading to poverty, environmental degradation, and a lack of appropriate technology, education, and healthcare (Otu and Anam, 2016; Rahman et al., 2022) [17,18]. Moreover, the prevalence of tobacco use among women has been increasing in low and middle-income countries due to the global spread of modern marketing and production practices (Tiwari et al., 2015; Shukla, 2021) [19,20]. These trends have serious implications for the health and well-being of rural women, who are often disproportionately affected by the adverse effects of tobacco use. Additionally, increasing women's access to resources such as credit, fertilizers, and improved seeds could significantly increase crop yields from female-controlled plots, leading to improved food security and nutrition, and increased income for rural women (D'Exelle and Riedl, 2018) [14]. This would not only benefit women directly, but also have positive spillover effects on their families and communities. However, it is important to note that such interventions must be designed with the specific needs and constraints of rural women.

Although women are disproportionately affected by the consequences of climate change, the discourse surrounding climate change adaptation has predominantly concentrated on its effects rather than delving into the strategies and resilience mechanisms employed by rural women to cope with these impacts. While its crucial to address climate change adaptation to safeguard those most susceptible, existing endeavors frequently lack cohesion, appear sporadic, and fall short in effectiveness. Therefore, there is a need to identify gender-sensitive adaptation and coping strategies to reduce food insecurity in the context of climate change. In this light, this paper investigates the adaptation and coping strategies employed by women to mitigate the negative effects of climate change in the study area.

Framework for Climate Change, Food Security, and Sustaining Livelihoods

The current research drew upon Fussel and Klein's (2006) [21] model concerning climate change, food security, and livelihoods (Figure 1). This framework underscores the multifaceted elements essential for understanding a community's susceptibility to shifting circumstances and its ability to adjust, especially concerning food security. This framework emphasizes the importance of considering the social, economic, and environmental factors that influence a community's resilience and adaptation strategies. The framework was used to guide the study's approach to understanding the impacts of climate change on women's livelihoods and food security, and their responses to these impacts.

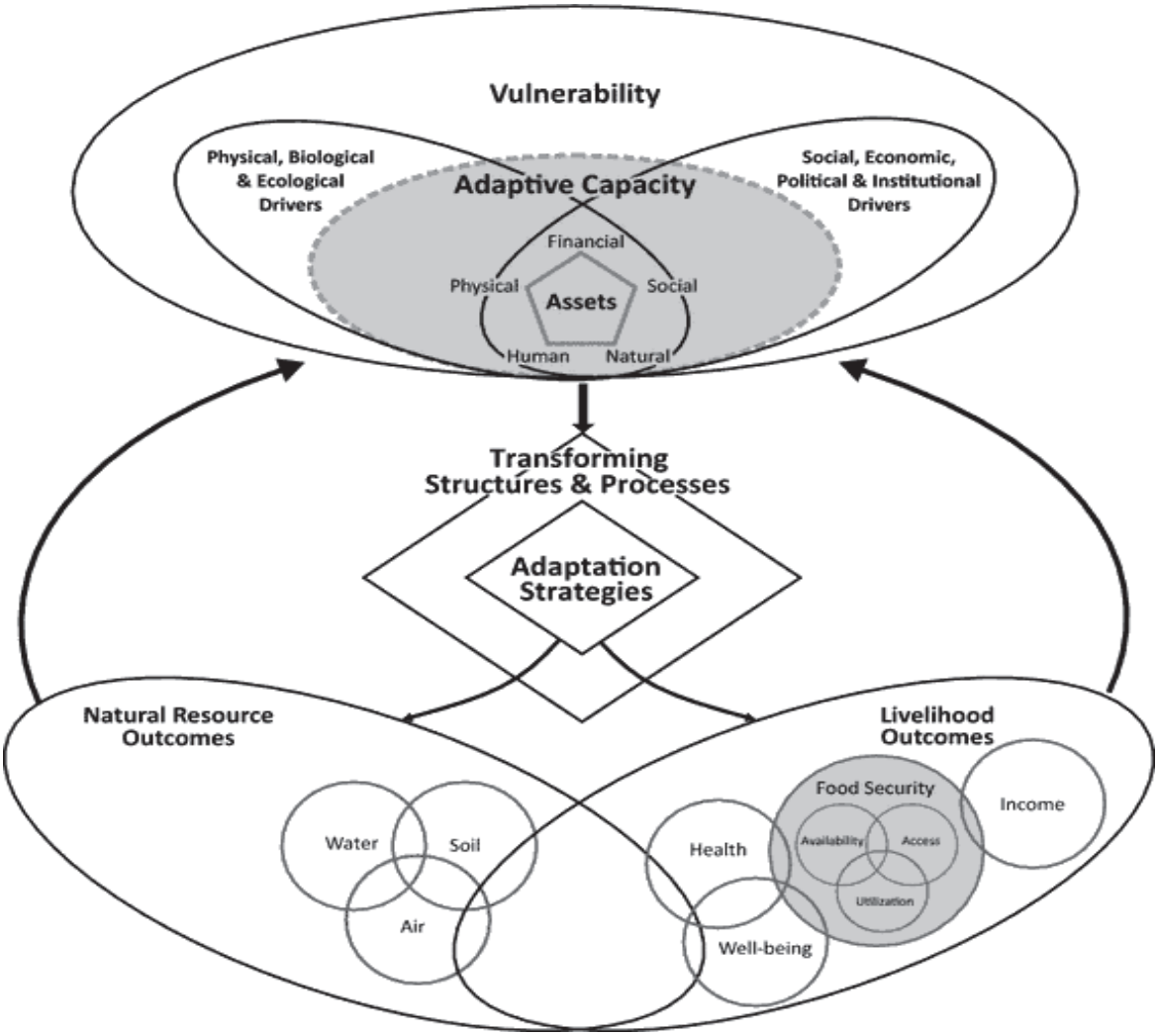

Figure 1. Framework for climate change, food security, and sustaining livelihoods. Source: Fussel and Klein's (2006) [21].

As depicted in the diagram, a community's vulnerability arises from numerous interconnected biophysical and socioeconomic elements that impact the community and influence its methods of adaptation (Figure 1). The framework recognizes that there are multiple dimensions of food security, and that they are linked and interdependent with other aspects of livelihood and the natural resources available to communities. The framework also highlights the important connections and interactions that must be considered when assessing the dynamic nature of a community's food security. This multi-dimensional perspective allows for a more comprehensive understanding of the complex factors that affect food security. Füssel (2007) and Füssel and Klein (2006) [21,22] contended that an integrated approach to vulnerability analysis aligns well with a definition of vulnerability that incorporates adaptive capacity, sensitivity, and exposure as its primary components. The framework's "exposure" element is considered external, while "sensitivity" and "adaptive capacity" are considered internal. This internal and external perspective on vulnerability is implicitly assumed in the integrated vulnerability assessment framework. This perspective allows for a more nuanced and comprehensive understanding of vulnerability. However, there is no universally agreed-upon method for integrating biophysical and socioeconomic indicators. This approach relies on a variety of data sources, from socioeconomic data such as race and age distribution, to biophysical data such as the frequency of earthquakes or droughts. These data sources are likely to have different weights, and the process of

assigning weight is not straightforward. Despite its limitations, this approach can provide valuable insights for policy decisions. This framework provides a broad overview of the factors and relationships that affect and constrain the nature and dynamics of a community's food security. This demonstrates that the resources crucial for a community's food security are at risk due to climate change, influenced by both biophysical (pertaining to the physical, biological, and ecological aspects) and socioeconomic (encompassing social, economic, political, and institutional factors) factors.

However, the level of vulnerability differs depending on the types of assets the community possesses. This approach provides a comprehensive perspective on the complex and multifaceted nature of food security. The vulnerability to climate change of people in a village depends on the assets they possess and how they are affected by biophysical and socioeconomic factors. This approach was used to analyze how women's adaptation and coping strategies can reduce food insecurity in a time of climate change. The analysis findings indicate that women encounter different levels of vulnerability based on their access to resources and their capacity to adapt to evolving circumstances, contingent upon their diverse assets. This suggests that a tailored approach to addressing food insecurity is needed, taking into account the unique circumstances of different communities.

The research topic "Adaptation and coping strategies by women to reduce food insecurity in an era of climate change: A case of Chireya district, Zimbabwe" was further explored by specifically investigating the adaptation and coping strategies employed by women in the Chireya district of Zimbabwe to reduce food insecurity in the context of climate change. This provides a more in-depth understanding of the specific challenges and solutions faced by women in this region and could help to inform policies and programs that address food insecurity. The existing literature provides valuable insights into gender-specific vulnerabilities, coping strategies, and food security in various settings. However, there is a lack of research focusing specifically on the challenges faced by women in the Chireya district, and how they cope with food insecurity in the face of climate change. This gap in the literature highlights the need for further research to gain a more nuanced understanding of the situation in this area, and to inform policy and intervention programs to reduce food insecurity. This research gap provides an opportunity to explore the experiences of women in the Chireya district, and how gender, socioeconomic factors, and environmental stressors intersect to affect their ability to cope with food insecurity in the context of climate change. This study investigated challenges faced by women in the Chireya district, their capacity to adapt to climate change, and the efficacy of their coping strategies. It also examined how women's experiences and coping strategies are shaped by their intersectional identities and the social, economic, and environmental contexts in which they live.

2. Methodology

This study employed an embedded mixed method case study design. An embedded mixed methods case study design involves integrating quantitative and qualitative methods within a case study. This is done to gain a more complete understanding of a particular case or situation. A rural village in Gokwe 22 kilometers from the Midlands Capital (Gweru) was the case in point. According to data from the Central Statistics Office (2013), the population density of the Chireya district ranges from 26 to 32 people per square kilometer. This means that the district is moderately populated, with an average of around 30 people living in each square kilometer of land. Given the district's location in rural Zimbabwe, this moderate population density likely reflects a mix of urban and rural settlements. The mean number of households is 6.5 of whom 3.9 are children. To gain a comprehensive understanding of the lived experiences of women in the Chireya district, a variety of research instruments was used, including key informant interviews, focus group interviews, non-formal interviews, and direct observations. This range of methods allowed for the collection of qualitative data from various perspectives, including community leaders, women themselves, and direct observation of the environment. Of the 64 respondents who participated in the study, 65% were female (35 respondents) and 35% were male (29 respondents). Of the 64 respondents,

13 were interviewed as key informants and 51 participated in focus group discussions. Three focus groups consisted of nine participants, while the other three consisted of eight participants. On 22 June 2022 simple random sampling was used to select a village from the seven villages in the Chireya district, to ensure that the sample was representative of the larger population. A simple random sampling method was chosen to select a village from the seven villages because it is a simple, unbiased, and straightforward method of sampling that ensures equal probability of selection for all villages. This method makes the sampling process efficient, transparent, and fair, and is therefore an appropriate choice for this study. This method also has the advantage of producing a sample that is representative of the larger population.

3. Results

3.1. Data Presentation and Analysis

3.1.1. Respondents' Gender Distribution

The results (Table 1) indicate a significant deviation from the pattern observed in other studies, such as Kongolo and Dlamini (2012) and Zenda and Malan's (2021) [23,24] studies, where male ownership of livestock dominates small-scale farming systems. In contrast, in the Chireya district, women make up a majority (62%) of small-scale farmers, while men account for only 33%, and village heads constitute a minor proportion (5%). This finding points to a need for further investigation into the unique factors that have led to such a shift in ownership patterns.

Table 1. Demographic information.

Gender Distribution	Percentage
Women	62
Men	33
Village heads	5
Ages	
50–60	58
61–70	40
75+	2
Education level	
Never went to school	3
Finished primary education	58
Secondary education	36
Tertiary education	3
Farming experience in years	
0–4	9
5–9	12
10–20	22
21 and above	57

3.1.2. Respondent Ages

The results of the survey (Table 1) revealed that respondents' education levels varied widely, with 58% of respondents having completed their primary education, 36% having completed their secondary education, 3% tertiary education, and 3% never went to school. This indicates that, while the respondents' level of literacy is reasonable, their education level may be limited in terms of fully grasping complex adaptation and coping strategies for climate change. Nonetheless, this level of education is deemed sufficient for the interpretation and understanding of basic adaptation and coping strategies to climate change, suggesting that education-based interventions may help improve adaptation and coping strategies to climate change in the area.

3.1.3. Respondents' Number of Years in Farming Experience

The survey results (Figure 2) revealed that a diverse range of experience levels was present among the respondents. About 58% of the respondents had less than 10 years of experience in farming (22% with 10–20 years, 13% with 5–9 years, and 8% with 0–4 years), while the remaining 42% had over 20 years of experience. This finding suggests that a mix of newer and more experienced farmers participated in the survey, offering a valuable perspective on sustainable sheep farming practices across different levels of experience.

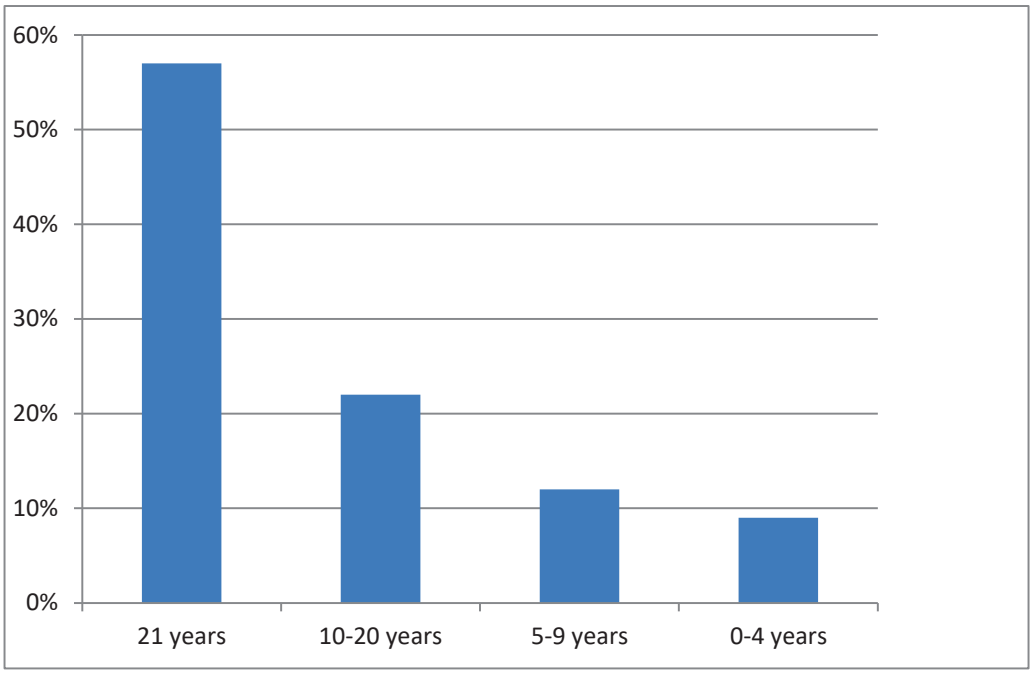

Figure 2. Duration of stay for the participants.

As shown in Figure 2, 57% of the residents interviewed had lived in the area for more than 21 years, indicating that they had extensive knowledge of the region's climatic patterns. While most respondents had lived in the area for a long time, a significant number reported migrating to the area from Masvingo, Chivi, and Mberengwa in search of better rainfall and pasture conditions following the drought of 1992. This suggests that the residents had firsthand experience of how the changing climate affects their livelihoods. Disasters and climate change can influence human migration patterns, necessitating a better understanding of the drivers behind such movements to inform disaster response and preparedness efforts (Parrish et al., 2020) [25]. In 2014, an estimated 184.6 million people were forced to leave their homes due to disasters such as floods, earthquakes, tropical storms, and volcanic eruptions, with 19.3 million people newly displaced during that year alone, according to the Internal Displacement Monitoring Center (IDMC). This instability and uncertainty have significant implications for the adaptive capacity of women in the face of climate change. The lack of permanent housing and a livelihood undermines their ability to adapt and cope with the changing climate and puts them at increased risk of food insecurity and other adverse impacts. Therefore, addressing the issue of disaster-induced displacement is critical to enhancing women's resilience to climate change.

3.2. Family Size of the Residents

The efficiency of coping mechanisms for tackling food insecurity needs to take into account the household's size. Household size is a key determinant of how well a family can adapt to climate change, as larger households often face greater challenges in meeting their needs. Therefore, it is important to consider household size when evaluating the efficacy of coping strategies and identifying potential areas for improvement.

As shown by the graph, the majority of households surveyed (61%) consisted of more than seven members, while 31% had between five and six members, and just 8% had four or fewer members (Figure 3). The researchers found that larger families had a harder time adapting and coping with climate change. This is likely due to the increased demands on resources, including food, water, and other necessities, which can be more difficult to meet with a larger household. This finding suggests that family size should be considered when developing policies and programs to help families adapt to climate change.

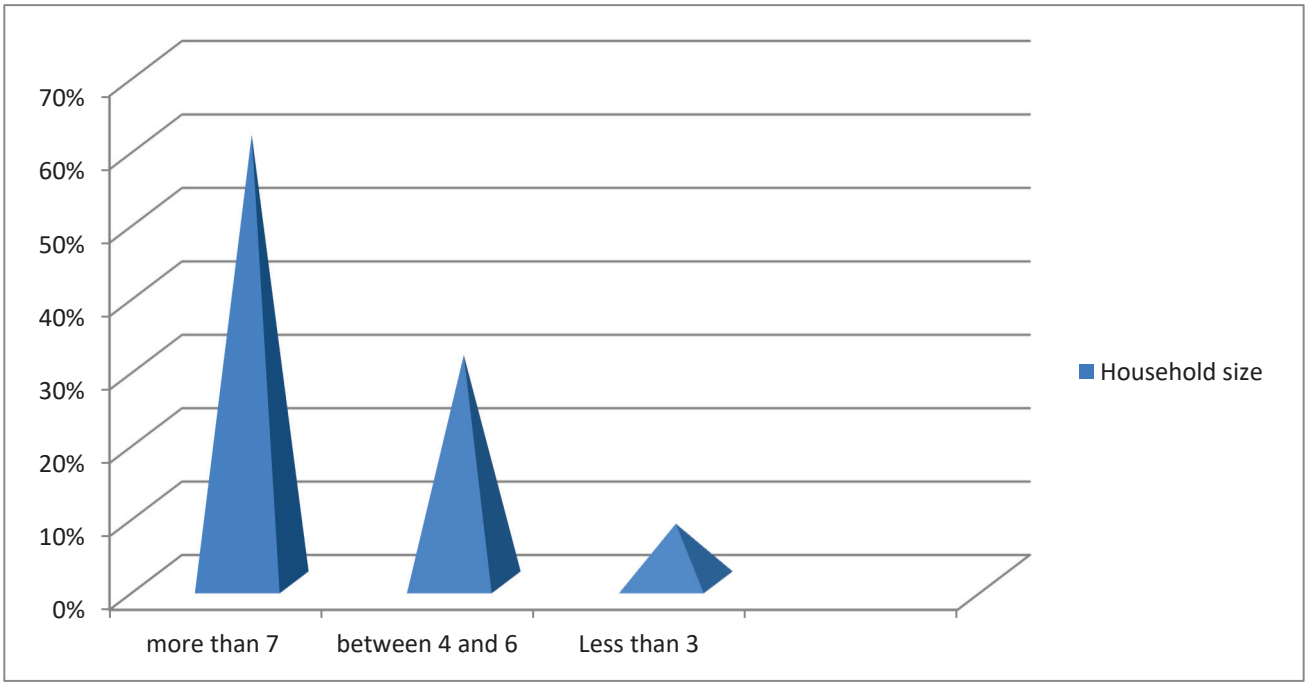

Figure 3. The family size is shown for the participants.

According to Li (2022) [26], women continue to fulfill traditional roles as mothers and caregivers in their families. While men may migrate in search of economic opportunities, women often remain in their homes to care for children, the elderly, and sick family members. Climate change greatly affects the ability to ensure access to household water, food, and fuel, responsibilities typically shouldered by women and girls. Top of Form.

This highlights the importance of considering gender roles and responsibilities in understanding and addressing the impacts of climate change. In times of drought and erratic rainfall, women and girls may have to travel longer distances and spend more time collecting water and fuel. Girls might be compelled to leave their education in order to assist their mothers with these duties, thus perpetuating a cycle of poverty and inequity. Climate change also has a negative impact on the health of crops and livestock, making it more difficult for women, who are often responsible for producing food for the household, to meet their families' needs. This highlights the gender-specific impacts of climate change on women's lives, including their health, education, and economic opportunities. Paniw et al. (2021) [27] assert that demographic patterns significantly impact both the difficulties posed by climate change and the potential remedies for addressing it. Rapid population growth can exacerbate vulnerability to the negative effects of climate change and expose an ever-growing number of people to climate risk. As populations continue to increase, especially in regions most vulnerable to climate change, the ability to adapt and cope with the impacts of climate change becomes more difficult. This suggests that addressing population growth is an important factor in efforts to mitigate and adapt to climate change. Not only does population growth exacerbate the negative effects of climate change, but it is also a driver of greenhouse gas emissions, which contribute to climate change. Meeting the needs for family planning and reproductive health can help build resilience to climate change

by reducing population growth and easing the challenges associated with adaptation. Furthermore, meeting family planning needs can help to reduce the growth of greenhouse gas emissions, and, thus, reduce the future impacts of climate change. In this way, meeting family planning needs is an important part of addressing the challenges of climate change.

The inhabitants of Ward 5, including both those interviewed separately and those involved in focus group discussions, generally concurred that there is evidence of climate change in the region, marked by a reduction in precipitation and a rise in ambient temperatures. During the focus group conversations, the majority of participants concurred that climate change is indeed occurring within their community. Among those interviewed individually, 60% agreed that climate change is taking place, while 40% were unsure whether the changes in precipitation were due to climate change or were a sign of God's anger with the people.

Inhabitants have indicated that they no longer experience the same rainfall patterns observed in the 1980s and 1990s, making it difficult for them to anticipate suitable conditions for planting crops. They reported the common rain names they used to receive, which include (the rain that washes away the chaff), (the rain that facilitates the blooming of the trees), and (the rains that signals the starting of the rainy season). They further clarified that they now receive only one type of rain, and that things have changed because there is no signaling of rainfall that tells them when to plant and/or prepare their agriculture activities.

One of the elderly women narrated: "Now we are not receiving the types of rains we used to get in this area long back, therefore we are now making use of every raindrop, regardless of when it falls)". This quote from the elderly woman captures the change in rainfall patterns that farmers in the area are experiencing, and the resulting need for adaptation and increased water efficiency. The expression "making use of every raindrop" conveys the sense of urgency and the importance of water conservation strategies, highlighting the adaptability and resilience of small-scale farmers in the face of climate change.

Residents also noted other changes in their local environment, such as an increased infestation of mopane trees by caterpillars during the spring, and the failure of fruit trees to bear fruit in some years. They also mentioned the increased population of crickets year-round, which indicates decreased precipitation. These changes, along with the changes in rainfall patterns, suggest a disruption in the natural cycles of the environment, which may be a consequence of climate change.

The residents reported the significant reduction of trees in the area as another indicator of climate change. One of them explained: "See now trees have been finished. When we arrived here there were many tree species, such that you could hardly move across the tress or bushes. Such things show that there is climate change". This quote captures a powerful observation by the residents, highlighting the rapid decline in tree populations as a potential sign of climate change. The loss of trees can have serious implications for the surrounding environment, including soil erosion, loss of biodiversity, and decreased carbon sequestration. The comment "when we arrived here" also alludes to the resident's long-term perspective, suggesting that the changes they have witnessed have been taking place over an extended period of time.

In the context of this paper, "climate change" refers to any change in climate over time, whether due to natural variability or as a result of human activity. A UNICEF report in 2010 indicates that climate change impacts in the sub-Sahara region will result in mortality and injury from extreme weather events; increase in risk of water scarcity; changes in the transmission, incidence, and distribution of water-, food-, and vector-borne diseases; migration and declining livelihoods; and heightened risk of food insecurity and child malnutrition (Hertel and Rosch, 2010; Baker and Anttila-Hughes, 2020) [28,29].

3.3. The Effects of Climate Change on Livelihoods

The graph depicts significant impacts of climate change as elucidated by the inhabitants (Figure 4). According to the graph above, 100% of residents noted that climate change resulted in decreased agricultural yields and increased livestock deaths. In total, 95% of the

respondents interviewed indicated experiencing a shortage of water and income, while 85% reported observing siltation in water reservoirs. Generally, this led to a reduction in the physical, human, financial, economic, natural, and social assets base thereby making the residents more vulnerable to facing climate change. Abid et al. (2015) [30] found that the farmers' main concern related to climate change is water insecurity. Farmers are facing challenges such as unpredictability in the monsoon rains, spatial and temporal variation in rainfall, increasing frequency of drought, rising water demands, falling groundwater levels, and declining water quality. These challenges make it difficult for farmers to grow crops and make a living. The impact of climate change on farmers' livelihoods necessitates a comprehensive approach that considers factors such as local infrastructure, education, economic development, and social security to ensure sustainable development (Wu, 2023) [31]. This is a compelling example of how climate change impacts can have complex and far-reaching consequences for different groups of people.

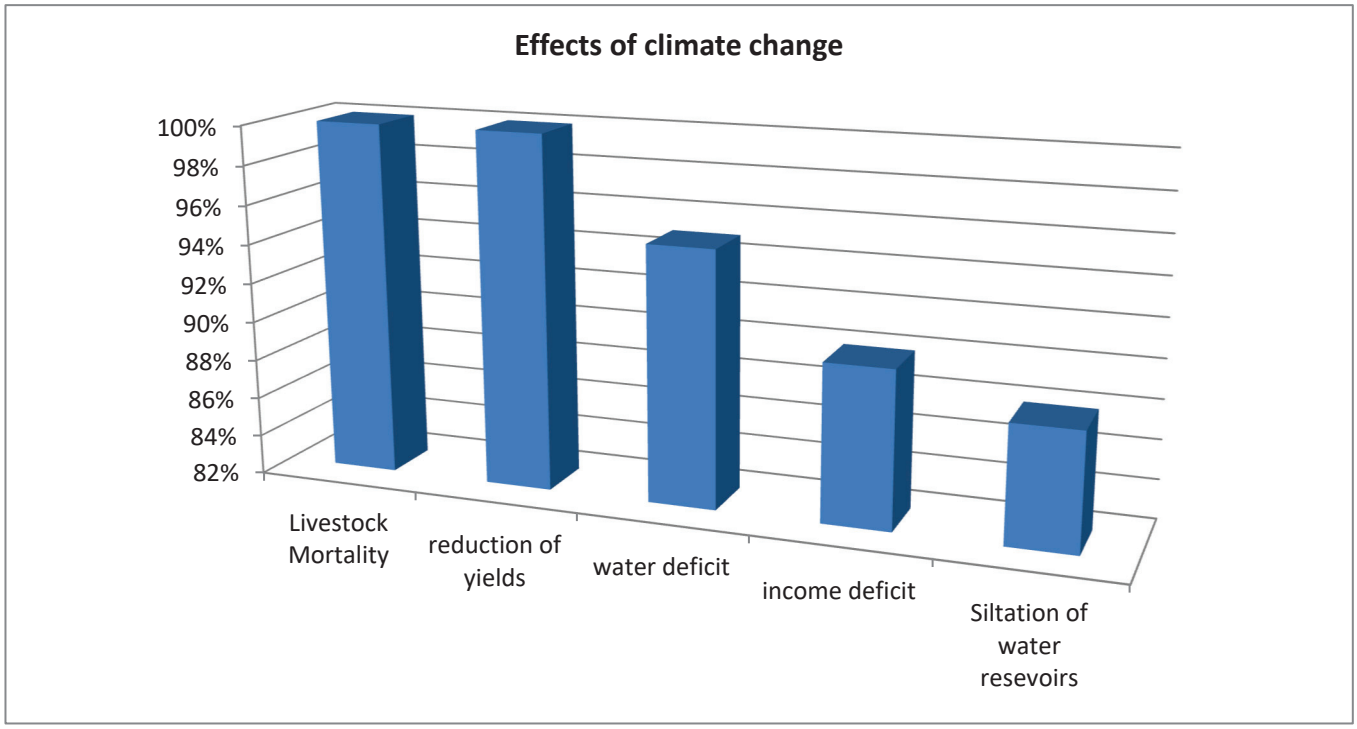

Figure 4. Effects of climate change on livelihoods.

Residents reported that the reduction in maize yields is due to high air temperatures and a significant reduction in precipitation. Since the year 2000, maize production has been negatively impacted, with some farmers unable to produce enough maize to feed their families through the next growing season. These changes have had a significant impact on the food security of the local community, and the farmers' inability to produce sufficient maize highlights the severity of the situation. This has led to increased poverty and hardship in the community.

The decrease in crop production was said to be exacerbated by significant livestock deaths, attributed to a scarcity of water and food during the dry season. One hundred households surveyed cited this as another consequence of climate change. One respondent narrated: "we just put our maize seeds without ploughing because our cattle died, due to lack of pastures. When rains come, they do not infiltrate. The water runs off. As a result, crops quickly dry up, especially during the dry spell and many households get poor crop yields and continue to impoverish the community". It was reported that this causes food insecurity and a reduction in the general livelihoods of people. The statement points to a vicious cycle caused by a combination of environmental, socioeconomic, and cultural

factors. The lack of cattle to plough the land reduces the amount of soil disturbance, which makes the soil more compacted and less able to absorb rainfall. This increases runoff and erosion, which leads to reduced water infiltration. The combination of these factors leads to soil degradation, which in turn reduces crop yields and negatively impacts the livelihoods of small-scale farmers. The cycle is perpetuated as impoverished households struggle to afford new livestock and the cycle of soil degradation and reduced crop yields continues.

Approximately 95% of respondents indicated experiencing water scarcity and reduced income due to the impacts of climate change, with 88% also mentioning the siltation of water reservoirs as another significant issue. One of them narrated: "people grow their crops along the flood plains. When rains come, they wash away the soil and deposit it in our dams, destroying work that was done. As a result, our cattle struggle to get water and eventually die". This quote illustrates the severe consequences of soil erosion on livestock farming. When heavy rains fall on deforested land, the soil loses its ability to hold water and sediment, resulting in floods that damage dams, impede access to water, and potentially cause livestock deaths. The direct connection between deforestation, soil erosion, and the impact on livestock farming is a stark reminder of the interconnectivity of environmental factors and the vulnerability of small-scale farmers to climate-related disasters.

At least 60% of participants highlighted that when water in the dams gets finished it becomes very smelly and causes many diseases such as red water to livestock and increases their mortality. As a result, people struggle for draught power at the onset of the season and struggle to sell their cattle in order to buy food because buyers need healthy cattle.

In total, 100% of the respondents reported high livestock mortality as an effect of climate change in the area. One of the elders said "our cattle drink water once in every two or three days during the dry season. As a result, many cattle would have died already by the time the rains falls. Some of us do not even have one. They all died". The quote from this elder powerfully communicates the tragic impact of climate change on livestock mortality in the area. The fact that 100% of respondents reported high livestock mortality due to climate change underscores the severity of the problem and the urgent need for action. The quote describes the dire circumstances faced by the local community, where cattle are forced to go without drinking water at increasingly prolonged intervals during the dry season, leading to severe dehydration and eventual death.

They further reported that most of the areas have no grass, especially during the dry season, and that little grass is found along river flood plains. They do not keep their cattle in the kraals during the night because they would want them to graze and avoid high temperatures during the day. Unfortunately, it is during this time that thieves come and drive the cattle away with the intention of stealing them. As a result, livelihoods are affected since cattle play a pivotal role in day to day living.

This also brought attention to the problem of inadequate soil fertility. The respondents mentioned that in the past, they relied on spreading cattle manure to enhance soil quality. However, with the absence of cattle, soil fertility has noticeably decreased. Consequently, despite receiving rainfall, crops struggle to grow quickly or yield satisfactory results due to the poor condition of the soil. A resident explained: "maize has its own days of maturity. When its time for the maize to mature, it does so even without reaching its full height. Therefore, it will not give good yields". They reported that this causes many households to be food insecure and in poverty. This quote illustrates the devastating effects of climate change on maize production and, consequently, food security and poverty levels in the area. The early maturity of maize plants due to inadequate rainfall and high temperatures results in stunted growth, leading to reduced yields. The resident's comment about maize having "its own days of maturity" highlights the vulnerability of maize production to climate change, as the natural cycles and rhythms of the crop are disrupted. The direct link between poor maize yields, food insecurity, and poverty underscores the far-reaching consequences of climate change for small-scale farmers and their communities.

Residents further explained that their poor livelihood as a result of climate change was not entirely the result of high temperatures and low rainfall but also wild animals.

It was reported that "due to the reduction of wild fruits and natural vegetation, wild animals such as baboons and wild pigs steal maize cobs at night. Sometimes the elephants come during the night and steal the maize only to leave us without food". This quote highlights the devastating consequences of climate change for the delicate balance between wildlife and agriculture in the area. As natural vegetation and wild fruits become scarce due to climate change, wild animals such as baboons, wild pigs, and elephants are forced to seek alternative food sources, often raiding maize fields at night. The destruction of crops by these animals further exacerbates the food security issues already plaguing the community, as farmers are left with little or no harvest to feed their families. This interaction between wildlife, agriculture, and climate change is a poignant example of the complex and far-reaching effects of environmental degradation.

It is estimated that the livelihoods of 70% of Africans are dependent on rain-fed agriculture, an activity that is characterized by small-scale, subsistence farms that are vulnerable to a variety of stresses, including those associated with climate change (Hlophe-Gindza and Mpandeli, 2021) [32]. Due to its largely adverse effects on African agriculture and livelihoods, climate change has a negative impact on food security (Challinor et al., 2007; Ribeiro and Rodriguez, 2020) [33,34].

The primary focus of research regarding the impact of climate change on food in Africa, as highlighted in assessments by the Intergovernmental Panel on Climate Change (IPCC), centers on changes in crop yields and food production (Pickson and Boateng, 2021) [35]. The literature discussing food security underscores that ensuring food security depends not only on food production but also on factors such as food access and utilization (Adepoju and Obialo, 2022) [36]. While food security is crucial for sustaining human life, individuals' well-being is also shaped by broader aspects of their livelihoods, including income, health, and assets (Bashir and Schilizzi, 2013; Schnitter and Berry, 2019) [37,38]. Studies on sustainable livelihoods suggest that livelihoods encompass various assets or capitals that enable people to pursue different strategies to achieve outcomes related to their livelihoods, including improved or worsened food security (Scoones, 1998; Carney et al., 1999) [39,40]. Implementing adaptation strategies is essential to ensure sustainable food security amidst climate change (Murniati & Mutolib, 2020) [41].

Toimil et al. (2020) [42] echoed similar concerns regarding the profound effects of prolonged climate-related crises on job prospects, financial stability, and particularly, the assurance of food supplies. The drought in 2015 notably worsened food insecurity in sub-Saharan Africa, a region already grappling with various developmental hurdles, reaching unprecedented levels. In Somalia, persistent drought and famine, compounded by ongoing violent conflict, have intensified forced displacement. As reported by Houessou et al. (2021) [43], approximately 855,000 individuals are confronting a crisis due to the unreliability of food availability.

3.4. Coping and Effectiveness of Strategies to Reduce Food Insecurity

This study delineated coping strategies as adjustments both within and beyond the farm that households utilize to endure. The table below illustrates these strategies employed by households to mitigate food insecurity amid climate change (Table 2). Residents disclosed actions such as selling assets, with 90% resorting to borrowing food, altering planting schedules, and selling livestock to alleviate food scarcity. Additionally, 36% mentioned exchanging food and money for work, while 20% indicated transferring their children temporarily to more affluent relatives as their sole recourse. Moreover, 12% reported resorting to marrying off their daughters to individuals better equipped to provide for them during times of hardship.

Table 2. Coping strategies to climate change.

Coping Strategy	Percentage of Women Using the Coping Strategy	Effectiveness
Selling items such as plows, harrows, and cultivators.	100%	60%
Altering the time of planting.	90%	80%
Selling domestic animals like cattle and goats, as well as domestic birds like chickens.	90%	65%
Borrowing from kins, friends, and from the chief.	90%	60%
Transitioning to drought-tolerant varieties of crops such as sorghum.	88%	75%
Informal employment.	80%	50%
Decreasing the frequency of daily meals.	80%	50%
Bartering pieces of land for grains.	80%	50%
Unlawful trade of firewood.	72%	35%
Buying on credit and paying after harvests or selling an asset.	70%	50%
Exchanging livestock and assets in return for crops.	70%	50%
Illegal mining activities.	70%	45%
Adding wild fruits to their diet as a supplement.	70%	30%
Depending on funding bodies or contributors.	67%	55%
Excavating deep wells alongside the flood plains.	60%	55%
Reducing the quantity and quality of meals.	60%	40%
Vending untamed fruits in rural hubs and urban areas.	50%	40%
Food for work and money for work programs.	36%	42%
Temporarily relocating children to more prosperous relatives, such as in-laws.	26%	20%
Consuming grains left aside as seeds.	26%	20%
Help from friends.	20%	20%
Arranging marriages for their daughters.	12%	10%

Marginalized social groups disproportionately suffer from the effects of climate change, primarily because of their heightened reliance on natural resources and their limited ability to adjust to these environmental shifts. It is notable that approximately two-thirds of impoverished individuals worldwide are women, underscoring their increased susceptibility to climate variations. This imbalance in power dynamics can lead to women being disproportionately affected by climate change, particularly in terms of their health, livelihoods, and overall well-being. Studies have shown that climate change exacerbates existing gender disparities, impeding women's growth potential (Okesanya, 2024) [44]. Women often bear the responsibility of ensuring their families' basic nutritional needs, yet they frequently lack access to and control over the resources necessary for this role, particularly when agricultural conditions deteriorate due to climate-related factors. Consequently, crop failures induced by climate change also jeopardize the food security of entire communities (Anderson et al., 2019; Suranny et al., 2022) [45,46].

Women face a significant deficiency in various rights, including land ownership, control over production resources, access to technology, financial resources, information, and training, particularly in areas such as climate adaptation and disaster preparedness (Okesenya, 2024) [44]. Research indicates that women and children are at a significantly higher risk of mortality in natural disasters, with studies suggesting a staggering 14-fold increase in their vulnerability (Hamidazada, et al., 2019) [47]. This susceptibility is further compounded by socio-cultural biases; for instance, public disaster warnings are often disseminated in locations inaccessible to women, exacerbating their vulnerability. Furthermore, the absence of land ownership titles presents a formidable challenge for women post-disaster, as it impedes their ability to secure new land for resettlement (Menon et al., 2014) [48]. Additionally, women are burdened with increased responsibilities post-disaster,

including cleanup efforts, sustaining livelihoods, and caring for the sick (Kretz et al., 2022) [49].

As a result, they not only find themselves with minimal time for activities that generate income but also face the risk of exhaustion and being overworked (Harris-Fry et al., 2020) [50]. Women, often subjected to discrimination in the allocation of resources like food and medicine, are at a heightened risk of illness compared to men. Additionally, due to economic or cultural barriers, they frequently encounter obstacles in accessing medical services (Bridge, 2008) [51]. Climate change exacerbates this situation by increasing the frequency of extreme weather events such as heat waves, leading to a rise in diseases. Higher temperatures facilitate the spread of infectious diseases like malaria and dengue fever (Anderson and Davies, 2016; Kulkarni et al., 2022) [52,53]. Furthermore, discrimination against women exacerbates the likelihood of their health deteriorating. In the aftermath of disasters, there is an increased risk of women falling victim to sexual violence (True, 2016; Memon, 2020) [54,55]. The impact of climate change on family income security also heightens the potential for domestic violence, as it disrupts the traditional role of the man as the primary breadwinner, causing psychological strain (Leslie and Wilson, 2020) [55].

In Mexico, particularly in Tlaxcala, small-scale farmers have adjusted to the challenges posed by climate variability (Below et al., 2012) [56]. For instance, they employ strategies like planting both quick-maturing but less productive corn varieties and slow-maturing but high-yield types. Additionally, they might switch from corn to wheat based on weather conditions. Farmers also adjust their use of fertilizers and pesticides according to climate patterns and diversify their land holdings across different areas. Moreover, households cope with hardships by tapping into savings, seeking loans from formal financial institutions, selling assets, or having their children work instead of attending school to supplement income (Jacoby and Skoufias, 1997) [57]. Other tactics involve managing income uncertainty through actions like taking on multiple jobs or engaging in informal economic activities after experiencing setbacks (Kochar, 1999; Morduch, 1995). [58,59]. These strategies traditionally help households mitigate the impact of unexpected income fluctuations over time. However, certain factors such as lower levels of education may heighten households' susceptibility to risk (Skoufias, 2007) [60].

3.5. Effectiveness of the Coping Strategies

According to the data presented above, approximately 80% of residents found that adjusting planting dates was effective, while 78% stated that transitioning to more drought-resistant crops yielded positive results. Those who had already made the switch to drought-resistant crops were reported to be in a better position compared to their counterparts.

Additionally, 42% of residents mentioned that obtaining assistance from donors and expanding cultivated land were effective measures. They noted that those cultivating larger plots were better off and even able to support those facing hunger. Strategies such as engaging in casual work, migration, foraging wild fruits, engaging in barter trade, reducing food consumption, and purchasing food on credit were reported by 42% as effective in mitigating food insecurity.

However, some residents expressed dissatisfaction with food aid from donor organizations, arguing that it only addresses short-term needs without providing sustainable solutions. They emphasized the importance of receiving training on improving agricultural yields in the face of climate change. Furthermore, tensions arise during food distribution due to insufficient supplies, leading to conflicts and resentment, especially among female-headed households who often receive inadequate support.

Concerns were also raised regarding borrowing and buying food on credit, as disputes often arise when borrowers fail to repay in a timely manner, leading to animosity within the community. Moreover, residents highlighted the exploitation they face in casual employment, particularly women, who often receive unfair treatment and inadequate compensation for their labor.

In summary, while certain strategies like adjusting planting practices and transitioning to drought-resistant crops have proven effective, challenges persist in accessing adequate support from donors and fair treatment in casual employment, highlighting the need for sustainable solutions and equitable practices.

3.6. Stakeholders Assisting the Communities to Cope with the Effects of Food Insecurity

The following table illustrates the stakeholders reportedly involved in aiding strategies aimed at alleviating food insecurity in the region while also fostering rural development (Table 3).

Table 3. Stakeholders assisting the communities to cope with the effects of food insecurity and their effectiveness.

Stakeholder	Duties
Local Government	• Department that is near the people in terms of service delivery. • It assisted to construct the dip tanks to manage livestock well. • Assisted with schools and clinics. • Managing the local shopping business centers.
Agritex	• It links the research science and technology to the needs of the farmers. • Farmers trainings. • Assists farmers with the seed type (hybrid) to plant. • They introduced use of bunds. • Introduced gardening projects at Zumba shopping center. • Assists in livestock management.
Grain Marketing Board	• The government of Zimbabwe's grain trade and marketing company. • It ensures that a number of households receive maize inputs at the onset of the season every year. • They reported that they stock maize grains and sell at an affordable price; distribute inputs of maize to the households.
Women affairs	• They reported that it assists with initiating and monitoring women's projects for sustainable development. • Women empowerment. • Coordinates all donor organizations that are into women and girl projects.
NGOs	Food and money distribution during the period in food insecurity situations.
Social welfare	• Assist the more vulnerable populations. • Distribute money to the vulnerable like the elderly and crippled to buy food, clothes, and sending children to school.
Environmental Management	Protect the environment from being exploited. They reported that it helped to mitigate veld fires; land degradation; siltation; deforestation.

The study found the following coping strategies were effective:

- Changing planting dates;
- Switching to early maturity drought-resistant crops;
- Crop rotation and diversification;
- Increasing the amount of land under cultivation;
- Digging the wells along the flood plains;
- Gardening (growing vegetables) to supplement diet;
- Water harvesting/dam construction;
- Income generating projects (IGPs) for both men and women.

To effectively adapt to changing climatic conditions, various measures across different sectors and levels are necessary. Specifically addressing climate change and gender, adaptation efforts aim to empower women by enhancing their livelihood opportunities.

In agriculture, where many women work to ensure family food security, adaptation measures include implementing cultivation and irrigation techniques to ensure crop resilience against natural resource depletion and unexpected weather events. Crop diversification and the use of locally produced organic fertilizers can optimize soil and irrigation use, mitigate erosion, and enhance crop survival during droughts or frost. These measures have the potential to increase production by maximizing existing resources. However, to fully benefit from these strategies, women require complementary training and agricultural extension services to learn about resource-efficient practices, as well as processing and marketing methods for agricultural products.

3.7. Implications of the Findings

This study on the effectiveness of coping strategies to address food insecurity amid climate change highlights numerous challenges leading to unsustainable coping mechanisms adopted by households. Based on the findings, the study has the following implications:

- The need for awareness among farmers regarding the harmful effects of environmental practices such as deforestation, veld fires, stream bank cultivation, and overuse of inorganic chemicals is emphasized. Government institutions responsible for environmental management should actively engage with rural communities to provide this awareness. Additionally, there is a call for the integration and implementation of a comprehensive framework for capacity building. This involves collaboration among government bodies such as the Ministry of Agriculture, Environmental Management Agency, and Local Government to educate farmers about the adverse impacts of environmental degradation.
- The Agriculture Research and Extension Services (Agritex) requires improvement to provide guidance on various drought-resistant crops, such as sorghum, and animals like donkeys. Additionally, there is a necessity to educate farmers about the significance of organic fertilizers and equip them with skills to adapt to fluctuations in precipitation and temperature. Furthermore, integrating indigenous knowledge systems is crucial for addressing climate challenges effectively.
- Government institutions, in collaboration with local communities, should implement improved water harvesting methods. These initiatives would assist communities in accessing domestic and drinking water for both humans and animals in the aftermath of rainfall. Additionally, this harvested water could be utilized for gardening purposes, thereby enhancing food supplies and dietary diversity.
- Early warning systems utilizing efficient information and communication technology are essential to swiftly distribute information to rural communities at the village level. Additionally, it is advisable to provide comprehensive training to farmers on managing various diseases.
- The Agriculture Research and Extension Services (Agritex) should promote the expansion and enhancement of non-farming income streams. This could involve implementing projects aimed at generating income, enhancing skills, and improving living standards for many individuals, enabling households to better withstand the impacts of climate change.
- To combat livestock illnesses, it is imperative to enhance production capabilities swiftly to mitigate losses and enhance productivity. Increasing veterinary extension services and providing training to existing personnel are highly recommended actions to decrease livestock mortality rates and enhance production levels.
- The Ministry of Women's Affairs, along with its partners, must raise awareness about the significance of empowering girls, and work towards diminishing instances of gender-based violence.

Further research is necessary to evaluate the contributions of both domestic and global organizations in combatting climate change and its impacts. Furthermore, more investigation is needed to develop frameworks aimed at aiding rural communities in effectively addressing challenges related to food security and climate change adaptation.

Author Contributions: E.M.—idea conceptualization, methodology, writing—original draft; writing—reviewing and editing. T.Z.—Idea conceptualization, writing, editing and proof reading—reviewing and editing original draft. M.Z.—Idea conceptualization, writing, editing and proof reading—reviewing and editing original draft. All authors have read and agreed to the published version of the manuscript.

Funding: This research received no external funding.

Data Availability Statement: Anonymised data are available by contacting the authors.

Conflicts of Interest: The authors declare no known competing financial interests or personal relationships that could have appeared to influence the work reported in this paper.

References

1. IPCC. Climate Change 2014: Impacts, Adaptation, and Vulnerability. In *Part A: Global and Sectoral Aspects. Contribution of Working Group II to the Fifth Assessment Report of the Intergovernmental Panel on Climate Change*; IPCC: Geneva, Switzerland, 2014; Chapter 24, p. 21.
2. Mikhaylov, A.; Moiseev, N.; Aleshin, K.; Burkhardt, T. Global climate change and greenhouse effect. *Entrep. Sustain. Issues* **2020**, *7*, 2897. [CrossRef]
3. Phiri, K.; Nhliziyo, M.; Madzivire, S.; Sithole, M.; Nyathi, D. Understanding climate smart agriculture and the resilience of smallholder farmers in Umguza district, Zimbabwe. *Cogent Soc. Sci.* **2021**, *7*, 1970425. [CrossRef]
4. Chanza, N.; Musakwa, W. Ecological and hydrological indicators of climate change observed by dryland communities of Malipati in Chiredzi, Zimbabwe. *Diversity* **2022**, *14*, 541. [CrossRef]
5. Rangarirai, W.; Marnani, C.; Rahmat, A. Analyzing the impact of community-based approaches on disaster preparedness to the risk of tropical cyclone induced flooding in Chimanimani district, Zimbabwe. *IOP Conf. Ser. Earth Environ. Sci.* **2023**, *1173*, 012070. [CrossRef]
6. Govere, S.; Nyamangara, J.; Nyakatawa, E. Review: Climate change and the water footprint of wheat production in Zimbabwe. *Water SA* **2019**, *45*, 513–526. [CrossRef]
7. Matsa, M. Climate change and lessons from world indigenous minority communities. In *Climate Change and Agriculture in Zimbabwe*; Springer: Berlin/Heidelberg, Germany, 2021; pp. 11–20.
8. Mushore, T.D.; Mhizha, T.; Manjowe, M.; Mashawi, L.; Matandirotya, E.; Mashonjowa, E.; Mutasa, C.; Gwenzi, J.; Mushambi, G.T. Climate change adaptation and mitigation strategies for small holder farmers: A case of Nyang district in Zimbabwe. *Front. Clim.* **2021**, *3*, 676495. [CrossRef]
9. Waha, K.; Müller, C.; Bondeau, A.; Dietrich, J.P.; Kurukulasuriya, P.; Heinke, J.; Lotze-Campen, H. Adaptation to climate change through the choice of cropping system and sowing date in sub-Saharan Africa. *Glob. Environ. Chang.* **2012**, *23*, 130–143. [CrossRef]
10. Sujakhu, N.; Ranjitkar, S.; He, J.; Schmidt-Vogt, D.; Su, Y.; Xu, J. Assessing the livelihood vulnerability of rural indigenous households to climate changes in central Nepal, Himalaya. *Sustainability* **2019**, *11*, 2977. [CrossRef]
11. Perkins, A.K. "The poor feel it the most": The Antilles bishops, the poor, and climate change. *Am. J. Econ. Sociol.* **2021**, *80*, 1155–1172. [CrossRef]
12. Dewi, K.H.; Sari, D.P.; Latifa, A. Sustainability of climate change issues in Indonesia: The voices of women's NGOs. *IOP Conf. Ser. Earth Environ. Sci.* **2022**, *1105*, 012005. [CrossRef]
13. Hlahla, S. Gender perspectives of the water, energy, land, and food security nexus in sub-Saharan Africa. *Front. Sustain. Food Syst.* **2022**, *6*, 719913. [CrossRef]
14. D'Exelle, B.; Riedl, A. Gender inequality and resource sharing: Evidence from rural Nicaragua. *J. Dev. Perspect.* **2018**, *2*, 62–87. [CrossRef]
15. Tigabie, A.; Teferra, B.; Abe, A. Access and control of resources by rural women in north Shewa zone, Amhara region, Ethiopia. *Res. World Agric. Econ.* **2022**, *3*, 36–47. [CrossRef]
16. Amporfu, E.; Grépin, K. Measuring and explaining changing patterns of inequality in institutional deliveries between urban and rural women in Ghana: A decomposition analysis. *Int. J. Equity Health* **2019**, *18*, 123. [CrossRef] [PubMed]
17. Otu, J.; Anam, B. The role of women in food production and poverty reduction in rural communities in cross river state. *Adv. Soc. Sci. Res. J.* **2016**, *3*. [CrossRef]
18. Rahman, M.M.; Dana, L.; Moral, I.H.; Anjum, N.; Rahaman, M.S. Challenges of rural women entrepreneurs in Bangladesh to survive their family entrepreneurship: A narrative inquiry through storytelling. *J. Fam. Bus. Manag.* **2022**, *13*, 645–664. [CrossRef]
19. Tiwari, R.; Gupta, A.; Agrawal, A.; Gandhi, A.; Gupta, M.; Das, M. Women and tobacco use: Discrepancy in the knowledge, belief and behavior towards tobacco consumption among urban and rural women in Chhattisgarh, central India. *Asian Pac. J. Cancer Prev.* **2015**, *16*, 6365–6373. [CrossRef] [PubMed]
20. Shukla, R.; Kanaan, M.; Siddiqi, K. Tobacco use among 1,310,716 women of reproductive age (15–49 years) in 42 low- and middle-income countries: Secondary data analysis from the 2010–2016 demographic and health surveys. *SSRN Electron. J.* **2021**, *23*, 2019–2027. [CrossRef]

21. Füssel, H.M.; Kein, R. Climate change vulnerability assessments: An evolution of conceptual thinking. *Clim. Chang.* **2006**, *75*, 301–329. [CrossRef]
22. Füssel, H. Vulnerability: A generally applicable conceptual framework for climate change research. *Glob. Environ. Chang.* **2007**, *17*, 155–167. [CrossRef]
23. Kongolo, M.; Dlamini, D.K. Small-scale livestock farming in developing areas of Swaziland and South Africa. *AFRREV STECH An Int. J. Sci. Technol. Bahir Dar Ethiop.* **2012**, *1*, 100–111.
24. Zenda, M.; Malan, P.J. The sustainability of small-scale sheep farming systems in the Northern Cape (Hantam Karoo), South Africa. *S. Afr. J. Agric. Extension* **2021**, *49*, 105–121. [CrossRef]
25. Parrish, R.; Colbourn, T.; Lauriola, P.; Leonardi, G.; Hajat, S.; Zeka, A. A critical analysis of the drivers of human migration patterns in the presence of climate change: A new conceptual model. *Int. J. Environ. Res. Public Health* **2020**, *17*, 6036. [CrossRef] [PubMed]
26. Li, Z. A review of research on the dilemma of motherhood in contemporary China. In *2022 6th International Seminar on Education, Management and Social Sciences*; Atlantis Press: Amsterdam, The Netherlands, 2022; pp. 1503–1509. [CrossRef]
27. Paniw, M.; James, T.D.; Ruth Archer, C.; Römer, G.; Levin, S.; Compagnoni, A.; Che-Castaldo, J.; Bennett, J.M.; Mooney, A.; Childs, D.Z.; et al. The myriad of complex demographic responses of terrestrial mammals to climate change and gaps of knowledge: A global analysis. *J. Anim. Ecol.* **2021**, *90*, 1398–1407. [CrossRef] [PubMed]
28. Hertel, T.W.; Rosch, S. Climate change, agriculture, and poverty. *Appl. Econ. Perspect. Policy* **2010**, *32*, 355–385. [CrossRef]
29. Baker, R.; Anttila-Hughes, J. Characterizing the contribution of high temperatures to child undernourishment in sub-Saharan Africa. *Sci. Rep.* **2020**, *10*, 18796. [CrossRef] [PubMed]
30. Abid, M.; Scheffran, J.; Schneider, U.A.; Ashfaq, M. Farmers' perceptions of and adaptation strategies to climate change and their determinants: The case of Punjab province, Pakistan. *Earth Syst. Dyn.* **2015**, *6*, 225–243. [CrossRef]
31. Wu, J. Impact of relocation in response to climate change on farmers' livelihood capital in minority areas: A case study of Yunnan province. *Int. J. Clim. Change Strateg. Manag.* **2023**, *15*, 790–809. [CrossRef]
32. Hlophe-Ginindza, S.; Mpandeli, N.S. The role of small-scale farmers in ensuring food security in Africa. In *Food Security in Africa*; IntechOpen: London, UK, 2021. [CrossRef]
33. Challinor, A.J.; Wheeler, T.; Garforth, C.; Craufurd, P.; Kassam, A. Assessing the vulnerability of food crop systems in Africa to climate change. *Clim. Chang.* **2007**, *83*, 381–399. [CrossRef]
34. Ribeiro, P.F.; Rodriguez, A.V.C. Emerging advanced technologies to mitigate the impact of climate change in Africa. *Plants* **2020**, *9*, 381. [CrossRef]
35. Pickson, R.B.; Boateng, E. Climate change: A friend or foe to food security in Africa? *Environ. Dev. Sustain.* **2021**, *24*, 4387–4412. [CrossRef] [PubMed]
36. Adepoju, A.O.; Obialo, A. Agricultural labour productivity growth and food insecurity transitions among maize farming households in rural Nigeria. *Ekon. Poljopr.* **2022**, *69*, 1093–1107. [CrossRef]
37. Bashir, M.K.; Schilizzi, S. The nexus between food security and livelihoods: A study on the determinants of food security in rural areas of Pakistan. *Food Secur.* **2013**, *5*, 327–337.
38. Schnitter, R.; Berry, P. The climate change, food security and human health nexus in Canada: A framework to protect population health. *Int. J. Environ. Res. Public Health* **2019**, *16*, 2531. [CrossRef] [PubMed]
39. Scoones, I. *Sustainable Rural Livelihoods: A Framework for Analysis*; IDS Working Paper 72; Institute of Development Studies: Brighton, UK, 1998.
40. Carney, D.; Drinkwater, M.; Rusinow, T.; Neefjes, K.; Wanmali, S.; Singh, N. *Livelihoods Approaches Compared*; Department for International Development: London, UK, 1999.
41. Murniati, K.; Mutolib, A. The impact of climate change on the household food security of upland rice farmers in Sidomulyo, Lampung province, Indonesia. *Biodiversitas J. Biol. Divers.* **2020**, *21*. [CrossRef]
42. Toimil, A.; Camus, P.; Losada, Í.J.; Cozannet, G.L.; Nicholls, R.J.; Idier, D.; Maspataud, A. Climate change-driven coastal erosion modelling in temperate sandy beaches: Methods and uncertainty treatment. *Earth-Sci. Rev.* **2020**, *202*, 103110. [CrossRef]
43. Houessou, M.D.; Cassee, A.; Sonneveld, B. The effects of the COVID-19 pandemic on food security in rural and urban settlements in benin: Do allotment gardens soften the blow? *Sustainability* **2021**, *13*, 7313. [CrossRef]
44. Okesanya, O.J.; Alnaeem, K.F.H.; Hassan, H.K.; Oso, A.T.; Adigun, O.A.; Bouaddi, O.; Olaleke, N.O.; Kheir, S.G.M.; Haruna, U.A.; Shomuyiwa, D.O.; et al. The intersectional impact of climate change and gender inequalities in Africa. *Public Health Chall.* **2024**, *3*, e169. [CrossRef]
45. Andersen, L.V.; Davis, M.D. Climate change and the epidemiology of selected tick-borne and mosquito-borne diseases: Update from the international society of dermatology climate change task force. *Int. J. Dermatol.* **2016**, *56*, 252–259.
46. Suranny, L.E.; Gravitiani, E.; Rahardjo, M. Impact of climate change on the agriculture sector and its adaptation strategies. *IOP Conf. Ser. Earth Environ. Sci.* **2022**, *1016*, 012038. [CrossRef]
47. Hamidazada, M.; Cruz, A.M.; Yokomatsu, M. Vulnerability factors of Afghan rural women to disasters. *Int. J. Disaster Risk Sci.* **2019**, *10*, 573–590. [CrossRef]
48. Memon, F. Climate change and violence against women: Study of a flood-affected population in the rural area of sindh, pakistan. *Pak. J. Women Stud. Alam-E-Niswan* **2020**, *27*, 65–85. [CrossRef]

49. Kretz, E.; Itaru, A.; Glas, M.; Waswa, L.; Jordan, I. Is responsive feeding difficult? a case study in teso south sub-county, kenya. *Nutrients* **2022**, *14*, 4677. [CrossRef] [PubMed]
50. Harris-Fry, H.; Nur, H.; Shankar, B.; Zanello, G.; Srinivasan, C.; Kadiyala, S. The impact of gender equity in agriculture on nutritional status, diets, and household food security: A mixed-methods systematic review. *BMJ Global Health* **2020**, *5*, e002173. [CrossRef] [PubMed]
51. Bridge, J. Barriers to accessing medical services: A review of economic and cultural factors. *J. Health Econ.* **2008**, *15*, 123–135.
52. Anderson, W.; Seager, R.; Baethgen, W.E.; Cane, M.A.; You, L. Synchronous crop failures and climate-forced production variability. *Sci. Adv.* **2019**, *5*, eaaw1976. [CrossRef] [PubMed]
53. Kulkarni, M.A.; Duguay, C.; Ost, K. Charting the evidence for climate change impacts on the global spread of malaria and dengue and adaptive responses: A scoping review of reviews. *Glob. Health* **2022**, *18*, 1–8. [CrossRef] [PubMed]
54. True, J. Gendered violence in natural disasters: Learning from New Orleans, Haiti and Christchurch. *Aotearoa N. Z. Soc. Work* **2016**, *25*, 78–89. [CrossRef]
55. Leslie, E.; Wilson, R. Sheltering in place and domestic violence: Evidence from calls for service during COVID-19. *J. Public Econ.* **2020**, *189*, 104241. [CrossRef]
56. Below, T.B.; Mutabazi, K.D.; Kirschke, D.; Franke, C.; Sieber, S.; Siebert, R.; Tscherning, K. Can farmers' adaptation to climate change be explained by socio-economic household-level variables? *Glob. Environ. Chang.* **2012**, *22*, 223–235. [CrossRef]
57. Jacoby, H.; Skoufias, E. Testing Theories of Consumption Behaviour Using Information on Aggregate Shocks: Income Seasonality and Rainfall in Rural India. *Am. J. Agric. Econ.* **1997**, *80*, 1–14. [CrossRef]
58. Kochar, A. Explaining household vulnerability to idiosyncratic income shocks. *Am. Econ. Rev.* **1999**, *89*, 159–164.
59. Morduch, J. Income smoothing and consumption smoothing. *J. Econ. Perspect.* **1995**, *9*, 103–114. [CrossRef]
60. Skoufias, E.; Rabassa, M.; Olivieri, S.; Brahmbhatt, M. The poverty impacts of climate Change. *PREM Policy Brief* **2011**, *51*, 1–35.

Disclaimer/Publisher's Note: The statements, opinions and data contained in all publications are solely those of the individual author(s) and contributor(s) and not of MDPI and/or the editor(s). MDPI and/or the editor(s) disclaim responsibility for any injury to people or property resulting from any ideas, methods, instructions or products referred to in the content.

sustainability

MDPI

Article

Predictive Analysis of Adaptation to Drought of Farmers in the Central Zone of Colombia

Jorge Armando Hernández-López [1,*], Diana Ximena Puerta-Cortés [2] and Hernán J. Andrade [3]

[1] Civil Engineering Program, Engineering Faculty, Universidad de Ibagué, Carrera 22 Calle 67 B/Ambalá, Ibagué 730001, Colombia
[2] Psychology Program, Universidad de Ibagué, Carrera 22 Calle 67 B/Ambalá, Ibagué 730001, Colombia; diana.puerta@unibague.edu.co
[3] Research Group PROECUT, Department of Production and Plant Health, Faculty of Agronomic Engineering, Universidad del Tolima, Ibagué 730006, Colombia; hjandrade@ut.edu.co
* Correspondence: Jorge.hernandez@unibague.edu.co; Tel.: +57-3138227133

Abstract: Drought constitutes one of the natural phenomena that causes the greatest socio-economic, and environmental losses in both the short and long term worldwide. Each year, these events are related to the presence of "El Niño—Southern Oscillation" (ENSO), which occurs throughout Colombia and has serious consequences in the agricultural and food sectors, as well as in most of the country's population. Farmers have adopted a number of strategies to mitigate the negative impact of droughts on food production. Certainly, when implementing future strategies, such strategies will be less effective if farmers' insights on ENSO are not considered. Consequently, this study was carried out to analyze the variables that predict adaptation to droughts in the dry zones of the department of Tolima. Three questionnaires were designed: socioeconomic vulnerability (SVT), risk perception (SRPT) and drought adaptation (SAT). A non-probability sample of 538 farmers was surveyed. Socio-economic vulnerability and drought perception were found to be predictive of drought adaptation in the study sample, and older people were found to be resilient to adaptation. The results of this research provide empirical evidence to analyze and formulate public policies about the impact of droughts on the most vulnerable populations.

Keywords: vulnerability; adaptation; perception; drought; farmers

1. Introduction

Global climate change affects agriculture and the lives of rural communities, threatening food sovereignty and rural people's sustainability, especially in developing countries [1–5]. Colombia is located on the equatorial strip, so it is under the influence of the Intertropical Confluence Zone (ITCZ), a determining factor in the spatiotemporal distribution of precipitation, temperature, and other climatic variables [2,6,7]. Due to its location in the northwest of South America and the influence of the processes that occur in the Atlantic and Pacific Oceans, Colombia is a country susceptible to catastrophes and natural disasters [7,8]. Frequently, the warm phase of the intertropical convergence zone oscillation, the Southern Oscillation System (ENSO), causes droughts, disrupting normal climate patterns [8–10]. The ENSO phenomenon has a strong effect on precipitation, the flow of rivers, and soil moisture [10]. The warming phase (El Niño) is associated with an increase in average air temperature, a decrease in soil moisture and evapotranspiration, a decrease in precipitation, and a consequent decrease in the average flow of rivers in western regions, the center, and the north of the country [6]. The opposite pattern, the cold reverse phase of ENSO, known as La Niña, is characterized mainly by sharp and abundant rainfall, increased river flow and subsequent flooding, and intensification of trade winds in the eastern Pacific Ocean, causing relatively colder deep waters along the equatorial Pacific, remain at the surface [11]. The abnormally intense trade winds exert a greater drag

effect on the ocean surface, increasing the difference in sea level between both ends of the equatorial Pacific [12].

Unlike other natural disasters, drought is one of the most complex and least understood climatic phenomena, because of its irregular distribution in time and space [13–15]. For this reason, it is difficult to provide a generic approach that includes all aspects and meets all expectations [2], which is why drought responds more to a climatic and environmental peculiarity, making it a phenomenon with a relative and elusive character [16].

Farmers suffer significant economic losses due to drought impacts over several years [16,17]. Crop production depends on financial, human, and social capitals that function as a whole system in which each capital influences and is influenced by other capitals, so the effects can be positive or negative [18,19]. To improve food livelihoods facing droughts, farming communities must develop context-specific adaptation measures [20,21]. Adaptation is defined as adjustments in ecological-socioeconomic systems in response to actual or expected climatic stimuli, effects, or impacts [22,23]. These adaptations can be autonomous, involuntary, planned, passive, reactive, or anticipatory and, to be successful, must address the sociopolitical, economic, and cultural interactions that determine access to livelihood resources [24,25]. Increasingly, adaptation studies recognize that people are not merely passive recipients, but also can overcome and adapt to change [26], albeit influenced by access to resources, local power dynamics, and other sociocultural, economic, and political dynamics [22].

Farming communities develop adaptation measures to minimize their vulnerability to droughts. Being vulnerable is defined as the degree and extent to which a specific hazard will affect the community and the environment [27–30]. There are three components to assess vulnerability: adaptive capacity, sensitivity, and exposure [31–33]. The ability of a structure to successfully adapt to climate extremes and variability is known as adaptive capacity [32,34,35]. Sensitivity refers to the responsiveness of the system to climatic influences and the degree to which climate change may affect its current form [27,36]. The nature, duration, and degree to which a system is exposed to considerable changes in climate are known as exposure [31].

Ongoing exposure to droughts means that communities that reside in agricultural areas have sufficient information to be able to perceive the risk. Drought risk perception is associated with education, resource acquisition, and awareness [37]. Understanding farmers' perceptions can play an important role in ensuring that drought adaptation strategies are successfully implemented and can improve food production [19,20,38].

The perceptions of farmers provide information for assessing climate change impacts as well as drought adaptation strategies [39,40]. Data on farmers' perceptions of drought are influenced by socioeconomic (gender, education level, household size, age, land tenure, off-farm income, livestock ownership), biophysical (agroecology, farm size and distance to market, rainfall and temperature), and institutional factors (extension services, access to credit, climate information, and humanitarian aid) [34,41–43].

Droughts have affected social welfare and food security throughout human history [10, 44,45]. It is one of the most devastating climatic threats to agriculture, because it causes the stoppage of food production. It also affects the growth of pastures, alters markets, and in extreme cases, results in the widespread death of animals [39,46–48].

From the socioeconomic perspective, one key factor that could drive or constrain the perception and adaptation to climate variability is gender [41]. Age is also an important socioeconomic factor in the perception and uptake of drought adaptation strategies [41]. Older farmers are prone to risk and are better at recognizing changes and using adaptation practices than younger smallholder farmers [41,49]. Older farmers also have more experience in farming and are more exposed to past climate shocks than younger farmers [41]. If most family members are of working age, the household will have enough labor and will be using better coping strategies [41,50].

Understanding farmers' perceptions can play an important role so that drought adaptation strategies are successfully implemented and can improve food production [51,52]. De-

spite the studies that have been carried out in Colombia so far, there is little research related to adaptation, socioeconomic vulnerability, and risk perception of farmers to droughts [53]. Therefore, there are no data to carry out effective interventions to minimize the impact of droughts in these communities. This research aims to analyze the variables that predict adaptation to droughts in the drylands of the department of Tolima in Colombia.

This research aims to analyze the variables that predict adaptation to droughts. The study is organized as follows: Section 2 includes a brief description of the study area, participants, questionnaires administered, and data analysis; the main results are presented in Section 3; Section 4 presents the discussion; and Section 5 shows the main conclusions. Finally, an annex of the questionnaires applied is included.

2. Materials and Methods

2.1. Spatial Coverage of the Survey

This research was developed in the dry area of the department of Tolima, located in the Alto Magdalena Valley, in central Colombia. The study area is located between 194 and 1000 m of altitude and has an area of 10,082.9 km^2. (Figure 1). The climatic conditions of these landscape units are characterized by an average annual temperature greater than 27 °C, average annual rainfall less than 1500 mm, and elevations between 300 and 400 m.

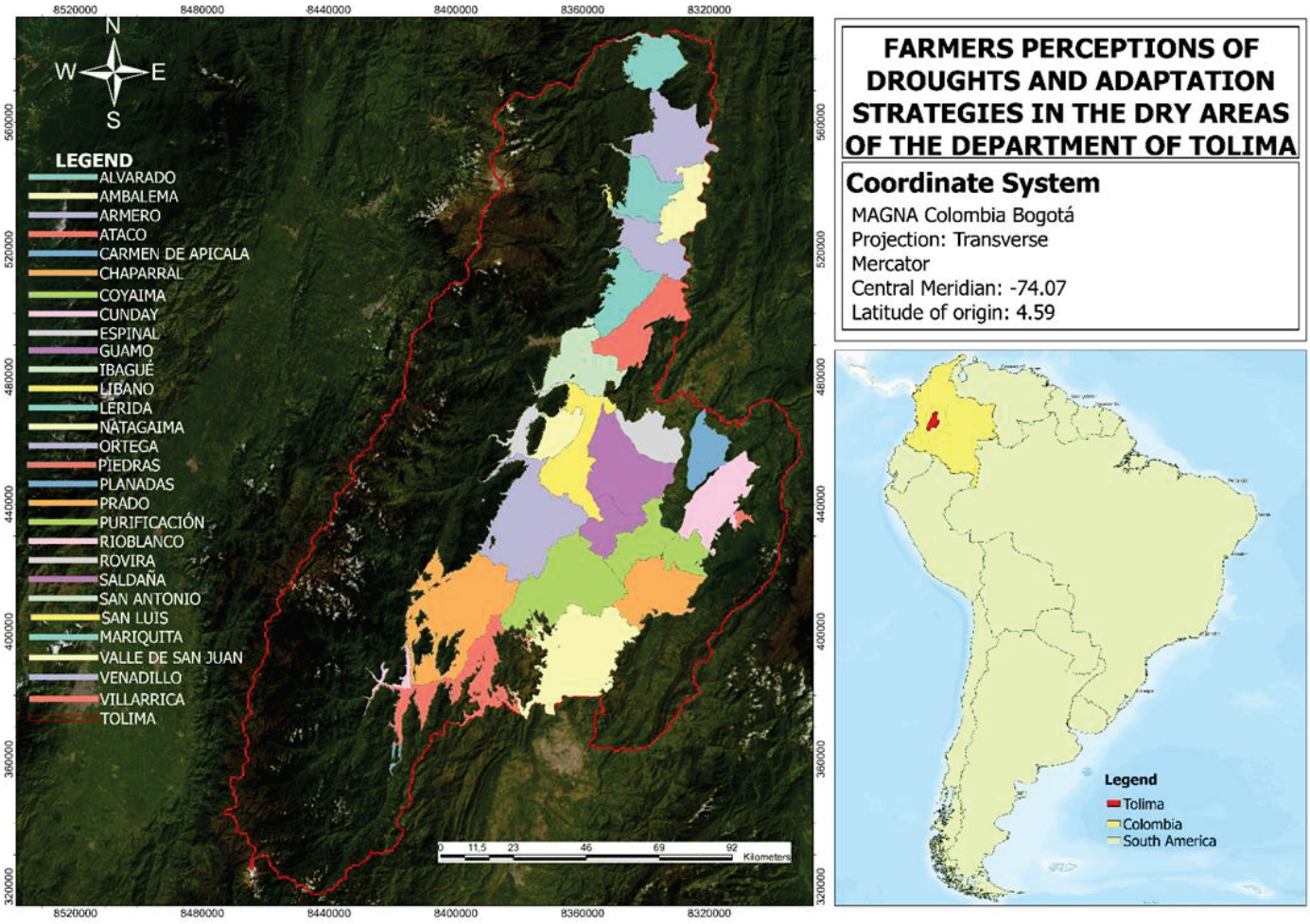

Figure 1. Study area in the dry zone of the department of Tolima, Colombia.

Historically, the territory's climate has been affected by ENSO, such as it has seen in the last 25 years (1985, 1988, 1991–1992, 1997–1998, 2001, 2009, 2015, and 2016) [54]. ENSO has negatively impacted the generation of electrical energy, shortages of agricultural

products, an increase in diseases, scarcity of drinking water, pests, and a reduction in agricultural productivity [55,56].

The Magdalena River crosses the department from south to north, affecting the weather in the area. The bioclimatic provinces in the study area are warm arid (CA), warm semi-arid (Csa), and warm semi-humid (Csh). The rain regime is bimodal, which is characterized by two quarterly rainy seasons between March and May, and from October to December, alternating with two seasons of low precipitation from January to February and from June to September [57]. In this ecosystem, there is great variation in physiographic units, presenting landscapes of alluvial valleys, hills, foothills, and mountains [56].

The land of the study area is mainly covered by natural pastures, managed pastures dedicated to extensive livestock grazing, cultivation of rice, cotton, corn, sorghum, small fruit crops, and vegetables, which are the main economic activities [57]. In the 43 municipalities of the study area, land use is generally distributed by mechanized and irrigated lands, mostly covered by natural pastures [56].

The natural cover has been almost completely destroyed, and the landscape is currently characterized by small groups of secondary forest and trees in living fences and pastures. Likewise, the productivity of livestock systems is limited mainly by the drastic decrease in forage, especially as a consequence of intense periods of drought, further accentuated by the high degree of deforestation. This situation causes low rates of productivity and profitability in both the agricultural and livestock systems of the area [57].

2.2. Survey Participants

The sample of the study was selected from 28 municipalities in the department of Tolima, Colombia. A total of 538 farmers participated; 24.7% of them were women and 75.2% were men. The respondents ranged in age from 18 to 85 years old. In the age group distribution, they were classified as: young people between 18 and 25 years old (8.8%); adults between 26 and 55 years old (57.5%) and older adults between 56 and 85 years old (33.7%). The predominant educational level in the questionnaires was primary school with 40.9%, followed by secondary school with 39.6%.

Data collection was carried out through a form applied by previously trained research assistants, who traveled to the dry zones of the study area. The respondents, whose participation was voluntary, were located in the population centers, at neighborhood meetings and on farms. Before the application of the questionnaire, the interviewers explained the objectives of the study to those interested, to them then it was shared the form containing the informed consent (voluntary participation, confidentiality, freedom to withdraw from the study and anonymity of their answers) and the questionnaires [58,59]. The application of the questionnaires was carried out from February to June 2022. The questionnaire was peer-reviewed to ensure its comprehensibility and acceptability by farmers [60,61].

2.3. Sample Survey

Different steps were taken to develop the SPRT and SAT questionnaires based on the methodology of McCoach [62]. This approach consists of a review of the literature to define the constructs, then the variables were operationalized and the items were drafted. In particular, the SPRT questionnaire was based on the theoretical aspects of Mooney [63], who identified and defined the three dimensions of risk perception in the face of climate change: perceived probability, perceived severity, and perceived consequences. The questionnaires on Drought Adaptation (SAT) and Socioeconomic Vulnerability (SVT) did not contain dimensions, therefore, they are categorized as unidimensional, and they only evaluate one construct.

After the questionnaires were designed, two experts evaluated the items of the scale, making linguistic adjustments, and then the scale was applied to 35 people, in order to obtain an initial evaluation. A four-point Likert scale was used to check whether the participants understood the item descriptions. The results showed that all respondents

fully understood the item descriptions. No modifications were made to the questionnaire or the scale, and the questionnaires were then applied to the study sample (see Appendix A).

Four questionnaires were applied: The first questionnaire, "Socio-demographic data and lifestyle in drought", consisted of 28 questions that inquired about the place of residence, name of the farm, name of the village, number of children, number of household members, main source of family income and income. Also, a total of 16 questions related to behaviors associated with the farmers' lifestyle during drought were formulated. These questions focused on four areas: land tenure, infrastructure and tools, access to water for irrigation and drinking water. The variables such as housing, time in housing and type of fuel for cooking (cooking with) are part of the characterization of the study sample in the section on sociodemographic variables which describe multidimensional poverty. For this reason, these elements may be compatible with other samples due to that most drought regions include farmers in poor areas.

The second questionnaire, "Socio-economic Vulnerability (SVT)", which was designed to evaluate social and economic vulnerability to droughts, consisted of 12 questions with a four-point Likert-type response, where one equals "Strongly disagree" and four equals "Strongly agree". The reliability analysis through Cronbach's alpha coefficient was 0.74 and showed a percentile classification in low vulnerability (27.7%), medium vulnerability (45.9%) and high vulnerability (26.4%).

Questionnaire number 3, "Drought risk perception (SPRT)", was designed with the objective of evaluating the farmers' perceptions of droughts. The SRPT consists of two climate perception questions and three dimensions: perceived probability with five questions, perceived severity with eight questions and perceived consequence with 14 questions. The Likert-type response scale is a four-point scale, where one equals "Strongly disagree" and four equals "Strongly agree". The reliability analysis of the SRPT using Cronbach's alpha = 0.88; for the perceived likelihood dimension 0.73; perceived severity 0.79 and perceived consequence 0.71.

The last questionnaire, "Drought Adaptation Test (SAT)", was designed with the objective of evaluating the adaptation of farmers to droughts. It consists of 12 questions with a four-point Likert-type response scale, where one equals "Strongly disagree" and four equals "Strongly agree". The reliability of the questionnaire through Cronbach's alpha was 0.76.

2.4. Survey Data Analysis

The data analysis was carried out according to the type of variables, the objectives of the study, and the scope of the research. This analysis started with bivariate analysis, then correlational, the reliability of the instruments was carried out, which corresponds to the measurement of the degree of stability of the results of the questionnaires when a measurement is repeated under identical conditions. Finally, a linear regression analysis to detect predictor variables was carried out.

The Statistical Package for the Social Sciences 25.0 (IBM SPSS), Rstudio, and Microsoft Excel v-2010 were used for data analysis [64–66]. We performed a bivariate analysis using the X2 test to detect and describe the relationship between sociodemographic variables, lifestyle-associated behaviors, SVT, SRPT, and SAT. The linear correlation between each of the dimensions (SRPT, SVT, and SAT) was estimated using the Pearson coefficient. The reliability of the questionnaires was assessed using Cronbach's Alpha internal consistency index, which was calculated using the item variance method, and a linear regression analysis was performed to detect predictor variables [54,59,67,68].

3. Results

3.1. Characterization of the Sample

A total of 73.8% of the participants in the study have lived in the study area for more than 5 years; 62.3% have their own home; 40.7% of the family group is made up of 3

to 4 people; the main source of income is agriculture (82.7%); and 41.1% earn less than one million pesos (Table 1).

Table 1. Socio-demographic variables of farmers in the dry zone of the department of Tolima, Colombia.

Group	Individual	Percentage (%)
Marital status	Single	21.0
	Married	36.1
	Widower	5.6
	Civil Union	35.5
	Divorced	1.9
Household members	1.0	7.2
	1 a 2	37.0
	3 a 4	40.7
	5>	15.1
Children	Yes	80.1
	No	19.9
Dependents	0	21.5
	1	24.2
	2	29.7
	≥3	24.5
Monthly income **	<1 million	41.1
	1 million	29.0
	1 a 2 million	18.2
	2 a 3 million	5.8
	4 a 5 million	2.4
	≥5 million	3.5
Housing	Own	62.3
	Rented	12.1
	Family	25.7
Time in housing	<1 year	3.0
	1 to 2 years	10.4
	3 to 4 years	12.8
	>5 years	73.8
Cooking with	Natural gas	30.5
	Firewood	27.7
	Gas cylinder	14.7
	Natural Gas + Firewood	1.1
	Natural Gas + Gas cylinder	1.1
	Firewood + Gas cylinder	24.9
Main source of income	Livestock	4.5
	Agriculture	82.7
	Fish farming	3.0
	Trade	4.8
	Other	1.7
	Livestock + Agriculture	3.2
	Trade + Agriculture	0.2

Note: ** 1.000.000 COP = 254 USD.

Most of the farmers (58.6%) own the land or plot of land, and 55.8% have their own agricultural machinery. About 55.4% of farmers have one to two workers, 84.5% have a maximum of 10 hectares of land, and 54.8% have access to water for irrigation purposes, while 56.3% do not have access to drinking water (Figure 2).

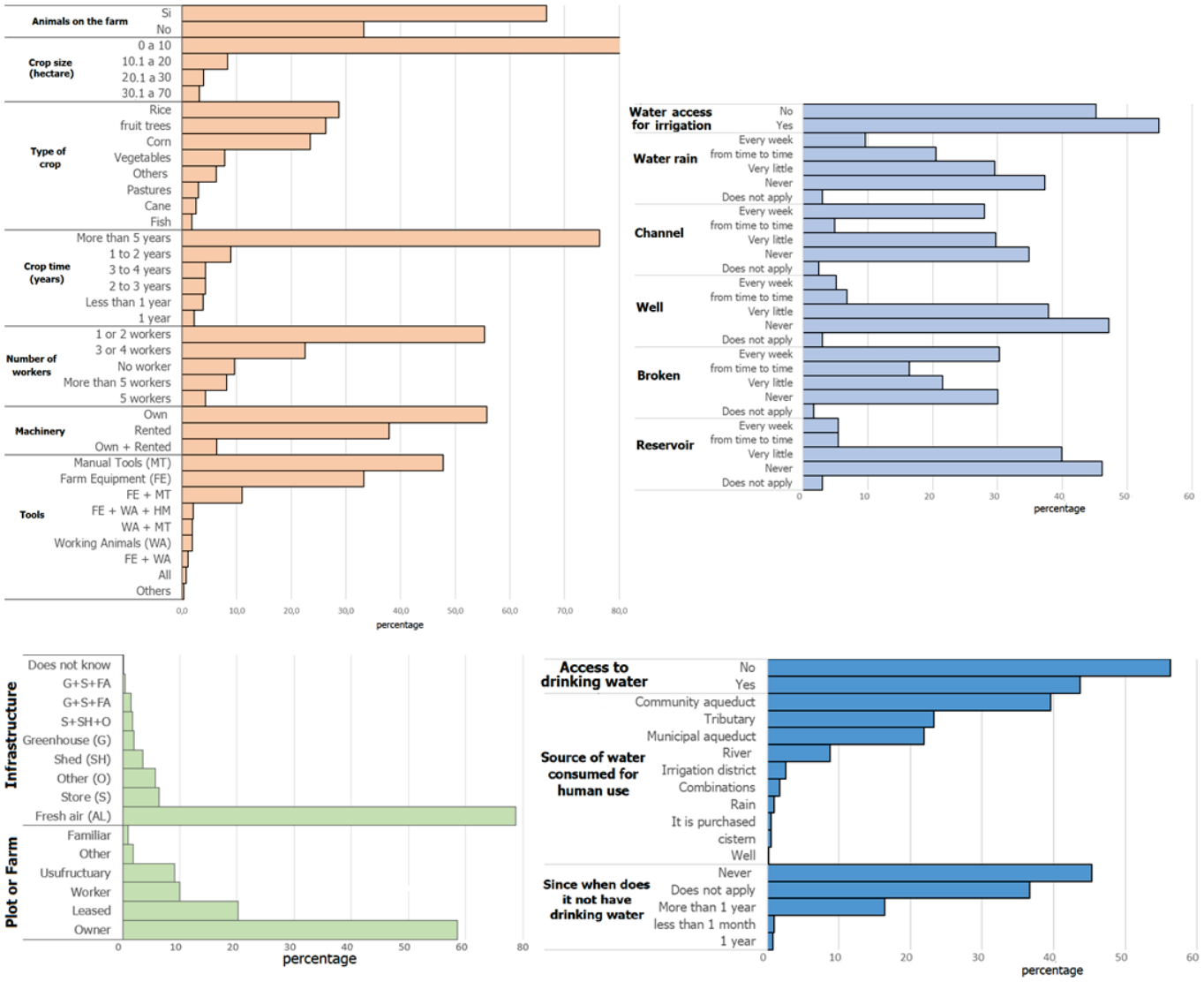

Figure 2. Lifestyle of farmers in the dry zone of the department of Tolima, Colombia.

3.2. Correlational Analysis between Age and Questionnaire Scores

The correlational analysis showed: (a) a negative and significant ($p < 0.05$) relationship between age and drought adaptation, and socioeconomic vulnerability index scores; (b) a positive and significant ($p < 0.05$) relationship between SAT, SVT, and SRPT index scores; and (c) and finally, a positive and significant ($p < 0.05$) relationship between SVT and SRPT (Table 2).

Table 2. Correlations between age, risk perception, socioeconomic vulnerability, and drought adaptation categories.

Variables	M (Pd)	SD	A	SAT	SVT	SRTP
1. Age (A)	48.17	14.75	1			
2. Adaptation to droughts (SAT)	31.17	6.93	−0.107 *	1		
3. Socio-economic vulnerability (SVT)	37.31	6.63	−0.148 **	0.540 **	1	
4. Perception of risk to droughts (SRPT)	76.19	14.20	−0.63	0.367 **	0.489 **	1

M: Mean; SD: Standard deviation; * Significant correlation at 0.05; ** Significant correlation at 0.01.

A linear regression was carried out to identify the predictor variables of farmers in the face of drought. The dependent variable was SAT scores. The covariates were age,

SVT and SRPT scores, socioeconomic vulnerability and perception were found to predict adaptation to drought in the study sample. As shown in Table 3, the model achieved a correct classification of 89.8% of the participants. The greatest resistance to change was evidenced by older people (95% CI = −0.047–0.020); with the greater vulnerability, more adaptation strategies are developed (95% CI = 0.405–0.576); people who have a perception of droughts assume strategies to adapt easily (95% CI = 0.026–0.106). Vulnerability and perception are predictors of adaptation to drought.

Table 3. Binary logistic regression analysis between the categories age, risk perception, socioeconomic vulnerability and adaptation to drought.

Variables	B	SD	BETA	t	Sig.	CI 95%	
Age	−0.01	0.02	−0.03	−0.796	0.427	−0.05	0.02
Socio-economic vulnerability (SAT)	0.491	0.04	0.469	11.25	<0.001	0.405	0.58
Perception of risk to droughts (SRPT)	0.066	0.02	0.135	3.268	0.001	0.026	0.11

B: Non-standard coefficient; SD: Standard deviation; BETA: Standard coefficient; t: Lower limit; Sig.: Upper limit; CI: Confidence interval.

4. Discussion

Questionnaires are a useful tool to provide an overview of droughts and provide feedback on participants' current perceptions [69]. Responses are based on subjective experiences and could be influenced temporarily or permanently by external factors, e.g., media coverage of current droughts, heat waves, and personal interest in the topic [70,71]. The SPRT risk perception questionnaire contained three dimensions: perceived probability, perceived severity, and perceived consequences. The SAT and SVT questionnaires were unidimensional. Table 4 describes the results of the questionnaires and also each dimension of the SPRT.

Table 4. Results of the questionnaires and also each dimension of the SPRT.

Study Questionnaires	Results
Adaptation to drought	On average, participants are adjusting to different drought adaptation measures, identifying new forms of water storage, improving agricultural techniques, and seeking other activities to improve income.
Socioeconomic vulnerability	In general, participants have a medium level of socio-economic vulnerability, indicating that some participants live in inequitable social contexts that make them more susceptible to droughts. However, despite the circumstances, they have water for farming and household activities, electricity, and access to health care.
Drought risk perception	Drought risk perception: On average, participants have the ability to detect, identify, and react to droughts, which may be influenced by the situations and their experiences. They are concerned about droughts and their consequences.
	Dimension perceived probability. For the most part, participants have a perceived probability at the medium level, indicating that not all significantly establish future experience of the event, observation of changes prior to the event, and adoption of the drought event. Dimension perceived severity. Most of the participants have a medium perceived probability, which indicates that the perception of the impact of agricultural droughts is not detected as serious. Dimension perceived consequences. Most of the participants have a perceived probability of the consequences of droughts at a medium level, in relation to what they cause in crop productivity. This is possibly due to already-developed adaptation mechanisms.

Knowledge and adaptation processes that are useful for individuals or communities to effectively adjust to modified environments over time are largely derived from empirical and analogical analyses [70,72]. The results of this study identified that agricultural land

size, geographic variations, and the number of adaptation activities implemented are key factors in recognizing variables that predict adaptation to drought in and around dry areas.

The study survey captured a representation of 73% male and 25% female farmers. Gender identity within agricultural communities meant potentially male participation in the dry areas of the department of Tolima. Most of the farmers surveyed, 309 respondents, were between 26 and 55 years old. This suggests that middle-aged and slightly older people were prominently engaged in agricultural activities. Furthermore, a substantial proportion of the farmers were within the age group of 56 to 85 years, possibly indicating a persistence of older people in the agricultural sector, such as those proposed by other authors [73–75].

The effectiveness of adaptations depends on socioeconomic factors and human system capacity that influence the selection of adaptation measures [76]. In our study, land tenure, access to water, level of schooling, size of agricultural land for cultivation, crop variations, and amount of implemented adaptation activities were identified as key factors determining the choice of adaptation measures. Farmers with access to water and larger farmland sizes are more likely to choose and adopt drought adaptation [77]. These factors also play an important role in determining an individual's economic status, whether they are wealthy or living in poverty [78,79].

Farmers' perceptions of drought impacts, and their adaptations, play a crucial role in reducing the effects of climate change on crop production [52,80,81]. Maintaining agricultural production is essential for farmers, but drought is severely influencing this [82]. The results show that vulnerability and perception are predictive of drought. Therefore, farmers' perception was identified as the dependent variable, which is widely used in similar studies [21]. According to the theoretical background of previous studies [52,60], people who perceive drought as a high-risk phenomenon seek adaptation strategies.

Scarcity of water, an increase in crop diseases, a reduction in crop yields, increased pest incidence, and a change in planting times are among the worst impacts of climate-related risks [83]. Table 5 compares the variables used in this study with research from other continents and Latin America. The study results provide a good overview of the challenges faced by farmers, focusing on the effects of droughts, and their preferred strategies to mitigate these effects. The older you are, the less adaptation you have, so there is greater resistance to change. People who perceive greater vulnerability are those who adapt faster because they perceive greater adaptation strategies.

Table 5. Comparison of variables used in the study with other research.

Author	Country	Variable	Results
[35]	Pakistan	Farmers' risk perception adaptation measures to climate change.	Age, education, farm size, household size, accessibility to credit, annual income, and perception of increasing temperature and decreasing precipitation significantly influenced the selection of adaptation strategies
[84]	Mongolia	Climate change risk perception	Climate change knowledge was associated with a positive stress response, which in turn was associated with perceived climate change risk.
[85]	Spain	Adaptation to drought Risk perception	Local experience is linked to risk perception, but does not necessarily drive adaptive behavior
[83]	Bangladesh	Drought threat perception Adaptation to drought	Agriculture, as well as the social life and health of farmers, are the most threatened. Farmer-owners are more capable of adopting new technologies than tenant farmers.
[86]	Chile	Risk perception of droughts	Factors influencing the perception of drought (years of experience, level of schooling, etc.) and adaptation strategies (farm size, gender, access to credit, etc.)
[87]	Cuba	Drought hazard perception	The population's perception of drought risk is medium

5. Conclusions

The SAT and SVT questionnaires were designed as a unidimensional tool to assess adaptation to drought. The SPRT is a valid and reliable questionnaire to evaluate the impact that drought has on farmers in Tolima. Therefore, the data collected help to identify the strategies to counteract the impact that this type of event has on the person and his community.

Older adults are the ones least able to adapt to droughts, so it is recommended that a detection and intervention program be developed to identify how this situation is affecting their health because of the stress caused by the phenomenon. It is also important to generate some community guidelines or public policies, so that the elderly can face droughts and improve their quality of life. However, the people who scored higher in their perception of droughts developed coping strategies, such as adaptation measures, since they cannot leave their territories due to socioeconomic reasons or security. According to our study, drought affects the agricultural economy, which generates food insecurity. The vulnerability of farmers living in these areas is associated with the lack of infrastructure, changes in rainfall and temperature patterns, and the lack of support from governmental and non-governmental institutions to solve the shortage of drinking water, and limited access to social, financial and human capital. Because of these conditions, farmers are even more vulnerable to the impacts of drought.

It is important to recognize that local communities are the main actors in addressing drought problems through a combination of traditional and contemporary practices developed through sustained interactions with their local environment. These results will enable policy makers, scientists, and program designers to realize adaptation strategies to ensure successful policy implementation. Likewise, having knowledge about droughts encourages farmers to adopt adaptation measures. Farmers will naturally play the most important role in adopting and implementing available adaptation methods, and the questionnaire results show the willingness of farmers to adopt adaptation measures.

The data from the questionnaires designed in this study allow developing countries, such as Colombia, to make decisions regarding risk management strategies in areas of significant agricultural potential, but with complex social needs and drought problems, in order to minimize the impact of droughts through the design of early warnings and effective interventions.

One of the limitations of the study is the use of a self-administered questionnaire and the participants' responses are based on subjective experiences and could be temporarily or permanently influenced by external factors, such as media coverage of current droughts, heat waves and personal interest in the topic. However, self-administered questionnaires have several advantages thanks to the flexible modality that allows them to be applied to a greater number of people, there is no pressure to answer the questions in a period of time, and they have a low investment. For future research, it is proposed to apply the instruments in other geographical areas to identify their internal consistency and their ability to generalize the data.

Author Contributions: Conceptualization, J.A.H.-L., D.X.P.-C. and H.J.A.; methodology, J.A.H.-L. and D.X.P.-C.; validation, J.A.H.-L., D.X.P.-C. and H.J.A.; formal analysis, J.A.H.-L., D.X.P.-C. and H.J.A.; investigation, J.A.H.-L. and D.X.P.-C.; data curation, J.A.H.-L., D.X.P.-C. and H.J.A.; writing—original draft preparation, J.A.H.-L., D.X.P.-C. and H.J.A.; writing—review and editing, J.A.H.-L., D.X.P.-C. and H.J.A.; visualization, J.A.H.-L., D.X.P.-C. and H.J.A.; supervision, J.A.H.-L., D.X.P.-C. and H.J.A. All authors have read and agreed to the published version of the manuscript.

Funding: This research was supported by the University of Ibagué [research project 19-500-INT, 2018].

Institutional Review Board Statement: Not applicable.

Informed Consent Statement: Not applicable.

Data Availability Statement: Data are contained within the article.

Conflicts of Interest: The authors declare no conflicts of interest.

Appendix A. Questionnaire to Evaluate Water Availability in Drought Scenarios

Before starting, please read the following:

The University of Ibagué is leading the project "Evaluation of the effect of water availability on agricultural production in the department of Tolima in drought scenarios." This questionnaire is part of the research project, and its objective is to evaluate the adaptation measures that agricultural workers use to protect their crops from drought scenarios (El Niño phenomenon), and how these scenarios affect agricultural, environmental, and social work, and the economy of the people.

Participation is completely voluntary and anonymity will be ensured, it does not present any risk to well-being and as a participant you are free to withdraw.

It is important that you answer with complete sincerity for the study to be successful, remember that there are no right or wrong answers.

Based on the above, you wish to participate in the study: Yes ___ No ___

General data

Age (Numbers): _____ Sex: F__ M___

Marital status: Single ____ Married ____ Widowed ___ Common law ____ Divorced ____

Level of education: Primary ___ Secondary ___ Baccalaureate ___ University ____ Technical studies ___ Postgraduate studies (Specialization, master's degrees and/or doctorate) ___

Place of birth: _____

Sociodemographic data questionnaire

1. Municipality where you live: _____

2. Name of the property:_____

3. Name of the Vereda: _____

4. Number of household members: 1 member ____ 1 to 2 members ___ 3 to 4 members ___ More than 5 members ___

5. Do you have children: Yes ___ No ___

6. If you have children, how many are they? 1 child ___ 2 to 3 children ___ 3 to 4 children ___ More than 5 children ___ I do not have children ___

7. How many people do you have in charge?: 1 person ___ 2 people ___ More than 3 people ___ I live alone ___ I don't have people in charge ___

8. Monthly income: Less than $1,000,000 ___ $1,000,000 ___ Between $1,000,000 to 2,000,000 ___ Between $2,000,000 to 3,000,000 ___ Between $4,000,000 to $5,000,000 ___ More than $5,000,000 ___

9. Housing: Own ___ Rented ___ Family _____

10. Time of residence in the home: Less than a year __ Between 1 to 2 years __ 3 to 4 years ___ More than 5 years ___

11. Cooking with: Natural gas ___ Firewood ___ Gas pipette ___

12. What is your family's main source of income? Livestock _ Agriculture _ Fish farming _ Commerce _ Other: _____

Land tenure

13. The plot or property where you work is: Owner ___ Leased ___ Usufructuary ___ Other ___

14. What infrastructure do you have on your farm or plot? Greenhouse ___ Warehouse ___ Shed ___ Outdoors ___ Other: _____

Infrastructure and tools

15. For agriculture, what tools do you use: Agricultural machinery ___ Work animals ___ Hand tools (pick, shovel, hoe, back pump, wheelbarrow, etc.) ___ Other: _____

16. Uses machinery: Own ___ Rented ___

17. Number of workers in charge: 1 to 2 workers ___ 3 to 4 workers ___ 4 to 5 workers ___ More than 5 workers ___

18. Time spent farming (in years): Less than 1 year _ 1 year __ 1 to 2 years __ 2 to 3 years __ 3 to 4 years __ More than 5 years ___

19. What do you grow at the moment? Vegetables __ Rice__ Wheat__ Beans__ Corn__ Other:_____

20. Size of the crop (hectares, bushels or square meters). Write with unit: _____

21. What other crops do you have during the year?: Cereals ___ Fruit trees ___ Legumes ___ Other: _____

22. You have animals: Yes ___ No ___

23. Type of animals: I do not have animals___ Cows___ Goats___ Sheep___ Fattening steers___ Pack animals (Horses, mules, donkeys)___ Pigs___ Dogs___ Fish___ Ducks-Geese___ Chickens___ Other_____

Water access for irrigation

24. Do you have access to water for irrigation: Yes ___ No ___

25. What are the sources of water supply for irrigation? Indicate the option with which you most identify according to the source of supply, with respect to scale (every week, from time to time, I have very little or no supply source):

	Every Week	From Time to Time	Never
Channel			
Well			
Reservoir			
Broken			
River			
Rainwater accumulation			

Access to drinking water

26. Do you have access to drinking water: Yes ___ No ___

27. Since when you do not have drinking water: Less than 1 month ___ 1 to 2 months ___ 3 to 6 months ___ 1 year ___ More than 1 year ___ Never ____ Not applicable___

28. The source of water consumed for human use is obtained from: River ___ Rain ___ Irrigation district ___ Community or village aqueduct ___ Municipal aqueduct ___ Birth _____

Perception of drought

To answer questions 29 and 30, take into account the following concepts:

The term precipitation is used in meteorology to refer to all the phenomena of water falling from the sky in any form: rain, hail, snow, etc.

Droughts are prolonged periods of dry weather caused by a lack of rain, resulting in water shortages. Periods of drought can cause water shortages and public health problems.

29. Perception of drought (In recent years):

	Increased	Diminished	There Are no Changes	Does not Know
The rainfall has:				
The drought has				

30. Number of precipitations per year: Below you will find the months of the year in the rows and the types of precipitation in the columns. According to the month, indicate the type of precipitation (Rain, dry or rain-Dry) for each month according to your experience.

	Rain	Dry	Rain-Dry
January			
February			
March			
April			

May			
June			
July			
August			
September			
October			
November			
December			

Socioeconomic vulnerability to droughts:

Below you will find a series of questions related to the experiences you have had with the drought. Respond according to your experience and indicate the answer that best identifies you based on the following scale:

1 = Strongly disagree
2 = Disagree
3 = Agree
4 = Totally agree.

Items	1	2	3	4
31. I have water for field activities				
32. I have drinking water for human consumption				
33. I have drinking water for household chores				
34. I have a rainwater storage system				
35. I eat less than three meals a day.				
36. I have a community that supports me economically, socially and/or emotionally				
37. The access roads to my property are paved				
38. There are conflicts over public order in my neighborhood				
39. The floors of my home are made of dirt				
40. The roof of my home is made of cardboard sheets or other recycling material				
41. My home guarantees physical security; i.e., protection against cold, humidity, heat, rain, wind or other health risks and structural hazards				
42. In my house, more than three adults sleep in a room.				

Drought risk perception

Below you will find a series of statements related to what you believe or think about the drought, responding according to your experience with the drought. Indicate the answer according to the option that best identifies you.

Perceived probability:

In this section, you will find a series of questions related to the changes in your life that you have observed due to the drought. Respond according to your experience, indicating the option that best identifies you based on the following scale:

1 = Strongly disagree
2 = Disagree
3 = Agree
4 = Totally agree.

Items	1	2	3	4
43. Summer is a threat that affects the water sources of my plot or farm				
44. I think the drought will come				
45. I am worried about the consequences of the next drought				
46. My family is worried that a drought is coming				
47. The next drought will have worse consequences than the previous one				

The perceived severity

In this section you will find a series of questions related to the negative impact that drought has on your life. According to your experience with drought, indicate the answer that best identifies you based on the following scale:

1 = Strongly disagree
2 = Disagree
3 = Agree
4 = Totally agree.

Items	1	2	3	4
48. Drought is the most serious thing that can happen to us				
49. The drought greatly affects the health of my family, that of my workers and myself				
50. Drought greatly affects the health and well-being of my animals				
51. Drought damages the quality of my crops				
52. The drought deteriorates my home				
53. My crop is affected by pests and/or diseases caused by droughts.				
54. The drought affects my harvest				
55. Drought seriously reduces water in my farm or plot				

Perceived consequences of droughts:

In this section, you will find a series of questions related to what you perceive causes the drought. Indicate the answer according to the option that best identifies you based on the following scale:

1 = Strongly disagree
2 = Disagree
3 = Agree
4 = Totally agree.

Items	1	2	3	4
56. Due to lack of water my family has health problems				
57. During a drought, water sources (rivers, streams, wells, streams, among others) are reduced.				
58. Water scarcity limits agricultural production				
59. In times of drought my crop loses life (withers or dies)				
60. A drought affects my agricultural work				
61. A drought can cause great economic losses				
62. I believe that in the event of a water shortage, children will have to miss school				
63. Drought generates significant losses in crop production				
64. Due to the drought I sell my harvest at a lower price				
65. Due to the drought I sell my property				
66. The scarcity of water affects the sanitary systems of my farm				
67. Due to the drought, I sold part of my assets and/or took out a mortgage on my home to obtain resources for my livelihood.				
68. I took out a bank loan due to the effects of the drought				
69. Due to the drought I have thought about changing my place of residence.				

Adaptation to droughts:

Below you will find a series of questions related to how you adapt or adjust to the drought, so please respond according to your experience, indicating the option that best identifies you based on the following scale:

1 = Strongly disagree
2 = Disagree
3 = Agree
4 = Totally agree.

Items	1	2	3	4
70. In the summer time he used seed that withstands the weather conditions				
71. To reduce the effect of drought on my crops, I have used pesticides, insecticides, and other inputs to control pests or diseases.				
72. Droughts have brought me new opportunities				
73. Due to the effects of the droughts, I have thought about changing my economic activity				
74. Due to the effects of the droughts I have changed jobs				
75. I have looked for new water storage alternatives on my farm or property.				
76. Despite the droughts, agriculture has generated stability for me				
77. The drought has allowed me to improve my agricultural techniques				
78. Due to the droughts I have had to carry out other extra activity(s) to increase income				
79. Due to the droughts I have modified the irrigation system for my crop				
80. Due to the droughts I began to use agrochemicals to improve production in my crop (insecticides, fungicides, pesticides, etc.)				
81. I have learned to use less labor to harvest the harvest in case of drought in my crop.				

References

1. Acibuca, V.; Kaya, A.; Kaya, T. Interregional comparative analysis of farmers' perceptions and expectations of climate change. *Ital. J. Agron.* **2022**, *17*, 1–8. [CrossRef]
2. Ávila Díaz, Á.J.; Carvajal Escobar, Y.; Gutiérrez Serna, S.E. Análisis de la influencia de El Niño y La Niña en la oferta hídrica mensual de la cuenca del río Cali. *Rev. Tecnura* **2015**, *18*, 120–133. [CrossRef]
3. Shah, A.A.; Khan, N.A.; Gong, Z.; Ahmad, I.; Naqvi, S.A.A.; Ullah, W.; Karmaoui, A. Farmers' perspective towards climate change vulnerability, risk perceptions, and adaptation measures in Khyber Pakhtunkhwa, Pakistan. *Int. J. Environ. Sci. Technol.* **2022**, *20*, 1421–1438. [CrossRef]
4. Streimikiene, D.; Dahal, K.R.; Dahal, P.; Adhikari, R.K.; Naukkarinen, V.; Panday, D.; Bista, N.; Helenius, J.; Marambe, B. Climate Change Impacts and Adaptation in a Hill Farming System of the Himalayan Region: Climatic Trends, Farmers’ Perceptions and Practices. *Climate* **2022**, *11*, 11. [CrossRef]
5. Yadav, S.S.; Hegde, V.S.; Habibi, A.B.; Dia, M.; Verma, S. Climate Change, Agriculture and Food Security. In *Food Security and Climate Change*; Yadav, S.S., Redden, R.J., Hatfield, J.L., Ebert, A.W., Hunter, D., Eds.; John Wiley & Sons: New York, NY, USA, 2019; pp. 1–24. [CrossRef]
6. Ojeda-Flechas, C.D.; Burbano-Rodríguez, J.A.; Carvajal-Escobar, Y.; Hernández-Torres, F.L. Characterization of comprehensive drought events associated with the enso warm phase through satellite images in the valle del cauca, colombia [Caracterización de eventos de sequía integral, asociados a la fase cálida de enos, mediante imágenes satelitale. *DYNA* **2020**, *87*, 204–214. [CrossRef]
7. Valencia, J.M.; García, C.E.; Montero, D. Anomalías de vegetación asociadas con el fenómeno del ENOS en el valle geográfico del río Cauca, Colombia. *Rev. Teledetec.* **2017**, *50*, 89–100. [CrossRef]
8. Poveda, G.; Álvarez, D.M.; Rueda, Ó.A. Hydro-climatic variability over the Andes of Colombia associated with ENSO: A review of climatic processes and their impact on one of the Earth's most important biodiversity hotspots. *Clim. Dyn.* **2011**, *36*, 2233–2249. [CrossRef]
9. Bedoya-Soto, J.M.; Poveda, G.; Trenberth, K.E.; Vélez-Upegui, J.J. Interannual hydroclimatic variability and the 2009–2011 extreme ENSO phases in Colombia: From Andean glaciers to Caribbean lowlands. *Theor. Appl. Climatol.* **2019**, *135*, 1531–1544. [CrossRef]
10. Loaiza Cerón, W.; Carvajal Escobar, Y.; Baquero Montoya, O.L. Índice estandarizado de precipitación (SPI) para la caracterización de sequías meteorológicas en la cuenca del río Dagua-Colombia. *Estud. Geogr.* **2016**, *76*, 557–578. [CrossRef]
11. Ballesteros, J.; Isaza, C. Adaptation Measures to Climate Change as Perceived by Smallholder Farmers in the Andes. *J. Ethnobiol.* **2021**, *41*, 428–446. [CrossRef]
12. Henao, F.; Viteri, J.P.; Rodríguez, Y.; Gómez, J.; Dyner, I. Annual and interannual complementarities of renewable energy sources in Colombia. *Renew. Sustain. Energy Rev.* **2020**, *134*, 110318. [CrossRef]
13. Chen, Y.; Penton, D.; Karim, F.; Aryal, S.; Wahid, S.; Taylor, P.; Cuddy, S.M. Characterisation of meteorological drought at sub-catchment scale in Afghanistan using station-observed climate data. *PLoS ONE* **2023**, *18*, e0280522. [CrossRef]
14. Dahir, A.; Omar, M.; Abukar, Y. Internet of things based agricultural drought detection system: Case study Southern Somalia. *Bull. Electr. Eng. Inform.* **2023**, *12*, 69–74. [CrossRef]
15. Espinosa, L.A.; Portela, M.M.; Matos, J.P.; Gharbia, S. Climate Change Trends in a European Coastal Metropolitan Area: Rainfall, Temperature, and Extreme Events (1864–2021). *Atmosphere* **2022**, *13*, 1995. [CrossRef]
16. Velasco, I.; Ochoa, L.; Gutiérrez, C. Sequía, un problema de perspectiva y gestión. *Región Y Soc.* **2017**, *17*, 35–71. [CrossRef]
17. Mpandeli, S.; Nesamvuni, E.; Maponya, P. Adapting to the Impacts of Drought by Smallholder Farmers in Sekhukhune District in Limpopo Province, South Africa. *J. Agric. Sci.* **2015**, *7*, 115–124. [CrossRef]
18. Mavhura, E.; Manatsa, D.; Matiashe, M. Adapting smallholder farming to climate change and variability: Household strategies and challenges in Chipinge district, Zimbabwe. *Clim. Chang.* **2017**, *3*, 903–913.

19. Mavhura, E.; Manyangadze, T.; Aryal, K.R. Perceived impacts of climate variability and change: An exploration of farmers' adaptation strategies in Zimbabwe's intensive farming region. *GeoJournal* **2022**, *87*, 3669–3684. [CrossRef]
20. Ogundeji, A.A.; Okolie, C.C. Perception and Adaptation Strategies of Smallholder Farmers to Drought Risk: A Scientometric Analysis. *Agriculture* **2022**, *12*, 1129. [CrossRef]
21. Van-Tilburg, A.J.; Hudson, P.F. Extreme weather events and farmer adaptation in Zeeland, the Netherlands: A European climate change case study from the Rhine delta. *Sci. Total Environ.* **2022**, *844*, 157212. [CrossRef] [PubMed]
22. Griffin, C.; Wreford, A.; Cradock-Henry, N.A. 'As a farmer you've just got to learn to cope': Understanding dairy farmers' perceptions of climate change and adaptation decisions in the lower South Island of Aotearoa-New Zealand. *J. Rural Stud.* **2023**, *98*, 147–158. [CrossRef]
23. Smith, W.; Davies-Colley, C.; Mackay, A.; Bankoff, G. Social impact of the 2004 Manawatu floods and the "hollowing out" of rural New Zealand. *Disasters* **2011**, *35*, 540–553. [CrossRef] [PubMed]
24. Eriksen, S.; Aldunce, P.; Bahinipati, C.S.; Martins, R.D.A.; Molefe, J.I.; Nhemachena, C.; O'Brien, K.; Olorunfemi, F.; Park, J.; Sygna, L.; et al. When not every response to climate change is a good one: Identifying principles for sustainable adaptation. *Clim. Dev.* **2011**, *3*, 7–20. [CrossRef]
25. Rahman, H.M.; Albizua, A.; Soubry, B.; Tourangeau, W. A framework for using autonomous adaptation as a leverage point in sustainable climate adaptation. *Clim. Risk Manag.* **2021**, *34*, 100376. [CrossRef]
26. Tanner, T.; Lewis, D.; Wrathall, D.; Bronen, R.; Cradock-Henry, N.; Huq, S.; Lawless, C.; Nawrotzki, R.; Prasad, V.; Rahman, M.A.; et al. Livelihood resilience in the face of climate change. *Nat. Clim. Chang.* **2015**, *5*, 23–26. [CrossRef]
27. Derbile, E.K.; Chirawurah, D.; Naab, F.X. Vulnerability of smallholder agriculture to environmental change in North-Western Ghana and implications for development planning. *Clim. Dev.* **2022**, *14*, 39–51. [CrossRef]
28. Fatorić, S. Vulnerability and Adaptation to Climate Change in the Mediterranean Region. Doctoral Thesis, Universidad Autónoma de Barcelona, Barcelona, España, 2014.
29. Keshavarz, M.; Maleksaeidi, H.; Karami, E. Livelihood vulnerability to drought: A case of rural Iran. *Int. J. Disaster Risk Reduct.* **2017**, *21*, 223–230. [CrossRef]
30. Sultana, R.; Irfanullah, H.M.; Selim, S.A.; Budrudzaman, M. Vulnerability and ecosystem-based adaptation in the farming communities of droughtprone Northwest Bangladesh. *Environ. Chall.* **2023**, *11*, 100707. [CrossRef]
31. Eze, J.N.; Onokala, P.C. Pattern of household vulnerability to desertification in Yobe state, Nigeria. *GeoJournal* **2022**, *87*, 2699–2717. [CrossRef]
32. Okolie, C.C.; Danso-Abbeam, G.; Ogundeji, A.A. Livelihood vulnerability to the changing climate: The experiences of smallholder farming households in the Free State Province, South Africa. *Clim. Serv.* **2023**, *30*, 100371. [CrossRef]
33. Virnodkar, S.S.; Pachghare, V.K.; Patil, V.C.; Jha, S.K. Remote sensing and machine learning for crop water stress determination in various crops: A critical review. *Precis. Agric.* **2020**, *21*, 1121–1155. [CrossRef]
34. Ali, S.; Ying, L.; Nazir, A.; Ishaq, M.; Shah, T.; Ye, X.; Tariq, A. Rural farmers perception and coping strategies towards climate change and their determinants: Evidence from Khyber Pakhtunkhwa province, Pakistan. *J. Clean. Prod.* **2021**, *291*, 125250. [CrossRef]
35. Khan, I.; Lei, H.; Shah, I.A.; Ali, I.; Khan, I.; Muhammad, I.; Huo, X.; Javed, T. Farm households' risk perception, attitude and adaptation strategies in dealing with climate change: Promise and perils from rural Pakistan. *Land Use Policy* **2020**, *91*, 104395. [CrossRef]
36. Bahta, Y.T.; Lombard, W.A. Nexus between Social Vulnerability and Resilience to Agricultural Drought amongst South African Smallholder Livestock Households. *Atmosphere* **2023**, *14*, 900. [CrossRef]
37. Khan, N.; Ma, J.; Kassem, H.S.; Kazim, R.; Ray, R.L.; Ihtisham, M.; Zhang, S. Rural Farmers' Cognition and Climate Change Adaptation Impact on Cash Crop Productivity: Evidence from a Recent Study. *Int. J. Environ. Res. Public Health* **2022**, *19*, 12556. [CrossRef]
38. Jha, S.; Kaechele, H.; Lana, M.; Amjath-Babu, T.S.; Sieber, S. Exploring farmers' perceptions of Agricultural Technologies: A Case Study from Tanzania. *Sustainability* **2020**, *12*, 998. [CrossRef]
39. Ahmed, Z.; Shew, A.M.; Mondal, M.K.; Yadav, S.; Jagadish, S.V.; Prasad, P.V.; Buisson, M.C.; Das, M.; Bakuluzzaman, M. Climate risk perceptions and perceived yield loss increases agricultural technology adoption in the polder areas of Bangladesh. *J. Rural Stud.* **2022**, *94*, 274–286. [CrossRef]
40. Aliyar, Q.; Zulfiqar, F.; Datta, A.; Kuwornu, J.K.M.; Shrestha, S. Drought perception and field-level adaptation strategies of farming households in drought-prone areas of Afghanistan. *Int. J. Disaster Risk Reduct.* **2022**, *72*, 102862. [CrossRef]
41. Gashure, S.; Wana, D. Smallholder farmers' perceptions, coping and adaptation strategies to climate variability in the UNESCO designated cultural landscapes of Konso. *Ethiopia* **2023**, *28*, 1243–1262. [CrossRef]
42. Marie, M.; Yirga, F.; Haile, M.; Tquabo, F. Farmers' choices and factors affecting adoption of climate change adaptation strategies: Evidence from northwestern Ethiopia. *Heliyon* **2020**, *6*, e03867. [CrossRef]
43. Sertse, S.F.; Khan, N.A.; Shah, A.A.; Liu, Y.; Naqvi, S.A.A. Farm households' perceptions and adaptation strategies to climate change risks and their determinants: Evidence from Raya Azebo district, Ethiopia. *Int. J. Disaster Risk Reduct.* **2021**, *60*, 102255. [CrossRef]
44. Olivares, B.O. Análisis temporal de la sequía meteorológica en localidades semiáridas de Venezuela. *UGCiencia* **2017**, *22*, 11–24. [CrossRef]

45. Ortega-Gaucin, D.; Velasco, I. Aspectos socioeconómicos y ambientales de las sequías en México. *Aqua-LAC* **2013**, *5*, 78–90. [CrossRef]
46. Melo-Leon, S.F.; Riveros-Salcedo, L.C.; Romero-Otalora, G.; Álvarez, A.C.; Diaz-Giraldo, C.; Calderón-Diaz, S.L. Efectos Económicos de Futuras Sequías en Colombia: Estimación a Partir del Fenómeno El Niño 2015. 2017. Available online: https://colaboracion.dnp.gov.co/CDT/Estudios%20Econmicos/466.pdf (accessed on 15 February 2024).
47. Li, J.; Huimin, L. Impacts of climate change on winter wheat and summer maize dual-cropping system in the North China Plain. *Environ. Res. Commun.* **2022**, *4*, 075014. [CrossRef]
48. Yao, P.; Qian, L.; Wang, Z.; Meng, H.; Ju, X. Assessing Drought, Flood, and High Temperature Disasters during Sugarcane Growth Stages in Southern China. *Agriculture* **2022**, *12*, 2117. [CrossRef]
49. Musafiri, C.M.; Macharia, J.M.; Ng'etich, O.K.; Kiboi, M.N.; Okeyo, J.; Shisanya, C.A.; Okwuosa, E.A.; Mugendi, D.N.; Ngetich, F.K. Farming systems' typologies analysis to inform agricultural greenhouse gas emissions potential from smallholder rain-fed farms in Kenya. *Sci. Afr.* **2020**, *8*, e00458. [CrossRef]
50. Asrat, P.; Simane, B. Household- and plot-level impacts of sustainable land management practices in the face of climate variability and change: Empirical evidence from Dabus Sub-basin, Blue Nile River, Ethiopia. *Agric. Food Secur.* **2017**, *6*, 61. [CrossRef]
51. Bwambale, N. Farmers' Knowledge, Perceptions, and Socioeconomic Factors Influencing Decision Making for Integrated Soil Fertility Management Practices in Masaka and Rakai Districts, Central Uganda. Master's Thesis, Iowa State University, Iowa, IA, USA, 2015.
52. Al Mamun, A.; Roy, S.; Islam, A.R.M.; Alam, G.M.; Alam, E.; Chandra Pal, S.; Sattar, A.; Mallick, J. Smallholder farmers' perceived climate-related risk, impact, and their choices of sustainable adaptation strategies. *Sustainability* **2021**, *13*, 11922. [CrossRef]
53. Rojas-Tiempo, J.; Díaz-Ruiz, R.; Álvarez-Gaxiola, F.; Ocampo-Mendoza, J.; Escalante-Estrada, A. Tecnología de producción de haba y características socioeconómicas de productores en Puebla y Tlaxcala. *Rev. Mex. Cienc. Agríc.* **2018**, *3*, 35–49. [CrossRef]
54. OMM. Guide to meteorological instruments and methods of observation. In World Meteorological Organization: Vol. I (Issue 8); WMO-No. 8: Measurement of Meteorological Variables; 2018. Available online: https://community.wmo.int/en/activity-areas/imop/wmo-no_8 (accessed on 19 June 2024).
55. UNGRD; IDEAM; MINAMBIENTE; CANCILLERÍA. Estrategia Nacional para la Gestión Integral de la Sequía en Colombia. 2018. Available online: https://faolex.fao.org/docs/pdf/col218772.pdf (accessed on 19 February 2024).
56. IGAC. *Estudio General de Suelos y Zonificación de Tierras Departamento del Tolima Escala 1: 100.000*, 1st ed.; In Instituto Geográfico Agustín Codazzi: Bogota, Colombia, 2016; pp. 1–545.
57. CORTOLIMA. *Plan de Gestión Ambiental Regional del Tolima 2013–2023. [Internet]*; Corporación Autónoma Regional del Tolima: Ibagué, Colombia, 2009. Available online: https://tolima.gov.co/images/transparencia/planeacion/formatos-de-empalme/gestion-del-desarrollo/lineamientos-seguimiento-plan-de-desarrollo/planes-sectoriales/gestion-del-riesgo/plan-de-gestion-ambiental-regional-2013_2023_tolima.pdf (accessed on 20 February 2024).
58. Anning, A.K.; Ofori-Yeboah, A.; Baffour-Ata, F.; Owusu, G. Climate change manifestations and adaptations in cocoa farms: Perspectives of smallholder farmers in the Adansi South District, Ghana. *Curr. Res. Environ. Sustain.* **2022**, *4*, 100196. [CrossRef]
59. Puerta-Cortés, D.; Carbonell, X. El modelo de los cinco grandes factores de personalidad y el uso problemático de Internet en jóvenes colombianos. *Adicciones* **2014**, *26*, 54. [CrossRef] [PubMed]
60. Dendir, Z.; Simane, B. Farmers' perceptions about changes in climate variables: Perceived risks and household responses in different agro-ecological communities, Southern Ethiopia. *Clim. Serv.* **2021**, *22*, 100236. [CrossRef]
61. Yiridomoh, G.Y.; Appiah, D.O.; Owusu, V.; Bonye, S.Z. Women smallholder farmers off-farm adaptation strategies to climate variability in rural Savannah, Ghana. *GeoJournal* **2021**, *86*, 2367–2385. [CrossRef]
62. McCoach, D.B.; Gable, R.K.; Madura, J.P. *Instrument Development in the Affective Domain*; Springer: New York, NY, USA, 2013; Volume 10, pp. 978–981.
63. Mooney, S.; O'Dwyer, J.; Lavallee, S.; Hynds, P.D. Private groundwater contamination and extreme weather events: The role of demographics, experience and cognitive factors on risk perceptions of Irish private well users. *Sci. Total Environ.* **2021**, *784*, 147118. [CrossRef] [PubMed]
64. Ayeri, O.S.; Christian, V.R.; Josef, E.; Michael, H. Local Perceptions and Responses to Climate Change and Variability: The Case of Laikipia District, Kenya. *Sustainability* **2012**, *4*, 3302–3325. [CrossRef]
65. Mekonnen, M.; Abeje, T.; Addisu, S. Integrated watershed management on soil quality, crop productivity and climate change adaptation, dry highland of Northeast Ethiopia. *Agric. Syst.* **2021**, *186*, 102964. [CrossRef]
66. Ngure, M.W.; Wandiga, S.O.; Olago, D.O.; Oriaso, S.O. Climate change stressors affecting household food security among Kimandi-Wanyaga smallholder farmers in Murang'a County, Kenya. *Open Agric.* **2021**, *6*, 587–608. [CrossRef]
67. Jia, J.J.; Wang, Y.; Liu, X.S.; Li, F.; Zhang, X.S. The response capability analysis of farmers on social-economic-natural complex ecosystem management in Alxa, Inner Mongolia. *Shengtai Xuebao* **2017**, *37*, 5836–5845. [CrossRef]
68. Maliki, M.A.; Pauline, N.M. Living and Responding to Climatic Stresses: Perspectives from Smallholder Farmers in Hanang' District, Tanzania. *Environ. Manag.* **2022**, *71*, 131–144. [CrossRef]
69. Von-Gehren, P.; Bomers, S.; Tripolt, T.; Söllinger, J.; Prat, N.; Redondo, B.; Vorss, R.; Teige, M.; Kamptner, A.; Ribarits, A. Farmers Feel the Climate Change: Variety Choice as an Adaptation Strategy of European Potato Farmers. *Climate* **2023**, *11*, 189. [CrossRef]
70. Darjee, K.B.; Neupane, P.R.; Köhl, M. Proactive Adaptation Responses by Vulnerable Communities to Climate Change Impacts. *Sustainability* **2023**, *15*, 10952. [CrossRef]

71. Weber, E.U.; Stern, P.C. Public Understanding of Climate Change in the United States. *Am. Psychol.* **2011**, *66*, 315–328. [CrossRef] [PubMed]
72. Smit, B.; Pilifosova, O. Adaptation to Climate Change in the Context of Sustainable Development and Equity. In *Climate Change 2003: Impacs, Adaption, and Vulnerability*; McCarthy, J.J., Canciany, O.F., Leary, N.A., Dokken, D.J., White, K.S., Eds.; Cambridge University Press: Cambridge, UK; New York, NY, USA, 2001; p. 1022.
73. Ayanlade, A.; Oluwatimilehin, I.A.; Ayanlade, O.S.; Adeyeye, O.; Abatemi-Usman, S. Gendered vulnerabilities to climate change and farmers' adaptation responses in Kwara and Nassarawa States, Nigeria. *Humanit. Soc. Sci. Commun.* **2023**, *10*, 911. [CrossRef]
74. Islam, M.S.; Kabir, M.H.; Ali, M.S.; Sultana, M.S.; Mahasin, M. Farmers' Knowledge on Climate Change Effects in Agriculture. *Agric. Sci.* **2019**, *10*, 386–394. [CrossRef]
75. Landaverde, R.; Rodriguez, M.T.; Niewoehner-Green, J.; Kitchel, T.; Chuquillanqui, J. Climate Change Perceptions and Adaptation Strategies: A Mixed Methods Study with Subsistence Farmers in Rural Peru. *Sustainability* **2022**, *14*, 6015. [CrossRef]
76. Smit, B.; Pilifosova, O. From adaptation to adaptive capacity and vulnerability reduction. In *Climate Change, Adaptive Capacity and Development*; World Scientific: Singapore, 2003; pp. 9–28. [CrossRef]
77. Mensah, M.; Vlek, P.L.G.; Fosu-Mensah, B.Y. Gender and climate change linkages in the semi-arid region of Ghana. *GeoJournal* **2022**, *87*, 363–376. [CrossRef]
78. Ahmed, Z.; Guha, G.S.; Shew, A.M.; Alam, G.M.M. Climate change risk perceptions and agricultural adaptation strategies in vulnerable riverine char islands of Bangladesh. *Land Use Policy* **2021**, *103*, 105295. [CrossRef]
79. Hossain, M.F. Impact of climate change in Bangladesh: Rainfall. *Int. J. Agric. Innov. Res.* **2014**, *2*, 860–863.
80. Karki, S.; Burton, P.; Mackey, B. The experiences and perceptions of farmers about the impacts of climate change and variability on crop production: A review. *Clim. Dev.* **2020**, *12*, 80–95. [CrossRef]
81. Waibel, H.; Pahlisch, T.H.; Völker, M. Farmers' Perceptions of and Adaptations to Climate Change in Southeast Asia: The Case Study from Thailand and Vietnam. *Clim. Smart Agric. Build. Resil. Clim. Chang.* **2018**, *52*, 137–160. [CrossRef]
82. Alam, G.M.M.; Alam, K.; Mushtaq, S. Climate change perceptions and local adaptation strategies of hazard-prone rural households in Bangladesh. *Clim. Risk Manag.* **2017**, *17*, 52–63. [CrossRef]
83. Habiba, U.; Shaw, R.; Takeuchi, Y. Farmer's perception and adaptation practices to cope with drought: Perspectives from Northwestern Bangladesh. *Int. J. Disaster Risk Reduct.* **2012**, *1*, 72–84. [CrossRef]
84. Sattler, D.N.; Bishkhorloo, B.; Graham, J.M. Climate change threatens nomadic herding in Mongolia: A model of climate change risk perception and behavioral adaptation. *J. Environ. Psychol.* **2021**, *75*, 101620. [CrossRef]
85. Iglesias, A.; Garrote, L.; Bardají, I.; Santillán, D.; Esteve, P. Looking into individual choices and local realities to define adaptation options to drought and climate change. *J. Environ. Manag.* **2021**, *293*, 112861. [CrossRef]
86. Suazo Muñoz, C.; Sandoval-Díaz, J. Revisión sistemática de la percepción de riesgo en agricultores ante la sequía: Factores de influencia, contenidos percibidos, estrategias de adaptación y prácticas asociadas. *Sci. Agropecu.* **2023**, *14*, 139–152. [CrossRef]
87. Núñez, E.G.; Lara, S.C.; García, I.R. Vulnerabilidad social y percepción del riesgo en la población cubana expuesta a la sequía. *Pers. Y Soc.* **2022**, *36*, 9–28. [CrossRef]

Disclaimer/Publisher's Note: The statements, opinions and data contained in all publications are solely those of the individual author(s) and contributor(s) and not of MDPI and/or the editor(s). MDPI and/or the editor(s) disclaim responsibility for any injury to people or property resulting from any ideas, methods, instructions or products referred to in the content.

climate

MDPI

Article

A Farmer-Centric Cost–Benefit Analysis of Climate-Smart Agriculture in the Gandaki River Basin of Nepal

Shobha Poudel [1,2,*], Rabin Thapa [3] and Bhogendra Mishra [1,4]

[1] Research Department, Science Hub, Kathmandu 44600, Nepal
[2] Fondazione Eni Enrico Mattei, Corso Magenta, 63, 20123 Milan, Italy
[3] Department of Agricultural Economics and Agribusiness Management, Faculty of Agriculture, Agriculture and Forestry University, Chitwan 44220, Nepal; rabin.thapa@nepal.gov.np
[4] Italian National Research Council (CNR), Institute for Electromagnetic Sensing of the Environmental, Via A. Corti 12, 20133 Milan, Italy; mishra.b@irea.cnr.it
* Correspondence: shobha.poudel@feem.it; Tel.: +39-02-40336934

Abstract: Climate-smart agriculture (CSA) is a climate-resilient practice that stands out globally as an important practice through which we can deal with emerging challenges through adaptation and mitigation to increase crop productivity and resilience. Despite its significance, a comprehensive cost–benefit analysis of the adoption of these practices has not yet been carried out. This study aims to bridge the knowledge gap between the cost and effectiveness of CSA practices adopted by small-scale farmers in growing rice, wheat and maize, the most staple crops in the Gandaki River Basin of Nepal. In this study, net present value (NPV), internal rate of return (IRR), benefit–cost (BC) ratio, net benefit investment (NK) ratio and payback period, along with the value of externalities (social and environmental), were employed to assess the profitability of CSA practices. The findings indicate that almost all the CSA practices analyzed were profitable, with the exception of solar water management in maize with very low IRR (6%) and a longer payback period. The outcome of this study offers valuable insights for farmers in choosing profitable CSA technology and for policy makers in promoting better CSA technology, upscaling CSA practices, and formulating new agricultural policies and programs in the context of the changing climate.

Keywords: climate change; climate-smart agriculture; cost–benefit analysis; externalities; investment appraisal; Nepal; smallholder farmers

1. Introduction

The world is facing the consequences of climate change in various ways. The increase in temperature, unevenly distributed precipitation, flood, landslides, and drought spells have created a change in agricultural patterns [1,2]. Additionally, these events have resulted in crop failures, exacerbating food and livelihood insecurity, amplifying water shortages, and increasing the likelihood of poverty [2,3]. Although there might be several factors influencing the fluctuating yield, climate change is considered a major one [4,5]. The changing climate has brought massive challenges for smallholder farmers who rely on rain-fed agriculture. Projections indicate that under the prevailing conditions, climate change is expected to lead to a decline in rain-fed maize yield, ranging from 3.3% to 6.4% by the year 2030 and 5.2% to 12.2% by 2050. Similarly, for irrigated maize yield, the decrease in yield is projected to be between 3% and 8% in 2030 and 5% and 14% in 2050, based on the cultivation of current varieties in South Asia [6]. In Nepal, the impact of climate change (CC) is anticipated to have the most pronounced negative effects on yield levels for maize, potato, sugarcane, and lentils. These crop yields are expected to decrease by 16.1%, 8.9%, 8.0%, and 4.9%, respectively, under CC conditions compared to a scenario without climate change (NoCC) by 2050. Additionally, rice and vegetable yields are also expected to be lower under CC compared to NoCC, but the projected differences are relatively small,

at −0.4% and −0.1%, respectively. The sustainability of rain-fed agricultural production systems may be jeopardized if we stay with business as usual (BAU) in the context of climate change. A sound policy recommendation for addressing the challenges posed by climate change involves promoting the adoption of climate-smart agriculture (CSA) practices as a means of adaptation. The Food and Agricultural Organization (FAO) of the United Nations defines CSA as a strategy through which to address the challenges of climate change and food security by sustainably increasing productivity, bolstering resilience, reducing GHG emissions, and enhancing achievement of national food security and development goals [7]. Adaptation, mitigation, and food security are the three pillars of CSA.

In Nepal, few villages from different ecological zones (Bardiya, Dang, Rupandehi, Nawalparasi, Gorkha, and Mahottari districts) have implemented CSA practices, which are vulnerable to changing climate and its possible effects. A study by Khatri-Chettri [8] on the benefits of implementing the CSA practices (including both experimental and in-field research) across South Asia revealed that the use of nutrient-supply- and irrigation-related technologies in rice led to an 83% and 23% increase in yield, respectively. Similarly, another study on the use of different irrigation-related CSA practices in winter maize reported an increased yield and significant improvement in the growth parameters [9]. Several studies suggest that the CSA practices could prove advantageous, but at the same time, the profitability of using different CSA practices in major crops grown by smallholder farmers needs to be ascertained. Therefore, by assessing the costs and benefits of agricultural investments, farmers and investors can adjust their decisions and prioritize the most effective techniques for successful adaptation [10]. The cost–benefit analysis (i) evaluates the impact of adopting specific CSA practices over time, providing farmers with information on the profitability of securing the necessary capital for the successful implementation and maintenance of CSA practices until profits are realized, and (ii) advises smallholder farmers on the potential of CSA practices to yield a return on invested capital. Assessment of CSA practices via discounted measures like net present value (NPV) and internal rate of return (IRR) not only provides a basis for choosing the most profitable practice but also indicates which practice should be chosen, considering long-term investment.

Similarly, a study reported that certain agricultural practices have a greater capacity to reduce greenhouse gas emissions (such as through carbon sequestration), enhance food security (for instance, by increasing productivity), and consequently contribute to the sustainability of the livelihoods of households [11]. CSA has the potential to provide environmental advantages that assist households in adapting to the impacts of climate change and variability [12]. The strategic selection of CSA practices plays a pivotal role in maximizing benefits while minimizing costs. However, this selection relies significantly on how farmers perceive these benefits. The farmers' perception of these benefits is a crucial factor influencing their decisions regarding acquiring loans for investing in new technologies [13]. Therefore, the implementation of cost–benefit analysis (CBA) becomes imperative, offering farmers crucial insights into the anticipated benefits of investing in specific CSA practices. By comparing these benefits with the associated costs, smallholder farmers can determine the time frame required to reach a break-even point.

In this light, this research aims to determine the major costs and benefits of adopting chosen CSA practices; carry out a profitability assessment of practices using net present value, payback period, IRR, B/C ratio and NK ratio; determine the value of social and environmental externalities created by the CSA practices; and include the estimated value of those externalities in the cost–benefit analysis of the different CSA practices in major cereal crops. This study focuses on evaluating six CSA practices that smallholder farmers in the Gandaki River Basin of Nepal consider to have the most substantial impact on food security, productivity, and mitigation. As farmers bear the investment costs and directly experience the economic benefits of adopting CSA practices, the analysis presented in this paper adopts a farmer-centric viewpoint rather than a public one. The primary objectives of this

paper include

1. Prioritization of the implemented CSA practices;
2. Evaluation of the costs and benefits associated with adopting six CSA practices recognized as climate-smart;
3. Estimation of the value of externalities linked to the implementation of these six CSA practices.

This study covers an important research gap that exists in the financial and externality assessment of CSA practices, along with a valuation of the externalities created by the CSA practices. The findings from this study can be a great asset to cereal growers in the regions of Gandaki River Basin as they choose appropriate CSA practices for sustainable farming systems in the context of the changing climate, and they will also help policy makers to prioritize the CSA practices in their program that are financially sound and will create welfare for society and the environment. However, this study has some limitations. It relies on the existing literature to gather additional evidence on the valuation of externalities associated with CSA practices. Furthermore, due to a lack of comprehensive data or minimal impact, the study was unable to assess the value generated by reducing soil and water contamination through certain CSA practices. Lastly, the small landholding size of cereal producers in the region constrained the calculation of the carbon balance, which was excluded from this analysis.

The structure of this paper is outlined as follows: Section 2 provides an overview of the study, detailing the selection and ranking process of the six climate-smart agriculture (CSA) practices, along with an explanation of data collection and analysis methods. Section 3 presents the key findings of the study and their discussion, and Section 4 includes our conclusions and policy recommendations.

2. Research Methods

2.1. Conceptual Framework

The conceptual framework of the study is shown in Figure 1 below. CSA encompasses smart practices in terms of energy, knowledge and nutrition [14]. These practices can help in adaptation to and mitigation of climate change stress and play a significant role in ensuring food security [5].

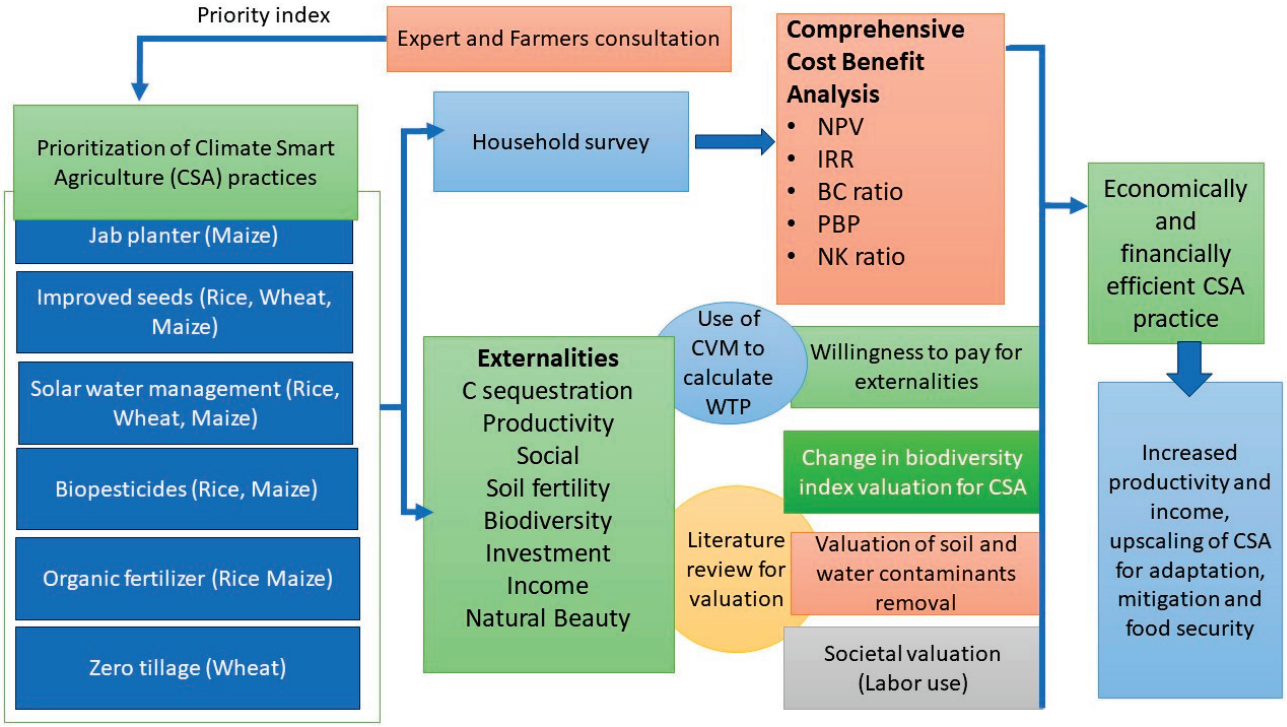

Figure 1. Conceptual framework of the study. Source: Author's own.

In this study, economically efficient CSA practices that are financially sound and produce high-value externalities were determined. The adoption of such CSA practices can have a twofold effect—increased productivity and income (i.e., the welfare effect) and decreased emission of greenhouse gases through upscaling of these practices.

2.2. Study Area

In Nepal, CSA practices have been implemented in selected villages from different ecological zones of the Gandaki River Basin with the support of the Consultative Group for International Agriculture Research (CGIAR) and coordination with different partners [15]. The pilot study is being carried out in six districts: Bardiya, Dang, Rupandehi, Nawlapur (formerly Nawalparasi), Gorkha, and Mahottari. These selected villages are vulnerable to changing climate and its impacts [15]. For our study, we have chosen the Nawalpur district (Figure 2).

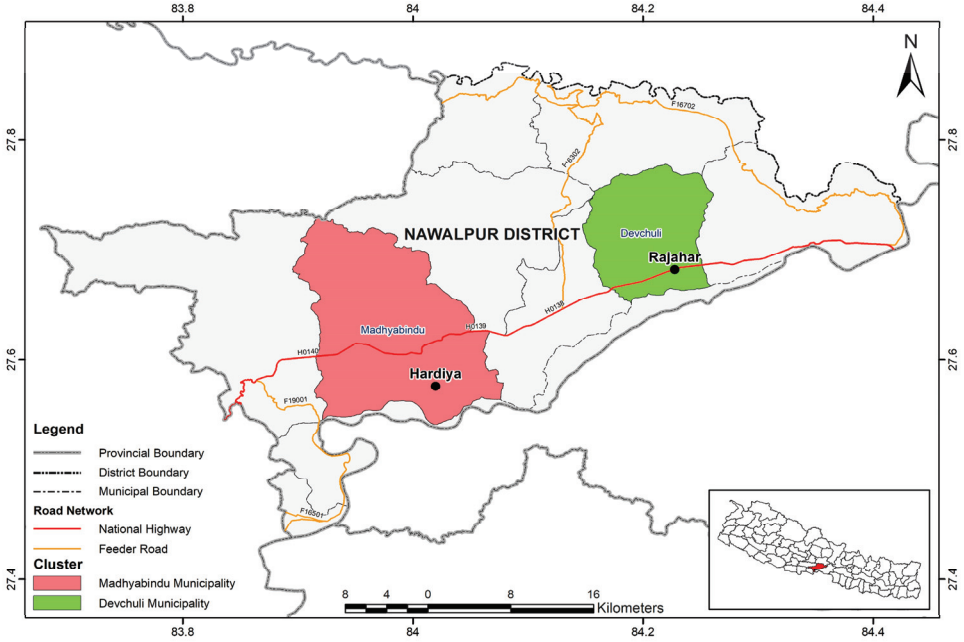

Figure 2. Map of the study area. Source: Author's own.

It is situated in Gandaki Province of Nepal centered at 27.32° N longitude and 83.40° E latitude. The district has a total population of 310,864 [16]. The altitudes vary from 91 m to 1936 m above mean sea level. Nawalpur is characterized by its tropical and sub-tropical climate zone. About half of the district is mainly populated by Brahmins, Magar, and Chhetri communities, while the Terai region is mainly populated by the Tharu community. The major occupation of the people in the district is farming. Nawalpur is a district vulnerable to the threats of the climate change [17], and it has relatively accessible sites in order to keep track of the agricultural farms. Furthermore, the future climate analog (2030), upon verification and evaluation at the Nawalpur site, has shown that the CSA areas for paddy and wheat will be appropriate for 1197 thousand hectares and 550 thousand hectares of land, respectively, across the country [8], which explains the rationale behind choosing the site.

2.3. Prioritization and Selection of CSA Practices

The CSA prioritization framework (CSA-PF) method involves consultation with experts and discussion with farmers and stakeholders to ascertain CSA practices and investment profiles. Farmers, agriculture officers and stakeholders of NGOs associated with climate-smart agriculture practices in the study sites were included in the CSA-PF process. The CSA-PF process encompassed the following steps: (a) in the first step, validation of the main farm typologies was carried out, as mentioned by [18]; (b) only small-scale subsistence cereal-growing farmers (referring to farmers with a small landholding size of less than 0.55 hectares) were selected [16]; (c) a list of existing and new CSA practices (specifically productivity, resilience, and low-emission development) that are adaptable to the varied typologies of the farms was made through focus group discussions with farmers and experts; (d) the listed practices were evaluated using the indicators in the CSA goals of productivity, resilience, and low-emission development. The major aim of the third step was to finally derive a shortlist which included the most applied and interested CSA practices for each type of farm; (e) we identified the most intriguing and applied practices prioritized by both farmers and experts; and (f) finally, we carried out an in-depth survey of farm households for the chosen CSA practices. In a nutshell, the first four steps involved 16 practices, among which only 6 practices were critically shortlisted in the priority ranking of CSA goals for CBA analysis. This paper specifically delves into the outcomes of step (d), conducting a comprehensive profitability assessment of the six high-priority CSA practices.

2.4. Data Collection

A structured questionnaire was prepared for the purpose of household survey data collection. The questionnaire aimed to obtain information on (1) general information about the study area; (2) the socio-economic characteristics and farming experience of household head; (3) field activities (no intervention); (4) adopted climate-smart practices; (5) yield, prices, inputs and costs of implementation of the practices (both before and after intervention); (7) household financial data; and (8) socio-economic and environmental impacts. Purposive sampling was carried out within the district, and a total of 100 farmers were selected who had practiced at least one of the six CSA practices in their farms for a period of at least two to five years (Table 1).

Table 1. Distribution of the households by CSA practices and types of crops in Nawalpur (N = 100).

Farm Practice	Crops Grown in a Calendar Year	Number of Respondents
Conventional Agriculture Practice (CAP)	Rice	100 (100)
	Maize	93 (93)
	Wheat	20 (20)
	Climate-Smart Agriculture Practices	
Jab planter	Rice	N/A
	Maize	58 (62.36)
	Wheat	N/A
Improved seeds (Local seeds)	Rice	27 (27)
	Maize	35 (37.63)
	Wheat	4 (20)
Solar water management	Rice	36 (36)
	Maize	49 (52.68)
	Wheat	4 (20)
Biopesticides	Rice	2 (2)
	Maize	5 (5.37)
	Wheat	N/A
Organic fertilizers	Rice	1 (1)
	Maize	2 (2.15)
	Wheat	N/A
Zero tillage	Rice	N/A
	Maize	N/A
	Wheat	10 (50)

Note: Figures in parentheses are the relative percentages of respondents. N/A means not applicable due to non-adoption of the particular practice.

Prior to the data collection, two enumerators were given training on questionnaire management, translation, and recording of the farm location and responses. Pre-testing of questionnaire was carried out by the enumerators, which was used to gain their preliminary experiences along with translation. All clandestine issues were found out and resolved. Prior to the survey, verbal consent was obtained from the respondents, ensuring that the collected data would only be used for the research purpose and would not be shared anywhere else. In each household, the household head was preferred for the interview. However, in their absence/inability to take part, we chose another member (>20 years old) of the farm household who had been farming for at least five years. In this study area, almost all of the CSA practices were observed to have been implemented recently (i.e., their adoption took place with uneven frequency from 2015 to 2019).

Conventional agriculture practice (CAP) refers to the farmers who had not applied any CSA practice in their field and were working under business-as-usual conditions before implementing CSA practices (i.e., before 2015). The same farmers before 2015 who were classified as CAP farmers were CSA farmers, provided they adopted at least one of the practices. From Table 1, it can be observed that not all (100) farmers adopted CSA practices.

The cropping system of farmers in the study area for cereals was R-W-M (rice–wheat–maize) in a calendar year, and hence it is possible that farmers grew rice, rice–maize, rice–wheat, maize–wheat or rice–wheat–maize; accordingly, the number of farmers growing particular crops were different. In the case of farmers adopting CSA practices, not all practices were applicable to all crops, and not all farmers adopted the particular CSA practices for that particular crop. For instance, jab planters are applicable to maize, and zero tillage is applicable to wheat only in this study area.

2.5. The Cost–Benefit Analysis Model

The CBA approach has a blended character of ex-ante and ex-post evaluation. It is an ex-post evaluation in a sense that practices were fostered and applied by the farmers, and ex-ante because their impact on yields or ecosystem services is not yet apparent, considering the span of the implemented practices. CBA is widely chosen for the evaluation of the benefits of expenditures in different sectors [19]. In this paper, the individual profitability of implementing CSA practices, i.e., the profitability for farmers who are implementing the practice, is determined by the CBA approach. The different CSA practices were appraised in terms of their relative profitability using the CBA approach, i.e., by comparing the differences between them in terms of the varying benefits and costs during the entire period of implementation. The cost incurred for the CAP was taken as the cost borne by the farmers for their regular agricultural activities prior to implementing the CSA practices. The cost incurred in adopting the CSA practices included the cost of the adoption, implementation, and maintenance of a given activity (per hectare of farmland). Thus, the calculations involve adoption, implementation and maintenance of the practices on a per-hectare basis, although farmers may have many activities taking place in an area of less than a hectare. Two popular discounted measures of CBA, (i.e., net present value (NPV) and internal rate of return (IRR) [20]) along with assessment of B/C ratio, net benefit investment ratio (NK ratio) and payback period (PBP) were applied for practices in rice, wheat and maize. Assessment of the individual profitability values can be determined by NPV, IRR, B/C ratio, NK ratio and the non-discounted measure; PBP (Formulas (1)–(5)) per hectare (ha) under CAP and CSA practices [21]. The comprehensive and multifaceted analysis of investment opportunities offers unique insights, and collectively, such insights ensure a thorough assessment of the financial viability and strategic value of the CSA practice under consideration.

$$\text{NPV} = \sum_{t=1}^{n} \frac{B_t - C_t}{(1+i)^t} \quad (1)$$

where NPV = net present value of implementing the CSA practice;
B_t = incremental benefit of the CSA practice in the t^{th} period;
C_t = incremental cost of the CSA practice in the t^{th} period;
n = number of years;
i = interest (discount) rate (%).

The NPV is defined as the summation of the present value of incremental net benefit over the time period considered [21]. The nature and description of the variables used for calculation of NPV is described in Table 2. The respective values used in the classical equation were determined using MS Excel and used to obtain the average NPV.

$$\text{IRR} = \text{LDR} + \Delta\text{DR} * \frac{NPV\ at\ LDR}{\sum PV\ of\ INB\ at\ two\ DR} \quad (2)$$

or the value of interest rate (i) at which NPV = 0.

Where LDR = lower discount rate; ΔDR = difference between discount rates; and INB = incremental net benefit.

The other indicator, IRR, can be defined as the interest rate that makes NPV zero, i.e., that which makes the present value of incremental net benefit zero. Unlike NPV, the cost of

capital (interest rate) need not be specified for the calculation of IRR. Upon calculation, it can be used as a yardstick for different probable values, and can thus be used to ascertain the profitability of diverse cases. A greater IRR (more than the discount rate) suggests a profitable investment.

The discounted B/C ratio and NK ratio were used to validate the profitability of different CSA practices. The discounted B/C ratio was estimated by dividing the present value of incremental benefit with the present value of incremental cost. A B/C ratio of greater than 1 is considered profitable.

$$\text{B/C ratio} = \frac{\sum_{t=1}^{n} \frac{B_t}{(1+i)^t}}{\sum_{t=1}^{n} \frac{C_t}{(1+i)^t}} \tag{3}$$

where

B/C = benefit–cost ratio of the CSA practice;
B_t = incremental benefit of the CSA practice in the t^{th} period;
C_t = incremental cost of the CSA practice in the t^{th} period;
n = number of years;
i = interest (discount) rate (%).

Similarly, an NK ratio of more than 1 is considered profitable for a business. It is the ratio of the sum of the positive value of incremental net benefit to the absolute negative value of incremental net benefit during the period considered [21].

$$\text{NK ratio} = \frac{sum\ of\ the\ incremental\ net\ benefit\ with\ positive\ value}{|sum\ of\ the\ incremental\ net\ benefit\ with\ negative\ values|} \tag{4}$$

The payback period (PBP) refers to the time needed to recover the initial investment.

$$\text{PBP} = \text{E} + \frac{B}{C} \tag{5}$$

where

PBP = payback period for implementing the CSA practice;
E = year immediately preceding the year of recovery;
B = amount left to be recovered;
C = cash flow during the final year of recovery.

We used the average values of the farm for the calculation of NPV, IRR, B/C ratio, and NK ratio. Furthermore, we considered a time period of 25 years for NPV, IRR, discounted B/C, and NK ratio estimation and kept the discount rate at 12% (representing the opportunity cost of capital affecting banks and financial organizations) on the basis of data obtained from farm households and considering the bank interest rate during the time period. The calculation was performed using different functions and formulas available in MS Excel. Each of these values were obtained from the individual farmers, and ultimately, the average values of each of the indicators were assessed. In order to represent the statistical variation present within the calculation of NPV, IRR, B/C ratio, and N/K ratio, standard deviations were assessed.

Table 2. Variables used in the NPV model for CBA.

Variable	Nature	Description
Cost of CSA practice (installation, operation and maintenance)	Random	A random character of the cost is assumed so as to capture the differences in production technology amid the farms in the study area
Price of the crops	Non-random	The data from survey showed minimal variation in prices of the cereal crops (expressed in USD) across the farms
Crop yield response	Random	The magnitude of the impact of implementing the CSA practice can be measured by the crop yield response
Time horizon, time response parameters (t1 and t2), and discount rate	Non-random	A specific feature of the practice defines the time horizon of the analysis

Note: Random means values can vary unpredictably due to inherent uncertainty, variability in data, or differences in conditions. Non-random means values are fixed or exhibit minimal variation within the context of the study, often because they are controlled or standardized across the analysis.

2.6. Crop Yield Response to Adoption of CSA

CSA emphasizes systems in agriculture that bolster the ecosystem services in a sustainable manner [22]. We presumed that the CSA practices would mostly enrich soil nutrient status, decrease soil erosion, and decrease water shortage due to proper management of irrigation in the field, so as to exhibit the impact of CSA practices on productivity of crops [23]. CSA practices in association with their aftermath have a subsidiary effect on productivity through enriched soil nutrient status [24].

Thus, the considerably longer time required for the yield response of the crops could be attributed to the preliminary soil destruction and other issues relating to soil characteristics. In order to build a proper model for the physical response pattern of crop yields after implementing CSA practices, we assume that the curve of response takes the form of a linear plateau preceded by a lag amid the implementation of the practices and the onset of yield response, as shown in Figure 3.

Figure 3 represents a production function [25] popularly used to demonstrate the biological process on par with the Liebig's law of the minimum. The discrepancy between Time 1 (t1) and Time 0 (t0) refers to the response lag. Similarly, Y_f is the highest possible increment in yield associated with the adoption of a CSA practice, and T refers to the entire time for which the practice is implemented. From the response survey among the farmers practicing CSA, both the yield response and maximum yield attainment took one year. T symbolizes the complete lifecycle of the practice, with the y-axis denoting productivity in quintal per hectare and the x-axis representing time in years.

The underlying principle of the Liebig production function is that at any given moment, only one factor, considered to be in minimal supply, constrains production (such as the level of nitrogen (N) in the soil) [26]. If the supply is augmented by using a nitrogen-rich fertilizer, production increases proportionally until it reaches a point at which a second factor, such as water availability, begins to constrain production. As depicted in Figure 3, there is a sudden shift from one limiting factor to another.

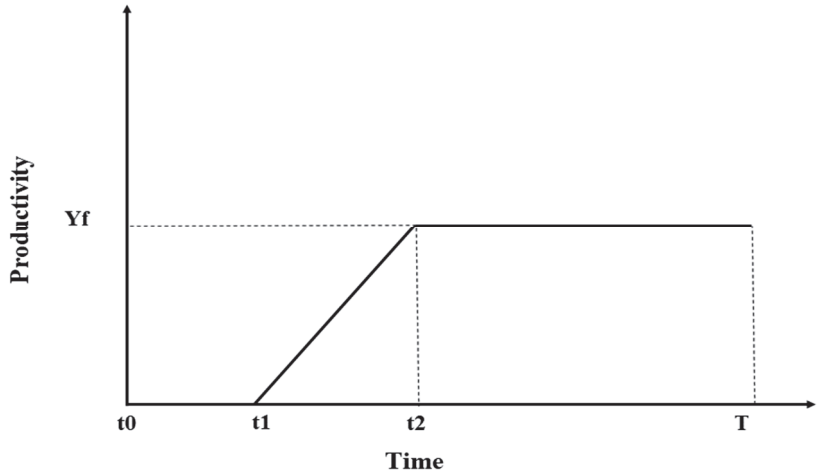

Figure 3. The productivity response function (the productivity increases in a linear plateau from t1 to t2, given one limiting factor, and then stabilizes over time when other factors limit production).

2.7. Environmental and Social Externalities

Every CSA practice creates external effects, which can be either positive or negative. In the context of this study, social and environmental externalities are considered to be generated upon application of CSA practices. Information on externalities was gathered from a survey of farmers and an experts' workshop, as well as various literature sources discussing the ramifications of adopting climate change adaptation strategies. These externalities encompass effects on crop and soil biodiversity and on ecosystem services, as well as other external effects like biodiversity, greenhouse gas emissions, soil fertility, social harmony, and social impact. The strength of the effects of the adoption of CSA practices on these externalities was qualitatively ascertained, based on the discussion with CSA farmers, to be "high", "non-significant" or "low". For instance, use of bio-pesticides might have non-significant impact on fertility of soil but a high impact on productivity.

2.7.1. Valuation of Externalities, Change in Biodiversity and Labor Requirement

For the valuation of externalities, the weighted value of change in externalities generated by the introduction of CSA practices was applied along with the respective shadow price-marginal amount someone is willing to pay (WTP) or willing to accept (WTA) for given external effects, which may be positive or negative. The estimation of the shadow prices with respect to external effects can be performed using different methods [27]. The contingent valuation method (CVM) is applied for estimation of the value of the benefits corresponding to the externalities, since it is the most flexible method of valuation in the case of a stated preference, i.e., non-market-based. CVM is a stated preference for the valuation of resources that cannot have market value but have an impact, either positively or negatively, on the environment [27–29]. The respondents were asked their WTP values for the externalities created by the adoption of CSA practices, which were later averaged to obtain a value which reflected the adopters' WTP for CSA practices at CAP, i.e., the amount they are willing to pay for an externality and to adopt a CSA practice within their conventional agriculture practices. Since not every farmer adopts every CSA practice, the valuation of externality was obtained from only the farmers associated with a particular CSA practice. For instance, the valuation of an externality created by the adoption of zero tillage (which in our case is wheat only) was obtained from the value of WTP obtained from farmers adopting the same.

The biodiversity index is an accurate and consistent measure of the richness of biodiversity in an area that allows for comparison of species' abundance between two systems [30]. The change in the biodiversity after the introduction of CSA practices was calculated, taking into consideration the associated externalities (social and environmental) and their benefits. This system of valuation works on the principle that any changes in land use

patterns indicate the amount of service provided to the environment [25]. For this purpose, a score was assigned in accordance with the type of land used to regulate or promote biodiversity. The topmost score of 1 was assigned to the forestland use pattern, owing to its greatest environmental services, whereas degraded land or intensive monoculture was assigned a score of 0 (at the bottom of the scale). To make the environmental service valuation proportionate, we considered a differential increment with respect to the base year 0. Furthermore, we assumed the price of alteration in biodiversity due to the implementation of a CSA practice. The distribution of prices was presumed to have a uniform nature, with a maximum value of USD 69/unit/year (USD 1 is taken to equal NPR 120.08 in our study, which is implied wherever the value is in USD, based on 4 December 2021) [31,32]. Ultimately, values were obtained by multiplying the change in biodiversity index due to the adoption of the respective CSA practice with the associated shadow price of the same level of biodiversity.

The societal impact or external consequences of implementing CSA strategies was assessed through their influence on changes in labor requirements. Furthermore, the calculation of the extra man days/ha/year for the practices was performed to assess the labor and employment as social externalities compared to the CAP. The value was obtained by asking the respondents about the additional labor required in adopting a particular CSA.

2.7.2. Soil and Water Conservation

The role of CSA practices in decreasing the effect of negative externalities like water pollution, particularly from agricultural chemicals, has been assessed [33,34]. Thus, this concept was incorporated by valuing the reduction in soil erosion and water pollution by using the opportunity cost. For this, we presumed an estimate of about USD 0.008/t of soil for the value of soil degradation due to land erosion [35]. The soil cover practice using mulch could effectively reduce loss of soil by about 91.1 t/Mz/year (1 Mz is equivalent to 0.7 ha) [36]. In the case of conservation tillage followed by mulching, an estimate of USD 1.04/ha was made [25]. This allowed us to consider the same value when using the jab planter and zero tillage.

2.8. Data Processing and Analysis

The collected data were carefully entered into MS Excel followed by data cleaning and curation. The collected data were arranged crop-wise, CSA practice-wise, and externality-wise (WTP) to prevent confusion upon further assessment. The collected data were analyzed using MS Excel and R Studio Version 4 for financial and economic analysis of the CSA practices.

3. Results

3.1. Prioritized Climate-Smart Practices

A list of CSA practices were developed and prioritized after consultation with experts, farmers, and stakeholders (Table 3). The practices thus listed were the most commonly adopted and most popular CSA practices in the study area. CSA practices or technologies that support the three pillars of CSA—production, resilience, and mitigation of climate change in agriculture—could be considered CSA technology. For this purpose, farmers were asked to score each technology on a scale of 0 to 4 based on productivity, adaptability, and mitigation. If farmers perceived that these practices made a substantial contribution to increasing productivity, enhancing adaptation, and supporting greenhouse gas (GHG) mitigation, they assigned a rank of 4. Conversely, if they did not recognize these benefits, the practices were assigned a rank of 0. They were free to score between 0 and 4 for each of the practices they have been applying as CSA practices. The top six most highly ranked CSA technologies which were prioritized for the economic analysis are briefly discussed below.

Table 3. Top prioritized CSA practices considered for cost–benefit analysis.

Practices	Descriptions
Jab planter	The use of a jab planter aims to reduce greenhouse gas emissions by avoiding the use of machinery, such as tractors, and soil disruption by ploughs.
Improved seeds	The adoption of hybrid seeds, as opposed to utilizing local or recycled seeds, increases production, while the application of other inputs like fertilizer, labor, and management remains constant.
Solar water management	Use of solar water management provides irrigation to replace the traditional petrol/diesel generator for irrigation, aiming to increase production and mitigate GHG emission.
Biopesticides	The use of biopesticides for controlling the pests aims to protect against the chemical contamination of the soil.
Organic fertilizers	Use of organic fertilizers like farmyard manure (FYM) compost minimizes the application of chemical fertilizers.
Zero tillage	Zero tillage and soil cover with straw as mulch minimize soil surface disruption and can occasionally replace the use of machinery, such as tractors or ploughs, on farms.

3.2. Cost–Benefit Analysis of Prioritized Climate-Smart Practices

A cost–benefit analysis was conducted for six climate-smart practices: use of a jab planter, improved seeds, solar water management, biopesticides, organic fertilizers, and zero tillage, as outlined in Table 4. The key indicators considered included the NPV, IRR, B/C ratio, NK ratio, discount rate, and payback period. The findings demonstrated the profitability and viability of prioritized climate-smart technologies. The discount rate was kept at 12%. The payback period of the CSA practices ranged between 2.2 years (organic fertilizer) and 14.17 years (solar water management). However, most of the CSA practices have a payback period of 2 to 4 years, indicating favorable conditions for smallholder farmers. This shorter payback period allows them to repay credit and enjoy investment profit simultaneously. Costs used in CBA calculations were associated with implementing, maintaining, and operating CSA practices on one hectare for one year, with constant input and output prices. The nature of cost within the CBA approach two kinds of cost: installation costs and operation and maintenance costs, both of which constitute materials and labor. Installation costs are incurred by the farmers during adoption. Operation and maintenance costs are mandatory, incurred over the entire lifecycle of CSA practices. Initial investment and operation and maintenance costs for different crops during different CSA practices are shown in Table 4.

Table 4. Initial investment and operation and maintenance costs for different crops during different CSA practices.

Farm Practice	Crops	Initial Investment (USD/ha)	Operation and Maintenance Cost (USD/ha)
Conventional agriculture practice (CAP)	Rice	479.17	510.33
	Maize	458.33	247.82
	Wheat	458.33	167.68
Climate-smart Agriculture Practices			
Jab planter	Rice Maize Wheat	204.17	411.21
Improved seeds	Rice	720.83	582.1
	Maize	720.83	369.11
	Wheat	720.83	152.2
Solar water management	Rice	1625	478.8
	Maize	1625	338
	Wheat	1625	240.7

Table 4. *Cont.*

Farm Practice	Crops	Initial Investment (USD/ha)	Operation and Maintenance Cost (USD/ha)
Biopesticides	Rice	625	655.82
	Maize	625	304.54
	Wheat		
Organic fertilizers	Rice	708.33	343.73
	Maize	708.33	247.63
	Wheat		
Zero tillage	Rice		
	Maize		
	Wheat	875	168.55

Source: Field survey (2019).

Private Profitability

In this study, a cost–benefit analysis was conducted to examine the economic implications of agricultural activities influenced by climate-smart agriculture (CSA). The assessment of costs and benefits considered the impact of a CSA practice on one hectare of land for analysis. Data regarding conventional agricultural practices or a business-as-usual scenario reflected input and output values before the implementation of the CSA; this relied on data recalled by the farmers. The jab planter was the most practiced (63%) CSA intervention, while households using biopesticides and organic fertilizer were minimal (7% and 3%, respectively).

From Table 5, it can be observed that almost all of the CSA practices were profitable, having positive NPV, an IRR higher than the discount rate, and a B/C ratio and NK ratio greater than 1, except for the practice of solar water management in maize. Among the profitability indicators discussed in the CBA, namely, NPV, IRR, B/C ratio, and NK ratio, NPV emerged as the most suitable measure for assessing the worthiness of a practice. While IRR and B/C ratio find applicability when there is only one alternative under consideration, NPV proves highly useful when multiple alternatives are available [10].

Table 5. NPV, IRR, B/C ratio, NK ratio, and payback period for different crops during different CSA practices.

Farm Practice	Crops	NPV (in USD ha^{-1} at 12%)	IRR (%)	B/C Ratio	NK Ratio	PBP (Years)
Conventional agriculture practice (CAP)	Rice	655.62 (±83.63)	42 (±5.35)	1.15 (±0.15)	3.18 (±0.4)	3.35
	Maize	328 (±24.95)	26 (±1.98)	1.14 (±0.09)	2.016 (±0.15)	4.67
	Wheat	332 (±53.72)	26 (±4.21)	1.19 (±0.19)	2.03 (±0.33)	4.65
Climate-smart Agriculture Practices						
Jab planter	Rice					
	Maize	282 (±33.37)	42 (±4.97)	1.08 (±0.13)	3.21 (±0.38)	3.35
	Wheat					
Improved seeds	Rice	530.4 (±118.58)	27 (±12.78)	1.10 (±0.52)	2.05 (±0.74)	4.66
	Maize	540.3 (±118.54)	27 (±7.96)	1.42 (±0.37)	2.07 (±0.49)	4.62
	Wheat	1029.5 (±850.56)	43 (±35.58)	2.44 (±1.16)	3.29 (±1.55)	3.30
Solar water management	Rice	1697 (±418.26)	33 (±8.53)	1.32 (±0.25)	2.56 (±0.47)	3.98
	Maize	−521 (±165.45)	6 (±1.61)	0.87 (±0.17)	0.61 (±0.12)	14.17
	Wheat	299.2 (±233.86)	15 (±11.50)	1.087 (±0.50)	1.24 (±0.56)	7.01

Table 5. *Cont.*

Farm Practice	Crops	NPV (in USD ha^{-1} at 12%)	IRR (%)	B/C Ratio	NK Ratio	PBP (Years)
Biopesticides	Rice	330 (±325.63)	22 (±21.13)	1.06 (±1)	1.72 (±1.68)	5.28
	Maize	494 (±235.16)	28 (±13.76)	1.16 (±0.68)	2.14 (±1.21)	4.48
	Wheat					
Organic fertilizers	Rice	1828 (±1801.88)	83 (±81)	1.54 (±1.50)	6.29 (±6.05)	2.20
	Maize	1034.5 (±1027)	45 (±44.1)	1.39 (±1.37)	3.38 (±3.32)	3.20
	Wheat					
Zero tillage	Rice					
	Maize					
	Wheat	317.6 (±275.6)	26 (±21.70)	1.18 (±0.90)	1.53 (±1.17)	4.29

Note: Figure in parentheses are standard deviations representing statistical variations in measures among farms.

In the case of solar water management used on wheat, the IRR was found to be 15%, a few percent more than the discount rate (12%), proving it to be a marginally profitable practice. The use of organic fertilizers in rice showed the highest IRR amid all the CSA practices. Despite the highest initial investment (Table 5), use of solar water management on rice exhibited a relatively higher NPV (USD 1697), which was only slightly lower than the NPV of using organic fertilizer on rice, which had the highest value (USD 1828). The BC and NK ratio were higher than 1 for all the practices except for solar water management use in maize and wheat (0.87 and 0.61, respectively), indicating a non-profitable practice. Most practices required a huge investment during the initial phase and a significantly greater amount of time to exhibit their impact on the return and yield from the crops. This could be attributed to the payback period (PBP). The PBP was within the range of 2 to 4 years for most of the CSA practices. A shortest recovery period of 2.2 years was found for rice cultivation with the practice of organic fertilizer application. Unlike other practices, the use of solar water management in maize and wheat required 14 and 7 years, respectively, to cover the investment in the initial phase.

3.3. Environmental and Social Externalities

Despite the different sets of externalities obtained from some of the CSA practices, eight externalities were generated that were determined to be relevant and feasible for valuation of the concerned parameters, as shown in Table 6. Practices like use of a jab planter, improved seeds, solar water, and zero tillage were associated with carbon sequestration due to low carbon emissions. In the case of increased productivity, all practices except for the organic fertilizer contributed to productivity. The use of organic fertilizer and zero tillage did not contribute to social harmony as an externality. In the case of soil fertility, except for the use of biopesticides, other practices contributed positively to soil fertility. All the CSA practices created positive externalities with respect to biodiversity. The use of a jab planter, improved seeds, solar water, and biopesticides was associated with higher income and added natural beauty as externalities.

Table 6. Externalities associated with different CSA practices in the Nawalpur district.

Practices	Externalities							
	Carbon Sequestration	Productivity	Social	Soil Fertility	Biodiversity	Investment	Income	Natural Beauty
Jab planter	Low carbon emissions	High	Social harmony	Low nitrogen emissions	Balanced environment	Low	High income	Adds to natural beauty

Table 6. *Cont.*

Practices	Externalities							
	Carbon Sequestration	**Productivity**	**Social**	**Soil Fertility**	**Biodiversity**	**Investment**	**Income**	**Natural Beauty**
Improved seeds	Low carbon emissions	High	Social harmony	Balanced	Eco-friendly	Low	High	No significant impact
Solar water management	Low carbon emissions	High	Social respect and harmony	Low nitrogen emissions	Balanced environment	Low	High	Adds to natural beauty
Biopesticides	Non-significant impact	High	Social harmony	Non-significant impact	Eco-friendly	Non-significant impact	High	Adds to natural beauty
Organic fertilizer	Non-significant impact	Non-significant impact	Non-significant impact	Balanced nitrogen	Eco-friendly	Non-significant impact	Non-significant impact	Non-significant impact
Zero tillage	Low carbon emissions	Low	Non-significant impact	Low nitrogen emissions	Eco-friendly	Low	Low	Non-significant impact

3.3.1. Willingness to Pay for Externalities and Change in Biodiversity

The willingness to pay (WTP) for the externalities of the farmers' adopting CSA is shown in Table 7. The farmers had higher WTP for the externalities of increased income (USD 69.27/ha) and enhanced productivity (USD 63.03/ha) thanks to the adoption of CSA practices, compared to other externalities. The CSA farmers had the lowest WTP (USD 16.22/ha) for the soil fertility externality created by CSA practices. These statistics reveal that farmers are more concerned with increased income and productivity upon adoption of CSA practices. The average value of WTP for externalities created by the adoption of CSA practices was USD 39.24/ha.

Table 7. WTP for externalities of CSA farmers.

Externalities	WTP (USD/ha)
Low greenhouse gas emissions	33.51
Increased productivity	63.03
Social benefit	41.92
Soil fertility	16.22
Biodiversity	36.7
Investment	24.1
Income	69.27
Natural beauty	29.17

The WTP for a unit change in biodiversity after the adoption of the CSA practices was between $8.75/ha and $51.3/ha (Table 8). The average value of WTP for a unit change in the biodiversity index was estimated to be USD 25.4/ha for the selected CSA practices of jab planter, improved seeds, solar water management, and zero tillage. Although the biopesticides and organic fertilizers have an impact on the biodiversity, we could not assess their effects due to lack of information.

Table 8. Estimated change in biodiversity index.

CSA Practices	Change in Biodiversity Index	WTP for Unit Change in Biodiversity (USD/ha)
Jab planter	0.64	51.3
Improved seeds	0.13	8.75
Solar water management	0.13	11.92
Zero tillage	0.64	29.6

Note: Biodiversity index adapted from [25].

3.3.2. Social Externalities Due to CSA Intervention

The study showed that on average, labor increased by 1 man-day/ha in the first year of establishment of practices and by 2 man days/ha per year for maintenance of the practices (Table 9) compared to CAP. On average, the value of increased labor was USD 19.44/ha in investment in the initial year, and an annual increase of USD 49.72/ha/year for the lifecycle of the practices. The valuation of externalities arising from CSA practices was carried out based on the CVM, which was estimated from the response of the respondents.

Table 9. Estimated impact on the level of labor as a result of introducing CSA practices.

CSA Practice	Increase in Labor (Man days/ha)		Increase in the Value of Labor (USD/ha)	
	Installation (Temporary)	Maintenance (Permanent)	Installation (Temporary)	Maintenance (Permanent)
Jab planter	0	3	0	30
Improved seeds	0	0	0	0
Solar water management	2	4	83.33	50
Biopesticides	4	1	33.33	8.33
Organic fertilizers	0	1	0	10
Zero tillage	0	3	0	200
Average	1	2	19.44	49.72

3.3.3. Soil and Water Conservation

The valuation of the two CSA practices which fell under the category of conservation tillage (with mulch), i.e., zero tillage and the use of a jab planter, was USD 4.75/ha, which represents the value of potential soil erosion that was prevented by adoption of the conservation tillage practice. In the case of agrochemicals, the use of organic fertilizer led to a valuation of USD 51/ha/year from the survey; the consequent avoidance of chemical fertilizer resulted in a reduction of USD 9.33/ha in pollutants.

4. Discussion

4.1. Costs and Benefits in Implementing CSA Practices

For any agricultural planner or policy maker, decision making regarding investments and regulatory practices primarily revolves around two key considerations: (1) the profitability of practices for individuals, and (2) the overall benefits these practices bring to the public. Cost–benefit analyses (CBAs) emerge as the preferred tool for decision makers when evaluating investment options, factoring in policy considerations and planning dynamics [37]. Various studies have made use of the CBA approach for determining the viability of practices in the context of changing climate [38]. This study utilizes two decision-making tools to assess climate-smart agriculture from the perspective of smallholder farmers in Nepal. Initially, the CSA-PF was employed to pinpoint the most prioritized CSA strategies. This involved ranking their significance in enhancing productivity, resilience, and mitigation benefits. Then, a cost–benefit analysis was conducted based on the data collected from the questionnaire survey and experts' workshops. The chosen practices not only provide social and economic benefit at the farm level under current conditions but

also have the ability to build resilience to climate change in the near future, thus providing a stable option [39,40].

Almost all the assessed practices demonstrated a profitable nature, signified by a net present value (NPV) greater than zero (Table 5) and an internal rate of return (IRR) surpassing the considered discount rate of 12%. However, the implementation of solar water management exhibited a negative NPV and a low IRR for maize, indicating an unprofitable aspect of this particular CSA practice in maize cultivation. This can be attributed to the substantial initial investment required for the installation of solar water management [41], with returns failing to recuperate the initial investment within the assessed timeframe. Solar water management also impacted wheat cultivation, revealing a lower NPV and an IRR marginally exceeding the discount rate, primarily due to the significant initial investment. Conversely, the utilization of organic fertilizer as a CSA practice in rice showcased the highest NPV and IRR, followed by solar water management in rice cultivation. These findings concur with [20], who reported highest NPV in case of organic fertilizer application, in their study in Kenya. Moreover, the benefit–cost (BC) ratio and NK ratio for nearly all practices exceeded 1, affirming the profitability of the CSA practices. The exception was the use of solar water management in maize, which diverged from the profitable trend. While choosing CSA practices, careful consideration should be given to the statistical variation within the measures used in this study.

For the determination of a cost–benefit analysis of the practices, the time required to recover initial investments is crucial. In this study, most of the CSA practices had a PBP of 2 to 4 years, which could be considered a relatively longer period for the small producers targeted by the CSA-PF. Use of organic fertilizers in rice and maize, improved seed cultivation by wheat farmers, and solar water management in rice cultivation were the top three practices with respect to their IRR, and they had payback periods of 2 to 3 years, indicating their potential to enhance food security within households, increase incomes, and enhance adaptation, despite their high associated costs. These emerged as the strongest choices among the CSA practices considered for the farmers in the region, with improved seeds in wheat, solar water management and organic fertilizers in rice, and organic fertilizers used in maize proving to be the promising practices for the individual crops. The use of solar water management in wheat had a PBP of 7.01 years. The longer payback period of solar water management has been reported by a previous study [42] in Burkina Faso, suggesting potential support from microfinancing institutes to irrigate via solar water pump systems. Practices that have a long PBP could be applicable to systems with a favorable environment (like a secured tenancy and institutional and political support) and in which diversified short-term livelihood alternatives are accessible [25]. The statistical variation within the measures should also be considered prior to their implementation.

4.2. Externalities Corresponding to CSA Practices

In understanding the economics of an agricultural practice, measures beyond a financial basis are equally crucial for making an assessment [43]. CBAs that solely emphasize the financial analysis can create a dilemma related to the adoption of practices, due to an inability to address the critical externalities in their approach [25]. This is highly relevant when we consider the implementation of CSA practices both on the farm and within the associated system of agro-ecology. It is evident that the non-market values associated with different practices could prove argumentative [44], but an inability to include the estimated values of external effects means they could go undiscussed. Our study prioritizes these externalities so as to include external effects in the discussion with concerned stakeholders within the CSA prioritization framework. This will assist in the choice of CSA practices within investment portfolios. The identified externalities of increased productivity and increased income, for which the farmers' willingness to pay was greater, are key in promoting CSA practices. Ref Anugwa et al. [45] reported that higher income and increased productivity due to adoption of CSA practices encourage a WTP of USD 115.63 per annum for adoption of CSA in rice cultivation in Nigeria. Decision makers can take into account

the externalities that respondents were more willing to pay for. The findings of our study are in line with [20,25] in Kenya and Guatemala, respectively, where the authors reported similar societal and environmental benefits upon adoption of different regionally based CSA practices. The implications of findings related to externalities have been described in relation to farmers' decision making. The valuation of externalities can help farmers and decision makers to make more holistic decisions regarding environmental benefits, risk reduction, and social co-benefits [46]. Most CSA practices have social benefits such as improved livelihoods for farmers, increased food security, and enhanced community resilience [47]. By valuing externalities related to social cohesion, decision makers can better understand the broader societal benefits of supporting CSA. This can inform policies and programs aimed at promoting sustainable agriculture. Similarly, CSA practices often enhance the resilience of agricultural systems to impacts of climate change such as droughts, floods, and extreme weather events. By valuing externalities related to risk reduction, such as increased water retention or improved pest management, decision makers can better assess the potential benefits of investing in CSA practices. This can also help farmers mitigate production risks and adapt to changing climatic conditions. CSA practices contribute to environmental conservation by reducing greenhouse gas emissions and preserving biodiversity. By valuing externalities related to environmental conservation, such as carbon sequestration or habitat restoration, decision makers can better assess the environmental impact of different agricultural practices. This can inform policies aimed at promoting sustainable land management and biodiversity conservation.

4.3. Potential Implementation and Adoption of CSA Practices

Although the approach of a cost–benefit analysis focuses on the determination of the profitability of individual farmers with respect to CSA practices, there were some constraints. One of the hindrances of the analysis is its inability to measure the degree of risk and uncertainty with respect to yields of cereal crops upon adoption of CSA practices compared with conventional farming. In order to overcome this restriction, we carried out a field survey of households who have implemented some CSA practices recently (in the last five years) but had undertaken conventional farming in the past. This tool could portray the difference in yield at the farm level. Furthermore, the price in real terms was averaged (between 2015–2020) so as to prevent any shortfalls with respect to short-term fluctuation in price. A mixed ex-ante and ex-post analysis was employed, as few CSA practices had been introduced very recently, thereby rendering it unfit for assessing the effectiveness of practicing CSA options.

CSA practices which could be cross-validated and evaluated were chosen along with policy makers, workshops, and farmers, thereby ameliorating constraints related to subjectivity [20]. In accordance with the findings of the study, most of the CSA practices had a positive NPV and a PBP of 4.21 years on an average; this presents an adequate justification for the Ministry of Agriculture and Livestock Development (MoALD), Nepal to encourage these promising CSA practices. The results provide convincing outcomes that can validate the government's promotion of these practices along with further research on these practices. CBA offers an opportunity and a tool for assessing probable adoption niches and can be enhanced upon combination with some interdisciplinary decision support tools.

4.4. Policy Planning

The findings of this study were shared and presented with research institutions, farmers' organizations, the agricultural ministry, non-government organizations working in climate change adaptation and mitigation, policy makers and concerned stakeholders in Kathmandu; then, the results were presented to concerned stakeholders. Furthermore, the different adjustments between the CSA goals (productivity, adaptation, mitigation) and the results of the economics of different practices used for the three crops were exhibited. Economic appraisal must be supplemented with other analyses of different conditions for prioritization of CSA practices. Thus, sufficient discussions to provide justification were

carried out during the workshop on CBA, which created an enabling environment for the implementation of CSA practices of the most interest to the concerned stakeholders. Further action plans were created, which outlined the financial support, technical assistance, and local leaders' roles required to scale up these practices. We hope that the findings of this study regarding climate-smart practices in the periphery of Gandaki River Basin can be scaled up via provision of our results to prospective researchers. This will create a favorable environment for potential research and provide a climate-smart path to upgrading farmers' conventional practices in the context of our changing climate. Furthermore, this study envisions roles for local stakeholders within the CBA approach and fills gaps in the literature data so as to allow for replication of our approach to then recommend impending decisions on the policy level. A major constraint on practitioners and policy makers is the development of programs which focus on inferential analysis and that can be managed well along with proper integration of the novel threat of climate change and up-to-date CSA data.

Adopting a CSA practice will require a decision to be made on investment. For this purpose, how one practice compares to the other needs to be analyzed and clarified on an economic basis. The CBA approach provides a unique method of determining impact along with individual profitability. Furthermore, the approach can be bolstered by coupling it with analysis of social and environmental externalities. This research revealed that nearly all the practices were observed to be profitable in nature but with varied time periods required to recover initial investments. The findings provide a means of rethinking and considering the practices that are being implemented in accordance with the current agricultural policies by the MoALD, Nepal. Similarly, a better understanding of corresponding externalities (social and environmental) that are associated with farmers' other policies and priorities is also provided by this study, which can have an impact on how these practices are adopted. Different practitioners, policy actors, and CSA-related stakeholders can modify the CBA approach so as to target investment activities to upscale novel practices in agriculture, which primarily focus on climate change adaptation, mitigation, resilience, and food security. Certain production systems will require a new approach that delimits the analysis, despite gaps in the data and uncertainty in measuring the impact of CSA practices. This study could not account for the valuation of carbon dioxide reduction, as the area under cultivation was too small to estimate the carbon balance using the FAO Ex-Act tool. The carbon balance could be calculated after a few years of CSA being practiced in a relatively larger land area. Similarly, the estimation of the reduction in cost of pesticides due to application of biopesticides as a CSA practice could not be addressed as an externality due to the practice being limited to very few households. The scope of this study is limited to smallholding farmers in the Gandaki River Basin of Nepal, given the similar climatic conditions, crop types, and farmers' production levels in this region. The findings from this study can reinforce the promotion of CSA practices and motivate farmers to adopt such practices in different regions, considering their financial viability and generation of welfare, as observed in our study. However, to recommend that farmers of a particular region adopt a particular CSA practice, their CSA practices need to be evaluated for financial viability and welfare generation. In such cases, the methodology used in this study will be useful for researchers who aim to evaluate CSA practices in different regions and countries.

5. Conclusions

Climate-smart agriculture is emerging as a resilient and adaptive approach through which to address the challenges posed by climate change. There are several studies in the field of climate change adaptation strategies. However, only a limited number of these studies have taken a comprehensive approach by calculating the costs versus the benefits of climate-smart agriculture. To effectively invest in climate-smart agriculture (CSA) practices among smallholder farmers, a thorough assessment is essential to comprehend the costs, advantages, and payback periods associated with each of the six CSA practices. This evaluation has the potential to significantly influence decisions regarding the expansion,

sustainability, and enhancement of food security for these practices. The current cost–benefit analysis (CBA) appraises CSA practices identified as optimal choices in terms of climate risk adaptation, financial returns, implementation costs, and the likelihood of investment loss. This study's findings offer vital information that farmers can use to to reconsider their investment strategies.

The CSA practices of implementing organic fertilization for rice and maize, introducing improved seeds for wheat, and adopting solar water management in rice cultivation, despite their initially high costs, emerged as the top three practices based on their internal rate of return (IRR). Their relatively short payback periods of 2 to 3 years highlight their potential to enhance food security, increase household income, and facilitate adaptation efforts. These practices stood out as the most favorable options among the CSA techniques evaluated for farmers in the region. Policy makers can develop and implement tailored training programs for farmers in the Gandaki River Basin that focus on climate-smart agricultural practices identified as cost-effective in the analysis. Similarly, focus should be directed to ensuring that farmers have access to the necessary resources, inputs, and technologies required to adopt climate-smart agricultural practices. This may include providing subsidies or financial assistance for the purchase of climate-resilient seeds, organic fertilizers, and water-saving irrigation systems, etc. The Ministry of Agriculture and Livestock Development of Nepal can utilize this information to prioritize initiatives in the agricultural sector, particularly in projects where decisions and outcomes for adaptation are unclear. This study's results provide insights into externalities and social benefits linked to the examined CSA practices, which are crucial for stakeholders to comprehend their true potential from the farmers' perspective. The adoption of these CSA practices, if implemented, would result in positive environmental and social impacts, contributing to achieving the three CSA goals: food security, adaptation, and mitigation.

Considering externalities in economic valuation is crucial and should be incorporated into the economic analysis of adaptation options to ensure robust economic evaluations in future studies. Such consideration would facilitate decision making during the selection of CSA options and guide the efficient allocation of scarce resources in the future. In this study, it was challenging to quantify one of the externalities arising from CSA—specifically, carbon sequestration for mitigation purposes—due to certain limitations. We recommend that future studies consider the measurement of carbon sequestration as a valuable metric for consideration which has the potential to broaden the information used to select and invest in appropriate CSA practices and to enhance future planning and decision making processes.

Author Contributions: S.P.: Conceptualization, Data curation, Funding acquisition, Investigation, Methodology, Resources, Supervision, Writing—original draft, Writing—review and editing. R.T.: Data curation, Formal analysis, Writing—original draft, Writing—review and editing. B.M.: Investigation, Project administration, Supervision, Visualization, Writing—review and editing. All authors have read and agreed to the published version of the manuscript.

Funding: The research was funded by the Organization for Women in Science for the Developing World (OWSD), in support of IDRC Canada (Award No.: 4500384867) and the Asia Pacific Network for Global Change Research (APN) Japan (Award No.: CRRP2021-10MYPoudel).

Data Availability Statement: The raw data supporting the conclusions of this article will be made available by the authors on request.

Conflicts of Interest: The authors declare no conflicts of interest.

References

1. Paudel, B.; Khanal, R.C.; Khatri-Chhetri, A.; Bhatta, K.; Chaudhari, P. *Climate-Smart Agriculture in Nepal: Champion Technologies and Their Pathways for Scaling Up*; Climate and Development Knowledge Network: London, UK, 2017.
2. Poudel, S.; Funakawa, S.; Shinjo, H. Household Perceptions about the Impacts of Climate Change on Food Security in the Mountainous Region of Nepal. *Sustainability* **2017**, *9*, 641. [CrossRef]
3. Poudel, S.; Funakawa, S.; Shinjo, H.; Mishra, B. Understanding households' livelihood vulnerability to climate change in the Lamjung district of Nepal. *Environ. Dev. Sustain.* **2020**, *22*, 8159–8182. [CrossRef]

4. Poudel, S.; Shaw, R. Climate Change and Its Impacts on Land Use/Cover Change and Food Security in Nepal. In *Land Use Management in Disaster Risk Reduction*; Springer: Tokyo, Japan, 2017. [CrossRef]
5. Thapa, R.; Dhakal, S.C. Climate change perception and adaptation strategies of rice seed growers in Chitwan district, Nepal. *Farming Syst.* **2024**, *2*, 100095. [CrossRef]
6. Tesfaye, K.; Zaidi, P.H.; Gbegbelegbe, S.; Boeber, C.; Rahut, D.B.; Getaneh, F.; Seetharam, K.; Erenstein, O.; Stirling, C. Climate change impacts and potential benefits of heat-tolerant maize in South Asia. *Theor. Appl. Climatol.* **2017**, *130*, 959–970. [CrossRef]
7. Chandra, A.; McNamara, K.E.; Dargusch, P. Climate-smart agriculture: Perspectives and framings. *Clim. Policy* **2018**, *18*, 526–541. [CrossRef]
8. Khatri-Chhetri, A.; Poudel, B.; Shirsath, P.B. Assessment of Climate-Smart Agriculture (CSA) Options in Nepal. 2017. Available online: https://cdkn.org/wp-content/uploads/2017/07/Assessment-of-CSA-in-Nepal_CCAFS-LI-BIRD-FINAL.pdf (accessed on 20 September 2021).
9. Gairhe, J.J.; Adhikari, M. Intervention of Climate Smart Agriculture Practices in Farmers Field to Increase Production and Productivity of Winter Maize in Terai Region of Nepal. *J. Inst. Agric. Anim. Sci.* **2018**, *35*, 59–66. [CrossRef]
10. Akinyi, D.P.; Karanja Ng'ang'a, S.; Ngigi, M.; Mathenge, M.; Girvetz, E. Cost-benefit analysis of prioritized climate-smart agricultural practices among smallholder farmers: Evidence from selected value chains across sub-Saharan Africa. *Heliyon* **2022**, *8*, e09228. [CrossRef]
11. Poudel, S.; Mishra, B.; Ghimire, S.; Luintel, N.; Thapa, P.; Sapkota, R. Climate change and agroecosystem: Impacts, adaption, and mitigation in South Asia. In *Developments in Weather and Climate Science*; Chatterjee, U., Shaw, R., Bhunia, G.S., Setiawati, M.D., Banerjee Community Response and Resilience, SBT-CC, Eds.; Elsevier: Amsterdam, The Netherlands, 2023; Volume 6, pp. 329–344.
12. Poudel, S.; Wickramasinghe, D.; Mukherjee, M.; Chowdhooree, I.; Chimi, C.; Mishra, B.; Abhinay, K.; Mitra, S.; Shaw, R. The status and prospect on nature-based solution in South Asia: A policy-based analysis. *PLoS Clim.* **2024**, *3*, e0000289. [CrossRef]
13. Nyang'au, J.O.; Mohamed, J.H.; Mango, N.; Makate, C.; Wangeci, A.N. Smallholder farmers' perception of climate change and adoption of climate smart agriculture practices in Masaba South Sub-county, Kisii, Kenya. *Heliyon* **2021**, *7*, e06789. [CrossRef]
14. Bhattacharyya, P.; Pathak, H.; Pal, S.; Bhattacharyya, P.; Pathak, H.; Pal, S. Dimensions of climate-smart agriculture. In *Climate Smart Agriculture: Concepts, Challenges, and Opportunities*; Springer: Berlin/Heidelberg, Germany, 2020; pp. 33–39.
15. Ghimire, R.; Khatri-Chhetri, A.; Chhetri, N. Institutional Innovations for Climate Smart Agriculture: Assessment of Climate-Smart Village Approach in Nepal. *Front. Sustain. Food Syst.* **2022**, *6*, 734319. [CrossRef]
16. Central Buareu of Statictics (CBS) Nepal. *National Sample Census of Agriculture*; CBS Nepal: Kathmandu, Nepal, 2023. Available online: https://www.agricensusnepal.gov.np/post/10_64fc3705ded11 (accessed on 20 August 2024).
17. Islam, A.; Shaw, R.; Mallick, F. National Adaptation Programme of Action. In *Climate Change Adaptation Actions in Bangladesh*; Springer: Tokyo, Japan, 2013; pp. 93–106. [CrossRef]
18. Karanja Ng'ang'a, S.; Miller, V.; Girvetz, E. Is investment in Climate-Smart-agricultural practices the option for the future? Cost and benefit analysis evidence from Ghana. *Heliyon* **2021**, *7*, e06653.
19. Mishan, E.J.; Quah, E. *Cost-Benefit Analysis*; Routledge: London, UK, 2020.
20. Karanja Ng'ang'a, S.; Notenbaert, A.; Mwungu, C.; Mwongera, C.; Girvetz, E. Cost and Benefit Analysis for Climate-Smart Soil Practices in Western Kenya. 2017, p. 37. Available online: https://cgspace.cgiar.org/handle/10568/82618 (accessed on 22 May 2019).
21. Dayananda, D.; Irons, R.; Harrison, S.; Herbohn, J.; Rowland, P. *Capital Budgeting—Financial Appraisal of Investments Projects*; Cambridge University Press: Cambridge, UK, 2002. Available online: http://www.cambridge.org/ (accessed on 20 March 2020).
22. Lipper, L.; Thornton, P.; Campbell, B.M.; Baedeker, T.; Braimoh, A.; Bwalya, M.; Caron, P.; Cattaneo, A.; Garrity, D.; Henry, K.; et al. Climate-smart agriculture for food security. *Nat. Clim. Chang.* **2014**, *4*, 1068–1072. [CrossRef]
23. Matson, P.A.; Parton, W.J.; Power, A.G.; Swift, M.J. Agricultural intensification and ecosystem properties. *Science* **1997**, *277*, 504–509. [CrossRef] [PubMed]
24. Kagabo, D.M.; Stroosnijder, L.; Visser, S.M.; Moore, D. Soil erosion, soil fertility and crop yield on slow-forming terraces in the highlands of Buberuka, Rwanda. *Soil Tillage Res.* **2013**, *128*, 23–29. [CrossRef]
25. Sain, G.; Loboguerrero, A.M.; Corner-Dolloff, C.; Lizarazo, M.; Nowak, A.; Martínez-Barón, D.; Andrieu, N. Costs and benefits of climate-smart agriculture: The case of the Dry Corridor in Guatemala. *Agric. Syst.* **2017**, *151*, 163–173. [CrossRef]
26. Paris, Q.; Knapp, K. Estimation of von Liebig response functions. *Am. J. Agric. Econ.* **1989**, *71*, 178–186. [CrossRef]
27. Brey, R.; Bergland, O.; Riera, P. A contingent grouping approach for stated preferences. *Resour. Energy Econ.* **2011**, *33*, 745–755. [CrossRef]
28. Karanja Ng'ang'a, S.; Miller, V.; Essegbey, G.O.; Karbo, N.; Ansah, V.; Nautsukpo, D.; Kingsley, S.; Girvetz, E.H. *Cost and Benefit Analysis for Climate-Smart Agricultural (CSA) Practices in the Coastal Savannah Agro-Ecological Zone (AEZ) of Ghana*; CGIAR: Montpellier, France, 2017.
29. Power, A.G. Ecosystem services and agriculture: Tradeoffs and synergies. *Philos. Trans. R. Soc. B Biol. Sci.* **2010**, *365*, 2959–2971. [CrossRef]
30. Lamb, E.G.; Bayne, E.; Holloway, G.; Schieck, J.; Boutin, S.; Herbers, J.; Haughland, D.L. Indices for monitoring biodiversity change: Are some more effective than others? *Ecol. Indic.* **2009**, *9*, 432–444. [CrossRef]

31. Gobbi, J.A.; Casasola, F. Comportamiento financiero de la inversión en sistemas silvopastoriles en fincas ganaderas de Esparza, Costa Rica. *Agroforestería Américas* **2003**, *10*, 39–40.
32. Pagiola, S.; Ramírez, E.; Gobbi, J.; de Haan, C.; Ibrahim, M.; Murgueitio, E.; Ruíz, J.P. Paying for the environmental services of silvopastoral practices in Nicaragua. *Ecol. Econ.* **2007**, *64*, 374–385. [CrossRef]
33. Johannsen, S.S.; Armitage, P. Agricultural Practice and the Effects of. *Freshw. Forum* **2010**, *28*, 45–55.
34. Kremen, C.; Iles, A.; Bacon, C. Diversified farming systems: An agroecological, systems-based alternative to modern industrial agriculture. *Ecol. Soc.* **2012**, *4*, 17. [CrossRef]
35. López, T. *Estado, Prioridades y Necesidades Para el Manejo Sostenible del Suelo en Costa Rica*; Instituto de Ciencias. Benemérita Universidad Autónoma de Puebla: Puebla, México, 2013; pp. 1–27.
36. FAO. *El Sistema Agroforestal Quesungual*; Food and Agriculture Organization: Rome, Italy, 2005.
37. Pearce, D.W. Valuing the Environment. Springer: Berlin/Heidelberg, Germany, 1970; Volume 228.
38. Azumah, S.B.; Adzawla, W.; Osman, A.; Anani, P.Y. Cost-Benefit Analysis of On-Farm Climate Change Adaptation Strategies in Ghana. *Ghana J. Geogr.* **2020**, *12*, 29–46. [CrossRef]
39. Dittrich, R.; Wreford, A.; Moran, D. A survey of decision-making approaches for climate change adaptation: Are robust methods the way forward? *Ecol. Econ.* **2016**, *122*, 79–89. [CrossRef]
40. de Bruin, K.; Goosen, H.; van Ierland, E.C.; Groeneveld, R.A. Costs and benefits of adapting spatial planning to climate change: Lessons learned from a large-scale urban development project in the Netherlands. *Reg. Environ. Chang.* **2014**, *14*, 1009–1020. [CrossRef]
41. Lefore, N.; Closas, A.; Schmitter, P. Solar for all: A framework to deliver inclusive and environmentally sustainable solar irrigation for smallholder agriculture. *Energy Policy* **2021**, *154*, 112313. [CrossRef]
42. Yamegueu, D.; Alokore, Y.; Corso, G. Potential of microfinanced solar water pumping systems for irrigation in rural areas of Burkina Faso. *Energy. Sustain. Soc.* **2019**, *9*, 8. [CrossRef]
43. Chaudhury, A.S.; Helfgott, A.; Thornton, T.F.; Sova, C. Participatory adaptation planning and costing. Applications in agricultural adaptation in western Kenya. *Mitig. Adapt. Strateg. Glob. Chang.* **2016**, *21*, 301–322. [CrossRef]
44. Scrieciu, S.Ş.; Barker, T.; Ackerman, F. Pushing the boundaries of climate economics: Critical issues to consider in climate policy analysis. *Ecol. Econ.* **2013**, *85*, 155–165. [CrossRef]
45. Anugwa, I.Q.; Onwubuya, E.A.; Chah, J.M.; Abonyi, C.C.; Nduka, E.K. Farmers' preferences and willingness to pay for climate-smart agricultural technologies on rice production in Nigeria. *Clim. Policy* **2022**, *22*, 112–131. [CrossRef]
46. Macháč, J.; Trantinová, M.; Zaňková, L. Externalities in agriculture: How to include their monetary value in decision-making? *Int. J. Environ. Sci. Technol.* **2021**, *18*, 3–20. [CrossRef]
47. Nyasimi, M.; Kimeli, P.; Sayula, G.; Radeny, M.; Kinyangi, J.; Mungai, C. Adoption and dissemination pathways for climate-smart agriculture technologies and practices for climate-resilient livelihoods in Lushoto, Northeast Tanzania. *Climate* **2017**, *5*, 63. [CrossRef]

Disclaimer/Publisher's Note: The statements, opinions and data contained in all publications are solely those of the individual author(s) and contributor(s) and not of MDPI and/or the editor(s). MDPI and/or the editor(s) disclaim responsibility for any injury to people or property resulting from any ideas, methods, instructions or products referred to in the content.

International Journal of
Geo-Information

MDPI

Article

Examining the Causal and Heterogeneous Influence of Three-Dimensional Urban Forms on CO_2 Emissions in 285 Chinese Cities

Weiting Xiong [1], Yedong Zhang [1] and Jingang Li [2,*]

[1] Department of Urban Design, College of Landscape Architecture, Nanjing Forestry University, No. 159 Longpan Road, Nanjing 210037, China; xwt@njfu.edu.cn (W.X.); zyd0505@njfu.edu.cn (Y.Z.)
[2] School of Architecture, Southeast University, Nanjing 210096, China
* Correspondence: lijingang@seu.edu.cn

Abstract: Despite the efforts to examine the influence of urban forms on CO_2 emissions, most studies have mainly measured urban forms from a two-dimensional perspective, with relatively little attention given to three-dimensional urban forms and their causal relationships. Utilizing the built-up area dataset from the Global Human Settlement Layer (GHSL) project and the carbon emission dataset from the China City Greenhouse Gas Working Group (CCG), we examine a causal and heterogeneous effect of three-dimensional urban forms on CO_2 emissions—specifically urban height, density, and intensity—in 285 Chinese cities. The empirical results reveal a robust and positive causal effect of 3D urban forms on carbon emissions. Even when incorporating the spatial spillover effect, the positive effect of 3D urban forms remains. Moreover, GDP per capita and total population have a greater impact on urban CO_2 emissions. Additionally, we find that the influence of 3D urban forms on CO_2 emissions is U-shaped, with total population serving as a moderating factor in this effect. Importantly, there is significant geographic and sectoral heterogeneity in the influence of 3D urban forms on CO_2 emissions. Specifically, the influence of 3D urban forms is greater in eastern cities than in non-eastern cities. Furthermore, 3D urban forms primarily influence household carbon emissions rather than industrial and transportation carbon emissions. Therefore, in response to the growing challenges of global climate change and environmental issues, urban governments should adopt various strategies to develop more rational three-dimensional urban forms to reduce CO_2 emissions.

Keywords: CO_2 emissions; three-dimensional urban forms; causal identification; heterogeneous impact; China

1. Introduction

Nowadays, global warming has emerged as an increasingly critical challenge to contemporary human existence [1]. Estimates suggest that global surface temperatures have risen more rapidly since 1970 than in any other 50-year period over the past 2000 years [2]. As the primary greenhouse gas resulting from human activities, carbon dioxide (CO_2) leads to remarkable increases in atmospheric temperature and thus significantly contributes to global warming and climate change [3]. However, despite international efforts to curb carbon emissions through agreements like the 2015 Paris Agreement, global carbon emissions continue to rise at an alarming rate, posing profound environmental and societal threats to human beings. For example, the International Energy Agency (IEA) points out that the world's CO_2 emissions associated with energy consumption increased by 1.1% in 2023, reaching a new record high of 37.4 billion tons [4]. Simultaneously, as cities have become major centers of population and economic activity, mitigating their environmental impact and promoting sustainable cities and communities have become

crucial aspects of global sustainable development. Consequently, how to reduce urban carbon emissions has attracted growing attention among scholars and policymakers.

The existing literature has demonstrated that CO_2 emissions are strongly linked to economic growth [5,6], industrial structure [7,8], technological progress [9,10] and urbanization rate [11,12], amongst many other social and economic factors. However, it is difficult and even unrealistic to reduce carbon emissions solely by restricting socioeconomic development, as this would undoubtedly hamper the improvement of human well-being. Therefore, in addition to socioeconomic factors, recent studies have increasingly focused on investigating other alternative factors that could influence carbon emissions. Among these factors, urban forms have obtained increasing attention. In fact, though occupying roughly 3% of the Earth's land, cities make up about 70% of the world's CO_2 emissions associated with energy consumption, with transport and buildings being among the largest contributors [2,13]. Moreover, it has been estimated that global urban land areas will grow by nearly two times during the 2000–2030 period [14]. Consequently, urban forms, which represent how cities are spatially and physically arranged, exert a profound effect on carbon emissions, as they influence people's transportation behaviors and energy consumption patterns.

The influence of urban forms on CO_2 emissions has been mainly explored from four aspects, these being land-use change, built environment, transportation network, as well as urban expansion pattern [15]. As for land use change, studies have shown that the urbanization process drives the transformation of agricultural land to urban construction land, which would decrease the carbon sink [16]. Furthermore, other scholars have argued that CO_2 emissions could be influenced by land use structure and land management strategies, as the capacities to generate and absorb carbon dioxide may vary among different categories of land uses [17]. With regard to the built environment, indicators such as population density [18,19] and land mixing degree [20] have been commonly used in empirical studies. For instance, in a case study of more than 120 of the largest urbanized areas in the US, Lee and Lee [18] showed that population density is negatively linked to CO_2 emissions from household travel. In another empirical study focusing on 268 Chinese cities, Li et al. [20] found that effect of land use mix on CO_2 emissions is U-shaped, indicating that a moderate level of land use mix is conducive to carbon reductions. In terms of transportation networks, empirical studies have mainly focused on accessibility, road network density, and other indicators that might influence carbon emissions by affecting people's travel behavior and cities' traffic environment. For example, Wang et al. [6] showed that transportation energy consumption is negatively linked to road network density, as a higher road network density usually leads to a higher accessibility and connectivity of urban traffic, thus reducing traffic congestion. As for urban expansion patterns, urban compactness [21] and urban polycentricity [22,23] are two indicators that have been widely used in empirical studies. While scholars have generally shown that more compact urban development is linked to less carbon emissions, the influence of urban polycentricity on CO_2 emissions is usually inconclusive. For instance, Sha et al. [24] showed that urban polycentricity helps improve carbon emission efficiency across 232 Chinese cities. However, Zhu et al. [25] found that the role of polycentric urban spatial structure in reducing CO_2 emissions could be moderated by urban economic strength.

Despite the efforts to examine the influence of urban forms on CO_2 emissions, most scholars have measured urban forms from a two-dimensional (2D) perspective, with relatively little attention being paid to three-dimensional (3D) urban forms. For example, Wang et al. [26] analyzed the effects of three two-dimensional urban form characteristics (extension, irregularity, and compactness) on CO_2 emission. However, urban forms represent not only how cities are horizontally structured but also how they are vertically organized. Furthermore, urban forms measured in 2D terms are not necessarily positively correlated with those in 3D terms. For instance, a compact city in 2D terms might not be regarded as compact if measured from a 3D perspective. Taking this a step further, we can argue that the positive influence of urban compact development in reducing CO_2 emissions from a 2D perspective, which has been verified in many studies [15,26], might not hold

if it is measured in 3D terms. Moreover, with increasing land use efficiency and tighter land resource supply, urban forms in many cities tend to grow taller rather than expand horizontally [27], making it increasingly important to examine the influence of 3D urban forms on CO_2 emissions.

Notably, some scholars have already examined how 3D urban forms are linked to CO_2 emissions. At the building scale, studies have shown that the operations of buildings make up over 1/3 of global final energy-related emissions [28]. As buildings continue to grow vertically, it can be expected that carbon emissions from buildings will rise [29]. Moreover, some studies have argued that high-rise and high-density buildings may increase carbon emissions through different mechanisms, such as reducing air flow and ventilation capacity [30], causing the urban heat island effect [31], increasing the frequent use of lights and air conditioners [32], and transforming the vertical roughness of urban landscapes [33]. Additionally, the shape, typology, and orientation of buildings have been found to be closely associated with CO_2 emissions [34].

At the city scale, since large-scale data on urban buildings are usually unavailable, empirical investigations of the role of 3D urban forms in reducing CO_2 emissions have been quite limited. One notable study is that by Xu et al. [35], which investigated the impact of 3D urban structures on CO_2 emissions across 86 Chinese cities. The empirical results show that the total building volume contributes the most to accelerated carbon emissions, followed by building height and building heat dissipation area. In addition, the results show that urban compactness measured in 3D terms might cause CO_2 emissions to rise. Another notable study is that by Du et al. [36], which explored how 2D and 3D urban forms influence CO_2 emissions across 2813 urban functional zones of Beijing. They found that commercial zones account for the highest carbon emissions, and factors such as building height, base area, and average building volume are all correlated with carbon emissions. Similarly, Lin et al. [37] adopted a random forest regression approach to examine the influence of 3D building structure on grid-level CO_2 emissions in Shenzhen. They found that carbon emissions are closely correlated with 3D urban form factors such as building coverage ratio and floor area ratio.

Overall, existing studies have contributed to our understanding of the effect of 3D urban forms on CO_2 emissions at the city scale. However, there remains much room for further investigation. First and perhaps foremost, existing studies have largely ignored the causal influence of 3D urban forms on CO_2 emissions. Nonetheless, identifying this causal relationship is crucial to revealing whether 3D urban forms truly exert an impact on carbon emissions, which is important for effectively making low-carbon strategies. Second, existing studies have mainly focused on a single Chinese city [36,37] or a group of Chinese cities [35]. An empirical study focusing on all the Chinese cities would thus contribute comprehensively to the literature. Third, it remains unclear whether the effect of 3D urban forms on CO_2 emissions is heterogeneous.

This paper contributes to the existing literature by conducting an empirical study of 285 Chinese cities at the prefecture and above level to investigate the causal and heterogeneous influence of 3D urban forms on CO_2 emissions at the city scale. Our empirical findings show a robust, positive causal influence of 3D urban forms on CO_2 emissions. This conclusion remains valid even when the spatial spillover effect is taken into account. Additionally, we provide evidence that the influence of 3D urban forms on CO_2 emissions is U-shaped and that total population plays a moderating role in this relationship. Importantly, the influence of 3D urban forms on CO_2 emissions exhibits geographic and sectoral heterogeneity. Specifically, the influence of 3D urban forms is greater in eastern cities than in non-eastern cities. Furthermore, 3D urban forms primarily affect household carbon emissions rather than industrial and transportation carbon emissions.

The structure of this paper is organized as follows. Section 2 describes the data and methodology used in this study. Then, Section 3 shows the regression results. Section 4 discusses the empirical results as well as policy implications. Finally, Section 5 concludes with future research suggestions.

2. Materials and Methods

2.1. Carbon Emissions and 3D Urban Forms Dataset

This paper takes prefecture-level and above cities in China as the research objects, excluding cities with missing data from Tibet, Hainan, and Xinjiang, resulting in a total of 285 cities. Data on carbon emissions for 285 Chinese cities at the prefectural and above level in 2020 were obtained from the China City Carbon Dioxide Emissions Dataset by the China City Greenhouse Gas Working Group (CCG) (https://www.cityghg.com/, accessed on 17 March 2024), which includes 137 persons from 76 organizations [35]. Given space constraints, a detailed description of how this dataset was produced is not provided here and can be found in Cai et al. [38] and Cai et al. [39]. Overall, the data provided in this dataset consist of two components: direct CO_2 emissions within the administrative boundaries of the cities, such as those from residential, industrial, commercial, and transportation related energy consumptions; and indirect CO_2 emissions from electricity purchases by the cities [38]. The CCG first established the 2015 dataset of CO_2 emissions for all Chinese cities and later extended it to establish a uniform carbon emissions inventory for 2005, 2010, 2015, and 2020 at the city level. Given the lack of official statistics on carbon emissions in Chinese cities, the reliability of this dataset for our analysis can be demonstrated by publications describing the datasets [38,39] and studies drawing upon the datasets [35]. The distribution of CO_2 emissions for 285 Chinese cities in 2020 is shown in Figure 1.

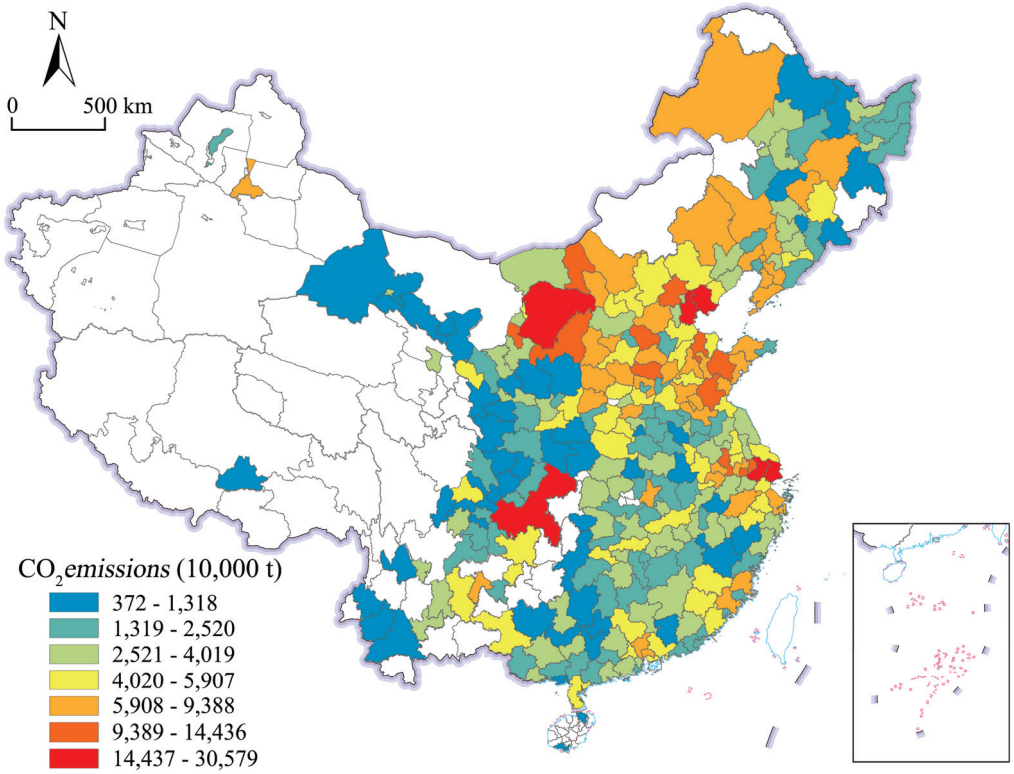

Figure 1. The distribution of CO_2 emissions for 285 Chinese cities.

Data on 3D urban forms for Chinese cities in 2020 were obtained from the 2023 data package released by the Global Human Settlement Layer (GHSL) project (https://human-settlement.emergency.copernicus.eu, accessed on 10 April 2024), which provides the spatial distribution of global human presence in the form of time series built-up maps, population density maps and settlement maps. For the purpose of this research, we utilized the built-up maps that include the datasets of GHS-BUILT-H (building heights), GHS-BUILT-S (built-up surfaces), and GHS-BUILT-V (built-up volume). Specifically, the GHS-BUILT-H dataset provides a spatial raster dataset with a resolution of 100 m, measured in meters, which describes the spatial distribution of building heights derived from a

combination of global DEM data and satellite imagery, filtered through linear regression techniques [40]. The GHS-BUILT-S dataset provides a spatial raster dataset with resolutions of 10, 100, and 1000 m, which shows the spatial distribution of built-up surfaces, measured in square meters [41]. The GHS-BUILT-V dataset provides a spatial raster dataset with resolutions of 10, 100, and 1000 m, which demonstrates the spatial distribution of built-up volumes, measured in cubic meters [42]. Note that the GHS-BUILT-H dataset only provides building height data for 2018, while the other two datasets provide data for 2020. Since building heights should be relatively stable within two years, we believe that this inconsistency is acceptable. To ensure consistency in resolution, all the three datasets were used with a resolution of 100 m.

2.2. Measurement of 3D Urban Forms

Three proxy indicators of 3D urban forms are considered here: building height, building density, and building intensity. Specifically, for each 100 m grid cell, we derived data on building heights, built-up surfaces, and built-up volumes from the above-mentioned three datasets, respectively. Given that each grid cell is at the 100 m scale, the values of building heights, built-up surfaces, and built-up volumes can directly represent each grid's building height (m), building density (m^2), and building intensity (m^3). We then calculated urban height (*H*), urban density (*D*), and urban intensity (*I*) at the city level. Since the grid-level spatial distributions of building heights, densities, and intensities are skewed (see Figure 2 for the distributions of the three indicators in representative cities), we use the median values of these metrics to represent the city-level building heights (m), densities (m^2), and intensities (m^3). Table 1 provides a descriptive statistical analysis of urban height, density and intensity.

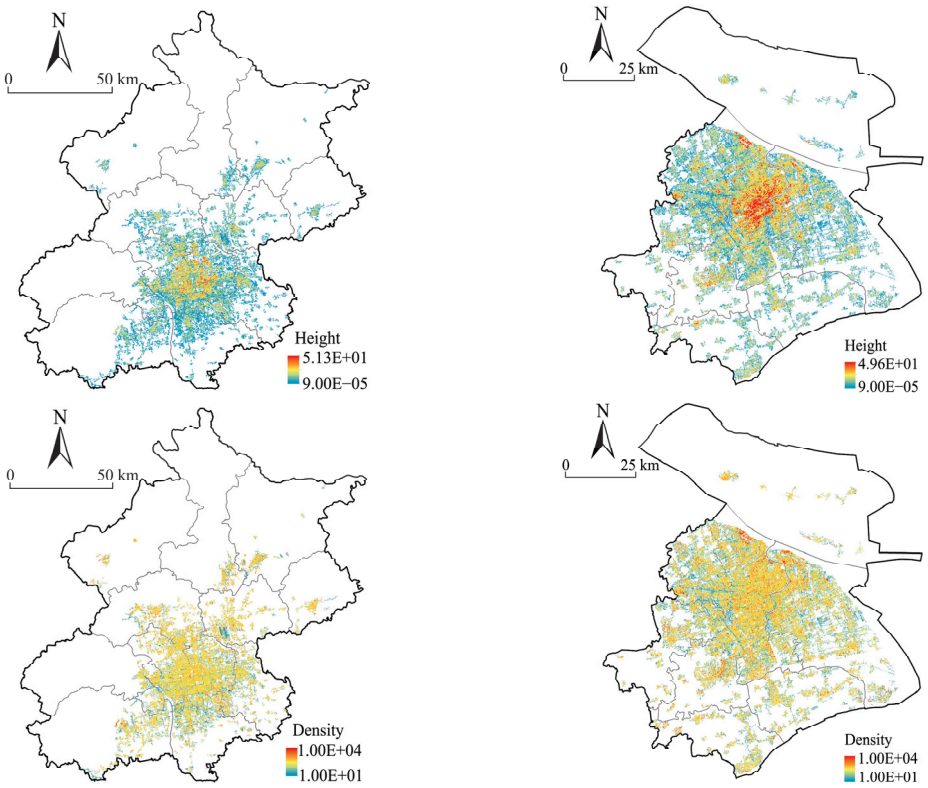

Figure 2. *Cont.*

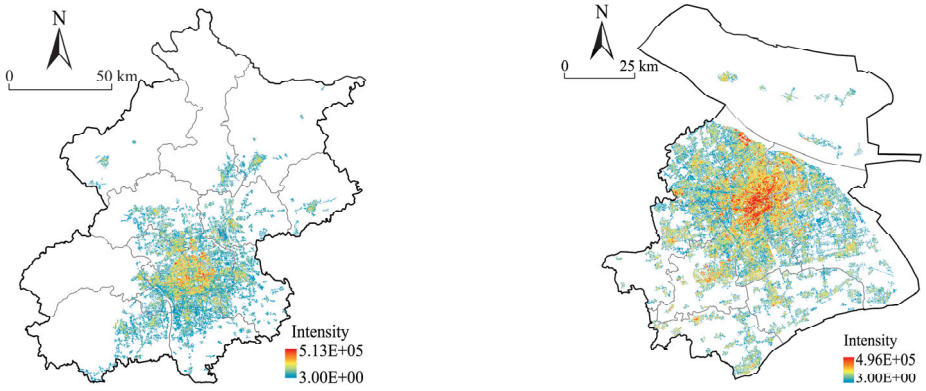

(**a**) Beijing (**b**) Shanghai

Figure 2. The distributions of the three indicators for representative cities.

Table 1. Description of urban height, density, and intensity.

3D Urban Forms	Mean	S.D.	Max	Min
Urban height	2.434	0.854	5.138	0.166
Urban density	2908.456	551.360	4276	612
Urban intensity	25,003.320	8512.944	51,561	1885

Though it could be ideal to include the three indicators together in regression models, we found a strong correlation among them, with the *KMO* statistic for the three indicators being 0.711. This would cause serious multicollinearity in regression models. Therefore, we adopted a principal component analysis (PCA) approach to downscale the three indicators. Specifically, in the PCA analysis, only one principal component had an eigenvalue greater than 1 and accounts for 93.77% of the variance, yielding a comprehensive 3D urban form indicator (*HDI*) (Figure 3).

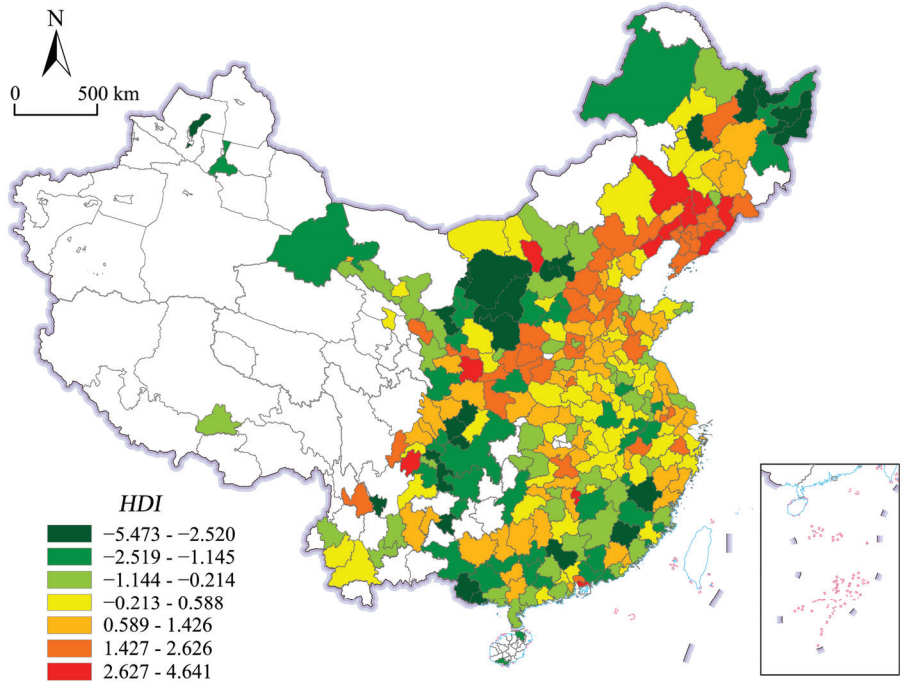

Figure 3. The distribution of *HDI* for 285 Chinese cities.

2.3. Model Specification

Given that the distribution of CO_2 emissions for Chinese cities exhibits strong spatial correlation, we utilize the following model to regress the effect of 3D urban forms on CO_2 emissions at the city scale:

$$CE_i = \alpha + \rho \sum_j w_{ij} CE_i + \beta HDI_i + \gamma X_i + \varepsilon_i \quad (1)$$

where CE_i denotes CO_2 emissions for city i. $\sum_j w_{ij} CE_i$ is the spatial lag term, with w_{ij} being the spatial components of the spatial weight matrix W. Here, we use the inverse distance weight matrix to capture the spatial relationships between cities i and j. HDI_i denotes the comprehensive 3D urban form indicator derived from the PCA analysis for city i, and X_i is a set of control variables affecting the city-level CO_2 emissions. ρ represents the spatial autoregressive coefficient, which captures the spatial dependence of carbon emissions. β is the coefficient of the key independent variable, while γ represents the coefficients of the control variables. α denotes the constant term and ε_i represents the error term.

Table 2 shows the measurement of all the variables. Except for the key independent variable, this paper includes a set of control variables that have been found to be associated with carbon emissions in existing studies. Specifically, we control for the impact of per capita GDP (*PGDP*) [19], population (*POP*) [24], population density (*POPDEN*) [19], industrial structure (*INS*) [22], economic openness (*OPEN*) [43], financial level (*FIN*) [22], government intervention (*GOV*) [44], and transportation infrastructure (*INF*) [12]. Data for these control variables were obtained from China Urban Construction Statistical Yearbook and China City Statistical Yearbook. To reduce the influence of heteroskedasticity, all control variables except for those measured in ratio forms (i.e., *INS*, *FIN*, and *GOV*) have been logarithmically transformed.

Table 2. Description of the variables.

Variables	Description
Carbon emissions (*CE*)	Total CO_2 emissions
3D urban forms (*HDI*)	The principal component of city-level height, density, and intensity
Economic level (*PGDP*)	Per capita GDP
Population (*POP*)	Total population
Population density (*POPDEN*)	Permanent resident population per km^2
Industrial structure (*INS*)	Ratio of value added of the secondary sector to total GDP
Economic openness (*OPEN*)	Volume of export trade
Financial level (*FIN*)	Ratio of deposit and loan balances of financial institutions to total GDP
Government intervention (*GOV*)	Ratio of fiscal expenditure to total GDP
Transportation infrastructure (*INF*)	Per capita road areas

3. Empirical Results

3.1. The Benchmark Regression Results

Table 3 shows the benchmark regression results. Specifically, in Model 1, we examine the effects of all control variables on CO_2 emissions. The empirical results show that the coefficients for *PGDP*, *POP*, *POPDEN*, and *INS* are statistically significant, while others are insignificant. Among them, the coefficients of *PGDP*, *POP*, and *INS* are positive and statistically significant at the 1% level, while *POPDEN* is negatively correlated at the 10% significance level. This indicates that the influences of per capita *GDP*, total population, and industrial structure on CO_2 emissions are significantly positive. This empirical finding aligns with those of many existing studies [22]. Conversely, population density (*POPDEN*) has a weak negative correlation with carbon emissions, suggesting that carbon emissions tend to decrease as urban population density increases. Theoretically, higher urban population density could lead to increased carbon emissions due to greater concentrations

of individuals and associated production and daily life activities [19]. However, higher population density can also enhance the development of public transportation, promote resource recycling, and improve energy efficiency, which may reduce CO_2 emissions [18,43]. Our empirical findings here indicate that the positive impact of population density might outweigh its negative impact on CO_2 emissions.

Table 3. Results of benchmark regressions.

Variable	Model 1	Model 2	Model 3	Model 4	Model 5	Model 6
HDI		0.097 ***	0.047 *	0.043 *	0.056 **	−0.412 **
		(0.028)	(0.027)	(0.024)	(0.026)	(0.206)
HDI^2					0.027 ***	
					(0.010)	
$HDI \times \ln POP$						0.082 **
						(0.036)
ln*PGDP*	0.536 ***		0.574 ***	0.636 ***	0.544 ***	0.485 ***
	(0.148)		(0.150)	(0.146)	(0.148)	(0.152)
ln*POP*	0.631 ***		0.619 ***	0.533 ***	0.626 ***	0.614 ***
	(0.084)		(0.084)	(0.093)	(0.083)	(0.086)
ln*POPDEN*	−0.104 *		−0.113 *	−0.091	−0.112 *	−0.138 **
	(0.063)		(0.063)	(0.057)	(0.063)	(0.065)
INS	0.018 ***		0.018 ***	0.015 ***	0.018 ***	0.018 ***
	(0.006)		(0.006)	(0.006)	(0.005)	(0.006)
ln*OPEN*	0.012		0.006	0.007	0.020	0.015
	(0.035)		(0.034)	(0.033)	(0.034)	(0.034)
FIN	0.000		0.000	−0.000	0.000	0.000
	(0.000)		(0.000)	(0.000)	(0.000)	(0.000)
GOV	0.666		0.759	0.709	0.743	0.414
	(0.744)		(0.762)	(0.627)	(0.731)	(0.742)
ln*INF*	0.038		0.069	0.038	0.101	0.058
	(0.123)		(0.125)	(0.116)	(0.123)	(0.122)
$\ln CE \times W$				0.036 **		
				(0.018)		
Constant	−3.072	7.982 ***	−3.492 *	−3.632 **	−3.555 *	0.485 ***
	(1.879)	(0.049)	(1.915)	(1.689)	(1.860)	(0.152)
Observations	285	285	285	285	285	285
R^2 / *Pseudo* R^2	0.410	0.038	0.418	0.414	0.434	0.432

Note: (1) *** $p < 0.01$, ** $p < 0.05$, * $p < 0.1$; (2) robust standard errors are in parentheses.

In Models 2 and 3, we further examine the effect of 3D urban forms on CO_2 emissions. In Model 2, without control variables, the result reveals that the influence of *HDI* on CO_2 emissions is positive and statistically significant. In Model 3, which includes the control variables, the positive estimated coefficient for HDI remains significant at the 10% level. These results align with the empirical findings shown in Xu et al. [35], suggesting that cities with higher building height, density, and intensity on average might lead to more carbon emissions. Furthermore, the estimated coefficients for *PGDP*, *POP*, *INS*, and *POPDEN* remain consistent with those in Model 1 with regard to their signs and significance, implying that the influence of these variables on CO_2 emissions is robust.

In Model 4, the influence of the spatial lag of the dependent variable is taken into account. Obviously, the estimated coefficient of $\ln CE \times W$ is positive at the 5% significance level, indicating that cities tend to produce more carbon emissions if their neighboring cities produce more carbon emissions. In line with the empirical results shown in Li et al. [20] and Zhu et al. [25], urban CO_2 emissions exhibit spatial correlation, and the influence of their spatial lag is significant. Despite this spatial correlation, the coefficient for *HDI* remains significantly positive, further demonstrating the positive influence of 3D urban forms on CO_2 emissions.

In Models 5 and 6, we added separately the squared term of *HDI* and the interaction term between *HDI* and ln*POP* to examine the nonlinear and moderating effects of 3D urban

forms on CO_2 emissions. The result in Model 5 shows that the coefficient of HDI^2 is positive and statistically significant at the 1% level, implying that the influence of 3D urban forms on carbon emissions is U-shaped. This suggests that below a certain threshold, an increase in 3D urban forms may intensify the use of land resources, protect the urban ecosystem, and improve energy use efficiency, thereby reducing energy consumption by residents and contributing to lower carbon emissions. However, when 3D urban forms exceed a certain threshold, the situation reverses. Thus, a moderate level of 3D urban forms might be conducive to reducing carbon emissions. In Model 6, the coefficient of $HDI \times \ln POP$ is positive and statistically significant at the 5% level, suggesting that total population plays a moderating role in the way that 3D urban forms affect carbon emissions. Specifically, when the total population is greater than 1.521 million (simply let $-0.412 + 0.082 \times \ln POP = 0$), an increase in the comprehensive indicator of 3D urban forms leads to more carbon emissions. Although 3D urban forms can enhance energy use efficiency, when a city's population size exceeds a certain threshold, the city's socioeconomic vitality and residents' living needs change significantly. As 3D urban forms continue to increase, the demand for resources and energy in these cities rises substantially, which would increase CO_2 emissions.

3.2. The Causal Effect of 3D Urban Forms on CO_2 Emissions

The influence of 3D urban forms on CO_2 emissions may be subject to potential endogeneity issues, such as reverse causality and omitted variables. Specifically, higher carbon emission intensity implies weaker environmental regulations and more extensive industrial structures, which can lead to disordered development and construction in cities, thereby affecting 3D urban forms. Additionally, although this study controls for a range of variables affecting carbon emissions based on existing studies, there may still be issues related to omitted variables. Consequently, this paper uses the instrumental variable (IV) approach [45] to address the endogeneity issues and investigate whether 3D urban forms are truly a driving force for carbon emissions.

Drawing on the approach adopted in Combes et al. [46], this paper uses the sum of distances from each city to 69 modern China treaty port cities, such as Guangzhou, Xiamen, Shanghai, Fuzhou, and Ningbo, as an IV, and employs the two-stage least squares method for estimation. The rationale for using this instrumental variable is as follows. On one hand, the presence of modern China treaty port cities has been in place for a long period and is unlikely to have a direct impact on carbon emissions in 2020, which provides strong exogeneity. On the other hand, modern China treaty port cities and their neighboring cities have been strongly influenced by western social, economic, and architectural forms, leading to profound changes in their socioeconomic and urban development. This, in turn, might affect the current spatial patterns of Chinese cities through the change of urban systems in China.

Table 4 presents the IV regression results. Specifically, the first-stage regression results show that the coefficients of the IV are negative and statistically significant, indicating that cities that are closer to modern China treaty port cities tend to have higher values of the comprehensive 3D urban form indicator. This is generally in line with our theoretical expectations, as cities closer to these treaty port cities are more likely to be influenced by western social, cultural, and architectural forms, leading to changes in their traditional low-density urban forms. The Kleibergen–Paap rk LM statistic is positive at the 1% significance level, and the Kleibergen–Paap rk Wald F statistic for instrumental variables exceeds 16.38, demonstrating that the instrumental variable passes both the under-identification and weak instrument tests. The second-stage regression results show that the coefficient of urban form is still significantly positive, indicating that we can capture the causal influence of 3D urban forms on CO_2 emissions while addressing the endogeneity issue. The effect estimated by the instrumental variable regression increases significantly compared to the benchmark regressions. This suggests that potential endogeneity does not change the direction of the influence of 3D urban forms on CO_2 emissions, and the positive influence of 3D urban forms may be underestimated in the baseline regression models.

Table 4. Results of the two-stage least squares estimation using IV.

Variable	First Stage: *HDI*	Second Stage: ln*CE*
DIS	−0.022 ***	
	(0.005)	
HDI		0.253 **
		(0.122)
ln*PGDP*	−0.634 **	0.740 ***
	(0.299)	(0.165)
ln*POP*	0.071	0.570 ***
	(0.202)	(0.099)
ln*POPDEN*	0.020	−0.149 **
	(0.151)	(0.074)
INS	−0.015	0.019 ***
	(0.014)	(0.007)
ln*OPEN*	0.109	−0.018
	(0.094)	(0.038)
FIN	−0.000	0.000
	(0.000)	(0.000)
GOV	−2.287	1.165
	(1.667)	(0.855)
ln*INF*	−0.828 ***	0.203
	(0.301)	(0.165)
Constant	10.756 ***	−5.332 **
	(3.797)	(2.114)
Kleibergen–Paap rk LM statistic	19.478 ***	
Kleibergen–Paap rk Wald F statistic	20.267	
Stock–Yogo critical value (10% maximal IV)	16.38	
Observations	285	285
R^2	0.192	0.270

Note: (1) *** $p < 0.01$, ** $p < 0.05$; (2) robust standard errors are in parentheses.

3.3. Heterogeneity Analysis

The IV approach is further used to examine whether the influence of 3D urban forms on CO_2 emissions is heterogeneous among different cities and sectors producing carbon emissions. Specifically, Models 1–2 compare the causal influence of 3D urban forms on CO_2 emissions in eastern cities with that in non-eastern cities, while Models 3–5 divide carbon emissions into those from industry, households, and transport sectors.

In Models 1 and 2 of Table 5, we observe that the *HDI* coefficients are positive and statistically significant. However, the *HDI* coefficient for eastern cities is larger than that for non-eastern cities, suggesting that the influence of 3D urban forms on CO_2 emissions is greater in eastern cities than in non-eastern cities. Furthermore, *PGDP*, *POP*, and *INS* have significant and positive effects on CO_2 emissions in non-eastern cities, but not in eastern cities. This disparity may be attributed to the substantial differences in urban expansion patterns and economic development structures between the two regions. In Model 1, the coefficient of *POPDEN* is negative at the 1% significance level, whereas it has a negative and statistically insignificant coefficient in Model 2. This indicates that in eastern cities, higher population density has a notable inhibiting influence on CO_2 emissions, likely due to its relatively advanced level of urban development. In fact, existing studies have also found that in more urbanized areas, increased population density might drive a rapid development of public transport systems and enhance resource recycling, reducing overall CO_2 emissions [18].

Table 5. Heterogeneity analysis estimates.

Variable	By Geography		By Sector		
	Model 1: Eastern	**Model 2: Non-Eastern**	**Model 3: Industry**	**Model 4: Household**	**Model 5: Transportation**
HDI	0.696 ***	0.212 *	0.270	0.435 ***	0.031
	(0.269)	(0.124)	(0.166)	(0.166)	(0.052)
ln*PGDP*	0.367	0.707 **	0.583 ***	0.477 **	0.590 ***
	(0.281)	(0.279)	(0.217)	(0.201)	(0.082)
ln*POP*	0.422	0.490 ***	0.595 ***	1.045 ***	0.844 ***
	(0.350)	(0.115)	(0.136)	(0.115)	(0.055)
ln*POPDEN*	−0.644 ***	−0.140	−0.282 **	−0.125	0.121 ***
	(0.249)	(0.088)	(0.111)	(0.089)	(0.045)
INS	−0.001	0.023 ***	0.033 ***	0.008	−0.007 *
	(0.013)	(0.009)	(0.011)	(0.008)	(0.003)
ln*OPEN*	−0.010	−0.031	−0.001	−0.161 ***	0.013
	(0.097)	(0.049)	(0.051)	(0.050)	(0.019)
FIN	0.000	0.000	0.000	0.000 **	−0.000 **
	(0.000)	(0.000)	(0.000)	(0.000)	(0.000)
GOV	−4.086	0.934	1.111	0.471	1.499 ***
	(2.972)	(1.068)	(1.017)	(1.162)	(0.318)
ln*INF*	−0.275	0.197	0.189	0.168	−0.123 *
	(0.311)	(0.216)	(0.204)	(0.197)	(0.069)
Constant	1.421	−4.797	−5.260 **	−6.449 **	−5.540 ***
	(4.301)	(3.472)	(2.523)	(2.648)	(0.874)
Kleibergen–Paap rk LM statistic	8.930 ***	16.481 ***	19.478 ***	19.478 ***	19.478 ***
Kleibergen–Paap rk Wald F statistic	10.075	19.272	20.267	20.267	20.267
Stock–Yogo critical value (10% maximal IV)	16.38	16.38	16.38	16.38	16.38
Observations	86	199	285	285	285
R^2	0.012	0.182	0.174	0.196	0.775

Note: (1) *** $p < 0.01$, ** $p < 0.05$, * $p < 0.1$; (2) robust standard errors are in parentheses.

In Models 3–5, the influence of *HDI* on household CO_2 emissions is positive at the 1% significance level, while its impact on industrial and transportation carbon emissions is not significant. The result suggests that the influence of 3D urban forms on CO_2 emissions is primarily focused on household carbon emissions. This is because 3D urban forms indirectly reflect the number of households. Higher height, density, and intensity of cities usually indicate a larger number of urban households, leading to increased household carbon emissions. In contrast, industrial carbon emissions mainly arise from the production of goods and services, which can be affected by urban population, economic growth, and industrial structure. Similarly, carbon emissions from the transportation sector are primarily affected by urban population and economic level. Specifically, cities with larger populations and higher economic levels tend to have more rail and air travel, resulting in higher levels of transportation-related carbon emissions.

3.4. Robustness Tests

The robustness of the causal influence of 3D urban forms on CO_2 emissions is tested by continuing to use the instrumental variable and excluding certain special samples. In Model 1 of Table 6, we exclude the samples of Beijing, Shanghai, Tianjin, and Chongqing, which are four centrally administered municipalities, and have larger populations and more built-up areas. Additionally, these cities are significantly more exposed to government and planning policy interventions than others. Based on Model 1, provincial capitals are further excluded in Model 2, as these cities tend to be supported by more development policies than other ordinary cities. In Model 3, we exclude megacities with an urban population exceeding 5 million. Taken together, the empirical findings of the three models show that the coefficients for *HDI* remain positive at the 5% significance level, suggesting that the causal influence of 3D urban forms on CO_2 emissions is robust.

Table 6. Robustness tests.

Variable	Model 1	Model 2	Model 3
HDI	0.257 **	0.221 **	0.242 **
	(0.125)	(0.111)	(0.105)
ln*PGDP*	0.632 ***	0.628 ***	0.522 ***
	(0.171)	(0.189)	(0.194)
ln*POP*	0.513 ***	0.609 ***	0.536 ***
	(0.104)	(0.102)	(0.108)
ln*POPDEN*	−0.152 **	−0.195 ***	−0.160 **
	(0.073)	(0.073)	(0.073)
INS	0.019 ***	0.027 ***	0.023 ***
	(0.007)	(0.007)	(0.008)
ln*OPEN*	−0.018	−0.025	−0.022
	(0.039)	(0.037)	(0.038)
FIN	0.000 *	0.000 **	0.000
	(0.000)	(0.000)	(0.000)
GOV	0.760	0.871	0.342
	(0.863)	(0.981)	(0.864)
ln*INF*	0.266	0.273 *	0.286 *
	(0.173)	(0.156)	(0.162)
Constant	−3.943 *	−5.368 **	−3.293
	(2.169)	(2.250)	(2.368)
Kleibergen–Paap rk LM statistic	18.722 ***	16.319 ***	23.685 ***
Kleibergen–Paap rk Wald F statistic	19.524	17.883	29.894
Stock–Yogo critical value (10% maximal IV)	16.38	16.38	16.38
Observations	281	258	264
R^2	0.230	0.323	0.231

Note: (1) *** $p < 0.01$, ** $p < 0.05$, * $p < 0.1$; (2) robust standard errors are in parentheses.

4. Discussion

Overall, our empirical findings demonstrate a significant, positive, and causal effect of 3D urban forms on carbon emissions, indicating that cities with higher building heights, density, and intensity contribute to greater carbon emissions. These findings generally align with those of other studies [35,37]. For instance, Xu et al. [35] showed that total building volume and average building height are positively related with CO_2 emissions. Theoretically, higher urban height results in increased solar radiation absorption, leading to higher carbon emissions for ventilation and cooling purposes [30]. Additionally, greater building height necessitates increased energy consumption for facilities such as water supply and elevator operation, thereby raising carbon emissions [47]. Higher building density and intensity indicate a greater proportion of impervious surfaces in the city, which not only enhances the urban heat island effect and increases carbon emissions due to ventilation and cooling needs [30], but also compresses green spaces such as urban green areas, wetlands, and farmlands, thereby reducing the carbon sink [37,48].

This paper also demonstrates a nonlinear and spatially autocorrelated influence of 3D urban forms on CO_2 emissions. In terms of the nonlinear relationship, we find that the influence of 3D urban forms on CO_2 emissions is U-shaped, and total population acts as a moderating factor in the influence of 3D urban forms on CO_2 emissions. This suggests that a moderate level of 3D urban forms might be conducive to reducing carbon emissions. Beyond this moderate level, the intensification of urban density and building heights may lead to the overconcentration of buildings and reduced green spaces, which can further intensify the urban heat island effect and raise energy consumption for cooling and ventilation [30]. Similarly, the influence of 3D urban forms on CO_2 emissions may be stronger in cities with larger populations, as the demand for energy and resources increases significantly with population growth. With regard to the spatially autocorrelated relationship, the results show that the influence of 3D urban forms on CO_2 emissions remains positive even when considering the spatial spillover effect of neighboring cities. As

noted in existing studies [20,25], ignoring the spatial correlation of carbon emissions may skew the results. In our analysis, when the spatial lag term for CO_2 emissions is included in the regression models, the influence of 3D urban forms on CO_2 emissions is reduced.

Our empirical findings also show significant geographic and sectoral heterogeneity in the influence of 3D urban forms on CO_2 emissions. According to the estimation results of sectoral heterogeneity, higher 3D urban forms significantly contribute to household carbon emissions, while the influence of 3D urban forms on industrial and transportation carbon emissions is not significant. Constrained by government urban planning, the proportion of land use for residential, industrial, and public service facilities is controlled, so 3D urban forms can indirectly reflect the number of urban households. In other words, higher 3D urban forms generally indicate more households, leading to greater energy consumption for maintaining daily urban life, which results in higher carbon emissions. Additionally, denser and taller residential buildings in a city lead to increased consumption of services and facilities, further raising the city's CO_2 emissions. Comparatively, CO_2 emissions from urban industries mainly come from the production of goods and services, which are influenced by urban economic development level, population size, and industrial structure. This finding is in line with the hypothesis of Xu et al. [35] that 3D urban forms are independent of agricultural and industrial energy consumption. The urban transportation CO_2 emissions primarily results from the energy consumption of cars, subways, trains, and airplanes, which also mainly depend on urban population size and economic development level. The sectoral heterogeneity in the influence of 3D urban forms on CO_2 emissions helps further explain the possible reasons for the geographic heterogeneity in the influence of 3D urban forms. Specifically, since 3D urban forms mainly affect household carbon emissions in cities, residents in eastern cities, compared to those in central and western cities, have higher incomes, pursue more comfortable living conditions, and have more diversified living service facilities. This, in turn, generates more energy consumption and carbon emissions. Studies on the influence of residents' income and energy consumption on CO_2 emissions show that higher income levels of the population may lead to higher energy consumption and CO_2 emissions [49].

Our empirical findings have some policy implications. Since 3D urban forms are important factors affecting carbon emissions, low-carbon city planning needs to account for 3D urban forms. Guided by the theory of agglomeration economies and the concept of compact city planning, vertical high-density cities have gradually become a key development mode for large cities worldwide. However, our empirical results show that greater height, density, and intensity of a city contribute to higher levels of carbon emissions. To achieve low-carbon development and address the climate change and environmental crises caused by excessive CO_2 emissions, policymakers, scholars, planners, and urban residents should collaborate to plan and build more rational 3D urban forms. First, urban planning should include control requirements for urban neighborhood construction to manage the height, density, and intensity of different functional neighborhoods and prevent disorderly building development. Second, promoting third spaces can facilitate multifunctional urban development and enhance the city's walkability [50], thereby reducing carbon emissions from residents' daily commutes. Third, protecting the urban ecosystem, increasing the proportion of green open spaces, and upgrading the greening of streets and squares can alleviate the urban heat island effect and reduce energy consumption for ventilation and cooling. Fourth, through vertical greening and green roofs, we can reduce solar radiation in summer and increase energy utilization efficiency in winter, which is conducive to decreasing CO_2 emissions from vertically high-density cities.

5. Conclusions

Recently, many studies have focused on the influence of urban forms on CO_2 emissions. However, due to the unavailability of large-scale data on urban buildings, scholars have mainly examined the impact of 2D urban forms on CO_2 emissions, while the causal and heterogeneous influences of 3D urban forms on CO_2 emissions have been significantly

underexplored. This paper aims to address this gap by examining the causal and heterogeneous influence of 3D urban forms on CO_2 emissions. Firstly, based on the 2022 global built-up area dataset, we constructed metrics for measuring the 3D urban forms of 285 Chinese cities. Furthermore, the causal influence of 3D urban forms on CO_2 emissions was validated through an econometric model and instrumental variable (IV) approach. The empirical results show that cities with greater height, density, and intensity are likely to have higher carbon emissions. Moreover, we find that the influence of 3D urban forms on CO_2 emissions remains positive even when considering the spatial spillover effect of neighboring cities. The influence of 3D urban forms on CO_2 emissions is U-shaped, and total population plays a moderating role in this relationship. The estimated results of instrumental variable regression further demonstrate a causal influence of 3D urban forms on CO_2 emissions. Besides this, the heterogeneity analysis shows significant geographic and sectoral differences in the influence of 3D urban forms on CO_2 emissions. Specifically, the influence of 3D urban forms is greater in eastern cities than in non-eastern cities. Furthermore, the influence of 3D urban forms on household carbon emissions is positive and statistically significant, while their influence on industrial and transportation carbon emissions is not significant. The empirical results remain robust even when excluding certain special samples. Overall, the empirical findings provide robust evidence that 3D urban forms exert a positive and causal influence on CO_2 emissions.

Our study has limitations that provide opportunities for future research. For instance, we used only three metrics—height, density, and intensity—to synthesize 3D urban forms. Future studies can establish a more comprehensive system of indicators for measuring 3D urban forms as large-scale building data become more available. Additionally, although this paper combines existing studies to theoretically elucidate the possible pathways through which 3D urban forms affect carbon emissions, subsequent studies should empirically test these pathways through methods such as structural equation modeling. Thirdly, since our study focuses on the overall urban scale, future studies can target individual cities and draw on the methodology of related studies [51] to predict the CO_2 emission pattern based on 3D urban forms. Fourthly, cities in different regions of China have varying climatic conditions, which may affect the relationship between 3D urban forms and CO_2 emissions from different sectors. Further research on this hypothesis is needed.

Author Contributions: Conceptualization, Weiting Xiong and Jingang Li; methodology, Jingang Li and Weiting Xiong; software, Yedong Zhang; validation, Weiting Xiong; formal analysis, Weiting Xiong and Jingang Li; resources, Jingang Li; data curation, Jingang Li; writing—original draft preparation, Yedong Zhang and Weiting Xiong; writing—review and editing, Weiting Xiong and Yedong Zhang; visualization, Jingang Li; supervision, Weiting Xiong and Jingang Li. All authors have read and agreed to the published version of the manuscript.

Funding: This research was funded by National Natural Science Foundation of China, grant number 52208063; Natural Science Foundation of Jiangsu Province, China, grant number BK20220424; The General Project of Basic Science (Natural Science) Research in universities of Jiangsu Province (Grant No. 22KJB560025) and The General Project of Philosophy and Social Science Research in Colleges and Universities in Jiangsu Province (Grant No. 2021SJA0143).

Data Availability Statement: The data used in this study are reasonably available through the corresponding author.

Conflicts of Interest: The authors declare no conflicts of interest.

References

1. Root, T.L.; Price, J.T.; Hall, K.R.; Schneider, S.H.; Rosenzweig, C.; Pounds, J.A. Fingerprints of Global Warming on Wild Animals and Plants. *Nature* **2003**, *421*, 57–60. [CrossRef] [PubMed]
2. Intergovernmental Panel on Climate Change. *Climate Change 2021: The Physical Science Basis. Contribution of Working Group I to the Sixth Assessment Report of the Intergovernmental Panel on Climate Change*; Cambridge University Press: Cambridge, UK, 2021.
3. Meinshausen, M.; Meinshausen, N.; Hare, W.; Raper, S.C.; Frieler, K.; Knutti, R.; Frame, D.J.; Allen, M.R. Greenhouse-Gas Emission Targets for Limiting Global Warming to 2 °C. *Nature* **2009**, *458*, 1158–1162. [CrossRef] [PubMed]

4. International Energy Agency. *CO_2 Emissions in 2023*; IEA: Paris, France, 2024.
5. Soytas, U.; Sari, R. Energy Consumption, Economic Growth, and Carbon Emissions: Challenges Faced by an EU Candidate Member. *Ecol. Econ.* **2009**, *68*, 1667–1675. [CrossRef]
6. Wang, S.; Liu, X.; Zhou, C.; Hu, J.; Ou, J. Examining the Impacts of Socioeconomic Factors, Urban Form, and Transportation Networks on CO_2 Emissions in China's Megacities. *Appl. Energy* **2017**, *185*, 189–200. [CrossRef]
7. Dong, B.; Ma, X.; Zhang, Z.; Zhang, H.; Chen, R.; Song, Y.; Shen, M.; Xiang, R. Carbon Emissions, the Industrial Structure and Economic Growth: Evidence from Heterogeneous Industries in China. *Environ. Pollut.* **2020**, *262*, 114322. [CrossRef]
8. Li, Y. Path-Breaking Industrial Development Reduces Carbon Emissions: Evidence from Chinese Provinces, 1999–2011. *Energy Policy* **2022**, *167*, 113046. [CrossRef]
9. Zhang, F.; Deng, X.; Phillips, F.; Fang, C.; Wang, C. Impacts of Industrial Structure and Technical Progress on Carbon Emission Intensity: Evidence from 281 Cities in China. *Technol. Forecast. Soc. Chang.* **2020**, *154*, 119949. [CrossRef]
10. Xie, Z.; Wu, R.; Wang, S. How Technological Progress Affects the Carbon Emission Efficiency? Evidence from National Panel Quantile Regression. *J. Clean. Prod.* **2021**, *307*, 127133. [CrossRef]
11. Luqman, M.; Rayner, P.J.; Gurney, K.R. On the Impact of Urbanisation on CO_2 Emissions. *NPJ Urban Sustain.* **2023**, *3*, 6. [CrossRef]
12. Pu, Y.; Wang, Y.; Wang, P. Driving Effects of Urbanization on City-Level Carbon Dioxide Emissions: From Multiple Perspectives of Urbanization. *Int. J. Urban Sci.* **2022**, *26*, 108–128. [CrossRef]
13. Seto, K.C.; Dhakal, S.; Bigio, A.; Blanco, H.; Carlo Delgado, G.; Dewar, D.; Huang, A.; Inaba, A.; Kansal, S.; Zwickel, T.; et al. *Human Settlements, Infrastructure, and Spatial Planning*; Cambridge University Press: Cambridge, UK, 2014.
14. Seto, K.C.; Güneralp, B.; Hutyra, L.R. Global Forecasts of Urban Expansion to 2030 and Direct Impacts on Biodiversity and Carbon Pools. *Proc. Natl. Acad. Sci. USA* **2012**, *109*, 16083–16088. [CrossRef] [PubMed]
15. Sun, C.; Zhang, Y.; Ma, W.; Wu, R.; Wang, S. The Impacts of Urban Form on Carbon Emissions: A Comprehensive Review. *Land* **2022**, *11*, 1430. [CrossRef]
16. Xu, Q.; Yang, R.; Dong, Y.X.; Liu, Y.X.; Qiu, L.R. The Influence of Rapid Urbanization and Land Use Changes on Terrestrial Carbon Sources/Sinks in Guangzhou, China. *Ecol. Indic.* **2016**, *70*, 304–316. [CrossRef]
17. Yang, B.; Chen, X.; Wang, Z.; Li, W.; Zhang, C.; Yao, X. Analyzing Land Use Structure Efficiency with Carbon Emissions: A Case Study in the Middle Reaches of the Yangtze River, China. *J. Clean. Prod.* **2020**, *274*, 123076. [CrossRef]
18. Lee, S.; Lee, B. The Influence of Urban Form on GHG Emissions in the U.S. Household Sector. *Energy Policy* **2014**, *68*, 534–549. [CrossRef]
19. Liu, Y.; Gao, C.; Lu, Y. The Impact of Urbanization on GHG Emissions in China: The Role of Population Density. *J. Clean. Prod.* **2017**, *157*, 299–309. [CrossRef]
20. Li, Q.; Chen, X.; Jiao, S.; Song, W.; Zong, W.; Niu, Y. Can Mixed Land Use Reduce CO_2 Emissions? A Case Study of 268 Chinese Cities. *Sustainability* **2022**, *14*, 15117. [CrossRef]
21. Xu, C.; Haase, D.; Su, M.; Yang, Z. The Impact of Urban Compactness on Energy-Related Greenhouse Gas Emissions across EU Member States: Population Density vs. Physical Compactness. *Appl. Energy* **2019**, *254*, 113671. [CrossRef]
22. Shi, K.; Liu, G.; Cui, Y.; Wu, Y. What Urban Spatial Structure Is More Conducive to Reducing Carbon Emissions? A Conditional Effect of Population Size. *Appl. Geogr.* **2023**, *151*, 102855. [CrossRef]
23. Li, Y.; Liu, X. How Did Urban Polycentricity and Dispersion Affect Economic Productivity? A Case Study of 306 Chinese Cities. *Landsc. Urban Plan.* **2018**, *173*, 51–59. [CrossRef]
24. Sha, W.; Chen, Y.; Wu, J.; Wang, Z. Will Polycentric Cities Cause More CO_2 Emissions? A Case Study of 232 Chinese Cities. *J. Environ. Sci.* **2020**, *96*, 33–43. [CrossRef] [PubMed]
25. Zhu, K.; Tu, M.; Li, Y. Did Polycentric and Compact Structure Reduce Carbon Emissions? A Spatial Panel Data Analysis of 286 Chinese Cities from 2002 to 2019. *Land* **2022**, *11*, 185. [CrossRef]
26. Wang, S.; Wang, J.; Fang, C.; Li, S. Estimating the Impacts of Urban Form on CO_2 Emission Efficiency in the Pearl River Delta, China. *Cities* **2019**, *85*, 117–129. [CrossRef]
27. Harris, A. Vertical Urbanisms: Opening Up Geographies of the Three-Dimensional City. *Prog. Hum. Geogr.* **2015**, *39*, 601–620. [CrossRef]
28. Zhong, X.; Hu, M.; Deetman, S.; Steubing, B.; Lin, H.X.; Hernandez, G.A.; Zhang, C.; Tukker, A.; Behrens, P. Global Greenhouse Gas Emissions from Residential and Commercial Building Materials and Mitigation Strategies to 2060. *Nat. Commun.* **2021**, *12*, 6126. [CrossRef] [PubMed]
29. Röck, M.; Saade, M.R.M.; Balouktsi, M.; Rasmussen, F.N.; Birgisdottir, H.; Frischknecht, R.; Habert, G.; Lützkendorf, T.; Passer, A. Embodied GHG Emissions of Buildings-The Hidden Challenge for Effective Climate Change Mitigation. *Appl. Energy* **2020**, *258*, 114107. [CrossRef]
30. Perini, K.; Magliocco, A. Effects of Vegetation, Urban Density, Building Height, and Atmospheric Conditions on Local Temperatures and Thermal Comfort. *Urban For. Urban Green.* **2014**, *13*, 495–506. [CrossRef]
31. Coseo, P.; Larsen, L. How Factors of Land Use/Land Cover, Building Configuration, and Adjacent Heat Sources and Sinks Explain Urban Heat Islands in Chicago. *Landsc. Urban Plan.* **2014**, *125*, 117–129. [CrossRef]
32. Yu, C.; Pan, W. Inter-Building Effect on Building Energy Consumption in High-Density City Contexts. *Energy Build.* **2023**, *278*, 112632. [CrossRef]

33. Cao, Q.; Luan, Q.; Liu, Y.; Wang, R. The Effects of 2D and 3D Building Morphology on Urban Environments: A Multi-Scale Analysis in the Beijing Metropolitan Region. *Build. Environ.* **2021**, *192*, 107635. [CrossRef]
34. Camporeale, P.E.; Mercader-Moyano, P. Towards Nearly Zero Energy Buildings: Shape Optimization of Typical Housing Typologies in Ibero-American Temperate Climate Cities from a Holistic Perspective. *Sol. Energy* **2019**, *193*, 738–765. [CrossRef]
35. Xu, X.; Ou, J.; Liu, P.; Liu, X.; Zhang, H. Investigating the Impacts of Three-Dimensional Spatial Structures on CO_2 Emissions at the Urban Scale. *Sci. Total Environ.* **2021**, *762*, 143096. [CrossRef] [PubMed]
36. Du, S.; Zhang, Y.; Sun, W.; Liu, B. Quantifying Heterogeneous Impacts of 2D/3D Built Environment on Carbon Emissions across Urban Functional Zones: A Case Study in Beijing, China. *Energy Build.* **2024**, *319*, 114513. [CrossRef]
37. Lin, J.; Lu, S.; He, X.; Wang, F. Analyzing the Impact of Three-Dimensional Building Structure on CO_2 Emissions Based on Random Forest Regression. *Energy* **2021**, *236*, 121502. [CrossRef]
38. Cai, B.; Cui, C.; Zhang, D.; Cao, L.; Wu, P.; Pang, L.; Zhang, J.; Dai, C. China City-Level Greenhouse Gas Emissions Inventory in 2015 and Uncertainty Analysis. *Appl. Energy* **2019**, *253*, 113579. [CrossRef]
39. Cai, B.; Liu, H.; Zhang, X.; Pan, H.; Zhao, M.; Zheng, T.; Nie, J.; Du, M.; Dhakal, S. High-Resolution Accounting of Urban Emissions in China. *Appl. Energy* **2022**, *325*, 119896. [CrossRef]
40. Pesaresi, M.; Politis, P. *GHS-BUILT-H R2023A—GHS Building Height, Derived from AW3D30, SRTM30, and Sentinel2 Composite (2018)*; European Commission, Joint Research Centre (JRC): Brussels, Belgium, 2023.
41. Pesaresi, M.; Politis, P. *GHS-BUILT-S R2023A—GHS Built-Up Surface Grid, Derived from Sentinel2 Composite and Landsat, Multitemporal (1975–2030)*; European Commission, Joint Research Centre (JRC): Brussels, Belgium, 2023.
42. Pesaresi, M.; Politis, P. *GHS-BUILT-V R2023A—GHS Built-Up Volume Grids Derived from Joint Assessment of Sentinel2, Landsat, and Global DEM Data, Multitemporal (1975–2030)*; European Commission, Joint Research Centre (JRC): Brussels, Belgium, 2023.
43. Yi, Y.; Wang, Y.; Li, Y.; Qi, J. Impact of Urban Density on Carbon Emissions in China. *Appl. Econ.* **2021**, *53*, 6153–6165. [CrossRef]
44. López, R.; Palacios, A. Why Has Europe Become Environmentally Cleaner? Decomposing the Roles of Fiscal, Trade and Environmental Policies. *Environ. Resour. Econ.* **2014**, *58*, 91–108. [CrossRef]
45. Li, Y.; Du, R. Polycentric Urban Structure and Innovation: Evidence from a Panel of Chinese Cities. *Reg. Stud.* **2022**, *56*, 113–127. [CrossRef]
46. Combes, P.P.; Démurger, S.; Li, S. Migration Externalities in Chinese Cities. *Eur. Econ. Rev.* **2015**, *76*, 152–167. [CrossRef]
47. Borck, R. Will Skyscrapers Save the Planet? Building Height Limits and Urban Greenhouse Gas Emissions. *Reg. Sci. Urban Econ.* **2016**, *58*, 13–25. [CrossRef]
48. Yu, S.; Hu, S.; Ren, Y.; Xu, H.; Song, W. Leverage Effect of New-Built Green Spaces on Housing Prices in a Rapidly Urbanizing Chinese City: Regional Disparities, Impact Periodicity, and Park Size. *Land* **2024**, *13*, 1663. [CrossRef]
49. Miao, L. Examining the Impact Factors of Urban Residential Energy Consumption and CO_2 Emissions in China-Evidence from City-Level Data. *Ecol. Indic.* **2017**, *73*, 29–37. [CrossRef]
50. Li, J.; Li, Y.; Tu, M.; Liu, X. Third Places as Catalysts for Technological Innovation? Evidence from a Grid Cell Level Analysis of Nanjing, China. *Int. J. Urban Sci.* **2024**, *28*, 105–123. [CrossRef]
51. Hu, X.; Zhu, W.; Shen, X.; Bai, R.; Shi, Y.; Li, C.; Zhao, L. Exploring the Predictive Ability of the CA–Markov Model for Urban Functional Area in Nanjing Old City. *Sci. Rep.* **2024**, *14*, 18453. [CrossRef]

Disclaimer/Publisher's Note: The statements, opinions and data contained in all publications are solely those of the individual author(s) and contributor(s) and not of MDPI and/or the editor(s). MDPI and/or the editor(s) disclaim responsibility for any injury to people or property resulting from any ideas, methods, instructions or products referred to in the content.

sustainability

MDPI

Article

Integrating Remote Sensing and Community Perceptions for Sustainable Climate Adaptation Strategies in Mountain Ecosystems

Ankita Pokhrel [1], Ping Fang [1,2,*] and Gaurav Bastola [3]

[1] United Nations Environment Program, Institute of Environment for Sustainable Development, College of Environment Science and Engineering, Tongji University, Shanghai 200070, China; ankita.pokhrel98@gmail.com
[2] Key Laboratory of Agro-Environment in Midstream of Yangtze Plain, Ministry of Agriculture and Rural Affairs, Hunan Academy of Agricultural Sciences, Institute of Agricultural Environment and Ecology of Hunan Province, Changsha 410125, China
[3] College of Civil Engineering, Tongji University, Shanghai 200070, China; gauravbastola@tongji.edu.cn
* Correspondence: fangping2000@tongji.edu.cn

Abstract: Mountain ecosystems, such as Nepal's Annapurna Conservation Area (ACA), are highly vulnerable to climate change, which threatens biodiversity, water resources, and livelihoods. This study examines Land Use Land Cover (LULC) changes, Normalized Difference Vegetation Index (NDVI) and Normalized Difference Snow Index (NDSI), climate variability, and community perception and adaptations over a 35-year period (1988–2023) using remote sensing, meteorological data, and community surveys. Vegetation expanded by 19,800 hectares, while barren land declined, reflecting afforestation and land reclamation efforts. NDVI showed improved vegetation health, while NDSI revealed significant snow cover losses, particularly after 1996. Meteorological analysis highlighted intensifying monsoonal rainfall and rising extreme precipitation events at lower elevations. Communities reported increased flooding, unpredictable rainfall, and reduced snowfall, driving adaptive responses such as water conservation, crop diversification, and rainwater harvesting. These findings demonstrate the value of integrating scientific data with local knowledge to inform sustainable adaptation strategies. Contributing to Sustainable Development Goals (SDGs) 6 and 13, the findings emphasize the importance of adaptive water management, resilient agriculture, and participatory conservation to enhance climate resilience in mountain ecosystems.

Keywords: climate adaptation; sustainable development; mountain ecosystem; community perceptions; Annapurna Conservation Area

1. Introduction

1.1. Background

Climate change is profoundly affecting ecosystems globally, with mountain ecosystems being particularly vulnerable due to their unique climatic and ecological characteristics. The impacts of climate change on mountain ecosystems manifest through various mechanisms, including alterations in temperature, precipitation patterns, and the dynamics of glacial and permafrost environments. These ecosystems occupy small environmental niches at higher elevations, making them particularly sensitive to climatic changes, which can lead to the loss of biodiversity and habitat [1,2]. Mountains, often referred to as the planet's "water towers", supply freshwater to billions of people and host rich biodiversity. The Annapurna

Conservation Area (ACA) in Nepal exemplifies this importance, spanning from subtropical lowlands to high-altitude alpine regions [3–6]. Such ecological and elevational diversity makes ACA an ideal setting to examine climate change impacts and develop sustainable adaptation strategies.

1.2. Literature Review

Over the past decade, numerous studies have explored climate adaptation strategies across various ecosystems, employing diverse methods to understand environmental changes [7–12]. Among these methods, remote sensing technologies have proven highly effective, offering detailed insights into Land Use/Land Cover (LULC) transformations and other key indicators of climate resilience [13–17]. Geospatial analyses, for example, have facilitated the tracking of deforestation, land degradation, and hydrological shifts in mountain regions, shedding light on spatial patterns of change [18–21]. Complementing these spatial assessments, time-series climate trend analyses using meteorological records have helped identify long-term shifts in temperature and precipitation regimes, revealing emerging anomalies and guiding adaptation efforts [14,22].

In addition to environmental indicators, recent research highlights the importance of local ecological knowledge and community perspectives [23]. Incorporating social dimensions into climate studies provides an understanding of how climatic changes are experienced, interpreted, and addressed at the grassroots level, thereby enriching the quantitative data derived from remote sensing and climate trend analyses [24,25]. Mountainous regions, including the ACA in Nepal, illustrate this complexity. Here, climatic changes influence biodiversity, including endangered species such as the snow leopard and red panda, and affect the livelihoods of communities who have long adapted to diverse environmental conditions [6].

While previous research in the ACA and similar mountainous ecosystems has generated valuable information—ranging from spatial LULC patterns to meteorological trends and community insights—many studies have focused primarily on one dimension of climate change [25–28]. This has left opportunities for more integrated approaches that combine these strands of knowledge. By drawing together remote sensing, long-term climate trend assessments, and local perceptions, there is the potential to form a more comprehensive understanding of climate resilience in vulnerable mountain ecosystems.

This study builds on existing foundations and advances the literature by integrating these three critical elements. Rather than addressing climate variability, LULC changes, or community perspectives independently, it synthesizes them into a single analytical framework. This integrated perspective not only enhances our understanding of climate resilience in the ACA but also provides policy-relevant insights that can guide sustainable resource management and conservation strategies in similar mountain regions worldwide.

1.3. Objective

This study adopts a socio-ecological systems framework to investigate the interplay between climatic changes, ecosystem dynamics, and community adaptive strategies in the ACA. By integrating remote sensing, climate time-series data, and community perceptions, this research provides a comprehensive understanding of climate resilience in mountain ecosystems over a 35-year period (1988–2023).

The study aims to detect patterns of LULC changes by analyzing shifts in vegetation, snow cover, barren land, and water bodies using high-resolution satellite imagery, enhanced through topographical correction to account for the complex mountainous terrain. Environmental changes are further assessed through vegetation health and snow cover trends using the Normalized Difference Vegetation Index (NDVI) and Normalized

Difference Snow Index (NDSI). To analyze climate variability, long-term temperature and precipitation trends are examined using meteorological data. Additionally, this study gathers community insights to understand local perceptions of climate change impacts and the adaptive strategies employed by residents.

As shown in Figure 1, the study integrates three critical components—remote sensing, climate time series, and community perspectives—to conduct a synthesis of environmental, climatic, and socio-cultural data. This integrated analysis contributes to a holistic understanding of climate resilience, informing evidence-based resource management and policy interventions. By aligning with the SDGs, particularly SDG 6 (Clean Water and Sanitation) and SDG 13 (Climate Action), the findings offer actionable insights for sustainable adaptation strategies in vulnerable mountain regions.

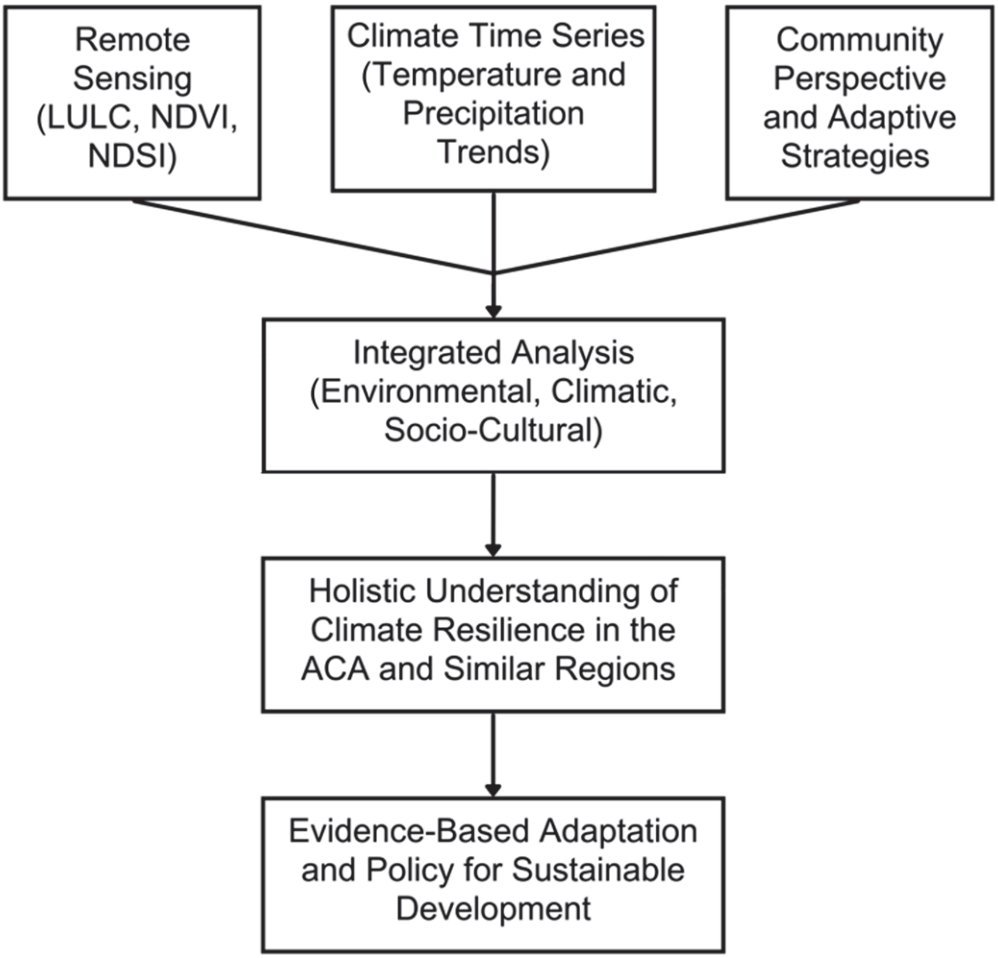

Figure 1. Conceptual theoretical framework of the study.

2. Materials and Methods

2.1. Study Area

ACA is located in central Nepal, stretching from 28°13′ N to 29°19′ N latitude and 83°29′ E to 84°53′ E longitude (Figure 2). Encompassing an area of 7629 square kilometers, the ACA exhibits a diverse range of ecosystems, from subtropical lowlands at elevations of about 1000 m to alpine regions exceeding 8000 m [6]. The region is characterized by significant climatic variation and supports a wide array of flora and fauna, including several endangered species. Figure 2 illustrates the geographical extent of the ACA, highlighting selected villages that represent the diverse ecological and climatic conditions within the study region.

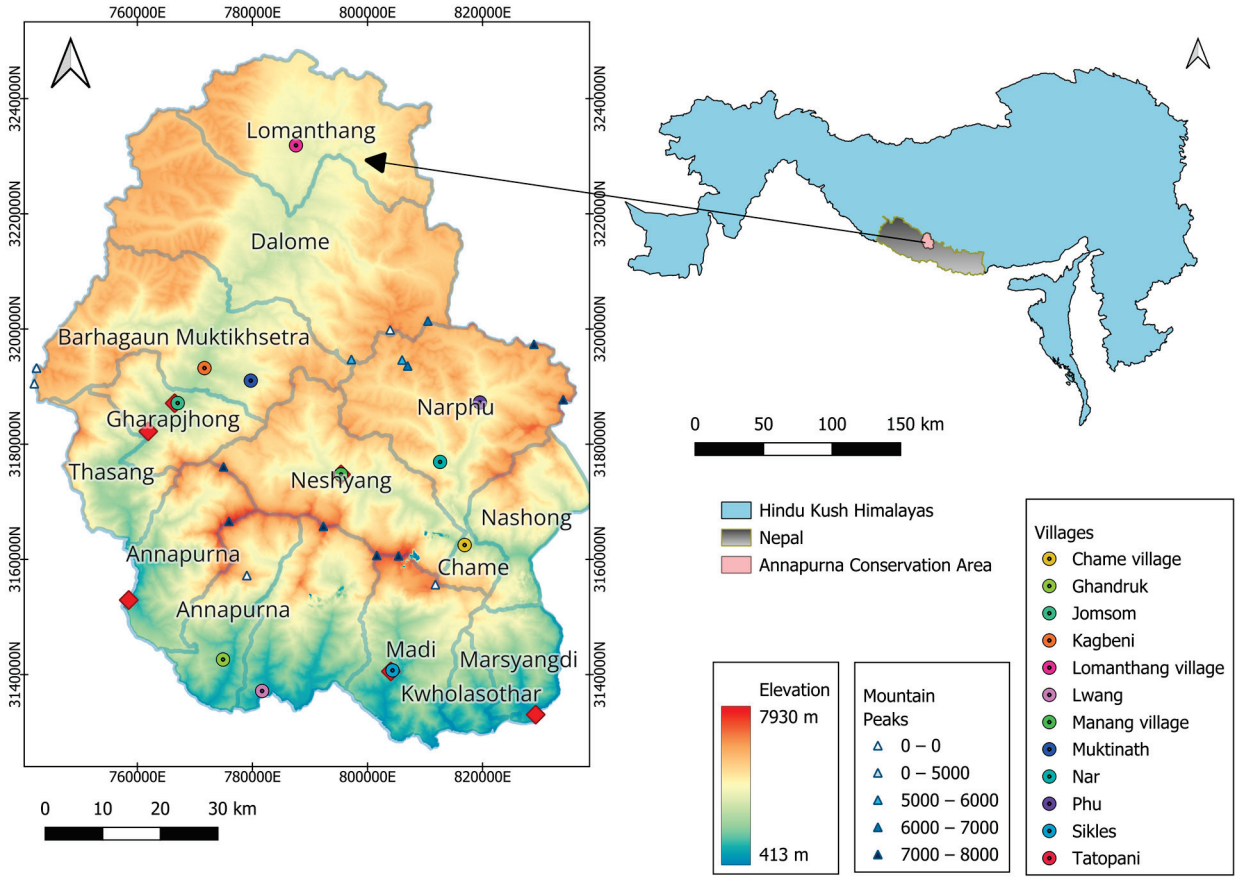

Figure 2. Map of the study area showing the Annapurna Conservation Area and selected villages.

2.2. Data Collection

2.2.1. Remote Sensing and GIS Analysis

Satellite Imagery Acquisition: Landsat satellite imagery from 1988 to 2023 was utilized to detect LULC changes in the ACA. Landsat Collection 2 Level 2 images were acquired from the United States Geological Survey (USGS) Earth Resources Observation and Science (EROS) Center Science Processing Architecture (ESPA) on-demand interface, which provides data preprocessed for atmospheric correction using the Landsat Ecosystem Disturbance Adaptive Processing System (LEDAPS) algorithm.

Table 1 outlines the key specifications of the Landsat satellite imagery utilized for this study, including acquisition dates, sensor types, and cloud cover. To ensure consistency, images were selected from the winter dry season months of November and December, minimizing the effects of cloud cover and seasonal vegetation changes.

Table 1. Landsat satellite imagery used in the study.

Date	Satellite/Sensor	Scene (Path/Row)	Sun Azimuth (°)	Sun Elevation	Cloud Coverage
20 November 1988	Landsat 5 TM	142/40	149.43	35.21	2%
12 December 1996	Landsat 5 TM	142/40	147.51	30.46	4%
27 December 2013	Landsat 8 OLI	142/40	155.30	33.57	1%
21 November 2023	Landsat 8 OLI	142/40	157.42	38.02	2%

2.2.2. Meteorological Data

Temperature and precipitation data were obtained from the Department of Hydrology and Meteorology (DHM) of Nepal for six meteorological stations within the ACA (Table 2).

Data spanning from 1983 to 2023 were collected, allowing for a comprehensive analysis of climatic trends.

Table 2. Meteorological stations and available data.

Station Index	Name	District	Latitude	Longitude	Elevation	Type of Station
0601	Jomsom	Mustang	28.7840111	83.7298167	2741	Temperature/Precipitation
0604	Thakmarpha	Mustang	28.740909	83.681614	2655	Temperature/Precipitation
0802	Khudi Bazar	Lamjung	28.28220833	84.35640278	838	Temperature/Precipitation
0820	Manang Bhot	Manang	28.66627083	84.02257194	3556	Precipitation
0824	Sikles	Kaski	28.355852	84.102068	1967	Precipitation
0606	Tatopani	Myagdi	28.477492	83.6404158	1161	Precipitation

2.2.3. Community Surveys

Structured interviews were conducted with residents from 11 villages within the ACA to understand local perceptions of climate change and adaptive strategies. A total of 110 respondents were surveyed, representing diverse demographics and occupations. The villages were selected to include a wide range of ecosystem and climatic conditions within the ACA region.

The survey questionnaire included sections on the following:

- Observed climatic changes (temperature, precipitation, snowfall);
- Impacts on water resources and agriculture;
- Adaptive measures undertaken by the community;
- Awareness of government policies and support mechanisms.

2.3. Data Analysis

2.3.1. LULC Change Analysis

Topographic correction: Given the mountainous terrain of the ACA, topographic effects were minimized using the Sun-Canopy-Sensor plus C (SCS+C) correction method [29]. This method accounts for the influence of terrain on illumination conditions, improving the accuracy of subsequent analyses [30]. Equation (1) shows the SCS+C correction formula used to mitigate topographic influence and enhance the accuracy of reflectance in the Landsat images.

$$L_n = L\frac{\cos\alpha\cos\theta + C}{\cos i + C} \quad (1)$$

The method utilizes the solar zenith angle (θ), the terrain's slope (α), and the solar incidence angle (i) to normalize the reflectance values (L_n) from the uncorrected reflectance (L).

Land cover classification: Next, we employed a multi-class classification approach using a suite of supervised image classification algorithms within the SAGA GIS environment to the acquired Landsat images [31]. We used the Winner Takes All (WTA) method, which integrates the outputs of multiple classification algorithms. The WTA method assigns each pixel to the class with the highest confidence or probability score across all selected classifiers, ensuring a robust and accurate final classification. Specifically, we tested these classifiers within the WTA framework, including Binary Encoding, Parallelepiped, Minimum Distance, Mahalanobis Distance, Maximum Likelihood, and Spectral Angle Mapping. Each algorithm computes class membership differently, ranging from simple geometric thresholds (e.g., Parallelepiped) to probabilistic approaches (e.g., Maximum Likelihood) and spectral similarity measures (e.g., Spectral Angle Mapping), thereby providing a comprehensive set of classification outcomes.

Our final LULC scheme included four primary classes—Barren Land, Snow, Vegetation, and Water—selected based on their prevalence, ecological importance, and distinct

spectral signatures in the study area. To ensure robust and unbiased results, the classification process was guided by a training dataset derived from a combination of in situ field observations, existing high-resolution imagery, and ancillary GIS datasets. Representative training samples were carefully selected to capture the spectral variability within each class, and these samples were divided into training and validation subsets.

Supervised classification was performed using the Maximum Likelihood algorithm. Training samples were selected for four major LULC classes: Vegetation, Snow Cover, Barren Land, and Water Bodies. Classification accuracy was assessed using confusion matrices and overall accuracy metrics.

2.3.2. NDVI and NDSI Analysis

Spatial and temporal variations in NDVI and NDSI were assessed. Mean, maximum, and minimum values were calculated for each year. NDVI and NDSI were calculated to assess changes in vegetation health and snow cover, respectively, using Equations (2) and (3), where B represents the band number:

For Landsat 5 TM,

$$\text{NDVI} = \frac{(\text{B4} - \text{B3})}{(\text{B4} + \text{B3})} \text{ and NDSI} = \frac{(\text{B2} - \text{B5})}{(\text{B2} + \text{B5})} \tag{2}$$

For Landsat 8 OLI,

$$\text{NDVI} = \frac{(\text{B5} - \text{B4})}{(\text{B5} + \text{B4})} \text{ and NDSI} = \frac{(\text{B3} - \text{B6})}{(\text{B3} + \text{B6})} \tag{3}$$

2.3.3. Climate Data Analysis

Temperature and precipitation trends were analyzed using the Mann–Kendall trend tests (Equation (4)) [32,33] and Sen-Slope Estimators [34]. Anomalies and deviations from long-term averages were identified to assess climate variability and trends. Seasonal and annual variations were also examined to understand the impact on water resources and ecosystems.

$$\begin{gathered} S = \sum_{i=1}^{n-1} \sum_{j=i+1}^{n} \operatorname{sgn}(x_j - x_i) \\ \text{where} \\ \operatorname{sgn}(x_j - x_i) = \begin{cases} +1 & \text{if} (x_j - x_i) > 0 \\ 0 & \text{if} (x_j - x_i) = 0 \\ -1 & \text{if} (x_j - x_i) < 0 \end{cases} \end{gathered} \tag{4}$$

2.3.4. Community Survey Analysis

Survey responses were coded and entered into a database for quantitative analysis. Descriptive statistics were used to summarize the data. Qualitative responses were analyzed thematically to identify common perceptions and adaptive strategies.

2.4. Ethical Considerations

Informed consent was sought from all participants, ensuring confidentiality and adherence to ethical guidelines for research involving human subjects. The study was conducted following all applicable guidelines and with the approval of the Department of National Parks and Wildlife Conservation (DNPWC) and Annapurna Conservation Area Project (ACAP), ensuring that the study's design and execution complied with national conservation laws and respected the ecological and cultural integrity of the area.

3. Results

3.1. LULC Changes

The supervised classification of Landsat images for the years 1988, 1996, 2013, and 2023 revealed significant changes in the distribution of land cover classes as shown in Figure 3. Table 3 provides a quantitative analysis of changes in LULC classes over the study period, revealing key trends such as the expansion of vegetation cover and reductions in barren land.

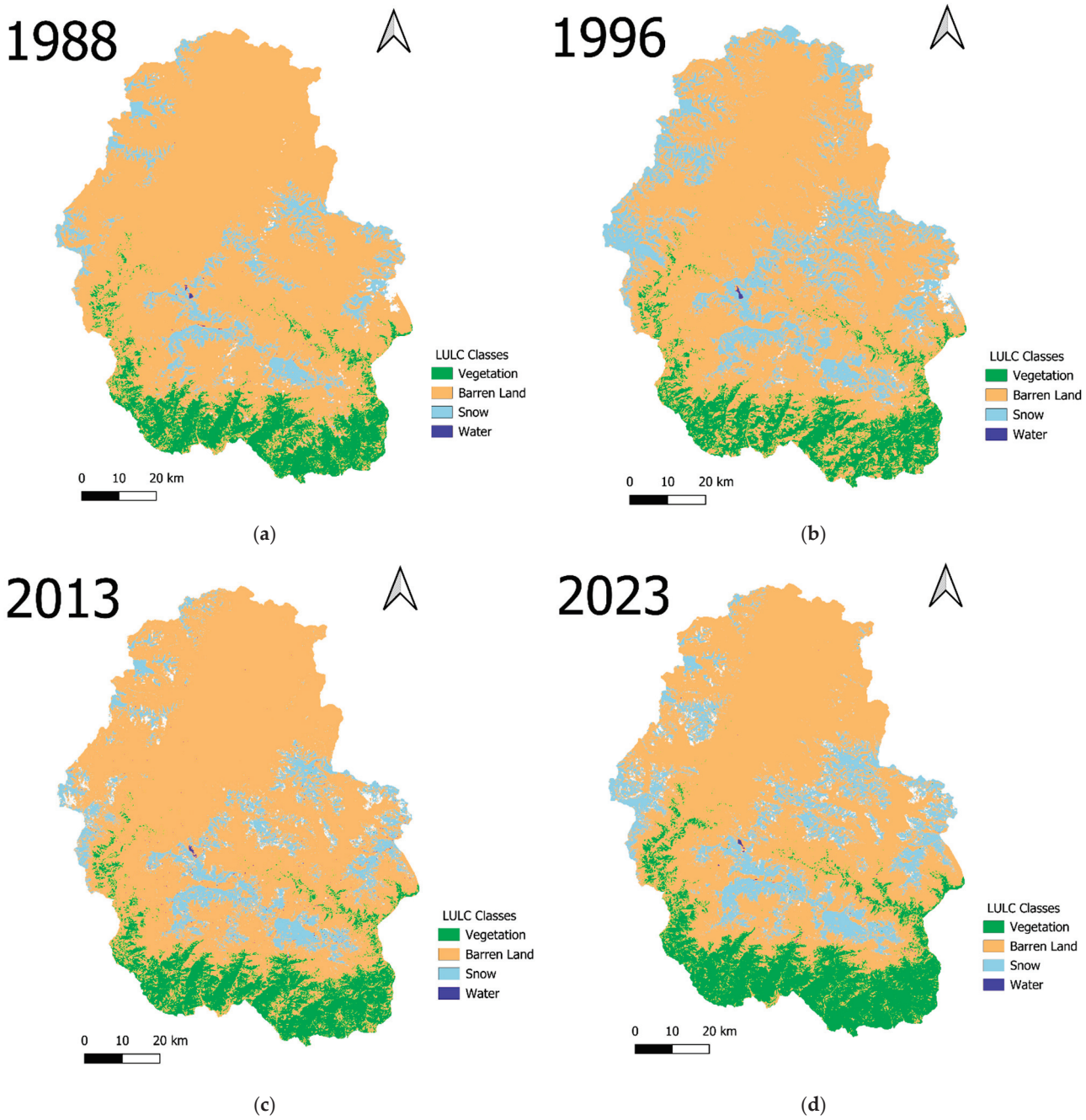

Figure 3. LULC classification maps of the ACA for the years (**a**) 1988, (**b**) 1996, (**c**) 2013, and (**d**) 2023.

From 1988 to 2023, notable changes were observed across all land cover classes in the Annapurna region. Vegetation cover expanded significantly from 57,858.84 ha in 1988 to 77,634.27 ha in 2023, reflecting conservation efforts, afforestation programs, and the effects of climate-induced shifts in vegetation zones. Snow cover exhibited variability,

peaking at 95,991.75 ha in 1996 but declining to 80,323.38 ha in 2023, indicating the impact of reduced snowfall and temperature increases. Barren land decreased consistently over the study period, from 389,018.9 ha in 1988 to 331,252.8 ha in 2023, driven by afforestation and land restoration efforts. Water bodies, while showing some fluctuations, remained relatively stable, increasing slightly from 207.72 ha in 1988 to 222.93 ha in 2023. These trends illustrate the interplay of conservation initiatives, climatic changes, and land use dynamics in shaping the region's landscape.

Table 3. Area (in hectares) of different land cover classes from 1988 to 2023.

Year	Class	Name	Area (ha)
1988	1	Vegetation	57,858.84
	2	Snow	49,583.25
	3	Barren	389,018.9
	4	Water	207.72
1996	1	Vegetation	54,111.6
	2	Barren	346,648.9
	3	Snow	95,991.75
	4	Water	177.21
2013	1	Vegetation	57,501.27
	2	Barren	369,110.8
	3	Snow	62,364.6
	4	Water	473.94
2023	1	Vegetation	77,634.27
	2	Snow	80,323.38
	3	Barren	331,252.8
	4	Water	222.93

3.2. Vegetation Health and Snow Cover Trends

NDVI values increased significantly, with the highest values observed in 2023 (up to +0.98) compared to the lowest in 1988 (up to +0.46) as shown in Table 4. Areas with high NDVI values expanded over time.

Table 4. NDVI and NDSI statistics from 1988 to 2023.

Years	NDVI Min.	NDVI Max.	NDVI Avg.	NDSI Min.	NDSI Max.	NDSI Avg.
1988	−0.324	0.461	0.069	−0.451	0.765	0.157
1996	−0.270	0.440	0.085	−0.440	0.791	0.176
2013	−0.331	0.989	0.329	−0.996	0.808	−0.094
2023	−0.304	0.983	0.340	−0.995	0.776	−0.109

For NDSI, the values in 2023 and 2013 averaged −0.109 and −0.094, respectively, suggesting a lower range of snow cover. The earlier years, 1996 and 1988, showed average values of 0.176 and 0.157, respectively, more than that of later years. For details, check Appendix A. Table 4 presents the minimum, maximum, and average NDVI and NDSI values.

3.3. Climate Variability Analysis

Temperature data from the meteorological stations were analyzed to identify trends in Tmax and Tmin temperatures. Figure 4 visualizes the annual mean Tmax and Tmin temperatures from 1983 to 2023, capturing long-term climatic trends and variability across the ACA.

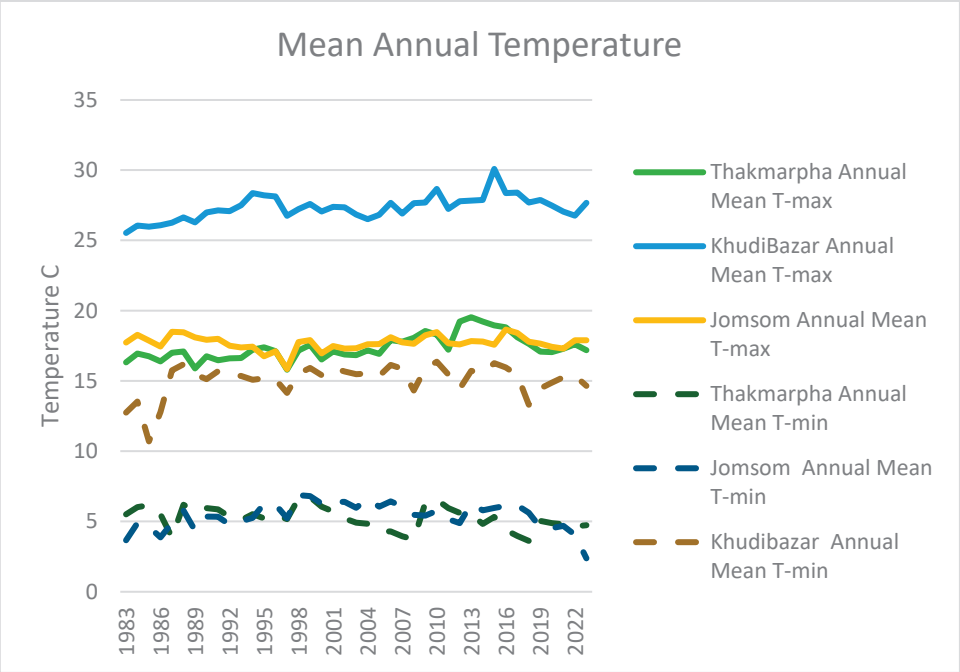

Figure 4. Annual mean Tmax and Tmin for Thakmarpha, Jomsom, and Khudi Bazar.

- Warming trends in Tmax: All stations showed a positive trend in Tmax. Thakmarpha and Khudi Bazar exhibited statistically significant increases ($p < 0.001$);
- Mixed trends in Tmin: Thakmarpha showed a significant negative trend in Tmin ($p = 0.001$), while Jomsom and Khudi Bazar had positive but non-significant trends. Table 5 presents the results of the Mann–Kendall trend test for temperature data, indicating statistically significant trends in maximum and minimum temperatures. Check Appendix B for trend graphs.

Table 5. Mann–Kendall trend test and sen-slope estimator results for temperature data.

Stations		Tmax	Tmin
Thakmarpha	*p*-value	<0.0001	0.001
	sen-slope	0.040	−0.033
	Trend	Positive	Negative
Jomsom	*p*-value	0.866	0.745
	sen-slope	0.001	0.006
	Trend	Positive	Positive
Khudibazar	*p*-value	<0.0001	0.328
	sen-slope	0.040	0.010
	Trend	Positive	Positive

Similarly, to the temperature data, annual precipitation data were analyzed for trends using the Mann–Kendall test. Figure 5 shows the annual precipitation trends for the stations.

- Positive trends: Thakmarpha and Jomsom exhibited positive trends in precipitation, with Jomsom's trend being statistically significant ($p < 0.001$);
- Negative trends: Khudi Bazar showed a negative but non-significant trend. Manang Bhot displayed a significant negative trend ($p = 0.001$);
- Variability: Precipitation patterns were highly variable, with anomalies such as droughts and extreme rainfall events. Table 6 provides the Mann–Kendall test results for precipitation.

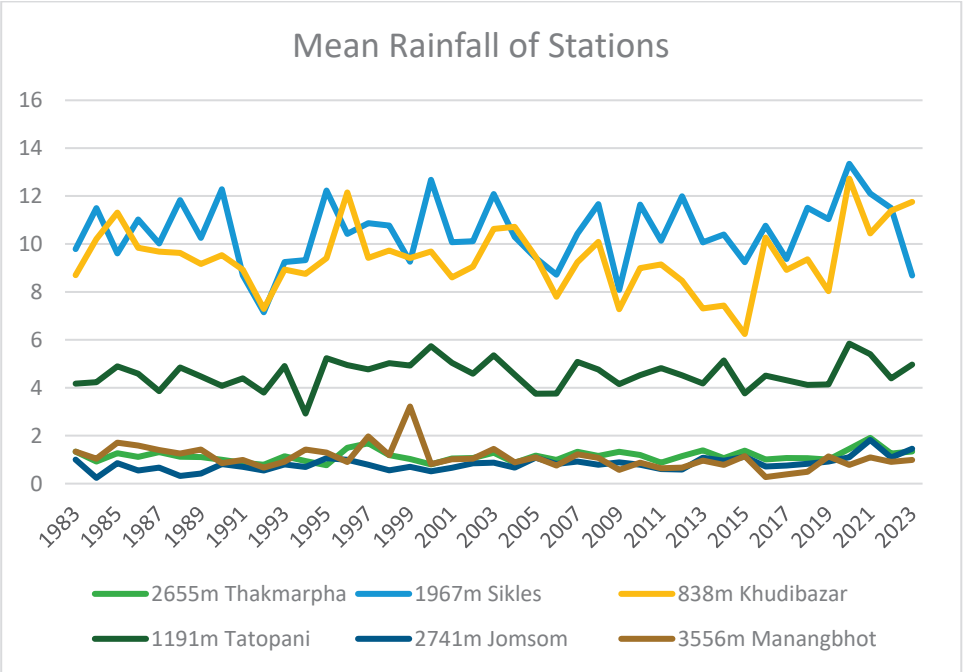

Figure 5. Annual precipitation for Thakmarpha, Jomsom, Khudi Bazar, Sikles, Manang Bhot, and Tatopani.

Table 6. Mann–Kendall trend test and sen-slope estimator results for precipitation data.

Stations		Precipitation
Thakmarpha	*p*-value sen-slope Trend	0.154 0.004 Positive
Jomsom	*p*-value sen-slope Trend	0.000 0.012 Positive
Khudibazar	*p*-value sen-slope Trend	0.661 −0.009 Negative
Sikles	*p*-value sen-slope Trend	0.465 0.016 Positive
Manang Bhot	*p*-value sen-slope Trend	0.001 −0.015 Negative
Tatopani	*p*-value sen-slope Trend	0.582 0.004 Positive

The frequency of extreme precipitation events in the Annapurna region has exhibited notable changes over the past four decades. An analysis of the data reveals that days with significant rainfall have generally increased across all stations. Figure 6 illustrates the normalized frequency of extreme precipitation events over the past four decades, emphasizing changes in rainfall patterns that influence flood risk and water resource management.

Increase in moderate extreme events: The percentage of days with rainfall exceeding 30 mm increased substantially over the decades. In 1983–1992, this percentage ranged from 6% to 12%, rising to 33% to 43% in 2003–2012. Days with rainfall over 50 mm also

increased, from 2 to 5% in 1983–1992 to 8 to 14% in 2003–2012. Despite the increase in moderate extremes, occurrences of rainfall exceeding 100 mm remain relatively rare, with only a slight rise from 0 to 1% in 1983–1992 to 2% in 2003–2012. The most recent decade (2013–2022) suggests a stabilization or slight decline in the frequency of these extreme events compared to the previous decade. The percentage of days with rainfall over 30 mm and 50 mm has not shown the same rate of increase as observed earlier.

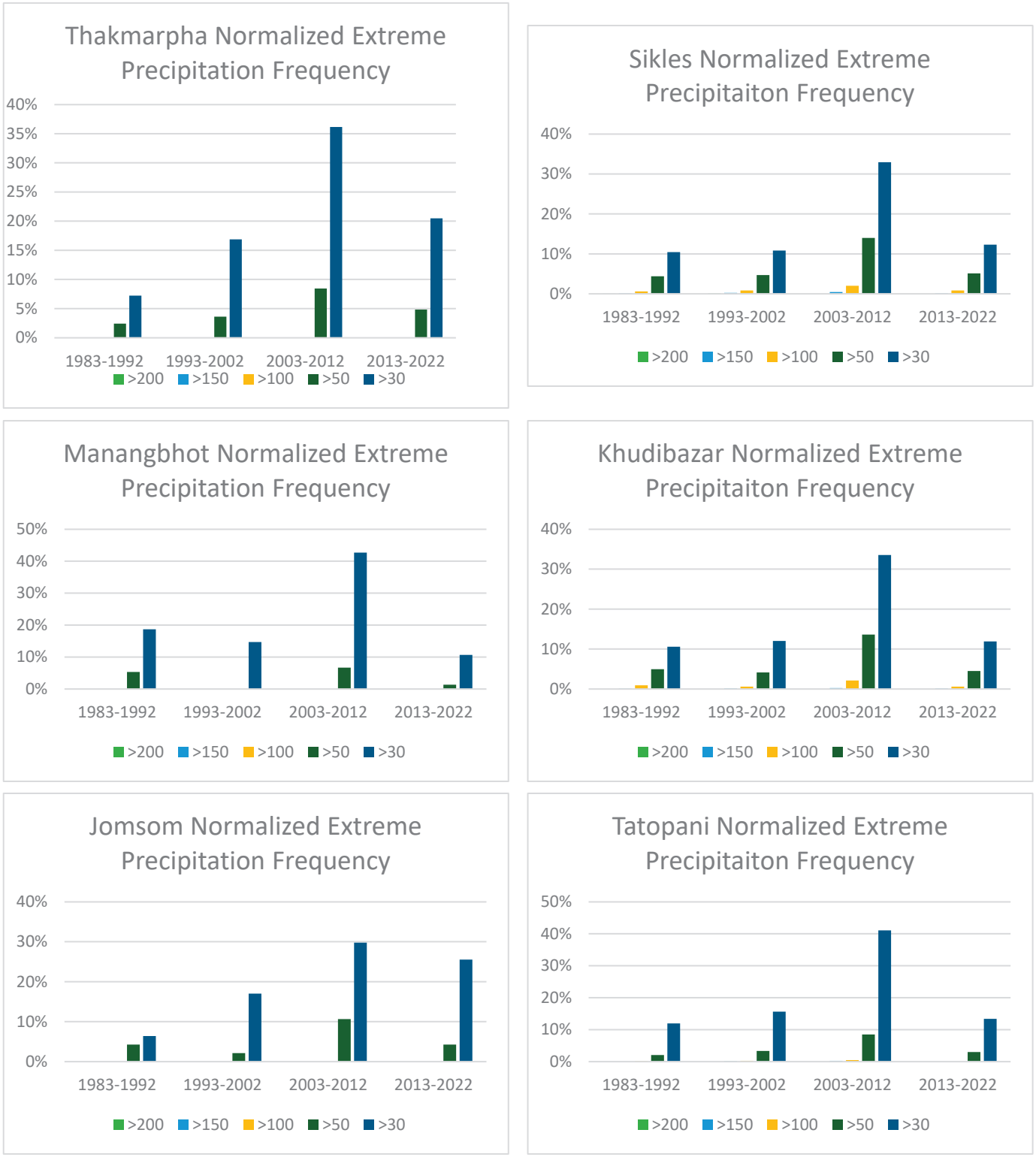

Figure 6. Normalized extreme precipitation frequency across stations.

An analysis of rainfall patterns across the Annapurna region reveals significant changes over the decades, with notable differences between higher elevation and lower elevation stations which is shown in Figure 7.

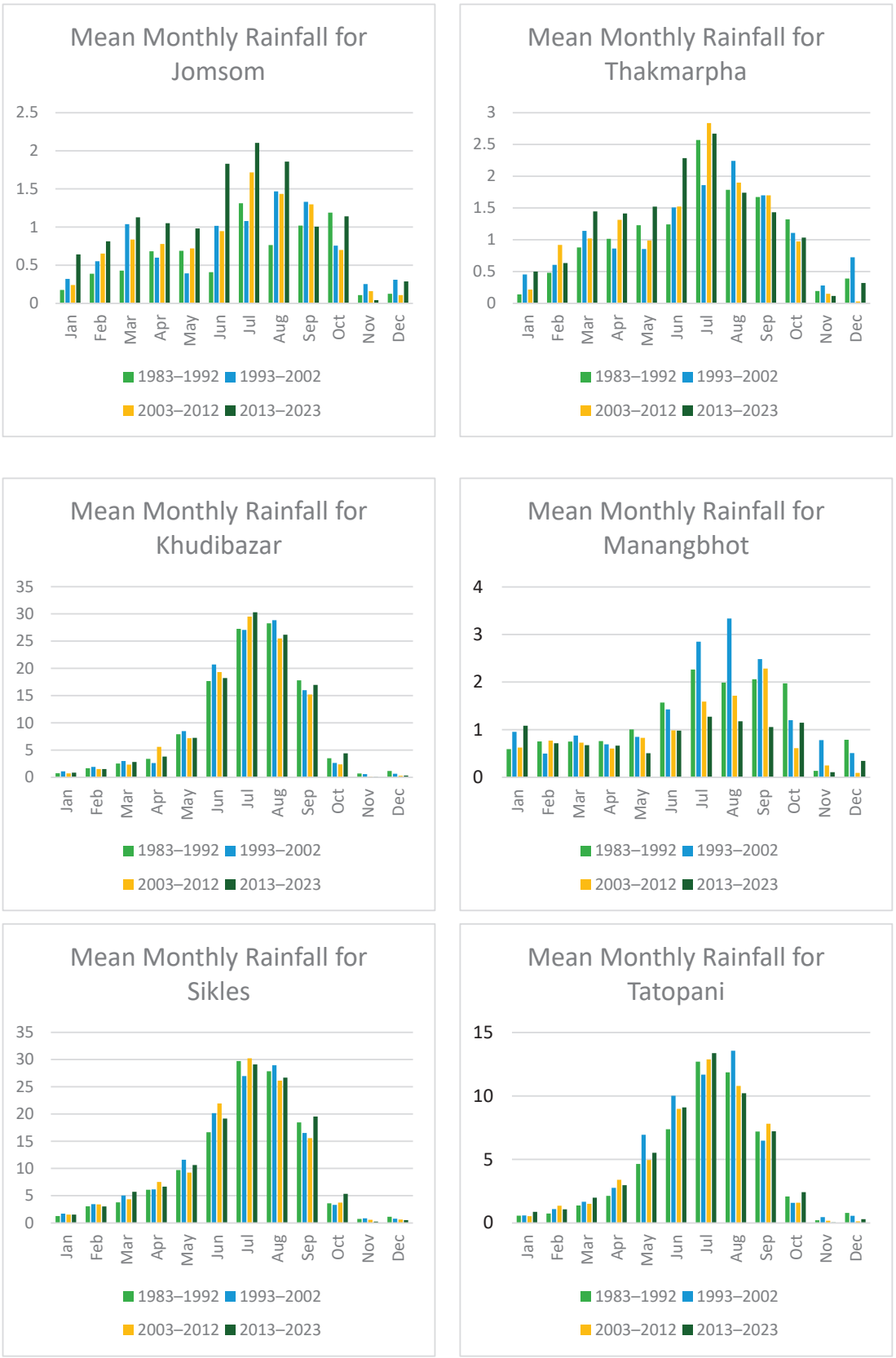

Figure 7. Decadal changes in precipitation pattern in given station.

Higher elevation stations such as Thakmarpha, Manang Bhot, and Jomsom exhibited a consistent increase in mean monthly rainfall during the monsoon months (July and August). Thakmarpha's July rainfall rose from 2.57 mm in 1983–1992 to 2.67 mm in 2013–2023. Jomsom's July rainfall increased from 1.31 mm to 2.10 mm over the same period.

Lower elevation stations like Sikles, Tatopani, and Khudi Bazar showed substantial increases in rainfall during the monsoon months. Sikles recorded July rainfall increases from 29.71 mm in 1983–1992 to 30.30 mm in 2013–2023. Khudi Bazar's July rainfall rose from 27.25 mm to 30.30 mm over the same period.

3.4. Community Perceptions and Adaptive Strategies

Appendix C includes the questionnaire and the demographic overview of the respondents.

Perception of climate change: Surveys conducted in 11 villages within the ACA indicate a high level of awareness regarding climate change among residents. (Figure 8) A significant majority (85%) reported noticeable changes in climatic patterns, particularly a decrease in snowfall and alterations in precipitation. Approximately 70% of respondents noted changes in water availability, which they attributed to these climatic shifts. Residents observed that these changes directly impacted on their agricultural practices, with shifts in crop types and growing seasons becoming necessary to adapt to the new conditions.

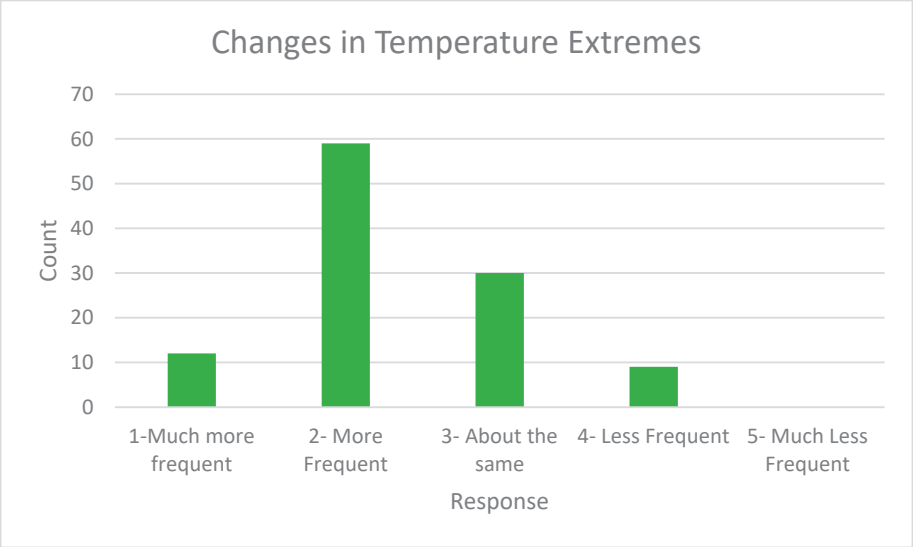

Figure 8. Responses for changes in temperature extremes.

Temperature extremes and weather patterns: The community's perception of climate change is notably well-informed, with a majority acknowledging its impacts on local ecosystems and livelihoods. Survey respondents have observed significant changes in local weather patterns, including more pronounced and frequent extreme weather events.

A significant number of respondents have observed changes in temperature extremes, with some noting that water now freezes less often, indicating milder winters. Rainfall patterns have been described as unpredictable, and several individuals have reported less snowfall, which aligns with the concerns about shorter winter seasons.

Water availability and infrastructure: As shown in Figure 9, the survey results present an encouraging trend in water availability and infrastructure within the community. Contrary to the challenges often faced in many regions, our data shows a marked improvement in access to water resources. Currently, all surveyed households report having access to piped water, a significant development compared to just a few years prior when such amenities were limited to a fraction of the population. It aligns with the 2023 Joint Monitor-

ing Program (JMP), and National Water, Sanitation and Hygiene (NWASH) data, which is also on a positive trend in achieving SDG 6 [35].

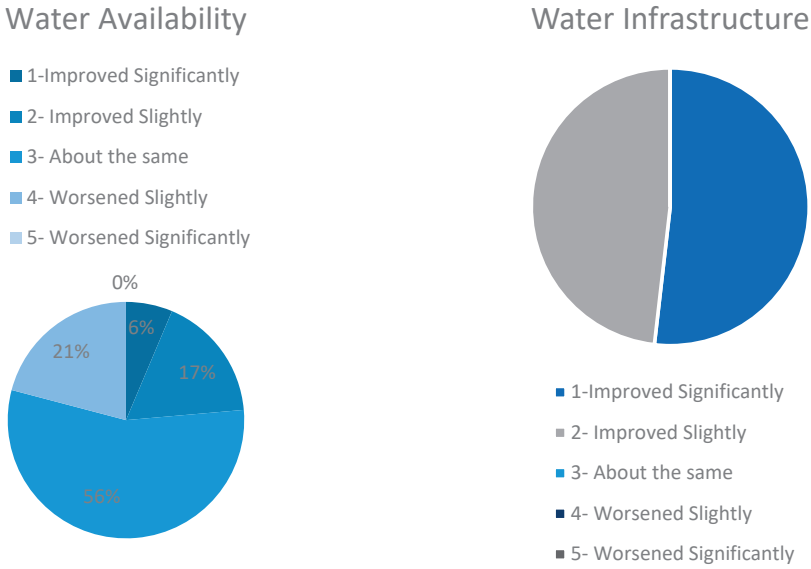

Figure 9. Responses on water availability and infrastructure.

This progress in water infrastructure is a testament to successful policy implementation and investment in the community's essential services. The upgrade has likely contributed to the community's well-being, as reliable access to clean water is a cornerstone of public health, economic development, and environmental sustainability. This positive shift also reflects a growing recognition of the importance of water security in the face of climate change, prompting proactive measures to ensure resilience and adaptability in water management systems.

The improved infrastructure sets a solid foundation for future initiatives to manage water resources sustainably. It is also a crucial step toward achieving related SDGs, particularly SDG 6, which calls for clean water and sanitation for all. The survey's findings can thus be a springboard for discussions on maintaining and furthering these gains, ensuring that water security remains a priority in policy planning and community development efforts.

Community involvement and social support: Figure 10 shows that the community engagement in local water management groups is mixed, with a significant number of respondents indicating moderate to high levels of involvement. This engagement suggests a community that is somewhat active and potentially receptive to initiatives for improving local resilience to climate change. On the other hand, a portion of the population is less involved, which may reflect barriers to participation or differing priorities. Understanding the factors that drive or hinder community involvement can inform strategies to foster more significant collective action in response to environmental challenges.

Open-ended responses: Open-ended responses highlight specific incidents, such as floods and landslides, directly impacting businesses and agriculture. Concerns about the changing climate patterns affecting the availability and quality of water sources are evident, with some respondents attributing these changes to climate change, deforestation, and natural variations. The survey data analysis reveals a community experiencing and observing tangible environmental changes due to climate change. There is a clear indication of altered weather patterns, water scarcity issues, and shifts in agricultural practices. Despite these challenges, the community's solid social support network and involvement in local environmental management suggest a capacity for resilience and adaptation. The data underscores

the need for continued monitoring, community engagement, and adaptive strategies to mitigate the impacts of climate change on these vulnerable mountain communities.

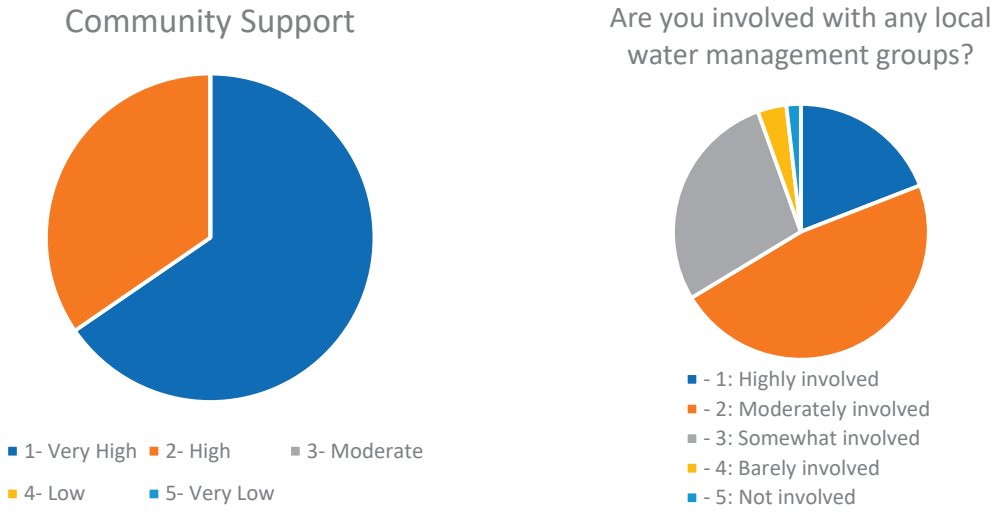

Figure 10. Responses on social support and involvement.

4. Discussion

4.1. LULC, Vegetation and Snow Cover Trends

The analysis of Landsat satellite imagery, corrected for topographical distortions, reveals significant land use and land cover (LULC) changes in the ACA over the 35-year period from 1988 to 2023. Vegetation cover increased substantially, expanding from 57,859 hectares in 1988 to 77,634 hectares in 2023, with a net gain of 19,775 hectares. This growth corresponds with a reduction in barren land, which decreased by 57,766 hectares, reflecting a shift toward afforestation and land reclamation. Snow cover displayed notable variability, peaking in 1996 before declining in subsequent years. Water bodies, meanwhile, exhibited relatively minor fluctuations over the study period. NDVI trends demonstrate a consistent improvement in vegetation health, with average NDVI values increasing from 0.069 in 1988 to 0.340 in 2023, and maximum values reaching 0.983, highlighting enhanced vegetation cover and a potential upward shift in vegetation zones to higher elevations due to warming temperatures.

The increase in vegetation cover aligns with regional findings by [26], who observed greening trends across the Central Himalayas due to warming-induced expansion of vegetation into higher elevations. Additionally, Bandyopadhyay et al., [17] documented a 28% reduction in areas devoid of vegetation (including glaciers) from 2000 to 2014, with these areas transitioning into vegetated land, particularly in the eastern Himalayas. Studies from other mountainous regions, such as the Scandinavian Mountain Range, have also documented increases in total tree canopy cover and field vegetation in alpine areas, while noting shifts in vegetation composition [36]. These findings further emphasize how regions adjacent to retreating glaciers or with favorable climatic conditions are transforming into vegetated landscapes. Our study builds on these findings by providing a longer-term, temporally consistent analysis spanning 35 years while incorporating topographical corrections to improve classification accuracy—a crucial step in mountainous terrains.

The observed increase in vegetation can be linked to several mechanisms. First, the establishment of the ACA as a protected area has significantly reduced deforestation while promoting natural regeneration and afforestation through community-led conservation programs [6]. Second, warming temperatures over recent decades may have extended the growing season and enabled vegetation to establish in areas previously covered by snow or barren land. This trend aligns with studies not just in the Himalayas but also

in other mountain areas, which highlight the upward shift in vegetation zones under climate warming. Furthermore, sustainable land management practices adopted by local communities have likely contributed to stabilizing degraded lands, as indicated by reduced barren areas. This trend highlights not only an expansion of vegetation cover but also a likely shift in vegetation zones toward higher elevations, as warming temperatures create favorable growing conditions in previously barren or snow-covered areas. This upward expansion, commonly observed in other mountainous regions worldwide, aligns with global findings on vegetation responses to climate change. For instance, similar trends have been reported in the Alps [37], Andes [38], and other regions of the Himalayas [21,39], where vegetation zones are migrating upward due to rising temperatures and extended growing seasons.

In contrast, the NDSI trends reveal a concerning pattern of declining snow cover over time, which aligns with broader global observations of shrinking cryospheric zones. Snow cover in the ACA showed significant seasonal fluctuations, with marked reductions during the winter months. Average NDSI values decreased from 0.157 in 1988 to −0.109 in 2023, reflecting a loss of snow cover extent and density. These trends are consistent with observations from similar mountain ecosystems [37–39]. The interplay between vegetation expansion and snow cover reduction underscores the complex ecological impacts of climate change in the ACA. On one hand, warmer temperatures and reduced snow cover provide opportunities for vegetation growth, particularly in alpine zones. On the other hand, the loss of snowpack has cascading effects on water availability, hydrological cycles, and habitat suitability for snow-dependent species. Declining snow cover also poses a threat to flagship species like the snow leopard in the ACA [40], which relies on snow-laden environments for prey availability and movement patterns. Moreover, communities downstream may experience altered water flow regimes due to changes in snowmelt timing and volume, emphasizing the critical need for adaptive water resource management.

The fluctuations in snow cover observed during the study period reflect the combined effects of rising temperatures and variable winter precipitation. While snow cover peaked in 1996, subsequent declines align with regional studies that attribute reduced snow accumulation to increased warming and melting in the Himalayas [17,41,42]. This loss of snowpack disrupts hydrological cycles, diminishing streamflow availability and impacting water-dependent agricultural and ecological systems. Snowpack reductions also pose risks to downstream ecosystems and communities, which rely on snowmelt during drier months. As snow serves as a critical natural reservoir, its loss could have far-reaching consequences for regional water security and ecological stability [41].

While these findings align with global trends, the ACA presents a unique case where both natural and anthropogenic factors interplay to drive ecological outcomes. The observed improvements in vegetation health suggest that conservation policies, such as afforestation and protection from deforestation, have effectively contributed to ecological resilience. However, the persistent loss of snow cover calls for urgent attention to mitigate its impacts on the region's hydrology and biodiversity. Further research should aim to disentangle the relative contributions of climate-driven changes and conservation measures, offering a more nuanced understanding of how to sustain these ecosystems under accelerating climatic pressures. By integrating scientific and local knowledge, future conservation strategies can better address these complex interactions and foster resilience in this vulnerable mountain ecosystem.

4.2. Climate Variables and Extremes

The analysis of temperature data across the ACA indicates a clear warming trend, particularly in maximum temperatures (Tmax). All meteorological stations showed positive

trends in Tmax, with statistically significant increases observed at Thakmarpha and Khudi Bazar ($p < 0.001$). For example, Thakmarpha recorded a sen-slope of +0.040 °C per year. These findings align with previous studies, which report similar warming trends across the Himalayan region [22]. In contrast, trends in minimum temperatures (Tmin) were more variable. Thakmarpha exhibited a significant decline in Tmin (sen-slope of −0.033 °C per year, $p = 0.001$), while Jomsom and Khudi Bazar recorded positive but non-significant trends. These divergent patterns may reflect the influence of microclimatic conditions, such as local topography, elevation, and vegetation cover, as well as variations in nighttime cooling rates in mountainous terrain.

Precipitation trends exhibited significant spatial variability across the ACA. Stations such as Jomsom showed a statistically significant increase in annual precipitation ($p < 0.001$, sen-slope of +0.012 mm/year), while Manang Bhot experienced a significant decline ($p = 0.001$, sen-slope of −0.015 mm/year). Thakmarpha and Sikles recorded positive but non-significant trends, whereas Khudi Bazar showed a non-significant negative trend. This spatial heterogeneity aligns with findings from [22], which emphasize the complex interactions between monsoonal dynamics and local topography in determining precipitation patterns in the Himalayas. An increasing frequency of extreme precipitation events was observed, particularly at lower elevation stations. Days with rainfall exceeding 30 mm increased significantly, rising from 6 to 12% in the 1983–1992 period to 33 to 43% in 2003–2012. Similarly, the frequency of days with rainfall exceeding 50 mm doubled, from 2 to 5% to 8 to 14% over the same period. However, rainfall exceeding 100 mm remained relatively rare, with only a slight increase from 0 to 1% to 2% during the study period. The most recent decade (2013–2023) suggested a stabilization or slight decline in the frequency of these extreme events, reflecting natural variability in precipitation patterns.

These trends are consistent with projections from global climate studies, which link warming-induced intensification of the hydrological cycle to an increased frequency of extreme rainfall events [43]. The spatial patterns observed in the ACA—greater intensification at lower elevations—may result from orographic effects and the enhanced capacity of warmer air to retain and release moisture during convective activity. Decadal analyses revealed contrasting trends between higher and lower elevations. At higher elevation stations, such as Thakmarpha and Jomsom, monsoonal rainfall during July and August showed consistent increases. For instance, Thakmarpha's mean July rainfall rose from 2.57 mm in 1983–1992 to 2.67 mm in 2013–2023. In contrast, lower elevation stations such as Sikles and Khudi Bazar exhibited more pronounced increases in monsoonal rainfall. Sikles recorded a July rainfall increase from 29.71 mm to 30.30 mm over the same period, reflecting the amplified impact of atmospheric warming and moisture availability at lower altitudes.

The observed climatic trends in the ACA can be attributed to a combination of global and regional mechanisms. Rising temperatures, driven by anthropogenic greenhouse gas emissions, are intensifying the hydrological cycle, leading to more frequent and intense rainfall events. The variability in precipitation trends across stations highlights the influence of local factors, including topography, vegetation cover, and proximity to moisture sources. At higher elevations, warming temperatures are likely accelerating glacial melt, contributing to altered streamflow regimes and seasonal water availability [44]. These dynamics are consistent with broader trends observed in other mountain regions.

The climatic changes observed in the ACA have profound implications for ecosystems, water resources, and human livelihoods. Increased Tmax and extreme precipitation events at lower elevations heighten the risks of flooding, soil erosion, and infrastructure damage. These changes pose challenges for agriculture, as altered rainfall patterns can disrupt planting schedules and reduce crop yields. At higher elevations, the retreat of glaciers and

reductions in snow cover threaten water security for downstream communities, particularly during the dry season [41].

4.3. Community Perception and Adaptation

The perceptions of local communities in the ACA regarding climate change provide critical insights into how environmental shifts are experienced and managed on the ground. Surveys conducted across 11 villages revealed a high level of awareness of climatic changes, with 85% of respondents noting a decrease in snowfall and alterations in precipitation patterns. These observations align with the environmental trends documented in this study, suggesting that communities are attuned to the impacts of climate variability. A significant proportion (70%) of respondents reported changes in water availability, attributing these to climatic shifts. The impacts on agriculture were particularly pronounced, with residents adjusting crop types and growing seasons to adapt to unpredictable rainfall and shorter winters. These findings echo those of, who similarly identified water conservation and crop diversification as primary adaptive strategies among Himalayan communities [45–48].

The community's perception of changing temperature extremes further underscores their understanding of local climate dynamics. Many respondents observed milder winters, with water freezing less frequently, and described rainfall patterns as increasingly erratic. These observations align with our findings on temperature trends and precipitation variability, which indicate significant warming and an increase in extreme rainfall events. This alignment between observed climatic trends and community perceptions highlights the validity of local knowledge as a complement to scientific data in understanding climate change's impacts.

Water availability and infrastructure improvements emerged as critical themes in the survey responses. Contrary to challenges often reported in other mountain regions, all surveyed households in the ACA now have access to piped water, reflecting significant progress in water infrastructure development. This improvement not only enhances community resilience to water scarcity but also aligns with global trends toward achieving SDG 6 (Clean Water and Sanitation). The community's proactive measures, such as rainwater harvesting and efficient irrigation practices, demonstrate their capacity to adapt to changing water dynamics. However, sustained efforts are needed to ensure that these gains are maintained and expanded to remote areas that may still face challenges in water access.

Community engagement in local water management and environmental initiatives shows a mixed picture. While many respondents reported moderate to high involvement, others highlighted barriers to participation, such as limited resources or competing priorities. This variation underscores the importance of fostering inclusive approaches to community engagement, with targeted support for vulnerable groups who may face greater barriers to participation. Strengthening local capacity and providing technical assistance can further enhance collective action in managing climate risks.

The survey also revealed the broader socio-economic implications of climate change. Respondents frequently mentioned floods and landslides as direct impacts on agriculture and livelihoods. These events, driven by increased extreme precipitation, exacerbate existing vulnerabilities in the region. Despite these challenges, the community's strong social support networks and active participation in conservation efforts reflect a capacity for resilience [49].

The adaptive strategies employed by the ACA communities are shaped by their direct experiences of climatic changes. Water conservation measures, adjustments in crop types and planting schedules, and participation in environmental initiatives highlight their resilience in the face of environmental challenges. However, these strategies require further support to address emerging risks and ensure long-term sustainability. Enhanced policy

frameworks, capacity-building initiatives, and investments in infrastructure are critical to strengthening adaptive capacities. For instance, integrating community-driven approaches into regional climate adaptation policies can ensure that strategies are both locally relevant and effective.

In conclusion, the alignment between community perceptions and observed climatic trends underscores the importance of integrating local knowledge into climate adaptation strategies. The proactive measures undertaken by the ACA communities provide valuable lessons for other mountain regions facing similar challenges. However, sustained policy support, capacity-building, and infrastructure investments are essential to build on these efforts and enhance the resilience of vulnerable mountain communities. By fostering stronger connections between scientific research and community-based initiatives, we can develop more effective and sustainable responses to the complex challenges posed by climate change.

4.4. Policy Implications and Sustainable Adaptation Strategies

By integrating scientific data, including remote sensing and meteorological analyses, with community insights, this study identifies key areas for policy intervention that align with SDG 6 and 13. These implications emphasize the interconnected nature of ecological, climatic, and socio-economic challenges and offer a pathway toward sustainable adaptation strategies.

The observed improvements in vegetation cover and reductions in barren land highlight the success of conservation efforts but also underscore the need for climate-smart resource management practices. Policies should prioritize initiatives such as promoting climate-resilient agriculture, including the introduction of drought-tolerant crop varieties and water-efficient irrigation systems, which can mitigate the risks posed by erratic rainfall patterns and water scarcity. Supporting agroforestry programs can enhance biodiversity, reduce soil erosion, and sequester carbon, offering both ecological and economic benefits. Moreover, addressing water resource challenges through the expansion of rainwater harvesting infrastructure and groundwater recharge systems is critical to ensuring year-round water availability for agriculture and household needs. Such measures will not only improve water security but also enhance resilience against seasonal variability and extreme weather events.

The findings related to snow cover fluctuations and the upward expansion of vegetation zones present unique challenges for biodiversity conservation. Cold-adapted species such as the snow leopard and red panda face shrinking habitats, while changes in snow cover threaten the hydrological cycles that sustain downstream ecosystems and communities. Conservation policies must incorporate measures to protect critical habitats, particularly in alpine and riparian zones, and promote the restoration of degraded ecosystems. Payment for Ecosystem Services (PES) programs could incentivize local communities to engage in conservation activities, such as afforestation, watershed management, and wildlife monitoring, ensuring both ecological preservation and community livelihoods.

Community perceptions of climate change impacts, such as reduced snowfall and changes in water availability, align closely with the scientific findings, reinforcing the importance of integrating local knowledge into policy frameworks. Strengthening the role of community-based water management groups through technical training and resource allocation can empower residents to manage water systems more effectively. Policymakers should also focus on enhancing the capacity of communities through education and training programs that promote awareness of climate adaptation strategies, such as sustainable farming practices and efficient water use. These initiatives should be designed to foster

inclusivity, addressing barriers to participation faced by marginalized groups and ensuring that adaptation efforts are equitable.

The observed increase in extreme precipitation events, particularly at lower elevations, highlights the need for policies that address disaster risk reduction. Investments in resilient infrastructure, such as flood-resistant roads and bridges, are essential to mitigate the impacts of flooding and landslides on livelihoods and critical services. Early warning systems for extreme weather events, combined with localized emergency response plans, can enhance community preparedness and reduce vulnerabilities. The integration of these measures into national climate adaptation plans will ensure that they are implemented systematically and sustainably.

Effective governance frameworks are crucial for translating these findings into actionable policies. Collaborative governance models that bring together government agencies, conservation organizations, and local communities can ensure that interventions are both scientifically sound and culturally relevant. Strengthening communication channels between national policymakers and grassroots stakeholders will enable bottom-up feedback mechanisms, ensuring that local needs and priorities are reflected in broader climate adaptation strategies. Furthermore, scaling up education campaigns on climate resilience can foster a deeper understanding of the challenges and solutions, empowering individuals and communities to contribute proactively to sustainability efforts.

In addition to local interventions, this study highlights the importance of leveraging technology and data integration to inform policy decisions. Expanding meteorological monitoring networks in high-altitude and remote areas can improve the resolution of climate trend analyses, while GIS-based tools can provide real-time data on land use changes, vegetation health, and snow cover dynamics. These advancements will support evidence-based policymaking and enable adaptive management strategies that respond to emerging challenges.

The alignment of the study's findings with SDGs 6 and 13 provides a clear framework for prioritizing policy actions. Table 7 outlines how our study's outcomes align with specific targets under SDGs 6 and 13, along with tailored recommendations to enhance sustainability efforts. For SDG 6, expanding access to clean water in underserved areas, promoting efficient irrigation techniques, and safeguarding water-related ecosystems are critical steps. For SDG 13, integrating local adaptation measures into national climate policies and providing technical and financial support for community-driven initiatives will strengthen resilience to climate-related hazards. Policymakers must ensure that these actions are coordinated and mutually reinforcing, balancing ecological conservation with socio-economic development.

Table 7. Alignment of study findings with relevant United Nations Sustainable Development Goals (SDGs) 6 and 13. The colors represent the following: Green indicates good progress or positive outcomes with minor improvements needed, Orange denotes mixed results or moderate progress with significant room for enhancement, and Red reflects poor progress or major issues requiring immediate attention.

Relevant SDG Target	Indicator	Assessment	Recommendation
6.1 Achieve universal and equitable access to safe and affordable drinking water for all	Piped water access in surveyed households, higher than recent years	High rate of access to piped water, indicating effective infrastructure improvements; however, ongoing maintenance and further expansion to remote areas is necessary	Continue infrastructure maintenance, expand piped water systems to underserved and remote areas, and monitor water quality regularly

Table 7. *Cont.*

Relevant SDG Target	Indicator	Assessment	Recommendation
6.4 Substantially increase water-use efficiency and ensure sustainable water withdrawals	Water availability and seasonal trends	Survey data shows mixed trends in water availability, with some areas experiencing seasonal scarcity due to changing climate patterns	Foster cross-sectoral cooperation for water management, implement efficient irrigation techniques, and explore rainwater harvesting initiatives
6.6 By 2020, protect and restore water-related ecosystems, including mountains, forests, wetlands, rivers, aquifers and lakes	Increase in vegetation cover change analysis, Fluctuations in snow cover (1988–2023) from the LULC	Positive ecosystem changes observed, attributed to conservation and reforestation efforts; snow cover fluctuations present challenges for hydrological cycles	Continue and expand conservation and reforestation efforts, integrate adaptive measures for snow cover management to balance hydrological needs
6.B Support and strengthen the participation of local communities in improving water and sanitation management	Involvement of locals in water management groups	Moderate engagement observed; community-driven water management initiatives show potential but require more structured support	Strengthen community participation in water governance through training, capacity building, and incentives for local leadership
13.1 Strengthen resilience and adaptive capacity to climate-related hazards and natural disasters in all countries	Community engagement in adaptation	High engagement among communities in adaptive measures, though limited by resource constraints	Expand resources and technical support for community-driven adaptation strategies, including early warning systems for extreme weather events
13.2 Integrate climate change measures into national policies, strategies and planning	Implementation of climate mitigation measures	Strong climate policies exist, but gaps remain in integrating local actions due to resource constraints and inconsistent support. Community initiatives often lack sufficient policy backing and technical resources.	Establish frameworks for effective collaboration between local communities and national governance structures, ensuring bottom-up communication channels will help reflect local needs in policy development and encourage broader community engagement in achieving national climate goals
13.3 Improve education, awareness-raising and human and institutional capacity on climate change mitigation, adaptation, impact reduction and early warning	Awareness and adaptation actions	Moderate to high levels of climate awareness among surveyed populations; further outreach and resource allocation are needed	Develop comprehensive climate education programs, offer community workshops on climate adaptation, and strengthen local knowledge-sharing networks

4.5. Limitations and Future Research Directions

This study provides critical insights into climate resilience in the Annapurna region through an integrated approach involving remote sensing, meteorological analyses, and community surveys. However, several limitations must be acknowledged to contextualize the findings and guide future research. The use of Landsat imagery, while providing a long-term perspective on land use and land cover changes, is constrained by its moderate spatial resolution, which may overlook fine-scale variations in the heterogeneous terrain of the study area. Although topographical corrections enhanced the accuracy of classifications, residual errors in steep slopes and shadowed regions remain a challenge. Vegetation health and snow cover trends, analyzed using NDVI and NDSI, offered valuable insights but oversimplified ecological processes in areas where vegetation and snow overlap. Additional indices or ground-based validation could improve the precision of such analyses.

The sparse meteorological station network, particularly in remote high-altitude areas, limited the resolution of climate variability assessments. Gaps in temperature and precipitation data may have introduced uncertainties, necessitating the expansion of monitoring networks and the use of satellite-based climate datasets to address spatial and temporal gaps. Community surveys, while capturing diverse perceptions from multiple villages, were limited by their sample size and the inherent subjectivity of self-reported data, which

may have emphasized recent climatic events. Larger, more representative samples, combined with participatory research methods, could provide a deeper understanding of community-level responses.

Future research should prioritize higher-resolution satellite imagery and advanced machine learning techniques to capture fine-scale land cover dynamics more accurately. Investigating the interactions between vegetation expansion and snow cover loss using additional ecological indices and process-based models will deepen understandings of ecosystem responses to climate change. Expanding meteorological station coverage and integrating high-resolution climate models will provide more granular data to support localized adaptation strategies. Socio-economic studies tracking the long-term impacts of climate variability on livelihoods and adaptation strategies could inform more actionable policies, while research on extreme weather events like floods and landslides would enhance disaster preparedness.

Addressing these limitations through interdisciplinary approaches and integrating local knowledge with scientific data will not only refine future analyses but also strengthen the development of adaptive strategies for climate resilience. By building on these findings, future research can contribute to more effective policies and sustainable resource management, supporting both ecological integrity and community well-being in vulnerable mountain ecosystems. This comprehensive understanding will also enhance alignment with global sustainability goals, ensuring a balanced approach to conservation and adaptation.

5. Conclusions

This study provides a comprehensive assessment of climate change impacts in Nepal's ACA over the past 35 years (1988–2023) by integrating remote sensing, climate data analysis, and community perspectives. The findings reveal significant environmental transformations, including a 34% increase in vegetation cover from 57,858.84 ha in 1988 to 77,634.27 ha in 2023, driven by effective afforestation and conservation initiatives. Concurrently, barren land decreased by approximately 14.9%, from 389,018.9 ha to 331,252.8 ha, highlighting successful land restoration efforts. However, snow cover has declined by 16.7%, decreasing from a peak of 95,991.75 ha in 1996 to 80,323.38 ha in 2023, underscoring the adverse effects of rising temperatures and reduced snowfall. These environmental changes are further evidenced by the significant improvement in vegetation health, with NDVI increasing from an average of 0.069 in 1988 to 0.340 in 2023, while NDSI declined from 0.157 to −0.109 over the same period.

Climate variability analysis reveals a complex pattern of warming and precipitation changes across the ACA. Tmax has shown a consistent warming trend, particularly in Thakmarpha and Khudi Bazar, with statistically significant increases of +0.040 °C per year ($p < 0.001$). Tmin exhibited mixed trends, including a significant decrease of −0.033 °C per year in Thakmarpha ($p = 0.001$). Precipitation patterns have become increasingly variable, with Jomsom experiencing a significant annual increase of +0.012 mm/year ($p < 0.001$) and Manang Bhot facing a significant decrease of −0.015 mm/year ($p = 0.001$). The frequency of extreme rainfall events has surged, with days exceeding 30 mm of rainfall rising from 6 to 12% in the 1983–1992 decade to 33 to 43% in 2003–2012, and days exceeding 50 mm increasing from 2 to 5% to 8 to 14%. These changes heighten the risks of flooding and landslides, posing substantial threats to both ecosystems and local communities.

Community surveys conducted across 11 villages within the ACA reveal a high level of climate change awareness, with 85% of respondents observing significant climatic shifts such as decreased snowfall and altered precipitation patterns. Approximately 70% reported changes in water availability, directly linking these to climate variability. These perceptions are reflected in tangible adaptations, including crop diversification and altered growing sea-

sons to accommodate new climatic conditions. Notably, all surveyed households now have access to piped water, a significant improvement that aligns with the 2023 Joint Monitoring Program (JMP) report [35], advancing progress toward SDG 6. Additionally, community engagement in water management groups is moderate to high, indicating a proactive stance towards enhancing resilience, although further efforts to increase participation could bolster collective adaptive capacity.

The integrated approach of this study—combining remote sensing, climate data, and community insights—provides a holistic understanding of the interplay between environmental changes and socio-economic impacts in the ACA. Quantitative data, such as the increase in NDVI and the significant rise in extreme rainfall events, align with global climate trends, reinforcing the study's broader relevance. The inclusion of community perceptions underscores the direct impact of environmental changes on local livelihoods and highlights effective adaptive strategies. These insights inform actionable recommendations, including the expansion of rainwater harvesting systems, promotion of climate-resilient agricultural practices, and implementation of robust disaster risk reduction measures. By merging scientific monitoring with community-based adaptation strategies, the study advocates for policies that are both scientifically robust and culturally relevant, ensuring sustainable and effective climate resilience. The study stresses the importance of strengthening community-based adaptation efforts, improving disaster risk reduction strategies, and fostering inclusive, technology-driven governance models. Additionally, it highlights the need for policies that protect water-related ecosystems, support local communities, and integrate local climate adaptation actions into national strategies.

In summary, this research advances understandings of climate change impacts in the ACA by offering a scalable framework applicable to other mountain regions. The significant environmental changes, coupled with high community awareness and adaptive responses, underscore both the challenges and the resilience of mountain ecosystems and their inhabitants. By leveraging an integrated methodological approach, the study delivers valuable insights and practical solutions essential for achieving sustainable development and enhancing climate resilience, directly supporting SDGs 6 and 13. The incorporation of detailed empirical data and community perspectives ensures that the recommendations are grounded in local realities, facilitating effective and sustainable policy and practice implementations.

Author Contributions: Conceptualization, A.P. and P.F.; methodology, A.P.; software, A.P.; validation, A.P. and P.F.; formal analysis, A.P.; investigation, A.P. and G.B.; resources, A.P. and G.B.; data curation, A.P. and G.B.; writing—original draft preparation, A.P.; writing—review and editing, P.F.; visualization, A.P.; supervision, P.F.; project administration, P.F.; funding acquisition, P.F. All authors have read and agreed to the published version of the manuscript.

Funding: This study was supported by the Science and Technology Commission of Shanghai Municipality (23HC1400300) and open fund of Key Laboratory of Agro-Environment in Midstream of Yangtze Plain, Ministry of Agriculture and Rural Affairs, P.R.China.

Institutional Review Board Statement: Ethical approval was not required as per Tongji University regulations. Research was conducted under the permissions granted by the Annapurna Conservation Area Project (ACAP), authorized by Nepal's Department of National Parks and Wildlife Conservation.

Informed Consent Statement: Informed consent was obtained from all subjects involved in the study.

Data Availability Statement: The original contributions presented in this study are included in the article. Further inquiries can be directed to the corresponding author.

Acknowledgments: The authors would like to express their deepest gratitude to everyone who contributed to the completion of this paper. We are immensely thankful to all the respondents from the 11 villages within the Annapurna Conservation Area (ACA) who generously shared their stories and experiences, providing invaluable insights for our study. Special thanks go to the local community leaders and organizations for their unwavering support and cooperation throughout the research process. We also appreciate the guidance and assistance from our research team, whose dedication and hard work were crucial in bringing this study to fruition. Additionally, we are grateful for the opportunity to conduct this important work, which aims to enhance climate resilience and support sustainable development in mountain ecosystems. Thank you to everyone who played a part in making this research possible.

Conflicts of Interest: The authors declare no conflicts of interest. The funders had no role in the design of the study; in the collection, analyses, or interpretation of data; in the writing of the manuscript; or in the decision to publish the results.

Appendix A

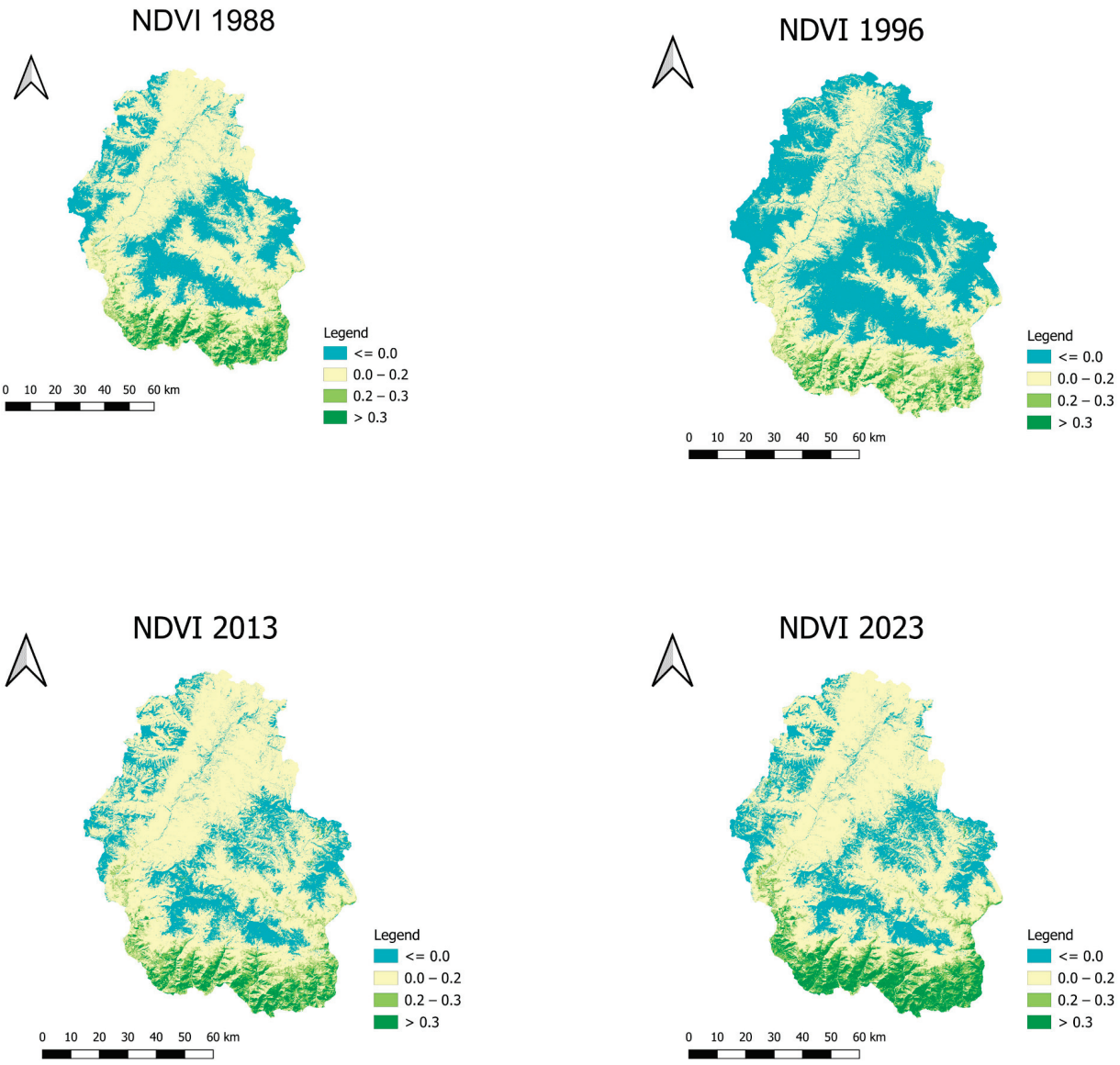

Figure A1. NDVI imagery of the study area in the years 1988, 1996, 2013, and 2023.

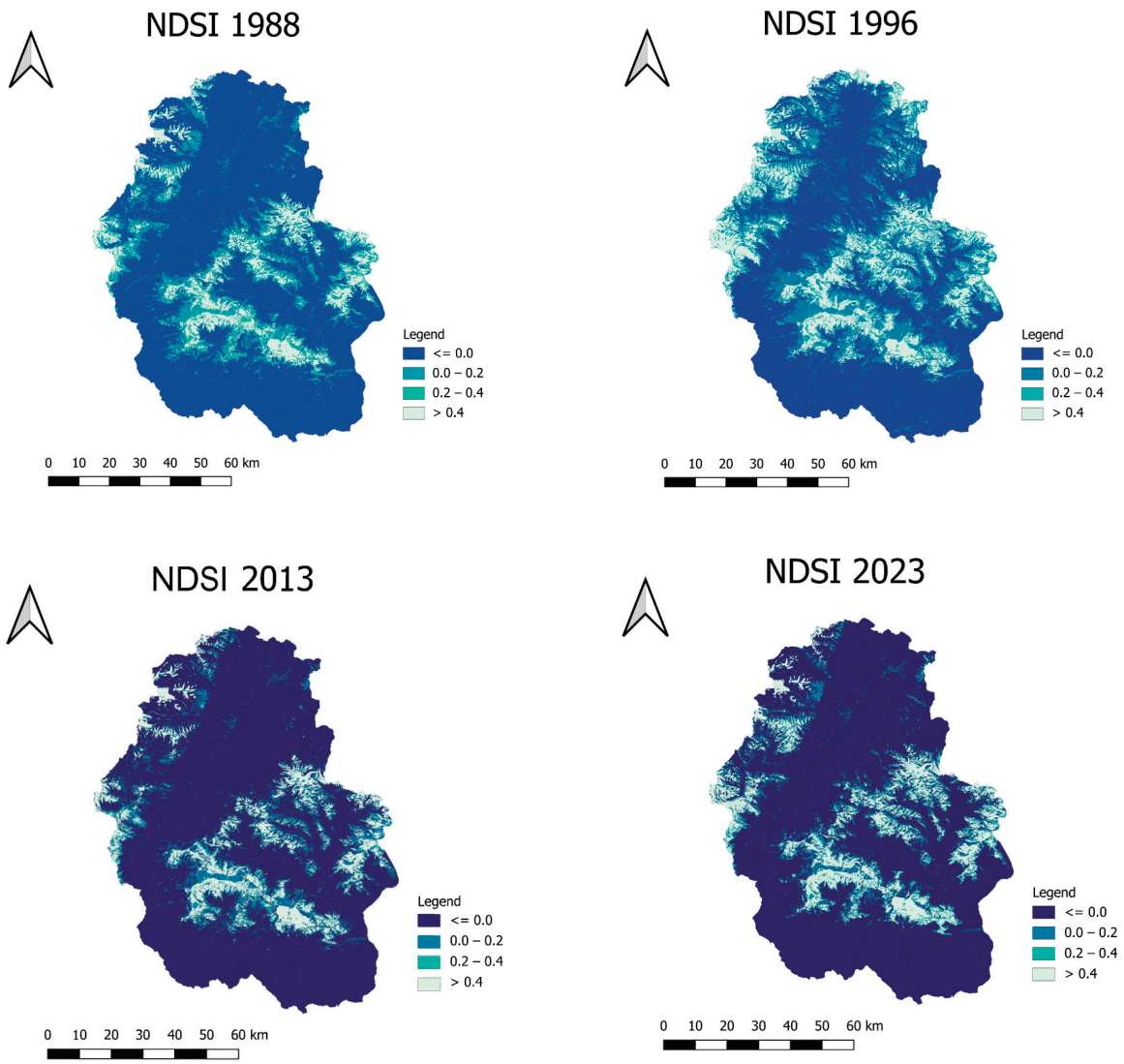

Figure A2. NDSI imagery of the study area in the years 1988, 1996, 2013, and 2023.

Appendix B

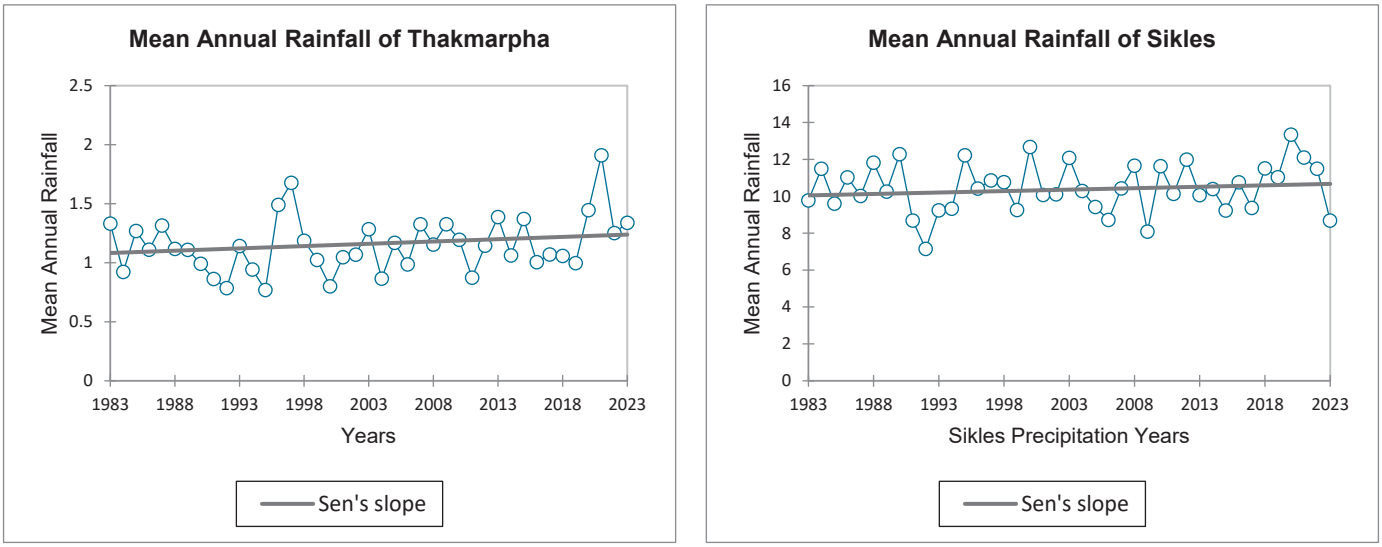

Figure A3. *Cont.*

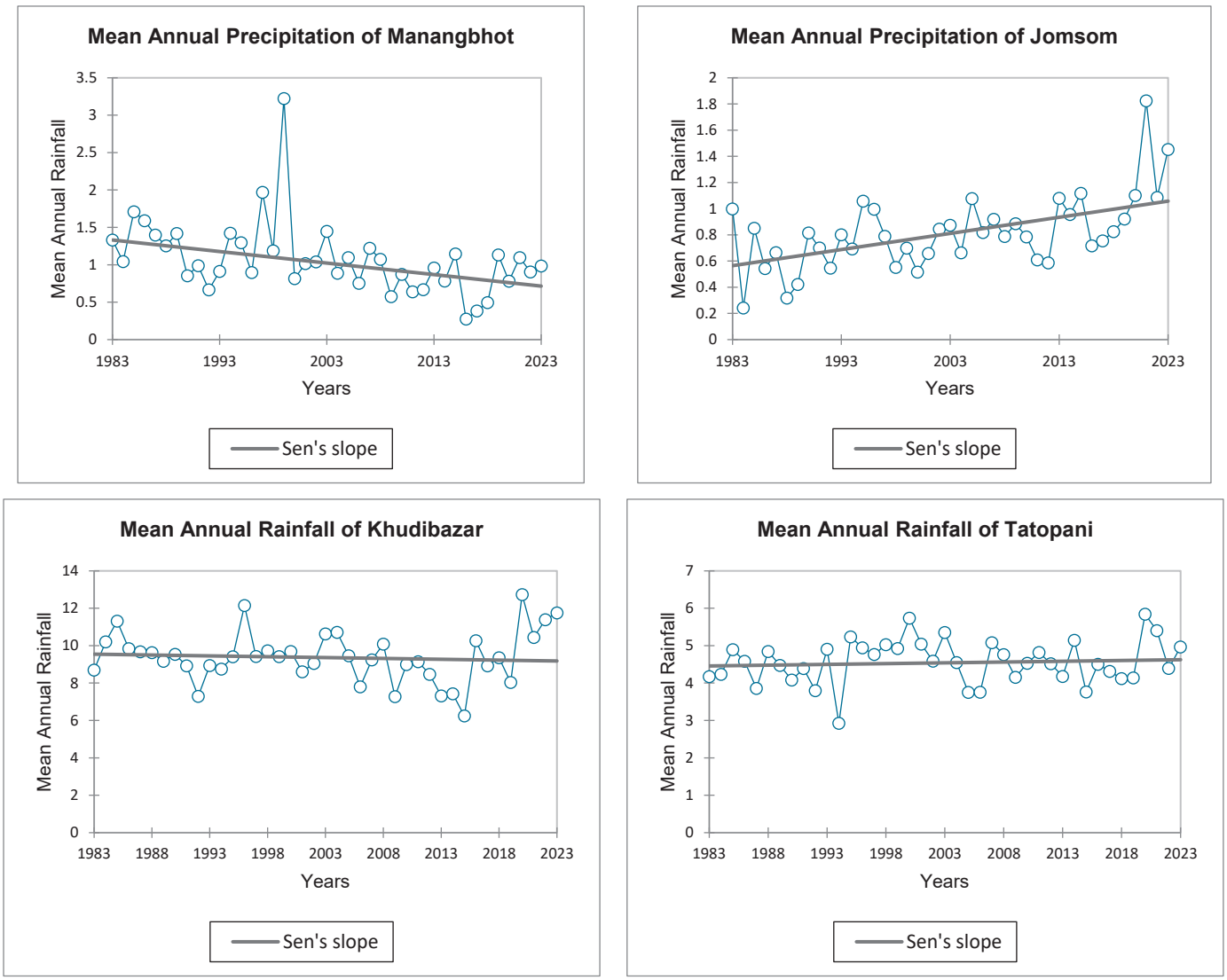

Figure A3. Man–Kendell trend test and sen-slope estimator chart for precipitation.

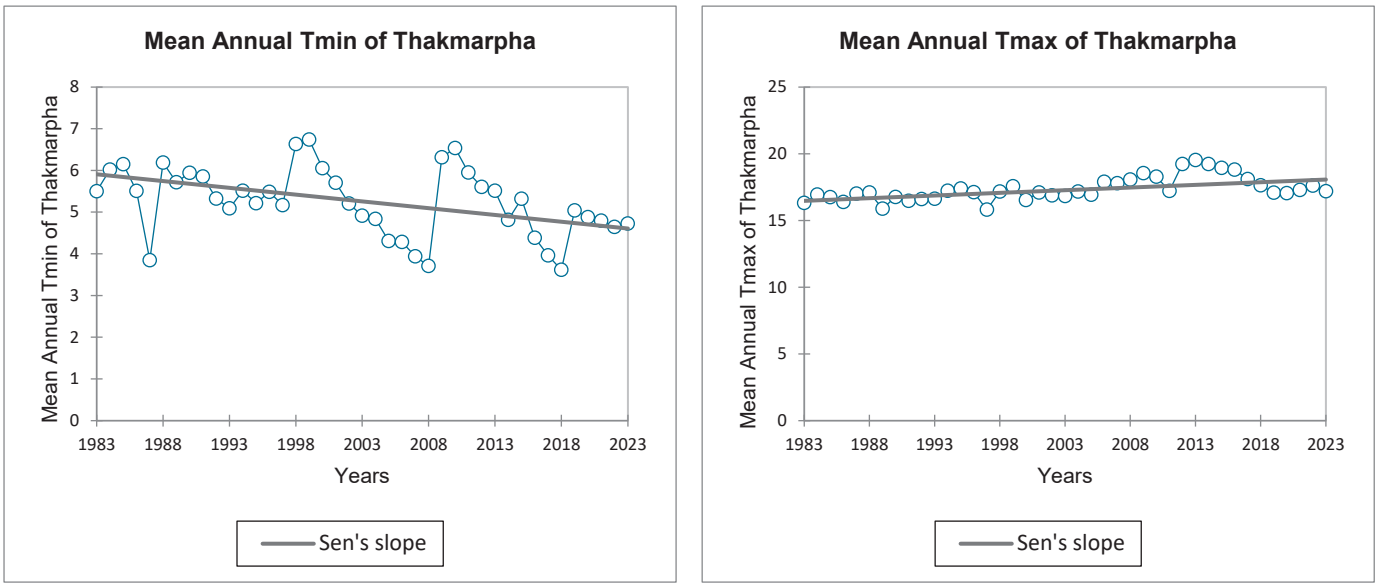

Figure A4. *Cont.*

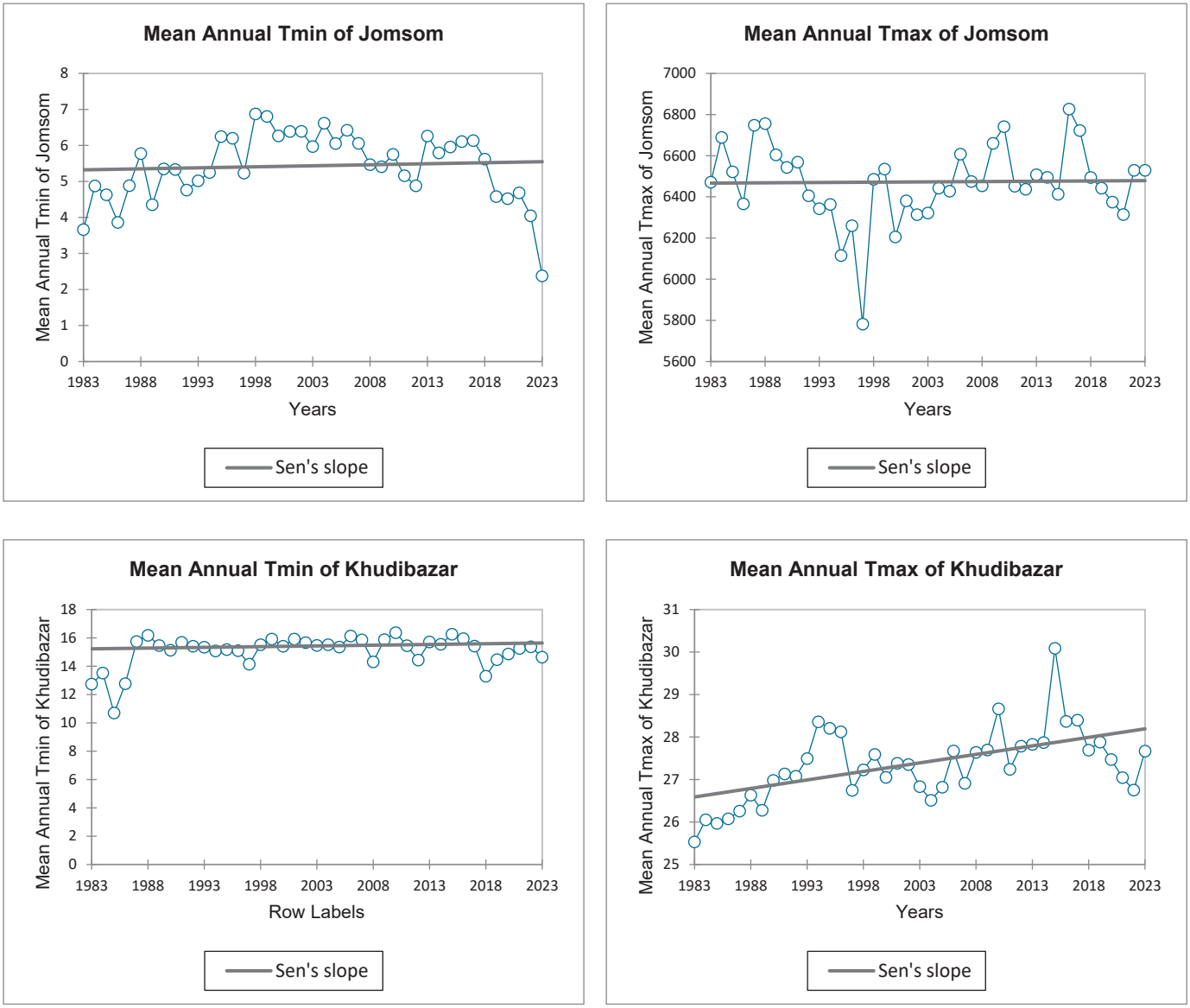

Figure A4. Man–Kendell trend test and sen-slope estimator chart for Tmin and Tmax.

Appendix C

Appendix C.1. Demographic Overview

The survey data collected from various individuals in different occupations and locations provides a rich dataset for understanding the perceptions and impacts of climate change on local communities. The respondents come from various age groups, occupations, and locations. The diversity in demographics allows for a comprehensive analysis of how climate change impacts vary across different population segments. The survey indicates a relatively balanced gender distribution among the respondents, with a near-even split between female and male participants. The age distribution of survey participants covers a diverse range, ensuring a broad perspective encompassing the views of younger and older community members. Notably, there is a predominance of respondents in the middle age brackets, which may reflect these age groups' active engagement and availability.

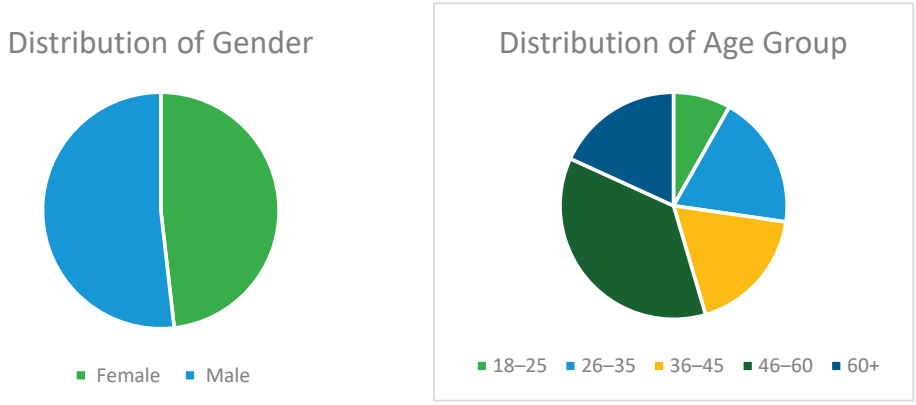

Figure A5. Demographic overview of the respondents.

Appendix C.2. Household Survey Questionnaire

Section 1: Demographic Information
- Name:
- Gender:
- Age:
- Occupation:
- Location:

Section 2: Climate and Environmental Changes
1. "Compared to 10-20 years ago, how would you describe changes in temperature extremes like heat waves or cold spells in your area?"
    - 1: Much more frequent
    - 2: More frequent
    - 3: About the same
    - 4: Less frequent
    - 5: Much less frequent

2. "Compared to 20 years ago, the winter season is now:"
    - 1: Much warmer
    - 2: Warmer
    - 3: About the same
    - 4: Cooler
    - 5: Much cooler

3. "In the last ten years, have extreme weather events like heavy rainfall/floods/droughts:"
    - 1: Increased significantly
    - 2: Increased slightly
    - 3: Remained the same
    - 4: Decreased slightly
    - 5: Decreased significantly

4. "During the winter season, is water now:"
    - 1: More available
    - 2: Somewhat more available
    - 3: About the same
    - 4: Somewhat less available

Section 3: Water Resources and Management

5. "How dependent is your household's income on local water availability?"
   - 1: Completely dependent
   - 2: Mostly dependent
   - 3: Somewhat dependent
   - 4: Slightly dependent
   - 5: Not dependent

6. "In the last ten years, has water infrastructure in your village:"
   - 1: Improved significantly
   - 2: Improved slightly
   - 3: Remained the same
   - 4: Worsened slightly
   - 5: Worsened significantly

Section 4: Community and Livelihood

7. "Are you involved with any local water management groups?"
   - 1: Highly involved
   - 2: Moderately involved
   - 3: Somewhat involved
   - 4: Barely involved
   - 5: Not involved

8. "How satisfied are you with opportunities to participate in local decisions?"
   - 1: Very satisfied
   - 2: Somewhat satisfied
   - 3: Neither satisfied nor dissatisfied
   - 4: Somewhat dissatisfied
   - 5: Very dissatisfied

9. "How reliable is your household's main water source?"
   - 1: Very reliable
   - 2: Somewhat reliable
   - 3: Neither reliable nor unreliable
   - 4: Somewhat unreliable
   - 5: Very unreliable

10. "During times of shortage, how difficult is it to get enough water?"
    - 1: Very difficult
    - 2: Somewhat difficult
    - 3: Neither easy nor difficult
    - 4: Somewhat easy

11. "How would you rate the condition/health of local water sources?"
    - 1: Very healthy
    - 2: Somewhat healthy
    - 3: Neither healthy nor unhealthy
    - 4: Somewhat unhealthy
    - 5: Very unhealthy

12. "How have stream flows or wetland/forest coverage changed over 20 years?"
    - 1: Increased significantly
    - 2: Increased slightly
    - 3: Remained the same
    - 4: Decreased slightly
    - 5: Decreased significantly

13. "How would you rate the level of social support in your community?"
    - 1: Very high
    - 2: High
    - 3: Moderate
    - 4: Low
    - 5: Very low

14. "During disasters, do community members help each other?"
    - 1: Always
    - 2: Often
    - 3: Sometimes
    - 4: Rarely
    - 5: Never

15. "To what extent has forest coverage increased in the local area over the past decade based on observations?"
    - 1: Increased significantly
    - 2: Increased slightly
    - 3: Remained the same
    - 4: Decreased slightly
    - 5: Decreased significantly

Open-Ended Questions

"How has the availability and quality of your local water sources been affected by changing climate patterns? Please provide detailed observations and experiences."

_____

"If you have noticed changes to local wildlife, plant species, or vegetation over the years, please describe them."

_____

"Please describe any observed changes in rainfall patterns, such as timing and amount, compared to the past."

_____

"How have growing seasons or timing of seasonal changes altered over the past decade based on your observations?"

_____

"In your view, what do you think has caused these observed changes to local climate patterns? Please explain, and feel free to select more than one option."

_____

Optional Questions with Multiple Choices

"Does your household engage in any of the following activities? (Check all that apply):"
· Agriculture
· Livestock rearing
· Trade
· Tourism services
· Other (please specify): [Open-ended response area]

"If involved in farming/livestock, have climate changes impacted (Check all that apply):"
· Crop yields
· Livestock health
· Planting/harvesting times
· Water availability for irrigation
· Pest and disease prevalence
· Other (please specify): [Open-ended response area]

"Is there a forest committee in your village? If yes, how does it work? (Optional)"
· Yes, and it functions effectively by...
· Yes, but it faces challenges such as...
· No, there is no forest committee

References

1. Knight, J. Scientists' Warning of the Impacts of Climate Change on Mountains. *PeerJ* **2022**, *10*, e14253. [CrossRef] [PubMed]
2. Schirpke, U.; Kohler, M.; Leitinger, G.; Fontana, V.; Tasser, E.; Tappeiner, U. Future Impacts of Changing Land-Use and Climate on Ecosystem Services of Mountain Grassland and Their Resilience. *Ecosyst. Serv.* **2017**, *26*, 79–94. [CrossRef]
3. Lutz, A.F.; Immerzeel, W.W.; Siderius, C.; Wijngaard, R.R.; Nepal, S.; Shrestha, A.B.; Wester, P.; Biemans, H. South Asian Agriculture Increasingly Dependent on Meltwater and Groundwater. *Nat. Clim. Chang.* **2022**, *12*, 566–573. [CrossRef]
4. Viviroli, D.; Dürr, H.H.; Messerli, B.; Meybeck, M.; Weingartner, R. Mountains of the World, Water Towers for Humanity: Typology, Mapping, and Global Significance. *Water Resour. Res.* **2007**, *43*, 7447. [CrossRef]
5. Immerzeel, W.W.; Lutz, A.F.; Andrade, M.; Bahl, A.; Biemans, H.; Bolch, T.; Hyde, S.; Brumby, S.; Davies, B.J.; Elmore, A.C.; et al. Importance and Vulnerability of the World's Water Towers. *Nature* **2020**, *577*, 364–369. [CrossRef]
6. NTNC National Trust for Nature Conservation. *Annual Report 2022 | The National Trust for Nature Conservation (NTNC)*, National Trust for Nature Conservation (NTNC) Khumaltar: Lalitpur, Nepal, 2022.
7. Dupuits, E.; Llambí, L.D.; Peralvo, M. Implementing Climate Change Adaptation Policies Across Scales: Challenges for Knowledge Coproduction in Andean Mountain Socio-Ecosystems. *Mt. Res. Dev.* **2022**, *42*, A1–A11. [CrossRef]

8. Aryal, J.P.; Sapkota, T.B.; Khurana, R.; Khatri-Chhetri, A.; Rahut, D.B.; Jat, M.L. Climate Change and Agriculture in South Asia: Adaptation Options in Smallholder Production Systems. *Environ. Dev. Sustain.* **2020**, *22*, 5045–5075. [CrossRef]
9. Sharma, A.; Goyal, M.K. Assessment of Ecosystem Resilience to Hydroclimatic Disturbances in India. *Glob. Chang. Biol.* **2018**, *24*, e432–e441. [CrossRef]
10. Nalau, J.; Verrall, B. Mapping the Evolution and Current Trends in Climate Change Adaptation Science. *Clim. Risk Manag.* **2021**, *32*, 100290. [CrossRef]
11. Galappaththi, E.K.; Ichien, S.T.; Hyman, A.A.; Aubrac, C.J.; Ford, J.D. Climate Change Adaptation in Aquaculture. *Rev. Aquac.* **2020**, *12*, 2160–2176. [CrossRef]
12. Long, A. REDD+, Adaptation, and Sustainable Forest Management: Toward Effective Polycentric Global Forest Governance. *Trop. Conserv. Sci.* **2013**, *6*, 384–408. [CrossRef]
13. Yi, Y.; Shi, M.; Wu, J.; Yang, N.; Zhang, C.; Yi, X. Spatio-Temporal Patterns and Driving Forces of Desertification in Otindag Sandy Land, Inner Mongolia, China, in Recent 30 Years. *Remote Sens.* **2023**, *15*, 279. [CrossRef]
14. Kumar, P.; Patel, A.; Rai, J.; Kumar, P. Environmental Challenges and Concurrent Trend of Weather Extremes over Uttarakhand Himalaya. *Theor. Appl. Climatol.* **2024**, *155*, 1217–1246. [CrossRef]
15. Paudel, B.; Zhang, Y.L.; Li, S.C.; Liu, L.S.; Wu, X.; Khanal, N.R. Review of Studies on Land Use and Land Cover Change in Nepal. *J. Mt. Sci.* **2016**, *13*, 643–660. [CrossRef]
16. Risna, R.A.; Prasetyo, L.B.; Lughadha, E.N.; Aidi, M.N.; Buchori, D.; Latifah, D. Forest Resilience Research Using Remote Sensing and GIS—A Systematic Literature Review. *IOP Conf. Ser. Earth Environ. Sci.* **2023**, *1266*, 012086. [CrossRef]
17. Bandyopadhyay, D.; Mukherjee, S.; Singh, G.; Coomes, D. The Rapid Vegetation Line Shift in Response to Glacial Dynamics and Climate Variability in Himalaya between 2000 and 2014. *Env. Monit Assess* **2022**, *195*, 70. [CrossRef] [PubMed]
18. Li, B.V.; Jenkins, C.N.; Xu, W. Strategic Protection of Landslide Vulnerable Mountains for Biodiversity Conservation under Land-Cover and Climate Change Impacts. *Proc. Natl. Acad. Sci. USA* **2022**, *119*, e2113416118. [CrossRef] [PubMed]
19. IPCC. *Climate Change and Land An IPCC Special Report on Climate Change, Desertification, Land Degradation, Sustainable Land Management, Food Security, and Greenhouse Gas Fluxes in Terrestrial Ecosystems*; IPCC: Geneva, Switzerland, 2019.
20. Lemenkova, P. Evaluating Land Cover Types from Landsat TM Using SAGA GIS for Vegetation Mapping Based on ISODATA and K-Means Clustering. *Acta Agric. Serbica* **2021**, *26*, 159–165. [CrossRef]
21. Demberel, O.; Munkhbat, B.; Dorjsuren, B.; Callaghan, T.V.; Tsogoo, B.; Zemtsov, V.A.; Shaarav, O.; Gongor, E.; Jargalsaikhan, Z.; Ganhuyag, N.; et al. Relationship between Dynamics of Modern Glaciers of the Mt. Munkhkhairkhan (Mongolian Altai) and Climate. *Water* **2023**, *15*, 1921. [CrossRef]
22. Dad, J.M.; Muslim, M.; Rashid, I.; Rashid, I.; Reshi, Z.A. Time Series Analysis of Climate Variability and Trends in Kashmir Himalaya. *Ecol. Indic.* **2021**, *126*, 107690. [CrossRef]
23. Barrett, K.; Bosak, K. The Role of Place in Adapting to Climate Change: A Case Study from Ladakh, Western Himalayas. *Sustainability* **2018**, *10*, 898. [CrossRef]
24. Baral, N.; Heinen, J.T. Regulatory Compliance of Community-Based Conservation Organizations: Empirical Evidence From Annapurna Conservation Area, Nepal. *Sustainability* **2020**, *12*, 9420. [CrossRef]
25. Baral, N.; Stern, M.J.; Heinen, J.T. Integrated Conservation and Development Project Life Cycles in the Annapurna Conservation Area, Nepal: Is Development Overpowering Conservation? *Biodivers. Conserv.* **2007**, *16*, 2903–2917. [CrossRef]
26. Shrestha, S.; Poudel, D.D.; Duex, T.W.; Yantis, R.B. Changing Climatic Conditions Affect Snow Cover in Annapurna Region of Nepal. *Strateg. Plan. Energy Environ.* **2023**, *41*, 215–240. [CrossRef]
27. Bhatta, K.P.; Aryal, A.; Baral, H.; Khanal, S.; Acharya, A.K.; Phomphakdy, C.; Dorji, R. Forest Structure and Composition under Contrasting Precipitation Regimes in the High Mountains, Western Nepal. *Sustainability* **2021**, *13*, 7510. [CrossRef]
28. Konchar, K.; Staver, B.; Salick, J.; Chapagain, A.; Joshi, L.; Karki, S.; Lo, S.; Paudel, A.; Subedi, P.; Ghimire, S.K. Adapting in the Shadow of Annapurna: A Climate Tipping Point. *J. Ethnobiol.* **2015**, *35*, 449–471. [CrossRef]
29. Soenen, S.; Peddle, D.; Coburn, C. A Modified Sun-Canopy-Sensor Topographic Correction in Forested Terrain. *IEEE Trans. Geosci. Remote Sens.* **2005**, *43*, 2148–2159. [CrossRef]
30. Sola, I.; González-Audícana, M.; Álvarez-Mozos, J. Multi-Criteria Evaluation of Topographic Correction Methods. *Remote Sens. Environ.* **2016**, *184*, 247–262. [CrossRef]
31. Conrad, O.; Bechtel, B.; Bock, M.; Dietrich, H.; Fischer, E.; Gerlitz, L.; Wehberg, J.; Wichmann, V.; Böhner, J. System for Automated Geoscientific Analyses (SAGA) v. 2.1.4. *Geosci. Model Dev.* **2015**, *8*, 1991–2007. [CrossRef]
32. Kendall, M.G. *Rank Correlation Methods*; Griffin: Oxford, UK, 1948.
33. Mann, H.B. Nonparametric Tests Against Trend. *Econometrica* **1945**, *13*, 245. [CrossRef]
34. Sen, P.K. Estimates of the Regression Coefficient Based on Kendall's Tau. *J. Am. Stat. Assoc.* **1968**, *63*, 1379–1389. [CrossRef]
35. WHO/UNICEF. Joint Monitoring Program for Water Supply, Sanitation and Hygiene (JMP)—Progress on Household Drinking Water, Sanitation and Hygiene 2000–2017. Available online: https://www.unwater.org/publications/who/unicef-joint-monitoring-program-water-supply-sanitation-and-hygiene-jmp-progress (accessed on 30 March 2024).

36. Hedenås, H.; Christensen, P.; Svensson, J. Changes in Vegetation Cover and Composition in the Swedish Mountain Region. *Environ. Monit. Assess.* **2016**, *188*, 452. [CrossRef] [PubMed]
37. Rumpf, S.B.; Gravey, M.; Brönnimann, O.; Luoto, M.; Cianfrani, C.; Mariethoz, G.; Guisan, A. From White to Green: Snow Cover Loss and Increased Vegetation Productivity in the European Alps. *Science* **2022**, *376*, 1119–1122. [CrossRef]
38. Saavedra, F.A.; Kampf, S.K.; Fassnacht, S.R.; Sibold, J.S. Changes in Andes Snow Cover from MODIS Data, 2000–2016. *Cryosphere* **2018**, *12*, 1027–1046. [CrossRef]
39. Shafiq, M.U.; Ahmed, P.; Islam, Z.U.; Joshi, P.K.; Bhat, W.A. Snow Cover Area Change and Its Relations with Climatic Variability in Kashmir Himalayas, India. *Geocarto Int.* **2019**, *34*, 688–702. [CrossRef]
40. Filla, M.; Lama, R.P.; Filla, T.; Heurich, M.; Balkenhol, N.; Waltert, M.; Khorozyan, I. Patterns of Livestock Depredation by Snow Leopards and Effects of Intervention Strategies: Lessons From the Nepalese Himalaya. *Wildl. Res.* **2022**, *49*, 719–737. [CrossRef]
41. Wood, L.R.; Neumann, K.; Nicholson, K.N.; Bird, B.W.; Dowling, C.B.; Sharma, S. Melting Himalayan Glaciers Threaten Domestic Water Resources in the Mount Everest Region, Nepal. *Front. Earth Sci.* **2020**, *8*, 128. [CrossRef]
42. Maurer, J.M.; Schaefer, J.M.; Rupper, S.; Corley, A. Acceleration of Ice Loss across the Himalayas over the Past 40 Years. *Sci. Adv.* **2019**, *5*, eaav7266. [CrossRef] [PubMed]
43. Trenberth, K.E. Changes in Precipitation with Climate Change. *Clim. Res.* **2011**, *47*, 123–138. [CrossRef]
44. Bajracharya, S.; Glaciology, P.M.-A. Glaciers, Glacial Lakes and Glacial Lake Outburst Floods in the Mount Everest Region, Nepal. *Ann. Glaciol.* **2009**, *50*, 81–86. [CrossRef]
45. KC, K.B.; Tzadok, E.; Pant, L. Himalayan Ecosystem Services and Climate Change Driven Agricultural Frontiers: A Scoping Review. *Discov. Sustain.* **2022**, *3*, 35. [CrossRef] [PubMed]
46. Subedi, A.; Raut, N.; Gurung, S. How Himalayan Communities Are Changing Cultivation Practices in the Context of Climate Change. *Reg. Sustain.* **2023**, *4*, 378–389. [CrossRef]
47. van Zonneveld, M.; Turmel, M.-S.; Hellin, J. Decision-Making to Diversify Farm Systems for Climate Change Adaptation. *Front. Sustain. Food Syst.* **2020**, 4. [CrossRef]
48. Kumar, M.; Rathod, R.; Mukherji, A. Water Security and Spring Conservation in the Himalaya. In *Climate Risks to Water Security: Framing Effective Response in Asia and the Pacific*; Ojha, H., Schofield, N., Camkin, J., Eds.; Springer International Publishing: Cham, Germany, 2023; pp. 15–36, ISBN 978-3-031-16648-8.
49. Restrepo-Mieth, A.; Perry, J.; Garnick, J.; Weisberg, M. Community-Based Participatory Climate Action. *Glob. Sustain.* **2023**, *6*, e14. [CrossRef]

Disclaimer/Publisher's Note: The statements, opinions and data contained in all publications are solely those of the individual author(s) and contributor(s) and not of MDPI and/or the editor(s). MDPI and/or the editor(s) disclaim responsibility for any injury to people or property resulting from any ideas, methods, instructions or products referred to in the content.

sustainability

MDPI

Article

Risk Spillover Effects in Energy Markets Under Climate Change: Evidence from the Chinese Market

Shufen Cao [1], Min Pang [1,*], Yongtan Ma [1], Qianyu Dong [1] and Yongping Tao [2]

[1] School of Economics and Management, Southwest Petroleum University, Chengdu 610500, China; a757970304@126.com (S.C.); mayongtan@163.com (Y.M.)
[2] China National Petroleum Corporation Drilling Fluid Technical Service Company, Sichuanqing Drilling Engineering Co., Chengdu 610051, China
* Correspondence: milier0106@163.com

Abstract: To ascertain the impact of climate change on risk spillovers in energy markets, the vector autoregressive (VAR) model and the impulse response function (IRF) were utilized to analyze risk spillover effects in China's energy markets between 2007 and 2023. The findings indicated that the risk spillover from climate change in China's energy markets is characterized by asymmetric and time-varying characteristics. A substantial degree of heterogeneity exists among distinct energy markets. Climate physical risk has a detrimental effect on risk spillovers in energy markets, while transition risk has a positive impact on risk spillover in fuel, LPG, and natural gas markets, and a negative effect on risk spillover in alcohol, gasoline, and diesel markets.

Keywords: climate change; Chinese energy market; risk spillover effects; VAR model; impulse response function (IRF); asymmetric dynamics; transition risk; physical risk

1. Introduction

In the twenty-first century, the frequency of extreme weather events has posed a direct threat to the survival of the human environment and has also had an unprecedented impact on the stability of the global economic system, particularly the energy market [1]. A substantial corpus of research has demonstrated that climate change has become one of the most pressing challenges confronting the global community. Climate change has far-reaching implications for risk spillovers in energy markets. Risk spillover is defined as the transmission of risk from one market to other institutions or markets through related operations or inter-market linkages. Extreme climate change affects energy supply and demand and energy market transformations, which in turn affects energy market risk spillovers [2]. On the one hand, the increased frequency of extreme weather events has led to a rise in energy demand, which in turn has triggered an imbalance between energy supply and demand as well as large fluctuations in energy prices [3]. On the other hand, persistent climate change has prompted governments to implement stringent emission reduction policies and to promote the energy transition, which in turn has affected risk spillovers in energy markets [4]. Consequently, a comprehensive examination of the interplay between climate change and its repercussions on the energy market is imperative to ensure its stability.

As the world's largest energy consumer and carbon emitter, China has a highly sophisticated and complex energy market. In recent years, the frequency and intensity of extreme weather events in China have significantly increased, further exacerbating the risk of spillover effects within the energy market [5,6]. Moreover, China's energy market

volatility exerts a substantial influence on the domestic economy, as well as on the global energy market through international trade and financial channels [7]. Therefore, this paper focuses on the impact of climate change on risk spillovers in China's energy markets, identifying how different types of risks (physical and transition risks) affect market stability.

We used the vector autoregressive (VAR) model and impulse response function (IRF) to analyze risk spillover effects in China's energy markets between 2007 and 2023 and found that the risk spillover from climate change of China's energy markets is asymmetric and time-varying. Clear heterogeneity exists between various energy markets: alcohol, gasoline, and diesel markets play the role of net spillovers, fuel and LPG markets play the role of spillover recipients, with risk spillover fluctuating between −20% and 25%. Risks posed by climate change can be categorized into physical and transition risks. Physical risk negatively impacts risk spillover in energy markets, but the impact of transition risk shows a different result. Transition risk positively impacts risk spillover in fuel, LPG, and natural gas markets, and negatively impacts risk spillover in alcohol, gasoline, and diesel markets.

This paper makes a significant contribution to the extant literature in several ways. Firstly, it explores the impact of climate change on risk spillovers in energy markets in terms of both physical risk and transition risk dimensions. This expands the perspective of existing studies that focus on transition risk. For example, Liu, Z. et al. analyzed the impact of climate policy uncertainty on risk spillovers between energy markets. In contrast, this paper further complements the physical risk dimension [4]. Secondly, this paper utilizes extensive energy market data encompassing various sectors, including fuel, alcohol, LPG, natural gas, petrol, and diesel, thereby expanding the scope beyond the limitations of previous studies that predominantly focused on oil and gas markets [8]. The objective is to furnish a scientific foundation and decision support for the formulation of climate-proofing policies for the energy market.

The remainder of this paper is organized as follows. Section 2 describes the literature review on the relationship between climate change and the energy market, and risk spillover effects in energy markets. Section 3 delineates data, variables, and methods. Section 4 reports the empirical results. Section 5 concludes the paper.

2. Literature Review

A substantial body of research has demonstrated the impact of climate change on risk spillovers in energy markets [9]. To analyze the impact of climate change on the risk spillover effect of energy markets in depth, the following discussion will be carried out at two levels. Firstly, existing studies and relevant theories on the relationship between climate change and energy markets and their mechanism of action will be systematically summarized and analyzed. Secondly, the methodology of measuring the risk spillover effect of energy markets from the perspective of climate change influencing the risk spillover effect of energy markets will be analyzed.

2.1. Climate Change and Energy Markets

In recent years, the increase in extreme weather events has brought the issue of climate change in energy markets to the forefront of growing academic attention. It is widely recognized in academia that the physical and transition risks associated with climate change pose a dual threat to the stability of energy markets. The term "physical risk" is used to denote the direct impact of extreme weather events on the energy market, while "transition risk" refers to the consequences of human actions aimed at addressing climate change. These actions may include the implementation of climate policies, technological upgrades, shifts in public sentiment, and disruptive innovations in business models [10].

Physical risk has been shown to exert a significant influence on the energy supply balance. From the supply-side perspective, physical risks, including natural disasters and extreme weather events such as droughts, heavy rains, and floods, have the potential to damage energy infrastructure, thereby affecting energy production and transportation, and thus energy prices and market stability. Furthermore, climate change may also affect energy supply through impacts on hydroelectric power generation (due to declining water levels resulting from increased evaporation from rivers and lakes) and renewable energy output (due to changes in wind speeds affecting the efficiency of wind power generation and changes in precipitation patterns affecting solar power generation) [11]. From the demand-side perspective, shifts in temperature and an escalation in the frequency and intensity of extreme weather events have the potential to disrupt established energy demand patterns [12]. For instance, high-temperature heat waves may lead to an increased demand for electricity, while cold snaps may result in a heightened demand for heating energy. These changes may consequently exert an influence on prices and the equilibrium between supply and demand within energy markets. In the long term, frequent extreme weather events may compel energy companies to reassess their production strategies in favor of investing in more resilient infrastructure, thus affecting the stability of energy supply and cost structure. A substantial body of research has demonstrated a considerable correlation between energy market volatility and climate change, with the latter posing a challenge to the stability of energy markets [13,14].

Transition risk exerts its influence on energy markets principally through policy effects, namely a series of policy measures formulated and implemented by governments to achieve the objectives of reducing greenhouse gas emissions, enhancing energy efficiency, and promoting the development of renewable energy sources [15]. These policies impact the energy market in terms of energy prices, energy supply and demand, energy investment, market structure, and technological innovation. Specifically, China has implemented policies such as the carbon tax and the carbon emissions trading system, which have increased the cost of fossil energy and thus affected energy prices. Furthermore, China has promoted a clean energy strategy, which has led to a decline in the demand for some traditional energy sources and a rise in the demand for clean energy. China has promoted an energy transition policy, which has led to an increase in investment in research and development of clean energy, and a significant increase in the supply of clean energy. China has proposed a carbon-neutral target for carbon peaks, which has led to a transformation of the energy mix and has significantly increased the supply of clean energy. These have contributed to the transformation of the energy mix, leading to an increase in the share of renewable energy sources such as wind and solar in the energy mix. Furthermore, China has encouraged energy-intensive industries to invest in energy-efficient technologies, leading to enhanced energy efficiency and optimized energy utilization [16,17]. In summary, policies drive energy markets. However, uncertainty surrounding the precise design of policies and their implementation may lead to increased concerns among market participants regarding the direction and cost of the market. Investors in energy markets are more sensitive to information about climate policies, which contributes to heightened uncertainty and risk spillover in energy markets [18,19].

Furthermore, it is evident that physical and transition risks do not operate in isolation within the energy market. Rather, they interact with each other, contributing to a dynamic and evolving risk landscape. In the event of transition risk being disregarded and inadequate policy measures being implemented to address climate change, there will be an increased likelihood of facing physical risk. Conversely, if radical transition measures are taken without considering the current state of industry development, higher transition risk

will be triggered in the short term. In summary, physical and transition risks interact in energy markets and together affect the stability of energy markets.

2.2. Risk Spillover Effects in Energy Markets

The energy market risk spillover effect is described as the process by which the risk of one market is transferred to another, thereby affecting the stability of the entire energy system [20]. In the context of globalization and the rapid development of financial markets, the increasing interdependence between energy markets has led to an increasingly significant risk spillover effect. In addressing this imperative, the academic community has devised an array of methodologies to investigate this phenomenon, encompassing vector autoregressive (VAR) models, generalized autoregressive conditional heteroskedasticity (GARCH) models, Copula methods and spillover index methods [21].

The utilization of VAR models, which possess the capacity to analyze the dynamic relationships between multiple time-series variables, can facilitate a more profound comprehension of the impacts of policy changes and external shocks on the energy market [22,23]. He Zhifang and Zhong Miaoqing examined the dynamic relationship between climate policy uncertainty, global energy prices, and stock prices through VAR models and found that the spillover effects of climate policy uncertainty on energy prices and stock prices have obvious time-varying characteristics [24]. Nonetheless, the majority of extant research in this area explores risk spillovers between energy markets from a single dimension only, thereby failing to fully integrate synergistic research on physical and transition risks.

GARCH models capture the volatility aggregation and conditional heteroskedasticity of time-series data, which helps to predict market volatility more accurately. Liu, Z. et al. utilized a GARCH model to analyze the impact of climate policy uncertainty on extreme risk spillover in the energy market [4]. Chai et al. utilized the DCC-GARCH model and the LSTAR model to analyze the time-varying linkages between the North American crude oil and natural gas markets, thereby providing insights into the nonlinear volatility characteristics of the trend-directed correlations between the two markets [25]. Qian et al. have investigated the intricate interdependency structure and risk spillovers among international markets by employing a range of models, including GARCH, EGARCH, and GJR-GARCH [25]. However, GARCH models present a challenge in analyzing the interdependencies among multiple time series simultaneously, thereby hindering the effective analysis of complex relationships among multiple energy markets.

The Copula approach has been extensively employed to model the dependence structure between markets, owing to its efficacy in handling nonlinear relationships and tail dependence. Chen Di et al. utilized the EVT-Copula-CoVaR model to quantify the risk spillover effects of the oil market on the Chinese carbon market, while the DCC-GARCH model was employed to capture the time-varying correlation of market fluctuations [26,27]. Diebold and Yilmaz proposed the spillover index method, which provides a direct measure to quantify the volatility spillover between markets [28]. Qingjun Zhang and Yanming Yang analyzed the risk spillover from carbon-intensive industries to the banking sector based on the DY index [29]. Nonetheless, the COVAR method prioritizes the examination of direct risk spillovers and places less emphasis on indirect risk spillover effects. This methodological approach may not always guarantee the requisite precision when confronted with nonlinear relationships. Furthermore, scholars have utilized Granger causal networks and dynamic network analysis to identify intricate relationships and risk propagation pathways between markets. Aiying Zhang et al. utilized nonlinear Granger causality to provide an in-depth analysis of the dynamic characteristics of China's energy price and stock market [30].

In summary, the utilization of VAR models in the analysis of climate change's impact on risk spillovers within energy markets offers three distinct advantages. Primarily, VAR models possess the capability to discern the dynamic interactions among multiple time series, rendering them well suited for the examination of the intricate relationship between climate change and energy markets. Secondly, the impact of climate change on the energy market is time-varying, particularly during extreme events (e.g., the New Crown epidemic, and the Russian–Ukrainian conflict). In such cases, the risk spillover effect is significantly enhanced, and the VAR model is capable of capturing this time-varying feature. Finally, the incorporation of multiple variables (e.g., various energy markets) into the VAR model facilitates simultaneous analysis, thereby enabling a comprehensive exploration of market interactions. In view of this, the present study adopts the VAR model combined with rolling windows to analyze the risk spillover effects in the energy market in order to reveal the trend of the risk spillover effects in different time periods. Through the utilization of impulse response analysis, the impact of climate change (physical risk and transition risk) on risk spillover in the energy market is explored in depth to reveal the dynamic transmission mechanism of climate change shocks and its characteristics over time. This provides a deeper understanding of how climate change propagates among energy markets and how climate change affects the stability of the energy market. Furthermore, it provides new perspectives and tools for the analysis of energy market stability and offers a more accurate perspective for relevant policy formulation and energy market risk management.

3. Data Description and Methodology

3.1. Data Description

Six representative energy prices of fuel (FM), alcohol (AM), liquefied petroleum gas (LPGM), natural gas (NGM), gasoline (GM), and diesel (DM) are selected as energy market metrics in China. We selected OPEC production cut data and WTI crude oil prices as our exogenous variables. The sample data of energy variables are obtained from the CEIC database. The OPEC production cut data are treated as a binary variable, where a value of 1 indicates the occurrence of an OPEC production cut in a given quarter, and a value of 0 indicates that no such cut occurred. The data were carefully compiled from the OPEC Monthly Oil Market Report. Considering the policy background, changes in the market environment, and data availability, the spot prices of the above six energy sources from January 2007 to December 2023 were selected as the study sample (see Table 1 and Figure 1).

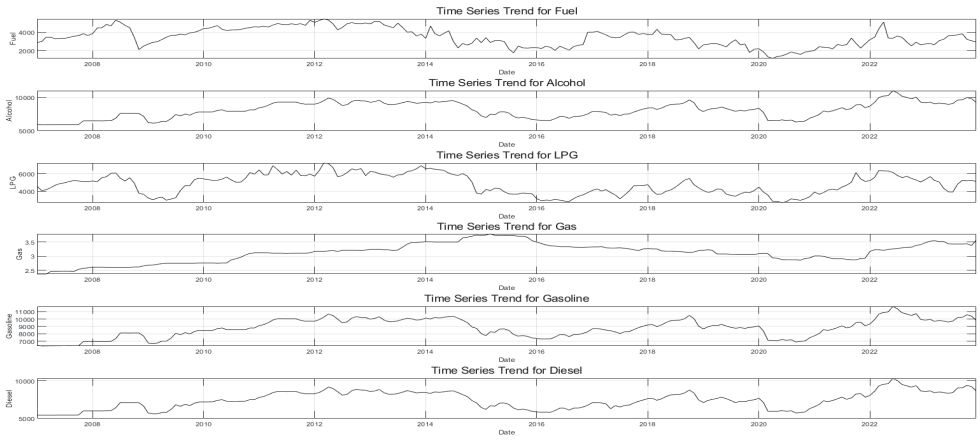

Figure 1. Monthly energy market data.

Table 1. Descriptive statistics.

Variable	Mean	Standard Deviation	Minimum	Median	Maximum	ADF
Fuel market (FM)	3472.39	1004.48	1161.00	3455.00	5450.00	−15.035 ***
Alcohol market (AM)	8110.62	1184.54	5900.50	8142.42	11,027.90	−10.367 ***
LPG market (LPGM)	4811.68	1133.86	2710.00	4950.00	8230.00	−11.900 ***
Natural gas market (NGM)	3.13	0.33	2.37	3.17	3.79	−9.800 ***
Gasoline market (GM)	8787.44	1236.96	6350.00	8791.06	11,713.78	−10.325 ***
Diesel market (DM)	7433.81	1140.16	5451.00	7402.59	10,341.62	−10.624 ***
Physical risk (PR)	37.12	12.50	12.25	36.50	56.33	−8.062 ***
Transition risk (TR)	52.55	3.30	47.59	52.51	61.20	−8.062 ***
OPEC production cuts	0.456	0.502	1.00	0.00	0.00	−11.402 ***
WTI crude oil	72.776	22.182	123.85	27.793	73.455	−6.381 ***

Note: * $p < 0.05$ level; ** $p < 0.01$; *** $p < 0.001$.

Physical risk refers to the direct damage to economic activities caused by extreme weather events and long-term climate trends resulting from climate change. Transition risk, on the other hand, represents the economic and financial risks to markets arising from factors such as changes in policy, technology, market sentiment, and consumer preferences as societies transition to a low-carbon economy. To quantify these risks in China, we have selected the climate risk index (CRI) and the Climate Change Performance Index (CCPI), both published by Germanwatch, as metrics for climate physical risk (PR) and transition risk (TR), respectively. The sample data for climate risk spans from 2007 to 2023, with all data being annual.

As a region with high climate vulnerability, China is highly susceptible to the significant impacts of climate change, and its climate physical risk index has been at a high level for a long time. Similar to small island countries and low-lying areas such as Bangladesh and the Philippines, which are more vulnerable to extreme weather events such as typhoons and floods, the climate risk index has also remained high. Transition risk is influenced by factors such as greenhouse gas emissions, the promotion of renewable energy, energy consumption, and the effectiveness of climate policies. In contrast, the Nordic countries, which are leaders in renewable energy utilization and climate policy implementation, have relatively low transition risks. China, on the other hand, has been at a relatively high level of transition risk due to its rapid industrialization, its energy structure still dominated by traditional fossil energy sources, and the fact that it is still in a stage of perfection in the promotion of renewable energy technologies and the implementation of climate policies.

Figure 2 provides information on the monthly volatility of six energy markets. Table 1 provides a descriptive statistical analysis of the data on China's energy market and climate risk indicators. The data in Table 1 demonstrates that, with regard to standard deviation, the volatility of the gasoline market (GM) is the most significant, with its standard deviation reaching 1236.96. This outcome aligns with market reality, given that gasoline, as the predominant energy source for transportation, possesses a relatively rigid demand, influenced by factors such as policy adjustments, international oil price fluctuations, and seasonal variations. Consequently, the gasoline market's volatility stands out. The mean values for alcohol (AM), gasoline (GM), and diesel (DM) are notably higher compared to those of other energy markets. This observation may be indicative of the heightened sensitivity of these three markets to external shocks, which may be associated with the pervasive utilization of these energy products in economic activities and the inflexible demand characteristics. Additionally, a degree of variability is observed in the statistical data between the variables in the table, which suggests that the selected variables can more effectively represent the diverse market characteristics and the level of risk. The

presence of such variability further validates the rationale behind the variable selection and establishes a robust foundation for the subsequent in-depth analysis. This discrepancy serves to reinforce the rationale behind variable selection, thereby establishing a robust foundation for the subsequent in-depth analysis.

Figure 2. Trends in price volatility.

The missing data are supplemented by the sample interpolation method, mainly because the energy market data involved in this study have certain nonlinear characteristics, and the sample interpolation method can better approximate these complex data relationships and provide more accurate estimates of the missing values. The effectiveness of this approach lies in its ability to reduce analytical bias due to missing data while preserving data smoothness and continuity, a crucial consideration in the study of dynamic relationships, such as those between climate change and its impact on the energy market. The spline interpolation method is notable for its numerical stability and convergence, which aid in avoiding the overfitting phenomenon and ensure the reliability of research outcomes.

This study employs the spline interpolation method for interpolation. To further evaluate the method's potential for data distortion and its impact on results. Setting 20% as the proportion of simulated missing data, the Mean Absolute Error (MAE) was calculated to be 44.3772, and the Relative Error was about 0.72%, which is significantly less than 1%. These findings demonstrate that the interpolation method does not distort the results.

To evaluate the smoothness of the data, we conducted the Augmented Dickey–Fuller (ADF) and Kwiatkowski–Phillips–Schmidt–Shin (KPSS) tests. The KPSS results showed that we could not reject the null hypothesis for all variables, confirming that the data were indeed smooth. The results of the ADF test indicated that we could reject the hypothesis of a unit root at the 1-percent significance level, further supporting the conclusion that the series was smooth (see Table 1).

3.2. Methodology

In this paper, the vector autoregressive (VAR) modeling framework is utilized and based on the generalized forecast error variance decomposition (FEVD) method to measure the linkages between energy markets.

The VAR model, in its smooth VAR (p) form with N-dimensional variables, is expressed in Equation (1). In order to ascertain the lag order p of the VAR model, the BIC information criterion is employed as a judgmental basis for selecting the optimal p as the model's final lag order.

$$x_t = \sum_{i=1}^{p} \varphi_i x_{t-i} + \varepsilon_t,\ \varepsilon_t \sim N(0,\ \sum) \tag{1}$$

x_t (t = 1,. . .,T) is a column vector of N dimensions, with ε_t representing the disturbance vector. The AVR (p) model is represented in the form of a vector moving average (VMA), as shown in Equation (2).

$$x_t = \sum_{i=1}^{\infty} A_i \varepsilon_{t-i} \tag{2}$$

A_i is an $N \times N$-dimensional coefficient matrix, satisfying $A_i = \varphi_1 A_{i-1} + \varphi_2 A_{i-2} + \cdots +]\varphi_p A_{i-p}$, $A_0 = I_{N\times N}$, $A_i = 0$, if $i < 0$.

The variance decomposition assesses the degree of influence of different variables on stochastic shocks by analyzing the H-period forecast error of any endogenous variable in the VAR (p) model and decomposing it into the contribution of stochastic shocks of each variable within the model. The traditional orthogonal variance decomposition is able to deal with the problem of inter-correlation of the stochastic disturbance terms of the endogenous variables of the model over the same period, but its results are susceptible to the ordering of the variables. In contrast, the generalized prediction error variance decomposition provides more robust decomposition results by accounting for the correlation of random shocks among variables based on the distributional properties of the random error terms in the historical data.

$\theta_{ij}(H)$ contribution of the random shock, defined as the H-step forecast mean square error of x_i ($i \neq j$), is calculated as shown in Equation (3).

$$\theta_{ij}(H) = \frac{\sigma_{ii}^{-1} \sum_{h=0}^{H-1} \left(e_i' A_h \sum e_j\right)^2}{\sum_{h=0}^{H-1} \left(e_i' A_h \sum A_h' e_i\right)} \tag{3}$$

σ_{ii} represents the standard deviation of the error term of the ith equation in the VAR model, and e_i represents the N-dimensional column vector whose ith component is 1 and the rest are 0. Due to the correlation between the components of the vector of random perturbation terms in the generalized prediction error variance decomposition, it follows that $\sum_{j=1}^{N} \theta_{ij}(H) \neq 1$.

In this paper, the comparability of the variance decomposition results is enhanced by standardizing the data across rows of the variance decomposition matrix. Concurrently, cognizance of the directionality of the role effect conduction is imperative, as it engenders an antithetical effect mechanism between each pair of variables. Consequently, $\widetilde{S}_{ij}(H)$ is used to represent the net effect of x_j on x_i, as delineated in Equations (4)–(6). In this paper, the observed energy market is used as x_i, and other energy markets are used as x_j, respectively, to test the net effect of the interaction between the energy markets [31].

$$S_{ij}(H) = \frac{\theta_{ij}(H)}{\sum_{J=1}^{N} \theta_{ij}(H)} \tag{4}$$

$$S_{ji}(H) = \frac{\theta_{ji}(H)}{\sum_{i=1}^{N} \theta_{ji}(H)} \tag{5}$$

$$\widetilde{S}_{ij}(H) = S_{ij}(H) - S_{ji}(H) \tag{6}$$

$S_{ji}(H)$ represents the mean of the effect of the influence of x_i on variable x_j, and $\widetilde{S}_{ij}(H)$ represents the mean difference in the interaction effect between the variables. Given that the distribution of the mean data is non-normal, it follows that traditional parametric tests may not be applicable. Consequently, this study employed the one-sided Wilcoxon rank sum test to ascertain statistical significance by comparing the rank order of the data [32].

4. Empirical Results and Analysis

4.1. Analysis of Risk Spillover Within Energy Markets

4.1.1. Static Analysis of Risk Spillover Within Energy Markets

The net spillover indices of the six energy markets are calculated to be 8.10%, 15.90%, 7.89%, 0.25%, 15.71%, and 15.83%. The static analysis of spillover effects reveals several noteworthy results. Firstly, the average spillover from the energy market as a whole is 10.61%. These data indicate that, in addition to the variables themselves, 10.61% of the extreme risk in the market is derived from the spillover effect between the energy markets. Secondly, the alcohol market, the gasoline market, and the diesel market have high spillover indices across the entire energy market, and there is a strong bi-directional volatility. It is evident that these three markets exhibit reduced susceptibility to volatility spillovers from other markets. Their own volatility spillovers to other markets exert a more substantial impact on the net spillover. Thirdly, the natural gas market demonstrates the weakest risk spillover and spillover effects, primarily due to natural gas's status as the most prevalent and relatively affordable energy source, which leads to a comparatively high level of price stability, and a comparatively limited ability to pass on volatility. Fourthly, the fuel and LPG markets both exhibit a net reception of spillovers from other markets, while being more influenced by spillovers from these markets.

4.1.2. Dynamic Analysis of Risk Spillover Within Energy Markets

In order to accurately capture the dynamic of the risk spillover effect within the energy market, this paper conducted a dynamic rolling spillover analysis of the sample data using a rolling window of 24 months to dissect the time-varying characteristics of the volatility spillover between the energy markets. The results of the analysis are shown in Figures 3 and 4. As demonstrated in Figures 3 and 4, the overall volatility level of energy markets is substantial, with a volatility range of −20% to 25%. This indicates that the total volatility spillover in energy markets exhibits significant time-varying characteristics and generally follows the law of gradual stabilization after sharp fluctuations.

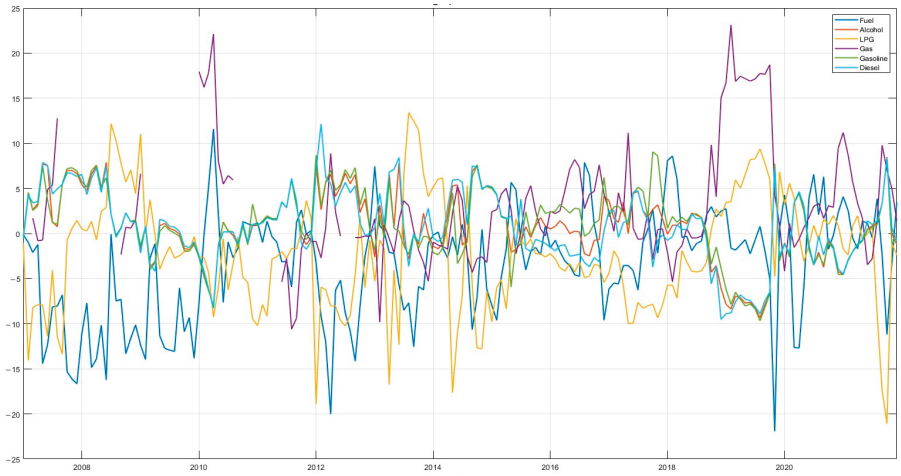

Figure 3. Dynamic spillover of risks within energy markets.

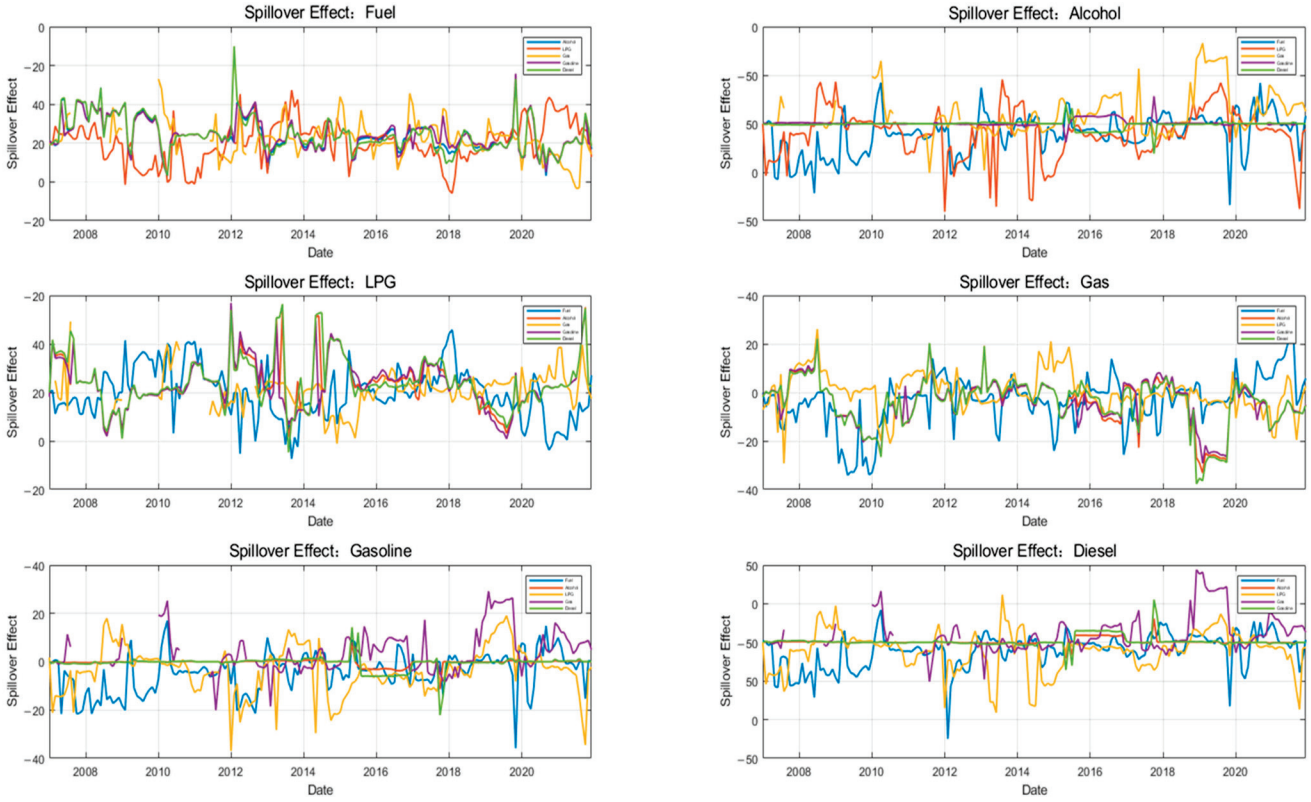

Figure 4. Dynamic spillover of risks within energy markets.

Specifically, the risk premium of each energy market is characterized by a clear asymmetry. The risk premium of the fuel market exhibits significant fluctuations, ranging from −20% to 10%, with the widest range of fluctuation. The spillover effect is predominantly negative, indicating that the fuel market is a recipient of risk premiums. This phenomenon is primarily attributable to the pivotal role of fuel in global energy consumption, its profound sensitivity to international crude oil prices, and the potential for significant risk spillovers in the fuel market in the event of supply disruptions or shifts in demand [33].

The risk spillover ranges for alcohol, gasoline, and diesel markets are −10% to 10%, with analogous overall spillover trends. This phenomenon may be attributed to the fact that gasoline and diesel are derived from analogous fuels and share common steps in their production and refining processes. Conversely, alcohol is predominantly utilized as a substitute or supplement for gasoline and diesel in transport fuels. The interplay between

supply and demand in the alcohol energy market exerts a significant influence on its prices and market volatility, which tend to exhibit a concomitant pattern [34].

The risk premium volatility of the LPG market ranges from −20% to 10%, with a wide range of fluctuations. This phenomenon can be attributed to the primary sourcing of LPG from refinery by-products, resulting in a strong correlation between LPG prices and international crude oil prices. Consequently, fluctuations in oil prices directly impact LPG prices. In contrast, the natural gas market exhibits a risk spillover volatility range of −10% to 20% and a frequent fluctuation range of between −10% and 10%, with a lower frequency of fluctuations. This is primarily attributable to the substantial size of the natural gas market, its relatively low price, and its relative stability.

It is evident that three distinct key points exist in the risk spillover across energy markets. Firstly, circa 2010, all five energy markets—fuel (FM), natural gas (NGM), alcohol (AM), gasoline (GM), and diesel (DM)—exhibited extreme values for that period. Specifically, the markets for fuel and natural gas exhibited remarkably high values, while the remaining three markets, namely alcohol, gasoline, and diesel, demonstrated significantly lower values. This observation suggests that the markets for fuel and natural gas experienced substantial risk spillovers during the observed period, while the markets for alcohol, gasoline, and diesel were subject to considerable risk spillover. This phenomenon may be attributed to the global economy's recovery from the 2010 financial crisis and the subsequent rise in demand for fuel and natural gas, driven by increased industrial activity in China.

Secondly, around 2012, the energy markets once again exhibited the extremes of that period. The three markets of fuel, LPG, and natural gas reached the extreme values of this phase, and the three markets of alcohol, gasoline, and diesel reached the extreme values of this phase. This indicates that the three markets of fuel, LPG, and natural gas exhibit large risk spillover, while the three markets of alcohol, gasoline, and diesel are subject to large risk spillover.

Thirdly, risk spillover across energy markets demonstrates sharp fluctuations between 2019 and 2020. The spillover effects in the fuel, LPG, gasoline, and diesel markets exhibit a rapid rise from a minimum to a maximum, while the natural gas and alcohol markets experience spillover effects that reach an extreme value and then rapidly decrease to a very small value. This phenomenon can be attributed primarily to the substantial impact of the COVID-19 outbreak on energy markets, which resulted in a notable shift in risk spillover across various energy sectors. This observation underscores the existence of a discernible correlation between energy markets. Subsequent to this, the energy markets have exhibited a return to a median volatility level, indicative of the robust resilience of the energy markets and the relative stability of the market [35].

4.2. Impulse Response of Physical Risk

This paper employs the technique of impulse response analysis in order to comprehensively assess the impact of climate change on energy market risk spillover. The impact of climate change on energy market risk spillover has been classified into physical risk and transition risk [36]. Consequently, this paper will analyze their impact on energy market risk spillover from the perspectives of physical risk and transition risk.

The time-series characteristics of each variable and the data situation are taken into account in the setting of the rolling window, which is set to 50. The horizontal axis indicates the duration of the shock effect in quarters, and the vertical axis indicates the size of the shock. The results of the impulse response analysis of physical risk to energy market risk spillover are illustrated in Figure 5.

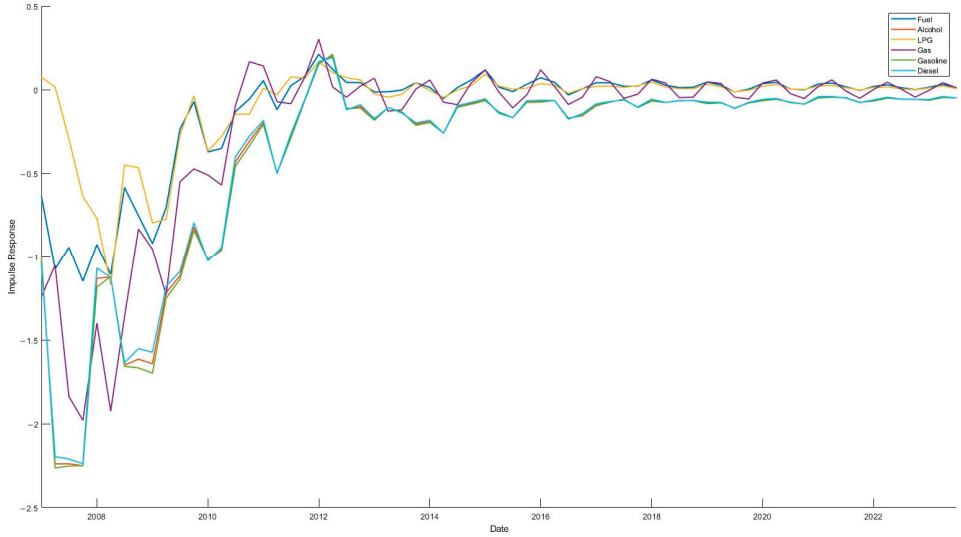

Figure 5. Physical risk impulse response analysis.

The findings reveal predominantly negative shocks, with shock values generally below zero. The trend of the impact of physical risk on each energy market is relatively similar, with all the sharp fluctuations gradually tending to be stable. By period 25, the volatility of each energy market narrows, and the fluctuations in the later period are seasonal, which is consistent with the basic law of energy demand and supply. This finding is consistent with the conclusions of Gu et al., which further corroborates the association between physical risk and risk spillover in energy markets [10].

The overall impact of physical risk on risk spillover in the energy market is predominantly negative, with shock values predominantly below zero. Specifically, the overall trend of physical risk shocks to the three markets—gasoline, alcohol, and diesel—is similar, with impulse response values fluctuating between −2.5 and 0, reaching a maximum negative shock in period 3 and a minimum response in period 21, followed by a reduction in the magnitude of the fluctuations, which ultimately leveled off. This finding suggests that this market segment is particularly susceptible to physical risk, primarily due to the primary application of these energies as a means of transportation, a sector that is susceptible to the impacts of extreme weather events. For instance, extreme weather events can result in the disruption of transport routes, the closure of petrol stations, or sudden fluctuations in demand, which can influence prices and the balance of supply and demand within these energy markets [3].

The impulse response values of physical risk to the natural gas market are between −2.0 and 0, indicating moderate volatility, with the maximum negative shock value occurring in period 4 and the minimum response value in period 21. This is followed by gradual small upward and downward fluctuations, eventually leveling off, and more pronounced seasonal fluctuations in the later periods. The primary factor contributing to this phenomenon is the classification of natural gas as a clean energy source. The market scale of natural gas is expanding in a gradual manner under the influence of clean energy policy and consumer preferences. Additionally, natural gas's predominant role as a heating energy source renders it more susceptible to seasonal fluctuations.

The impulse responses of physical risk to the LPG and fuel markets are all between −1.5 and 0, with maximum negative shocks in periods 4 and 6, respectively, and a minimum in period 21, followed by small upward and downward fluctuations and eventually leveling off. This observation indicates that the market demonstrates a relatively smoother response to physical risks, which may be attributable to the utilization of these energy sources being more decentralized and generally characterized by more stable supply and storage systems.

4.3. Impulse Response of Transition Risk

The time-series characteristics of each variable and the data situation are taken into account, and the rolling window is set to 50. The horizontal axis indicates the duration of the shock effect in quarters, and the vertical axis indicates the size of the shock. The results of the impulse response analysis of transition risk on energy market risk spillover are illustrated in Figure 6.

The findings reveal a consistent trend in the transition risk shocks across various energy markets, with a gradual shift towards smoother performance as the volatility of sharp fluctuations diminishes. The initial shocks of transition risk to energy market risk spillover are predominantly negative, reflecting the concerns of each energy market about the uncertainty of transition, while subsequent positive shocks reflect the energy market's awareness of the new opportunities that transition may bring. As the market becomes acclimatized to the transition risk, the shock to energy markets from this risk gradually diminishes and tends to zero, thereby demonstrating the market's capacity for self-regulation and adaptation to the new normal.

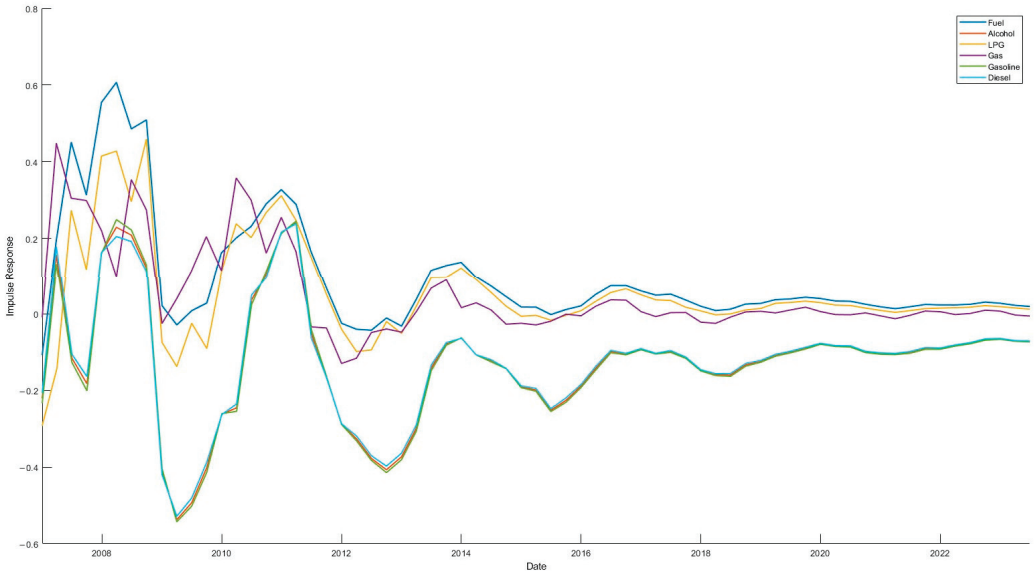

Figure 6. Transition risk impulse response analysis.

The impact of transition risk on the gasoline, alcohol, and diesel markets has been shown to exhibit a similar overall trend, characterized by significant fluctuations in the impulse response value, ranging from −0.6 to 0.2. These fluctuations reach a negative maximum in period 10, a positive maximum in the 18th period, and subsequently a negative minimum in period 25. Thereafter, a gradual decrease in the magnitude of the fluctuations is observed, leading to a state of relative stability. This observation indicates that this market segment is more susceptible to transition risks, primarily due to the potential for significant fluctuations in demand during the transition phase. Conventional energy sources such as gasoline and diesel may be impacted by the substitution of novel energy sources, and the promotion of biofuels and renewable energy sources may exert an influence on the alcohol and diesel markets [3].

The impulse response values of transition risk to the natural gas market range from −0.1 to 0.4, indicating moderate volatility and predominantly positive shocks. It attains a positive maximum in period 3, after which the positive shocks exhibit a weakening trend, and the response value attains a negative maximum in period 21, followed by gradual small upward and downward fluctuations, which eventually level off, with seasonal fluctuations becoming more pronounced in the later period. This phenomenon can be attributed, at

least in part, to the pivotal role that natural gas, recognized for its clean and efficient characteristics, plays in the broader context of the energy transition. The expansion of the natural gas market has been influenced by the implementation of clean energy policies and consumer preferences, resulting in a gradual increase in market size. Transition policies have had a strengthening effect on the construction and operation of the natural gas market, thus helping to guarantee the security and stability of natural gas supply [37].

The impulse response value of transition risk to fuel market shocks ranges from -0.1 to 0.6, reaching a negative maximum in period 1, a positive maximum in period 6, and a response value of 0 in period 21, after which it undergoes small upward and downward fluctuations before ultimately stabilizing. The impulse response value of the transition risk to the LPG market shock ranges from -0.3 to 0.4, reaching a negative maximum in period 1, a positive maximum in period 8, and a response value of 0 in period 21, after which it gradually fluctuates up and down by a small margin and eventually stabilizes.

4.4. External Factors Analysis

This study aims to further explore the impact of external variables on risk spillovers in energy markets. To this end, OPEC production reduction policy and WTI crude oil price volatility are selected as external variables to be analyzed. The results indicate that both OPEC production reduction policy and WTI crude oil price volatility have an impact on risk spillover in the energy market, with WTI crude oil price volatility exhibiting a more significant impact.

The results of the impulse response analysis of the OPEC production cut policy on risk spillovers in the energy market are shown in Figure 7. The impact of OPEC production cuts on the alcohol, gasoline, and diesel markets is relatively analogous, with all generating negative shocks that peak in period 5, followed by sharp fluctuations, and then converge to zero in period 30, followed by reduced fluctuations and eventual leveling off. This phenomenon is primarily attributable to the direct correlation between OPEC production cuts and the subsequent increase in crude oil prices. The alcohol, gasoline, and diesel markets exhibit a high degree of correlation with crude oil prices. An increase in crude oil prices leads to higher production costs for these products, thereby generating a negative shock to the market. There is a similar impact of OPEC production cuts on fuel and LPG markets: the former exhibits a more pronounced positive shock in period 1, followed by a period of heightened volatility, attaining its maximum negative shock value in period 14, with the shock eventually converging to 0 in period 20. This is followed by a decline in fluctuations and subsequent stabilization. This phenomenon is primarily attributable to the diminished sensitivity of the fuel and LPG markets to fluctuations in crude oil prices, coupled with the prevailing market assumption that diminished supply will result in price escalation during the nascent phase of production cuts. The impact of OPEC's production cuts is most pronounced on the natural gas market, manifesting as a positive shock in period 1, followed by pronounced fluctuations, culminating in the maximum negative shock value in period 9, approaching zero in period 25, and subsequently exhibiting a decline in volatility. The fluctuations then decrease and eventually level off.

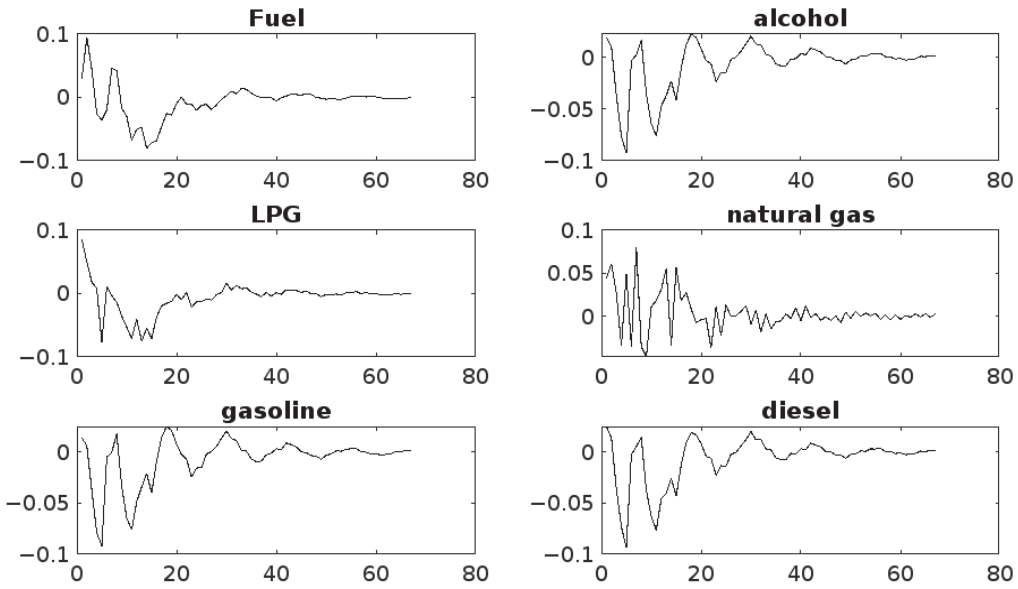

Figure 7. OPEC production cuts impulse response analysis.

The results of the impulse response analysis of the WTI crude oil price on risk spillovers in the energy market are shown in Figure 8. The impact of WTI crude oil price volatility on the fuel, alcohol, LPG, gasoline, and diesel markets is relatively similar. Alcohol, gasoline, and diesel markets reach their maximum shocks in period 3, LPG in period 4, and fuel market in period 8, and then the shock response decreases gradually, approaching zero in period 25, and then the volatility decreases and eventually stabilizes. This is mainly due to the fact that these markets are highly correlated with crude oil prices, as their production costs are directly dependent on crude oil prices, and fluctuations in WTI crude oil prices are quickly transmitted to these markets, leading to price changes. Fuel markets are relatively less responsive to crude oil price fluctuations, possibly because their production processes and inventory adjustments take longer. WTI crude oil price fluctuations have a more frequent impact on natural gas markets, with a maximum shock in period 2, followed by sharp fluctuations, a maximum negative shock in period 9, a maximum shock in period 14, and then decreasing fluctuations and eventually leveling off. This is mainly due to the uniqueness of the natural gas market, which is linked to the crude oil market but has significant differences. The supply and demand structure of natural gas is more complex, and its price is not only affected by the volatility of crude oil prices, but is also closely related to seasonal demand (e.g., winter heating), regional supply capacity, and policy direction.

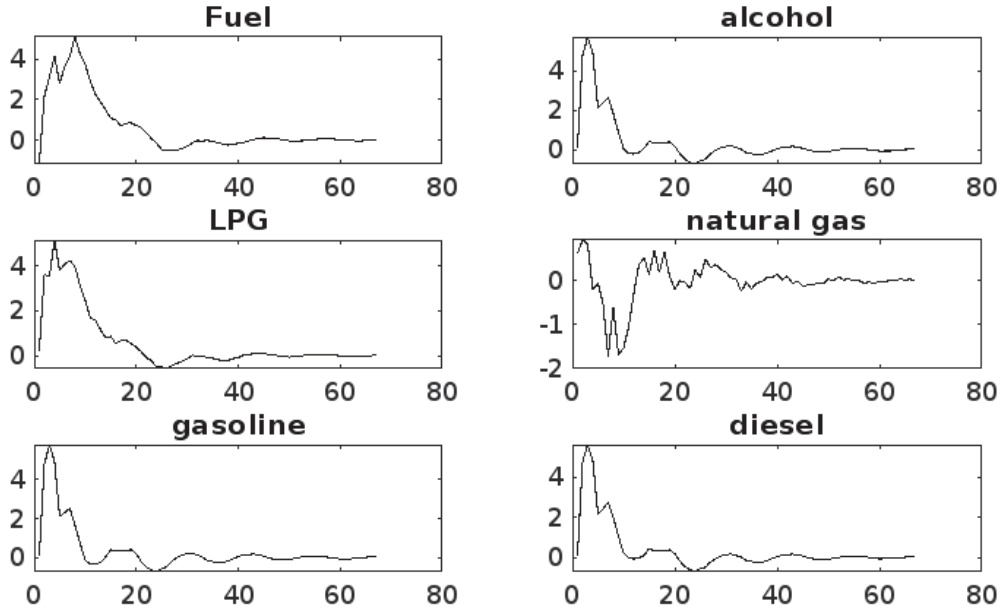

Figure 8. WTI crude oil impulse response analysis.

4.5. Robustness Testing

In the preceding section of this paper, the VAR model was used to analyze the energy market risk spillover effect of the energy market, to further validate the model VAR robustness. In the following, the test is performed by adjusting the model, specifically by using the GARCH model to re-examine the energy market risk spillover effect.

The estimation results of the univariate GARCH (1,1) and GARCH (1,0) models for each energy submarket in China are reported in Table 2. ω is the constant term, β is the coefficient of the GARCH term, and α is the coefficient of the ARCH term. From the results of the GARCH (1,1) model test, the coefficients of the constant term, the coefficients of the ARCH term, and the coefficients of the GARCH term for alcohol, LPG, and gasoline are all significant at the 1% level. The coefficients of the constant term, and the coefficients of the ARCH term for fuel, natural gas, and diesel were significant, but the coefficients of the GARCH term were not significant, so GARCH (0,1) was used for reestimation.

Table 2. GARCH model estimation result.

Market	GARCH (1,1)						GARCH (0,1)			
	ω	t	β	t	α	t	ω	t	α	t
FM	0.097	5.106	0.000	0.000	0.391	3.529	0.071	11.612	0.391	4.008
AM	0.023	4.213	0.175	1.967	0.576	4.252	0.033	7.812	0.608	4.088
LPGM	0.036	2.035	0.428	2.334	0.266	2.680	0.086	8.557	0.228	2.394
NGM	0.014	2.863	0.000	0.000	0.140	2.251	0.014	22.219	0.140	2.316
GM	0.021	4.457	0.208	2.369	0.562	4.217	0.033	7.971	0.582	3.964
DM	0.036	5.670	0.000	0.000	0.585	4.006	0.036	8.079	0.585	4.010

Note: FM = fuel market; AM = alcohol market; LPGM = liquefied petroleum gas market; NGM = natural market; GM = gasoline market; DM = diesel market.

A thorough validation of the GARCH model and the VAR model's impulse response analysis substantiates the rational self-consistency of the conclusions presented in this study. The study posits that the repercussions of climate change on risk spillover in the energy market can be elucidated by the differentiation mechanism of physical risk and transition risk. Furthermore, the volatility characteristics of disparate energy products are found to be intimately associated with their sensitivity and adaptive capacity to climate shocks. The

short-term abruptness characteristics of physical risk (e.g., extreme weather) are significant in high-ARCH-effect products (gasoline, alcohol, and diesel), whose volatility is mainly driven by upfront shocks and decays quickly, consistent with the phenomenon of impulse response in which violent negative shocks are followed by rapid stabilization. Conversely, low-ARCH-effect products, such as natural gas and LPG, exhibit a greater reliance on long-term fundamentals, attributable to the enhanced stability of their supply chains. This observation is reflected in a flat trend in the impulse response, indicative of a more stable underlying dynamic.

The long-term policy effect of transition risk is reflected by products with significant GARCH terms (alcohol, LPG, gasoline), whose volatility persistence ($\alpha + \beta \approx 0.7$) reflects the market's adaptation process to the gradual adjustment of the transition policy, and matches the dynamic path of the impulse response, whereby initial negative shocks gradually turn to the positive direction, and eventually stabilize. Conversely, the pure ARCH effect products (diesel, fuel) exhibit a lack of long-term volatility persistence, thereby directly reflecting the short-term impact of policy substitution. This observation aligns with the characteristics of the transition risk impulse response, which is characterized by small fluctuation amplitude and rapid decay. Additionally, natural gas, positioned as a clean energy transition catalyst, demonstrates low ARCH coefficients and seasonal fluctuation characteristics, thereby reinforcing its role as a policy dividend supporter. The impulse response of the positive shock dominant results is particularly noteworthy. In summary, the VAR model demonstrates robust performance.

5. Conclusions and Policy Implications

5.1. Conclusions

As the frequency and intensity of extreme weather events increased, energy markets faced more volatility and risk. China has implemented a variety of policies to address the energy market risks posed by climate change. However, frequent policy adjustments also affect energy markets and may exacerbate market volatility, thereby threatening energy security. In order to quantify the risk spillovers between energy markets in China and the impact of climate change on risk spillovers in energy markets, this study employs a VAR model to analyze risk spillovers between energy markets and applies an impulse response to analyze the impact of climate change on risk spillovers in energy markets. The primary conclusions that can be drawn from this analysis are as follows.

The average volatility spillover in the energy market is 10.61%, which is indicative of marked asymmetry, with heightened spillover levels observed in the alcohol, gasoline, and diesel markets, which are classified as net spillovers, in the fuel and LPG markets, designated as spillover recipients, and in the natural gas market, which exhibits the least pronounced risk spillover effect.

The overall volatility level of the energy market exhibits substantial fluctuations, ranging from −20% to 25%, and the total volatility spillover displays discernible time-varying characteristics. The total spillover level of the fuel market is more volatile, while the overall spillover level of the alcohol, gasoline, and diesel markets is similar, and the whole shows a flat state. The risk spillover of the natural gas market has a smaller range of fluctuations and a lower frequency of spillovers.

The physical risk significantly exacerbates the risk spillover between energy markets, and most of its impulse response values are below 0, and there is a clear negative shock. The transition risk exerts a divergent effect on the risk spillover of diverse energy markets. The nature of risk spillover is contingent on the specific market in question; for instance, shocks to the fuel, LPG, and natural gas markets predominantly engender positive

shocks, while shocks to the alcohol, gasoline, and diesel markets predominantly engender negative shocks.

5.2. Policy Implications

Each energy market should consider its own risk volatility characteristics and response characteristics to different climate change risks to develop appropriate risk response policies to improve energy market stability: Establishing a risk-monitoring mechanism and strengthening market risk management. Developing and improving the risk-monitoring system for the energy market to monitor market fluctuations and risk spillover in real time. Constructing risk early warning indicators and utilizing big data and artificial intelligence technology to monitor and analyze market risks in multiple dimensions and frequencies. Setting risk thresholds so that timely early warning will be issued and measures are taken when market fluctuations exceed the normal range [38]. Stabilizing the policy environment and establishing risk buffer mechanisms. Establishing energy risk management tools to help companies and investors effectively manage market risks and reduce losses caused by uncertainty. Enhancing the transparency of market information disclosure, publishing regular market reports, analyzing market dynamics and potential risks, and ensuring that market participants have access to accurate market information. Establishing personalized risk buffer mechanisms according to different types of energy markets, such as strategic reserves to cope with market volatility for net spillovers (e.g., natural gas market) and risk funds for net recipients (e.g., fuel market) to mitigate the negative impact of risk spillover. Strengthening physical risk management and building energy security defenses. Strengthening the construction and maintenance of energy infrastructure, and improving the ability to withstand physical risks such as natural disasters by reinforcing key facilities, upgrading engineering design standards, and adopting advanced early warning systems. Formulating detailed contingency plans to ensure that prompt and effective action can be taken in the face of extreme weather events and other unforeseen circumstances. Strengthening cross-sectoral coordination to ensure the rational allocation and rapid deployment of resources in order to minimize the impact on energy supply. Developing adaptive strategies to address transition risks. Formulating flexible policies to support technological innovation and business model changes in the process of the energy transition. Encouraging energy enterprises to carry out technological upgrading and innovation to adapt to the new trend of low-carbon development and ensure the long-term sustainable development of the energy market. Strengthening regulation and policy implementation to ensure that all relevant measures are effectively implemented. Promoting cooperation between regulators and energy enterprises to ensure that risk management measures are adequately considered and implemented and regularly assess their effectiveness. Promoting international cooperation and exchanges, sharing best practices and experiences in energy transition, and utilizing international platforms to promote technology transfer and joint research and development, so as to jointly address the challenges of energy transition [39].

Author Contributions: Conceptualization, S.C. and M.P.; methodology, Y.M.; software, S.C. and Y.M.; validation, M.P., S.C. and Y.M.; formal analysis, S.C. and Y.M.; investigation, M.P.; resources, M.P.; data curation, S.C. and Y.M.; writing—original draft preparation, S.C.; writing—review and editing, S.C., M.P., Y.M., Q.D. and Y.T.; visualization, S.C.; funding acquisition, M.P. All authors have read and agreed to the published version of the manuscript.

Funding: This research was funded by the 2022 National Social Science Foundation Major Project, grant number 22&ZD105; 2020 National Social Science Foundation Western Program, grant number 20XJY006.

Data Availability Statement: The data used to support the findings of this study are available from the corresponding author upon request.

Conflicts of Interest: Author Yongping Tao was employed by the company China National Petroleum Corporation Drilling Fluid Technical Service Company of Sichuanqing Drilling Engineering Co. The remaining authors declare that the research was conducted in the absence of any commercial or financial relationships that could be construed as a potential conflict of interest.

References

1. Shaw, R.; Luo, Y.; Cheong, T.S.; Halim, S.A.; Chaturvedi, S.; Hashizume, M.; Insarov, G.E.; Ishikawa, Y.; Jafari, M.; Kitoh, A.; et al. 2022: Asia. In *Climate Change 2022: Impacts, Adaptation and Vulnerability*; Contribution of Working Group II to the Sixth Assessment Report of the Intergovernmental Panel on Climate Change; Cambridge University Press: Cambridge, UK; New York, NY, USA, 2022; pp. 1457–1579.
2. Chen, J.; Chen, Y.; Zhou, W. Relation exploration between clean and fossil energy markets when experiencing climate change uncertainties: Substitutes or complements? *Humanit. Soc. Sci. Commun.* **2024**, *11*, 691. [CrossRef]
3. Gonçalves, A.C.R.; Costoya, X.; Nieto, R.; Liberato, M.L.R. Extreme weather events on energy systems: A comprehensive review on impacts, mitigation, and adaptation measures. *Sustain. Energy Res.* **2024**, *11*, 4. [CrossRef]
4. Liu, Z.H.; Ding, Z.H.; Duan, Z.P. Does climate policy uncertainty exacerbate extreme risk spillovers among energy markets? *Syst. Eng. Theory Pract.* **2023**, *43*, 1651–1667.
5. Zhang, S.; Aibai, A. The impact of extreme weather on regional financial risk. *Financ. Econ.* **2024**, *1*, 30–40. [CrossRef]
6. Li, K.; Cai, B.; Wang, Z. Accessing the Climate Change Impacts in China Through a Literature Mapping. *Int. J. Environ. Res. Public Health* **2022**, *19*, 13411. [CrossRef]
7. Ding, S.; Liang, Z.; Chen, J. A study on the spillover effects of climate policy uncertainty and energy and metal markets under the time-frequency perspective. *Syst. Eng. Theory Pract.* **2023**, *43*, 2222–2235.
8. Guo, N.; Zhang, J. Study on the volatility spillover effect between China's energy market and stock market--an empirical study based on TVP-VAR-DY model. *J. Southwest Univ. Natl. (Humanit. Soc. Sci. Ed.)* **2022**, *43*, 122–133.
9. Jin, Y.; Zhao, H.; Bu, L.; Zhang, D. Geopolitical risk, climate risk and energy markets: A dynamic spillover analysis. *Int. Rev. Financ. Anal.* **2023**, *87*, 102597. [CrossRef]
10. Zheng, L.; Ye, N.; Gan, Y.; Lai, C. The impact of extreme weather event shocks on bank stability. *Wuhan Financ.* **2024**, *7*, 28–37. Available online: https://kns.cnki.net/kcms2/article/abstract?v=CdHX_LbaUYy6TLvsH41oNRF6G7JIaNNlVIAElKHDHvVqWFqh7i9xMpe_XgxvoOrsjpKglo-W2SjruGut9xo1S8PdTTXizO2iEdVPvBDCuC-1MF9TmwsjhnQ8yVM_HsTn5SXzbEIg2o0EBNmYfJIXA6ZAsa_u4yKMwYQ1EF63n6HLi2bzhm0m5AMIqqTRNixK&uniplatform=NZKPT&language=CHS (accessed on 8 October 2024).
11. Liu, L.; He, G.; Wu, M.; Liu, G.; Zhang, H.; Chen, Y.; Shen, J.; Li, S. Climate change impacts on planned supply–demand match in global wind and solar energy systems. *Nat. Energy* **2023**, *8*, 870–880. [CrossRef]
12. Gong, X.; Lai, P.; He, M.; Wen, D. Climate risk and energy futures high frequency volatility prediction. *Energy* **2024**, *307*, 132466. [CrossRef]
13. Liu, Z.; Xie, Y.; Niu, Y. Energy market, financial market green concern and commercial banks' climate risk—a frequency domain analysis based on quantile vector autoregressive model. *Shanghai Financ.* **2024**, *4*, 56–69. [CrossRef]
14. Li, J. How will climate change affect China in the future? *Ecol. Econ.* **2024**, *40*, 9–12.
15. Moon, T.H.; Kim, D.-H.; Park, C.S.; Lee, D.-S. Policy Analysis to Reduce Climate Change-Induced Risks in Urban and Rural Areas in Korea. *Sustainability* **2017**, *9*, 524. [CrossRef]
16. Calcaterra, M.; Reis, L.A.; Fragkos, P.; Briera, T.; de Boer, H.S.; Egli, F.; Emmerling, J.; Iyer, G.; Mittal, S.; Polzin, F.H.J.; et al. Reducing the cost of capital to finance the energy transition in developing countries. *Nat. Energy* **2024**, *9*, 1241–1251. [CrossRef]
17. Guo, W.; Luo, S. Geopolitical risks, energy price volatility and global inflation. *Financ. Econ.* **2023**, *4*, 40–52.
18. Gu, Q.; Li, S.; Tian, S.; Wang, Y. Impact of climate risk on energy market risk spillover: Evidence from dynamic heterogeneous network analysis. *Energy Econ.* **2024**, *137*, 107775. [CrossRef]
19. Hafezi, M.; Sahin, O.; Stewart, R.A.; Mackey, B. Creating a Novel Multi-Layered Integrative Climate Change Adaptation Planning Approach Using a Systematic Literature Review. *Sustainability* **2018**, *10*, 4100. [CrossRef]
20. Lupu, R.; Călin, A.C.; Zeldea, C.G.; Lupu, I. Systemic Risk Spillovers in the European Energy Sector. *Energies* **2021**, *14*, 6410. [CrossRef]
21. Hwang, Q.; Yao, M.; Li, S.; Wang, F.; Luo, Z.; Li, Z.; Liu, T. Risk Spillovers Between China's Carbon and Energy Markets. *Energies* **2023**, *16*, 6820. [CrossRef]
22. Li, C.; Li, J.; Chen, W. Risk spillovers between financial markets and major sectors of the real economy. *Financ. Econ.* **2024**, *1*, 18–29.

23. Du, R.; Xu, P. Time-Varying Spillover Effects Between Clean and Traditional Energy Under Multiple Uncertainty Risk: Evidence from the U.S. Market. *Sustainability* **2024**, *16*, 9164. [CrossRef]
24. He, Z.; Zhong, M. A study of the dynamic impact of climate policy uncertainty on global energy prices and stock prices. *Syst. Sci. Math.* **2024**, 1–24. Available online: https://link.cnki.net/urlid/11.2019.o1.20240903.1029.002 (accessed on 8 October 2024).
25. Qian, L.; Jiang, Y.; Long, H. Extreme risk spillovers between China and major international stock markets. *Mod. Financ.* **2023**, *21*, 30–34. [CrossRef]
26. Chen, D.; Hu, H.; Zhang, H. Research on risk spillover effect of oil market on China's carbon market based on EVT-Copula-CoVaR. *Oper. Res. Manag.* **2024**, *33*, 108–115.
27. Yao, C.-Z.; Zhang, Z.-K.; Li, Y.-L. The Analysis of Risk Measurement and Association in China's Financial Sector Using the Tail Risk Spillover Network. *Mathematics* **2023**, *11*, 2574. [CrossRef]
28. Chai, J.; Lin, J.; Liang, T. A study on the linkage of crude oil and natural gas in North American market-an empirical analysis based on Bayesian DCC-GARCH and LSTAR models. *Manag. Rev.* **2021**, *33*, 16–28. [CrossRef]
29. Zhang, Q.; Yang, Y. Research on the risk spillover effect of carbon-intensive industries on the banking industry under the background of low-carbon transition. *Financ. Econ.* **2024**, *7*, 25–37.
30. Zhang, A.-Y.; He, Y.-D.; Wen, H. Research on the interaction effect between energy price and energy stocks based on continuous wavelet. *Econ. Issues* **2020**, *12*, 18–28.
31. Ma, Y.; Lu, J.; Lin, P.; Xie, Q. Structural correlation effect of global financial development and economic growth—an analysis based on financial cycle and financial stability mechanism. *Financ. Sci.* **2021**, *10*, 1–14.
32. Zhu, B.; Ma, Y.; Chen, D. The mechanism of the role of debt financing mode on the spillover effect of industry financial risk. *Financ. Sci.* **2018**, *1*, 15–27. Available online: https://kns.cnki.net/kcms2/article/abstract?v=CdHX_LbaUYxuq-yQd0ka7kSkiqvEZUqhn9OsoJn3yTgQIAYETXIeK8pau5K-zxF0cRX48WMW_2i2fCu2zAy2vwf8ij_44mQVOmfrqvif9QymEkSCBsdJrh-fzYOyDg7o46p1NmfsGHMpKKEgjxLRGW3H7WbAciZIXyPNrFd1bRh2_gDiyHDMhy-7RsH4RRlB&uniplatform=NZKPT&language=CHS (accessed on 8 October 2024).
33. Zhong, W.; Li, H. A study of tail risk spillover effects of international oil prices, macroeconomic variables and Chinese stock market. *China Manag. Sci.* **2022**, *30*, 27–37. [CrossRef]
34. Li, H.; Li, W.; Hu, Y.; Zhang, R.; Li, Y.; Chang, Y. Analysis and trend forecast of refined oil prices in 2024. *J. Beijing Inst. Technol. (Soc. Sci. Ed.)* **2024**, *26*, 59–67.
35. Akyildirim, E.; Cepni, O.; Molnár, P.; Uddin, G.S. Connectedness of energy markets around the world during the COVID-19 pandemic. *Energy Econ.* **2022**, *109*, 105900. [CrossRef]
36. Li, B.; Zhang, J.; Shen, X. Is there a stock premium effect for climate change risk. *Financ. Sci.* **2024**, *6*, 31–47. Available online: https://kns.cnki.net/kcms2/article/abstract?v=CdHX_LbaUYw3zwiiDXo1eBosuXZ5t81JTNREzqZB45Q7k5EhPGK9o0mCE4GDsF6eias0Mn12BS10ejazNpTqYqTciK-JsRhD2KNlDLtMzcTq179rJti0G4cRpESB6ubehR-OKuIl_eofyXt6C6nH6ifoUSwTiCigV9E3mlnVanlMUDeXGP61NkBhTGG9UQvc&uniplatform=NZKPT&language=CHS (accessed on 8 October 2024).
37. Wang, L.; Wang, X.; Liang, C. Natural gas volatility prediction via a novel combination of GARCH-MIDAS and one-class SVM. *Q. Rev. Econ. Financ.* **2024**, *98*, 101927. [CrossRef]
38. Bao, M.; Ding, Y.; Zhou, X.; Guo, C.; Shao, C. Risk assessment and management of electricity markets: A review with suggestions. *CSEE J. Power Energy Syst.* **2021**, *7*, 1322–1333. [CrossRef]
39. Zhang, D.; Zhao, M.; Wang, Y.; Vigne, S.A.; Benkraiem, R. Technological innovation and its influence on energy risk management: Unpacking China's energy consumption structure optimisation amidst climate change. *Energy Econ.* **2024**, *131*, 107321. [CrossRef]

Disclaimer/Publisher's Note: The statements, opinions and data contained in all publications are solely those of the individual author(s) and contributor(s) and not of MDPI and/or the editor(s). MDPI and/or the editor(s) disclaim responsibility for any injury to people or property resulting from any ideas, methods, instructions or products referred to in the content.

sustainability

MDPI

Article

Linking Perceptions, Emotions, and Actions: How Psychological Distance, Media Framing, and Guilt About Climate Crisis Promote Communication and Pro-Environmental Behavior

Juhyun Hong [1] and Chang-Young Jeon [2,*]

[1] School of Media & Advertising, Kookmin University, Seoul 02707, Republic of Korea; joohssy@kookmin.ac.kr
[2] Media Research Center, Korea Press Foundation, Seoul 04518, Republic of Korea
* Correspondence: cyjeon8@kpf.or.kr

Abstract: This study explored the impact of psychological distance, media coverage, and guilt on communication behavior and eco-friendly actions and found that environmental interest was a significant predictor of behavior. The findings indicate that perceptions of the severity of the climate crisis and media coverage facilitated information seeking and interpersonal communication, which in turn led to eco-friendly behavior. Additionally, guilt strongly predicted information seeking and eco-friendly product purchase intention. Information seeking and interpersonal communication positively influenced eco-friendly product purchases and energy conservation. Women and younger individuals favored face-to-face communication and public transport, while older individuals focused on energy conservation and eco-friendly purchases. Perceptions of climate crisis severity and media coverage influenced communication and eco-friendly purchases. Guilt strongly predicted information seeking and purchase intention, which emphasizes the effectiveness of emotion-based messages. The findings highlight the need for targeted strategies across demographics and political orientations to promote pro-environmental behavior.

Keywords: psychological distance; media framing; climate crisis; pro-environmental behavior; guilt and communication behavior

1. Introduction

According to a 2023 report by WWF Korea, Koreans' perceptions of environmental issues have evolved over time. In 2018, environmental concerns were seen as fragmented, but by 2022, they were recognized as interconnected. Media coverage also changed, with keywords shifting from broad environmental terms in 2018 to a more diverse range of topics in 2022, including consumer behavior, carbon neutrality, fine dust, and business agreements. Additionally, an analysis of YouTube comments revealed that public awareness and concern about environmental crises spread more rapidly through social media than through traditional news outlets [1]. As awareness grows and environmental issues become more complex, the study highlighted the importance of eco-friendly behaviors.

The escalating climate crisis underscores the urgent need to elucidate the factors that drive pro-environmental behavior [2,3]. Effective environmental management requires collective action at the local, regional, national, and global levels. Feldman and Hart [4] found that message content, more than media framing, significantly influences perceptions of climate change severity and behavioral intention for mitigation or adaptation, which highlights its impact on public behavior [4].

Scholars identified cognitive awareness, including knowledge on the severity of climate crisis, as a key predictor of pro-environmental behavior. Kollmuss and Agyeman (2002) argued that individuals who understand the consequences of climate change and its severity are more likely to engage in environmentally friendly behavior [5].

Cognitive awareness is essential for action, but emotional engagement, perceived efficacy, and social norms are crucial for bridging the gap between knowledge and behavior. Combining knowledge with emotional engagement and action opportunities fosters pro-environmental behavior [6].

Emotions related to the climate crisis, such as guilt, pride, and anger, also form pro-environmental behavioral intentions. Harth, Leach, and Kessler (2013) demonstrated that guilt about environmentally harmful actions encourages individuals to feel responsible and take compensatory actions [7]. Similarly, their analysis of guilt, anger, and pride revealed that individuals who feel guilt over the harmful environmental actions of their group are more likely to take responsibility and adopt compensatory behaviors, while self-esteem reinforces continually eco-friendly actions. Conversely, anger negatively impacts pro-environmental intentions [8].

This study examines the combined influence of cognitive and emotional factors on communication behavior and pro-environmental actions by exploring the effects of emotional variables and climate crisis severity on eco-friendly behavior. Information seekers exhibit stronger pro-environmental behavioral intentions. Choo (2023) investigated the effects of information seeking on environmental attitudes and behaviors and found that individuals who frequently seek information on climate change are more aware of its severity and display more positive attitudes toward environmental protection. A higher frequency of information seeking was also correlated with a stronger intention to act in environmentally friendly ways [9]. Similarly, Hovick et al. (2021) reported that exposure to environmental health risk messages increases risk perceptions, which motivates individuals to seek information and adopt behaviors that reduce environmental impacts [10]. Han and Xu (2020) mentioned that interpersonal communication, especially with family and friends, strongly increased environmental risk awareness and promoted pro-environmental behavior. Social media was effective when combined with interpersonal communication, whereas traditional media exhibited no direct impact [11].

This study explores how cognitive and emotional factors, including awareness and emotional engagement with the climate crisis, drive communication behavior and eco-friendly action, thus offering insights for effective climate advocacy strategies. This study examines how perceptions of the climate crisis, media framing, and guilt influence communication and eco-friendly behavior. This study utilized quantitative research methods to explore the relationships between emotions, including those related to the climate crisis and guilt, communication behaviors, and eco-friendly actions. The data for this analysis were obtained from the annual surveys conducted by the Korea Institute of Environmental Policy Evaluation (KEI). Understanding how cognitive factors and the guilt associated with psychological distance drive eco-friendly behavior is essential for developing effective climate change communication strategies. Given the impact of interpersonal communication on eco-friendly behavior, policymakers, businesses, and media organizations can play a crucial role in structuring climate messages and promoting sustainable consumer and societal behaviors.

2. Theoretical Background

2.1. Climate Crisis, Sustainability, and Eco-Friendly Actions

The climate crisis, driven by human activities such as fossil fuel consumption and deforestation, causes global warming, extreme weather, biodiversity loss, and rising sea

levels. It threatens sustainability by depleting resources, disrupting ecosystems, and worsening social inequality. Sustainability is a development approach that meets present needs without compromising the ability of future generations to meet their needs [12].

Proposed by Olson (1965) [13], collective action theory emphasizes the importance of individual contributions in achieving group goals. According to this theory, in solving the climate crisis, individual eco-friendly practices (e.g., waste reduction, energy conservation, and support of sustainable products) cumulatively contribute to the reduction of greenhouse gas emissions and resource depletion [2]. Social practice theory emphasizes how everyday practices are shaped by cultural norms, material conditions and individual actions, in which small individual actions can trigger wider social change, normalizing sustainability and creating systemic change.

Eco-friendly behavior refers to actions taken by individuals to minimize negative impacts on the environment based on factors such as personal values, social norms, and external influences [5,7,9]. Specifically, it refers to environmentally friendly behavior in daily life such as energy conservation, recycling, and use of public transportation. In addressing the climate crisis, individual actions can drive important collective change, and consumer demand. for eco-friendly products can foster changes in markets and encourage policymakers to implement sustainable regulations. Notably, individual eco-friendly actions can help solve the climate crisis by relying on public support and cooperation.

In the same context, discussions on sustainability emphasize the role of individual and collective actions in solving the climate crisis. Theories, such as value–belief–norm theory (VBN) and social practice theory examine how attitudes, norms, and everyday practices shape environmental behavior [14]. Many factors influence the relationship between the climate crisis and individual behavior. According to VBN theory, behavior is influenced by values, beliefs, and perceived obligations [14]. Awareness of the climate crisis is central to green action. People with altruistic or eco-centric values are more likely to engage in pro-environmental behavior. If individuals recognize the negative impacts and severity of the crisis, then they are motivated to act sustainably. Those aware of the crisis but do not practice eco-friendly behavior may experience cognitive dissonance, which prompts them to adopt environmentally friendly actions to resolve it.

2.2. Interconnections Between Psychological Distance, Interpersonal Communication, and Environmental Behavior

The theory of planned behavior (TPB) explains various social behaviors, including individual eco-friendly actions. According to TPB, human behavior is determined by behavioral intention, which is shaped by attitude, subjective norms, and perceived behavioral control [8]. Based on this theoretical framework, this study examines the role of perceptions and emotional factors related to environmental issues as predictors of eco-friendly behavior, with a particular focus on the moderating effect of interpersonal communication [15].

Interpersonal communication directly influences subjective norms and perceived behavioral control, two key components of TPB. Through the process of sharing environmental information with others, individuals may experience increased social pressure to engage in eco-friendly behavior, thereby reinforcing subjective norms. Additionally, interpersonal communication facilitates the exchange of practical knowledge on eco-friendly practices, enhancing perceived behavioral control by increasing individuals' confidence in their ability to act. Moreover, interpersonal discussions about environmental issues can reduce psychological distance, making such issues feel more personally relevant and thereby influencing behavioral change [16].

In summary, a shorter psychological distance leads to a more positive attitude toward eco-friendly behavior. Meanwhile, interpersonal communication strengthens subjective

norms and enhances perceived behavioral control, reinforcing the likelihood of engaging in pro-environmental actions in accordance with the TPB framework.

This study explores how perceptions of the climate crisis, emotions such as guilt, and media framing influence communication behavior and environmental actions. The theory of planned behavior (TPB) provides a foundational framework for understanding how an individual's attitude, subjective norms, and perceived behavioral control affect their intention to engage in eco-friendly behavior. The concept of psychological distance, a cognitive element in this study, aligns with TPB's notion that perceptions shape attitudes and offers a basis for explaining how factors such as guilt and media framing influence eco-friendly actions. The key moderating variable in this study, interpersonal communication, impacts subjective norms (social pressure to behave in an eco-friendly manner) and perceived behavioral control (confidence in one's ability to act), further supporting the TPB's assertion that perceptions shape attitudes and behaviors.

The relationship between knowledge, attitudes, and actions in this study is complex and dynamic, influenced by a range of cognitive, emotional, and situational factors. Various theories attempt to explain how these elements interact, but the path from knowledge to behavior is not always straightforward. For instance, individuals may feel motivated to protect the environment due to cognitive dissonance, yet engage in excessive consumption. When psychological distance from environmental issues is high, individuals' motivation to engage in eco-friendly behavior decreases. Moreover, social and economic systems that promote environmentally harmful behaviors, such as industrial production and endless consumption, can hinder individuals' ability to adopt eco-friendly behaviors. Self-interest can also disrupt environmental actions [17]. Emotions like fear, hope, anger, and guilt, as discussed by Kleres and Wettergren (2017), interact with individuals' motivation to engage in climate activism. These emotional responses can either drive action or become barriers, depending on how they are framed and managed. Understanding the impact of these emotions on behavior is critical for designing effective communication strategies that promote sustainable actions and policy change [15].

This study focuses on how emotional and cognitive factors shape decision-making and behavior in the context of environmental action. Knowledge, attitudes, and actions are interconnected, but their relationships are influenced by various psychological, social, and situational factors. These interactions do not always follow a linear progression, making it essential to understand their complexity in order to predict and encourage pro-environmental behavior.

2.3. Psychological Distance from the Climate Crisis and Environmental Behavior

Recognizing the severity of the impacts of climate change increases one's sense of urgency and encourages environmentally friendly behavior. The theory of planned behavior (TPB) explains how the perception of the severity of environmental problems influences attitudes toward pro-environmental behavior and increases the likelihood of the adoption of such behaviors [8]. Promoting environmentally friendly attitudes through social influence and demonstrating social acceptance can enhance the motivation to adopt eco-friendly behavior.

Building on previous research that focused on the level of awareness and severity of climate change [9], this study hypothesizes that perceived severity in terms of beliefs leads to pro-environmental behavior and that differences exist in behavior between individuals who recognize the severity of the climate crisis and those who do not. It highlights behavioral differences between these groups. According to VBN theory, individuals who perceive the climate crisis as serious are more likely to engage in pro-environmental behavior if their values (e.g., biosphere values or altruism) align with sustainability. While

previous studies concentrated on perceived severity, the present study examines recipients' perceptions of the severity of the climate crisis from various aspects based on psychological distance theory.

Psychological distance theory provides a framework for understanding why individuals frequently perceive the climate crisis as a distant problem, which influences the motivation to engage in pro-environmental behavior. Psychological distance from climate change is related to pro-environmental behavior [14]. This concept is central to construal level theory [18], which posits that individuals mentally represent events based on perceived distance across four dimensions, namely temporal, spatial, social, and virtual.

First, temporal distance leads to the perception of climate change as a problem in the distant future, with its effects expected to occur decades later. Regarding spatial distance, individuals typically believe that climate change will primarily affect distant places instead of their country. Social distance promotes the view of climate change as a problem that affects other groups except for oneself, which can diminish personal responsibility and empathy [19]. Virtual distance is a psychological perception that leads to the view of climate change.

When a problem is perceived as psychologically distant (high-level construal), individuals tend to think abstractly and focus on the *why* (e.g., climate change is a global issue). This abstract thinking can reduce the perceived relevance of pro-environmental actions. When the problem is psychologically close (low-level construal), individuals think more specifically and focus on the *how* (e.g., taking concrete actions such as recycling). This specific way of thinking promotes pro-environmental behavior. Reducing psychological distance increases risk perception and personal relevance, both of which are important predictors of environmental protection behavior [20].

Based on previous research, this study focuses on temporal, social, and virtual distance in terms of psychological distance and examines the relationship between these perceptions and pro-environmental behavior.

H1a–c: Perception of the severity of the climate crisis ([a] distance, [b] social, and [c] virtual distance) will positively affect pro-environmental behavior.

2.4. Cognitive Seriousness of Climate Crisis-Related Media Reports

The media plays a crucial role in the formation of public perceptions and attitudes by determining which issues receive attention [21]. As a major intermediary between scientific knowledge and public understanding, the media influences how individuals and society recognize the urgency and relevance of climate change. The media not only selects which topics to cover but also influences the public's interpretation of information by framing environmental problems in particular ways [22]. By emphasizing certain aspects and downplaying others, the media shapes perception and emotional response, thus acting as a cognitive framework that guides individuals in understanding and evaluating complex phenomena such as the climate crisis.

Framing theory highlights that the emphasis of the media on potential dangers or benefits can increase or decrease the intention to engage in specific behaviors [23]. Environmental frames that emphasize long-term damages due to climate change can highlight its importance and severity. Feldman and Hart [4] underscored the significance of framing in climate change communication by analyzing the influence of message design on perceptions and behavioral intentions regarding climate change [23]. The findings suggested that an environmental frame that focuses on ecological impacts (e.g., biodiversity loss and habitat destruction) was not significantly more effective than other frames (e.g., economic or health) in raising awareness about the severity of climate change. In other words, environmental messages alone may not be sufficient for changing attitudes or increasing the

perceived seriousness of climate change, especially among audiences previously exposed to similar content.

Media frames play an important role in forming public perceptions and actions on environmental issues [24], economic frames, moral frames, environmental and biological frames, and public health frames [25]. Economic frames can prevent eco-friendly behavior by emphasizing economic losses to individuals. Moral frames can promote eco-friendly behavior by causing responsibility and guilt. Public health frames can affect the introduction of policies that reduce individual and companies' carbon emissions by connecting with individual health.

This indicates that respondents have likely previously encountered climate-related messages, and their perception of the severity of the climate crisis was not notably affected by whether the message was framed around environmental, economic, or health concerns. Emphasizing the interpretation of climate news based on prior attitudes and values, Nisbett [24] stressed the importance of framing in enhancing the effectiveness of climate change communication. The effects of specific frames are dependent on public values, political tendencies, and prior knowledge. Previous scholars demonstrated that environmental framing is particularly impactful in such contexts.

Media reports on the climate crisis can be exaggerated, factual, or reduced. Exaggerated portrayals may lead to anxiety or helplessness, whereas accurate reports enable informed decision-making. When the crisis is downplayed, it can lead to disengagement, indifference, or resentment toward environmental advocates, as audiences may view them as alarmists.

This study stands apart in that it considers individual perceptions of media reports on the climate crisis. While the actual framing of media coverage is important, individual judgment about the severity of these reports also influences eco-friendly behavior.

H2: The perceived seriousness of media reports on the climate crisis will positively influence eco-friendly behavior.

2.5. Emotional Factors That Affect Eco-Friendly Behavior: Guilt

This study focuses on guilt as a motivation for environmentally friendly behavior, particularly in comparison with other emotions such as anger and fear, as discussed in the climate crisis research conducted by Mallett and Melchiori [25]. Their analysis highlights the role of guilt and message framing in influencing public support for environmental policies. The authors found that guilt-inducing messages were more effective in increasing public support for environmental bills compared with neutral messages, as guilt motivated participants adopt a more responsible stance on environmental protection.

Self-determination theory (Ryan and Deci, 2000) [26] emphasizes the importance of internal motivations, such as guilt and pride, in shaping behavior. According to this theory, feelings of guilt and shame related to nonenvironmentally friendly behaviors promote social responsibility and motivate individuals to adopt eco-friendly practices [26]. As suggested by Bamberg and Moser (2007), guilt as a result of environmental destruction can foster self-control and encourage sustainable practices, while pride associated with eco-friendly actions can reinforce such behavior [27].

An emotional response to one's perceived responsibility for environmental harm, guilt plays a significant role in motivating pro-environmental behavior. The guilt hypothesis proposes that individuals act to alleviate guilt by engaging in behaviors that are linked to environmental protection [28]. This emotional appeal is further supported the appraisal theory of emotion (Lazarus, 1991) [29], which posits that guilt arises when individuals perceive their actions as harmful and recognize their responsibility for such actions. This emotional state can prompt individuals to adopt compensatory strategies, including eco-

friendly behaviors, to address their perceived wrongdoing [4]. Recognizing the negative outcomes of one's actions and feeling personally responsible trigger guilt, which encourages prosocial behavior aligned with personal norms [30].

H3: Guilt related to the climate crisis will positively affect eco-friendly behavior.

2.6. Interpersonal Communication and Its Role in Environmental Behavior

2.6.1. Information Seeking

Personal communication behaviors, such as information seeking and interpersonal communication, are vital in addressing the climate crisis by influencing awareness, attitudes, and behaviors, which are connected to eco-friendly actions through the psychological, social, and cognitive pathways.

According to the TPB (Ajzen, 1991), the pursuit of information increases awareness, attitude formation, subjective norms, and perceived behavioral control over environmental issues, which directly predict pro-environmental behavior [8]. Individuals actively seek information related to the climate crisis to fulfill specific needs such as understanding its causes and impacts. In this context, information seeking facilitates the development of environmental understanding, which is a fundamental element of decision-making and behavior change based on acquired information. Therefore, individuals who actively seek information are more likely to adopt eco-friendly behaviors [31].

2.6.2. Interpersonal Communication

Interpersonal communication plays a crucial role in shaping environmental behavior by spreading norms, values, and behaviors through social networks. For example, discussing climate issues with colleagues and family can normalize green practices and promote collective action. These conversations help foster behavioral change by strengthening personal responsibility and making climate issues feel immediate and relevant.

According to social influence theory, interpersonal communication promotes the spread of norms, values, and behaviors within social networks [32]. Through conversations about climate issues within social circles, individuals contribute to collective action against climate change by challenging unsustainable norms and promoting pro-environmental behaviors.

Communication behaviors, such as individual information seeking and interpersonal communication, can create positive feedback, including raising awareness of climate policies and strengthening public support for systemic change. Interpersonal discussions can amplify individual responsibility and motivate behavioral change by making climate issues feel more urgent and relevant. Sharing experiences and strategies also promotes social learning, which makes pro-environmental behavior more accessible and acceptable.

Interpersonal communication enables individuals to exchange information, discuss concerns, and influence one another's perceptions of environmental issues. These interactions can further enhance awareness and increase the adoption of environmentally friendly behaviors.

In summary, recognizing the seriousness of media coverage and engaging in interpersonal communication are crucial for promoting pro-environmental behavior. Media informs and structures discourses, while personal communication reinforces messages, which makes climate issues feel immediate and relevant. Shared emotions, such as guilt or hope, help spread pro-environmental norms and encourage action.

H4a,b: Climate crisis-related communication behavior ([a] information seeking and [b] interpersonal communication) will positively affect pro-environmental behavior.

2.7. Climate Crisis Communication Prediction Forecasts

In the relationship between temporal distance and information seeking, recognizing that temporal distance is long can reduce the need for information seeking about climate change. The reason is that results may seem distant and not immediate [33]. When people perceive the climate crisis as an event that will occur in the distant future (i.e., with a large temporal distance), then they are less likely to engage in interpersonal discussions [18]. Social distance refers to the perceived closeness or similarity between oneself and others affected by climate change; empathy and concern increase with the increase in social distance. In relation to information seeking, individuals with low levels of social distance (e.g., feeling connected to people affected by climate change) are more likely to seek information to understand and address the problem [34].

In the case of interpersonal communication, closer social ties or decreased social distance may motivate discussions on the climate crisis, in particular, sharing concerns or solutions [20]. Perceived severity of media coverage refers to one's judgment of how alarming or serious the media portrays the climate crisis. The higher the perceived severity, the more likely an individual will be to seek more information to understand risks and take actions [33].

Guilt occurs when individuals feel responsible for contributing to climate change or failing to sufficiently act to address it. Guilt can be a powerful motivator of communicative behavior. Regarding information seeking, guilt can lead individuals to seek information as a means of reducing cognitive dissonance and mitigating their contribution to the crisis [35]. Guilt can also lead to discussions with colleagues as a way of expressing concerns, sharing knowledge, and motivating collective action [26,35].

2.8. Communication as a Control Variable

This study examined the moderating effect of communication behavior on the relationship between the perceived severity of the climate crisis, emotions, and environmentally friendly behavior. According to the TPB, information seeking increases knowledge and shapes attitudes, perceived norms, and perceived behavioral control, which are predictors of behavior [8]. When individuals feel guilty about the climate crisis or perceive it as severe, active information seeking helps bridge the gap between emotional reactions and informed action by providing factual knowledge or actionable solutions. This process strengthens the association between perceived severity or guilt and pro-environmental behavior.

The risk information seeking and processing model (Griffin et al., 1999) states that individuals seek information based on their perception of risk and uncertainty [36]. When the climate crisis is perceived as severe, individuals who actively seek information are more likely to take informed action (e.g., save energy and reduce waste). This moderating effect occurs because information seeking reduces uncertainty and provides clarity about actionable steps, thereby reinforcing the perceived need for environmentally friendly behavior.

Regarding the moderating effect of interpersonal communication, social influence theory (Bandura, 1991) states that interpersonal communication promotes the spread of norms, attitudes, and behaviors [37]. Discussing the severity of the climate crisis or the guilt associated with environmental harm with others can normalize pro-environmental practices and amplify the emotional intensity of the issue. Discussing environmental issues with others increases awareness, reinforces norms, and increases the likelihood of environmentally friendly behavior [38].

2.9. Eco-Friendly Behavioral Preceding Variable

2.9.1. Demographic Factors

Among the demographic factors, gender and age consistently predict environmentally friendly behavior. Previous studies have demonstrated that women tend to exhibit stronger environmentally friendly attitudes and behaviors than men, potentially due to their higher levels of environmental concern and empathy [39]. Age influences behavior differently: older individuals may favor practices such as energy conservation, which are frequently rooted in long-standing habits, while younger individuals may be more receptive to the adoption of new eco-friendly behaviors, such as using public transportation [40].

2.9.2. Environmental Concern

In this study, the interest in the environment is assumed to be a prior factor because it is the basis for forming individual attitudes, intentions, and actions in eco-friendly practices. Environmental interests, defined by individual interest in environmental issues, are an important motivational driver of eco-friendly behavior. The VBN theory assumes that individuals with stronger biological values and those that believe in ecological damage are likely to adopt eco-friendly norms that lead to eco-friendly actions [14]. Interest in the environment originates from altruistic values, and interest in environmental issues emphasizes the dangers of deterioration and belief in individual responsibilities. Norms are activated, and individuals act in an environmentally friendly manner. Those who are interested in environmental issues are likely to be an environmentally conscious person and integrate this identity into their concepts [41,42].

2.9.3. Political Tendency

Political tendencies are closely correlated with environmental attitudes, in which progressive individuals typically display greater interest in climate change and participate more actively in environmental protection activities compared with conservatives [43]. Ideology influences behavioral intentions by shaping the sense of responsibility and the need for collective action.

Moral foundations theory (Haidt, 2007) suggests that differences in moral priorities influence the perceptions of issues. Progressive individuals tend to prioritize environmental protection based on the moral foundations of harm and care [43]. Similarly, the norm activation model (Schwartz, 1977) argues that personal norms, activated by awareness of consequences and a sense of responsibility, predict environmentally friendly behavior [31].

Progressive individuals are more likely to experience guilt or the moral obligation to act on climate issues due to their openness to information on anthropogenic climate change. Conversely, conservatives may view climate change as exaggerated or caused by external factors (e.g., natural cycles or actions by foreign countries), which can reduce feelings of guilt or responsibility.

From the perspective of value systems and moral foundations, progressives are more likely to perceive climate change as a moral issue, which prompts them to engage in behaviors such as recycling, reducing energy consumption, and supporting climate policies [41,44]. Conversely, conservatives may exhibit skepticism toward environmental policies, particularly when these policies are perceived as threats to economic stability, individual freedom, or traditional structures.

2.10. Research Framework: Research Questions and Hypotheses

This study examines the psychological and communication factors influencing eco-friendly behavior. Specifically, it explores how awareness of the climate crisis, media framing, and emotions (such as guilt) shape communication behaviors (e.g., informa-

tion seeking and interpersonal communication) and pro-environmental actions. The key research questions (RQ) and hypotheses (H) are as follows.

RQ 1. What are the factors that influence climate crisis-related communication behavior (e.g., additional information exploration and interpersonal communication)?

RQ 1-1. How does the preliminary void (sex, age, political tendency, and environmental interest) influence communication behavior?

RQ 1-2. Cognitive seriousness; how do time and social distance influence communication behavior?

RQ 1-3. How does the seriousness of media reports affect communication behavior?

RQ 1-4. How do emotions affect communication behavior?

RQ2. What are the factors that influence eco-friendly behaviors related to climate crisis ([a] purchase, [b] public transportation, and [C] energy saving)?

RQ 2-1. How does the preliminary void (sex, age, political tendency, environmental interest) affect eco-friendly behavior?

RQ 2-2. How did the recognized severity (time and social distance) affect eco-friendly behavior?

H1: The severity of the climate crisis ([a] time, [b] social, and [c] virtual distance) will exert a positive effect on eco-friendly behavior.

RQ 2-3. How does the severity of media reports influence eco-friendly behavior?

H2: The severity of media reports related to the climate crisis will positively influence eco-friendly behavior.

RQ 2-4. How does emotion (guilt) affect eco-friendly behavior?

H3: Guilt about the climate crisis will positively affect eco-friendly behavior.

RQ 2-5. How does communication acts ([a] additional information search and [B] interpersonal communication) affect eco-friendly behavior?

H4: Communication behavior related to climate crisis ([a] additional information exploration and [b] interpersonal communications) will positively affect eco-friendly behavior.

RQ 3. Communications ([a] additional information search and [b] interpersonal communication) will exert a regulatory effect in the relationship between recognized severity and eco-friendly behavior related to climate change.

2.11. Research Model

Figure 1 illustrates the relationships among cognition, emotion, and behavior. For RQ 1, individuals seek and discuss information when perceiving the climate crisis or media reports as severe or feeling guilt. RQ 2 explores the impact of severity, media, guilt, and communication behavior on eco-friendly actions. Communication behavior acts as a mediator and an amplifier, connecting perceptions and emotions to behaviors. The model highlights how perceived seriousness and guilt can directly or indirectly drive eco-friendly behavior through enhanced communication, which boosts participation in sustainable practices.

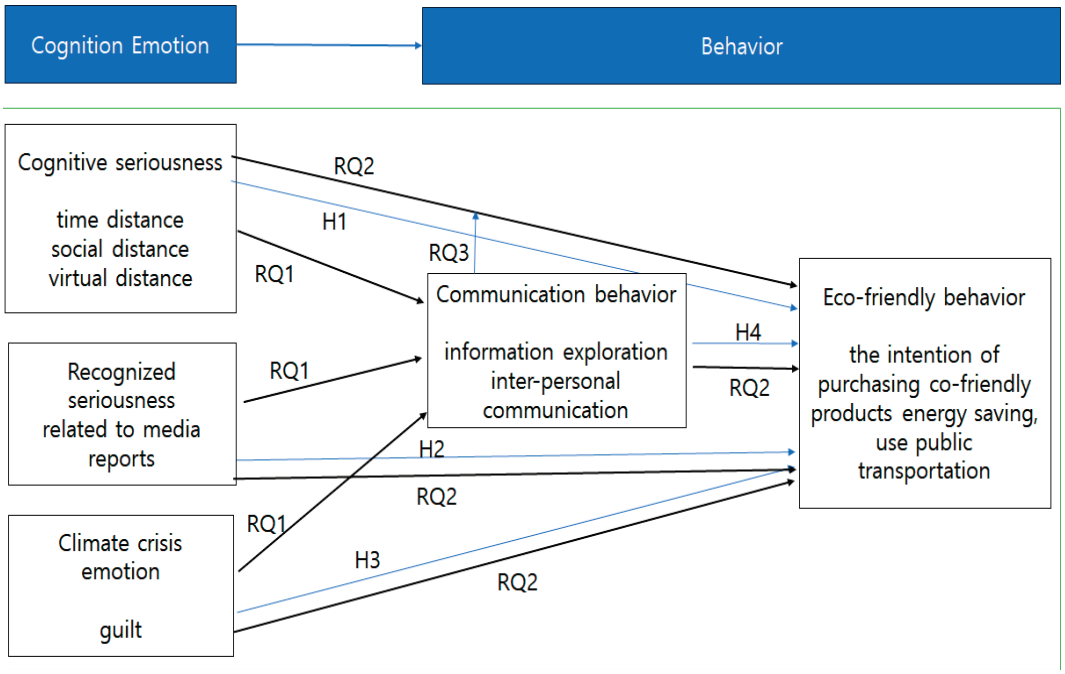

Figure 1. Model of predictors of pro-environmental behavior.

3. Materials and Methods

3.1. Data Collection and Analysis Target

This study utilizes data from the National Environmental Awareness Survey, an annual survey conducted by the Korea Environment Institute (KEI), which aims to assess public perceptions of environmental issues. The survey was administered online to a sample of 3088 respondents, who participated via mobile phones or personal computers through a web-based questionnaire. The questionnaire, based on the 2021 revised version, includes four primary sections: environmental awareness, environmental attitudes and practices, environmental demands, and environmental policies, with additional items introduced to address emerging environmental concerns.

Hierarchical regression analysis was employed to explore the relationships between environmental awareness, emotions, and eco-friendly behaviors, with a focus on testing the moderating role of communication behaviors such as information seeking and interpersonal communication. By sequentially entering independent variables, hierarchical regression allows for the assessment of the incremental explanatory power of each predictor and controls for potential confounding factors. This methodology is particularly well-suited for identifying causal relationships and understanding the complex, sequential influences of cognitive and emotional factors on environmental behaviors.

The Environmental Awareness Survey reorganizes question codes, content, and scales. An online survey was conducted with 3088 adults (aged 19–69 years) nationwide using proportional allocation by region, gender, and age. The survey was conducted by a professional company and lasted 8 days (21–28 September 2023).

3.2. Operational Definition and Measurement of Variables

3.2.1. Psychological Distance: Temporal, Social, and Virtual Distance

Psychological distances related to climate change were identified based on prior studies, including temporal, social, and virtual distance [19]. Temporal distance was measured using the question, “Do you think our country will be negatively affected by climate change?” The options were: “It will not be affected at all” (1 point), “It will not be

affected within 100 years" (2 points), "It will be affected within 50 years" (3 points), "It will be affected within 20 years" (4 points), and "It will be affected within 10 years" (5 points).

The study assessed social distance using the question, "How serious an impact does you think climate change has had on society?" Virtual distance was measured by asking, "How serious an impact do you think climate change has had on you?" Social and virtual distances were measured using a five-point scale (5 = *very serious*, temporal distance [mean = 1.74, SD = 1.10], social distance [mean= 4.12, SD = 0.66], and virtual distance [mean = 3.63, SD = 0.74]).

3.2.2. Recognized Seriousness of Media Reports

The recognized seriousness of media reports was assessed using the item, "How do you think that you are dealing with environmental and environmental issues in the media?" (5 = media reduces the seriousness, 1 = media exaggerates the seriousness), A score of 5 means that the seriousness of the environmental problem is overly reduced (mean = 2.97, SD = 0.89).

3.2.3. Guilt

Guilt was measured by asking participants to indicate the extent to which they agree with the statement, "I sometimes engage in harmful actions and feel guilty", using a five-point scale (5 = *strongly agree*, mean = 3.26, SD = 0.91).

3.3. Adjustable Variables

3.3.1. Communication Behavior

Additional information about information seeking was measured by rating the item "I try to obtain more information about the environment" using a five-point scale (mean = 3.31, SD = 0.76). Interpersonal communication was measured using a five-point scale by asking, "I talk to people around me about new facts I learned about the environment" (mean = 3.24, SD = 0.83). A score of 5 means *strongly agree*.

3.3.2. Pro-Environmental Behavior

Pro-environmental behavior was examined using items on the intention to purchase eco-friendly products ("I consider purchasing products with eco-friendly or recycling marks first"), use public transportation ("I use eco-friendly transportation (walking, bicycle, public transport) when traveling short distances"), and energy saving (I use water and electricity sparingly to reduce water and electricity bills at my house) rated on a five-point scale (5 = *strongly agree*). The results are as follows: intention to purchase eco-friendly products: mean = 3.14, SD = 0.91; using public transportation: mean = 3.67, SD = 1.05; and energy saving: mean= 3.87, SD= 0.87.

3.4. Antecedent Variable

Gender, age, interest in environmental issues, and political inclination were assumed to be the antecedent variables that influence eco-friendly behavior.

Interest in environmental issues was assessed using the item "How interested are you in environmental issues on a daily basis?" rated on a five-point scale (5 = *very interested*; mean = 3.79, SD = 0.76).

Political inclination was measured by asking, "To what extent do you consider yourself politically progressive or conservative?" and was assessed using a five-point scale (1 = *very liberal*, 5 = *very conservative*, mean = 3.16, SD = 1.13).

3.5. Hierarchical Regression Analysis

Hierarchical regression analysis was used to examine the predictors of eco-friendly behaviors through six blocks: demographics (gender, age, environmental interest, and political tendency), psychological distance (time, social, and virtual), severity of media reports, emotions (guilt), communication behaviors (information seeking and interpersonal communication), and eco-friendly behaviors (product purchase, public transportation use, and energy saving).

4. Results

4.1. Correlation Analysis Between the Major Variables

Table 1 presents the results of the correlation analysis among guilt, seriousness, and social distance with the variables information seeking, interpersonal communication, and environmentally friendly behavior. The study observed that environmentally friendly behavior (e.g., energy saving and use of public transportation) is interconnected with these psychological and emotional factors.

The severity of climate crisis-related reports was correlated with virtual (0.1653 *) and social (0.2043 *) distance. The greater the recognized severity, the closer people feel at this level. The weak negative correlation with temporal distance (−0.1127 *) indicates that perceived severity slightly decreases temporal distance. Cognitive seriousness exhibited a positive, moderate correlation with guilt (0.1157 *) and additional information seeking (0.1467 *). In other words, the higher the severity of cognitive seriousness, the more the guilt, and the exploration of additional information tend to increase slightly.

Guilt displayed a positive correlation with the variables virtual distance (0.1556 *), social distance (0.1525 *), additional information seeking (0.2357 *), and interpersonal communication (0.2013 *). This result indicates that guilt motivates participation in additional information seeking and interpersonal communication. Guilt was also positively correlated with the intention to purchase eco-friendly products (0.3086 *).

Additional information seeking was strongly correlated with interpersonal communication (0.5645 *). This finding indicates that individuals who seek more information are more likely to discuss it with others. Additional information seeking also pointed to a certain degree of correlation with environmentally friendly behaviors such as energy saving (0.2899 *) and public transportation (0.1852 *).

Regarding eco-friendly behavior, energy saving displays positive correlations with all variables, but has a particularly strong relationship with public transportation (0.3959 *), which implies that individuals who engage in one environmentally friendly behavior are likely to participate in others as well. Other notable correlations included social distance (0.1894 *) and additional information seeking (0.2899 *). The use of public transportation is correlated with additional information seeking (0.1852 *) and energy saving (0.3959 *), thus reflecting patterns of participation in eco-friendly behaviors. Purchase intentions exhibit a positive relationship with guilt (0.3086 *) and the pursuit of additional information (0.3422 *), which indicates that emotional and cognitive factors influence consumer behavior.

In general, correlation coefficients above 0.5 in social science research may suggest a strong relationship, but it is necessary to apply more quantitative criteria to determine multicollinearity. Therefore, this study further examined the Variance Inflation Factor (VIF). The results showed that all variables had VIF values of 3.0 or less, indicating that multicollinearity is not a concern.

Table 1. Correlation matrix of major variables (N = 3088).

	Virtual Distance	Social Distance	Temporal Distance	Recognized Severity of Media Reports	Guilt	Additional Information Seeking	Interpersonal Communication	Intention to Purchase Eco-Friendly Products	Transportation	Energy Saving
Virtual distance	1.0000									
Social distance	0.5024 *	1.0000								
Temporal distance	−0.1578 *	0.2656 *	1.0000							
Recognized severity of media reports	0.1653 *	0.2043 *	0.1127 *	1.0000						
Guilt	0.1556 *	0.1525 *	0.0518	0.1157 *	1.0000					
Additional information seeking	0.2902 *	0.2084 *	0.0599 *	0.1467 *	0.2357 *	1.0000				
Interpersonal communication	0.2390 *	0.1774 *	0.0623 *	0.1223 *	0.2013 *	0.5645 *	1.0000			
Intention to purchase eco-friendly products	0.1694 *	0.1313 *	−0.0732 *	0.1028 *	0.3086 *	0.3422 *	0.2922 *	1.0000		
Use of public transportation	0.1247 *	0.1210 *	0.0856 *	0.0458	0.0596 *	0.1852 *	0.1463 *	0.0806 *	1.0000	
Energy saving	0.1689 *	0.1894 *	0.1409 *	0.0680 *	0.0959 *	0.2899 *	0.2236 *	0.1685	0.3959 *	1.0000

Note. * $p < 0.05$.

4.2. RQ 1: Hierarchical Regression Analysis of Communication Predictions

The first stage included preceding variables such as performance age, environmental interest, and political tendency; in the second stage, the recognized serious variables were added. In the third stage, the recognized severe variable for media reports was added. *In* the fourth stage, guilt, an emotional variable, *was added*. Table 2 *presents* the results of the analysis of the prediction variable of information exploration and interpersonal communication behavior.

Table 2. Hierarchical regression analysis of predictors of communication behavior.

Variables	Information Seeking			Interpersonal Communication		
	β	*t*	*SE*	β	*t*	*SE*
Block 1						
Gender (female)	0.04	1.63 **	0.02	0.13	4.58 ***	0.03
Age	0.01	0.40	0.01	−0.00	−0.80	0.01
Political ideology	−0.03	−1.96 ***	0.01	−0.04	−2.36 ***	0.01
Environment interest	0.39	20.39 ***	0.02	0.37	17.45 ***	0.02
R^2 (F)	0.16 (108.90) ***			0.13 (86.13) ***		
Block 2						
Temporal distance Timing of negative cons.	0.02	0.65	0.01	−0.01	−0.42	0.02
Social distance Impact on society	0.03	1.00	0.02	0.02	0.56	0.01
Virtual distance Impact on individuals	0.19	8.93 **	0.02	0.15	6.61 ***	0.03
R^2 (F)	0.19 (35.78) ***			0.14 (19.18) ***		
Block 3						
Media report severity	0.06	4.03 ***	0.01	0.05	2.61 ***	0.02
R^2 (F)	0.20 (16.25) **			0.15 (6.79) **		
Block 4						
Emotion (guilt)	0.13	7.97 ***	0.02	0.11	6.98 ***	0.02
R^2 (F)	0.22 (63.51) **			0.16 (41.27) ***		

Note. ** $p < 0.01$. *** $p < 0.001$.

The final model describes the difference in information exploration of 22% and 16% of interpersonal communication. *The results indicate that* emotional factors (e.g., guilt) and environmental interest play an important role in predicting this behavior. Specifically, the results *of the* hierarchical regression analysis *on* Block 1 are an important predicting variable for both behaviors (information search: β = 0.39, interpersonal communication: β = 0.37, both *p*s < 0.001). Gender (female) *exerts* a small but significant positive impact, especially *on* interpersonal communication (β = 0.13, $p < 0.001$). Political ideology *exhibits* a negative connection (information exploration: β = −0.03, $p < 0.001$, interpersonal communication: −0.04, $p < 0.001$). The impact on the individual in *terms of the* perception of the impact of Block 2 climate crisis positively predicted both behaviors (β = 0.19, $p < 0.01$ for information search = 0.15, $p < 0.001$). The *severity* of Block 3 (media reports) *exerted* positive impacts *on information search* (β = 0.06, $p < 0.001$) *and interpersonal communication* (β = 0.05, $p < 0.001$). Block 4 *stands for* guilt, *which* strongly predicted *the* two behaviors (β = 0.13, $p < 0.001$ for information exploration, β = 0.11, $p < 0.001$).

4.3. Eco-Friendly Behavior Prediction Variable Hypothesis and Results of Analysis for RQ 2

This study explored the predictors of eco-friendly behavior and focused on psychological distance, media framing, guilt, and communication behavior. It analyzed the impact

of demographics, perceived severity of the climate crisis, media coverage, emotions, and communication on three pro-environmental behaviors, namely purchase intention, transportation, and energy saving. Table 3 shows the results of hierarchical regression analysis by dividing eco-friendly behavioral predictions into five blocks. The analysis results were presented as follows.

Table 3. Hierarchical regression analysis of predictors of pro-environmental behavior.

Variables	Purchase Intention			Public Transportation			Energy Saving		
	β	*t*	*SE*	β	*T*	*SE*	β	*t*	*SE*
Block 1									
Gender (female)	0.10	2.91 ***	0.03	0.17	4.61 ***	0.03	0.12	4.04 ***	0.03
Age	0.09	7.52 ***	0.01	−0.08	−6.33 ***	0.01	0.08	7.48 ***	0.01
Political ideology	−0.04	−2.24 **	0.01	0.03	1.51	0.02	0.02	1.10	0.01
Environment interest	0.27	12.25 ***	0.02	0.26	10.20 ***	0.03	0.32	14.92 ***	0.02
R^2 (F)	0.09 (63.84) ***			0.04 (37.54) ***			0.11 (89.93) ***		
Block 2									
Temporal distance Timing of negative cons.	0.00	0.01	0.01	−0.07	−3.06 ***	0.02	−0.10	−5.19 ***	0.02
Social distance Impact on society	0.01	0.44	0.03	0.06	1.80 *	0.01	0.08	2.89 ***	0.01
Virtual distance Impact on individuals	0.12	4.38 ***	0.03	0.07	2.24 **	0.03	0.05	2.02 **	0.03
R^2 (F)	0.10 (9.01) ***			0.06 (9.42) ***			0.13 (18.87) ***		
Block 3									
Media report severity	0.06	3.02 ***	0.02	−0.01	−0.24	0.02	0.01	0.52	0.02
R^2 (F)	0.11 (9.09) **			0.06 (0.06)			0.13 (0.27)		
Block 4									
Emotion (guilt)	0.27	12.83 ***	0.02	0.01	0.57	0.02	0.04	2.02 *	0.02
R^2 (F)	0.17 (164.48) ***			0.06 (0.33)			0.14 (4.07)		
Block 5									
Information seeking	0.21	7.97 ***	0.03	0.16	5.00 ***	0.03	0.20	7.06 ***	0.03
Interpersonal communication	0.11	4.78 ***	0.02	0.04	1.30	0.03	0.05	1.90 *	0.02
R^2 (F)	0.22 (74.22) ***			0.08 (20.05) ***			0.17 (40.70) ***		

Note. * $p < 0.05$. ** $p < 0.01$. *** $p < 0.001$.

In the hierarchical regression model, demographic variables (i.e., gender, age, environmental interest, and political orientation) were included in the first step, followed by perceived severity in the second step, severity of media coverage in the third, guilt in the fourth, and communication behavior in the fifth. The final model explained 22% of purchase intention, 8% of public transportation use, and 17% of energy saving. Information seeking and environmental concerns emerged as consistent predictors across all behaviors.

H1 (temporal distance) was partially supported, as it positively predicted public transportation use (β = −0.07, $p < 0.001$) and energy saving (β = −0.10, $p < 0.001$) but not purchase intention. H2 (social distance) was also partially supported, as it positively predicted public transportation use (β = 0.08, $p < 0.001$) and energy saving (β = 0.06, $p < 0.001$) but not purchase intention. H3 (virtual distance) was fully supported, as it positively predicted purchase intention (β = 0.12, $p < 0.001$), public transportation use (β = 0.07, $p < 0.05$), and energy saving (β = 0.05, $p < 0.05$). H4 (perceived severity of media coverage) was partially supported, because it positively influenced purchase intention (β = 0.06, $p < 0.001$) but not the other behaviors. H5 (guilt) was partially supported, significantly predicting

purchase intention (β = 0.27, $p < 0.001$) and energy saving (β = 0.04, $p < 0.05$) but not the use of public transportation.

Block 1 (demographics) demonstrated that women and those with high levels of environmental concerns engaged more in eco-friendly behaviors. Younger people preferred public transportation, while older individuals focused on energy saving and eco-friendly products. Block 2 (perception of impact) affected all behaviors, while Block 3 (media coverage) influenced purchase intention. Guilt (Block 4) strongly predicted purchase intention. Block 5 (communication behavior) significantly influenced all behaviors with information seeking and interpersonal communication enhancing purchase intention and energy saving.

These findings highlight the importance of demographic factors, emotional appeals, and communication strategies in promoting eco-friendly behaviors.

Figure 2 illustrates the values presented in Table 1, focusing on the relationship between the independent and dependent variables. By incrementally incorporating an eco-friendly rinse-based predictor variable, the figure presents the results of a hierarchical regression analysis used to assess the contribution of the independent variables. A positive coefficient indicates that the dependent variable increases as the independent variable increases, whereas a negative coefficient signifies that the dependent variable decreases as the independent variable increases.

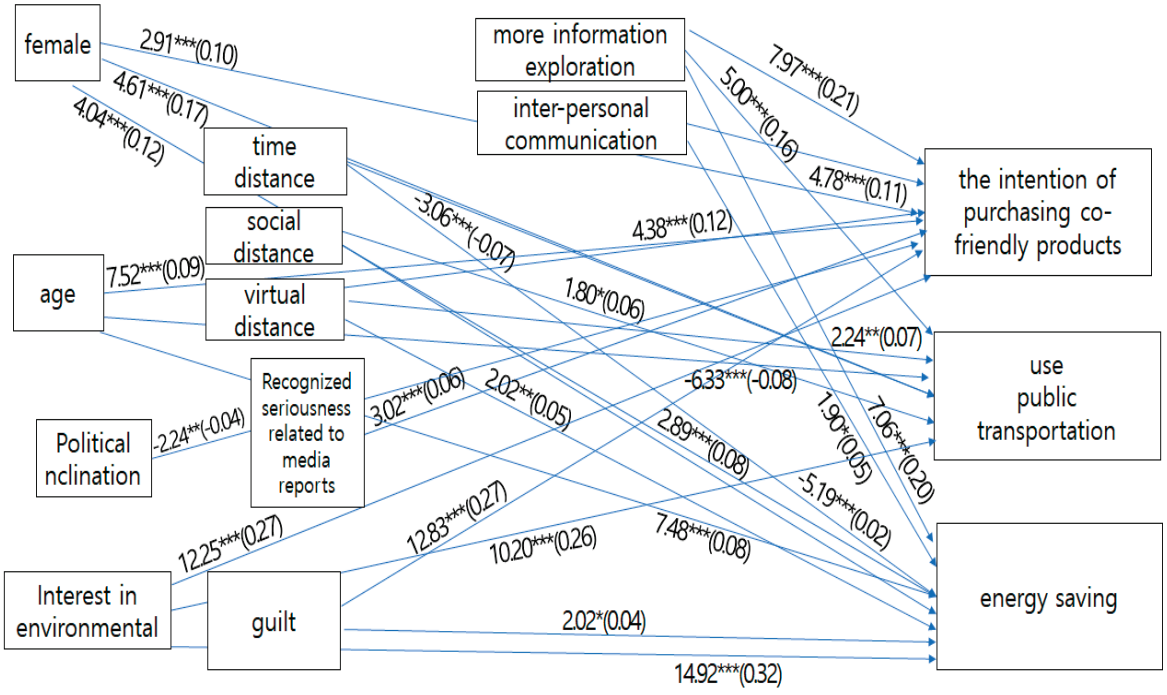

Figure 2. Results of hierarchical regression analysis. Note. * $p < 0.05$. ** $p < 0.01$. *** $p < 0.001$.

4.4. Results of the Analysis of Eco-Friendly Behavioral Control for RQ 3

Interpersonal communication exerted a positive influence on the relationship between virtual distance and environmentally friendly behavior (energy saving). It also exerted a positive moderating effect on the relationship between the temporal distance and energy conservation. Table 4 presents the results of the analysis of the moderating effect of communication behavior on the relationship between perceived seriousness and eco-friendly behavior.

Table 4. Moderating effect of communication behavior on relationship between perceived severity and pro-environmental behavior.

Energy Saving	**Coef.**	**Std. Err.**	***t***	***p*** **> |** ***t*** **|**	**[95% Confidence Interval]**	
Virtual distance	−0.0914217	0.0755374	−1.21	0.226	−0.2395304	0.0566869
Interpersonal communication	−0.06263	0.0838019	−0.75	0.455	−0.2269431	0.1016831
Virtual distance: interpersonal communication	0.0726037	0.0224037	3.24	0.001	0.0286693	0.1165481
_cons	3.538153	0.2752349	12.86	0.000	2.99849	4.077815
Use of public transportation	**Coef.**	**Std. Err.**	***t***	***p*** **> |** ***t*** **|**	**[95% Confidence interval]**	
Temporal distance	−0.2970804	0.0632019	−0.12	0.002	−0.3210024	−0.0731583
Interpersonal communication	0.2092843	0.0403777	−2.70	0.007	0.0300134	0.18833531
Time distance-interpersonal communication	0.048859	0.0190892	2.04	0.042	0.0014301	0.076288
_cons	3.439068	0.13559255	25.30	0.000	3.172354	3.703582

The relationship between virtual distance and energy saving displayed a negative but statistically nonsignificant direct effect (coefficient = −0.0914, $p = 0.226$). This result indicates that virtual distance alone does not exert a significant direct impact on energy saving behavior. Similarly, interpersonal communication exerted a negative but nonsignificant direct effect (coefficient = −0.0626, $p = 0.455$). However, when virtual distance interacted with interpersonal communication (coefficient = 0.0726, $p = 0.001$), the interaction effect was positive and statistically significant. This finding implies that interpersonal communication moderates the effect of virtual distance on energy conservation, which amplifies its positive impact.

The direct effect of temporal distance on the use of public transportation was negative and statistically significant (coefficient = −0.2971, $p = 0.002$). This result denotes that the likelihood of using public transportation decreases with the increase in the perceived temporal distance of eco-friendly behavior. Conversely, interpersonal communication exerted a significant and positive direct effect (coefficient = 0.2093, $p = 0.007$), which indicates that it encourages the use of public transportation. Furthermore, the effect of the interaction between temporal distance and interpersonal communication (coefficient = 0.0489, $p = 0.042$) was positive and statistically significant. This result indicates that interpersonal communication mitigates the negative impact of temporal distance on the use of public transportation.

5. Discussion

This study examined the predictors of communication behavior, particularly information seeking and interpersonal communication, in the context of the climate crisis. It performed hierarchical regression analysis to analyze individual and situational factors, including demographics, environmental concerns, perceived severity, and guilt.

The perceived severity of the climate crisis strongly predicted information seeking and interpersonal communication with women more engaged in discussions. Conservative political tendencies hindered these behaviors, which indicates the need for targeted strategies. Perceptions of psychological distance decreased the adoption of eco-friendly behavior, which emphasizes the importance of local and immediate impacts. Media coverage enhanced communication, while guilt motivated information seeking as a coping mechanism. Women exhibited higher levels of participation in pro-environmental behaviors, while younger individuals favored the use of public transportation and older ones

prioritized energy conservation and eco-friendly products. Environmental concern was the strongest predictor wherein practical benefits influence purchase decisions more than perceived distances.

Guilt strongly predicted purchase intentions but exerted limited effects on other behaviors, thus highlighting the need for complementary strategies. Information seeking was a key predictor across behaviors, while interpersonal communication significantly influenced purchase intention and energy conservation. It also moderated psychological distances, thus bridging the gap between immediate actions and long-term climate benefits. Guilt can serve as a strong motivator for immediate eco-friendly behavior, but it is unlikely to sustain long-term behavioral change unless reinforced by positive emotions such as pride or self-efficacy [30]. Excessive guilt may lead to anxiety, stress, or feelings of helplessness, which can hinder eco-friendly actions [36]. This study highlights guilt as a significant predictor of eco-friendly behavior but emphasizes the need for a balance between guilt and other motivational factors, such as pride, to maintain long-term engagement in sustainable practices.

This study builds on previous research that links proximity to environmental issues, such as climate change, to stronger eco-friendly behavior. It demonstrates that perceptions of the climate crisis' severity, influenced by psychological distance, motivate individuals to seek information and engage in environmentally responsible actions. Media coverage of the climate crisis plays a pivotal role in promoting such behaviors by fostering information seeking and interpersonal communication, aligning with theories that media reports shape public interest and inspire action.

The study also reinforces the theory that guilt is a powerful motivator for eco-friendly behavior. Negative emotions, particularly guilt, have been shown to strongly predict information seeking and eco-friendly purchasing intentions, highlighting the effectiveness of emotion-based messaging in promoting environmental action.

Demographic differences were observed in communication preferences and eco-friendly behaviors, with women and younger individuals favoring interpersonal communication and public transportation, while older individuals focused more on energy conservation and eco-friendly purchases. This suggests that communication preferences and behaviors may not align with existing theoretical models, underscoring the need for tailored strategies that consider demographic factors such as age and gender.

The findings provide valuable insights for stakeholders, including policymakers and environmental communicators. Policymakers can emphasize the immediacy and relevance of climate threats, while environmental communicators can develop messages that resonate emotionally with individuals, tailored to specific demographic groups. Overall, this study advocates for a multifaceted, targeted approach to promoting eco-friendly behavior that accounts for emotional drivers, demographic differences, and media framing.

6. Conclusions

This study examines the effects of cognitive and emotional factors, including psychological distance, media framing, and guilt, on communication and pro-environmental behavior. It emphasizes the reduction of psychological distance through personalized messages and the use of guilt to drive eco-friendly actions, while balancing guilt with positive emotions such as pride for sustaining long-term changes in behavior.

The study highlights guilt as a key emotional driver but suggests the exploration of other emotions such as pride, fear, and anger. It calls for cross-cultural, longitudinal, and norm-based research, as well as investigation into the interaction between online and offline behaviors through digital platforms for further insights.

The current research offers valuable contributions to an enhanced understanding of the relationship among perceptions, emotions, and behaviors in the context of the climate crisis, helping to design other effective communication strategies and policies to encourage sustainable practices.

This study offers valuable insights into the relationship between the climate crisis, guilt, communication behavior, and eco-friendly actions, yet several limitations must be acknowledged. While the study establishes clear correlations, the use of time-series data would provide a more robust understanding of causal relationships and the long-term effects of media framing on eco-friendly behavior. The focus on a specific demographic limits the generalizability of the findings; thus, conducting similar research across diverse cultural and regional contexts would enhance the broader applicability of the results. Additionally, while this study primarily emphasizes guilt as an emotional driver, future research should examine other emotions, such as fear, pride, or shame, as potential motivators of pro-environmental behavior. Finally, investigating the long-term effects of emotions, media frames, and psychological distance on eco-friendly behavior would deepen our understanding of how individual perceptions and behaviors evolve over time, contributing to a more comprehensive view of the sustainability of eco-friendly actions.

In this study, the emotions considered as key predictors of eco-friendly behavior are socially constructed and vary significantly across cultures. The experience of emotions such as guilt, fear, and responsibility in environmental issues is shaped by cultural norms at both the individual and group levels [45]. Additionally, individuals from different cultural backgrounds perceive the psychological distance and risks associated with the climate crisis differently, which in turn influences their emotional engagement and behavioral responses [45].

Therefore, when interpreting and generalizing research findings from a specific region, such as Korea, it is essential to consider cultural differences in emotional responses and the role of media in framing climate issues. These factors may lead to varying perceptions and reactions among different populations, underscoring the importance of cultural context in climate crisis communication and behavior.

Author Contributions: Conceptualization, J.H.; methodology, J.H. and C.-Y.J.; software, C.-Y.J.; validation, J.H. and C.-Y.J.; formal analysis, C.-Y.J.; data curation, C.-Y.J.; writing—original draft preparation, J.H.; writing—review and editing, C.-Y.J. All authors have read and agreed to the published version of the manuscript.

Funding: This research received no external funding.

Institutional Review Board Statement: This study utilized publicly available data that did not contain personally identifiable information, as provided on the Korea Environment Institute (KEI)'s homepage (https://doi.org/10.23160/keidata.12) a government-affiliated organization of South Korea. Data Connection Date: 19 November 2024. According to Chapter 2, Article 6 of the Korea Environment Institute's Research Ethics Regulations, the Research Ethics Committee is responsible for reviewing and approving research through deliberation and voting on the initiation of preliminary surveys and the approval of research findings (https://www.kei.re.kr/menu.es?mid=a10503000000/https://www.kei.re.kr/board.es?mid=a20609010000&bid=0061).

Informed Consent Statement: Informed consent was obtained from all subjects involved in the study.

Data Availability Statement: The data presented in this study are available on request from the corresponding author.

Conflicts of Interest: Author Chang-Young Jeon was employed by the company Korea Press Foundation. The remaining authors declare that the research was conducted in the absence of any commercial or financial relationships that could be construed as a potential conflict of interest.

References

1. World Wide Fund for Nature (WWF) Korea. The Environmental Perception of Korean Society Through Big Data Analysis. Available online: https://wwfkorea.or.kr/data/file/korean_report/1794572195_LVUsXNcj_01ba13033992c5a3e94adc9f5dc3ecfcb491a74d.pdf?utm_source=chatgpt.com (accessed on 4 February 2025).
2. Ostrom, E. Polycentric systems for coping with collective action and global environmental change. *Glob. Environ. Chang.* **2010**, *20*, 550–557. [CrossRef]
3. Korea Environmental Research Institute (KEI). National Environmental Awareness Survey. 2023. Available online: https://www.kei.re.kr/elibList.es?mid=a10101010000&elibName=researchreport&class_id=&act=view&c_id=760172 (accessed on 4 February 2025).
4. Li, N.; Su, L.Y. Message Framing and Climate change communication: A Meta-Analytical Review. *J. Appl. Commun.* **2018**, *102*, 4. [CrossRef]
5. Kollmuss, A.; Agyeman, J. Mind the gap: Why do people act environmentally and what are the barriers to pro-environmental behavior? *Environ. Educ. Res.* **2002**, *8*, 239–260. [CrossRef]
6. Gifford, R.; Nilsson, A. Personal and social factors that influence pro-environmental concern and behaviour: A review. *Int. J. Psychol.* **2014**, *49*, 141–157. [CrossRef]
7. Harth, N.S.; Leach, C.W.; Kessler, T. Guilt, anger, and pride about in-group environmental behaviour: Different emotions predict distinct intentions. *J. Environ. Psychol.* **2013**, *34*, 18–26. [CrossRef]
8. Ajzen, I. The theory of planned behavior. *Organ. Behav. Hum. Decis. Process.* **1991**, *50*, 179–211. [CrossRef]
9. Choo, C.W. Climate change information seeking. *J. Assoc. Inf. Sci. Technol.* **2023**, *74*, 1086–1099. [CrossRef]
10. Hovick, S.R.; Bigsby, E.; Wilson, S.R.; Thomas, S. Information seeking behaviors and intentions in response to environmental health risk messages: A test of a reduced risk information seeking model. *Health Commun.* **2021**, *36*, 1889–1897. [CrossRef]
11. Han, R.; Xu, J. A comparative study of the role of interpersonal communication, traditional media and social media in pro-environmental behavior: A China-based study. *Int. J. Environ. Res. Public Health* **2020**, *17*, 1883. [CrossRef]
12. Atkins, W.A. *Energy: In Context*; Lerner, B.W., Lerner, K.L., Riggs, T., Eds.; World Commission on Environment and Development: Farmington Hills, MI, USA, 1986; Volume 2, pp. 903–933. Available online: https://go-gale-com-ssl.proxy.kookmin.ac.kr/ps/i.do?v=2.1&u=keris183&it=r&id=GALE%7CCX3627100233&p=GVRL&sw=w&aty=ip (accessed on 4 February 2025).
13. Olson, M. *The Logic of Collective Action: Public Goods and the Theory of Groups*; Harvard University Press: Cambridge, UK, 1965; Available online: http://commres.net/wiki/_media/olson.pdf (accessed on 4 February 2025).
14. Stern, P.C. New environmental theories: Toward a coherent theory of environmentally significant behavior. *J. Soc. Issues* **2000**, *56*, 407–424. [CrossRef]
15. Kleres, J.; Wettergren, Å. Fear, hope, anger, and guilt in climate activism. *Soc. Mov. Stud.* **2017**, *16*, 507–519. [CrossRef]
16. Jones, C.; Hine, D.W.; Marks, A.D. The future is now: Reducing psychological distance to increase public engagement with climate change. *Risk Anal.* **2017**, *37*, 331–341. [CrossRef] [PubMed]
17. DeSombre, E.R. *Why Good People Do Bad Environmental Things*; Oxford University Press: Oxford, UK, 2018.
18. Trope, Y.; Liberman, N. Construal-level theory of psychological distance. *Psychol. Rev.* **2010**, *117*, 440–463. [CrossRef] [PubMed]
19. Gifford, R. The dragons of inaction: Psychological barriers that limit climate change mitigation and adaptation. *Am. Psychol.* **2011**, *66*, 290–302. [CrossRef] [PubMed]
20. Spence, A.; Poortinga, W.; Pidgeon, N. The psychological distance of climate change. *Risk Anal.* **2012**, *32*, 957–972. [CrossRef]
21. McCombs, M.E.; Shaw, D.L. The agenda-setting function of mass media. *Public Opin. Q.* **1972**, *36*, 176–187. [CrossRef]
22. Entman, R.M. Framing: Toward clarification of a fractured paradigm. *J. Commun.* **1993**, *43*, 51–58. [CrossRef]
23. Chong, D.; Druckman, J.N. Framing theory. *Annu. Rev. Political Sci.* **2007**, *10*, 103–126. [CrossRef]
24. Nisbet, M.C. Communicating Climate Change: Why Frames Matter for Public Engagement. *Environ. Sci. Policy Sustain. Dev.* **2009**, *51*, 12–23. [CrossRef]
25. Mallett, R.K.; Melchiori, K.J. Guilt and environmental message framing: How guilt impacts public support for environmental legislation. *J. Environ. Psychol.* **2016**, *45*, 34–45. [CrossRef]
26. Ryan, R.M.; Deci, E.L. Autonomy is no illusion: Self-determination theory and the empirical study of authenticity, awareness, and will. In *Handbook of Experimental Existential Psychology*; Greenberg, J., Koole, S.L., Pyszczynski, T., Eds.; Guilford Press: New York, NY, USA, 2000; pp. 449–479. Available online: https://www.researchgate.net/publication/232506712 (accessed on 4 February 2025).
27. Bamberg, S.; Möser, G. Twenty years after Hines, Hungerford, and Tomera: A new meta-analysis of psycho-social determinants of pro-environmental behavior. *J. Environ. Psychol.* **2007**, *27*, 14–25. [CrossRef]
28. Schneider, C.R.; Zaval, L.; Weber, E.U.; Markowitz, E.M. The influence of anticipated pride and guilt on pro-environmental decision making. *PLoS ONE* **2017**, *12*, e0188781. [CrossRef] [PubMed]
29. Lazarus, R.S. *Emotion and Adaptation*; Oxford University Press: New York, NY, USA, 1991. [CrossRef]

30. Baumeister, R.F.; Stillwell, A.M.; Heatherton, T.F. Guilt: An interpersonal approach. *Psychol. Bull.* **1994**, *115*, 243–267. [CrossRef] [PubMed]
31. Schwartz, S.H. Normative influences on altruism. *Adv. Exp. Soc. Psychol.* **1977**, *10*, 221–279. [CrossRef]
32. Vrselja, I.; Pandžić, M.; Rihtarić, M.L.; Ojala, M. Media exposure to climate change information and pro-environmental behavior: The role of climate change risk judgment. *BMC Psychol.* **2024**, *12*, 262. [CrossRef]
33. Sparkman, G.; Howe, L.; Walton, G. How social norms are often a barrier to addressing climate change but can be part of the solution. *Behav. Public Policy* **2021**, *5*, 528–555. [CrossRef]
34. Leiserowitz, A. Climate change risk perception and policy preferences: The role of affect, imagery, and values. *Clim. Chang.* **2006**, *77*, 45–72. [CrossRef]
35. Mallett, R.K.; Harrison, P.R.; Melchiori, K.J. Guilt and Environmental Behavior. In *Encyclopedia of Quality of Life and Well-Being Research*; Michalos, A.C., Ed.; Springer Netherlands: Dordrecht, The Netherlands, 2014; pp. 2622–2626. [CrossRef]
36. Griffin, R.J.; Dunwoody, S.; Neuwirth, K. Proposed model of the relationship of risk information seeking and processing to the development of preventive behaviors. *Environ. Res.* **1999**, *80 Pt 2*, S230–S245. [CrossRef]
37. Bandura, A. Social cognitive theory of self-regulation. *Organ. Behav. Hum. Decis. Process.* **1991**, *50*, 248–287. [CrossRef]
38. Moser, S.C.; Dilling, L. *Creating a Climate for Change: Communicating Climate Change and Facilitating Social Change*; Cambridge University Press: Cambridge, UK, 2007; pp. 163–164. [CrossRef]
39. Zelezny, L.C.; Chua, P.P.; Aldrich, C. New ways of thinking about environmentalism: Elaborating on gender differences in environmentalism. *J. Soc. Issues* **2000**, *56*, 443–457. [CrossRef]
40. Ágoston, C.; Balázs, B.; Mónus, F.; Varga, A. Age differences and profiles in pro-environmental behavior and eco-emotions. *Int. J. Behav. Dev.* **2024**, *48*, 132–144. [CrossRef]
41. Clayton, S.; Opotow, S. (Eds.) Clayton, S.; Opotow, S. (Eds.) Environmental identity: A conceptual and an operational definition. In *Identity and the Natural Environment: The Psychological Significance of Nature*; The MIT Press: Cambridge, MA, USA, 2003; pp. 45–66. [CrossRef]
42. McCright, A.M.; Dunlap, R.E. The politicization of climate change and polarization in the American public's views of global warming, 2001–2010. *Sociol. Q.* **2011**, *52*, 155–194. [CrossRef]
43. Haidt, J. The new synthesis in moral psychology. *Science* **2007**, *316*, 998–1002. [CrossRef] [PubMed]
44. Fielding, K.S.; Hornsey, M.J. A social identity analysis of climate change and environmental attitudes and behaviors: Insights and opportunities. *Front. Psychol.* **2016**, *7*, 121. [CrossRef]
45. Markus, H.R.; Kitayama, S. Culture and the self: Implications for cognition, emotion, and motivation. *Psychol. Rev.* **1991**, *98*, 224–253. [CrossRef]

Disclaimer/Publisher's Note: The statements, opinions and data contained in all publications are solely those of the individual author(s) and contributor(s) and not of MDPI and/or the editor(s). MDPI and/or the editor(s) disclaim responsibility for any injury to people or property resulting from any ideas, methods, instructions or products referred to in the content.

agronomy

MDPI

Article

Agriculture Resilient at Three Irrigation Modules of Zacatecas, Mexico: Water Scarcity and Climate Variability

Carlos Bautista-Capetillo [1,†], Hugo Pineda-Martínez [1,†], Luis Alberto Flores-Chaires [1,*] and Luis Felipe Pineda-Martínez [2]

[1] Educational Program of Doctorado en Ciencias de la Ingeniería, Universidad Autónoma de Zacatecas "Francisco García Salinas", Campus UAZ Siglo XXI, Carretera, Zacatecas-Guadalajara Km. 6, La Escondida, Zacatecas 98160, Mexico; baucap@uaz.edu.mx (C.B.-C.); hpineda@uaz.edu.mx (H.P.-M.)

[2] Educational Program of Doctorado en Ciencias Sociales, Universidad Autónoma de Zacatecas "Francisco García Salinas", Campus Universitario II, Avenida Preparatoria s/n, Fraccionamiento Progreso, Zacatecas 98065, Mexico; lpineda@uaz.edu.mx

* Correspondence: luischaires@uaz.edu.mx; Tel.: +52-492-544-3340

† These authors contributed equally to this work.

Abstract: Agriculture is the largest consumer of freshwater resources, accounting for approximately 70% of total water withdrawals. In semi-arid regions like Zacatecas, Mexico, water scarcity and climate variability pose critical challenges to small-scale farmers. This study evaluates the effectiveness of integrating modern irrigation technologies with traditional water management practices to enhance agricultural resilience. Analysis of climatic data (1961–2020) revealed a statistically significant increase in annual precipitation of 2.01 mm year^{-1} in the Leobardo Reynoso module ($p < 0.05$), while the Miguel Alemán module exhibited a decline ranging from -0.54 mm year^{-1} to -2.22 mm year^{-1}, exacerbating water scarcity. Pressurized irrigation systems in Leobardo Reynoso improved application efficiency to 87.5%, compared to 50% in traditional furrow irrigation. Despite these advancements, conveyance efficiency remains low (60%) due to extensive open canal networks. Climate projections indicate a 6–11% increase in irrigation water demand for staple crops by 2065, driven by rising evapotranspiration rates. Findings underscore the need for policy interventions, infrastructure upgrades, and financial support to sustain agricultural productivity in water-stressed environments.

Keywords: agriculture; water use efficiency; traditional plus modern irrigation strategies; climate resilience

1. Introduction

Small-scale agriculture underpins global food security, particularly in developing countries where it accounts for over 80% of food production [1]. It sustains rural livelihoods, contributes significantly to local economies, and plays a vital role in managing natural resources [2]. However, water scarcity and climate variability threaten the sustainability of these systems, challenging their ability to alleviate rural poverty [3,4]. Water scarcity, currently affecting 40% of the global population, poses a substantial obstacle to agricultural productivity, especially in water-stressed regions [5]. This challenge is compounded by disrupted rainfall patterns and the increased frequency of extreme weather events [6], which intensify global temperature rises, amplify growing season unpredictability, and raise the risk of crop failures [7]. Smallholder farmers, who rely heavily on rain-fed agriculture, are particularly vulnerable due to limited access to alternative water sources, irrigation infrastructure, and financial resources for implementing adaptive measures [8].

Without effective water management strategies, small-scale agriculture faces declining productivity, heightened vulnerability, and increased risks of food insecurity [9].

Irrigation has long been recognized as a critical adaptation strategy to mitigate the impacts of water scarcity and climate variability. By providing a reliable water supply, irrigation systems stabilize yields, improve water productivity, and reduce smallholder farmers' dependence on erratic rainfall [10]. However, despite its potential, access to advanced irrigation technologies remains limited for many small-scale farmers due to economic, technical, and social barriers [11]. Additionally, existing irrigation systems often suffer from inefficiencies, with significant water losses through evaporation, runoff, or poor design [12,13]. Enhancing water-use efficiency and adopting innovative irrigation methods are urgently needed to achieve sustainable water use in agriculture.

Traditional water management practices, often low-cost and environmentally sustainable, remain underutilized in modern frameworks. Techniques such as terracing, mulching, infiltration ditches, rainwater harvesting, and crop pattern rotation show promise for enhancing soil moisture retention and optimizing water use in smallholder systems [2,14]. Derived from local knowledge, these practices offer cost-effective solutions for smallholder farmers lacking access to expensive irrigation systems. Integrating modern irrigation technologies with traditional practices may provide the most effective solution for building resilience in water-scarce and climate-vulnerable regions [7]. Community-based water management initiatives, such as shared irrigation schemes and water user associations, have demonstrated potential in improving equitable access to water resources and fostering collective action for water conservation [15].

Despite growing research on irrigation and water management strategies, significant gaps remain in understanding how these solutions can be tailored to the unique needs of smallholder farmers. Most government policies focus on large-scale irrigation systems and fail to adequately address socio-economic and cultural constraints influencing adoption at the small-scale level [16]. Furthermore, limited empirical evidence exists regarding the long-term impacts of combining modern and traditional irrigation practices on agricultural resilience, particularly in regions experiencing acute water stress. For instance, while drip irrigation systems improve water-use efficiency, their high initial costs and maintenance requirements often deter adoption by resource-constrained smallholders [17]. The integration of traditional and modern practices remains poorly explored, leaving opportunities for synergies largely underutilized. These knowledge gaps hinder the development of targeted policies and practices that could promote the widespread adoption of effective water management solutions for small-scale agriculture.

This study analyzes specific water management strategies for irrigation in small-scale agricultural systems of Zacatecas, Mexico. It focuses on three regions affected by water scarcity and climate variability. The research evaluates pressurized irrigation methods' advantages in terms of rational water use, as well as their capacity to face the complexity of challenges that arise to meet crop water needs in an environment of increasing climatic variability, and how, from a holistic context, technology limitations can be remedied to prolong the productive life of irrigation modules, contributing to agricultural resilience and the viability of small farmers to stay cropping their plots.

2. Materials and Methods

2.1. Study Area

The research was conducted in Zacatecas, a region in northern Mexico characterized by semiarid climatic conditions, where effective water management is crucial for sustaining agricultural productivity. Geographically, Zacatecas lies between latitudes 21°01′45.0″ N and 25°07′21.5″ N, and longitudes 100°43′34.3″ W and 104°43′34.3″ W. The region features

diverse physiographic characteristics, including the Sierra Madre Occidental to the west, the Meseta Central Highlands in the central portion, and the Sierra Madre Oriental to the north. Elevations range from 1000 m in the valleys to 3200 m above sea level in mountainous areas. Zacatecas experiences a semi-arid climate, with an annual average precipitation of approximately 350 mm, 80% of which occurs between June and September during the rainy season. Rainfall variability is high, both spatially and temporally, and prolonged droughts are common. Annual temperatures range from an average low of 6.5 °C in January to a high of 29.6 °C in May. These climatic conditions pose significant challenges for water resource management, particularly in irrigated agriculture, where potential evapotranspiration far exceeds precipitation.

Agriculture remains a vital economic activity in Zacatecas, covering approximately 1.7 million hectares, with 13% of this area under irrigation. The primary crops grown in the region include vegetables (such as peppers, garlic, onions, and tomatoes), grains (including maize, beans, oats, wheat, and sorghum), and forage crops such as alfalfa. Among the irrigated areas, Irrigation District No. 034 stands out, covering 18,000 hectares and plays a significant role in the regional economy. Within this district, three irrigation modules —Julián Adame (JA), Miguel Alemán (MA), and Leobardo Reynoso (LR)—were selected for analysis. These modules collectively span 11,971 hectares and rely on a combination of lined and unlined canal networks for water distribution (Figure 1).

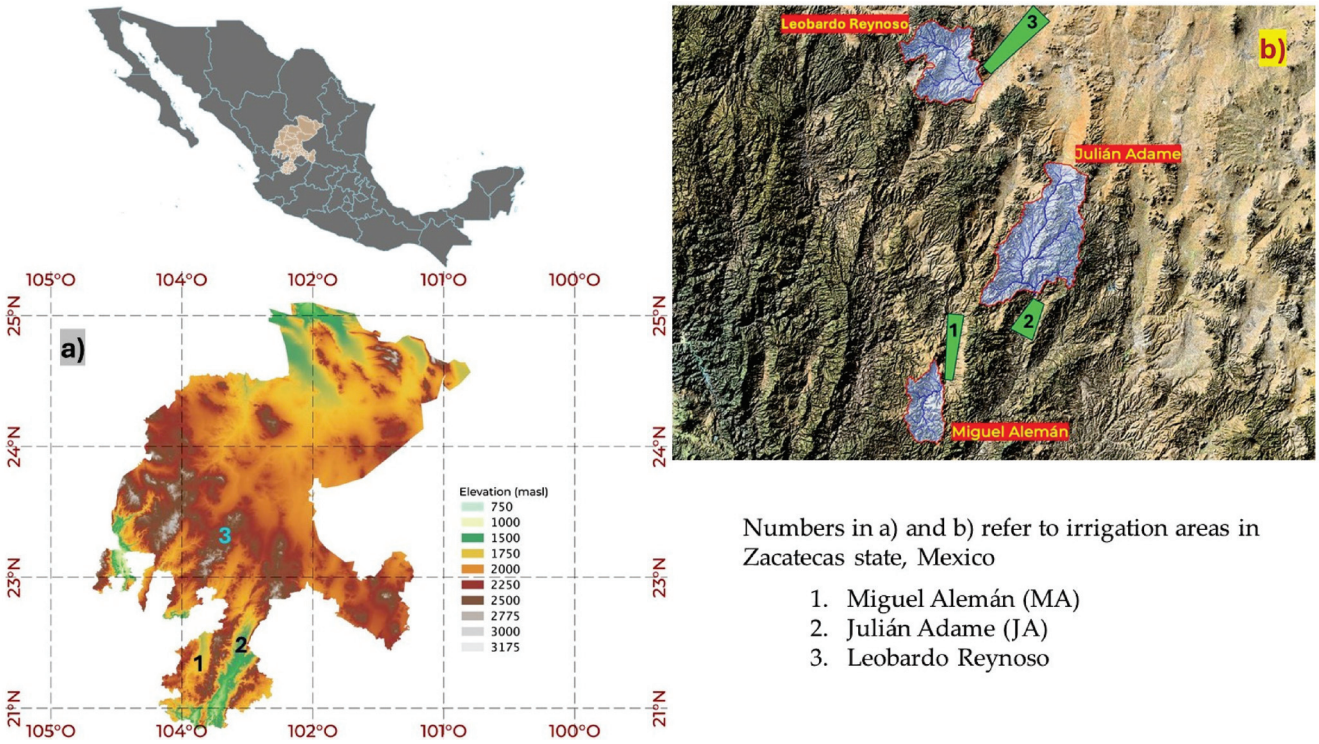

Figure 1. A sketch depiction of Leobardo Reynoso (LR), Julian Adame (JA) and Miguel Aleman (MA) irrigation module's location.

2.2. Statistical Analysis of Rainfall and Temperature Trends

Long-term rainfall and temperature time series were analyzed from 16 meteorological stations strategically distributed across Zacatecas, to assess climatic variability and its implications for water resources into three irrigation modules. These stations, monitored by the Servicio Meteorológico Nacional (SMN) of México [18], encompass daily and monthly precipitation and temperature records spanning the period from 1961 to 2020. Prior to statistical evaluation, a robust pre-processing protocol was implemented to rectify data

deficiencies and ensure integrity. Stations exhibiting less than 15% missing data were retained for analysis, and minor gaps of up to three days per month were interpolated using the monthly station-specific means. In cases where data gaps exceeded the defined threshold, missing values were reconstructed using either Inverse Distance Weighting (IDW) or linear regression (Lreg), leveraging data from nearby stations [19,20]. IDW was selected due to the observed negative correlation between station distance and the similarity of climatic variables (rainfall and temperature), indicating that closer stations tend to exhibit more similar precipitation trends. This relationship supports the use of IDW, as proximity is a key condition for effective interpolation [21–23]. To ensure data reliability, outlier detection and correction followed stringent quality control methodologies [24].

The selection of IDW as the most accurate interpolation method was justified through a quantitative validation process using independent testing data [25]. Specifically, approximately 20% of observed data was excluded from the interpolation process and later used to assess IDW's accuracy against alternative methods. Mean Absolute Error (MAE) and Root Mean Square Error (RMSE) were used to measure deviations between actual and interpolated values. For precipitation data, IDW achieved an MAE of 49.92 mm and an RMSE of 64.02 mm, performing comparably to Ridge spatial regression (48.59 mm MAE, 63.96 mm RMSE) and simplified Kriging (46.37 mm MAE, 65.45 mm RMSE), while spline performance showed higher errors (60.04 mm MAE, 81.96 mm RMSE). For temperature data, a qualitative assessment confirmed that IDW effectively captured spatial and temporal trends without introducing significant biases or distortions. While alternative methods such as spline yielded slightly lower errors, they required higher computational resources and were more sensitive to data gaps, leading to unrealistic fluctuations in interpolated values.

To explain climatic variability within the region, seasonal and annual precipitation and temperature patterns were examined using comprehensive descriptive statistical measures, involving central tendency, dispersion metrics, and variability coefficients [26]. The characterization of temporal trends in these hydroclimatic variables was performed using the Mann-Kendall (MK) test, a non-parametric method designed to identify monotonic trends in time series data independent of underlying distributional assumptions [27–30]. Statistical significance of observed trends was evaluated based on a normalized test statistic, applying a 95% confidence threshold to ensure rigor in inference. To mitigate the risk of inflated trend significance attributable to serial correlation, pre-whitening procedures were systematically employed. Furthermore, complementary statistical methodologies [31,32] were incorporated to validate findings and attenuate potential autocorrelation effects, thereby reinforcing the robustness of trend assessments.

To detect discontinuities and structural changes in the mean or variance of precipitation and temperature time series, multiple statistical tests were applied to enhance diagnostic accuracy. The Pettitt test, a rank-based non-parametric technique, was utilized to identify potential change points indicative of abrupt climatic shifts [33]. The Standard Normal Homogeneity Test (SNHT) facilitated comparative assessment of mean values before and after detected change points [34]. The Buishand Range Test [35] was employed to evaluate systematic shifts in the mean of observed records through cumulative deviation analysis, while the Von Neumann Ratio Test [36] provided an independent measure of randomness within the time series.

In order to identify cyclic patterns within precipitation and temperature time series, the Fast Fourier Transform (FFT) was employed. This process entailed FFT application to data set, dominant frequencies identification associated with relevant climatic cycles, spectral filtering implementation to remove high-frequency noise components, and the reconstruction of the series using the Inverse Fourier Transform (IFFT) [37]. Consequently, a smoothed version of the data was obtained, emphasizing recurrent climatic patterns,

devoid of random fluctuations. Thereafter, an Autoregressive Integrated Moving Average (ARIMA) model is implemented to capture unaccounted trends as well as residual variability unexplained by the FFT. This implied the series stationarities through differencing, when necessary, the selection of the ARIMA model order (p, d, q) based on Akaike (AIC) and Bayesian (BIC) information criteria [38], and the evaluation of the fit using metrics such as Mean Squared Error (MSE) and Coefficient of Determination (R^2) [39]. Finally, the fitted model was used to generate projections of precipitation and temperature for the period 2025–2065.

2.3. Crop Water Requirements and Water Use Efficiency

Following climatic trend analysis, crop water requirements (CWR) were calculated to optimize irrigation practices in the region. CWR represents the amount of water needed to compensate for evapotranspiration (ETc) losses, ensuring optimal crop growth under favorable conditions [40]. To estimate reference evapotranspiration (ET_0), the Penman-Monteith equation was applied, considering multiple climatic parameters such as net radiation, air temperature, humidity, and wind speed. This equation integrates factors including latent heat of vaporization, energy balance, vapor pressure deficit, air density, specific heat of air, and resistance to water vapor transfer. Once ET_0 was determined, it was multiplied by a dimensionless crop coefficient (Kc) to compute ETc, which varies depending on crop and growth stage.

The methodology for determining ET_0 and Kc is extensively detailed in FAO Irrigation and Drainage Paper No. 56 [41], which serves as a global reference for calculating evapotranspiration and crop water requirements under different climatic conditions. To determine the actual water requirement for crops in the irrigation modules, the CROPWAT 8.0 software developed by the FAO was employed [42]. This tool processes climatic, crop, and soil data to simulate irrigation needs under different environmental conditions, offering essential insights for water management in semi-arid regions. To improve water conveyance efficiency in the irrigation modules (JA, MA, LR), hydraulic performance was assessed using three established methodologies: the Irrigation Unit Coefficient, Clement's method, and Clemmens' technique. These methods evaluate the ability of canals to effectively conduct water, providing a comprehensive understanding of irrigation efficiency. Detailed implementation procedures for these methodologies can be found in the corresponding references [43–48].

Water use efficiency was analyzed by estimating losses within the distribution network and agricultural plots through three key indicators: application efficiency, conduction efficiency, and uniformity efficiency, as proposed by Christiansen [49]. Application efficiency measures the proportion of water effectively applied to the crop in relation to the required amount. Conduction efficiency evaluates the volume of water transported through the irrigation network relative to the intended amount, accounting for losses along distribution system. Uniformity efficiency determines how evenly water is distributed across the field by analyzing variations in infiltration at different locations.

To further analyze the hydraulic behavior of the canal networks, EPANET® Version 2.2 software was used to simulate flow conditions. This tool solves flow continuity and head loss equations to assess the pressure, flow rates, and overall performance of water distribution systems under varying operational scenarios. The Darcy-Weisbach equation was applied to estimate friction losses within the canals, enabling the identification of inefficiencies in the irrigation network [50]. These analyses provide crucial insights for optimizing water distribution and improving the overall performance of irrigation systems. With a view to demonstrating that the difference in application efficiency between gravity irrigation and pressurized irrigation decreases when traditional furrow irrigation is carried out

under controlled conditions. This paper includes findings from an experiment published in 2020 relating to two experimental plots established in the LR irrigation module [51] and thus evaluating how water volume in the storage source derived from the surface area that must be irrigated with run-off water because its topography makes it unsuitable for pressurized irrigation, evolves.

3. Results

3.1. Rainfall and Temperature Trends at Irrigation Modules Context

An integrated analysis of precipitation and temperature trends from 1961 to 2020 across LR, JA, and MA irrigation modules reveals significant climatic dynamics, illustrating notable changes in rainfall and temperature patterns over time. These variations are influenced by mesoscale atmospheric processes, topographical effects, and broader climatic phenomena. Figure 2 illustrates the spatial distribution of mean rainfall and temperature during the 1961–2020 period, highlighting a clear precipitation gradient that ranges from approximately 410 mm year^{-1} in the northwest to over 730 mm year^{-1} in the southeast. The northwest, depicted in pale blue hues, experiences arid to semi-arid conditions, while the southeast, represented by darker blue shades, receives substantially higher precipitation, a pattern likely influenced by orographic lifting, prevailing wind patterns, and regional moisture transport mechanisms. Notable locations such as MA irrigation module exhibit the highest precipitation levels, whereas JA irrigation module experiences moderate rainfall, and LR irrigation module falls within a lower precipitation zone compared to MA irrigation module. This spatial variability underscores the complex geographic and climatic interactions shaping the region's hydrometeorological patterns.

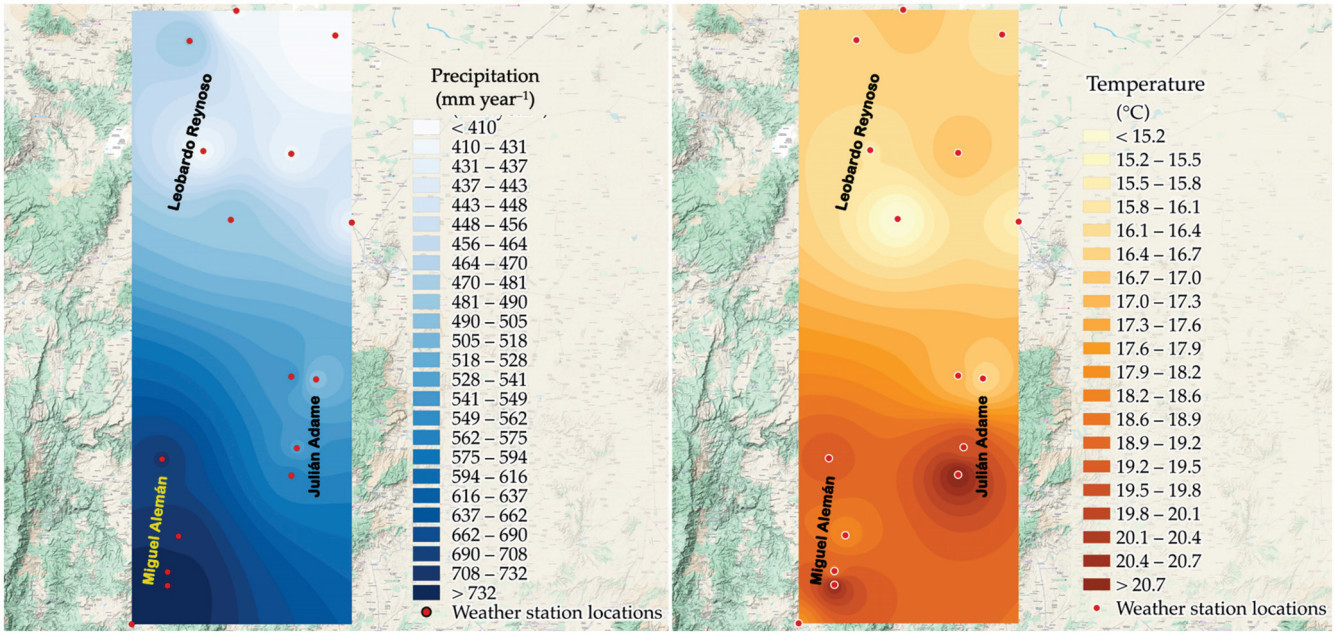

Figure 2. Precipitation and temperature average evolution at LR, JA, and MA irrigation modules during 1961–2020 period.

The temperature distribution exhibits a well-defined gradient, ranging from below 15.2 °C in the cooler northern regions to above 20.7 °C in the warmer southern zones. Cooler temperatures, represented by lighter shades, are predominantly associated with higher altitudes and reduced solar radiation, whereas the darker orange to brown tones in the south correspond to elevated temperatures, likely influenced by subtropical climatic dynamics and lower elevations. A clear inverse correlation is observed between precip-

itation and temperature, where regions with lower precipitation, such as the northwest, generally exhibit cooler conditions, while areas receiving higher precipitation, particularly in the southeast, tend to display warmer thermal profiles. These spatial climatic patterns have significant implications for agricultural practices, water resource management, and ecological sustainability. Areas with higher precipitation and moderate temperatures, such as those surrounding MA irrigation module, provide favorable conditions for agricultural productivity and human settlement. In contrast, regions like LR irrigation module, where precipitation is lower despite moderate temperatures, are likely to encounter considerable challenges related to water availability and resource management. To further enhance the understanding of these climatic interactions, future research should incorporate additional variables, including wind patterns, atmospheric humidity, and solar radiation.

An analysis of long-term precipitation trends reveals both increasing and declining patterns across the study area (see Table 1). The LR irrigation module exhibited a statistically significant annual increase in rainfall of 2.01 mm per year ($p < 0.05$) for the Fresnillo weather station and 1.40 mm per year ($p < 0.05$) for the Santa Rosa weather station, resulting in a cumulative increase ranging from 84.0 to 120.6 mm over the 60-year study period, suggesting a transition toward wetter conditions. The observed upward trends in precipitation are likely attributable to localized orographic effects and mesoscale atmospheric convergence, which have been shown to intensify rainfall patterns in elevated terrains, such as those found in Santa Rosa (2236 masl) and Fresnillo (2201 masl).Conversely, while records at weather stations within the LR irrigation module, which is situated at an elevation below 2100 masl, also demonstrate an increase in annual rainfall, these records do not attain statistical significance. A similar observation can be made for the JA irrigation module, a geographical region with an elevation below 2100 masl, which also exhibited an annual increase in precipitation. However, the statistical significance of this increase is negligible, akin to the observations made in the LR irrigation module.

Table 1. Precipitation tendency into LR, MA, and JL irrigation modules for 1961–2020 period.

Irrigation Module	Weather Station	Latitude (Degrees)	Longitude (Degrees)	Elevation (Masl)	MK Tau	SS (mm Year^{-1})	Lreg. (mm Year^{-1})	Trend
Leobardo Reynoso	Calera	22.91	−102.66	2097	0.050	0.341	0.343	Upward
	Cañitas	23.60	−102.73	2046	0.139	0.253	0.302	
	Fresnillo *	23.17	−102.89	2201	0.159	2.005	1.905	
	El Sauz	23.28	−103.11	2096	0.021	0.430	0.430	
	Sain Alto	23.58	−103.26	2071	0.071	0.845	0.636	
	Santa Rosa *	22.93	−103.11	2236	0.202	1.403	1.365	
	El Cazadero	23.69	−103.09	1862	0.068	0.739	0.739	
Julián Adame	El Chique	22.00	−102.89	1648	0.084	0.697	1.002	
	Tayahua	22.10	−102.87	1729	0.028	0.460	0.761	
	Villanueva	22.36	−102.89	1935	0.060	0.584	0.633	
	Palomas	22.35	−102.80	2025	0.033	0.328	0.719	
Miguel Alemán	Excamé	21.65	−103.34	1740	−0.090	−1.092	−1.276	Downward
	La Villita	21.60	−103.34	1786	−0.168	−2.220	−2.188	
	Casa Llanta	22.06	−103.36	1730	−0.046	−0.536	−0.571	
	Tlaltenango	21.77	−103.31	1685	−0.123	−1.563	−1.721	
	Teul	21.47	−103.46	1909	−0.093	−1.037	−0.983	

* Statistically Significant ($p < 0.05$).

The LR irrigation module exhibited an increase in precipitation ranging from 0.25 to 0.85 mm year^{-1}, while the JA module demonstrated a range between 0.33 and 0.70 mm per year. The findings indicate that while precipitation levels increase with increasing elevation, they also decrease with increasing latitude (Table 1). Conversely, the MA irrigation module exhibited a negative precipitation trend, characterized by a decline ranging from −0.54 mm year^{-1} to −2.22 mm year^{-1}, resulting in a cumulative reduction between 34.2 mm and 133.2 mm between 1961 and 2020. This decline points to an elevated vul-

nerability to water scarcity. The driest periods in MA irrigation module coincided with prolonged droughts lasting up to nine years, as identified through a threshold-based analysis that classified dry years as those with annual precipitation below 595.7 mm. In contrast, wet years, defined by precipitation exceeding 909.3 mm, were relatively less frequent but often associated with intense and irregular rainfall events.

Annual precipitation variability was particularly pronounced in stations such as Calera, Cañitas, and El Sauz, where trends ranged from 0.3 to 0.8 mm per year, although these changes were not statistically significant. Such results align with the high interannual variability characteristic of northern Mexico's semi-arid regions. For example, JA irrigation module recorded 32 wet years and 28 dry years, whereas MA module experienced 26 wet years and 34 dry years, highlighting the considerable differences in pluviometry regimes across the study area (Figure 3). The cyclical nature of wet and dry periods was evident, with droughts lasting up to nine years in some cases, followed by shorter yet intense wet periods. During dry years, precipitation levels fell significantly below the annual means, often leading to critical water deficits in reservoirs and agricultural systems.

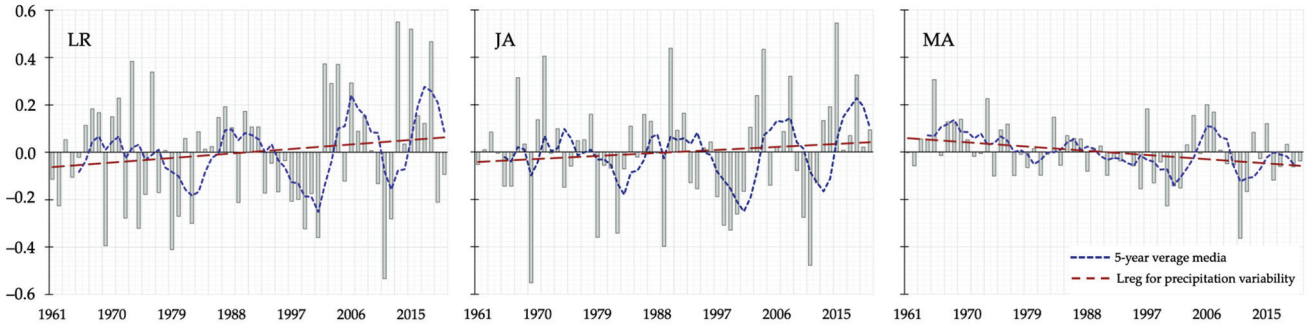

Figure 3. Precipitation variability at LR, JA, and MA irrigation modules during 1961–2020. From left to right, Leobardo Reynoso, Julián Adame, and Miguel Alemán.

From 1961 to 2020, rainfall patterns in the study modules showed alternating periods of surplus and deficit. Typically, dry spells lasted one to two years, but prolonged droughts could extend up to nine years. In contrast, wet years were shorter, occurring every one to three years. Figure 3 presents these trends, showing annual rainfall anomalies (red bars) alongside a 5-year moving average (blue dash line) for a clearer view of variability over time. JA irrigation module exhibits pronounced interannual oscillations, while LR irrigation module's moving average indicates a discernible upward trend despite considerable variability. In contrast, MA irrigation module's trend appears more stable, with notable deviations around 2010, followed by a gradual recovery. Persistent variability in LR irrigation module, particularly during the 1970s and mid-2000s, stabilizes toward the latter years of the study period, reflecting broader-scale climatic influences and localized anomalies.

The post-2010 recovery trend observed across all regions may indicate the re-establishment of stable rainfall regimes. Notably, the 1970s emerge as a period of amplified variability, underscoring the impact of larger climatic phenomena. Superimposed localized anomalies further highlight the intricate interplay between regional and site-specific drivers. By analyzing the persistence and variability of wet and dry periods across LR, JA, and MA irrigation modules, key insights into climatic behaviors and their underlying mechanisms were obtained. Wet and dry periods typically persisted for one to two years, with wet periods exhibiting slightly longer durations, suggesting a regional hydrological regime dominated by surplus precipitation. LR and JA irrigation modules displayed heightened interannual variability, marked by frequent state transitions, indicating sensitivity to macro-atmospheric oscillations.

In contrast, MA irrigation module displayed prolonged persistence, indicative of its dependence on localized hydrological factors like soil moisture dynamics and evapotranspiration. Synchrony and divergence among modules were further explored. LR and JA irrigation modules showed strong alignment during wet periods, driven by common atmospheric dynamics, while MA irrigation module often diverged during dry periods, emphasizing its distinct drivers. Cross-correlation analysis reinforced previous statement, with high synchronization (r = 0.83) between LR and JA irrigation modules, moderate correlation (r = 0.53) between LR and MA, and weak correlation (r = 0.25) between JA and MA irrigation modules, substantiating the hypothesis of independent climatic mechanisms for MA irrigation module. As Figure 4 displays, a reconstruction of cyclic signals reveals predominant patterns. Overlapping wet periods in LR and JA highlight common climatic drivers, while MA irrigation module reveals independent cycles driven by hydrological mechanisms such as soil moisture retention and evaporation. Amplitude analysis reveals significant interannual variability in the JA irrigation module, with cycles oscillating between ±5.0 units, in contrast to the moderate amplitude of around ±3.0 units observed in the LR irrigation module. The frequency of cycles and high amplitude (±4.5 units) of the MA irrigation module are indicative of long-term driver control or tidal influences. In addition, the phase difference observed in MA compared to LR and JA suggests that its cycles are not directly influenced by the same climatic drivers, but rather by internal hydrological processes.

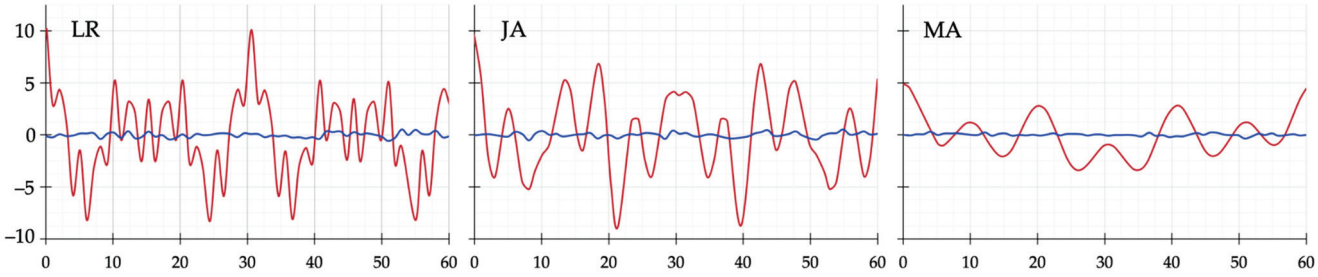

Figure 4. Dominant multiyear cycles for precipitation at LR, JA, and MA irrigation modules.

As for rainfall trends in irrigation modules, Figure 5 illustrates tendencies for all agricultural units under examination. As previously stated, LR and JA irrigation modules at a regional scale exhibit an upward rainfall trend from 1961 to 2020. LR module exhibits a consistent upward trend in precipitation from 1961 to 2020, with an approximate increase of +8.8 mm per decade, as indicated by the regression line. JA module similarly demonstrates an increasing trend, with a slope of +7.6 mm per decade. Both modules exhibit moderate interannual variability without abrupt deviations from the trend. In contrast, MA irrigation module shows a clear downward trend, with a linear regression slope of −14.6 mm per decade. This module also exhibits slightly higher variability compared to LR and JA. While the upward trends in LR and JA are not statistically significant according to MK test ($p > 0.05$), the downward trend in the MA module is statistically significant, with a p-value of 0.03. These modules have upward Sen's slopes of 8.2 mm per decade and 6.6 mm per decade, respectively. In contrast, the MA irrigation module shows a Sen's slope of approximately −13.9 mm per decade.

Temperature trends vary by altitude and latitude, directly affecting agriculture. In the LR module, maximum temperatures range from 14.9 °C (Santa Rosa) to 17.0 °C (Fresnillo and El Cazadero), while minimums fall between −13.0 °C (Sain Alto) and 8.3 °C (Table 2). The region's higher elevation helps stabilize temperatures, benefiting heat-sensitive crops. However, large nighttime temperature swings—often exceeding 10 °C—can disrupt key growth stages like germination and flowering. The JA module exhibited intermediate

thermal conditions, with average maximum temperatures ranging from 16.4 °C to 21.0 °C and minimums spanning from −16.0 °C to 23.5 °C. Heatwaves, particularly at stations such as El Chique, contributed to annual maximum temperatures surpassing 40.0 °C in certain years. While the elevated average temperatures facilitate an extended growing season, they also accelerate evapotranspiration rates, intensifying water demand and increasing vulnerability to drought stress. The MA module recorded the highest temperatures, with average maximums reaching 20.8 °C in La Villita and minimums averaging 10.1 °C. Extreme temperatures peaked at 45.0 °C, reflecting the module's lower altitude and latitude.

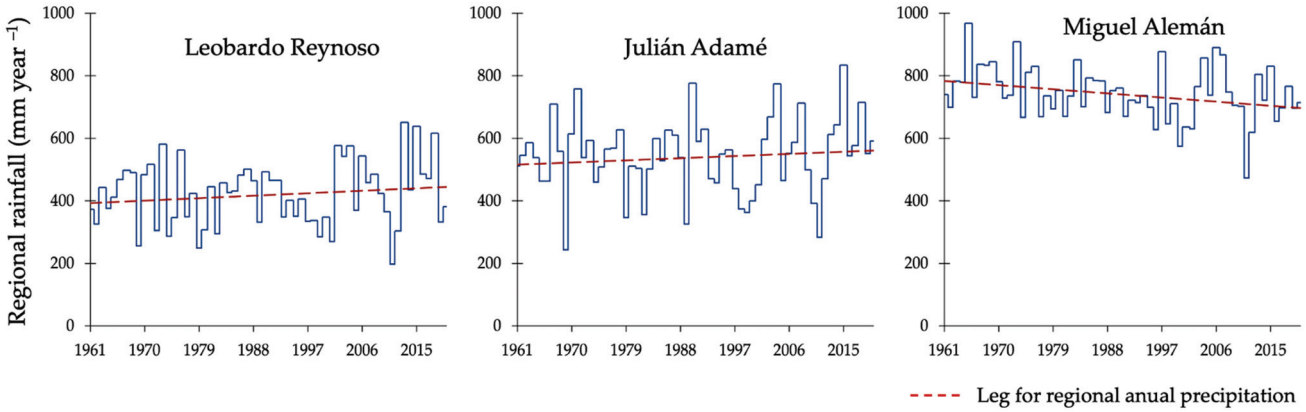

Figure 5. Yearly rainfall evolves for 1961–2020 period at LR, JA, and MA irrigation modules.

Table 2. Minimum and maximum daily temperature statisticians for 1961–2020 period.

Irrigation Module	Temperature Minimum (°C)				Temperature Maximum (°C)			
	$\bar{X}$	SD	X_{min}^{min}	X_{max}^{min}	$\bar{X}$	SD	X_{min}^{max}	X_{max}^{max}
Julián Adame	8.6	5.4	−16.0	22.5	26.8	4.3	2.0	41.0
Leobardo Reynoso	8.3	5.2	−13.0	21.5	26.4	4.5	−2.0	42.0
Miguel Alemán	10.1	5.1	−10.5	23.5	27.4	4.9	−1.0	45.0

The analysis of climatic evolution highlights key patterns in precipitation and temperature over time. In LR and JA irrigation modules, cumulative increases of 52.8 mm and 45.6 mm in annual precipitation, respectively, were observed during the 1961–2020 period. This trend reflects a gradual shift toward wetter conditions, offering opportunities for water resource recharge but also necessitating effective management to mitigate risks cumuli such as soil erosion during wet years. On the other hand, MA irrigation module showed a tie decrease of 25.8 mm over the same period, indicating increasing vulnerability to prolonged droughts. These trends were accompanied by notable interannual variability, with cycles of dry and wet years; in LR irrigation module, dry years recorded precipitation below 310.3 mm, while in JA irrigation module, wet years exceeded 676.9 mm.

3.2. Crop Water Requirements and Agriculture Systems Efficiency

Management of water resources in semi-arid regions presents a complex challenge for resilience and sustainability of agro-ecological systems. As climate conditions become more variable, it is crucial to reassess how water is distributed and applied in agriculture. Improving irrigation methods can help farmers adapt to these changes and maintain productivity. A regional climatological analysis of LR irrigation module (Figure 6), covering the period from 1961 to 2020, reveals statistically significant trends indicative of an evolving climate regime [52]. Dataset exhibits a decadal thermal increase of 0.16 °C, juxtaposed with a marginal upward shift of 8.8 mm in precipitation. However, interannual stability

of temperature is markedly greater than that of precipitation, demonstrating around nine-fold lower variability. In semi-arid regions, agricultural water management constitutes a significant challenge to sustainability of those communities residing in such areas.

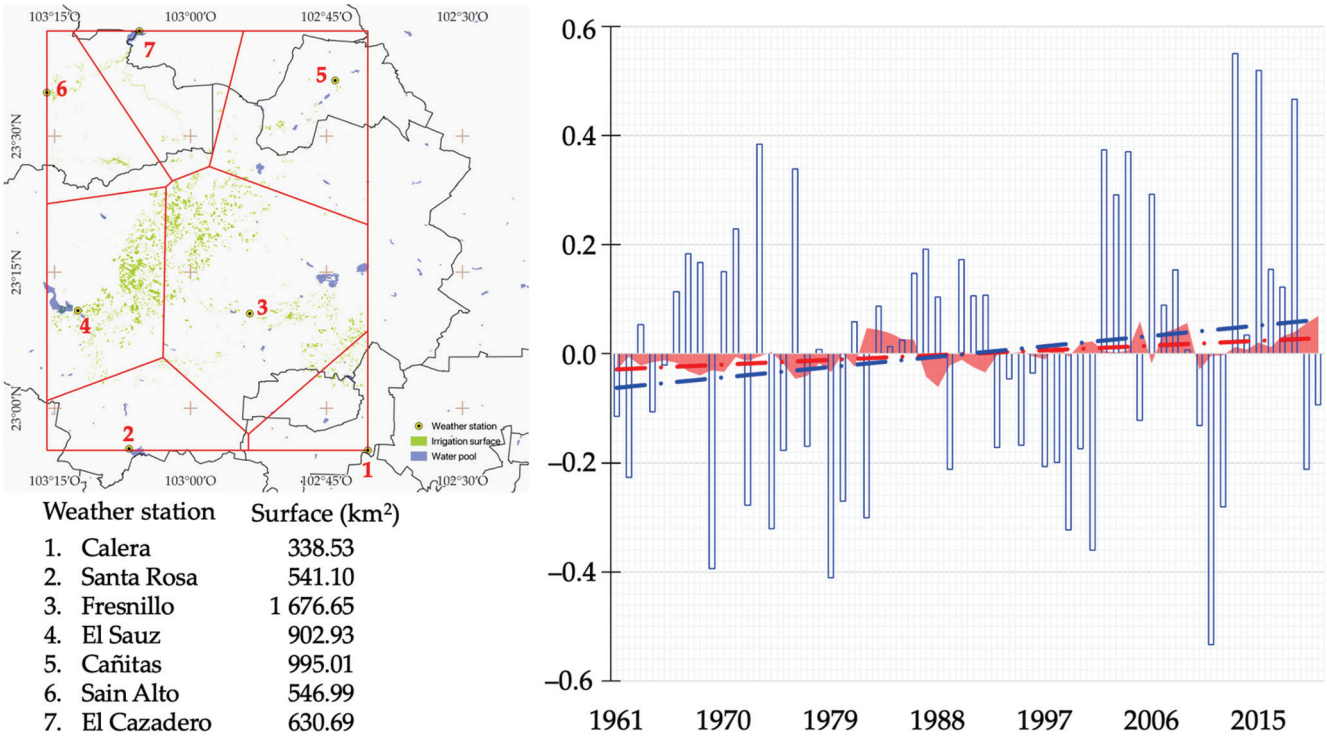

Weather station	Surface (km²)
1. Calera	338.53
2. Santa Rosa	541.10
3. Fresnillo	1 676.65
4. El Sauz	902.93
5. Cañitas	995.01
6. Sain Alto	546.99
7. El Cazadero	630.69

Figure 6. Precipitation (blue bars) and temperature regional (red polygon) anomalies for Leobardo Reynoso irrigation module. Red and blue dash lines are regressions for temperature and precipitation, respectively.

Homogeneity tests (Pettitt's test, SNHT, Buishand's test, and von Neumann's test) showed irregularities in climate trends. A significant temperature shift occurred around 1997 ($p < 0.0001$), marking a clear warming trend. However, precipitation remained within historical normal without major changes. To further analyze these trends, the Mann-Kendall test and Sen's slope estimation were used. The results confirmed a strong warming pattern ($\tau = 0.415$, $p < 0.0001$), with temperatures rising by 0.016 °C per year. While precipitation also showed a significant trend ($\tau = 0.084$, $p = 0.005$), an increase of 0.819 mm year^{-1} was too small to impact overall water availability. Climate changes will impact irrigation needs, especially for maize and grasslands. Maize will grow adequately with 6% less water than it currently requires, while pasture will need to consume 11% more water to avoid stress.

However, both crops will have to meet their water needs with more water from irrigation, since the forecast indicates that effective precipitation in dry years will be up to three times lower than currently observed. Although in wet years, rainfall alone would be sufficient for maize to grow without yield loss and pasture would need to be supplied with about 12% irrigation water, the increase in rainfall variability leads to a scenario in which uncertainty plays a major role. These results support stated by Íñiguez-Covarrubias et al. [53], who noted that shorter plant cycles often meet water needs in most years. However, unlike this study, they did not account for projected rainfall declines due to climate anomalies. Then, sustained temperature increases, rising potential evapotranspiration, and growing irrigation demand are expected to challenge the region's productive capacity within 35 years, as infrastructure struggles to accommodate escalating water requirements.

In furtherance of preceding assertions, attention is directed to LR irrigation module, a subject of particular pertinence in Zacatecas, a state in which drip irrigation is not usually alternative for irrigate plots. In contrast, this irrigation method has been spread in over 3000 hectares at LR irrigation module plus 800 hectares using sprinkler irrigation, resulting in a substantial enhancement in irrigation efficiency, with certain instances exhibiting values approaching 95%. However, on average, the module attains an application efficiency of 87.5%. Despite the significant efforts of farmers to operate a system that, while resulting in improved water application at the plot level, also entails higher production costs, their efforts are ultimately undermined when calculating global efficiency, given that the efficiency corresponding to conduction is despite farmers' efforts to manage a system that leads to enhanced water application at the plot level, the resulting higher production cost is not conducive to global efficiency. This is primarily due to an extensive network of over 21 km of main canal, facilitate water conveyance from the headworks to a point where it is released into the free surface and the beginning of piped lines (Figure 7).

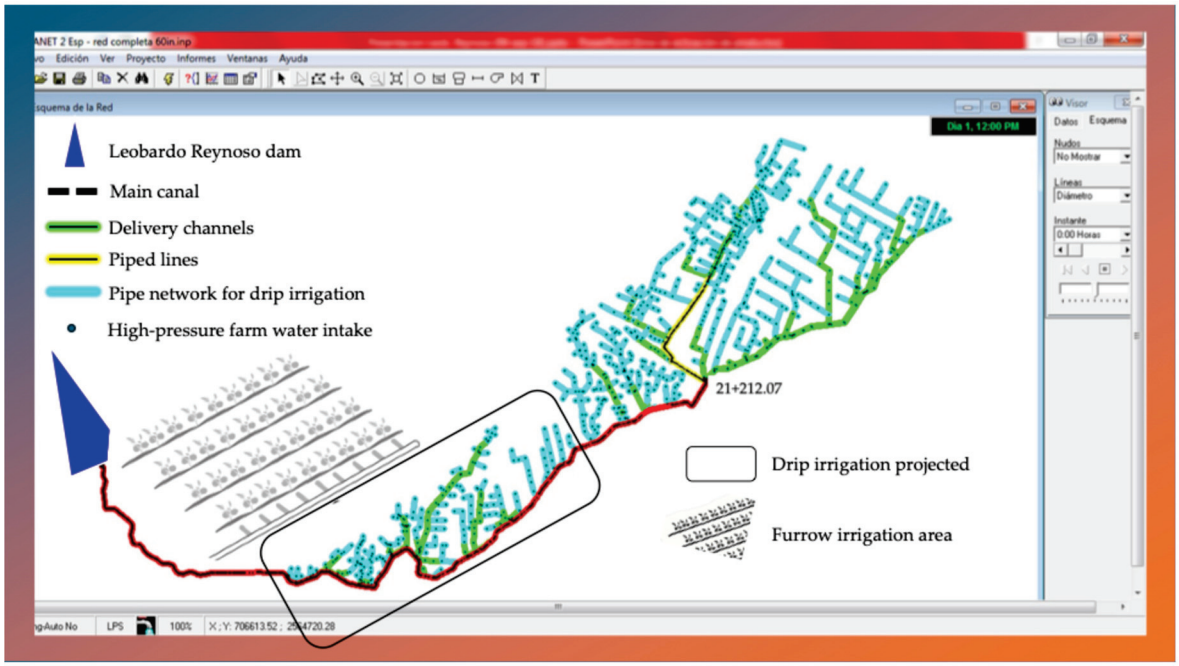

Figure 7. Schematic display of water conveyance network in Leobardo Reynoso irrigation module.

While it is true that nearly 81.5% percent of the irrigated land is currently covered by pressurized irrigation systems, it is also true that the LR irrigation module has had to go through several stages to reach this level of development. The first years of operation were characterized by furrow irrigation with a conveyance system consisting of lined and unlined canals, which at best allowed about 70% of the current irrigated area to be under irrigation (Figure 8). In the late 1970s and early 1980s, the first pressurized irrigation systems, mainly center pivot and to a lesser extent front-end, began to appear. Undoubtedly, technification has been a fundamental factor in reaching 100% of irrigable land. From the implementation of sprinkler irrigation in conjunction with wet years—in the period 1984–1988, runoff ranged between 28 and 40 Hm3— it allowed, after 38 years, for the first time to have a reservoir at maximum capacity. However, seven years later, the dam only had 50% of its stored volume and two years later it reached its minimum operating level.

Even though a gradual increase in irrigated land had been sufficient for almost 950 farmers irrigating with water from Leobardo Reynoso dam to keep their plots in production. However, climate projections indicate that in addition to bringing a supplementary 500 hectares into modern drip irrigation between 2025 and 2030, users will have to

consider a wider crop pattern than is usually established in that irrigation module in order to maximize water productivity. In other words, introducing technology to 4300 hectares with sprinkler and drip irrigation would prolong the LR irrigation module's production until 2040, with 4660 hectares being cultivated, 50% of which producing corn, and a further 1000 hectares with crops such as alfalfa, grass, chili, garlic, onion and tomato. On the other hand, it is possible to extent, beyond 2040, productive life in this irrigation zone if, in dry years, a decision is made to reduce per-hectare volume according to water deficit. The most critical case would involve extracting 18.5 Hm^3 of the stored volume (2400 m^3 ha^{-1}), less than half that granted annually per hectare, a sufficient amount to establish beans or tomatoes in cases where producers have application efficiencies of around 95%.

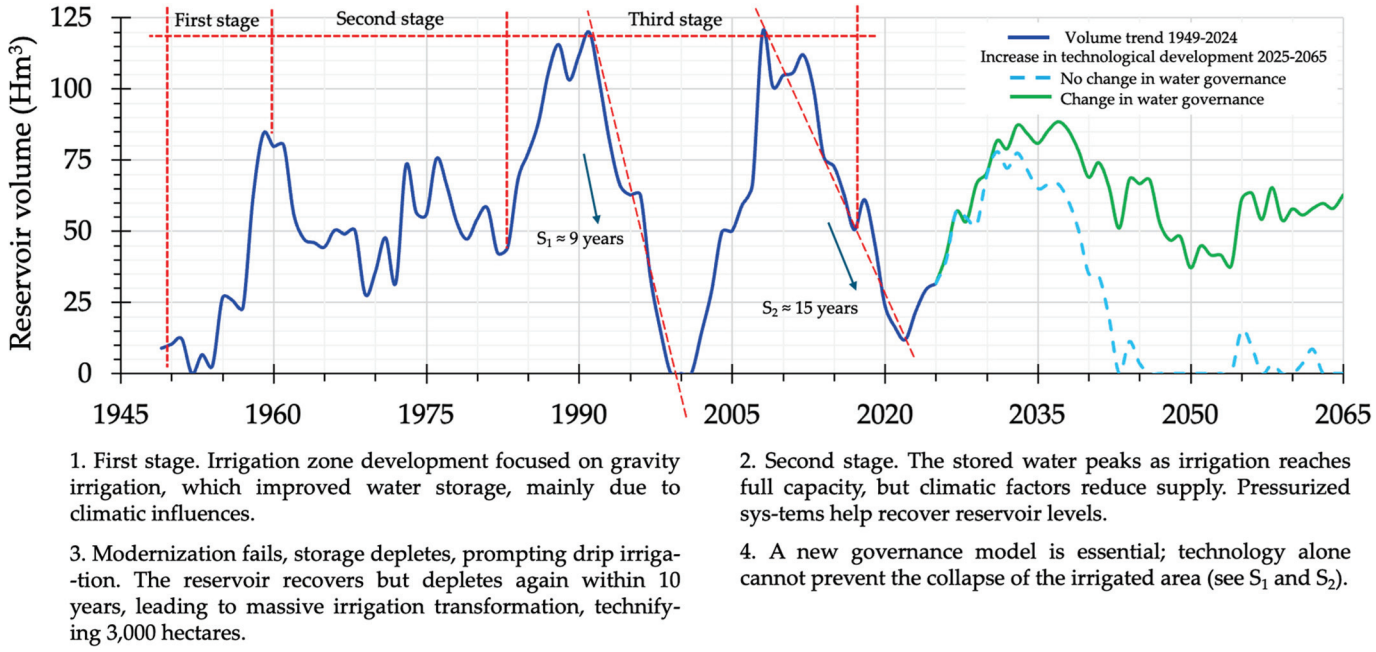

Figure 8. Reservoir volume evolution from 1949 to 2024, and projected from 2025 to 2065.

Rising temperatures and increasing evapotranspiration rates are intensifying irrigation demands, putting pressure on existing infrastructure. Without modernization—such as upgrading intake structures, expanding storage, and improving conveyance efficiency—water shortages may significantly impact food security and agricultural productivity [54]. The amount of water that is discharged by each irrigation module depends on the area that is sown as well as the crops that are grown during a particular agricultural season, then projections of water discharge rates through CUR, Clemens, and Clement methods. Critical rates for controlled demand were derived from CUR method as follows: 2.7 m^3 s^{-1} in JA irrigation module, 5.3 m^3 s^{-1} in MA irrigation module, and 4.9 m^3 s^{-1} in LR irrigation module. However, these calculations assume static climate conditions, ignoring projected water demand increases due to climate alterations —prolonged droughts and extreme weather—[55]. Beyond this consideration, the intake structure for each irrigation module does not have the capacity to supply such discharges, even with a hydraulic load at the level of ordinary maximum water levels. This will result in a diversion dam being built with enough capacity to supply any flow in excess of hydraulic capacity of existing headworks.

Pressurized irrigation has been shown to enhance efficiency, with LR benefiting from a 1.5 m diameter pipeline, while JA and MA continue to rely on less efficient canal-based systems. Pressure levels ranged from 103.9 to 455.9 kPa in LR, where 98.5% of the surface is suitable for drip irrigation. However, lower hydraulic pressure values in JA and MA irrigation modules, limit the viability of the pressurized system, with 45% of hydrants

below 147.0 kPa. High-pressure zones—98.5% in LR, 54.7% in JA, and 53.7% in MA—are ideal for pressurized irrigation, which improves water use and crop quality [56]. The installation of pressure regulating valves is recommended for pressures above 490.0 kPa [57]. Efficiency comparisons highlight the advantages of pressurized systems, and they are a fundamental piece of data in the hydraulic modeling of the network as a whole. In this regard, the on-site assessments conducted on the irrigation modules that currently operate with diverse irrigation methods have yielded uniformity coefficients of 82.6% and 87.1%, and application efficiencies equivalent to 82.2% and 86.0%, for drip irrigation and sprinkler irrigation, respectively [58,59].

Conversely, furrow irrigation exhibited a markedly lower efficiency, with an average of 50.0%, with only marginal enhancements in MA (58.1%) [54]. Water transport efficiency constitutes a pivotal factor. Open channel systems in MA, LR, and JA demonstrate an average efficiency of 60.0%, resulting in substantial water losses. Conversely, pressurized pipes have been shown to achieve efficiencies exceeding 95.0%, underscoring the limitations of conventional infrastructure [58]. Expanding pressurized systems in high-pressure zones is essential for optimizing water use, nutrient delivery, and resource efficiency [60]. Crop diversification strategies can further improve resilience to climate variability [61,62]. As climate conditions become increasingly unpredictable, upgrading irrigation infrastructure is crucial to sustaining agricultural productivity. Without these measures, water shortages will continue to threaten food security and long-term sustainability.

4. Discussion

The semi-arid climate of Zacatecas exacerbates water scarcity and agricultural vulnerability, particularly due to recurrent droughts and erratic precipitation. Traditional irrigation methods are inefficient, characterized by significant water losses through seepage and evaporation, and limited adaptability to changing climatic conditions [63]. These inefficiencies reduce agricultural productivity and threaten ecosystem sustainability, necessitating the modernization of irrigation systems. Studies such as [64] highlight the potential of improved irrigation practices to reduce water demand in arid regions significantly. Similarly, [65] demonstrated that integrating nutrient-efficient practices with advanced irrigation technologies enhances agricultural outputs [66–69] further emphasized the role of topographical adjustments and crop diversification in optimizing water and nutrient use efficiency in regions with extreme climatic variability, such as Zacatecas. Government initiatives, particularly those led by the Comisión Nacional del Agua (Conagua) [70], have focused on rehabilitating and modernizing irrigation infrastructure, achieving water conveyance efficiencies as high as 98% in certain districts. These efforts enhance irrigation effectiveness and contribute to community resilience by stabilizing agricultural incomes.

Increased atmospheric evaporative demand is projected to elevate potential evapotranspiration (ET_0) while reducing effective precipitation (Pe). In irrigated areas with limited water supply, ETc may be constrained by water availability, increasing competition for resources and potentially compromising agricultural productivity. Additionally, accelerated crop phenological cycles due to elevated temperatures do not necessarily translate into increased biomass production. A shorter growth cycle restricts cumulative photosynthetic activity, limiting carbon assimilation and yield potential. Surpassing physiological thermal thresholds (24–30 °C for maize) may exacerbate photosynthetic inefficiencies, impair reproductive development, and reduce grain filling. These conditions heighten the risk of hydric stress, lower water use efficiency and threaten agronomic sustainability. Findings highlight a fundamental shift in regional climatic dynamics, primarily driven by progressive atmospheric warming. While long-term water availability may remain within historical bounds, rising temperatures necessitate a reassessment of water balance parameters.

4.1. Modernization of Irrigation Modules: Climate Adaptation and Agricultural Sustainability

Zacatecas' distinct rainfall patterns pose challenges across its three primary irrigation modules. JA irrigation module receives an annual average of 535.5 mm of rainfall, but precipitation variability exacerbates soil erosion and necessitates costly infrastructure repairs. While MA irrigation module experiences greater annual rainfall (714.4 mm) but high variability, alternating between drought-induced planting disruptions and waterlogging from heavy rains. LR irrigation module, with an annual average of 417.6 mm, relies on high-salinity water from the Leobardo Reynoso dam, further limiting viable crop options. Maize cultivation, spanning 1985 hectares, is deeply embedded in the region's agricultural tradition but places significant pressure on water resources due to application between seven and nine cubic decameter of water per hectare [71], exceeding by far, crops such as tomatoes, beans, or oats. Recent diversification strategies, including intercropping with drought-resistant species like sorghum and beans in MA irrigation module, have reduced water use by 15% and improved soil fertility through nitrogen fixation.

Pressurized irrigation technologies, including drip and sprinkler systems, have replaced traditional open canals, reducing water losses by 30–35% [72,73]. Hydraulic modeling through EPANET has improved water delivery uniformity by 15% and reduced losses by 20% at waterworks distribution networks. Irrigation efficiency in JA irrigation module has increased to 70%, stabilizing maize and alfalfa production. MA irrigation module has achieved 70.4% efficiency, mitigating climatic variability impacts. The LR irrigation module has been shown to exhibit an 80% efficiency rate, a notable achievement attributed to its fully pressurized pipeline network. However, the region's groundwater sources continue to be a significant concern, as the withdrawal rate has surpassed the natural recharge rate. This has led to a decline in the water supply potential of the aquifers in the area. These advancements have yielded substantial socio-economic and environmental benefits, increasing farmers' incomes by 40% through high-value crops such as tomatoes, peppers, and avocados [74,75].

4.2. Integration of Traditional and Modern Practices

Hybrid approaches that blend modern irrigation technologies with traditional agricultural practices have emerged as a critical strategy for enhancing resilience and sustainability. Drip and sprinkler systems, which deliver precise amounts of water directly to crop root zones, are complemented by holistic practices such as rainwater harvesting, contour farming, mulching, cropping pattern rotation, basic food basket crops with regional climate resilience [76]. In MA irrigation module, these hybrid approaches have increased water retention by 25.0% and boosted crop yields by 20.0%. The FAO's 2021 [1] report highlights the role of these systems in improving soil health, enhancing water-use efficiency, and reducing vulnerability to climate change. Similarly, IWMI [77] has identified hybrid systems as instrumental in achieving sustainable agricultural development in semi-arid regions.

Despite its successes, the modernization of irrigation in Zacatecas faces persistent challenges. The high cost of pressurized irrigation—ranging from $1200 to $2500 per hectare—remains a major challenge, especially for small farmers. From now on, irrigation modules will have to restructure their governance models since in critical dry years they will have to be subject to volumes below their annual concession. The LR irrigation module—equal for JA and MA irrigation modules—in low-water periods will have to agree to use less than 50% of the total annual volume, establishing low-profitability crops, which contrasts with production costs of irrigation systems that maintain a large percentage of irrigated land. A paradigm shift will have to emerge in the coming years: during dry seasons, the profitability of land should be distributed among those who are willing to cede their volume to those with perennial or fruit crops or to those who grow agricultural

products with higher consumption than that established for a specific year. The cost of climatic anomalies should be borne by all users, and the benefit should be distributed equitably, and that will only be feasible to the extent that it is established in prevailing regulations in each case.

Expanding financial support through subsidies, low-interest loans, and cooperative funding is crucial. Training programs are also needed to help farmers operate and maintain these systems effectively. To ensure sustainability, policies should encourage renewable energy use and crop diversification while minimizing carbon emissions. Long-term success will also depend on financial reforms and better infrastructure maintenance. The modernization of irrigation systems by addressing inefficiencies, enhancing resilience, and fostering sustainability, illustrates the transformative potential of targeted investments in technology and governance. Continued investment in capacity building, environmental stewardship, and inclusive policies will be essential to consolidating these gains and achieving long-term agricultural sustainability.

5. Conclusions

This study evaluated the impact of irrigation modernization on small-scale agriculture in Zacatecas, Mexico, highlighting the challenges posed by water scarcity and climate variability. The integration of modern irrigation technologies with traditional water management practices significantly enhances water-use efficiency and agricultural resilience. The transition from open canal systems to pressurized irrigation networks has resulted in substantial improvements in water distribution and application efficiency, particularly in the Leobardo Reynoso (LR) module, where efficiencies reached 87.5%.

The analysis of long-term climatic trends revealed increasing temperature and precipitation variability, indicating that future irrigation demands for staple crops like maize and pastures are likely to increase. Modeling projections also highlighted the rising evapotranspiration rates, which further emphasize the need for adaptive, climate-responsive irrigation strategies that align with the evolving environmental conditions. Additionally, hydraulic and crop modeling analyses confirmed the significant gains in efficiency with the implementation of modern irrigation systems. The results demonstrated that pressurized irrigation systems substantially outperformed traditional gravity-based systems, reducing water losses and optimizing the allocation of resources. These models provided valuable insights into the potential improvements in water-use efficiency under different climate scenarios and confirmed the effectiveness of the proposed strategies for addressing water scarcity.

Despite these advancements, challenges remain, particularly related to financial constraints and infrastructure limitations. Modernizing irrigation systems must go beyond infrastructure improvements and include expanded institutional support, policy reforms, and financial incentives. Furthermore, equitable water distribution during dry periods will require collaborative governance models to ensure sustainability and economic viability for smallholder farmers. Looking ahead, further research should focus on optimizing hybrid irrigation systems that integrate modern technologies with traditional water management practices. Long-term studies on the socio-economic and environmental impacts of irrigation modernization will also be crucial for guiding policy and investment decisions. As irrigation systems reach their full capacity, especially for smaller farmers, embracing cooperative management and traditional practices will be essential to reduce production costs and sustain agricultural productivity, particularly in dry years.

Overall, this study reinforces the importance of continued investment in irrigation modernization, supported by modeling results that validate the proposed water conservation strategies. The integration of infrastructure upgrades, policy reforms, and community

engagement will be key to ensuring the long-term sustainability of agricultural production in Zacatecas, particularly in the face of increasing water scarcity and climate variability.

Author Contributions: Conceptualization, C.B.-C. and H.P.-M.; methodology, C.B.-C. and H.P.-M.; software, L.A.F.-C.; validation, C.B.-C. and H.P.-M.; formal analysis, C.B.-C., H.P.-M. and L.F.P.-M.; investigation, C.B.-C., H.P.-M., L.A.F.-C. and L.F.P.-M.; writing—original draft preparation, C.B.-C. and H.P.-M.; writing—review and editing, L.F.P.-M.; visualization, L.A.F.-C.; supervision, C.B.-C., H.P.-M., L.A.F.-C. and L.F.P.-M. All authors have read and agreed to the published version of the manuscript.

Funding: This research received no external funding.

Data Availability Statement: Major data sets were obtained of Mexican agencies; in this sense historical records and time series were analyzed considering raw data downloaded from follow web sites. 1. https://smn.conagua.gob.mx/es/climatologia/informacion-climatologica/informacion-estadistica-climatologica (accessed on 18 September 2024), 2. https://sinav30.conagua.gob.mx:8080/SINA/?opcion=repda (accessed on 10 June 2024), 3. https://www.inegi.org.mx/default.html (accessed on 28 January 2025), 4. https://datos.gob.mx/ (accessed on 12 November 2024), 5. https://sih.conagua.gob.mx/ (accessed on 25 March 2024), 6. https://www.dof.gob.mx/#gsc.tab=0 (accessed on 14 September 2024) www.dof.gob.mx/index.php#gsc.tab=0. Besides, information from https://dataspace.copernicus.eu/ (accessed on 18 September 2024) was used in the study.

Acknowledgments: The authors acknowledge to Universidad Autónoma de Zacatecas «Francisco García Salinas» for extensive and unrestricted support for spending part of their contrac ted time with such institution to carry out the research.

Conflicts of Interest: The authors declare no conflicts of interest.

References

1. Food and Agriculture Organization (FAO). The State of Food and Agriculture 2021. In *Food and Agriculture Organization of the United Nations*; Food and Agriculture Organization (FAO): Rome, Italy, 2021.
2. Rockström, J.; Barron, J.; Fox, P. Water productivity in rain-fed agriculture: Challenges and opportunities for small-holder farmers in drought-prone tropical agroecosystems. *Water Resour. Manag.* **2007**, *21*, 43–56.
3. Carr, E.R.; Fleming, G.; Kalala, T. Understanding women's access to agricultural extensions services in Zambia: Opportunities and barriers. *J. Rural Stud.* **2019**, *71*, 49–58.
4. Altieri, M.A.; Nicholls, C.I.; Montalba, R. Technological approaches to sustainable agriculture at a crossroads: An agroecological perspective. *Sustainability* **2015**, *7*, 4518–4526. [CrossRef]
5. UN-Water. *The United Nations World Water Development Report 2021: Valuing Water*; United Nations: San Francisco, CA, USA, 2021.
6. Intergovernmental Panel on Climate Change (IPCC). *Climate Change 2021: The Physical Science Basis*; Intergovernmental Panel on Climate Change: Geneva, Switzerland, 2021.
7. Lal, R. Enhancing crop yields in the developing world through soil organic carbon sequestration. *Adv. Agron.* **2013**, *118*, 155–176.
8. Adhikari, U.; Nejadhashemi, A.P.; Woznicki, S.A. Climate change and eastern Africa: A review of impact on major crops. *Food Energy Secur.* **2015**, *4*, 110–132. [CrossRef]
9. Abhilash, P.C.; Dubey, R.K.; Tripathi, V.; Gupta, V.K.; Singh, H.B. Plant growth-promoting microorganisms for environmental sustainability. *Trends Biotechnol.* **2016**, *34*, 847–850. [CrossRef]
10. Ward, F.A.; Pulido-Velazquez, M. Water conservation in irrigation can increase water use. *Proc. Natl. Acad. Sci. USA* **2008**, *105*, 18215–18220. [CrossRef]
11. Lybbert, T.J.; Sumner, D.A. Agricultural technologies for climate change adaptation in developing countries: Policy options for innovation and technology diffusion. *Food Policy* **2012**, *37*, 114–123. [CrossRef]
12. Bouman, B.A.M. Water productivity in rainfed agriculture. *Irrig. Sci.* **2007**, *25*, 181–196.
13. Van Der Ploeg, M.J.; Gooren, H.P.; de Rooij, G.H. Innovative approaches to enhance water productivity in small-holder agriculture. *Hydrol. Earth Syst. Sci.* **2020**, *24*, 1051–1062.
14. Meinzen-Dick, R. Property rights and sustainable irrigation: A developing country perspective. *Agric. Water Manag.* **2014**, *145*, 23–31. [CrossRef]
15. Giordano, M. and de Fraiture, C. 2014. Small private irrigation: Enhancing benefits and managing trade-offs. *Agric. Water Manag.* **2014**, *131*, 175–182.

16. Namara, R.E.; Upadhyay, B.; Nagar, R.K. Adoption and impacts of micro-irrigation technologies: Empirical results from India. *Irrig. Sci.* **2010**, *31*, 693–705.
17. Servicio Meteorológico Nacional (SMN). *Información Estadística Climatológica*; Comisión Nacional del Agua, Gobierno de México: Ciudad de México, Mexico, 2024.
18. Campos-Aranda, D.F. Búsqueda de tendencias en la precipitación anual del estado de Zacatecas, México; en 30 registros con más de 50 años. *Ing. Investig. Tecnol.* **2015**, *16*, 355–368.
19. Yozgatligil, C.; Aslan, S.; Iyigün, C.; Batmaz, İ. Comparison of missing value imputation methods in time series: The case of Turkish meteorological data. In *Theoretical and Applied Climatology*; Springer: Berlin/Heidelberg, Germany, 2013. [CrossRef]
20. Mair, A.; Fares, A. Comparison of rainfall interpolation methods in a mountainous region of a tropical island. *J. Hydrol. Eng.* **2011**, *16*, 371–383.
21. Vicente-Serrano, S.; Saz-Sánchez, M.; Cuadrat, J. Comparative analysis of interpolation methods in the middle Ebro Valley (Spain): Application to annual precipitation and temperature. *Clim. Res.* **2003**, *24*, 161–180.
22. Di Piazza, A.; Lo Conti, F.; Noto, L.V.; Viola, F.; La Loggia, G. Comparative analysis of different techniques for spatial interpolation of rainfall data to create a serially complete monthly time series of precipitation for Sicily, Italy. *Int. J. Appl. Earth Obs. Geoinf.* **2011**, *13*, 396–408.
23. García-Vera, M.A.; Abaurrea, J.; Asín-Lafuente, J.; Centelles-Nogués, A. Evolución de las precipitaciones en la cuenca del Ebro: Caracterización espacial y análisis de tendencias. In *VII Reunión Nacional de Climatología*; Grupo de Clima de la Asociación de Geógrafos Españoles: Albarracín, Spain, 2002.
24. Wilks, D.S. Indices of Rank Histogram Flatness and Their Sampling Properties. *Am. Meteorol. Soc. Mon. Weather Rev.* **2019**, *17*, 763–769.
25. Hashemi, M.; Peralta, R.C.; Yost, M. Balancing Results from AI-Based Geostatistics versus Fuzzy Inference by Game Theory Bargaining to Improve a Groundwater Monitoring Network. *Mach. Learn. Knowl. Extr.* **2024**, *6*, 1871–1893. [CrossRef]
26. Mann, H.B. Nonparametric tests against trend. *Econom. J. Econom. Soc.* **1945**, *13*, 245–259. [CrossRef]
27. Kendall, M. Rank correlation measures. *Charles Griffin* **1975**, *202*, 15.
28. Sen, P.K. Estimates of the regression coefficient based on Kendall's tau. *J. Am. Stat. Assoc.* **1968**, *63*, 1379–1389.
29. von Storch, H.; Navarra, A. *Analysis of Climate Variability: Applications of Statistical Techniques*, 2nd updated and extended ed.; Springer: Berlin/Heidelberg, Germany, 1999.
30. Hamed, K.H.; Rao, A.R. A modified Mann–Kendall trend test for autocorrelated data. *J. Hydrol.* **1998**, *204*, 182–196.
31. Yue, S.; Wang, C. The Mann–Kendall test modified by effective sample size to detect trend in serially correlated hydrological series. *Water Resour. Manag.* **2004**, *18*, 201–218.
32. Pettitt, A.N. A non-parametric approach to the change-point problem. *Appl. Stat.* **1979**, *28*, 126–135.
33. Alexandersson, H. A Homogeneity Test Applied to Precipitation Data. *J. Climatol.* **1986**, *6*, 661–675. [CrossRef]
34. Buishand, T.A. Some Methods for Testing the Homogeneity of Rainfall Records. *J. Hydrol.* **1982**, *58*, 1127.
35. von Neumann, J. Distribution of the Ratio of the Mean Square Successive Difference to the Variance. *Ann. Math. Stat.* **1941**, *12*, 367–395.
36. Press, W.H.; Teukolsky, S.A.; Vetterling, W.T.; Flannery, B.P. *Numerical Recipes: The Art of Scientific Computing*, 3rd ed.; Cambridge University Press: Cambridge, UK, 2007.
37. Box, G.E.; Jenkins, G.M.; Reinsel, G.C.; Ljung, G.M. *Time Series Analysis: Forecasting and Control*, 5th ed.; John Wiley & Sons: Hoboken, NJ, USA, 2015.
38. Hyndman, R.J.; Athanasopoulos, G. *Forecasting: Principles and Practice*, 2nd ed.; OTexts: Melbourne, Australia, 2018.
39. Pereira, L.S.; Alves, I. Crop Water Requirements. In *Reference Module in Earth Systems and Environmental Sciences*; Elsevier: Amsterdam, The Netherlands, 2013.
40. Allen, R.G.; Pereira, L.S.; Raes, D.; Smith, M. Crop Evapotranspiration—Guidelines for Computing Crop Water Requirements. In *Irrigation and Drainage, Paper No. 56*; FAO: Rome, Italy, 1998.
41. Surendran, U.; Sushanth, C.M.; Mammen, G.; Joseph, E.J. Modelling the Crop Water Requirement Using FAO-CROPWAT and Assessment of Water Resources for Sustainable Water Resource Management: A Case Study in Palakkad District of Humid Tropical Kerala, India. *Aquat. Procedia* **2015**, *4* (Suppl. C), 1211–1219.
42. Espinosa Espinosa, B.; Flores Magdaleno, H.; Ascencio Hernández, R.; Carrillo Flores, G. Diseño de un sistema de riego hidrante parcelario con los métodos por Turnos y Clement: Análisis técnico y económico. *Terra Latinoam.* **2016**, *34*, 431–440.
43. Leal-Pinedo, A.; Domínguez-Hernández, F.; Morales-García, A. Aplicación del método de Clément en el diseño de un sistema de riego parcelario. *Tecnol. Cienc. Agua* **2016**, *7*, 431–445.
44. Íñiguez-Covarrubias, M.; De León, M.B.; Prado, H.J.V.; Rendón, P.L. Análisis y comparación de tres métodos para determinar la capacidad de conducción de canales, aplicados en el distrito de riego La Begoña. *Ing. Hidráulica* **2007**, *XXII*, 81–90.

45. Abadía, R.; Ruiz, A.; Rocamora, M.C.; Puerto, H.; Andréu, J.; Pastor, J.J.; García, F.; Del Amor, M.A. Aplicación del método de Clément al cálculo de los caudales de línea en redes colectivas de distribución de agua a presión con servicio a la demanda modificada, para sistemas de riego por goteo. In Proceedings of the I Congreso Nacional de Ingeniería para la Agricultura y el Medio Rural, Valencia, Spain, 20 September 2001.
46. Clement, R. *Computation of flow in Irrigation Systems Operating 'On Demand'. La Société du Canal de Provence et d'Aménagement de la Region Provencale*; Le Tholonet, 13 December 1965; U.S. Bureau of Reclamation: Denver, CO, USA, 1979.
47. Clemmens, A.J. Delivery System Schedules and Required Capacities. In *Planning, Operation, Rehabilitation and Automation of Irrigation Water Delivery Systems: Symposium Proceedings*; ASCE: New York, NY, USA, 1987.
48. Christiansen, J.E. *Irrigation by Sprinkling*; University of California Agricultural Experiment Station: San Diego, CA, USA, 1942; Bulletin No. 670.
49. Rossman, L.A. *EPANET 2.0 User Manual*; Water Supply and Water Resources Division, National Risk Management Laboratory, USEPA: Cincinnati, OH, USA, 2000.
50. González-Trinidad, J.; Júnez-Ferreira, H.; Bautista-Capetillo, C.; Ávila, D.L.; Robles, R.C.O. Improving the water-use efficiency and the agricultural productivity: An application case in a modernized semiarid region in North-Central Mexico. *Sustainability* **2020**, *12*, 8122. [CrossRef]
51. Organización Meteorológica Mundial (WMO). *Los Indicadores del Cambio Climático Alcanzaron Niveles sin Precedentes en 2023*; Organización Meteorológica Mundial: Geneva, Switzerland, 2024; Available online: https://wmo.int/es/news/media-centre/los-indicadores-del-cambio-climatico-alcanzaron-niveles-sin-precedentes-en-2023-omm (accessed on 14 February 2025).
52. Ojeda-Bustamante, W.; Sifuentes-Ibarra, E.; Iñiguez-Covarrubias, M.; Montero-Martínez, M. Impacto del cambio climático en el desarrollo y requerimientos hídricos de los cultivos. *Agrociencia* **2011**, *45*, 1–11.
53. Íñiguez-Covarrubias, M.; Ojeda-Bustamante, W.; Flores-Velázquez, J.; Díaz-Delgado, C. Planning of irrigation distribution, demand, and canal conduction capacity. *Rev. Mex. Cienc. Agrícolas* **2020**, *11*, 41–54.
54. FAO. *Water and Agriculture: Sustainability, Markets, and Policies*; Food and Agriculture Organization: Rome, Italy, 2019.
55. Döll, P. Impact of climate change and variability on irrigation requirements: A global perspective. *Clim. Change* **2002**, *54*, 269–293.
56. Nourelahi, O.; Khaledian, M.; Kavoosi-Kalashami, M.; Pirmoradian, N. Factors affecting the adoption of collective pressurized irrigation systems. *Environ. Dev. Sustain.* **2022**, *24*, 12367–12386. [CrossRef]
57. Phocaides, A. *Handbook of Pressurized Irrigation Systems*, 2nd ed.; Food and Agriculture Organization of the United Nations: Rome, Italy, 2007.
58. Bolognesia, A.; Bragallia, C.; Lenzib, C.; Artina, S. Energy efficiency optimization in water distribution systems. *Procedia Eng.* **2014**, *70*, 181–190.
59. Andrés, R.; Cuchí, J.A. Analysis of sprinkler irrigation management in the LASESA district, Monegros (Spain). *Agric. Water Manag.* **2014**, *131*, 95–107. [CrossRef]
60. Fishman, R.; Giné, X.; Jacoby, H.G. Efficient irrigation and water conservation: Evidence from South India. In *The Policy Research Working Paper Series*; World Bank: Washington, DC, USA, 2023.
61. Hufnagel, J.; Reckling, M.; Ewert, F. Diverse approaches to crop diversification in agricultural research. A review. *Agron. Sustain. Dev.* **2020**, *40*, 1–17. [CrossRef]
62. Brumbelow, K.; Georgakakos, A. Consideration of climate variability and change in agricultural water resources planning. *J. Water Resour. Plan. Manag.* **2007**, *133*, 275–285.
63. Buyukcangaz, H.; Demirtas, C.; Yazgan, S.; Korukcu, A. Efficient water use in agriculture in Turkey: The need for pressurized irrigation systems. *Water Int.* **2007**, *32* (Suppl. 1), 776–785. [CrossRef]
64. Hernández-Mendoza, J.; López-Martínez, A.; Ramírez-Gutiérrez, J. Inefficiencies in Traditional Irrigation Systems and Their Impact on Agricultural Productivity. *Water* **2020**, *12*, 1342. [CrossRef]
65. Daccache, A.; Lamaddalena, N.; Fratino, U. Assessing pressure changes in an on-demand water distribution system on drip irrigation performance—Case study in Italy. *J. Irrig. Drain. Eng.* **2010**, *136*, 261–270. [CrossRef]
66. Andrade, J.F.; Poggio, S.L.; Ermácora, M.; Satorre, E.H. Land use intensification in the Rolling Pampa, Argentina: Diversifying crop sequences to increase yields and resource use. *Eur. J. Agron.* **2017**, *82*, 1–10. [CrossRef]
67. Alam, M.J.; Humphreys, E.; Sarkar, M.A.R.; Sudhir-Yadav. Intensification and diversification increase land and water productivity and profitability of rice-based cropping systems on the High Ganges River Floodplain of Bangladesh. *Field Crops Res.* **2017**, *209*, 10–26. [CrossRef]
68. Torres, R.; Aguilar, J. The Role of Drip Irrigation in Reducing Water Demand in Arid Regions. *Irrig. Sci.* **2022**, *40*, 785–799.
69. López, M.; García, R.; Pérez, A. Efficient Water Use through Modern Irrigation Systems in Mexico: A Case Study. *Sustainability* **2019**, *11*, 5438. [CrossRef]
70. Ortega, L.; Fernández, C.; Gómez, P. Irrigation Modernization and Water Use Efficiency: A Review of Technological Advances. *Agronomy* **2018**, *8*, 226.
71. Comisión Nacional del Agua (Conagua). *National Water Management Report*; Conagua: Mexico City, Mexico, 2021.

72. García, P.; Martínez, F.; Ramírez, C. Climate Variability and Water Availability in Zacatecas: Implications for Agricultural Sustainability. *Climate* **2018**, *6*, 95. [CrossRef]
73. Ortega, L.; Sánchez, M.; Domínguez, R. Water Consumption and Crop Selection in Semi-Arid Regions: A Comparative Analysis. *Water* **2021**, *13*, 1742.
74. Clement, R.; Martínez, H.; López, G. Hydraulic Modeling and Optimization of Irrigation Networks Using EPANET. *Water Resour. Manag.* **2015**, *29*, 2421–2437.
75. González-Prieto, J.; Fernández, A. Reducing Groundwater Extraction through Pressurized Irrigation Systems: A Case Study. *Water Supply* **2018**, *18*, 1290–1303. [CrossRef]
76. Santos, F.; Ramírez, J. The Role of Sustainable Agriculture in Preventing Soil Degradation and Salinization. *Land Degrad. Dev.* **2016**, *27*, 1413–1421. [CrossRef]
77. International Water Management Institute (IWMI). *Water Productivity and Agricultural Sustainability in Drylands*; IWMI: Colombo, Sri Lanka, 2020.

Disclaimer/Publisher's Note: The statements, opinions and data contained in all publications are solely those of the individual author(s) and contributor(s) and not of MDPI and/or the editor(s). MDPI and/or the editor(s) disclaim responsibility for any injury to people or property resulting from any ideas, methods, instructions or products referred to in the content.

sustainability

MDPI

Article

Knowledge Alliances for Global Change Adaptation: A Relational Approach Based on Traditional Ecological Knowledge, Territorial Management, and Community Practices in the Chilean Context

Patricio Silva-Ávila [1,2,*], Jorge Rojas Hernández [2,3] and Ricardo O. Barra [1,2]

[1] Facultad de Ciencias Ambientales y Centro EULA-Chile, Universidad de Concepción, Concepción 4030000, Chile; ricbarra@udec.cl
[2] Water Research Center for Agriculture and Mining (CRHIAM), Concepcion 4070411, Chile; jrojas@udec.cl
[3] Facultad de Ciencias Sociales, Departamento de Sociología, Universidad de Concepción, Concepción 4030000, Chile
* Correspondence: patsilva.avila@gmail.com

Abstract: This study explores how traditional ecological knowledge in Chile can contribute to adaptation strategies within increasingly complex socio-ecological landscapes. It addresses the need for innovative approaches to knowledge production and application in the face of climate change and related crises. Through an exploratory, multi-sited qualitative methodology—integrating ethnographic observation, participatory methods, and in-depth interviews across various regions—this research identifies patterns, contrasts, and synergies in TEK practices related to water management, agroecology, community resource governance, and cultural heritage. The results show that TEK is not a static repository but rather a set of dynamic and adaptive practices and understandings shaped over centuries of interaction with heterogeneous environments. Although pressures such as migration, industrialization, resource privatization, and climatic threats endanger its continuity, TEK demonstrates the ability to integrate with scientific and political frameworks, enabling culturally relevant adaptation driven by local communities. These findings highlight the relevance of relational and transdisciplinary approaches to reduce epistemic gaps, foster cooperation, and guide more equitable, multi-level environmental governance. In conclusion, strengthening TEK's role—through supportive policies, collaborative research, and inclusive dialogues—can enhance resilience, guide sustainable transitions, and enrich global adaptation strategies that respect local contexts and cultural diversity, thereby advancing progress toward the SDGs.

Keywords: traditional ecological knowledge; climate change adaptation; relational approach; agroecology; resilience; community-based resource governance

1. Introduction

In an era marked by complex, uncertain, and immeasurable challenges—environmental, social, economic, and geopolitical in nature [1,2]—there is an urgent need to broaden and diversify the search for sustainable transition and adaptation strategies for these crisis scenarios [3,4] while profoundly re-evaluating conventional paradigms of knowledge production and application. These processes require an innovative approach to knowledge theories that seeks appropriate responses to the multiple problems and challenges faced by modern society [5]. In this context, alternatives have emerged that open spaces

to re-comprehend and integrate [6,7] the various expressions of traditional ecological knowledge (TEK) that have been extensively validated by Indigenous peoples and rural societies [8,9]. Historically, these worldviews have offered a systemic understanding of the landscape, diverse productive experiences, and resilient community dynamics within changing environments [10]. TEK, as a reservoir of sustainable practices and community resilience strategies, presents a valuable contribution to sustainable development goals by aligning traditional knowledge with ecological balance, food security, and equitable resource management.

The objective of this research is to explore, in an exploratory manner, TEK expressions in certain Chilean contexts, examining their local dynamics and the synergistic potential they may represent among different territorial realities. It aims to understand and foster an adaptive process, situated at multiple scales and co-constructed under a relational approach, in response to the socio-climatic crisis confronting Chilean society as well as other Latin American societies.

By focusing the analysis on different regions of Chile, we seek to understand how these TEK expressions, articulated at local scales under contrasting environmental conditions, can generate synergies between distinct territorial realities. This approach not only intends to provide a conceptual and empirical basis for better understanding TEK's role in climate change adaptation and sustainability but also to lay foundations for future collaborative initiatives—across various scales—that strengthen its incorporation into territorial governance. Recent studies [11–13] underscore the importance of TEK in natural resource management and climate change adaptation, offering transformative perspectives to mitigate environmental impacts and develop culturally congruent and ecosystemically effective adaptation strategies. These efforts align directly with the overarching goals of sustainability science, which emphasize integrated, interdisciplinary approaches to address global environmental change while respecting local knowledge systems and community agency.

Co-constructing and integrating TEK experiences and practices into adaptation measures not only takes advantage of the long-standing traditions and conceptions these communities hold regarding their environment [14] but also ensures the preservation of socio-cultural, productive, and ecosystemic heritage—integral elements for advancing toward resilient adaptation [15,16]. These heritage dimensions reflect TEK's critical role in sustaining biodiversity, promoting environmental justice, and strengthening social cohesion, thereby enriching its contribution to sustainable land-use planning and governance.

Transitioning toward these paradigm shifts allows for a relational and interdependent understanding among knowledge systems, governance dynamics, and ecosystem states, establishing points of interaction that manifest in the territory and mediate among domestic, community, and productive environments of diverse local contexts [17]. Discussions related to agroecological production systems [18], as historically resilient and community-based agricultural management experiences [19,20], reaffirm TEK as an alternative paradigm that also provides a vital response to crises of biodiversity loss, ecosystem degradation, and structural inequality fostered by agro-industrial models [21]. These insights align with the principles of sustainable development, wherein TEK contributes to ecological restoration, climate resilience, and inclusive economic frameworks that respect local knowledge.

Fostering the development of new scientific fields from the interactions of traditional and contemporary knowledge systems aims to progressively reduce the dialogical and operational gaps among decision-makers, members of productive sectors, and local actors [22]. This implies strengthening a collaborative approach—pointing toward transdisciplinary methodologies—that values co-production and involves stakeholders, horizontally incorporating Indigenous communities and rural societies into the process. Such integration

not only advances sustainability science but also positions TEK as a pivotal framework for addressing global socio-environmental transformations [23,24].

All of this means advancing toward new knowledge alliances that can gather, situate, and apply these TEK discussions into concrete cases. Under this relational approach [25], these alliances can resiliently weave collaborative processes capable of overcoming cultural, political, and institutional barriers [26], consolidating spaces for TEK within governance and land-use planning processes, and preventing its degradation and loss in the face of multiple threats [27]. These efforts reinforce TEK's role as a cornerstone of sustainability, linking traditional practices with contemporary challenges to build adaptive, inclusive, and resilient pathways for the future.

2. Theoretical–Conceptual Review

Briefly, this review aims to emphasize the fundamental role of traditional ecological knowledge (TEK) in discussions regarding adaptation and mitigation in contemporary crisis scenarios.

2.1. Traditional Ecological Knowledge: Expanding the Pathways for Adaptation in Times of Crisis

The wide array of TEK expressions represents centuries of community interactions, learning, and observation, brought together by Indigenous peoples and rural societies who systematically adapted to their ecosystems, encapsulating practices, beliefs, and techniques for their survival and sustainability [28].

These knowledge systems [29–31] are characterized by a holistic and systematic understanding of the world [32,33], a diversity of trades, practices, and techniques [34,35], and a cohesive dynamic passed down through generations [36]. Such dynamics are reflected in the cultural institutions that peoples and communities have built from their worldviews [37]. Historically, communities have maintained a close relationship with their environment [38], enabling them to undergo profound adaptive processes in response to local contextual changes, progressively adjusting their productive management methods and governance strategies around hydro-productive–ecological management of their surroundings [18,39].

The adaptability and dynamic nature of TEK [40] enable contributions to the design of ecologically viable adaptation and mitigation strategies that are also pertinent to diverse local socio-cultural realities [41,42]. TEK complements scientific methods with nuanced data and understandings of environmental changes often overlooked by conventional science [22]. This integrative path of various forms of knowledge requires moving beyond the historical perspective—rooted in traditional science—of "instrumentalizing" TEK expressions [43,44], thereby avoiding compartmentalizing their integral understanding of the environment or reducing them to seemingly irrelevant perceptions in decision-making processes [45,46].

2.2. Toward a Relational Society–Nature Vision Through a Reinterpretation of TEK

Understanding and integrating TEK into contemporary adaptive processes requires transcending the fragmented views that have historically dominated knowledge management [14]. It calls for advancing toward a relational approach that connects these traditional expressions to the need to rethink the relationships between society and nature [47,48]. In various contexts, the relational approach [49,50] is gaining relevance, converging diverse cooperative initiatives into collective efforts to replicate and learn from these experiences at multiple scales [51].

The relational approach in sustainability science emphasizes the dynamic and interdependent relationships among human and non-human actors. Rather than treating these

as isolated components, this perspective focuses on the interactions and interconnections that shape socio-ecological systems [52,53]. This approach aligns with the idea that sustainability outcomes are deeply rooted in the quality and nature of these interactions, where communities, ecosystems, and governance structures are inherently interlinked. These relationships form the foundation of their adaptive and resilient potential [54–56].

For instance, in the context of TEK, the relational approach highlights the embeddedness of knowledge systems within cultural practices, spiritual beliefs, and ecological interactions. Indigenous relational ontologies, as Whyte [26] has explored, conceive humans as integral components of ecosystems, fostering stewardship practices that sustain both biodiversity and cultural identity. This framework transcends reductionist views, providing a more nuanced understanding of how TEK can contribute to resilience and sustainability. By applying this approach in practice [57,58], significant advancements have been made in the co-management of natural resources, territorial planning, and transitions toward sustainable models [59,60]. Examples from global experiences [61–65] demonstrate that co-constructing knowledge through reciprocal and respectful interactions with Indigenous worldviews can guide transformative and just sustainability pathways [66–68].

Knowledge alliances, on the other hand, represent structured collaborations between diverse epistemological systems—scientific, local, and Indigenous—to address complex socio-environmental challenges. These alliances are not merely aggregations of knowledge but dynamic, co-creative processes aimed at fostering synergies across epistemic traditions. As Puri [69] explains, knowledge alliances facilitate the integration of context-specific Indigenous knowledge with scientifically codified practices through participatory frameworks and mediating tools, such as boundary objects, which enable mutual understanding and collective problem-solving.

2.3. Co-Construction of Knowledge Alliances from an Inter- and Transdisciplinary Perspective

The global distribution of TEK [70] offers a unique opportunity to establish wide-ranging dialogues among worldviews and practices, enabling the integration of trades, techniques, and experiences into a common adaptive framework [71]. On this path, inter- and transdisciplinarity emerge as essential epistemological approaches [72–74], guiding the development of new sub-disciplines toward creating adaptation strategies and plans that understand the complexity of socio-ecological interactions [75] as well as building truly collaborative and horizontal alliances [76,77].

Knowledge alliances, grounded in reciprocity and trust, promote horizontal dialogue that not only integrates diverse worldviews but also creates innovative spaces for formulating inclusive and equitable policies [78]. These alliances allow for the successful replication and adaptation of strategies in different contexts, strengthening sustainability and socio-environmental justice [79]. The co-construction of knowledge, under an inter- and transdisciplinary epistemology [80], provides a robust framework to address contemporary challenges, integrating TEK into a relational approach that enriches both the scientific discourse [81] and public policy formulation.

This approach presents significant methodological challenges, such as the need to slow down certain stages of the investigative and reflective processes [82] to promote deep integration of diverse worldviews [83,84], further strengthening trust-based relationships among actors at different scales and in various contexts. At the same time, there are opportunities to reimagine certain strategies in local decision-making and territorial management [85], seeking solutions that are not only ecologically viable but also culturally resonant and socially equitable [86].

The success of these alliances lies in their ability to articulate multi-scalar mitigation and adaptation strategies that respond to local realities but also have global resonance and projectable longevity [87].

2.4. Chile and the Socio-Environmental Crisis: A Diverse Setting for Reconceiving TEK

Chile's great ecosystemic and cultural diversity [88] offers a broad and interesting scenario for the study and understanding of TEK [89]. Indigenous peoples such as the Mapuche or Aymara [90,91], together with rural agrarian societies formed in the central regions [92–94], have developed intricate knowledge systems that have been fundamental for environmental management [95–97]. They have adapted to their daily practices, ecosystemic particularities, and territorial transformations [98–100]. These dynamics, deeply rooted in local culture, constitute a strategic resource for Chile to more resiliently address contemporary environmental problems and challenges, such as the severe water crisis [101] or the increase in extreme events [102], including floods and wildfires [103].

Indeed, the country faces a scenario of growing environmental vulnerability [104], intensified by the impacts of climate change [105]. The water crisis—marked by a prolonged megadrought and overexploitation of water in various territories [106,107]—is a clear example of these threats, affecting both biodiversity and the sustainability of traditional knowledge systems [27,108] and community livelihoods. This scenario is further aggravated by certain territorial conflicts and tensions [109,110], along with various migration processes [111,112], putting the country's biocultural richness at risk [113] and progressively eroding the intergenerational transmission channels of TEK itself [90].

However, Chile has taken steps toward safeguarding TEK and integrating it into contemporary environmental management. For instance, national programs like the Indigenous Territorial Development Program (PDTI) and PRODESAL, implemented by INDAP (Institute for Agricultural Development), provide financial and technical support to Indigenous and rural communities to sustain traditional agricultural practices while addressing environmental challenges. Similarly, legal frameworks like the Environmental Framework Law (Ley N° 19.300) emphasize the sustainable management of natural and cultural heritage, providing a policy basis to protect TEK practices. Initiatives like the revitalization of the Itata Valley or the Denomination of Origin programs for traditional products further illustrate how TEK can merge with modern governance models to promote resilience and sustainability.

Adopting a relational and transdisciplinary perspective in managing Chile's socio-environmental crisis offers another pathway to address the threats, strengthening these traditional knowledge systems. This approach requires reciprocity and (re)establishment of trust between those who carry or preserve traditional knowledge and those who actively participate in decision-making [114,115]. For example, collaborative initiatives like *La Despensa de O'Higgins* demonstrate how community-based efforts can successfully bridge TEK and modern market demands, ensuring the continuation of sustainable practices. Such integration not only reinforces the socio-ecological resilience of local communities but also contributes to consolidating new models to resiliently tackle complex environmental problems on a global scale [116,117].

3. Methods

This research adopted an exploratory, multi-sited, and predominantly qualitative methodological strategy, structured into three main stages (Figure 1), aimed at characterizing and interrelating various TEK expressions in four areas representative of Chile's ecosystemic and socio-cultural diversity. The inherent complexity of TEK systems [32], their intricate relationship with territory, and community dynamics required an adaptive

research strategy capable of capturing the specificities and nuances of this knowledge in particular local contexts [118,119].

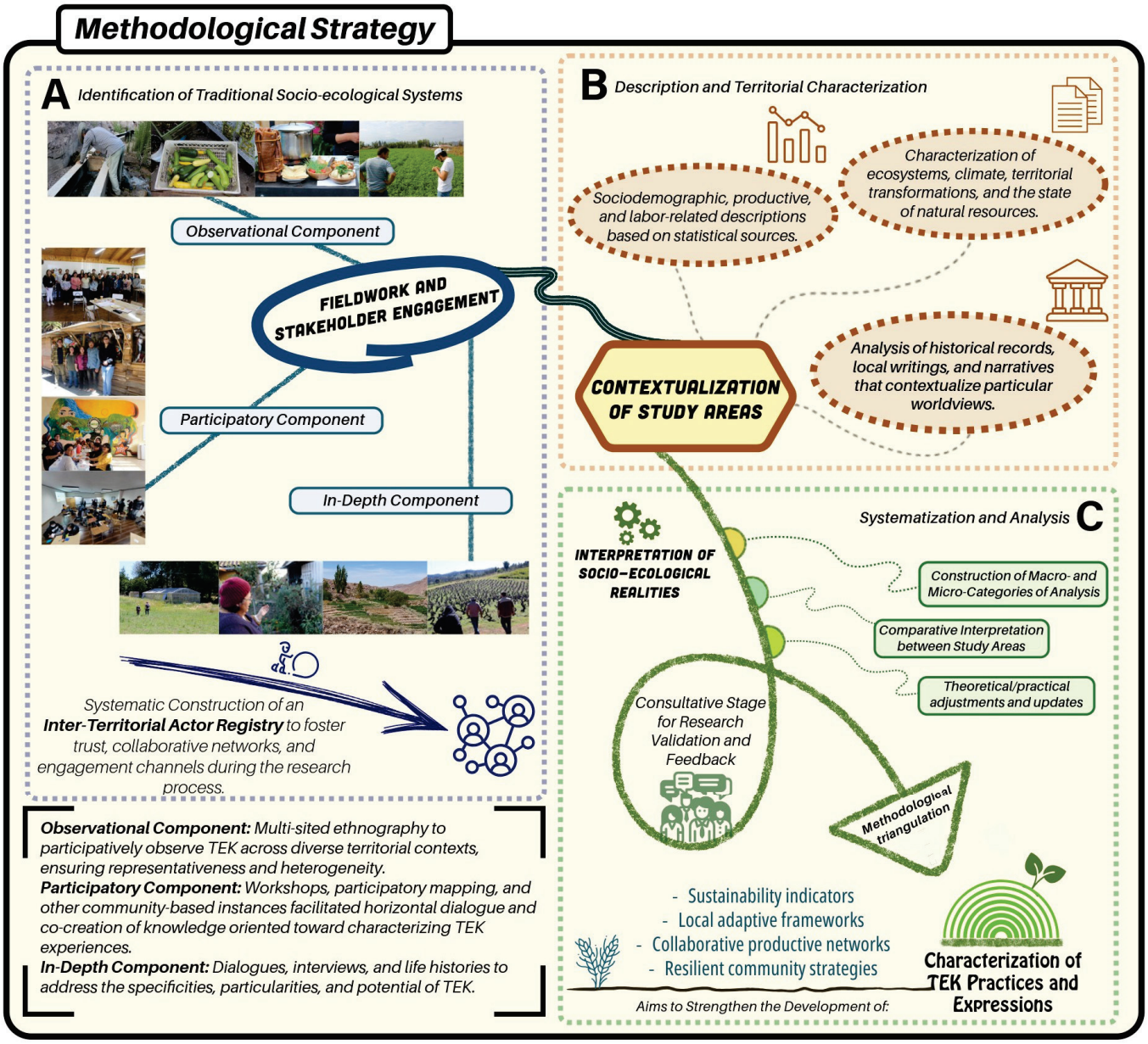

Figure 1. Methodological strategy.

3.1. Identification of Actors and Traditional Socio-Ecological Systems

The central and core stage of this research involved the integration of ethnographic techniques, participatory methodologies, and an in-depth exploration of each territory's narratives. These processes also entailed ongoing engagement and interaction with a variety of actors in the studied territories, consolidating an inter-territorial roster of actors connected to TEK experiences. This made it possible to envision future opportunities for collaboration and knowledge exchange.

3.1.1. Observational Component

An initial approach under a multi-sited ethnographic framework [82,120] made it possible to study TEK systems in different territorial contexts, scalable under a common thematic–analytical framework [121,122]. This process also centered on conducting participant observation [123,124], immersing the researcher in the daily practices and rituals of

the studied communities. Such immersion enabled a holistic and contextualized understanding of the environment and the dynamics of its natural resource management [35,125]. Over a three-year period, visits were made to each study area during different seasons, productive periods, and key community dates, building and strengthening relationships with key actors, institutions, and significant TEK experiences [126]. This iterative approach effectively integrated the design of instruments and data collection techniques [127].

3.1.2. Participatory Component

Expanding the research scope through participatory instances proved fundamental for collaboratively strengthening a TEK characterization that not only reflected a scientific perspective [128] but also democratized the knowledge production process [129]. Ensuring applicability and scalability to different local contexts, this involved community forums, workshops, participatory mapping, shared meals, and collaboration in tasks related to water and land management. These activities fostered horizontal dialogue with the study participants [130,131]. Not only did these activities validate TEK's local relevance, but meaningful participation also added a special dynamic to this research. It enriched the central aspects of this study and facilitated knowledge exchange among the involved actors [132], closing epistemological gaps and strengthening mutual trust [133,134].

3.1.3. In-Depth Component

The third component focused on deepening the understanding of TEK through semi-structured interviews with more than 20 key actors [135,136], delving into their life histories and experiences. This was complemented by extensive visits to community and productive environments, gaining a more detailed knowledge of the particularities, differences, and adaptive capacities within TEK expressions [137]. By continuously iterating between collected data, recorded narratives, and analyzed theory, following the constant comparative method [138], it became easier to identify patterns, categories, and variations among the different studied territories [139,140]. This facilitated the coding process and guided the subsequent analysis and inductive theory-building around TEK cases.

3.2. Description, Contextualization, and Territorial Characterization

This stage involved analyzing and reviewing secondary data to complement previously conducted qualitative work. It allowed for contextualizing and enriching the initial findings, strengthening this research's conceptual frameworks, and adjusting the thematic guidelines used in the fieldwork [118]. Moreover, this approach broadened the research scope in both longitudinal and geographical terms, contributing to a more in-depth analysis and minimizing the burden on participants [141].

The central objective was to delve into the historical–cultural, socio-demographic, ecosystemic, productive, and labor dimensions of the study areas. This was achieved by using official statistical sources, historical records, and previous studies. Employing secondary data also offered significant advantages for the research process, such as saving time, accessing large volumes of information, and reducing data collection costs [142].

3.3. Systematization, Analysis, and Interpretation of Socio-Ecological Realities

At this stage, data were systematized, analyzed, and interpreted, applying grounded theory principles [138,143,144]. Triangulating methods and data sources strengthened the validity of results, allowing for the comparison and corroboration of qualitative findings with the quantitative and contextual information obtained in the previous stage [145]. Continuous iteration between theory and empirical data adjusted and enriched the research's conceptual framework [146–148]. This approach made it possible to address problems by considering scale and time from the practices shaping the studied scenarios. We progressed

in constructing macro-categories of analysis based on different studied realities, establishing comparisons and particularities in TEK experiences obtained from dynamic interactions with communities and their socio-ecological, productive, and cultural environments.

Community validation through workshops, feedback sessions, and result-sharing provided cultural and human sensitivity, utility, and relevance to the involved communities [129]. Simultaneously, this process strengthened trust and promoted the communities' appropriation of generated knowledge, integrating it into their daily practices. In this way, the practical application of the findings with future perspectives was made possible.

3.4. Ethical Considerations

A pertinent ethical protocol was implemented, including informed consent from each participant, data confidentiality, and the commitment to return results to communities in a comprehensible and useful manner [149]. Sensitive information was anonymized, and the rights and dignity of all participants were respected. Additionally, a gender perspective was integrated, and the inclusion of diverse voices at all levels of this study was promoted [150].

Building trust was fundamental to the success of this research. The flexibility of the methodological approach allowed for adjusting procedures according to participants' needs, sensitivities, and worldviews, ensuring ethical, respectful, and inclusive research [119]. This ethical commitment not only strengthened this study but also increased its impact and reach by fostering lasting and collaborative relationships with communities [133].

4. Study Areas

Chile, a country stretching approximately 4300 km from the Atacama Desert in the north to the austral regions of Patagonia, is a paradigmatic example of ecological, climatic, and geomorphological diversity [88]. This longitudinal diversity underpins the distinct socio-ecological interactions that shape territorial management and traditional knowledge systems across its regions. This research focuses on four study areas—Tarapacá, O'Higgins, Ñuble-Biobío, and Los Ríos-Los Lagos—selected based on theoretical and practical criteria that prioritize representation of heterogeneous territorial, cultural, and ecological contexts (Figure 2). These regions not only reflect diverse environmental conditions but also illustrate the varied interactions between traditional ecological knowledge (TEK), governance frameworks, and productive practices throughout Chile's history.

In recent years, the country has faced an unprecedented water crisis, marked by a persistent megadrought that has profoundly altered water availability [107]. Overexploitation of aquifers, the expansion of exotic forest plantations, and agricultural intensification have placed pressure on water sources, raising tensions and conflicts among productive sectors, rural communities, and local ecosystems [110]. This delicate scenario is further aggravated by institutional limitations, legal tensions, and epistemological barriers that hinder the transition toward more equitable water governance [101].

The selected study areas encompass a geographic diversity that reflects the main climatic and ecosystemic characteristics of Chile. The Tarapacá region, in the extreme north, is characterized by a desert climate with minimal rainfall and extreme temperatures [151]. High-Andean ecosystems, such as *Bofedales*, play a crucial role in water management and biodiversity preservation, being fundamental to local communities' resilience in the face of water scarcity. This region also presents a marked altitudinal transition, from the arid coast to the heights of the Altiplano.

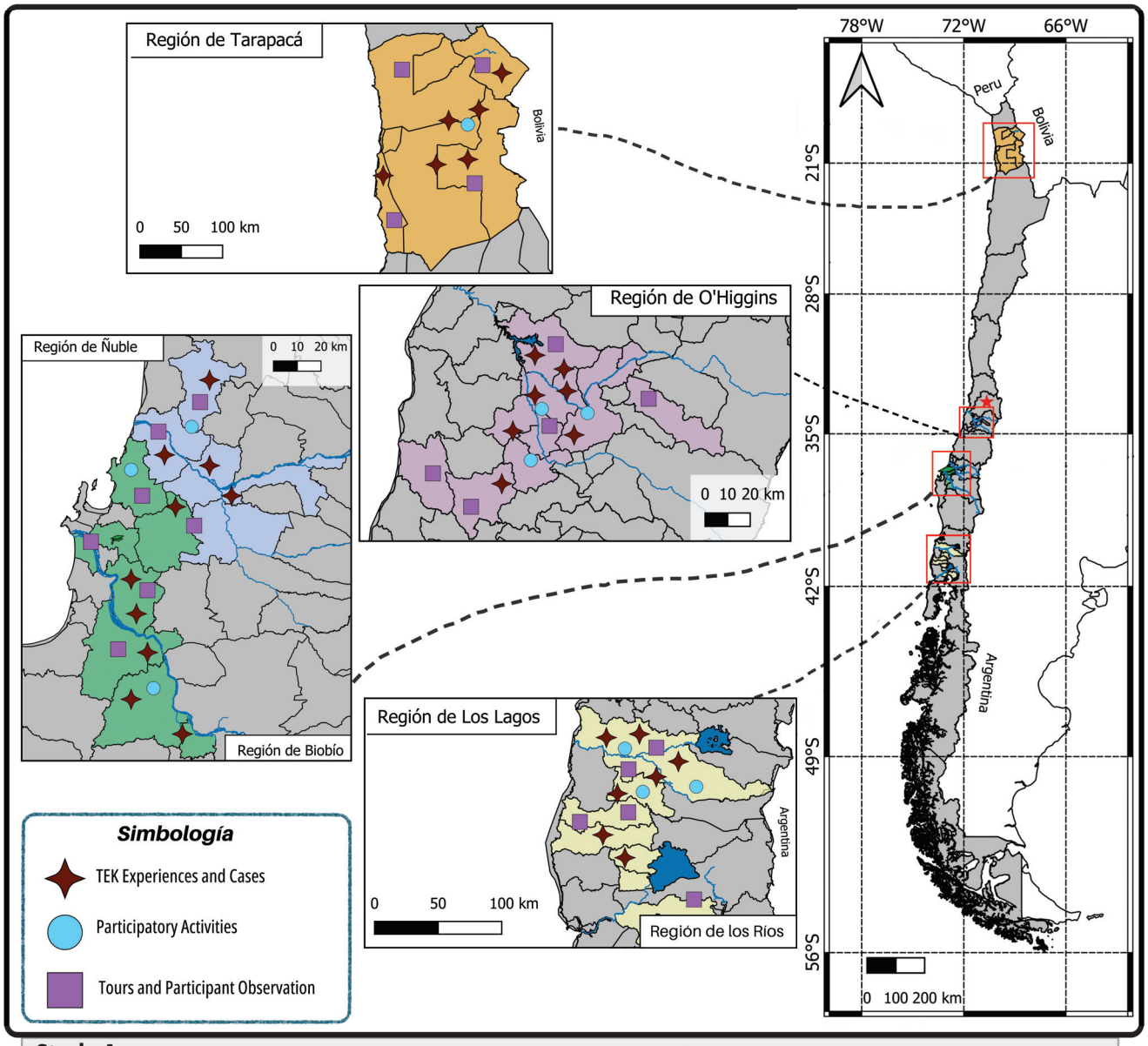

Figure 2. Study areas.

In contrast, the O'Higgins, Ñuble, and Biobío regions in central and southern Chile experience Mediterranean and temperate rainy climates, with key fluvial and agricultural ecosystems. Irregular precipitation patterns and water overexploitation in the Cachapoal and Tinguiririca rivers in O'Higgins, as well as the fragmentation of the Itata and Ñuble rivers, have affected the sustainability of productive and ecological systems. In Biobío, the expansion of forest monocultures and the increase in wildfires exacerbate biodiversity conservation and sustainable land management issues, also complicating governance in significant basins such as that of the Biobío River. The Biobío is one of the country's main water bodies and poses a series of challenges in terms of water governance, continuously interacting with industrial activities, hydroelectric projects, numerous stakeholders, and

traditional productive experiences [152]. Finally, in the Los Ríos and Los Lagos regions, the temperate–rainy climate, combined with deforestation, changes in rainfall patterns, landscape transformation through land subdivision, and land-use changes, all increase the territory's vulnerability, affecting agricultural production and the preservation of fluvial systems.

Challenges in these regions include deforestation, shifting rainfall patterns, and fragmentation due to land subdivision, all of which heighten vulnerability to climate change. However, the resilience of TEK practices, such as sustainable livestock grazing and soil conservation techniques, demonstrates the capacity of local communities to adapt. Moreover, the prevalence of cooperatives, such as those focused on dairy production or wool processing, illustrates how traditional practices can be integrated into modern economic frameworks, creating opportunities for knowledge exchange and innovation in sustainability.

The selected regions were chosen based on their ability to represent the ecological and cultural diversity of Chile while reflecting key socio-ecological dynamics. The criteria included the following:

- Ecosystemic Diversity: Capturing distinct climatic zones (arid, Mediterranean, and temperate) to reflect the variability of TEK applications across different environmental contexts.
- Historical Significance: Highlighting regions with pivotal roles in Chile's socio-economic development, from the Andean highlands' early agricultural innovations to the colonial and post-independence transformations of the central valleys and southern territories.
- Functional Representation of TEK: Showcasing a range of TEK practices, including water management, agroecology, and hybridized land-use systems, to illustrate how traditional knowledge informs sustainable practices across different landscapes.
- Governance Complexities: Focusing on regions with active socio-environmental conflicts or collaborative governance initiatives to explore how TEK interfaces with policy and management frameworks.

5. Results

5.1. Tarapacá: TEK Conservation in an Arid Context

In Tarapacá, TEK expressions represent a remarkable model of sustainability in one of the world's most arid ecosystems (Figure 3). The practices developed, maintained, and transmitted by peoples (Aymara, Quechua, and Diaguita, among others present in the area) reflect centuries of adaptation to their environment, practicing efficient and sustainable natural resource management [100]. Traditional productive systems in the region are deeply integrated with the landscape, combining agricultural, pastoral, and water-related practices with cultural and spiritual expressions that reinforce social cohesion.

Water management in this area is characterized by the application of a variety of traditional techniques and practices fundamental to sustaining both productive and community activities (Figure 3B). High-Andean Bofedales, key ecosystems for water regulation in the Altiplano, support a range of productive and cultural activities. In these ecosystems, traditional techniques such as "champeo" (Figure 3A) are employed, involving monitoring, channeling, and redistributing water to retain and release it during dry seasons, thereby facilitating camelid grazing and crop viability in critical periods. Additionally, sowing and harvesting water practices, based on rainwater capture and storage, complement other water management strategies, enabling communities to anticipate climatic variability. These practices have parallels with water collection systems in Tunisia and Peru, evidencing their potential replicability in other arid regions [153,154].

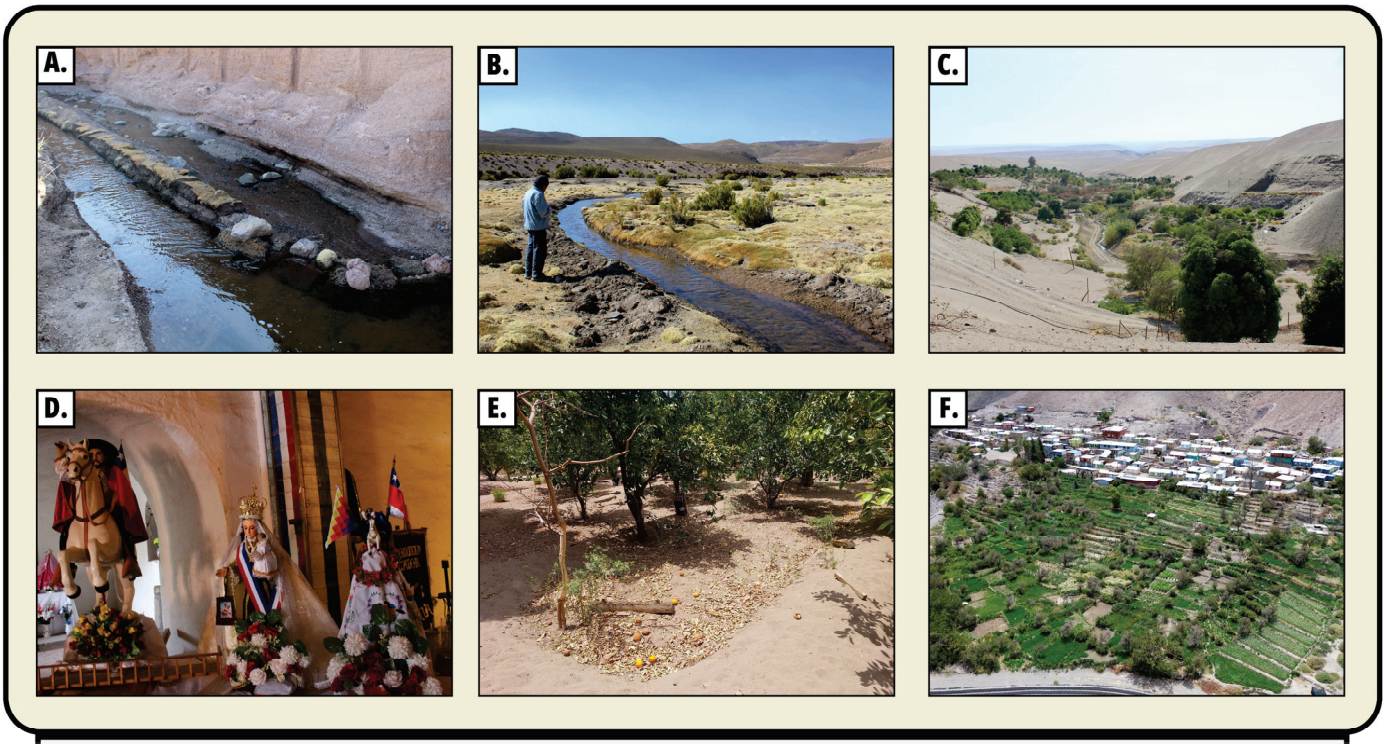

Figure 3. TEK in Tarapacá.

Another crucial aspect of water management is the development of irrigation systems that take advantage of the landscape's morphology, such as the ancestral installation of "qochas" in places like Pica, Matilla, and the Quisma Valley. Qochas are water reservoirs collecting runoff and rainwater, increasing water availability for agricultural use. These systems have evolved historically, gradually complemented by some canalization and infiltration technologies introduced by Spanish colonizers who leveraged the area's productive potential during the 16th and 17th centuries [98,155].

In this area, another fundamental TEK component is the ancestral use of agricultural terraces, a practice widespread throughout the Andes [91]. These terraces, extensively found in sectors like the Tarapacá Gorge (Figure 3F), have been essential for maximizing moisture retention, minimizing erosion, and preserving fertile soils—crucial factors to produce crops such as quinoa, oregano, citrus, Pascua pear, and quince (Figure 3F). However, currently, these terraces are not being used at their full capacity. The pressure from extractive activities, especially mining, has negatively affected crop maintenance and productivity. Additionally, generational turnover among farmers hinders the continuity of agricultural activities, since younger generations often migrate to urban coastal areas in the region. Despite these challenges, there is potential and capacity to revitalize agricultural terraces through support programs and the promotion of sustainable practices. Restoring these structures would not only contribute to food security and local economic development but also allow the preservation of the region's cultural heritage and ecological landscape. Studies in other Andean areas have shown that rehabilitating agricultural terraces can be

successful when TEK is combined with modern techniques and the local community is actively involved, suggesting that similar initiatives could be implemented in Tarapacá to reverse the current trend and strengthen agricultural resilience. Comparable to rice terraces in China [156] and dryland systems in Thailand [157], these practices demonstrate their effectiveness in different agroclimatic contexts and their potential integration into global adaptation strategies.

Some remnants of Tarapacá's viticultural tradition remain structurally embedded in the development and establishment of the area's settlements. In Matilla, precisely, the production of wines such as Oporto-type, developed between the 16th and 18th centuries, once achieved international recognition. Although this practice declined after the War of the Pacific due to strategic and developmental factors that led to the expropriation of water from peasants in the Quisma Valley (Figure 3C), there are currently inter-institutional collaborative initiatives aimed at reviving these crafts [97]. These initiatives seek new productive niches through the revitalization of these traditions, integrating modern techniques with native varieties and promoting sustainability through wine tourism.

The cultural aspect of TEK is inseparable from its spiritual dimension. Various religious festivities (Figure 3D) distributed among the valleys and gorges (such as La Tirana or San Antonio in Matilla) symbolize a religious and cultural syncretism that reinforces elements for the intergenerational transmission of traditional knowledge. These celebrations act as spaces to reactivate community dynamics and exchange knowledge and practices with the new generations who, during these festivities, return to their traditional villages.

5.2. O'Higgins: Agroecology, Water, and Seeds—Sustaining Ancestral Knowledge

Historically, this area has been a key agricultural center for Chile, with a rich heritage dating back to pre-Hispanic and colonial periods [92,158]. During the hacienda period, a mixture of knowledge about valley management was consolidated, where the syncretism between ancestral practices—of Indigenous peoples—and European practices—brought by Spanish colonizers—gave rise to unique agricultural systems. TEK in this region (Figure 4) has been nurtured by this history, consolidating over generations of peasants who have preserved and adapted traditional practices, both in landscape management and in maintaining spaces and productive methods at different scales.

A representative example is the use of "Azudas" in Larmahue, commune of Pichidegua (Figure 4A); they are ancestral waterwheels introduced during the colonial period, still used to lift water and irrigate fields in dryland areas. These structures have been maintained and rebuilt by local artisans, reflecting the integration of traditional techniques with current needs. The preservation of this system is possible thanks to the active role of peasantry in conserving these techniques, including trades such as carpentry and blacksmithing, essential for the construction and maintenance of azudas. Several studies reaffirm and explore in depth the active role of these irrigation systems in the region's development and the maintenance of community dynamics [93,95,96].

In the Cachapoal and Rapel valleys, agriculture rooted in family farming conserves ancestral agroecological practices (Figure 4E), such as refined pruning and artisanal food preservation methods. However, less water-efficient techniques persist, such as furrow or flood irrigation (Figure 4B), as well as seasonal soil burning. Although traditional, these practices lack the necessary efficiency in the face of the current water crisis and the growing demand for sustainable production.

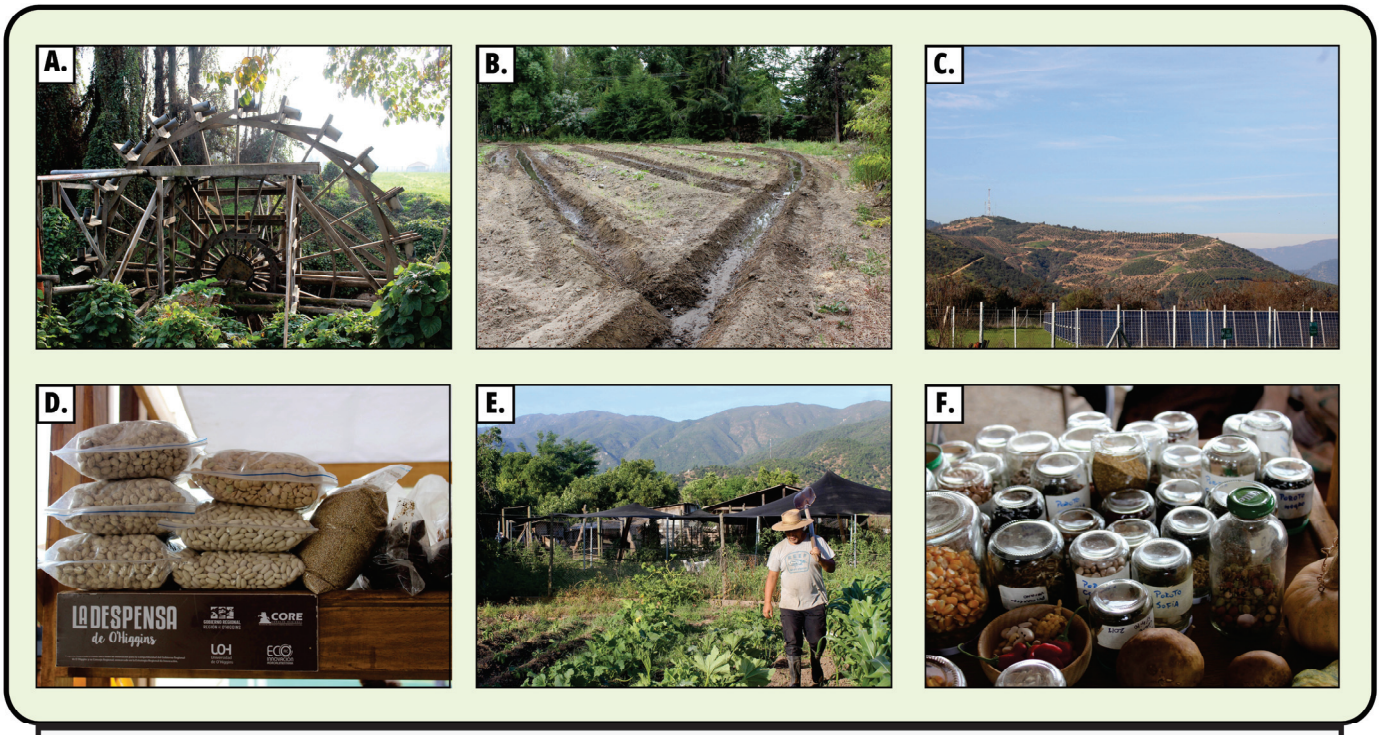

TEK in O´Higgins: Some of the studied expressions or cases were: **A.** Use of waterwheels or "Azudas" for water management in dryland areas; Lo Argentina, Pichidegua. **B.** Furrow irrigation among the diverse irrigation methods used in the area; San Luis, Pichidegua. **C.** Landscape transformation associated with the industrialization of productive sectors and the promotion of new technologies; Llallauquén, Las Cabras. **D.** Initiatives like "La Despensa de O´Higgins" promote the revival of local products, preserving ancestral cultures and preparations of the territory. **E.** Agroecological garden work, part of the traditional agriculture in O'Higgins; Codao, Peumo. **F.** Seed guardians in the Cachapoal Valley maintain seed recovery and conservation, conducting constant exchanges and bartering, fulfilling an educational role and fostering community well-being.

Figure 4. TEK in O'Higgins.

Seed guardians in the Cachapoal Valley represent a strategic dimension of TEK in the area (Figure 4F). Cases such as that of Mrs. Ana Yañez Antillanca—an agroecological gardener, researcher of ancestral cuisine, and community educator—through the conservation, selection, and improvement of ancestral crop varieties not only contribute to the genetic resilience of agricultural systems but also reinforce the socio-cultural fabric around the use, preparation, and exchange of foods. Her holistic perspective integrates the safeguarding of plant species with culinary practices, oral traditions, and the strengthening of local networks, evidencing that TEK is not a mere static repository but a dynamic field capable of adapting and generating productive alternatives in the face of climatic variability and pressures on water resources. The work of these seed guardians transcends the productive sphere to become a pedagogical and cultural reference, expanding the repertoire of options available to communities and enabling innovative ways to articulate TEK as a key tool in transitioning toward sustainable and socially just forms of global adaptation. Through local markets and fairs, these guardians' agroecological dynamics have recently been strengthened, allowing for the expansion of spaces for exchange, intergenerational dialogue, and the productive capacity of small farmers. Community initiatives such as "La Despensa de O'Higgins" (Figure 4D) have revitalized the production and consumption of traditional foods, promoted food security, and strengthened the valleys' cultural identity. The impetus of this initiative allows us to envision the development of these small traditional value chains in other contexts.

Viticulture is another fundamental practice in O'Higgins. During the hacienda period, vineyards expanded, and vine management techniques were transmitted from generation to generation. This knowledge has allowed maintaining the quality and diversity of local varieties, highlighting the Cachapoal Valley and its revitalization of grape varieties like Carmenere. Traditional pruning is not only an agricultural technique but also a niche for exchanging knowledge among local communities. Several actors emphasize the importance of the intergenerational transmission of this knowledge and how industrialization and the introduction of new crops have posed greater difficulties in preserving it.

TEK faces challenges such as agricultural intensification, the industrialization of traditional niches like wine, and the expansion of monocultures and solar fields on fertile lands, creating a fragmented territorial matrix (Figure 4C). This landscape transformation dynamic concentrates resources and displaces ancestral practices, while global market adaptation limits interaction between generations, reducing opportunities to share knowledge.

5.3. Ñuble and Biobío Regions: Socio-Ecological Adaptation Under Territorial and Productive Pressures

In these regions, whose administrative separation in 2018 has introduced new governance dynamics, TEK expressions face a complex scenario marked by tensions between ancestral practices and contemporary productive pressures [159,160]. On one hand, the intensive expansion of forest monocultures (pine and eucalyptus) has made water access difficult, altered soil fertility and productivity, fragmented the landscape, and directly affected rural communities along with their traditional agricultural dynamics [161]. On the other hand, the Biobío River basin—one of the country's most significant—serves as a strategic axis for multiple actors, making it even more complex to implement actions that enhance socio-ecological resilience.

In the face of these scenarios, TEK manifests in agroecological practices, centuries-old trades, and adaptive techniques that aim to sustain the zone's productive and cultural diversity (Figure 5). The Itata Valley, for example, is renowned for its viticultural tradition with grape varieties such as País or Moscatel de Alejandría, managed (Figure 5B) through manual pruning, fermentation with native yeasts, and the use of centennial vines—more than 200 years old in some sectors like Portezuelo or Nacimiento (Figure 5E). This knowledge, transmitted through generations, has found new ways to persist by recovering earthenware jars for winemaking and the technological control of fermentation parameters (Figure 5F). The balance generated between ancestral heritage and contemporary innovation reveals TEK's potential to address climatic and commercial challenges, preserving a unique territorial and patrimonial identity. Local studies reaffirm Itata's historical, productive, and cultural value [162,163]; international experiences, such as climate change innovations in Australian wine regions, also show how regions can adapt to environmental challenges through sustainable practices and the conservation of cultural heritage [164].

In rural sectors of Hualqui or Florida, water management stands out through the utilization of springs, ravines, and small traditional infrastructures (Figure 5A), supporting domestic tasks and maximizing the efficiency of available water resources. These practices, together with the recovery of community spaces like gardens, provide bases to move toward food self-sufficiency and the strengthening of the social fabric. The "Unión Comunal de Huertos Orgánicos" (UCHO) in Tomé (Figure 5D), for instance, illustrates how citizen participation revitalizes the maintenance and exchange of seeds and agricultural knowledge, fostering crop diversity on a peri-urban scale.

However, challenges are not limited to forestry pressure or climatic variability. The industrialization of productive niches, especially in viticulture, has driven transformations that strain ancestral practices. Although adapting grape varieties and rescuing traditional methods such as cooperage and the production of "pipeño" wines remain valid, com-

petition in global markets and demand for standardized products pose obstacles to the continuity of artisanal systems. Similarly, in Santa Juana, the Ají and Merkén Producers' Cooperative represents how local innovation, led by women like Mrs. Inés Olate, can redefine the gastronomic value of a culturally rooted product. Merkén, a traditional Mapuche spice, thus finds diffusion channels that revalue its role as intangible heritage, promoting TEK's recognition in broader culinary circuits.

TEK in Ñuble and Biobío: Some of the studied expressions or cases were: **A.** Among the daily uses in spring water management was the installation of washing basins or "Bateas"; Unihue, Hualqui. **B.** Cleaning and pruning vineyards in the Itata Valley, a crucial winter preparation stage influencing productivity in the following season. **C.** The expansion of forest monocultures has impacted the productive landscape of the area, reducing the presence of traditional viticulture and other productions; Guarilihue, Coelemu. **D.** Community activities and maintenance in the gardens of the Unión Comunal de Huertos Orgánicos; Tomé. **E.** Centenary grapevines trained "en cabeza" (head-trained) taking advantage of dryland conditions in the area; San Ramón, Nacimiento. **F.** Part of the innovation in viticulture is to include clay barrels recovered for wine fermentation, combined with technology that allows controlling and adjusting parameters to meet market demands.

Figure 5. TEK in Ñuble and Biobío.

Administrative fragmentation between Ñuble and Biobío adds complexity when coordinating public policies and action plans. This is reflected in the difficulty of generating medium-scale projects that strengthen the agricultural and cultural history of valleys like Itata or implementing joint strategies to promote the export of local products without losing territorial specificity. Managing the Biobío River basin, with multiple interests at stake, requires a polycentric and transdisciplinary approach integrating community, scientific, and political perspectives. Only in this way will it be possible to minimize the logistical and commercial gaps that hinder the competitiveness of small producers while respecting the diversity of practices and work rhythms associated with the local agricultural calendar.

Associativity emerges as a promising pathway. Community networks, cooperatives, and training workshops allow sharing experiences and adjusting techniques in response to external pressures. Migration, although a factor of instability, also introduces new knowledge and practices that, if well integrated, can enrich the productive repertoire. In sum, the realities of Ñuble and Biobío show how TEK is a living and strategic component

that, despite the tensions generated by territorial (Figure 5C), forestry, and productive transformations, offers alternatives toward a resilient transition.

5.4. Los Ríos and Los Lagos Regions: Cooperativism, Cultural Diversity, and TEK as Resilience Practices

The Los Ríos and Los Lagos regions—administratively separated in 2007—present a singular TEK tapestry (Figure 6), shaped by the interaction between ancestral knowledge of Indigenous peoples (Mapuche, Huilliche, and Lafkenche) and the technical–productive legacy introduced by European colonizers in the early 20th century. These dynamics have given rise to a syncretism between what is ancestral and what is modern, despite contemporary socio-economic and environmental transformations.

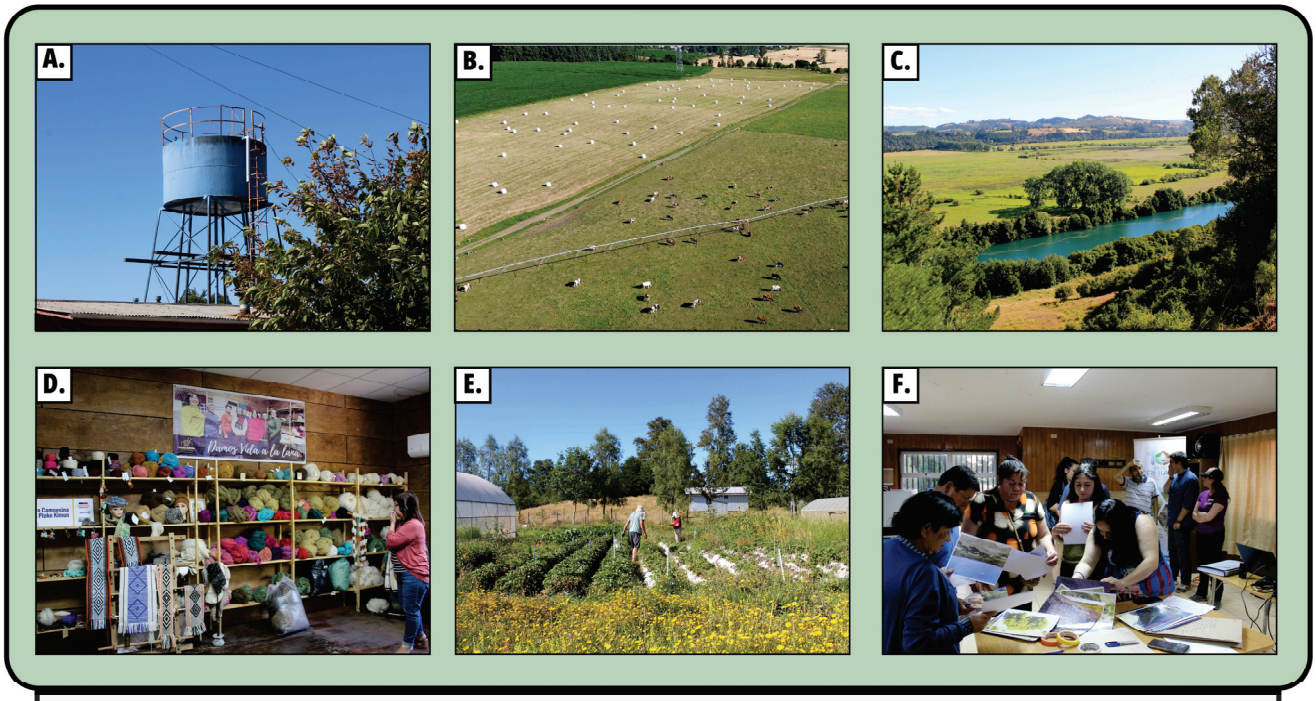

TEK in Los Ríos and Los Lagos: Some of the studied expressions or cases were: **A.** Experiences from the "Aldea Campesina Georgia" in water and community management, promoted by public policies during the 20th century; La Unión. **B.** Pasture management and the introduction of irrigation technologies associated with the industrialization of livestock production; Osorno. **C.** Pastures reflecting landscape transformation and soil management; Tronlico, La Unión. **D.** Cooperativism and multi-scale associativity developed through the PDTI at Casona Cultural los Castaños; Río Negro. **E.** Harvest and pest control activities in orchards managed by the Agroecological Women's Peasant Cooperative of Osorno. **F.** Territorial dialogues and actor coordination in various rural sectors of La Unión, strengthening community strategies and fostering knowledge exchange.

Figure 6. TEK in Los Ríos and Los Lagos.

One of the pillars of rural development in these regions has been cooperativism, whose origin dates to the impetus of German colonists and state policies that encouraged agricultural associativity. Significant cases include international cooperation initiatives such as the peasant villages built in the mid-20th century. For example, the Georgia peasant village in La Unión remains a paradigmatic case of autonomy and water governance (Figure 6A). Although strained by development, generational turnover, and the orientation toward water privatization in Chile, they have maintained an essential part of the collective dynamics required to sustain solid community relations.

Traditional cooperatives of national relevance, like COLUN, have played a crucial role in strengthening activities such as livestock farming and the dairy industry in the area, integrating TEK elements in their origins (Figure 6B). However, with economic

growth and development, technologization and the progressive loss of traditional trades and techniques—such as artisanal dairy production and the elaboration of typical beverages like apple chicha—have ensued. In contrast, other emerging cooperatives, like the Agroecological Women's Peasant Cooperative of Osorno (AgroeCoop), led by women, have demonstrated how associativity can empower small-scale producers, promoting agroecological techniques that fuse traditional knowledge with contemporary innovations (Figure 6E). This model not only strengthens family peasant agriculture but also generates support and advisory networks contributing to sustainability and food sovereignty.

Comparisons with other contexts stand out. Experiences of cooperativism in France and Ethiopia have demonstrated the potential of community organizations to improve technical efficiency and the sustainability of small agricultural operations [165,166]. In Pakistan [39], integrating TEK into resource management has shown positive results in climate change adaptation, providing valuable lessons that could be replicated in these territories.

At the cultural infrastructure level, the Casona Cultural Los Castaños in Río Negro has been key to revitalizing local economies and generating new job opportunities for Mapuche women (Figure 6D). In this space, the Indigenous Territory Development Program (PDTI) has fostered the integration of technologies and the creation of cooperatives that articulate ancestral and contemporary knowledge around local production (honey, blue eggs, and wool). These initiatives allow women to break with traditional dynamics that relegated them to the domestic sphere, promoting their empowerment and active participation in the public sphere as agents of change [167].

In the textile field, the Corazón de Vellón cooperative in Los Lagos demonstrates an exemplary initiative to keep artisanal wool production alive. This organization brings together artisans and their families, promoting community activities such as "wool washing," which not only preserve traditional techniques but also reinforce social bonds. These practices reflect another example of TEK's role and its expressions in constructing resilient community networks and adapting to a changing socio-economic context (Figure 6F).

However, the region also faces significant challenges. The expansion of monocultures, such as forest plantations or hazelnut production, generates tensions in water resource management and biodiversity conservation. Additionally, land burning, historically used for territorial development and community establishment in past centuries, continues to be widespread, exacerbating soil degradation and contributing to landscape transformation (Figure 6C). These practices underscore the urgent need to incorporate agroecological approaches and strengthen environmental education to ensure long-term sustainability.

5.5. Core Insights and Synthesis

The findings of this study underscore the diverse manifestations and adaptive capacities of Traditional Ecological Knowledge (TEK) across Chile's distinct geographic and climatic regions. Each region showcases specific TEK practices (Figure 7) that address localized environmental, social, and economic challenges while contributing meaningfully to broader sustainable development goals.

Territories / Key Points	Tarapacá	O´Higgins	Ñuble/Biobío	Los Ríos/Los Lagos
Climatic Conditions	Arid desert climate with extreme temperatures.	Mediterranean climate with irregular precipitation.	Temperate rainy climate with significant forestry pressures.	Temperate rainy climate with agroecological diversity.
Key TEK Practices/Techniques	Water harvesting (e.g., "champeo," qochas), agricultural terraces, irrigation systems.	Waterwheels (Azudas), furrow irrigation, seeds Keepers and conservation of biodiversity.	Viticulture techniques, centenary vine management, organic gardens.	Cooperativism, wool production, agroecological orchards.
General Description of TEK	TEK emphasizes sustainable water and soil management in conditions of extreme water scarcity. Integrates spiritual traditions with productive techniques, ensuring resources for traditional crops like quinoa and citrus. Bofedales act as ecological regulators under ancestral management.	Blends ancestral Indigenous techniques with colonial agricultural innovations, focusing on water management, seed conservation, and agroecology. Initiatives like "La Despensa de O'Higgins" and local fairs promote traditional value chains.	TEK manifests in viticulture, traditional water management, and agroecological practices. Combines ancestral knowledge with technological innovations, addressing challenges like landscape fragmentation and resource exploitation.	Integrates Indigenous knowledge with European agricultural techniques. Highlights gender equity in cooperatives, cultural preservation, and innovative agroecological practices.
Socio-Environmental Challenges	Mining pressures, water scarcity, urban migration, generational turnover.	Water inefficiency, intensification of monocultures, globalized market pressures.	Forestry monocultures, water governance conflicts, industrial agriculture.	Expansion of monocultures, water conflicts, landscape degradation.
Contributions to Sustainability	Strengthens water governance in arid regions, ensures food security, revitalizes cultural heritage, and fosters resilience in fragile ecosystems.	Promotes agroecological diversification, seed conservation, community food security, and the revitalization of ancestral agricultural practices.	Preserves viticulture as cultural heritage, supports socio-ecological resilience through agroecology, promotes innovation in artisanal practices.	Enhances community empowerment, sustains cooperativism, preserves cultural heritage, and promotes sustainable agroecological systems.

Figure 7. Cases synthesis.

The following points encapsulate the principal insights, illustrating the interplay between traditional practices, contemporary challenges, and pathways to resilience.

- *Diversity of Practices:* Across regions, TEK reflects a harmonious integration of ancestral and modern knowledge systems. This is evident in the adaptation of water management techniques in Tarapacá, agroecological innovations in O'Higgins, viticulture resilience in Ñuble and Biobío, and cooperative models in Los Ríos and Los Lagos.
- *Socio-Environmental Contributions:* TEK supports ecological regulation, biodiversity conservation, food security, and cultural preservation, proving its value as a tool for addressing climate change and socio-economic transformations.
- *Challenges to TEK:* The findings also reveal shared threats, including land-use pressures, generational knowledge loss, and insufficient integration into contemporary governance frameworks.
- *Sustainability Pathways:* Collaborative initiatives, such as seed conservation networks, community cooperatives, and agroecological practices, illustrate how TEK can foster

resilience, environmental justice, and sustainable transitions when supported by appropriate institutional frameworks and community participation.

6. Discussion

The findings presented in this study outline a complex and heterogeneous panorama of traditional ecological knowledge (TEK) in Chile, evidencing both its adaptive relevance to global climate change and the tensions and challenges that communities face as they attempt to sustain and project these practices within dynamic socio-environmental scenarios. In a context marked by climatic impacts, water crises, productive transformations, and migrations of varying scope, this exploratory, multi-sited research carried out in various regions of the country has made it possible to characterize, contextualize, and compare TEK expressions, identifying common patterns, specificities, and potentialities for their consolidation as a strategic pillar in the transition toward sustainable adaptation.

A key initial point is that TEK, far from representing a static repository, is confirmed as a set of dynamic knowledge, subject to processes of adaptation, hybridization, and reconfiguration. In arid territories of the north, such as Tarapacá, ancestral hydro-productive practices (like champeo, qochas, or the use of agricultural terraces) demonstrate local communities' capacity to manage their resources under scarcity, anticipate climatic variability, and preserve spiritual traditions associated with the landscape. These practices parallel water sowing and harvesting systems in Ibero-America [168], such as the amunas of Peru and albarradas of Ecuador, which have been instrumental in ensuring water availability for agriculture while maintaining ecosystem health. Both examples highlight how TEK contributes to water governance in fragile and arid ecosystems, offering replicable models for other regions facing water scarcity.

Similarly, in the central part of the country (O'Higgins, Ñuble, Biobío), there are instances of traditional knowledge linked to water management, agricultural production, viticulture, and agroecology. These practices are constantly reconfigured as they interact with contemporary productive pressures—such as agrarian intensification, forest monocultures, and the globalized demands of markets—generating local arrangements that combine ancestral knowledge with technical innovations. This dynamic is echoed in agroforestry practices in northern Ghana [169], where small-scale farmers integrate TEK with soil fertility management to enhance productivity and resilience under changing climatic conditions. Such parallels reinforce the universality of TEK in sustaining agricultural systems while addressing global climate challenges.

In the south, TEK is expressed in the memory of traditional trades, associativity, agroecology, and cooperativism, integrating Indigenous worldviews and technical legacies from European colonization processes. This syncretism is evident in cooperative initiatives that combine innovation, gender equity in traditional spaces, and the strengthening of family peasant agriculture. These efforts align with revitalization initiatives in Alpine Europe [170], where TEK has been successfully integrated into biodiversity conservation and sustainable land use practices, demonstrating the value of co-management frameworks in enhancing socio-ecological resilience.

From a comparative perspective, Chilean dynamics show parallels with experiences in other countries where the co-production of knowledge and inter-epistemic dialogue have proven effective in addressing water crises, food security, and climate uncertainty. For example, in the Indian Himalayas, communities employ TEK to monitor snowmelt and glacial cycles, guiding irrigation and agricultural practices in high-altitude environments. These practices resonate with the Andean TEK in Chile's high-altitude ecosystems, where community-based hydrological knowledge supports adaptive water governance. Similarly, ethnomedical systems in Bolivia and Ecuador emphasize the intersection of biodiversity

conservation and community well-being [171], aligning with Mapuche approaches in Chile that integrate cultural heritage and ecological management.

The relational approach adopted—centered on the interdependencies among communities, ecosystems, technologies, productive practices, and regulations—provides a more comprehensive vision of TEK. It transcends the simple transfer of information, focusing on processes of co-creation of knowledge and territorial governance. This approach is particularly relevant in a context where adaptation to contemporary challenges cannot depend solely on conventional science but must incorporate local understandings of hydrological cycles, biodiversity, and seasonal rhythms. For example, the integration of TEK into governance frameworks in Vanuatu demonstrates how local ecological knowledge can inform disaster risk reduction and resilience-building strategies [172], a principle that has significant potential for replication in Chile and other regions facing climate vulnerabilities [173].

However, structural tensions and power asymmetries among actors highlight limitations and challenges. In this regard, the intensification of forest monocultures, the expansion of agro-industries, and water privatization weaken the socio-ecological base on which TEK depends, generating territorial conflicts and uncertainties about future resource availability. Other factors, such as internal and international migration dynamics, the aging of those who preserve traditional knowledge, the departure of young people to urban centers, and administrative fragmentation among regions, hinder the intergenerational continuity of practices. Moreover, certain traditional methods prove ill-suited to new climatic conditions, requiring their re-evaluation and possible modification without losing their cultural essence.

Addressing this research through an exploratory, multi-sited, and predominantly qualitative methodological strategy has made it possible to capture nuances and complexities impossible to approach solely through quantitative indicators. Participant observations, semi-structured interviews, and interaction with local actors across several territories have revealed how TEK in Chile is not limited to a productive dimension but integrates cultural, spiritual, and affective values, shaping lived territories where daily practices build socio-ecological adaptation. In the future, it will be valuable to advance toward mixed methodological approaches, integrating quantitative analyses, evaluating the long-term impact of TEK incorporation into public policies and climate adaptations, as well as the effectiveness of knowledge co-production in collaborative governance processes.

In this line, there is a need to design policy instruments and institutional spaces that recognize territorial specificities and the legitimacy of TEK, ensuring its articulation with contemporary scientific knowledge. The Chilean experience shows that forming and strengthening knowledge alliances can increase community resilience and environmental justice if appropriate normative frameworks, stable financing, and institutional capacity are consolidated to ensure community participation. Similarly, linking with academia, the public sector, and civil society can foster integrated monitoring and evaluation systems, generating constant feedback and guiding decision-making in changing scenarios.

Each territory presents singularities that are difficult to replicate without contextual adjustments. Likewise, the lack of quantitative indicators hinders the exact measurement of TEK's impact on adaptation. Nevertheless, the qualitative richness and the rigor in data triangulation establish solid conceptual and empirical foundations for future studies. A promising direction is to delve deeper into the role of TEK in polycentric water governance, productive diversification, and the restoration of degraded landscapes, as well as to seek strategies to revitalize ancestral knowledge among younger generations.

In summary, this study shows that TEK, understood from a relational and integrative approach, constitutes a strategic factor for confronting Chile's socio-climatic crisis. Far from being a vestige of the past, TEK emerges as dynamic knowledge, capable of hybridizing

with science, technology, and public policies, providing culturally pertinent and ecologically viable adaptive pathways. The experiences gathered in different territories and other regions worldwide reveal that it is not only about rescuing ancestral knowledge but about understanding it as part of a socio-ecological continuum, where alliances and co-production of knowledge enable paths toward resilience, environmental justice, and the transition to sustainability.

7. Conclusions

This study deepens the understanding of traditional ecological knowledge (TEK) in Chile, positioning it as a dynamic and strategic system that broadens comparative perspectives with other contexts. By interpreting TEK through a relational lens, this research highlights its value as a resource for addressing complex socio-environmental transformations and fostering adaptive strategies across diverse scenarios. Strengthening its integration into institutional frameworks, public policies, and collaborative research projects represents a decisive step toward fostering more just, resilient, and sustainable societies. This aligns with the goals of the scientific community and the urgent demands of a humanity facing rapid global changes, such as those highlighted in the Sustainable Development Goals (SDGs).

The findings highlight those ancestral practices in water management, agroecology, cooperativism, and traditional viticulture, among others, that not only enhance socio-ecological resilience but also promote intercultural dialogue, social cohesion, and sustainability across multiple scales. These TEK expressions provide a robust foundation for co-creating climate change adaptation strategies, employing participatory methodologies, applying inter- and transdisciplinary approaches, and consolidating knowledge alliances that respect and integrate epistemic and cultural diversity. By fostering such alliances, TEK becomes a key driver in the transition to sustainable development pathways, contributing to equitable resource management and biodiversity conservation.

Looking ahead, there is a pressing need to advance mixed methodological approaches that quantitatively evaluate TEK's impact in global change scenarios, thus reinforcing its legitimacy and applicability among decision-makers. Comparative research and longitudinal studies will play a pivotal role in identifying the key factors that enable TEK's adaptability across diverse socio-cultural and ecological contexts, enhancing its scalability and its incorporation as a mainstream environmental policy tool. These efforts will require the promotion of collaborative spaces among communities, academia, and policy-makers, encouraging active participation and knowledge exchange to address the interconnected challenges of the 21st century. By doing so, TEK can contribute significantly to achieving sustainability goals, fostering resilience, and guiding transformative actions in an era of unprecedented global change.

Author Contributions: Conceptualization, P.S.-Á., J.R.H. and R.O.B.; methodology, P.S.-Á.; validation, P.S.-Á., J.R.H. and R.O.B.; formal analysis, P.S.-Á.; investigation, P.S.-Á.; resources, P.S.-Á.; data curation, P.S.-Á.; writing—original draft preparation, P.S.-Á.; writing—review and editing, P.S.-Á. and J.R.H.; visualization, R.O.B.; supervision, J.R.H. and R.O.B.; project administration, P.S.-Á. and J.R.H.; funding acquisition, J.R.H. and R.O.B. All authors have read and agreed to the published version of the manuscript.

Funding: This research was funded by the National Doctoral Scholarship, grant number 21211340, provided by the National Agency for Research and Development. Also, this research received support of the Water Resources Center for Agriculture and Mining (CRHIAM) ANID/FONDAP/15130015-ANID/FONDAP/1523A0001.

Institutional Review Board Statement: The study was carried out in accordance with the Declaration of Helsinki and under the regulations approved by the Ethics, Bioethics and Biosafety Committee of the University of Concepción in decree No. 2017-083 of 19 June 2017.

Informed Consent Statement: Informed consent was obtained from all subjects involved in this study.

Data Availability Statement: The data that support the results of this study are available on request from the corresponding author, P.S. The data are not publicly available due to ethical considerations and to protect the privacy of those who participated.

Acknowledgments: Special thanks to communities, organizations, and institutions that collaborated in the development of this research.

Conflicts of Interest: The authors declare no conflicts of interest.

References

1. Meyer, R. Uncertainty as a science policy problem. *Clim. Change* **2012**, *110*, 1–2. [CrossRef]
2. Workman, M.; Dooley, K.; Lomax, G.; Maltby, J.; Darch, G. Decision making in contexts of deep uncertainty—An alternative approach for long-term climate policy. *Environ. Sci. Policy* **2019**, *103*, 77–84. [CrossRef]
3. Nakashima, D.J.; McLean, K.G.; Thulstrup, H.D.; Castillo, A.R.; Rubis, J.T. *Weathering Uncertainty: Traditional Knowledge for Climate Change Assessment and Adaptation*; UNESCO: Paris, France, 2012.
4. IPCC. *Global Warming of 1.5 °C. Summary for Policymakers*; Reporte Especial del Panel Intergubernamental del Cambio Climático; IPCC: Geneva, Switzerland, 2018.
5. Kassam, K. Transdisciplinary research, Indigenous knowledge, and wicked problems. *Rangelands* **2021**, *43*, 133–141. [CrossRef]
6. Raymond, C.M.; Fazey, I.; Reed, M.S.; Stringer, L.C.; Robinson, G.M.; Evely, A.C. Integrating local and scientific knowledge for environmental management. *J. Environ. Manag.* **2010**, *91*, 1766–1777. [CrossRef] [PubMed]
7. Alexander, C.; Bynum, N.; Johnson, E.; King, U.; Mustonen, T.; Neofotis, P.; Oettlé, N.; Rosenzweig, C.; Sakakibara, C.; Shadrin, V.; et al. Linking Indigenous and Scientific Knowledge of Climate Change. *BioScience* **2011**, *61*, 477–484. [CrossRef]
8. Berkes, F. *Sacred Ecology*, 3rd ed.; Routledge: New York, NY, USA, 2012.
9. Berkes, F.; Colding, J.; Folke, C. Rediscovery of Traditional Ecological Knowledge as Adaptive Management. *Ecol. Appl.* **2000**, *10*, 1251–1262. [CrossRef]
10. Gómez-Baggethun, E.; Reyes-García, V. Reinterpreting change in traditional ecological knowledge. *Hum. Ecol.* **2013**, *41*, 643–647. [CrossRef]
11. Gwandure, C.; Lukhele-Olorunju, P. Women's use of indigenous knowledge in Africa. *Soc. Sci. Humanit. Open* **2023**, *8*, 100741. [CrossRef]
12. Hosen, N.; Nakamura, H.; Hamzah, A. Adaptation to Climate Change: Does Traditional Ecological Knowledge Hold the Key? *Sustainability* **2020**, *12*, 676. [CrossRef]
13. Lemi, T. The role of traditional ecological knowledge (TEK) for climate change adaptation. *Int. J. Environ. Sci. Nat. Resour.* **2019**, *18*, 28–31. [CrossRef]
14. Olazabal, M.; Chu, E.; Broto, V.C.; Patterson, J. Subaltern forms of knowledge are required to boost local adaptation. *One Earth* **2021**, *4*, 828–838. [CrossRef]
15. Wibeck, V.; Eliasson, K.; Neset, T. Co-creation research for transformative times: Facilitating foresight capacity in view of global sustainability challenges. *Environ. Sci. Policy* **2021**, *128*, 290–298. [CrossRef]
16. Kumar, V. Role of Indigenous Knowledge in Climate Change Adaptation Strategies: A Study with Special Reference to North-Western India. *J. Geogr. Nat. Disasters* **2015**, *5*. [CrossRef]
17. Novalia, W.; Malekpour, S. Theorising the role of crisis for transformative adaptation. *Environ. Sci. Policy* **2020**, *112*, 361–370. [CrossRef]
18. Šūmane, S.; Kunda, I.; Knickel, K.; Strauss, A.; Tisenkopfs, T.; Rios, I.D.I.; Rivera, M.; Chebach, T.; Ashkenazy, A. Local and farmers' knowledge matters! How integrating informal and formal knowledge enhances sustainable and resilient agriculture. *J. Rural Stud.* **2017**, *59*, 232–241. [CrossRef]
19. Altieri, M.A. Agroecología: Principios y estrategias para diseñar sistemas agrícolas sostenibles. *Agroecol. Y Desarro. Rural Sustentable* **2011**, *1*, 25–37.
20. Altieri, M.A.; Toledo, V.M. The agroecological revolution in Latin America: Rescuing nature, ensuring food sovereignty and empowering peasants. *J. Peasant Stud.* **2011**, *38*, 587–612. [CrossRef]
21. Altieri, M.A.; Nicholls, C.I. Agroecology and the reconstruction of a post-COVID-19 agriculture. *J. Peasant Stud.* **2020**, *47*, 881–898. [CrossRef]

22. Ludwig, D.; Poliseli, L. Relating traditional and academic ecological knowledge: Mechanistic and holistic epistemologies across cultures. *Biol. Philos.* **2018**, 33. [CrossRef]
23. Pohl, C.; Klein, J.T.; Hoffmann, S.; Mitchell, C.; Fam, D. Conceptualising transdisciplinary integration as a multidimensional interactive process. *Environ. Sci. Policy* **2021**, *118*, 18–26. [CrossRef]
24. Arnott, J.C.; Neuenfeldt, R.J.; Lemos, M.C. Co-producing science for sustainability: Can funding change knowledge use? *Glob. Environ. Change* **2019**, *60*, 101979. [CrossRef]
25. Foggin, J.M.; Brombal, D.; Razmkhah, A. Thinking Like a Mountain: Exploring the Potential of Relational Approaches for Transformative Nature Conservation. *Sustainability* **2021**, *13*, 12884. [CrossRef]
26. Whyte, K.P. On the role of traditional ecological knowledge as a collaborative concept: A philosophical study. *Ecol. Process.* **2013**, *2*, 7. [CrossRef]
27. Reyes-García, V.; Guèze, M.; Luz, A.C.; Paneque-Gálvez, J.; Macía, M.J.; Orta-Martínez, M.; Pino, J.; Rubio-Campillo, X. Evidence of traditional knowledge loss among a contemporary indigenous society. *Evol. Hum. Behav.* **2013**, *34*, 249–257. [CrossRef]
28. Albuquerque, U.; Cantalice, A.; Oliveira, D.; Oliveira, E.S.; Santos, E.B.d.; Santos, F.I.R.d.; Soldati, G.T.; Lima, I.d.S.; Silva, J.V.M.; Abreu, M.B.; et al. ¿Por qué se mantiene el conocimiento ecológico tradicional (CTE)? Una respuesta a Hartel et al. *Biodivers. Conserv.* **2024**, *33*, 859–866. [CrossRef]
29. Hill, R.; Adem, Ç.; Alangui, W.V.; Molnár, Z.; Aumeeruddy-Thomas, Y.; Bridgewater, P.; Tengo, M.; Thaman, R.; Yao, C.Y.A.; Berkes, F.; et al. Working with indigenous, local and scientific knowledge in assessments of nature and nature's linkages with people. *Curr. Opin. Environ. Sustain.* **2020**, *43*, 8–20.
30. Singh, R.K.; Singh, A.; Sheoran, P.; Sharma, D.K.; Sharma, P.C. 'Mera Gaon, Mera Gaurav' policy: A source of hypothesis for the co-production of adaptive agricultural knowledge. *Indian J. Agric. Sci.* **2019**, *89*, 1410–1414. [CrossRef]
31. Biró, M.; Molnár, Z.; Babai, D.; Dénes, A.; Fehér, A.; Barta, S.; Sáfián, L.; Szabados, K.; Kiš, A.; Demeter, L.; et al. Reviewing historical traditional knowledge for innovative conservation management: A re-evaluation of wetland grazing. *Sci. Total Environ.* **2019**, *666*, 1114–1125. [CrossRef]
32. Berkes, F.; Berkes, M.K. Ecological complexity, fuzzy logic, and holism in indigenous knowledge. *Futures* **2009**, *41*, 6–12. [CrossRef]
33. Acosta, A.; Vivir, E.B. *Sumak Kawsay, Una Oportunidad Para Imaginar Otros Mundos*; Editorial Icaria: Barcelona, Spain, 2013.
34. Abasolo, V. Revalorización de los saberes tradicionales campesinos relacionados con el manejo de tierras agrícolas. *Rev. De Cienc. Soc. De La Univ. Iberoam.* **2011**, *6*, 98–120.
35. Rai, S.; Mishra, P. Conocimiento ecológico tradicional y gestión de recursos: Un marco conceptual. In *Conocimiento Ecológico Tradicional de la Gestión de Recursos en Asia*; Rai, S.C., Mishra, P.K., Eds.; Springer: Cham, Switzerland, 2022. [CrossRef]
36. Malapane, O.L.; Chanza, N.; Musakwa, W. Transmission of indigenous knowledge systems under changing landscapes within the vhavenda community, South Africa. *Environ. Sci. Policy* **2024**, *161*, 103861. [CrossRef]
37. Cacho, M.M.Y.T.G.; Giraldo, O.F.; Aldasoro, M.; Morales, H.; Ferguson, B.G.; Rosset, P.; Khadse, A.; Campos, C. Bringing agroecology to scale: Key drivers and emblematic cases. *Agroecol. Sustain. Food Syst.* **2018**, *42*, 637–665. [CrossRef]
38. Zhang, X.; Khachatryan, H.; Knuth, M. Relating Knowledge and Perception of Sustainable Landscape Practices to the Adoption Intention of Environmentally Friendly Landscapes. *Sustainability* **2021**, *13*, 14070. [CrossRef]
39. Jamil, A.; Zubair, M.; Manzoor, S.A. A Herder's eye view: Traditional ecological knowledge based indicators for monitoring rangeland conditions in Thal, Pakistan. *Environ. Dev.* **2022**, *42*, 100699. [CrossRef]
40. Audefroy, J.F.; Sánchez, B.N.C. Integrating local Knowledge for Climate Change Adaptation in Yucatán, Mexico. *Int. J. Sustain. Built Environ.* **2017**, *6*, 228–237. [CrossRef]
41. Gudynas, E. Extractivismos y corrupción en América del Sur. Estructuras, dinámicas y tendencias en una íntima relación. *RevIISE* **2017**, *10*, 73–87.
42. Williams, P.A.; Sikutshwa, L.; Shackleton, S. Acknowledging Indigenous and Local Knowledge to Facilitate Collaboration in Landscape Approaches—Lessons from a Systematic Review. *Land* **2020**, *9*, 331. [CrossRef]
43. Nadasdy, P. The Politics of Tek: Power and the "Integration" of Knowledge. *Arct. Anthropol.* **1999**, *36*, 1–18. Available online: http://www.jstor.org/stable/40316502 (accessed on 7 October 2024).
44. Huntington, H. Using Traditional Ecological Knowledge in Science: Methods and Applications. *Ecol. Appl.* **2000**, *10*, 1270–1274.
45. Mistry, J.; Berardi, A. Bridging indigenous and scientific knowledge. *Science* **2016**, *352*, 1274–1275. [CrossRef]
46. McCarter, J.; Gavin, M.C.; Baereleo, S.; Love, M. The challenges of maintaining indigenous ecological knowledge. *Ecol. Soc.* **2014**, *19*, 39. [CrossRef]
47. Hackfort, S.; Burchardt, H. Analyzing socio-ecological transformations—A relational approach to gender and climate adaptation. *Crit. Policy Stud.* **2016**, *12*, 169–186. [CrossRef]
48. Klenk, N.; Meehan, K. Climate change and transdisciplinary science: Problematizing the integration imperative. *Environ. Sci. Policy* **2015**, *54*, 160–167. [CrossRef]
49. Pormon, M.M.M.; Lejano, R.P. Relational epistemologies for sustainability and resilience towards disasters. *Prog. Disaster Sci.* **2022**, *17*, 100272. [CrossRef]

50. West, S.; Haider, L.J.; Stålhammar, S.; Woroniecki, S. A relational turn for sustainability science? Relational thinking, leverage points and transformations. *Ecosyst. People* **2020**, *16*, 304–325. [CrossRef]
51. O'Brien, K.; Carmona, R.; Gram-Hanssen, I.; Hochachka, G.; Sygna, L.; Rosenberg, M. Fractal approaches to scaling transformations to sustainability. *AMBIO* **2023**, *52*, 1448–1461. [CrossRef]
52. Shein, P.P.; Sukinarhimi, P. Taboos as a Social Mechanism Keeping the Human-Nature Balance: Core Values and Practices of Rukai Traditional Ecological Knowledge of Water. *Sustainability* **2022**, *14*, 2032. [CrossRef]
53. Menatti, L.; Bich, L.; Saborido, C. Health and environment from adaptation to adaptivity: A situated relational account. *Hist. Philos. Life Sci.* **2022**, *44*, 38. [CrossRef]
54. Siders, A. Adaptive capacity to climate change: A synthesis of concepts, methods, and findings in a fragmented field. *Wiley Interdiscip. Rev. Clim. Change* **2019**, *10*, e573. [CrossRef]
55. Pelling, M. *Adaptation to Climate Change: From Resilience to Transformation*; Routledge: London, UK, 2011.
56. Armitage, D.; Berkes, F.; Doubleday, N. (Eds.) *Adaptive Co-Management: Collaboration, Learning, and Multi-Level Governance*; UBC Press: Vancouver, BC, Canada, 2007.
57. Djenontin, I.N.S.; Meadow, A.M. The art of co-production of knowledge in environmental sciences and management: Lessons from international practice. *Environ. Manag.* **2018**, *61*, 885–903. [CrossRef]
58. Boiral, O.; Heras-Saizarbitoria, I.; Brotherton, M. Improving environmental management through indigenous peoples' involvement. *Environ. Sci. Policy* **2019**, *103*, 10–20. [CrossRef]
59. Bouzarovski, S. Just Transitions: A Political Ecology critique. *Antipode* **2022**, *54*, 1003–1020. [CrossRef]
60. DeLonge, M.S.; Miles, A.; Carlisle, L. Investing in the transition to sustainable agriculture. *Environ. Sci. Policy* **2016**, *55*, 266–273. [CrossRef]
61. Akinnagbe, O.M.; Iroh, I.J. Agricultural adaptation strategies to climate change impacts in Africa: A review. *Bangladesh J. Agric. Res.* **2014**, *39*, 407–418.
62. Harisha, R.P. Traditional Ecological Knowledge (TEK) and its importance in South India: Perspective from local communities. *Appl. Ecol. Environ. Res.* **2016**, *14*, 311–326. [CrossRef]
63. Saylor, C.R.; Alsharif, K.A.; Torres, H. The importance of traditional ecological knowledge in agroecological systems in Peru. *Int. J. Biodivers. Sci. Ecosyst. Serv. Manag.* **2017**, *13*, 150–161. [CrossRef]
64. Flores, J.C.G.; Cedillo, J.G.G.; Plata, M.Á.B.; Pérez, J.I.J. Análisis del conocimiento ecológico tradicional y factores socioculturales sobre huertos familiares en el Altiplano Central Mexicano. *Cuadernos Geogr.* **2019**, *58*, 260–281. [CrossRef]
65. Keats, B.; Evans, P. Traditional knowledge and resource management in the northwest territories, Canada: Definitions, disciplinary divides, and reasons for decisions. *Extr. Ind. Soc.* **2020**, *7*, 1309–1318. [CrossRef]
66. Moser, S.C. Can science on transformation transform science? Lessons from co-design. *Curr. Opin. Environ. Sustain.* **2016**, *20*, 106–115. [CrossRef]
67. Gram-Hanssen, I.; Schafenacker, N.; Bentz, J. Decolonizing transformations through 'right relations'. *Sustain. Sci.* **2021**, *17*, 673–685. [CrossRef]
68. Leonardsson, H.; Kronsell, A.; Andersson, E.; Burman, A.; Blanes, R.; Da Costa, K.; Hasselskog, M.; Stepanova, O.; Öjendal, J. Achieving peaceful climate change adaptation through transformative governance. *World Dev.* **2021**, *147*, 105656. [CrossRef]
69. Puri, N. Integrating Scientific with Indigenous Knowledge: Constructing Knowledge Alliances for Land Management in India. *MIS Q.* **2007**, *31*, 355. [CrossRef]
70. Aswani, S.; Lemahieu, A.; Sauer, W.H.H. Global trends of local ecological knowledge and future implications. *PLoS ONE* **2018**, *13*, e0195440. [CrossRef]
71. Kuhlicke, C.; De Brito, M.M.; Bartkowski, B.; Botzen, W.; Doğulu, C.; Han, S.; Hudson, P.; Karanci, A.N.; Klassert, C.J.; Otto, D.; et al. Spinning in circles? A systematic review on the role of theory in social vulnerability, resilience and adaptation research. *Glob. Environ. Change* **2023**, *80*, 102672. [CrossRef]
72. Mauser, W.; Klepper, G.; Rice, M.; Schmalzbauer, B.S.; Hackmann, H.; Leemans, R.; Moore, H. Transdisciplinary global change research: The co-creation of knowledge for sustainability. *Curr. Opin. Environ. Sustain.* **2013**, *5*, 420–431. [CrossRef]
73. Berke, P.R.; Quiring, S.M.; Olivera, F.; Horney, J.A. Addressing Challenges to Building Resilience Through Interdisciplinary Research and Engagement. *Risk Anal.* **2018**, *41*, 1248–1253. [CrossRef]
74. Smetschka, B.; Gaube, V. Co-creating formalized models: Participatory modelling as method and process in transdisciplinary research and its impact potentials. *Environ. Sci. Policy* **2019**, *103*, 41–49. [CrossRef]
75. Birchall, S.J.; MacDonald, S.; Slater, T. Anticipatory planning: Finding balance in climate change adaptation governance. *Urban Clim.* **2021**, *37*, 100859. [CrossRef]
76. Bollier, D. *Pensar Desde Los Comunes*; Sursiendo, de Sueños, T., Limón, T., Eds.; Cornucopia y Guerrilla Translation: Amherst, MA, USA, 2016; ISBN 978-84-945978-1-7.
77. Boon, W.P.C.; Hessels, L.K.; Horlings, E. Knowledge co-production in protective spaces: Case studies of two climate adaptation projects. *Reg. Environ. Change* **2019**, *19*, 1935–1947. [CrossRef]

78. Turnhout, E.; Metze, T.; Wyborn, C.; Klenk, N.; Louder, E. The politics of co-production: Participation, power, and transformation. *Curr. Opin. Environ. Sustain.* **2019**, *42*, 15–21. [CrossRef]
79. Posner, E.; Weisbach, D. *Climate Change Justice*; Princeton University Press: Princeton, NJ, USA, 2010.
80. Darbellay, F. Rethinking inter- and transdisciplinarity: Undisciplined knowledge and the emergence of a new thought style. *Futures* **2014**, *65*, 163–174. [CrossRef]
81. Arnott, J.C.; Mach, K.J.; Wong-Parodi, G. Editorial overview: The science of actionable knowledge. *Curr. Opin. Environ. Sustain.* **2020**, *42*, A1–A5. [CrossRef]
82. Grandia, L. Slow ethnography: A hut with a view. *Crit. Anthropol.* **2015**, *35*, 301–317. [CrossRef]
83. Morin, E. *La Mente Bien Ordenada. Repensar la Reforma. Reformar el Pensamiento*; Seix Barral: Barcelona, Spain, 2001.
84. Stock, P.V.; Forney, J. Farmer autonomy and the farming self. *J. Rural Stud.* **2014**, *36*, 160–171. [CrossRef]
85. Ludwig, D.; Macnaghten, P. Traditional ecological knowledge in innovation governance: A framework for responsible and just innovation. *J. Responsible Innov.* **2019**, *7*, 26–44. [CrossRef]
86. Fernández-Llamazares, Á.; Díaz-Reviriego, I.; Luz, A.C.; Cabeza, M.; Pyhälä, A.; Reyes-García, V. Rapid ecosystem change challenges the adaptive capacity of Local Environmental Knowledge. *Glob. Environ. Change* **2015**, *31*, 272–284. [CrossRef]
87. Jimenez, A.; Delgado, D.; Merino, R.; Argumedo, A. A Decolonial Approach to Innovation? Building Paths Towards Buen Vivir. *J. Dev. Stud.* **2022**, *58*, 1633–1650. [CrossRef]
88. Sarricolea, P.; Herrera-Ossandon, M.; Meseguer-Ruiz, Ó. Climatic regionalisation of continental Chile. *J. Maps* **2016**, *13*, 66–73. [CrossRef]
89. Guerrero-Gatica, M.; Mujica, M.I.; Barceló, M.; Vio-Garay, M.F.; Gelcich, S.; Armesto, J.J. Traditional and Local Knowledge in Chile: Review of Experiences and Insights for Management and Sustainability. *Sustainability* **2020**, *12*, 1767. [CrossRef]
90. Barreau, A.; Ibarra, J.T.; Wyndham, F.S.; Rojas, A.; Kozak, R.A. How Can We Teach Our Children if We Cannot Access the Forest? Generational Change in Mapuche Knowledge of Wild Edible Plants in Andean Temperate Ecosystems of Chile. *J. Ethnobiol.* **2016**, *36*, 412–432. [CrossRef]
91. Cortez, H.G.; Kröll, H.G. La propiedad de la tierra entre los Aymara del altiplano chileno, 1880–2020. *Rev. De Geogr. Norte Gd.* **2022**, *83*, 67–86. [CrossRef]
92. Canales, M.; Hernández, M.C. Del fundo al mundo. Cachapoal, un caso de globalización agropolitana. *Espac. Abierto* **2011**, *20*, 579–605.
93. Larenas, J.; Sahady, A.; Bravo, M.; Quilodrán, C.; Fuster, X. Las ruedas de Larmahue: Una manifestación de construcción de territorio y paisaje agrario. *Rev. INVI* **2014**, *29*, 189–216. [CrossRef]
94. Salazar, P.A. Fiestas costumbristas en la Región del Libertador General Bernardo O'Higgins, Chile: Tradiciones, gastronomía y religiosidad en el centro de la fiesta. *Rev. RIVAR* **2020**, *8*, 179–197. [CrossRef]
95. Sahady, A.; Bravo, J.; Quilodrán, C. Azudas de Larmahue: Al rescate del recurso hídrico en medio de un terreno secano, en pleno valle del Cachapoal, Sexta Región. *AUS* **2012**, *12*, 18–21. [CrossRef]
96. Bravo Sánchez, J.M.; Sahady Villanueva, A.; Quilodrán Rubio, C. *Azudas en Chile: Un Vernáculo Sistema de Riego en Tierras de Secano*; Papeles de Geografía; Universidad de Murcia: Murcia, Spain, 2013.
97. Alar, M.L. Vino del Desierto. Una oportunidad para recuperar una tradición de la agricultura del desierto. *Idesia* **2019**, *37*, 3–4. [CrossRef]
98. Rojas, C.D. Modernización y Conflicto Social. La Expropiación de las Aguas de Regadío a los Campesinos del Valle de Quisma (Oasis de Pica) y el Abastecimiento Fiscal a Iquique, 1880–1937. *Chungara* **2012**, *44*, 195–196. [CrossRef]
99. Meza, M.; Pereira, K.; Jofré, J. Saberes y estrategias de adaptación a la disponibilidad hídrica en las yungas secas del norte de Chile. *Rev. De Geogr. Norte Gd.* **2020**, *76*, 255–277. [CrossRef]
100. Meseguer-Ruiz, Ó.; Prieto, M.; Carimán, K.V.G. Conocimiento ecológico tradicional en el Altiplano chileno: Entre la variabilidad climática y la percepción local. *Rev. De Geogr. Norte Gd.* **2022**, *83*, 107–123. [CrossRef]
101. Becerra, P.; Sepúlveda, P. Water crisis in Chile: Hydrological governance and the role of indigenous knowledge. *Water Int.* **2021**, *46*, 696–711.
102. Carrasco-Escaff, T.; Garreaud, R.; Bozkurt, D.; Jacques-Coper, M.; Pauchard, A. The key role of extreme weather and climate change in the occurrence of exceptional fire seasons in south-central Chile. *Weather Clim. Extrem.* **2024**, *45*, 100716. [CrossRef]
103. Peterson, V.A.; Castillo, E.J.; Reyes, L.A. Fires in central-southern Chile's (sustainable) green suburbs. *Resour. Environ. Sustain.* **2023**, *13*, 100123. [CrossRef]
104. Cortina, M.; Madeira, C. Exposures to climate change's physical risks in Chile. *Lat. Am. J. Cent. Bank.* **2023**, *4*, 100090. [CrossRef]
105. Centro de Ciencia del Clima y la Resiliencia CR2. El Antropoceno en Chile: Evidencias y Formas de Avanzar. 2019. Available online: http://www.cr2.cl/wp-content/uploads/2019/03/Informe-Antropoceno-castellano-2.pdf (accessed on 28 November 2024).
106. Garreaud, R.D.; Boisier, J.P.; Rondanelli, R.; Montecinos, A.; Sepúlveda, H.H.; Veloso-Aguila, D. The Central Chile Mega Drought (2010–2018): A climate dynamics perspective. *Int. J. Climatol.* **2020**, *40*, 421–439. [CrossRef]

107. Boisier, J.P.; Alvarez-Garreton, C.; Cordero, R.R.; Damiani, A.; Gallardo, L.; Garreaud, R.D.; Lambert, F.; Ramallo, C.; Rojas, M.; Rondanelli, R. Anthropogenic drying in central-southern Chile evidenced by long-term observations and climate model simulations. *Elem. Sci. Anthr.* **2018**, *6*, 74. [CrossRef]
108. Cámara-Leret, R.; Bascompte, J. Language extinction triggers the loss of unique medicinal knowledge. *Proc. Natl. Acad. Sci. USA* **2021**, *118*, e2103683118. [CrossRef]
109. Robles, C. The agrarian historiography of Chile: Foundational interpretations, conventional reiterations, and critical revisionism. *Historia Agraria Revista de Agricultura e Historia Rural*, 1 August 2020; pp. 93–122. [CrossRef]
110. Panez-Pinto, A.; Faúndez-Vergara, R.; Mansilla-Quiñones, C. Politización de la crisis hídrica en Chile: Análisis del conflicto por el agua en la provincia de Petorca. *Agua Y Territ./Water Landsc.* **2017**, *10*, 131. [CrossRef]
111. Rodrigo, L.M.; Mateo-Peinado, L. Internal migration and economic mobility in Chile. *Reg. Stud.* **2023**, *58*, 1377–1389. [CrossRef]
112. Rueda-Salazar, S.; García, J. The public health challenges of female migration: The Venezuelan diaspora in Andean countries. *Int. J. Equity Health* **2024**, *23*, 210. [CrossRef]
113. Rojas, J.; Silva Ávila, P.; Barra, R.; Figueroa, R.; Arumi, J.L.; Hansen-Rojas, G. *Bienes Comunes y Diversidad Biocultural en Tiempos de Crisis: Escasez Hídrica, Pandemia y Cambio Climático*; CRHIAM (ANID/FONDAP 15130015), Universidad de Concepción; RIL Editores: Santiago, Chile, 2021; ISBN 978-84-18982-17-0.
114. Pettenger, M.E. (Ed.) *The Social Construction of Climate Change: Power, Knowledge, Norms, Discources*; Routledge: London, UK, 2007.
115. Cologna, V.; Kotcher, J.; Mede, N.G.; Besley, J.; Maibach, E.W.; Oreskes, N. Trust in climate science and climate scientists: A narrative review. *PLoS Clim.* **2024**, *3*, e0000400. [CrossRef]
116. Melo, O.; Báez, N.; Acuña, D. Towards Sustainable Agriculture in Chile, Reflections on the Role of Public Policy. *Int. J. Agric. Nat. Resour.* **2021**, *48*, 186–209. [CrossRef]
117. Ocampo-Melgar, A.; Urquiza, A. *Estudio de la Gestión Adaptativa en Chile: Descubriendo Elementos Para la Resiliencia*; Universidad de Chile: Santiago, Chile, 2024. [CrossRef]
118. Uiterkamp, A.J.M.S.; Vlek, C. Practice and Outcomes of Multidisciplinary Research for Environmental Sustainability. *J. Soc. Issues* **2007**, *63*, 175–197. [CrossRef]
119. Parsons, M.; Fisher, K.; Nalau, J. Alternative approaches to co-design: Insights from indigenous/academic research collaborations. *Curr. Opin. Environ. Sustain.* **2016**, *20*, 99–105. [CrossRef]
120. Marcus, G.E. Ethnography in/of the World System: The Emergence of Multi-Sited Ethnography. In *Ethnography Through Thick and Thin*; Marcus, G.E., Ed.; Princeton University Press: New Jersey, NY, USA, 1995; pp. 79–104.
121. Hage, G. A not so multi-sited ethnography of a not so imagined community. *Anthropol. Theory* **2005**, *5*, 463–475.
122. Lützhöft, M.; Nyce, J.M.; Petersen, S. Epistemology in ethnography: Assessing the quality of knowledge in human factors research. *Theor. Issues Ergon. Sci.* **2010**, *11*, 532–545. [CrossRef]
123. Shah, A. Ethnography? *Hau J. Ethnogr. Theory* **2017**, *7*, 45–59. [CrossRef]
124. Uldam, J.; McCurdy, P. Studying Social Movements: Challenges and Opportunities for Participant Observation. *Sociol. Compass* **2013**, *7*, 941–951. [CrossRef]
125. Dawson, N.; Coolsaet, B.; Sterling, E.; Loveridge, R.; Gross-Camp, N.; Wongbusarakum, S.; Sangha, K.; Scherl, L.; Phuong Phan, H.; Zafra-Calvo, N.; et al. El papel de los pueblos indígenas y las comunidades locales en la conservación eficaz y equitativa. *Ecol. Soc.* **2021**, *26*, 19. [CrossRef]
126. Dominique, M.; Chavez, D.; Gavin, M. Una evaluación global de la participación de las comunidades indígenas en la investigación climática. *Environ. Res. Lett.* **2018**, *13*, 123005. [CrossRef]
127. Qureshi, H.A.; Ünlü, Z. Beyond the Paradigm Conflicts: A Four-Step Coding Instrument for Grounded Theory. *Int. J. Qual. Methods* **2020**, *19*, 1–10. [CrossRef]
128. Keahey, J. Sustainable Development and Participatory Action Research: A Systematic Review. *Syst. Pract. Action Res.* **2021**, *34*, 291–306. [CrossRef]
129. Verwoerd, L.; Klaassen, P.; Van Veen, S.; De Wildt-Liesveld, R.; Regeer, B. Combining the roles of evaluator and facilitator: Assessing societal impacts of transdisciplinary research while building capacities to improve its quality. *Environ. Sci. Policy* **2019**, *103*, 32–40. [CrossRef]
130. García-Nieto, A.P.; Quintas-Soriano, C.; García-Llorente, M.; Palomo, I.; Montes, C.; Martín-López, B. Collaborative mapping of ecosystem services: The role of stakeholders' profiles. *Ecosyst. Serv.* **2015**, *13*, 141–152. [CrossRef]
131. Jerolmack, C.; Khan, S. Talk Is Cheap: Ethnography and the Attitudinal Fallacy. *Sociol. Methods Res.* **2014**, *43*, 178–209.
132. Rodela, R. The social learning discourse: Trends, themes and interdisciplinary influences in current research. *Environ. Sci. Policy* **2012**, *25*, 157–166. [CrossRef]
133. Scoones, I.; Stirling, A.; Abrol, D.; Atela, J.; Charli-Joseph, L.; Eakin, H.; Ely, A.; Olsson, P.; Pereira, L.; Priya, R.; et al. Transformations to sustainability: Combining structural, systemic and enabling approaches. *Curr. Opin. Environ. Sustain.* **2020**, *42*, 65–75. [CrossRef]

134. Davis, A.; Ruddle, K. Construyendo confianza: Escepticismo racional e investigación sistemática en la investigación del conocimiento ecológico local. *Ecol. Appl.* **2010**, *20*, 880–894. [CrossRef]
135. King, N.; Horrocks, C. *Interviews in Qualitative Research*; Sage: London, UK, 2010.
136. Kvale, S.; Brinkmann, S. *Interviews: Learning the Craft of Qualitative Research Interviewing*; Sage: London, UK, 2009.
137. Cardoso, A.R.; Fernandes, C.; Honrado, J.P. Social-ecological memory: From concepts and methods to applications. *Geogr. Res.* **2024**, 1–20, Early View. [CrossRef]
138. Glaser, B.; Strauss, A. *The Discovery of Grounded Theory*; Aldine Publishing Company: Hawthorne, NY, USA, 1967.
139. Olson, J.; McAllister, C.; Grinnell, L.; Walters, K.G.; Appunn, F. Applying Constant Comparative Method with Multiple Investigators and Inter-Coder Reliability. *Qual. Rep.* **2016**. [CrossRef]
140. Deterding, N.M.; Waters, M.C. Flexible Coding of In-depth Interviews: A Twenty-first-century Approach. *Sociol. Methods Res.* **2018**, *50*, 708–739. [CrossRef]
141. Chatfield, S.L. Recommendations for Secondary Analysis of Qualitative Data. *Qual. Rep.* **2020**, *25*, 833–842. [CrossRef]
142. Perez-Sindin Lopez, X. Secondary Data: Advantages and disadvantages. In *The SAGE Encyclopedia of Communication Research Methods*; Allen, M., Ed.; SAGE: Thousand Oaks, CA, USA, 2017; pp. 1578–1579.
143. Strauss, A.; Corbin, J. *Basics of Qualitative Research: Grounded Theory Procedures and Techniques*; Sage: Newbury Park, CA, USA, 2008.
144. Qureshi, H.A. Rethinking sampling in grounded theory: Reflections for novice grounded theorists. *Int. J. Contemp. Res. Rev.* **2018**, *9*, 20187–20194. [CrossRef]
145. Allen, N.; Davey, M. The Value of Constructivist Grounded Theory for Built Environment Researchers. *J. Plan. Educ. Res.* **2017**, *38*, 222–232. [CrossRef]
146. Walker, D.; Myrick, F. Grounded theory: An exploration of process and procedure. *Qual. Health Res.* **2006**, *16*, 547–559. [CrossRef]
147. Timmermans, S.; Tavory, I. Theory Construction in Qualitative Research: From Grounded Theory to Abductive Analysis. *Sociol. Theory* **2012**, *30*, 167–186.
148. Charmaz, K.; Thornberg, R. The pursuit of quality in grounded theory. *Qual. Res. Psychol.* **2020**, *18*, 305–327. [CrossRef]
149. Lacey, J.; Howden, S.M.; Cvitanovic, C.; Dowd, A. Informed adaptation: Ethical considerations for adaptation researchers and decision-makers. *Glob. Environ. Change* **2015**, *32*, 200–210. [CrossRef]
150. Arnold, D.G. (Ed.) *The Ethics of Global Climate Change*; Cambridge University Press: Cambridge, UK, 2011.
151. Grünewal, V.; Figueroa, R.; Parra, O. Recursos hídricos asociados a la actividad minera en territorio Aymara. In *Gobernanza del agua en Latinoamérica y Europa: Actores Sociales, Conflictos y Territorialidad*; Jacobi, P., Almeida, P., Eds.; Editorial Annablume: São Paulo, Brasil, 2009; p. 225.
152. Díaz, M.E.; Figueroa, R.; Vidal-Abarca, M.R.; Suárez, M.L. Exploring the complex relations between water resources and social indicators: The Biobío basin (Chile). *Ecosyst. Serv.* **2018**, *31*, 84–92.
153. Jebari, S.; Berndtsson, R.; Bahri, A. Challenges of Traditional Rainwater Harvesting Systems in Tunisia. *Middle East Crit.* **2015**, *24*, 289–306. [CrossRef]
154. Huasasquiche, J.; Kómetter, R. El aporte de los saberes comunales andinos en la utilización de los bienes y servicios ecosistémicos. *Ser. Bosques Andin.* **2017**, *27*. Available online: https://www.cooperacionsuiza.pe/30-de-agosto-de-2017/ (accessed on 15 May 2024).
155. Castro, C.L.; Rivera, C.N. La sociedad rural del oasis de Pica frente al proceso chilenizador: Conflictos, interacciones y reacomodos (Tarapacá, norte de Chile 1880–1900). *Estud. Ibero-Am.* **2011**, *37*, 271–300.
156. Wang, N.; Fang, M.; Beauchamp, M.; Jia, Z.; Zhou, Z. An indigenous knowledge-based sustainable landscape for mountain villages: The Jiabang rice terraces of Guizhou, China. *Habitat Int.* **2021**, *111*, 102360. [CrossRef]
157. Mungsunti, A.; Parton, K.A. The Price of Sustainability of a Traditional Irrigation System in Northern Thailand. *Sustainability* **2021**, *13*, 1375. [CrossRef]
158. Bengoa, J. *Historia Social de la Agricultura Chilena. Tomo I: El Poder y la Subordinación*; Ediciones SUR: Santiago, Chile, 1988.
159. Torres, R.; Azócar, G.; Rojas, J.; Montecinos, A.; Paredes, P. Vulnerability and resistance to neoliberal environmental changes: An assessment of agriculture and forestry in the Biobio region of Chile (1974–2014). *Geoforum* **2015**, *60*, 107–122. [CrossRef]
160. Klubock, T. *La Frontera: Forests and Ecological Conflict in Chile's Frontier Territory*; Duke University Press: Durham, NC, USA, 2014.
161. Silva Ávila, P. Prácticas y saberes de gestión comunitaria y productiva del agua bajo contexto de escasez. Experiencias de las regiones del Biobío y Ñuble. In *Seguridad Hídrica: Derechos de Agua, Escasez, Impactos y Percepciones Ciudadanas en Tiempos de Cambio Climático*; Rojas, J., Barra, R., Eds.; RIL Editores: Santiago, Chile, 2020; pp. 127–154.
162. Serra, I.; Calderón-Orellana, A.; Hidalgo, M. Heroic Viticulture in Itata Valley, Chile: Characteristics and Challenges for the Development of Unique Wines in Southern Chilean Vineyards. In *Latin American Viticulture Adaptation to Climate Change*; Gutiérrez Gamboa, G., Fourment, M., Eds.; Springer: Cham, Switzerland, 2024. [CrossRef]
163. Cid-Aguayo, B.E.; Letelier-Araya, E.; Saravia-Ramos, P.; Vanhulst, J. Terroir y Territorio. Casos de la pequeña vitivinicultura en el centro sur de Chile. *Rev. Urbano* **2020**, *23*, 112–123. [CrossRef]

164. Galbreath, J. Exploratory Study of Climate Change Innovations in Wine Regions in Australia. *Reg. Stud.* **2015**, *50*, 1903–1918. [CrossRef]
165. Abate, G.T.; Francesconi, G.N.; Getnet, K. Impact of agricultural cooperatives on smallholders' technical efficiency: Empirical evidence from Ethiopia. *Ann. Public Coop. Econ.* **2014**, *85*, 257–286. [CrossRef]
166. Massera, M.L.; Cuatrín Sperati, E.; Locher, M.V. Cooperativismo agrícola en el contexto de globalización. Un estudio exploratorio en el sur de Francia. *Eutopía. Rev. Desarro. Econ. Territ.* **2020**, *18*, 95–116. [CrossRef]
167. Acevedo-Ortiz, M.A.; Lugo-Espinosa, G.; Ortiz-Hernández, Y.D.; Pérez-Pacheco, R.; Ortiz-Hernández, F.E.; Granados-Echegoyen, C.A. Women's Leadership in Sustainable Agriculture: Preserving Traditional Knowledge Through Home Gardens in Santa Maria Jacatepec, Oaxaca. *Sustainability* **2024**, *16*, 9513. [CrossRef]
168. Martos-Rosillo, S.; Durán, A.; Castro, M.; Vélez, J.J.; Herrera, G.; Martín-Civantos, J.M.; Mateos, L.; Durán, J.J.; Jódar, J.; Gutiérrez, C.; et al. Ancestral Techniques of Water Sowing and Harvesting in Ibero-America: Examples of Hydrogeoethical Systems. In *Advances in Science, Technology & Innovation*; Springer: Cham, Switzerland, 2021; pp. 489–492. [CrossRef]
169. Boafo, Y.A.; Saito, O.; Kato, S.; Kamiyama, C.; Takeuchi, K.; Nakahara, M. The role of traditional ecological knowledge in ecosystem services management: The case of four rural communities in Northern Ghana. *Int. J. Biodivers. Sci. Ecosyst. Serv. Manag.* **2015**, *12*, 24–38. [CrossRef]
170. Ianni, E.; Geneletti, D.; Ciolli, M. Revitalizing Traditional Ecological Knowledge: A Study in an Alpine Rural Community. *Environ. Manag.* **2015**, *56*, 144–156. [CrossRef] [PubMed]
171. Zank, S.; Júnior, W.S.F.; Hanazaki, N.; Kujawska, M.; Ladio, A.H.; Santos, M.L.M.; Blanco, G.D.; Nascimento, A.L.B.D. Local ecological knowledge and resilience of ethnomedical systems in a changing world—South American perspectives. *Environ. Sci. Policy* **2022**, *135*, 117–127. [CrossRef]
172. McCarter, J.; Gavin, M.C. Local Perceptions of Changes in Traditional Ecological Knowledge: A Case Study from Malekula Island, Vanuatu. *AMBIO* **2013**, *43*, 288–296. [CrossRef]
173. Naylor, A.; Ford, J.; Pearce, T.; Van Alstine, J. Conceptualizing Climate Vulnerability in Complex Adaptive Systems. *One Earth* **2020**, *2*, 444–454. [CrossRef]

Disclaimer/Publisher's Note: The statements, opinions and data contained in all publications are solely those of the individual author(s) and contributor(s) and not of MDPI and/or the editor(s). MDPI and/or the editor(s) disclaim responsibility for any injury to people or property resulting from any ideas, methods, instructions or products referred to in the content.

sustainability

MDPI

Article

Compassion Towards Nature and Well-Being: The Role of Climate Change Anxiety and Pro-Environmental Behaviors

Armando Prata * and Marcela Matos

Center for Research in Neuropsychology and Cognitive Behavioral Intervention (CINEICC), Faculty of Psychology and Educational Sciences, University of Coimbra, Rua do Colégio Novo, 3000-115 Coimbra, Portugal; marcela.s.matos@gmail.com

* Correspondence: armando.s.prata@student.fpce.uc.pt

Abstract: The current study examined the structure and psychometric characteristics of the Portuguese version of the Climate Change Anxiety Scale (CAS), exploring the climate change anxiety and environmental action mediator effects on the relationship between connection to nature and well-being, and whether self-compassion and receiving compassion from others would moderate these associations. The sample was composed of 522 participants from the general population who completed a set of self-report measures through an online survey. Exploratory factor analysis results of the CAS extracted four factors, and a confirmatory factor analysis revealed an acceptable fit of this structure to the data ($\chi 2$ (164) = 328.67; $p < 0.001$, CMIN/DF = 2.004; CFI = 0.94; TLI = 0.93; RMSEA = 0.06 [90% CI 0.05–0.07; $p < 0.001$]). The CAS demonstrated good internal consistency ($\alpha = 0.92$) and convergent, concurrent, and divergent validities. Two moderated mediation models showed a significant direct effect of connection to nature on well-being, and self-compassion and compassion from others significantly moderating this relationship. Furthermore, in both models, climate change anxiety and environmental action significantly mediate the association between connection to nature and well-being. Overall, connection with nature seems to enhance well-being in lower and medium levels of self-compassion and from others but may increase climate change anxiety in all compassion levels, reinforcing the importance of promoting nature-based interventions combined with compassion-focused programs to foster well-being.

Keywords: compassion; connection to nature; climate change anxiety; well-being; pro-environmental behaviors

1. Introduction

Currently, climate change issues represent one of the foremost challenges confronting humanity. Media outlets frequently report on severe weather events such as intensified storms, hurricanes, extreme heat, and sea-level rise, attributing them to anthropogenic impacts on the climate [1]. Reports from the Intergovernmental Panel on Climate Change underscore the role of human activities in driving atmospheric, oceanic, and terrestrial warming. Hence, there has been a notable increase in weather and climate extremes, including heatwaves, heavy precipitation, droughts, and tropical cyclones, resulting in widespread damage to ecosystems and posing threats to food and water security [2]. Moreover, there is an elevated risk of epidemics and pandemics due to these climate-related changes [3]. Climate change has also had significant impacts on human physical and mental health. Specifically, extreme climate events have been linked to adverse mental health outcomes, including poor mental health, increased psychiatric hospitalizations,

elevated mortality rates among individuals with mental illness, and heightened suicide rates [4]. This risk is particularly heightened among populations with pre-existing mental illness, low- and middle-income individuals, and those residing in tropical climate zones. Research has demonstrated a positive association between mortality and organic mental disorders, suicides, and self-harm, as well as between morbidity and mood disorders, organic mental disorders, schizophrenia, and anxiety disorders [5]. Furthermore, studies have identified challenges in coping with emotions such as fear, anxiety, worry, guilt, and sadness in the face of climate-related stressors [6]. Thus, direct exposure to extreme events and environmental disasters often leads to profound psychological trauma, characterized by feelings of terror, anger, and shock. This exposure is also linked to elevated rates of various psychopathological conditions, including post-traumatic stress disorder, generalized anxiety disorder, depression, phobias, as well as substance abuse disorders involving alcohol and drugs [7].

1.1. Connection to Nature, Mental Health, and Well-Being

From an evolutionary standpoint, humans have been intimately intertwined with the natural world since time immemorial, evolving within this relationship to adapt and survive. Through the utilization of senses, emotions, and cognition, humanity has adapted to the overarching goals of survival and reproduction. Mental patterns have evolved in ancestral minds, facilitating the achievement of these goals [8] (pp. 49–66). One such example is the intrinsic need for belonging, where ancestral human species recognized that staying together increased chances of survival, particularly during times of scarcity [9]. Attachment theory elucidates this process, highlighting the intrinsic motivation of young children to seek comfort and security from their attachment figures [10]. Additionally, the concept of place attachment underscores the search for places that provide comfort and security [11] (pp. 3–37). Despite nature offering sustenance and shelter, it also presented numerous dangers, threatening human lives. The evolution of higher mental processes, such as planning, anticipation, and imagination, enabled humanity to develop better defenses, distancing itself from the perils of the natural world. Nevertheless, physical and mental health, as well as overall well-being, remain reliant on nature, given that 99% of human existence transpired within this environment [8]. Moreover, the biophilic hypothesis [12] posits the existence of an intrinsic affinity towards life within human identity. This hypothesis encompasses various aspects, including attraction, rationality, aversion, exploitation, affection, control, self-identity, and symbolism, all of which contribute to a deep-seated connection with nature [13]. Summarily, the biophilic hypothesis asserts a biological predisposition towards being attracted to, dependent on, and affiliative with nature [14].

Three classical theories have been proposed to elucidate the benefits of connecting with nature. Firstly, the stress-reduction theory [15] posits that exposure to non-threatening natural environments reduces stress levels and negative emotions while improving sustained attention. Secondly, the attention-restoration theory [16] suggests that interacting with nature aids in restoring attention by shifting from top-down attentional processes (e.g., thoughts, rumination) to bottom-up processes (e.g., sensory engagement). Lastly, the prospect-refuge theory [17] argues that landscapes offering both expansive views (prospect) and places for concealment and protection (refuge) contribute to enhanced cognitive restoration [18]. Presently, research is beginning to demonstrate that increased engagement in nature-based activities, such as forest bathing (FB), can improve mental health and well-being [19,20]. Furthermore, combining FB with compassion-focused interventions (e.g., compassion mind training) has been shown to improve nature connection scores. Consequently, the development of a reliable measure of connection to nature becomes crucial,

prompting environmental psychologists to conceptualize this construct. Various measures, such as the Connectedness to Nature Scale [21], emphasize the presence of emotions associated with belonging to the natural world, while others, like the Inclusion of Nature in the Self, focus on cognitive beliefs [22]. Additionally, the Commitment to Nature scale [23] proposes an interpersonal relationship between humans and nature, highlighting their deep interdependence on well-being. Multidimensional scales, such as the Environmental Identity Scale [24], assess interaction with nature, the importance of nature, membership in nature, and positive emotions towards nature. Overall, there exists a robust convergence among these measures, except for the Inclusion of Nature in the Self [25]. Consequently, a broader construct termed "Connection to Nature" has been delineated, emphasizing its strong association with well-being and pro-environmental behaviors [25], grounded in the innate connection between human beings and nature. In addition, a meta-analysis has shown that more connection to nature predicts more pro-environmental behaviors [26].

In this study, nature is defined expansively, encompassing all spaces where plants grow, whether by human design or not, referring to areas typically characterized by greenery and the presence of water [27].

1.2. Connection to Nature and Climate Change Anxiety

In the latest report, the Directorate-General for Climate Action of the European Commission [28] highlights that Portuguese residents over 15 years old perceive climate change as the third most serious global issue, with 89% considering it an extremely severe problem. Furthermore, 68% of respondents have taken action to combat climate change in the past six months, and 28% of them believe they are personally responsible for these efforts [28]. Climate change poses a psychologically distant risk to humans, as it is anticipated to occur in the future and affects other people and places [29]. Therefore, understanding climate change risk perception necessitates consideration of four psychological dimensions: cognitive, experiential, socio-cultural, and sociodemographic characteristics. Moreover, an anxiety cycle emerges only when a perception of threat is present [30], with research indicating varied risk perceptions across these dimensions [31].

In the cognitive dimension, knowledge about climate change contributes to increasing risk perception, although distinctions between subjective and objective knowledge remain unclear. The experiential process involves affect and emotion guiding information processing [32], with individual experiences and affective evaluations from media influencing risk perception, particularly when directly experiencing climate change events [33]. While indirect experiences of climate change exist, their impact on risk perception is lower. Socio-cultural influences, encompassing culture, values, worldviews, and social norms, contribute to variations in climate change risk perception. This includes differences between environmental domains with egoistic values, which prioritize individual outcomes, socio-altruistic values, oriented towards caring for others, and biospheric values, focused on caring for non-human nature and the biosphere itself [34,35]. Overall, evidence suggests that younger individuals, females, those with higher education levels, politically liberal individuals, and racial minorities exhibit greater concerns about climate change [36].

Henceforth, individuals exhibiting higher scores in connection with nature also demonstrate elevated levels of climate change risk perception and heightened anxiety. This emotional response serves an adaptive purpose, as it is oriented towards the future, involving the anticipation of potential threats and the formulation of strategies to mitigate them and has a survival function by priming both the physical body and mind for rapid action [37]. However, excessive anxiety can have maladaptive consequences, leading to emotional dysregulation [38]. Within the realm of climate psychology, this specific manifestation of anxiety is conceptualized as climate change anxiety. Consequently, individuals who feel a

stronger connection to nature and exhibit greater environmental concern are more likely to be vigilant towards climate change threats and thus experience heightened anxiety [39]. Nevertheless, several factors influence the escalation of climate change anxiety. For instance, individuals who lack a sense of connection to nature but have experienced climate change-related events directly or indirectly, such as storms, droughts, or loss of habitat, are prone to heightened anxiety characterized by worry and trauma [36]. Conversely, individuals who harbor a stronger sense of connection to nature, accompanied by heightened feelings of care and concern, tend to exhibit greater vigilance towards environmental threats. Consequently, they experience elevated levels of climate change anxiety, along with increased symptoms of stress and depression, and lower levels of overall well-being [39].

1.3. Climate Change Anxiety, Mental Health, and Well-Being

The threat of climate change is intricately linked to mental health outcomes, though the nature of this association varies in its relation to mortality and morbidity. Certain populations, particularly those in tropical and subtropical regions, as well as individuals aged over 65 years, exhibit greater vulnerability to these mental health impacts [5]. Additionally, a relationship has been identified between latitude, temperature, and mortality, with lower minimum mortality rates observed in higher latitudes. Moreover, numerous studies have linked high ambient temperatures with an increased risk of suicide [4,40], as well as an elevated risk of mental-health-related emergency department visits [40,41], and higher mortality rates among individuals with pre-existing mental health conditions [4]. One study even reported that increased suicide rates in the United States and Mexico were influenced by the use of depressive language on social media [40].

Furthermore, the threat of climate change is directly associated with trauma and indirectly affects community well-being [42]. This impact is particularly pronounced among family farmers, leading to a compromised sense of self-identity and chronic forms of place-based distress, heightening perceived risks of depression and suicide [43]. Conversely, individuals in the United States and New Zealand may choose to go childfree for both biospheric and altruistic reasons [23].

1.4. Climate Change Anxiety and Pro-Environmental Behavior

The challenges posed by anxiety often prompt individuals to engage in a range of coping mechanisms, especially those associated with defensive responses to (physical, social, or psychological) threats, such as fight, flight, or freeze behaviors. Flight behavior typically involves denial of climate change, freezing behavior may include attempts at distraction or pathological worry [44], and fight behavior often results in the adoption of pro-environmental behaviors [45]. Furthermore, research indicates that individuals with a stronger connection to nature are more inclined to engage in the latter [26]. Pro-environmental behaviors are conscious actions aimed at reducing the negative impact of human activity on the natural or built environment [46]. These behaviors are influenced by internal factors like personality traits and values, as well as external factors such as political, social, cultural, and economic circumstances.

Moreover, environmental consciousness encompasses knowledge (e.g., understanding climate change), emotions (e.g., fear of climate change), and values/attitudes (e.g., concern for the natural world) [46]. Values that drive pro-environmental behaviors include childhood experiences in nature, witnessing environmental degradation, familial and organizational values, influence from role models such as friends or teachers, and educational background [47].

Additionally, individuals with higher levels of biospheric environmental concerns are more inclined to perceive ecological stress, employ ecological coping strategies, and

demonstrate pro-environmental behaviors [48]. Conversely, those with social-altruistic concerns may engage in ecological coping without necessarily perceiving ecological stress, while individuals with egoistic concerns neither perceive ecological stress nor engage in ecological coping [48].

In another study, evidence suggests that risk perception indirectly influences anxiety and worry, while response efficacy (belief in one's effectiveness and desired consequences) indirectly and directly influences behavior, and psychological adaptation (affective, cognitive, and motivational readiness to address climate change issues) directly influences behavior [29]. Conversely, individuals with a strong green identity (someone who identifies as friendly to the natural environment) are more likely to exhibit pro-environmental behaviors [49].

Moreover, research highlights various motives associated with different pro-environmental behaviors, without discernible patterns [50]. These motives are often linked to emotions, with empathic feelings and attitudes, stemming from perspective-taking, fostering helping behaviors [34]. Different studies have identified a range of emotions that drive pro-environmental behaviors, including anxiety [39], worry [44], fear, guilt, and hope [51], as well as eco-anger, eco-anxiety, and eco-depression [52] and feelings of hopelessness [53].

Interestingly, these behaviors can manifest as either individualistic actions (e.g., recycling, conserving energy) or collective endeavors (e.g., participating in political protests), and individuals with the same motives may exhibit either individual or collective behaviors [50].

1.5. Pro-Environmental Behavior, Mental Health, and Well-Being

Although ecological coping has been shown to decrease depressive symptoms [48] and sustainable behaviors have been associated with increased happiness [54], psychopathology linked to anxiety often arises when coping mechanisms, such as pro-environmental behaviors, prove ineffective in addressing and resolving the underlying issue, thereby perpetuating a sense of threat perception. For example, in the context of the climate change threat, the sixth report from the Intergovernmental Panel on Climate Change underscores the ongoing escalation of the threat [2]. Consequently, coping behaviors like denying the problem (flight), engaging in distraction or pathological worry (freeze), or actively participating in pro-environmental actions (fight) may not yield the desired outcomes, thereby exacerbating anxiety and diminishing overall mental health and well-being [55].

Furthermore, pro-environmental behaviors could exacerbate distress and anxiety because they may fail as a coping strategy [56]. Different emotions predict varying coping outcomes, with one study identifying that eco-anger predicts better mental health compared to eco-depression and eco-anxiety, which are less adaptive and lead to lower well-being [52].

Overall, there is more evidence suggesting that environmental activism protects against mental distress and improves well-being compared to individual pro-environmental behavior [57]. It acts as a buffer, with a study concluding that collective activism significantly attenuated the association between climate change anxiety and major depressive disorder more than individual pro-environmental behavior [45]. It is asserted that activism protects against feelings of hopelessness [53], lowers symptoms of general anxiety disorder, and fosters feelings of empowerment and social support [58], contributing to long-term mental health [59].

1.6. The Role of Compassion

Compassion is a concept deeply rooted in various spiritual and moral philosophical traditions, originating from the Latin term "compassio", which denotes the act of sharing suffering with others. It encompasses understanding another person's pain, empathizing

with their perspective, and desiring to alleviate their suffering [60]. Compassion plays an evolutionary role intertwined with attachment processes, fostering affiliative and cooperative behaviors through physiological mechanisms such as the activation of the vagus nerve [61]. As an evolved motivational system, compassion emerges from a blend of innate caregiving motives shared with other mammals and higher-order cognitive processes associated with social and emotional intelligence unique to humans [62]. Compassion entails various competencies and motivations, including care for well-being, sensitivity (attentiveness to suffering), sympathy (emotions arising from experiencing suffering), distress tolerance (ability to tolerate feelings arising when engaging with suffering), empathy (seeing the world through others' eyes), and non-judgment (open acceptance that aids distress tolerance). These competencies facilitate wise actions such as attentive behavior (recalling knowledge and wisdom), imagery (envisioning compassionate practices), reasoning (sound judgment), behaviors (compassionate actions), sensory awareness (being aware of bodily states and cultivating compassionate bodily states), and feelings (emotions of compassion) [62]. Within a compassionate mindset, three flows are recognized: self-compassion, compassion towards others, and others' compassion towards oneself. Furthermore, compassion is depicted as an intra- and interpersonal dynamic process involving these three flows [63]. Viewing compassion as motivation prompts consideration of its role in the relationship between connection to nature, climate change threat perception, pro-environmental behaviors, and their consequent impacts on well-being. There is evidence in the literature indicating an association between connection to nature and compassion. On one hand, prosocial behaviors are known to increase with a stronger connection to nature [64,65]. A common hypothesis explaining this association involves the experience of self-transcendent emotions, which include wonder, awe, gratitude, and compassion [66]. On the other hand, heart rate variability (HRV), a marker of parasympathetic nervous system activity, has been found to be associated with both compassion [67] and connection to nature [68]. Thus, enhancing one's connection to nature might elevate levels of compassion, and both factors can increase HRV, thereby fostering prosocial behavior [69] and pro-environmental behaviors [65]. Furthermore, Cassidy and Elliot [70] hypothesized a mediation of self-compassion [71] in the association of pro-environmental behaviors and mental well-being, linking self-compassion with hope. They concluded that higher levels of self-compassion are associated with increased pro-environmental behaviors and higher levels of well-being but did not clarify the direction of causality between self-compassion, pro-environmental behaviors, and well-being.

Interestingly, some research has established a link between connection to nature and the theoretical construct of nondual compassion [72]. Nondual compassion is described as a state of unified compassion and unconditional love, coupled with a comprehensive understanding of the nature of the mind [73]. This construct is characterized as an altered state of consciousness and is viewed as a trait that functions along a spectrum of compassion for self, others, and both self and others [72]. It is associated with nondual awareness, which is characterized by human experience devoid of the dualities of subject and object, self and other, and mind versus body [74,75]. Changes have been observed in delta, alpha, and theta brain activity in response to both exposure to nature and nondual awareness [76] leading to an integration of internal and external experiences [72], simultaneously activating the default mode network and goal-oriented networks [74], and evidencing a state of oneness, uniting extrinsic and intrinsic experiences. Additionally, feeling a part of a broader system, such as nature, rather than separate from it, could increase nondual compassion and understanding interconnection and interdependence of all life forms, promoting a harmonious and compassionate relationship with the natural world.

1.7. The Current Study

In the Anthropocene era, a term coined by Paul Crutzen and Eugene Stoermer [77] to describe the current geological epoch marked by significant human impact on Earth and climate change, it is crucial to understand and improve the relationship between humans and nature to create a balanced, win-win interaction. Numerous studies indicate that a better relationship with nature enhances well-being and physical and mental health [25]. However, the nature of this relationship can vary significantly based on how individuals relate to nature [34]. For instance, a person who has greater concerns with environmental issues will have decreased well-being and mental health when closer to nature. Therefore, it is essential to understand the mechanisms that underline the connection between nature and well-being. By doing so, we can enhance our social, economic, and political systems to foster human and environmental well-being as a symbiotic entity. Exposure to nature, which enhances well-being, could also increase awareness of climate change, potentially leading to direct or indirect suffering. Emotions elicited by climate change (e.g., anxiety) can drive coping mechanisms, such as pro-environmental behaviors, decreasing anxiety, and thereby enhancing well-being [54]. Interestingly, literature differentiates between individual and collective actions, showing varied outcomes based on the type of behavior [57]. Consistent with existing research, we hypothesize that environmental action positively influences well-being by improving physical and mental health, fostering social connections, promoting economic benefits, and ensuring long-term sustainability and equity [58]. Given the presence of suffering when humans interact with nature through increased awareness of climate change, which is associated with difficult emotions such as fear, anxiety, guilt, and anger [78], and considering that compassion is a motivational construct with strong evidence linking it to improved well-being and mental health [79], we hypothesized that compassion may play a role in the relationship between humans and nature. Moreover, it is important to distinguish between receiving compassion (from the self and others), which entails engaging and acting towards the prevention/alleviation of one's own suffering, and compassion for others, which entails engaging with and preventing/alleviating the suffering of others [63].

From a psychological standpoint, recognizing and understanding suffering is the initial step towards alleviating it. We hypothesize that individuals who are more aware of their own suffering may experience lower levels of climate change anxiety. Although awareness of others' suffering can lead to prosocial behaviors and pro-environmental behaviors [48], these actions are responses to human suffering rather than environmental suffering. Individuals with higher compassion for others may not necessarily demonstrate increased compassion for nature.

Therefore, the main aim of the current study was to investigate what mechanisms/factors could explain the relationship between connection to nature, climate change anxiety and well-being, and whether, among individuals with higher levels of self-compassion and compassion from others, a stronger connection to nature is associated with lower climate change anxiety and higher well-being. The specific aims were to: (1) Adapt the Climate Change Anxiety Scale [39] to the Portuguese language and examine its factor structure and psychometric properties in the Portuguese population; (2) Analyze a moderated mediation model, with connection to nature as a predictor of well-being, mediated by climate change anxiety and pro-environmental behaviors; (3) Examine compassion's flow towards oneself (from self and others) as moderator, investigating whether higher levels of compassion's flow towards oneself, are associated with a weaker relationship between connection to nature and climate change anxiety and a stronger relationship between connection to nature and well-being.

Deriving from Specific Aims 2 and 3, the following hypotheses were formulated: (1) Connection to nature would be associated with well-being and with climate change anxiety; (2) Climate change anxiety would mediate association between connection to nature and pro-environmental behaviors, and between connection to nature and well-being; pro-environmental behaviors would mediate the relationship between connection to nature and well-being, and between climate change anxiety and well-being; (3) Compassion flow towards oneself (from self and others), would moderate the associations between connection to nature and climate change anxiety, and between connection to nature and well-being.

2. Materials and Methods

2.1. Ethics

Ethics approval for the present study was granted by the Ethics and Deontology of Research Commission at the Faculty of Psychology and Education Sciences in the University of Coimbra (UC; CEDI:FPCEUC:81/4). All research was performed in accordance with regulations specified in the ethics approval and in accordance with the Declaration of Helsinki.

2.2. Procedure

Participants were recruited online from the Portuguese general population between February and March 2024, informed about the study's aims and procedures, provided informed consent prior to participation, and guaranteed complete anonymity. The study was conducted using an online survey, self-paced and about 20 min long, combining different measures, hosted at the University of Coimbra institutional account in the online platform https://www.limesurvey.org/pt/ (accessed on 20 May 2024), and was disseminated through social media platforms, institutional emailing lists, and using snowball sampling, and there was no payment for completing the survey. Inclusion criteria were being between 18 and 65 years of age and living in Portugal.

2.3. Participants

A sample of 522 participants was recruited. The average age of participants was 44.49 years (*SD* = 11.68), with ages ranging from 18 to 65 years. The sample consisted of 361 identified as cisgender women (69.16%), 158 as cisgender males (30.27%), 1 non-binary (0.19%), and 2 not answered (0.38%). Marital status distribution included 320 individuals (61.3%) who were married or living with a partner, and 202 individuals (38.7%) who were single, divorced, or widowed. The majority of participants were Caucasian (n = 445, 85.2%). Participants resided in urban areas (n = 234, 44.8%), rural areas (n = 209, 40%), and suburban areas (n = 79, 15.1%). Educational attainment varied, with 333 participants (63.8%) having completed high school and 189 participants (36.2%) having completed basic or secondary education. Most participants had children (n = 350, 67%), while 172 participants (33%) did not have children. Regarding socioeconomic status, 243 participants (46.6%) were at a medium level, 122 participants (23.4%) at a low level, 106 participants (20.3%) at a high level, and 51 participants (9.8%) did not provide income information. Most participants reported good physical health (n = 265, 50.8%) and good mental health (n = 266, 51%). A minority of participants were undergoing psychiatric or psychological treatment (n = 67, 12.8%), while 453 participants (86.8%) were not. Additionally, the majority (77.8%) did not engage in daily contemplative practice, whereas 109 participants (20.9%) reported having contemplative practice.

For this study, the sample was randomly subdivided into two subsets (*n1* = 261 and *n2* = 261). These two subsets didn't present statistically significant differences regarding

distribution of sociodemographic information (age, gender, area of residence, ethnicity, education level, marital status, having children, socioeconomic level, physical and mental health level, psychiatric or psychological counseling (yes/no), and contemplative practices (Table A1 of Appendix A).

2.4. Measures

2.4.1. Climate Anxiety Scale (CAS) [39]

Climate Change Anxiety Scale is a self-reported questionnaire, designed to measure anxiety to climate changes, with two subscales, Cognitive–Emotional Impairments with 8 items (e.g., "I have nightmares about climate change") describing difficult thoughts and feelings related to climate changes, and Functional Impairments with 5 items (e.g., "My friends say I think about climate change too much"), describing difficulties in daily routines and relationships related to climate changes. Higher scores indicate higher levels of anxiety about climate change. Clayton and Karazsia also identified as two factors related to climate changes anxiety, Experience of Climate Change with 3 items (e.g., "I was directly affected by climate change"), describing direct experience with climate change phenomenon, and Behavioral Engagement with 6 items (e.g., "I recycled"), describing pro-environmental behaviors. Those 22 items were included in the exploratory (EFA) and confirmatory (CFA) factor analysis. Participants indicated how often they experienced each statement over the last two weeks with a 5-point Likert scale (1 = *never*, 2 = *rarely*, 3 = *sometimes*, 4 = *often*, 5 = *almost always*). The Cronbach alphas indicated good internal consistencies (Cognitive–Emotional = 0.97, Functional = 0.79, Experience = 0.86, and Behavioral = 0.94). These scales were then translated and adapted to the Portuguese population, and the back translations were examined by a bilingual English teacher to examine the accuracy and fidelity of the original scales.

2.4.2. Hogg Eco-Anxiety Scale (HEAS) [80,81]

The Hogg Eco-Anxiety Scale is a self-reported questionnaire designed to measure eco-anxiety with four subscales: Affective Symptoms with four items (e.g., "Feeling afraid"), Rumination with three items (e.g., "Unable to stop thinking about losses to the environment"), Behavioral Symptoms with three items (e.g., "Difficulty sleeping"), and Personal Impact Anxiety with three items (e.g., "Feeling anxious about the impact of your personal behaviors on the earth"). Higher scores indicate higher levels of eco-anxiety. Participants indicated how often they experienced each factor of eco-anxiety over the last two weeks when thinking about climate change and other global environmental conditions with a 4-point Likert scale (0 = *not at all*, 1 = *several of the days*, 2 = *over half the days*, 3 = *nearly every day*). The Cronbach alphas indicated good internal consistencies, with Affective Symptoms = 0.92 (Portuguese version = 0.85), Rumination = 0.90 (Portuguese version = 0.89), Behavioral Symptoms = 0.86 (Portuguese version = 0.86), and Personal Impact Anxiety = 0.88 (Portuguese version = 0.92). In this study, the Cronbach alpha was 0.85, 0.89, 0.85, and 0.91, respectively.

2.4.3. Environmental Action Scale (EAS) [57,82]

The Environmental Action Scale is a self-reported questionnaire, aimed at evaluating the degree of involvement of people in collective actions in favor of the environment, with two subscales, Participatory Actions with 10 items (e.g., "Participated in an educational event") and Leadership Actions with 8 items (e.g., "Organized an educational event"). Higher scores indicate higher involvement in collective actions. Participants indicated, in the last six months, how often, if at all, they have engaged in the related environmental activities and actions with a 4-point Likert scale (0 = *never*, 2 = *sometimes*, 4 = *frequently*). The Cronbach alphas indicated good internal consistencies in Participatory Actions = 0.92

(Portuguese version = 0.90) and Leadership Actions = 0.92 (Portuguese version = 0.96). In this study, the Cronbach alphas were 0.90 and 0.83, respectively.

2.4.4. Brief Version Connectedness to Nature Scale (CNS-Brief Version) [83,84]

Brief Version Connectedness to Nature Scale is a self-reported questionnaire, designed to measure connection to nature with 7 items (e.g., "I often feel a kinship with animals and plants"). Higher scores indicate higher connection to nature. Participants were invited to answer, on a 5-point Likert scale ranging from 1 (*completely disagree*) to 5 (*completely agree*). The Cronbach alpha indicated good internal consistency, $\alpha = 0.87$ (Portuguese version = 0.83). In this study the Cronbach alpha was 0.89.

2.4.5. Compassionate Engagement and Action Scales (CEAS) [85,86]

This self-report questionnaire encompasses three subscales measuring the three orientations/flows of compassion: Self-compassion, Compassion to Others, and Compassion from Others [85]. Each subscale has 13 items and is divided into two sections. The first (engagement) is related to the motivations and capacities to deal with suffering. It includes the six compassion engagement elements: motivation to care for well-being, attention/sensitivity to suffering, sympathy, distress tolerance, empathy, and being accepting and non-judgmental [85]. The second section (compassionate action) is related to the ability to pay attention to learn about and act on what is helpful—developing the wisdom and commitment to do something about it. It includes compassion action elements: directing attention to what is helpful, thinking and reasoning about what is likely to be helpful, taking helpful actions, and creating feelings of support, kindness, helpfulness, and encouragement to deal with distress. The items are rated on a 10-point Likert scale (1–10). Higher scores indicate higher levels of compassion. The CEAS was found to have robust psychometric properties. In the scale Compassion to Others—engagement (e.g., "I tolerate the various feelings that are part of other people's distress"), the Cronbach alpha was $\alpha = 0.90$ (Portuguese version $\alpha = 0.82$), and in this study, 0.88. The Cronbach alpha for "Compassion to others—Actions" (e.g., "I am able to take the actions and do the things that will be helpful to others.") was $\alpha = 0.94$ (Portuguese version $\alpha = 0.90$), and in this study, 0.95. In Compassion for Self—engagement the Cronbach alpha for the 2 items emotional sensitivity scale (e.g., "I am emotionally moved by my distressed feelings or situations.") was $\alpha = 0.77$ (Portuguese version $\alpha = 0.72$; in this study 0.68) and $\alpha = 0.72$ (Portuguese version $\alpha = 0.63$; in this study 0.82) for the 4 items' engagement with suffering scale (e.g., "I am motivated to engage and work with my distress when it arises"). In the scale Compassion for Self—actions (e.g., "I direct my attention to what is likely to be helpful to me."), the Cronbach alpha was $\alpha = 0.90$ (in this study was 0.94), like in the Portuguese version. In Compassion from Others—engagement (e.g., "Others are emotionally moved by my distressed feelings."), the Cronbach alpha was $\alpha = 0.89$, like in the Portuguese version (in this study was 0.93). Finally, in the scale Compassion from Others-Actions (e.g., "Others direct their attention to what is likely to be helpful to me."), the Cronbach alpha was $\alpha = 0.91$ (Portuguese Version $\alpha = 0.92$; in this study 0.95). For the purposes of this study, participants completed the Compassion for Self and Compassion from Others subscales.

2.4.6. Depression, Anxiety, and Stress Scale (DASS 21) [87,88]

The Depression, Anxiety, and Stress Scale is a self-reported questionnaire, designed with three subscales, Depression (e.g., "I felt that life was meaningless"), Anxiety (e.g., "I was aware of dryness of my mouth") and Stress (e.g., "I found myself getting agitated"), with 7 items each one. Higher scores indicate higher levels of depression, anxiety, and stress. Participants were invited to answer, on a 4-point Likert scale ranging from 0 (*did not apply to me at all*) to 3 (*applied to me very much, or most of the time*). The Cronbach alphas

indicated good internal consistencies in Depression, $\alpha = 0.91$ (Portuguese version = 0.85; in this study 0.90), in Anxiety, $\alpha = 0.84$ (Portuguese version = 0.74; in this study 0.88), and in Stress, $\alpha = 0.90$ (Portuguese version = 0.81; in this study 0.91).

2.4.7. PERMA-Profiler (PERMA) [89,90]

PERMA-Profiler is a self-reported questionnaire, designed with seven subscales: Positive Emotion (P) with 3 items (e.g., "In general, to what extent do you feel contented?"); Engagement (E), 3 items (e.g., "In general, to what extent do you feel excited and interested in things?"); Relationship (R), 3 items (e.g., "To what extent do you feel loved?"); Meaning (M), 3 items (e.g., "In general, to what extent do you lead a purposeful and meaningful life?"); Accomplishment (A), 3 items (e.g., "How often are you able to handle your responsibilities?"); Negative Emotion, 3 items (e.g., "In general, how often do you feel anxious?"); Physical Health, 3 items (e.g., "In general, how would you say your health is?"); Loneliness, 1 item ("How lonely do you feel in your daily life?"); and Happiness, 1 item ("Taking all things together, how happy would you say you are?"). The average of Happiness together with the 15 PERMA items shapes the overall well-being subscale. The answers range on a Likert scale from an 11-point response format. The results of the PERMA-Profiler are calculated by averaging the items that make up each factor. The scores of the PERMA-Profiler indicate the flourishing psychological profile, the level of overall well-being, negative emotion, physical health, and loneliness. The Cronbach alpha of scale Positive Emotion was $\alpha = 0.88$ (Portuguese version = 0.87; in this study 0.94), of Engagement was $\alpha = 0.72$ (Portuguese version = 0.56; in this study 0.73), of Relationship was $\alpha = 0.82$ (Portuguese version = 0.77; in this study 0.79), of Meaning was $\alpha = 0.90$ (Portuguese version = 0.84; in this study 0.88), of Accomplishment was $\alpha = 0.79$ (Portuguese version = 0.71; in this study 0.82), of Negative Emotion was $\alpha = 0.71$ (Portuguese version = 0.71; in this study 0.76), and of Physical Health was $\alpha = 0.92$ (Portuguese version = 0.86; in this study 0.90).

2.5. Data Analysis

Data were analyzed using the Statistical Package for Social Sciences (IBM SPSS, version 27.0) and AMOS 27 software [91]. Preliminary analyses of all variables in the study assessed the normality of the data distribution, following Kline's recommendations [92]. Normality was examined based on skewness (SK) and kurtosis (Ku) values, considering values above |3| and |10|, respectively, as indicative of non-normal distribution (see Table A2 of Appendix A). To address the first research objective, which involves examining the factor structure and psychometric properties of the CAS, the sample was randomly divided into two subsets. In one subset, an EFA was conducted using the principal component analysis approach with direct oblimin (oblique) rotation. Criteria for factor extraction included examination of the low loading items ($r < 0.3$) [93], Kaiser-Meyer-Olkin Measure ($KMO > 0.6$) [93], and Bartlett's Test of Sphericity ($\chi 2$, $p \leq 0.050$) [93]. The Kaiser criterion (i.e., eigenvalues greater than 1.0) was used, and the scree plot was inspected to determine the optimal number of factors [93]. To confirm whether the structure of the CAS derived from the EFA presents an adequate fit to the data in the Portuguese population, a confirmatory factor analysis (CFA) using maximum likelihood estimation was conducted in AMOS 27 software [91] in the other randomly generated sample subset. The structure was specified to have a second-order factor, the Climate Anxiety Scale (CAS), which contains two subscales: Cognitive Impairment and Functional Impairment. The specified model includes two other intercorrelated factors, Experience of Climate Change and Behavioral Engagement, correlated with the CAS (Figure 1).

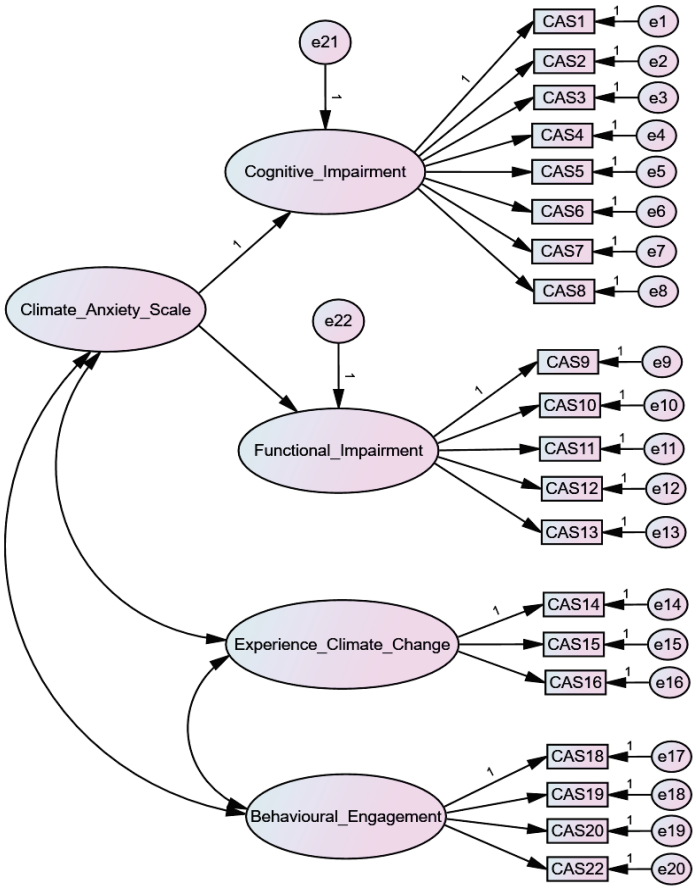

Figure 1. CFA theoretical model for CAS factorial structure and two more factors associated and emerged in EFA.

The normality of the items was evaluated by the Sk and Ku values (Table A3 of Appendix A). No item had indicators of severe violations to the normal distribution (Sk < |3| and Ku < |10|) [92]. Multivariate outliers were screened using the Mahalanobis squared distance (D^2) method [92], and 12 outliers were removed to improve the model fit. However, removing the thirteenth and subsequent outliers resulted in a decrease in model fit, so these outliers were retained. The sociodemographic differences between the subsets (see Table A1 of Appendix A) were observed through Student's t-test, to continuous variables and chi-square to categorial variables. It also analyzed the magnitude of effect, through Cohen's d (continuous variables; <0.02, small; 0.021–0.079, moderate; >0.08, large) [94], and through V of Cramér (categorial variables; 0.10–0.29, small; 0.30–0.49, moderate; >0.50, large) [94,95]. Model fit was ascertained using Normed chi-square ($\chi 2/df$), with 2 to 5 indicating a good fit. Because the chi-square index ($\chi 2$) is very sensitive to sample size and to minor or potentially nonconsequential violations of model fit, we assessed the fit of the model with three additional indicators: the comparative fit index (CFI), the Tucker–Lewin Index (TLI), and the root-mean-square error of approximation (RMSEA). Criteria for adequate and good model fit were CFI and TLI values above 0.90 and RMSEA values between ≤ 0.05 and ≤ 0.08 [92,93,96]. The mean (M) and standard deviation (DP) of each factor were calculated, and reliability was assessed by estimating Cronbach's alpha coefficients for each subscale, classified as acceptable ($\geq$0.70) and good ($\geq$0.80) [97].

To examine the validity of the CAS, Pearson product-moment correlation coefficients were computed. Cohen's [94] guidelines were used to describe the effect sizes of Pearson's correlations (i.e., weak for correlations between 0.10 and 0.29, medium for those between

0.30 and 0.49, and strong for correlations at 0.50 or higher). Convergent validity was evaluated using Pearson correlation coefficients between the CAS and subscales and the Depression, Anxiety, and Stress Scale [87] and with the Experience of Climate Change factor [39]. Concurrent Validity was assessed by evaluating the Pearson correlation coefficients between the CAS and the Hogg Eco-Anxiety Scale [80]. Divergent validity was assessed by evaluating the correlation between the CAS and the Behavioral Engagement factor [39].

Finally, to accomplish the second and third objectives of our study, two sequential moderated mediation models were evaluated. Although some differences were found in the study variables when comparing levels/categories within the sociodemographic variables (see Table A4 of Appendix A), an inspection of the potential covariance of sociodemographic variables revealed small effect sizes ($\eta 2$ = 0.01, small; 0.6, moderate; 0.14, large) [94] and weak-to-moderate correlations (see Table A5 of Appendix A) with the variables included in the model, and therefore these were not included as covariates. In the moderated mediation models, we examined the direct and indirect effects, considering climate change anxiety (CAS) and pro-environmental behaviors (EAS), as sequential mediators, in the association between connection to nature (CNS) and well-being (PERMA; Figures 2 and 3), using PROCESS macro for SPSS [98]. To maintain a parsimonious model, compassion (self-compassion—Figure 2 and compassion from others—Figure 3) was hypothesized as a moderator in the more theoretically relevant but minimum number of paths to reduce the possibility of Type I error. Therefore, in this study, compassion for self and from others were hypothesized as moderators of the associations between connection to nature and well-being, and between connection to nature and climate change anxiety. To illustrate the moderation effect, a graphic was plotted considering one line for each of the three levels of the moderator ($M - SD$, M, $M + SD$) [99]. For tests of mediation, the significance of direct, indirect, and total effects was assessed using $\chi 2$ tests [92]. The bootstrapping resampling method was further used to test the significance of the mediational paths, using 5000 bootstrap samples and 95% confidence intervals (CI) [92]. For all the analyses performed in this study, results were considered statistically significant at a p-value lower than 0.05.

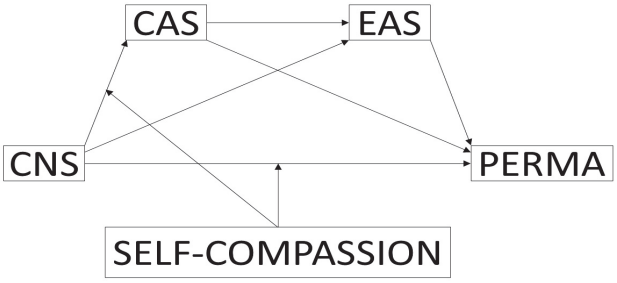

Figure 2. Moderated mediation model with self-compassion as a moderator.

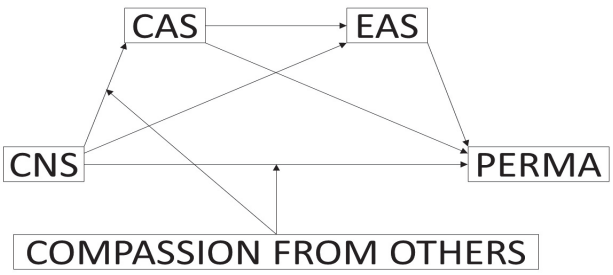

Figure 3. Moderated mediation model with compassion from others as a moderator.

3. Results

3.1. Climate Change Anxiety Scale

3.1.1. Exploratory Factor Analysis

In one of the subsets (n = 261), an EFA was conducted, using the principal component analysis with direct oblimin (oblique) rotation. Although a solution emerged with five factors with eigenvalue above one, after analyzing the scree plot, and in line with the original study [39], one factor, with an eigenvalue of 1.002, was dismissed. Moreover, one of the factors, which in the original study included Items 17, 18, 19, 20, 21, and 22, emerged in this study formed by Items 18, 19, 20, and 22 (Cronbach's α of 0.72). The fifth factor, with Items 17 and 21, was not retained (Cronbach's α of 0.53). The model, with four factors, accounted for 60.98% of the variance among the items. Factor loadings are presented in Table 1.

Table 1. Exploratory factor analysis using principal component analysis (n = 261).

Items	FACTOR				
	1	**2**	**3**	**4**	**5**
CAS1	0.69				
CAS2	0.76				
CAS3	0.75				
CAS4	0.79				
CAS5	0.80				
CAS6	0.78				
CAS7	0.67				
CAS8	0.78				
CAS9					0.79
CAS10					0.78
CAS11					0.80
CAS12					0.78
CAS13					0.56
CAS14			−0.85		
CAS15			−0.87		
CAS16			−0.80		
CAS17 [a]				−0.69	
CAS18		0.79			
CAS19		0.70			
CAS20		0.84			
CAS21 [a]				−0.65	
CAS22		0.60			
Cronbach's alpha	0.89	0.72	0.80	0.53	0.83

[a] not retained.

All the presented factor loadings range between 0.56 and 0.87. Factor 1 measures Cognitive and Emotional Impairment in response to climate change, Factor 2 is related to Behavioral Engagement, Factor 3 represents Personal Experience of Climate Change, and Factor 5 measures Functional Impairment influenced by concern about climate change.

3.1.2. Confirmatory Factor Analysis

In the other sample subset (n = 261), a CFA was conducted using the four factors that resulted from the EFA (Figure 1), similar to the original study [39]. Results showed that this model has a poor fit to the data: $\chi 2$ (165) = 455.54; $p < 0.001$, CMIN/DF = 2.76; CFI = 0.89; TLI = 0.87; RMSEA = 0.08 [90% CI 0.07–0.09; $p < 0.001$]. Furthermore, the intercorrelation between the CAS and Behavioral Engagement was removed because it was not statistically significant. Outliers were screened using the Mahalanobis squared

distance and 12 of them were removed to improve the model fit: $\chi 2$ (166) = 413.12; $p < 0.001$, CMIN/DF = 2.49; CFI = 0.91; TLI = 0.90; RMSEA = 0.08 [90% CI 0.07–0.09; $p < 0.001$]. An inspection of the modification indices indicated that correlating the measurement errors of two pairs of items of the Cognitive Impairment factor (Items 1 and 2; Items 5 and 8) would significantly increase the model fit. After correlating these two pairs of items, results revealed an improvement in the model fit (Figure 4), with this adjusted model presenting an acceptable fit to the data $\chi 2$ (164) = 328.67; $p < 0.001$, CMIN/DF = 2.004; CFI = 0.94; TLI = 0.93; RMSEA = 0.06 [90% CI 0.05–0.07; $p < 0.001$]. The first-order factors, Cognitive Impairment and Functional Impairment, were significantly loaded on the second-order factor of Climate Change Anxiety (0.93 and 0.91, respectively). Regarding local fit, in the Cognitive Impairment subscale, items revealed standardized regression weights (SRW) ranging from 0.56 (Item 1) to 0.92 (Item 6), and in the Functional Impairment subscale from 0.63 (Item 10) to 0.92 (Item 12; Figure 3). Squared multiple correlations (SMC) results indicated that in the Cognitive Impairment factor, values ranged from 0.31 (Item 1) to 0.85 (Item 6), and from 0.40 (Item 10) to 0.85 (Item 12) in the Functional Impairment subscale.

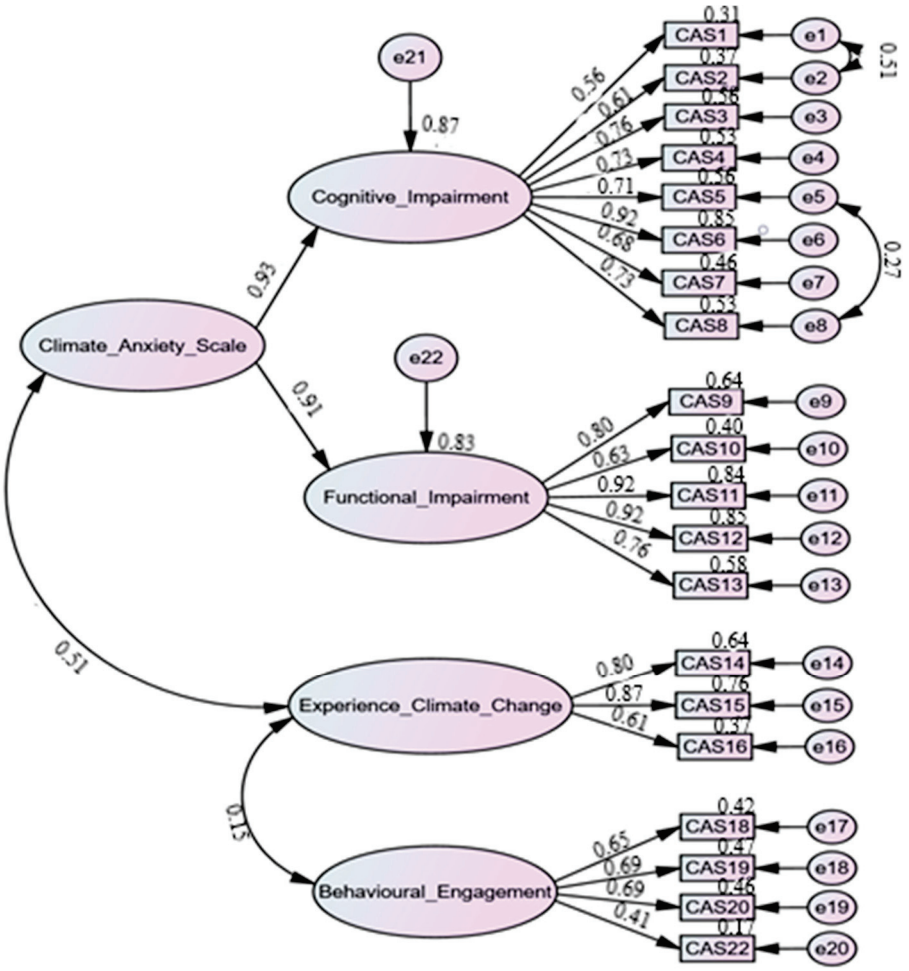

Figure 4. CFA model for the Climate Anxiety Scale factorial structure adjusted.

3.1.3. Descriptive Statistics and Reliability

Table 2 shows the means, standard deviation, and Cronbach's alpha of each factor, and other scales (N = 510). The Climate Anxiety Scale had a Cronbach's alpha of 0.92, with 0.89 in the Cognitive Impairment subscale, and 0.85 in the Functional Impairment subscale, indicating a good internal consistency. Experience with climate change had $\alpha = 0.79$, and Engagement behavior $\alpha = 0.70$.

Table 2. Descriptive statistics—variables under study.

Scale	*M* (*SD*)	Range	Cronbach's α
Climate Anxiety Scale	18.92 (6.89)	13–55	0.92
Cognitive impairment	11.80 (4.45)	8–35	0.89
Functional Impairment	7.12 (2.91)	5–20	0.86
Experience with climate change	5.78 (2.64)	3–15	0.79
Engagement behaviour	16.41 (2.74)	4–20	0.70
HEAS	5.33 (6.18)	0–34	0.94
EAS	13.96 (12.66)	0–62	0.93
CNS	25.59 (6.56)	7–35	0.89
CEAS-SC	65.98 (16.55)	10–100	0.90
CEAS-CFO	58.20 (18.13)	10–100	0.96
Well-Being (PERMA)	7.08 (1.69)	0–10	0.96

Note. *N* = 510. CAS = Climate Change Anxiety Scale; HEAS = Hogg Eco-Anxiety Scale; EAS = Environmental Action Scale; CNS = Brief Version Connectedness to Nature Scale; CEAS–SC = Compassionate Engagement and Action–Self-Compassion Scale; CEAS–CFO = Compassionate Engagement and Action–Compassion from Others Subscale.

Table 3 shows the correlation between these subscales and the other scales. Behavioral engagement was not correlated with cognitive or functional impairment. Moreover, Factors 1 and 5 were strongly correlated.

Table 3. Correlation matrix—variables under study.

Variables	1	2	3	4	5	6	7	8	9	10	11
CAS	1										
Cognitive impairment	0.96 **	1									
Functional Impairment	0.90 **	0.74 **	1								
Experience with Climate Change	0.46 **	0.43 **	0.44 **	1							
Behavioral Engagement	0.08	0.06	0.10 *	0.18 **	1						
HEAS	0.74 **	0.68 **	0.70 **	0.38 **	0.09	1					
EAS	0.32 **	0.26 **	0.36 **	0.38 **	0.33 **	0.36 **	1				
CNS	0.15 **	0.13 **	0.15 **	0.23 **	0.40 **	0.16 **	0.35 **	1			
CEAS-SC	−0.09 *	−0.08	−0.09	0.04	0.19 **	−0.11 *	0.10 **	0.29 **	1		
CEAS-CFO	−0.04	−0.03	−0.05	0.12 **	0.19 **	−0.03	0.08	0.20 **	0.46 **	1	
Well-Being (PERMA)	−0.19 **	−0.17 **	−0.19 **	0.03	0.18 **	−0.19 **	0.14 **	0.25 **	0.56 **	0.45 **	1
DASS-21	0.35 **	0.32 **	0.35 **	0.18 **	−0.05	0.46 **	0.08	0.07	−0.17 **	−0.09 *	−0.37 **

Note. *N* = 510. CAS = Climate Change Anxiety Scale; HEAS = Hogg Eco-Anxiety Scale; EAS = Environmental Action Scale; CNS = Brief Version Connectedness to Nature Scale; CEAS–SC = Compassionate Engagement and Action–Self-Compassion Scale; CEAS–CFO = Compassionate Engagement and Action-Compassion from Others Subscale; DASS-21 = Depression, Anxiety, and Stress Scale. * $p < 0.050$. ** $p < 0.010$.

Additionally, the analysis identified a moderate multicollinearity risk between the variables CAS, Cognitive Impairment, and Functional Impairment. The variance inflation factor (VIF) was 2.24, falling within the range indicative of moderate multicollinearity [100,101], while the tolerance value of 0.45 exceeded the critical threshold of 0.1, suggesting no substantial multicollinearity risk [100].

3.1.4. Convergent, Concurrent, and Divergent Validity

For the convergent validity, correlation analyses indicated a moderate association between the Depressive Anxiety and Stress Scale with the Climate Change Anxiety Scale ($r = 0.35$; $p < 0.010$), Cognitive Impairment ($r = 0.32$; $p < 0.010$), and Functional Impairment ($r = 0.35$, $p < 0.010$). Experience of Climate Change was also moderately correlated with the CAS ($r = 0.46$; $p < 0.010$), Cognitive Impairment ($r = 0.43$; $p < 0.010$), and Functional Impairment ($r = 0.44$, $p < 0.10$). Moreover, Hogg Eco-Anxiety Scale [80] was strongly

correlated with the CAS ($r = 0.74$; $p < 0.010$), Cognitive Impairment ($r = 0.68$; $p < 0.010$), and Functional Impairment ($r = 0.70$; $p < 0.010$), thus supporting concurrent validity. Conversely, for discriminant validity, behavioral engagement showed weak correlations with the CAS ($r = 0.08$), Cognitive Impairment ($r = 0.06$), and Functional Impairment ($r = 0.10$; $p < 0.050$).

3.2. Moderated Mediation Model Analysis

Two moderated mediation models were analyzed (Figures 2 and 3). Tables 4 and 5 present the results of the direct and indirect effects of each model. Correlations between the study variables and the sociodemographic variables revealed weak to moderate effect sizes (between 0.01 and 0.37; see Table A5 of Appendix A). Consequently, these sociodemographic variables were not included in the models as covariates. Results of the direct effects of connection to nature on well-being are presented at low, medium, and high levels of the significant moderators, self-compassion, and compassion from others.

Table 4. Direct effects on different levels of self-compassion and indirect effects.

Effect	Path	Unstandardized Coefficient	95% Confidence Interval	
			Lower	Upper
Direct	CNS -> WB	0.100 ***	0.042	0.162
Direct	CNS -> WB | Self-compassion = −1 SD	0.040 ***	0.019	0.066
Direct	CNS -> WB | Self-compassion = 0 SD	0.020 *	0.002	0.042
Direct	CNS -> WB | Self-compassion = +1 SD	0.002	−0.023	0.028
Indirect	CNS -> CAS -> WB	−0.009	−0.016	−0.004
Indirect	CNS -> EAS -> WB	0.010	0.003	0.016
Indirect	CNS -> CAS -> EAS -> WB	0.002	0.001	0.003

Note. $N = 510$. CAS = Climate Change Anxiety Scale; EAS = Environmental Action Scale; CNS = Brief Version Connectedness to Nature Scale; WB = Well-Being (PERMA). * $p < 0.050$. *** $p < 0.001$.

Table 5. Direct effects on different levels of compassion from others and indirect effects.

Effect	Path	Unstandardized Coefficient	95% Confidence Interval	
			Lower	Upper
Direct	CNS -> WB	0.123 ***	0.067	0.178
Direct	CNS -> WB | Compassion from others = −1 SD	0.065 ***	0.040	0.090
Direct	CNS -> WB | Compassion from others = 0 SD	0.039 ***	0.018	0.059
Direct	CNS -> WB | Compassion from others = +1 SD	0.012	−0.016	0.040
Indirect	CNS -> CAS -> WB	−0.009	−0.016	−0.004
Indirect	CNS -> EAS -> WB	0.010	0.004	0.016
Indirect	CNS -> CAS -> EAS -> WB	0.001	0.000	0.003

Note. $N = 510$. CAS = Climate Change Anxiety Scale; EAS = Environmental Action Scale; CNS = Brief Version Connectedness to Nature Scale; WB = Well-Being (PERMA). *** $p < 0.001$.

Regarding the first model with self-compassion as moderator presented in Figure 2, results showed a significant direct effect of connection to nature on well-being ($b = 0.10$, $SE = 0.031$, $p < 0.001$, 95% CI = [0.042, 0.162]), with a significant moderation effect of self-compassion ($b = -0.0012$, $SE = 0.0004$, $p < 0.010$, 95% CI = [−0.0021, −0.0003]; see Table 4).

As depicted in Figure 5, increased connection to nature was significantly associated with enhanced levels of well-being in participants with low ($b = 0.040$, $SE = 0.012$, $p < 0.001$, 95% CI = [0.019, 0.066]) and medium ($b = 0.020$, $SE = 0.010$, $p < 0.050$, 95% CI = [0.002, 0.042]) levels of self-compassion, but not in participants scoring high self-compassion ($b = 0.002$, $SE = 0.013$, $p = 0.87$, 95% CI = [−0.023, 0.028]).

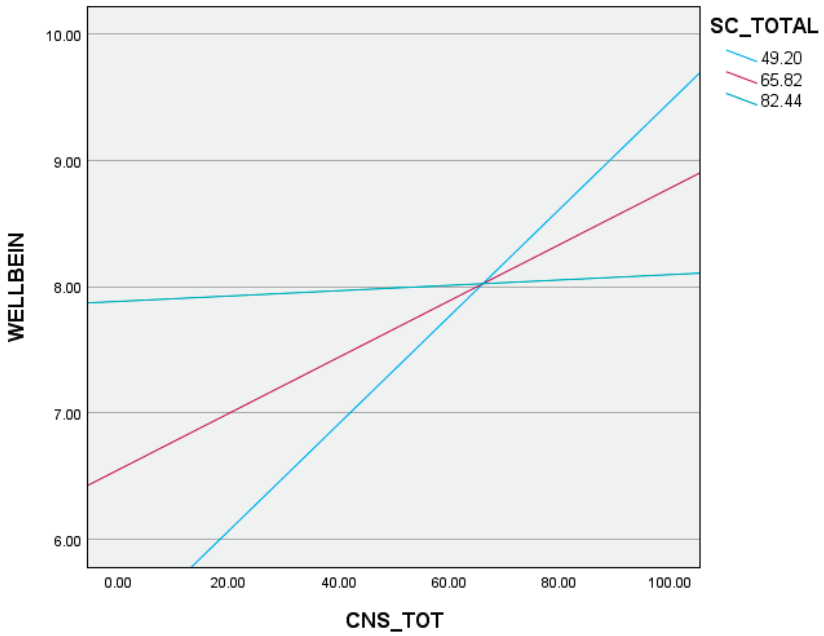

Figure 5. Graphic of Moderation of Self-Compassion. CNS_TOT = Connectedness to Nature Scale total score; WELLBEIN = Well-Being (PERMA) total score; SC_TOTAL = Compassionate Engagement and Action–Self-Compassion scale total score at level $M - SD$ (49.20), level M (65.82), and level $M + SD$ (82.44).

There was also a significantly indirect effect of connection to nature on well-being, significantly mediated by climate change anxiety ($b = -0.009$, $SE = 0.003$, 95% CI = [−0.016, −0.004]), an indirect effect of connection to nature on well-being significantly mediated by environmental action ($b = 0.010$, $SE = 0.003$, 95% CI = [0.003, 0.016]), and an indirect effect of connection to nature on well-being significantly mediated by climate change anxiety/environmental action ($b = 0.002$, $SE = 0.001$, 95% CI = [0.001, 0.003]).

The moderation effect of self-compassion on the association between connection to nature and climate change anxiety was not significant ($b = -0.002$, $SE = 0.002$, $p = 0.435$, 95% CI = [−0.006, 0.003]). Therefore, the index of moderated mediation in the overall model was not significant, $b = 0.000$, $SE = 0.000$, 95% CI = [−0.0001, 0.000], meaning that self-compassion did not moderate the mediation path (between connection to nature and climate change anxiety), only the direct effect of connection to nature on well-being. This mediation model with a moderation of direct effect explained 36.89% of the variance of well-being.

In regard to the model with compassion from others as a moderator and presented in Figure 3, results showed a significant direct effect of connection to nature on well-being ($b = 0.123$, $SE = 0.028$, $p < 0.001$, 95% CI = [−0.067, 0.178]), with a significant moderator effect of compassion from others ($b = -0.001$, $SE = 0.001$, $p < 0.010$, 95% CI = [−0.002, −0.001]; see Table 5).

The inspection of the graphic of moderation indicates that higher connection to nature was significantly associated with enhanced levels of well-being, in participants with low ($b = 0.065$, $SE = 0.013$, $p < 0.001$, 95% CI = [0.040, 0.090]) and medium levels ($b = 0.039$, $SE = 0.011$, $p < 0.001$, 95% CI = [0.018, 0.059]) of compassion from others, but not in participants with increased levels of compassion from others ($b = 0.012$, $SE = 0.014$, $p = 0.39$, 95% CI = [−0.016, 0.040]; Figure 6).

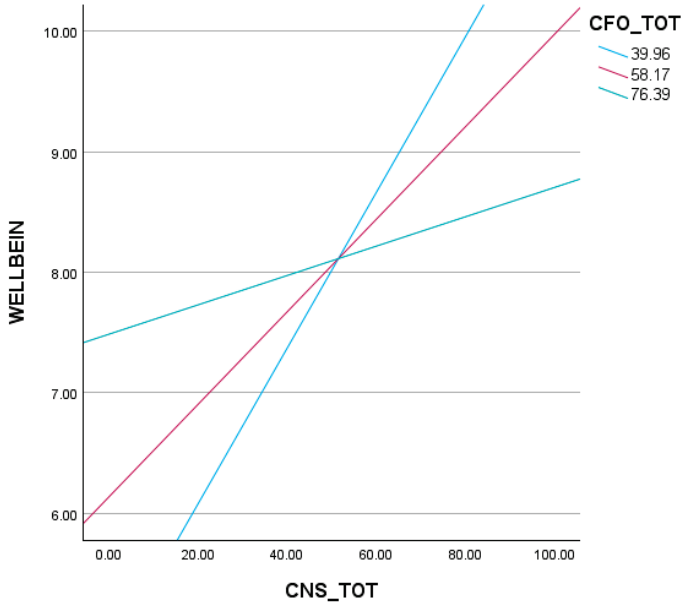

Figure 6. Graphic of moderation of compassion from others. Note. CNS_TOT = Connectedness to Nature Scale total score; WELLBEIN = Well-Being (PERMA) total score; CFO_TOTAL = Compassionate Engagement and Action—Compassion from Others Subscale total score at level $M - SD$ (39.96), level M (58.17), and level $M + SD$ (76.39).

There was also a significantly indirect effect of connection to nature on well-being, significantly mediated by climate change anxiety ($b = -0.009$, $SE = 0.003$, 95% CI = [−0.016, −0.004]), an indirect effect of connection to nature on well-being, significantly mediated by environmental action ($b = 0.010$, $SE = 0.003$, 95% CI = [0.004, 0.016]) and an indirect effect of connection to nature on well-being, significantly mediated by climate change anxiety/environmental action ($b = 0.001$, $SE = 0.001$, 95% CI = [0.000, 0.003]). The moderation effect of compassion from others on the association between connection to nature and climate change anxiety was not significant ($b = -0.002$, $SE = 0.002$, $p = 0.435$, 95% CI = [−0.007, 0.002]). Therefore, the index of moderated mediation in the overall model was not significant, $b = 0.000$, $SE = 0.000$, 95% CI = [−0.0001, 0.000], meaning that compassion from others did not moderate the mediation path (between connection to nature and climate change anxiety), only the direct effect of connection to nature on well-being. Thus, the mediation model with a moderation of this direct effect explained 29.79% of the variance of well-being.

4. Discussion

In a world facing increasing challenges related to climate change caused by human activities, known as the Anthropocene Era [77], understanding how humans relate to nature could help change behaviors and promote a balanced life. Climate change anxiety is an emotional reaction that can stem from various causes, particularly socio-altruistic values (caring for others) and biospheric values (caring for non-human nature and the biosphere itself), but not from egoistic values [34]. Given the intrinsic motivation for interdependence with nature [14], people who feel a stronger connection to nature and have greater environmental concern are more likely to be vigilant towards climate change threats, experiencing heightened anxiety [39], poorer mental health, and lower levels of well-being [1]. Pro-environmental behaviors are deliberate actions aimed at reducing the negative impact of human activity on the natural or built environment and function as a coping mechanism [46]. Individuals with higher levels of biospheric values are more inclined to perceive ecological stress and engage in pro-environmental behaviors. Those

with higher levels of socio-altruistic values also engage in pro-environmental behaviors but without necessarily perceiving ecological stress [48]. Additionally, individuals with higher levels of self-compassion and compassion from others exhibit more pro-environmental behaviors and higher levels of well-being [70]. Therefore, the current study aimed to better understand the relationship between connection to nature and well-being by examining the mediator role of climate change anxiety and environmental action and the moderator effect of self-compassion and compassion from others on this association.

Following the adaptation of the CAS to Portuguese, we studied its factor structure and psychometric properties within the Portuguese population. The original study by Clayton and Karazsia [39], an exploratory factor analysis (EFA), identified four factors, named Cognitive Impairment, Functional Impairment, Personal Experience with Climate Change, and Behavioral Engagement. Our EFA revealed five factors. Three of these matched the original study, namely Cognitive Impairment (factor loadings between 0.67 and 0.80), Functional Impairment (factor loadings between 0.56 and 0.80), and Personal Experience with Climate Change (factor loadings between -0.80 and -0.87). However, the Behavioral Engagement factor, comprising Items 17 to 22, was subdivided into two factors in our study: one included Items 17 and 21 and exhibited unacceptable internal consistency, and the other comprised Items 18, 19, 20, and 22 with acceptable internal consistency. Due to the differing grammatical construction and focus on consequences of not acting pro-environmentally, Items 17 ("I wish I behaved more sustainably") and 21 ("I feel guilty if I waste energy") were hence excluded from the final scale composition in this Portuguese adaptation. Consequently, in our study, Behavioral Engagement is represented by Items 18, 19, 20, and 22.

In line with the original study [39], a confirmatory factor analysis (CFA) using a four-factor structure was then conducted and tested for a second-order factor (Climate Change Anxiety Scale) comprising the cognitive engagement and functional impairment factors. Initially, this second-order factor was estimated to be correlated with the personal experience climate change factor and the behavioral engagement factor. The CFA results indicated a poor model fit and revealed a weak correlation between the Climate Change Anxiety Scale and the Behavioral Engagement factor. Upon inspecting the Mahalanobis distance and measurement error covariances, we identified significant outliers and covariation between the measurement errors of Item 1 with Item 2 and Item 5 with Item 8, which differ from the CAS's original study [39]. Items 1 and 2 that start with "Tenho dificuldades em. . ." in the Portuguese language differed grammatically from the other items in the Cognitive Impairment subscale. Similarly, Items 5 and 8, starting with "Penso: Porque é que. . ." in the Portuguese language, showed covariation due to their distinct grammatical structure.

The model was thus respecified by removing extreme outliers and covarying the measurement errors of Items 1 with 2 and 5 with 8. The CFA of the adjusted model indicated an adequate model fit, corroborating the factor structure with four factors: Cognitive Impairment, Functional Impairment, Personal Experience Climate Change, and Behavioral Engagement. The CAS demonstrated good internal consistency and reliability, evidencing internal validity similar to the original study [39]. It was also important to compare the CAS with other scales that measure similar and different constructs. The CAS evidenced good convergent validity with a scale that measures anxiety (DASS-21) and with a scale that measures personal experience with climate change [39]. Interestingly, results from this research differed from the original study. In our study, the Cognitive and Functional Impairment subscales showed a low-moderate correlation with the DASS-21 and a higher-moderate correlation with Personal Experience with Climate Change compared to the original study [39]. The Hogg Eco-Anxiety Scale [80] was translated and validated in Portugal [81] and measures eco-anxiety, which includes anxiety related to climate change

issues and various environmental calamities. Unlike the CAS, which focuses solely on climate change-related cognitive and functional impairment, the Hogg scale addresses a broader range of environmental concerns. Therefore, extending the original CAS study [39], we included this scale in our study and verified its concurrent validity through a strong correlation with the CAS. Nevertheless, our study was cross-sectional, indicating that future research in Portugal should seek to explore the temporal consistency of the CAS.

Although the Experience Climate Change factor was moderately correlated with Cognitive Impairment and Functional Impairment, Clayton and Karazsia proposed a second-order factor (Climate Anxiety Scale) comprising Cognitive and Functional Impairment [39]. The correlation analysis revealed a moderate multicollinearity risk among CAS, Cognitive Impairment, and Functional Impairment. VIF indicated a moderate but non-severe multicollinearity, and the tolerance value suggests no substantial multicollinearity risk. Therefore, it aligned with previous validation studies of this scale across diverse cultural contexts [102–105] that have retained the two-factor structure despite similar multicollinearity levels. Given the absence of severe multicollinearity in our data and alignment with established methodological precedents, we elected to maintain the original two-factor structure for consistency and comparability. Studies have found an association between natural disasters and poorer mental health [7], suggesting that future research could examine the impact of direct and indirect climate change experiences on climate change anxiety. This could help explain the observed correlations and enable the design of more effective psychological programs for individuals affected by climate change events. Overall, the CAS proved to be a reliable measure for assessing climate change anxiety. The increasing number of people experiencing direct or indirect effects of climate change underscores the need for validated measures in Portugal to assess anxiety related to this issue. Although the Portuguese validation of the CAS was conducted with the general population, resulting in possible floor effects (i.e., low mean scores for each item), it is crucial to study the CAS in a clinical population and in specific groups, such as climate change activists [57] or in younger or female populations [36], to identify cut-off points that distinguish adaptive anxiety from clinical anxiety.

Robust evidence linking nature connection to well-being raises questions about potential mediator and moderator mechanisms on this relationship. Our second and third aims are an attempt to answer those questions. A moderated mediation model was evaluated by examining whether climate change anxiety and environmental action would function as mediators on the association between connection to nature and well-being and testing whether self-compassion and receiving compassion from others would moderate the associations between connection to nature and climate change anxiety and connection to nature and well-being.

4.1. Connection to Nature and Climate Change Anxiety

Results from our model indicated that a greater connection to nature was associated with increased climate change anxiety. Participants with a stronger connection to nature may exhibit heightened environmental concern and are more likely to be vigilant to climate change threats, leading to an emotional response such as climate change anxiety [39].

4.2. Connection to Nature and Environmental Action

Our findings indicated that a stronger connection to nature was associated with increased environmental action. Participants who identify closely with nature and possess a sense of self-care may perceive the protection and care of nature as analogous to taking care of themselves. This aligns with previous research, which found that empathic feelings

and attitudes, derived from perspective-taking, serve as a motivation for engaging in pro-environmental behaviors [34].

4.3. Connection to Nature and Well-Being

Our findings indicate that a stronger connection to nature enhances well-being. Previous research has described that feeling connected to nature can evoke emotions such as wonder, awe, gratitude, and compassion [66]. Additionally, psychological theories suggest that psychopathology is often associated with mental inflexibility [62,106]. Therefore, a connection to nature may facilitate a shift from a narrow self-perspective to a broader perspective, thereby promoting psychological flexibility.

4.4. Climate Change Anxiety as a Mediator

Our results demonstrated that climate change anxiety mediated the association between connection to nature and well-being, as well as between connection to nature and environmental action. Numerous studies have correlated climate change with poor mental health and lower levels of well-being [4,40,41]. Therefore, participants with a higher connection to nature exhibited worse well-being, which could be attributed to an anxiety response related to environmental concern and heightened vigilance to climate change threats [39].

Additionally, a stronger connection to nature was linked to increased environmental actions, an association also mediated by climate change anxiety [39]. Previous studies have identified this mediation, suggesting that environmental action serves as a coping mechanism to alleviate the distress caused by climate change anxiety [59]. Furthermore, it has been found that collective environmental activism significantly reduces the impact of climate change anxiety on major depressive disorder more effectively than individual pro-environmental behavior [45]. Our results are in line with these previous studies, but further research is needed to explore and compare the effects of collective environmental activism and individual pro-environmental behaviors as responses to climate change anxiety.

4.5. Environmental Action as a Mediator

Our study confirmed that environmental action acts as a mediator in the relationship between climate change anxiety and well-being, as well as between connection to nature and well-being. Consistent with other research, our findings suggest that environmental activism enhances well-being and mitigates climate change anxiety [45,57]. Furthermore, we found that a stronger connection to nature predicts higher well-being. This can be explained by the similarity between feelings, attitudes, and behaviors towards nature and the concept of self-care and consequently by environmental action [34].

4.6. Self-Compassion and Receiving Compassion from Others as Moderators

In our models, self-compassion and receiving compassion from others emerged as moderators in the direct effect of connection to nature on well-being. The results indicated that, for participants with lower to medium levels of self-compassion (both self-directed and received from others), a higher connection to nature significantly enhanced well-being. We initially predicted that greater self-compassion would strengthen the positive impact of connection to nature on well-being. However, the findings revealed that among participants with higher levels of self-compassion, a greater connection to nature did not further enhance well-being. This suggests that individuals with higher self-compassion might have already achieved their maximum potential well-being, thus, a greater connection to nature does not seem to enhance well-being in them.

It is important to note that the construct of connection to nature encompasses various aspects such as heightened sensitivity (attentiveness to the suffering of nature), sympa-

thy (emotional responses to the suffering of nature), empathy (seeing the world from nature's perspective), care for nature's well-being, distress tolerance (ability to endure feelings arising from nature's suffering), and non-judgement (open acceptance that aids distress tolerance). These attributes seem to closely resemble the competencies and motivations associated with compassion. Future research could seek to further examine the potential correspondence and associations between the competencies/components of both constructs.

Additionally, physiological markers like heart rate variability, an indicator of parasympathetic nervous system activity, are associated with both connection to nature [68] and compassion [67]. Numerous studies have found a strong correlation between compassion and well-being [79,107]. This raises the question: Could interventions that combine nature immersion with compassion training accelerate the development of compassion's competencies and motivations and have beneficial psychophysiological effects? Aligned with studies that integrate connection to nature with compassion [19], future research could explore this relationship further. Specifically, examining the psychophysiological effects of psychological intervention programs that target both connection to nature and compassion, such as forest bathing [20] and compassionate mind training [61], could provide valuable insights into the feasibility, usefulness, and effectiveness of such interventions to improve well-being.

Conversely, self-compassion and receiving compassion from others did not moderate the association between connection to nature and climate change anxiety. Across varying levels of self-compassion and compassion from others, a higher connection to nature was consistently linked to increased climate change anxiety. This sample, drawn from the general population, exhibited a potential floor effect in the CAS results. Consequently, the levels of climate change anxiety observed can be considered normative and adaptive. Therefore, higher levels of compassion did not mitigate the increase in climate change anxiety associated with a greater connection to nature. Future research could investigate this model within a clinical sample and in specific groups (e.g., climate change activists, youth, or female populations) where non-adaptive climate change anxiety could be more prevalent.

5. Limitations

This study has limitations that should be considered when interpreting our findings and that future research should seek to address. First, as a cross-sectional study, the CAS was not evaluated for temporal stability. The observed multicollinearity between factors may suggest limited discriminant validity in the bifactor structure of the scale. However, variance inflation factor (VIF) values fell below critical thresholds (VIF < 5), indicating moderate rather than severe multicollinearity. Tolerance metrics supported this interpretation, with values exceeding 0.1, which aligns with established thresholds for acceptable collinearity. Furthermore, in our moderated mediation model, the directionality of the effects was hypothesized based on existing literature; however, the results should be regarded as preliminary. We encourage the scientific community to replicate this cross-sectional study. Nevertheless, the causality of the relationship between variables cannot be determined from our findings, without longitudinal or experimental research, causal inferences regarding these relationships cannot be drawn, as the associations may be bidirectional. In addition, this model explained 37% of the variance in levels of well-being, raising the question of whether there are other variables that could better explain variance in levels of well-being when associated with a higher connection to nature. Furthermore, our study did not assess compassion towards nature. The CEAS self-compassion scale and receiving compassion from others scale do not have items addressing questions related to compassion engagement and action towards nature suffering. Interestingly, some literature

links connection to nature to a different form of compassion, known as unified compassion. This type of compassion is characterized by a human experience that transcends the dualities of subject and object, self and other, and mind versus body [74,75]. Due to the absence of a measure for this construct, this study was unable to assess its existence.

The sample was collected exclusively online, and although routine strategies were used to mitigate the risks associated with the online modality [108], the sample might not be representative of the population due to self-selection bias. Finally, participants using self-response instruments are influenced by social desirability factors, which can bias their answers due to these factors.

6. Conclusions

Adapting the CAS assessment tool to Portuguese and evaluating its psychometric properties is a crucial step towards validating its use in clinical psychology and advancing climate change research. The study underscores the complex relationship between humans and nature, showing that a stronger connection to nature can both enhance well-being and increase climate change anxiety. This dual effect highlights the evolutionary roots of human interactions with nature and the challenges posed by modern environmental issues. Importantly, the research found that individuals with lower levels of self-compassion and compassion from others experience greater improvements in well-being when they feel more connected to nature, whereas this benefit is not as pronounced in those with higher compassion. These findings suggest that nature-based interventions, when combined with compassion-focused approaches such as compassionate mind training, could be particularly effective in promoting well-being and helping individuals cope with climate change anxiety. Overall, fostering both a connection to nature and compassion may be key to supporting mental health and encouraging sustainable behaviors in the face of environmental challenges.

Author Contributions: Conceptualization, A.P. and M.M.; methodology, A.P and M.M.; validation, A.P and M.M.; formal analysis, A.P. and M.M.; investigation, A.P. and M.M.; resources, A.P. and M.M.; data curation, A.P.; writing—original draft preparation, A.P. and M.M.; writing—review and editing, A.P. and M.M.; visualization, A.P. and M.M.; supervision, M.M.; project administration, A.P. and M.M. All authors have read and agreed to the published version of the manuscript.

Funding: This work was supported by CINEICC's strategic project UID/PSI/00730/2020 funded by the Portuguese Foundation for Science and Technology (FCT—Fundação para a Ciência e a Tecnologia, I.P./MCTES).

Institutional Review Board Statement: Ethics approval for the present study was granted by Ethics and Deontology of Research Commission at Faculty of Psychology and Education Sciences in University of Coimbra (UC; CEDI:FPCEUC:81/4). All research was performed in accordance with regulations specified in the ethics approval and in accordance with the Declaration of Helsinki.

Informed Consent Statement: Informed consent was obtained from all subjects involved in the study.

Data Availability Statement: This study is an ongoing study, and data that supports the findings are available from the corresponding author, AP, upon reasonable request.

Conflicts of Interest: The authors declare no conflicts of interest.

Appendix A

Table A1. Sociodemographic differences between samples.

Variables	Sample 1 (*n* = 261)	Sample 2 (*n* = 261)	t/χ2	d/V
Age *M(SD)*	44.29 (11.82)	44.65 (11.71)	−0.34 (520)	0.03
Gender *n* (%) *Female*	187 (71.6)	168 (67.47)	3.97	0.09
Residence *n* (%) *Urban*	115 (44.06)	113 (45.38)	1.16	0.05
Ethnia *n* (%) *Caucasian*	214 (81.99)	220 (88.35)	10.64	0.14
Education level *n* (%) *Higher education*	165 (63.22)	160 (64.26)	0.06	0.01
Marital status *n* (%) *Married*	163 (62.45)	148 (59.44)	0.49	0.03
Children *n* (%) *Yes*	183 (70.11)	159 (63.86)	2.26	0.07
Socioeconomic level *n* (%) *Medium*	123 (47.13)	117 (40.21)	0.01	0.00
Physical health *n* (%) *Good*	145 (55.56)	115 (46.18)	8.02	0.13
Mental health *n* (%) *Good*	131 (50.19)	130 (52.21)	2.25	0.07
Psi/psi counseling *n* (%) *No*	227 (86.97)	216 (86.75)	0.01	0.00
Contemplative practices *n* (%) *No*	207 (79.30)	190 (76.31)	2.38	0.07

Table A2. Normality analysis of variables in study.

Variables	*M*	*SD*	Skewness	Kurtosis
CNS	25.53	6.59	−0.52	−0.29
Cognitive impairment	11.80	4.45	1.78	3.94
Functional impairment	7.12	2.91	1.72	2.83
CAS	18.92	6.89	1.82	4.02
Participatory action	11.11	8.73	1.12	1.00
Leadership action	2.85	4.63	2.26	5.06
Environmental action	13.96	12.66	1.43	1.84
Wellbeing	7.08	1.69	−1.10	2.04
Self-compassion engagement	37.58	9.99	−0.52	0.59
Self-compassion action	28.24	8.31	−0.60	−0.13
Self-compassion_total	65.82	16.62	−0.67	0.60
Compassion from others engagement	34.11	10.84	−0.11	−0.26
Compassion from others action	24.07	8.01	−0.27	−0.23
Compassion from others_total	58.17	18.22	−0.19	−0.25

Note. CNS = Brief Version Connectedness to Nature Scale; CAS = Climate Change Anxiety Scale.

Table A3. Normality Analysis Of Items Of CAS.

Items	*M*	*SD*	Skewness	Kurtosis
CAS1	1.99	0.95	0.59	−0.47
CAS2	1.72	0.82	0.90	0.26
CAS3	1.40	0.72	2.01	4.23
CAS4	1.27	0.60	2.43	6.03
CAS5	1.51	0.80	1.48	1.28
CAS6	1.25	0.59	2.66	7.70
CAS7	1.25	0.61	2.60	6.37
CAS8	1.41	0.73	1.88	3.22
CAS9	1.35	0.67	1.96	3.36
CAS10	1.77	0.94	0.97	−0.01
CAS11	1.29	0.58	2.29	6.36
CAS12	1.32	0.63	2.17	5.13
CAS13	1.39	0.78	2.20	4.43
CAS14	1.68	0.92	1.24	0.81
CAS15	1.79	1.02	1.09	0.30
CAS16	2.32	1.19	0.48	−0.74
CAS17	2.88	1.10	−0.01	−0.56
CAS18	4.28	0.96	−1.30	1.11
CAS19	4.45	0.76	−1.57	3.25
CAS20	4.03	0.94	−1.00	1.05
CAS21	3.20	1.26	−0.20	−0.95
CAS22	3.65	1.09	−0.51	−0.31

Table A4. Comparing categories within sociodemographic variables in study variables.

F Test	Gender				Area					NSE					Etnia			
	F	M	*F* Test	η^2	R	SU	U	*F* Test	η^2	L	M	H	*F* Test	η^2	*F* Test	*DF*	*p*-Value	η^2
Variable	M (SD)	M (SD)			M(SD)	M(SD)	M(SD)			M(SD)	M(SD)	M(SD)						
CNS	26.17 (6.40)	24.02 (6.82)	4.37 **	0.03	25.23 (6.45)	27.88 (5.46)	25.04 (6.90)	5.74 **	0.02	25.27 (6.89	25.26 (6.70)	26.56 (5.35)	1.06	0.01	0.97	10.499	0.47	0.02
CAS	19.33 (7.32)	17.99 (5.73)	1.70	0.01	19.43 (7.66)	19.25 (7.03)	18.34 (6.05)	1.48	0.01	20.46 (7.72)	18.40 (6.58)	18.39 (5.94)	2.65 *	0.02	2.08	10.499	0.02	0.04
EAS	14.10 (12.32)	13.57 (13.51)	0.24	0.00	14.93 (12.88)	15.03 (14.39)	12.73 (11.77)	1.96	0.01	14.45 (14.11)	14.91 (13.57)	11.37 (8.33)	1.97	0.01	0.41	10.499	0.94	0.01
WB	7.09 (1.67)	7.05 (1.71)	1.53	0.01	7.20 (1.64)	7.32 (1.59)	6.89 (1.75)	2.76	0.01	6.56 (1.78)	7.20 (1.69)	7.42 (1.32)	5.60 ***	0.03	0.76	10.499	0.67	0.02
SC	67.59 (15.92)	61.79 (17.26)	7.12 ***	0.04	66.29 (16.38)	67.09 (17.16)	64.96 (16.69)	0.60	0.00	64.42 (16.90)	65.63 (17.49)	68.27 (12.33)	1.09	0.01	1.79	10.499	0.06	0.04
CFO	59.20 (18.52)	55.46 (17.27)	2.40	0.01	57.54 (17.35)	58.71 (18.44)	58.57 (18.96)	0.21	0.00	57.81 (18.29)	57.48 (18.83)	60.33 (15.44)	0.62	0.00	0.39	10.499	0.95	0.01

* $p < 0.050$ ** $p < 0.010$ *** $p < 0.001$. CNS = Brief Version Connectedness to Nature Scale; CAS = Climate Change Anxiety Scale; EAS = Environmental Action Scale; WB = Well-Being (PERMA); SC = Compassionate Engagement and Action–Self-Compassion scale; CFO = Compassionate Engagement and Action-Compassion from Others Subscale; F = female; M = male; R = rural; SU = semi-urban; U = urban; L = low; M = middle; H = high.

Table A5. Correlation table between sociodemographic variables and variables in study.

Correlation (r/r_s)	CNS	CAS	EAS	WB	SC	CFO
Education level [a] (r)	0.08	−0.10 *	0.14 **	0.06	0.11 *	0.11 *
Marital_Status [b] (r)	0.01	0.02	−0.03	0.09 *	−0.09 *	−0.09 *
Children [c] (r)	0.03	0.05	−0.01	0.01	−0.03	−0.15 **
Psi/psi counseling [d] (r)	−0.09	−0.06	−0.07	0.09	0.03	0.04
Contemplative practices [e] (r)	0.21 **	0.08	0.14 **	0.06	0.10 *	0.02
Age (r_s)	0.17 **	0.10 *	0.05	0.10 *	0.01	−0.12 **
Physical health (r_s)	−0.01	−0.14 *	−0.01	0.27 **	0.15 **	0.11 *
Mental health (r_s)	0.01	−0.19 **	−0.07	0.39 **	0.24 **	0.15 **

* $p < 0.050$. ** $p < 0.010$. Note. (r) Pearson's r; (r_s) Spearman's rho; [a] Education: 0 = secondary school or below, 1 = Higher education. [b] Current marital status: 0 = single, 1 = married. [c] Children: 0 = no children; 1 = children. [d] Psychological or psychiatric counseling: 0 = no; 1 = yes. [e] Contemplative practices: 0 = no; 1 = yes. CNS = Brief Version Connectedness to Nature Scale; CAS = Climate Change Anxiety Scale; EAS = Environmental Action Scale; WB = Well-Being (PERMA); SC = Compassionate Engagement and Action–Self-Compassion scale; CFO = Compassionate Engagement and Action-Compassion from Others Subscale.

References

1. Clayton, S.; Manning, C.; Speiser, M.; Hill, A. *Mental Health and Our Changing Climate: Impacts, Inequities, Responses*; American Psychological Association, and ecoAmerica: Washington, DC, USA, 2021. Available online: https://www.apa.org/news/press/releases/mental-health-climate-change.pdf (accessed on 8 June 2024).
2. IPCC. Contribution of Working Groups I, II and III to the Sixth Assessment Report of the Intergovernmental Panel on Climate Change. In *Climate Change 2023: Synthesis Report*; Lee, H., Romero, J., Eds.; IPCC: Geneva, Switzerland, 2023; pp. 35–115. [CrossRef]
3. Gupta, S.; Rouse, B.; Sarangi, P. Did Climate Change Influence the Emergence, Transmission, and Expression of the COVID-19 Pandemic? *Front. Med.* **2021**, *8*, 769208. [CrossRef]
4. Charlson, F.; Ali, S.; Benmarhnia, T.; Pearl, M.; Massazza, A.; Augustinavicius, J.; Scott, J.G. Climate Change and Mental Health: A Scoping Review. *Int. J. Environ. Res. Public Health* **2021**, *18*, 4486. [CrossRef]
5. Liu, J.; Varghese, B.; Hansen, A.; Xiang, J.; Zhang, Y.; Dear, K.; Gourley, M.; Driscoll, T.; Morgan, G.; Capon, A.; et al. Is there an association between hot weather and poor mental health outcomes? A systematic review and meta-analysis. *Environ. Int.* **2021**, *153*, 106533. [CrossRef] [PubMed]
6. Obradovich, N.; Migliorini, R.; Paulus, M.P.; Rahwan, I. Empirical evidence of mental health risks posed by climate change. *Proc. Natl. Acad. Sci. USA* **2018**, *115*, 10953–10958. [CrossRef] [PubMed]
7. Beaglehole, B.; Mulder, R.; Frampton, C.; Boden, J.; Newton-Howes, G.; Bell, C. Psychological distress and psychiatric disorder after natural disasters: Systematic review and meta-analysis. *Br. J. Psychiatry* **2018**, *213*, 716–722. [CrossRef]
8. Kellert, S.R. *Birthright: People and Nature in the Modern World*; Yale University Press: New Haven, CT, USA, 2012; pp. 49–66. [CrossRef]
9. Baumeister, R.F.; Leary, M.R. The need to belong: Desire for interpersonal attachments as a fundamental human motivation. *Psychol. Bull.* **1995**, *117*, 497–529. [CrossRef] [PubMed]
10. Bowlby, J. Attachment and loss: Retrospect and prospect. *Am. J. Orthopsychiatry* **1982**, *52*, 664–678. [CrossRef]
11. Bachelard, G. *The Poetics of Space*; Orion Press, Inc.: Phoenix, AZ, USA, 1964; pp. 3–37.
12. Fromm, E. *The Heart of Man: Its Genius for Good and Evil*, 2nd ed.; Harper & Row: San Francisco, CA, USA, 1980; Volume 12.
13. Wilson, E.O. *Biophilia*; Harvard University Press: Cambridge, MA, USA, 1984.
14. Kellert, S.R.; Wilson, E.O. *The Biophilia hypothesis*; Island Press: Washington, DC, USA, 1993.
15. Ulrich, R.S. View through a window may influence recovery from surgery. *Science* **1984**, *224*, 420–421. [CrossRef]
16. Kaplan, S. The restorative benefits of nature: Toward an integrative framework. *J. Environ. Psychol.* **1995**, *15*, 169–182. [CrossRef]
17. Appleton, J. The experience of landscape. *Landsc. Res.* **1975**, *1*, 15–16. [CrossRef]
18. Gatersleben, B.; Andrews, M. When walking in nature is not restorative-the role of prospect and refuge. *Health Place* **2013**, *20*, 91–101. [CrossRef] [PubMed]
19. McEwan, K.; Giles, D.; Clarke, F.J.; Kotera, Y.; Evans, G.; Terebenina, O.; Minou, L.; Teeling, C.; Basran, J.; Wood, W.; et al. A Pragmatic Controlled Trial of Forest Bathing Compared with Compassionate Mind Training in the UK: Impacts on Self-Reported Wellbeing and Heart Rate Variability. *Sustainability* **2021**, *13*, 1380. [CrossRef]
20. McEwan, K.; Potter, V.; Kotera, Y.; Jackson, J.E.; Greaves, S. 'This Is What the Colour Green Smells Like!': Urban Forest Bathing Improved Adolescent Nature Connection and Wellbeing. *Int. J. Environ. Res. Public Health* **2022**, *19*, 15594. [CrossRef]
21. Mayer, F.S.; Frantz, C.M. The connectedness to nature scale: A measure of individuals' feeling in community with nature. *J. Environ. Psychol.* **2004**, *24*, 503–515. [CrossRef]
22. Perrin, J.L.; Benassi, V.A. The connectedness to nature scale: A measure of emotional connection to nature? *J. Environ. Psychol.* **2009**, *29*, 434–440. [CrossRef]
23. Davis, J.L.; Green, J.D.; Reed, A. Interdependence with the environment: Commitment, interconnectedness, and environmental behaviour. *J. Environ. Psychol.* **2009**, *29*, 173–180. [CrossRef]
24. Clayton, S. Environmental Identity: A Conceptual and an Operational Definition. In *Identity and the Natural environment: The Psychological Significance of Nature*; Clayton, S., Opotow, S., Eds.; MIT Press: Cambridge, MA, USA, 2003; pp. 45–65. [CrossRef]
25. Tam, K.P. Concepts and measures related to connection to nature: Similarities and differences. *J. Environ. Psychol.* **2013**, *34*, 64–78. [CrossRef]
26. Mackay, C.M.L.; Schmitt, M.T. Do people who feel connected to nature do more to protect it? A meta-analysis. *J. Environ. Psychol.* **2019**, *65*, 101323. [CrossRef]
27. Kaplan, R.; Kaplan, S. *The Experience of Nature: A Psychological Perspective*; Cambridge University Press: Cambridge, UK, 1989.
28. European Commission Directorate-General for Communication (2023). Special Eurobarometer 538 Climate Change. In *Special Eurobarometer 538 Climate Change-Report*; Directorate-General for Climate Action (European Commission), Ed.; Directorate-General for Communication: Brussels, Belgium, 2023. [CrossRef]
29. Spence, A.; Poortinga, W.; Pidgeon, N. The psychological distance of climate change. *Risk Anal.* **2012**, *32*, 957–972. [CrossRef]

30. Kennerley, H.; Kirk, J.; Westbrook, D. *An Introduction to Cognitive Behaviour Therapy*, 3rd ed.; SAGE Publications: Thousand Oaks, CA, USA, 2016.
31. van der Linden, S. The social-psychological determinants of climate change risk perceptions: Towards a comprehensive model. *J. Environ. Psychol.* **2015**, *41*, 112–124. [CrossRef]
32. Damásio, A. *O Erro de Descartes, Emoção, Razão e Cérebro Humano*; Temas e Debates: Lisboa, Portugal, 1994.
33. Swim, J.K.; Stern, P.C.; Doherty, T.J.; Clayton, S.; Reser, J.P.; Weber, E.U.; Gifford, R.; Howard, G.S. Psychology's contributions to understanding and addressing global climate change. *Am. Psychol.* **2011**, *66*, 241–250. [CrossRef]
34. Schultz, P.W. Empathizing with nature: The effects of perspective taking on concern for environmental issues. *J. Soc. Issues* **2000**, *56*, 391–406. [CrossRef]
35. Stern, P.C.; Dietz, T.; Kalof, L. Value orientations, gender, and environmental concern. *Environ. Behav.* **1993**, *25*, 322–348. [CrossRef]
36. van der Linden, S. Determinants and measurements of climate change risk perception, worry, and concern. In *The Oxford Encyclopedia of Climate Change Communication*; Nisbet, M.C., Schafer, M., Markowitz, E., Ho, S., O'Neill, S., Thaker, J., Eds.; Oxford University Press: Oxford, UK, 2017. [CrossRef]
37. Beck, J.S.; Liese, B.S.; Najavits, L.M. Cognitive Therapy. In *Clinical Textbook of Addictive Disorders*, 3rd ed.; Frances, R.J., Miller, S.I., Mack, A.H., Eds.; Guilford Publications: New York, NY, USA, 2005; pp. 474–501.
38. Barlow, D.H. *Anxiety and Its Disorders: The Nature and Treatment of Anxiety and Panic*, 2nd ed.; The Guilford Press: New York, NY, USA, 2002.
39. Clayton, S.; Karazsia, B.T. Development and validation of a measure of climate change anxiety. *J. Environ. Psychol.* **2020**, *69*, 101434. [CrossRef]
40. Burke, M.; González, F.; Baylis, P.; Heft-Neal, S.; Baysan, C.; Basu, S.; Hsiang, S. Higher temperatures increase suicide rates in the United States and Mexico. *Nat. Clim. Change* **2018**, *8*, 723–729. [CrossRef]
41. Nori-Sarma, A.; Sun, S.; Sun, Y.; Spangler, K.R.; Oblath, R.; Galea, S.; Gradus, J.L.; Wellenius, G.A. Association between ambient heat and risk of emergency department visits for mental health among US adults, 2010 to 2019. *JAMA Psychiatry* **2022**, *79*, 341–349. [CrossRef]
42. Berry, H.L.; Bowen, K.; Kjellstrom, T. Climate change and mental health: A causal pathways framework. *Int. J. Public Health* **2010**, *55*, 123–132. [CrossRef]
43. Ellis, N.R.; Albrecht, G.A. Climate change threats to family farmers' sense of place and mental wellbeing: A case study from the Western Australian Wheatbelt. *Soc. Sci. Med.* **2017**, *175*, 161–168. [CrossRef]
44. Verplanken, B.; Marks, E.; Dobromir, A.I. On the nature of eco-anxiety: How constructive or unconstructive is habitual worry about global warming? *J. Environ. Psychol.* **2020**, *72*, 101528. [CrossRef]
45. Schwartz, S.E.O.; Benoit, L.; Clayton, S.; Parnes, M.F.; Swenson, L.; Lowe, S.R. Climate change anxiety and mental health: Environmental activism as buffer. *Curr. Psychol.* **2022**, *42*, 16708–16721. [CrossRef]
46. Kollmuss, A.; Agyeman, J. Mind the Gap: Why do people act environmentally and what are the barriers to pro-environmental behaviour? *Environ. Educ. Res.* **2002**, *8*, 239–260. [CrossRef]
47. Chawla, L. Significant life experiences revisited: A review of research on sources of environmental sensitivity. *J. Environ. Educ.* **1998**, *29*, 11–21. [CrossRef]
48. Helm, S.V.; Pollitt, A.; Barnett, M.A.; Curran, M.A.; Craig, Z.R. Differentiating environmental concern in the context of psychological adaption to climate change. *Glob. Environ. Change* **2018**, *48*, 158–167. [CrossRef]
49. Bradley, G.L.; Babutsidze, Z.; Chai, A.; Reser, J.P. The role of climate change risk perception, response efficacy, and psychological adaptation in pro-environmental behavior: A two nation study. *J. Environ. Psychol.* **2020**, *68*, 101410. [CrossRef]
50. Steg, L.; de Groot, J. *Environmental Psychology: An Introduction*, 2nd ed.; Wiley: Hoboken, NJ, USA, 2018. [CrossRef]
51. Kleres, J.; Wettergren, A. Fear, hope, anger, and guilt in climate activism. *Soc. Mov. Stud.* **2017**, *16*, 507–519. [CrossRef]
52. Stanley, S.; Hogg, T.; Leviston, Z.; Walker, I. From anger to action: Differential impacts of eco-anxiety, eco-depression, and eco-anger on climate action and well-being. *J. Clim. Change Health* **2021**, *1*, 100003. [CrossRef]
53. DeAngelo, L.; Schuster, M.T.; Stebleton, M.J. California DREAMers: Activism, identity, and empowerment among undocumented college students. *J. Divers. High. Educ.* **2016**, *9*, 216–230. [CrossRef]
54. Corral-Verdugo, V.; Durón, F.; Frías, M.; Tapia, C.O.; Fraijo, B.; Gaxiola, J. Socio-physical environmental factors and sustainable behaviour as indicators of family positivity. *PsyEcol. Biling. J. Environ. Psychol.* **2015**, *6*, 146–168. [CrossRef]
55. Clayton, S. Climate Change and Mental Health. *Curr. Environ. Health Rep.* **2021**, *8*, 1–6. [CrossRef]
56. Albright, J.N.; Hurd, N.M. Activism, social support, and trump-related distress: Exploring associations with mental health. *J. Divers. High. Educ.* **2023**, *16*, 1–12. [CrossRef]
57. Alisat, S.; Riemer, M. The environmental action scale: Development and psychometric evaluation. *J. Environ. Psychol.* **2015**, *43*, 13–23. [CrossRef]
58. Flanagan, C.A.; Cumsille, P.; Gill, S.; Gallay, L.S. *Sense of Community Connectedness Scale [Database Record]*; APA PsycTests: Washington, DC, USA, 2007. [CrossRef]

59. Boehnke, K.; Wong, B. Adolescent political activism and long-term happiness: A 21-year longitudinal study on the development of micro- and macrosocial worries. *Personal. Soc. Psychol. Bull.* **2011**, *37*, 435–447. [CrossRef] [PubMed]
60. Gilbert, P. The evolution and social dynamics of compassion. *Soc. Personal. Psychol. Compass* **2015**, *9*, 239–254. [CrossRef]
61. Gilbert, P. *Compassion: Conceptualisations, Research and Use in Psychotherapy*; Routledge: Abingdon, UK, 2005. [CrossRef]
62. Gilbert, P. *The Compassionate Mind: A new Approach to the Challenge of Life*; Constable & Robinson: London, UK, 2009.
63. Gilbert, P. *Compassion Focused Therapy: The CBT Distinctive Features Series*; Routledge: Abingdon, UK, 2010. [CrossRef]
64. Castelo, N.; White, K.; Goode, M.R. Nature promotes self-transcendence and prosocial behavior. *J. Environ. Psychol.* **2021**, *76*, 101639. [CrossRef]
65. Zelenski, J.M.; Dopko, R.L.; Capaldi, C.A. Cooperation is in our nature: Nature exposure may promote cooperative and environmentally sustainable behavior. *J. Environ. Psychol.* **2015**, *42*, 24–31. [CrossRef]
66. Stellar, J.E.; Gordon, A.M.; Piff, P.K.; Cordaro, D.; Anderson, C.L.; Bai, Y.; Maruskin, L.A.; Keltner, D. Self-transcendent emotions and their social functions: Compassion, gratitude, and awe bind us to others through prosociality. *Emot. Rev.* **2017**, *9*, 200–207. [CrossRef]
67. Kim, J.J.; Cunnington, R.; Kirby, J.N. The neurophysiological basis of compassion: An fMRI meta-analysis of compassion and its related neural processes. *Neurosci. Biobehav. Rev.* **2020**, *108*, 112–123. [CrossRef] [PubMed]
68. Farrow, M.R.; Washburn, K. A Review of Field Experiments on the Effect of Forest Bathing on Anxiety and Heart Rate Variability. *Glob. Adv. Health Med.* **2019**, *8*, 2164956119848654. [CrossRef]
69. Kirby, J.N.; Tellegen, C.L.; Steindl, S.R. A Meta-Analysis of Compassion-Based Interventions: Current State of Knowledge and Future Directions. *Behav. Ther.* **2017**, *48*, 778–792. [CrossRef]
70. Cassidy, T.; Elliott, E. Beliefs, attitudes and intentions towards environmental issues: The role of self-compassion and wellbeing. *J. Psychol. Clin. Psychiatry* **2024**, *15*, 87–92. [CrossRef]
71. Neff, K.; Germer, C. Self-compassion and psychological well-being. In *The Oxford Handbook of Compassion Science*; Seppälä, E.M., Simon-Thomas, E., Brown, S.L., Worline, M.C., Cameron, C.D., Doty, J.R., Eds.; Oxford University Press: Oxford, UK, 2017; pp. 371–385.
72. Manneh, A. A mind, brain, health and education approach to nature-induced compassion: Assessment of the potential of exposure to nature as a protective factor to induce nondual compassion in adults. *ResearchGate* **2021**, preprint. [CrossRef]
73. Schoenberg, P.L.A.; Vago, D.R. Mapping meditative states and stages with electrophysiology: Concepts, classifications, and methods. *Curr. Opin. Psychol.* **2019**, *28*, 211–217. [CrossRef]
74. Josipovic, Z. Neural correlates of nondual awareness in meditation. *Ann. New York Acad. Sci.* **2014**, *1307*, 9–18. [CrossRef] [PubMed]
75. Josipovic, Z. Love and compassion meditation: A nondual perspective. *Ann. New York Acad. Sci.* **2016**, *1373*, 65–71. [CrossRef]
76. Imperatori, C.; Massullo, C.; De Rossi, E.; Carbone, G.A.; Theodorou, A.; Scopelliti, M.; Romano, L.; Del Gatto, C.; Allegrini, G.; Carrus, G.; et al. Exposure to nature is associated with decreased functional connectivity within the distress network: A resting state EEG study. *Front. Psychol.* **2023**, *14*, 1171215. [CrossRef] [PubMed]
77. Crutzen, P.J.; Stoermer, E.F. The 'Anthropocene' (2000). In *Paul J. Crutzen and the Anthropocene: A New Epoch in Earth's History*; Benner, S., Lax, G., Crutzen, P.J., Pöschl, U., Lelieveld, J., Brauch, H.G., Eds.; Springer: Berlin, Germany, 2021; Volume 1, pp. 19–21. [CrossRef]
78. Galway, L.P.; Beery, T. Exploring climate emotions in Canada's provincial north. *Front. Psychol.* **2022**, *13*, 920313. [CrossRef]
79. Gilbert, P. Evolution, Compassion, and Wellbeing. In *Toward an Integrated Science of Wellbeing*; Rieger, E., Costanza, R., Kubiszewski, I., Dugdale, P., Eds.; Oxford Academic Press: Oxford, UK, 2023; pp. 87–107. [CrossRef]
80. Hogg, T.L.; Stanley, S.K.; O'Brien, L.V.; Wilson, M.S.; Watsford, C.R. The Hogg Eco-Anxiety Scale: Development and validation of a multidimensional scale. *Glob. Environ. Change* **2021**, *71*, 102391. [CrossRef]
81. Sampaio, F.; Costa, T.; Teixeira-Santos, L.; de Pinho, L.G.; Sequeira, C.; Luís, S.; Loureiro, A.; Soro, J.C.; Roldán Merino, J.; Moreno Poyato, A.; et al. Validating a measure for eco-anxiety in Portuguese young adults and exploring its associations with environmental action. *BMC Public Health* **2023**, *23*, 1905. [CrossRef] [PubMed]
82. Carmona, B.; Loureiro, A.; Aguilar-Luzón, M.C. Environmental Action Scale: Psychometric properties of the Portuguese version (Escala de Acciones Ambientales: Propiedades psicométricas de la versión portuguesa). *Psyecology* **2021**, *12*, 24–44. [CrossRef]
83. Pasca, L.; Aragonés, J.I.; Coello, M.T. An analysis of the connectedness to nature scale based on item response theory. *Front. Psychol.* **2017**, *8*, 1330. [CrossRef]
84. Loureiro, A.; Olivos, P. The role of environmental values, environmental identity, and contact with nature, in predicting support for pro-environmental behaviours. In Proceedings of the International Conference on Environmental Psychology, A Coruña, Spain, 30 August–1 September 2017.
85. Gilbert, P.; Catarino, F.; Duarte, C.; Matos, M.; Kolts, R.; Stubbs, J.; Ceresatto, L.; Duarte, J.; Pinto-Gouveia, J.; Basran, J. The development of compassionate engagement and action scales for self and others. *J. Compassionate Health Care* **2017**, *4*, 4. [CrossRef]

86. Matos, M.; Duarte, C.; Pinto-Gouveia, J. Constructing a self-protected against shame: The importance of warmth and safeness memories and feelings on the association between shame memories and depression. *Int. J. Psychol. Psychol. Ther.* **2015**, *15*, 317–335.
87. Lovibond, P.F.; Lovibond, S.H. The Structure of Negative Emotional States: Comparison of the Depression Anxiety Stress Scales (DASS) with the Beck Depression and Anxiety Inventories. *Behav. Res. Ther.* **1995**, *33*, 335–343. [CrossRef] [PubMed]
88. Pais-Ribeiro, J.L.; Honrado, A.; Leal, I. Contribuição para o Estudo da Adaptação Portuguesa das Escalas de Ansiedade, Depressão e Stress de Lovibond e Lovibond. *Psicol. Saúde Doenças* **2004**, *36*, 229–239.
89. Butler, J.; Kern, M.L. The PERMA-Profiler: A brief multidimensional measure of flourishing. *Int. J. Wellbeing* **2016**, *6*, 1–48. [CrossRef]
90. Alves, M.; Lourenço, M.; Brito, A.; Gouveia, M. Confirmação da estrutura fatorial da versão portuguesa do questionário de Florescimento Psicológico—PERMA-Profiler 2016. In Proceedings of the 3º Congresso da Ordem dos Psicólogos Portugueses, Porto, Portugal, 28 September–1 October 2016.
91. Arbuckle, J. *Amos*; (Version 27.0); [Computer Program]; IBM: Chicago, IL, USA, 2020.
92. Kline, R.B. *Principles and Practice of Structural Equation Modelling*, 3rd ed.; Guilford Press: New York, NY, USA, 2011.
93. Tabachnick, B.G.; Fidell, L.S. *Using Multivariate Statistics*, 6th ed.; Pearson Education: London, UK, 2013.
94. Cohen, J. *Statistical Power Analysis for the Behavioural Sciences*, 2nd ed.; Routledge: Abingdon, UK, 1988. [CrossRef]
95. Field, A. *Discovering Statistics Using SPSS*, 5th ed.; Sage Publications, Inc.: Thousand Oaks, CA, USA, 2018.
96. Byrne, B. *Structural Equation Modeling with AMOS*, 3rd ed.; Routledge: New York, NY, USA, 2016. [CrossRef]
97. George, D.; Mallery, P. *Using SPSS for Windows Step by Step: A Simple Guide and Reference*, 4th ed.; Pearson Education: London, UK, 2003.
98. Hayes, A.F. *Introduction to Mediation, Moderation, and Conditional Process Analysis: A Regression-Based Approach*, 2nd ed.; Guilford Press: New York, NY, USA, 2013.
99. Cohen, J.; Cohen, P.; West, S.G.; Aiken, L.S. *Applied Multiple Regression/Correlation Analysis for the Behavioral Sciences*, 3rd ed.; Lawrence Erlbaum Associates Publishers: Mahwah, NJ, USA, 2003.
100. Kutner, M.; Nachtsheim, C.; Neter, J.; Li, W. *Applied Linear Statistical Models*, 5th ed; McGraw-Hill: Irwin, NY, USA, 2005.
101. Kyriazos, T.; Poga, M. Dealing with multicollinearity in factor analysis: The problem, detections, and solutions. *Open J. Stat.* **2023**, *13*, 404–424. [CrossRef]
102. Mouguiama-Daouda, C.; Blanchard, M.; Coussement, C.; Heeren, A. On the Measurement of Climate Change Anxiety: French Validation of the Climate Anxiety Scale. *Psychol. Belg.* **2022**, *62*, 123–135. [CrossRef]
103. Cruz, S.; High, A. Psychometric properties of the Climate Change Anxiety Scale. *J. Environ. Psychol.* **2022**, *84*, 101905. [CrossRef]
104. Innocenti, M.; Santarelli, G.; Vanessa Faggi, V.; Castellini, G.; Manelli, I.; Magrini, G.; Galassi, F.; Ricca, V. Psychometric properties of the Italian version of the Climate Change Anxiety Scale. *J. Clim. Change Health* **2021**, *3*, 2667–2782. [CrossRef]
105. Larionow, P.; Sołtys, M.; Izdebski, P.; Mudło-Głagolska, K.; Golonka, J.; Demski, M.; Rosińska, M. Climate Change Anxiety assessment: The psychometric properties of the Polish version of the Climate Anxiety Scale. *Front. Psychol.* **2022**, *13*, 870392. [CrossRef]
106. Hayes, S.; Strosahl, K.; Wilson, K. *Acceptance and Commitment Therapy: The Process and Practice of Mindful Change*, 2nd ed.; Guilford Press: New York, NY, USA, 2012.
107. Matos, M.; Albuquerque, I.; Galhardo, A.; Cunha, M.; Pedroso Lima, M.; Palmeira, L.; Petrocchi, N.; McEwan, K.; Maratos, F.A.; Gilbert, P. Nurturing compassion in schools: A randomized controlled trial of the effectiveness of a Compassionate Mind Training program for teachers. *PLoS ONE* **2022**, *17*, e0263480. [CrossRef] [PubMed]
108. Godinho, A.; Schell, C.; Cunningham, J.A. Out damn bot, out: Recruiting real people into substance use studies on the internet. *Subst. Abus.* **2020**, *41*, 3–5. [CrossRef] [PubMed]

Disclaimer/Publisher's Note: The statements, opinions and data contained in all publications are solely those of the individual author(s) and contributor(s) and not of MDPI and/or the editor(s). MDPI and/or the editor(s) disclaim responsibility for any injury to people or property resulting from any ideas, methods, instructions or products referred to in the content.

remote sensing

MDPI

Article

Enhancing Seasonal PM2.5 Estimations in China through Terrain–Wind–Rained Index (TWRI): A Geographically Weighted Regression Approach

Boqi Peng [1,2], Busheng Xie [1,2], Wei Wang [1,2] and Lixin Wu [1,2,*]

[1] School of Geosciences and Info-Physics, Central South University, Changsha 410083, China; pengboqi@csu.edu.cn (B.P.)
[2] Laboratory of Geohazards Perception, Cognition and Predication, Central South University, Changsha 410083, China
* Correspondence: wulx66@csu.edu.cn

Abstract: PM2.5 concentrations, closely linked to human health, are significantly influenced by meteorological and topographical factors. This study introduces the Terrain–Wind–Rain Index (TWRI), a novel index that integrates the Terrain–Wind Closed Index (TWCI) with relative humidity to quantitatively examine the coupling effect of natural elements on PM2.5 concentration and its application to PM2.5 inversion. By employing Geographically Weighted Regression (GWR) models, this study evaluates the inversion results of PM2.5 concentrations using TWRI as a factor. Results reveal that the annual average correlation between TWRI and site-measured PM2.5 concentrations increased from 0.65 to 0.71 compared to TWCI. Correlations improved across all seasons, with the most significant enhancement occurring in summer, from 0.51 to 0.66. On the inversion results of PM2.5, integrating TWRI into traditional models boosted accuracy by 1.3%, 5.4%, 4%, and 7.9% across four seasons, primarily due to the varying correlation between TWRI and PM2.5. Furthermore, the inversion results of coupled TWRI more effectively highlight the high value areas in closed areas and the low value areas in humid areas.

Keywords: TWRI; PM2.5; AOD; GWR; coupling effect

1. Introduction

The atmosphere is one of the fundamental elements that humans rely on for survival and development [1,2]. Emerging studies have shown that long-term exposure to air pollutants, particularly PM2.5, increases the risk of respiratory and cardiovascular diseases [3–5]. PM2.5 primarily originates from human activities and is influenced by meteorological conditions [6–8]. Sources of PM2.5 primarily include human activities such as industrial operations, agriculture, and transportation [9,10], with concentrations also being influenced by natural meteorological factors like wind speed, relative humidity, terrain, and planetary boundary layer, etc. [6,11,12]. Despite significant economic progress, China faces severe air pollution, with PM2.5 being a significant concern [13,14]. In response to this issue, China initiated the nationwide air quality monitoring in 2013 to monitor air pollutants in real-time. However, the network, with uneven and sparse spatial distribution, cannot meet the requirements of high spatial and temporal resolution air pollution monitoring [15].

Thanks to the swift progress in satellite technology, employing remote sensing techniques combined with observation stations to monitor and retrieve PM2.5 has become feasible in recent years. Past research has revealed a robust correlation between Aerosol Optical Depth (AOD) and PM2.5, facilitating the remote-sensing-based inversion of PM2.5 concentrations using satellite-derived AOD [16,17]. Most research focuses on refining models to enhance the accuracy of PM2.5 estimation from AOD [18–20]. Particularly, statistical models, mainly through linear or nonlinear regression methods for inversion, have been

extensive implemented [21]. Given the significant geographic variability of PM2.5 concentrations, Geographically Weighted Regression (GWR) is commonly employed to model and estimate the concentrations accurately. Distinct from traditional linear regression models, GWR functions as a local linear regression model, where regression coefficients are adjusted according to geographic location changes, which can better express the influence of regional natural factors. This adaptation enables GWR to accurately reflect the local variability of PM2.5 concentrations [22,23].

Given that meteorological and topographical factors have a great impact on the relationship between PM2.5 and AOD, these factors are often used as auxiliary variables in estimation models, such as boundary layer height, relative humidity, wind speed, elevation, etc. [22–24]. Various natural factors impact PM2.5 concentrations through diverse mechanisms [25,26]. Chen and Ye found that wind acts as a significant driving force, influencing the deposition and dispersion of air pollutants. Regions with lower wind speeds tend to exhibit increased pollutant concentrations, whereas areas with higher wind speeds see reduced levels of pollutants [12]. Similarly, Karle also found that the Planetary Boundary Layer (PBLH) affects pollutant concentrations through various mechanisms. On one hand, it compresses the space available for pollutant emissions, thereby increasing concentration levels. On the other hand, temperature inversions occurring within the planetary boundary layer inhibit the dispersion of pollutants [27]. Conversely, several studies employ various methods to select the optimal factors in inversion processes. Tang found that applying principal component analysis to determine the optimal parameters can improve the accuracy of inversion before GWR [28]. Similarly, Ding found also that employing a principal component analysis to select optimal inversion factors can achieve similar improvement in accuracy before using the LSTM model [29]. Furthermore, Zhang found that employing the variance inflation factor to determine the optimal set of factors can achieve notably enhanced results in the inversion accuracy [30].

Lately, it has been increasingly recognized that merely analyzing the impact of a single meteorology or topographical factor on PM2.5 alone is qualitatively insufficient. Consequently, Wu quantitatively proposed the Terrain–Wind–Closed Index (TWCI) model to account for the coupled–closed effect of terrain and meteorological factors on PM2.5 [31]. They found that integrating meteorological and topographical factors can effectively interpret the spatiotemporal distribution of PM2.5. However, the impact of rainfall, indicated by relative humidity, on a broad temporal and spatial scale remains underexplored in TWCI.

A quantitative coupling model can capture and explain the impact of natural factors on PM2.5 from a new perspective. Thus, to better describe the impact of relative humidity, the Terrain–Wind Closed Index (TWCI) model is extended into a TWRI (Terrain–Wind–Rained Index) model by incorporating the relative humidity and the spatiotemporal distribution and correlation are compared on an annual and seasonal basis in this study. In addition, to explore the utility of this coupling effect relative to PM2.5 inversion, the results with TWRI as a PM2.5 inversion parameter are compared through geographically weighted regression. The efficacy of each model is evaluated using 10-fold cross-validation, and the spatial distribution of seasonal PM2.5 concentrations is compared on both national and regional scale.

2. Materials and Method

2.1. Materials

2.1.1. Site-Based PM2.5 Levels

Air pollution monitoring stations were established by the Chinese government in 2013 to enable the monitoring of air quality. Daily average PM2.5 data from 1674 monitoring stations were obtained from the China Environmental Monitoring Center [15] (CEMC, http://www.cnemc.cn/, accessed on 1 January 2024) (see Figure 1). The study used the PM2.5 measurements obtained from 1 January 2020 to 31 December 2020 for a whole year analysis.

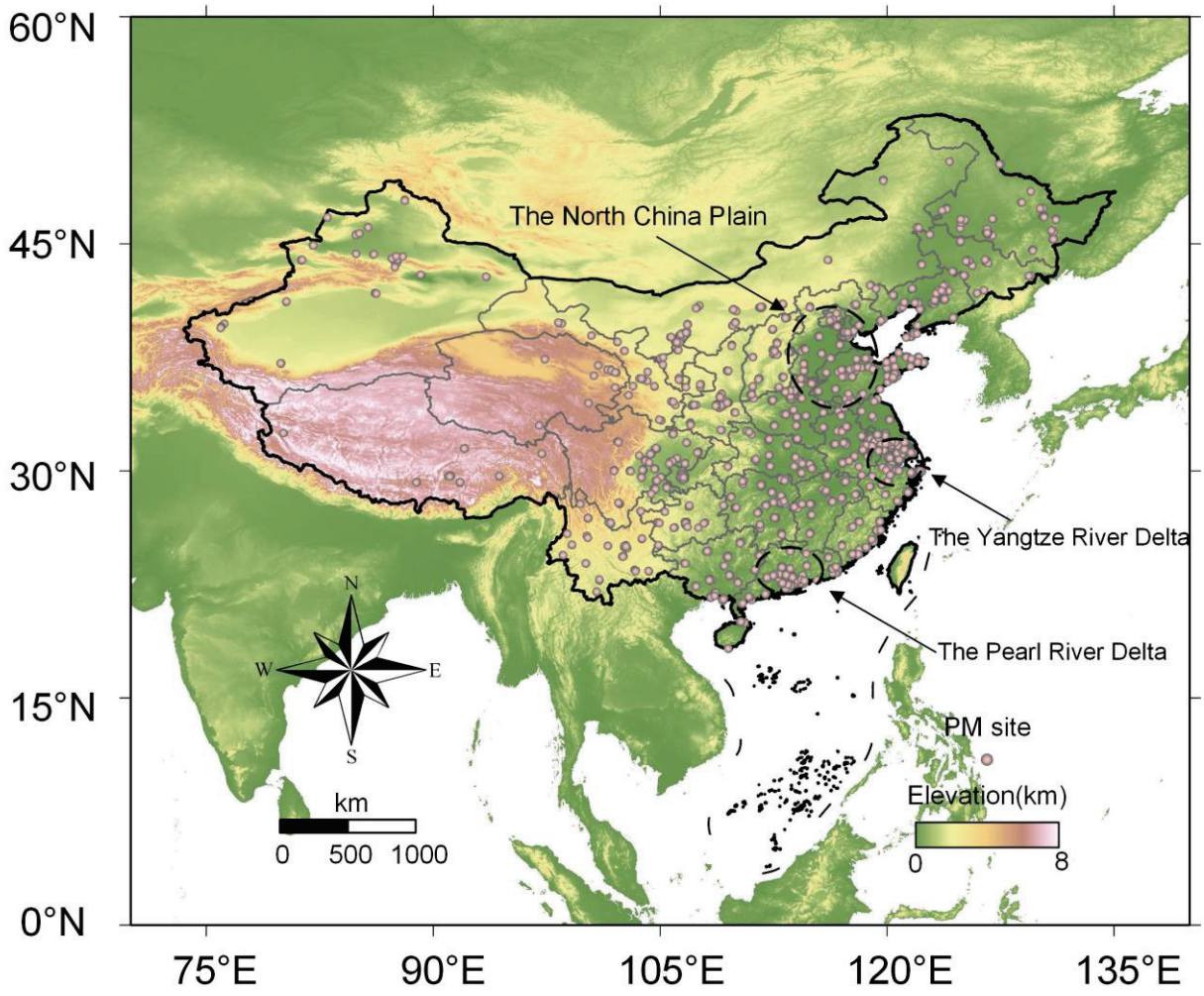

Figure 1. Spatial distribution of the study area and PM monitoring network in China.

2.1.2. MODIS AOD

This study used the MODIS's AOD dataset, MCD19A2, which provides daily data at 1 km × 1 km resolution. MCD19A2 is derived from the fusion of MODIS data from Terra and Aqua satellites, processed using the MAIAC algorithm and resulting in the generation of the daily 1 km resolution product. Released by NASA, the MCD19A2 product represents the latest MODIS_C6 aerosol product iteration, facilitating global aerosol monitoring with enhanced spatial and temporal resolution [32]. The data are freely available at https://search.earthdata.nasa.gov/search, accessed on 1 January 2024.

2.1.3. Meteorological Factors

This study used meteorological products sourced from ERA-5 (https://cds.climate.copernicus.eu/cdsapp#!/search?type=dataset, accessed on 1 January 2024). Compared to ERA-Interim, ERA-5 exhibits significant enhancements in spatial resolution, temporal resolution, and atmospheric pressure layer coverage. Four meteorological variables—10 m U/V wind components (m/s), relative humidity (RH; %), boundary layer height (BLH; m)—are included, provided at a resolution of 0.25° × 0.25° [33].

2.1.4. Digital Elevation Model

This study used the Digital Elevation Model (DEM) sourced from USGS with a resolution of 90 m (https://search.earthdata.nasa.gov/search, accessed on 1 January 2024). Terrain aspect and elevation were extracted as parameters based on the DEM to participate in the calculation of the Terrain–Wind–Rain Index (TWRI).

2.1.5. Data Processing

To ensure consistency across various spatial resolutions, all parameters used were resampled to a uniform spatial resolution of $0.01° \times 0.01°$ using linear interpolation. Given that the aim of this study was to obtain quarterly average concentration of PM2.5, the quarterly averages data within 3 km radius around the site were used for modeling. The sources and spatiotemporal resolutions of the data used are summarized in Table 1.

Table 1. The main information of the obtained parameters in this study.

Variable Name	Source	Spatial Resolution	Temporal Resolution	Unit
Wind speed	ERA5	$0.25° \times 0.25°$	1 month	m/s
Wind direction	ERA5	$0.25° \times 0.25°$	1 month	°
Boundary layer height	ERA5	$0.25° \times 0.25°$	1 month	m
Relative humidity	ERA5	$0.25° \times 0.25°$	1 month	%
DEM	USGS	90 m	-	m
MODIS-AOD	MODIS	$0.01° \times 0.01°$	1 day	-
Ground-level PM2.5	CNEMC	-	1 h	$\mu g/m^3$
Grid-level PM2.5	WUSTL	$0.01° \times 0.01°$	1 month	$\mu g/m^3$

2.2. Method

2.2.1. The Construction of TWRI

Research indicates that natural topographical and meteorological factors impact PM2.5 concentrations, including wind speed, boundary layer height, relative humidity, terrain elevation, etc. [19,34]. Each factor contributes to the concentration of particulate matter through different mechanisms [35,36].

In the horizontal direction, the dispersion of PM2.5 is primarily influenced by wind and mountainous terrain, while, in the vertical direction, it is affected by the boundary layer height. Consequently, mountains, wind, and the planetary boundary layer collectively form an approximate 3D box dynamically, representing the local activity space of atmospheric particles [31]. In addition, precipitation, characterized by relative humidity, acts on the particulate matters through the process of deposition. Horizontal dispersion, vertical dispersion, and deposition are all independent processes; therefore, their combined effect can be described by the product of these factors.

Thus, based on the above analysis, *TWRI* can be calculated using the following formula:

$$TWRI(i,j) = TWI(i,j) \times PBLH(i,j) \times (1 - RH(i,j)) \quad (1)$$

where $TWI(i,j)$ refers to the terrain–wind index, which represents the closed coupling effect from terrain and wind at grid(i, j). $PBLH(i,j)$ is the closed effect represented by the height of the boundary layer at grid(i, j). $RH(i,j)$ is the relative humidity at grid(i, j).

As mentioned above, considering the wind speed in the horizontal direction and in some places, the terrain can form a completely closed area in the horizontal dimension alone, but in other places, such as semi-closed areas, wind has a significant impact on the terrain closed effect. Therefore, the terrain orientation and wind direction jointly act on the closed effect, and *TWI* can be obtained by the following formula:

$$TWI(i,j) = \frac{1}{4w^2} \sum_{m,n=i-w}^{m,n=i+w} max[ACI_{m,n}, WCI_{m,n}] \times W_{m,n}^{dist} \quad (2)$$

Among them, $ACI_{m,n}$ and $WCI_{m,n}$ are closed indices calculated based on the slope direction and wind direction of the surrounding points at grid(m, n) around grid(i, j), respectively; w is the size of the buffer window, in kilometers; $W_{m,n}^{dist}$ represents the weight derived from the horizontal distance of the observation grid(i, j). More details can be found in Wu [31].

2.2.2. Geographically Weighted Regression Model (GWR)

The geographically weighted regression model is a commonly used regression model for AOD–PM2.5, which is a local linear regression model that allows regression coefficients to change with changes in geographic location. In the following geographically weighted regression models, the Gaussian function was uniformly used as the kernel density function, and the bandwidth was determined using the AIC (Akaike Information Criterion), which could lead to a better fitting result [37].

To explore the effectiveness of applying TWRI to AOD–PM2.5 inversion, traditional, coupled, and optimized models were constructed for comparative analysis. The formula employed in the traditional model is as follows:

$$PM2.5 = \alpha_{u1,v1} AOD_{u1,v1} + \alpha_{u2,v2} RH_{u2,v2} + \alpha_{u3,v3} PBLH_{u3,v3} + \alpha_{u4,v4} WS_{u4,v4} + \alpha_{u5,v5} DEM_{u5,v5} + b_i \quad (3)$$

The coupled model formula is:

$$PM2.5 = \alpha_{u1,v1} AOD_{u1,v1} + \alpha_{u2,v2} TWRI_{u2,v2} + b_i \quad (4)$$

The optimized model formula is:

$$PM2.5 = \alpha_{u1,v1} AOD_{u1,v1} + \alpha_{u2,v2} RH_{u2,v2} + \alpha_{u3,v3} PBLH_{u3,v3} + \alpha_{u4,v4} WS_{u4,v4} + \alpha_{u5,v5} DEM_{u5,v5} + \alpha_{u6,v6} TWRI_{u5,v5} + b_i \quad (5)$$

where $\alpha_{u1,v1}$, $\alpha_{u2,v2}$, ... $\alpha_{un,vn}$ are the regression coefficients in location (u, v), X_N represents the value of predictor in location (u, v), and b_i is the random error.

This study investigates the potential of TWRI to substitute the multifactorial effects on particulate matter in coupled models and directly integrate with AOD for inversion purposes. Additionally, the study examines whether incorporating TWRI into traditional models can improve the precision of PM2.5 inversion.

To mitigate overfitting, ten-fold Cross-Validation (CV) was employed. The Pearson's correlation coefficient (R) was used to determine the relationship between parameters and model inversion performance. Model efficacy was assessed by comparing estimated outcomes to actual measurements and calculating the coefficient of determination (R-squared), Root Mean Square Error (RMSE), and Mean Absolute Error (MAE). The comprehensive workflow of this study is depicted in Figure 2.

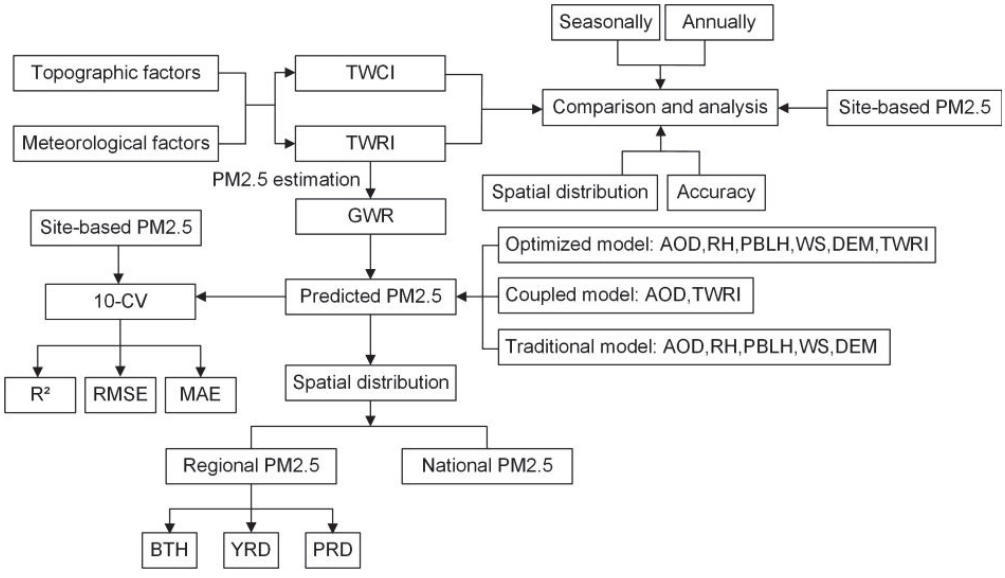

Figure 2. The overall workflow for this study.

3. Results

3.1. Comparison between TWRI and TWCI

3.1.1. Comparison between Annual TWRI and TWCI

Based on the method above, the seasonal TWRI and TWCI models in China were constructed. To assess the strengths and weaknesses of the two models, the correlation between each model and PM2.5 values at different windows were compared, as shown in Figure 3:

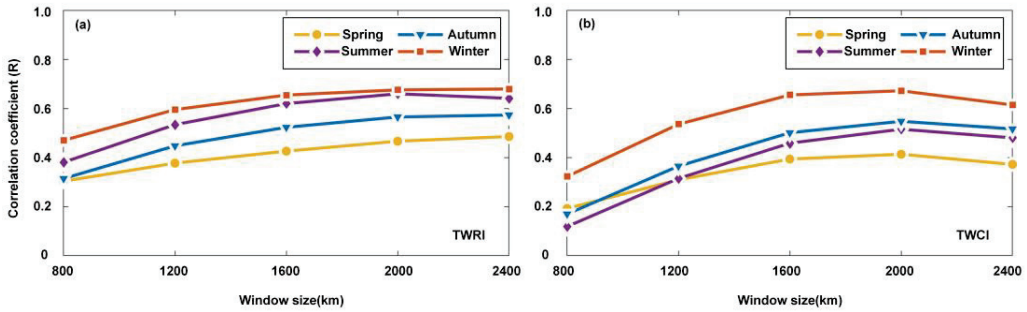

Figure 3. The correlation coefficient (R) between quarterly TWRI (**a**) and TWCI (**b**) with PM2.5 at stations vary with different window sizes.

Seasonal variability analysis indicates that winter was consistently associated with the highest PM2.5 in both models, whereas spring exhibited the weakest correlation. In the TWRI model, the correlation in summer was significantly higher than in autumn compared to TWCI. Additionally, for both the TWCI and the TWRI models, the correlation increased with the enlargement of the window size. The growth rate of the correlation in the TWRI model was smaller compared to the significant changes observed in the TWCI model as the window size varied. When the window range was 2000 km, the correlation between the two model values and the PM2.5 concentration reached its highest level. In a comparative analysis of the two models, the TWRI model demonstrated a consistently higher correlation with PM2.5 concentrations across all windows than the TWCI model. However, the difference was not significant in the optimal window size during spring, autumn, and winter, but the TWRI model exhibited a notably higher correlation in summer than the TWCI model (0.66–0.51).

The observed increase in the correlation of the model during summer can be attributed to the higher precipitation and relative humidity which more effectively capture the scouring effect of rainfall on particulate matter, enhancing the model's correlation in summer. Across different window sizes, TWRI consistently outperformed TWCI, indicating that TWRI offers better stability and robustness.

Beyond window selection, Figure 4 compares the spatial distribution of annual TWCI and TWRI. Spatially, there are distinct differences between the two models. TWCI (Figure 4a) showed high-value areas concentrated in regions like the Junggar Basin, Sichuan Basin, Fen-Wei River Valley, Songliao Basin, and from North to Central China, extending to the Yangtze River Plain. In contrast, the TWRI (depicted in Figure 4b) displayed high-value regions predominantly in the North China Plain and the eastern Tarim Basin, with markedly lower values observed in Southern China. Relative to TWCI, the spatial distribution of TWRI distinctly delineates the differences between China's northern and southern regions.

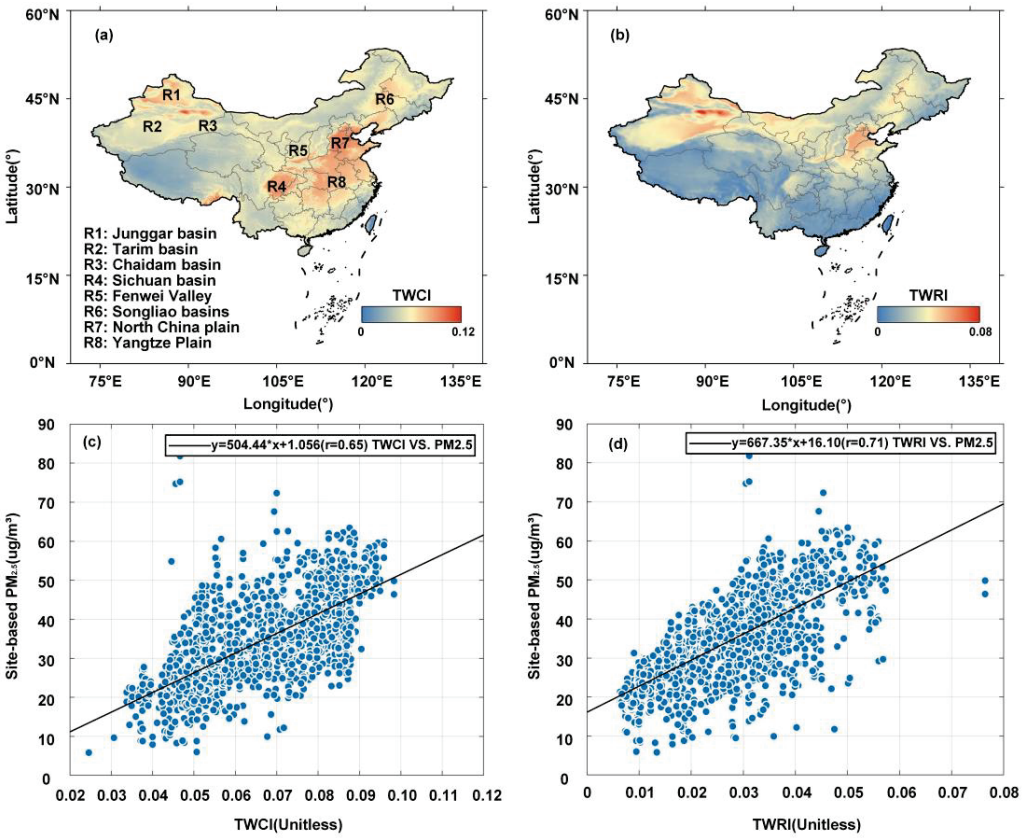

Figure 4. Spatial distributions of annual TWCI (**a**) and TWRI (**b**). Scatterplots of annual TWCI (**c**) and TWRI (**d**) with site-based PM2.5.

Furthermore, the correlation between annual TWRI and site-based PM2.5 was compared, improving from the previous 0.65 to 0.71, showing a slight enhancement in correlation. Consequently, the TWRI model, which incorporates relative humidity, provided a more accurate simulation of the coupling effect of natural elements affecting PM2.5 concentrations compared to TWCI.

3.1.2. Comparison between Seasonal TWRI and TWCI

Figure 5 illustrates that the R value (correlation coefficients) between TWRI and PM2.5 across different seasons in China varied from 0.46 to 0.67, with specific values for spring, summer, autumn, and winter being 0.46, 0.66, 0.56, and 0.67, respectively. In contrast, the R values between TWCI and PM2.5 ranged from 0.41 to 0.67, with seasonal values of 0.41, 0.51, 0.54, and 0.67, respectively. TWRI significantly enhanced the correlation with PM2.5 concentration in summer, while other seasons showed slight improvements compared to TWCI. This may be due to the most significant deposition being caused by summer rainfall.

Figure 6 illustrates the quarterly changes in the spatial distribution of TWRI, TWCI, and PM2.5. TWRI maintained a relatively high value in closed areas within a year compared to TWCI, such as the Junggar basin (R1), Tarim basin (R2), Chaidam basin (R3), Sichuan (R4) basin, the Fenwei Valley (R5), Song Liao basins (R6) and the North China plain (R7). The difference is that the Yangtze Plain (R8) had a significant low value compared to TWCI.

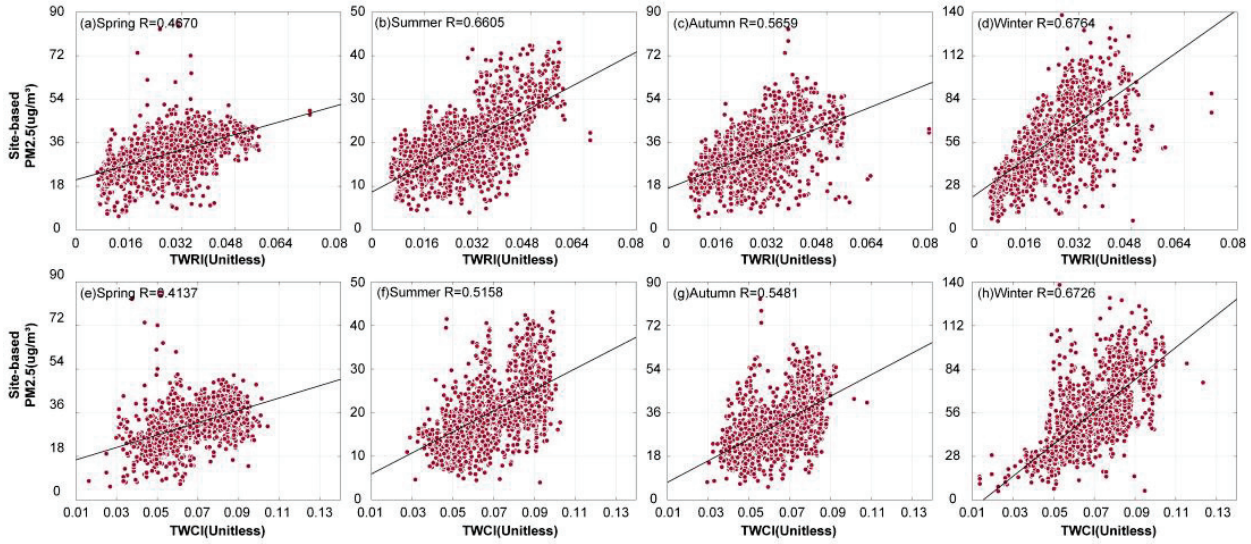

Figure 5. Scatter plot of seasonal TWRI (**a**–**d**) and TWCI (**e**–**h**) with PM2.5 concentration at different stations.

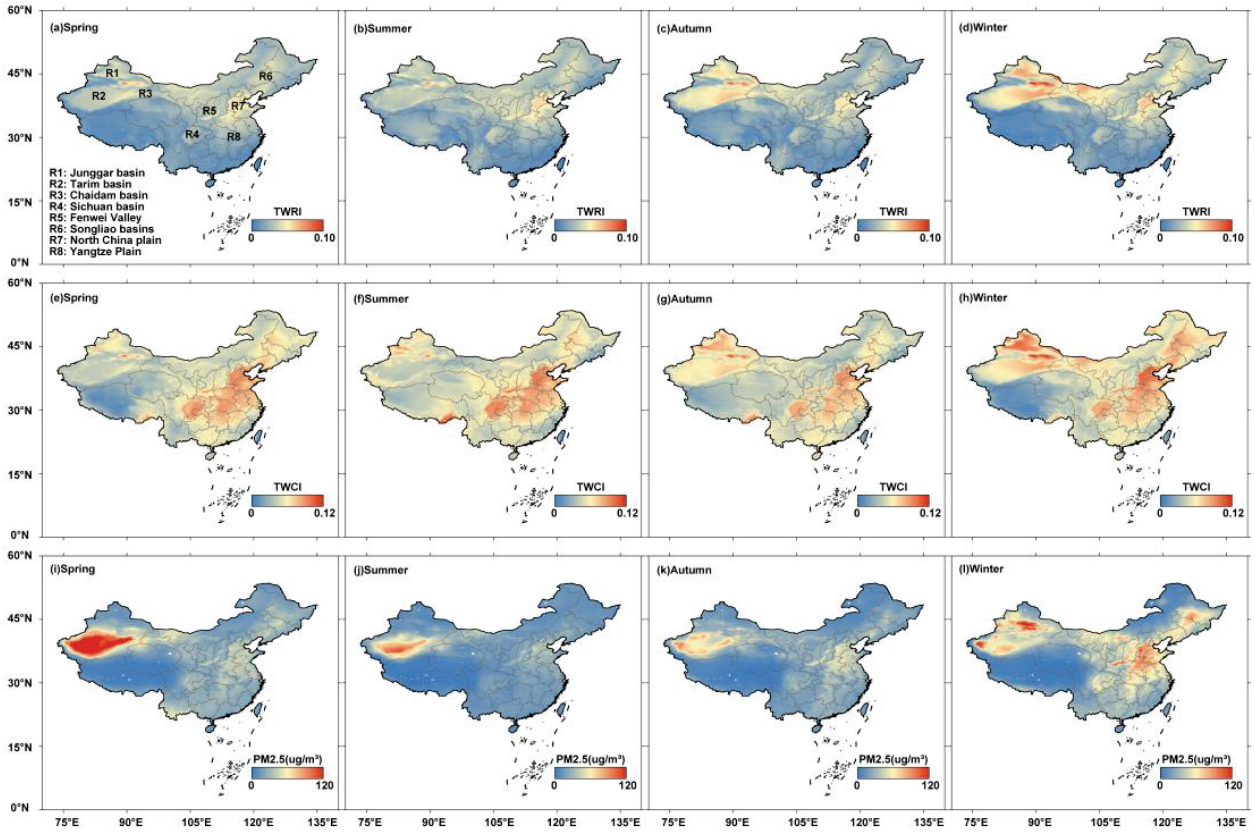

Figure 6. Spatial distribution of seasonal (**a**–**d**) TWRI, (**e**–**h**) TWCI, and(**i**–**l**) PM2.5 concentration for spring (**a**,**e**,**i**), summer (**b**,**f**,**j**), autumn (**c**,**g**,**k**), and winter (**d**,**h**,**l**) in China.

Correspondingly, the quarterly spatial distributions of PM2.5 and TWCI are shown in Figure 6e–h,i–l. The seasonal temporal and spatial distributions of TWCI (Figure 6e–h) did not reflect the differences between humid and arid regions in China, resulting in almost identical TWCI values in the Sichuan Basin, North China plain, and Central China plain, an output which was significantly different from the seasonal spatio-temporal distribution of PM2.5. Taking the North China Plain in summer as an example, it exemplifies a typical semi-

enclosed region where the Yanshan Mountains to the north and the Taihang Mountains to the west restrict the dispersion of air pollutants toward the west and the north, respectively. The dominant southerly winds, interacting with these mountain ranges, create a fully closed area that obstructs the horizontal diffusion of PM2.5. Additionally, the planetary boundary layer acts as a barrier to the vertical dispersion of pollutants, forming a closed three-dimensional space delineated by the TWCI. In the summer, however, the prevailing southerly winds contribute to significant rainfall in the area, promoting the deposition of pollutants and, thereby, reducing PM2.5 concentrations. This phenomenon is more pronounced in southern China and subtropical regions and is characterized by the TWRI.

3.2. PM2.5 Estimation

3.2.1. Descriptive Statistics

Table 2 summarizes the mean changes in the variables used in the PM2.5 prediction model for each season in China. The annual PM2.5 concentration in China was 38.68 ± 32.28 $\mu g/m^3$, with the highest concentration observed in winter at 58.27 ± 23.51 $\mu g/m^3$ and the lowest observed in summer at 19.95 ± 7.86 $\mu g/m^3$. The annual average AOD in China was 0.22 ± 0.21, with little seasonal variation: the values from spring to winter were 0.12 ± 0.07, 0.04 ± 0.03, 0.08 ± 0.05, and 0.10 ± 0.16, respectively. The relative humidity was highest in summer, with a value of $73.67 \pm 10.75\%$, while it attained its lowest in winter, with a value of $58.99 \pm 15.36\%$. The boundary layer was at its lowest in winter, at 0.38 ± 0.10 km, while it was at its highest in the summer, at 1.16 ± 0.51 km. The highest wind speed was recorded in winter and reached 1.31 ± 0.74 m/s, while the lowest was recorded in autumn, reaching 0.77 ± 0.19 m/s. TWRI also varied, but the difference was not significant: from spring to winter, the values were 28.01 ± 12.07, 28.40 ± 13.08, 26.42 ± 11.65, and 28.87 ± 14.22, respectively. Most parameters almost reached their extreme values during summer and winter, a phenomenon which may be influenced by both meteorological factors and seasonal emission differences.

Table 2. Descriptive statistics of all variables for each season in China.

Season		PM2.5 ($\mu g/m^3$)	AOD	RH (%)	PBLH (km)	WS (m/s)	TWRI × 1000	DEM (m)
Spring	Min	7.18	0	20.25	0.22	0.16	6.27	0
N = 1484	Max	187.28	0.37	85.72	1.42	3.40	74.98	4101
	Mean	55.27	0.12	58.99	0.58	0.97	28.01	426
	Std.	23.51	0.07	15.36	0.16	0.52	12.07	725
Summer	Min	4.00	0	22.17	0.21	0.17	5.46	-
N = 1486	Max	83.35	0.27	90.50	1.16	4.34	69.73	-
	Mean	19.95	0.04	73.67	0.51	1.17	28.40	-
	Std.	7.86	0.03	10.75	0.13	0.62	13.08	-
Autumn	Min	5.40	0	27.34	0.17	0.22	6.53	-
N = 1481	Max	82.92	0.24	87.28	0.90	5.72	82.54	-
	Mean	31.39	0.08	66.34	0.44	1.30	26.42	-
	Std.	11.15	0.05	10.63	0.09	0.77	11.65	-
Winter	Min	7.18	0	17.67	0.07	0.19	6.38	-
N = 1447	Max	187.28	0.27	87.09	1.28	5.16	94.18	-
	Mean	55.27	0.10	64.69	0.38	1.31	28.87	-
	Std.	23.51	0.06	10.97	0.10	0.74	14.22	-

Table 3 details the correlations between various variables and PM2.5 concentrations at the monitoring stations. Research has shown that AOD has the highest correlation with PM2.5, followed by TWRI. In addition, the correlation between all variables and PM2.5 was almost at its weakest in spring, while it attained its highest in autumn or winter.

Table 3. The correlation coefficient (R) between PM2.5 concentration and all variables in each season in China.

Season/R	AOD	RH (%)	PBLH (km)	WS (m/s)	TWRI	DEM
Spring	0.5888	−0.2975	0.1129	−0.2502	0.4603	−0.2553
Summer	0.7258	−0.2917	0.0201	−0.3296	0.6577	−0.2123
Autumn	0.7540	−0.4059	−0.3159	−0.4138	0.5667	−0.2829
winter	0.5684	−0.3480	−0.4571	−0.5077	0.6950	−0.2906

3.2.2. Model Fitting and Validation

The results of the fitting and validation are illustrated in Table 4 for three models in 2020 for China. It is observed that the fitting and validation accuracies of the three models were not significantly different, indicating that the model fitting effect was valid and there was no overfitting phenomenon. The optimized model had the best fitting effect for the entire year, with R^2 values > 0.8, and RMSE and MAE values of < 10 μg/m^3 and 7 μg/m^3, respectively. The coupled model had the lowest fitting effect, with R^2 values of 0.68, 0.70, 0.75, and 0.74 for a year, while the R^2 values of traditional models remained stable at 0.78.

Table 4. Model fitting and sample cross-validation results under different parameter combinations.

Model	Model Fitting				Model Validation			
	Spring	Summer	Autumn	Winter	Spring	Summer	Autumn	Winter
GWR (traditional model)	R^2 = 0.78 RMSE = 4.71 MAE = 3.57	R^2 = 0.77 RMSE = 3.81 MAE = 2.90	R^2 = 0.78 RMSE = 5.24 MAE = 3.95	R^2 = 0.78 RMSE = 10.97 MAE = 7.95	R^2 = 0.75 RMSE = 5.04 MAE = 3.78	R^2 = 0.74 RMSE = 3.99 MAE = 3.04	R^2 = 0.76 RMSE = 5.51 MAE = 4.16	R^2 = 0.76 RMSE = 11.61 MAE = 8.35
GWR (coupled model)	R^2 = 0.68 RMSE = 5.95 MAE = 4.53	R^2 = 0.70 RMSE = 4.57 MAE = 3.55	R^2 = 0.72 RMSE = 6.16 MAE = 4.74	R^2 = 0.74 RMSE = 11.99 MAE = 8.47	R^2 = 0.66 RMSE = 6.13 MAE = 4.66	R^2 = 0.68 RMSE = 4.67 MAE = 3.63	R^2 = 0.71 RMSE = 6.30 MAE = 4.84	R^2 = 0.73 RMSE = 12.40 MAE = 8.69
GWR (optimized model)	R^2 = 0.80 RMSE = 4.47 MAE = 3.32	R^2 = 0.80 RMSE = 3.52 MAE = 2.67	R^2 = 0.82 RMSE = 4.80 MAE = 3.60	R^2 = 0.84 RMSE = 9.52 MAE = 6.61	R^2 = 0.76 RMSE = 4.90 MAE = 3.56	R^2 = 0.78 RMSE = 3.73 MAE = 2.83	R^2 = 0.79 RMSE = 5.12 MAE = 3.84	R^2 = 0.82 RMSE = 10.12 MAE = 7.00

Similarly, there was a similar trend in verifying accuracy. Among the three models, the optimized model had the highest R^2 values of 0.76, 0.78, 0.79, and 0.82 for the four seasons, respectively. The coupled model had the lowest R^2 values, which were 0.66, 0.68, 0.71, 0.73 for the four seasons, respectively. Although relatively low, such values are not far from traditional models, with values of 0.74, 0.74, 0.75, 0.76.

In addition, the coupled model and optimized model had the lowest R^2 in spring (0.66, 0.76, respectively), and the highest in winter (0.73, 0.82, respectively), showing similar seasonal characteristics. This is related to the poor ability of TWRI to capture particulate matter concentration in spring and its better ability to capture particulate matter concentrations in winter. Furthermore, summer had the lowest RMSE and MAE values, while winter had the highest RMSE and MAE estimates among all models, a phenomenon which is related to increased anthropogenic emissions during winter and rainfall during summer [38].

Figure 7 illustrates the density scatterplots of the validation results for the traditional model, the coupled model, and the optimized model. There was no significant difference in the distribution of predicted and observed values in the four seasons among the three models, and there was an underestimation phenomenon in all models, with slopes < 0.85. The scatter points of the optimized model were more concentrated, while the scatter points of the coupled model were more scattered, a phenomenon which is related to its R^2.

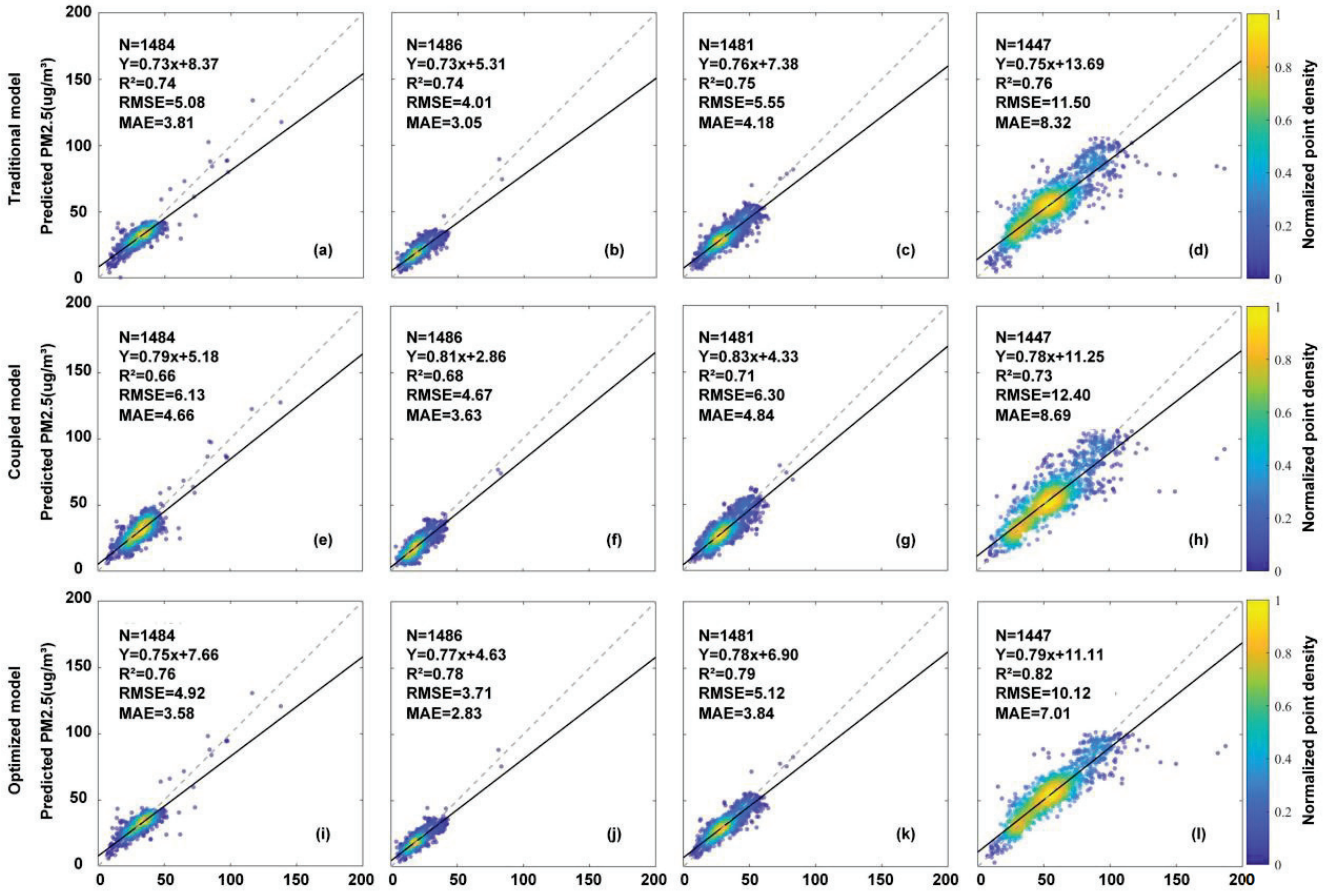

Figure 7. Density scatterplots of 10-CV results from the GWR with traditional, coupled, and optimized models for spring (**a**,**e**,**i**), summer (**b**,**f**,**j**), autumn (**c**,**g**,**k**), and winter (**d**,**h**,**l**) in China. The dashed line and the solid line represent the 1:1 line and the linear regression line, respectively.

3.2.3. PM2.5 Spatial Distribution

Figure 8 illustrates the quarterly PM2.5 spatial distribution across China from three models in 2020. On the seasonal scale, data are missing in southern China and northeastern and northwestern China because of the cloud cover in summer and the snow cover in winter. In terms of overall spatial distribution, all three models share the same characteristics in terms of seasonal variation. Significant areas of high concentration were identified in the Tarim Basin and the North China Plain, whereas significantly low concentration areas were observed in northeastern and southern China. Additionally, seasonal variations revealed significant spatial differences in fine particulate pollution. Winter experienced the most severe air pollution (50.01 ± 49.49, 43.55 ± 25.62, 51.59 ± 47.38 $\mu g/m^3$), while summer experienced the lowest level of air pollution (16.51 ± 13.69, 17.74 ± 12.77, 15.57 ± 18.99 $\mu g/m^3$). On the one hand, the seasonal fluctuations in PM2.5 levels can be attributed to lower emissions in summer and higher emissions in winter due to heating requirements. On the other hand, the summer monsoon contributes to increased rainfall that helps mitigate pollution levels, whereas in winter lower wind speeds and shallower boundary layers hinder the dispersion of pollutants. Moreover, PM2.5 concentrations tend to be less pronounced during the spring and autumn seasons.

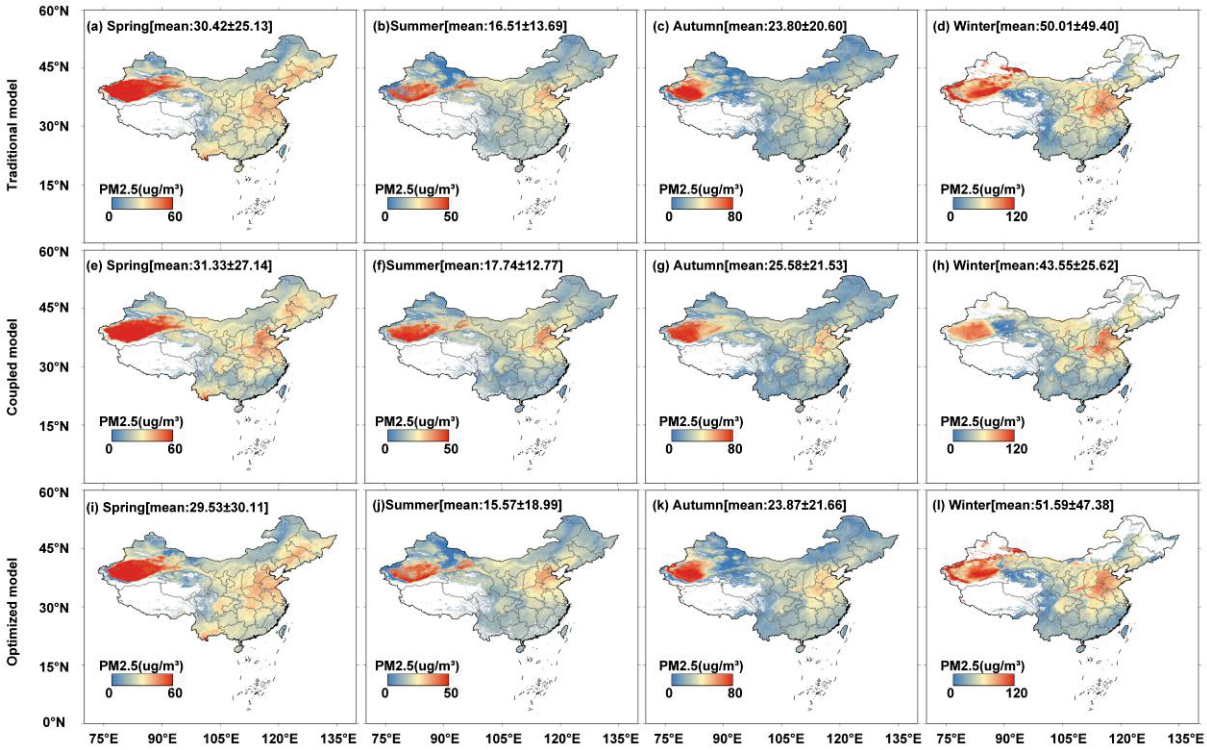

Figure 8. Seasonal mean distributions of PM2.5 concentrations of three models for spring (**a**–**i**), summer (**b**–**j**), autumn (**c**–**k**), and winter (**d**–**l**) in 2020 across China.

Additionally, the inversion results from the coupled model were more centralized, mainly evidenced by the high concentration values that were concentrated in closed areas such as basins and valleys, in stark contrast with the surrounding results. The traditional model produced a more averaged distribution, with indistinct boundaries of high concentration and no significant differences between the central and southern regions. The optimized model merged the advantages of both, offering more distinct boundaries for high concentration areas while also providing relatively lower predicted results in the southern regions.

3.2.4. Regional PM2.5

The North China Plain, the Yangtze River Delta region, and the Pearl River Delta region were selected as heavily polluted areas for regional analysis. Quarterly performance of three models in these regions was evaluated to assess their effectiveness in capturing variations in pollution levels.

(1) North China Plain

A comparison of three different models for the seasonal variation in PM2.5 over the North China Plain is shown in Figure 9. Consistent with previous studies, the models indicated lower concentrations during summer, higher in winter, and comparable levels in spring and autumn. The coupled model consistently exhibited the lowest mean concentrations across all seasons, but also the highest standard deviation. This suggests that the inverted results from the coupled model featured a broad distribution, highlighting the disparities between high and low concentrations, particularly between the Taihang Mountains and the North China Plain (highlighted by the red line frame on the left side of Figure 9). Furthermore, in comparison with the traditional model, the coupled model captured lower values in the Taishan Mountain range (Figure 9e,g, highlighted by the red line frame on the right side). The optimized model bore more resemblance to the traditional model, yet it captured variations in the Taishan Mountains (Figure 9 i,k,l), though these were not significant. In addition, its measurements were marginally lower in the Taihang

and Yanshan Mountains, with more distinct differences observed between the mountains and the plains.

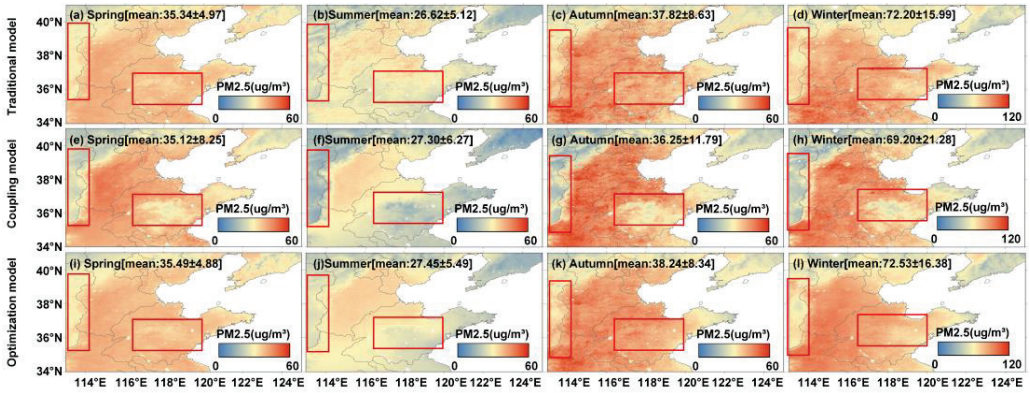

Figure 9. Zoomed-in map of seasonal distribution of PM2.5 concentration in 2020 of three models in the North China Plain: Traditional model (**a**–**d**), Coupling model (**e**–**h**) and Optimization model (**i**–**l**). The red wireframe indicates areas with significant differences among the three models.

Table 5 shows the accuracy verification results associated with stations located in the North China Plain. Overall, among the three models, the optimized model had the highest inversion accuracy, followed by the traditional model and the coupled model, which had the lowest inversion accuracy. In terms of quarterly changes, the three models achieved the highest accuracy in autumn with R^2 values of 0.72, 0.64, and 0.79, respectively, while the lowest occurred in summer with R^2 values of 0.49, 0.42, and 0.60, respectively.

Table 5. Model sample cross-validation results under different parameter combinations in North China Plain.

Model	Model Validation			
	Spring	**Summer**	**Autumn**	**Winter**
Traditional model	R^2 = 0.6038 MAE = 3.1961 RMSE = 4.3009	R^2 = 0.4951 MAE = 4.2243 RMSE = 5.2480	R^2 = 0.7209 MAE = 4.5146 RMSE = 5.8526	R^2 = 0.6391 MAE = 9.2194 RMSE = 13.5801
Coupled model	R^2 = 0.4812 MAE = 4.3503 RMSE = 5.4718	R^2 = 0.4205 MAE = 4.4136 RMSE = 5.5517	R^2 = 0.6480 MAE = 5.4437 RMSE = 6.8394	R^2 = 0.5728 MAE = 10.4857 RMSE = 15.031
Optimized model	R^2 = 0.6459 MAE = 3.0781 RMSE = 4.1251	R^2 = 0.6028 MAE = 3.7031 RMSE = 4.5989	R^2 = 0.7932 MAE = 3.9485 RMSE = 5.0712	R^2 = 0.7078 MAE = 8.0193 RMSE = 12.231

(2) Pearl River Delta

As shown in Figure 10, the concentration of PM2.5 in the Pearl River Delta varied seasonally. There was, typically, a decrease in PM2.5 levels during the summer and an increase in PM2.5 levels during the winter, with minimal variation during spring and autumn. Since seasonal emissions showed minimal variation, this is primarily influenced by meteorological factors. The summer monsoon, bringing rainfall, leads to pollutant deposition and reduced PM2.5 concentrations. Conversely, during winter, weaker winds and a lower planetary boundary layer promote particle accumulation. Among the three models, the coupled model consistently exhibited lower average concentrations throughout the year. In comparison with the traditional model, both the coupled and optimized models emphasized areas of high concentration surrounding Guangzhou (Figure 10e–l, marked by a red wireframe). The coupled and optimized models also showed lower values in

the northern mountainous regions of the Pearl River Delta compared with the traditional model (Figure 10d,h,l).

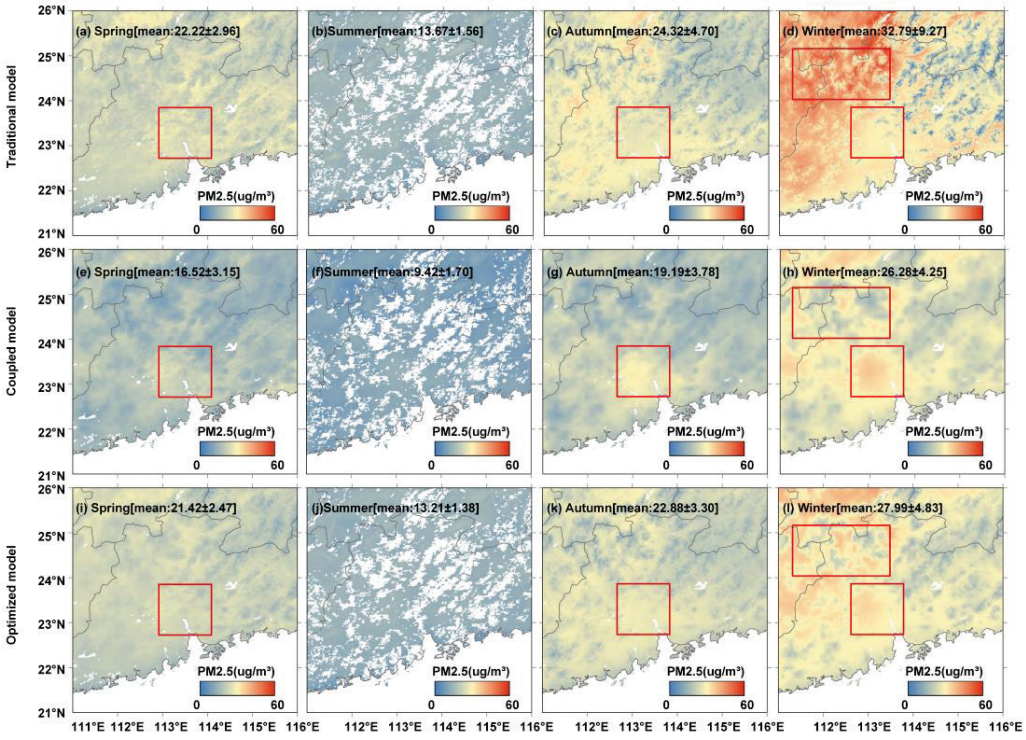

Figure 10. Zoomed-in map of seasonal concentration of PM2.5 in 2020 for three models in the Pearl River Delta: Traditional model (**a**–**d**), Coupling model (**e**–**h**) and Optimization model (**i**–**l**). The red wireframe indicates areas with significant differences among the three models.

Table 6 shows the accuracy verification results associated with stations located in the Pearl River Delta. Similarly to the North China Plain, the optimized model had the highest inversion accuracy, followed by the traditional model and the coupled model, which had the lowest inversion accuracy. However, there was no significant indication of change regarding the seasonal variations. In the traditional model, the accuracy was highest in summer and lowest in autumn, with values of 0.5901 and 0.3351, respectively. In the coupled model, the accuracy was highest in spring and lowest in autumn, with values of 0.2936 and 0.1782, respectively. In the optimized model, the accuracy was highest in summer and lowest in winter, with values of 0.6287 and 0.4363, respectively.

Table 6. Model sample cross-validation results under different parameter combinations in the Pearl River Delta.

Model	Model Validation			
	Spring	**Summer**	**Autumn**	**Winter**
Traditional model	R^2 = 0.4199 MAE = 2.7604 RMSE = 3.3114	R^2 = 0.5901 MAE = 1.8302 RMSE = 2.3255	R^2 = 0.3351 MAE = 2.6256 RMSE = 3.1117	R^2 = 0.3779 MAE = 4.6836 RMSE = 6.1177
Coupled model	R^2 = 0.2936 MAE = 2.5943 RMSE = 3.3598	R^2 = 0.1852 MAE = 2.6615 RMSE = 3.5591	R^2 = 0.1782 MAE = 3.3697 RMSE = 4.5965	R^2 = 0.2816 MAE = 3.3234 RMSE = 4.0667
Optimized model	R^2 = 0.5299 MAE = 1.8325 RMSE = 2.3227	R^2 = 0.6287 MAE = 1.7368 RMSE = 2.2703	R^2 = 0.4757 MAE = 2.0630 RMSE = 2.7055	R^2 = 0.4363 MAE = 2.7679 RMSE = 3.4448

(3) Yangtze River Delta

Figure 11 illustrates the PM2.5 concentrations across the Yangtze River Delta. Consistent with the two other areas, the concentration of PM2.5 in this region also varied seasonally—low values in summer, high values in winter, and minimal differences between spring and autumn. There were significant north–south disparities in PM2.5 levels, with higher concentrations observed in the north and lower concentrations observed in the south. This pattern largely stems from the northern area location on the Jianghuai Plain, where a dense population and industrial activities contribute to greater emissions, unlike the less populated hilly and mountainous terrain in the south which generates fewer emissions. Of the three models analyzed, the coupled model consistently exhibited the lowest average inversion values on a seasonal scale, while the optimized model exhibited the highest average. Spatially, however, no significant differences were evident among the models in this region.

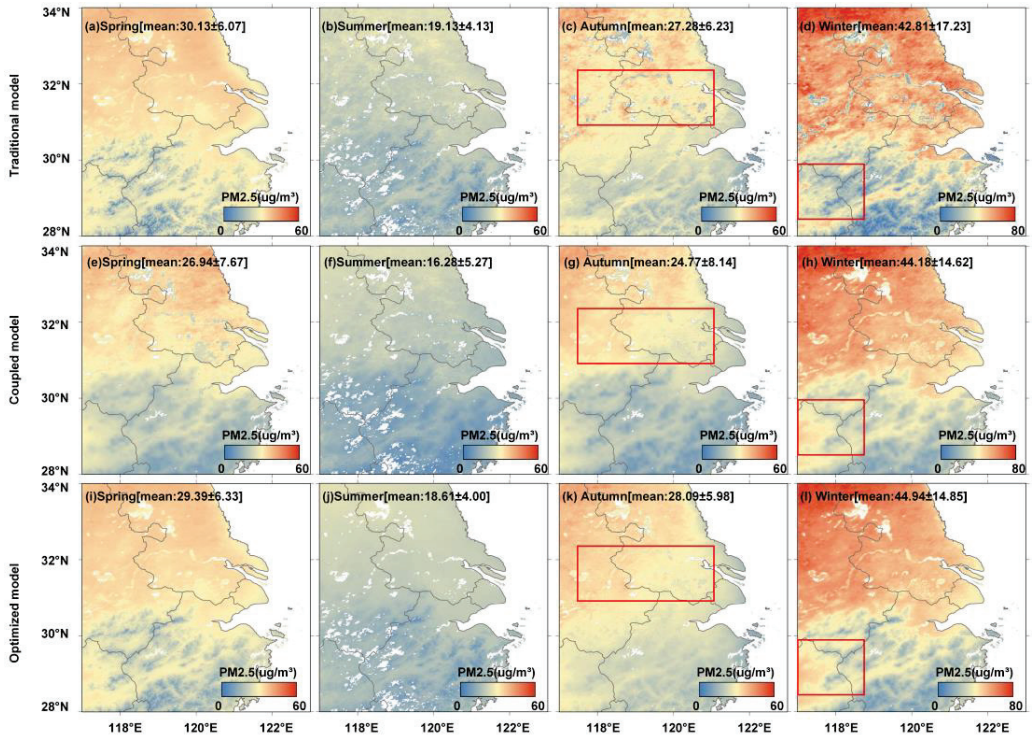

Figure 11. Zoomed-in map of the seasonal concentration of PM2.5 in 2020 for three models in the Yangtze River Delta region: Traditional model (**a**–**d**), Coupling model (**e**–**h**) and Optimization model (**i**–**l**). The red wireframe indicates areas with significant differences among the three models.

Table 7 shows the accuracy verification results associated with stations located in the Yangtze River Delta. Similarly to the first two regions, the optimized model still achieved the highest accuracy among the three models. However, in this region, the coupled model exhibited slightly higher accuracy values than the traditional model in autumn and winter, and lower in spring and summer. In terms of quarterly changes, the three models achieved the highest accuracy in winter with R^2 values of 0.5852, 0.7595, and 0.7713, respectively, while the lowest occurred in summer with R^2 values of 0.2722, 0.2011, and 0.3292, respectively.

Table 7. Model sample cross-validation results under different parameter combinations in the Yangtze River Delta.

Model	Model Validation			
	Spring	**Summer**	**Autumn**	**Winter**
Traditional model	R^2 = 0.4622 MAE = 3.4077 RMSE = 4.4071	R^2 = 0.2722 MAE = 2.6890 RMSE = 3.3348	R^2 = 0.5203 MAE = 3.7955 RMSE = 5.1042	R^2 = 0.5852 MAE = 7.7003 RMSE = 9.6655
Coupled model	R^2 = 0.4520 MAE = 3.8866 RMSE = 5.0530	R^2 = 0.2011 MAE = 3.5427 RMSE = 4.4939	R^2 = 0.5909 MAE = 3.8037 RMSE = 4.8866	R^2 = 0.7595 MAE = 5.3997 RMSE = 7.2528
Optimized model	R^2 = 0.5317 MAE = 3.1902 RMSE = 4.1344	R^2 = 0.3492 MAE = 2.5069 RMSE = 3.1245	R^2 = 0.6337 MAE = 3.3545 RMSE = 4.3711	R^2 = 0.7713 MAE = 5.3192 RMSE = 7.1304

3.3. Discussion

Considering the impact of rainfall deposition on particulate matter, along with relative humidity and TWCI, the TWRI model was proposed. Compared to the TWCI model, TWRI exhibited enhanced stability and robustness, particularly manifesting increased boundary effects in closed areas, especially during summer and in South China. This suggests that TWRI more effectively captured the restrictive impact of topographical and meteorological factors on PM2.5 concentrations, primarily attributed to the predominant deposition effects brought by summer rainfall in humid regions, such as Southern China.

Subsequently, we employed a geographically weighted regression to use TWRI as an index for seasonal inversion. We compared the fitting and verification accuracies of traditional, coupled, and optimized models. The results revealed that: (1) using TWRI alone resulted in a slight decrease in accuracy compared to traditional models, yet the difference was minimal. Integrating the TWRI factor, however, led to improved accuracy. (2) There was little difference in fitting accuracy across seasons in the traditional model, but the lowest fitting accuracy was observed in spring, and the highest in winter within the coupled and optimized models incorporating the TWRI factor. This can be attributed to the fact that (a) TWRI represents a coupling effect of natural factors which does not encompass all mechanisms, thus solely using TWRI and AOD for inversion led to decreased accuracy; (b) in the optimized model, all natural factors were included, reflecting their individual impacts considered in traditional models, although the coupling effect represented by TWRI was not considered, hence its inclusion improved the accuracy; lastly, (c) the differential seasonal fitting performance, with spring being the worst and winter the best, also influenced the inversion accuracy, resulting in poorer performance in spring and enhanced performance in winter.

The spatial distribution of inversion results was analyzed across the different seasons on mainland China using the three models, with a particular emphasis on hotspot regions including the North China Plain, the Pearl River Delta, and the Yangtze River Delta. The results show that using TWRI alone resulted in higher concentration values being more concentrated in closed areas, with clearer boundaries between high- and low-value areas. This primarily stems from the fact that traditional models consider only the magnitude of meteorological and topographical factors, without accounting for the combined effects of these factors on closed areas, where the boundaries of these coupling effects are more distinct.

Furthermore, a comparative analysis of site-specific inversion accuracies revealed that, generally, the accuracies of all models were lower at the local level than at the national level, likely due to the utilization of nationwide data for model fitting. Additionally, within the three studied regions, the optimized model consistently demonstrated the highest inversion accuracy, followed by the traditional model, with the coupled model exhibiting the lowest accuracy. Notably, the coupled model integrating the TWRI achieved its highest accuracy in the North China Plain, with decreased accuracy in the Yangtze River Delta and

the lowest accuracy in the Pearl River Delta. This variation can be attributed to the more pronounced coupled meteorological characteristics (closed effect) represented by TWRI in the North China Plain, as opposed to the weaker effects in the Yangtze and Pearl River Deltas. These findings suggest that inversion models incorporating TWRI are particularly effective in areas characterized by significant closed effects, such as basins and valleys, whereas their performance may be less pronounced in plains and mountainous regions.

However, some limitations/errors remain in this study. First, the TWRI model primarily uses relative humidity to represent changes in rainfall, overlooking the hygroscopic growth effect of relative humidity. Secondly, owing to a lack of daily TWRI data, seasonal averages were used in model fitting and validation, resulting in an insufficient number of sample points.

4. Conclusions

In this article, we introduce the TWRI model to represent the coupling effects of meteorological and topographical factors on PM2.5 concentrations and utilize this index to estimate seasonal surface PM2.5 concentrations. Compared to the TWCI model, TWRI more accurately simulates the spatial distribution and seasonal variations of particulate matter concentrations. By incorporating TWRI into PM2.5 inversions, seasonal accuracy improved by 1.3%, 5.4%, 4%, and 7.9% compared to the traditional model. Furthermore, inversions using TWRI more effectively delineate the boundaries and disparities between high and low concentration areas, especially in humid regions like South China. TWRI introduces a novel parameter in the PM2.5 inversion process, enhancing estimation accuracy and improving the fidelity of spatial distributions. It offers new insights into the coupling effects of natural meteorological elements on particulate matter and provides fresh perspectives for PM2.5–AOD inversion studies.

Future research should focus on developing coupled models that consider hygroscopic growth effects and on creating daily TWRI to enable PM2.5 inversions based on daily data.

Author Contributions: L.W. initiated and supervised this research. B.P. conducted the modeling and analysis and drafted the manuscript guided by L.W. and W.W. B.X. developed the original TWCI model guided by L.W. and W.W. and provided support for the development of the presented TWRI model. All authors have read and agreed to the published version of the manuscript.

Funding: This study was jointly supported by the Basic Science-Center Project of National Natural Science Foundation of China (72088101), the National Key Research and Development Program of China under Grant (2023YFE0208000), and the National Natural Science Foundation of China (42371392).

Data Availability Statement: The original contributions presented in the study are included in the article, further inquiries can be directed to the corresponding author.

Acknowledgments: The authors are grateful to CNEMC, ERA, the data center of NASA, and USGS for providing the datasets used in this study.

Conflicts of Interest: The authors declare no conflict of interest.

References

1. Yin, P.; Brauer, M.; Cohen, A.J.; Wang, H.D.; Li, J.; Burnett, R.T.; Stanaway, J.D.; Causey, K.; Larson, S.; Godwin, W.; et al. The effect of air pollution on deaths, disease burden, and life expectancy across China and its provinces, 1990-2017: An analysis for the Global Burden of Disease Study 2017. *Lancet Planet. Health* **2020**, *4*, E386–E398. [CrossRef] [PubMed]
2. Steffen, W.; Richardson, K.; Rockström, J.; Cornell, S.E.; Fetzer, I.; Bennett, E.M.; Biggs, R.; Carpenter, S.R.; de Vries, W.; de Wit, C.A.; et al. Planetary boundaries: Guiding human development on a changing planet. *Science* **2015**, *347*, 1259855. [CrossRef] [PubMed]
3. Cohen, A.J.; Brauer, M.; Burnett, R.; Anderson, H.R.; Frostad, J.; Estep, K.; Balakrishnan, K.; Brunekreef, B.; Dandona, L.; Dandona, R.; et al. Estimates and 25-year trends of the global burden of disease attributable to ambient air pollution: An analysis of data from the Global Burden of Diseases Study 2015. *Lancet* **2017**, *389*, 1907–1918. [CrossRef] [PubMed]
4. Dominici, F.; Peng, R.D.; Bell, M.L.; Pham, L.; McDermott, A.; Zeger, S.L.; Samet, J.M. Fine particulate air pollution and hospital admission for cardiovascular and respiratory diseases. JAMA-J. Am. Med. Assoc. 2006, 295, 1127–1134. [CrossRef]

5. Liu, C.; Hu, H.; Zhou, S.; Chen, X.L.; Hu, Y.T.; Hu, J.L. Change of Composition, Source Contribution, and Oxidative Effects of Environmental PM2.5 in the Respiratory Tract. *Environ. Sci. Technol.* **2023**, *57*, 11605–11611. [CrossRef] [PubMed]
6. Shu, Z.; Zhao, T.; Liu, Y.; Zhang, L.; Ma, X.; Kuang, X.; Li, Y.; Huo, Z.; Ding, Q.; Sun, X.; et al. Impact of deep basin terrain on PM(2.5) distribution and its seasonality over the Sichuan Basin, Southwest China. *Environ. Pollut.* **2022**, *300*, 118944. [CrossRef] [PubMed]
7. Qi, L.; Zheng, H.; Ding, D.; Ye, D.; Wang, S. Effects of Meteorology Changes on Inter-Annual Variations of Aerosol Optical Depth and Surface PM2.5 in China—Implications for PM2.5 Remote Sensing. *Remote Sens.* **2022**, *14*, 2762. [CrossRef]
8. Zhai, S.X.; Jacob, D.J.; Wang, X.; Shen, L.; Li, K.; Zhang, Y.Z.; Gui, K.; Zhao, T.L.; Liao, H. Fine particulate matter (PM2.5) trends in China, 2013–2018: Separating contributions from anthropogenic emissions and meteorology. *Atmos. Chem. Phys.* **2019**, *19*, 11031–11041. [CrossRef]
9. Lelieveld, J.; Evans, J.S.; Fnais, M.; Giannadaki, D.; Pozzer, A. The contribution of outdoor air pollution sources to premature mortality on a global scale. *Nature* **2015**, *525*, 367–371. [CrossRef] [PubMed]
10. Ding, Y.T.; Zhang, M.; Qian, X.Y.; Li, C.R.; Chen, S.; Wang, W.W. Using the geographical detector technique to explore the impact of socioeconomic factors on PM2.5 concentrations in China. *J. Clean. Prod.* **2019**, *211*, 1480–1490. [CrossRef]
11. Liu, B.; Ma, X.; Ma, Y.; Li, H.; Jin, S.; Fan, R.; Gong, W. The relationship between atmospheric boundary layer and temperature inversion layer and their aerosol capture capabilities. *Atmos. Res.* **2022**, *271*, 106121. [CrossRef]
12. Chen, X.; Ye, J. When the wind blows: Spatial spillover effects of urban air pollution in China. *J. Environ. Plan. Manag.* **2018**, *62*, 1359–1376. [CrossRef]
13. Liu, B.Y.; Wang, L.L.; Zhang, L.; Bai, K.X.; Chen, X.F.; Zhao, G.N.; Yin, H.T.; Chen, N.; Li, R.; Xin, J.Y.; et al. Evaluating urban and nonurban PM2.5 variability under clean air actions in China during 2010-2022 based on a new high-quality dataset. *Int. J. Digit. Earth* **2024**, *17*, 2310734. [CrossRef]
14. Zhang, Q.; Zheng, Y.X.; Tong, D.; Shao, M.; Wang, S.X.; Zhang, Y.H.; Xu, X.D.; Wang, J.N.; He, H.; Liu, W.Q.; et al. Drivers of improved PM2.5 air quality in China from 2013 to 2017. *Proc. Natl. Acad. Sci. USA* **2019**, *116*, 24463–24469. [CrossRef] [PubMed]
15. Zhang, Y.-L.; Cao, F. Fine particulate matter (PM2.5) in China at a city level. *Sci. Rep.* **2015**, *5*, 14884. [CrossRef] [PubMed]
16. Yang, Z.M.; Zdanski, C.; Farkas, D.; Bang, J.; Williams, H. Evaluation of Aerosol Optical Depth (AOD) and PM2.5 associations for air quality assessment. *Remote Sens. Appl.-Soc. Environ.* **2020**, *20*, 100396. [CrossRef]
17. Yang, Q.; Yuan, Q.; Yue, L.; Li, T.; Shen, H.; Zhang, L. The relationships between PM2.5 and aerosol optical depth (AOD) in mainland China: About and behind the spatio-temporal variations. *Environ. Pollut.* **2019**, *248*, 526–535. [CrossRef] [PubMed]
18. Xu, W.; Wang, W.; Wang, N.; Chen, B. A New Algorithm for Himawari-8 Aerosol Optical Depth Retrieval by Integrating Regional $PM_{2.5}$ Concentrations. *IEEE Trans. Geosci. Remote Sens.* **2022**, *60*, 4106711. [CrossRef]
19. Yang, Q.; Yuan, Q.; Yue, L.; Li, T. Investigation of the spatially varying relationships of PM2.5 with meteorology, topography, and emissions over China in 2015 by using modified geographically weighted regression. *Environ. Pollut.* **2020**, *262*, 114257. [CrossRef] [PubMed]
20. Hammer, M.S.; van Donkelaar, A.; Li, C.; Lyapustin, A.; Sayer, A.M.; Hsu, N.C.; Levy, R.C.; Garay, M.J.; Kalashnikova, O.V.; Kahn, R.A.; et al. Global Estimates and Long-Term Trends of Fine Particulate Matter Concentrations (1998–2018). *Environ. Sci. Technol.* **2020**, *54*, 7879–7890. [CrossRef] [PubMed]
21. Zhu, S.T.; Tang, J.Y.; Zhou, X.L.; Li, P.; Liu, Z.L.; Zhang, C.C.; Zou, Z.Y.; Li, T.; Peng, C.H. Research progress, challenges, and prospects of PM2.5 concentration estimation using satellite data. *Environ. Rev.* **2023**, *31*, 605–631. [CrossRef]
22. Wang, W.; Mao, F.; Du, L.; Pan, Z.; Gong, W.; Fang, S. Deriving Hourly PM2.5 Concentrations from Himawari-8 AODs over Beijing–Tianjin–Hebei in China. *Remote Sens.* **2017**, *9*, 858. [CrossRef]
23. Bai, Y.; Wu, L.; Qin, K.; Zhang, Y.; Shen, Y.; Zhou, Y. A Geographically and Temporally Weighted Regression Model for Ground-Level PM2.5 Estimation from Satellite-Derived 500 m Resolution AOD. *Remote Sens.* **2016**, *8*, 262. [CrossRef]
24. He, Q.; Huang, B. Satellite-based mapping of daily high-resolution ground PM2.5 in China via space-time regression modeling. *Remote Sens. Environ.* **2018**, *206*, 72–83. [CrossRef]
25. Song, S.; Gao, M.; Xu, W.; Sun, Y.; Worsnop, D.R.; Jayne, J.T.; Zhang, Y.; Zhu, L.; Li, M.; Zhou, Z.; et al. Possible heterogeneous chemistry of hydroxymethanesulfonate (HMS) in northern China winter haze. *Atmos. Chem. Phys.* **2019**, *19*, 1357–1371. [CrossRef]
26. Ning, G.; Wang, S.; Ma, M.; Ni, C.; Shang, Z.; Wang, J.; Li, J. Characteristics of air pollution in different zones of Sichuan Basin, China. *Sci. Total Environ.* **2018**, *612*, 975–984. [CrossRef] [PubMed]
27. Karle, N.N. *Studies of the Planetary Boundary Layer and their Impact on Air Pollution in a Semi-Arid Region with Complex Terrain*; The Unisversity of Texas: El Paso, TX, USA, 2021.
28. Tang, Y.; Xie, S.; Huang, L.; Liu, L.; Wei, P.; Zhang, Y.; Meng, C. Spatial Estimation of Regional PM2.5 Concentrations with GWR Models Using PCA and RBF Interpolation Optimization. *Remote Sens.* **2022**, *14*, 5626. [CrossRef]
29. Ding, W.; Zhu, Y. Prediction of PM2.5 Concentration in Ningxia Hui Autonomous Region Based on PCA-Attention-LSTM. *Atmosphere* **2022**, *13*, 1444. [CrossRef]
30. Zhang, T.; Zang, L.; Wan, Y.; Wang, W.; Zhang, Y. Ground-level PM2.5 estimation over urban agglomerations in China with high spatiotemporal resolution based on Himawari-8. *Sci. Total Environ.* **2019**, *676*, 535–544. [CrossRef] [PubMed]
31. Wu, L.; Xie, B.; Wang, W. Quantifying the impact of terrain–wind–governed close-effect on atmospheric polluted concentrations. *J. Clean. Prod.* **2022**, *367*, 132995. [CrossRef]

32. Lyapustin, A.; Wang, Y. MCD19A2 MODIS/Terra+Aqua Land Aerosol Optical Depth Daily L2G Global 1 km SIN Grid V006. [Dataset], NASA EOSDIS Land Processes DAAC, 2018. Available online: https://lpdaac.usgs.gov/products/mcd19a2v006/ (accessed on 9 June 2024).
33. Urraca, R.; Huld, T.; Gracia-Amillo, A.; Martinez-de-Pison, F.J.; Kaspar, F.; Sanz-Garcia, A. Evaluation of global horizontal irradiance estimates from ERA5 and COSMO-REA6 reanalyses using ground and satellite-based data. *Sol. Energy* **2018**, *164*, 339–354. [CrossRef]
34. Schnell, J.L.; Naik, V.; Horowitz, L.W.; Paulot, F.; Mao, J.; Ginoux, P.; Zhao, M.; Ram, K. Exploring the relationship between surface PM2.5 and meteorology in Northern India. *Atmos. Chem. Phys.* **2018**, *18*, 10157–10175. [CrossRef]
35. Liu, S.; Xing, J.; Sahu, S.K.; Liu, X.; Liu, S.; Jiang, Y.; Zhang, H.; Li, S.; Ding, D.; Chang, X. Wind-blown dust and its impacts on particulate matter pollution in Northern China: Current and future scenarios. *Environ. Res. Lett.* **2021**, *16*, 114041. [CrossRef]
36. Zhang, L.; Guo, X.; Zhao, T.; Gong, S.; Xu, X.; Li, Y.; Luo, L.; Gui, K.; Wang, H.; Zheng, Y.; et al. A modelling study of the terrain effects on haze pollution in the Sichuan Basin. *Atmos. Environ.* **2019**, *196*, 77–85. [CrossRef]
37. Oshan, T.M.; Smith, J.P.; Fotheringham, A.S. Targeting the spatial context of obesity determinants via multiscale geographically weighted regression. *Int. J. Health Geogr.* **2020**, *19*, 11. [CrossRef]
38. Wei, J.; Huang, W.; Li, Z.; Xue, W.; Peng, Y.; Sun, L.; Cribb, M. Estimating 1-km-resolution PM2.5 concentrations across China using the space-time random forest approach. *Remote Sens. Environ.* **2019**, *231*, 111221. [CrossRef]

Disclaimer/Publisher's Note: The statements, opinions and data contained in all publications are solely those of the individual author(s) and contributor(s) and not of MDPI and/or the editor(s). MDPI and/or the editor(s) disclaim responsibility for any injury to people or property resulting from any ideas, methods, instructions or products referred to in the content.

sustainability

MDPI

Article

Sustainable Geoinformatic Approaches to Insurance for Small-Scale Farmers in Colombia

Ahmad Abd Rabuh [1], Richard M. Teeuw [2,*], Doyle Ray Oakey [3], Athanasios V. Argyriou [4], Max Foxley-Marrable [5] and Alan Wilkins [6]

[1] Analytics, IS & Operations Department, Oxford Brookes University, Oxford OX3 0BP, UK; aabd-rabuh@brookes.ac.uk
[2] Centre for Applied Geoscience, University of Portsmouth, Portsmouth PO1 3QL, UK
[3] Primer Sol Consulting, Monument, CO 80132, USA
[4] Laboratory of Geophysical—Satellite Remote Sensing & Archaeo-Environment (GeoSat ReSeArch), Institute for Mediterranean Studies (IMS), Foundation for Research & Technology Hellas (FORTH), 74100 Rethymno, Greece; nasos@ims.forth.gr
[5] Revolution Data Platforms, Ottawa, ON K2J, Canada
[6] Mercari Risk Management Ltd., Southampton SO45 5TE, UK
* Correspondence: richard.teeuw@port.ac.uk; Tel.: +44-2392-842267

Abstract: This article presents a low-cost insurance system developed for smallholder farms in disaster-prone regions, primarily using free Earth observation (EO) data and free open source software's (FOSS), collectively termed "sustainable geoinformatics." The study examined 30 farms in Risaralda Department, Colombia. A digital elevation model (12.5 m pixels) from the ALOS PALSAR satellite sensor was used with a geographic information system (GIS) to map the terrain, drainage, and geohazards of each farming district. Google Earth Engine (GEE) was used to carry out time-series analysis of 15 EO and weather datasets for 1998 to 2020. This analysis enabled the levels of risk from hydrometeorological hazards to be determined for each farm of the study, providing key data for the setting of insurance premiums. A parametric insurance product was developed using a proprietary mobile phone app that collected GPS-tagged, time-stamped mobile phone photos to verify crop damage, with further verification of crop health also provided by daily near-real-time satellite imagery (e.g., PlanetScope with 3 m pixels). Machine learning was used for feature identification with the photos and the satellite imagery. Key features of this insurance system are its low operational cost and rapid damage verification relative to conventional approaches to farm insurance. This relatively fast, low-cost, and affordable approach to insurance for small-scale farming enhances sustainable development by enabling policyholder farmers to recover more quickly from disasters.

Keywords: digital data poverty; disaster risk management; earth observation; extreme weather; GIS; machine learning; parametric insurance; small farms; sustainable geoinformatics

1. Introduction

Climate change is affecting food security via increasing temperatures, changing precipitation patterns, and greater frequency of extreme weather events [1]. According to the World Health Organization, 828 million people are affected by hunger, and 670 million people (8 percent of the world population) will still be facing hunger in 2030 [2]. This research contributes to reducing food insecurity, contributing to the United Nations Sustainable Development Goals (SDGs) of "Zero Hunger" and "Life on Land".

Workers in low-income countries are the most affected by climate change. They struggle to find insurance as insurers begin to avoid risky regions [3]. Those who are vulnerable due to poverty, limited education, and financial exclusion are more likely to be impacted by extreme weather events [4]. Insurance can spread the risk of the losses from disasters. However, the increasing frequency and severity of extreme weather events

is making insurance much more challenging. This has led to increases in prices of the premiums charged for insurance cover, a cost barrier that low-income populations find difficult to cross [5].

The aim of this research is to develop an insurance system that is affordable to insurers and small-scale farm owners. We illustrate how this can be done using free open source software (FOSS), geographic information system (GIS), data from Earth observation (EO) satellites, and the application of machine learning and deep learning algorithms to detect features in mobile phone photos. From an insurance sector perspective, the objectives are to: (i) provide insurance access to small-scale farms, allowing them to run a viable business by increasing crop sustainability and resilience to extreme weather events; (ii) allow underwriters to predict risks, thus setting more affordable premiums; and (iii) optimize claims and verify damages using an automated system.

This study examines the feasibility of using sustainable geoinformatics and machine learning with EO satellite and mobile phone technologies, seeking to demonstrate that those technologies can be integrated into an insurance system that is affordable to small-scale farmers. Figure 1 shows how the feasibility study was conducted, with a pre-disaster underwriting stage having a better estimation of the underlying asset (i.e., crop), a better awareness of potential geohazards affecting insured farms, and a historical outlook on previous disaster events in the farming district. The diagram illustrates how a parametric insurance model estimating disaster damage can use machine learning models to detect changes in satellite images and classify mobile phone photos uploaded by impacted farmers, triggering an automated insurance payout.

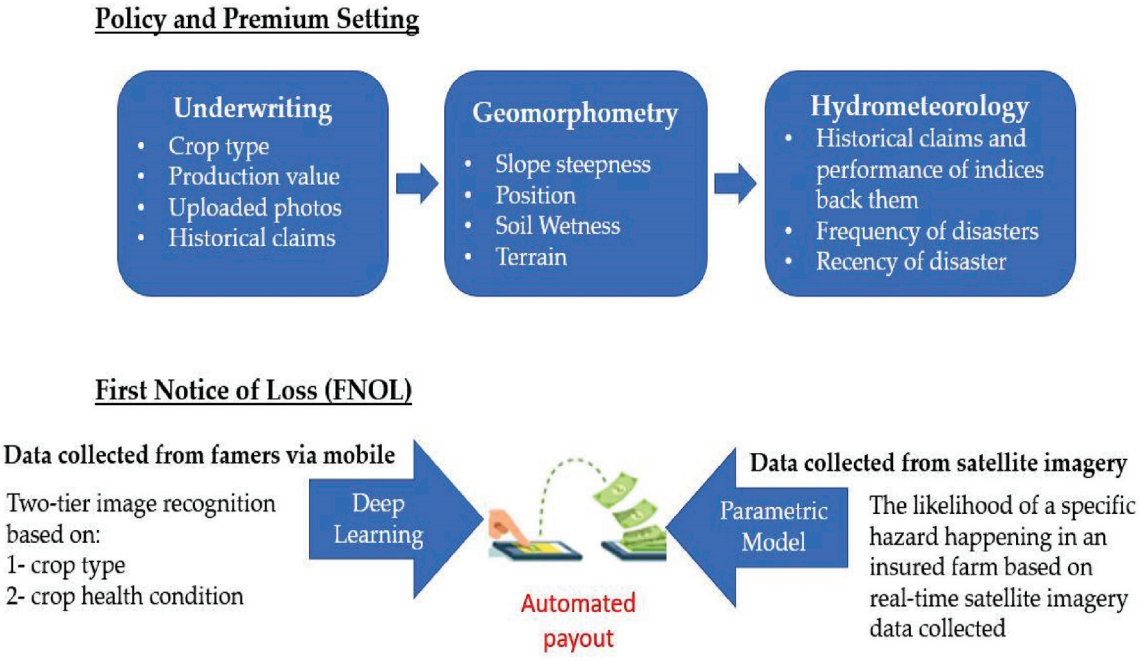

Figure 1. Conceptual model of the insurance system and its geoinformatic components.

The organization of this manuscript is as follows. The introduction reviews the impacts of extreme weather events on farming and how such risks have been managed, including the provision of insurance for the farming sector. The next section covers the data types and analytical methods. Next comes the reporting of results, followed by a discussion, including recommendations, and conclusions.

1.1. Climate Change, Disasters, and Farming

In 2018, the UK Space Agency predicted that "Climate change is expected to result in more frequent and intensive climate-related hazards. It will also reduce the predictabil-

ity and change the geographic distribution of extreme climatic hazards, such as extreme temperatures, floods and droughts, heat waves, wild fires and storms" [6]. That prediction has largely been verified by numerous extreme weather events, often with records broken [1,7]. Therefore, many scholars focused their research on reducing risk in disaster-prone areas by building a resilient climate change ecosystem [8], in which a key factor is food security [9,10]. Other factors are decreasing the likelihood of crop failure (i.e., damaged, diseased, or destroyed [11]), as well as mitigating the risk of damage to farm infrastructure [12].

This research contributes to the shifting of the climate risk assessment framework to a sustainable climate-resilient ecosystem. This can be done by (1) predicting where andwhen extreme weather events are most likely and (2) ensuring farmers' business continuity and thus the provision of sustainable livelihoods. This comes in line with the findings of the Intergovernmental Panel on Climate Change (IPCC), which asserted that climate change exacerbates land degradation [1].

1.2. Disaster Risk Management

Managing the risk of disaster has two main components: (i) reducing the risk of a disaster occurring, which requires research into the main drivers of disasters (hazards, exposure, vulnerability) to identify appropriate mitigation activities; and (ii) managing disaster risk as effectively as possible, which involves emergency management (from preparedness and early warning systems, to rapid response, then recovery, following "Build Back Better" guidelines), as well as strengthening resilience, e.g., by reducing socio-economic impacts via insurance.

Oliveira [7] conducted a systematic review of pre- and post-disaster studies and highlighted the importance of building back better in the post-disaster phase in light of the Sendai Framework. The aforementioned framework was published in 2015 by the UN Office for Disaster Risk Reduction, aiming to achieve seven global sustainable targets by 2030. In light of the above, impacts of extreme weather disasters were seen as a threat to food security and agriculture.

The term "resilience" became prominent towards the end of the last century with conceptual frameworks [13]. Lu and Yang [14] argued that disasters come with a social factor, which can be measured using social networks. Accordingly, Wu and Cui [15] monitored tweets and measured sentiment during Hurricane Sandy.

Geoinformatics and Farm Risk Management

The focus on food security has shifted the attention to secure vulnerable sources of food with advanced technologies. The suggestion of relying on information and communication technologies to increase resilience, especially in low- and middle-income countries, was introduced by many researchers followed by the emergence of a sub-discipline known as "ICT for Resilience and Sustainable Development (ICT4RS)" [4,16]. Research by Heeks and Ospina [17] introduced e-Resilience, a framework that explains the interplay between information systems and humans during disasters. They conducted a survey and reported on the usage of ICT (via mobile phones and internet-connected laptops/tablets) in relation to the respondents' demographics. Similarly, Longo, Zardo [8] used ArcGIS version 10.4.1 software to map land cover and assess its resilience to climate change, creating the Ecosystem Service Climate Change Adaptation (ESCCA) framework.

The global abundance of freely available digital map data and Earth observation data with relatively detailed pixels (in the 3 m to 300 m range), has given scientists the opportunity to integrate many datasets at locations such as farm fields to detect, map and monitor types of vegetation coverage and hazard zones [18]. As a result, space agencies started different programs to eliminate food insecurity and protect agriculture productivity. The Global Agriculture Monitoring (GLAM) project [9] aims at monitoring crop conditions using remotely sensed data [19]. Similarly, the National Aeronautics and

Space Administration (NASA) started the "Harvest Africa" program to monitor crops and issue early warnings in the sub-Saharan Africa (SSA) region [20].

Leidig and Teeuw [21] considered disaster risk management applications of free or low-cost remote sensing data and geospatial analysis software, termed "sustainable geoinformatics." This article is inspired by the aforementioned term and presents a low-cost EO-based farm insurance system. This is also consistent with what the UK Space Agency had stated: "*EO enables accurate mapping of land use and monitoring of changes in crops and the land itself. This data is useful for finance companies that need access to data concerning land used by growers in order to be able to offer them financial products such as insurance or credit. For many small-scale producers in developing countries, these financial products are prohibitively expensive, not designed for their needs, or simply not available at all. . .*" [6], page 11. This research examines the feasibility of using sustainable geoinformatics for disaster risk management with small farms. This has involved a combination of digital elevation data from satellite remote sensing, daily EO imagery and archive EO data from the past two decades, supported by time-stamped GPS-tagged photos from farmers' mobile phones and data processing using deep learning. Of the various studies that focused on using geoinformatics/EO and ICT to support agriculture, the majority focused on the African continent in different scopes (e.g., West Africa, sub-Saharan Africa, etc.). Additionally, until now, no study has discussed the AI deep learning model for crop damage detection from an actuarial point of view and how that would affect the underwriting process.

1.3. Provision of Insurance for Small-Scale Farmers

Insurance helps to maintain economic stability, especially for vulnerable societies [22]. However, due to its volatility in weather conditions, many insurers stopped covering disasters such as floods [5]. The impacts of climate change are greater with small-scale farmers because they typically do not have the capacity to cope, due to their limited resources and the cost barrier that they face if they seek farm insurance [6]. This can be explained by "social identity theory," which asserts that generations and social classes can impact climate policies [23]. Meanwhile, the development of an agricultural insurance system is a complex and multifaceted process, where production system, crop types, farm size, farm location, data availability, sales channels and other risk factors make it difficult for insurers to offer the right policy and set the right premium [24].

In agriculture, of the world's 570 million smallholder farms, 87% are less than 2 Ha in size [25]. In addition to cost, agriculture insurance remains low in developing countries, where many small farms are concentrated, due to institutional and technological constraints [26] as well as the high cost of loss estimation/verification [27]. In the Latin American region, only 4 percent of small to medium enterprises (SMEs) working in the farming business have insurance, generally due to lack of governmental support, except for Mexico and Brazil [28]. In addition, premiums are estimated to be around USD 72 per hectare, which is a significantly high amount for smallholding farm owners. Overall, the insured farmed land in Latin America is estimated to be 29 million hectares out of a total of 138 million hectares [28]. As a result, many smallholder farmers have formed cooperative groups in order to improve productivity and spread risks, as is the case in many farming districts of Colombia, where this research is focused.

Decisions associated with disasters have been characterized as having an heuristics nature [29] instead of being data-driven. Consistently, "parametric insurance" uses indices to guide insurance payouts based on pre-defined thresholds [27]. In other words, its ultimate payment is not based on individual losses, but determined according to a measure (be it an earthquake magnitude or wind speed). In this research, the combination of EO data, GIS, geospatial analysis and machine learning methods is utilized to identify the right measure(s) per disaster type while arguing that insurance payouts can still be individualized using deep learning technology.

Parametric insurance offers payouts to claimants when a disaster exceeds a threshold measured by an index or multiple indices. The adoption of parametric insurance has been

challenging and controversial. Figueiredo, Martina [27] implied that at the heart of its design, parametric insurance violates risk assessment principles since it issues automated payouts regardless of actual losses. Nevertheless, parametric insurance has been common when it comes to agricultural products. A framework of how parametric insurance can be used in Africa was developed by Ibarra and Securities [26]. Subsequently, many studies focused on different aspects of such novel adoption in various countries. For example, Figueiredo, Martina [27] focused on methods to estimate risks by calculating the probability of a flood event happening in Jamaica using a logistic regression model. They based their study on the premise that the target variable has a binary nature: disaster/no disaster. A study by Prokopchuk [30] used temperature, humidity and precipitation to estimate the growth level of grains within Ukraine and linked that to insurance. Inspired by the importance of predictability and the emergence of machine learning, Cesarini, Figueiredo [31] suggested integrating multiple sources of weather data then applying supervised machine learning (ML) techniques, such as support vector machines and artificial neural networks (ANNs) to classify impacts of drought and floods in the Dominican Republic between 2000 and 2019. The study of Benso, Gesualdo [22] examined weather indices in Brazil and how those affect soybean farms: they argued that disasters could be interrelated and proposed a multi-hazard risk assessment approach. During the 2023 United Nations Climate Change Conference, the former secretary of the United States, Hillary Clinton, indicated that she is pioneering new reforms of the insurance industry by working with the Arsht-Rock Foundation Resilience Center to recognize parametric insurance as a form of climate change resilience [3].

2. Materials and Methods

2.1. The Study Area

The study area for this research is the Dosquebradas farming district in Risaralda Department, Colombia (Figure 2).

Figure 2. Location of the study area in Riseralda Department, Colombia. Areas of forest are shown in dark green. The inset box indicates the area shown in detail within Figure 3 (map source: OpenStreetMap).

Farm Locations and Disaster Events

In Dosquebradas, 30 farms were surveyed (Figure 3). These were mostly growing coffee, with a few fields of avocado. Examination of disaster data on the website of Colombia's Institute of Hydrology, Meteorology and Environmental Studies (IDEAM) (http://ideam.gov.co, accessed on 15 September 2020) yielded information about 31 disasters

affecting Risaralda Department since 1998, e.g., event dates, areas affected, casualties (see Appendix A). Earthquakes were also included in the database because they often cause landslides, which can severely damage farm infrastructure.

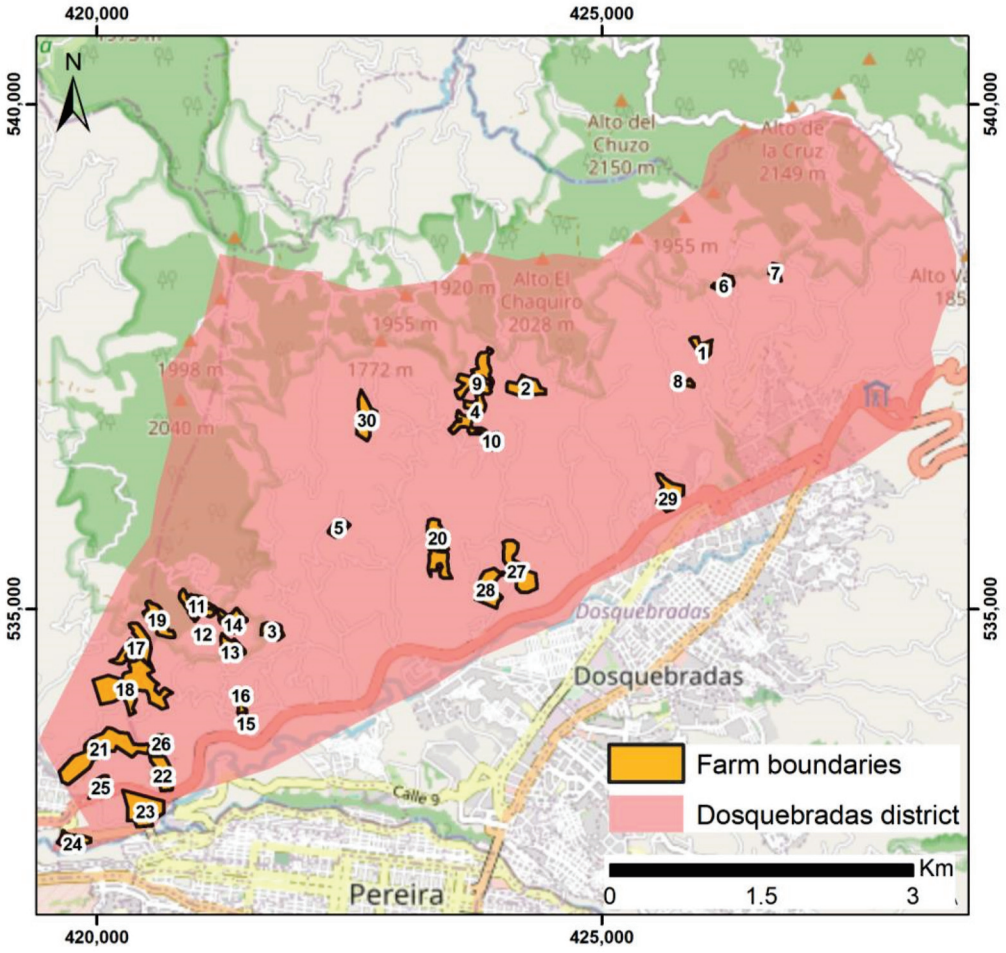

Figure 3. The Dosquebradas study area (corresponding to the inset box in Figure 2): locations and areal extents of the farms included in the testing of the insurance system.

2.2. Data Sources

According to Ibarra and Securities [26], data of high quality is essential in building a parametric insurance model. Satellite imagery and digital elevation model (DEM) data were used to examine the study area, involving mapping of terrain (geomorphometry), and monitoring of land cover, crop types and weather (temperature and precipitation). After pre-processing, the various datasets were integrated using QGIS version 3.10. Archive geospatial datasets were processed using Google Earth Engine (GEE), with time-series analyses of vegetation and hydro-meteorological indices. Finally, GPS time-stamped photos provided via mobile phone apps were used for verification purposes, where deep learning was used to identify crop types and health conditions.

2.2.1. Earth Observation (EO) Imagery

Satellite EO imagery forms the basis of many global datasets on vegetation types, soil features, and land surface temperature [5]. In this feasibility study, various geoinformatic datasets were used and these are summarized in Table 1. The farming district was mapped and monitored for vegetation cover and ground surface temperature using imagery from the Moderate Resolution Imaging Spectroradiometer (MODIS: 250 m pixels), analyzing an archive of MODIS imagery dating back to 2000. Detailed EO-based mapping of farms and

individual fields (vegetation cover, crop types, stages of crop growth and photosynthetic activity) was carried out using visible and infrared imagery from PlanetScope (3.8 m pixels) and Sentinel-2 (10 m pixels), for which archive imagery extends back to 2015.

Table 1. Geospatial datasets (VIR = visible and infraRed; VNIR = visible and near infrared).

Dataset	Type	Pixel Size (m)	Derived Indices	Data Provider
ALOS PALSAR (L-band radar)	Digital Elevation Model (DEM)	12.5	Landform types, slope steepness, floodplains, topographic wetness	https://search.asf.alaska.edu/#/, accessed on 9 November 2020
MODIS	VIR imagery	250	NDVI (vegetation photosynthesis)	https://modis.gsfc.nasa.gov/data/. accessed on 9 November 2020
Sentinel-2 Multi Spectral Instrument	VIR imagery	10	NDVI: vegetation photosynthesis, bare ground, crop type	https://earth.esa.int/web/sentinel/user-guides/sentinel-2-msi/product-types/level-2a, accessed on 9 November 2020
PlanetScope	VNIR imagery	3.0		https://www.planet.com/products/planet-imagery/, accessed on 9 November 2020
Geological maps	GIS—1:100,000	1000	Geology Land cover type	http://www.ideam.gov.co/, accessed on 9 November 2020
OpenStreetMap	Open Source topography	Variable to 1:10 k scale	Topography: drainage, roads, bridges, buildings	https://www.openstreetmap.org/#map=13/4.8540/-75.7178&layers=C, accessed on 9 November 2020
Google Earth Pro	Maps and archive EO imagery	0.3–30	Digital globe and map with 3D visualization of terrain	https://www.google.com/intl/en_uk/earth/versions/, accessed on 9 November 2020
Google Earth Engine (GEE)	Archive EO imagery	10–500	Search engine and data analysis platform	https://code.earthengine.google.com/, accessed on 2 October 2020

2.2.2. Digital Elevation Models (DEMs) and Geomorphometrics

The ALOS PALSAR global DEM (12.5 m pixels) produced by the University of Alaska Space Facility was used to carry out geomorphometric analyses of the terrain within the two farming districts. The methodology of Argyriou, Sarris [32] and Argyriou, Teeuw [33] was used to produce DEM-derived maps of slope steepness, slope aspect, terrain wetness, drainage networks, and landform types.

2.2.3. Mobile Phone Photos

Using a customized mobile phone app, time-stamped photos with global positioning system (GPS) longitude/latitude coordinates accurate to $+/-5$ m were collected in September 2020 within the sampled farms. A total of 748 farm photos were saved on the InsurTech server (Figure 4) as KML files. That KML format enabled administrative users to see the locations via Google Earth, thus linking mobile phone photos to insured items on farms, as well as providing locations that could be examined using EO satellite imagery.

2.3. Data Analysis

GPS-located phone photos were collected around the boundaries of each insured farm, enabling the area of each crop type on the farm to be calculated. Thereafter, a change detection analysis could be applied to calculate the area of the "damaged" pixels and thus estimate losses. This can also be done using daily imagery from PlanetScope or other high-resolution satellite imagery (e.g., Maxar, Iceye) with pixels in the 3m to 0.3m range.

Figure 4. Satellite image of a studied farm, overlain with locations of GPS-tagged time-stamped photos from the InsurTech mobile phone app, taken at 50 m intervals around a field boundary, with inset example photo.

In this study, the research framework of Wagstaff [34] was followed, with its three stages: preparation, ML contribution, and impact. In preparation, the problem was identified and relevant data were collected while generating features and labeling classes. In the ML contribution, random forest (RF) was used to classify vegetation types, while LSTM was used to detect extreme weather events in the time-series analysis of the satellite data. Additionally, deep learning (DL) was used to recognize images collected from the mobile app and classify those. The impact results were presented in a parametric model form where insurers would adopt a new process and become part of the InsurTech ecosystem. Those results are shared with relevant communities such as policymakers, technology developers, agriculture supply chain players and insurers who would benefit from the accessible EO capabilities. This research encouraged the adoption of the new geoinformatic approach in order to sustain small-scale farming businesses.

There were four analyses that were performed in this research: (i) terrain analysis of farming districts and individual farms, using DEM-based geomorphometrics; (ii) mapping land cover and crop types by applying a machine learning random forest (RF) algorithm on satellite imagery; (iii) time-series analysis of farming districts, monitoring hydrometeorological indices before, during, and after historical extreme weather events, using long short-term memory (LSTM); and (iv) image recognition via computer vision to classify mobile phone photos into crop type and health condition, using deep learning (DL).

2.3.1. Mapping Terrain and Landforms: DEM Geomorphometrics

A DEM of a given landscape can be analyzed using geomorphometrics to identify key components that will have distinct morphologies. This is subject to specific Earth surface processes and thus contains predictable soil and regolith types. A freely available DEM with near-complete global coverage was used in this research: the 12.5 m-pixel ALOS PALSAR DEM (Table 1). Three geomorphometric features were mapped in the study area and calculated within QGIS version 3.10, as follows.

1. Slope steepness: Slope gradient (SG) shows the change occurring in elevation between each pixel of the DEM and its neighbors. Flat surfaces are characterized by low values, while a steep relief is indicated by higher values [35]. The direction of slope, known as the slope aspect, was also mapped because some slopes receive more rainfall as they face towards the dominant direction of winds during the wetter seasons of the year.
2. Topographic position index (TPI), showing landform types: This is a geomorphological measure that classifies landforms into 10 types: canyons and deeply incised valleys, mid-slope drainage, upland drainage, U-shaped valleys, plains, foot slopes, upper slopes, local ridges, mid-slope ridges, and high ridges [33,36].

3. Topographic wetness index (TWI): This measure determines the slope of a given field in order to estimate soil moisture and surface saturation of that area. A high TWI value indicates an accumulation of soil moisture and surface saturation [37,38]. A low TWI value indicates susceptibility to soil erosion, whereas a high TWI value indicates an area with limited moisture [33,39,40].

2.3.2. Vegetation Mapping and Monitoring

- Vegetation detection with satellite imagery: Sentinel-2 and PlanetScope imagery (Table 1) were used to discriminate between vegetation and areas of bare soil in the study areas. The detection of land cover types through machine learning predictive modeling informed our parametric insurance model and helped in price setting, as detailed later in this paper. This was done using a random forest (RF) machine learning classification algorithm [41]. High prediction accuracy and high tolerance to outliers and noise are the main advantages of RFs [41]. In addition, they estimate correlations between covariates and dependent variables by evaluating the relative importance of covariates [42]. RF classification was applied to cloud-free Sentinel-2 imagery, based on training samples, to discriminate land cover types.
- Normalized Difference Vegetation Index (NDVI): The NDVI "is the primary vegetation index for monitoring crop conditions" [9]. It is widely used due to its ability to measure photosynthesis activity and thus correlate with vegetation density and vitality [43,44]. The NDVI is derived from satellite imagery in the visible and near-infrared (VNIR) parts of the electromagnetic spectrum. The NDVI derived from MODIS can be used for assessing vegetation dynamics during the past 20 years [45]. The NDVI has been at the center of calculations pertaining to food insecurity whenever EO is used to spot anomalies in the growth of crops [9]. Bégué, Madec [9] conducted spatiotemporal analysis of NDVI performance in West Africa: impacts of extreme weather events could be evaluated based on NDVI values before, during, and after disaster events.

2.3.3. Time-Series Analysis

Datasets were sourced via Google Earth Engine (GEE) to analyze various bioclimatic and hydrometeorological indices for our study area, examining data for the past 20 years and focusing on extreme weather events affecting those areas since 1998. Monthly datasets were compiled and analyzed from various climatic data archives: Climate Hazards group InfraRed Precipitation with Station data (CHIRPS), ERA5 Climate, TerraClimate, Palmer Drought Severity Index (PDSI) and the Cloud Classification System-Climate Data Record (CCS-CDR), details of which are provided in Appendix B. Those hydrometeorological datasets were used to examine periods of extreme weather events, such as intense rainfall and flooding (La Niña), dryness, drought and wildfires (El Niño).

MODIS 16-day rolling mean and medians of NDVI, Precipitation Estimation from Remotely Sensed Information using Artificial Neural Networks (PERSIANN), CHIRPS precipitation indices and the Palmer Drought Severity Index (PDSI) were plotted on a time-series axis. Also, periods of extreme weather were shaded in colors: blue for floods, light brown for drought, and dark red for periods with frequent wildfire (Figure 5).

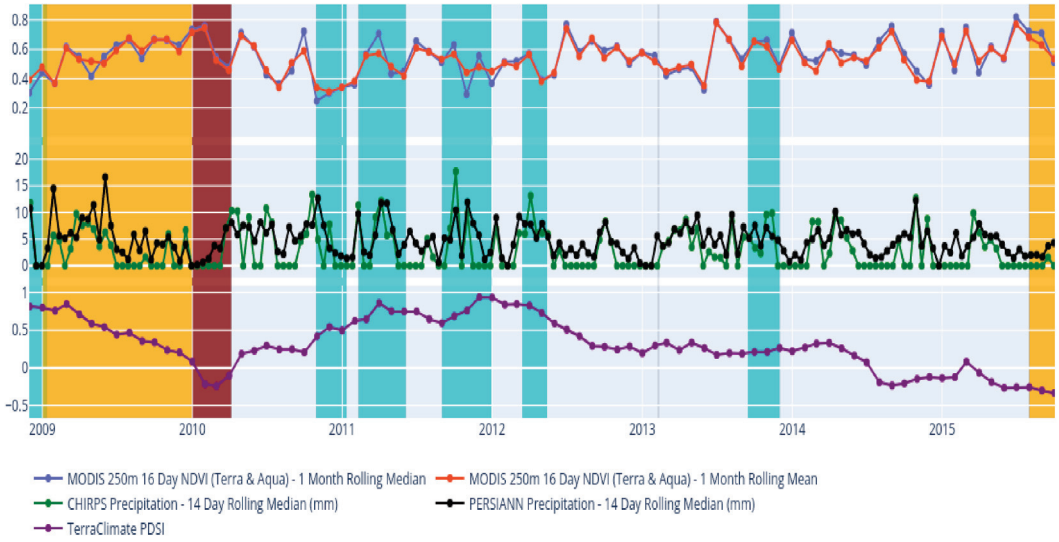

Figure 5. An excerpt from the timeline chart of climate indices and MODIS NDVI for the Dosquebradas district from 2009 to 2015. Periods with flooding are highlighted in blue and periods of drought are shown in orange, with brown indicating drought with numerous wildfires.

2.3.4. Damage Detection via Deep Learning (DL)

For geoinformatics to contribute to social resilience and sustainable food security, local knowledge must be incorporated in the implementation of the technology. Therefore, a digital business model was adopted, where insured farmers input their data by uploading time-stamped and geotagged photos via their mobile phones. Deep learning (DL) models have been utilized as an effective way to detect objects within photos in disaster management. For example, Chaudhuri and Bose [29] applied a convolutional neural network deep learning model for geotagged photos to verify damage in buildings and survivors in the case of earthquakes. Nakalembe and Kerner [46] argued the plausibility of using deep learning models in lieu of machine learning decision trees and random forest approaches for crop-type classifications.

Long Short-Term Memory (LSTM)

A sequence learning method has been developed for this research with thousands of time steps via a recurrent neural network known as long short-term memory (LSTM) model. The batch size and time steps were used as input features, with the output being a softmax function used in the output (final) layer. The model was trained using many instances of the disaster dataset with a look-back window of day/week/month (n + 1) onward. Every time the one-step-ahead feature is predicted, its observed parameters can be used to refine the network state, before moving the time window one step (Figure 6). This procedure provides an up-to-date network, updating every time new information is available.

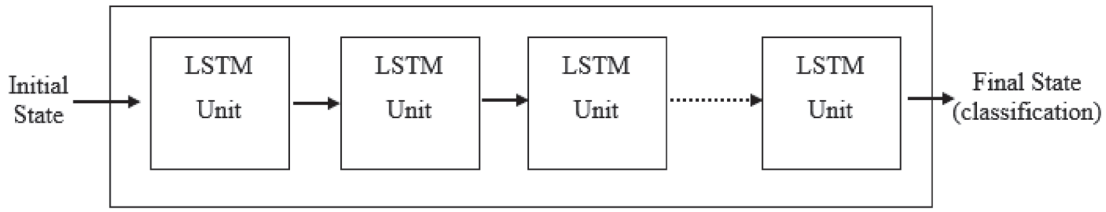

Figure 6. Long short-term memory (LSTM) layers.

DL was used for image recognition and classification with the photos of the mobile phone app, aiming to detect labeled crop types and verify damage due to extreme weather events. In this feasibility study, the focus was on avocado and coffee crops.

To ensure correct pre-processing, hyper-parameters were set at the start of the learning to the shape and size of the crop images, specifically, rescaling the photos to 28 rows by 28 columns since neural networks work on square images [29]. The inputs are trained images with their labels as well as a holdout sample (or subset) for testing purposes. Both sequential and activation functions were run on the training datasets to derive initial weights. A forward pass happens when the aforementioned data and parameters are passed to the model.

Mathematical operations (linear algebraic and integral) were performed to assess the correctness of model definitions in predicting the pre-known labels. Thereafter, a backward pass took place where an optimizer aimed at minimizing the loss value using differential operation. This was run sequentially until loss was at its minimum value. As a result, weights were set to predict classes of crop type and subsequently detect crop health condition, while the iterative learning process was used to set parameters (Figure 7).

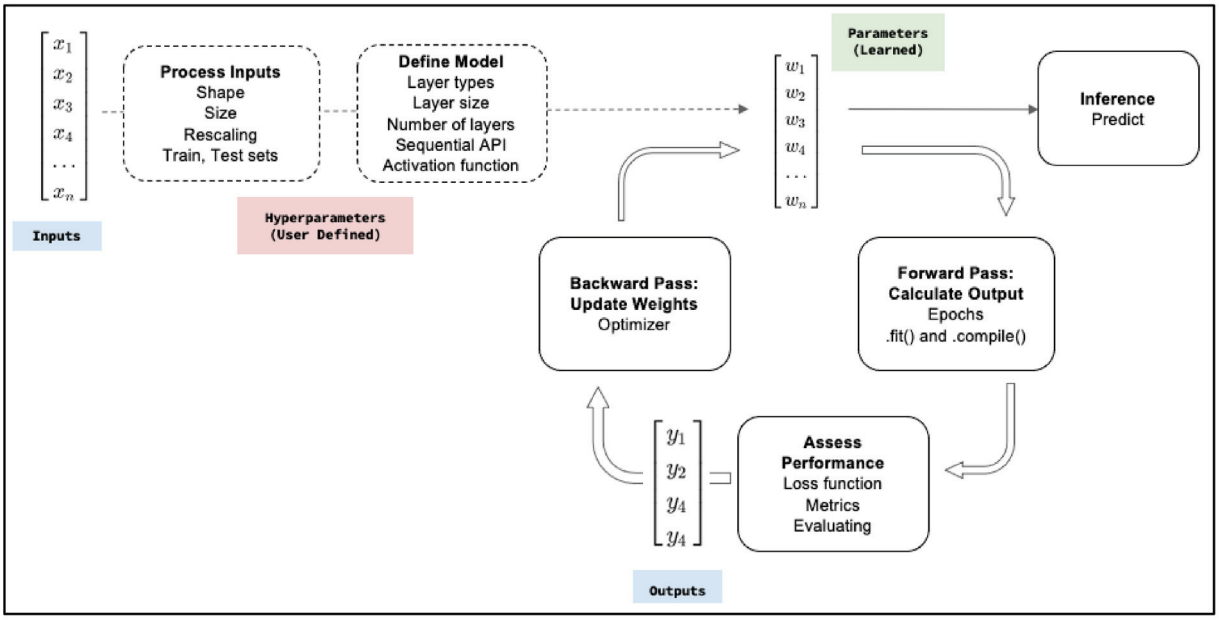

Figure 7. Parameter setting and loss value optimization to derive unbiased weights.

3. Results

3.1. Terrain and Infrastructure Risks

The information provided by the detailed, farm-specific, DEM-based geomorphometric risk analysis (Figure 8) enables the insurer to evaluate the level of risk that any given farm's infrastructure and crops are exposed to, thereby guiding the setting of premiums for any given farm. For example, in the Dosquebradas district, most farms were found to have relatively minor exposure to flood hazards. However, farms 17 and 18 showed a risk of landslides and soil erosion due to steep slopes and topographic wetness in the eastern part of the farm (Figure 9a), while in the western part of the farm, there is severe flood risk due to topographic wetness and floodplain locations (Figure 9b).

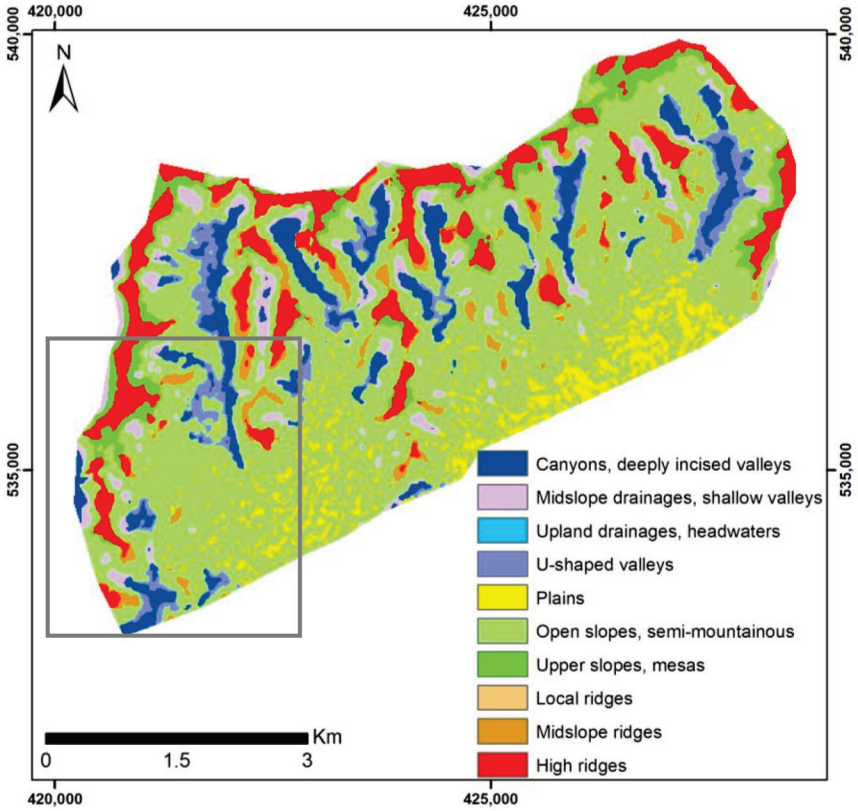

Figure 8. Landform types of Dosquebradas district produced from DEM geomorphometrics. The inset box indicates the area examined in detail within Figure 9a,b.

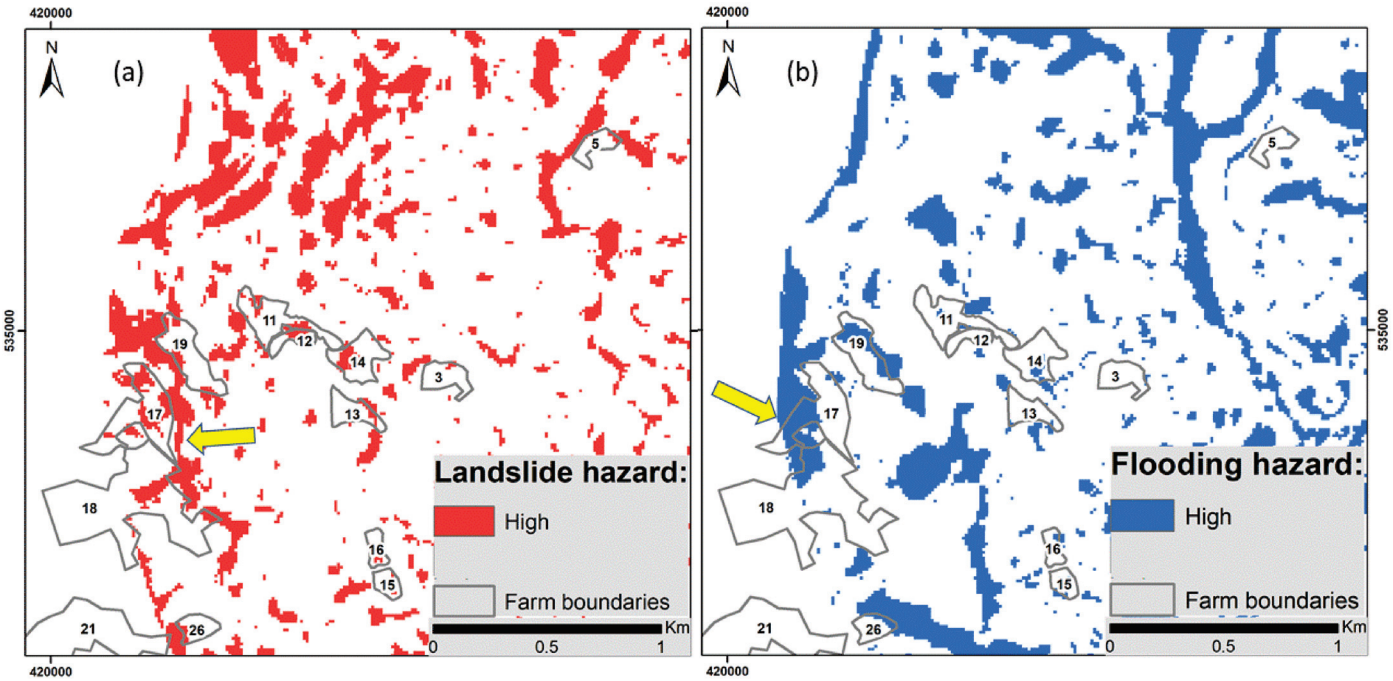

Figure 9. The Dosquebradas study area, with overlain outlines of the surveyed farms: (**a**) landslide hazard zones, with the arrow pointing at the eastern border of farms 17 and 18; (**b**) flood hazard zones, with the arrow pointing at parts of farms 17 and 18 at risk of flooding.

3.2. Indices and Predictions: Climate and Vegetation over Time

The Palmer Drought Severity Index (PDSI) demonstrated a constant trend in normal time and varied during extreme weather events. The most obvious downward trend was associated with wildfires, where PDSI values demonstrated a sharp decline. However, both those and periods of flooding recorded moderate inclines in PDSI values, so PDSI cannot be used to differentiate between the two types of extreme weather.

The MODIS NDVI time-series plots exhibited a constant trend during disaster-free times. During floods, the NDVI values remained constant with less volatility. When it comes to drought, an upward trend is demonstrated. Conversely, the NDVI trend sustained a sharp decline in the periods dominated by wildfires.

3.3. Deep Learning and Mobile Phone Photos of Crops

The aim of using DL is to create two-tier layers by classifying crops into: (1) coffee beans (class I) vs. avocados (class II); and (2) healthy crops vs. unhealthy (or damaged) crops. The dataset consisting of 748 photos of crops was divided into a training set and a testing set with an 80:20 split ratio in order to prevent overfitting. Our binary classification algorithm resulted in an overall 0.8473 accuracy. Table 2 shows the performance of the model based on 748 photos collected from 30 farms in the Dosquebradas study area.

Table 2. Results of 2-tier DL model.

Metric	Score
Accuracy	0.8473
Precision	0.8917
Sensitivity (recall)	0.9175
F1 score	0.9044
Specificity	0.7947

4. Discussion

4.1. Parametric Insurance Model

A parametric insurance model has been developed that incorporates crop type, crop value/yield, historic claims–loss data and satellite remote sensing data, as well as photos of the crops at the time of buying the policy. To estimate the crop yield, underwriters can use tools such as the Global Agriculture Monitoring (GLAM) decision support system to quantitatively forecast crop yields or they can rely on historical production numbers and selling prices. In contrast to GLAM, the system presented here also considers geomorphometrics and historical trends (via monthly data, for 20 years) of hydrometeorological indices for risk assessment of the underlying asset (i.e., insured farm and crops). Geomorphometrics indicate the likelihood of flooding, erosion, and landslides.

Historical extreme weather disasters can be studied in terms of types, recency, frequency and monetary claims. This helps with setting acceptable ranges for the two indices included (i.e., NDVI and PDSI) for the farm to be insured at a low risk of damage to the crops and farm infrastructure.

The design of a parametric model should assist in determining outputs to be used in underwriting an insurance policy. Those outputs are:

- Actuarial rate tables—premiums, reserves, cash values and dividends.
- Interest rates.
- Loading rates, expense charges, and policy fees.
- Date bands and face amount bands.
- Premium calculation rules.
- Billing and collection rules.
- Underwriting rules.

The aforementioned outputs will be unbiased and set more fairly since those are based on indices captured from EO, geomorphometry, and topography. Additionally, for

underwriting, both policy and premium setting would change automatically as the first notification of loss (FNOL) is issued.

4.1.1. Insurance Claim Verification

The claim verification process is a tedious task that can take a long time to be processed. Machine learning and deep learning models help automate the process while cutting time and costs. In addition, the ability of the system operators to freely download and analyze globally available daily to weekly satellite EO imagery overcomes site access limitations in developing countries. Furthermore, when analyzing data-driven claims, the opportunity of prescriptive analytics emerges when insurers, re-insurers, creditors and governmental agencies aim to minimize damage to agricultural products.

4.1.2. Automated Decision Making

Having an automated hazard detection would recommend to farmers the next best course of action, through what is known as "digital nudging" [47], for example, recommending drip irrigation for areas that the 20-year NDVA records indicate are prone to drought.

4.2. Impact

This research has a direct impact on risk transfer within the agricultural supply chain. Additionally, it has a wider impact on society with fairer and inclusive effects.

4.2.1. Applications of EO for Finance and Insurance Services

It has been argued by Longo, Zardo [8] that despite having knowledge of climate change adaptation frameworks, this knowledge needs to be integrated in practice. Therefore, the focus in this research was on the farmers–insurers relationship in practical terms. Additionally, the findings can be generalized and risk can be distributed by extending it across agricultural supply chains. Actors in such supply chains can benefit from predicting extreme weather disasters (Figure 10). In addition, insurance credit can be allowed using the parametric insurance model for re-insurers. In summary, we have demonstrated how banks and agricultural fund managers can apply EO models and techniques to estimate the projected return on their financial investment in commodities.

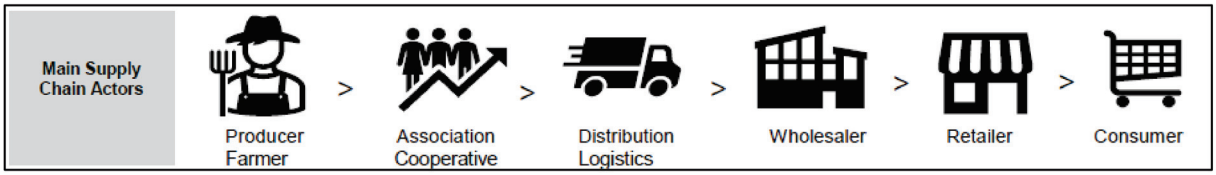

Figure 10. Agriculture supply chain.

4.2.2. Moral Hazard and Information Asymmetry

When using parameters to gauge risks, both parties, insurance provider and insured farmer, would have access to similar information about parameters leading to elimination of information asymmetry. Similarly, moral hazards (mainly represented by fraudulent claims) are significantly reduced because of the widespread availability of indices provided by third-party weather agencies [22].

4.2.3. Digital Divide and Data Poverty

The "digital divide" highlights the gap between those with ready access to digital services through information and communication technologies (ICT) and those who are without such access [48]. The digital divide is caused by geographical, economic, educational, attitudinal, generational or even physical factors. It has been argued that disasters affect people unequally by harming those who are most digitally excluded, i.e. those that

are experiencing 'Data Poverty' [49,50]. Additionally, data generated from limited ICT devices and services are of low quality and can have negative effects due to their unreliability [51]. Furthermore, this research has contributed to digital inclusivity [52] within the Colombian farming community. The level of community intelligence, determined by ICT access, determines its resilience and ability to generate reliable information [29].

4.2.4. Sustainability

In this research, the authors were able to improve sustainability by assisting communities in hedging the risk of hunger while offering a low-cost insurance plan. This paper outlines how the insurance ecosystem may use the affordable and publicly available data and FOSS to apply DL for image classification as well as ML for mapping terrain and estimating extreme weather risks. Not only is this new process affordable for insurers and farmers, but it is also relatively rapid and accurate. Specifically, an alert is raised automatically as soon as an indicator (or a parameter) exceeds or drops below a pre-determined acceptable range driving up the likelihood of an extreme weather disaster. This automated decision is also complemented by an image recognition algorithm that uses deep learning to verify the crop type and its condition as soon as a farmer submits a claim. Finally, ML algorithms such as RF are used to capture changes in topography and approve loss claims. The findings of this paper contribute to the farming business continuity and to the rapid recovery of farmers' livelihoods, thus boosting sustainable development and improving quality of life.

4.2.5. Policymaking

Policymakers can make use of geoinformatics and satellite data for social good. This is consistent with the framework proposed by Oktari, Munadi [53], who concluded that ICT artifacts are the primary driver for sustainability and policies. This research unlocks many opportunities for farmers, insurers, and credit associations in many ways. Specifically, when suggesting that insured individuals (in this research, farmers) contribute to the claim verification process, this creates social recognition and thus contributes to institutional trust and a sustainable pro-environmental attitude towards climate change policies [23]. In return, the InsurTech mobile application can make recommendations such as building a glasshouse or installing a new irrigation system that is suitable for the soil of a specific area, which is known as "digital nudging" [47] and farmers would respond to that positively. Similarly, credit/financing societies can provide loans to ensure continuation of the supply of crops in that area based on an InsurTech recommendation system. Meanwhile, more variables and data can benefit better risk modeling, such as the growth cycles of different crops being used to better estimate losses.

4.3. Limitations

There have been some challenges with technology and fieldwork for data collection.

4.3.1. Technological Challenges

In technology, when exporting interactive maps using the GEE API, the maps expired after a few days due to authentication issues with GEE. Since they are used for research purposes, the authors could not request that the maps work permanently. Instead, maps were reproduced by running Python code.

Additionally, cloud coverage hindered the use of optical satellite imagery (e.g., Sentinel-2 and PlanetScope), which prevented the investigation of photosynthetic activity in crops. On the other hand, radar satellite imagery (e.g., Sentinel-1) is able to penetrate cloud cover and can detect land surface features and crop types, although it did not perform well in areas with steep slopes. Consequently, both radar and optical satellite imagery had to be included in the damage verification component of the insurance ecosystem.

4.3.2. Data Challenges

Collecting farm data presented a challenge, which affected the deep learning model. Specifically, photos were collected during the period of COVID-19 and many restrictions were in place for our collaborators to navigate in Colombia in March–April 2020. As a result, the mobile photos dataset was relatively small (748 photos).

On the other hand, when labeling the photos, an imbalanced dataset was produced, leading to better classification of coffee beans in comparison with avocados. This was because of the imbalance between the two classes in the dataset. This has affected the accuracy of the DL model (currently at a moderate 0.85 classification accuracy). Nevertheless, there is huge potential for improvement with the app deployment and more regions signing up onto it.

4.4. Recommendations

One of the recommendations is to extend the damage detection from crops to farming infrastructure (e.g., access roads, bridges, processing facilities).

Insurance companies can benefit from automated verification of extreme weather disasters and correct triggering of claims—thus issuing a payout to the insured farmer with less administrative cost. This can be done by ongoing monitoring of EO-derived indices such as the NDVI. Finally, the use of mobile phone photos (time-stamped and GPS-located) can identify the crop, reveal its condition, and save verification costs for the insurers.

4.5. Future Agenda

4.5.1. Wider Coverage

In terms of the underlying asset (crop), the value of crop insured can be better estimated by adding the level of growth (of the crop) at the time of the disaster. This means that a farmer with damaged crops in the sowing season would not have lost the value of a whole season of the insured crop. This is because such farmers can restart the season immediately as soon as a small payout is approved by the insurer to compensate for the value of the seeds. Conversely, when a disaster happens during the harvesting season (especially toward the end of the season), a significant loss can be expected. This is because the whole season would have to be written off. The Food and Agriculture Organization (FAO) provides an interactive tool known as the "Crop Calendar" for farm planning (by country, crop, and activity).

The FAO also summarizes the output of the tool by issuing a timeline of crop calendars per country. The aforementioned factor (growth level) can feed into the insurance model to increase transparency and information symmetry.

Researchers in the future could determine whether insuring a specific product in a specific location is viable and subsequently determine the level of risk associated with it, thus setting fair insurance premiums by integrating such tools in their actuarial insurance model.

4.5.2. Multiple Data Sources

It has been argued that disasters are hard to verify unless first responders and affected people contribute to the disaster data [54]. This can be done by integrating different data sources. In data science and information systems, one of the main features is data integration. In this research, EO was used for pre- and post-disaster damage verification, along with photographic evidence from client farmer phones. However, other sources can also be used, such as scrapping online digital texts from national disaster agencies and using AI to analyze the content of such texts. This would detect any paradigm shift in the semantics describing weather indices [55]. Additionally, exchanges on social media platforms have been effective when communicating emergency situations, specifically when a shared vision and language is present [14].

5. Conclusions

This research has examined the terrain where farms are located to understand their exposure to extreme weather events based on geomorphological measures (e.g., slope steepness, topographic wetness) derived from a freely available satellite-derived global elevation model. As a result, estimating the damage that extreme weather disasters caused to farms was possible in terms of the likelihood at a given site of geohazards such as flooding, landslides and soil erosion. Satellite data were also used to determine the historical occurrences of extreme weather events within farming districts, as well as the vegetation coverage, crop types and crop health. When it comes to insurance and crop damage verification, faster decisions resulted from utilizing a mobile phone app that can provide time-stamped, GPS-located photos of crop damage, with a DL image recognition algorithm improving the verification process.

Key features of this insurance system are its low operational cost and rapid damage verification relative to conventional approaches to farm insurance. It is an affordable form of insurance for small-scale farmers, with the rapid verification and payment of claims enabling policyholders to potentially recover more quickly from disasters.

The insurance ecosystem presented here assists sustainable development in two main ways:

(i) By the use of affordable EO data and sustainable geoinformatics, resulting in low-cost insurance, affordable to smallholder farmers.
(ii) Via relatively rapid processing and verification of damage loss claims—i.e., with payouts potentially within days, rather than months—facilitating business continuity and enabling rapid recovery of farmer livelihoods.

Author Contributions: Conceptualization: R.M.T., A.V.A., D.R.O., and A.W.; methodology: R.M.T. and A.V.A.; writing: A.A.R.; data collection: D.R.O. and M.F.-M.; data analysis and modeling: A.A.R. and M.F.-M.; mobile app development: D.R.O.; review and edit: A.A.R., R.M.T., and A.V.A.. All authors have read and agreed to the published version of the manuscript.

Funding: This research was funded by the Space Research and Innovation Network for Technology (SPRINT), grant OC2020DCYg/OW131379Z7.

Institutional Review Board Statement: Not applicable.

Informed Consent Statement: Not applicable.

Data Availability Statement: Data are publicly available through the links provided in the manuscript and Appendix B.

Acknowledgments: The authors acknowledge the assistance received from staff, who attended our brainstorming meetings from the University of Portsmouth. Special thanks to Mathias Leidig, Andrew Lundgren, and Risto Talas.

Conflicts of Interest: Author Doyle Ray Oakey was employed by the company Parametrica.ai. Author Max Foxley-Marrable was employed by the company Revolution Data Platforms. Author Alan Wilkins Mercari was employed by the company Mercari Risk Management Ltd. The remaining authors declare that the research was conducted in the absence of any commercial or financial relationships that could be construed as a potential conflict of interest.

Appendix A. Natural Hazards in Dosquebradas, Colombia, 1998–2020 (Compiled from IDEAM Online Database)

	Disaster	Start Date	End Date
1	Drought	1998-01-01	1999-01-01
2	Flood	1999-01-10	1999-05-19
3	Earthquake	1999-01-25	1999-01-26

	Disaster	Start Date	End Date
4	Flood	1999-10-28	1999-12-31
5	Flood	2000-05-18	2000-05-24
6	Wildfire	2001-08-01	2001-09-01
7	Drought	2002-01-01	2003-01-01
8	Flood	2002-04-24	2002-04-29
9	Flood	2003-08-01	2003-12-01
10	Flood	2004-01-01	2004-06-28
11	Drought	2004-01-01	2005-01-01
12	Flood	2005-04-12	2005-05-07
13	Flood	2005-09-15	2005-11-17
14	Flood	2006-01-01	2006-04-27
15	Drought	2006-01-01	2007-01-01
16	Flood	2007-10-20	2007-10-26
17	Flood	2008-01-01	2008-05-19
18	Flood	2008-11-16	2009-01-12
19	Drought	2009-01-01	2010-01-01
20	Wildfire	2010-01-01	2010-04-06
21	Flood	2010-10-30	2011-01-12
22	Flood	2011-02-10	2011-06-05
23	Flood	2011-09-01	2011-12-31
24	Flood	2012-03-15	2012-05-14
25	Earthquake	2013-02-09	2013-02-09
26	Flood	2013-09-15	2013-12-01
27	Drought	2015-08-01	2016-02-01
28	Storm	2016-09-20	2016-09-23
29	Flood	2017-03-17	2017-05-16
30	Flood	2017-12-01	2018-01-07
31	Drought	2018-01-01	2020-01-01
32	Flood	2019-02-20	2019-02-26
33	Flood	2020-06-10	2020-07-10

Appendix B. Datasets analyzed in Google Earth Engine

	Dataset	Google Earth Engine	Dataset Provider
1	Sentinel-2 MSI: MultiSpectral Instrument, Level-2A	https://developers.google.com/earth-engine/datasets/catalog/COPERNICUS_S2_SR, accessed on 9 November 2022	https://earth.esa.int/web/sentinel/user-guides/sentinel-2-msi/product-types/level-2a, accessed on 9 November 2022
2	Sentinel-2: Cloud Probability	https://developers.google.com/earth-engine/datasets/catalog/COPERNICUS_S2_CLOUD_PROBABILITY, accessed on 9 November 2022	https://earth.esa.int/web/sentinel/user-guides/sentinel-2-msi/product-types/level-1c, accessed on 9 November 2022
3	Sentinel-1 SAR GRD: C-band SAR Radar Ground Range Detected, log scaling	https://developers.google.com/earth-engine/datasets/catalog/COPERNICUS_S1_GRD, accessed on 9 November 2022	https://sentinel.esa.int/web/sentinel/user-guides/sentinel-1-sar/, accessed on 9 November 2022

	Dataset	Google Earth Engine	Dataset Provider
4	USGS Landsat 8 Surface Reflectance Tier 1	https://developers.google.com/earth-engine/datasets/catalog/LANDSAT_LC08_C01_T1_SR, accessed on 9 November 2022	https://www.usgs.gov/core-science-systems/nli/landsat/landsat-8, accessed on 9 November 2022
5	USGS Landsat 7 Surface Reflectance Tier 1	https://developers.google.com/earth-engine/datasets/catalog/LANDSAT_LE07_C01_T1_SR, accessed on 9 November 2022	https://www.usgs.gov/core-science-systems/nli/landsat/landsat-7, accessed on 9 November 2022
6	USGS Landsat 5 Surface Reflectance Tier 1	https://developers.google.com/earth-engine/datasets/catalog/LANDSAT_LT05_C01_T1_SR, accessed on 9 November 2022	https://www.usgs.gov/core-science-systems/nli/landsat/landsat-5, accessed on 9 November 2022
7	MOD13Q1.006 Terra Vegetation Indices 16-Day Global 250m	https://developers.google.com/earth-engine/datasets/catalog/MODIS_006_MOD13Q1, accessed on 9 November 2022	https://lpdaac.usgs.gov/products/mod13q1v006/, accessed on 9 November 2022
8	MYD13Q1.006 Aqua Vegetation Indices 16-Day Global 250m	https://developers.google.com/earth-engine/datasets/catalog/MODIS_006_MYD13Q1, accessed on 9 November 2022	https://lpdaac.usgs.gov/products/myd13q1v006/, accessed on 9 November 2022
9	CHIRPS Daily (v.2): Climate Hazards Group InfraRed Precipitation with Station Data	https://developers.google.com/earth-engine/datasets/catalog/UCSB-CHG_CHIRPS_DAILY, accessed on 9 November 2022	https://chc.ucsb.edu/data/chirps, accessed on 9 November 2022
10	PERSIANN-CDR: Precipitation Estimation from Remotely Sensed Information ANN-Climate Data Record	https://developers.google.com/earth-engine/datasets/catalog/NOAA_PERSIANN-CDR, accessed on 9 November 2022	https://data.nodc.noaa.gov/cgi-bin/iso?id=gov.noaa.ncdc:C00854, accessed on 9 November 2022
11	TerraClimate: Monthly Climate and Climatic Water Balance for Global Terrestrial Surfaces.	https://developers.google.com/earth-engine/datasets/catalog/IDAHO_EPSCOR_TERRACLIMATE, accessed on 9 November 2022	http://www.climatologylab.org/terraclimate.html, accessed on 9 November 2022
12	ERA5 Daily aggregates—Latest climate reanalysis produced by ECMWF/Copernicus Climate Service	https://developers.google.com/earth-engine/datasets/catalog/ECMWF_ERA5_DAILY, accessed on 9 November 2022	https://cds.climate.copernicus.eu/cdsapp#!/dataset/reanalysis-era5-single-levels, accessed on 9 November 2022

	Dataset	Google Earth Engine	Dataset Provider
13	ERA5 Monthly aggregates—Latest climate reanalysis produced by ECMWF/Copernicus Climate Service	https://developers.google.com/earth-engine/datasets/catalog/ECMWF_ERA5_MONTHLY, accessed on 9 November 2022	https://cds.climate.copernicus.eu/cdsapp#!/dataset/reanalysis-era5-single-levels, accessed on 9 November 2022
14	GPM: Global Precipitation Measurement (GPM) v6	https://developers.google.com/earth-engine/datasets/catalog/NASA_GPM_L3_IMERG_V06, accessed on 9 November 2022	https://disc.gsfc.nasa.gov/datasets/GPM_3IMERGHH_06/summary, accessed on 9 November 2022
15	GPM: Monthly Global Precipitation Measurement (GPM) v6	https://developers.google.com/earth-engine/datasets/catalog/NASA_GPM_L3_IMERG_MONTHLY_V06, accessed on 9 November 2022	https://disc.gsfc.nasa.gov/datasets/GPM_3IMERGM_06/summary, accessed on 9 November 2022

References

1. Shukla, P.R.; Skeg, J.; Calvo Buendia, E.; Masson-Delmotte, V.; Pörtner, H.O.; Roberts, D.C.; Zhai, P.; Slade, R.; Connors, S.; van Diemen, S.; et al. IPCC, 2019: Climate Change and Land: An IPCC Special Report on Climate Change, Desertification, Land Degradation, Sustainable Land Management, Food Security, and Greenhouse Gas Fluxes in Terrestrial Ecosystems. 2019. Available online: https://philpapers.org/rec/SHUCCA-2 (accessed on 8 August 2023).
2. WHO. Global Hunger Numbers Rose to as Many as 828 Million in 2021. 2022. Available online: https://www.who.int/news/item/06-07-2022-un-report--global-hunger-numbers-rose-to-as-many-as-828-million-in-2021 (accessed on 8 August 2023).
3. Reuters. Hilary Clinton at Cop28 Climate Talks Calls for Insurance Reform. 2023. Available online: https://www.marketscreener.com/news/latest/Hillary-Clinton-at-COP28-climate-talks-calls-for-insurance-reform-45490148/ (accessed on 4 February 2024).
4. Sigit, A.; Koyama, M.; Harada, M. Flood Risk Assessment Focusing on Exposed Social Characteristics in Central Java, Indonesia. *Sustainability* **2023**, *15*, 16856. [CrossRef]
5. Medium. Issue 96: Insurance. Future 2023. Available online: https://medium.com/@planetsnapshots/issue-96-insurance-1caa45991937 (accessed on 3 December 2023).
6. UKSA. *Space for Agriculture in Developing Countries*; UK Space Agency International Partnerships Programme; UK Space Agency: Swindon, UK, 2018.
7. Oliveira, M. What Is the Role of Information and Communication Technologies (Ict) in Building Resilience Aspects in Case of Disaster? *2023.* Available online: https://aisel.aisnet.org/ecis2023_rp/251/ (accessed on 30 January 2024).
8. Longo, A.; Zardo, L.; Maragno, D.; Musco, F.; Burkhard, B. Let's Do It for Real: Making the Ecosystem Service Concept Operational in Regional Planning for Climate Change Adaptation. *Sustainability* **2024**, *16*, 483. [CrossRef]
9. Begue, A.; Madec, S.; Lemettais, L.; Leroux, L.; Interdonato, R.; Becker-Rescheff, I.; Barker, B.; Justice, C.; Kerdiles, H.; Meroni, M. How well do EO-based food security warning systems for food security agree? Comparison of NDVI-based vegetation anomaly maps in West Africa. *IEEE J. Sel. Top. Appl. Earth Obs. Remote Sens.* **2023**, *16*, 1641–1653. [CrossRef]
10. Xu, Y.; Zhao, Y.; Zhai, P. Advances in scientific understanding on climate change and food security from IPCC special report SRCCL. *Adv. Clim. Change Res.* **2020**, *16*, 37.
11. Challinor, A.J.; Simelton, E.S.; Fraser, E.D.; Hemming, D.; Collins, M. Increased crop failure due to climate change: Assessing adaptation options using models and socio-economic data for wheat in China. *Environ. Res. Lett.* **2010**, *5*, 034012. [CrossRef]
12. Rozaki, Z.; Wijaya, O.; Rahmawati, N.; Rahayu, L. Farmers' disaster mitigation strategies in Indonesia. *Rev. Agric. Sci.* **2021**, *9*, 178–194. [CrossRef] [PubMed]
13. Tobin, G.A. Sustainability and community resilience: The holy grail of hazards planning? *Glob. Environ. Change Part B Environ. Hazards* **1999**, *1*, 13–25. [CrossRef]
14. Lu, Y.; Yang, D. Information exchange in virtual communities under extreme disaster conditions. *Decis. Support Syst.* **2011**, *50*, 529–538. [CrossRef]
15. Wu, D.; Cui, Y. Disaster early warning and damage assessment analysis using social media data and geo-location information. *Decis. Support Syst.* **2018**, *111*, 48–59. [CrossRef]
16. Bertschek, I.; Polder, M.; Schulte, P. ICT and resilience in times of crisis: Evidence from cross-country micro moments data. *Econ. Innov. New Technol.* **2019**, *28*, 759–774. [CrossRef]

17. Heeks, R.; Ospina, A.V. Conceptualising the link between information systems and resilience: A developing country field study. *Inf. Syst. J.* **2019**, *29*, 70–96. [CrossRef]
18. Li, G.; Zhao, J.; Murray, V.; Song, C.; Zhang, L. Gap analysis on open data interconnectivity for disaster risk research. *Geo-Spat. Inf. Sci.* **2019**, *22*, 45–58. [CrossRef]
19. Becker-Reshef, I.; Justice, C.; Sullivan, M.; Vermote, E.; Tucker, C.; Anyamba, A.; Doorn, B. Monitoring global croplands with coarse resolution earth observations: The Global Agriculture Monitoring (GLAM) project. *Remote Sens.* **2010**, *2*, 1589–1609. [CrossRef]
20. Nakalembe, C.; Justice, C.; Kerner, H.; Justice, C.; Becker-Reshef, I. Sowing Seeds of Food Security in Africa. *Eos* **2021**, 102. Available online: https://www.researchgate.net/profile/Catherine-Nakalembe-2/publication/348790680_Sowing_Seeds_of_Food_Security_in_Africa/links/611d88fe169a1a01030ef7d3/Sowing-Seeds-of-Food-Security-in-Africa.pdf (accessed on 19 October 2023). [CrossRef]
21. Leidig, M.; Teeuw, R. Free software: A review, in the context of disaster management. *Int. J. Appl. Earth Obs. Geoinf.* **2015**, *42*, 49–56. [CrossRef]
22. Benso, M.R.; Gesualdo, G.C.; Silva, R.F.; Silva, G.J.; Rápalo, L.M.C.; Navarro, F.A.R.; Marques, P.A.A.; Marengo, J.A.; Mendiondo, E.M. Design and evaluation of weather index insurance for multi-hazard resilience and food insecurity. *Nat. Hazards Earth Syst. Sci.* **2023**, *23*, 1335–1354. [CrossRef]
23. Jütersonke, S.; Groß, M. The Effect of Social Recognition on Support for Climate Change Mitigation Measures. *Sustainability* **2023**, *15*, 16486. [CrossRef]
24. Aleskerova, Y.; Kovalenko, L.; Havryliuk, V. Innovative financial criteria for methodological approaches to the assessment of agrarian insurance. *Balt. J. Econ. Stud.* **2019**, *5*, 34–41. [CrossRef]
25. Lowder, S.K.; Skoet, J.; Raney, T. The number, size, and distribution of farms, smallholder farms, and family farms worldwide. *World Dev.* **2016**, *87*, 16–29. [CrossRef]
26. Ibarra, H.; Securities, I.L. *Parametric Insurance: General Market Trends and Perspectives for the African Insurance Sector*; Insurance Linked Securities; Partnerre New Solutions Inc.: Bermuda, Germany, 2010.
27. Figueiredo, R.; Martina, M.L.V.; Stephenson, D.B.; Youngman, B.D. A probabilistic paradigm for the parametric insurance of natural hazards. *Risk Anal.* **2018**, *38*, 2400–2414. [CrossRef] [PubMed]
28. Iturrioz, R.; Arias, D. *Agricultural Insurance in Latin America: Developing the Market*; World Bank: Washington, DC, USA, 2010.
29. Chaudhuri, N.; Bose, I. Exploring the role of deep neural networks for post-disaster decision support. *Decis. Support Syst.* **2020**, *130*, 113234. [CrossRef]
30. Prokopchuk, O.; Prokopchuk, I.; Mentel, G.; Bilan, Y. Parametric insurance as innovative development factor of the agricultural sector of economy. *AGRIS -Line Pap. Econ. Inform.* **2020**, *12*, 69–86. [CrossRef]
31. Cesarini, L.; Figueiredo, R.; Monteleone, B.; Martina, M.L.V. The potential of machine learning for weather index insurance. *Nat. Hazards Earth Syst. Sci.* **2021**, *21*, 2379–2405. [CrossRef]
32. Argyriou, A.V.; Sarris, A.; Teeuw, R.M. Using geoinformatics and geomorphometrics to quantify the geodiversity of Crete, Greece. *Int. J. Appl. Earth Obs. Geoinf.* **2016**, *51*, 47–59. [CrossRef]
33. Argyriou, A.V.; Teeuw, R.M.; Rust, D.; Sarris, A. GIS multi-criteria decision analysis for assessment and mapping of neotectonic landscape deformation: A case study from Crete. *Geomorphology* **2016**, *253*, 262–274. [CrossRef]
34. Wagstaff, K. Machine learning that matters. *arXiv* **2012**, arXiv:1206.4656.
35. Reuter, H.; Nelson, A. Geomorphometry in ESRI Packages. *Dev. Soil Sci.* **2009**, *33*, 269–291.
36. Tağıl, Ş.; Jenness, J. GIS-based automated landform classification and topographic, landcover and geologic attributes of landforms around the Yazoren Polje, Turkey. *J. Appl. Sci.* **2008**, *8*, 910–921. [CrossRef]
37. Beven, K.J.; Kirkby, M.J. A physically based, variable contributing area model of basin hydrology/Un modèle à base physique de zone d'appel variable de l'hydrologie du bassin versant. *Hydrol. Sci. J.* **1979**, *24*, 43–69. [CrossRef]
38. Sörensen, R.; Zinko, U.; Seibert, J. On the calculation of the topographic wetness index: Evaluation of different methods based on field observations. *Hydrol. Earth Syst. Sci.* **2006**, *10*, 101–112. [CrossRef]
39. Hjerdt, K.N.; McDonnell, J.J.; Seibert, J.; Rodhe, A. A new topographic index to quantify downslope controls on local drainage. *Water Resour. Res.* **2004**, *40*, W05602. [CrossRef]
40. Migoń, P.; Kasprzak, M.; Traczyk, A. How high-resolution DEM based on airborne LiDAR helped to reinterpret landforms: Examples from the Sudetes, SW Poland. *Landf. Anal.* **2013**, *22*, 89–101. [CrossRef]
41. Breiman, L. Random forests. *Mach. Learn.* **2001**, *45*, 5–32. [CrossRef]
42. Kubosova, K.; Brabec, K.; Jarkovsky, J.; Syrovatka, V. Selection of indicative taxa for river habitats: A case study on benthic macroinvertebrates using indicator species analysis and the random forest methods. *Hydrobiologia* **2010**, *651*, 101–114. [CrossRef]
43. Justice, C.; Townshend, J.; Vermote, E.; Masuoka, E.; Wolfe, R.; Saleous, N.; Roy, D.; Morisette, J. An overview of MODIS Land data processing and product status. *Remote Sens. Environ.* **2002**, *83*, 3–15. [CrossRef]
44. Tucker, C.J. Red and photographic infrared linear combinations for monitoring vegetation. *Remote Sens. Environ.* **1979**, *8*, 127–150. [CrossRef]
45. Kern, A.; Marjanović, H.; Barcza, Z. Spring vegetation green-up dynamics in Central Europe based on 20-year long MODIS NDVI data. *Agric. For. Meteorol.* **2020**, *287*, 107969. [CrossRef]

46. Nakalembe, C.; Kerner, H. Considerations for AI-EO for agriculture in Sub-Saharan Africa. *Environ. Res. Lett.* **2023**, *18*, 041002. [CrossRef]
47. Jesse, M.; Jannach, D. Digital nudging with recommender systems: Survey and future directions. *Comput. Hum. Behav. Rep.* **2021**, *3*, 100052. [CrossRef]
48. Cullen, R. Addressing the digital divide. *Online Inf. Rev.* **2001**, *25*, 311–320. [CrossRef]
49. Masiero, S.; Nielsen, P. Resilient ICT4D: Building and sustaining our community in pandemic times. *arXiv* **2021**, arXiv:2108.09712.
50. Leidig, M.R.; Teeuw, M.; Gibson, A.D. Data poverty: A global evaluation for 2009 to 2013-implications for sustainable development and disaster risk reduction. *Int. J. Appl. Earth Obs. Geoinf.* **2016**, *50*, 1–9. [CrossRef]
51. Pan, S.L.; Zhang, S. From fighting COVID-19 pandemic to tackling sustainable development goals: An opportunity for responsible information systems research. *Int. J. Inf. Manag.* **2020**, *55*, 102196. [CrossRef] [PubMed]
52. Taylor, L. What is data justice? The case for connecting digital rights and freedoms globally. *Big Data Soc.* **2017**, *4*, 2053951717736335. [CrossRef]
53. Oktari, R.S.; Munadi, K.; Idroes, R.; Sofyan, H. Knowledge management practices in disaster management: Systematic review. *Int. J. Disaster Risk Reduct.* **2020**, *51*, 101881. [CrossRef]
54. Hertzum, M. How do journalists seek information from sources? *A systematic review. Inf. Process. Manag.* **2022**, *59*, 103087. [CrossRef]
55. Abd Rabuh, A.; El-Masri, M.; Al-Yafi, K. A Text Analytics Approach to Evaluate Paradigm Shifts in Information Systems Research. Available online: https://www.researchgate.net/profile/Ahmad-Abd-Rabuh/publication/326088441_Australasian_Conference_on_Information_Systems_A_Text_Analytics_Approach_to_Evaluate_Paradigm_Shifts_in_Information_Systems_Research/links/5b37792caca2720785fa34d9/Australasian-Conference-on-Information-Systems-A-Text-Analytics-Approach-to-Evaluate-Paradigm-Shifts-in-Information-Systems-Research.pdf (accessed on 26 July 2021).

Disclaimer/Publisher's Note: The statements, opinions and data contained in all publications are solely those of the individual author(s) and contributor(s) and not of MDPI and/or the editor(s). MDPI and/or the editor(s) disclaim responsibility for any injury to people or property resulting from any ideas, methods, instructions or products referred to in the content.

agronomy

MDPI

Article

Interpolation of Nitrogen Fertilizer Use in Canada from Fertilizer Use Surveys

James Arthur Dyer [1,*], Angela Pearson [2] and Raymond Louis Desjardins [3]

[1] Independent Researcher, 122 Hexam Street, Cambridge, ON N3H 3Z9, Canada
[2] Serecon Inc., 600 First Edmonton Place, 10665 Jasper Ave, Edmonton, AB T5J 3S9, Canada; angelapearson727@gmail.com
[3] Science and Technology Branch, Agriculture and Agri-Food Canada, 960 Carling Avenue, Ottawa, ON K1A 0C6, Canada; ray.desjardins@agr.gc.ca
* Correspondence: jamesdyer@sympatico.ca; Tel.: +1-519-653-2995

Abstract: Canadian nitrogen (N) fertilizer use has more than doubled since 1990 (1.2 to 2.9 MtN by 2021). Consequently, a better understanding of this trend is needed. A comprehensive set of recommended N rates (RNRs) that agreed with the fertilizer sales data from 1996 and 2001 was compared with the Fertilizer Use Survey (FUS). The FUS was conducted from 2014 to 2021, with 2017 being the most representative year for these data. Using non-parametric statistics, confidence intervals were derived from the histograms used to present the FUS data. N application rates from the RNR for canola, spring and Duram wheat, and oats in the west were all below their respective FUS confidence intervals, whereas N application rates for grain corn showed almost no difference in N use between the RNR and FUS. Crop-specific N application rates interpolated from the RNR and FUS were integrated over their respective crop areas and plotted against national fertilizer sales records from 1990 to 2021. The rapid increase in N use between 2001 and 2017 (0.89 MtN), 90% of it (0.80 MtN) in Western Canada, was primarily due to the increased application rates per crop, rather than crop area changes. The RNR-FUS interpolations were a good approximation of N sales records and could improve farm GHG emissions modelling. The economically important crops in Western Canada should be the main focus for N-related GHG reduction measures, but production losses need to be avoided.

Keywords: nitrogen fertilizer; Fertilizer Use Survey; recommended application rates; non-parametric mean deviation; fertilizer sales records; fertilizer use trends; interpolated trends

1. Introduction

There has been a rapid increase in nitrogen (N) fertilizer use in Canada over the last four decades [1]. The national records of fertilizer shipments [2], hereafter referred to as fertilizer sales, have shown that N fertilizer use has tripled since 1981. This increase is part of a global trend [3]. After levelling off between 1996 and 2006, sales increased steadily until 2021. The Fertilizer Use Survey (FUS) provides the first opportunity in 20 years to evaluate this change. The N application rates reported by the FUS were derived from a series of surveys conducted between 2014 and 2021 [4].

This rapid increase has major implications for two of the elements in Canada's agricultural carbon footprint. N fertilizer is the largest source of N_2O emissions [5–7] and N fertilizer manufacture is the largest user of fossil fuel in the farm energy budget [8]. On a per weight basis, N_2O represents the most potent GHG emissions from agriculture. The N fertilizer that leaches into ground water, or is lost with surface runoff, has a major impact on the biodiversity of downstream habitats [9–12], and drinking water [13,14]. However, the world would not be able to meet its food production needs without chemical fertilizers [12,15–17]; the largest share of which is nitrogen [3].

Canada has committed to reduce current GHG emissions from fertilizer by 30% below 2020 levels by 2030 [10,18], with almost all of this reduction projected to come from improved fertilizer management [4]. The rapid increase in nitrogen use since 1990 (Figure 1) has major implications for this commitment. Given these changes and the importance of N fertilizer to food production, there is a need to better understand the historical trend of this essential farm input [19].

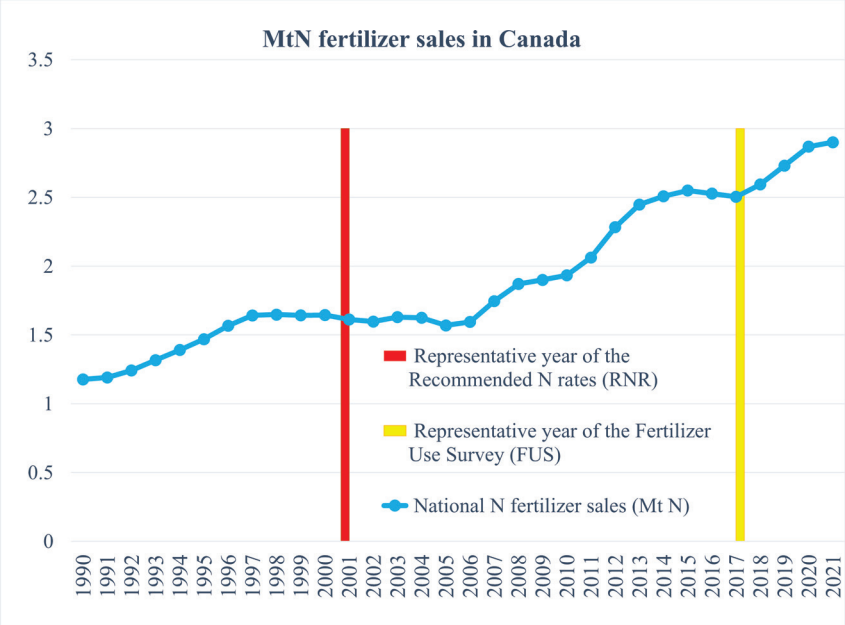

Figure 1. Time series of the national N fertilizer sales in Canada (blue) from 1990 to 2021 and the representative years (vertical bars) for the recommended N rates (RNRs) (red) and the Fertilizer Use Survey (FUS) (yellow).

1.1. Early N Fertilizer Recommendations

In this analysis, the recent fertilizer use data from the FUS were compared with the Recommended N Rates (RNRs) [20], based on a statistical measure of the differences in the respective N application rates. The N fertilizer rates from the Yang et al. paper [20] were reported to have agreed well with national fertilizer sales data from 1996 and 2001. The relatively flat N sales period between 1996 and 2006 made 2001 an appropriate representative year for the RNRs in Figure 1. Prior to the FUS, numerous Canadian GHG budget studies relied on the RNR estimates [5,10,21–25]. Without an update on these RNRs, it was not possible in these assessments to determine the cause of this trend in Canadian fertilizer use or to identify crops with the biggest increase in N fertilizer use. Instead, the industry-wide trend in fertilizer sales had to be used as a "one size fits all" index calculation [19]. Used together, these two data sets could show how much of this trend was due to application rate changes in crops but not others, if there is a general increase in N rates for all crops, or if the shift was towards crops that required more N fertilizer.

1.2. The Fertilizer Use Survey

The FUS covered 13 crops in five Canadian provinces from 2014 to 2021 [4]. As the mid-point year, 2017 is the representative year for the FUS in Figure 1. However, only two of the thirteen crops in the FUS (canola for the three Prairie Provinces and grain corn in Ontario) were surveyed in all eight years of the FUS. It did not include any surveys in British Columbia or the Atlantic Provinces and many crops were not surveyed in all of the provinces where they are grown. Two crops, sunflower and flaxseed, were only surveyed in Manitoba. The sampling for Quebec winter wheat was found to be inadequate. Most of the spatial gaps occurred because most major field crops are region-specific in Canada.

For example, grain corn, soybeans, and winter wheat are not grown to any extent in the west. Due to limited resources and the expense of large scale surveys, the FUS database has numerous temporal data gaps. In spite of these weaknesses, the FUS provides the only up-to-date data on Canadian N fertilizer use.

If the FUS is to have a role in an improved trend analysis, then whether the N fertilizer application rates derived from the FUS were significantly different from the RNRs needs to be determined. Finding a significant difference could help to explain the rapid increase in N fertilizer consumption. A quantitative answer to this question depended on a measure of the dispersion of observed application rates from the FUS. In this paper, the RNR-FUS relationship will be analyzed and it will be integrated over the 21 field crops used in the Sustainability Metrics (SMs) program in Canada [5,26]. These 21 SM crops are all listed in the annual crop inventory [27] and they account for all but five of the field crops monitored by this inventory. The five exclusions, potatoes, canary seed, ginseng, buckwheat, and triticale, are all considered either minor crops in Canada or horticultural, rather than agronomic, crops.

2. Methodology

2.1. Deriving the Mean Deviations

Because the FUS was subject to confidentiality restrictions, the recorded data from the FUS were only available as histograms [4]. The FUS only provided sufficient data to generate histograms for 11 of the 21 SM crops. In spite of this data access constraint, it was possible to estimate mean N fertilizer application rates and a measure of dispersion for each rate from these histograms. In addition, the data access constraint required a non-parametric statistical methodology to quantify this dispersion. Arkin and Colton [28] provided a non-parametric technique for estimating the mean deviation (MD) from histograms.

2.2. Mean Deviation (MD) Calculations

$$MD = (1/\eta) \times \sum^{n}(f \times |d|) \quad (1)$$

where

MD = mean deviation;
Mn = arithmetic mean;
v = mid-point value of each frequency class, *n*;
f = frequency (%) of records in each class;
η = total number of all frequencies over all classes ($\sum^{n}f$);
d = difference of each value (v) from the mean;
$d_n = (Mn - v_n)$;
$\sum$ = cumulative (integration); and
|d| = mode (sign ignored) value of (d)

Since MD is a function of Mn, a non-parametric calculation of Mn was computed as follows:

$$Mn = \sum^{n} (v \times f)/\sum^{n} f \quad (2)$$

The Mn and MD values derived from the FUS histograms for each available crop, province, and year are listed in Appendix A. The crop–province averages over all available years for Mn and MD are also shown in Appendix A.

2.3. N Application Rate Confidence Intervals

Figure 2 compares the RNR with the FUS Mn rates and confidence intervals (CI). Upper and lower CIs for each of the 23 crop–province cases are defined by Mn plus or minus MD derived from Equations (1) and (2). Each stacked bar in Figure 2 is only represented by the one average rate from Appendix A, regardless of how many years each crop was sampled in that province. The yellow bars in Figure 2 show the upper CIs and the blue

bars show the lower CIs for the 23 crop–province cases. The top of the white bars simply define the smallest value of the lower CIs. Figure 2 shows whether the RNRs (red line) are within or outside their respective CI intervals. RNRs that are within their respective CIs are identified by overlaps with either the blue or the yellow bars. These overlaps suggest a lack of significant difference in N use rates between the FUS and RNRs for each case. The Mn rates (Equation (2)) are shown by the margin between the blue and yellow bars. If the red RNR line is above the blue–yellow margin (into the yellow bars), then that RNR value exceeds the FUS Mn value.

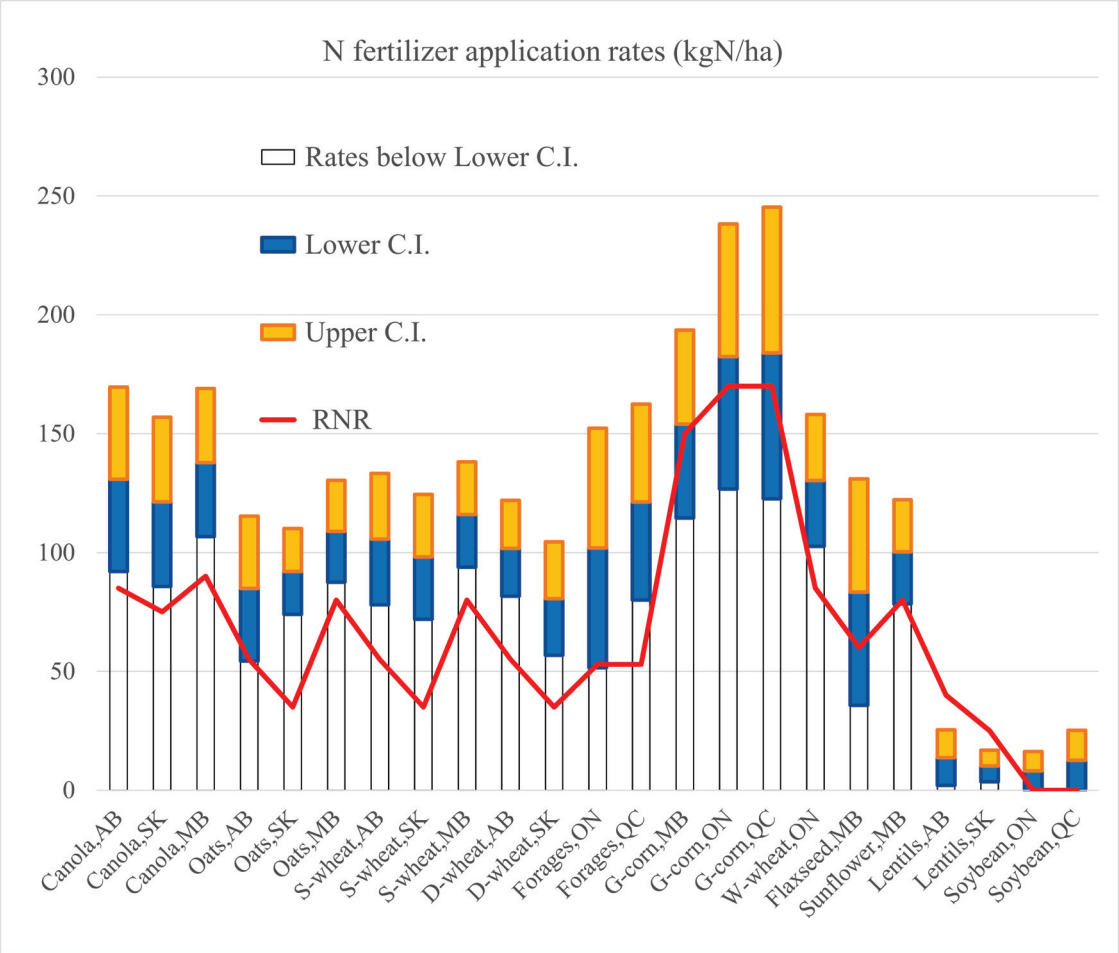

Figure 2. Comparing estimates and confidence intervals (C.I.) of national N fertilizer use from the Fertilizer Use Survey (FUS) with the recommended fertilizer rates (RNRs) from Yang et al. [20] by crop and province. Abbreviated prefixes for the wheats, D, S, and W, stand for "Duram", "Spring", and "Winter", respectively. The abbreviated prefix, G, for corn stands for "Grain" and "Forages" refers to hay from perennial grass.

However, because the measure of dispersion in this analysis was a non-parametric MD calculation, the CI estimates in Figure 2 are not meant to be a substitute for rigorous confidence interval computations from quadratic means and standard deviations derived from the source non-grouped data. The latter methodology would be essential to determine the true significance of the CIs, or whether or not a future set of surveys would statistically replicate the FUS. The main purpose of the CIs in Figure 2 was to highlight the relative Mn to RNR differences among the crop-province cases included in the 2021 FUS. Regardless of those differences, there was no reason not to apply all of the Mn-RNR differences to a trend analysis.

2.4. Centralizing the FUS to a Single Year

For the ease of applying the RNR-FUS interpolation process to all crop–province (cp) combinations, a constant time interval was needed between the RNR and the FUS. This required an objective estimate of a year that would best represent all of the individual survey results in Appendix A. Towards an estimate of the average survey year (Y_{as}), the cp combinations with data in each year were counted. Then each year's count (C) was multiplied by the year (Y) of that count. As shown in Equation (3), these year–count products were summed over all eight years and divided by the total number of counts of cp cases with the survey histograms in Appendix A. Y_{as} was found to be a third into 2017, rounded to 2017.

$$Y_{as} = \sum^{y,cp} (Y_{y,cp} \times C_{y,cp}) / \sum^{y,cp} C_{y,cp} \quad (3)$$

Figure 3 demonstrates a lack of stationarity over the eight years of the FUS. So, a further correction following Equation (3) was for the effect of the temporal differences in the FUS N use rates (S) due to the sequence of cp survey histograms within the eight years of the FUS. This correction linked the N use difference to the difference between Y_{cp} and Y_{as}. The Y_{cp} to Y_{as} shift was indexed to the period (years) between the RNRs (Y = 2001) and the FUS (Y = 2017). This index, calculated using Equation (4), is a dimensionless temporal shift factor (Z) that is distributed about one. To cover cp cases with more than one year of survey, Y_{cp} was replaced by the average Y_{cp} of those years ($Y_{cp,ave}$).

$$Z_{cp} = 1 + ((Y_{cp,ave} - Y_{as}) / (Y_{as} - Y_{RNR})) \quad (4)$$

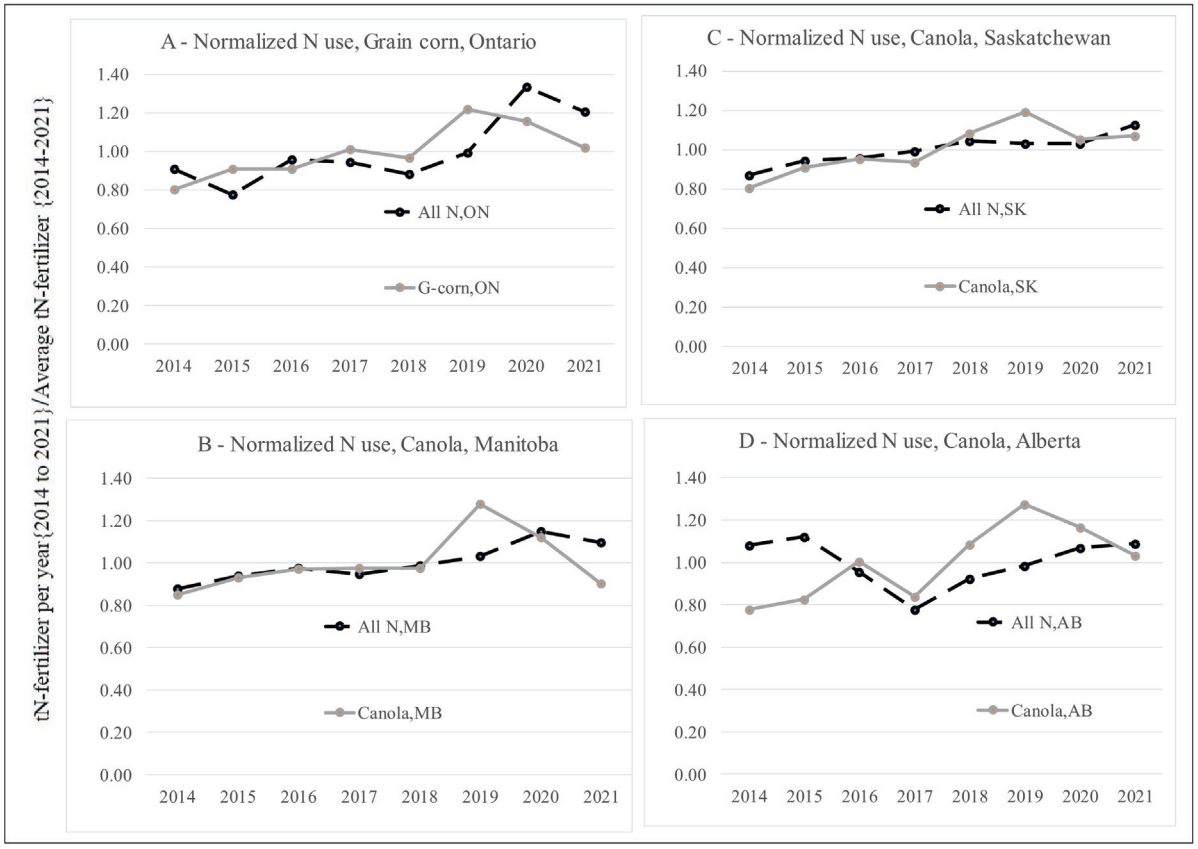

Figure 3. Plots of N fertilizer use for grain corn in Ontario (**A**) and canola in Manitoba (**B**), Saskatchewan (**C**), and Alberta (**D**) with N fertilizer sales records for these four provinces over the eight years of the Fertilizer Use Survey (FUS), where fertilizer use rates and N sales data were normalized to their respective eight-year averages.

The corrected N fertilizer rate from the FUS (S'_{cp}) is computed using Equation (5) from Z_{cp} and the respective cp N fertilizer application rates from the FUS and the RNRs. In Equation (5), Z is only applied to the difference between the FUS and RNR N rates for each RNR-FUS pair.

$$S'_{FUS,cp} = S_{RNR,cp} + Z_{cp} \times (S_{FUS,cp} - S_{RNR,cp}) \quad (5)$$

All of the four cp combinations with histograms in all eight years exhibited some change (lack of stationarity) over the eight years of the FUS. Although these four rates of change may not be statistically significant, they reflect the change in N use between the RNRs and the FUS. To assess this potential impact, these four eight-year time series were plotted with provincial N sales records from the respective provinces over the same eight years in Figure 3. In order for FUS N use and N sales to have comparable scales in each sub-figure, the data in all eight series were normalized to their respective eight-year averages. Therefore, although the FUS time series are per ha rates and the N sales time series are integral N totals, their slopes are still comparable because they are both sets of dimensionless numbers distributed about one.

2.5. FUS to RNR Differences for Crops with No CI

Table 1 pairs the mean application rates for 15 of the 21 SM crops with the respective RNRs. As well as the 11 crops in Figure 2, Table 1 shows four additional crops (barley, dry peas, chickpeas and dry beans) for which recent data on their application rates were available. For the five crops for which CI intervals could not be calculated in one or more provinces, those provinces are shown in italics and grey. With an unreliable histogram, Quebec winter wheat was also shown in grey and italics. For dry peas and barley, and soybeans in Manitoba, the FUS provided mean values, but no histograms.

Table 1. Fifteen crops included in the sustainability metrics analysis, with both a recent and a 2001 provincial N fertilizer rate estimate available. For the 13 pairs shown as shaded and in italics, histograms were either not available or not reliable.

	Alberta		**Saskatchewan**		**Manitoba**		**Ontario**		**Quebec**	
	FUS [1]	**RNRs** [2]	**FUS**	**RNRs**	**FUS**	**RNRs**	**FUS**	**RNRs**	**FUS**	**RNRs**
Crop	**kgN/ha**		**kgN/ha**		**kgN/ha**		**kgN/ha**		**kgN/ha**	
Barley	*84*	*55*	*45*	*35*	*77*	*75*				
Canola	131	85	121	75	138	90				
Oats	85	55	92	35	109	80				
S-wheat	106	55	98	35	116	80				
D-wheat	102	55	81	35						
Lentils	14	40	10	25						
Forages							102	53	121	53
G-corn					154	150	182	170	184	170
W-wheat							130	85	*44*	*85*
Flax					83	60				
Sunflower					100	80				
Soybean					*4*	*0*	*7*	0	8	0
Chick peas [3]	*42*	*40*	*42*	*25*						
Dry beans [3]	*71*	*40*			*39*	*15*	*64*	*25*		
Dry peas	*10*	*10*	*3*	*9*	*9*	*10*				

[1], FUS = Fertilizer Use Survey (See Appendix A for mean deviation estimates); [2], RNRs = recommended nitrogen [application] rates; [3], two pulse crops in the FUS columns use N rates from other sources.

N application rates for chickpeas and dry beans were taken from two online extension publications [29,30]. The average rates for chickpeas in Alberta and Saskatchewan came from the Saskatchewan Pulse Growers website [30]. Since dry beans (including both white and colored beans) are poor N-fixers compared to other pulses, the Manitoba Pulse and Soybean Growers website [29] recommended that dry beans be treated like non-legumes. Hence, for dry beans in Alberta, the Manitoba and Ontario application rates recommended by unidentified provincial experts are used in Table 1. While the sources for these two crops were subjective, both crops are very minor in Canada.

The cp cases surveyed in the FUS accounted for 93% of the land that supported the 21 SM field crops in 2017 (calculation not shown). However, only 39 of the 75 possible cp combinations in Table 1 (not counting the Atlantic Province or British Columbia) are filled with N use rates. The reasons that those 39 FUS N rates could account for so much farm land were, first, the FUS targeted the most economically important crops, and second, most of the 21 SM crops, particularly the dominant ones, are concentrated in climatically homogeneous regions. For example, spring wheat and canola are almost all grown in the prairies and grain corn is mostly grown in Ontario and Quebec.

Nevertheless, a national N use estimate from the FUS must include all areas growing each crop, even if they were not included in the FUS. The two minor crops not covered by the FUS and the limited production of the 13 FUS crops in other provinces accounted for small amounts of additional N fertilizer use. Hence, N application rates from the FUS were extrapolated to the non-FUS cp cases. The rates of FUS crops that are in provinces not covered by the FUS were assigned the RNR-FUS average rate from each respective crop. For crops with more than one province with an FUS N rate (expressed as percentages of their respective RNRs), an area-weighted average rate was calculated. Given the indexing of FUS rates to RNRs, the rates in the non-FUS provinces are (by default) all 100% (of RNR). Thus, each non-FUS default rate was replaced by the midpoint (average) of the area-weighted FUS average rate (expressed as %) and RNRs (expressed as 100%).

The six SM crops not shown in Table 1 include fall rye, sugar beets, mustard seed, silage corn, alfalfa and other small grains (treated as one crop). For five of these crops, the rate from the most closely related crop in the FUS was used as a proxy. Yang et al. [20] suggested that all small grain cereal crops are statistically much the same. Therefore, barley was the proxy for fall rye, other small grains and sugar beets. Canola was used for mustard seed and grain corn was used for silage corn. Due to inadequate sampling, the Quebec winter wheat rate was replaced with the winter wheat rate from Ontario. The Ontario and Quebec forage rates from the FUS were not considered good proxies for tame hay in the other provinces, nor for alfalfa in any province. Therefore, tame hay outside of these two provinces and all alfalfa retained their RNRs.

To test the impact of additional uses of N fertilizer on the FUS, these additional N weights were calculated with the respective RNR N application rates instead of the proxy FUS rates. The results were a 24% drop in the east, a 9% drop in the west, and a Canada-wide drop of 11%, or 0.28 less MtN applied across Canada than the 2.6 MtN shown in Figure 4 (blue curve) for 2017. Although they are small relative to the actual FUS data set, the proxy FUS rates still played an important part in the N sales-FUS agreement for 2017 demonstrated in Figure 4.

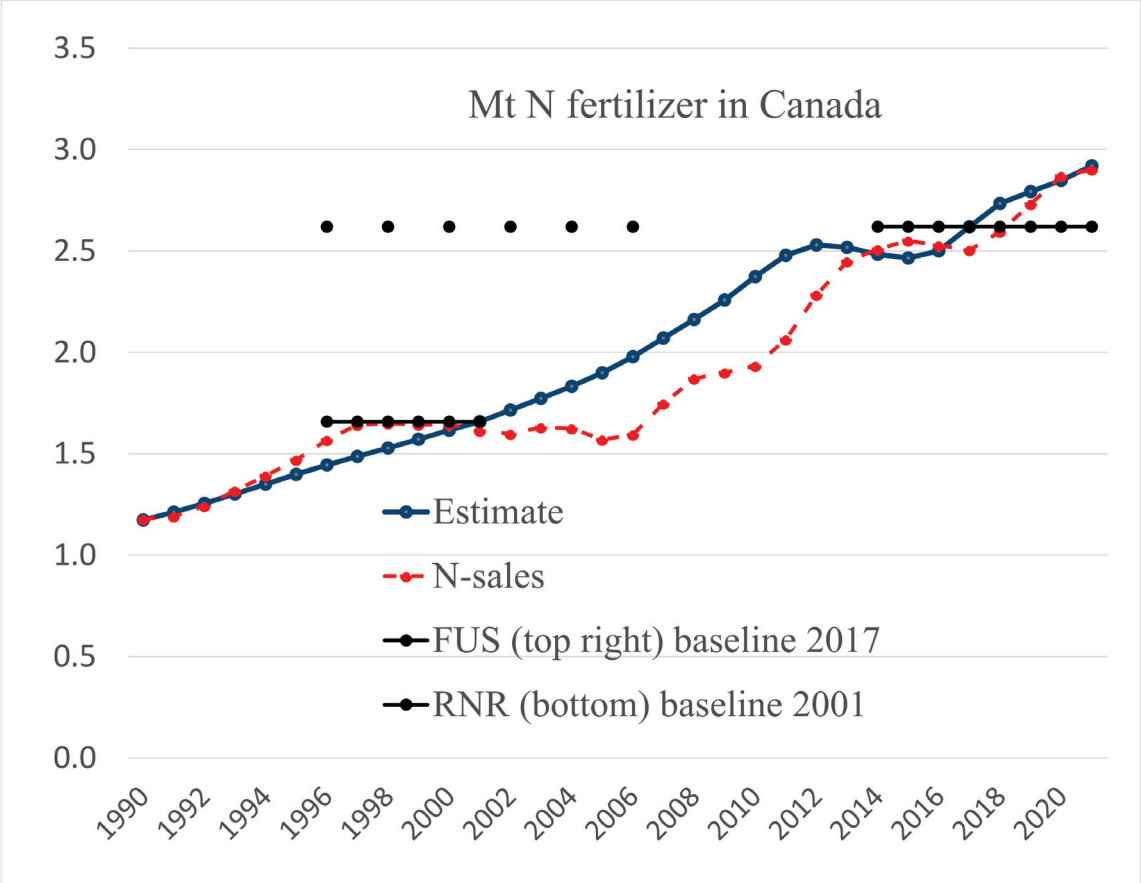

Figure 4. Time-series comparison of N fertilizer use for 21 field crops in Canada estimated from the FUS and RNRs (blue) with reported N fertilizer sales in Canada (red) from 1990 to 2021. The two black lines show the RNR and FUS average national N use, and the black dots show the FUS average N use projected back to 1996-2006.

2.6. Historical N Fertilizer Use Trends

Figure 4 shows two trend lines for the total weights of N fertilizer use in Canada from 1990 to 2021. The dashed red line shows the national N fertilizer sales. The integrated N from the FUS and RNR interpolations is shown in solid blue. These annual integrations were performed over all of the SM crop areas and cp cases. The smoother blue line shows a derived time series of total national N fertilizer applications. The weights of N for the FUS and RNR years (2001 and 2017) shown in Figure 1 are represented in Figure 4 by two short horizontal black lines. Since the interpolated time line was derived from these two short lines, this precise intersection of the blue line and the two short black lines at 2001 and 2017, respectively, was expected.

Since the integrated N based on the N application rates from Yang et al. [20] agreed closely with the fertilizer sales records for the census years 1996 and 2001, this short horizontal line, shown in black in Figure 4, covers all four inter-census years. For the FUS, the horizontal black line covered 2014 to 2021, the FUS survey period. The fertilizer sales data [2], shown in Figure 4 by the dashed red line, initially showed significant fluctuations. So, instead of just the raw annual N sales (I) from each year (y), a binomial computation of N sales (I′) was generated to smooth the curve for I as follows:

$$I'_y = (I_{y-1} + 2 \times I_y + I_{y+1})/4 \quad (6)$$

In spite of this binomial smoothing, the national fertilizer sales data (red) trend line in Figure 4 is still quite non-linear, especially after 1996.

2.7. The Interpolation of N Fertilizer Use Estimates

The interpolated N fertilizer rate (B) was calculated for each cp and year (Y). Because (as described above) the FUS was represented as a percent of RNRs, then the RNRs in all cases become 1 (always 100%) and each FUS rate is a percent of the respective RNR. The interpolation process depends on the time between RNR and FUS (ΔY), defined as:

$$\Delta Y = Y_{FUS} - Y_{RNR} \quad (7)$$

The flatness of the N sales curve just before 2001, the representative RNR year, in Figure 4 means that B will not be very sensitive to the year representing the RNR (Y_{RNR}). But Figure 3 shows that B is sensitive to the year representing the FUS (Y_{FUS}), thus requiring Equation (3). The RNR to FUS interpolation of B (blue) was:

$$B_{cp,y} = B_{RNR,cp} + ((Y - Y_{RNR})/\Delta Y) \times (B_{FUS,cp} - B_{RNR,cp}) \quad (8)$$

For 2001 and 2017, the B_{cp} estimates replicate their respective N rates, as reported by Yang et al. [20] and shown by the two short flat lines in Figure 4. The calculated percentages for B must be multiplied by the N fertilizer rate from Yang et al. [20] to apply this interpolation to each cp and to provide actual N application rates.

Equation (8) was extrapolated backward from 2001 to 1990, the Kyoto baseline year [31]. There was a boundary condition placed on the extrapolations to the years before 2001 that before 2001 B was not allowed to go below 40% of R. Where the RNRs exceeded the FUS rates (e.g., lentils), B for the pre-2001 years was not allowed to exceed 160% of the RNRs. These arbitrary 60% boundary conditions only applied occasionally to the pre-RNR extrapolations. For extrapolating forward from 2017 to 2021, no boundary conditions were applied.

2.8. Integrating Fertilizer Applications over Crop Areas

To get from B to the national N use shown in Figure 4, each B_{cp} must be integrated over its respective crop area. The national N consumption (F) was calculated annually by multiplying each B by its crop area (A) from each year (y) for each cp case and integrating the set of B and A products over all cp cases, as follows:

$$F_y = \Sigma^{cp} B_{cp,y} \times A_{cp,y} \quad (9)$$

The difference between the one size fits all approach and the interpolation process is illustrated in Figure 4 by the six black dots from 1996 to 2006 which overlap the years for which the fixed (black) RNR line applies. The vertical difference between these dots and the RNR baseline approximates the amount N fertilizer that is accounted for by the RNR-FUS interpolations (blue) curve. The change in F over ΔY for each cp is the alternative to the one size fits all indexing of either the RNR or FUS data directly to N fertilizer sales records.

2.9. Secondary Trend Line Corrections

The interpolated rates still required a partial one size fits all correction in order to fully simulate the fertilizer sales. This secondary correction to B (B′) used the ratio of the fertilizer sales data (I) to F, with each ratio being specific to each year. Equation (9) was then recalculated with the set of corrected B. The new set of B (B′) was generated as follows:

$$B'_{cp,y} = (I_y/F_y) \times B_{cp,y} \quad (10)$$

To understand the secondary correction, consider 2006, the census year with the biggest sales–interpolations difference. This illustration assumes that the dots extending from the 2017 FUS baseline to the 2006 N sales in Figure 4 represent the totally uncorrected fertilizer use based solely on the FUS. The gap between the dots and 2006 N sales (red) also represents the total required correction to the FUS for 2006. Instead of correcting the FUS N

total by 0.97 MtN (in the absence of the interpolations), the secondary correction for 2006 (between the blue to red lines) would only require a 0.38 MtN reduction.

The interpolation for 2006 only reduced the necessary one size fits all correction to 63% of the required correction without the interpolation. However, for most of the 32 years in Figure 4, the required secondary correction was much smaller. Because the curve for the secondary correction would be exactly the same as the sales curve, that curve is not shown in Figure 4. Instead, the red sales curve in Figure 4 represents both the N sales data and the secondarily corrected RNR-FUS interpolations.

2.10. Regional Demonstration of the Interpolation Process

Although Figure 4 presents the interpolation process on a national scale over all crops, the actual calculations were executed provincially for each crop, which matches the operating scale of the field print calculator model [32,33]. It is useful to examine the Canadian N fertilizer industry on a semi-national basis, given the distinct agro-climatic and farming system differences between Eastern and Western Canada [34].

Figure 5 gives the interpolations and the sales records of N fertilizer for both the east and the west over the same time series as Figure 4. The two N sales curves in Figure 5 are shown by dashed red lines and the two interpolated curves are shown by solid blue lines. As in Figure 4, the red curves also represent the secondary correction of the interpolations. Also shown in Figure 5 are two flat black lines from 1996 to 2001, the RNR baseline. Because the N use changes in Figures 4 and 5 are integrated over their respective SM crop areas, these graphs do not differentiate the impacts of N application rate changes from land use changes.

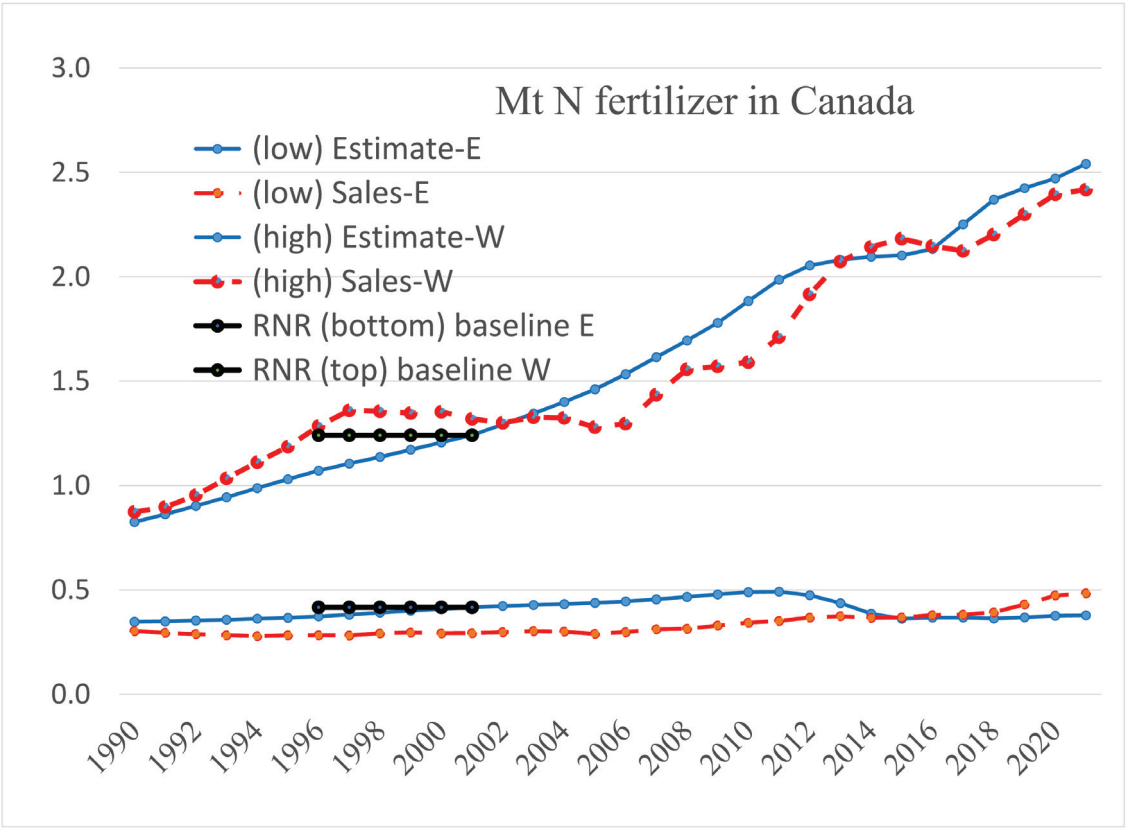

Figure 5. Time-series comparison of N fertilizer use for SM field crops in Eastern (the lower pair) and Western (the higher pair) Canada estimated from the FUS and RNRs (blue) with reported N fertilizer sales (red) in Canada from 1990 to 2021.

To isolate the impact of land use change, Figure 6 shows the possible changes in total N fertilizer use when the N application rates are fixed at the 2001 baseline RNR. As in Figure 5, Figure 6 shows an east–west breakdown of N fertilizer use, as well as the simulated national weight of N fertilizer use (as in Figure 4). Figure 6 focusses on just the truly interpolative years (2001 to 2017) of Figures 4 and 5 between the RNRs and FUS. The Eastern Canada curve is green, the Western Canada curve is yellow, and the Canada curve is blue. The N fertilizer weights associated with the RNRs for the east, west, and Canada are indicated by the short dotted black bars at 2000 and 2001 at the start of each curve. These three baseline bars in Figure 6 equate to the east and west RNR bars in Figure 5 and the RNR bar in Figure 4, respectively.

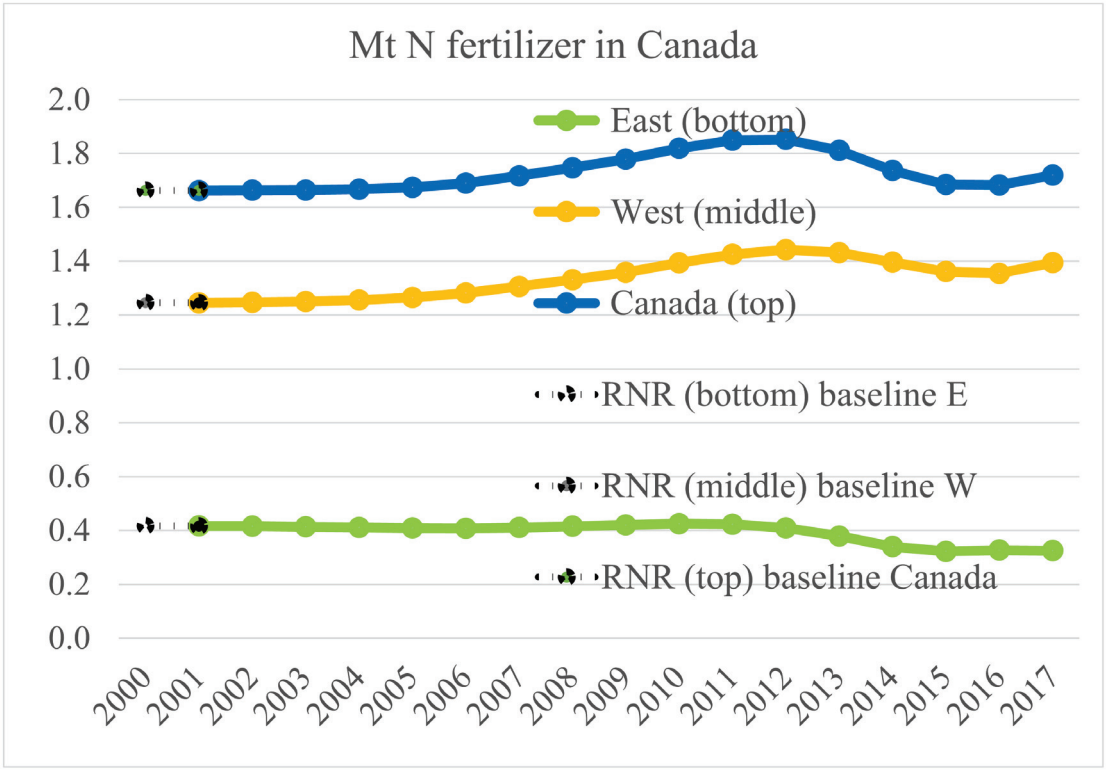

Figure 6. Theoretical time-series of N fertilizer use for 21 field crops in Eastern (green/bottom) and Western (yellow/middle) Canada, and Canada (blue/top) where N application rates are fixed at the 2001 RNRs.

3. Results

Figure 2: Except for the two cases for lentils, the RNRs were all below their respective Mn rates derived from the FUS histograms. The RNR (red) line intersects the lower (white) parts of the CI bars in almost all of the cp cases in the west. The RNRs for canola, all three wheats, oats in Manitoba and Saskatchewan, and sunflower were all below their respective CIs. Oats in Alberta only marginally intersected its lower CI. Flaxseed in Manitoba had an RNR value well within its CI, while the RNR for Manitoba sunflower seed was only just within its CI. In contrast, the RNRs for grain corn were all well within their respective CIs (blue bars), including Manitoba. The RNR for the perennial forage crop in Ontario was just within its CI, whereas the RNR for Quebec forage (with a slightly smaller CI than Ontario) was well below its CI. Winter wheat in Ontario was well below its CI; however, due to its inadequate sample size, winter wheat in Quebec was not included in Figure 2. For most of the crops in Figure 2, the combined widths of blue and yellow bars compared to the white bars were quite consistent. The exceptions included the two pulses (which require very little N fertilizer), flaxseed (a minor crop with only one histogram), and forages.

Table 1: The FUS/RNR ratios for barley were quite similar to the FUS/RNR ratios for the three wheat crops, except for winter wheat in Quebec. N rate recommendations for chickpeas and dry beans have substantially increased since the RNR. As well as having quite low application rates, Ontario soybeans did not show any substantial change since 2001. The RNR for winter wheat in Quebec was inexplicably high (hence, deemed unreliable), whereas the RNRs for this crop in Ontario behaved similarly to barley and the other two wheats relative to the RNRs. Table 1 also provided some guidance for the crops without any MD estimates and excluded from Figure 2. MD/Mn ratios that can be computed from Table 1 reflect the relative CI widths described for Figure 2. When the exceptional cases noted for Figure 1 were excluded, the range among the MD/Mn ratios in Table 1 was from 19% to 36%, resulting in a relative standard deviation for MD/Mn of 21%.

Figure 3: In Figure 3B,C, there is a close fit between the FUS and N sales for most years. This was because in Manitoba (Figure 3B) and Saskatchewan (Figure 3C) canola is the dominant land user. In Alberta, canola is less dominant, which is reflected by the poor agreement in Figure 3D. For grain corn in Figure 3A, there was a moderately good agreement between the FUS and the N sales. The N sales and FUS N curves in Figure 3A–C all appear to have similar slopes, which suggests that three of the four 8-year cp cases in the FUS captured a portion of the increase in N use between the RNR and the FUS. Figure 3D, however, illustrates the potential for error when extrapolating crop-specific N use based on the one size fits all N sales trend. The moderate slopes apparent in all four sub-figures were also justification for the temporal centralizing of the FUS data by Equations (3)–(5).

Figure 4: The interpolation process was most in need of the secondary correction between 2005 and 2012. The best fit of the interpolated N use curve was (not surprisingly) near the two years that represent the RNRs and FUS (Figure 1). Normalizing the set of Mn from the FUS to Y_{as} (Equation (3)) contributed to the close fit, especially after 2015. Figure 4 shows that by 2021, Canadian N fertilizer use has more than doubled since 1990 (1.2 to 2.9 MtN). Figure 4 also shows that the steepest increase in N fertilizer sales was between 2006 and 2014. The weight of N that the cp interpolation process accounted for was demonstrated in Figure 4 by the vertical difference between the RNR black bar and the black dots from 1996 to 2006. This difference indicates a 0.96 MtN increase between 2001 and 2017. The difference over that period for the N sales curve (red) was 0.89 MtN.

Figure 5: The difference in the two pairs of curves over the whole time series in Figure 5 shows that most of the N fertilizer use by 2021 (83%) was in the west. More importantly, 90% of the change in Canada's N use between 2001 and 2017 (0.80 MtN, red curves) was also in the west. In the east, the N sales (red curve) are flat until 2017, while the interpolated N use (blue curve) goes down slightly. This would make the 2017 western share of N use change based on interpolation (blue curves) even higher than 90%.

The 0.80 MtN increase in Western Canada (red curve) between the RNRs and the FUS accounts for 28% of the 2.9 MtN that was sold to Canadian farmers in 2020 (Figure 4), the threshold year for Canada's N-related GHG reduction goal [10,18]. In both the east and west, the uncorrected interpolation estimates were reasonably close to the N sales curve, particularly after 2013. The decreased rate of change after 2013 in the west is consistent with the modest slopes seen for the FUS years in Figure 3. Meanwhile, in the east, the agreement between the interpolations and N sales was consistent from 1990 to 2013; for the west, this relationship showed much the same reversal in 2002 as is seen in Figure 4.

Figure 6: All three curves in Figure 6 are much flatter than the curves in Figures 4 and 5. In the east (green curve), Figure 6 holds steady from the 2001 RNR baseline rate, dropping by only 0.09 MtN by 2017, but decreasing slightly faster after 2012. This decline closely mimics the eastern blue curve in Figure 5. But the Eastern N sales (red) curve in Figure 5 increased slightly after 2016. Thus, the impact of changes in N fertilizer application rates is almost non-existent in Eastern Canada. However, Figure 6 shows a modest increase in the west (yellow) which peaks at 2012. This change was only 0.20 MtN since 2001. By 2017, this change has decreased to 0.15 MtN. The N rate increases attributable to crop area

changes were only 16% and 12% of the overall increase in N use in the west for 2012 and 2021, respectively.

The 0.80 MtN change in the western N sales curve (Figure 5, upper red) represents an increase of 61% by 2017 over 2001. With the 12% impact of crop area changes in the west (Figure 6), this 61% change is reduced to the portion attributed to just the increased N application rate. With this adjustment for crop areas, the western RNR-FUS increase by 2017 over 2001 is 49%. The western RNR-FUS change is due solely to increased N application rates, and after the secondary correction is reduced to 0.61 MtN. With this adjustment, the 28% of the total 2.9 MtN of sales in Canada in 2020 is down to just 23%.

Table 2: To help explain Figure 5, the areas used by the crops from Figure 2, plus barley and dry peas, are shown in Table 2. Because their areas across Canada were less than 100 thousand ha, flaxseed, sunflower and winter wheat are not included in Table 2. Due to the lack of change demonstrated in Figure 6, only 2017 (Y_{as}) is shown. The five coastal provinces, which were not represented in the FUS, are excluded from Table 2.

Table 2. Areas growing 10 agronomic crops in 2017 that were assessed in the Fertilizer Use Survey (FUS) in five Canadian provinces [1].

	Quebec	Ontario	Manitoba	Saskatchewan	Alberta	Canada
Crops			**Mha of Cropland**			
Commercial						
Canola	0.0	0.0	*1.3*	*4.9*	*2.7*	8.9
Spring wheat	0.1	0.0	*1.1*	*2.8*	*2.3*	6.4
Duram wheat	0.0	0.0	0.0	*1.8*	*0.4*	2.2
Feed crops						
Grain corn	0.4	*0.8*	0.2	0.0	0.0	1.4
Oats	0.1	0.0	0.2	0.5	0.2	1.0
Barley	0.1	0.0	0.1	*0.9*	*1.1*	2.2
Forages	*0.6*	*0.7*	*0.6*	*1.4*	*1.7*	4.9
Legumes						
Soybeans	*0.4*	*1.2*	*0.8*	*0.2*	0.0	2.6
Lentils	0.0	0.0	0.0	*1.6*	*0.2*	1.8
Dry Peas	0.0	0.0	0.0	*0.8*	*0.7*	1.6
Total areas	1.6	2.8	4.3	15.1	9.2	33.0

[1], In order to highlight the major crops in each category, the eight largest crop-province areas in each group are shown in grey and in italics.

Table 2 divided crops into three groups: commercial, livestock feed, and legumes (livestock feed and edible pulses). While areas in the eastern provinces were dominated by feed crops, the western crop areas, particularly Saskatchewan, were primarily devoted to the commercial group. Two crops, canola and spring wheat (in grey and italics), dominate the commercial group and both show a clear separation in Figure 2 between the FUS CIs and the RNRs. Their area dominance, combined with this separation, is a probable explanation for the steep slope in the west in Figure 5. Grain corn and soybeans (in grey and italics), on the other hand, with no RNR-FUS separation in Figure 2, provide an explanation for the lack of slope in the east in Figure 5. Although the six million ha in legumes across Canada were appreciable, their low N fertilizer rates resulted in very little impact on Figure 5.

An east–west pair of per ha N use rates is calculated from the 2017 interpolations in Figure 5 and the east–west area summaries in Table 2. These multi-crop, regional average N application rates were 83 kgN/ha in the east and 79 kgN/ha in the west. At least for 2017, these two rates were very close. This likely reflects the offsetting of the high grain corn N use by the almost zero N use by soybeans in the east to closely resemble the N use rates by canola, and spring and Duram wheat in the west.

4. Discussion

Rather than treating the FUS rates as replacements for the RNRs, the real value of the FUS was to use it in conjunction with the RNRs to interpolate N use in any other year. The RNR-FUS interpolation process gave rise to the crop-specific N use interpolations (CSNIs) model, which limits reliance on the one size fits all indexing to N sales to just the secondary correction (Equation (10)). The advantage of CSNIs over total reliance on one size fits all is that each cp time series of N application rates has its own trend line. The one size fits all approach can introduce significant errors in many crops. In relation to crops for which N rates changed very little, too much N would be added, whereas the crops for which N rates underwent a big increase would not be assigned enough increase in N use.

The CSNI model's sensitivity to crop diversity has implications for Canada's agricultural GHG emissions budget. This sensitivity involves the fossil energy for fertilizer manufacture [8] and chemical fertilizer N_2O emissions [5,6]. With food production systems typically having unique crop complexes [34], crop-related N use differences can, in turn, have appreciable impacts on commodity GHG budget comparisons. With the secondary correction, the CSNI model fits the sales data exactly, while still capturing the crop-specific changes. This close agreement with N sales data (Figures 4 and 5) also suggests that the selected 21 SM crops for this analysis adequately accounted for Canada's agronomic land base.

The close relationship shown nationally in Figure 4 mostly holds true on an east–west basis (Figure 5), especially in the west. The close relationship of the 1996 to 2001 sales data with the RNRs, as stated by Yang et al. [20], appears to involve an error compensation, with the N sales curve in the east being below the black RNR bar and above the black RNR bar in the west. However, these differences are small compared to the change in N rates between 2001 and 2017, and over the entire 1990–2021 period. Figure 5 also illustrates (by both the sales and interpolation curves) that almost all of the growth in N fertilizer use in Canada has taken place in the west.

The dramatic east–west difference in slopes in both the interpolated and sales curves in Figure 5 is supported by the crop-specific differences in Figure 2 and the areas of the dominant crops in Table 2. With nearly all of the cp cases with RNRs below their respective CIs also being in the west (Figure 2), the steepness of the two western curves in Figure 5 was to be expected. Additionally, most of these wide RNR to FUS differences were for the most economically important crops in the west, spring wheat and canola (Table 2). Conversely, in Figure 2, the closeness of the FUS mean and RNRs for grain corn and soybean, the most economically important crops in the east, explains the flatness of the two eastern curves in Figure 5. This correlation between Figures 2 and 5 further demonstrates the effectiveness of the CSNI model.

Except for the 2002 to 2011 dip in N sales, the uncorrected CSNI model was a reasonable first approximation of the N sales curve, given that it was derived independently from those national sales data, and that there were no data comparable to either the FUS or the RNRs in that 2002 to 2011 period. Although the RNR to FUS application rate changes in the west were only 23% of the total Canadian N consumption in 2020, that 23% shift in the west equates to 77% of Canada's goal of reducing GHG emissions from fertilizer use by 30% [10,18].

Figure 6 clarified the overwhelming impact that the per-crop N application rate increases had on N use compared to land use changes among crops. The uncorrected N application rate interpolations (Equation (9)) were close to linear from 2001 to 2017. However, the slight upward bend at 2012 in both blue curves in Figure 5 could be related to the slight upward distortions in the green and yellow curves in Figure 6, since Equation (9) is sensitive to crop area integrations.

5. Conclusions

Most of the increased N use in Canada was applied to a few economically important crops in the west, whereas land use changes among the major crops is far less important. Table 1, Appendix A, and the extrapolations (proxies) required for the non-FUS crop–province cases all draw attention to the gaps in the FUS data set. These gaps reflect the asymmetric distribution of Canadian agronomic crops demonstrated in Table 2. However, the close agreement between the N sales and FUS in 2017, the 93% of Canadian cropland accounted for by the FUS, and the sensitivity test on the proxy FUS N rates indicate that the FUS was sufficiently comprehensive.

While there were wide CIs around the crop-specific N use rates in the FUS, most of these increases since 2001 appear to be significant (at least by the non-parametric assessment in Figure 2). Combined with the secondary correction, the CSNI model is well suited to both historical and predictive N fertilizer applications. For example, CSNI should be a useful tool for the environmental assessment of excess N applications by helping to identify the source crops. Figures 4 and 5 suggest that, even without the secondary correction, the interpolation process would still be a reasonably accurate N use model in Canada if no N sales data were available. With the secondary correction, it is a definite improvement on the decades of N use estimates based solely on one size fits all indexing crop-specific N use to fertilizer sales data. Limiting the one size fits all approach to just the secondary correction will increase crop sensitivity in the GHG inventory models.

Although there were considerable extrapolations in this analysis, mainly from the crops covered in the FUS to the crops that were not covered, the FUS was surprisingly representative of the eight years of N sales records surrounding 2017. Conversely, the RNRs were based on information gleaned from provincial agricultural extension publications and from soil and crop advisers [20]. But (as shown by Figures 4 and 5), they still adequately represent the 1996–2001 period, as claimed by the RNR authors. Seen in this light, the FUS should not be viewed as a replacement for the RNR: each was shown to be valid for the periods in which they were derived. Similarly, while the FUS rates represent current N use rates, the FUS should not be taken as recommendations or guidelines for current crop production.

The CSNI approach identified the crops where the greatest attention to changing N application rates is most warranted. However, since they include two economically important export crops, this approach could prove to be a major policy challenge. In spite of being the heaviest user of N fertilizer of all the FUS crops, grain corn (at least from 2001 onward) did not contribute appreciably to the national N use increase over the last three decades.

The RNRs suggest that N use in Canada should be well below the FUS rates. As shown above, a 23% reduction in just the actual per-crop N application rates in the west could theoretically achieve 77% of the Canada's N fertilizer-related GHG emissions target [10,18]. Caution is needed, though, that this is likely not possible without at least some corresponding declines in crop yields. However, while improved fertilizer management [4] represents the essential alternative, this analysis identified where and for what crops these improvements might be the most effective.

The success of the CSNI model satisfied the goal of this paper. The CSNI model could significantly improve the monitoring of CO_2 emissions from N fertilizer manufacturing and N_2O and water pollution which will lead to more accurate targeting on mitigation measures. But the next step is to understand why N application rate increases since 2001 were greater in some crops than in others. Prior to the FUS, this question would not arise. With only the RNRs, there was no information available on crop-specific N application rates at another point in the time series to infer crop-specific trends.

Even with the FUS providing a second set of points in the time series, explaining the rate increases is still beyond the scope of this paper. While crop yield records are standard terms in agriculture census and survey records, relating interpolated N application rates to crop yield statistics leaves too much to assumption. Other factors, including plant genetics,

improved pesticides, changing climate, and the market value of the crop, can increase crop yields. Research on these factors is expected as part of Canada's commitment for a 30% reduction in N-related GHG emissions [10,18]. This research should include field testing under controlled conditions to isolate these factors. This research will likely facilitate finding a relationship with crop yields. Even without this understanding, however, the CSNI model should still be a useful tool for agricultural GHG inventory reports.

Author Contributions: Conceptualization, J.A.D. and A.P.; methodology, J.A.D.; formal analysis, J.A.D.; resources, A.P. and R.L.D.; writing—original draft preparation, J.A.D.; writing—review and editing, R.L.D.; funding acquisition, A.P. and R.L.D. All authors have read and agreed to the published version of the manuscript.

Funding: The research was funded by Serecon Inc., Edmonton, Alberta, Canada (a private sector consulting firm).

Data Availability Statement: Due to confidentiality restrictions the raw survey data are not publically available. The survey histograms are available upon request from Fertilizer Canada and the derived means and means deviations derived from the histograms are listed in Appendix A.

Acknowledgments: The authors acknowledge the support of Serecon Inc. for funding the analysis described in this paper and to Fertilizer Canada and Serecon Inc. for providing access to the Fertilizer Use Survey histograms. We are grateful to Devon Worth, Science and Technology Branch, AAFC, for making the national records of fertilizer shipments available for this analysis and for reviewing an early draft of this paper. We acknowledge the Science and Technology Branch, AAFC, for their ongoing support and encouragement for this work and for funding much of the background work under the Sustainability Metrics initiative leading up to this project.

Conflicts of Interest: Author Angela Pearson was employed by the company Serecon. The remaining authors declare that the research was conducted in the absence of any commercial or financial relationships that could be construed as a potential conflict of interest.

Appendix A

Table A1. Output from the non-parametric analysis of the Fertilizer Use Survey (FUS) histograms from all years (2014–2021), 11 crops and five Canadian provinces. Abbreviated prefixes for wheats, D, S and W, stand for "Duram", "Spring" and "Winter", respectively. For corn, the prefix, G, stands for "Grain".

Survey Years:		**2014**		**2015**		**2016**		**2017**		**2018**		**2019**		**2020**		**2021**		**Averages**	
										kg N/ha									
Crop	**Province**	**Mn**	**MD**	**Mn**	**MD**	**Mn**	**MD**	**Mn**	**MD**	**Mn**	**MD**	**Mn**	**MD**	**Mn**	**MD**	**Mn**	**MD**	**Mn**	**MD**
Canola	AB	102	32	108	27	131	57	110	48	142	24	167	50	152	40	135	32	**131**	**39**
	SK	98	38	110	29	116	63	114	40	131	23	145	40	128	22	130	30	**121**	**36**
	MB	117	33	128	22	134	47	134	30	134	25	176	44	154	21	124	28	**138**	**31**
G-corn	MB							174	28							134	51	**154**	**39**
	ON	147	66	166	27	166	83	185	62	176	64	223	54	211	34	186	55	**182**	**56**
	QC	150	68	192	29	183	97	210	52									**184**	**61**
Oats	AB									85	30							**85**	**30**
	SK									92	18							**92**	**18**
	MB									109	21							**109**	**21**
S-wheat	AB	91	27			99	23									127	33	**106**	**28**
	SK	83	31			92	19									119	28	**98**	**26**
	MB	107	21			109	23									132	23	**116**	**22**
D-wheat	AB					102	20											**102**	**20**
	SK					81	24											**81**	**24**
Forages	ON									102	50							**102**	**50**
	QC									121	41							**121**	**41**
Lentils	AB					14	12											**14**	**12**
	SK					10	7											**10**	**7**
Soybean	ON					7	9											**7**	**9**
	QC					8	18											**8**	**18**
W-wheat	ON			109	41			132	22					149	21			**130**	**28**
	QC			44	49													**44**	**49**
Flaxseed	MB															83	48	**83**	**48**
Sunflower	MB															100	22	**100**	**22**

References

1. Qualman, D. *Tackling the Farm Crisis and the Climate Crisis: A Transformative Strategy for Canadian Farms and Food Systems, Discussion Document*; Collaboration with the National Farmers Union (NFU): London, UK, 2019; 102p.
2. Statistics Canada. Fertilizer Shipments to Canadian Agriculture Markets, by Nutrient Content and Fertilizer Year, Cumulative data (×1000) Table: 32-10-0039-01 (formerly CANSIM 001-0069). 2023; Release date: 2023-02-21. Available online: https://www150.statcan.gc.ca/t1/tbl1/en/tv.action?pid=3210003901 (accessed on 1 July 2024).
3. Statista. Global Consumption of Agricultural Fertilizer from 1965 to 2021, by Nutrient (in Million Metric Tons). 2024. Available online: https://www.statista.com/statistics/438967/fertilizer-consumption-globally-by-nutrient/ (accessed on 1 July 2024).
4. Fertilizer Canada. A Summary of the Fertilizer Use Survey Conducted from 2014 to 2021: 4R Nutrient Stewardship, Grower Adoption across Canada. 2022. Available online: https://fertilizercanada.ca/wp-content/uploads/2022/08/SPARK-FERTILIZER-USE-IN-CANADA-REPORT-2022-VF_08_04_2022.pdf (accessed on 1 July 2024).
5. Dyer, J.A.; Vergé, X.P.C.; Desjardins, R.L.; Worth, D.E. District Scale GHG Emission Indicators for Canadian Field Crop and Livestock Production. *Agronomy* **2018**, *8*, 190. [CrossRef]
6. Janzen, H.H.; Angers, D.A.; Boehm, M.; Bolinder, M.; Desjardins, R.L.; Dyer, J.; Ellert, B.H.; Gibb, D.J.; Gregorich, E.G.; Helgason, B.L.; et al. A proposed approach to estimate and reduce net greenhouse gas emissions from whole farms. *Can. J. Soil Sci.* **2006**, *86*, 401–418. [CrossRef]
7. Pulse Canada. Application of Sustainable Agriculture Metrics to Selected Western Canadian Field Crops, Final Report. 2011. Available online: https://www.serecon.ca/public/download/documents/6679 (accessed on 1 July 2024).
8. Dyer, J.A.; Desjardins, R.L. A review and evaluation of fossil energy and carbon dioxide emissions in Canadian agriculture. *J. Sustain. Agric.* **2009**, *33*, 210–228. [CrossRef]
9. Brune, D.; SKillpack, C.; Buchholz, D. Nitrogen in the Environment: How Nitrogen Enters Groundwater. Univ. Missouri Extension Factsheet. 2002. Available online: https://extension.missouri.edu/publications/wq256 (accessed on 1 July 2024).
10. NFU. Agricultural Greenhouse Gas Emissions in Canada: A New, Comprehensive Assessment. National Farmers Union (NFU). 2022. Available online: https://www.nfu.ca/publications/a-new-comprehensive-assessment-ghg-emissions-canada-2022/ (accessed on 1 July 2024).
11. Philpott, T. A Brief History of Our Deadly Addiction to Nitrogen Fertilizer. Mother Jones. 2013. Available online: https://www.motherjones.com/food/2013/04/history-nitrogen-fertilizer-ammonium-nitrate/ (accessed on 1 July 2024).
12. Simpson, S. Nitrogen Fertilizer: Agricultural Breakthrough-And Environmental Bane. 2009. Available online: https://www.scientificamerican.com/article/nitrogen-fertilizer-anniversary/ (accessed on 1 July 2024).
13. MacDonald, K.B. Risk of water contamination by nitrogen. In *Environmental Sustainability of Canadian Agriculture: Report of the Agri-Environmental Indicator Project*; McRae, T., Smith, C.A.S., Gregorich, L.J., Eds.; Agriculture and Agri-Food Canada: Ottawa, ON, Canada, 2000; pp. 117–123.
14. Quinte Conservation. Drinking Water Source Protection. Factsheet. 2014. Available online: https://www.quinteconservation.ca/en/watershed-management/resources/Documents/commercial_fertilizer.pdf (accessed on 1 July 2024).
15. Erisman, J.; Sutton, M.; Galloway, J.; Klimont, Z.; Winiwarter, W. How a century of ammonia synthesis changed the world. *Nat. Geosci.* **2008**, *1*, 636–639. [CrossRef]
16. Roberts, T.L. The Role of Fertilizer in Growing the World's Food. TopCrop Manager Factsheet. 1999. Available online: https://www.topcropmanager.com/the-role-of-fertilizer-in-growing-the-worlds-food-10387/ (accessed on 1 July 2024).
17. Thakur, N. Food Security, Safety and Environmental Concerns: Restoring Long-term Agricultural Sustainability. *Acad. Lett.* **2021**, *888*. [CrossRef]
18. Government of Canada. Discussion Document: Reducing Emissions Arising from the Application of Fertilizer in Canada's Agriculture Sector. 2022. Available online: https://agriculture.canada.ca/en/department/transparency/public-opinion-research-consultations/share-ideas-fertilizer-emissions-reduction-target/discussion (accessed on 9 May 2024).
19. Huffman, T.; Ogston, R.; Fisette, T.; Daneshfar, B.; Gasser, P.-Y.; White, L.; Maloley, M.; Chenier, R. Canadian agricultural land-use and land management data for Kyoto reporting. *Can. J. Soil Sci.* **2006**, *86*, 431–439. [CrossRef]
20. Yang, J.Y.; De Jong, R.; Drury, C.F.; Huffman, E.; Kirkwood, V.; Yang, X.M. Development of a Canadian agricultural nitrogen budget model (CANB v2.0): Simulation of the nitrogen indicators and integrated modelling for policy scenarios. *Can. J. Soil Sci.* **2006**, *87*, 153–165. [CrossRef]
21. Karimi, R.; Pogue, S.J.; Kröbel, R.; Beauchemin, K.A.; Schwinghamer, T.; Janzen, H.H. An updated nitrogen budget for Canadian agroecosystems. *Agric. Ecosyst. Environ.* **2020**, *304*, 107046. [CrossRef]
22. Vergé, X.P.C.; Dyer, J.A.; Desjardins, R.L.; Worth, D. Long Term trends in greenhouse gas emissions from the Canadian poultry industry. *J. Appl. Poult. Res.* **2009**, *18*, 210–222. [CrossRef]
23. Vergé, X.P.C.; Dyer, J.A.; Desjardins, R.L.; Worth, D. Greenhouse gas emissions from the Canadian pork industry. *Livest. Sci.* **2009**, *121*, 92–101. [CrossRef]
24. Vergé, X.P.C.; Dyer, J.A.; Desjardins, R.L.; Worth, D. Greenhouse gas emissions from the Canadian beef industry. *Agric. Syst.* **2008**, *98*, 126–134. [CrossRef]
25. Vergé, X.P.C.; Dyer, J.A.; Desjardins, R.L.; Worth, D. Greenhouse gas emissions from the Canadian dairy industry during 2001. *Agric. Syst.* **2007**, *94*, 683–693. [CrossRef]

26. McConkey, B.; Lee, D.; Martin, T.; Cerkowniak, D.; Thiagarajan, A.; Lenton, L.; Jamieson, T. AAFC Sustainability Metrics Project. Agriculture and Agri-Food Canada. 2017. Available online: https://sustainablecrops.ca/images/pdf/AAFC_SustainabilityMetricsProject_NOV23_2107.pdf (accessed on 1 July 2024).
27. AAFC. *Annual Crop Inventory*; Government of Canada, Agriculture and Agri-Food Canada (AAFC), Science and Technology Branch: Ottawa, ON, Canada, 2016. Available online: https://open.canada.ca/data/en/dataset/ba2645d5-4458-414d-b196-6303ac06c1c9 (accessed on 1 July 2024).
28. Arkin, H.; Colton, R.C. *Statistical Methods as Applied to Economics, Business, Psychology, Education and Biology*, 4th ed.; Barnes and Noble College Outline Series; Barnes & Noble: New York, NY, USA, 1967; 273p, LCCCN: 55-8987.
29. Manitoba Pulse and Soybean Growers. Crop Nutrition Factsheet. Available online: https://www.manitobapulse.ca/production/dry-bean-production/crop-nutrition/#:~:text=The%20majority%20of%20dry%20bean,about%2090%20lbs%20N/ac (accessed on 1 July 2024).
30. Saskatchewan Pulse Growers. Available online: https://saskpulse.com/growing-pulses/chickpeas/seeding/ (accessed on 1 July 2024).
31. United Nations. Kyoto Protocol to the United Nations Framework Convention on Climate Change. 1998. Available online: https://unfccc.int/resource/docs/convkp/kpeng.pdf (accessed on 1 July 2024).
32. Buttenham, M. Canadian Field Print Initiative. Ontario Grain Farmer Magazine. April 2019. Available online: https://ontariograinfarmer.ca/2019/04/01/canadian-field-print-initiative/ (accessed on 1 July 2024).
33. Serecon. The Canadian Field Print Calculator. 2023. Available online: https://www.serecon.ca/public/download/documents/8730 (accessed on 1 July 2024).
34. Dyer, J.A.; Vergé, X.P.C.; Kulshreshtha, S.N.; Desjardins, R.L.; McConkey, B.G. Areas and greenhouse gas emissions from feed crops not used in Canadian livestock production in 2001. *J. Sustain. Agric.* **2011**, *35*, 780–803. [CrossRef]

Disclaimer/Publisher's Note: The statements, opinions and data contained in all publications are solely those of the individual author(s) and contributor(s) and not of MDPI and/or the editor(s). MDPI and/or the editor(s) disclaim responsibility for any injury to people or property resulting from any ideas, methods, instructions or products referred to in the content.

remote sensing

MDPI

Article

Revealing Cropping Intensity Dynamics Using High-Resolution Imagery: A Case Study in Shaanxi Province, China

Yadong Liu [1,2], Hongmei Li [1], Lin Zhu [3], Bin Chen [4], Meirong Li [1], Huijuan He [1], Hui Zhou [1], Zhao Wang [1] and Qiang Yu [2,*]

[1] Shaanxi Meteorological Service Center of Agricultural Remote Sensing and Economic Crops, Xi'an 710016, China; liuyadong@snu.ac.kr (Y.L.); lee8003@163.com (H.L.); 15339178813@163.com (M.L.); hehuijuan618@gmail.com (H.H.); hytux@163.com (H.Z.); sandstom@163.com (Z.W.)
[2] State Key Laboratory of Soil Erosion and Dryland Farming on the Loess Plateau, Northwest A&F University, Yangling 712100, China
[3] College of Natural Resources and Environment, Northwest A&F University, Yangling 712100, China; 2023050823@nwafu.edu.cn
[4] College of Soil and Water Conservation Science and Engineering, Northwest A&F University, Yangling 712100, China; 2022050855@nwafu.edu.cn
* Correspondence: yuq@nwafu.edu.cn

Abstract: Reliable and continuous information on cropping intensity is crucial for assessing cropland utilization and formulating policies regarding cropland protection and management. However, there is still a lack of high-resolution cropping intensity maps for recent years, particularly in fragmented agricultural regions. In this study, we combined Landsat-8 and Sentinel-2 imagery to generate cropping intensity maps from 2019 to 2023 at a 10 m resolution for Shaanxi Province, China. First, the satellite imagery was harmonized to construct 10-day composite enhanced vegetation index (EVI) time series. Then, the cropping intensity was determined by counting the number of valid EVI peaks within a year. Assessment based on 578 sample points showed a high level of accuracy, with overall accuracy and Kappa coefficient values exceeding 0.96 and 0.93, respectively. We further analyzed the spatiotemporal patterns of cropping intensity and generated a map of abandoned cropland in Shaanxi. The results indicated that cropland in Shaanxi Province was mainly utilized for single-cropping (52.9% of area), followed by double-cropping (35.2%), with non-cropping accounting for 11.9%. Cropping intensity tended to be lower in the north and higher in the south. Temporally, the average cropping intensity of Shaanxi increased from 1.1 to over 1.3 from 2019 to 2023. Despite this upward trend, large areas of cropland were abandoned in northern Shaanxi. These results demonstrate the potential of utilizing Landsat-8 and Sentinel-2 imagery to identify cropping intensity dynamics in fragmented agricultural regions and to guide more efficient cropland management.

Keywords: cropland use; multiple cropping; multi-source remote sensing; rainfed agriculture

1. Introduction

Understanding the spatiotemporal dynamics of cropping intensity is pivotal for effective cropland management and sustainable agricultural development. Cropping intensity, defined as the cultivation frequency on a cropland plot within a year, serves as a crucial indicator of cropland utilization efficiency and productivity [1]. In China, the multiple cropping system, i.e., harvesting two or more crops within a single year, has a long history dating back to the first century [2]. This strategic approach to land use aims to increase crop production within the constraints of limited cropland area, thereby maximizing the utilization of agroclimatic resources [3].

Shaanxi Province, located in northwestern China, is a typical agricultural region characterized by diverse topography and climatic conditions. Shaanxi was one of three

pilot provinces at the beginning of the Grain for Green program in 1999 in which steeply sloping cropland was converted to forest or grassland [4]. Consequently, there has been a substantial reduction in cropland area in Shaanxi [5,6]. Yet, large portions of abandoned cropland have also been observed in gently sloping areas [7]. Since 2020, Shaanxi has implemented several measures aimed at the recultivation of abandoned cropland to increase food supply. Thus, the period from 2019 to 2023 marked a critical juncture in the trajectory of cropland management in Shaanxi.

Remote sensing technology has played a crucial role in agricultural land use mapping since the 1970s [8]. Over the past few decades, research in crop mapping using remote sensing has grown significantly, with an increasing reliance on time series imagery to monitor crop phenology and seasonal variability [9,10]. Medium-resolution imagery, such as from the Moderate Resolution Imaging Spectroradiometer (MODIS), has been extensively used for generating cropping intensity assessments [11,12]. For example, [12] produced a global cropping intensity dataset from 2001 to 2019 using MODIS enhanced vegetation index (EVI) time series with a 16-day temporal resolution.

While earlier studies have made significant progress in crop intensity mapping using remote sensing, many still rely on data from a single sensor [8], which involves trade-offs between spatial and temporal resolution due to the physical limitations of individual sensors [13]. For example, Landsat imagery provides a high spatial resolution (30 m), but its temporal resolution is often insufficient to capture cropping patterns [14]. To address these limitations, spatiotemporal fusion techniques have been developed, combining fine- and coarse-resolution imagery to generate datasets with high spatiotemporal resolutions [15,16]. By fusing Landsat and MODIS data, it is possible to create 8-day-interval time series with a 30 m spatial resolution [17]. Additionally, the fusion of Landsat-8 and Sentinel-2 imagery offers even richer observations, achieving a temporal resolution of less than 5 days [18], enabling more detailed analysis of seasonal cropland dynamics. Given the substantial data volume and computational complexity involved, cloud computing platforms like Google Earth Engine (GEE) have become indispensable, offering planetary-scale processing capabilities for handling large datasets efficiently [19]. By leveraging its multi-petabyte data catalog and freely accessible computational service, GEE has been widely used for large-scale crop mapping and agricultural monitoring [20–22].

Despite these advancements, the potential of high-spatiotemporal-resolution imagery to accurately reveal cropping intensity remains underexplored, particularly in fragmented agricultural regions with complex cropping patterns like Shaanxi Province [23]. Although some studies have employed fused data to develop cropping intensity maps for individual years [14,24,25], these is still a notable gap in the availability of continuous, high-resolution cropping intensity maps for such challenging regions.

The primary objective of this study was to create a continuous, high-resolution cropping intensity dataset for Shaanxi Province from 2019 to 2023. Using a combination of Landsat-8 and Sentinel-2 imagery processed through GEE, we aimed to capture the spatiotemporal dynamics of cropping intensity and identify abandoned cropland in this region. Our findings will provide valuable insights to inform more effective cropland management strategies, and the methodology developed in this research offers the potential for broader applicability, facilitating continuous monitoring of the cropping intensity in other regions by leveraging multi-source remote sensing data.

2. Materials and Methods

2.1. Study Area

This study was conducted for Shaanxi Province (105°29′–111°15′E, 31°42′–39°35′N) in China, which has a total land area of 20.56×10^4 km^2 (Figure 1a). Shaanxi exhibits a varied range of altitudes and climates. Geographically, it is characterized by three natural zones from north to south: the Loess Plateau, the Guanzhong Plain, and the Qinba mountainous region. Shaanxi spans three climate zones: temperate, warm temperate, and northern subtropical regions. In recent years, the annual accumulated temperature above 0 °C

ranged between 4000 and 6000 °C (Figure 1b), while annual precipitation increased from 400 mm in the north to 1400 mm in the south (Figure 1c). Cropland is dispersed throughout the entire province, with the majority concentrated in central Shaanxi. The cropping system in Shaanxi transitions from single-cropping in the north to double-cropping in the south.

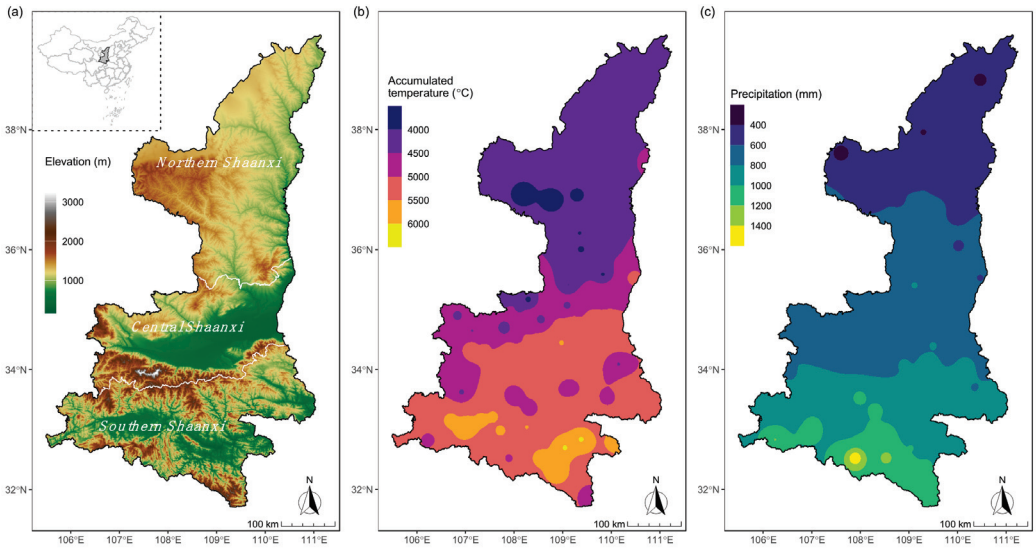

Figure 1. The geographical location of Shaanxi Province in China and the distribution of agroclimatic resources within Shaanxi. (**a**) Geographical location of Shaanxi Province and its regions along with elevation distribution. (**b**) Spatial distribution of the average annual accumulated temperature above 0 °C during 2019–2023. (**c**) Spatial distribution of the average annual precipitation during 2019–2023.

2.2. Workflow

The data and workflow for generating cropping intensity are presented in Figure 2. First, Sentinel-2 and Landsat-8 imagery were processed and harmonized to create a high-spatiotemporal-resolution dataset. Next, we constructed a consistent EVI time series through compositing, gap-filling, and smoothing techniques. Subsequently, cropping intensity was derived by counting the number of valid EVI peaks within a year. The accuracy of the generated product was then assessed using a large number of sample points.

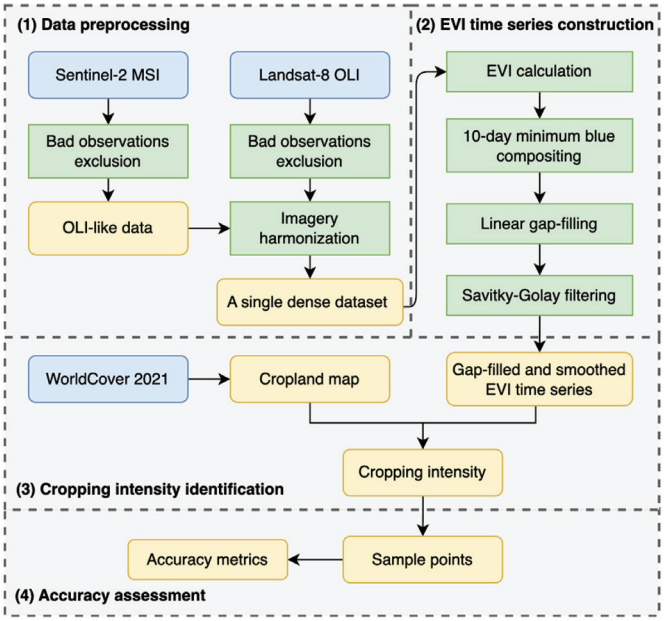

Figure 2. Data and workflow for generating cropping intensity.

2.3. Satellite Imagery

To gather cropland planting information, we utilized Landsat and Sentinel time series data spanning from 2019 to 2023. On a globe scale, the dual Sentinel satellite constellations (S2A and S2B) revisit every 3.8 days, and incorporating Landsat-8 data will further reduce the interval to 2.9 days on average [18]. The surface reflectance products of Landsat-8 Operational Land Imager (OLI) and Sentinel-2 MultiSpectral Instrument (MSI) were processed through GEE [19]. Low-quality observations were identified and excluded from further processing. We used the quality assurance layers QA60 and QA_PIXEL for Sentinel-2 and Landsat-8, respectively, to remove clouds and other low-quality observations.

Imagery harmonization was conducted to merge Landsat-8 and Sentinel-2 time series. We used the red, blue, and near-infrared bands from two sources: OLI bands 2, 4, and 5, and MSI bands 2, 4, and 8A [26]. First, given the spectral response similarities of OLI and MSI sensors, as shown in Table 1 and Figure 3, we employed linear models described by [27] to transform MSI data into OLI-like data. Then, to reconcile the difference in spatial resolutions, bands with 20 m or 30 m resolution were downscaled to 10 m. Finally, two normalized datasets with comparable spectral ranges and spatial resolutions were merged into a single dense dataset.

Table 1. The spectral band characteristics of Landsat-8 OLI and Sentinel-2 MSI sensors and the transformation equations.

Spectral Band	OLI		MSI-2A		MSI-2B		Transformation Equation
	Central Wavelength (nm)	Bandwidth (nm)	Central Wavelength (nm)	Bandwidth (nm)	Central Wavelength (nm)	Bandwidth (nm)	
Blue	482.0	60	492.7	65	492.3	65	OLI = 0.0003 + 0.9570 MSI
Red	654.6	37	664.6	30	664.9	31	OLI = 0.0041 + 0.9533 MSI
NIR	864.7	28	864.7	21	864.0	21	OLI = 0.0077 + 0.9644 MSI

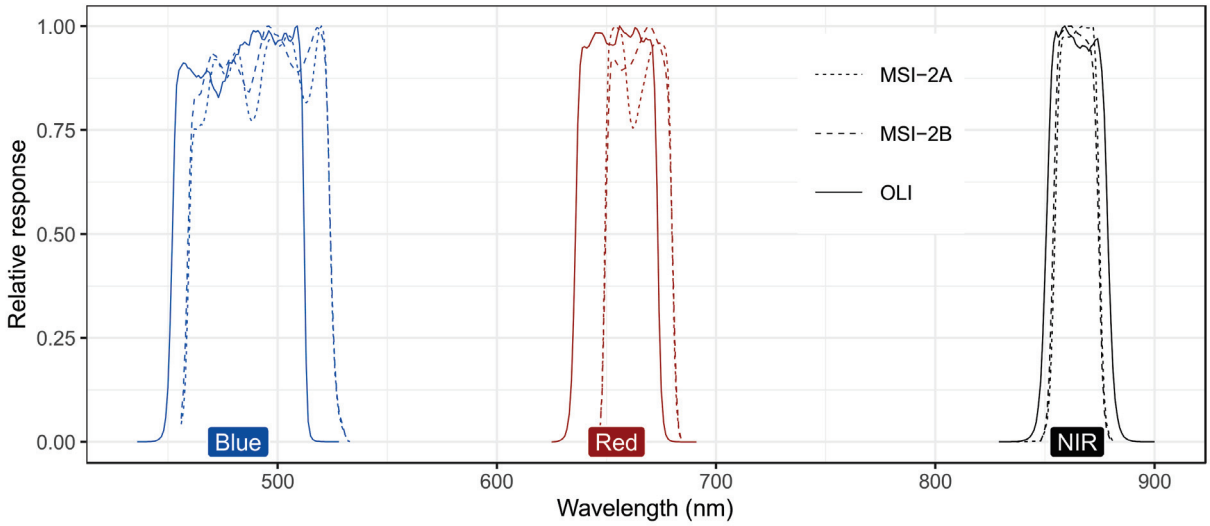

Figure 3. Spectral response functions of Landsat-8 OLI and Sentinel-2 MSI for the approximately equivalent bands utilized in this study [28,29].

We counted the total number of observations and the number of good-quality observations per pixel in Shaanxi throughout 2021 as an example (Figure 4). On average, the Sentinel-2 constellations and Landsat-8 exhibited revisit cycles of approximately 2.9 days

and 13 days, respectively. Their combination resulted in a more frequent observation interval, reduced to 2.4 days. After the removal of cloud-affected data, the frequency of good-quality observations remained reasonably high. To provide a comparative perspective, the revisit cycles for Landsat-8, Sentinel-2, and the combined Landsat-8 and Sentinel-2 datasets were approximately 21.2 days, 4.8 days, and 3.9 days, respectively.

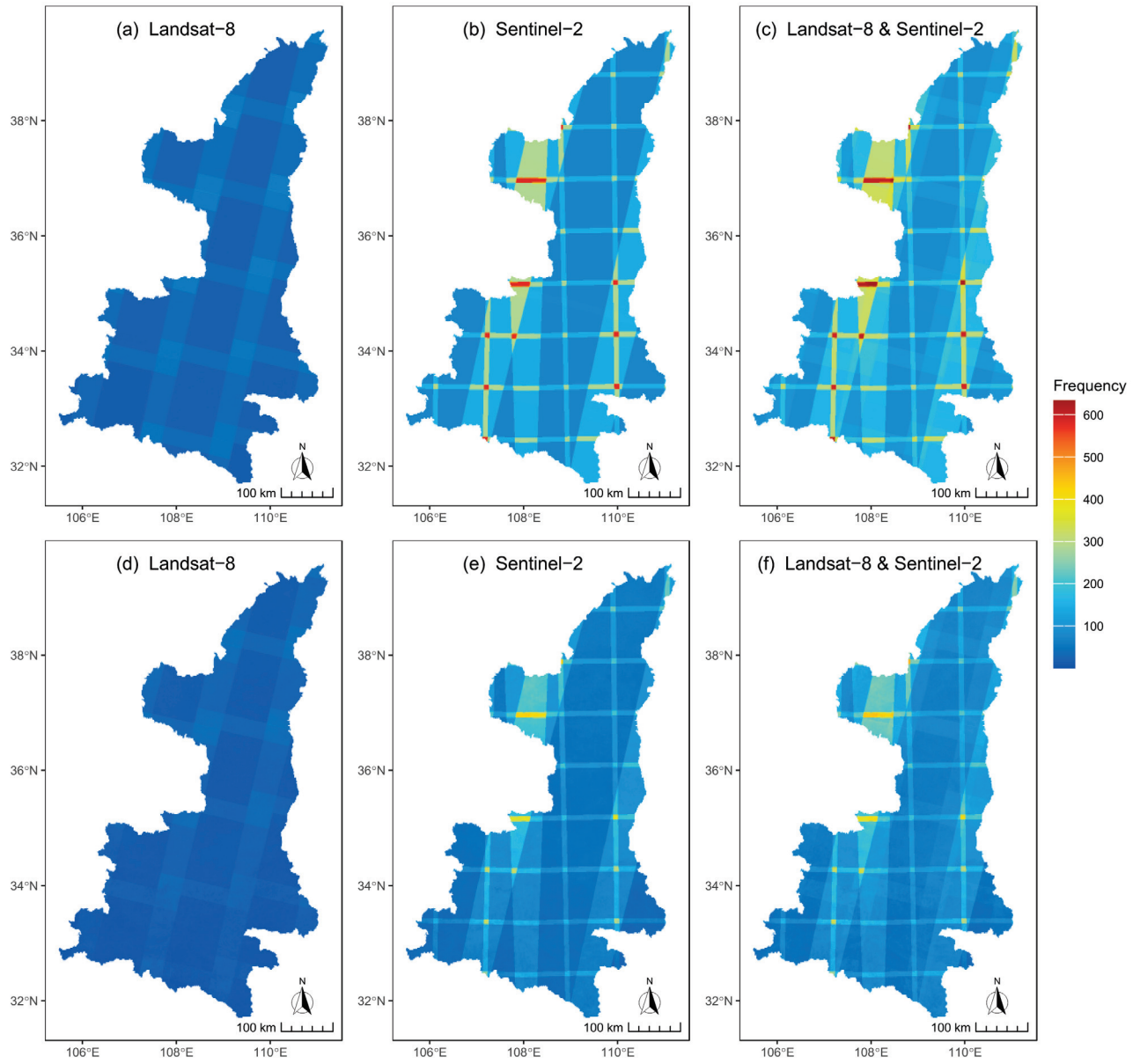

Figure 4. Distributions of total observations (**a**–**c**) and good-quality observations (**d**–**f**) in data from various sensors during 2021 in Shaanxi Province.

2.4. WorldCover Product

We used the European Space Agency (ESA) WorldCover land cover product to prepare the cropland basemap (Figure 5a). This product was the first global land cover product at 10 m resolution based on both Sentinel-1 and Sentinel-2 data. The WorldCover 2021 product [30] represents the global land cover for 2021 and is the successive version of the initial product obtained for 2020. It was generated with an improved algorithm (v200 vs. v100), leading to an overall improved retrieval and an increased accuracy (76.6% vs. 74.7%). As shown in Figure 5a, extensive croplands in Shaanxi are predominantly situated within the Guanzhong Plain, characterized by the prevalence of moderate- and large-sized crop

fields. Conversely, the Loess Plateau in northern Shaanxi, as well as the Qinba mountainous area of southern Shaanxi, exhibit small-sized crop fields.

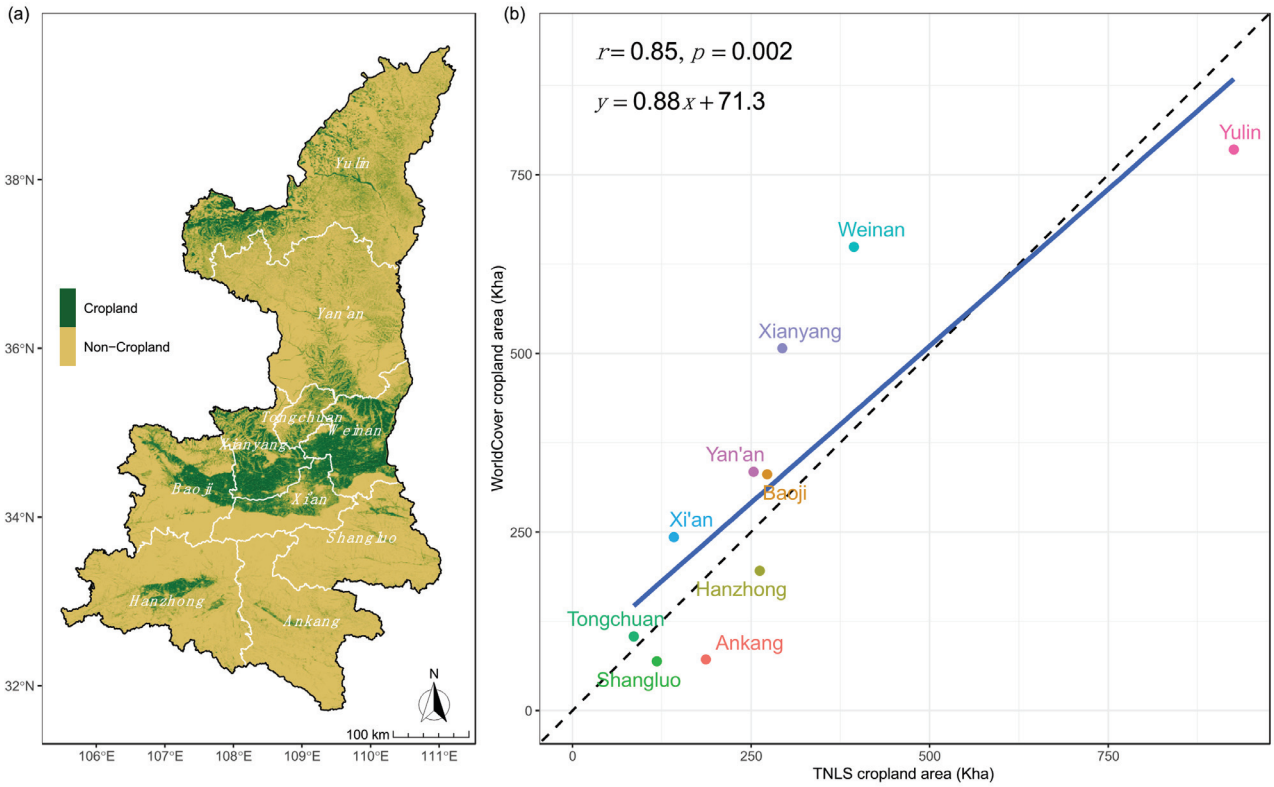

Figure 5. Cropland map of Shaanxi Province and accuracy at city levels. (**a**) Cropland map of Shaanxi derived from the WorldCover 2021 product. (**b**) Comparison between cropland area estimated from the map and data acquired from the Third National Land Survey (TNLS) results for cities in Shaanxi Province.

The Third National Land Survey (TNLS) data of Shaanxi Province, released in 2022, served as the benchmark for evaluating the derived cropland basemap. This dataset resulted from tremendous efforts integrating field surveying, drones, and satellite imagery with a resolution of less than or equal to one meter [31]. By collecting the cropland area figures from the TNLS result for each city, ranging from 85.6 Kha to 926 Kha, we assessed the accuracy of the WorldCover cropland product. To achieve this, we calculated the cropland area for each city using the cropland basemap and compared it with the TNLS data, employing linear regression for analysis.

For cropland area at the city level, the derived cropland map from the WorldCover product exhibited reasonably good agreement with the TNLS dataset. The correlation coefficient between these two datasets was 0.85, and the regression line closely approximated the 1:1 line, as depicted in Figure 5b. For most cities, the data points were near to the 1:1 line. As a whole, the cropland area estimated from the WorldCover product was higher than the area from the TNLS dataset by about 354 Kha. Consequently, the WorldCover product shows promise as a reliable source for generating a land use map for Shaanxi, particularly for extracting the distribution of cropland.

2.5. EVI Calculation

EVI has shown a strong correlation with canopy structural attributes, such as leaf area index and chlorophyll content, making it a prevalent indicator of green vegetation [32]. EVI time series have been employed extensively to effectively identify crop phenological traits, reflecting various growth stages, such as time of planting and harvesting. Notably,

different cropping intensities exhibit distinct EVI patterns within one year [11]. Therefore, EVI has been used in several studies for crop intensity mapping [11,12]. The EVI calculation formula is as follows:

$$EVI = 2.5 \times \frac{NIR - Red}{NIR + 6 \times Red - 7.5 \times Blue + 1} \quad (1)$$

where *NIR*, *Red*, and *Blue* represent the surface reflectances in the near-infrared, red, and blue bands, respectively.

2.6. Time Series Construction

The minimum blue compositing method [11] was employed to create EVI products with uniform intervals. Within each compositing period, the EVI value with the lowest reflectance in the blue band was extracted. This approach is particularly effective in identifying the clearest conditions owing to the blue band's sensitivity to aerosol contamination [33]. Considering the good-quality satellite observations and typical crop phenology in Shaanxi, a 10-day compositing period was chosen to generate 10-day composite EVI time series. Still, the composite time series might contain gaps due to a continuous absence of good-quality observations during the compositing period. Linear interpolation was utilized to fill these gaps by referencing EVI values before and after the respective time of the data gap.

We utilized the Savitzky–Golay filter [34] to smooth the composite EVI time series. Disturbances in the observations caused by snow and other factors often result in dramatic fluctuations within EVI curves. These fluctuations, theoretically, should not normally manifest themselves due to the limited duration of crop growth. Therefore, it was imperative to apply smoothing techniques to the composite time series before further analysis. The Savitzky–Golay filter is a widely used approach for reconstructing vegetation index time series [35,36]. This method performs polynomial least squares fitting over successive sets of adjacent values within a temporal window. The window size dictates the number of observations considered, while the polynomial degree regulates the order of the smoothing function. We implemented a moving window comprising nine composite dates, considering that the crop growth period typically exceeds 90 days in Shaanxi. A second-order polynomial was chosen to preserve subtle information related to crop phenology. Consequently, we generated a gap-filled and smoothly refined 10-day composite EVI time series for subsequent analysis (Figure 6).

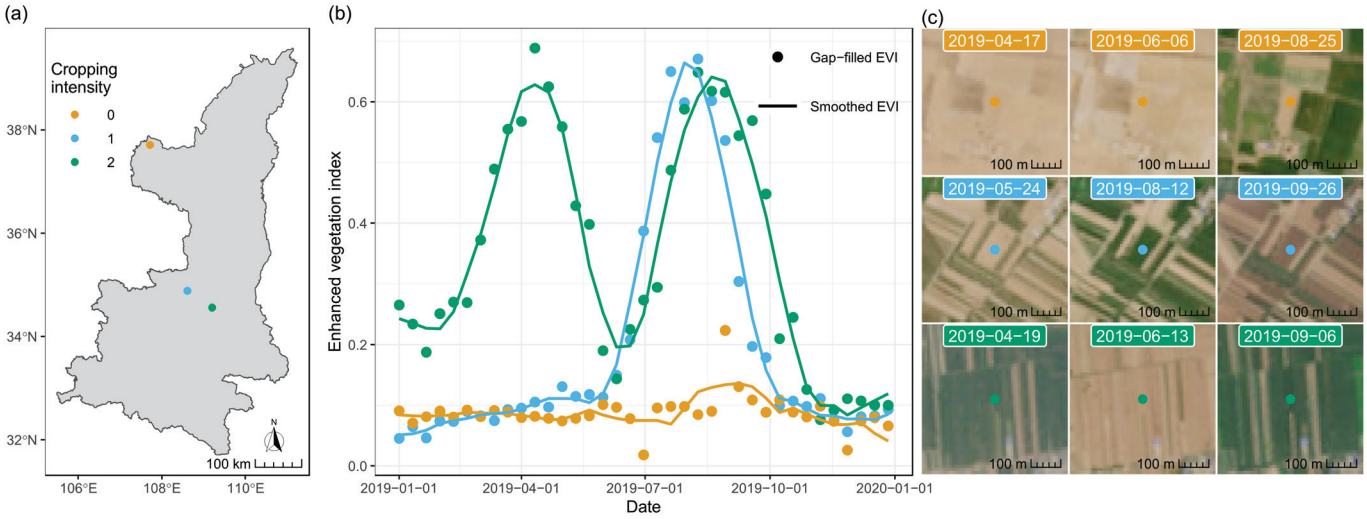

Figure 6. Typical enhanced vegetation index (EVI) patterns of different cropping intensities throughout a year in Shaanxi Province. (**a**) Spatial locations of three sites in Shaanxi. (**b**) EVI time series derived from Sentinel-2 and Landsat-8 data. Symbol and line colors correspond to the label colors in panel (**a**). (**c**) True color Sentinel-2 images at three sites.

2.7. Cropping Intensity Identification

The determination of cropping intensity relied on the extraction of phenological characteristics from smoothed EVI time series. Throughout a crop growing season, EVI values take a distinctive pattern: a gradual increase during the vegetative growth stage, reaching a peak when the canopy closes, and declining through the reproductive growth stage until harvest. Within one year, single-cropping systems will exhibit one distinctive cycle, whereas double-cropping systems will display two complete cycles. In contrast, non-cropping areas or fallow lands tend to have consistently low EVI values or significantly lower EVI peaks during the growing season. Therefore, the count of EVI peaks serves as a robust indicator of cropping intensity (Figure 6b). In this study, potential peaks in the EVI time series were identified as local maxima using a moving window spanning nine composite dates. Peaks with an EVI value lower than 0.35 were disregarded as spurious peaks [17]. Furthermore, peaks occurring after late October were excluded because winter wheat could exhibit a peak before entering dormancy. Cropping intensity was quantified by tallying the total count of peaks observed within the calendar year. Finally, we obtained the annual cropping intensity map for Shaanxi during 2019–2023.

2.8. Accuracy Assessment

The accuracy of cropping intensity quantification was assessed at the pixel scale using a stratified random sampling dataset. Sample points were randomly collected from each cropping intensity region estimated for the year 2019. The actual cropping intensity was independently determined through visual interpretation of EVI time series, very high-resolution imagery, and true color Sentinel-2 images. This process utilized tools such as Collect Earth v1.20.6 [37] and the Copernicus Browser [38]. Notably, during the interpretation, the points whose buffer zones contained noisy features such as ridges and trees were deliberately excluded. As a result, a total of 578 individual sample points were retained for the accuracy assessment (Figure 7). To enhance the independence of the validation, only sample points for the years from 2020 to 2023 were used for assessment, with each year containing more than 500 sample points. Subsequently, the confusion matrix and various metrics were calculated, such as overall accuracy and the Kappa coefficient. The overall accuracy serves as a fundamental metric for assessing the performance in terms of correct classifications across the entire dataset. It is determined as follows:

$$p_o = \frac{t}{n} \tag{2}$$

where p_o represents the overall accuracy, t is the number of correctly classified samples, and n is the total number of samples. The Kappa coefficient is a statistic that measures the performance considering class imbalances and the possibility of agreement occurring by chance. It is calculated as follows:

$$k = \frac{p_o - p_e}{1 - p_e} \tag{3}$$

where p_e is the expected proportion of samples correctly classified by chance. The Kappa coefficient (k) ranges from -1 and 1, with a value of 1 indicating perfect agreement between the truth and predictions.

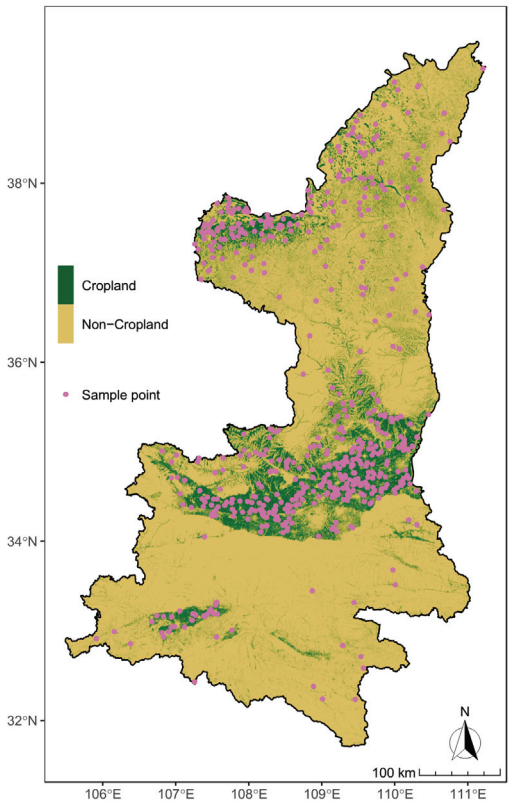

Figure 7. Spatial distribution of sample points in Shaanxi Province used for accuracy assessment.

3. Results

3.1. Spatial Distribution of Cropping Intensity

The spatial distribution of cropping intensity and the corresponding area in Shaanxi Province during 2019–2023 are shown in Figure 8. In agricultural practice, single-cropping dominates in Shaanxi, followed by double-cropping, with non-cropping being the least common. In terms of the percentage of cropland area occupied by each cropping intensity, single-cropping consistently maintained the highest proportion of the total cropland area from 2019 to 2023, averaging approximately 52.9%. Double-cropping accounted for 35.2% of the total cropland area, while non-cropping occupied 11.9% of the total cropland area.

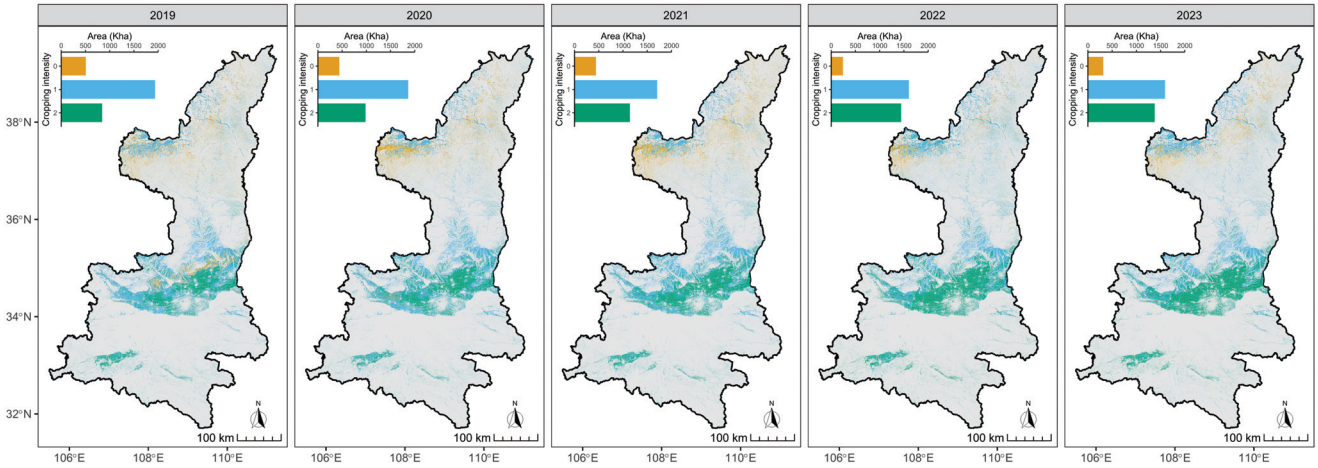

Figure 8. Cropping intensity (0, 1, 2) maps and cropland area statistics in Shaanxi Province from 2019 to 2023.

A considerable amount of cropland in northern Shaanxi has remained idle (Figure 9). For instance, in 2019, nearly 1/3 of the cropland in northern Shaanxi (366.4 Kha) had a cropping intensity of 0, constituting 72.3% of the non-cropping cropland in the entire province. This proportion remained consistently high, reaching or exceeding 90% from 2020 to 2023, peaking at 96.1% in 2021. This indicates that the majority of idle cropland was concentrated in northern Shaanxi, which is also evidenced by Figure 8. In contrast, there was very little idle cropland in central and southern Shaanxi, both in terms of absolute area and proportion, which were far lower than observed for the northern region. For example, in central Shaanxi, the proportion of idle cropland was 7.4% in 2019, the highest in the past five years, and subsequently remained below 2%.

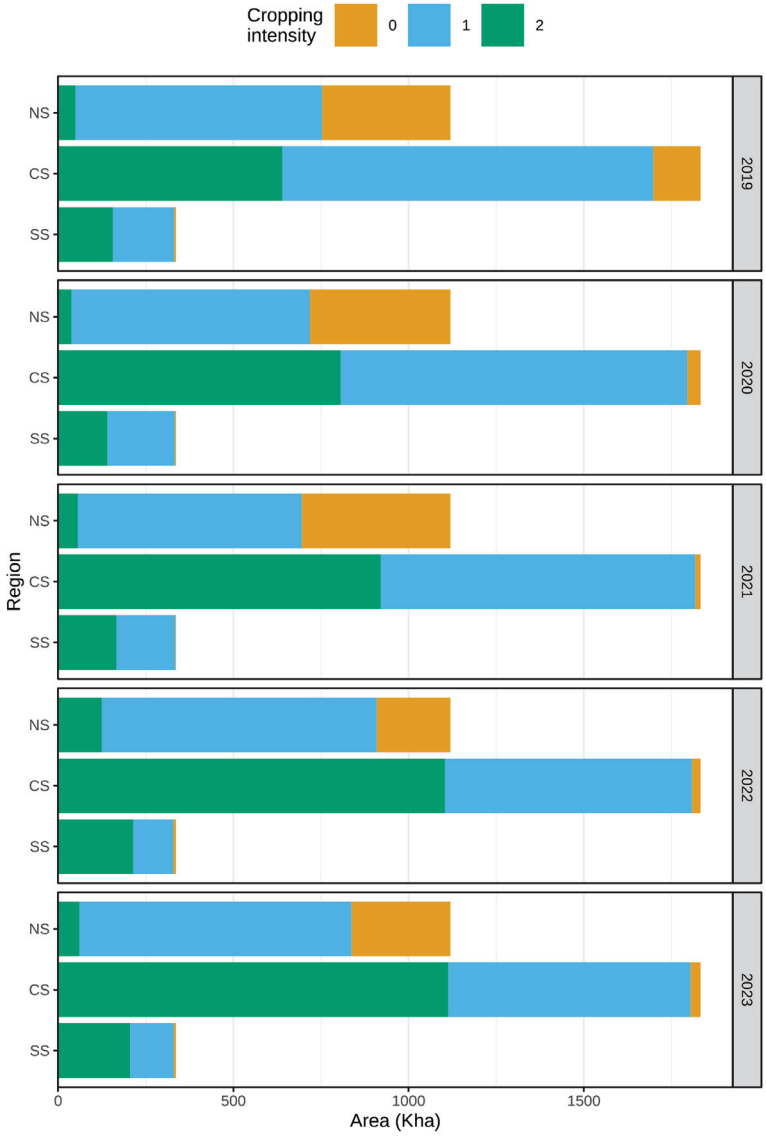

Figure 9. Cropland area for each cropping intensity in different regions of Shaanxi Province from 2019 to 2023. NS: Northern Shaanxi, CS: Central Shaanxi, SS: Southern Shaanxi.

3.2. Temporal Dynamics of Cropping Intensity

Temporally, the cropping intensity of most cropland in Shaanxi has undergone transitions over the past five years (Figure 10a). Only about 1/3 of cropland maintained a consistent cropping intensity during this period, including 100.4 Kha of non-cropping, 614.1 Kha of single-cropping, and 390.7 Kha of double-cropping cropland. In adjacent years, transitions primarily occurred between 1 and 2 or between 0 and 1. For example, from

2019 to 2020, the cropping intensity of 368.5 Kha of cropland increased from 1 to 2, while 267.0 Kha declined from 2 to 1. Additionally, 188.8 Kha and 160.9 Kha transitioned from 0 to 1 and from 1 to 0, respectively. When comparing 2019 and 2023, approximately 62% of croplands maintained their cropping intensity, with the remaining 656.8 Kha transitioning from 1 to 2, 233.1 Kha transitioning from 0 to 1, and 183 Kha and 104 Kha transitioning from 2 to 1 and from 1 to 0, respectively (Figure 10b).

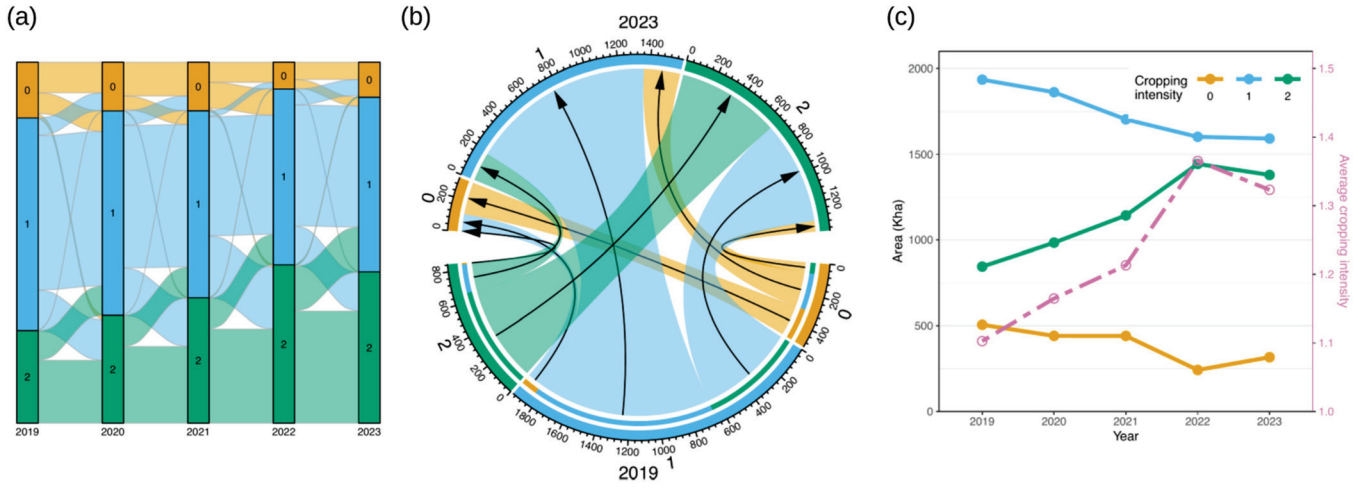

Figure 10. Temporal transitions of cropping intensity (0, 1, 2) in Shaanxi Province during 2019–2023. (**a**) Alluvial plot with temporal transitions of cropping intensity during 2019–2023. (**b**) Transition of cropping intensity between 2019 and 2023. (**c**) Cropland area of each cropping intensity and the average cropping intensity for Shaanxi Province from 2019 to 2023.

The transition of cropping intensity has led to an increasing trend in the utilization of cropland in Shaanxi Province (Figure 10c). From 2019 to 2022, the area of double-cropping cropland steadily increased from 844.9 Kha to 1443.7 Kha. Although there was a slight decrease in 2023, the decline was relatively small. In contrast, the area of single-cropping cropland decreased annually from 2019 to 2023. The area of idle cropland exhibited a significant decrease in 2022, reduced by 45% compared to the preceding year. Consequently, the average cropping intensity of Shaanxi, which was 1.10 in 2019, increased to 1.37 in 2022 and 1.32 in 2023.

3.3. Distribution of Abandoned Cropland

The abandoned cropland map of Shaanxi Province was derived from cropping intensity maps, as shown in Figure 11. The definition of abandoned cropland varies across previous studies, particularly in terms of the duration of time for which the land remains uncultivated [39–41]. In this study, we followed the FAO's definition, considering cropland that has been idle for at least five consecutive years as abandoned [42]. Cropland with a cropping intensity of zero for the period 2019–2023 was recognized as abandoned. In total, Shaanxi Province has 100.4 Kha (about 3%) of abandoned cropland, primarily concentrated in northern Shaanxi. At the city level, Yulin and Yan'an account for 90.0 Kha and 8.4 Kha of the abandoned cropland, respectively. Of the other regions, Weinan has the largest area of abandoned cropland, at approximately 0.58 Kha.

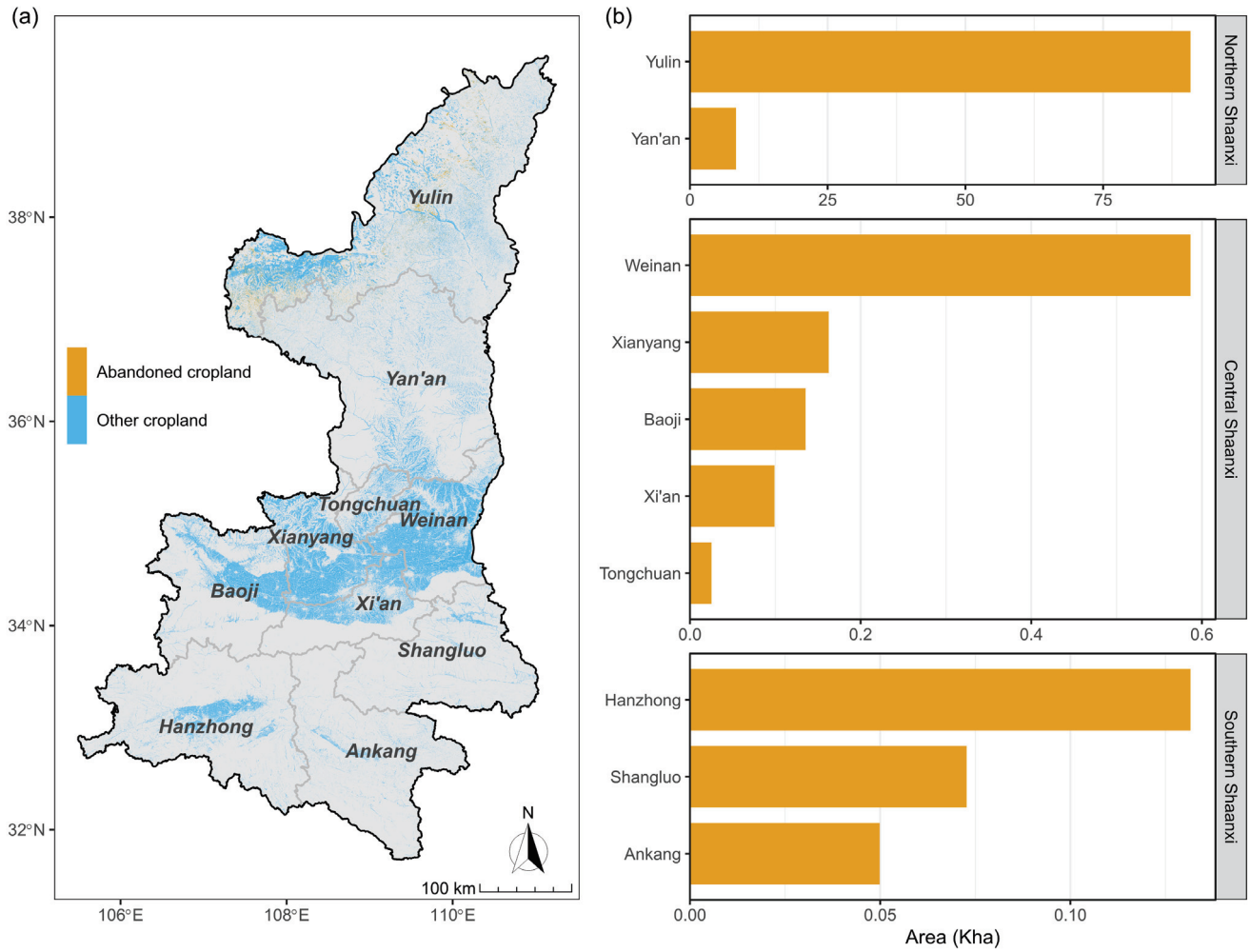

Figure 11. Distribution of abandoned cropland in Shaanxi Province and its area by city. (**a**) Map of abandoned cropland in Shaanxi Province. (**b**) Area of abandoned cropland in each city of Shaanxi Province.

3.4. Accuracy of Cropping Intensity Based on Sample Points

The accuracy assessment, conducted on 578 sample points, exhibited a high level of accuracy in extracting cropping intensity. Detailed confusion matrix and accuracy metrics for estimating the cropping intensity from 2020 to 2023 are presented in Table 2. On average, the overall accuracy and Kappa coefficient values reached 0.969 and 0.947, respectively. Moreover, for each year, the overall accuracy and Kappa coefficient values exceeded 0.96 and 0.93, respectively. Thus, the proposed approach could accurately detect the cropping intensity across multiple years in Shaanxi.

Table 2. The confusion matrix and accuracy metrics for estimating cropping intensity for Shaanxi Province in 2020–2023.

2020				
		Truth		
Prediction		0	1	2
	0	76	4	0
	1	1	255	4
	2	0	10	175
Overall Accuracy: 0.964				
Kappa Coefficient: 0.940				

2021				
		Truth		
Prediction		0	1	2
	0	73	4	0
	1	0	247	2
	2	0	5	200
Overall Accuracy: 0.979				
Kappa Coefficient: 0.966				

2022				
		Truth		
Prediction		0	1	2
	0	30	3	0
	1	4	265	1
	2	0	11	199
Overall Accuracy: 0.963				
Kappa Coefficient: 0.933				

2023				
		Truth		
Prediction		0	1	2
	0	43	3	0
	1	1	252	1
	2	0	10	201
Overall Accuracy: 0.971				
Kappa Coefficient: 0.949				

4. Discussion

4.1. Distribution of Cropping Intensity and Influencing Factors

Cropping intensity in Shaanxi generally exhibited a distribution pattern of lower in the north and higher in the south, aligning with the spatial pattern of thermal conditions. We examined the annual accumulated temperature above 0 °C from 2019 to 2023, a reliable indicator for assessing the suitability of multiple cropping systems [1,43,44]. This parameter was calculated as the sum of daily average air temperature consistently above 0 °C, with the beginning and end dates determined using a moving average method over five days. Based on the average values during 2019–2023 (Figure 1b), most parts of Shaanxi had accumulated temperatures $\geq$ 0 °C ranging between 4000 and 6000 °C, with less in the north and more in the south. Recent research by [45] suggested that the minimum accumulated temperature requirement was about 4400 °C for double-cropping systems, and 6000 °C for triple-cropping systems. In northern Shaanxi, accumulated temperatures mostly ranged between 4000 and 4500 °C, making the area suitable for single-cropping, while central and southern Shaanxi had accumulated temperatures ranging between 4500 and 6000 °C, sufficient to support double-cropping, but inadequate for triple-cropping.

Topography likely plays the dominant role in shaping the distribution of idle cropland in Shaanxi. Topographical attributes have been demonstrated to have a significant influence on agricultural production, affecting the spatial arrangement of soil nutrients, water resources, and cultivation practices [46,47]. The abandoned cropland map (Figure 11) illustrates that idle cropland in Shaanxi is predominantly concentrated in high-altitude regions of northern Shaanxi. To delve deeper, we conducted a statistical analysis of the area of idle cropland under different relief degrees of land surface (RDLSs) (Figure 12). The RDLS, originally proposed by [48], is a synthetic representation of the regional altitude and surface cutting degree. Leveraging the RDLS dataset for China [49], we projected it to align with the cropping intensity map prior to analysis. The findings suggested that during 2020–2023, more than 80% of idle cropland was concentrated in regions where the RDLS ranged from 0.9 to 1.6, with a sparse distribution observed in flat areas.

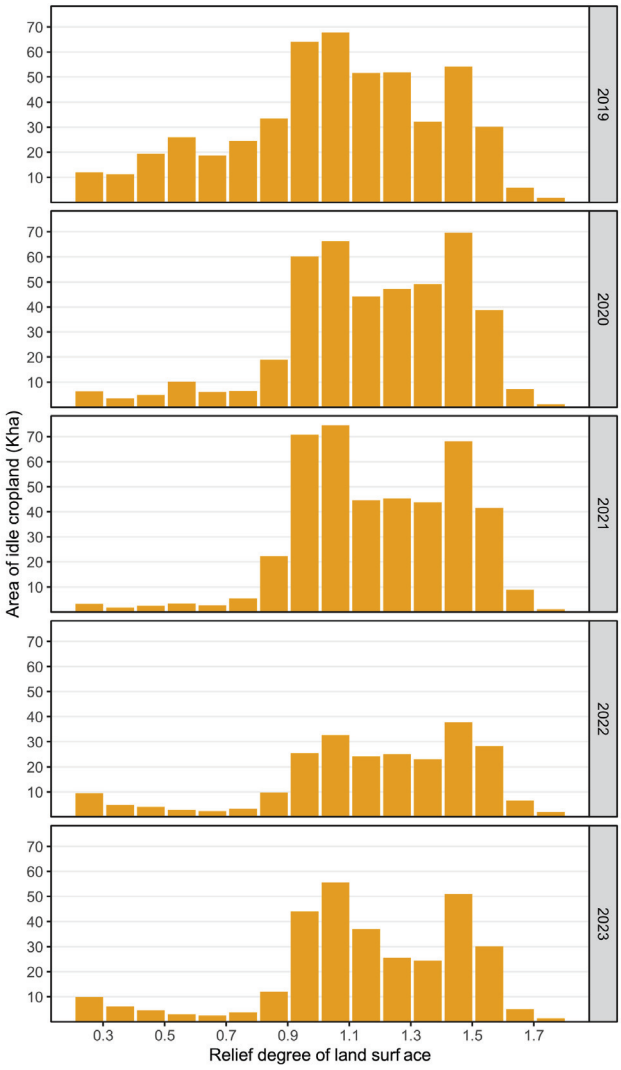

Figure 12. Histogram depicting the distribution of idle cropland area across different land surface relief degrees in Shaanxi Province.

4.2. Implication for Cropland Management

The rise in cropping intensity in Shaanxi was closely linked to the strong cropland protection policies implemented in recent years. China has devoted great efforts to cropland protection, and the 14th Five-Year Development Plan has reinforced the strictest cropland protection system to ensure national food security [41]. Guidance from the Ministry of Agriculture and Rural Affairs emphasized the urgent need to rehabilitate abandoned cropland in plain areas for cultivation. Our findings revealed a notable decline in idle cropland area in central Shaanxi in 2020 (Figures 8 and 9). Additionally, the increasing trend in the utilization of cropland over the past five years reflects the efficacy of the "storing grain in land" strategy.

We found that there were still some idle croplands in the hilly and mountainous areas of northern Shaanxi, which should be the areas of focus for the recultivation of abandoned cropland. This region has complex terrain, with alternating ridges and hills, numerous gullies, and serious fragmentation of cropland. Additionally, there are some areas affected by salinization and wind erosion. Therefore, we recommend the development of diverse agricultural production based on the local conditions, and thereby growing suitable crops for different areas, such as staple crops, miscellaneous grains, and forage grasses, to increase the supply of diversified products.

The northern part of central Shaanxi Province also exhibited cropping intensity gaps. This region is primarily dominated by single-cropping cultivation, and there are also scattered idle croplands. In terms of the thermal conditions, the accumulated temperature $\geq$0 °C in this region has exceeded 4500 °C in recent years, which is sufficient to meet the requirements for double-cropping (Figure 1b). Additionally, the annual precipitation in this region has also surpassed 600 mm in recent years (Figure 1c). Furthermore, climate change may increase the production potential of this area in the future [50]. However, the lack of water infrastructure makes this region a typical rainfed agriculture area. On the one hand, rainfed farming techniques and water-saving irrigation can be promoted to elevate non-cropping to single-cropping. On the other hand, improving irrigation conditions through construction of water infrastructure could help further increase cropping intensity, thereby fully exploiting the production potential of thermal and water resources.

4.3. Potential of Landsat-8 and Sentinel-2 Imagery to Identify Cropping Intensity

The combination of Landsat-8 and Sentinel-2 has demonstrated significant potential for mapping cropping intensity. Globally, the median revisit interval of their combination is 2.9 days [18]. For Shaanxi Province, our results showed an even shorter interval of 2.4 days. After eliminating cloud-affected, low-quality data, the fusion still offers frequent observations at a 3.9-day interval. This short revisit cycle allows for the creation of dense time series, enabling the capture of seasonal variability and the assessment of cropping intensity. Additionally, the high spatial resolution enhances the ability to monitor fragmented cropland, which is common in Shaanxi and similar agricultural regions, as compared to previous studies [11,12]. The long historical archive of Landsat-8 and Sentinel-2 also supports continuous temporal analysis, facilitating the identification of cropland abandonment. The combination delivers the data needed for high-accuracy and consistent cropping intensity mapping, ultimately supporting more effective cropland management strategies.

4.4. Potential Sources of Uncertainty

Several factors may affect the accuracy of cropping intensity maps generated from the proposed algorithms. Firstly, we utilized the WorldCover product to derive the cropland basemap of Shaanxi Province. While the extracted cropland areas were largely consistent with the TNLS results, there were still some disparities. For example, the cropland areas appeared slightly smaller in southern Shaanxi (Figure 5b). This could be attributed to the high degree of fragmentation in these regions [51], where individual cropland plots may be smaller than the size of a single pixel, leading to misclassification as other land cover types. Secondly, in some areas of Shaanxi, the two-year–three-crop rotation system is practiced [52]. However, this study did not specifically distinguish this category, but rather broke it down into a single-cropping and a double-cropping classification. While this approach may slightly impact the calculated cropping intensity, its effect was limited due to the relatively small area of these plots.

4.5. Limitations and Future Directions

At present, there are numerous spectral indices available in addition to the EVI used in this study. Although EVI alone showed a high accuracy, incorporating additional indices could potentially enhance the robustness of the results. For example, the land surface water index may improve the differentiation of cropping cycles [23]. Furthermore, the cropping intensity generation method in this study relies on the shape characteristics of the EVI time series, which can be effectively extracted using deep learning techniques [8]. Applying deep learning to automate the feature extraction process could significantly improve the efficiency of cropping intensity assessments. In summary, while this study demonstrates the effectiveness of EVI in mapping cropping intensity, future research should consider integrating multiple spectral indices and deep learning techniques to provide more robust and reliable assessments.

5. Conclusions

We explored the potential of fused high spatiotemporal remote sensing imagery for revealing cropping intensity dynamics. Using Shaanxi Province, China, as a case study, we combined Landsat-8 and Sentinel-2 imagery to generate cropping intensity maps at a 10 m resolution from 2019 to 2023. Subsequently, we investigated the spatiotemporal characteristics of cropping intensity and the distribution of abandoned cropland. Our findings revealed that single-cropping dominated crop production in Shaanxi (52.9% of cropland area), followed by double-cropping (35.2%), with non-cropping accounting for 11.9%. Cropping intensity tended to be lower in the north and higher in the south. While the transition in cropping intensity led to an upward trend in cropland utilization, large areas of cropland were abandoned, particularly in northern Shaanxi. These findings demonstrate the capability of high-resolution imagery to identify cropland utilization dynamics in fragmented agricultural regions and offer valuable guidance for effective cropland management practices.

Author Contributions: Conceptualization, Y.L. and Z.W.; data curation, H.L., B.C., and M.L.; formal analysis, Y.L.; methodology, Y.L. and L.Z.; project administration, Z.W.; supervision, Q.Y.; visualization, Y.L., H.H., and H.Z.; writing—original draft, Y.L.; writing—review and editing, Z.W. and Q.Y. All authors have read and agreed to the published version of the manuscript.

Funding: This research was funded by the National Natural Science Foundation of China (Grant number 42101304), and the Key Research and Development Projects of Shaanxi Province (Grant number 2024NC-YBXM-213).

Data Availability Statement: The data presented in this study are available on request from the corresponding author due to privacy.

Conflicts of Interest: The authors declare no conflicts of interest.

References

1. Yin, X.; Song, Z.; Shi, S.; Bai, Z.; Jiang, Y.; Zheng, A.; Huang, W.; Chen, N.; Chen, F. Developments and Prospects of Multiple Cropping in China. *Farming Syst.* **2024**, *2*, 100083. [CrossRef]
2. Liu, X.; Xang, C.; Han, X. Multiple Cropping in China. *China Rep.* **1983**, *19*, 11–21. [CrossRef]
3. Ray, D.K.; Foley, J.A. Increasing Global Crop Harvest Frequency: Recent Trends and Future Directions. *Environ. Res. Lett.* **2013**, *8*, 044041. [CrossRef]
4. Qian, C.; Shao, L.; Hou, X.; Zhang, B.; Chen, W.; Xia, X. Detection and Attribution of Vegetation Greening Trend Across Distinct Local Landscapes Under China's Grain to Green Program: A Case Study in Shaanxi Province. *Catena* **2019**, *183*, 104182. [CrossRef]
5. Zhou, X.; Zhou, Y. Spatio-Temporal Variation and Driving Forces of Land-Use Change from 1980 to 2020 in Loess Plateau of Northern Shaanxi, China. *Land* **2021**, *10*, 982. [CrossRef]
6. Ye, J.; Hu, Y.; Feng, Z.; Zhen, L.; Shi, Y.; Tian, Q.; Zhang, Y. Monitoring of Cropland Abandonment and Land Reclamation in the Farming–Pastoral Zone of Northern China. *Remote Sens.* **2024**, *16*, 1089. [CrossRef]
7. Zhao, X.; Wu, T.; Wang, S.; Liu, K.; Yang, J. Cropland Abandonment Mapping at Sub-Pixel Scales Using Crop Phenological Information and MODIS Time-Series Images. *Comput. Electron. Agric.* **2023**, *208*, 107763. [CrossRef]
8. Alami Machichi, M.; Mansouri, L.E.; Imani, Y.; Bourja, O.; Lahlou, O.; Zennayi, Y.; Bourzeix, F.; Hanadé Houmma, I.; Hadria, R. Crop Mapping Using Supervised Machine Learning and Deep Learning: A Systematic Literature Review. *Int. J. Remote Sens.* **2023**, *44*, 2717–2753. [CrossRef]
9. Zhang, M.; Zhou, Q.; Chen, Z.; Liu, J.; Zhou, Y.; Cai, C. Crop Discrimination in Northern China with Double Cropping Systems Using Fourier Analysis of Time-Series MODIS Data. *Int. J. Appl. Earth Obs. Geoinf.* **2008**, *10*, 476–485. [CrossRef]
10. Bégué, A.; Arvor, D.; Bellon, B.; Betbeder, J.; De Abelleyra, D.; PD Ferraz, R.; Lebourgeois, V.; Lelong, C.; Simões, M.; Verón, S.R. Remote Sensing and Cropping Practices: A Review. *Remote Sens.* **2018**, *10*, 99. [CrossRef]
11. Li, L.; Friedl, M.; Xin, Q.; Gray, J.; Pan, Y.; Frolking, S. Mapping Crop Cycles in China Using MODIS-EVI Time Series. *Remote Sens.* **2014**, *6*, 2473–2493. [CrossRef]
12. Liu, X.; Zheng, J.; Yu, L.; Hao, P.; Chen, B.; Xin, Q.; Fu, H.; Gong, P. Annual Dynamic Dataset of Global Cropping Intensity from 2001 to 2019. *Sci. Data* **2021**, *8*, 283. [CrossRef] [PubMed]
13. Karmakar, P.; Teng, S.W.; Murshed, M.; Pang, S.; Li, Y.; Lin, H. Crop Monitoring by Multimodal Remote Sensing: A Review. *Remote Sens. Appl. Soc. Environ.* **2024**, *33*, 101093. [CrossRef]
14. Liu, L.; Xiao, X.; Qin, Y.; Wang, J.; Xu, X.; Hu, Y.; Qiao, Z. Mapping Cropping Intensity in China Using Time Series Landsat and Sentinel-2 Images and Google Earth Engine. *Remote Sens. Environ.* **2020**, *239*, 111624. [CrossRef]
15. Belgiu, M.; Stein, A. Spatiotemporal Image Fusion in Remote Sensing. *Remote Sens.* **2019**, *11*, 818. [CrossRef]

16. Xiao, J.; Aggarwal, A.K.; Duc, N.H.; Arya, A.; Rage, U.K.; Avtar, R. A Review of Remote Sensing Image Spatiotemporal Fusion: Challenges, Applications and Recent Trends. *Remote Sens. Appl. Soc. Environ.* **2023**, *32*, 101005. [CrossRef]
17. Li, L.; Zhao, Y.; Fu, Y.; Pan, Y.; Yu, L.; Xin, Q. High Resolution Mapping of Cropping Cycles by Fusion of Landsat and MODIS Data. *Remote Sens.* **2017**, *9*, 1232. [CrossRef]
18. Li, J.; Roy, D. A Global Analysis of Sentinel-2A, Sentinel-2B and Landsat-8 Data Revisit Intervals and Implications for Terrestrial Monitoring. *Remote Sens.* **2017**, *9*, 902. [CrossRef]
19. Gorelick, N.; Hancher, M.; Dixon, M.; Ilyushchenko, S.; Thau, D.; Moore, R. Google Earth Engine: Planetary-Scale Geospatial Analysis for Everyone. *Remote Sens. Environ.* **2017**, *202*, 18–27. [CrossRef]
20. Xiong, J.; Thenkabail, P.S.; Gumma, M.K.; Teluguntla, P.; Poehnelt, J.; Congalton, R.G.; Yadav, K.; Thau, D. Automated Cropland Mapping of Continental Africa Using Google Earth Engine Cloud Computing. *ISPRS J. Photogramm. Remote Sens.* **2017**, *126*, 225–244. [CrossRef]
21. Liu, X.; Zhai, H.; Shen, Y.; Lou, B.; Jiang, C.; Li, T.; Hussain, S.B.; Shen, G. Large-Scale Crop Mapping From Multisource Remote Sensing Images in Google Earth Engine. *IEEE J. Sel. Top. Appl. Earth Obs. Remote Sens.* **2020**, *13*, 414–427. [CrossRef]
22. Htitiou, A.; Boudhar, A.; Chehbouni, A.; Benabdelouahab, T. National-Scale Cropland Mapping Based on Phenological Metrics, Environmental Covariates, and Machine Learning on Google Earth Engine. *Remote Sens.* **2021**, *13*, 4378. [CrossRef]
23. Guo, Y.; Xia, H.; Pan, L.; Zhao, X.; Li, R.; Bian, X.; Wang, R.; Yu, C. Development of a New Phenology Algorithm for Fine Mapping of Cropping Intensity in Complex Planting Areas Using Sentinel-2 and Google Earth Engine. *ISPRS Int. J. Geo-Inf.* **2021**, *10*, 587. [CrossRef]
24. Liu, L.; Kang, S.; Xiong, X.; Qin, Y.; Wang, J.; Liu, Z.; Xiao, X. Cropping Intensity Map of China with 10 m Spatial Resolution from Analyses of Time-Series Landsat-7/8 and Sentinel-2 Images. *Int. J. Appl. Earth Obs. Geoinf.* **2023**, *124*, 103504. [CrossRef]
25. Pan, L.; Xia, H.; Yang, J.; Niu, W.; Wang, R.; Song, H.; Guo, Y.; Qin, Y. Mapping Cropping Intensity in Huaihe Basin Using Phenology Algorithm, All Sentinel-2 and Landsat Images in Google Earth Engine. *Int. J. Appl. Earth Obs. Geoinf.* **2021**, *102*, 102376. [CrossRef]
26. Mandanici, E.; Bitelli, G. Preliminary Comparison of Sentinel-2 and Landsat 8 Imagery for a Combined Use. *Remote Sens.* **2016**, *8*, 1014. [CrossRef]
27. Zhang, H.K.; Roy, D.P.; Yan, L.; Li, Z.; Huang, H.; Vermote, E.; Skakun, S.; Roger, J.-C. Characterization of Sentinel-2A and Landsat-8 Top of Atmosphere, Surface, and Nadir BRDF Adjusted Reflectance and NDVI Differences. *Remote Sens. Environ.* **2018**, *215*, 482–494. [CrossRef]
28. Spectral Response of the Operational Land Imager In-Band, Band-Average Relative Spectral Response | Landsat Science. Available online: https://landsat.gsfc.nasa.gov/satellites/landsat-8/spacecraft-instruments/operational-land-imager/spectral-response-of-the-operational-land-imager-in-band-band-average-relative-spectral-response/ (accessed on 12 July 2024).
29. S2 Mission. Available online: https://sentiwiki.copernicus.eu/web/s2-mission (accessed on 12 July 2024).
30. Zanaga, D.; Van De Kerchove, R.; Daems, D.; De Keersmaecker, W.; Brockmann, C.; Kirches, G.; Wevers, J.; Cartus, O.; Santoro, M.; Fritz, S.; et al. ESA WorldCover 10 m 2021 V200. *Zenoto* **2022**. [CrossRef]
31. Chen, X.; Yu, L.; Du, Z.; Liu, Z.; Qi, Y.; Liu, T.; Gong, P. Toward Sustainable Land Use in China: A Perspective on China's National Land Surveys. *Land Use Policy* **2022**, *123*, 106428. [CrossRef]
32. Huete, A.; Didan, K.; Miura, T.; Rodriguez, E.P.; Gao, X.; Ferreira, L.G. Overview of the Radiometric and Biophysical Performance of the MODIS Vegetation Indices. *Remote Sens. Environ.* **2002**, *83*, 195–213. [CrossRef]
33. Grogan, K.; Fensholt, R. Exploring Patterns and Effects of Aerosol Quantity Flag Anomalies in MODIS Surface Reflectance Products in the Tropics. *Remote Sens.* **2013**, *5*, 3495–3515. [CrossRef]
34. Abraham, S.; Golay, M.J.E. Smoothing and Differentiation of Data by Simplified Least Squares Procedures. *Anal. Chem.* **1964**, *36*, 1627–1639. [CrossRef]
35. Chen, J.; Jönsson, P.; Tamura, M.; Gu, Z.; Matsushita, B.; Eklundh, L. A Simple Method for Reconstructing a High-Quality NDVI Time-Series Data Set Based on the Savitzky–Golay Filter. *Remote Sens. Environ.* **2004**, *91*, 332–344. [CrossRef]
36. Zhou, J.; Jia, L.; Menenti, M.; Gorte, B. On the Performance of Remote Sensing Time Series Reconstruction Methods—A Spatial Comparison. *Remote Sens. Environ.* **2016**, *187*, 367–384. [CrossRef]
37. Bey, A.; Sánchez-Paus Díaz, A.; Maniatis, D.; Marchi, G.; Mollicone, D.; Ricci, S.; Bastin, J.-F.; Moore, R.; Federici, S.; Rezende, M.; et al. Collect Earth: Land Use and Land Cover Assessment Through Augmented Visual Interpretation. *Remote Sens.* **2016**, *8*, 807. [CrossRef]
38. Copernicus Browser. Available online: https://browser.dataspace.copernicus.eu/ (accessed on 12 July 2024).
39. Alcantara, C.; Kuemmerle, T.; Prishchepov, A.V.; Radeloff, V.C. Mapping Abandoned Agriculture with Multi-Temporal MODIS Satellite Data. *Remote Sens. Environ.* **2012**, *124*, 334–347. [CrossRef]
40. Zhu, X.; Xiao, G.; Zhang, D.; Guo, L. Mapping Abandoned Farmland in China Using Time Series MODIS NDVI. *Sci. Total Environ.* **2021**, *755*, 142651. [CrossRef]
41. Jiang, Y.; He, X.; Yin, X.; Chen, F. The Pattern of Abandoned Cropland and Its Productivity Potential in China: A Four-Years Continuous Study. *Sci. Total Environ.* **2023**, *870*, 161928. [CrossRef]
42. Zheng, Q.; Ha, T.; Prishchepov, A.V.; Zeng, Y.; Yin, H.; Koh, L.P. The Neglected Role of Abandoned Cropland in Supporting Both Food Security and Climate Change Mitigation. *Nat. Commun.* **2023**, *14*, 6083. [CrossRef]
43. Liu, X.; Han, X. *China's Multiple Cropping System*; Beijing Agricultural University Press: Beijing, China, 1987.

44. Gao, J.; Yang, X.; Zheng, B.; Liu, Z.; Zhao, J.; Sun, S.; Li, K.; Dong, C. Effects of Climate Change on the Extension of the Potential Double Cropping Region and Crop Water Requirements in Northern China. *Agric. For. Meteorol.* **2019**, *268*, 146–155. [CrossRef]
45. Jiang, Y.; Yin, X.; Wang, X.; Zhang, L.; Lu, Z.; Lei, Y.; Chu, Q.; Chen, F. Impacts of Global Warming on the Cropping Systems of China Under Technical Improvements from 1961 to 2016. *Agron. J.* **2021**, *113*, 187–199. [CrossRef]
46. Han, Z.; Song, W. Abandoned Cropland: Patterns and Determinants Within the Guangxi Karst Mountainous Area, China. *Appl. Geogr.* **2020**, *122*, 102245. [CrossRef]
47. Eyre, R.; Lindsay, J.; Laamrani, A.; Berg, A. Within-Field Yield Prediction in Cereal Crops Using LiDAR-Derived Topographic Attributes with Geographically Weighted Regression Models. *Remote Sens.* **2021**, *13*, 4152. [CrossRef]
48. Feng, Z.; Tang, Y.; Yang, Y.; Zhang, D. The Relief Degree of Land Surface in China and Its Correlation with Population Distribution. *Acta Geogr. Sin.* **2007**, *62*, 1073–1082. [CrossRef]
49. You, Z.; Feng, Z.; Feng, Z.; Yang, Y.; Yang, Y. Relief Degree of Land Surface Dataset of China (1km). *Dightal J. Glob. Change Data Repos.* **2018**. [CrossRef]
50. Liang, Z.; Sun, L.; Tian, Z.; Fischer, G.; Yan, H. Increase in Grain Production Potential of China Under Climate Change. *PNAS Nexus* **2023**, *2*, pgad057. [CrossRef]
51. Ye, S.; Ren, S.; Song, C.; Du, Z.; Wang, K.; Du, B.; Cheng, F.; Zhu, D. Spatial Pattern of Cultivated Land Fragmentation in Mainland China: Characteristics, Dominant Factors, and Countermeasures. *Land Use Policy* **2024**, *139*, 107070. [CrossRef]
52. Yibin, W.; Jian, W.; Fei, L.; Xiaolin, L.; Dan, Z. Can the Transition of Multiple Cropping Systems Affect the Cropland Change? *Agric. Syst.* **2024**, *214*, 103815. [CrossRef]

Disclaimer/Publisher's Note: The statements, opinions and data contained in all publications are solely those of the individual author(s) and contributor(s) and not of MDPI and/or the editor(s). MDPI and/or the editor(s) disclaim responsibility for any injury to people or property resulting from any ideas, methods, instructions or products referred to in the content.

International Journal of Geo-Information

MDPI

Article

A Novel Approach for Ex Situ Water Quality Monitoring Using the Google Earth Engine and Spectral Indices in Chilika Lake, Odisha, India

Subhasmita Das [1], Debabrata Nandi [1], Rakesh Ranjan Thakur [2], Dillip Kumar Bera [3], Duryadhan Behera [4], Bojan Đurin [5] and Vlado Cetl [6,*]

[1] Department of Remote Sensing & GIS, Maharaja Sriram Chandra Bhanja Deo University, Baripada 757003, Odisha, India; dsubhasmita75@gmail.com (S.D.); debabrata.gis@gmail.com (D.N.)
[2] Odisha State Disaster Management Authority, Revenue and Disaster Management Department, Bhubaneswar 751023, Odisha, India; rakeshgeo@hotmail.com
[3] School of Civil Engineering, KIIT Deemed to Be University, Bhubaneswar 751024, Odisha, India; dberafce@kiit.ac.in
[4] Department of Earth Sciences, Sambalpur University, Sambalpur 768019, Odisha, India; dbehera@suniv.ac.in
[5] Department of Civil Engineering, University North, 42000 Varazdin, Croatia; bojan.durin@unin.hr
[6] Department of Geodesy and Geomatics, University North, 42000 Varazdin, Croatia
* Correspondence: vlado.cetl@unin.hr

Abstract: Chilika Lake, a RAMSAR site, is an environmentally and ecologically pivotal coastal lagoon in India facing significant emerging environmental challenges due to anthropogenic activities and natural processes. Traditional in situ water quality monitoring methods are often labor intensive and time consuming. This study presents a novel approach for ex situ water quality monitoring in Chilika Lake, located on the east coast of India, utilizing Google Earth Engine (GEE) and spectral indices, such as the Normalized Difference Turbidity Index (NDTI), Normalized Difference Chlorophyll Index (NDCI), and total suspended solids (TSS). The methodology involves the integration of multi-temporal satellite imagery and advanced spectral indices to assess key water quality parameters, such as turbidity, chlorophyll-a concentration, and suspended sediments. The NDTI value in Chilika Lake increased from 2019 to 2021, and the Automatic Water Extraction Index (AWEI) method estimated the TSS concentration. The results demonstrate the effectiveness of this approach in providing accurate and comprehensive water quality assessments, which are crucial for the sustainable management of Chilika Lake. Maps and visualization are presented using GIS software. This study can effectively detect floating algal blooms, identify pollution sources, and determine environmental changes over time. Developing intuitive dashboards and visualization tools can help stakeholders engage with data-driven insights, increase community participation in conservation, and identify pollution sources.

Keywords: water quality monitoring; NDTI; NDCI; TSS; GEE; GIS

1. Introduction

Water quality monitoring is one of the core practices in protecting the integrity of water bodies and safeguarding the health of the ecosystems and populations depending on them [1–3]. It systematically analyzes water's physical, chemical, and biological properties to determine water quality or its vulnerability to and impairment by contaminant exposure [4,5]. Turbidity, chlorophyll, and total suspended solids levels are monitored in water to ascertain aquatic environments' overall health and functioning [6,7]. Remote sensing, a means to collect information on objects or phenomena without direct physical contact, has become a potent tool for water quality monitoring. In remote sensing, this is realized through the measurement of reflectance or radiance of water bodies across the spectral bands of the electromagnetic spectrum [8–10]. It has been discovered that remote sensing techniques are effective in detecting floating algal blooms, identifying sources of

pollution, and determining changes over time in the condition of the environment. Some water quality monitoring platforms exist in the remote sensing domain, including the Google Earth Engine (GEE) [11–13]. Based on the cloud environment, the GEE provides users with the full library of satellite imagery and geospatial datasets and a suite of analysis and visualization tools. Resources such as this, when applied, empower the GEE as a tool through which researchers, policymakers, and environmental practitioners can carry out long-term and in-depth assessments of water quality dynamics at regional, national, and global scales [14–16]. The GEE's flexibility goes beyond data access and includes deploying algorithms and models tuned for one's water quality monitoring objectives [17–19]. In this sense, remote-sensing data enable one to tap into sophisticated processing capabilities so that users can find actionable insights, identify trends, and evaluate the efficacy of their strategies for managing water. Furthermore, with the aid of the GEE, dynamic water quality maps, charts, and indicators enhance effective decision-making as they encourage environmental stewardship [20–22].

In addition to its analytical capabilities, the GEE has a user-friendly and intuitive interface that fosters the creation of web applications and interactive platforms to disseminate water quality information. The development of intuitive dashboards and visualization tools may help stakeholders engage with data-driven insights, make them aware of the issues related to water quality, and increase community participation in conservation. In this sense, the inclusion of the GEE in this effort represents a paradigm shift on a global scale in impact assessment and monitoring [23–25]. In so doing, the GEE can harness the cloud remote sensing technology promptly and cost-effectively in monitoring water resources, thus enabling an individual to put into place proactive measures in the management of water resources to be assured of the integrity of the ecosystems as well as ensuring public health [26–28]. Water quality monitoring, therefore, requires the assistance of remote sensing and the GEE to achieve the sustainable management and protection of water resources [29–31]. They might be used to gain deeper insights into ecosystems and aquatic environments, spot emerging threats, and focus the interventions in such a manner so as to ensure the long-term viability of freshwater environments for generations to come [32,33].

2. Materials and Methods

2.1. Study Area

In Odisha, on the east coast of India, at the mouth of the Daya River, which drains into the Bay of Bengal, sits the Chilika Lagoon, a RAMSAR site. It extends at latitude 19°43′ N and longitude 85°19′ E (Figure 1). It lies in the three coastal districts of Odisha, Puri, Khordha, and Ganjam, and has a total area of more than 1165 square kilometers.

The lake is a complex hydrological and ecological system receiving freshwater inflows from 52 streams and rivers, with saline tidal influx from the Bay of Bengal, and with several mouths around its periphery that open and close seasonally. The corresponding gradient of the depth and salinity categorizes the northern, central, southern, and outer channel zones. It is enriched with aquatic flora and fauna in addition to rare and endangered species like the Irrawaddy dolphin, fishing cat, and Chilika buffalo. The lake also hosts millions of migratory birds who visit the lake every winter. The lake is a source of livelihood for more than 0.2 million fisher folk and other communities. Several thousands of species of fish, birds, reptiles, invertebrates, and amphibians live in the lake. The lake also offers multiple ecosystem services, including water purification, control of floods, regulation of climate, and recreation. Some of the threats and challenges the lake faces include pollution, siltation, invasive species, habitat loss, and overexploitation of resources. Additionally, it has been designated as a priority site for Indian conservation and management, which is a Ramsar Site (an intergovernmental convention was adopted in 1971 in the Iranian city of Ramsar that aims to conserve and use wetlands sustainably and recognizes wetlands).

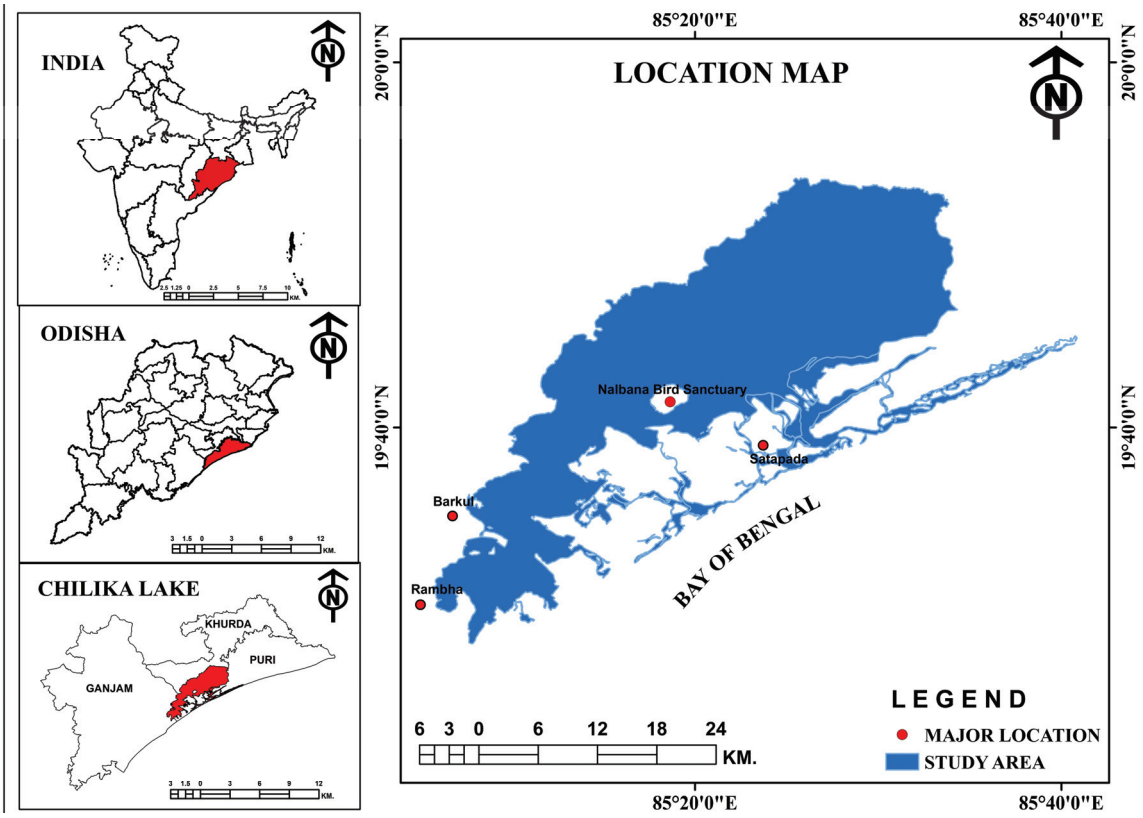

Figure 1. Study area.

2.2. Data and Indices Used

2.2.1. Satellite Imagery

For this research, Sentinel-2 Level 2A (MSI) imagery was used (Table 1). The images provide surface reflectance (SR) corrected for atmospheric conditions, and the atmospheric effects were removed, allowing for a more accurate analysis of land cover features. Sentinel-2 Level 2A products are generated by applying atmospheric correction algorithms to level-1C data.

Table 1. Sentinel-2 Level 2A imagery datasets.

MSI Bands (Spatial Resolution)	Central Wavelength (nm)	Band Width (nm)	Lref W/(m^2 sr µm)
B1—(60 m)	443.9 (Aerosols)	21	0.0001
B2—(10 m)	496.6 (Blue)	66	0.0001
B3—(10 m)	560 (Green)	36	0.0001
B4—(10 m)	664.5 (Red)	31	0.0001
B5—(20 m)	703.9 (Red-edge 1)	15	0.0001
B6—(20 m)	740.2 (Red-edge 2)	15	0.0001
B7—(20 m)	782.5 (Red-edge 3)	20	0.0001
B8—(10 m)	835.1 (NIR)	106	0.0001
B8-A—(20 m)	864.8 (Red-edge 4)	21	0.0001
B9—(60 m)	945 (Water Vapor)	20	0.001
B10—(60 m)	1375 (SWIR)	31	1
B11—(20 m)	1613.7 (SWIR 1)	91	0.0001
B12—(20 m)	2202.4 (SWIR 2)	175	0.0001

ESRI (Environmental System Research Institute)-based ArcGIS Pro software (2023) was used to perform the pre-processing stages on the imagery. The Apparent Reflectance Function calculates the top of atmosphere reflectance and sun angle adjustment by cali-

brating the digital number (DN) values of data obtained from satellite sensors. Maps are presented using the software ArcGIS 10.8.

2.2.2. Google Earth Engine (GEE)

It is a cloud-based service that uses satellite imagery and geospatial datasets to analyze Earth's surface changes, trends, and differences [34]. It offers access to a vast catalog of historical and current imagery, data, and tools for processing and visualizing them [35]. Users can interact with the platform through web-based code editors, explorer apps, or Python and JavaScript client libraries. It supports applications like remote sensing, natural resource management, disease prediction, and environmental monitoring. It is free for academic and research use.

2.2.3. Water Quality Data

Data on the water quality of Chilika Lake in Odisha were gathered from the GEE Data Catalogue [36,37]. The study's models were created using ex situ measurements of Chilika Lake and Sentinel-2 images [38]. The research was carried out using a variety of water quality measures, including total suspended solids, chlorophyll, and turbidity, using different seasonal imagery, as shown in Table 2.

Table 2. Details of the study area with no indices and different seasonal imagery.

Study Area	Area of Lake (km^2)	No. of Indices	Different Seasonal Imagery
Chilika lake, Odisha, India	1165	• NDTI • NDCI • TSS	Winter season (January–February) Pre-Monsoon Season (March–May) Monsoon Season (June–August) Post-Monsoon Season (September–November)

2.3. Methodology

The data acquisition stage involves gathering Sentinel-2 satellite imagery, a multispectral data collection initiative by the European Space Agency. The image interpretation stage uses the Automated Water Extraction Index (AWEI) technique to identify water bodies using visible and near-infrared wavelengths [39]. The final output is a map or image highlighting the extracted water bodies, helpful in monitoring water resources, mapping floodplains, or studying wetland ecosystems. This simplified process allows for efficient water body extraction from Sentinel-2 satellite imagery, which is portrayed in Figure 2, and the detailed process is discussed below.

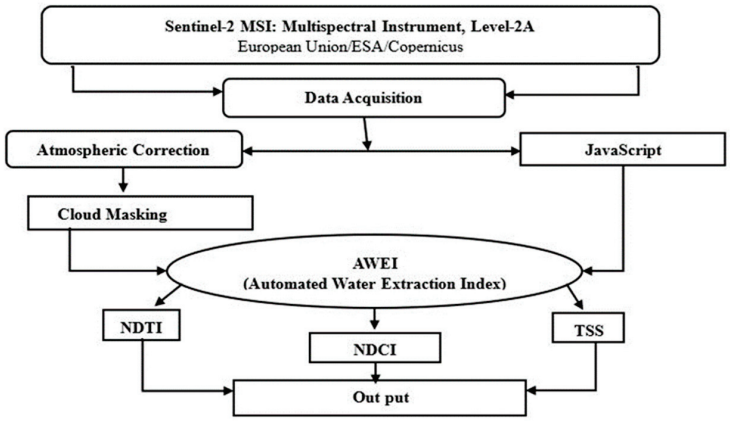

Figure 2. Flow chart of the methodology.

2.3.1. Atmospheric Correction

Sentinel-2 is a constellation of twin polar-orbiting satellites with a high 5-day revisit period of the equator [40]. MSI data offer thirteen spectral bands, precise spatial resolution, and twelve-bit quantization. They are helpful for vegetation research, water quality applications, aerosol and coastal retrievals, and inland water research [41–43]. The sensor's bottom-of-atmosphere reflectance photo underwent atmospheric effect correction, and alternative algorithms have been proposed for water quality monitoring in the GEE [44,45].

SIAC: Sensor Invariant Atmospheric Correction estimates surface reflectance of land and water pixels. Assumes spectrally smooth atmospheric scattering. Validated for Sentinel-2 land pixels. Limited accuracy for water pixels [46].

ACOLITE: The Sentinel-2 Sensor Algorithm uses dark pixel subtraction to correct atmospheric effects and estimates water quality parameters like turbidity and chlorophyll-a from surface reflectance [47]. A modified Atmospheric Correction algorithm improves accuracy and spatial resolution by adjusting Sentinel-2 reflectance using a linear regression model [48]. Both algorithms use different formulas to calculate satellite images' surface reflectance and water quality parameters. The SIAC algorithm estimates surface reflectance at band i.

$$\rho_i = \pi L_i - \alpha_i / \beta_i \tag{1}$$

where ρ_i is the surface reflectance, L_i is the top-of-atmosphere (TOA) radiance, and αi and β_i are the coefficients derived from the sensor-invariant relationship.

The ACOLITE algorithm uses the following formula to estimate the surface reflectance at band i:

$$\rho_i = \pi L_i - L_{dark,i} / F_0 \cos(\theta_s) \tag{2}$$

where ρ_i is the surface reflectance, L_i is the TOA radiance, $L_{dark,\ i}$ is the dark pixel radiance, F_0 is the solar irradiance and θ_s is the solar zenith angle.

2.3.2. Cloud Masking

Cloud masking is supposed to remove pixels from the Sentinel-2 images affected by clouds or their shadows. Various methods are available in this regard [49].

2.3.3. Water Masking

Water masking is a method used to identify water pixels in satellite images, with increasing applications in water quality monitoring, flood mapping, and hydrological modeling [50]. One method is the Automatic Water Extraction Index (AWEI), which combines spectral information from different bands. To apply the AWEI to Sentinel-2 images in the Google Earth Engine (GEE), load the image collection, filter by date, region, and cloud, select required bands like blue, green, red, NIR, and SWIR, and define the AWEI function to calculate the water index.

$$AWEI = 4 \times (Green - SWIR1) - (0.25 * NIR + 2.75 * SWIR1) \tag{3}$$

The AWEI function maps images to a binary image, assigning 1 to water pixels and 0 to non-water pixels. A threshold value is set to indicate water pixels, with values above this threshold representing water pixels and values below this threshold representing non-water pixels [51]. For instance, a zero threshold would indicate that all positive AWEI values are water pixels. Display the water mask image on the map and export the results to a vector layer or a raster file.

2.3.4. Indices Used for Monitoring Water Quality Monitoring in the GEE

For this research work, we used these indices

(a) NDTI (Normalized Difference Turbidity Index)

An NDTI band index is described as follows:

$$\text{NDTI} = \text{Red} - \text{Green}/\text{Red} + \text{Green}$$

The NDTI, a satellite-based water turbidity measure, is crucial for assessing water quality and aquatic ecosystems, indicating pollution, erosion, and sediment transport [52].

2.3.5. JavaScript for NDTI Estimation in the GEE

The processing steps for deriving TSI maps from satellite imagery are detailed below. The NDTI uses the reflectance properties of water and vegetation to estimate vegetation abundance. It indirectly provides access to water quality parameters such as turbidity and chlorophyll-a concentration [53,54]. The formula is:

Steps in the GEE:

(a) Import Imagery:

Choose Sentinel-2 images as they offer suitable green and NIR bands. Filter by date (Winter season, Pre-Monsoon Season, Monsoon Season, or Post Monsoon Season), cloud cover, and other criteria relevant to your study area and objectives.

(b) Load and Process: Load the selected image collection using ee.ImageCollection(). Apply cloud masking, atmospheric correction, and other pre-processing steps as needed.

(c) NDTI Calculation:

The function to calculate the NDTI using JavaScript is as follows (Figure 3):

```
var calcNDTI = function(img) {
        var ndti = img.expression(
            '(A_t * (p_w * scale_factor) / (1 - ((p_w * scale_factor )/ C)))', {
                'p_w': img.select('B4').divide(10000), //red band mid wv_len = 645.5nm
                'A_t': 366.14, //calib param (ACOLITE)
                'B_t': 0.33, //calib param (ACOLITE)
                'C': 0.19563, //calib param (ACOLITE)
                'pi': Math.PI,
                'scale_factor': 1.0 //band info
            }).rename('NDTI');
        return img.addBands(ndti)
}
```

Figure 3. JavaScript code for NDTI calculation.

(d) Add a visualization parameter:

The function to visualize the NDTI using JavaScript is as follows (Figure 4):

```
var ndtiViz={min:0,max:100, palette: ['darkblue','blue','lightblue','cyan','limegreen']};
Map.addLayer(NDTI.mean().clip(ROI), ndtiViz , 'ndti') // ROI is our study area
```

Figure 4. JavaScript code for NDTI visualization.

2.3.6. JavaScript for NDCI Estimation in the GEE

NDCI (Normalized Difference Chlorophyll Index)

An NDCI band index is described as follows:

$$\text{NDCI} = \text{Red edge 1} - \text{Red}/\text{Red edge1} + \text{Red}$$

Chlorophyll, a pigment in green plants and algae, indicates water quality and eutrophication. Remote sensing and the Google Earth Engine (GEE) can help monitor water quality trends globally by estimating chlorophyll-a concentrations [55]. Sentinel-2 satellite photos and the GEE enable accurate approximation of chlorophyll concentrations [56]. However, high readings call for further investigation and management to prevent harmful algal blooms and protect water bodies.

The NDCI is calculated using specific spectral bands to estimate chlorophyll-a concentration, an indicator of phytoplankton biomass and water quality [57,58].

Steps in the GEE:

(a) Import Satellite Imagery: Choose Sentinel-2 imagery due to its suitable green and red bands. Filter by date (Winter season, Pre-Monsoon Season, Monsoon Season, or Post-Monsoon Season), cloud cover, and other criteria relevant to your study area and objectives.

(b) Load and Process: Load the selected image collection using ee.ImageCollection(). Apply cloud masking, atmospheric correction, and other pre-processing steps as needed.

(c) NDCI (Normalized Difference Chlorophyll Index) calculation: The function to calculate the NDCI using the formula above is written in JavaScript as follows (Figure 5)

```
var calcNDCI = function(img) {
  var ndci = img.normalizedDifference(['B5','B4']).rename('NDCI');
  return img.addBands(ndci);
};//The normalized difference is computed as (first - second) / (first + second)
```

Figure 5. JavaScript code for NDCI calculation.

(d) Add a visualization parameter: The function to visualize the NDTI using JavaScript is as follows (Figure 6):

```
var ndciViz={min:-1 ,max:1, palette:['darkblue', 'blue', 'cyan', 'limegreen', 'yellow', 'orange', 'orangered','darkred']};

var NDCI = COLL.select('NDCI');

  var rgbNDCI = NDCI.map(function(img) {
    return img.visualize(ndciViz).clip(ROI);
  });

Map.addLayer(NDCI.mean().clip(ROI), ndciViz, 'ndci')
```

Figure 6. JavaScript code for NDCI visualization.

2.3.7. JavaScript for TSS Estimation in the GEE

TSS (Total Suspended Solids)

Suspended matter, a significant source of pollution in surface water, is crucial for water quality management [59]. Total suspended solids (TSS), a critical indicator of water quality, are monitored using remote sensing techniques like the GEE [60]. Algorithms like Doxaran and Markov models provide a synoptic view of TSS dynamics, improving water quality management and prediction [61].

(a) The function to calculate TSS using the formula above is written in JavaScript as follows (Figure 7).

```
var calcTSS = function(img){
  var tss=img.expression(
    '(RED+(NIR1/RED))/2', {
    RED:img.select('B4').divide(65565),
    NIR1:img.select('B8').divide(65565),
    }).rename('TSS');

  var tss_res = tss.expression('((TSS**2) * 93011) - (TSS * 82773) + 18442 ',{
    TSS:tss.select('TSS')
  }).rename('TSS')

  return img.addBands(tss_res);
}
```

Figure 7. JavaScript code for TSS calculation.

(b) Add a visualization parameter: The function to visualize TSS using JavaScript is as follows (Figure 8):

```
var tssViz = {
  bands: 'TSS',
  min:0,
  max:6000,
  palette: ['darkblue', 'blue', 'cyan', 'limegreen', 'yellow', 'orange', 'orangered','darkred']
};
Map.addLayer(TSS.mean().clip(ROI), tssViz, 'TSS')
```

Figure 8. JavaScript code for TSS visualization.

3. Results

Chilika Lake follows the new Caledonian barrier reef; this is why it has been listed as a World Heritage Site. The salinity of the Chilika water varies by region, from freshwater to oceanic salinity due to tidal influx [62]. As it is a World Heritage Site, many tourists visit this place, which makes the surroundings more polluted. There are other polluting factors involved due to migratory birds [63]. Due to this, we studied various indices of water quality monitoring concerning seasonal and yearly data.

3.1. Seasonal Water Quality Variation

As per the Indian Metrological Department, Odisha experiences four major seasons (i.e., Winter, Pre-Monsoon, Monsoon, and Post-Monsoon). In the current study, a detailed analysis of the NDTI, NDCI, and TSS for all four seasons was carried out and is discussed below.

3.1.1. Winter Season

NDTI (Normalized Difference Turbidity Index)

The NDTI is a valuable tool for assessing water quality, offering insights into turbidity, sedimentation, and algal blooms [64]. High NDTI values result in reduced light penetration and impact aquatic photosynthesis, habitats, and biodiversity. A lower NDTI value may help improve the reduction in sedimentation and preserve habitats and biodiversity [65]. In the current study, we found that in 2019, the FNU maximum was recorded at 118.17, while the lowest recorded value was 26.655. The NDTI reached the highest value of 158.606 FNU and the lowest value of 19.806 FNU in 2021. In 2023, the NDTI recorded a high of 1909.83 FNU and a low of 370.775 FNU (Figure 9). Regular monitoring of turbidity using the NDTI during winter can provide valuable data for conservation efforts. It helps identify any unusual changes in water quality that might indicate pollution or other environmental issues, enabling timely intervention [66]. As the study area is a popular tourist destination, especially in winter, lower turbidity levels enhance the aesthetic appeal of the lake, attracting more tourists. This can have positive economic implications for the local communities dependent on tourism [67].

NDCI (Normalized Difference Chlorophyll Index)

A high NDCI value leads to excessive algal growth, potentially toxic to humans and aquatic life, and a low value indicates low nutrient levels, which impact aquatic productivity. During winter, the low temperature and lower nutrient inflow from the catchment area decrease the chlorophyll concentration. The NDCI can effectively monitor these changes, providing insights into the seasonal variations in phytoplankton biomass. Regular monitoring of chlorophyll levels using the NDCI during winter provides valuable data for water quality management [68].

Chlorophyll has a maximum value of 0.135 mg and a minimum value of −0.068 mg in 2019, according to the above maps and statistical data. In 2021, there was a maximum of 0.042 mg of chlorophyll-a and a minimum of −0.006 mg. In 2023, there was a high

of 0.078 mg chlorophyll-a and a low of −0.028 mg (Figure 10). Monitoring chlorophyll levels using the NDCI during winter helps manage fish populations and ensure sustainable fishing practices. Lower chlorophyll levels can indicate healthier water conditions, which benefit fish growth and reproduction [69].

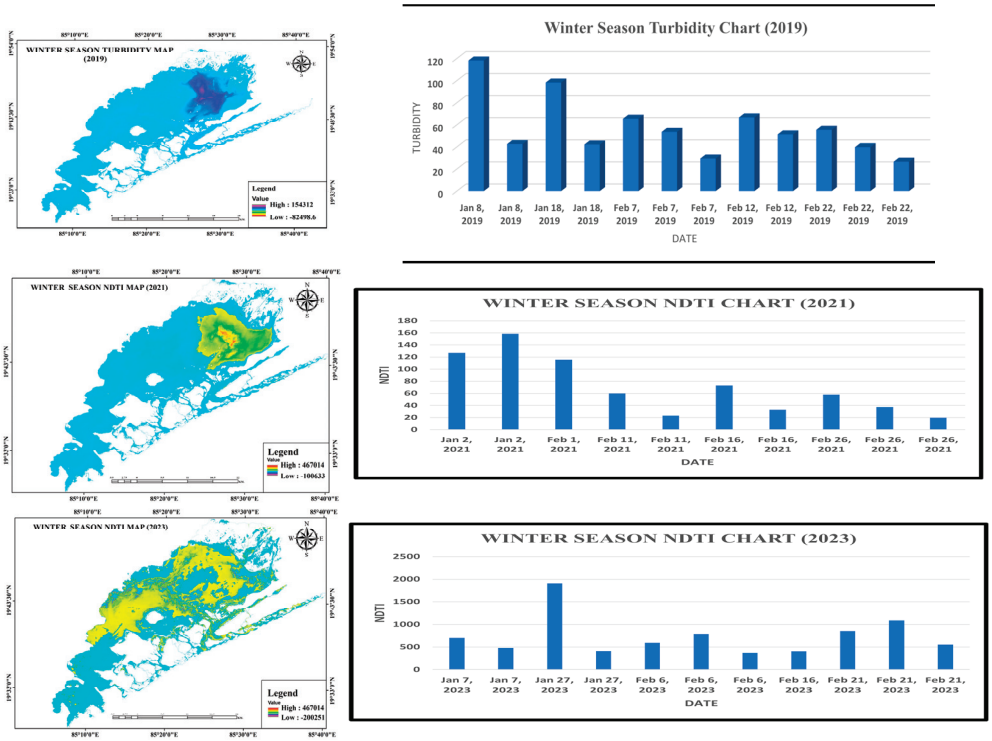

Figure 9. Winter season NDTI map and chart (2019/2021/2023).

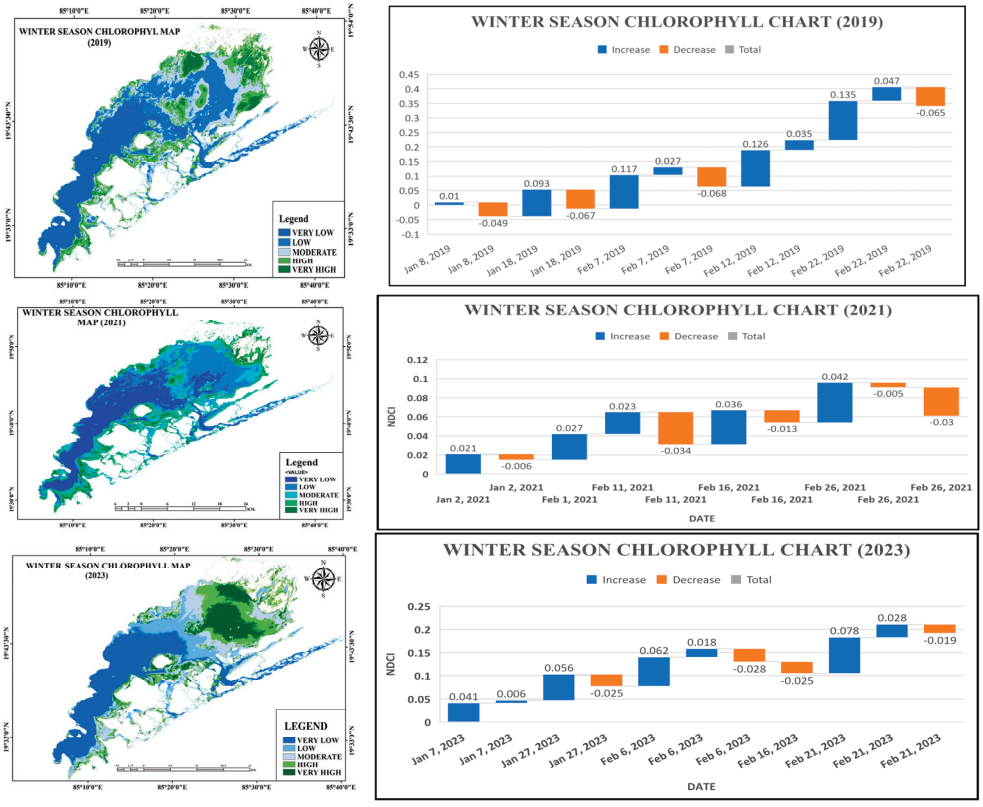

Figure 10. Winter season NDCI map and chart (2019/2021/2023).

TSS (Total Suspended Solids)

During winter, less rainfall in the catchment area leads to lower sediment inflow, which results in lower TSS levels, which enhances water quality and impacts TSS, with it having a maximum value of 6701.34 mg/L and a minimum value of 1914.76 mg/L in 2021. The TSS in 2023 had a minimum value of 315.965 mg/L and a maximum value of 1113.42 mg/L (Figure 11). Lower TSS levels can improve fish health and growth by providing a more transparent and oxygen-rich environment. This can enhance fish populations and support sustainable fishing practices. Regular monitoring of TSS levels during winter offers valuable data for conservation efforts [70–72].

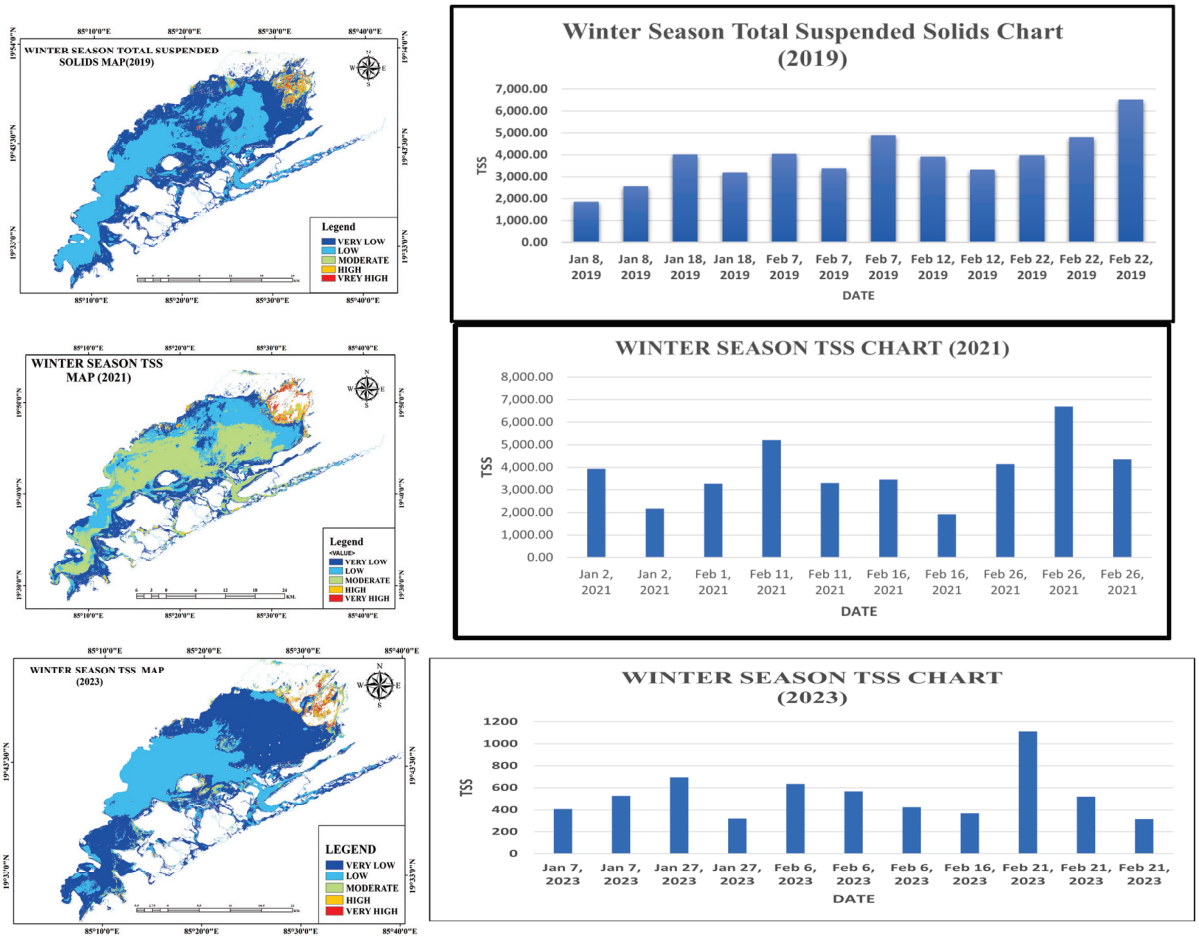

Figure 11. Winter season TSS map and chart (2019/2021/2023).

3.1.2. Pre-Monsoon Season

NDTI (Normalized Difference Turbidity Index)

In the pre-monsoon period, sediment load increases due to agricultural activities and soil erosion in the catchment area. Elevated turbidity levels affect aquatic life by reducing light penetration, essential for photosynthesis in marine plants [73]. Higher turbidity levels can affect fish health and breeding conditions. Higher turbidity levels can reduce the aesthetic appeal of the lake, affecting tourism [74]. The NDTI for the year 2019 had a maximum value of 702.304 FNU and a minimum value of 35.038 FNU, according to the mapping and statistical data above. The NDTI had a maximum value of 356.244 FNU and a minimum value of 39.683 FNU in 2021. In 2023, the NDTI reached a high of 1326.35 FNU and a low of −77.251 FNU (Figure 12). Monitoring turbidity using the NDTI during the pre-monsoon period is crucial for water quality management and also for attracting tourists [75].

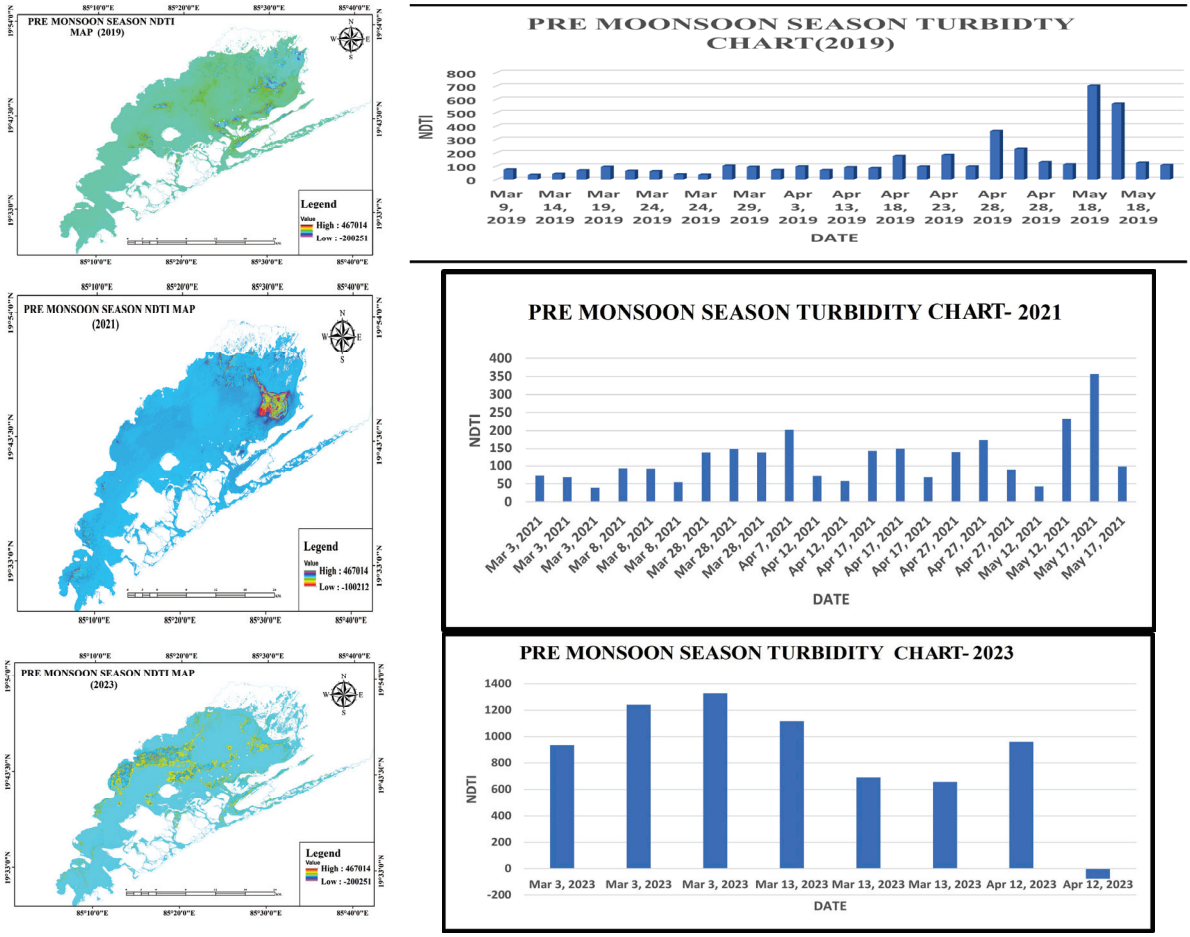

Figure 12. Pre-monsoon season NDTI map and chart (2019/2021/2023).

NDCI (Normalized Difference Chlorophyll Index)

During the pre-monsoon period, there is an increase in agricultural activity and soil erosion, leading to higher nutrient runoff into Chilika Lake and resulting in a hike in chlorophyll levels [76]. Higher chlorophyll levels indicate increased phytoplankton biomass, which can affect the lake's ecological balance. Elevated nutrient levels can lead to eutrophication, causing algal blooms that deplete oxygen in the water and harm aquatic life [77]. Higher chlorophyll levels can affect the food web dynamics in Chilika Lake. Monitoring chlorophyll levels using the NDCI during the pre-monsoon period can help manage fish populations and ensure sustainable fishing practices. Understanding phytoplankton dynamics is crucial for predicting fish stock health and availability [78].

According to the mapping mentioned above and statistical data, the highest and minimum values of chlorophyll-a in 2019 were 0.113 mg and −0.001 mg, respectively. In 2021, there was a maximum of 0.046 mg chlorophyll-a and a minimum of −0.016 mg. Chlorophyll-a had a maximum value of 0.083 mg and a minimum value of −0.013 mg in 2023 (Figure 13). Regular monitoring using the NDCI helps maintain water quality, essential for attracting tourists and supporting the local economy [79]. Regularly tracking chlorophyll levels using the NDCI during the pre-monsoon period provides valuable data for water quality management. It helps identify any unusual changes in phytoplankton biomass that might indicate pollution or other environmental issues, enabling timely intervention [80].

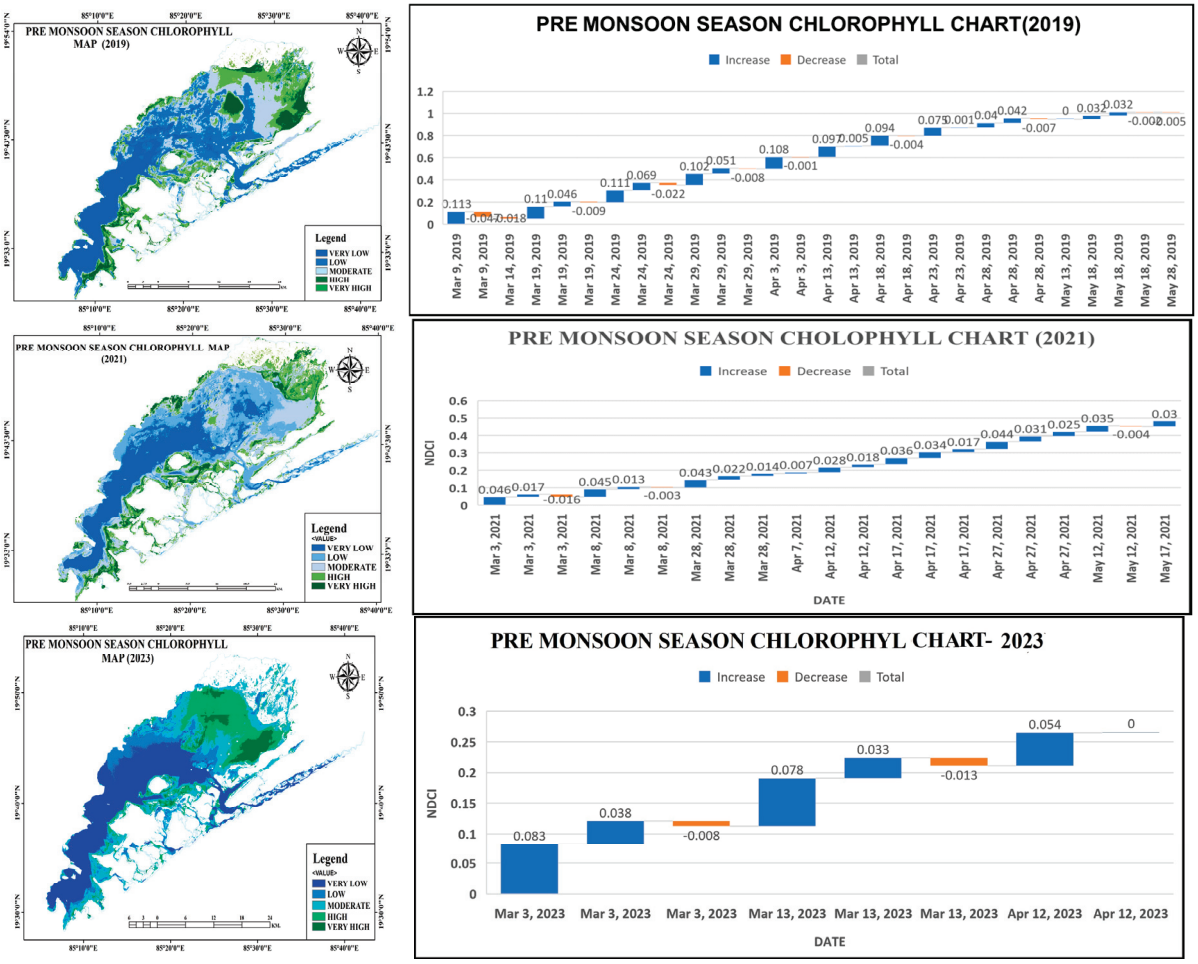

Figure 13. Pre-monsoon season NDCI map and chart (2019/2021/2023).

TSS (Total Suspended Solids)

In the pre-monsoon period, higher sediment runoff into Chilika Lake resulted in elevated TSS levels. Elevated TSS levels can reduce water clarity and quality, affecting the health of the aquatic ecosystem [81]. High TSS can carry pollutants and nutrients, leading to eutrophication, algal blooms, and oxygen depletion. Regular monitoring helps identify pollution sources and implement management strategies. High TSS levels can negatively impact aquatic life by reducing light penetration, essential for photosynthesis in aquatic plants [82]. The fishing community around Chilika Lake relies heavily on its resources. Elevated TSS levels can affect fish health and breeding conditions, reducing fish populations [83]. Monitoring TSS helps manage fish stocks and ensure sustainable fishing practices. Monitoring these levels is crucial for understanding sediment dynamics and their impact on the lake's ecosystem [84].

According to the mapping and statistical data above, the TSS for the year 2019 had a maximum value of 3339.34 mg/L and a minimum value of 208.886 mg/L. The TSS in 2021 had a minimum value of 188.934 mg/L and a maximum value of 3176.90 mg/L. The minimum value of 175.206 mg/L and the maximum value of 817.706 mg/L for TSS were found in 2023 (Figure 14).

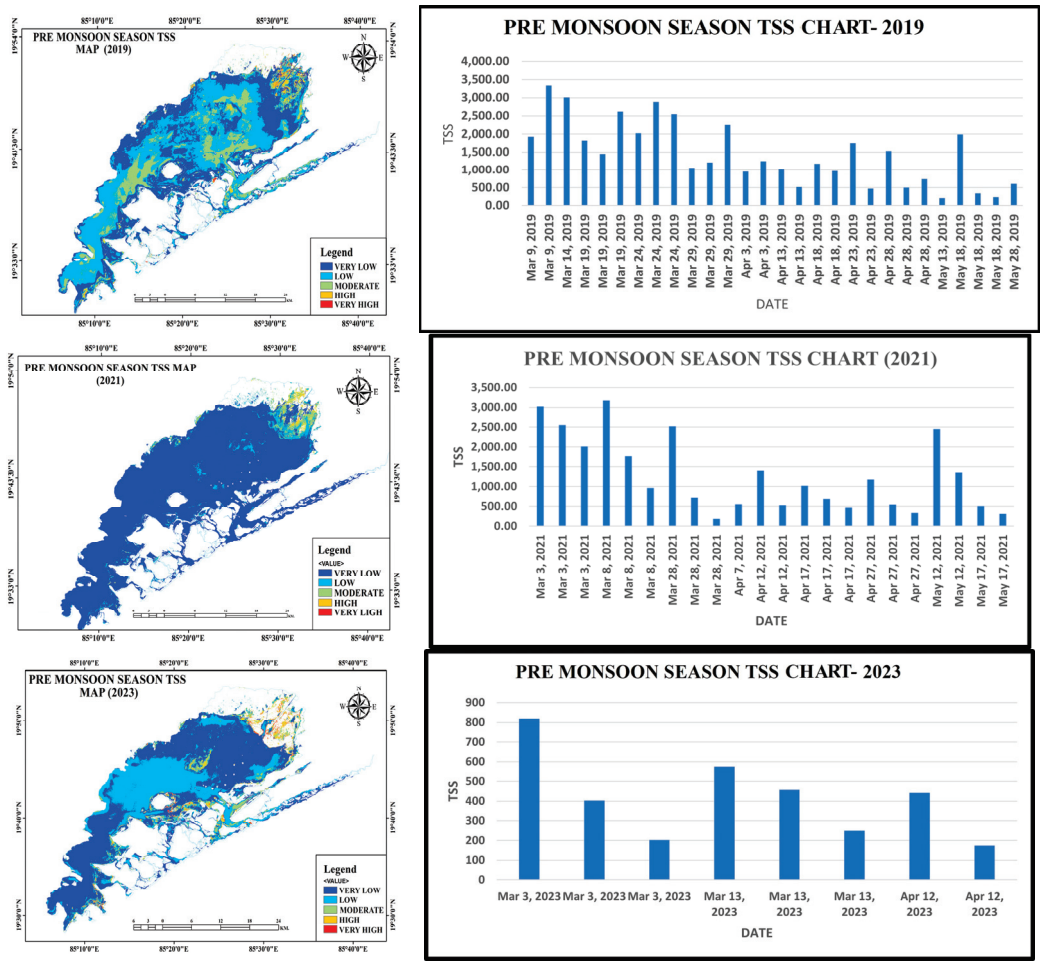

Figure 14. Pre-monsoon season TSS map and chart (2019/2021/2023).

3.1.3. Monsoon Season

NDTI (Normalized Difference Turbidity Index)

The monsoon season brings heavy rainfall, increasing runoff from the surrounding catchment areas. This runoff carries a high load of sediments into Chilika Lake, resulting in elevated turbidity levels [85]. The NDTI can effectively monitor these changes, providing valuable data on sediment dynamics. High turbidity levels during the monsoon season can affect water quality by reducing light penetration and increasing the concentration of suspended particles [86]. Monitoring turbidity using the NDTI helps identify areas with poor water quality, enabling timely interventions to mitigate pollution and maintain the lake's health [54]. Elevated turbidity levels can negatively impact aquatic life by reducing the availability of light for photosynthesis in aquatic plants [87]. The NDTI helps to assess these impacts and plan conservation measures. Monitoring these levels using the NDTI helps to manage fish populations and ensure sustainable fishing practices. Monitoring turbidity levels using the NDTI can help predict and manage flood events by providing data on sediment load and water flow patterns [88]. The NDTI for the year 2019 had a maximum value of 644.353 FNU and a minimum value of −118.078 FNU, according to the mapping and statistical data above. The NDTI had a minimum value of 75.631 FNU and a maximum value of 342.902 FNU in 2021. In 2023, the highest value of the NDTI was 84.481 FNU, while the lowest value was 319.128 FNU (Figure 15).

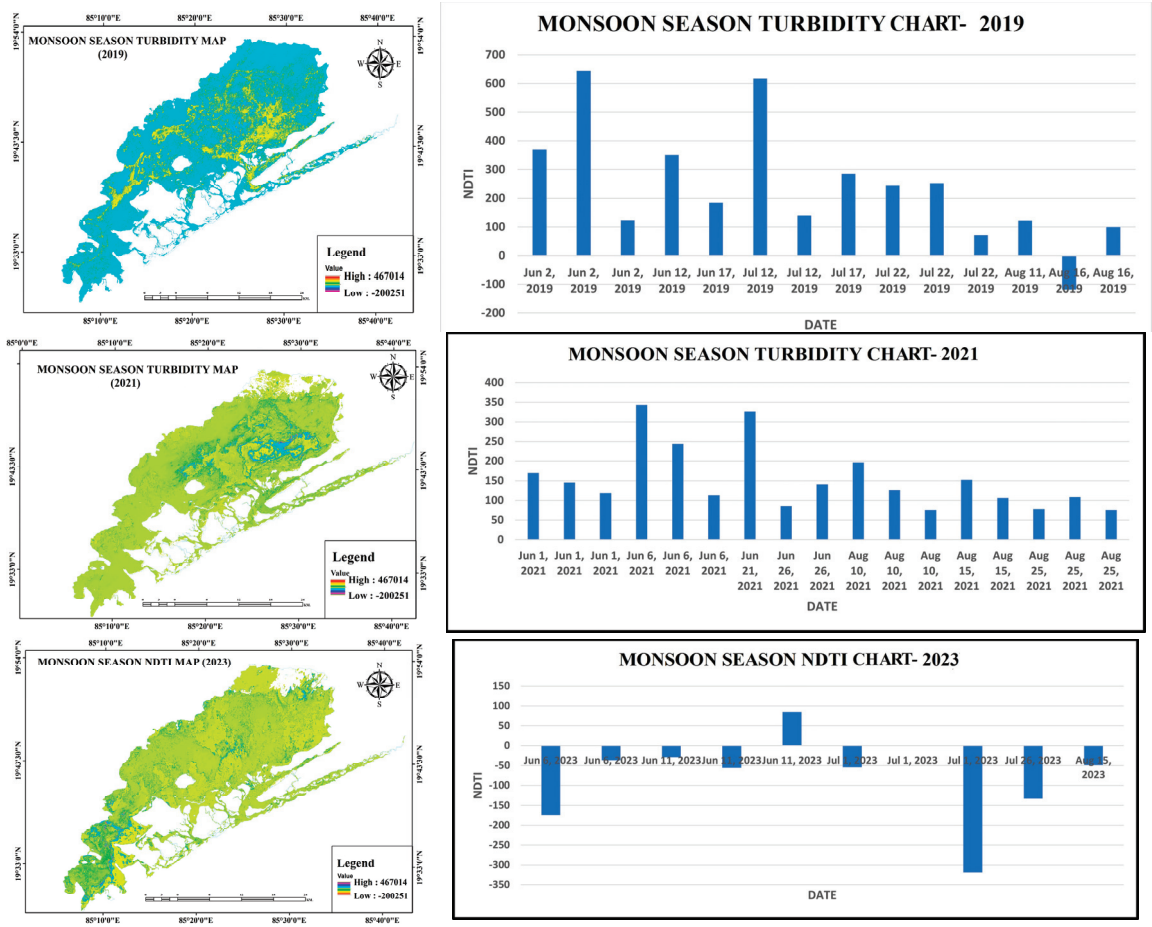

Figure 15. Monsoon season NDTI map and chart (2019/2021/2023).

NDCI (Normalized Difference Chlorophyll Index)

The monsoon season brings heavy rainfall, increasing runoff from agricultural lands and surrounding areas. This runoff carries a high load of nutrients into Chilika Lake, resulting in elevated chlorophyll levels [89]. The elevated nutrient levels can lead to eutrophication, causing algal blooms that deplete oxygen in the water and harm aquatic life. Monitoring chlorophyll levels using the NDCI helps in the early detection of eutrophication, allowing for timely management interventions to prevent adverse effects on the lake's ecosystem. Higher chlorophyll levels can affect the food web dynamics in Chilika Lake [90]. Monitoring chlorophyll levels using the NDCI during the monsoon period can help to manage fish populations and ensure sustainable fishing practices. Understanding phytoplankton dynamics is crucial for predicting fish stock health and availability. Regular monitoring of chlorophyll levels using the NDCI during the monsoon season provides valuable data for water quality management. It helps identify any unusual changes in phytoplankton biomass that might indicate pollution or other environmental issues, enabling timely intervention [91].

According to the given mapping and statistical data, the maximum and minimum values of chlorophyll-a in 2019 were 0.054 mg and −0.039 mg, respectively. The maximum and minimum amounts of chlorophyll-a in 2021 were 0.057 mg and 0.005 mg, respectively. In 2023, there was a maximum of 0.039 mg chlorophyll-a and a minimum of −0.007 mg (Figure 16).

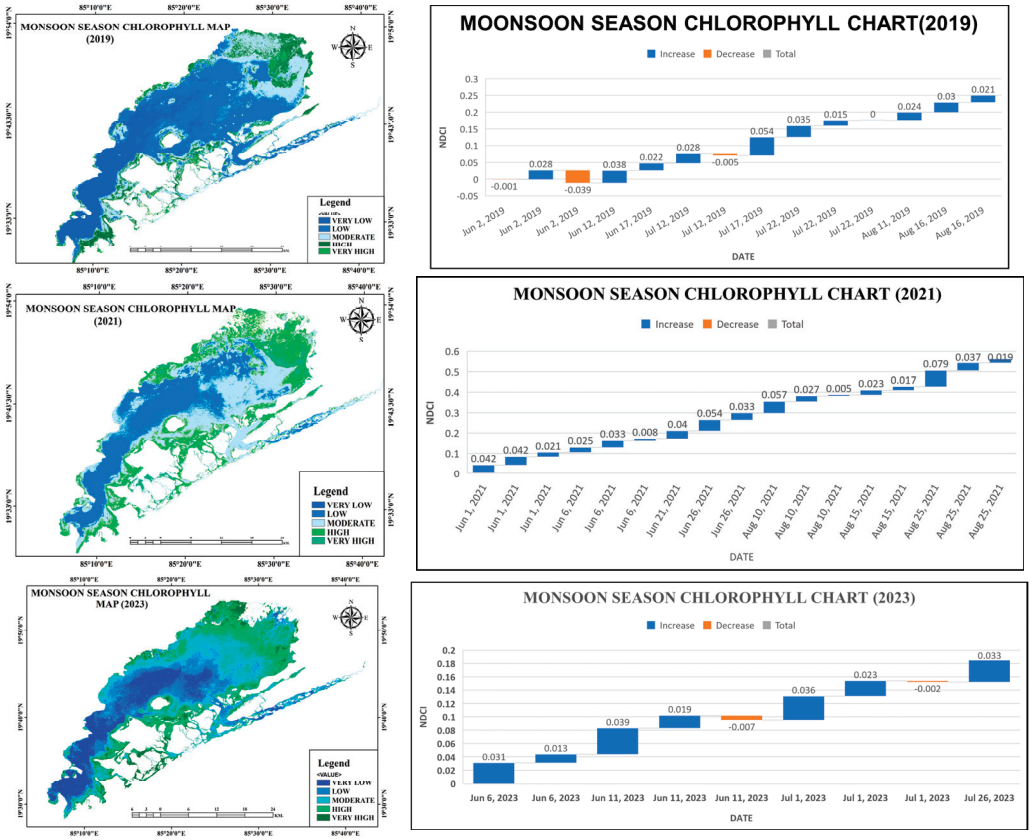

Figure 16. Monsoon season NDCI map and chart (2019/2021/2023).

TSS (Total Suspended Solids)

The monsoon season brings heavy rainfall, leading to substantial runoff from the surrounding catchment areas. This runoff carries a high load of sediments into Chilika Lake, resulting in elevated TSS levels [92]. Higher TSS levels have implications like reduced water clarity, impacting aquatic photosynthesis and recreational use; increased sedimentation, affecting habitats and biodiversity; higher risk of waterborne diseases and pathogens and decreased dissolved oxygen levels, harming aquatic life; and increased turbidity, interfering with ultraviolet (UV) disinfection [93]. Moderate TSS levels result in algal growth promotion, potentially leading to eutrophication, nutrient transport, and cycling impacts, changes in aquatic food webs, and sedimentation impacts on aquatic habitats. Low TSS levels result in improved water clarity, enhancing aquatic photosynthesis, reducing sedimentation, preserving habitats and biodiversity, and lowering the risk of waterborne diseases and pathogens [94].

Monitoring these levels is crucial for understanding sediment dynamics and their impact on the lake's ecosystem. Elevated TSS levels can reduce water clarity and quality, affecting the health of the aquatic ecosystem. High TSS levels can carry pollutants and nutrients, contributing to eutrophication, and leading to algal blooms and oxygen depletion [95]. Regular monitoring helps to identify pollution sources and implement management strategies. High TSS levels can negatively impact aquatic life by reducing light penetration, essential for photosynthesis in aquatic plants [96]. This can disrupt the food web and affect the overall biodiversity of the lake. Fish and other organisms may also experience stress due to increased sedimentation [97]. High TSS levels can reduce the aesthetic appeal of the lake, affecting tourism. Clearwater is important for recreational activities such as boating and bird watching. Regular monitoring helps maintain water clarity and supports the local tourism industry [98]. The local community is crucial in maintaining water clarity and supporting the local tourism industry. The monsoon season often brings the risk of flooding. Monitoring TSS levels helps to predict and manage flood

events by providing data on sediment load and water flow patterns. This information is crucial for designing effective flood control measures [99].

The TSS for the year 2019 had a maximum value of 5252.09 mg/L and a minimum value of 388.392 mg/L, according to the mapping and statistical data above. TSS has a maximum value of 2453.94 mg/L and a minimum value of 438.239 mg/L in 2021. With a high value of 518.07 mg/L and a low value of 110.72 mg/L, the TSS in 2023 (Figure 17).

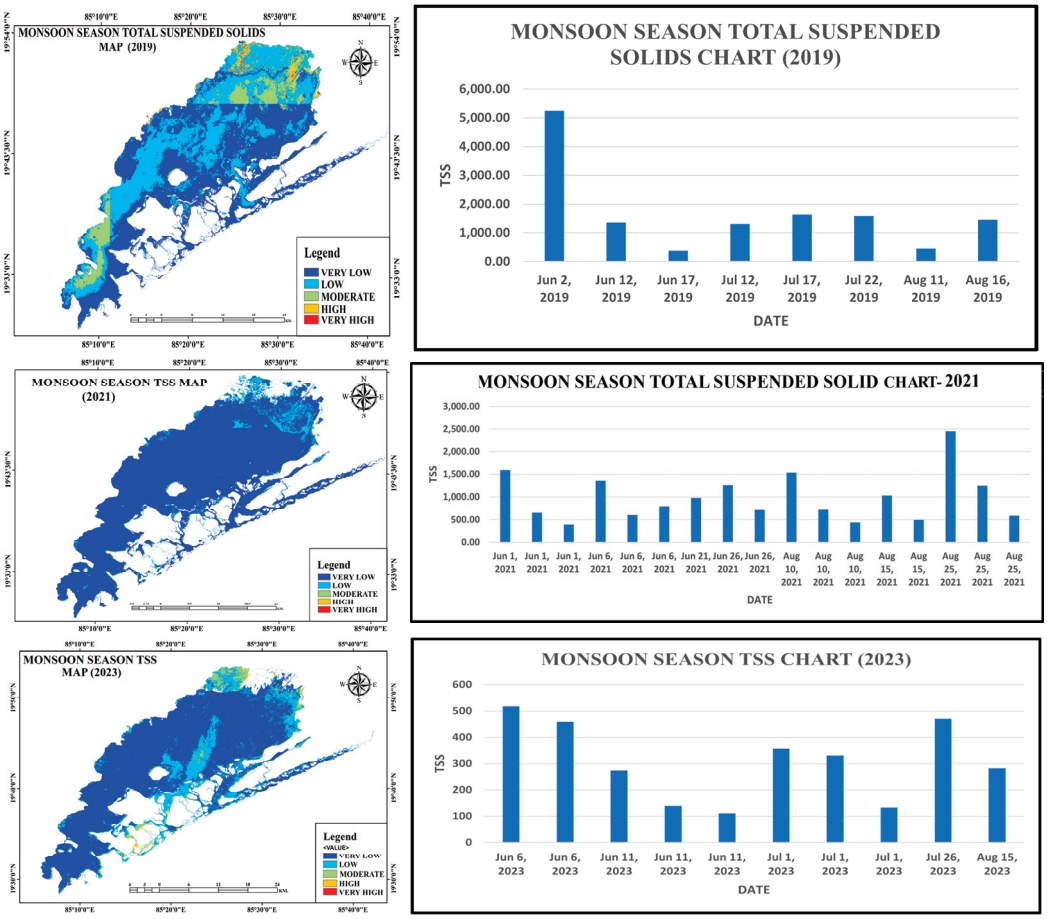

Figure 17. Monsoon season TSS map and chart (2019/2021/2023).

3.1.4. Monsoon Season

NDTI (Normalized Difference Turbidity Index)

In the post-monsoon season, the lagoon receives significant river freshwater inflow carrying sediments and nutrients. The NDTI helps to monitor the increased turbidity levels due to sediment resuspension and runoff [100]. High turbidity can reduce water clarity, impacting aquatic life and the overall health of the lagoon. The post-monsoon period is characterized by high sediment deposition from riverine inputs. The NDTI can track these changes, providing insights into sediment dynamics and their impact on water quality [101]. The influx of nutrients from agricultural runoff and other sources during the post-monsoon season can lead to eutrophication. Turbidity influences light penetration in the water column, affecting phytoplankton growth [102]. Post-monsoon, increased turbidity can limit light availability, potentially reducing phytoplankton growth. The NDTI can detect changes in turbidity due to pollution events, such as industrial discharge or urban runoff [103]. Monitoring these changes during the post-monsoon season helps in the early detection and mitigation of pollution sources, ensuring that the lagoon's water quality remains within safe limits [104]. By understanding turbidity patterns and their implications, stakeholders can make informed decisions to protect and sustain Chilika Lagoon's biodiversity and ecological balance.

According to the mapping and statistical data above, the NDTI for the year 2019 had a maximum value of 262.823 FNU and a minimum value of 23.312 FNU. In 2021, it had a minimum value of 31.013 FNU and a maximum value of 75.244 FNU. In 2023, it had a maximum value of 504.286 FNU and a minimum value of 81.351 FNU (Figure 18).

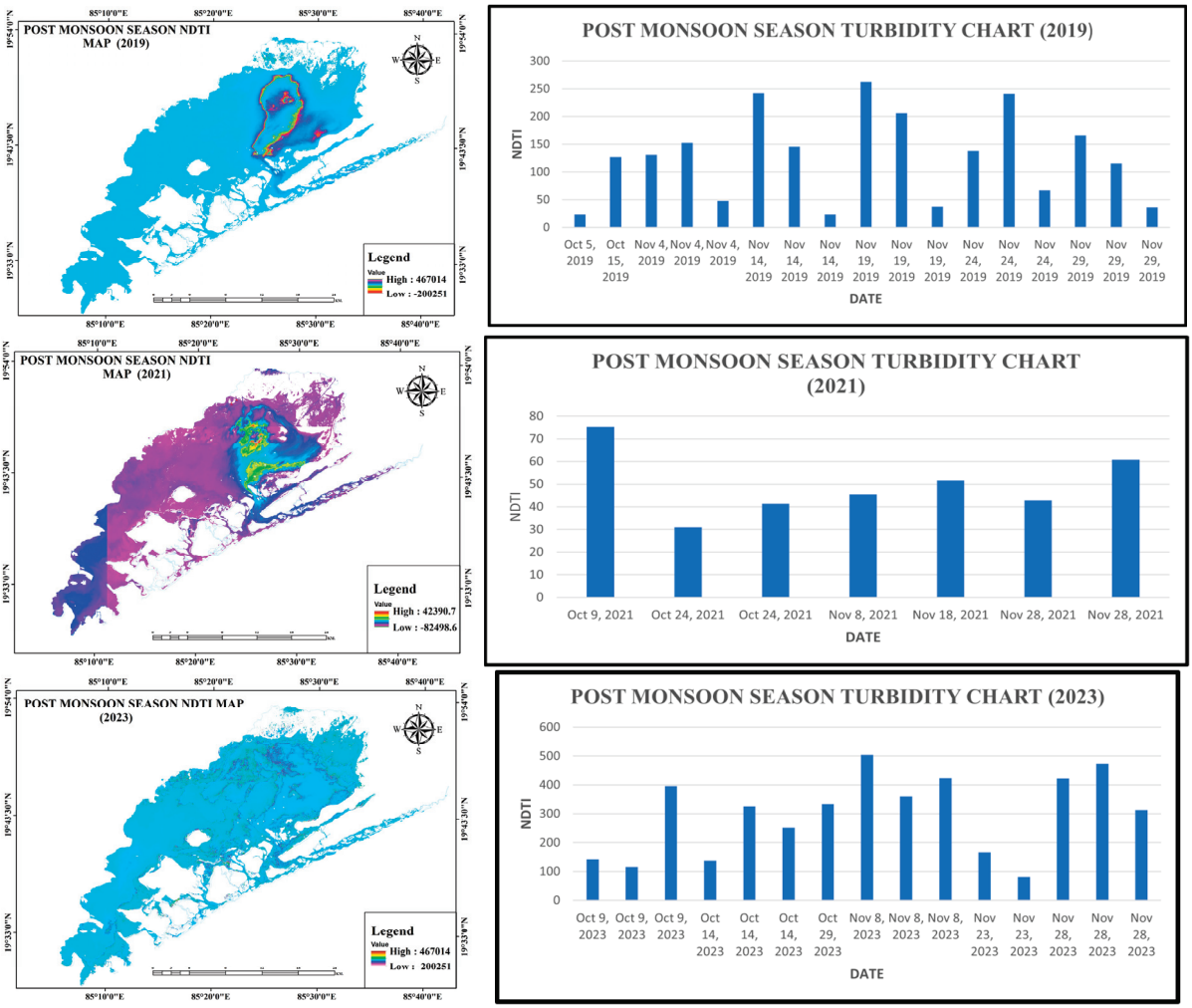

Figure 18. Post-monsoon season NDTI map and chart (2019/2021/2023).

NDCI (Normalized Difference Chlorophyll Index)

Post monsoon, the influx of nutrients from riverine runoff can lead to phytoplankton blooms. The NDCI helps detect these blooms by measuring chlorophyll-a concentrations [105]. High NDCI values indicate increased phytoplankton biomass, which can affect the lagoon's primary productivity and food web dynamics [106]. The post-monsoon season often brings nutrient-rich runoff from agricultural fields and urban areas. The NDCI can monitor the extent of eutrophication by tracking chlorophyll-a levels [107]. Elevated chlorophyll-a concentrations can lead to hypoxic conditions, affecting aquatic life and water quality [108]. High phytoplankton biomass can reduce light penetration in the water column, affecting submerged aquatic vegetation and other photosynthetic organisms. NDCI data can help understand these changes and their implications for the lagoon's ecological health.

According to the preceding mapping and statistical data, the maximum and minimum values of chlorophyll-a in 2019 were 0.043 mg and −0.061 mg, respectively. In 2021, there was a maximum of 0.101 mg of chlorophyll-a and a minimum of −0.017 mg. In 2023, the highest concentration of chlorophyll-a was found to be 0.027 mg, while the lowest concentration was found to be 0.019 mg (Figure 19).

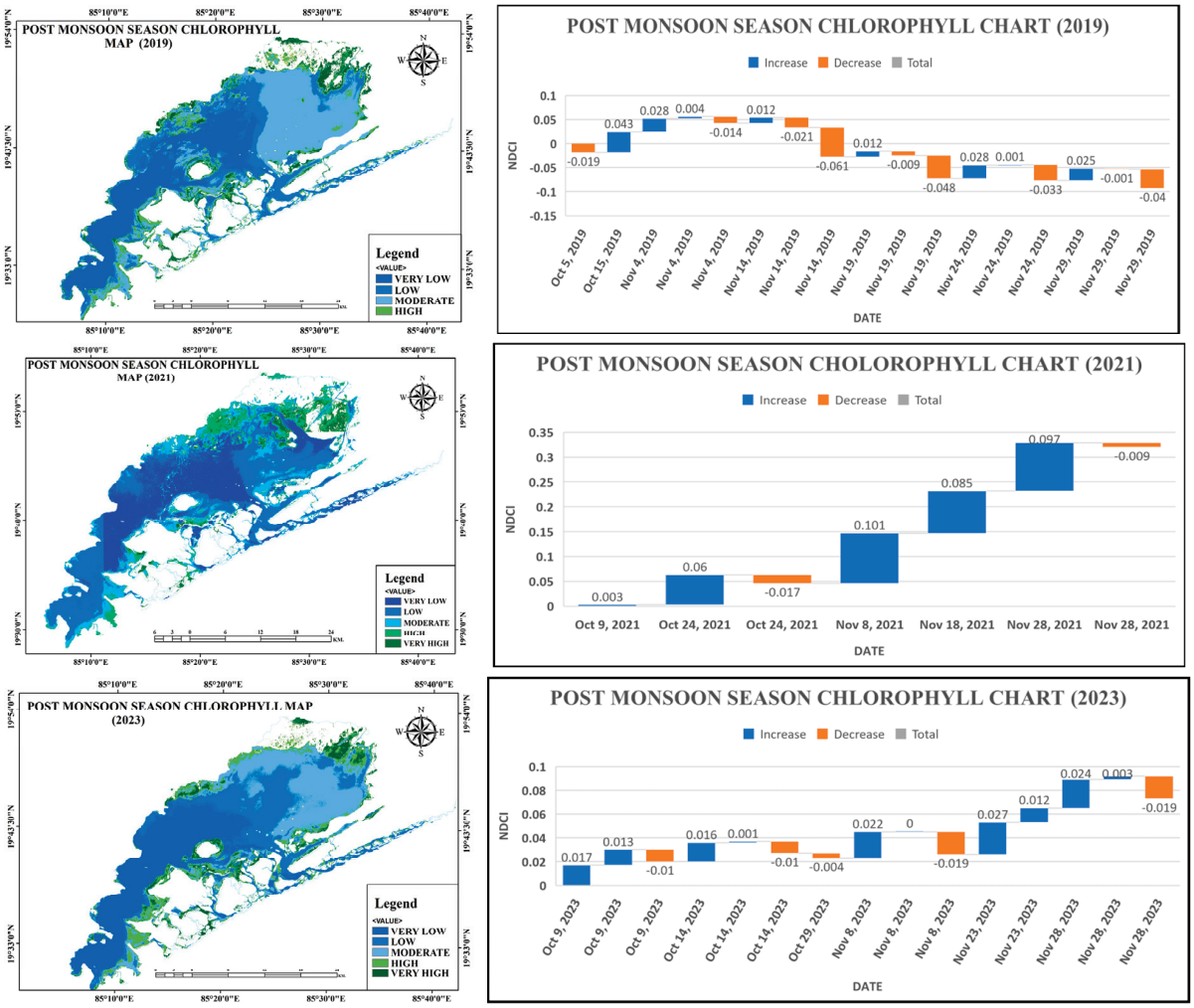

Figure 19. Post-monsoon season NDCI map and chart.

TSS (Total Suspended Solids)

In the post-monsoon season, the lagoon receives substantial freshwater inflow from rivers, carrying sediments and organic matter, leading to increased TSS levels and higher turbidity [109]. Elevated turbidity can reduce light penetration, affecting photosynthesis and the growth of submerged aquatic vegetation [110]. The post-monsoon period is characterized by significant sediment deposition from riverine inputs. High TSS levels indicate increased sediment load, which can alter the lagoon's geomorphology and impact habitats for aquatic organisms [111]. High TSS levels can also indicate the presence of pollutants, such as heavy metals and pesticides, attached to sediment particles. Monitoring TSS helps identify pollution sources and assess their impact on water quality [112]. Increased TSS can clog fish gills, reduce feeding efficiency, and smother benthic habitats. This can lead to a decline in fish populations and affect the overall biodiversity of the lagoon [113].

According to the mapping above and statistical data, the TSS in 2019 had a high value of 4479.57 mg/L and a low value of 1450.71 mg/L. The year 2021 saw a maximum TSS value of 6309.97 mg/L and a minimum value of 708.087 mg/L. The TSS had a maximum value of 794.806 mg/L and a minimum value of 90.01 mg/L in 2023 (Figure 20).

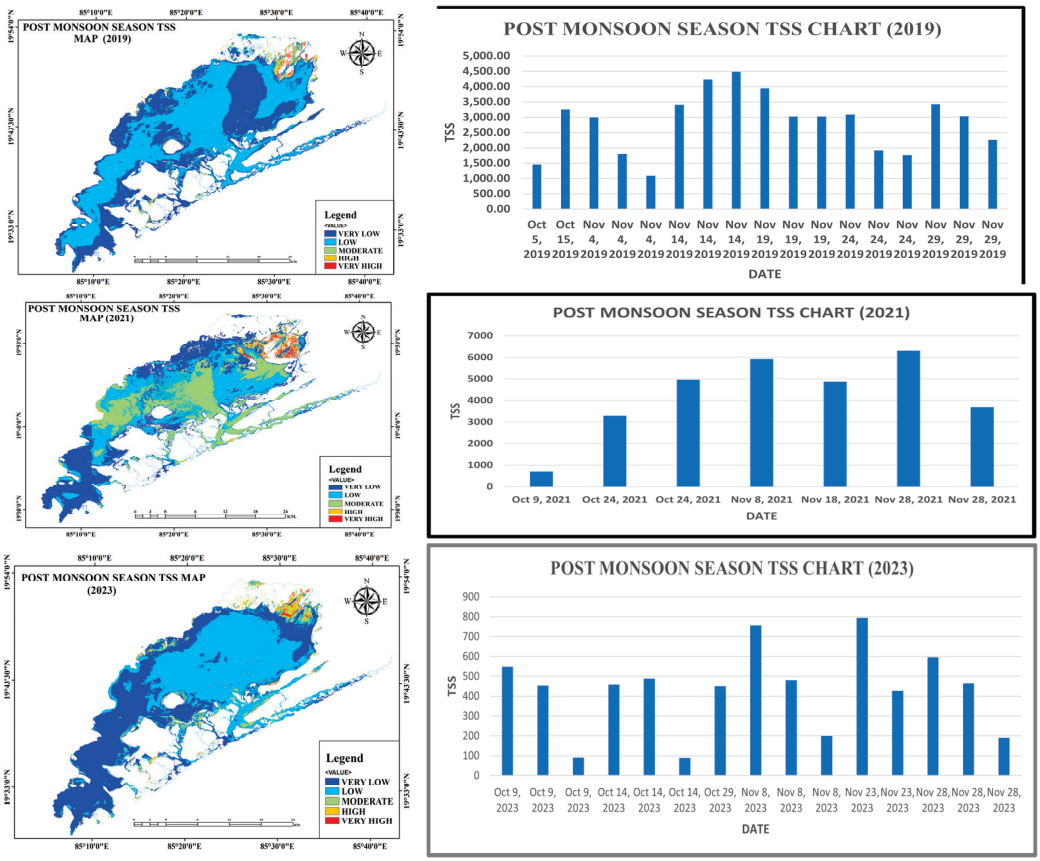

Figure 20. Post-monsoon season TSS map and chart (2019/2021/2023).

4. Discussion

Based on our observations, we found that the NDTI value of the water in Chilika Lake climbed gradually from 2019 to 2021 before sharply increasing in 2023. While the water NDTI increased explicitly in the pre-monsoon and monsoon seasons in 2019 and 2021, it increased in the winter and post-monsoon seasons in 2023. In the monsoon season, however, it decreased to a modest value, indicating that the water is somewhat clearer and more obvious than in previous years [114,115]. There was an increase in the amount of chlorophyll-a, as observed when using the NDCI. By year, it grew progressively between 2019 and 2023. Additionally, it was noted that chlorophyll-a rose quickly throughout the pre-monsoon and monsoon seasons; in contrast, there was a significant increase in chlorophyll-a during the winter and pre-monsoon seasons of 2021 [116]. With the help of all of these observations, we can see that the amount of chlorophyll-a in Chilika Lake has been rising annually.

Based on our most recent TSS indices, it was concluded that the TSS value increased mainly during the winter and monsoon seasons in 2019. By 2021, we noted that the growing value shifted to the winter and post-monsoon seasons [117]. Conversely, we observe that the winter and pre-monsoon seasons significantly increased the TSS value. As we can see from the above, the TSS value primarily increased during the winter months each year. These days, the quality of the water is improving. The value of TSS generally increases over the years, indicating an improvement in the water quality these days [118–120].

Upon creating a unified map with all of the monthly data for a given year, we noticed that the NDTI, NDCI, and TSS values climbed from 2019 to 2021 to 2023 [121,122]. Additionally, one can see that while the NDTI and NDCI values increased in 2023, the TSS value decreased compared to the year before [123,124]. This is likely because the composite data we used to create the value were primarily an average or mean value, which is what caused the TSS value to decrease in 2023 (Table 3).

Table 3. Yearly overview of maximum and minimum values of water quality indices.

Year																	
2019						2021						2023					
NDTI (FNU)		NDCI (mg)		TSS (mg/L)		NDTI (FNU)		NDCI (mg)		TSS (mg/L)		NDTI (FNU)		NDCI (mg)		TSS (mg/L)	
MAX	MIN	MAX	MIN	MAX	MIN	MAX	MIN	MAX	MIN	MAX	MIN	MAX	MIN	MAX	MIN	MAX	MIN
702.304	23.312	0.135	−0.073	9282	208.886	365.224	−5.187	0.106	−0.084	7608.18	188.934	2105.41	−433.419	0.083	−0.0321	1178.01	90.01

4.1. Interpretation

This study using the GEE coupled with spectral indices provides a cost-effective and efficient method for monitoring water quality in Chilika Lake, which can be replicated in other aquatic ecosystems [125]. The findings can inform decision-makers and stakeholders about the lake's water quality status to develop targeted management strategies to mitigate pollution and employ conservative approaches [126]. The findings can contribute to conservation efforts by identifying areas with poor water quality [127]. The GEE and spectral indices can help monitor the impacts of climate change on water quality, enabling researchers to understand the complex relationships between climate variables and water quality parameters [128]. The integrated approaches of classical monitoring along with Remote sensing-based studies have always proved to be an accurate and precise means to study different water quality parameters, and both approaches suffice each other [129–134]. The identified areas with poor water quality in our research can be addressed by the concerned authorities. As the water is affected by different industries neighboring the lake, which contribute to water deterioration [135], decision-makers have employed initiatives to address these issues, and over the course of time, some prominent positive outcomes can be noticed like improved salinity levels, fish landings, a decrease in invasive species, recovery of lost habitats for important species, etc. Further rigid and spatial targets can be planned by decision-makers based on the findings for the sustainable water quality management of the Chilika lagoon [136]. These points highlight their significance and emphasize their potential to contribute to effective water quality monitoring, informed decision-making, conservation efforts, climate change research, and scalability [137].

4.2. Limitations

The spatial resolution may not capture all small-scale water quality variations, particularly in areas with complex shoreline features [138]. Our approach provides depth-integrated measurements, which may not accurately represent water quality at specific depths or in regions with stratified water columns. Atmospheric and environmental factors, such as cloud cover, aerosols, and sediment resuspension, can affect the accuracy of spectral indices and water quality retrievals [139]. The availability and quality of ground truth data may limit the accuracy of our approach, particularly in areas with limited in-situ measurements [140]. Our study focuses on a specific period, and our results may not represent long-term water quality trends or seasonal variations. Spectral indices may not be specific to certain water quality parameters, potentially leading to ambiguous interpretations [141,142]. While we used available in-situ data for validation, more extensive in-situ measurements would strengthen the accuracy and reliability of our approach [143–147].

4.3. Recommendations

We recommend the following avenues for further studies or analyses based on our findings: a combined GEE-derived spectral index with extensive in situ water quality measurements to improve accuracy and validation; extension of the study period to capture seasonal and inter-annual water quality variations, enabling a better understanding of Chilika Lake's dynamics; utilization of high-resolution satellite or aerial imagery to capture small-scale water quality variations and complex shoreline features; exploration of the application of machine learning algorithms to improve the accuracy and robustness of spectral index-based water quality retrievals; integration of GEE-derived water quality parameters into hydrodynamic or water quality models to simulate and predict Chilika

Lake's water quality; and conducting comparative studies with other lakes or coastal ecosystems to evaluate the transferability and scalability of our approach. To enhance confidence in our findings, we could validate our results with alternative data sources, such as autonomous underwater vehicles (AUVs) or unmanned aerial vehicles (UAVs).

5. Conclusions

The NDTI, NDCI, and TSS are the primary indices we used to monitor water quality throughout our study. TSS and the NDTI indicate the water's purity and are indirectly related to water quality. Additionally, the NDCI is a separate indicator that displays the rate of chlorophyll-a growth. Our research demonstrates that other elements, such as climatic or meteorological conditions, rain, flooding, tourism, etc., occasionally affect the water quality in Chilka Lake. The water quality index primarily varied throughout the winter and monsoon seasons, as we can see. Even though foreign birds migrate through Chilka, it is a popular tourist destination. Additionally, the geographic location of Chilika contributed to the water contamination there. Its water is salty, which is a relief. According to our research, Chilika Lake water is becoming more contaminated than it was in 2019. During winter, it makes sense that human activity, natural disasters, and migratory animals are the leading causes of pollution in Chilika Lake water.

Author Contributions: Subhasmita Das, Debabrata Nandi, and Rakesh Ranjan Thakur: conceptualization and writing—original draft; Dillip Kumar Bera and Duryadhan Behera contributed to all sections; Bojan Đurin and Vlado Cetl: supervision and review, and editing of the manuscript. All authors have read and agreed to the published version of the manuscript.

Funding: This research was partially funded by University North, Croatia, Scientific project UNIN-TEH-24-1-16 "The role of geodesy and geomatics in the development of smart spaces" (2024).

Data Availability Statement: Data will be provided upon request.

Acknowledgments: All authors acknowledge the Remote Sensing and GIS Department for use of their software and infrastructure to prepare the manuscript.

Conflicts of Interest: The authors declare that there are no conflicts of interest regarding the publication of this paper.

References

1. Ramanaiah, S.V.; Potoroko, I.; Malinin, A.; Tsaturov, A.; Kadi, A.; Aleksandrovna, D.T.; Vyacheslavovna, V.I. Monitoring of Water Quality in Selected Water Bodies in the Chelyabinsk, Russian Federation. *Sustain. Water Resour. Manag.* **2023**, *9*, 53. [CrossRef]
2. Latwal, A.; Rehana, S.; Rajan, K.S. Detection and Mapping of Water and Chlorophyll-a Spread Using Sentinel-2 Satellite Imagery for Water Quality Assessment of Inland Water Bodies. *Environ. Monit. Assess.* **2023**, *195*, 1304. [CrossRef] [PubMed]
3. Tripathi, A.K. Water Quality Models and their Use in Monitoring the Quality of Surface Water Bodies. *Int. J. Res. Appl. Sci. Eng. Technol.* **2021**, *9*, 445–448. [CrossRef]
4. Roy, R.; Mrinmoy, M. Assessment of Water Quality Trends in Loktak Lake, Manipur, India. *Environ. Earth Sci.* **2019**, *78*, 383. [CrossRef]
5. Lin, Y.; Pan, S.; Chang, H.; Yu, M.; Lin, W. Will Extreme Drought Impact the Reservoir Water Quality? A 30-Year Observational Study. *Agric. Water Manag.* **2023**, *289*, 108574. [CrossRef]
6. Fitriani, N.; Wahyudianto, F.; Salsabila, N.F.; Radin Mohamed, R.; Kurniawan, S. Performance of Modified Slow Sand Filter to Reduce Turbidity, Total Suspended Solids, and Iron in River Water as Water Treatment in Disaster Areas. *Inżynieria Ekol.* **2023**, *24*, 1–18. [CrossRef]
7. Adjovu, G.E.; Stephen, H.; James, D.; Ahmad, S. Overview of the Application of Remote Sensing in Effective Monitoring of Water Quality Parameters. *Remote Sens.* **2023**, *15*, 1938. [CrossRef]
8. Sedighkia, M.; Datta, B.; Saeedipour, P.; Abdoli, A. Predicting Water Quality Distribution of Lakes through Linking Remote Sensing–Based Monitoring and Machine Learning Simulation. *Remote Sens.* **2023**, *15*, 3302. [CrossRef]
9. Ndou, N. Geostatistical Inference of Sentinel-2 Spectral Reflectance Patterns to Water Quality Indicators in the Setumo Dam, South Africa. *Remote Sens. Appl. Soc. Environ.* **2023**, *30*, 100945. [CrossRef]
10. Zhao, M.; O'Loughlin, F. Mapping Irish Water Bodies: Comparison of Platforms, Indices and Water Body Type. *Remote Sens.* **2023**, *15*, 3677. [CrossRef]
11. Alharbi, B. Remote Sensing Techniques for Monitoring Algal Blooms in the Area between Jeddah and Rabigh on the Red Sea Coast. *Remote Sens. Appl. Soc. Environ.* **2023**, *30*, 100935. [CrossRef]

12. Jin, H.; Fang, S.; Chen, C. Mapping of the Spatial Scope and Water Quality of Surface Water Based on the Google Earth Engine Cloud Platform and Landsat Time Series. *Remote Sens.* **2023**, *15*, 4986. [CrossRef]
13. Zhang, T.; Wang, H.; Hu, S.; You, S.; Yang, X. Long-Term and Bimonthly Estimation of Lake Water Extent Using Google Earth Engine and Landsat Data. *Remote Sens.* **2022**, *14*, 2893. [CrossRef]
14. Boukhennaf, A.; Khoudir, M. Long and Short-Term Evolution of the Algerian Coastline Using Remote Sensing and GIS Technology. *Reg. Stud. Mar. Sci.* **2023**, *61*, 102893. [CrossRef]
15. Saeid, A.; Ayad, A. Remote Sensing in Water Quality and Water Resources Management. *Int. J. Res. Appl. Sci. Biotechnol.* **2022**, *9*, 163–170. [CrossRef]
16. Dube, T.; Shekede, M.D.; Massari, C. Remote Sensing for Water Resources and Environmental Management. *Remote Sens.* **2023**, *15*, 18. [CrossRef]
17. Sherjah, P.Y.; Sajikumar, N.; Nowshaja, P.T. Quality Monitoring of Inland Water Bodies Using Google Earth Engine. *J. Hydroinform.* **2023**, *25*, 432–450. [CrossRef]
18. Chen, Z.; Zhao, S. Automatic Monitoring of Surface Water Dynamics Using Sentinel-1 and Sentinel-2 Data with Google Earth Engine. *Int. J. Appl. Earth Obs. Geoinf.* **2022**, *113*, 103010. [CrossRef]
19. Condeça, J.; Nascimento, J.; Barreirasl, N. Monitoring the Storage Volume of Water Reservoirs Using Google Earth Engine. *Water Resour. Res.* **2022**, *58*, e2021WR030026. [CrossRef]
20. Zhao, J.; Jin, S.; Zhang, Y. Dynamic Water Quality Changes in the Main Stream of the Yangtze River from Multi-Source Remote Sensing Data. *Remote Sens.* **2023**, *15*, 2526. [CrossRef]
21. Adjovu, G.E.; Stephen, H.; James, D.; Ahmad, S. Measurement of Total Dissolved Solids and Total Suspended Solids in Water Systems: A Review of the Issues, Conventional, and Remote Sensing Techniques. *Remote Sens.* **2023**, *15*, 3534. [CrossRef]
22. Chu, H.-J.; He, Y.C. Remote Sensing Water Quality Inversion Using Sparse Representation: Chlorophyll-a Retrieval from Sentinel-2 MSI Data. *Remote Sens. Appl. Soc. Environ.* **2023**, *31*, 101006. [CrossRef]
23. Jeon, M.; Guerra, H.B.; Choi, H.; Kwon, D.; Kim, H.; Kim, L.-H. Stormwater Runoff Treatment Using Rain Garden: Performance Monitoring and Development of Deep Learning-Based Water Quality Prediction Models. *Water* **2021**, *13*, 3488. [CrossRef]
24. Kruger, A.; Pieters, R.; Horn, S.; Van Zijl, C.; Aneck-Hahn, N. The Role of Effect-Based Methods to Address Water Quality Monitoring in South Africa: A Developing Country's Struggle. *Environ. Sci. Pollut. Res. Int.* **2022**, *29*, 84049–84055. [CrossRef] [PubMed]
25. Kumar, L.; Kumari, R.; Kumar, A.; Tunio, I.A.; Sassanelli, C. Water Quality Assessment and Monitoring in Pakistan: A Comprehensive Review. *Sustainability* **2023**, *15*, 6246. [CrossRef]
26. Ahmed, H. Monitoring and Assessing the Quality of Water in Lake Edku Using the Remote Sensing Technology and the Geographic Information System (GIS). *Aquat. Sci. Fish Resour.* **2023**, *24*, 29–39. [CrossRef]
27. Acharyya, N.; Panda, S.; Bandyopadhyay, J. Structural Classification and Monitoring Development Status of Impounded Water Resources Using Spatial Information Technology of Purba Medinipur District, India. *Sustain. Water Resour. Manag.* **2022**, *8*, 100. [CrossRef]
28. Yakymchuk, V. Simulation Mathematical Modeling of Hydroecological Monitoring of Water Resources Using Space Images of the Earth. *Ukr. J. Remote Sens.* **2022**, *9*, 37–42. [CrossRef]
29. Jodhani, K.H.; Gupta, N.; Parmar, A.D.; Bhavsar, J.D.; Patel, H.; Patel, D.; Singh, S.K.; Mishra, U.; Omar, P.J. Synergizing Google Earth Engine and Earth Observations for Potential Impact of Land Use/Land Cover on Air Quality. *Results Eng.* **2024**, *22*, 102039. [CrossRef]
30. Kaplan, G.; Mateo, G. Large-Scale Mapping and Monitoring Inland Waters by Google Earth Engine and Remote Sensing Techniques. In *Geospatial Information Handbook for Water Resources and Watershed Management*; CRC Press: Boca Raton, FL, USA, 2022; pp. 17–31.
31. Nguyen, U.N.; Pham, L.T.; Dang, T.D. An automatic water detection approach using Landsat 8 OLI and Google Earth Engine cloud computing to map lakes and reservoirs in New Zealand. *Environ. Monit. Assess.* **2019**, *191*, 235. [CrossRef]
32. Baxter, A.J.; Bryan, R.D. Palaeoecological insights for the conservation of aquatic ecosystems in dryland environments: A case study of the Verlorenvlei system, South Africa. *Aquat. Conserv. Mar. Freshw. Ecosyst.* **1994**, *4*, 255–271. [CrossRef]
33. Mobariz, M.; Kaplan, G. Monitoring Amu Darya river channel dynamics using remote sensing data in Google Earth Engine. In Proceedings of the 5th International Electronic Conference on Water Sciences, Online, 16–30 November 2020; p. 8012.
34. Molnár, T.; Géza, K. Forest Monitoring Based on Sentinel-2 Satellite Imagery, Google Earth Engine Cloud Computing, and Machine Learning. *Preprints* **2023**. [CrossRef]
35. Bright, J. Geospatial Survey Tools for Planning, Processing, Visualizing, and Assessing Marine Magnetic Survey Data for Archeological Resources. In Proceedings of the Offshore Technology Conference, Houseton, TX, USA, 1–6 May 2019.
36. Goswami, S.; Samal, R.N.; Choudhury, S.B. Coastal Ecosystem Monitoring Using Long-Term Satellite Data Records: A Case Study of Chilika Lake, Odisha. *PeerJ* **2018**. [CrossRef]
37. Yang, L.; Driscol, J.; Sarigai, S.; Wu, Q.; Lippitt, C.D.; Morgan, M. Towards Synoptic Water Monitoring Systems: A Review of AI Methods for Automating Water Body Detection and Water Quality Monitoring Using Remote Sensing. *Sensors* **2022**, *22*, 2416. [CrossRef] [PubMed]
38. Lock, M.; Saintilan, N.; Van Duren, I.; Skidmore, A. Monitoring Coastal Water Body Health with Sentinel-2 MSI Imagery. *Remote Sens.* **2023**, *15*, 1734. [CrossRef]

39. Kumar, A.; Manu, M. Investigating the Applicability of a Simple Iterative Approach for Aerosol Optical Depth (AOD) Retrieval over Diverse Land Surface Types from Landsat 8 and Sentinel 2 Using Visible and near-Infrared (VNIR) Spectral Bands. *Atmos. Environ.* **2023**, *314*, 120082. [CrossRef]
40. Lahaie, P. Autonomous Atmospheric Correction Algorithm for Long Wave Infrard Hyperspectral Imagery. In Proceedings of the 9th Workshop on Hyperspectral Image and Signal Processing: Evolution in Remote Sensing (WHISPERS), Amsterdam, The Netherlands, 23–26 September 2018; Volume 28, pp. 1–5.
41. Bukata, R.P. Applications of water quality products to environmental monitoring. In *Satellite Monitoring of Inland and Coastal Water Quality*; CRC Press: Boca Raton, FL, USA, 2005; pp. 81–110.
42. Mazzoni, F.; Alvisi, S.; Franchini, M.; Blokker, M. Exploiting High-Resolution Data to Investigate the Characteristics of Water Consumption at the End-Use Level: A Dutch Case Study. *Water Resour. Ind.* **2023**, *29*, 100198. [CrossRef]
43. Paulino, R.S.; Martins, V.S.; Novo, E.M.L.M.; Barbosa, C.C.F.; de Carvalho, L.A.S.; Begliomini, F.N. Assessment of Adjacency Correction over Inland Waters Using Sentinel-2 MSI Images. *Remote Sens.* **2022**, *14*, 1829. [CrossRef]
44. Kwong, I.H.; Wong, F.K.; Fung, T. Automatic Mapping and Monitoring of Marine Water Quality Parameters in Hong Kong Using Sentinel-2 Image Time-Series and Google Earth Engine Cloud Computing. *Front. Mar. Sci.* **2022**, *9*, 871470. [CrossRef]
45. Jia, M.; Wang, Z.; Mao, D.; Ren, C.; Wang, C.; Wang, Y. Rapid, robust, and automated mapping of tidal flats in China using time series Sentinel-2 images and Google Earth Engine. *Remote Sens. Environ.* **2021**, *255*, 112285. [CrossRef]
46. Li, M.; Zhao, C.; Duan, Z.; Cheng, H.; Lian, Y.; Wang, G. Mechanically and accurately calculate river width in vegetation areas by coupling Sentinel-1 and -2 imageries within land-water-mixed pixels. *J. Hydrol.* **2024**, *643*, 131913. [CrossRef]
47. Warren, M.A.; Simis, S.G.; Selmes, N. Complementary water quality observations from high and medium resolution Sentinel sensors by aligning chlorophyll-a and turbidity algorithms. *Remote Sens. Environ.* **2021**, *265*, 112651. [CrossRef] [PubMed]
48. Wang, L.-C.; Ma, C.-X. A One-dimensional Linear Regression Model Based Spatial and Temporal Data Compression Algorithm for Wireless Sensor Networks. *J. Electron. Inf. Technol.* **2010**, *32*, 755–758. [CrossRef]
49. Candra, D.S.; Phinn, S.; Scarth, P. Cloud and cloud shadow masking for Sentinel-2 using multitemporal images in global area. *Int. J. Remote Sens.* **2019**, *41*, 2877–2904. [CrossRef]
50. Shaban, A.; El-Baz, F. Landsat Satellite Images for Lineaments Detection: A Tool to Identify Groundwater Productivity in Lebanon. In *Satellite Monitoring of Water Resources in the Middle East*; Springer Water: Berlin/Heidelberg, Germany, 2022; pp. 251–271.
51. Sharma, A.; Castro-Bolinaga, C. *River Mask Before and After the Elwha Dam Removals, WA*; HydroShare Resources: Chapel Hill, NC, USA, 2021.
52. Randhawa, S.; Guruprasad, R.; Balivada, S.; Hirani, P.; Guha, S. BLUEWATER EYE: Using satellite as a low-cost water pollution sensor: Analytics for deriving long term pollution insights based on mapping water turbidity. In Proceedings of the SPIE Remote Sensing, Berlin, Germany, 10–13 September 2018; Remote Sensing for Agriculture, Ecosystems, and Hydrology XX; Volume 16, p. 50.
53. Sibilia, C.D.; Aguirre-Gutiérrez, J.; Mowbray, L.; Malhi, Y. Effects of submerged aquatic vegetation and water quality on waterfowl abundance by foraging guild. *Ecol. Solut. Evid.* **2021**, *3*, e12137. [CrossRef]
54. Rawat, K.S.; Sahu, S.R.; Singh, S.K.; Chander, S.; Gujrati, A. Water Quality Analysis Using Normalized Difference Chlorophyll Index (NDCI) and Normalized Difference Turbidity Index (NDTI), Using Google Earth Engine Platform. In Proceedings of the 2023 International Conference on Modeling, Simulation & Intelligent Computing (MoSICom), Dubai, United Arab Emirates, 7–9 December 2023; pp. 408–413.
55. Karle, N.; Wolf, T.; Heege, T.; Schenk, K.; Klinger, P.; Schulz, K. Satellite remote sensing of chlorophyll and Secchi depth for monitoring lake water quality: A validation study. In Proceedings of the Earth Resources and Environmental Remote Sensing/GIS Applications X, Strasbourg, France, 9–12 September 2019; p. 61. [CrossRef]
56. Ivanda, A.; Šerić, L.; Bugarić, M.; Braović, M. Mapping Chlorophyll-a Concentrations in the Kaštela Bay and Brač Channel Using Ridge Regression and Sentinel-2 Satellite Images. *Electronics* **2021**, *10*, 3004. [CrossRef]
57. Boyer, J.N.; Kelble, C.R.; Ortner, P.B.; Rudnick, D.T. Phytoplankton bloom status: Chlorophyll a biomass as an indicator of water quality condition in the southern estuaries of Florida, USA. *Ecol. Indic.* **2009**, *9*, S56–S67. [CrossRef]
58. Vanderhoof, M.K.; Alexander, L.; Christensen, J.; Solvik, K.; Nieuwlandt, P.; Sagehorn, M. High-Frequency Time Series Comparison of Sentinel-1 and Sentinel-2 Satellites for Mapping Open and Vegetated Water across the United States (2017-2021). *Remote Sens. Environ.* **2023**, *288*, 113498. [CrossRef]
59. Albiac, J.; Dinar, A. Sustainable Water Management and Non-point Source Pollution Control in Spain and the European Union. In *The Management of Water Quality and Irrigation Technologies*; Albiac, J., Mema, M., Calvo, E., Eds.; Taylor Francis: Abingdon, UK, 2012; pp. 77–98.
60. Zhang, X.; Huang, J.; Chen, J.; Zhao, Y. Remote Sensing Monitoring of Total Suspended Solids Concentration in Jiaozhou Bay Based on Multi-Source Data. *Ecol. Indic.* **2023**, *154*, 110513. [CrossRef]
61. Liu, C.; Pan, C.; Chang, Y.; Luo, M. Water Quality Autoregression Prediction Model Based on Markov-Switching Theory Using Crow Search Algorithm. In Proceedings of the EGU General Assembly 2020, Online, 4–8 May 2020. [CrossRef]
62. Pham, T.T.; Nguyen, T.; Tham, H.T.; Truong, T.N.; Lam-Dao, N.; Nguyen-Huy, T. Specifying the Relationship between Land Use/Land Cover Change and Dryness in Central Vietnam from 2000 to 2019 Using Google Earth Engine. *J. Appl. Remote Sens.* **2021**, *15*, 024503. [CrossRef]

63. Manoj, M.; Dhilip Kumar, V.; Arif, M.; Bulai, E.-R.; Bulai, P.; Geman, O. State of the Art Techniques for Water Quality Monitoring Systems for Fish Ponds Using IoT and Underwater Sensors: A Review. *Sensors* **2022**, *22*, 2088. [CrossRef] [PubMed]
64. Singh, R.; Saritha, V.; Pande, C.B. Monitoring of wetland turbidity using multi-temporal Landsat-8 and Landsat-9 satellite imagery in the Bisalpur wetland, Rajasthan, India. *Environ. Res.* **2024**, *241*, 117638. [CrossRef]
65. Tan, K.; Sun, M.; Sun, D.; Liu, X.; Liu, X.; Wang, B.; Dou, W.; Zhang, H.; Lun, F. Mapping of nearshore bathymetry using Gaofen-6 images for the Yellow River Delta-Laizhou Bay, China. *Ecol. Inform.* **2024**, *80*, 102497. [CrossRef]
66. Mishra, K.; Choudhary, B.; Fitzsimmons, K.E. Predicting and evaluating seasonal water turbidity in Lake Balkhash, Kazakhstan, using remote sensing and GIS. *Front. Environ. Sci.* **2024**, *12*, 1371759. [CrossRef]
67. Baloch, Q.B.; Shah, S.N.; Iqbal, N.; Sheeraz, M.; Asadullah, M.; Mahar, S.; Khan, A.U. Impact of tourism development upon environmental sustainability: A suggested framework for sustainable ecotourism. *Environ. Sci. Pollut. Res.* **2022**, *30*, 5917–5930. [CrossRef]
68. Zhang, J.; Meng, F.; Fu, P.; Jing, T.; Xu, J.; Yang, X. Tracking changes in chlorophyll-a concentration and turbidity in Nansi Lake using Sentinel-2 imagery: A novel machine learning approach. *Ecol. Inform.* **2024**, *81*, 102597. [CrossRef]
69. Chen, J.; Liu, Z.; Xiao, S.; Chen, R.; Luo, C.; Zhu, T.; Cao, T.; Ni, L.; Xie, P.; Su, H.; et al. Effects of benthivorous fish disturbance on chlorophyll a contents in water and the growth of two submersed macrophytes with different growth forms under two light regimes. *Sci. Total Environ.* **2020**, *704*, 135269. [CrossRef]
70. Devlin, A.; Pan, J.; Shah, M.; Nuhu, A.; Cummins, K.; Zarges, C.; Fierro, P.; Olmos, V.; Dirisu, A.; Olomukoro, J.; et al. *Inland Waters—Dynamics and Ecology*; IntechOpen: London, UK, 2020. [CrossRef]
71. Jain, V.; Benyoucef, L. New Approaches for Modeling and Evaluating Agility in Integrated Supply Chains. In *Supply Chain the Way to Flat Organisation*; InTech: London, UK, 2009. [CrossRef]
72. Imen, S.; Chang, N.; Yang, Y.J. Developing the Remote Sensing-Based Early Warning System for Monitoring TSS Concentrations in Lake Mead. *J. Environ. Manag.* **2015**, *160*, 73–89. [CrossRef]
73. Austin, Å.N.; Hansen, J.P.; Donadi, S.; Eklöf, J.S. Relationships between aquatic vegetation and water turbidity: A field survey across seasons and spatial scales. *PLoS ONE* **2017**, *12*, e0181419. [CrossRef]
74. Sahoo, D.; Anandhi, A. Conceptualizing turbidity for aquatic ecosystems in the context of sustainable development goals. *Environ. Sci. Adv.* **2023**, *2*, 1220–1234. [CrossRef]
75. Hale, R.C.; Gallo, K.P.; Loveland, T.R. Influences of Specific Land Use/Land Cover Conversions on Climatological Normals of Near-surface Temperature. *J. Geophys. Res.* **2008**, *113*. [CrossRef]
76. Rutherford, G.N.; Guisan, A.; Zimmermann, N.E. Evaluating Sampling Strategies and Logistic Regression Methods for Modelling Complex Land Cover Changes. *J. Appl. Ecol.* **2007**, *44*, 414–424. [CrossRef]
77. Rawat, K.S.; Singh, S.K. Monitoring water spread and aquatic vegetation using earth observational data for Nani-High Altitude Lake (N-HAL) of Uttarakhand State, India. *J. Eng. Res.* **2023**, *12*, 64–74. [CrossRef]
78. Patra, S.; Basuri, C.K.; Muduli, P.R.; Kanuri, V.V.; S., R.R.; Dipnarayan, G.; R., A.K.; Avvari, L.; Panda, U.S.; K., D.S.; et al. Determination of biogeochemical rate constants for Chilika Lake, a tropical brackish water lagoon on the east coast of India. *Front. Mar. Sci.* **2024**, *11*, 1323229. [CrossRef]
79. Akinnawo, S.O. Eutrophication: Causes, consequences, physical, chemical and biological techniques for mitigation strategies. *Environ. Chall.* **2023**, *12*, 100733. [CrossRef]
80. Lomartire, S.; Marques, J.C.; Gonçalves, A.M. The key role of zooplankton in ecosystem services: A perspective of interaction between zooplankton and fish recruitment. *Ecol. Indic.* **2021**, *129*, 107867. [CrossRef]
81. Fan, X.; Liu, Y.; Wu, G.; Zhao, X. Compositing the Minimum NDVI for Daily Water Surface Mapping. *Remote Sens.* **2020**, *12*, 700. [CrossRef]
82. Zhang, Y.; Gao, W.; Li, Y.; Jiang, Y.; Chen, X.; Yao, Y.; Messyasz, B.; Yin, K.; He, W.; Chen, Y. Characteristics of the Phytoplankton Community Structure and Water Quality Evaluation in Autumn in the Huaihe River (China). *Int. J. Environ. Res. Public Health* **2021**, *18*, 12092. [CrossRef]
83. Du, Y.; Song, K.; Wang, Q.; Li, S.; Wen, Z.; Liu, G.; Tao, H.; Shang, Y.; Hou, J.; Lyu, L.; et al. Total suspended solids characterization and management implications for lakes in East China. *Sci. Total Environ.* **2022**, *806*, 151374. [CrossRef]
84. Alimi, O.S.; Farner Budarz, J.; Hernandez, L.M.; Tufenkji, N. Microplastics and Nanoplastics in Aquatic Environments: Aggregation, Deposition, and Enhanced Contaminant Transport. *Environ. Sci. Technol.* **2018**, *52*, 1704–1724. [CrossRef] [PubMed]
85. Bilotta, G.S.; Brazier, R.E. Understanding the influence of suspended solids on water quality and aquatic biota. *Water Res.* **2008**, *42*, 2849–2861. [CrossRef] [PubMed]
86. Geng, M.; Qian, Z.; Jiang, H.; Huang, B.; Huang, S.; Deng, B.; Peng, Y.; Xie, Y.; Li, F.; Zou, Y.; et al. Assessing the impact of water-sediment factors on water quality to guide river-connected lake water environment improvement. *Sci. Total Environ.* **2024**, *912*, 168866. [CrossRef] [PubMed]
87. Jargal, N.; Lee, E.; An, K. Monsoon-induced response of algal chlorophyll to trophic state, light availability, and morphometry in 293 temperate reservoirs. *J. Environ. Manag.* **2023**, *337*, 117737. [CrossRef]
88. Ganesh, V.; Goswami, S.; Nagendra, H. Long-Term Surface Water Variability in Chilika Lake Using Archival Remote Sensing Data. *Environ. Sci. Proc.* **2024**, *29*, 33. [CrossRef]
89. Teng, W.; Guoxiang, W.; Qiang, L. Effects of Water Turbidity on the Photosynthetic Characteristics of *Myriophyllum spicatum* L. *Asian J. Plant Sci.* **2007**, *6*, 773–780. [CrossRef]

90. Organisation for Economic Co-operation and Development. *Test No. 239: Water-Sediment Myriophyllum Spicatum Toxicity Test. (n.d.)*; OECD Publishing: Paris, France, 2014. [CrossRef]
91. Jones, R.C.; Adams, M.S. Seasonal variations in photosynthetic response of algae epiphytic on *Myriophyllum spicatum* L. *Aquat. Bot.* **1982**, *13*, 317–330. [CrossRef]
92. Salls, W.B.; Schaeffer, B.A.; Pahlevan, N.; Coffer, M.M.; Seegers, B.N.; Werdell, P.J.; Ferriby, H.; Stumpf, R.P.; Binding, C.E.; Keith, D.J. Expanding the Application of Sentinel-2 Chlorophyll Monitoring across United States Lakes. *Remote Sens.* **2024**, *16*, 1977. [CrossRef]
93. Tweddle, J.F.; Gubbins, M.; Scott, B.E. Should phytoplankton be a key consideration for marine management? *Mar. Policy* **2018**, *97*, 1–9. [CrossRef]
94. Grober, B.L.; Bennett, S. Modeling Surface Runoff of Spring Lake Watershed. *Geol. Soc. Am. Abstr. Programs* **2018**, *50*. [CrossRef]
95. Sharma, S.; Bhattacharya, A. Drinking water contamination and treatment techniques. *Appl. Water Sci.* **2016**, *7*, 1043–1067. [CrossRef]
96. Azha, S.F.; Sidek, L.M.; Ahmad, Z.; Zhang, J.; Basri, H.; Zawawi, M.H.; Noh, N.M.; Ahmed, A.N. Enhancing river health monitoring: Developing a reliable predictive model and mitigation plan. *Ecol. Indic.* **2023**, *156*, 111190. [CrossRef]
97. Hauer, C.; Leitner, P.; Unfer, G.; Pulg, U.; Habersack, H.; Graf, W. The Role of Sediment and Sediment Dynamics in the Aquatic Environment. In *Riverine Ecosystem Management*; Springer: Berlin/Heidelberg, Germany, 2018; pp. 151–169. [CrossRef]
98. Kumar, A.; Equeenuddin, S.M.; Mishra, D.R.; Acharya, B.C. Remote monitoring of sediment dynamics in a coastal lagoon: Long-term spatio-temporal variability of suspended sediment in Chilika. *Estuar. Coast. Shelf Sci.* **2016**, *170*, 155–172. [CrossRef]
99. Noe, G.B.; Cashman, M.J.; Skalak, K.; Gellis, A.; Hopkins, K.G.; Moyer, D.; Webber, J.; Benthem, A.; Maloney, K.; Brakebill, J.; et al. Sediment dynamics and implications for management: State of the science from long-term research in the Chesapeake Bay watershed, USA. *Wiley Interdiscip. Rev. Water* **2020**, *7*, e1454. [CrossRef]
100. Feng, X.; Zhu, C.; Liu, J.P.; Jia, Y. Sediment Dynamics in Coastal and Marine Environments: Scientific Advances. *Water* **2023**, *15*, 1404. [CrossRef]
101. Quevauviller, P.; Borchers, U.; Thompson, K.C.; Simonart, T. (Eds.) *The Water Framework Directive: Ecological and Chemical Status Monitoring*; Wiley: Hoboken, NJ, USA, 2008.
102. Chander, S.; Gujrati, A.; Abdul Hakeem, K.; Garg, V.; Issac, A.M.; Dhote, P.R.; Kumar, V.; Sahay, A. Water Quality Assessment of River Ganga and Chilika Lagoon using AVIRIS-NG Hyperspectral Data. *Curr. Sci.* **2019**, *116*, 1172. [CrossRef]
103. Nukapothula, S.; Yunus, A.P.; Kaushal, S.; Chen, C.; Narayana, A. Turbidity dynamics in Indian peninsular river mouths derived from Kd490 reveals key anthropogenic drivers. *Sci. Total Environ.* **2023**, *896*, 165162. [CrossRef]
104. Das, S.; Sangode, S.J.; Kandekar, A.M.; Meshram, D.C.; Tarolli, P. Interrelation between factors controlling sediment yield in the largest catchment of Peninsular India. *J. Hydrol.* **2023**, *622*, 129680. [CrossRef]
105. Ansari, A.A.; Singh, I.B.; Tobschall, H.J. Role of monsoon rain on concentrations and dispersion patterns of metal pollutants in sediments and soils of the Ganga Plain, India. *Environ. Geol.* **2000**, *39*, 221–237. [CrossRef]
106. Talbot, C.J.; Bennett, E.M.; Cassell, K.; Hanes, D.M.; Minor, E.C.; Paerl, H.; Raymond, P.A.; Vargas, R.; Vidon, P.G.; Wollheim, W.; et al. The impact of flooding on aquatic ecosystem services. *Biogeochemistry* **2018**, *141*, 439–461. [CrossRef]
107. Kramer, S.J.; Maritorena, S.; Cetinić, I.; Jeremy Werdell, P.; Siegel, D.A. Phytoplankton communities quantified from hyperspectral ocean reflectance correspond to pigment-based communities. *Opt. Express* **2024**, *32*, 34482–34491. [CrossRef]
108. Haraguchi, L.; Carstensen, J.; Abreu, P.C.; Odebrecht, C. Long-term changes of the phytoplankton community and biomass in the subtropical shallow Patos Lagoon Estuary, Brazil. *Estuar. Coast. Shelf Sci.* **2015**, *162*, 76–87. [CrossRef]
109. Lemos, V.M.; Lanari, M.; Copertino, M.; Secchi, E.R.; De Abreu, P.C.; Muelbert, J.H.; Garcia, A.M.; Dumont, F.C.; Muxagata, E.; Vieira, J.P.; et al. Patos Lagoon estuary and adjacent marine coastal biodiversity long-term data. *Earth Syst. Sci. Data* **2022**, *14*, 1015–1041. [CrossRef]
110. Albanai, J.A.; Karam, Q.; Ali, M.; Annabi-Trabelsi, N. Physicochemical factors affecting chlorophyll-a concentrations in the north-western Arabian Gulf and Kuwait's territorial waters. *Arab. J. Geosci.* **2022**, *15*, 1671. [CrossRef]
111. Dewata, I.; Hamdi, H.; Putra, A. Water quality of batang merao watershed and implementation of landsat 8 oli for the transparency of lake kerinci waters. *J. Sustain. Sci. Manag.* **2024**, *19*, 108–119. [CrossRef]
112. Mishra, D.R.; Kumar, A.; Muduli, P.R.; Acharyya, T.; Acharya, P.; Singh, S.; Rastogi, G. Landfall season is critical to the impact of a cyclone on a monsoon-regulated tropical coastal lagoon. *Sci. Total Environ.* **2021**, *770*, 145235. [CrossRef]
113. Gray, A.B. The impact of persistent dynamics on suspended sediment load estimation. *Geomorphology* **2018**, *322*, 132–147. [CrossRef]
114. Leifels, M.; Sirikanchana, K.; Ebdon, J. Microbiological impact of diffuse pollution sources on water quality. In *Land Use and Water Quality: The Impacts of Diffuse Pollution*; Kajitvichyanukul, P., D'Arcy, B., Eds.; IWA Publishing: London, UK, 2022; pp. 73–82.
115. Franco, A.; Franzoi, P.; Malavasi, S.; Riccato, F.; Torricelli, P. Fish assemblages in different shallow water habitats of the Venice Lagoon. Developments in Hydrobiology. *Hydrobiologia* **2006**, *555*, 159–174. [CrossRef]
116. Naskar, P.R.; Katiyar, S.; Bondyopadhyay, S. Pre-Monsoon and Post-Monsoon Groundwater Chemical Analysis For Burdwan (West Bengal), India. *Mausam* **2021**, *72*, 859–864. [CrossRef]
117. Bid, S.; Siddique, G. Identification of seasonal variation of water turbidity using NDTI method in Panchet Hill Dam, India. *Model. Earth Syst. Environ.* **2019**, *5*, 1179–1200. [CrossRef]

118. Sonwani, S.; Saxena, P. Water-Insoluble Carbonaceous Components in Rainwater over an Urban Background Location in Northern India during Pre-Monsoon and Monsoon Seasons. *Environ. Sci. Pollut. Res. Int.* **2021**, *28*, 53058–53073. [CrossRef] [PubMed]
119. Yaroshenko, I.; Kirsanov, D.; Marjanovic, M.; Lieberzeit, P.A.; Korostynska, O.; Mason, A.; Frau, I.; Legin, A. Real-Time Water Quality Monitoring with Chemical Sensors. *Sensors* **2020**, *20*, 3432. [CrossRef]
120. Chen, J.; Huang, J.; Zhang, X.; Chen, J.; Chen, X. Monitoring total suspended solids concentration in Poyang Lake via machine learning and Landsat images. *J. Hydrol. Reg. Stud.* **2023**, *49*, 101499. [CrossRef]
121. Doxaran, D.; Lamquin, N.; Park, Y.; Mazeran, C.; Ryu, J.; Wang, M.; Poteau, A. Retrieval of the seawater reflectance for suspended solids monitoring in the East China Sea using MODIS, MERIS and GOCI satellite data. *Remote Sens. Environ.* **2014**, *146*, 36–48. [CrossRef]
122. Feng, L.; Hu, C.; Chen, X.; Tian, L.; Chen, L. Human Induced Turbidity Changes in Poyang Lake between 2000 and 2010: Observations from MODIS. *J. Geophys. Res. Ocean.* **2012**, *117*. [CrossRef]
123. Mncube, Z.; Xulu, S. Progress of Nighttime Light Applications within the Google Earth Engine Cloud Platform. *Geocarto Int.* **2022**, *18*, 1–22. [CrossRef]
124. Hui, Y.; Huang, Z.; Alahi, M.E.E.; Nag, A.; Feng, S.; Mukhopadhyay, S.C. Recent Advancements in Electrochemical Biosensors for Monitoring the Water Quality. *Biosensors* **2022**, *12*, 551. [CrossRef]
125. Olias, L.G.; Di Lorenzo, M. Microbial Fuel Cells for In-Field Water Quality Monitoring. *RSC Adv.* **2021**, *11*, 16307–16317. [CrossRef]
126. Mukonza, S.S.; Chiang, J.-L. Meta-Analysis of Satellite Observations for United Nations Sustainable Development Goals: Exploring the Potential of Machine Learning for Water Quality Monitoring. *Environments* **2023**, *10*, 170. [CrossRef]
127. Ma, C.; Zhao, J.; Ai, B.; Sun, S.; Yang, Z. Machine Learning Based Long-Term Water Quality in the Turbid Pearl River Estuary, China. *J. Geophys. Res. Ocean.* **2022**, *127*, e2021JC018017. [CrossRef]
128. Cosgrove, W.J.; Loucks, D.P. Water management: Current and future challenges and research directions. *Water Resour. Res.* **2015**, *51*, 4823–4839. [CrossRef]
129. Kavzoglu, T.; Goral, M. Google Earth Engine for Monitoring Marine Mucilage: Izmit Bay in Spring 2021. *Hydrology* **2022**, *9*, 135. [CrossRef]
130. Ziemińska-Stolarska, A.; Adamiec, J.; Imbierowicz, M.; Imbierowicz, E.; Jaskulski, M.; Zbiciński, I. Surface water quality monitoring in a large dam reservoir, Poland. *Desalination Water Treat.* **2018**, *101*, 130–142. [CrossRef]
131. Feyisa, G.L.; Meilby, H.; Fensholt, R.; Proud, S.R. Automated Water Extraction Index: A New Technique for Surface Water Mapping Using Landsat Imagery. *Remote Sens. Environ.* **2014**, *140*, 23–35. [CrossRef]
132. Yue, L.; Li, B.; Zhu, S.; Yuan, Q.; Shen, H. A Fully Automatic and High-Accuracy Surface Water Mapping Framework on Google Earth Engine Using Landsat Time-Series. *Int. J. Digit. Earth* **2023**, *16*, 210–233. [CrossRef]
133. Mansourmoghaddam, M.; Ghafarian Malamiri, H.R.; Rousta, I.; Olafsson, H.; Zhang, H. Assessment of Palm Jumeirah Islands Construction Effects on the Surrounding Water Quality and Surface Temperatures during 2001–2020. *Water* **2022**, *14*, 634. [CrossRef]
134. Pereira, A.C.; Mulligan, C.N.; Veetil, D.P.; Bhat, S. An In-Situ Geotextile Filtration Method for Suspended Solids Attenuation and Algae Suppression in a Canadian Eutrophic Lake. *Water* **2023**, *15*, 441. [CrossRef]
135. George, T.E.; Karatu, K.; Edward, A. An evaluation of the environmental impact assessment practice in Uganda: Challenges and opportunities for achieving sustainable development. *Heliyon* **2020**, *6*, e04758. [CrossRef]
136. Publications. (n.d.). Chilika Lake—Asia's Largest Brackish Water Lagoon. Available online: https://www.chilika.com/publications.php (accessed on 20 August 2024).
137. Kumar, R.; Parvaze, S.; Huda, M.B.; Allaie, S.P. The changing water quality of lakes—A case study of Dal Lake, Kashmir Valley. *Environ. Monit. Assess.* **2022**, *194*, 228. [CrossRef]
138. Shams, M.Y.; Elshewey, A.M.; El-kenawy, E.M.; Ibrahim, A.; Talaat, F.M.; Tarek, Z. Water quality prediction using machine learning models based on grid search method. *Multimed. Tools Appl.* **2023**, *83*, 35307–35334. [CrossRef]
139. Mishra, V.; Limaye, A.S.; Muench, R.E.; Cherrington, E.A.; Markert, K.N. Evaluating the performance of high-resolution satellite imagery in detecting ephemeral water bodies over West Africa. *Int. J. Appl. Earth Obs. Geoinf.* **2020**, *93*, 102218. [CrossRef]
140. Saber, A.; James, D.E.; Hayes, D.F. Estimation of water quality profiles in deep lakes based on easily measurable constituents at the water surface using artificial neural networks coupled with stationary wavelet transform. *Sci. Total Environ.* **2019**, *694*, 133690. [CrossRef] [PubMed]
141. Barzegar, R.; Adamowski, J.; Moghaddam, A.A. Application of wavelet-artificial intelligence hybrid models for water quality prediction: A case study in Aji-Chay River, Iran. *Stoch. Environ. Res. Risk Assess.* **2016**, *30*, 1797–1819. [CrossRef]
142. Zhou, C.; Su, F.; Harvey, F.; Xu, J. Analyzing the Uncertainties of Ground Validation for Remote Sensing Land Cover Mapping in the Era of Big Geographic Data. Advances in Geographic Information Science. In *Spatial Data Handling in Big Data Era*; Sun, B., Chen, X., Zhou, Q., Eds.; Springer: Berlin/Heidelberg, Germany, 2017; pp. 31–38.
143. Fowler, J.; Waldner, F.; Hochman, Z. All pixels are useful, but some are more useful: Efficient in situ data collection for crop-type mapping using sequential exploration methods. *Int. J. Appl. Earth Obs. Geoinf.* **2020**, *91*, 102114. [CrossRef]
144. Ibrahim, A.; Wayayok, A.; Shafri, H.Z.; Toridi, N.M. Remote Sensing Technologies for Unlocking New Groundwater Insights: A Comprehensive Review. *J. Hydrol. X* **2024**, *23*, 100175. [CrossRef]
145. Meghla, N.T.; Urmy, S.Y.; Mahamud, M.R. Assessment of the Seasonal Variations of Lakes Water Quality in Bangladesh. *Biomed. Sci. Clin. Res.* **2023**, *2*. [CrossRef]

146. Huang, C.; Chen, Y.; Zhang, S.; Wu, J. Detecting, Extracting, and Monitoring Surface Water from Space Using Optical Sensors: A Review. *Rev. Geophys.* **2018**, *56*, 333–360. [CrossRef]
147. Zhang, G.; Yao, T.; Xie, H.; Yang, K.; Zhu, L.; Shum, C.; Bolch, T.; Yi, S.; Allen, S.; Jiang, L.; et al. Response of Tibetan Plateau Lakes to Climate Change: Trends, Patterns, and Mechanisms. *Earth-Sci. Rev.* **2020**, *208*, 103269. [CrossRef]

Disclaimer/Publisher's Note: The statements, opinions and data contained in all publications are solely those of the individual author(s) and contributor(s) and not of MDPI and/or the editor(s). MDPI and/or the editor(s) disclaim responsibility for any injury to people or property resulting from any ideas, methods, instructions or products referred to in the content.

International Journal of Geo-Information

MDPI

Article

GIS-Based Dashboards as Advanced Geospatial Applications for Climate Change Education and Teaching the Future

Rafael De Miguel González [1,2,*], Juan Mar-Beguería [1], María Sebastián López [1] and Ondrej Kratochvíl [1]

[1] ARGOS, Institute for Research in Environmental Sciences of Aragon, IUCA, University of Zaragoza, 50009 Zaragoza, Spain; j.mar@unizar.es (J.M.-B.); msebas@unizar.es (M.S.L.); onkra@unizar.es (O.K.)
[2] EUROGEO, B8020 Waardamme, Belgium
* Correspondence: rafaelmg@unizar.es

Abstract: ArcGIS Dashboard technology allows for the integration and visualization of various maps, charts, and indicators within a single interface, using databases underneath a geographic information system. The two dashboards of the European project Teaching the Future address the dual objective of (i) cartographically displaying the evolution in four phases of climate change data experienced across the entire planet from 1954 to 2021 in vectorial cells measuring one degree of latitude by one degree of longitude and (ii) spatially representing three scenarios (low, medium, and high greenhouse gas emissions) up to the year 2100, showing potential temperature increases in those same cells. In addition to the maps, the different data and charts contribute to the understanding of anomalies relative to the average, the global increase in each selected area by zooming in on the map, and the evolution of both observed and projected data. Both dashboards represent an accurate and reliable treatment of the data, as well as a cartographic expression that is easy for map readers to understand, making them powerful resources for teaching climate change at any educational level, whether in higher education or schools and for a general audience.

Keywords: ArcGIS Dashboard; geospatial competences; geographical education; climate change

1. Introduction

Educators and scientists are deeply concerned about the climate crisis. Teaching the Future (https://teachingthefuture.eu) is a European Union-funded project aimed at enhancing climate change education, embedded within the European Commission's "Education for Climate Coalition" as a flagship initiative of the European Education Area and a horizontal priority in the Erasmus Plus program to develop green competences for lifelong learning [1]. This project, led by the EUROGEO (European Association of Geographers) [2], seeks to provide easy access to scientific data and climate information through a comprehensive climate data dashboard and maps. These tools support a teacher training program designed to disseminate effective knowledge on climate education. The project also focuses on equipping young people with the skills to work with high-quality scientific data and reliable information sources to address the challenges posed by climate change. The skills are related to the EU competence frameworks DigComp (skills in data literacy, communication, content creation, safety, and problem-solving) and the GreenComp (skills in embodying sustainability values, embracing complexity, envisioning sustainable futures, and acting for sustainability). Consequently, these maps become powerful resources for promoting active citizenship, encouraging young people to engage with their local communities using inquiry-based approaches to citizen science to examine and tackle climate issues.

The project is grounded in an analysis of secondary education curricula across several European countries, with a particular focus on geography. This analysis highlights both the deficiencies and the potential of climate education within national standards. As a result, an online climate data dashboard, primarily composed of maps, has been developed as a teaching resource for educators in both school and higher education. This resource adopts an interdisciplinary approach that extends beyond geographical science. The maps are based on open data initiatives, utilizing geospatial information from European sources, such as the European Environment Agency Climate Data Centre, the European Space Agency Climate Initiative, and the EU Open Data Portal. These resources can be further enriched with global datasets from organizations like NASA and the Intergovernmental Panel on Climate Change (IPCC).

Integrating these reliable data sources, accessible to the public and produced by leading scientists, into climate education represents a highly innovative approach. Currently, there is little to no awareness in most European schools of the availability of open data or related scientific resources, such as data visualization and presentation tools that are freely available through maps and dashboards. These tools have the potential to enhance education and lifelong learning at all levels, including school education, higher education, and adult education.

2. Climate Change Education with Geoinformation and Dashboards: Context

Climate change education is a topic of growing interest in scientific research [3], with nearly 1000 references currently available on the Web of Science related to this topic, many of them in geographic education or natural sciences education. However, very few of these bibliographic references explicitly mention the importance of maps and geoinformation as essential teaching resources for the instruction and learning of climate change. When mentioned, it is often indirectly, focusing on issues such as prior knowledge and misconceptions (what the student and teacher know), curricular content (what the student needs to know), teacher training (what the teacher needs to know), learning methods (particularly inquiry-based learning), the assessment of learning outcomes, and technological approaches through audiovisual resources and communication strategies that can foster comprehensive climate change education (knowing, doing, and being), as well as a personal and collective commitment to climate change adaptation and mitigation measures [4–8].

If references to maps are scarce, those maps and cartographic resources created with geospatial technologies and GIS are even rarer unless they are local case studies [9]. This contrasts with the recent dominance of geoinformation as an essential element for acquiring geographic and geospatial competencies in geographic education, both in school education and higher education [10–14], and particularly to achieve meaningful learning, spatial and geographical thinking, and powerful knowledge in geographical issues like climate change [15–20].

Some of the references that highlight the role of maps in climate change education showcase the learning opportunities provided by interactive maps and Story Maps [21,22] or the vast amount of information offered by raster maps generated with data from remote sensing for climate change education [23,24]. Other contributions also demonstrate the massive climate educational potential of geospatial information through MOOCs [25] or emphasize its contribution to education on the SDGs, one of which (number 13) focuses on climate action [26].

Finally, there are not many studies that analyze dashboards that include maps despite the fact that at the recent Esri User Conference 2024, the Governor of Minnesota, Tim

Walz, stated that the COVID-19 Map created by Johns Hopkins University using ArcGIS Dashboard technology has become the most viewed map in the history of geography. He made this statement with the agreement of his presenter, Esri President Jack Dangermond. The recent selection of Tim Walz as a candidate for Vice President of the United States in the 2024 elections, along with his self-description as a "GIS nerd", has led to more discussion of this dashboard-based example in the international press than in academic circles.

In fact, the main references that analyze and highlight the cartographic power of maps included in dashboards are related to the COVID-19 Map [27–29] or other disciplines within geography, such as urban geography [30] or mobility [31]. In geographic education, some good teaching practices with dashboards and maps have also been published [2,32]. Two recent specific publications are relevant: one that cited climate as one of the topics for innovative instruction in geography using dashboards [33] and another that disseminates a specific example of ArcGIS Dashboard for data climate data visualization [34]. In this way, the climate dashboard developed in the *Teaching the Future project* aims to contribute to increasing mapping references in climate change education.

3. Materials and Methods

The design of the thematic maps and their time series, along with the accompanying charts, involved using various data sources and types depending on the variables analyzed and the time range. The initial stage included a quality control check of the original dataset to eliminate the most obvious errors, following the methodology previously implemented [35]. A paleoclimatic perspective was incorporated by comparing recent instrumental data with previously published proxy-based temperature reconstructions and future-modeled climate data layers based on representative concentration pathways (RCPs 2.6, 4.5, and 8.5). The climate projections are based on Representative Concentration Pathway (RCP)/Shared Socioeconomic Pathway (SSP) scenarios. The ensemble (and some single-model) datasets were harmonized using regular latitude–longitude grids with horizontal resolutions of 2° (CMIP5), 1° (CMIP6), 0.5° (ORAS5), 0.25° (CORDEX-CORE and ERA5), 0.125° (CORDEX-EUR-11, E-OBS), and 0.1° (ERA5-Land).

3.1. Copernicus Data Source

The use of dashboards alongside spatial and cartographic information offers the unique advantage of enabling interactive and dynamic visualization of geospatial data. Users can interact with maps and charts by zooming in and out, filtering, and exploring the data in various ways. These dashboards are accessible from any device with an internet connection, allowing users to access information from anywhere. However, a notable limitation is that ArcGIS Dashboards have a limited capacity to handle raster data natively. Although raster data formats, such as GeoTIFF, can be used as background or reference layers, analyzing and interacting directly with these data often requires conversion to vector formats (shapefile and feature class) for better integration and functionality within the dashboard.

For this reason, the data obtained from the Copernicus Climate Change Service in NetCDF format [36–38], which were used to develop the climate dashboard for the Teaching the Future project, required conversion through Python, followed by processing in ArcGIS Pro and ArcGIS Online, to be integrated into the ArcGIS Dashboard. Along with the spatial dimension, the creation of this climate dashboard has allowed the cartographic visualization of the temporal variable, as expressed in Table 1, which details the metadata used in the spatial modeling of the data.

Table 1. Data source for Teaching the Future climate dashboard.

	Study Area	Typology of Climate Data	Spatial Resolution	Temporary Coverage
1	World	Observed average annual temperatures	1° latitude and longitude	1954–2019
2	World	Average annual temperatures modeled according to RCP scenarios	1° latitude and longitude	2006–2100
3	Europe	Observed average annual temperatures (average, maximum, and minimum) and rainfall	0.2° latitude and Longitude	1950–2021

Source: Copernicus Climate Change Service (2018).

The temperature in both the observed and projected dashboards is generated at 2 m above the surface. On the other hand, the precipitation data were provided in the datasets as mean precipitation flux (kg m^{-2} s^{-1}). This is the amount of water per unit area and time, and it was converted to annual rainfall (mm/year).

In this paper, 1 kg $m^{-2}s^{-1}$ is equivalent to 1 mm/s^1 because 1 kg m^{-2} corresponds to 1 mm of water depth. As a year has 31,536,000 s, the precipitation flux value should be multiplied by this constant.

Precipitation (mm/year) = Precipitation flux (kg $m^{-2}s^{-1}$) × 31,536,000

The ensemble (and some single-model) datasets were harmonized using regular latitude–longitude grids with horizontal resolutions of 2° (CMIP5), 1° (CMIP6), 0.5° (ORAS5), 0.25° (CORDEX-CORE and ERA5), 0.125° (CORDEX-EUR-11 and E-OBS), and 0.1° (ERA5-Land).

3.2. Dashboard Generation Process

Teaching the Future consists of six different dashboards. However, the cartographic and methodological process for designing these dashboards follows the same phases and procedures, which include (i) processing the raw NetCDF data with Python, (ii) further processing with ArcGIS Pro, and (iii) the design of climate maps and dashboards through various ArcGIS Online applications (Figure 1).

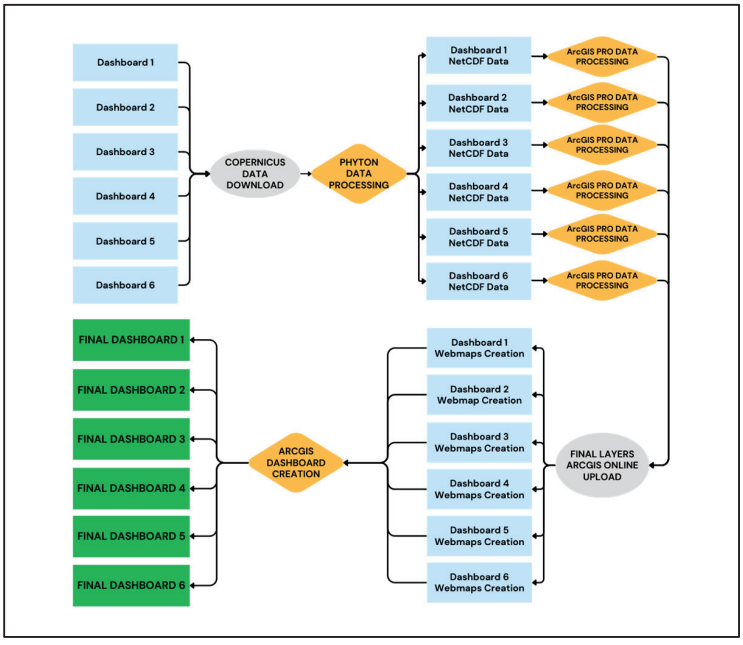

Figure 1. From NetCDF data to ArcGIS Dashboard.

3.3. Data Processing with Python

The data, downloaded from the official Copernicus portal of the EU (Climate Data Store), were processed using Python to consolidate the vast amount of data from each dataset into a single NetCDF file. This was necessary because the nature and arrangement of the data—sometimes daily or even at smaller temporal scales, other times monthly or annually—made them impossible to handle due to their size and volume. The Python script in Figure 2 was used for this process.

```
import os
import numpy as np
import xarray as xr
import rioxarray as rio
from netCDF4 import Dataset
def nc_to_geotiff(input_nc: str, output_tiff: str = None) -> str:
    """ Converts a NetCDF file to GeoTIFF by computing the average of all
relevant layers.

    Parameters:
        input_nc (str): Path to the input NetCDF file.
        output_tiff (str, optional): Path to the output GeoTIFF file. If
not provided,
                                     the input filename will be used with a
.tif extension.
        Returns:
        str: 'ok' if the conversion was successful, 'error' otherwise.
    """    variables = ['tas', 'tasmax', 'tasmin', 'tasavg', 'tassum',
'pr',            'prmin', 'prmax', 'pravg', 'prsum', 'rr',         'rrmin',
'rrmax', 'rravg', 'rrsum']

    try:
        with Dataset(input_nc, mode='r') as nc:
            nc.set_auto_mask(False)

            for var in variables:
                if var in nc.variables:
              data = nc[var][:]
              avg_data = np.mean(data, axis=0)

                    lat = nc['lat'][:]
                    lon = nc['lon'][:]

                    data_xr = xr.DataArray(avg_data, coords={'y': lat, 'x':
lon}, dims=["y", "x"])
                                        output_tiff = output_tiff or
f"{os.path.splitext(input_nc)[0]}.tif"
                    data_xr.rio.to_raster(output_tiff)
    return 'ok'
    except Exception as e:
        print(f"Error processing {input_nc}: {e}")
        return 'error'
        return 'error'
def process_nc_directory(directory: str):
        Processes all NetCDF files in a directory and converts them to Geo-
TIFF.
        Parameters:
        directory (str): Path to the directory containing NetCDF files.
       for filename in os.listdir(directory):
       if filename.endswith(".nc"):
            input_path = os.path.join(directory, filename)
            print(f"Processing: {input_path}")
            result = nc_to_geotiff(input_path)
            print(f"Result: {result}")
# Input directory configuration
nc_directory = r'C:/Users/ ' process_nc_directory(nc_direc-
tory)
```

Figure 2. Python script.

The script's objective is to unify multiple NetCDF files from a directory into a single *xarray* data structure and perform annual resampling. From this resampling, several

statistics are derived: mean, maximum, minimum, standard deviation, median, sum, and product. Additionally, given that months and leap years have different durations, the script also calculates the time-weighted average and weighted sum.

The script is designed to work with dimensions set as indexes, as long as they are numeric (coordinates) or date-type values. The statistics are calculated for all numeric columns, excluding the indexes, to avoid issues related to variables with different names. Each derived statistic is saved in a separate file to facilitate management and take advantage of Esri software's visualization options. This allows the sequence of data to be visualized using the "play" functionality in ArcGIS Pro.

Running the script automates the data preparation work, which is typically time-consuming and labor-intensive. Although developing the script required significant effort, testing has proven its effectiveness. Once opened, the NetCDF files can be handled, like a *pandas dataframe* or an *xarray*, making them easier to edit and analyze and enabling the preparation of more complex functions or simulations.

3.4. From ArcGIS Pro to ArcGIS Online

Once the necessary processing of the Copernicus climate files was completed using Python (with NetCDF data homogenized to annual temporal scales), the data were processed using ArcGIS Pro, following the cartographic design shown in Figure 3. One of the peculiarities of ArcGIS Online Dashboards is that they only accept spatial data in a shapefile format, relegating raster data (such as TIFF files) to visual support elements, similar to base maps.

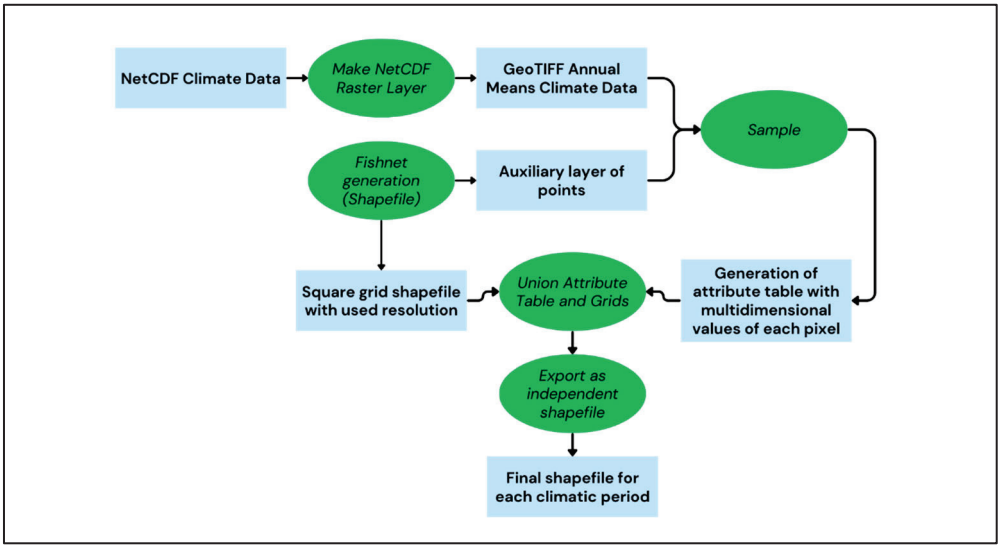

Figure 3. Shapefile creation process.

Therefore, with ArcGIS Pro, prior to uploading the information to ArcGIS Online, the data were processed to generate vector format layers (shapefiles). Additionally, ArcGIS Pro was used to create extra thematic information from the raw data, such as calculating the means of the standard 30-year climatic periods (1961–1990; 1971–2000; 1981–2010; and 1991–2020) or the annual thermal or precipitation anomalies relative to the reference climatic period (1961–1990). The same approach was applied to the future modeled climate data layers based on Representative Concentration Pathways (RCPs 2.6, 4.5, and 8.5). These RCPs are climate change scenarios that project future greenhouse gas concentrations. They describe future greenhouse gas concentrations and have been formally adopted by the IPCC.

This thorough process ensured that the data were appropriately formatted and enhanced for effective visualization and analysis within the ArcGIS Online Dashboard environment.

4. Results

Once all the adjustments and processing of each layer to be used in the dashboards were completed and uploaded to the ArcGIS Online servers, the final process of creating the dashboards was divided into two phases: (i) the design of the web maps to be included in each dashboard and (ii) the final generation of each dashboard with its widgets and unique elements.

Regarding the creation of each web map, decisions were made on the value range for the legend and color scale and the values and type of cartographic representation, as well as other aesthetic values and parameters typical of thematic cartography [39]. Additionally, unlike conventional cartographic elements, being dynamic maps, other utilities were developed, such as pop-ups with extra thematic information within each cell. These pop-ups present elements from the attribute table in a more user-friendly way for the intended audience of the dashboards, using different fonts, colors, or graphics instead of standard cells. Once the cartography was processed from the ArcGIS online server, the different dashboards were generated.

In total, six dashboards were carried out, as shown in Figure 4: two main ones that cover the entire world and four complementary dashboards that map climate change in Europe with greater detail, which are all available at the webpage of the project https://teachingthefuture.eu/climate-dashboards/ (accessed on 14 February 2025).

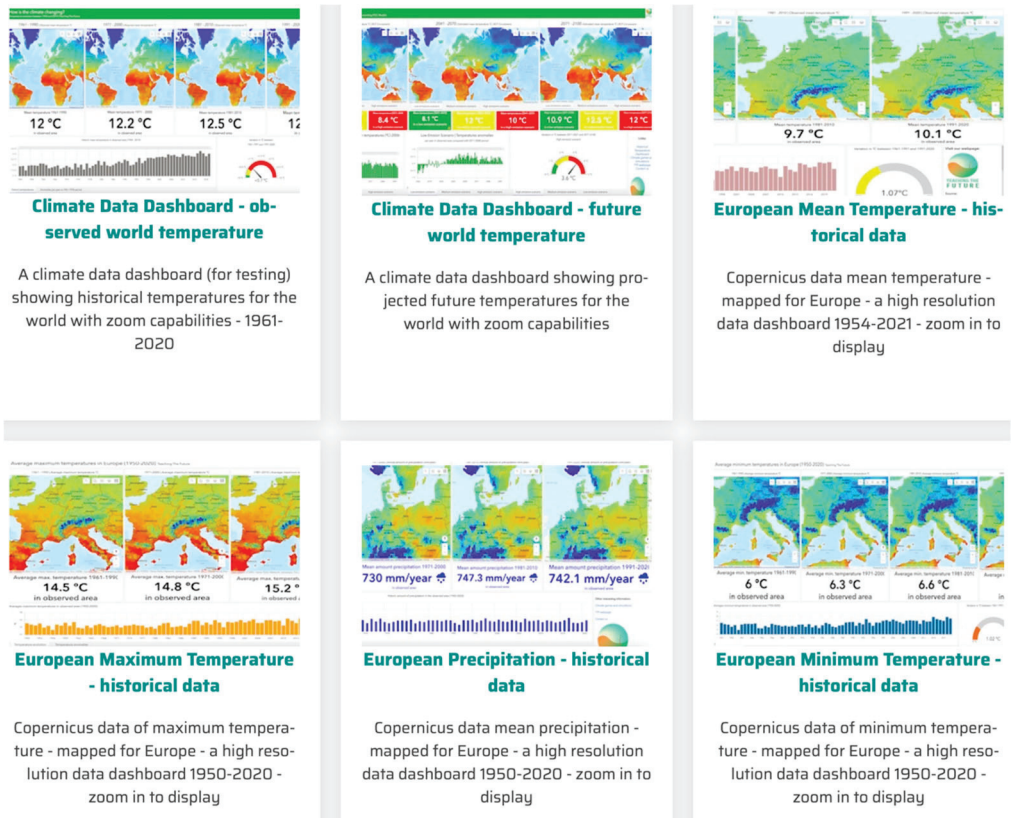

Figure 4. Teaching the Future climate dashboards.

- Climate data dashboard: observed mean temperature, world, 1961;
- Climate data dashboard: estimated mean temperature, world, 2011–2100;

- Climate data dashboard: observed mean temperature, Europe, 1961–2020;
- Climate data dashboard: observed average maximum temperature, Europe, 1961–2020;
- Climate data dashboard: observed average minimum temperature, Europe, 1961–2020;
- Climate data dashboard: observed annual precipitations, Europe, 1961–2020.

There are five dashboards featuring observed data, each consisting of four maps, one for each standard 30-year climatic period (1961–1990, 1971–2000, 1981–2010, and 1991–2020). One dashboard for projected future data consists of three maps corresponding to the three mentioned IPCC RCP scenarios (2.6, 4.5, and 8.5) for the periods 2011–2040, 2041–2070, and 2070–2100, making a total of twenty-three maps.

These maps include pop-up elements, where clicking on a specific area of the map provides detailed information about that area, such as the average temperature for the observed period, a chart showing the variation in annual average temperatures across periods, and the thermal variation between periods (Figure 5). Additionally, the dashboards offer features like a geographic search tool, spatial bookmarks, a legend, and the ability to toggle layers on and off (Figure 6).

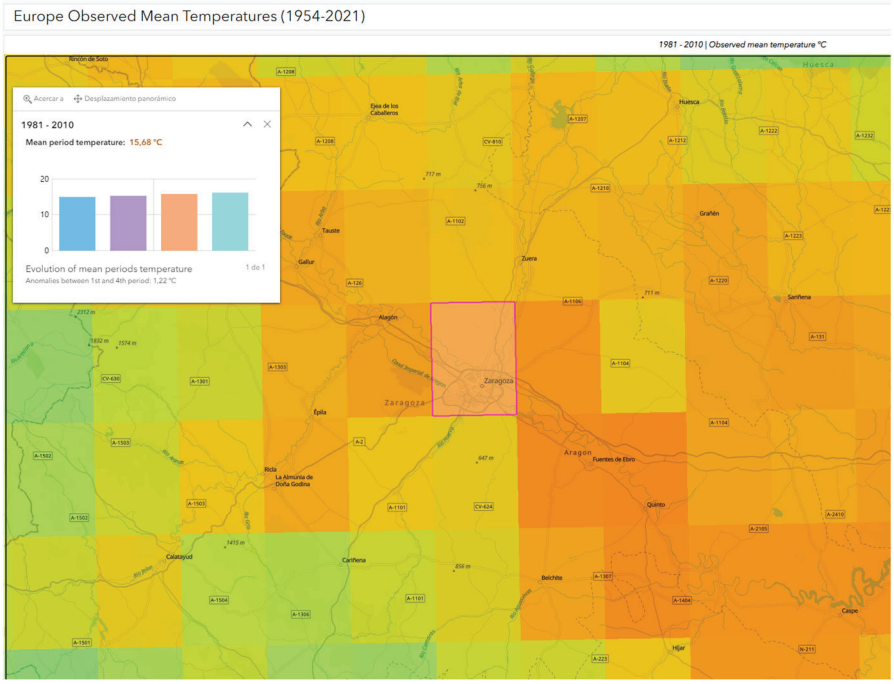

Figure 5. Detailed data of a cell raster with pop-up window: average temperature and chart.

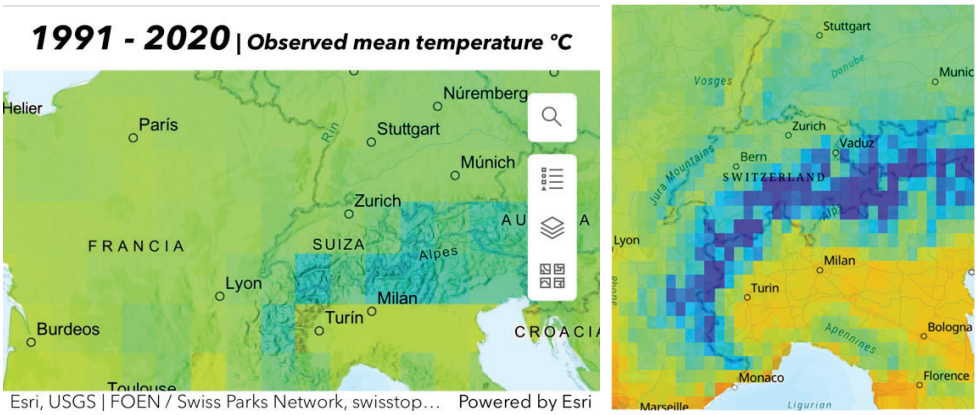

Figure 6. Difference in raster cell size between the world map (**left**) and the European map (**right**).

Additionally, each dashboard's set of maps includes a three-part complement, thus increasing the interactivity of the map reader with the map and the graphical and numerical spatial information:

- Indicators: The observed annual mean temperature for each period within the observed area;
- Calipers: They display the thermal variation (°C) between the 1961–1991 climate period and the 1991–2020 climate period. Depending on the degree of temperature increase, it is displayed using a traffic light system (green, yellow, and red);
- Charts: Two graphs are provided in each dashboard, according to the maps. These charts show the annual evolution of mean temperatures per year, as well as the thermal anomalies for each year relative to the reference climate period. The data observed in the charts (Figure 7), dependent on the observable scale, can be downloaded as a ".csv" file in accordance with the interoperability requirements of the project.

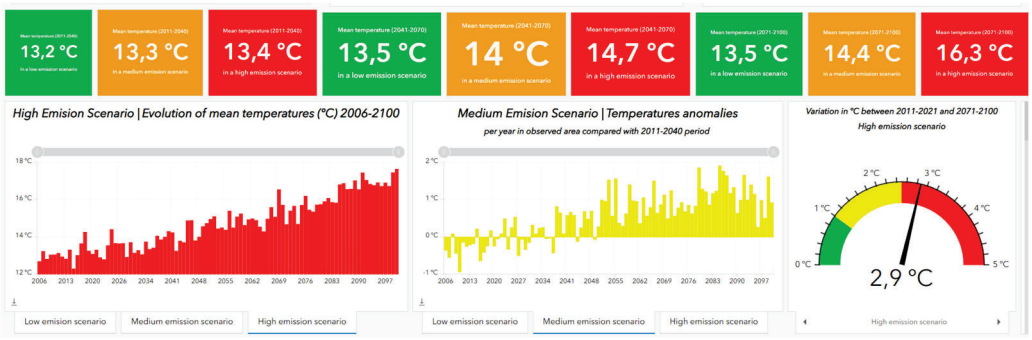

Figure 7. Data and charts associated with the maps in the climate dashboard.

5. Discussion

Once the six dashboards were developed, the discussion focused on validating these cartographic resources based on geoinformation as educational materials that effectively contribute to climate education in real school contexts. This discussion has been extensively addressed in the report on curriculum and digital teaching resources, which was developed within the framework of the *Teaching the Future* project, as well as in some of the previously cited references [2–5,14,16,33,34] and others [40,41], which have highlighted the benefits of Web_GIS in addressing key challenges—such as climate education—in geography education while also emphasizing essential strategies to develop geospatial, digital, and sustainability-related skills. This debate has been further reinforced by the recent publication of the *Handbook of Geography Education* [42], which, in several of its chapters, highlights the comparative advantage of GIS (and even GIS dashboards) over other climate education studies or resources.

Following the previous discussion, a second debate arises regarding the selection of the best approach to integrate project-based learning with problem-based learning in geospatial education. In this regard, the academic literature [43] concludes that the geo-inquiry approach is capable of integrating three fundamental dimensions for meaningful learning: geo-instructional, geo-progressions, and geo-capabilities.

As a result, the dashboards have led to the development of a lesson plan on climate change and a proposed geo-inquiry scaffolded in five steps—engage → explore → explain → elaborate → evaluate—following the 5E instructional model [44] for science education. The materials, alongside others, like climate simulations, to implement experiential learning activities, are available on the project's website (https://teachingthefuture.eu/module-4/ (accessed on 14 February 2025)) and have been widely disseminated through geography

teacher training programs in secondary education, as well as in 53 schools across Europe, particularly in Belgium, Spain, Greece, and Italy.

6. Concluding Remarks

This study demonstrates the value of climate dashboards as a powerful educational resource for climate change teaching and learning. By integrating spatial and temporal data visualization, the *Teaching the Future* climate dashboards provide an interactive, data-driven approach to understanding climate change at multiple scales. These tools bridge the gap between scientific climate data and classroom instruction, making complex climate trends more accessible and fostering critical thinking in students and the general public.

Climate action, as outlined in SDG 13—and specifically target 13.3, which promotes climate education, awareness-raising, and the enhancement of human and institutional capacity for climate change mitigation, adaptation, impact reduction, and early warning—is a key focus aligned with the UN Sustainable Development Goals. This initiative supports countries in adopting the Paris Agreement, with the goal of limiting global temperature rise to well below 2 degrees Celsius and addressing the global impacts, whether they be environmental, economic, or social.

The primary goal of creating this climate dashboard was to develop a cartographic tool that simplifies the understanding of a complex phenomenon with multiple consequences. To achieve this, the visual representation of climatic phenomena, particularly the global increase in temperatures, has been crucial in the design of the six dashboards, as well as in each individual map that they comprise. Dashboards are a visual approach that effectively displays climate data, as they clearly communicate information and aid in interpreting spatial climate data.

The dashboards leverage high-quality, authoritative datasets from the European Commission's Copernicus Program and the IPCC, ensuring reliability and scientific rigor. Consequently, the climate dashboard is designed to facilitate climate education using accurate and reliable information not based on biases or fake information that often prevail in denialist or alarmist discourses on climate change. Their user-friendly design facilitates engagement with climate change data, empowering educators, students, and citizens to explore historical trends and future projections based on different emission scenarios. This approach not only strengthens spatial literacy and geographical thinking but also combats misinformation by promoting data-backed climate education.

It offers a scientific perspective grounded in spatial data, which can be replicated in citizen science exercises due to its ease of reading, understanding, and use by school students, university students, and the general public alike. This is further enhanced by the dashboard's combination of spatial and temporal information, observed data with scientifically based forecasts, easy access, and interactive features, allowing for data downloads, information reuse, and map customization. Specifically, it offers cartography that is both local and global, as the zoom-in/out function enables users to understand the phenomenon of climate change at a local to global scale.

In conclusion, the climate dashboard is the primary tool of the European project *Teaching the Future*, which aims to promote climate education and strengthen "green education" as one of the prominent focus areas of the European Education Area. This European Union initiative fosters collaboration between Member States and stakeholders to build more resilient and inclusive national education systems for lifelong learning. Green education seeks to develop green competencies in students, and the climate dashboard aims to implement a comprehensive instructional model based on geographical knowledge, spatial thinking skills, and, most importantly, spatial citizenship, raising awareness of the challenges of global climate change. The *Teaching the Future* climate dashboard encourages

its users to move from knowledge to individual and collective action, with measures that contribute to climate change mitigation, adaptation, and impact reduction, thus promoting a powerful resource for powerful and transformative involvement.

Our future work involves promoting teacher training courses and instructional materials based on geospatial inquiry-based learning using the climate dashboard in combination with other resources, such as local case studies, national policies, and global debates on climate change challenges. The open-access user interface, interdisciplinary approach, and transnational nature of this project aim to enhance the impact of these six climate dashboards and maps—which have so far exceeded 13,000 views—in schools, universities, and among stakeholders engaged in climate change education. The EUROGEO's role in the Advisory Group of the European Commission's *Education for Climate Coalition*, as a participatory community supporting teaching and learning for the green transition, will also contribute to this effort.

Additionally, our future research will aim to gather evidence on the implementation and effectiveness of the geo-inquiry approach in climate education, as well as its impact on skills acquisition. This will involve analyzing learning outcomes—through both quantitative and qualitative methods—collected from thousands of users of the climate dashboards. Moreover, we will actively engage in dialogue with users of the *Teaching the Future* climate dashboards and maps to gather feedback, enhance user experience, and further improve the tool's functionality, ensuring the dashboards remain a dynamic and evolving tool for climate education.

Ultimately, the *Teaching the Future* climate dashboards serve as a model for leveraging geospatial technology in education, transforming climate data into actionable knowledge that inspires both awareness and meaningful action toward climate mitigation and adaptation.

Author Contributions: Rafael De Miguel González: conceptualization, visualization, writing—original draft, writing—review and editing, investigation, project administration; Juan Mar-Beguería: data curation, methodology, visualization, investigation, writing—original draft; writing—review and editing; María Sebastián López and Ondrej Kratochvíl: investigation, writing—original draft; writing—review and editing. This paper is part of a doctoral thesis supervised by the first signatory (Rafael De Miguel González) and carried out by the second signatory (Juan Mar-Beguería), financed by the University of Zaragoza (code PI-PRD-001/2023). All authors have read and agreed to the published version of the manuscript.

Funding: This research was funded by the European Commission project *Teaching the Future*, grant number 2021-1-BE02-KA220-SCH-000034478.

Data Availability Statement: Data that support the findings of this study are openly available on Copernicus websites: https://cds.climate.copernicus.eu/datasets/derived-era5-land-daily-statistics?tab=overview, https://cds.climate.copernicus.eu/datasets/insitu-gridded-observations-europe?tab=overview, https://cds.climate.copernicus.eu/datasets/projections-cmip5-monthly-single-levels?tab=overview (all accessed on 14 February 2025).

Acknowledgments: The authors would like to acknowledge the people who contributed to this project, either at the EUROGEO or the University of Zaragoza, the other project partners, and the teachers and students who piloted and tested the dashboards. This acknowledgment is specially given to Karl Donert, Luc Zwartjes, María Luisa de Lázaro, Miguel Ángel Saz, Martín de Luis, Samuel Esteban, María Zúñiga, and Ángel Pueyo.

Conflicts of Interest: The authors declare no conflicts of interest.

References

1. Bianchi, G.; Pisiotis, U.; Cabrera, M. *GreenComp The European Sustainability Competence Framework*; Publications Office of the European Union: Luxembourg, 2022. [CrossRef]
2. Mar-Begueria, J.; Saz, M.A.; De Miguel, R. Geoinformación y ciencia geográfica para la enseñanza y aprendizaje del cambio climático en educación secundaria: El proyecto Teaching the future. In *The Geography of the Place. The Place of Geography*; Editions University Castilla La Mancha: Ciudad Real, Spain, 2023; pp. 707–720.
3. Monroe, M.; Plate, R.; Oxarart, A.; Bowers, A.; Chaves, W.A. Identifying effective climate change education strategies: A systematic review of the research. *Environ. Educ. Res.* **2017**, *25*, 791–812. [CrossRef]
4. Chang, C.H. Climate Change Education. In *Knowing, Doing and Being*; Routledge: Abingdon, UL, USA, 2023; 246p.
5. Favier, T.; Van Gorp, B.; Cyvin, J.B.; Cyvin, J. Learning to teach climate change: Students in teacher training and their progression in pedagogical content knowledge. *J. Geogr. High. Educ.* **2021**, *45*, 594–620. [CrossRef]
6. Leal, W.; Lackner, B.; McGhie, H. *Addressing the Challenges in Communicating Climate Change Across Various Audiences*; Springer: Cham, Switzerland, 2019; 673p. [CrossRef]
7. Mitchell, J. Wicked from the Start: Educational Impediments to Teaching about Climate Change (and How Geography Education Can Help). *Educ. Sci.* **2023**, *13*, 1174. [CrossRef]
8. Hammond, L.; Fargher, M.; Walshe, N. Geography teacher educators' perspectives on education for sustainability: Identity and agency in a period of rapid education policy change in England. *Int. Res. Geogr. Environ. Educ.* **2024**, 1–18. [CrossRef]
9. Tabor, L. Using a GIS-Based Framework to Teach Climate Change in Kansas. Ph.D. Thesis, Kansas State University, Manhattan, KS, USA, 2016.
10. De Miguel, R.; Donert, K.; Koutsopoulos, K. *Geospatial Technology in Geography Education*; Springer: Cham, Switzerland, 2019; 219p. [CrossRef]
11. De Miguel, R.; De Lázaro, M.L. WebGIS Implementation and Effectiveness in Secondary Education Using the Digital Atlas for Schools. *J. Geogr.* **2020**, *119*, 74–85. [CrossRef]
12. De Miguel, R.; Donert, K. Geography and International Education. In *A Geographical Century: Essays for the Centenary of the International Geographical Union*; Springer: Cham, Switzerland, 2022; pp. 135–154. [CrossRef]
13. De Miguel, R.; Sebastián, M. Education on Sustainable Development Goals: Geographical Perspectives for Gender Equality in Sustainable Cities and Communities. *Sustainability* **2022**, *14*, 4042. [CrossRef]
14. Sebastián, M.; De Miguel, R. Mobile Learning for Sustainable Development and Environmental Teacher Education. *Sustainability* **2020**, *12*, 9757. [CrossRef]
15. De Miguel, R. Powerful geography and the future of geographic education. *Dialogues Hum. Geogr.* **2024**, *14*, 5–8. [CrossRef]
16. Fargher, M. WebGIS for Geography Education: Towards a GeoCapabilities Approach. *ISPRS Int. J. Geo-Inf.* **2018**, *7*, 111. [CrossRef]
17. Fargher, M.; Healy, G. Empowering geography teachers and students with geographical knowledge: Epistemic access through GIS. In *Geography Education in the Digital World: Linking Theory and Practice*; Walshe, N., Healy, G., Eds.; Routledge: Abingdon, UK, 2020; pp. 102–116.
18. He, Y.; Tani, S.; Puustinen, M. GeoCapabilities Approach to Climate Change Education: Developing an Epistemic Model for Geographical Thinking. *J. Geogr.* **2024**, *123*, 23–31. [CrossRef]
19. Zadrozny, J.; Crane, M.; Boehm, R.; Solem, M. Teaching Climate Change through Powerful Geography. *Geogr. Teach.* **2023**, *20*, 141–149. [CrossRef]
20. Owen, C.; Taylor, A. *Thinking Critically in Geography: Teaching Climate Change*; Geographical Association: Manchester, UK, 2024; 60p.
21. Schnitzler, C. Telling Human Stories of Climate Change with ArcGIS Story Maps. *Geogr. Teach.* **2020**, *17*, 169–172. [CrossRef]
22. Thürkow, D.; Lindau, A.; Schmidt, G.; Illiger, P.; Krause, C.; Gertsmann, H.; Schürmann, A. Using Interactive Story Maps Enriched by Direct Knowledge Queries for the Development of E-Learning Modules on Climate Change. *KN J. Cartogr. Geogr. Inf.* **2019**, *69*, 195–204. [CrossRef]
23. Cox, H.; Kelly, K.; Yetter, L. Using Remote Sensing and Geospatial Technology for Climate Change Education. *J. Geosci. Educ.* **2014**, *62*, 609–620. [CrossRef]
24. Asimakopoulou, P.; Nastos, P.; Vassilakis, E.; Hatzaki, M.; Antonarakou, A. Earth Observation as a Facilitator of Climate Change Education in Schools: The Teachers' Perspectives. *Remote Sens.* **2021**, *13*, 1587. [CrossRef]
25. Codato, D.; Tha, C.; Pappalardo, S.; Peroni, F.; Facchinelli, F.; Crescini, E.; De Marchi, M. Geo-ICTs for good: A MOOC on Gis-science for climate justice. *Int. Arch. Photogramm. Remote Sens. Spat. Inf. Sci.* **2022**, *48*, 103–110. [CrossRef]
26. De Lázaro, M.L.; De Miguel, R. *Sustainable Development goals in Europe. A Geographical Approach*; Springer: Cham, Switzerland, 2023; 371p. [CrossRef]
27. Adams, A.M.; Chen, X.; Li, W.; Zhang, C. Normalizing the pandemic: Exploring the cartographic issues in state government COVID-19 dashboards. *J. Maps* **2023**, *19*, 2235385. [CrossRef]

28. Haynes, D.; Ahmadkhani, M.; Numainville, J. The next generation of dashboards: A spatial online analytical processing (SOLAP) platform for COVID-19. *J. Maps* **2024**, *20*, 2276763. [CrossRef]
29. Geraghty, E.; Kerski, J. The Impact of COVID-19 on Geography, GIS, and Education. *J-Reading. J. Res. Didact. Geogr.* **2020**, *2*, 53–66. [CrossRef]
30. Logan, T.; Hobbs, M.; Conrow, L.; Reid, N.; Young, R.; Anderson, M. The x-minute city: Measuring the 10, 15, 20-minute city and an evaluation of its use for sustainable urban design. *Cities* **2022**, *131*, 103924. [CrossRef]
31. Conrow, L.; Fu, C.; Huang, H.; Andrienko, N.; Andrienko, G.; Weibel, R. A conceptual framework for developing dashboards for big mobility data. *Cartogr. Geogr. Inf. Sci.* **2023**, *50*, 495–514. [CrossRef]
32. Dundar, E. How Can A GIS Application Develop Geographical Skills of Students: The Case Dashboards. *J. Hum. Soc. Sci.* **2023**, *6*, 55–74. [CrossRef]
33. Kerski, J. Innovative Instruction Using Field Surveys, Interactive Maps, Dashboards, and Infographics. *Geogr. Teach.* **2021**, *18*, 45–54. [CrossRef]
34. Case, N. *Creating an ArcGIS Dashboard for Climate Data Management And Visualization*; Senior Independent Study Theses; The College of Wooster: Wooster, OH, USA, 2022; p. 9708.
35. Serrano, R.; Beguería, S.; de Luis, M. STEAD: A high-resolution daily gridded temperature dataset for Spain. *Earth Syst. Sci. Data* **2019**, *11*, 1171–1188. [CrossRef]
36. Copernicus Climate Change Service, Climate Data Store. CMIP5 Monthly Data on Single Levels. Copernicus Climate Change Service (C3S) Climate Data Store (CDS). 2018. Available online: https://cds.climate.copernicus.eu/datasets/projections-cmip5-monthly-single-levels?tab=overview (accessed on 14 February 2025).
37. Cornes, R.; Van der Schrier, G.; Van den Besselaar, E.; Jones, P. An Ensemble Version of the E-OBS Temperature and Precipitation Datasets. *J. Geophys. Res. Atmos.* **2018**, *123*, 9391–9409. [CrossRef]
38. Muñoz Sabater, J. ERA5-Land Monthly Averaged Data from 1950 to Present. Copernicus Climate Change Service (C3S) Climate Data Store (CDS). 2019. Available online: https://cds.climate.copernicus.eu/datasets/reanalysis-era5-land-monthly-means?tab=overview (accessed on 14 February 2025).
39. Zúñiga, M.; Pueyo, A.; Calvo, J.L. The Spanish population during the twentieth century and beyond. *J. Maps* **2012**, *8*, 386–391. [CrossRef]
40. Kerski, J.; Baker, T. Infusing Educational Practice with Web GIS. In *Geospatial Technologies in Geography Education*; Springer: Cham, Switzerland, 2019; pp. 3–19. [CrossRef]
41. Kerski, J. Teaching and Learning Geography with a Web GIS Approach. In *Re-Visioning Geography. Supporting the SDGs in the Post-COVID Era*; Springer: Cham, Switzerland, 2023; pp. 113–135. [CrossRef]
42. Bednarz, S.; Mitchell, J. *Handbook of Geography Education*; Springer: Cham, Switzerland, 2025; 961p. [CrossRef]
43. De Miguel, R.; de Lázaro Torres, M.L. Spain: Geography Education for Global Understanding. In *Geography Education for Global Understanding*; Springer: Cham, Switzerland, 2018; pp. 182–192. [CrossRef]
44. Bybee, R. *The BSCS 5E Instructional Model: Origins, Effectiveness, and Applications*; Biological Sciences Curriculum Study: Springs, CO, USA, 2006.

Disclaimer/Publisher's Note: The statements, opinions and data contained in all publications are solely those of the individual author(s) and contributor(s) and not of MDPI and/or the editor(s). MDPI and/or the editor(s) disclaim responsibility for any injury to people or property resulting from any ideas, methods, instructions or products referred to in the content.

International Journal of Geo-Information

MDPI

Article

Geoinformatics and Machine Learning for Shoreline Change Monitoring: A 35-Year Analysis of Coastal Erosion in the Upper Gulf of Thailand

Chakrit Chawalit [1], Wuttichai Boonpook [1,*], Asamaporn Sitthi [1], Kritanai Torsri [2], Daroonwan Kamthonkiat [3], Yumin Tan [4], Apised Suwansaard [5] and Attawut Nardkulpat [1]

[1] Department of Geography, Faculty of Social Sciences, Srinakharinwirot University, Bangkok 10110, Thailand; chakrit.chawalit@g.swu.ac.th (C.C.); asamaporn@g.swu.ac.th (A.S.); attawut.nardkulpat@g.swu.ac.th (A.N.)
[2] Hydro-Informatics Institute, Ministry of Higher Education, Science, Research and Innovation, Bangkok 10900, Thailand; kritanai@hii.or.th
[3] Department of Geography, Faculty of Liberal Arts, Thammasat University, Rangsit Campus, Khlong Nueng 12120, Thailand; daroonwan.k@arts.tu.ac.th
[4] School of Transportation Science and Engineering, Beihang University, Beijing 100191, China; tanym@buaa.edu.cn
[5] Department of Civil Engineering, Faculty of Engineering, Rajamangala University of Technology Rattanakosin, Salaya, Nakhon Pathom 73170, Thailand; apised.suw@rmutr.ac.th
* Correspondence: wuttichaib@g.swu.ac.th

Abstract: Coastal erosion is a critical environmental challenge in the Upper Gulf of Thailand, driven by both natural processes and human activities. This study analyzes 35 years (1988–2023) of shoreline changes using geoinformatics, machine learning algorithms (Random Forest, Support Vector Machine, Maximum Likelihood, Minimum Distance), and the Digital Shoreline Analysis System (DSAS). The results show that the Random Forest algorithm, utilizing spectral bands and indices (NDVI, NDWI, MNDWI, SAVI), achieved the highest classification accuracy (98.17%) and a Kappa coefficient of 0.9432, enabling reliable delineation of land and water boundaries. The extracted annual shorelines were validated with high accuracy, yielding RMSE values of 13.59 m (2018) and 8.90 m (2023). The DSAS analysis identified significant spatial and temporal variations in shoreline erosion and accretion. Between 1988 and 2006, the most intense erosion occurred in regions 4 and 5, influenced by sea-level rise, strong monsoonal currents, and human activities. However, from 2006 to 2018, erosion rates declined significantly, attributed to coastal protection structures and mangrove restoration. The period 2018–2023 exhibited a combination of erosion and accretion, reflecting dynamic sediment transport processes and the impact of coastal management measures. Over time, erosion rates declined due to the implementation of protective structures (e.g., bamboo fences, rock revetments) and the natural expansion of mangrove forests. However, localized erosion remains persistent in low-lying, vulnerable areas, exacerbated by tidal forces, rising sea levels, and seasonal monsoons. Anthropogenic activities, including urban development, mangrove deforestation, and aquaculture expansion, continue to destabilize shorelines. The findings underscore the importance of sustainable coastal management strategies, such as mangrove restoration, soft engineering coastal protection, and integrated land-use planning. This study demonstrates the effectiveness of combining machine learning and geoinformatics for shoreline monitoring and provides valuable insights for coastal erosion mitigation and enhancing coastal resilience in the Upper Gulf of Thailand.

Keywords: coastal erosion; machine learning; shoreline extraction; Upper Gulf of Thailand; remote sensing; digital shoreline analysis system (DSAS)

1. Introduction

Coastal erosion is a natural process influenced by dynamic forces such as wave action, wind, water flow, sea level rise, and sediment transport [1]. In recent years, global warming has intensified these processes, leading to rapid glacier melting, rising sea levels, and stronger storm surges [2]. Rising sea levels and climate change exacerbate coastal erosion, endangering ecosystems, disrupting local economies, and threatening the livelihoods of millions of coastal residents. With a coastline extending approximately 3151 km, Thailand faces significant challenges due to coastal erosion. The Gulf of Thailand accounts for 2039.78 km of this coastline, while the Andaman Sea contributes 1111.35 km. According to the Department of Marine and Coastal Resources report [3], about 69.74 km of Thailand's coastline experienced erosion in 2022, categorized into high erosion (29.88 km), medium erosion (26.79 km), and low erosion (13.07 km). Since 1995, the upper Gulf of Thailand has experienced severe erosion, with rates exceeding 25 m per year. This erosion is mainly caused by rising sea levels and extreme weather events, severely impacting muddy and sandy beaches with floodplain topography.

To monitor coastal erosion, there are two primary methods: ground surveys, and remote sensing technology. Ground surveys, while highly accurate, require significant manpower, time, and financial resources [4]. For example, Bird et al. [5] employed radar-based methods to monitor coastal morphological changes. While these methods offer real-time monitoring capabilities, they are limited by their smaller spatial coverage. In contrast, remote sensing techniques utilize two main data sources including aerial photographs and satellite imagery. Aerial photographs [6,7] and unmanned aerial vehicle (UAV) images [8,9] provide high spatial resolution and broad coverage. However, their use can be costly due to the need for frequent flights and the complexity of image processing. Satellite imagery offers high spatial resolution, wide coverage, multispectral capabilities, and frequent data acquisition, making it ideal for continuous coastal monitoring [10]. Synthetic aperture radar (SAR) imagery provides systematic, near-daily acquisitions with all-weather capabilities. Its meter-level spatial resolution makes it highly effective for shoreline extraction [11]. However, SAR images do not represent land use features, making it challenging to identify specific land use changes. In contrast, optical satellite imagery provides clearer land use features, making it more suitable for detecting and monitoring land use changes over time. For example, Xu [12] used Landsat imagery from 1986 to 2015 to monitor shoreline dynamics in Texas, revealing significant erosion, with 52.58% of the coastline affected over 30 years. In Thailand, Kamthonkiat et al. [13] utilized time-series remotely sensed data from Landsat and ASTER between 1991 and 2010 to estimate erosion and accretion rates before and after the 2004 Indian Ocean tsunami. Ajira Thiangtrong [14] used Landsat 5 imagery to monitor coastal changes in Ban Laemsing, Samut Prakan, improving the differentiation between land and sea using multispectral bands. The study identified significant erosion, particularly exacerbated by human activities, and highlighted its impact on mangrove forests. Similarly, Supawat Inkerd et al. [15] used Landsat imagery and aerial photographs to digitize shorelines and monitor changes in the Andaman Sea region, identifying significant erosion and accretion between 1995 and 2019, particularly in areas such as Chang Lang Beach and Pak Meng Beach. Pattrakorn Nidhinarangkoon and Sompratana Ritphring [4] conducted a comparative study of shoreline detection methods, utilizing satellite imagery from Google Earth to digitize shorelines and monitor coastal

changes, with a focus on correcting for tidal effects. In recent years, satellite remote sensing has become increasingly pivotal for coastal monitoring, providing valuable data on shoreline dynamics at both local and global scales.

Manual digitization methods can provide accurate shoreline extraction but are time-consuming and costly, prompting researchers to explore more efficient techniques. Recent advances in remote sensing have enabled the integration of automated image-processing techniques to improve shoreline monitoring. Several studies have utilized indices such as the Modified Normalized Difference Water Index (MNDWI) and the Normalized Difference Water Index (NDWI) for coastal line extraction. For instance, Kim et al. [16] applied MNDWI on Landsat imagery from 1985 to 2011, combined with the Canny Edge Detection Algorithm, to automatically extract and monitor shoreline changes. Their analysis revealed an average coastal erosion rate of 6.4 m per year, with a total coastline retreat of approximately 166 m over 26 years. Similarly, Ghosh et al. [17] also used MNDWI on Landsat imagery from 1989 to 2010 to digitize shorelines, revealing significant erosion in the northern and western parts of Hatiya Island, along with accretion in the southern and eastern regions. Furthermore, Maglione et al. [18] enhanced shoreline extraction using NDVI and NDWI indices, combined with pan-sharpening techniques on high-resolution WorldView-2 imagery, resulting in more accurate coastline delineation in the Campania region of Italy. The integration of satellite imagery with machine learning (ML) techniques has transformed coastal monitoring by allowing the automated extraction of shoreline features with higher precision and efficiency [19].

ML algorithms have gained prominence in shoreline extraction and classification tasks due to their ability to handle complex datasets and improve classification accuracy. For instance, Fatah et al. [20] employed multiple ML models, including XGBoost (version 1.6.2), Random Forest (RF), and Decision Tree (DT), to delineate groundwater potential zones (GWPZs) in Iraq's Kurdistan region using geoinformatics-based modeling. Similarly, Rash et al. [21] utilized multi-temporal Landsat imagery to analyze LULC changes over three decades in the Kurdistan Region, Iraq, demonstrating that RF outperformed other classifiers in accuracy and consistency. Recent studies have further refined these techniques; Sun et al. [22] found that that Landsat and Sentinel-2 have significantly advanced the ability to monitor coastal changes over time. This provides more frequent revisits and multispectral capabilities, enhancing the precision of coastline delineation. ML algorithms, such as the Minimum Distance Classifier (MDC), Maximum Likelihood Classifier (MLC), K-Nearest Neighbor (KNN), K-Means, ISODATA, Artificial Neural Networks (ANNs), Random Forest (RF), and Support Vector Machines (SVM), have proven effective for feature classification. These methods improve the accuracy and efficiency of distinguishing features like land, water, and vegetation compared to traditional techniques. For instance, a recent study by Kannan et al. [23] explored the use of SVM for shoreline extraction. Choung and Jo [24] compared traditional water-index methods with ML algorithms, demonstrating the superiority of SVM for shoreline extraction, particularly in challenging coastal conditions. Similarly, Minghelli et al. [25] focused on improving shoreline extraction by addressing foam pixel interference in WorldView-2 imagery, demonstrating that SVM outperformed traditional classification methods in accurately delineating shorelines, especially in coastal areas affected by natural events like the Tohoku tsunami. Bamdadinejad et al. [26] compared shoreline extraction methods using Landsat imagery and found that SVM outperformed MLC in detecting shoreline changes along the Persian Gulf, particularly in areas affected by erosion and accretion. Zhou et al. [27] reviewed the growing importance of ML in coastline extraction, emphasizing its ability to efficiently process large-scale data. Algorithms like RF, SVM, and Convolutional Neural Networks (CNNs) have proven effective for classifying

coastal features such as land, water, and vegetation. Additionally, indices like NDWI and MNDWI have improved coastline detection accuracy across various environments.

As a recent and effective method for shoreline extraction, Vos et al. [28] introduced CoastSat as a reliable platform for global shoreline extraction, demonstrating its ability to produce accurate results. Curoy et al. [29] further validated CoastSat's performance by using it to digitize a time series of shoreline positions in southern Thailand. However, local environmental factors, such as sediment type, seasonal monsoon effects, and water clarity, can influence the accuracy of shoreline extraction. Therefore, customizing the algorithm to account for these regional variations is essential for capturing shoreline dynamics accurately in specific coastal regions. Additionally, the choice of ML algorithm plays a crucial role in ensuring the accuracy and reliability of shoreline extraction. Applying multiple indices enhances feature differentiation, improving the classification of coastal features. This study employs MDC, MLC, SVM, and RF for shoreline extraction, each chosen for its strengths. MDC is fast and efficient for well-separated spectral classes, while MLC handles spectral overlaps, making it robust for coastal mapping. SVM excels in complex land–water boundaries, and RF, a powerful ensemble method, ensures high accuracy with minimal tuning. This selection provides a comprehensive evaluation, optimizing shoreline classification accuracy.

For coastal change analysis, the Digital Shoreline Analysis System (DSAS) has been widely adopted for monitoring and analyzing shoreline changes [30,31]. The DSAS was applied to calculate rates of change using a series of historical shoreline positions extracted from remote sensing imagery. Numerous studies have successfully adopted the DSAS in different regions. Kannan et al. [23] employed the DSAS to assess shoreline changes along the Visakhapatnam coast from 1989 to 2015, utilizing multi-temporal satellite imagery from Landsat and IRS-P6 LISS sensors. Goksel et al. [32] focused on the Black Sea region in Istanbul, Turkey, using the DSAS alongside the MLC of Landsat-7 and Landsat-8 imagery to analyze shoreline changes between 2009 and 2016. Similarly, Wang et al. [33] utilized the DSAS to study coastal changes in Ningbo, China, specifically in Hangzhou Bay, Xiangshan Bay, and Sanmen Bay from 1976 to 2015, employing automatic shoreline extraction using NDWI and MNDWI indices. Darwish and Smith [34] compared the performance of Landsat-8, PlanetScope, and Sentinel-2 imagery for detecting coastline changes in El-Alamein, Egypt, from 2016 to 2021, utilizing the DSAS to analyze shoreline dynamics. Rumahorbo et al. [35] applied the DSAS to monitor shoreline changes in Supiori Regency, Indonesia, revealing significant erosion rates ranging from 1.22 to 1.46 m per year, and accretion rates ranging from 1.05 to 1.68 m per year. Chettiyam Thodi et al. [36] integrated remote sensing and GIS techniques for shoreline monitoring in coastal islands of Kerala, India, from 1973 to 2019, utilizing Landsat imagery for shoreline digitization and applying the DSAS to calculate erosion and accretion change rates. Quang et al. [37] employed the DSAS to analyze shoreline changes in Quang Nam, Vietnam, using the MNDWI index to extract annual shorelines from Landsat and Sentinel-2 imagery.

In Thailand, Oraon Sarajit and Kanchana Kakhapalorn [38] assessed coastal erosion in Phetchaburi province using Landsat TM-5 and THEOS imagery from 2001 to 2011. Their study focused on the impacts of seasonal monsoons on shoreline changes. Similarly, Wuttipong Sangmanee and Chanchai Thanawut [39] used the DSAS to assess shoreline changes in Pattani province from 1975 to 2011, emphasizing the influence of coastal defense structures on erosion and accretion rates. Aekkarak Faiboob and Wutthipong Seangmenee [40] analyzed shoreline changes at the estuary of Songkhla lake, focusing on the impact of coastal engineering structures over 48 years (1967–2015) using remote sensing data and the DSAS. Anutin Kongkhan [41] utilized time-series remote sensing imagery to analyze shoreline changes and assess coastal erosion in Samut Prakan and Chachoengsao provinces from

2017 to 2020. More recently, Pawornprach Imlamai et al. [42] utilized Landsat 8 imagery and applied the DSAS to assess shoreline changes and evaluate erosion in Phetchaburi province, employing the Normalized Shoreline Change Index (NSMI) and Normalized Difference Shoreline Index (NDSSI) for enhanced shoreline area analysis. It was reported that coastal erosion remains high in the Upper Gulf of Thailand. While these studies demonstrate the effectiveness of the DSAS in tracking shoreline changes, many rely on medium-resolution imagery, limited machine-learning approaches, and shorter temporal scopes.

This research builds upon previous work by addressing the severe coastal erosion observed in the Upper Gulf of Thailand through the use of modern geoinformatics techniques. This study uses remote sensing data and ML algorithms (MDC, MLC, SVM, and RF) to automatically extract and classify coastal lines over a 35-year period (1988–2023), leveraging their efficiency and accuracy in handling complex datasets. Additionally, multiple normalized indices are applied to enhance land use feature extraction, water frequency index (WFI) is used for shoreline extraction, and the DSAS is used to analyze coastal changes and erosion rates. The goal is to develop a more efficient and accurate approach to monitoring coastal changes and informing strategies to mitigate the impacts of coastal erosion.

2. Study Area

This research focuses on the Upper Gulf of Thailand, encompassing the coastlines of eight provinces: Prachuap Khiri Khan, Phetchaburi, Samut Songkhram, Samut Sakhon, Samut Prakan, Bangkok, Chachoengsao, and Chonburi. The study area spans approximately 407 km along the coastline, as depicted in Figure 1. This region was selected due to its high susceptibility to coastal erosion, consistently observed from 1995 to 2023. The majority of the coastline consists of sandy and muddy beaches with a flat terrain. These features make it highly vulnerable to coastal retreat caused by tidal surges and other natural forces.

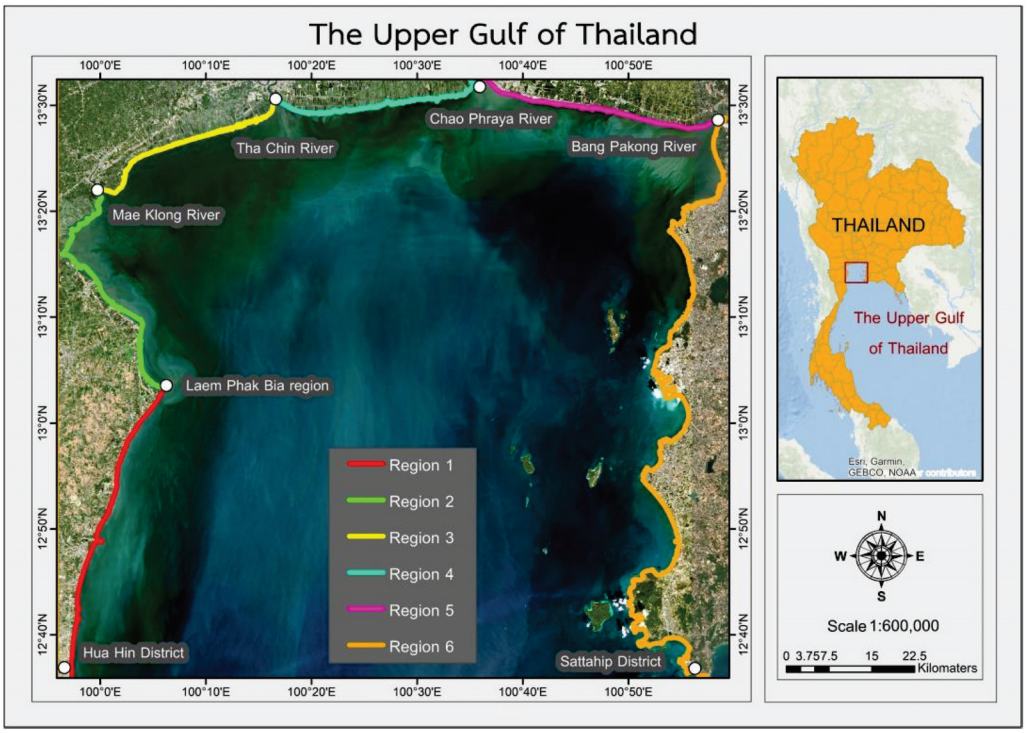

Figure 1. Map of the study area in the Upper Gulf of Thailand which is divided into six regions based on physical characteristics.

The study area is characterized by low-lying, flat coastal plains, particularly in regions with extensive mudflats. The flat terrain and proximity to sea level make the region highly susceptible to flooding, amplifying the effects of tidal action, storm surges, and extreme weather events. While storm surges and cyclonic events can cause rapid and severe coastal changes, it is crucial to understand their interaction with sea-level rise, as storms often amplify the impacts of rising sea levels in vulnerable areas. For example, storm surges associated with tropical storms and cyclones can lead to short-term, high-intensity erosion events, accelerating shoreline retreats in regions already stressed by gradual sea-level rise. This dynamic interplay between long-term processes, like sea-level rise, and short-term events, such as storms, adds complexity to the interpretation of coastal changes observed through satellite imagery. Differentiating between gradual erosion driven by sea-level rise and episodic, intense changes caused by storms is essential for accurate coastal monitoring. Natural features such as mangrove forests and mudflats provide some protection against storms and rising sea levels, but the overall low elevation of the region amplifies its vulnerability to both gradual and sudden coastal changes.

The climate of the Upper Gulf of Thailand is tropical monsoon, with three distinct seasons: the rainy season (May to October), the summer season (March to May), and the winter season (November to February). The rainy season is dominated by the southwest monsoon, which brings heavy rainfall that contributes to storm surges, exacerbating coastal erosion in low-lying areas. During this season, the wind pattern drives a clockwise circulation, especially along the western coast. The summer season experiences high temperatures and generally dry conditions, with occasional thunderstorms. During this transitional period, water flows from the south, moving eastward or southward based on monsoonal influences. The winter season is dominated by the northeast monsoon, which brings cooler and drier air, accompanied by moderate winds that reduce the intensity of coastal erosion compared to the rainy season. During this period, counterclockwise circulation prevails, driven by northeast winds that push water into the southern part of the gulf and out through the eastern coast [43,44]. The coastal changes in the study area result from a complex interplay of factors, including long-term sea-level rise, seasonal variations in storm intensity, and episodic extreme weather events. These dynamic drivers, coupled with the region's low-lying topography, make the Upper Gulf of Thailand particularly vulnerable to both gradual and rapid coastal change processes. Despite these challenges, this study primarily focuses on the slow, progressive effects of sea-level rise, which has been identified as the dominant long-term driver of coastal erosion in the region.

Due to the large size of the study area and its diverse physical characteristics, the region was divided into six sub-regions for analysis, as shown in Figure 1. These sub-regions are Hua Hin District–Laem Phak Bia (Region 1), Laem Phak Bia–Mae Klong River (Region 2), Mae Klong River–Tha Chin River (Region 3), Tha Chin River–Chao Phraya River (Region 4), Chao Phraya River–Bang Pakong River (Region 5), and Bang Pakong River–Sattahip District (Region 6).

3. Materials and Methods

3.1. Materials

To monitor coastal erosion, satellite imagery, geospatial data, and other relevant datasets were employed to analyze shoreline changes in the Upper Gulf of Thailand over an extended period. A summary of the data used is provided in Table 1. The research employs two primary datasets, one focused on shoreline changes and the other on physical geography. The first dataset focuses on analyzing shoreline changes. It includes Landsat imagery for land and water classification, used to create annual shoreline data and generate training and validating datasets. Shoreline data for 2018 and 2023 serve as reference points

for validation. Additionally, land use shapefiles provide yearly information on LULC changes in coastal areas. The second dataset provides physical geography insights. It includes sea-depth data for underwater topography, a digital elevation model (DEM) for onshore topography, and annual global sea level and temperature data for tracking trends. Additionally, it includes local sea level and temperature data from the Upper Gulf of Thailand and geological maps for analyzing coastal characteristics.

Table 1. Summary of datasets used for shoreline analysis in the Upper Gulf of Thailand.

Data Type	Period	Details	Source
Landsat 5, 7, 8, 9	1988–2023	A 30 m spatial resolution collected from Path 129/Row 051 which underwent atmospheric correction, representing the Upper Gulf of Thailand for land–water classification and shoreline extraction.	United States Geological Survey (USGS)
Land Use/Land Cover Types	1988, 1994, 2000, 2006, 2011, 2018, 2023	ESRI shapefiles covering coastal provinces in the Upper Gulf of Thailand, used for analyzing land use and coastal changes.	Land Development Department, Thailand
Shoreline Data	2019, 2022	ESRI shapefiles derived from digitization combined with GNSS surveys, used to validate extracted shorelines.	Department of Marine and Coastal Resources, Thailand
Digital Elevation Model	2000	A 90 m spatial resolution covering the Upper Gulf of Thailand, used to represent onshore topography	United States Geological Survey (USGS)
Annual Global Mean Sea Level Data	1987–2023	Represents global annual sea level averages in centimeters.	The National Aeronautics and Space Administration (NASA), USA
Annual Global Average Temperature Data	1987–2023	Represents global annual temperature averages in degrees Celsius.	The National Aeronautics and Space Administration (NASA), USA
Annual Mean Sea Level (Upper Gulf of Thailand)	1987–2023	Collected from four stations around the Gulf of Thailand (Bang Pakong, Ban Laem, Samut Sakhon, Ao Udom), representing local annual sea level trends in centimeters.	Marine Department, Thailand
Annual Average Temperature (Upper Gulf of Thailand)	1987–2023	Collected from weather stations (Phetchaburi, Bangkok, Samut Prakan, Chonburi) to monitor regional temperature changes.	Meteorological Department, Thailand
Sea Depth Data	-	Sixteen nautical chart sections of the Upper Gulf of Thailand presented in raster format representing underwater topography.	Hydrographic Department, Royal Thai Navy
Geological Maps	-	Scale of 1:250,000 covering four sections of the Upper Gulf of Thailand, used to analyze geological characteristics.	Department of Mineral Resources, Thailand.

3.2. Methods

The process of this research is divided into several key steps, including data preparation, training data, ML classification, accuracy assessment, shoreline extraction, shoreline assessment, shoreline change analysis, and the analysis of the causes of coastal changes. The process of each step is shown in Figure 2 and is explained in the following sections.

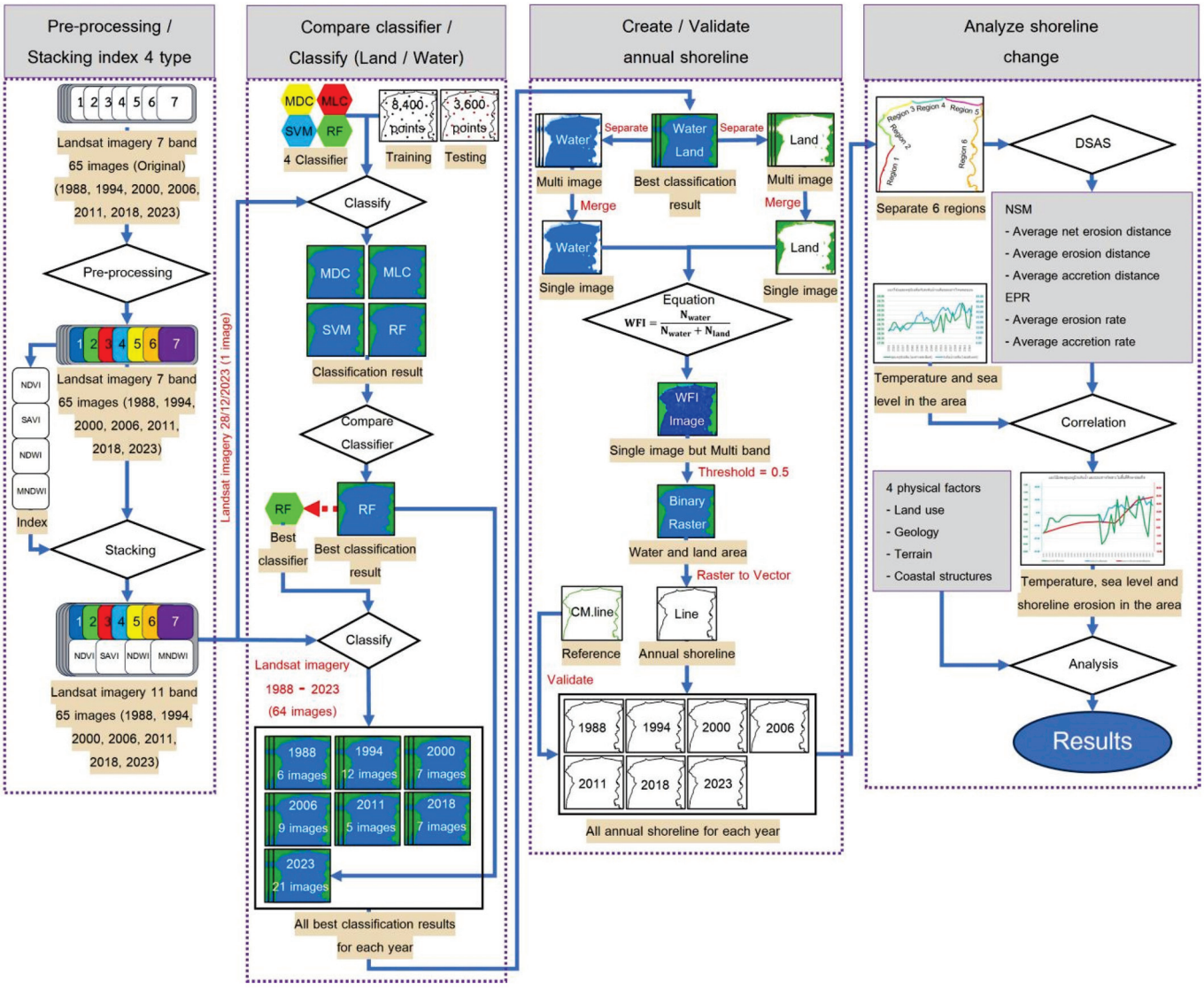

Figure 2. Workflow of the research methodology used for shoreline change analysis in the Upper Gulf of Thailand.

3.2.1. Data Preparation

Data Preprocessing

The collected satellite images and geospatial data were preprocessed to ensure correct data formats and coordinate systems. All Landsat imagery was georeferenced to a reference image using the UTM WGS84 zone 47N coordinate system to ensure spatial consistency. All shapefiles used in this research were reprojected to align with the Landsat data.

Index Calculation

Spectral Indices are used to improve the land–water distinction. These indices serve a specific role in enhancing shoreline detection. They provide a more comprehensive approach to accurately detecting and mapping shorelines.

The Normalized Difference Water Index (NDWI), as shown in Equation (1), is designed to enhance water bodies in satellite images by maximizing the difference between near-infrared (*NIR*) and green wavelengths. This index is effective in separating water from land and enhances the shoreline boundary, making it suitable for identifying the water–land transition zone. However, it may misclassify shallow water mixed with vegetation as land.

$$\text{NDWI} = \frac{Green - NIR}{Green + NIR} \tag{1}$$

The Modified Normalized Difference Water Index (MNDWI), as shown in Equation (2), is an adjustment of the NDWI that replaces the *NIR* band with a shortwave infrared (*SWIR*) band. This modification helps reduce noise caused by built-up areas and vegetation, improving the distinction between water and non-water features, particularly in urbanized coastal zones. The MNDWI sharpens the boundary between water and land, making it more effective in areas with significant anthropogenic features. However, it is less effective in distinguishing water from non-vegetated land.

$$\text{MNDWI} = \frac{Green - SWIR}{Green + SWIR} \tag{2}$$

In contrast, the NDWI was chosen for this study due to the natural characteristics of the Upper Gulf of Thailand, where water–land boundaries are primarily defined by natural features such as beaches and mangroves. The NDWI proved effective in these regions, while MNDWI may be more suitable for coastal zones with greater urbanization.

The Normalized Difference Vegetation Index (NDVI), as shown in Equation (3), is primarily used for vegetation analysis. It takes advantage of the fact that healthy vegetation reflects more *NIR* light and absorbs visible red light. This index is often used to assess the presence and condition of vegetation. It can indirectly assist shoreline analysis by identifying and excluding vegetated areas along the coastline and refining water–land boundary detection, especially in mangrove areas. In contrast, it performs poorly in distinguishing water from non-vegetated land.

$$\text{NDVI} = \frac{NIR - Red}{NIR + Red} \tag{3}$$

The Soil Adjusted Vegetation Index (SAVI), as shown in Equation (4), is a modification of NDVI that accounts for the influence of soil brightness in areas with sparse vegetation. It introduces a correction factor (L) to minimize soil effects, making it useful in areas where vegetation does not fully cover the soil. It is helpful in coastal areas with sparse vegetation or where bare soil is present. It improves shoreline mapping by distinguishing vegetation from soil, thus refining the boundary between vegetated land and water. However, it struggles with pure water detection and misclassifies blended vegetation and soil.

$$\text{SAVI} = \frac{(1 + L)(NIR - Red)}{NIR + Red + L} \tag{4}$$

Layer Stacking

This process produced a set of stacked spectral bands and expanded indices. For Landsat 5 and Landsat 7, the stacked images included the bands Blue, Green, Red, Near Infrared (*NIR*), Shortwave Infrared 1 (SWIR1), and Shortwave Infrared 2 (SWIR2), along with the indices NDVI, NDWI, MNDWI, and SAVI. For Landsat 8 and 9, the stacked images included Coastal Aerosol, Blue, Green, Red, NIR, SWIR1, SWIR2, and the same four indices. These stacked images are used in land-use classification.

3.2.2. Training Data

To prepare the training data for classification, land use data were simplified into two main categories: water and land. The number of samples was determined by using the ratio of water and land. This was combined with a stratified sampling strategy to ensure an appropriate distribution of sample points that accurately represented the different land cover types. All 65 Landsat images were used to collect data samples. A stratified random sampling approach was applied to ensure that the sample groups were well distributed across the study area and proportionally representative of water and land cover types. The total of the data samples is 12,000 sets. To create the training dataset, 70% of the sample sets were designated as training data, while the remaining 30% were used as testing data as shown in Table 2. This division ensured that the training and testing datasets were mutually exclusive, preventing overlap and enhancing the reliability of the classification model.

Table 2. Number of data samples used for training and testing in the land and water classification process.

Sample Sets	Training	Testing
Land cover types (Land/Water)	8400	3600

3.2.3. Machine Learning Classification

To classify land and water areas using Landsat imagery, Kim et al. [45] highlighted the frequent application of RF, ANN, and SVM in environmental research. This study draws from the findings of Sun et al. [22], who highlighted the increasing role of ML algorithms in coastal extraction. The performance of algorithms such as SVM, MLC, and RF, which demonstrated high accuracy, was also noted by Kannan et al. [23], Choung and Jo [24], Bamdadinejad et al. [26], Goksel et al. [32], and Zhou et al. [27]. These algorithms were selected for their respective strengths in handling the complexities of coastal image data, fast processing capabilities, and minimal parameter requirements. While CNNs excel in high-resolution imagery, their high computational demands and extensive training requirements make them less suitable for multi-decadal shoreline monitoring with Landsat imagery. Based on these considerations, four ML algorithms were employed in this study including MDC, MLC, SVM, and RF. Each algorithm was chosen for its specific advantages and suitability for the task of shoreline classification. MDC was included as a baseline method due to its simplicity, speed, and efficiency, particularly in cases where computational resources are limited or when quick classifications are needed. MDC is effective in scenarios with well-separated classes where there is little overlap between land and water. The algorithm calculates the Euclidean distance between pixel values in the feature space, assigning each pixel to the class with the nearest mean value. MLC was selected for its probabilistic approach, assuming that data within each class follows a normal distribution. This method performs well when the classes are well-defined, and the data meet these assumptions. MLC is robust in handling overlapping classes, which is common in coastal environments where water, sand, and vegetation may blend. SVM was included due to its strength in handling nonlinear boundaries and its capability to perform well with high-dimensional data, such as satellite imagery with many bands. SVM is well-regarded for its robustness in creating hyperplanes that maximize the margin between classes, making it effective even with smaller training datasets. However, it requires careful tuning of parameters to achieve optimal performance. In this study, the regularization parameter (C) and kernel parameters (gamma and epsilon) were optimized, with gamma set to 30,000 and error control set to 600. The Radial Basis Function (RBF) kernel was chosen due to its effectiveness in mapping data into higher-dimensional spaces, enhancing the separability of classes. To further improve the algorithm's performance, grid search combined with

cross-validation was applied to systematically fine-tune the parameters. RF was selected for its capability to handle complex and heterogeneous datasets, as well as its robustness to noise, as confirmed by Agarwal et al. [46], who demonstrated its effectiveness in modeling groundwater storage variations with minimal sensitivity to noise and data heterogeneity. This characteristic is particularly essential for coastal regions characterized by diverse land cover, water reflections, and seasonal variability. RF operates as an ensemble learning method, combining multiple decision trees to reduce the risk of overfitting and enhance classification accuracy. In this study, the RF hyperparameters were optimized using random search to achieve optimal performance. The key parameters included the number of trees set to 20, the maximum depth set to 600, and the minimum number of samples required for splitting nodes set to 20.

To compare the effectiveness of these algorithms, Landsat-8 imagery from 28 December 2023 was selected as the test dataset due to its cloud-free conditions and minimal atmospheric distortion, and the algorithm with the best performance in terms of both overall accuracy and Cohen's Kappa was then applied to classify the remaining 64 Landsat images from 1988 to 2023, ensuring consistency in shoreline extraction across the entire study period.

3.2.4. Accuracy Assessment

The classification results were validated using 30% of the data as testing data, distinct from the training data. The accuracy of the classifications was calculated using two metrics such as overall accuracy, and Cohen's Kappa coefficient. The accuracy results of the four classification methods were then evaluated for the performance of land-use classification.

3.2.5. Shoreline Extraction

In this process, classification images are used to generate annual shoreline representations. This approach aims to minimize the effects of varying sea levels in different images, ensuring more consistent and accurate shoreline detection. One consideration in this process is the potential impact of tidal range on shoreline position. While tidal fluctuations can lead to short-term variations in shoreline location, the methodology used in this study focuses on mean sea level and does not explicitly account for tidal range variations. Given the relatively flat topography of the study area and focus on annual shoreline changes, the tidal range is assumed to have a minimal impact on the overall shoreline extraction process. The first step in shoreline extraction is the binary raster creation. The classification results of all 65 satellite images were divided into seven time periods. The classified images were reprocessed into Binary Raster maps, separating them into two maps: water map and land map. In the water map, water pixels were assigned a value of 1, and land pixels were assigned a value of 0. In contrast, in the land map, land pixels were assigned a value of 1, and water pixels were assigned a value of 0. The results were a set of binary raster maps distinguishing water and land. The second step is the aggregation of the water raster. The binary raster maps for water areas (water = 1, land = 0) from each image were aggregated to create a single water raster for that year. Similarly, the binary raster maps for land areas (water = 0, land = 1) were aggregated to generate a single land raster for each year. The third step is the Water Frequency Index (*WFI*) calculation. This method calculated the *WFI* from the water and land raster maps based on Equation (5). The output is a *WFI* image that represents the separation between land and water.

$$WFI = \frac{N_{Water}}{N_{Water} + N_{Land}} \tag{5}$$

where N_{Water} is the number of water pixels and N_{Land} is the number of land pixels.

The fourth step involves thresholding each *WFI* image to create the shoreline. A threshold of 0.5 was used, where pixel values greater than or equal to 0.5 were defined as water areas, and pixel values less than 0.5 were defined as land areas. This thresholding process follows the approach by Quang et al. [37] and Xu et al. [12]. The output of the thresholding process is a set of binary raster shoreline images. The fifth step is the conversion of raster to vector. The binary raster shoreline images were then converted into vector files (ESRI shapefile format), representing the shoreline as a line feature for each period. Lastly, the sixth step is the refinement of shoreline data. The vector line data for all seven years were refined by removing estuary and canal areas, focusing exclusively on the coastal shorelines. The result was a single annual shoreline vector.

3.2.6. Shorelines Assessment

Due to the large size of the study area and the long duration of the study, there were limitations in accessing historical shoreline data for certain years, including 1988, 1994, 2000, 2006, and 2011. The shoreline data for the Upper Gulf of Thailand, as generated by the Department of Marine and Coastal Resources for their report on Thailand's coastal conditions, was used. This included data for two years, 2018 (using 2019 data as a substitute) and 2023 (using 2022 data as a substitute), to verify the accuracy of the extracted annual shorelines. The verification process involved the following steps. The first step is to buffer the shoreline data by 30 m. This buffer parameter is to match the resolution of the Landsat images. The result is a reference shoreline in the polygon feature type with a 30 m width on both sides for the years 2019 and 2022. The second step is to verify the accuracy of the extracted annual shorelines. This involved overlaying the extracted annual shorelines in the line feature types for the years 2018 and 2023 with the reference shoreline in the polygon feature types for the years 2019 and 2022. The intersected areas were then calculated, and the accuracy was expressed as a percentage using the following Equation (6). The result was the accuracy of the extracted shorelines for the years 2018 and 2023.

$$\text{Percentage of shoreline accuracy} = \frac{\text{Length of Intersect Line}}{\text{Length of Extracted Shoreline}} \times 100 \tag{6}$$

While the percentage overlap method is simple and effective for general validation, it does not account for regional specificities and may overlook smaller errors that can be significant in certain areas, especially where classification errors are more pronounced. To address this limitation, the Root Mean Square Error (*RMSE*) metric was incorporated for a more comprehensive evaluation. *RMSE* quantifies the difference between the reference and extracted shorelines by squaring the errors, averaging them, and then taking the square root, as shown in Equation (7). This metric is particularly effective in highlighting larger discrepancies, which are more common in regions with complex shorelines.

$$RMSE = \sqrt{\frac{1}{n}\sum_{i=1}^{n}(x_i - y_i)^2} \tag{7}$$

where x_i and y_i are the coordinates of the reference and extracted shorelines, respectively. n is the total number of corresponding points used to calculate the error between the reference and extracted shorelines.

RMSE offers a more comprehensive validation of the shoreline extraction process by addressing both average errors and larger discrepancies that may occur in certain regions. When combined with the percentage overlap, they provide a more robust measure of the accuracy of the extracted shorelines, particularly in areas with complex coastal features or significant classification errors.

3.2.7. Analysis of Shoreline Changes Using the Digital Shoreline Analysis System (DSAS)

To analyze shoreline changes in the Upper Gulf of Thailand, this study employed the Digital Shoreline Analysis System (DSAS) following a structured workflow. The analysis consisted of four main steps. The first step is baseline creation. It involved the generation of inland baselines using verified annual shorelines. To establish an initial reference, a uniform buffer distance of 25 m per year was applied, based on the maximum recorded coastal erosion rate. To account for regional and temporal variations, buffer distances were adjusted according to observed erosion rates for each time period including 1988–1993 (6 years) set to 150 m, 1993–1999 (6 years) set to 150 m, 1999–2005 (6 years) set to 150 m, 2005–2010 (5 years) set to 125 m, 2010–2017 (7 years) set to 175 m, and 2017–2023 (5 years) set to 125 m. For the entire study period (1988–2023, 35 years), a cumulative buffer distance of 875 m was applied, calculated by multiplying the critical erosion rate (25 m per year) by the total number of years. The resulting baseline features were created as line datasets with attribute information corresponding to each period. The second step is annual shoreline preparation. This step involved processing annual shorelines, ensuring consistency and accuracy. Attribute data were assigned to each shoreline, with a default positional uncertainty of 30 m to reflect the spatial resolution of Landsat imagery. These shorelines were systematically organized for analysis across all six sub-regions and time periods. The third step is geodatabase creation and transect generation. A personal geodatabase was developed to store shoreline and baseline data for all sub-regions and time intervals. Transects were automatically generated at 50 m intervals along the shorelines, ensuring a systematic and spatially consistent framework for analysis. The final step is shoreline change calculation. The DSAS was used to compute two key shoreline change metrics including Net Shoreline Movement (NSM) measuring the total perpendicular movement of the shoreline over time, and End Point Rate (EPR) determining the rate of shoreline change by dividing the NSM by the corresponding time interval.

To maintain the accuracy of the analysis, estuaries and man-made structures along the coastline were excluded. The severity of shoreline changes was classified using the Department of Marine and Coastal Resources (DMCR) criteria, which categorize erosion and accretion rates into seven classes including Severe Erosion (>5 m/year), Moderate Erosion (1–5 m/year), Minor Erosion (0.5–1 m/year), Stable (−0.5–0.5 m/year), Minor Accretion (0.5–1 m/year), Moderate Accretion (1–5 m/year), and High Accretion (>5 m/year). The result was a spatially explicit map visualizing shoreline change severity, along with data on perpendicular shoreline movement across six time periods in six sub-regions.

3.2.8. Analysis of the Causes of Coastal Changes

To analyze the coastal change, three statistics were analyzed: annual average temperature from meteorological stations in or near the study area, annual average water level from water level stations in or near the study area, and annual average accumulated coastal erosion distance, calculated using the Digital Shoreline Analysis System (DSAS). The trends of these three statistics were observed to determine how they influenced the coastline in each sub-region. The analysis also considered other factors such as the area's topography, geology, land use, seasonal currents, and coastal structures. The result was an identification of the causes of coastal changes in each sub-region of the study area.

4. Results

In this study, the monitoring of shoreline changes was conducted using remote sensing, combined with shoreline analysis through the Digital Shoreline Analysis System (DSAS). The causes of shoreline changes were also analyzed based on various factors in the Upper Gulf of Thailand. The results of the study are coastal area classification results, annual

shoreline creation, accuracy verification of the annual shoreline, and coastal analysis using the digital shoreline analysis system.

4.1. Coastal Area Classification Results

To evaluate the performance of classification methods in the coastal area. Landsat-8 captured on 28 December 2023 was used for the classification test. A total of 12,000 points were used for both training data and testing data, with no overlap between the two datasets, as shown in Table 2. The coastal area was classified into two categories: water and land, using four classification methods: Minimum Distance to Means (MDC), Maximum Likelihood Classifier (MLC), Support Vector Machine (SVM), and Random Forest (RF). The overall accuracy and Cohen's Kappa Coefficient were used for evaluating these classification methods. The results are presented in Figure 3.

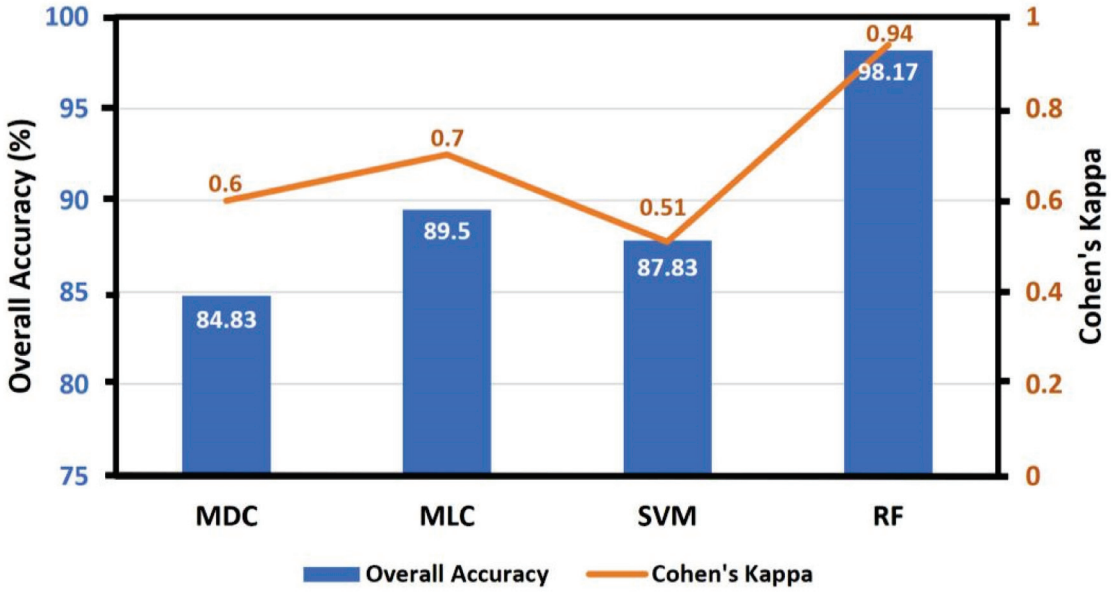

Figure 3. Compare the performance of classification algorithms including Minimum Distance, Maximum Likelihood Classifier, Support Vector Machine, and Random Forest in overall accuracy and Cohen's Kappa Coefficient.

As seen in Figure 3, the Random Forest (RF) method achieved the highest overall accuracy with 98.17% and 0.94 of Cohen's Kappa Coefficient. This method overcomes the maximum likelihood classifier method with 89.50% of overall accuracy and 0.69 of Cohen's Kappa Coefficient, the Support Vector Machine method with 87.83% of overall accuracy and 0.50 of Cohen's Kappa Coefficient, and the Minimum Distance to Mean (MDC) with 84.83% of overall accuracy and 0.59 of Cohen's Kappa Coefficient.

The classification results for land and water classes varied across the different algorithms as shown in Figure 4. The Minimum Distance algorithm struggled with errors, particularly misclassifying land as water in coastal fishing areas. Similarly, the Support Vector Machine (SVM) algorithm also showed high classification errors, especially in distinguishing coastal fishing areas and mangrove forests, where it often incorrectly classified mangrove areas as water. The Maximum Likelihood algorithm performed better in classifying mangrove forests but still encountered misclassification issues in coastal fishing zones. In contrast, the Random Forest algorithm significantly reduced classification errors in these challenging areas, particularly between water and coastal fishing regions. While the Random Forest algorithm provided more accurate results compared to the other methods, some minor errors persisted in regions where the distinction between land and water was not clearly defined in the imagery.

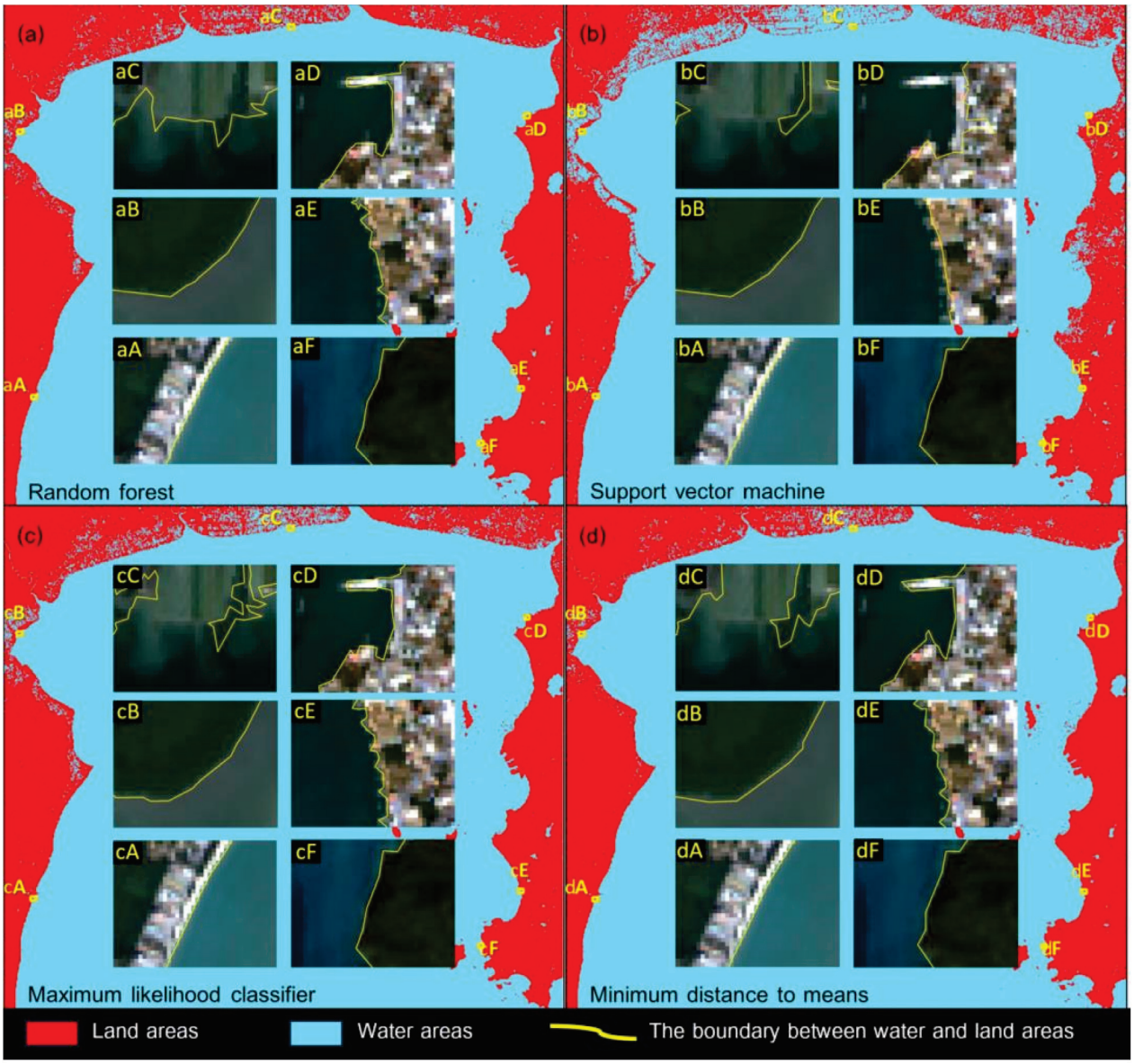

Figure 4. Classification results using four ML methods—Random Forest (**a**), Support Vector Machine (**b**), Maximum Likelihood Classifier (**c**), and Minimum Distance (**d**), for the Upper Gulf of Thailand. Each classification result illustrates the boundary between land and water in sample areas, including beach (**aA**,**bA**,**cA**,**dA**), mangrove forest (**aB**,**bB**,**cB**,**dB**), coastal fishing areas (**aC**,**bC**,**cC**,**dC**), shoreline protection structures (**aD**,**bD**,**cD**,**dD**), and steep cliffs (**aF**,**bF**,**cF**,**dF**).

Therefore, it was concluded that the most effective classification method is Random Forest. It was applied for classifying all 64 images that were captured from 1988 to 2023. The classification results shown in Figure 5 demonstrate that the overall accuracy ranged from 93.67% to 99.83%. Cohen's Kappa Coefficient ranged from 0.81 to 0.99. The average overall accuracy of over 65 images is 97.54%. These results confirmed that these classification results indicate excellent classification performance and are suitable for shoreline extraction.

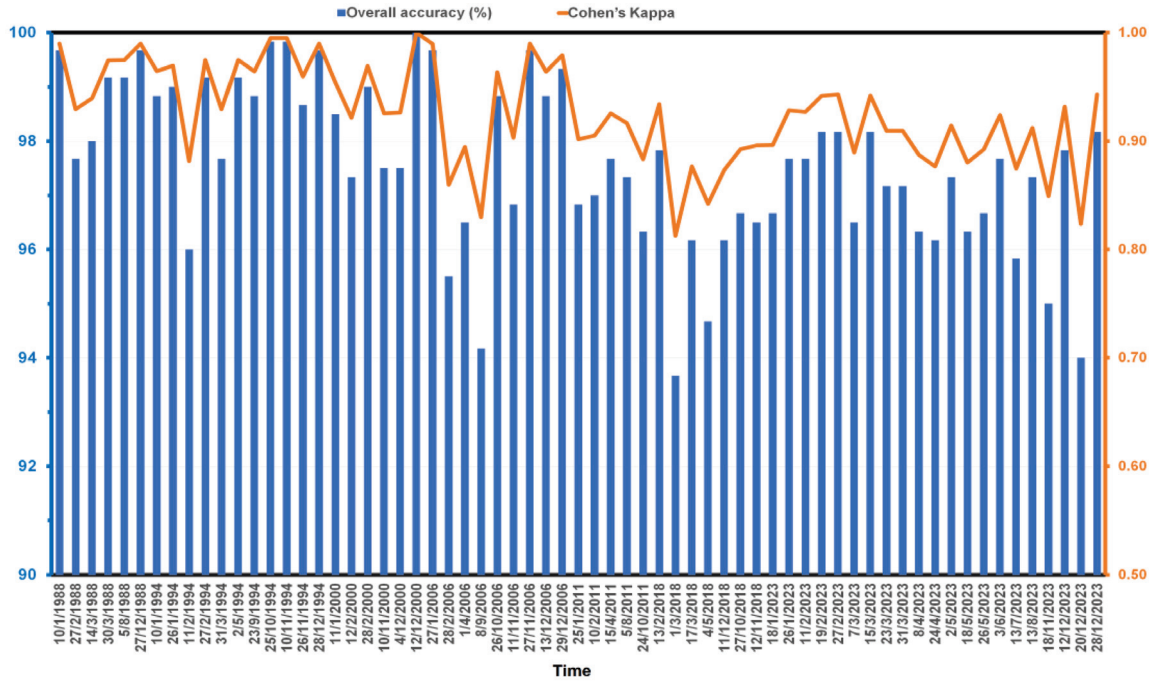

Figure 5. Overall accuracy and Cohen's Kappa Coefficient for the Random Forest classification method applied to 65 satellite images from 1988 to 2023.

4.2. The Results of Annual Shoreline Creation

The classification results of coastal areas were derived from 65 images spanning 1988 to 2023, which were used for shoreline extraction. To monitor shoreline change, images were grouped into seven time periods (1988, 1994, 2000, 2006, 2011, 2018, and 2023). Land and water areas were separated and analyzed using the water frequency index, with values ranging from 0 to 1, and a threshold of 0.5 was applied to distinguish between land (0) and water (1). The resulting data were converted from raster to vector format, and non-coastal water bodies such as rivers and canals were removed to focus on actual shoreline changes. The results of shoreline creation from seven periods are shown in Figure 6.

The annual shorelines remained consistent and continuous across all seven periods, successfully eliminating classification issues related to shallow water and clouds. Additionally, the method effectively delineated fishponds, which act as barriers between land and sea, despite their small size relative to the satellite image resolution. Most artificial structures in the sea were also successfully classified. However, challenges remained in differentiating ports and certain coastal infrastructure.

Ports often consist of breakwaters, piers, and docks that extend into the sea, creating mixed land–water boundaries that are difficult to classify using spectral indices alone. These structures, particularly when connected to the mainland, were sometimes misclassified as land, leading to overestimation of the shoreline extent in those areas. Additionally, large industrial docks and harbors may have water surfaces that appear similar to natural coastal features, further complicating classification. Despite efforts to refine classification accuracy, some artificial coastal structures were still partially misclassified due to spectral similarities with natural shorelines.

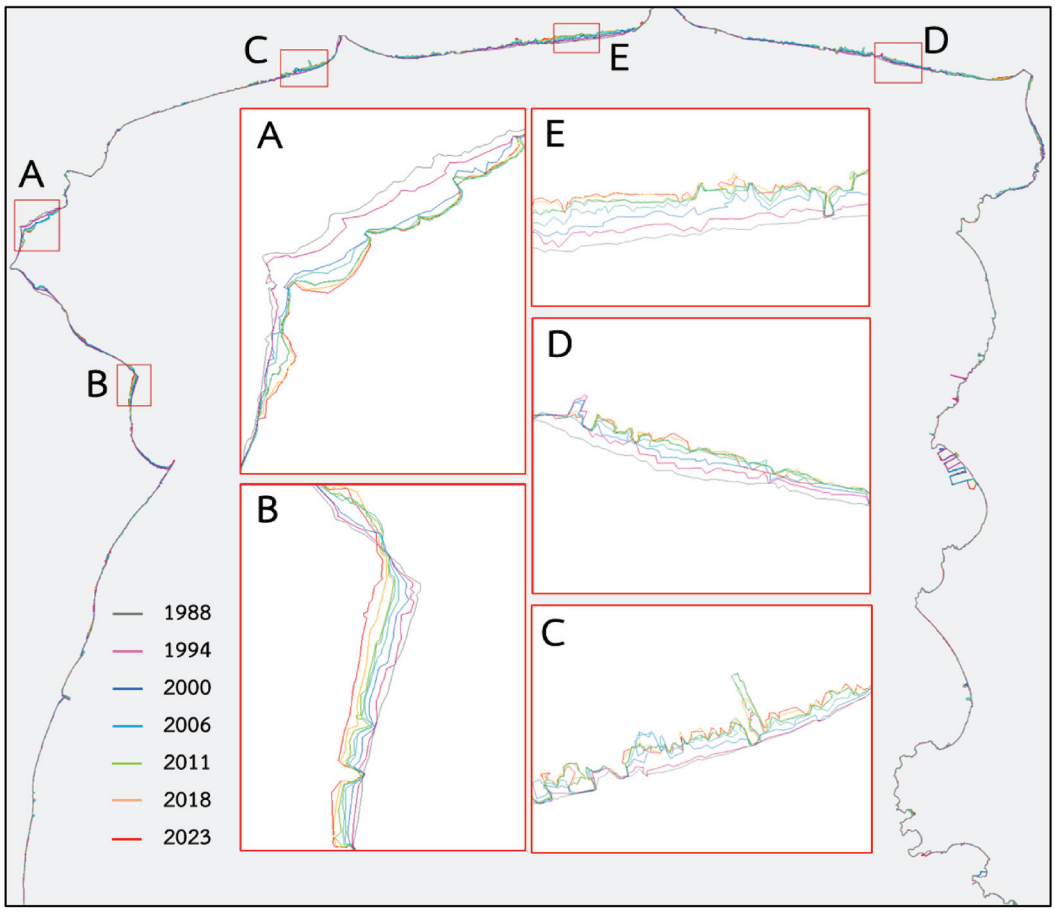

Figure 6. Overlay of the extracted shorelines from seven time periods (1988, 1994, 2000, 2006, 2011, 2018, and 2023) in the Upper Gulf of Thailand. (**A**) represents shoreline changes at the Klong Yi San Kao estuary, (**B**) represents shoreline changes at Pak Thalenai, (**C**) represents shoreline changes at the mangrove area in Bang Krachao, (**E**) represents shoreline changes at Khun Samut Chin, and (**D**) represents shoreline changes at Khlong Nang Hong.

4.3. The Annual Shoreline Assessment

This section presents the results of accuracy verification for the extracted annual shorelines for the years 2018 and 2023. The extracted shorelines were compared against the 30 m buffer of the reference shorelines for 2019 and 2022, provided by the Department of Marine and Coastal Resources. As for accuracy verification (Percentage Overlap), for the shoreline assessment in 2018, the accuracy of the extracted shoreline was 81.78%, with a correct distance of 362,961.60 m out of a total distance of 443,823.62 m. The error distance was 80,862.02 m (18.22%), with discrepancies primarily observed around ports on the eastern side and large beaches on the western side of the Upper Gulf of Thailand (Figure 7a).

For 2023, the accuracy was 80.01%, with a correct distance of 363,164.24 m out of a total distance of 453,917 m. The error distance was 90,752.76 m (19.99%), showing similar errors around ports and large beaches (Figure 7b). Both extracted shorelines demonstrated accuracy above 80%, confirming their reliability for further coastal analysis.

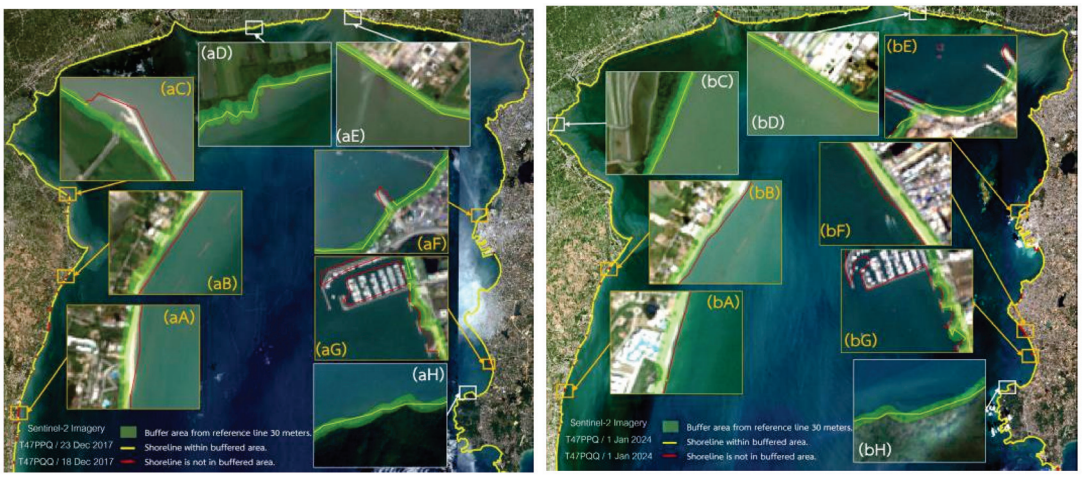

(**a**) (**b**)

Figure 7. Assessment of annual shoreline extraction compared to the reference shorelines in 2018 (**a**) and 2023 (**b**) in the Upper Gulf of Thailand. Shoreline locations in 2018: (**aA**) Hua Hin Beach, (**aB**) Chaosamran Beach, (**aC**) Pak Thale Nok, (**aD**) Bang Khun Thian, (**aE**) Bang Pu, (**aF**) Udom Bay, (**aG**) Na Chom Thian Beach, and (**aH**) Bang Sare. Shoreline locations in 2023: (**bA**) Hua Hin Beach, (**bB**) Chaosamran Beach, (**bC**) Bang Tabun estuary, (**bD**) Bang Khun Thian, (**bE**) Udom Bay, (**bF**) Jomtien Beach, (**bG**) Na Chom Thian Beach, and (**bH**) Bang Sare.

To further assess the accuracy, Root Mean Square Error (RMSE) values were calculated using 374 validation points for both years; for the shoreline assessment in 2018, the RMSE was 13.59 m, indicating an average deviation of 13.59 m between the extracted and reference shorelines. The higher RMSE reflects discrepancies in areas with complex coastal features, such as water–land boundaries and ports. For 2023, the RMSE improved to 8.90 m, demonstrating reduced error and improved shoreline extraction accuracy. This improvement is attributed to refined processing techniques, higher-quality satellite imagery, and enhanced classification algorithms.

The verification results confirm that the extracted shorelines for 2018 and 2023 are reliable, with accuracy exceeding 80% and RMSE values showing measurable improvement. The lower RMSE in 2023 highlights the effectiveness of advancements in remote sensing, improved image resolution, and enhanced shoreline extraction techniques. This confidence extends to the extracted shorelines for earlier years (1988, 1994, 2000, 2006, and 2011), despite the lack of validation data for those years.

4.4. The Results of the Digital Shoreline Analysis System (DSAS)

The shoreline change results were derived from the analysis of annual shoreline data across six time periods. As shown in Table 3 and Figure 8, from 1988 to 1994, Region 4 experienced the highest rate of coastal erosion at 13.55 m per year, followed by Region 5 with an average of 6.02 m per year. Region 2 had the highest rate of accretion, with a rate of 10.09 m per year, followed by Region 1 with 2.01 m per year. From 1994 to 2000, Region 4 continued to exhibit the highest erosion rate at 12.50 m per year, while Region 5 had the second-highest erosion rate at 6.68 m per year. Region 2 again saw the highest accretion rate, averaging 8.89 m per year. Between 2000 and 2006, Region 4 remained the most eroded, with an erosion rate of 10.35 m per year, followed by Region 5 at 6.77 m per year. Region 2 saw the highest accretion rate during this period, at 2.94 m per year. From 2006 to 2011, Region 5 had the highest erosion rate at 4.55 m per year, followed by Region 4 at 3.95 m per year. Accretion was observed in Region 1 at 2.81 m per year and Region 2 at 2.41 m per year. Between 2011 and 2018, Region 4 again had the highest erosion rate at 3.88 m per year, with Region 6 ranking second at 2.05 m per year. Region 1 saw

minor accretion at 0.10 m per year. From 2018 to 2023, Region 2 experienced the highest erosion rate at 1.55 m per year, followed by Region 4 with 0.54 m per year. Region 5 saw the highest accretion rate during this period, at 3.30 m per year. Over the entire period from 1988 to 2023, Region 4 exhibited the highest total erosion rate at 8.41 m per year, followed by Region 5 at 3.95 m per year and Region 3 at 2.14 m per year. Region 1 and Region 6 experienced erosion rates of less than 1 m per year, with 0.33 and 0.23 m per year, respectively. The highest overall accretion rate was observed in Region 2, at 3.44 m per year.

Table 3. The average rate of shoreline erosion in each region of the Upper Gulf of Thailand from 1988 to 2023.

Period	The Average of Shoreline Erosion (−) and Accretion Rate (Meters/Year)					
	Region 1	**Region 2**	**Region 3**	**Region 4**	**Region 5**	**Region 6**
1988–1994	2.01	10.09	0.01	−13.55	−6.02	−0.64
1994–2000	−0.40	8.89	−5.22	−12.50	−6.68	−0.48
2000–2006	−0.04	2.94	−1.21	−10.35	−6.77	−0.10
2006–2011	2.81	2.41	−1.80	−4.55	−5.18	0.19
2011–2018	−0.71	−0.18	−1.31	−3.88	0.10	−2.05
2018–2023	−1.55	−0.54	1.31	−0.40	3.30	−0.40

4.5. The Analysis of the Coastal Changes

The DSAS analysis reveals significant changes in the coastline along the Upper Gulf of Thailand from 1988 to 2023, primarily driven by rising sea levels closely linked to global warming. As illustrated in Figures 9 and 10, increasing global temperatures have led to the melting of polar ice caps and mountain glaciers, subsequently elevating global sea levels. This relationship is reflected in the strong correlation coefficient (0.8632) shown in Figure 10a, highlighting the interconnected nature of rising temperatures and sea levels. Furthermore, the correlations between global sea level, temperature, and coastal erosion are also significant, with values of 0.7659 and 0.8633, respectively, as shown in Figure 10b,c. These findings underscore the role of rising temperatures and sea levels as primary drivers of coastal erosion. On a regional scale, data from meteorological stations across the Upper Gulf of Thailand confirm that this area follows the global trend. A strong correlation (0.8136) between mean sea level and coastal erosion is observed in Figure 10f, indicating that rising sea levels play a dominant role in reshaping the coastline. However, while both average temperature and annual sea level demonstrate steady increases, the relationship between temperature and sea level rise within the region is weaker (correlation of 0.5117, Figure 10d). This suggests that local environmental factors including sediment supply, monsoonal currents, coastal geomorphology, and extreme weather events contribute to sea-level impacts and erosion processes in the region. In addition to long-term sea-level rise, short-term climatic events such as storm surges, tropical storms, and monsoonal variations have played a crucial role in shaping the shoreline dynamics of the Upper Gulf of Thailand. The impact of these events is evident in episodic erosion spikes that deviate from the general long-term trend of progressive shoreline retreat. For example, storm surges associated with seasonal monsoons temporarily elevate water levels, exacerbating erosion, especially in low-lying areas. While our analysis focuses on the dominant influence of global warming-induced sea-level rise, integrating localized storm data could further refine our understanding of coastal change dynamics and provide more precise insights into extreme weather impacts.

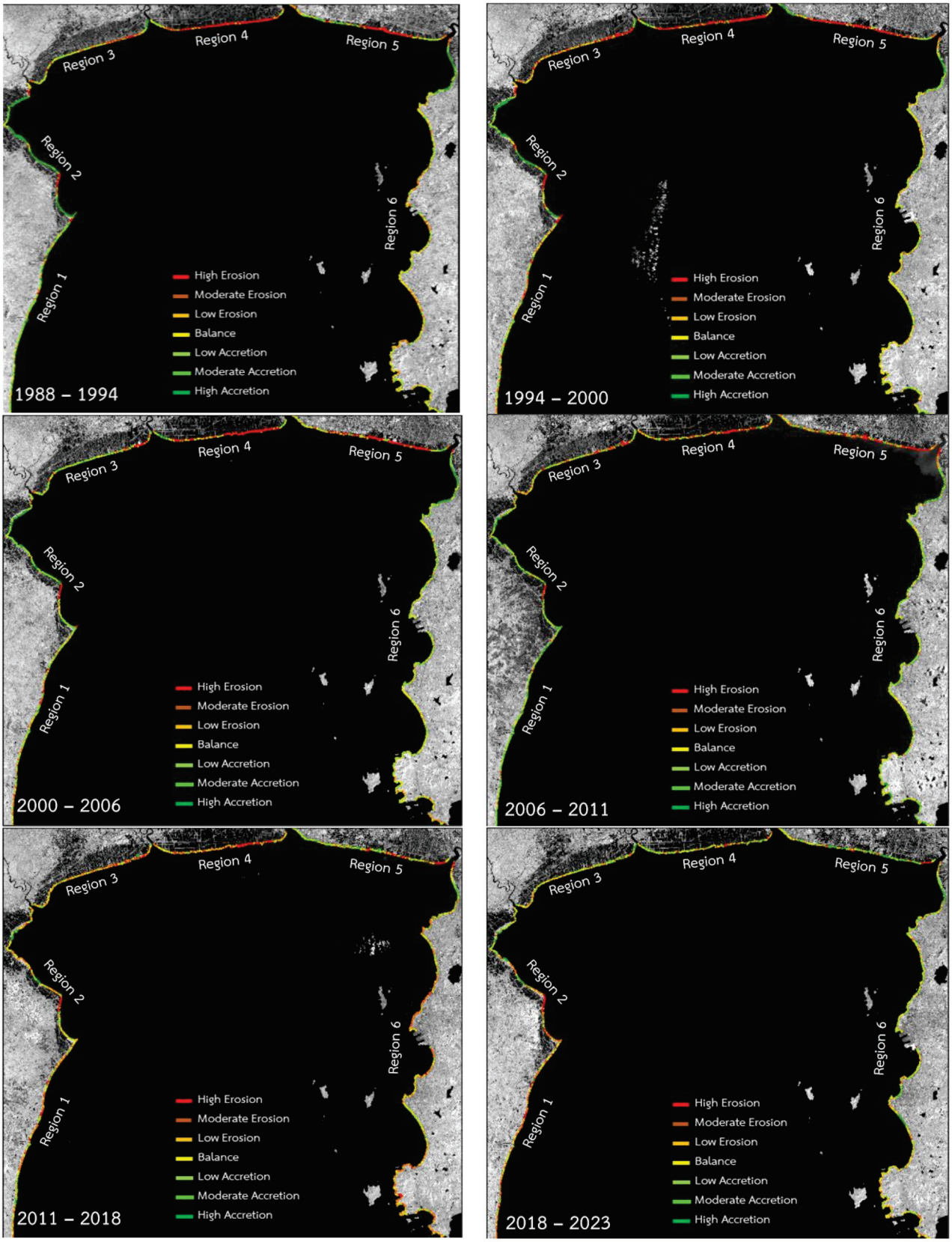

Figure 8. Results of shoreline change analysis using the Digital Shoreline Analysis System (DSAS) for the Upper Gulf of Thailand.

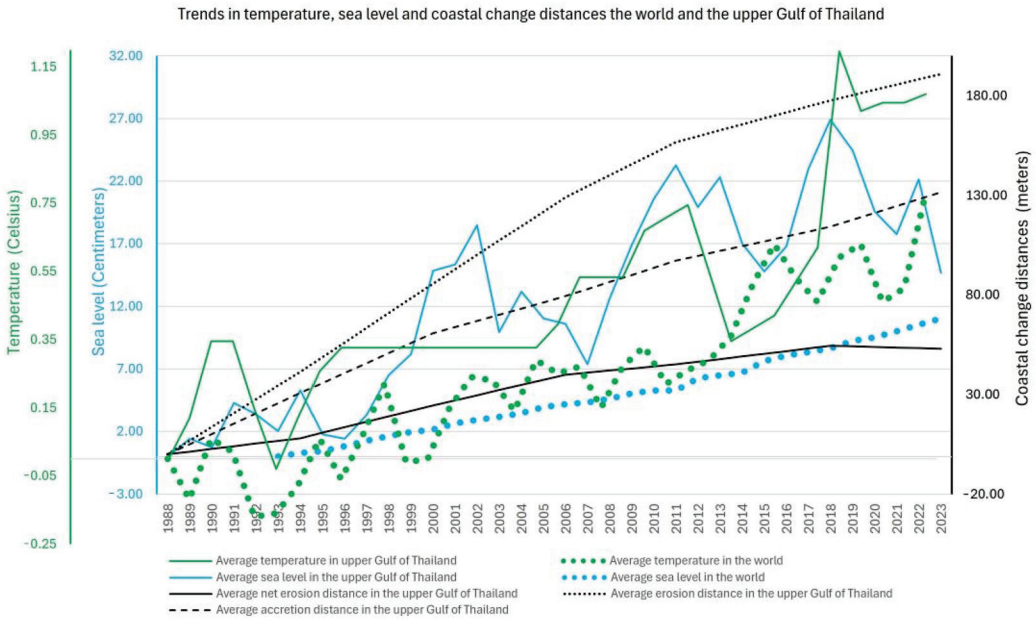

Figure 9. Trends in global mean sea level and average temperature, along with mean sea level, average temperature, and accumulated shoreline erosion in the Upper Gulf of Thailand.

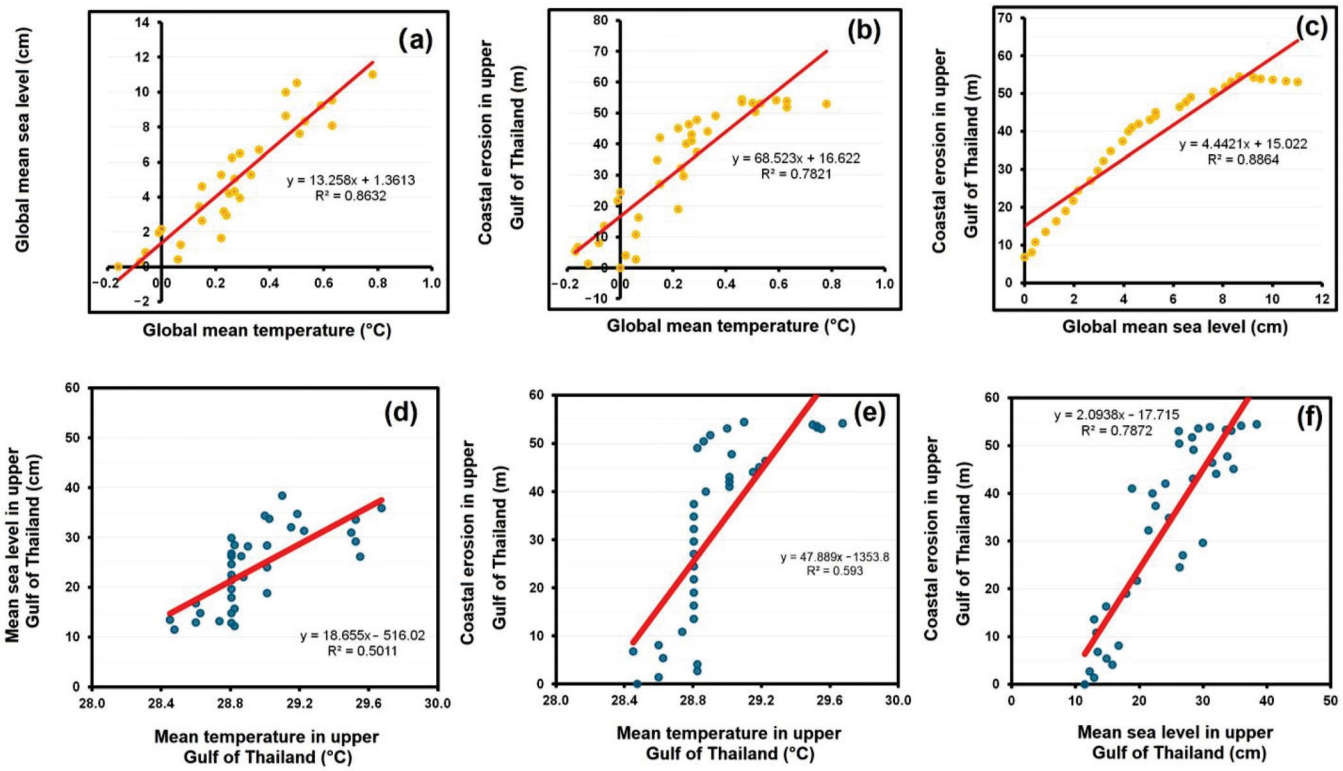

Figure 10. Correlation analyses between sea level, temperature, and coastal erosion: (**a**) Global mean sea level vs. global average temperature (**b**). Coastal erosion in the Upper Gulf of Thailand vs. global mean temperature (**c**). Coastal erosion in the Upper Gulf of Thailand vs. global mean sea level (**d**). Mean sea level vs. mean temperature in the Upper Gulf of Thailand (**e**). Coastal erosion vs. mean temperature in the Upper Gulf of Thailand (**e**), (**f**) Coastal erosion vs. mean sea level in the Upper Gulf of Thailand.

To better understand the factors contributing to coastal erosion including topography, geology, land use, seasonal currents, coastal structures, human activities, and extreme weather events, the study area was divided into six regions, as illustrated in Figure 1. This

division facilitates a more localized assessment of erosion patterns, sediment deposition, and the effectiveness of coastal protection measures across the study area.

4.5.1. Region 1: Hua Hin District–Laem Phak Bia

The coastal area between Hua Hin District and Laem Phak Bia demonstrates significant variability in erosion and accretion patterns over the past several decades (1988–2023) as shown in Figure 11.

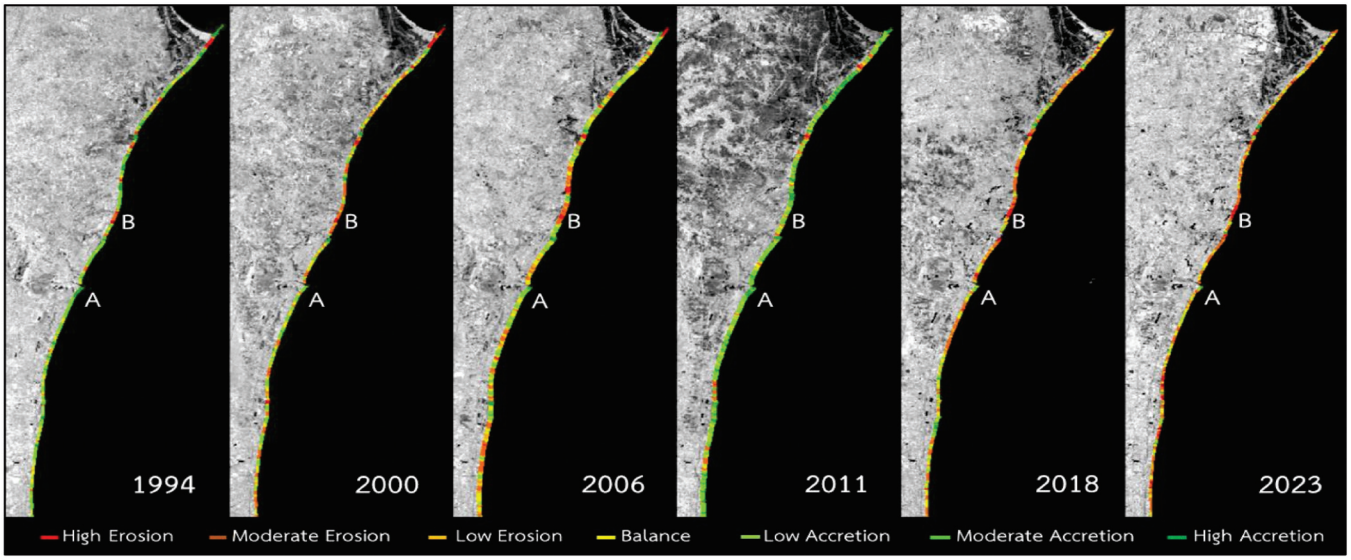

Figure 11. Shoreline changes over six time periods from Hua Hin District to Laem Phak Bia region. (A) represents shoreline changes in the northern part of Cha-Am Beach, and (B) represents shoreline changes in Bang Kao Beach.

As seen, land use along the coastal area is built up and beach forest. This region features low-lying coastal plains with flat, sandy beaches, fine sediments, and estuarine mudflats, making it highly vulnerable to erosion, particularly during the southwest monsoon and storm surges. The coastline is composed of mud, sand, and gravel, with most beaches being sandy, which enhances its susceptibility to erosion. The moderately steep slope of the coastline, combined with rising sea levels and intensifying ocean currents, exacerbates erosion on flat, sandy beaches, which are particularly prone to sediment loss. The dynamics of sediment transport and erosion in the region are heavily influenced by seasonal currents. The southwest monsoon (May–October) generates stronger northward currents that intensify erosion by displacing sediments from more exposed areas, particularly along flat, sandy beaches. Additionally, storm surges and extreme weather events during the southwest monsoon have caused episodic erosion, accelerating shoreline retreat in vulnerable regions. For example, Bang Kao Beach reveals localized trends of both erosion and accretion. From 1988 to 2006, continuous erosion was observed, particularly in the central and northern parts of Cha-am Beach. Erosion rates decreased between 2006 and 2011, with noticeable sand deposition on several beaches, driven by sediment transport and localized sediment accumulation. However, after 2011, erosion rates began to rise again. For example, the central region near the Cha-am Fishing Pier has experienced continuous erosion over multiple decades, while Bang Kao Beach, though showing moderate accretion in 2011, returned to severe erosion by 2018 and 2023. The absence of effective coastal protection measures in these areas, combined with the intensification of southwest monsoonal currents, has resulted in shoreline instability.

An analysis of specific areas such as Area A, located closer to estuarine zones (Figure 12c), has experienced consistent sediment accretion as shown in Figure 12a, averag-

ing 4.07 m per year. Between 2017 and 2023, accretion rates peaked at 4.41 m per year, as sediment from river discharge and estuarine processes accumulated along the shoreline. However, despite its overall positive sediment balance, Area A remains susceptible to episodic erosion during storm surges and extreme weather events, particularly in areas where mangrove forests have been cleared. The removal of mangroves and land reclamation for agriculture or infrastructure has further exposed the shoreline to tidal forces and erosion. In contrast, in Area B, located in the exposed sections of the coastline (Figure 12d), erosion has been the dominant process, as shown in Figure 12b, with an average rate of 3.42 m per year between 1988 and 2023.

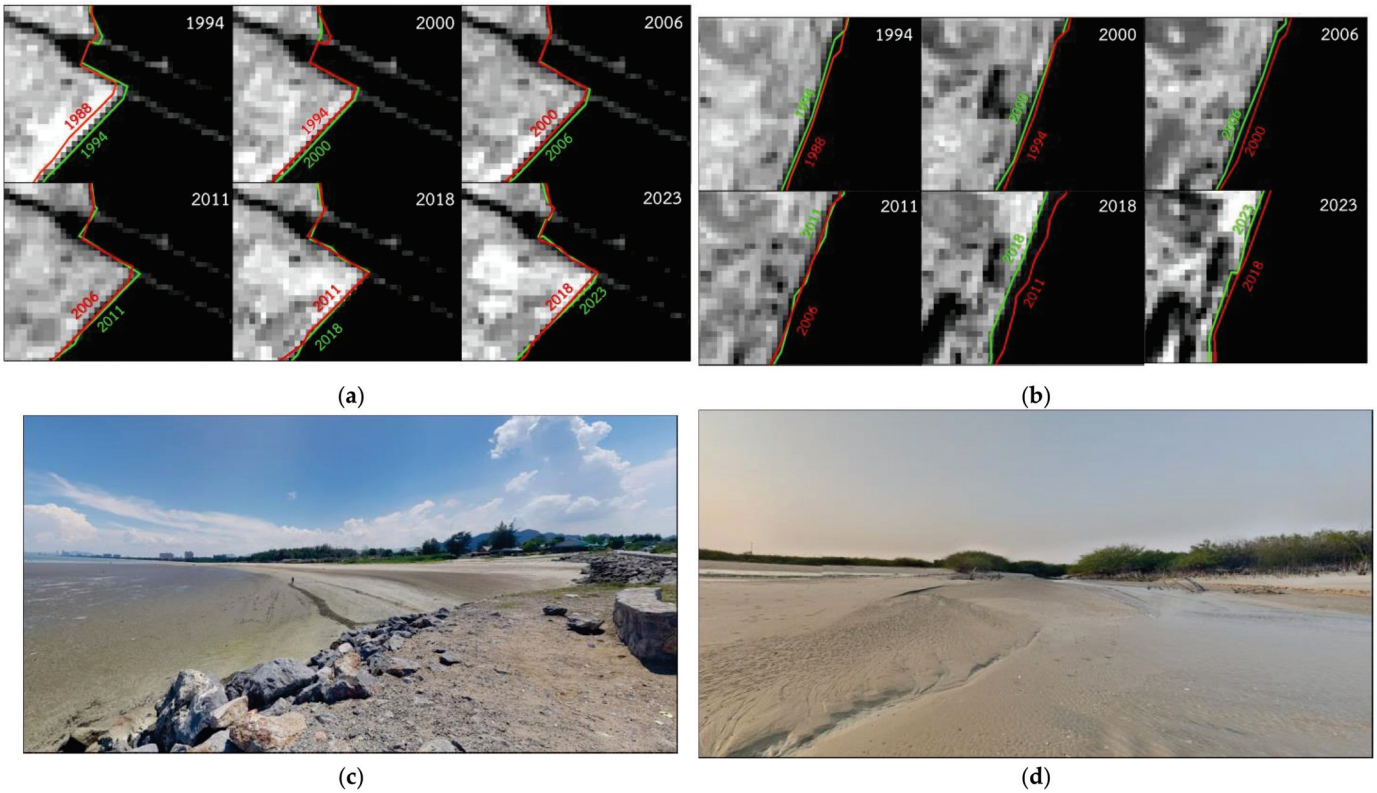

Figure 12. Shoreline change analysis: sample of shoreline changes (**a**) over six time periods in Saphan Pla Cha-am (**c**), and sample of shoreline changes (**b**) over six time periods in the coastal area Bang Kao Subdistrict, Cha-am District, Phetchaburi (**d**).

The shoreline retreat in this area has been influenced by its flat topography, strong tidal forces, and exposure to southwest monsoonal currents. Erosion was particularly severe during 1988–1994, when rates peaked at 8.88 m per year, leading to an erosion of 12.05 m. Although erosion rates temporarily decreased between 1994 and 2006, the trend intensified again between 2006 and 2011, with erosion rates reaching 10.37 m per year. This period corresponds to increased wave energy during the southwest monsoon and the absence of effective coastal protection structures. By 2023, the cumulative erosion in Area B reached 10.82 m, underscoring the area's vulnerability to rising sea levels, tidal forces, and extreme weather events. Overall, the analysis of Region 1 highlights a dynamic interplay between erosion and accretion processes, with distinct variability between Area A and Area B. However, both areas remain vulnerable to the impacts of rising sea levels, tidal forces, and storm surges. Between 1988 and 2023, the region experienced a net shoreline change with a cumulative sediment loss of 10.82 m.

4.5.2. Region 2: Laem Phak Bia–Mae Klong River

The coastal area between Laem Phak Bia and the Mae Klong River is characterized by an alluvial plain formed by sediment deposition at the estuary, with extensive mangrove forests and mudflats sustained by sediment carried and deposited by the Mae Klong River and Khlong Bang Tabun. The flat topography and the presence of fine sediments make the area highly susceptible to erosion, particularly during the southwest monsoon when stronger currents displace sediments from south to north. In contrast, the northeast monsoon (November–February) facilitates sediment deposition as slow-moving currents transport material from north to south, contributing to mangrove expansion and mudflat formation near estuarine zones. Extreme weather events have further shaped the region's shoreline dynamics, with storms and tropical cyclones contributing to episodic erosion. These events brought high storm surges and strong wave action that accelerated shoreline retreat, particularly in vulnerable areas like the southern Mae Klong estuary.

The analysis of coastal changes in Region 2 highlights a dynamic interplay between erosion and accretion processes. Between 1988 and 2023, the region experienced significant net shoreline erosion and accretion as shown in Figure 13, particularly in Area A, which includes the southern part of the Mae Klong estuary. Area A has shown an average annual accretion rate of 18.40 m per year, resulting in a cumulative shoreline expansion of 139.64 m by 2023 as shown in Figure 14a. This significant accretion is primarily driven by sediment deposition from strong tidal forces and riverine processes, particularly during the northeast monsoon season, when slower currents facilitate sediment accumulation near estuarine zones. This area features flat coastal plains and mudflats that are conducive to sediment deposition. The riverine forces of the Mae Klong River play a critical role in delivering sediment loads to the estuary, while the tidal forces during seasonal monsoons further contribute to sediment retention in the area. Additionally, the gradual accumulation of sediments has been observed in the southern Mae Klong estuary, where estuarine mudflats provide a stable environment for accretion processes (Figure 14c).

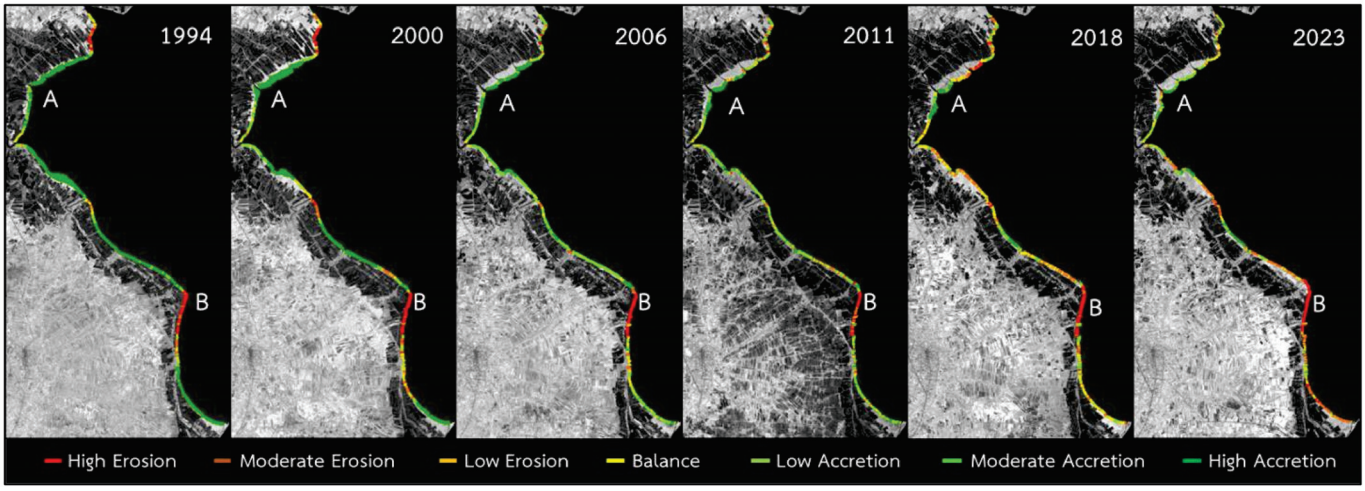

Figure 13. Shoreline changes over six time periods from Laem Phak Bia–Mae Klong River. (A) represents shoreline changes at the Klong Yi San Kao estuary, and (B) represents shoreline changes at Pak Thalenai.

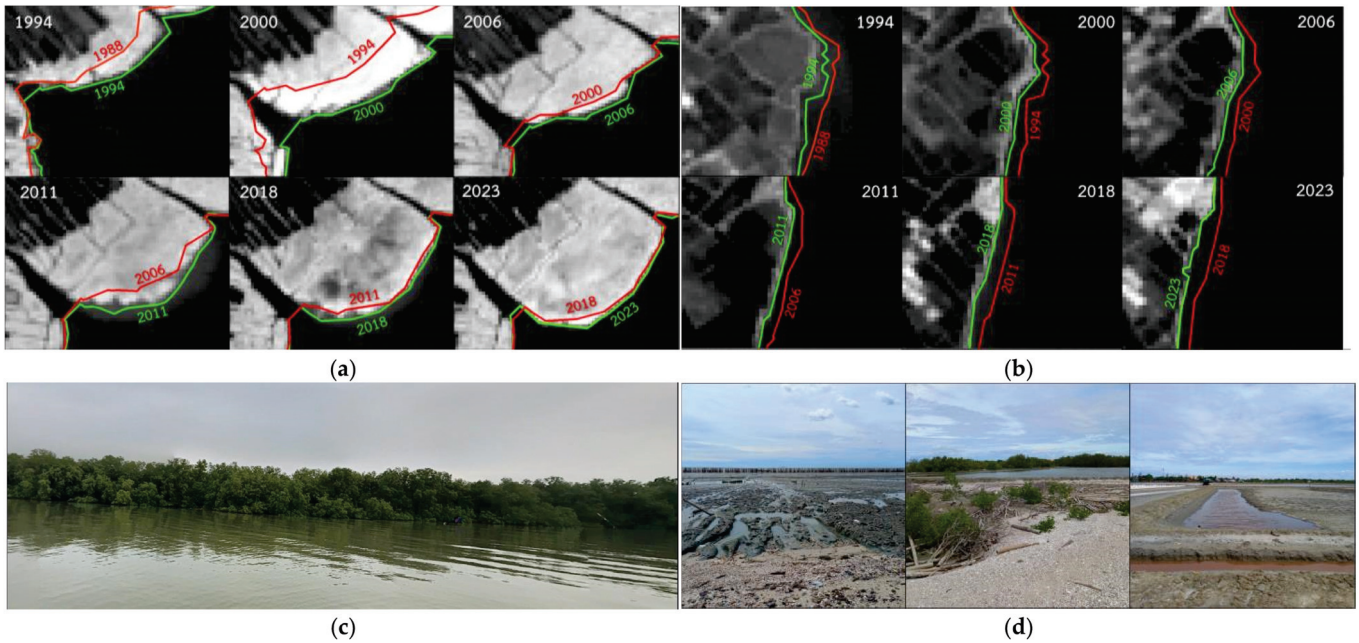

Figure 14. Shoreline change analysis: sample of shoreline changes (**a**) over six time periods in the coastal area between the Mae Klong estuary and the Khlong Bang Tabun estuary (**c**), and sample of shoreline changes (**b**) over six time periods in the coastal area Pak Thale Conservation Area, Pak Thale Subdistrict, Ban Laem District, Phetchaburi Province (**d**).

In contrast, Area B, a coastal area situated near the Pak Thale Conservation area, has experienced persistent erosion rather than accretion in recent decades as shown in Figure 14b, with an average annual erosion rate of 13.39 m per year between 1988 and 2023. Despite its proximity to sediment-rich environments, this erosion is primarily driven by strong tidal currents, particularly during the southwest monsoon (May–October), which displaces sediments away from the shoreline and reduces sediment deposition. Erosion pressures have intensified, driven by the combined effects of stronger tidal currents, rising sea levels, and human activities. The conversion of mangrove forests into agricultural land and salt farms has significantly reduced the natural sediment retention capacity of the shoreline, leaving the area more vulnerable to tidal forces and wave action. Efforts to combat erosion in Area B have included the installation of coastal protection measures, such as bamboo fences, which aim to absorb wave energy and promote sediment accumulation (Figure 14d). While these measures have proven effective in stabilizing certain sections of the shoreline, they have not been sufficient to counteract the over-arching erosion trends, particularly in zones where human disturbances and tidal forces remain dominant. In summary, the coastal area between Laem Phak Bia and the Mae Klong River reflects a dynamic balance of erosion and accretion driven by natural processes and human interventions. While regions such as Area A have benefited from sediment deposition facilitated by seasonal currents and mangrove expansion, Area B faces continuous erosion due to tidal forces, storm surges, and human activities.

4.5.3. Region 3: Mae Klong River–Tha Chin River

The coastal area between the Mae Klong River and Tha Chin River estuaries in the Upper Gulf of Thailand demonstrates dynamic variability in erosion and accretion processes during 1988–2023 as shown in Figure 15. This region is primarily characterized by extensive mudflats formed from alluvial soil deposition at river estuaries, combined with low-lying coastal plains that slope gently toward the sea. The flat terrain and fine sediments make the area highly prone to erosion, particularly during strong tidal forces and

rising sea levels, while the presence of mangrove forests provides some natural resilience to erosion. The flat, low-lying terrain, combined with mudflats and fine sediments, makes the shoreline particularly vulnerable to seawater intrusion and sediment displacement caused by strong tidal currents. The land used in this area includes coastal fishing and salt farming, which have encroached on mangrove forests and disrupted natural sediment retention processes (Figure 16d). Removing mangroves to accommodate salt pans and fish farms has exposed large portions of the shoreline to tidal and wave action, accelerating erosion rates, especially in Area A. Seasonal monsoonal currents significantly influence the region's sediment dynamics. The southwest monsoon (May–October) produces stronger northward-moving currents that displace sediments from more exposed areas, intensifying erosion. Extreme weather events, including tropical storms and storm surges, have accelerated episodic erosion in vulnerable areas. The combination of rising sea levels and stronger wave energy during storms has contributed to significant shoreline retreats, particularly in exposed sections of Area A.

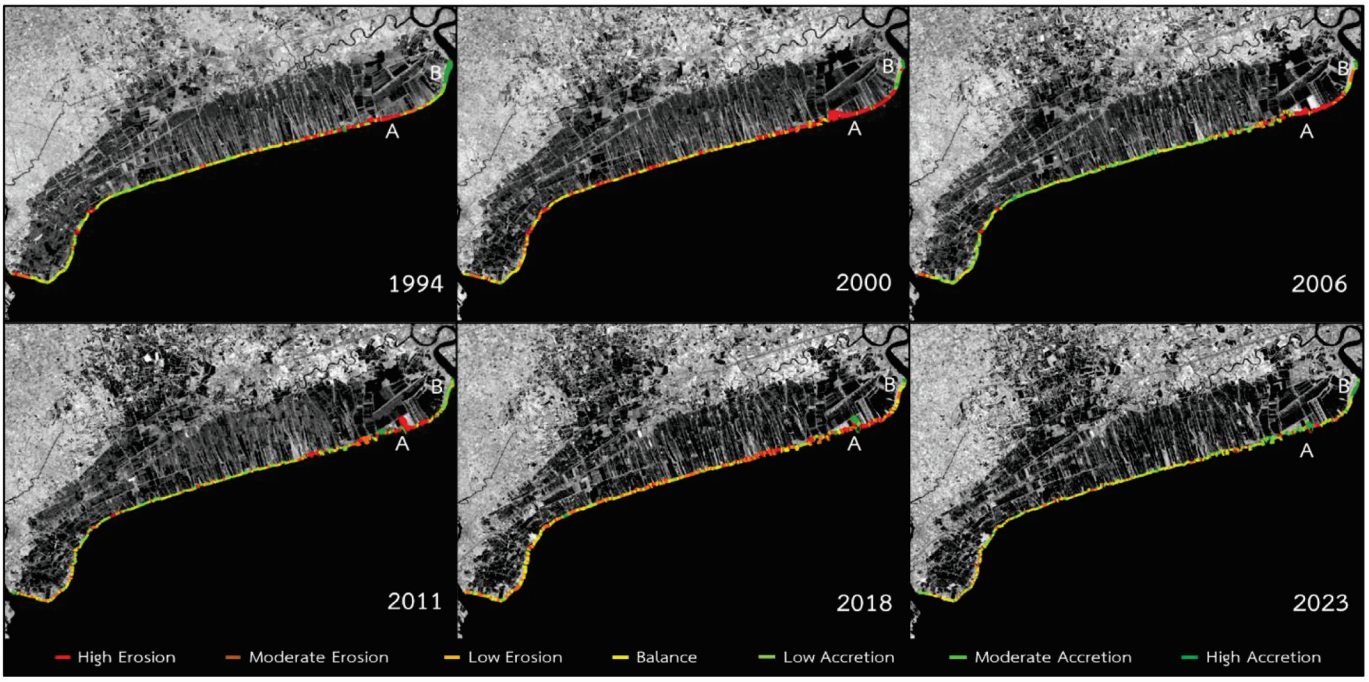

Figure 15. Shoreline changes over six time periods from Mae Klong River to Tha Chin River. (A) represents shoreline changes at the mangrove area in Bang Krachao, and (B) represents shoreline changes at Ao Mahachai Mangrove Forest Study Centre.

For northeast monsoons, it generates slow-moving currents that promote sediment deposition along sheltered mudflat areas, contributing to shoreline stability, with the construction of coastal protection since 2000. Soft measures such as bamboo fences have been implemented to trap sediments and stabilize sections of the shoreline (Figure 16c), particularly in Area B, where accretion has been more consistent. Additionally, hard structures, such as rock revetments and embankments, have been built to reduce erosion in highly exposed zones. However, in Area A, these measures have proven less effective due to the combined pressures of rising sea levels, strong tidal currents, and the lack of natural buffers like mangrove forests. For the analysis of shoreline changes in specific areas, Area A is situated in more exposed coastal sections as shown in Figure 16a; Area A has experienced consistent net erosion at an average rate of 8.86 m per year. Erosion was particularly severe between 1988 and 2011, with rates peaking at 30.72 m per year during the 1993–2000 period. By 2023, the cumulative shoreline retreat had reached 50.18 m, underscoring the long-term

vulnerability of this area to tidal forces and sea-level rise. Land reclamation for fish and salt farming, combined with embankment collapses caused by seawater intrusion, has exacerbated erosion in this zone. In contrast, Area B located further inland and closer to estuarine environments has shown consistent net accretion at an average rate of 7.42 m per year as shown in Figure 16b. Between 2017 and 2023, accretion rates peaked at 12.16 m per year, reflecting the continued role of mangrove expansion and sediment retention facilitated by calmer currents. Overall, between 1988 and 2023, shoreline erosion in Area A reached 50.18 m, while Area B demonstrated consistent shoreline accretion.

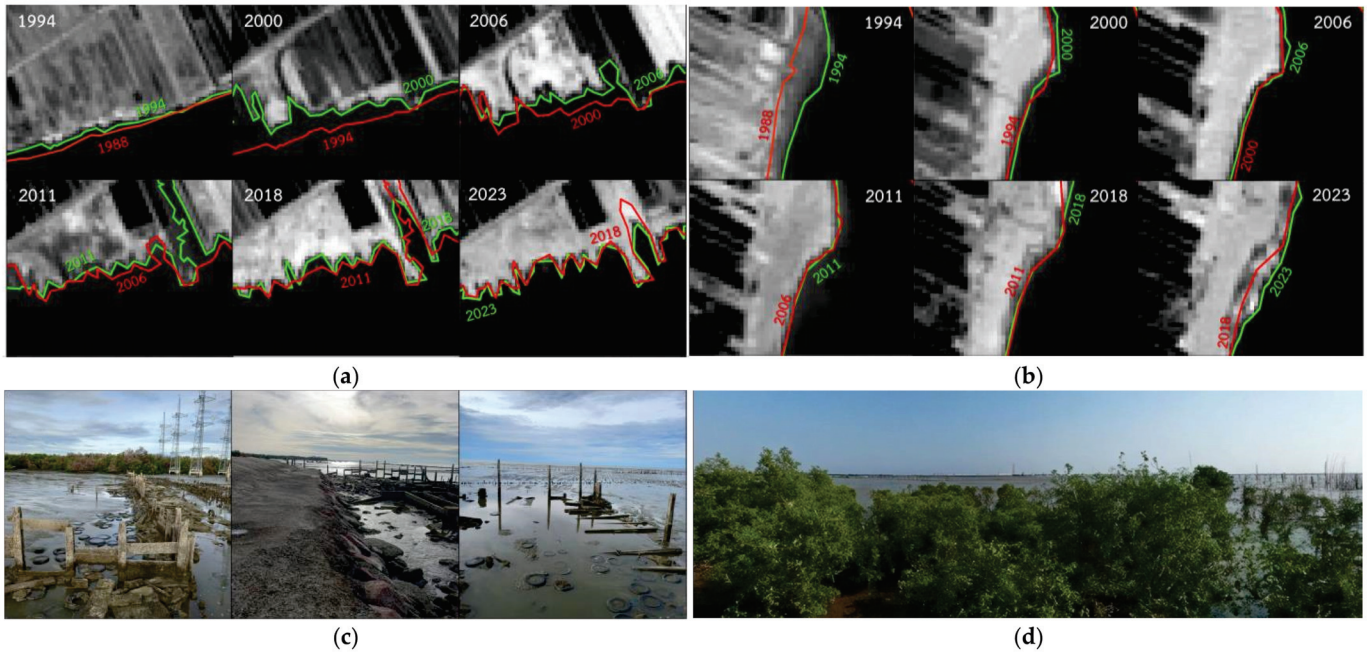

Figure 16. Shoreline change analysis: sample of shoreline changes (**a**) over six time periods in the coastal area Bang Phraek Subdistrict, Mueang District, Samut Sakhon Province (**c**), and a sample of shoreline changes (**b**) over six time periods in the coastal area Ao Mahachai Mangrove Forest Natural Education Center, Bang Phraek Subdistrict, Mueang District, Samut Sakhon Province (**d**).

4.5.4. Region 4: Tha Chin River–Chao Phraya River

The coastal area between the Tha Chin River and Chao Phraya River estuaries, located in the northernmost part of the Gulf of Thailand, demonstrates significant variability in erosion and accretion processes during 1988–2023 as shown in Figure 17. This region primarily consists of flat coastal plains with gentle slopes formed by alluvial soil deposits from the estuaries, making the area highly vulnerable to seawater intrusion and coastal erosion. The geological composition, dominated by mud and sand, supports the growth of mangrove forests, which provide some natural resilience against erosion. The region's low-lying terrain and flat coastal plains make it particularly susceptible to rising sea levels and sediment displacement caused by tidal currents. Extensive salt farming and the conversion of mangrove forests into agricultural or residential zones have significantly disrupted the natural sediment balance, weakening the shoreline's resilience to erosion. The collapse of embankments in salt farm areas, combined with sediment removal during extreme tidal conditions, has further exacerbated erosion. The northeast monsoon brings slow-moving currents that facilitate sediment deposition, contributing to shoreline accretion and mangrove expansion. In contrast, the southwest monsoon generates stronger northward currents that displace sediments, intensifying erosion. Soft structures, such as bamboo fences (Figure 18c), were implemented in 2000 to trap sediments and reduce wave energy, particularly in accretion-prone areas. Hard structures, such as rock revetments and vertical

barriers (Figure 18d), were constructed to stabilize the shoreline in severely eroded zones. Extreme weather events, including storm surges and tropical cyclones, have intensified sediment displacement and shoreline retreat in exposed areas. The combined effects of rising temperatures, higher sea levels, and extreme tidal conditions during storm events have accelerated episodic erosion, particularly in low-lying sections of Area A.

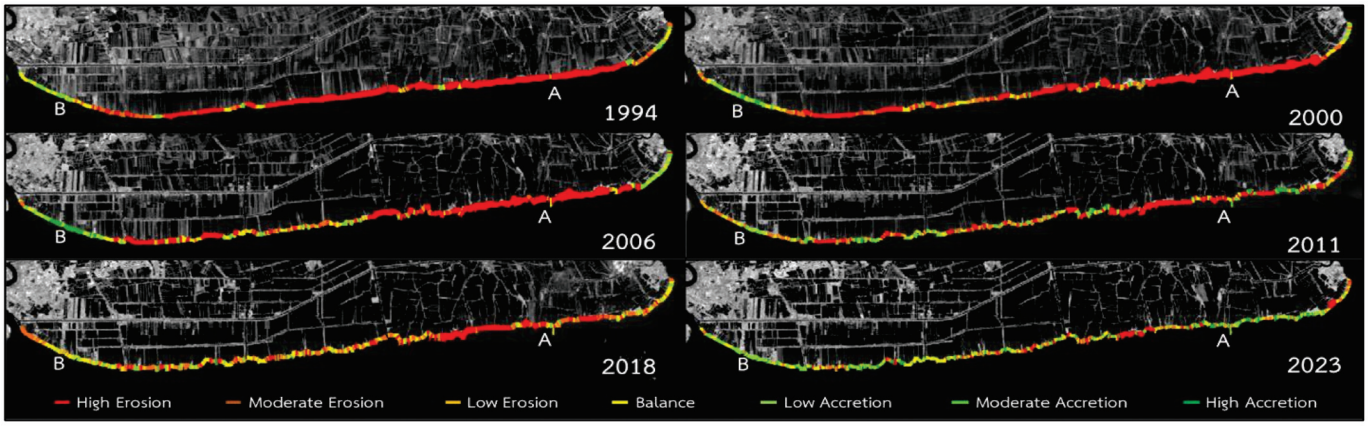

Figure 17. The shoreline changes over six time periods from Tha Chin River to Chao Phraya River. (A) represents shoreline changes at Khun Samut Chin, and (B) represents shoreline changes at the Tha Chin estuary.

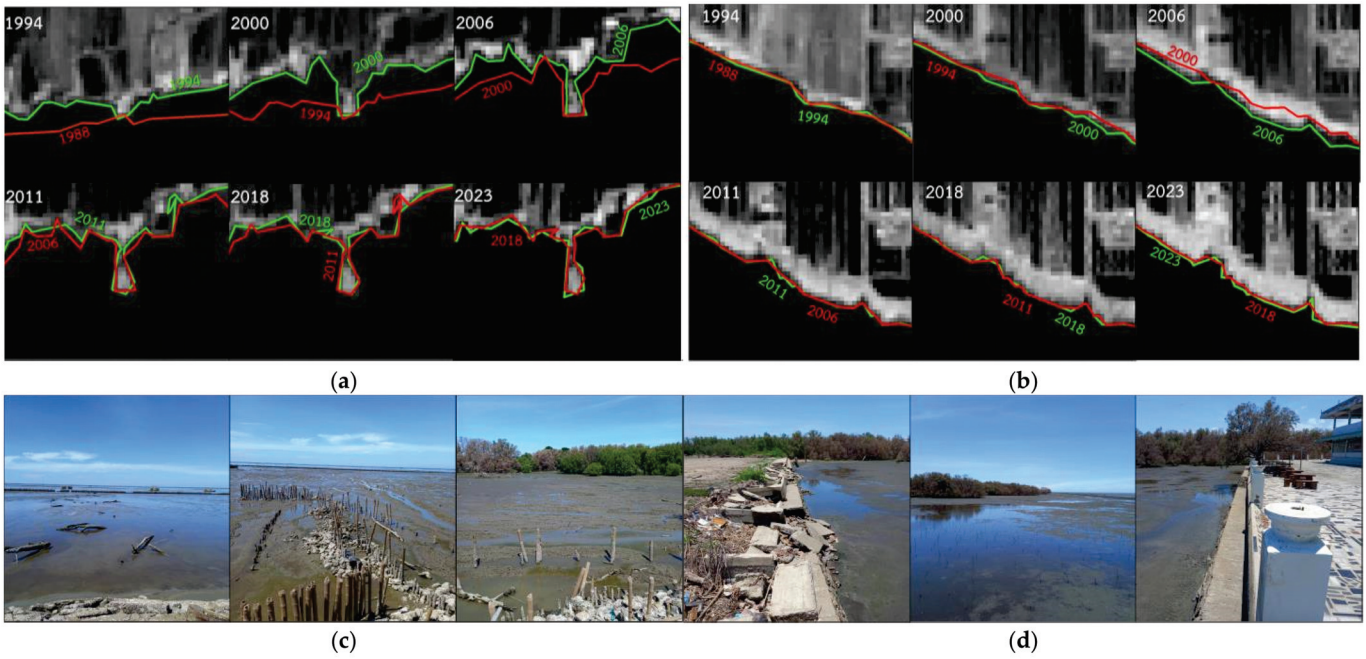

Figure 18. Shoreline change analysis: sample of shoreline changes (**a**) over six time periods in the coastal area Ban Khun Samut Chin, Laem Fa Pha Subdistrict, Phra Samut Chedi District, Samut Prakan Province (**c**), and sample of shoreline changes (**b**) over six time periods in the coastal area Marine and Coastal Resources Office, Samut Sakhon Mueang District, Samut Sakhon Province (**d**).

The analysis of shoreline changes in Region 4 reveals a predominantly erosional trend in exposed areas and localized accretion in more sheltered zones. For example, Area A is situated in exposed sections of the coastline and has experienced severe erosion as shown in Figure 18a, with an average annual erosion rate of 15.47 m per year between 1988 and 2023. The shoreline erosion reached 270.30 m by 2023, indicating the long-term vulnerability of this area to rising sea levels and tidal forces. The period between 1988 and 2000 saw the

most significant erosion rates, peaking at 31.22 m per year during 1993–2000, as rising sea levels and seasonal currents displaced sediments from the shoreline. Although erosion rates slowed to 2.66 m per year between 2011 and 2018, the cumulative effects of seawater intrusion, strong tidal currents, and embankment collapse associated with salt farming and fish farming continued to exacerbate sediment loss. In contrast, Area B, located in more sheltered estuarine zones, has demonstrated net accretion with an average rate of 2.94 m per year as shown in Figure 18b. Between 1999 and 2005, accretion rates peaked at 11.21 m per year, reflecting the influence of slow-moving tidal currents and sediment retention near mangrove forests. More recently, between 2017 and 2023, accretion rates averaged 2.50 m per year, highlighting the continued role of natural sediment dynamics in stabilizing portions of the shoreline. Overall, while Area A has suffered persistent shoreline retreat, with a cumulative loss of 270.30 m, due to rising sea levels, tidal forces, and human disturbances, Area B has shown consistent sediment accretion facilitated by natural tidal currents and mangrove forest expansion.

4.5.5. Region 5: Chao Phraya River–Bang Pakong River

The coastal area between the Chao Phraya River and Bang Pakong River estuaries exhibits complex shoreline changes from 1988 to 2023 as shown in Figure 19. This region is a lowland area formed by river sedimentation, with a geological composition dominated by mud and sand. The flat terrain and low elevation make the region highly vulnerable to flooding during high tides and coastal erosion, particularly when exposed to strong wave action during the southwest monsoon season. The region's flat lowlands and muddy shorelines are prone to erosion due to their low elevation and weak geological composition. Extensive salt farming and the conversion of mangrove forests into aquaculture and residential zones have disrupted natural sediment dynamics and removed critical coastal buffers. Fish farming embankments, particularly near exposed shorelines, have frequently collapsed due to rising sea levels and strong tidal forces, further accelerating erosion by displacing sediments into tidal currents. Extreme weather events, including storm surges and high wave action during the southwest monsoon (May–October), have accelerated episodic erosion and generated strong northward currents, which intensify erosion in exposed areas. These currents displace sediments and exacerbate shoreline retreat, particularly where natural buffers like mangrove forests have been removed.

In contrast, the northeast monsoon (November–February) promotes sediment deposition in sheltered zones. A combination of soft and hard coastal protection structures has been implemented since 2001. Soft structures, such as bamboo fences, have effectively trapped sediments and reduced wave energy in sheltered zones, promoting localized accretion (Figure 20c). Hard structures, including rock walls (Figure 20d) and vertical coastal barriers, have been constructed to protect exposed areas with heavy fishing and industrial activity. While these measures have helped stabilize some sections of the shoreline, their effectiveness has been limited to regions with severe erosion and frequent embankment failures. The region's vulnerability to erosion has been exacerbated by land use practices, including the expansion of urban settlements, salt farming, and fish farming, which have reduced the natural resilience of the coastline. The removal of mangroves and the collapse of embankments have left the shoreline exposed to tidal forces and storm surges.

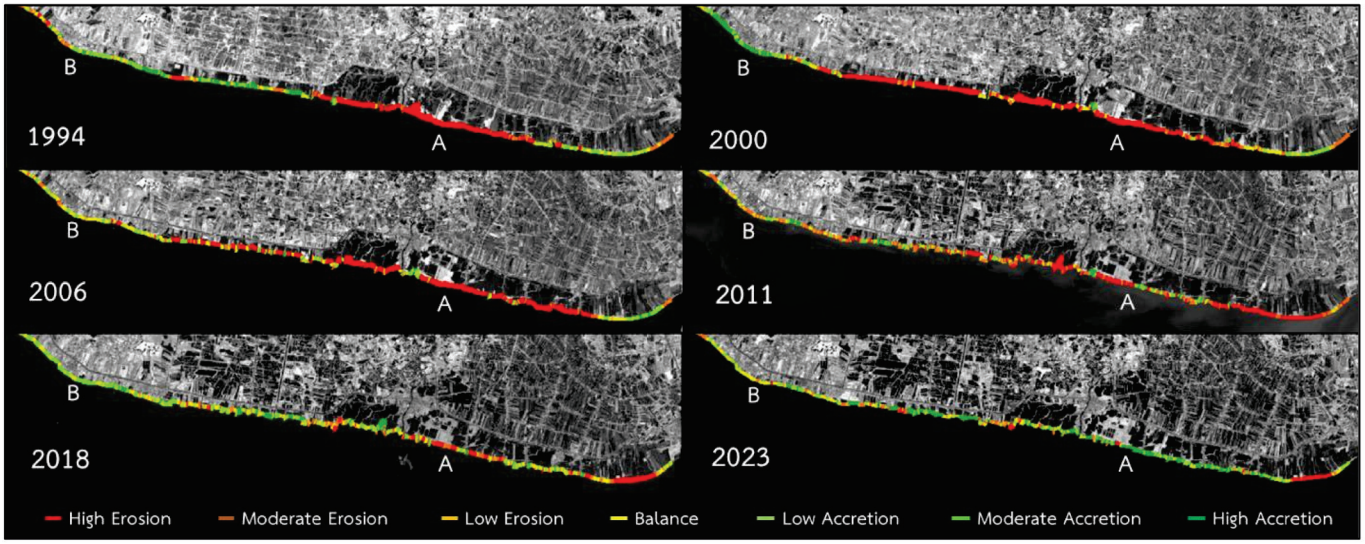

Figure 19. Shoreline changes over six time periods from Chao Phraya River to Bang Pakong River. (A) represents shoreline changes at Khlong Nang Hong, and (B) represents shoreline changes at Bang Pu Mai.

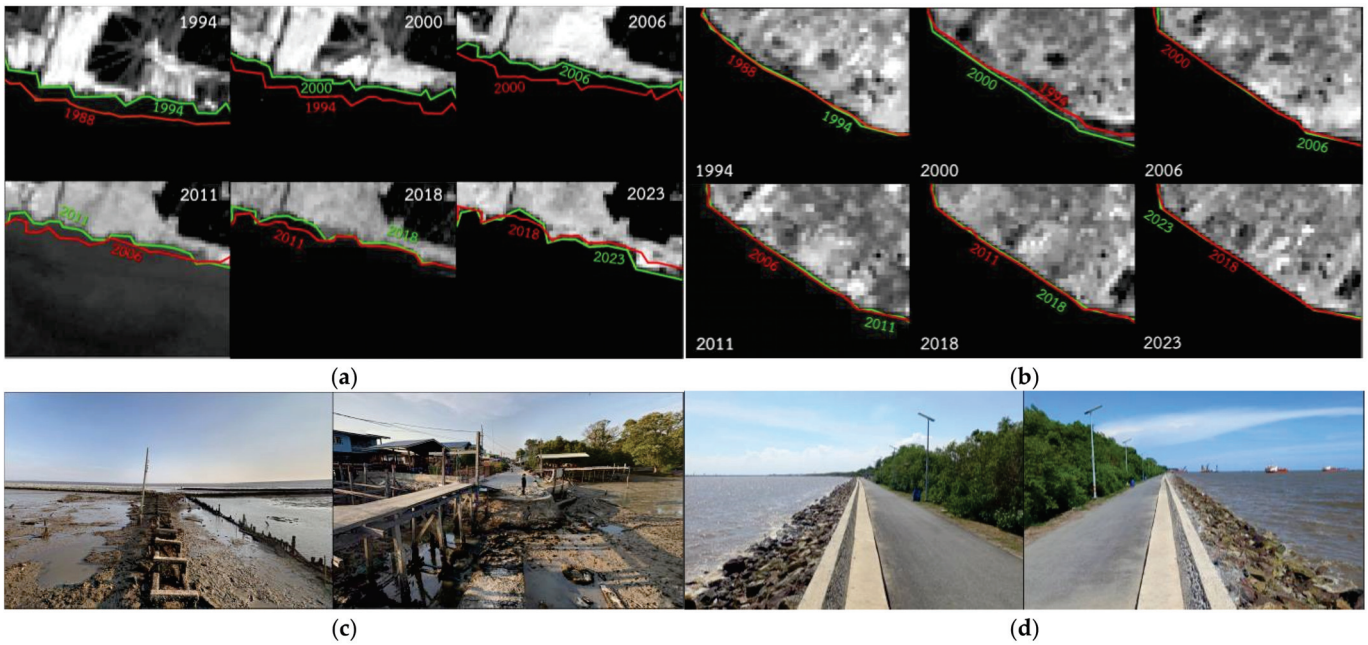

Figure 20. Shoreline change analysis: sample of shoreline changes (**a**) over six time periods in the coastal area Khlong Dan Subdistrict, Bang Bo District, Samut Prakan Province (**c**), and sample of shoreline changes (**b**) over six time periods in the coastal area Bang Pu Subdistrict, Mueang District, Samut Prakan Province (**d**).

The analysis of shoreline changes in Region 5 reveals a predominance of erosion with some localized accretion, influenced by tidal forces, human activities, and seasonal dynamics. For example, Area A is located in the more exposed sections of the coastline. Area A has experienced consistent erosion as shown in Figure 20a, with an average annual rate of 11.51 m per year between 1988 and 2023. The cumulative shoreline retreat reached 125.50 m by 2023, reflecting the long-term vulnerability of this area to rising sea levels and strong tidal forces. The period between 1988 and 2011 saw the most intense erosion, particularly during 1988–1994, when rates peaked at 23.36 m per year, resulting in a cumulative loss of 36.12 m by 1994. Although erosion rates slowed to 4.70 m per year

between 2011 and 2018, the area continued to experience gradual retreat due to the collapse of fish farming embankments and the reduction of natural sediment retention provided by mangrove forests. In recent years, from 2017 to 2023, a slight reversal occurred with an accretion rate of 6.13 m per year, likely driven by the installation of soft coastal protection structures that trapped sediments and stabilized sections of the shoreline. In contrast, Area B, situated in more sheltered estuarine environments, has exhibited minor but consistent accretion as shown in Figure 20b, averaging 1.10 m per year. Between 1993 and 2000, accretion rates peaked at 6.30 m per year, as slow-moving currents and river sediment delivery promoted localized sediment buildup. However, from 2000 to 2011, sediment deposition declined, with accretion rates dropping to 0.96 m per year. In recent years (2017–2023), the area has stabilized, with modest accretion averaging 0.26 m per year, aided by bamboo fences and natural sediment dynamics. Overall, while Area A has suffered persistent shoreline retreat, with a cumulative loss of 125.50 m, due to rising sea levels, tidal currents, and the collapse of human-made structures, Area B has shown minor accretion facilitated by natural sediment dynamics and northeast monsoonal currents.

4.5.6. Region 6: Bang Pakong River–Sattahip District

The coastal area between the Bang Pakong River and Sattahip District, located along the eastern Gulf of Thailand, exhibits diverse erosion and accretion patterns over the period 1988–2023 as shown in Figure 21. This region can be divided into three distinct sections: the upper region dominated by alluvial plains, the central region characterized by mixed sediments of sandstone and gravel, and the southern region featuring rocky formations and cliffs that naturally resist erosion.

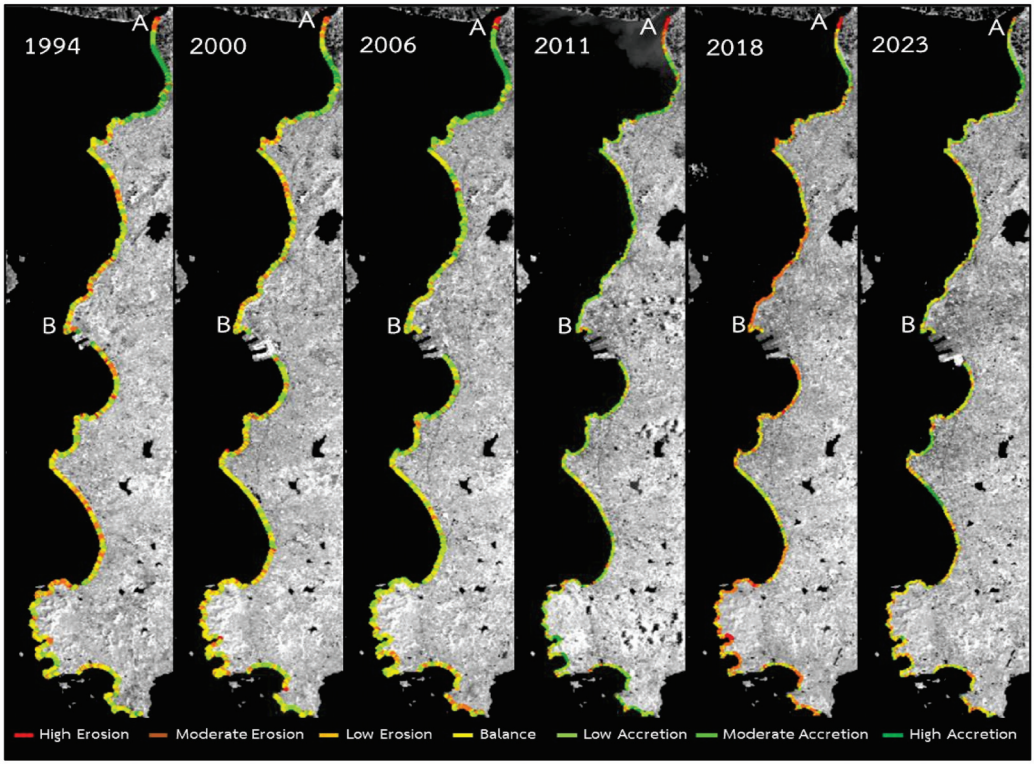

Figure 21. Shoreline changes over six time periods from Bang Pakong River to Sattahip District. (A) represents shoreline changes at the Bang Pakong estuary, and (B) represents shoreline changes at Laem Chabang Port.

The upper region of Region 6 is dominated by lowlands with extensive alluvial deposits of mud and sand, making it particularly vulnerable to erosion under rising sea levels

and strong wave action. This area is heavily used for coastal fisheries and aquaculture. The central and southern regions, in contrast, are composed of sandstone, gravel, and rocky outcrops, which are naturally resistant to erosion. The presence of cliffs with moderately sloping bases further enhances erosion resilience, reducing shoreline retreat in these areas. However, land use changes, including urbanization and port construction, have disrupted natural sediment dynamics in localized sections. Extreme weather events, such as storm surges during the southwest monsoon (May–October) and localized tropical storms, have exacerbated erosion and intensified northward tidal currents, displacing sediments and accelerating erosion in exposed areas, particularly in Area A (Figure 22a), where natural buffers like mangroves have been degraded. Conversely, the seasonal northeast monsoon (November–February) promotes sediment deposition by driving slow-moving currents from north to south, particularly in sheltered estuarine zones. Various coastal protection measures have been implemented across Region 6. Soft structures, such as bamboo fences in mangrove-rich areas, have been installed since 2015, effectively reducing erosion rates by trapping sediments and dissipating wave energy. Hard structures, including vertical barriers, piers, and rock revetments, have been constructed in urbanized areas since 2002 to stabilize shorelines. In the central and southern regions, offshore breakwaters and large ports have provided effective erosion control since 1988. Moreover, human activities, particularly the expansion of fish farms and urban development, have significantly impacted sediment transport and coastal stability. The conversion of mangroves to aquaculture has weakened natural sediment retention, increasing the vulnerability of soft coastal plains to erosion.

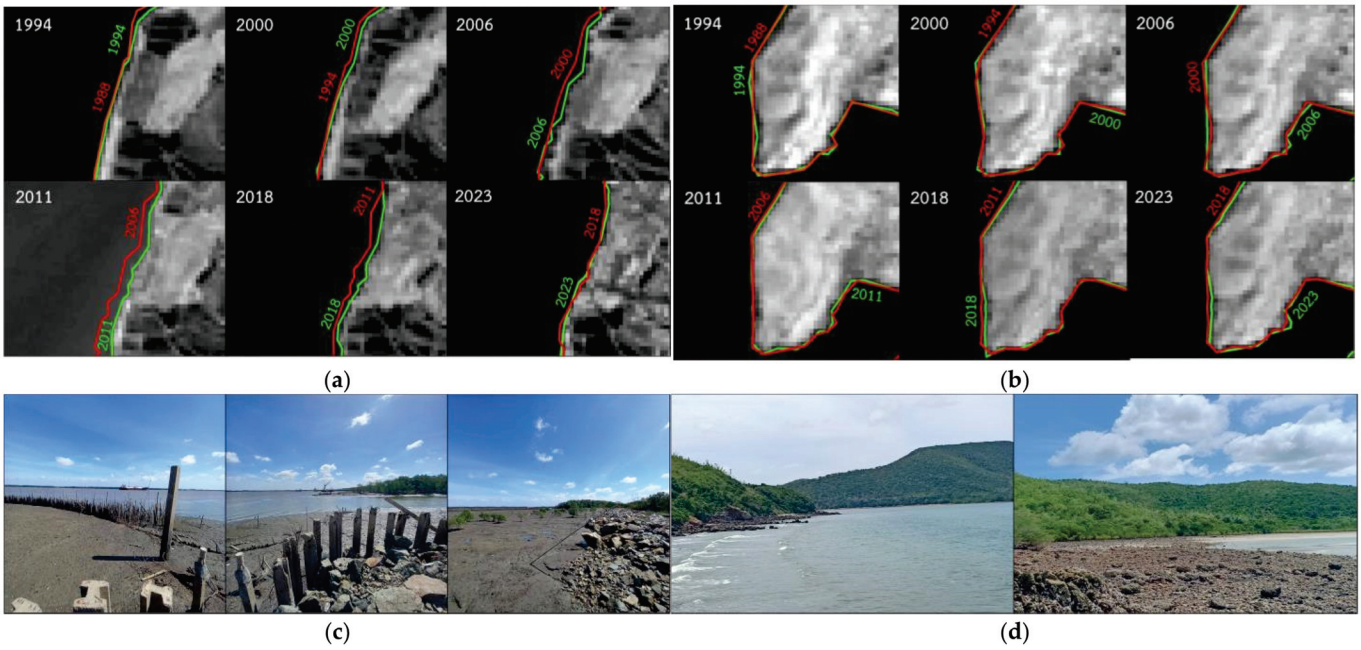

Figure 22. Shoreline change analysis: sample of shoreline changes (**a**) over six time periods in the coastal area Bang Pakong estuary, Khlong Tamhru Subdistrict, Mueang District, Chonburi Province (**c**), and sample of shoreline changes (**b**) over six time periods in Laem Chabang coastal area, Thung Sukhla Subdistrict, Sri Racha District, Chonburi Province (**d**).

The analysis of shoreline changes in Region 6 highlights variability between erosion-prone zones in the upper region and more stable, resistant areas in the central and southern sections. For example, Area A, situated in the upper coastal plain with soft mud and sand deposits, has experienced significant erosion as shown in Figure 22a, averaging 5.50 m per year. The shoreline erosion reached 22.68 m by 2023, emphasizing its long-

term vulnerability to tidal forces, seasonal monsoons, and rising sea levels. Between 1988 and 2011, erosion rates steadily increased, peaking at 11.74 m per year during the period 2005–2011. This intensification corresponds to stronger wave action during the southwest monsoon and the widespread conversion of mangrove forests into fish farms. Mangrove loss has reduced the natural buffering capacity of the coastline, leaving the area exposed to tidal currents and storm surges. In recent years (2017–2023), erosion rates declined slightly, with accretion recorded at 1.32 m per year, likely due to the installation of soft coastal structures such as bamboo wave barriers, which trap sediments and reduce wave energy (Figure 22c). Area B is located further south, consisting of mixed sandy and gravelly terrain, where erosion rates have been relatively lower, averaging 0.43 m per year as shown in Figure 22b. This area experienced minor accretion during certain periods, such as 1993–2006. However, between 2011 and 2018, erosion returned, with rates reaching 1.22 m per year, driven by tidal forces, rising sea levels, and localized urbanization impacts. The shoreline erosion in Area B reached 22.68 m by 2023, reflecting a gradual, long-term shoreline instability exacerbated by wave action and human activities.

Overall, while Area A has experienced persistent shoreline retreat, with a cumulative loss of 22.68 m, Area B has remained relatively stable due to its mixed geology and occasional sediment deposition (Figure 22d). The implementation of coastal protection structures has contributed to recent stabilization, but the region remains vulnerable to tidal forces, rising sea levels, and human activities.

5. Discussion

This research demonstrates remote sensing techniques, ML-based classification, and the DSAS for analyzing the shoreline changes in the Upper Gulf of Thailand over the past 35 years (1988–2023). The results illustrated the efficiency of coastal area classification, annual shoreline creation, annual shoreline assessment, DSAS-based metrics, and observed coastal changes.

One core aspect of this study was evaluating the performance of ML algorithms in classifying satellite imagery into land and water categories. Significant spectral bands (Blue, Green, Red, NIR, SWIR1, and SWIR2) and indices (NDVI, NDWI, MNDWI, SAVI) were used to enhance the shoreline separation. These elements allowed for precisely identifying shoreline boundaries and classifying complex coastal environments, including mudflats, mangroves, sandy beaches, and urban areas. For instance, NDWI and MNDWI proved particularly effective for differentiating water and land features near estuarine and tidal zones, while SAVI enhances the differentiation of sparse vegetation and bare soils. Similarly, NDVI distinguishes vegetated areas (e.g., mangrove and beach forests) from non-vegetated zones. The integration of spectral bands and indices with ML algorithms (RF, SVM, MLC, and MDC) demonstrated high overall accuracy results of over 80%. RF outperformed other classifiers, achieving the highest accuracy (98.17%) and a Cohen's Kappa Coefficient of 0.9432, demonstrating strong classification performance along the shoreline. However, key challenges remain, particularly in handling complex coastal features such as mangrove forests, estuarine mudflats, and urbanized areas, which can introduce classification uncertainties. Additionally, RF is susceptible to overfitting, especially when working with highly correlated features. To optimize performance and reduce computational demands, RF requires careful hyperparameter tuning (e.g., adjusting the number of trees and tree depth) and often larger training datasets to ensure robust generalization. Meanwhile, other algorithms experienced misclassifications in areas with mixed pixels, especially in regions where water and vegetation boundaries overlap, highlighting the importance of spectral indices for detecting subtle shoreline changes. SVM can be robust and handle complex boundaries well, yet they may not match RF's accuracy in large, high-dimensional datasets.

Traditional methods such as the statistical MLC and the distance-based MDC often rely on simpler assumptions about data distribution and distance metrics, making them less effective in highly complex, overlapping spectral environments. Furthermore, the performance of RF was also confirmed when it was applied to classify 64 additional images, achieving an average overall accuracy of 97.54%. These classification images were grouped into seven periods to generate the annual shoreline, utilizing a water frequency index with a threshold of 0.5 to effectively distinguish between land and water. The annual shoreline assessments for 2018 and 2023 demonstrated high accuracy, with an overlapping percentage exceeding 80% and RMSE values of 13.59 m in 2018 and 8.90 m in 2023. These results confirm the reliability of the shoreline extraction process, as the observed shoreline shifts remained less than a single pixel (30 m), consistent with the resolution of Landsat imagery. This highlights that Landsat imagery is well-suited for long-term shoreline monitoring and change detection, providing a cost-effective and reliable solution for regional-scale coastal studies. Nevertheless, the overall accuracy supports the reliability of shorelines extracted for earlier years (1988, 1994, 2000, 2006, and 2011), despite lacking direct validation data.

The results of the DSAS from 1988 to 2023 illustrate distinct patterns of erosion and accretion in the Upper Gulf of Thailand across six periods. These results demonstrate the variability in erosion intensity and accretion trends, which can be attributed to a combination of natural processes, including tidal forces, seasonal currents, and rising sea levels, as well as human interventions, such as coastal development, land use changes, and the implementation of protective structures. During 1988–1994, the Upper Gulf of Thailand experienced the most severe erosion, particularly in Region 4 (-13.55 m/year) and Region 5 (-6.02 m/year). This period marked the beginning of significant shoreline retreat, driven by rising sea levels, increased wave energy, low-lying topography, and human interventions. Notably, the conversion of over 45% of mangrove areas into aquaculture and agriculture in Region 4 significantly weakened coastal defenses, correlating with the highest recorded erosion rates in this study. In Region 5, urban expansion and port development disrupted sediment transport, contributing to shoreline retreat exceeding 3 m per year. Other regions, such as Region 1 and Region 6, showed minor erosion rates, indicating localized impacts of tidal forces on sediment transport. In contrast, Region 2 experienced notable accretion (10.09 m/year), primarily influenced by sediment deposition near estuarine zones, which facilitated sediment retention. The 1994–2000 period continued to experience significant erosion, though at slightly reduced rates. Region 4 remained the most eroded (-12.50 m/years), while Region 5 increased (-6.68 m/years). However, Region 3, was previously stable, possibly due to sediment redistribution during this period (-5.22 m/years). Region 2 maintained high accretion (8.89 m/years), reinforcing the role of sediment-laden rivers in stabilizing certain sections of the coastline. This period reflects localized variability, where erosion rates persisted in exposed regions, while accretion occurred in sediment-rich estuarine zones. From 2000 to 2006, the rate of erosion declined compared to previous periods, although Region 4 remained highly vulnerable (-10.35 m/year), followed by Region 5 (-6.77 m/year). This decline may be attributed to the early implementation of coastal protection structures, including rock revetments and soft barriers. The expansion of mangrove forests helped buffer certain regions against wave energy. Notably, Region 2 showed a reduced accretion rate (2.94 m/year), indicating a possible shift in sediment dynamics or rising sea levels that hindered deposition. During the 2006–2011 period, erosion rates continued to decline in most regions, suggesting a stabilizing effect of coastal management efforts (coastal protection structures (e.g., bamboo fences and rock revetments)) and natural processes (the expansion of mangrove forests). Region 5 recorded the highest erosion rate, with shoreline retreat reaching -5.18 m/year, primarily due to the collapse of fish farming embankments and insufficient protection. In

Region 4, erosion persisted at an average rate of −4.55 m/year, exacerbated by ongoing mangrove loss and sediment depletion. In contrast, Region 1 saw an accretion rate increase of 2.81 m/year. Meanwhile, minor accretion was recorded in Region 2 (2.41 m/year), reinforcing the role of sediment deposition near estuarine zones. The results indicate localized erosion persistence in vulnerable areas while regions with natural sediment dynamics, like mangrove zones, showed slight recovery. Between 2011 and 2018, erosion rates declined further, with some regions experiencing stabilization and minor accretion. Region 4 had erosion rates reduced (−3.88 m/year), while Region 6 showed localized erosion (−2.05 m/year). Region 5 saw minor accretion during this period (0.10 m/year), suggesting the effectiveness of soft coastal protection measures such as bamboo fences in trapping sediments. This period reflects a transition toward shoreline stabilization due to improved management practices, despite ongoing challenges posed by rising sea levels and wave action. The 2018–2023 period demonstrates a mixed trend of erosion and accretion, with regional variability. Region 2, which previously exhibited high accretion, shifted to erosion (−0.54 m/year), indicating changing sediment transport dynamics and increased exposure to tidal forces. In contrast, Region 5 experienced notable accretion (3.30 m/year), likely due to the successful implementation of coastal protection structures and sediment redistribution. Other regions, such as Region 4 and Region 6, exhibited minimal erosion (−0.40 m/year), signaling the effects of stabilization measures and natural geological resistance in these areas. This period highlights the dynamic interplay of natural processes, human activities, and coastal management interventions, where localized erosion persists in some regions while others benefit from sediment stabilization and protection structures.

Global warming has significantly influenced global temperatures and sea levels, both of which strongly correlate with shoreline erosion in the Upper Gulf of Thailand. While climate change is a key driver, regional factors such as sediment supply, tidal forces, and storm surges also shape shoreline dynamics. Our findings highlight that rising sea levels contribute to long-term coastal retreat, with a strong correlation between mean sea level and erosion. However, localized climatic events, such as monsoonal currents and extreme storms, lead to episodic fluctuations in erosion rates, highlighting the need for further studies focusing on short-term coastal changes and their immediate impacts on shoreline dynamics. This region's coastal processes reflect a complex interplay between natural forces and anthropogenic influences. Key factors, including topography, geology, land use, seasonal currents, coastal structures, and human activities, collectively drive the observed shoreline changes. These interconnected elements govern erosion and accretion patterns and underscore the region's heightened vulnerability to rising sea levels, intensified wave energy, and human-induced modifications. Sea-level rise accelerates shoreline retreat, especially in low-lying coastal areas, where even small increases exacerbate erosion and permanent land loss. The western part of the Upper Gulf of Thailand slopes gently from west to east, creating long beaches and mangrove forests near river estuaries. These long beaches remain relatively stable with minimal erosion, primarily due to natural sediment dynamics. Meanwhile, the mangrove forests in this region have experienced moderate sediment accumulation, influenced by the sloping topography and natural sediment deposition. Over time, however, the rate of accumulation has steadily declined, particularly between 2011 and 2023. Erosion is driven by seawater intrusion and stronger wave action, which disrupts mudflats, alters sediment transport, and degrades mangrove ecosystems. Rising sea levels further reduce sediment retention in mangroves, diminishing their natural defense against coastal erosion. The northern region consists of a flat alluvial plain, formed by sediment deposits from four major rivers: the Mae Klong, Tha Chin, Chao Phraya, and Bang Pakong rivers. The geology in this area is dominated by mud and sand, supporting the growth of extensive mangrove forests that serve as natu-

ral buffers against erosion. However, these mangroves have been increasingly degraded due to human encroachment, urban expansion, and the conversion of coastal zones for aquaculture and agriculture, which has weakened the region's natural resilience to erosion. The eastern region of the Upper Gulf exhibits a diverse landscape. The northern part comprises mudflats and mangrove forests that stabilize the coastline, while the central region features sandy beaches, deep-sea ports, urban centers, and tourist attractions. This central area supports substantial industrial and commercial activities that disrupt sediment dynamics and contribute to localized erosion. In contrast, the southern part transitions into rocky beaches and cliffs, which are more resistant to erosion compared to the sandy and muddy coastal areas further north. Seasonal currents play a critical role in shaping the sediment dynamics and erosion processes in the Upper Gulf of Thailand. Furthermore, during the southwest monsoon (May to October), this region is temporarily affected by extreme weather events. It contributes to storm surges and currents redistribute sediments, intensify wave energy, and accelerate erosion, especially in vulnerable coastal areas with weak defenses. It also generates stronger south-to-north currents, which intensify erosion by redistributing sediments away from vulnerable coastal areas. Regions with low-lying topography and limited protective structures are particularly affected during this period. The Upper Gulf of Thailand's coastal dynamics is shaped by a complex interaction of natural and human-induced factors, including topographical variation, sediment availability, seasonal monsoons, and anthropogenic influences such as urbanization, mangrove deforestation, and coastal infrastructure development. The region demonstrates a dynamic and often unstable coastline, with variations in erosion and sediment deposition that require region-specific management strategies.

While this study demonstrates the application of ML to coastal change, it acknowledges the need for further exploration into the cause-and-effect relationships between different drivers and the complex interactions among them. Future research should aim to deepen the understanding of these processes by integrating multiple data sources, advanced models, local environmental factors, short-term temporal variations, such as seasonal impacts, to enhance the understanding of coastal dynamics. This approach will help improve the predictive power of shoreline change models and support more effective coastal management in the face of climate change and sea-level rise.

6. Conclusions

This study analyzed shoreline changes in the Upper Gulf of Thailand over a 35-year period (1988–2023) using remote sensing, ML techniques, and the DSAS. The results highlight the dynamic and complex patterns of erosion and accretion influenced by both natural processes and human activities. For the coastal area classification, the RF algorithm achieved the highest accuracy and Cohen's Kappa Coefficient among the four tested ML methods, demonstrating its robustness for classifying land and water areas. Spectral indices such as NDWI, MNDWI, NDVI, and SAVI were critical in enhancing feature extraction, enabling the accurate delineation of shorelines and coastal land cover. The seven periods of annual shoreline extraction and accuracy revealed consistent and reliable results, validated through overlay assessments and RMSE calculations. The shorelines extracted for 2018 and 2023 achieved high accuracy, with small RMSE values, indicating suitability for long-term shoreline monitoring using Landsat imagery. The DSAS results showed significant temporal and spatial variability in shoreline erosion and accretion across six periods. Severe erosion occurred between 1988–1994 and 1994–2000, particularly in Region 4 (Tha Chin River–Chao Phraya River) and Region 5 (Chao Phraya River–Bang Pakong River), where erosion rates exceeded 10 m per year. In contrast, Region 2 (Laem Phak Bia–Mae Klong River) exhibited consistent accretion, largely driven by sediment deposition in estuarine environments and

mangrove expansion. However, erosion rates stabilized in recent decades, coinciding with the implementation of coastal protection measures, including soft and hard structures. The analysis reveals that coastal changes are driven by a combination of natural factors (tidal forces, seasonal monsoons, rising sea levels, and extreme weather events exacerbate erosion in low-lying areas with fine sediments) and anthropogenic factors (land use changes, the conversion of mangrove forests to aquaculture and salt farming, and urban development have weakened natural coastal defenses). Given the strong correlation between rising sea levels, temperatures, and shoreline erosion, proactive measures are needed to enhance the resilience of vulnerable coastal regions in the Upper Gulf of Thailand. Future studies should focus on integrating higher-resolution imagery and advanced deep-learning techniques to further improve shoreline extraction and change analysis. Incorporating hydrodynamic and sediment transport models could enhance the understanding of coastal processes. Additionally, considering the impacts of sea-level rise and storm surges would provide a more comprehensive perspective on short-term coastal evolution. Integrating more regional studies on these factors can further improve predictive shoreline change models, supporting more effective coastal management strategies in response to climate change.

Author Contributions: Conceptualization: Chakrit Chawalit, Wuttichai Boonpook, Asamaporn Sitthi, Kritanai Torsri, Daroonwan Kamthonkiat and Yumin Tan; methodology: Chakrit Chawalit, Wuttichai Boonpook, Asamaporn Sitthi, Kritanai Torsri and Apised Suwansaard; software: Chakrit Chawalit and Attawut Nardkulpat; validation: Chakrit Chawalit, Kritanai Torsri and Wuttichai Boonpook; formal analysis: Chakrit Chawalit and Wuttichai Boonpook; investigation: Chakrit Chawalit and Wuttichai Boonpook; resources: Chakrit Chawalit and Apised Suwansaard; data curation: Chakrit Chawalit and Attawut Nardkulpat; writing—original draft preparation: Chakrit Chawalit and Wuttichai Boonpook; writing—review and editing: Chakrit Chawalit, Wuttichai Boonpook, Asamaporn Sitthi, Daroonwan Kamthonkiat and Yumin Tan; visualization: Chakrit Chawalit and Wuttichai Boonpook; supervision: Wuttichai Boonpook and Asamaporn Sitthi; project administration: Chakrit Chawalit and Wuttichai Boonpook; funding acquisition: Wuttichai Boonpook and Apised Suwansaard. All authors have read and agreed to the published version of the manuscript.

Funding: This research was funded by the Faculty of Social Sciences, Srinakharinwirot University (No. 313/2566).

Data Availability Statement: The data presented in this study are available on request from the corresponding author. The data are not publicly available due to the permission of the data sharing policy.

Acknowledgments: All authors would like to thank the Faculty of Social Science and the Graduate School of Srinakharinwirot University for their research funding and facilities. We also extend our gratitude to the Hydrographic Department of the Royal Thai Navy, the Land Development Department, the Department of Marine and Coastal Resources, the Marine Department, the Meteorological Department, and the Department of Mineral Resources in Thailand, as well as the United States Geological Survey (USGS) and the National Aeronautics and Space Administration (NASA) in the USA for providing the spatial data used in the analysis process. We sincerely thank the reviewers and editors for their beneficial, careful, and detailed comments and suggestions that helped improve the paper.

Conflicts of Interest: The authors declare no conflicts of interest.

References

1. Li, K.; Zhang, L.; Chen, B.; Zuo, J.; Yang, F.; Li, L. Analysis of China's coastline changes during 1990–2020. *Remote Sens.* **2023**, *15*, 981. [CrossRef]
2. WMO. *State of the Global Climate 2022*; UN: New York, NY, USA, 2023.
3. Department of Marine and Coastal Resources. *Annual Report on the State of Marine and Coastal Resources and Coastal Erosion in Thailand, 2022*, 1st ed.; Do Connection Company Limited: Bangkok, Thailand, 2024.

4. Ritphring, S.; Nidhinarangkoon, P. The comparative study of shoreline detection methods. In Proceedings of the 24th National Convention on Civil Engineering, Udonthani, Thailand, 10–12 July 2019.
5. Bird, C.O.; Bell, P.S.; Plater, A.J. Application of marine radar to monitoring seasonal and event-based changes in intertidal morphology. *Geomorphology* **2017**, *285*, 1–15. [CrossRef]
6. Sesli, F.A. Mapping and monitoring temporal changes for coastline and coastal area by using aerial data images and digital photogrammetry: A case study from Samsun, Turkey. *Int. J. Phys. Sci.* **2010**, *5*, 1567–1575.
7. Gonçalves, J.A.; Bastos, L.; Pinho, J.; Granja, H. Digital aerial photography to monitor changes in coastal areas based on direct georeferencing. In Proceedings of the 5th EARSeL Workshop on Remote Sensing of the Coastal Zone, Prague, Czech Republic, 1–3 June 2011; pp. 1–3.
8. Novais, J.; Vieira, A.; Bento-Gonçalves, A.; Silva, S.; Folharini, S.; Marques, T. The Use of UAVs for Morphological Coastal Change Monitoring—A Bibliometric Analysis. *Drones* **2023**, *7*, 629. [CrossRef]
9. Ahmed, T.; Creedon, L.; Gharbia, S.S. Low-Cost Sensors for Monitoring Coastal Climate Hazards: A Systematic Review and Meta-Analysis. *Sensors* **2023**, *23*, 1717. [CrossRef]
10. Geo-Informatics and Space Technology Development Agency Public Organization. *Textbook on Space Technology and Geo-Informatics*, 1st ed.; Amarin Printing and Publishing Public Company Limited: Bangkok, Thailand, 2009.
11. Zheng, H.; Li, X.; Wan, J.; Xu, M.; Liu, S.; Yasir, M. Automatic coastline extraction based on the improved instantaneous waterline extraction method and correction criteria using SAR imagery. *Sustainability* **2023**, *15*, 7199. [CrossRef]
12. Xu, N. Detecting coastline change with all available landsat data over 1986–2015: A case study for the state of Texas, USA. *Atmosphere* **2018**, *9*, 107. [CrossRef]
13. Kamthonkiat, D.; Koshimura, S.; Matsuoka, M. Time series analysis of shoreline positions in the pre-and post-2004 Indian Ocean Tsunami in Phang Nga Province, Thailand. *J. Earth Sci. Eng.* **2012**, *2*, 35–41.
14. Thiangtrong, A. Remote Sensing Applications for Change Detection in Coastal Region, Ban Laemsing Samut Parkarn Province. Master's Thesis, Chulalongkorn University, Bangkok, Thailand, 2006.
15. Supawat Inkerd, N.O.; Kwanthong, N.; Klompong, N.; Khankajorn, T. Remote Sensing Applications for Change Detection in The Andaman Sea Coastal Region, Sikao District, Trang Province. *Wichcha J. Nakhon Si Thammarat Rajabhat Univ.* **2018**, *37*, 84–98.
16. Kim, M.K.; Sohn, H.G.; Kim, S.P.; Jang, H.S. Automatic coastline extraction and change detection monitoring using Landsat imagery. *J. Korean Soc. Geospat. Inf. Sci.* **2013**, *21*, 45–53.
17. Ghosh, M.K.; Kumar, L.; Roy, C. Monitoring the coastline change of Hatiya Island in Bangladesh using remote sensing techniques. *ISPRS J. Photogramm. Remote Sens.* **2015**, *101*, 137–144. [CrossRef]
18. Maglione, P.; Parente, C.; Vallario, A. Coastline extraction using high resolution WorldView-2 satellite imagery. *Eur. J. Remote Sens.* **2014**, *47*, 685–699. [CrossRef]
19. Vitousek, S.; Buscombe, D.; Vos, K.; Barnard, P.L.; Ritchie, A.C.; Warrick, J.A. The future of coastal monitoring through satellite remote sensing. *Camb. Prism. Coast. Futures* **2023**, *1*, e10. [CrossRef]
20. Fatah, K.K.; Mustafa, Y.T.; Hassan, I.O. Groundwater potential mapping in arid and semi-arid regions of kurdistan region of Iraq: A geoinformatics-based machine learning approach. *Groundw. Sustain. Dev.* **2024**, *27*, 101337. [CrossRef]
21. Rash, A.; Mustafa, Y.; Hamad, R. Quantitative assessment of Land use/land cover changes in a developing region using machine learning algorithms: A case study in the Kurdistan Region, Iraq. *Heliyon* **2023**, *9*, e21253. [CrossRef]
22. Sun, W.; Chen, C.; Liu, W.; Yang, G.; Meng, X.; Wang, L.; Ren, K. Coastline extraction using remote sensing: A review. *GIScience Remote Sens.* **2023**, *60*, 2243671. [CrossRef]
23. Kannan, R.; Kanungo, A.; Murthy, M. Detection of shoreline changes Visakhapatnam coast, Andhra Pradesh from multi-temporal satellite images. *J. Remote Sens. GIS* **2016**, *5*, 157.
24. Choung, Y.-J.; Jo, M.-H. Comparison between a Machine-Learning-Based Method and a Water-Index-Based Method for Shoreline Mapping Using a High-Resolution Satellite Image Acquired in Hwado Island, South Korea. *J. Sens.* **2017**, *2017*, 8245204. [CrossRef]
25. Minghelli, A.; Spagnoli, J.; Lei, M.; Chami, M.; Charmasson, S. Shoreline extraction from WorldView2 satellite data in the presence of foam pixels using multispectral classification method. *Remote Sens.* **2020**, *12*, 2664. [CrossRef]
26. Bamdadinejad, M.; Ketabdari, M.J.; Chavooshi, S.M.H. Shoreline extraction using image processing of satellite imageries. *J. Indian Soc. Remote Sens.* **2021**, *49*, 2365–2375. [CrossRef]
27. Zhou, X.; Wang, J.; Zheng, F.; Wang, H.; Yang, H. An Overview of Coastline Extraction from Remote Sensing Data. *Remote Sens.* **2023**, *15*, 4865. [CrossRef]
28. Vos, K.; Splinter, K.D.; Harley, M.D.; Simmons, J.A.; Turner, I.L. CoastSat: A Google Earth Engine-enabled Python toolkit to extract shorelines from publicly available satellite imagery. *Environ. Model. Softw.* **2019**, *122*, 104528. [CrossRef]
29. Curoy, J.; Ward, R.D.; Barlow, J.; Moses, C.; Nakhapakorn, K. Coastal dynamism in Southern Thailand: An application of the CoastSat toolkit. *PLoS ONE* **2022**, *17*, e0272977. [CrossRef] [PubMed]
30. Hossen, M.F.; Sultana, N. Shoreline change detection using DSAS technique: Case of Saint Martin Island, Bangladesh. *Remote Sens. Appl. Soc. Environ.* **2023**, *30*, 100943. [CrossRef]

31. Nassar, K.; Mahmod, W.E.; Fath, H.; Masria, A.; Nadaoka, K.; Negm, A. Shoreline change detection using DSAS technique: Case of North Sinai coast, Egypt. *Mar. Georesour. Geotechnol.* **2019**, *37*, 81–95. [CrossRef]
32. Goksel, C.; Senel, G.; Dogru, A.O. Determination of shoreline change along the Black Sea coast of Istanbul using remote sensing and GIS technology. *Desalination Water Treat.* **2020**, *177*, 242–247. [CrossRef]
33. Wang, X.; Liu, Y.; Ling, F.; Liu, Y.; Fang, F. Spatio-temporal change detection of Ningbo coastline using Landsat time-series images during 1976–2015. *ISPRS Int. J. Geo-Inf.* **2017**, *6*, 68. [CrossRef]
34. Darwish, K.; Smith, S. A comparison of landsat-8 oli, sentinel-2 msi and planetscope satellite imagery for assessing coastline change in el-alamein, egypt. *Eng. Proc.* **2021**, *10*, 23. [CrossRef]
35. Rumahorbo, B.T.; Warpur, M.; Hamuna, B. Detection of Shoreline Changes due to Abrasion and Accretion Using Landsat Imagery–A Case Study in the Coastal Areas of Supiori Regency, Indonesia. *Ecol. Eng. Environ. Technol.* **2023**, *24*, 161–171. [CrossRef]
36. Chettiyam Thodi, M.F.; Gopinath, G.; Surendran, U.P.; Prem, P.; Al-Ansari, N.; Mattar, M.A. Using RS and GIS Techniques to Assess and Monitor Coastal Changes of Coastal Islands in the Marine Environment of a Humid Tropical Region. *Water* **2023**, *15*, 3819. [CrossRef]
37. Quang, D.N.; Ngan, V.H.; Tam, H.S.; Viet, N.T.; Tinh, N.X.; Tanaka, H. Long-term shoreline evolution using dsas technique: A case study of Quang Nam province, Vietnam. *J. Mar. Sci. Eng.* **2021**, *9*, 1124. [CrossRef]
38. Oraon Sarajit, K.N. Geo-information Application for Coastal Erosion Situation, Phetchaburi Province. *Thai Sci. Technol. J.* **2014**, *6*, 789–800.
39. Wuttipong Sangmanee, C.T. Integration remote sensing data for monitoring shoreline changesin Pattani province. *J. Humanit. Soc. Sci. Prince Songkla Univ.* **2017**, *13*, 69–102.
40. Aekkarak Faiboon, W.S. Geospatial Monitoring and Forecasts of Coastal Engineering Structures' Shoreline Transformational Impact at Songkhla Lake Mouth. *Princess Naradhiwas Univ. J.* **2019**, *11*, 165–179. Available online: https://li01.tci-thaijo.org/index.php/pnujr/article/view/160033 (accessed on 14 February 2025).
41. Khongkhan, A. Incorporating the Use of Time Series Remote Sensing Data to Assess the Vulnerability of the Thai Coast to Climate Change Induced Coastal Hazards. *J. Sci. Technol.* **2021**, *4*, 1–18.
42. Pawornprach Imlamai, S.W.; Phaksopa, J. Monitoring Study of Coastal Morphological Change from Coastal Engineering Structures at Mrigadayavan Palace, Phetchaburi Province Using Geo-Informatics. *Burapha Sci. J.* **2023**, *28*, 730–751.
43. Buranapratheprat, A. Circulation in the Upper Gulf of Thailand: A Review. *Burapha Sci. J.* **2024**, *13*, 75–83.
44. Lorpittayakorn, P. Circulation Patterns in the Gulf of Thailand from Model. *Thai Sci. Technol. J.* **2015**, *23*, 446–465.
45. Kim, Y.I.; Park, W.H.; Shin, Y.; Park, J.-W.; Engel, B.; Yun, Y.J.; Jang, W.S. Applications of Machine Learning and Remote Sensing in Soil and Water Conservation. *Hydrology* **2024**, *11*, 183. [CrossRef]
46. Agarwal, V.; Akyilmaz, O.; Shum, C.; Feng, W.; Yang, T.-Y.; Forootan, E.; Syed, T.H.; Haritashya, U.K.; Uz, M. Machine learning based downscaling of GRACE-estimated groundwater in Central Valley, California. *Sci. Total Environ.* **2023**, *865*, 161138. [CrossRef] [PubMed]

Disclaimer/Publisher's Note: The statements, opinions and data contained in all publications are solely those of the individual author(s) and contributor(s) and not of MDPI and/or the editor(s). MDPI and/or the editor(s) disclaim responsibility for any injury to people or property resulting from any ideas, methods, instructions or products referred to in the content.

MDPI AG
Grosspeteranlage 5
4052 Basel
Switzerland
Tel.: +41 61 683 77 34

MDPI Books Editorial Office
E-mail: books@mdpi.com
www.mdpi.com/books

Disclaimer/Publisher's Note: The title and front matter of this reprint are at the discretion of the Topic Editors. The publisher is not responsible for their content or any associated concerns. The statements, opinions and data contained in all individual articles are solely those of the individual Editors and contributors and not of MDPI. MDPI disclaims responsibility for any injury to people or property resulting from any ideas, methods, instructions or products referred to in the content.

Academic Open
Access Publishing

mdpi.com

ISBN 978-3-7258-5822-4